2013 Project Review

Consortium Project on Seismic Inverse Methods for Complex Structures

CWP Faculty

Jyoti Behura
Norman Bleistein (Prof. Emeritus)
Dave Hale (CWP Director)
Ken Larner (Prof. Emeritus)
Paul Sava
Roel Snieder
Ilya Tsvankin

CWP Students

Farhad Bazargani
Filippo Broggini
Pengfei Cai
Stefan Compton
Esteban Díaz Pantin
Johannes Douma
Yuting Duan
Ashley Fish
Clément Fleury
Detchai Ittharat
Oscar Jarillo Michel
Jason Jennings
Nishant Kamath
Chinaemerem Kanu
Allison Knaak
Myoung Jae Kwon
Vladimir Li
Simon Luo
Yong Ma
Andrew Muñoz
Nori Nakata
Conrad Newton
Natalya Patrikeeva
Francesco Perrone
Bharath Shekar
Satyan Singh
Steven Smith
Xiaoxiang Wang
Xinming Wu
Tongning Yang

Long-Term Visitors

Michael Behm, University of Vienna
Pablo García López, Oviedo School of Mines
Ernst Niederleithinger, Federal Institute for Materials Research and Testing (BAM), Berlin
Joost van der Neut, Delft University of Technology

CWP Staff/Administration

Shingo Sean Ishida, Communications
Pamela Kraus, Program Assistant
John Stockwell, Research Associate
Diane Witters, Writing Consultant

Consortium Project on Seismic Inverse Methods for Complex Structures
2013 Annual Meeting
Golden, Colorado, May 13-16, 2013

Center for Wave Phenomena
Colorado School of Mines
924 16th Street, Golden, Colorado 80401
+1.303.384.2178 cwpcsm@dix.mines.edu

www.cwp.mines.edu

Contents

3) Anisotropic velocity and attenuation analysis

---

4) Time-lapse seismic

---

5) Image processing

---

6) Wavefield focusing

6) Wavefield focusing (continued)

---

7) Seismic interferometry

Acknowledgments

This Project Review book is prepared for the sponsors of the Consortium Project on Seismic Inverse Methods for Complex Structures ("Consortium") at the Center for Wave Phenomena. The Consortium provides substantial funding for the overall research and educational program at CWP.

We are extremely grateful for the support of our Consortium sponsors (in alphabetical order):

Aramco Services Co.
BGP Inc.
BHP Billiton Petroleum (Americas) Inc.
BP America Production Co.
CGG
Chevron Energy Technology Co.
China Petrochemical Technology Co.
Cimarex Energy
ConocoPhillips
Devon Energy Corp.
Eni S.p.A.
ExxonMobil Upstream Research Co.
Geokinetics
Hess Corp.
Instituto Mexicano del Petróleo
ION Geophysical Corp.
Japan Oil, Gas and Metals National Corp.
Landmark/Halliburton
Marathon Oil
Nexen Petroleum USA Inc.
Paradigm Geophysical Corp.
PDVSA Intevep
Petrobras America Inc.
Repsol Services Co.
Shell International Exploration and Production
Statoil
Talisman Energy Inc.
TGS-Nopec Geophysical Co.
Total E&P Recherche Développement
Transform Software and Services
WesternGeco

CWP also received additional financial support, research grants, fellowships and scholarships during this project year from the following agencies and organizations (in alphabetical order):

BP America
ConocoPhillips
Eni
ExxonMobil
King Abdulaziz City for Science and Technology (KACST)
National Space and Aeronautics Administration
The Petroleum Institute, Abu Dhabi
Shell
Unconventional Natural Gas Institute (UNGI) at CSM
U.S. Department of Energy

CWP policy on proprietary material

New reports and printed material produced at the Center for Wave Phenomena with Consortium support is presented to Sponsors before it is released to the general public. We delay general publication by at least 60 days.

During this delay period, Sponsors may use the material within their organizations as they wish. We ask that all Sponsors respect the rights of other Sponsors and of CWP by not publishing these results externally and independently, in advance of this 60-day delay period. For additional information, please refer to your Consortium Membership Agreement, the paragraph entitled "Sponsor Confidentiality Obligation."

3D image-domain wavefield tomography using time-lag extended images

Tongning Yang and Paul Sava
Center for Wave Phenomena, Colorado School of Mines

ABSTRACT

Image-domain wavefield tomography is a technique that reconstructs the velocity model by extracting information from migrated images. In time-lag extended images, velocity model accuracy can be evaluated by reflection focusing error, which represents the traveltime residual in the image domain. The model is updated by minimizing an objective function similar to the one used by wave-equation traveltime inversion. Unlike wave-equation traveltime inversion wherein traveltime residual is obtained from crosscorrelation of a single-shot data, the focusing error is extracted from time-lag gathers, which are wavefield crosscorrelations based on multiple experiments. Because the signal-to-noise ratio is higher in common-image gathers than that in common-shot gathers, our technique is able to measure focusing error more accurately in presence of noisy data and complex geologic structures. In addition, the image-domain approach is robust as it does not suffer from cycle-skipping, which is common in conventional data-domain full-waveform inversion. We also use the focusing error to precondition the gradient of the objective function in order to improve the convergence of the inversion. This is done by constructing a gradient mask which restricts the model updates to areas where the accumulated focusing error exceeds a certain threshold. This preconditioning of the gradient limits the model update to areas containing the velocity model errors. We illustrate the method using both synthetic and field data. The North Sea 3D field data example demonstrates that the technique is effective in optimizing the velocity model and improving image quality. In addition, the method is efficient in 3D because only the time-lag extensions are computed and stored, in contrast to differential semblance optimization which requires costlier inline and crossline space-lag extensions.

Key words: wavefield tomography, 3D, extended images, adjoint-state method, focusing error

1 INTRODUCTION

In seismic imaging, building an accurate and reliable velocity model remains one of the biggest challenges. The need for high-quality velocity models is driven by the wide-spread use of advanced imaging techniques such as one-way wave-equation migration (WEM) and reverse-time migration (RTM) (Etgen et al., 2009).

In the past decade, velocity model-building methods using full seismic wavefields (Tarantola, 1984; Pratt, 1999; Vigh and Starr, 2008; Symes, 2009) have become popular mainly because of their accuracy and because the availability of increased computational power. One can divide the family of such velocity-estimation techniques into data-domain methods (Sirgue and Pratt, 2004; Plessix, 2009) and image-domain methods (Sava and Biondi, 2004; Shen and Symes, 2008; Yang and Sava, 2011). Data-domain methods adjust the velocity model by minimizing the difference between simulated and recorded data (Tarantola, 1984; Pratt, 1999). This formulation is based on the strong assumption that the wave equation used for data simulation is consistent with the physics of the earth, which is often violated in practice. In addition, the methods also require low-frequency data and sufficiently accurate initial model to avoid the cycle-skipping problem.

Unlike the data-domain approaches, image-domain methods update the velocity model by optimizing the image quality. As stated by the semblance principle (Al-Yahya, 1989;

Yilmaz, 2001), the image obtained by multiple and redundant seismic experiments is optimized when the correct velocity model is used to migrate the data. The common practice is to optimize image coherency in common-image gathers by iteratively updating the velocity model. In complex geology, image-domain wavefield tomography is capable of handling complicated wave propagation because it uses a wave-equation engine to simulate the wavefields. Furthermore, the band-limited wavefields used in the velocity model building are consistent with the wave-equation migration algorithms used in imaging.

The cycle-skipping problem in conventional data-domain full-waveform inversion is mainly caused by its objective function, which is the L-2 norm of the difference between the observed and simulated data. Cycle-skipping occurs when the initial model is not accurate enough or the data do not have sufficiently low frequency components. To overcome this problem, wave-equation traveltime inversion was proposed to reconstruct the velocity model in complex geologic environments (Luo and Schuster, 1991; Zhang and Wang, 2009; van Leeuwen and Mulder, 2010). The essential idea behind this method is to invert the velocity model using only the traveltime information rather than full waveforms. In this way, the nonlinearity of the objective function with respect to the model is significantly reduced, and the objective function is less sensitive to data noise and the accuracy of the initial model. For wave-equation traveltime inversion, the traveltime residual is obtained from the cross-correlation between the recorded and simulated data, and then spread along the wavepath computed by solving the wave equation in the background model. Nonetheless, these techniques aim to invert for a velocity model using transmission waves, and not reflected waves. As a result, they are limited to cross-well experiments or to surface experiments with diving waves.

Velocity model updates using traveltime residuals are also performed in the image domain, by techniques known as *focusing analysis* (Faye and Jeannot, 1986). The traveltime residual is defined as *focusing error*, since it uses the focusing of reflections as a measure for the coherence of migrated images. Such information indicates the accuracy of the velocity model and thus can be used for model building. For wave-equation migration, one can extract focusing information from time-lag extended images (Sava and Fomel, 2006); focusing is quantified as the reflection focus shift along the time-lag axis. Wang et al. (2005) propose a velocity analysis method using time focusing applied to re-datumed data sets. Their approach is ray-based and thus may become unstable when the complex geology results in multi-pathing. Higginbotham and Brown (2008) and Brown et al. (2008) also propose a model-building method that converts the focusing error into velocity updates using an analytic formula. However, the formula is derived under the 1D assumption, the focusing error is transformed into vertical updates only, and therefore the accuracy of the method is degraded in areas with strong lateral velocity variations. Wang et al. (2008, 2009) illustrate that focusing analysis can be used as an image-enhancement tool to improve the image quality and to update subsalt velocity models. Yang and Sava (2010a) analyze the relationship between the focusing error and velocity model accuracy, and develop a wave-equation migration velocity analysis based on this relationship (Yang and Sava, 2010b).

Here, we propose a methodology for 3D image-domain tomography using the focusing information of migrated images. The essential idea is to extract focusing error from time-lag extended images and then convert it into velocity updates by a procedure similar to wave-equation traveltime inversion (Luo and Schuster, 1991). In addition, we use focusing error to constrain the updates only in target areas where velocity error exists and to speed up the convergence of the inversion. We begin by defining an objective function based on measured image focusing. We discuss its gradient computation and illustrate how the focusing error can be used to construct a mask for preconditioning the gradient. Then we use a simple synthetic model to illustrate the workflow of the method and present an application of the method to a North Sea 3D OBC field dataset. The improved image quality and flatter events in angle-domain common-image gathers demonstrate that the method is a robust and effective 3D velocity model-building tool. Finally, we compare and contrast our approach to other wave-equation-based velocity model building methods.

2 THEORY

The objective function for our wavefield tomography approach is

$$J = \frac{1}{2}\|\Delta\tau\|^2 \,. \tag{1}$$

Here $\Delta\tau$ stands for the focusing error, which is the time lag of reflection focus away from zero measured in extended images. Time-lag extended images are the crosscorrelation between extrapolated wavefields (u_s and u_r)

$$R(\mathbf{x},\tau) = \sum_j \sum_\omega \overline{u_s(j,\mathbf{x},\omega)} u_r(j,\mathbf{x},\omega)\, e^{-2i\omega\tau} \,, \tag{2}$$

where j is the shot index, ω is the angular frequency, and $\mathbf{x}$ are the space coordinates $\{x,y,z\}$. The source and receiver wavefields u_s and u_r satisfy

$$\begin{bmatrix} \mathcal{L}(\mathbf{x},\omega,m) & 0 \\ 0 & \mathcal{L}^*(\mathbf{x},\omega,m) \end{bmatrix} \begin{bmatrix} u_s(j,\mathbf{x},\omega) \\ u_r(j,\mathbf{x},\omega) \end{bmatrix} = \begin{bmatrix} f_s(j,\mathbf{x},\omega) \\ f_r(j,\mathbf{x},\omega) \end{bmatrix} , \tag{3}$$

where $\mathcal{L}$ and $\mathcal{L}^*$ are forward and adjoint frequency-domain wave operators, and f_s and f_r are the source and receiver data. The wave operator $\mathcal{L}$ and its adjoint $\mathcal{L}^*$ propagate the wavefields forward and backward in time, respectively, using a two-way wave equation, i.e., $\mathcal{L} = -\omega^2 m - \Delta$, where m represent slowness squared and Δ is the Laplacian operator.

The objective function in equation 1 is the same as that defined in wave-equation traveltime inversion (Luo and Schuster, 1991; Zhang and Wang, 2009). However, the physical meanings of $\Delta\tau$ in the objective functions differ. In our approach, $\Delta\tau$ is the focusing error measured from the stack over shots of image obtained by wavefield crosscorrelation. In contrast, $\Delta\tau$ in wave-equation traveltime inversion is the travel-

time misfit measured between observed and simulated data at the known receiver locations for a single shot.

We compute the gradient of our objective function using the adjoint-state method (Plessix, 2006). The first step is to construct state variables u_s and u_r, which relate the objective function to the model parameters (equation 3). The next step is to construct the adjoint sources, which are used to obtain adjoint-state variables. The adjoint sources are the derivative of the objective function with respect to the state variables. In our case, as $\Delta\tau$ is not directly dependent on the wavefields, we use the *connective function* similar to the one developed by Luo and Schuster (1991). Since the focusing error represents the time lag when the reflection events focus, we have

$$R(\mathbf{x},\Delta\tau) = max\{R(\mathbf{x},\tau)\,|\tau\in[-T,T]\}\,. \tag{4}$$

As a result, the connective function can be written as

$$\dot{R}_{\Delta\tau} = \left.\frac{\partial R}{\partial\tau}\right|_{\Delta\tau} \tag{5}$$

$$= \sum_j\sum_\omega (-2i\omega)\,\overline{u_s(j,\mathbf{x},\omega)}u_r(j,\mathbf{x},\omega)\,e^{-2i\omega\Delta\tau}\,. \tag{6}$$

The adjoint sources are then obtained as

$$g_s(j,\mathbf{x},\omega) = \frac{\partial J}{\partial(u_s)} = \Delta\tau\frac{\partial(\Delta\tau)}{\partial(u_s)} = \Delta\tau\frac{\frac{\partial(\dot{R}_{\Delta\tau})}{\partial(u_s)}}{\frac{\partial(\dot{R}_{\Delta\tau})}{\partial(\Delta\tau)}} \tag{7}$$

$$= \frac{\Delta\tau}{E}(2i\omega)\,\overline{u_r(j,\mathbf{x},\omega)}e^{2i\omega\Delta\tau} \tag{8}$$

and

$$g_r(j,\mathbf{x},\omega) = \frac{\partial J}{\partial(u_r)} = \Delta\tau\frac{\partial(\Delta\tau)}{\partial(u_r)} = \Delta\tau\frac{\frac{\partial(\dot{R}_{\Delta\tau})}{\partial(u_r)}}{\frac{\partial(\dot{R}_{\Delta\tau})}{\partial(\Delta\tau)}} \tag{9}$$

$$= \frac{\Delta\tau}{E}(-2i\omega)\,u_s(j,\mathbf{x},\omega)\,e^{-2i\omega\Delta\tau}\,, \tag{10}$$

where

$$E = \sum_j\sum_\omega 4\omega^2\overline{u_s(j,\mathbf{x},\omega)}u_r(j,\mathbf{x},\omega)\,e^{-2i\omega\Delta\tau}\,. \tag{11}$$

The adjoint-state variables are constructed similarly to state variables as follows:

$$\begin{bmatrix}\mathcal{L}^*(\mathbf{x},\omega,m) & 0\\ 0 & \mathcal{L}(\mathbf{x},\omega,m)\end{bmatrix}\begin{bmatrix}a_s(j,\mathbf{x},\omega)\\ a_r(j,\mathbf{x},\omega)\end{bmatrix} = \begin{bmatrix}g_s(j,\mathbf{x},\omega)\\ g_r(j,\mathbf{x},\omega)\end{bmatrix}\,. \tag{12}$$

The gradient of the objective function is simply the crosscorrelation between state and adjoint-state variables:

$$\frac{\partial J}{\partial m} = \tag{13}$$

$$\sum_j\sum_\omega \frac{\partial\mathcal{L}}{\partial m}\left(u_s(j,\mathbf{x},\omega)\,\overline{a_s(j,\mathbf{x},\omega)} + u_r(j,\mathbf{x},\omega)\,\overline{a_r(j,\mathbf{x},\omega)}\right)\,, \tag{14}$$

where $\frac{\partial\mathcal{L}}{\partial m}$ is just $-\omega^2$.

One common problem for image-domain wavefield tomography is that the computed gradient always distributes the measured misfit along the wavepaths from image points to the surface. This is because the focusing error actually measures velocity model error accumulated from top to bottom, and the gradient spreads the updates all the way up to the surface. If certain areas above the image point do not contain error in the velocity model, the inversion needs additional iterations to eliminate the update in this region, which consequently slows the convergence of the inversion. To ameliorate this problem, we use the focusing error as a constraint for the inversion. The focusing error is associated with the accuracy of the velocity model and accumulated from top to bottom in a way similar to the velocity model error. Therefore, the integral of the focusing error absolute value over depth indicates the distribution of the velocity model error. If this integral in a certain area is close to zero, then the velocity model for this area and above is accurate and needs no updates. Therefore, we can construct a gradient mask to mute areas where no model update is required. We define the gradient mask W as:

$$W(\mathbf{x}) = \begin{cases} 0 & \text{if } \int_0^z |\Delta\tau(x,y,z)|dz < \tau_0 \\ 1 & \text{elsewhere}\end{cases}\,, \tag{15}$$

where τ_0 is a user-defined threshold. By applying the gradient mask and limiting the model updates in the target regions, we reduce the number of iterations needed by the inversion and improve the convergence of the method. This idea is similar to applying layer-stripping in velocity model building: we first update the model in the shallow regions, and then proceed to updates of the deeper portion of the model while keeping the upper portion fixed.

3 EXAMPLES

We demonstrate the gradient computation and preconditioning of our method using a synthetic horizontally layered model, and then we apply the method to a North Sea 3D OBC field dataset.

Figure 1(a) shows the velocity profile of the synthetic model. The model has two interfaces located at $z = 0.5$ km and $z = 1.1$ km, and the velocities for the three layers from top to bottom are 1.5, 1.7, and 2.3 km/s. We simulate the data using acoustic two-way wave-equation finite-difference modeling. The initial model used for imaging is constant using the velocity from the first layer in the true model, i.e. 1.5 km/s. We use this model to migrate the data and to obtain the image and the time-lag gathers. As the initial model is correct in the first layer, we expect that the first interface be correctly imaged, and the second interface shifted. The migrated image in Figure 1(b) indeed shows that the first reflector is correctly imaged at $z = 0.5$ km, and that the second reflector is too shallow, at $z = 1.0$ km. Figure 2 shows a gather located at the center of the model. Using such gathers, we can extract the focusing error $\Delta\tau$ by measuring the lag of the focus from zero time lag. Here, the time-lag gathers accurately capture the velocity information: as there is no velocity model error associated with the first layer, the corresponding reflection focus is

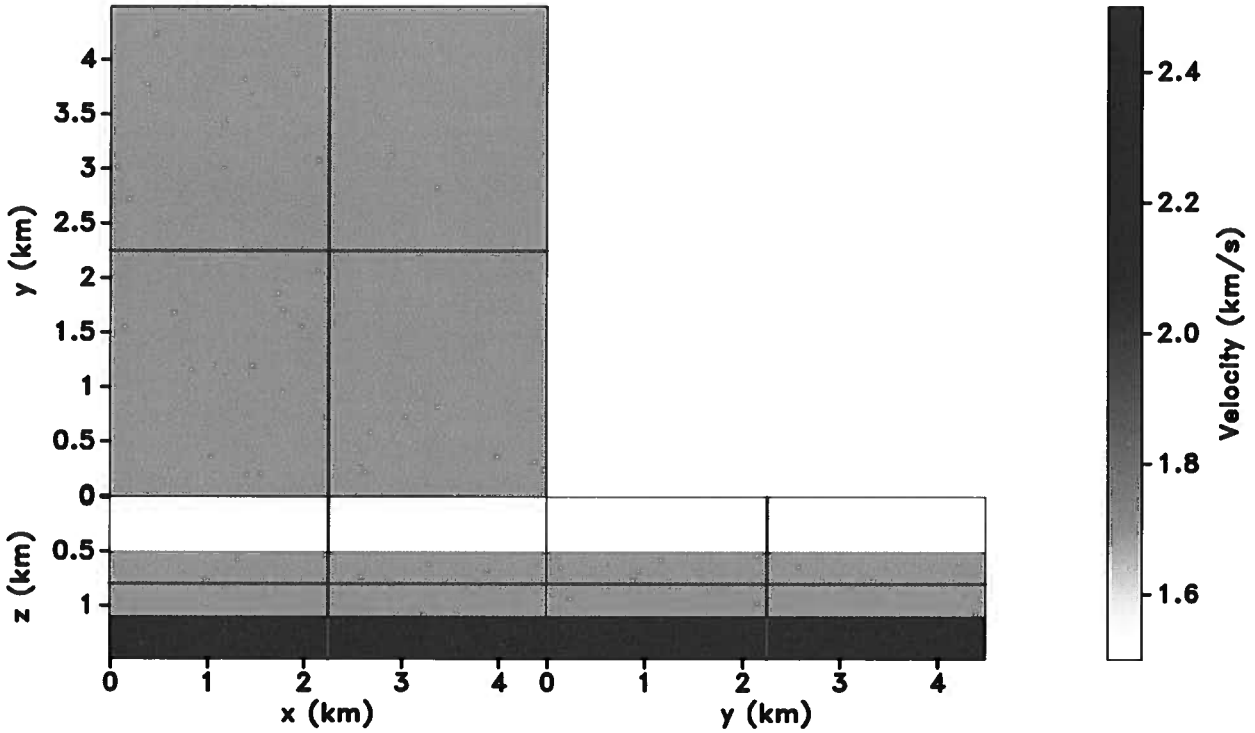

(a)

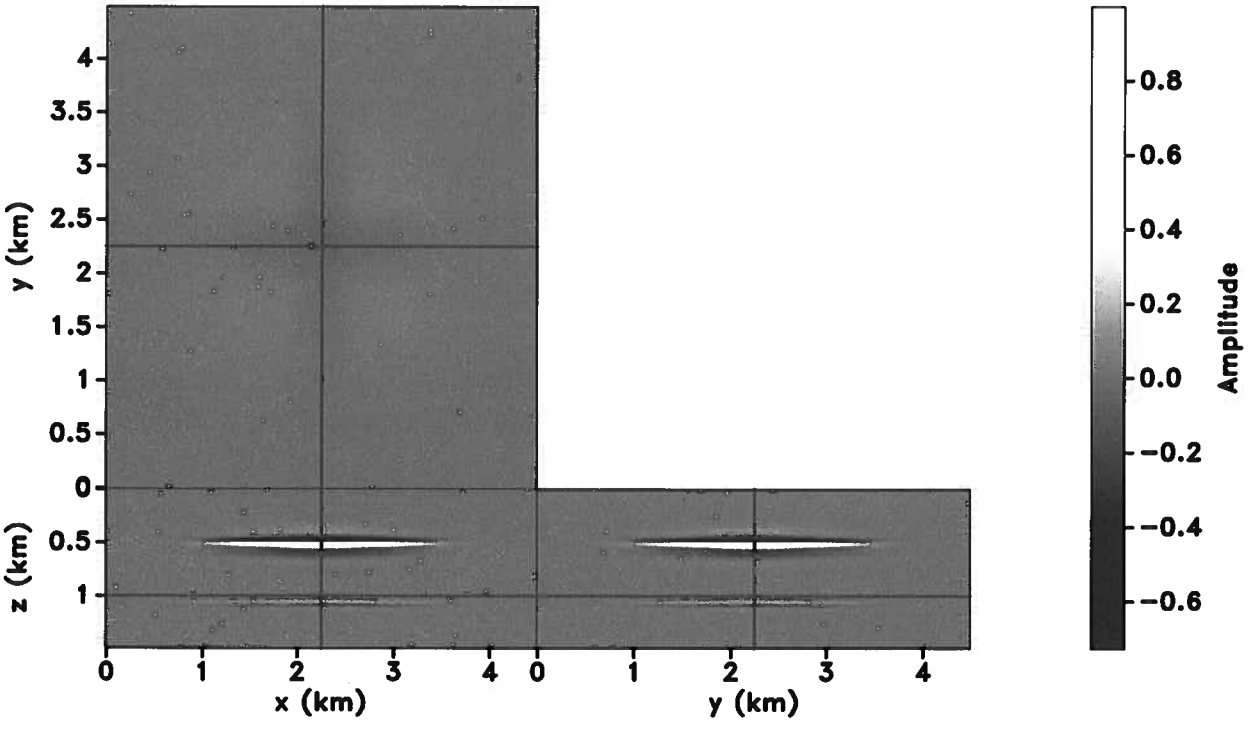

(b)

Figure 1. (a) The layered velocity model, and (b) migrated image obtained with the initial model, the constant with velocity from the first layer in the true model, i.e. 1.5 km/s.

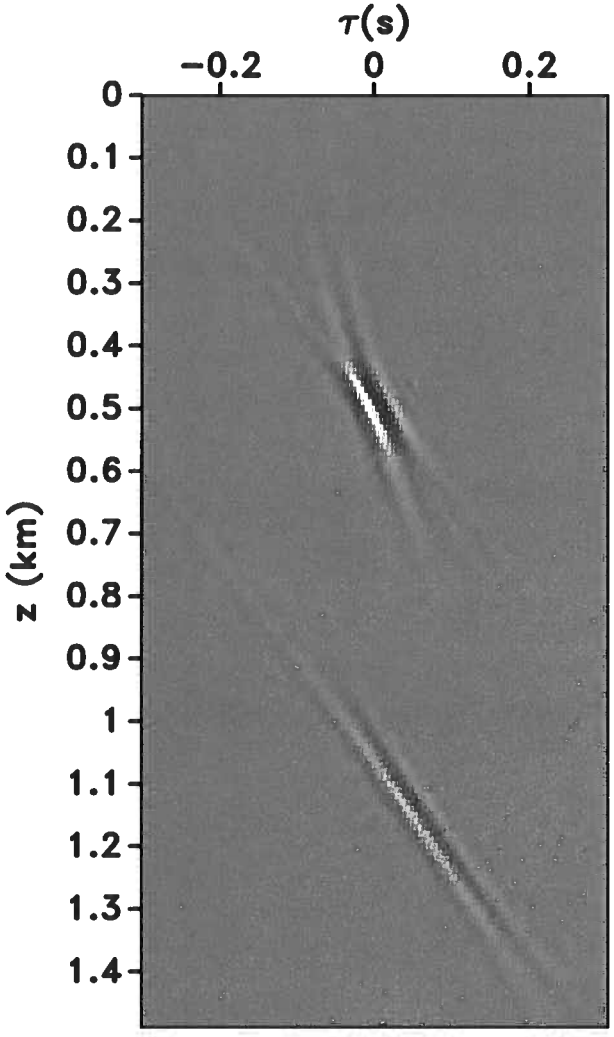

Figure 2. Time-lag gathers obtained with the initial model. The gather is located at at $x = 2.25$ km, $y = 2.25$ km. The reflection focus of the top layer is located at zero lag as there is no velocity error. The focus of the second layer shifts to positive 0.1 s due to the incorrect initial model.

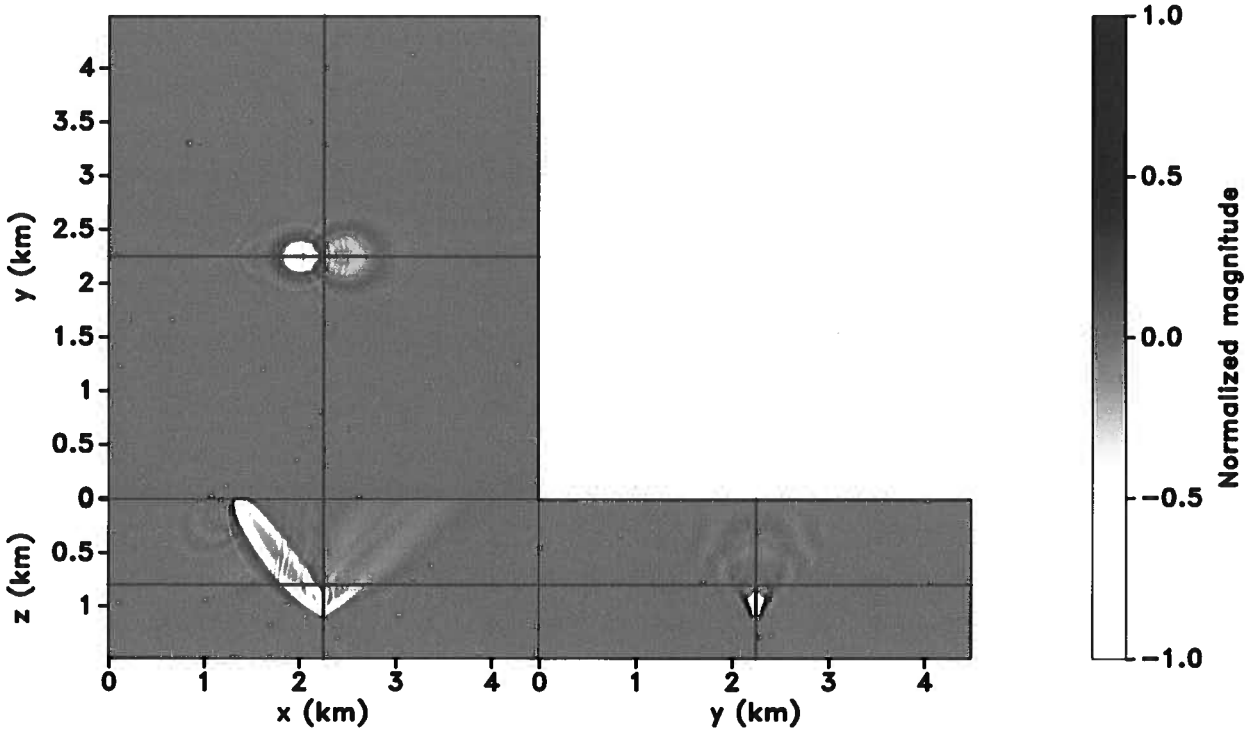

(a)

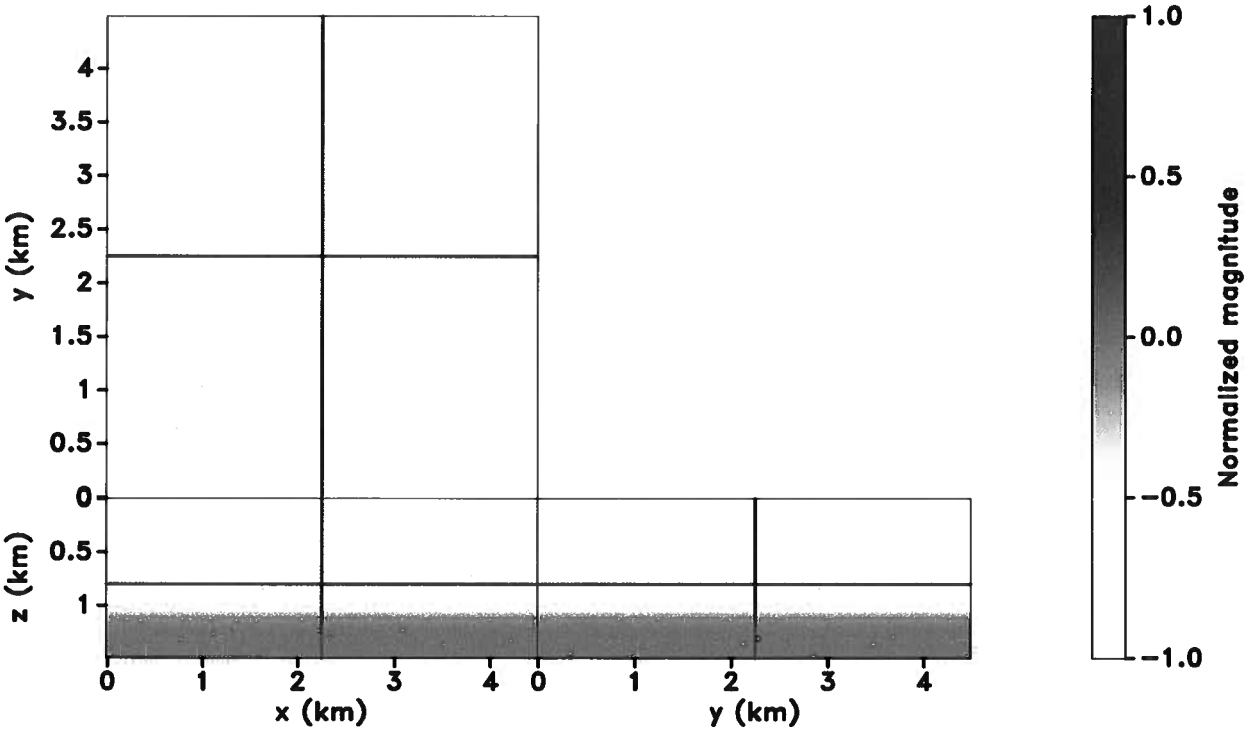

(b)

Figure 3. (a) The gradient obtained with a single shot, which corresponds to the sensitivity kernel of our method, and (b) the gradient obtained with all shots.

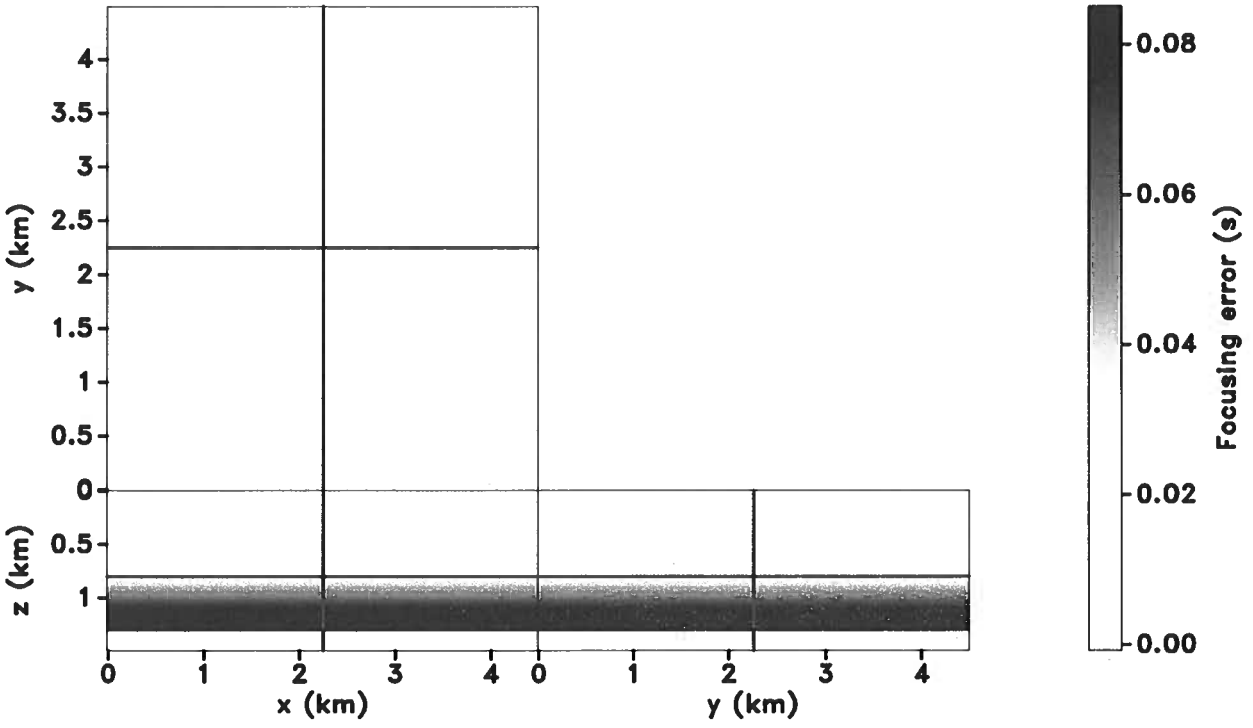

(a)

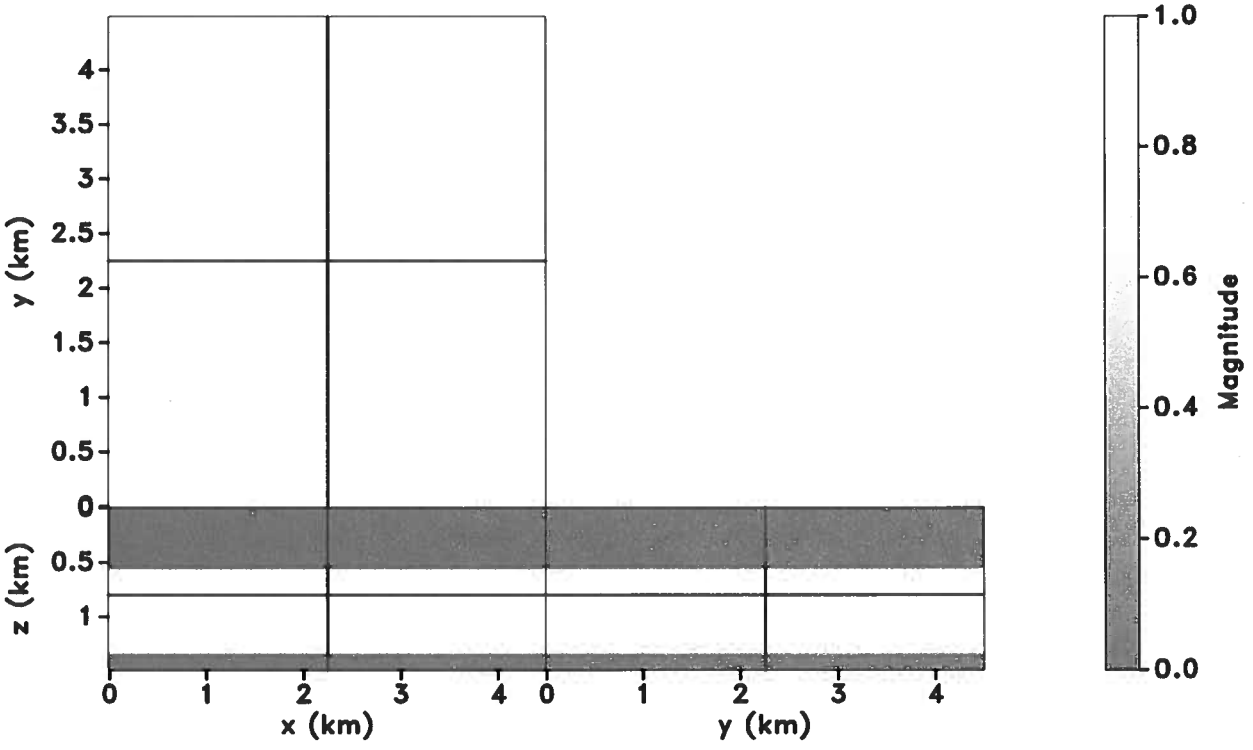

(b)

Figure 4. (a) The focusing error extracted from the time-lag gathers. (b) The gradient mask obtained using equation 11.

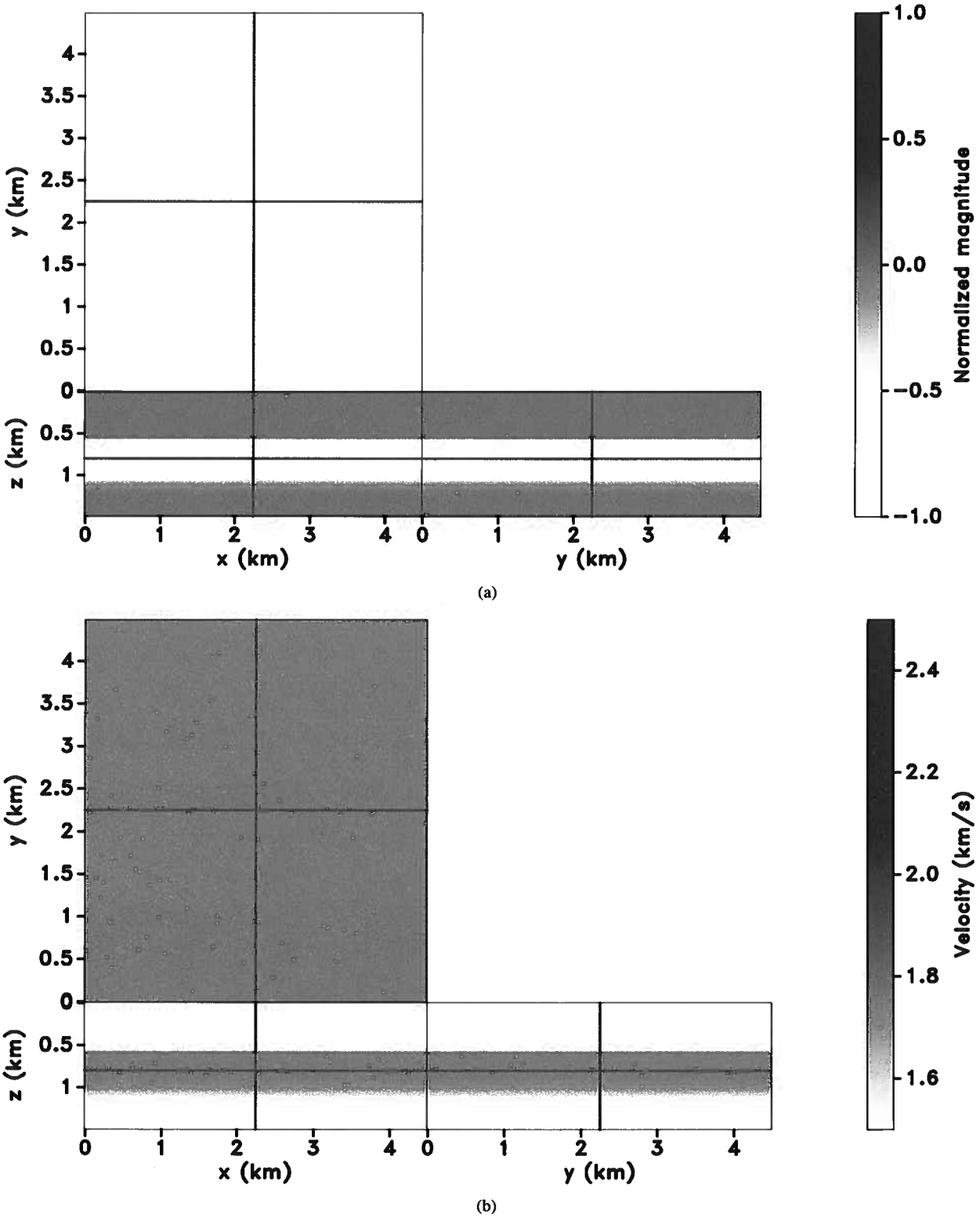

Figure 5. (a) The gradient obtained after applying the mask. (b) The updated model using the gradient in (a) after one iteration.

located at zero time lag. In contrast, the reflection focus of second layer is shifted to $\tau = 0.1$ s indicating that the migration velocity is lower than that of the true model. Using the focusing error, we construct the objective function and compute the gradient following the workflow discussed in the previous section. Figure 3(a) plots the gradient obtained for one gather at the center of the model and one shot located at $x = 1.1$ km, $y = 2.25$ km. This single-shot gradient corresponds to the sensitivity kernel of the method. The kernels connecting the source and receivers to the image point on the second layer. Figure 3(b) plots the gradient obtained for all gathers and all shots. The gradient is negative, indicating that the velocity of the initial model should be increased, which agrees with our experimental setup. The gradient in Figure 3(b) also suggests a update in the area between $z = 0$ km and $z = 0.5$ km, because the sensitivity kernels for the second layer distributes the focusing error along the path from the source to image points to receivers. However, the focusing error (Figure 4(a)), which characterizes the velocity model error distribution, is zero in the top layer because there is no velocity error in this area. This demonstrates that the computed gradient is not consistent with the velocity error distribution, so we need to restrict the updates from the top layer. Using the focusing error as a priori information, we construct the gradient mask using equation 15, as shown in Figure 4(b). Because the mask is zero in the first layer, this effectively removes the updates there. The final preconditioned gradient, after applying the mask, is plotted in Figure 5(a). The update is now limited to the second layer only, and results in a faster convergence for the inversion. In this simple case, we reconstruct the model shown in Figure 5(b) after only one iteration.

The North Sea 3D OBC field dataset was acquired in the Volve field, and the construction of the initial model is described in Szydlik et al. (2007). The Earth model is anisotropic and can be described using the Thomsen parameters V_p, ϵ, and δ (Thomsen, 1986). Here we assume that the medium is isotropic and use only the V_p model to test our algorithm. Figures 6(a) and 7(a) show the initial model obtained by a layer-stripping method and the corresponding migrated image. Using the objective function and gradient computation discussed in the previous section, we run the inversion for five iterations. The updated velocity model and its corresponding migrated image are plotted in Figures 6(b) and 7(b). Observe that the inversion increases the velocity around the center part of the model between $z = 2.5$ km-4.0 km. This update improves the image quality, as the main reflections around $z = 2.8$ km are more focused and coherent, and the continuity of the deeper reflections improves as well. These improvements can be better observed in the zoom-in inline sections extracted at $y = 3.5$ km in Figures 8(a) and 8(b). To further assess the model improvement, we construct angle-domain common-image gathers before and after the inversion. Figures 9(a)-9(c) and Figures 10(a)-10(c) plot angle gathers sampled in the inline direction at three different crossline locations using the initial and updated models, respectively. Notice that the main reflector around $z = 2.8$ km is characterized by flatter gathers after the inversion, indicating the model improvement.

4 DISCUSSION

We demonstrate an image-domain wavefield tomography approach that can be used as an alternative to data-domain wave-equation traveltime inversion. We use focusing to measure a traveltime error, which depends on the velocity model error, i.e., we formulate an objective function by minimizing the focusing error.

Our method shares many similarities with wave-equation traveltime inversion, e.g., the objective function construction. The main difference between these two techniques, however, lies in how the focusing information is extracted. In wave-equation traveltime inversion, the traveltime residual $\Delta\tau$ is obtained from the cross-correlation between recorded and simulated data in individual shot gathers. In contrast, our method estimates the focusing error $\Delta\tau$ from time-lag gathers, which are the cross-correlations of extrapolated source and receiver wavefields stacked over all experiments. In general, the signal-to-noise ratio in common-image gathers is higher than in shot gathers due to the stacking process. Thus, the approach proposed here is expected to render more accurate focusing information in presence of noise and complex geology. Besides, wave-equation traveltime inversion is designed to extract the traveltime information from transmission waves, which can be used only in cross-well geometry or for diving waves in surface acquisition. Our approach, in contrast, extracts the traveltime information from reflected waves, and thus it is capable of inverting the velocity model in deeper target regions.

Furthermore, our method requires less computational efforts compared to differential semblance optimization (DSO). DSO uses space-lag gathers and needs to compute the lags in both inline and crossline directions in 3D. This leads to 5D image hypercubes which are too expensive to compute and store. In comparison, our method requires only the time lag to evaluate velocity information even in 3D. As a result, the computational and storage cost is at least one order of magnitude lower than in the case of space-lag gathers. Nonetheless, the azimuthal resolution of our method is lower than that provided by DSO since the time-lag itself is not sufficient to characterize the azimuth information in the gathers.

5 CONCLUSION

We develop a 3D image-domain velocity model building technique based on time-lag extended images, which characterize the traveltime residual due to velocity error by reflection focusing. We formulate the optimization problem by minimizing the focusing error based on images constructed by wave-equation migration, which puts our technique in the family of wavefield tomography techniques. We speed up inversion by exploiting focusing information as a priori information to precondition the gradient. A North Sea field data example illustrates that our method is effective in improving model accu-

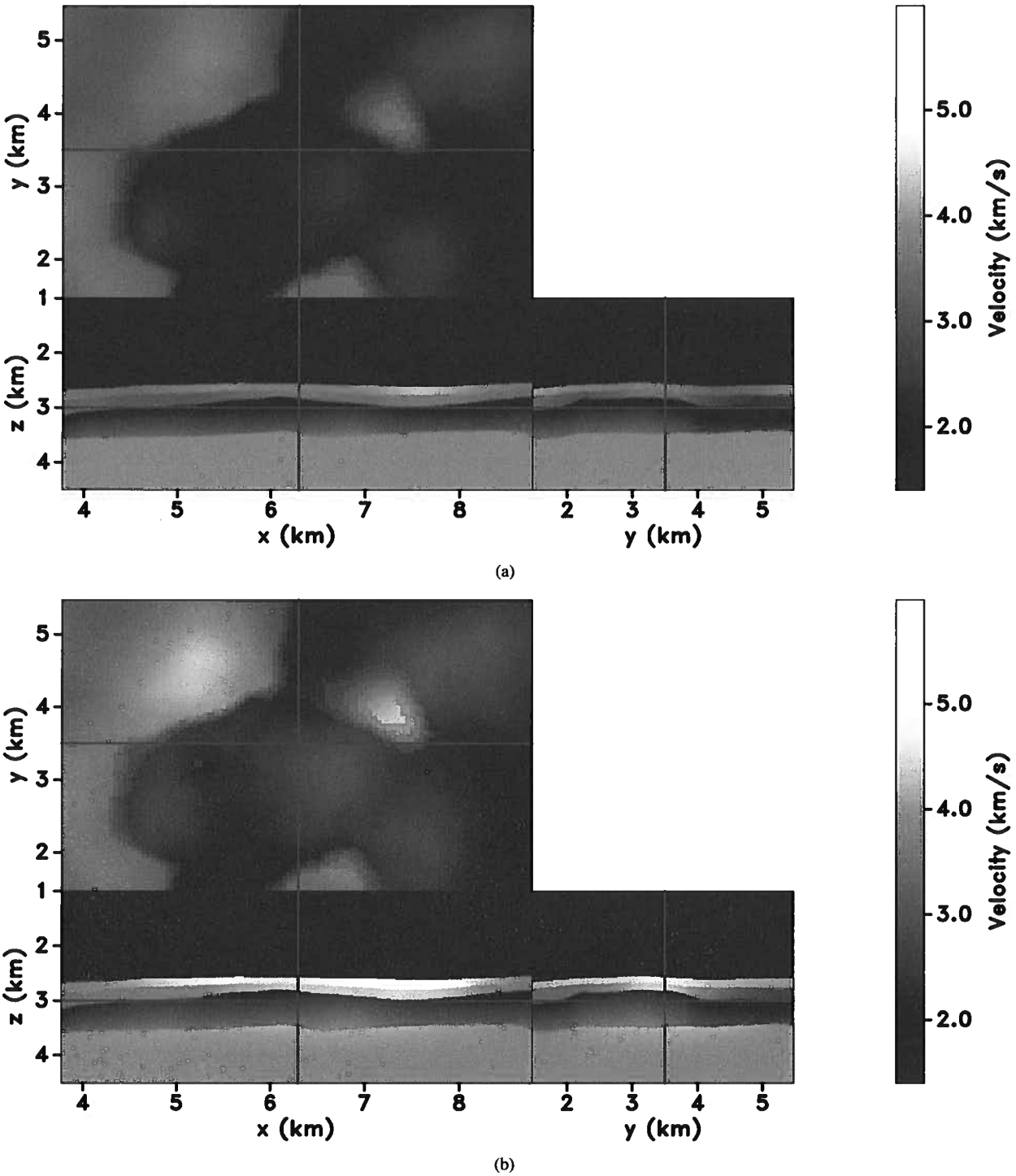

Figure 6. North Sea field data example. (a) The initial model used for the inversion, and (b) the updated model obtained after the inversion.

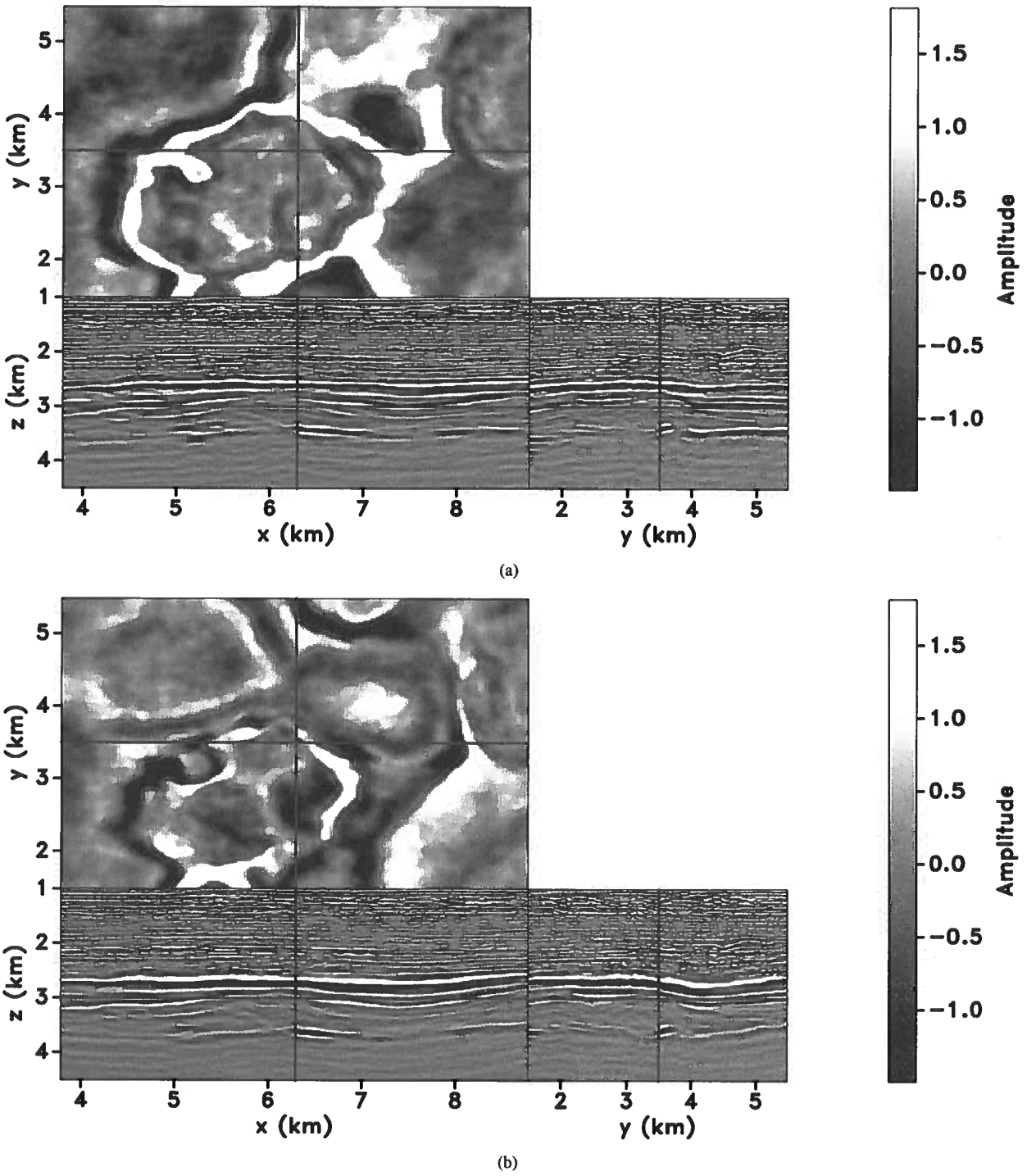

Figure 7. North Sea field data example. (a) The migrated image obtained with the initial model, and (b) the migrated image obtained with the updated model.

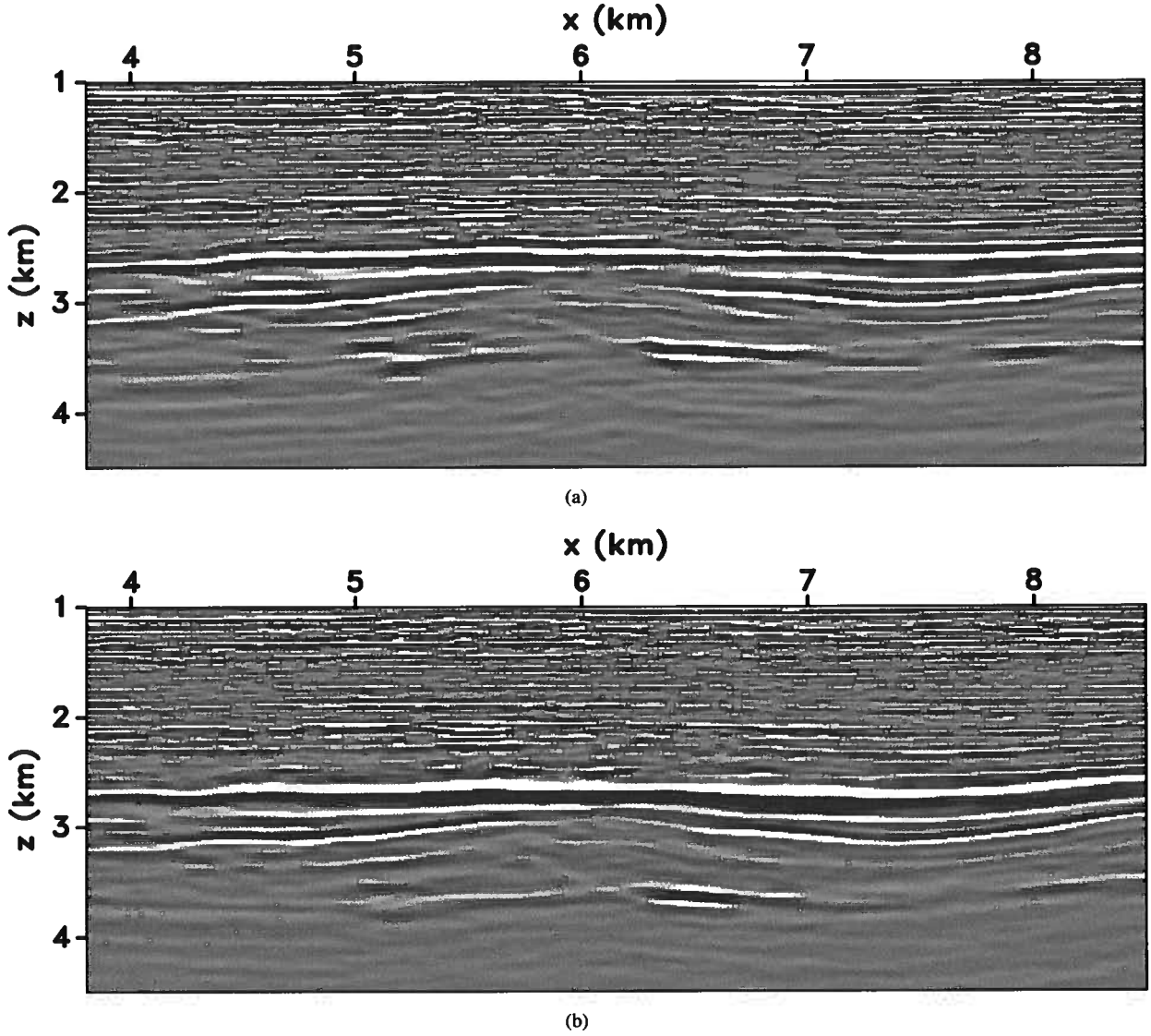

Figure 8. North Sea field data example. Zoom-in image extracted at $y = 3.5$ km to highlight the difference in image quality. (a) The image obtained with the initial model and (b) the image obtained with the updated model.

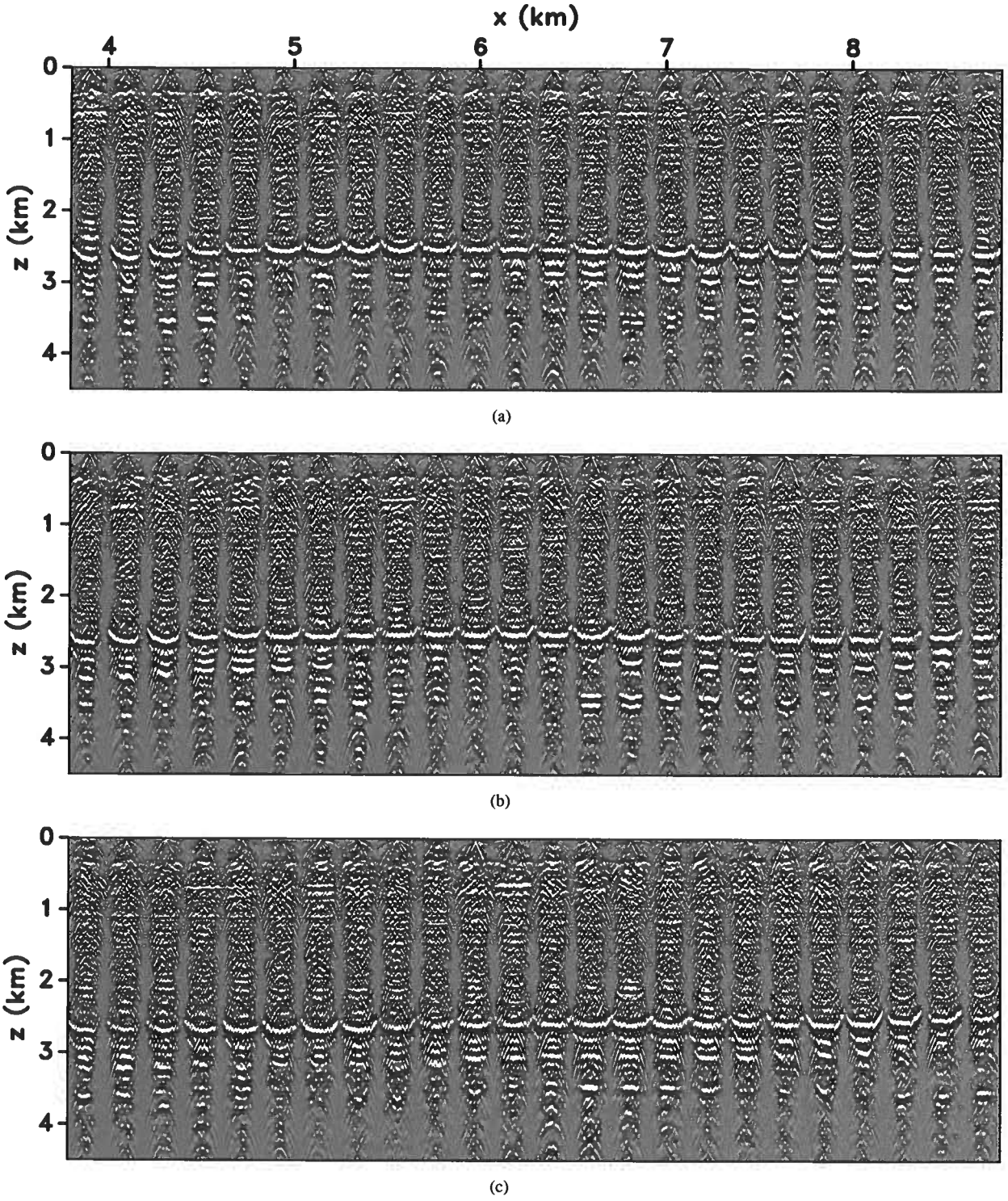

Figure 9. Angle-domain gathers obtained with the initial model at (a) $y = 3$ km, (b) $y = 6$ km, and (c) $y = 9$ km. The angle range is from $-60°$ to $60°$.

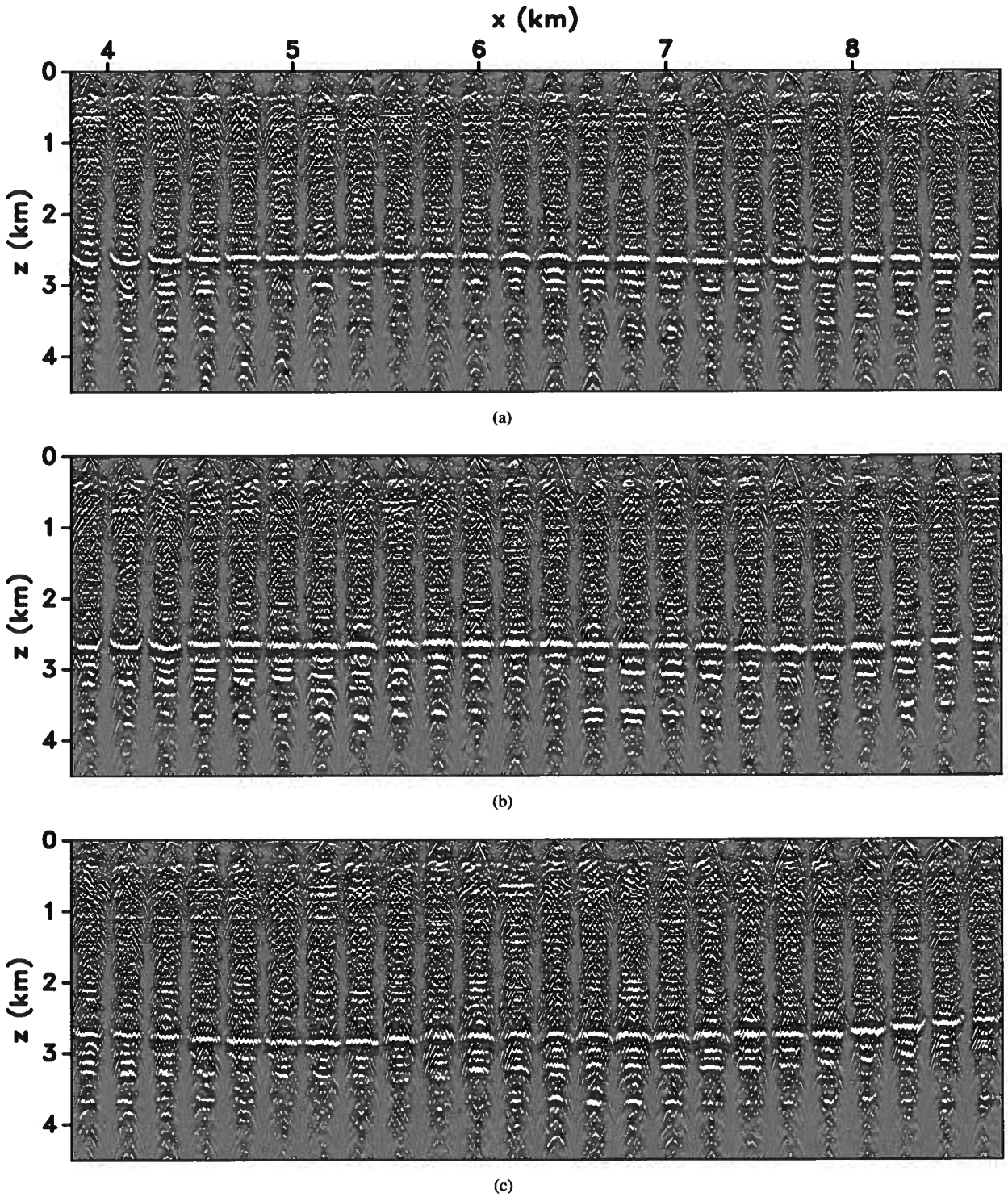

Figure 10. Angle-domain gathers obtained with the updated model at (a) $y = 3$ km, (b) $y = 6$ km, and (c) $y = 9$ km. The angle range is from $-60°$ to $60°$.

racy and image quality. In addition, the method is computationally efficient in 3D velocity model building applications.

6 ACKNOWLEDGMENTS

We thank sponsor companies of the Consortium Project on Seismic Inverse Methods for Complex Structures, whose support made this research possible. The authors would also like to thank Statoil ASA and the Volve license partners ExxonMobil E&P Norway and Bayerngas Norge, for the release of the Volve data. The reproducible numeric examples in this paper use the Madagascar open-source software package freely available from http://www.ahay.org.

7 DISCLAIMER

The views expressed in this paper belong to the authors and do not necessarily reflect the views of Statoil ASA and the Volve field license partners.

REFERENCES

Al-Yahya, K., 1989, Velocity analysis by iterative profile migration: Geophysics, **54**, 718–729.

Brown, M. P., J. H. Higginbotham, and R. G. Clapp, 2008, Velocity model building with wave equation migration velocity focusing analysis: 78th Annual International Meeting, SEG, Expanded Abstracts, 3078–3082.

Etgen, J., S. H. Gray, and Y. Zhang, 2009, An overview of depth imaging in exploration geophysics: Geophysics, **74**, WCA5–WCA17.

Faye, J. P., and J. P. Jeannot, 1986, Prestack migration velocities from focusing depth analysis: 56th Annual International Meeting, SEG, Expanded Abstracts, 438–440.

Higginbotham, J. H., and M. P. Brown, 2008, Wave equation migration velocity focusing analysis: 78th Annual International Meeting, SEG, Expanded Abstracts, 3083–3086.

Luo, Y., and G. Schuster, 1991, Wave equation traveltime inversion: Geophysics, **56**, 645–653.

Plessix, R.-E., 2006, A review of the adjoint state method for computing the gradient of a functional with geophysical applications: Geophysical Journal International, **167**, 495–503.

———, 2009, Three-dimensional frequency-domain full-waveform inversion with an iterative solver: Geophysics, **74**, WCC53–WCC61.

Pratt, R. G., 1999, Seismic waveform inversion in the frequency domain, Part 1: Theory and verification in a physical scale model: Geophysics, **64**, 888–901.

Sava, P., and B. Biondi, 2004, Wave-equation migration velocity analysis - I: Theory: Geophysical Prospecting, **52**, 593–606.

Sava, P., and S. Fomel, 2006, Time-shift imaging condition in seismic migration: Geophysics, **71**, S209–S217.

Shen, P., and W. W. Symes, 2008, Automatic velocity analysis via shot profile migration: Geophysics, **73**, VE49–VE59.

Sirgue, L., and R. Pratt, 2004, Efficient waveform inversion and imaging: A strategy for selecting temporal frequencies: Geophysics, **69**, 231–248.

Symes, W., 2009, Migration velocity analysis and waveform inversion: Geophysical Prospecting, **56**, 765–790.

Szydlik, T., P. Smith, S. Way, L. Aamodt, and C. Friedrich, 2007, 3-d pp/ps prestack depth migration on the volve field: First break, **25**, 43–47.

Tarantola, A., 1984, Inversion of seismic reflection data in the acoustic approximation: Geophysics, **49**, 1259–1266.

Thomsen, L., 1986, Weak elastic anisotropy: Geophysics, **51**, 1954–1966. (Discussion in GEO-53-04-0558-0560 with reply by author).

van Leeuwen, T., and W. A. Mulder, 2010, A correlation-based misfit criterion for wave-equation traveltime tomography: Geophysical Journal International, **182**, 1383–1394.

Vigh, D., and E. W. Starr, 2008, 3D prestack plane-wave, full-waveform inversion: Geophysics, **73**, VE135–VE144.

Wang, B., Y. Kim, C. Mason, and X. Zeng, 2008, Advances in velocity model-building technology for subsalt imaging: Geophysics, **73**, VE173–VE181.

Wang, B., C. Mason, M. Guo, K. Yoon, J. Cai, J. Ji, and Z. Li, 2009, Subsalt velocity update and composite imaging using reverse-time-migration based delayed-imaging-time scan: Geophysics, **74**, WCA159–WCA166.

Wang, B., F. Qin, V. Dirks, P. Guilaume, F. Audebert, and D. Epili, 2005, 3-d finite angle tomography based on focusing analysis: 78th Annual International Meeting, SEG, Expanded Abstracts, 2546–2549.

Yang, T., and P. Sava, 2010a, Moveout analysis of wave-equation extended images: Geophysics, **75**, S151–S161.

———, 2010b, Wave-equation migration velocity analysis with time-lag imaging: Geophysical Prospecting, submitted for publication.

———, 2011, Waveform inversion in the image domain: Presented at the 73th EAGE Conference and Exhibition, Extended Abstracts.

Yilmaz, O., 2001, Seismic Data Analysis (2nd edition): Society of Exploration Geophysicists.

Zhang, Y., and D. Wang, 2009, Traveltime information-based wave-equation inversion: Geophysics, **74**, WCC27–WCC36.

Wavefield tomography using RTM backscattering

Esteban Díaz and Paul Sava
Center for Wave Phenomena, Colorado School of Mines, Golden CO 80401

ABSTRACT
Reverse time migration (RTM) backscattering contains kinematic information that can be used to constrain velocity models. The backscattering results from the correlation between forward scattered and backscattered wavefields from sharp interfaces, i.e. sediment-salt interfaces. The synchronization between these wavefields depends on the velocity of the sediment section and the correct interpretation of the sharp boundary. Therefore, we can use these events along with reflection and diving waves to define a joint optimization problem for velocity model building. As in RTM images, in gradient computation the backscattering and diving information produces cross-talk. In order to avoid the cross-talk, we use a directional filter based on the Poynting vector which preserves the components of the wavefield that travel in the same direction. Using backscattered waves for constraining the velocity in the sediment section requires defining the top of salt in advance, which would imply a dynamic workflow for model building in salt environments where both sediment velocity and salt interface change iteratively during inversion.

Key words: RTM backscattering, wavefield tomography, Poynting vector

1 INTRODUCTION

The two-way way equation is the engine of reverse-time migration (RTM) (Baysal et al., 1983; McMechan, 1983; Whitmore, 1983). This imaging technology is used routinely to obtain high fidelity images of the subsurface. Despite the computing cost, the two-way operator has many advantages over other modeling approaches, like downward continuation or Kirchhoff modeling. This technique is especially suited for complex geological settings such as those with strong velocity gradients, sharp boundaries (e.g. salt bodies), and strong lateral variations. The reason for the RTM success is that a wavefield reconstructed with the two-way operator can easily handle any dip, multi-pathing, and reflections from steep structures (Gray et al., 2001; Etgen et al., 2009).

RTM also produces low wave-number events in seismic images, which are usually referred to as RTM artifacts. The low wave-number energy is produced by the correlation of waves that propagate in the same direction, thus violating the assumptions of the conventional cross correlation imaging condition (Claerbout, 1985). Such events include backscattered waves, head-waves, and diving waves. The backscattered events obstruct the image representing the subsurface reflectivity, and so are usually considered noise. Numerous techniques can be employed to remove the RTM noise. In terms of filtering approach, we could divide such methods in two categories: pre-imaging filtering (Fletcher et al., 2005; Yoon et al., 2004; Liu et al., 2011) and post-imaging filtering (Youn and Zhou, 2001; Guitton et al., 2007; Zhang and Sum, 2009; Kaelin and Carvajal, 2011).

Although the low wavenumber energy is noise for imaging purposes, it can be used for velocity model-building. This energy is the result of the correlation of waves traveling in the same direction, thus coinciding in space and time. This space and time coincidence only occurs when the wavefields extrapolation is accurate. Therefore, if the velocity model is correct, the RTM backscattering is strong simply because the wavefields are synchronized (Díaz and Sava, 2012). For reflected data, the space-time synchronization criterion also applies at the reflector position. Since both types of waves (transmitted and reflected) share the same kinematic behaviour, we can design a joint optimization problem that improves the synchronization of all the data simultaneously,thus allowing us to refine the model and to use the RTM backscattering as a source of information instead of treating it as noise.

To optimize the velocity model, one can choose a method that is consistent with the modeling operator (two-way). Such an inverse problem could be formulated by finding a model that produces data which resembles the observed data, as is done in Full Waveform Inversion (Tarantola, 1984; Pratt, 1999). This data-domain approach relies on the kinematic and dynamic consistencies between modeled and observed data. Therefore, if the propagation engine used is not dynamically consistent with the data, i.e. the modeled amplitudes are not accurate, then the chances for convergence diminish. Alternatively, one can optimize the model in the image space using

techniques from the family usually referred to as wavefield tomography (Woodward, 1992; Sava and Biondi, 2004; Fliedner and Bevc, 2008; Shen and Symes, 2008; Yang and Sava, 2011a). The image domain approach seeks the kinematic synchronization of the wavefields at an image location. Therefore, the aim of this method is to improve the image focusing rather than to match the dynamic information of the wavefields as in done in the data-domain approach. This increases the robustness of the method, but decreases its ability to construct high resolution models. One way to formulate the problem in the image space is by using extended images (Rickett and Sava, 2002; Sava and Fomel, 2006; Sava and Vasconcelos, 2011), from which we can extract wavefield similarities in space and time (Shen et al., 2003; Yang and Sava, 2010). Extended images are normally used for optimizing the reflected data information, but Díaz and Sava (2012) show that similar to reflected data, the RTM backscattered energy also maps to zero time-lag and space-lag when the velocity model is correct.

In this paper, we demonstrate that it is possible to use the backscattered and diving waves for image-domain wavefield tomography. Using the two-way wave equation operator allows simultaneous inversion based on the reflected, diving and backscattered waves. We formulate the tomography problem using the adjoint state method (ASM), which is an efficient technique for gradient-based optimization (Plessix, 2006). However, the gradient computed using the ASM suffers from cross-talk between forward and backscattered waves, which produces undesirable reflector-like evens. In order to avoid the unwanted correlations, we apply a directional filter designed to keep the contributions between wavefields traveling in the same direction during the correlation step of the gradient computation. This filter is based on the Poynting vectors of the extrapolated wavefields (Yoon et al., 2004), although other filtering techniques can be used instead.

We start this paper with a brief review of the RTM backscattering kinematic properties and the mapping patterns in extended images, and then we review wavefield tomography using extended images. We show how this methodology can be adapted to backscattering energy and define an objective function and its gradient, which are essential for inversion. We then illustrate how we can make use of the backscattering information for wavefield tomography, and demonstrate our method using a complex synthetic based on the Sigsbee model (Paffenholz et al., 2002).

2 RTM BACKSCATTERING REVISITED

RTM backscattering is produced in the presence of sharp models, e.g. sediment-salt interfaces. In such cases, wavefields extrapolated with a two-way operator (e.g. the scalar wave equation)

$$\frac{1}{v^2(\mathbf{x})}\frac{\partial^2 u(\mathbf{x},t)}{\partial t^2} - \nabla^2 u(\mathbf{x},t) = f(\mathbf{x},t) \qquad (1)$$

contains forward and backscattered components. Here, $u(\mathbf{x},t)$ the reconstructed wavefield, $v(\mathbf{x})$ the medium velocity and $f(\mathbf{x},t)$ the source function. Therefore, we can write the source wavefield as a superposition of two components

$$u_s(\mathbf{x},t) = u_s^b(\mathbf{x},t) + u_s^f(\mathbf{x},t), \qquad (2)$$

where the superscripts ^{b} and ^{f} correspond to the backscattered and forward scattered wavefields from the sharp boundary, respectively. Similarly, the receiver wavefield can be decomposed into two components with the equivalent naming convention:

$$u_r(\mathbf{x},t) = u_r^b(\mathbf{x},t) + u_r^f(\mathbf{x},t). \qquad (3)$$

2.1 Conventional imaging condition

The source and receiver wavefields allow one to construct an image with the conventional imaging condition (Claerbout, 1985) defined as the zero-lag correlation between source and receiver wavefields:

$$R(\mathbf{x}) = \sum_e \sum_t u_s(e,\mathbf{x},t) u_r(e,\mathbf{x},t). \qquad (4)$$

Here e refers to the experiment index, e.g. shot number or plane-wave take-off angle.

If the wavefields used in imaging contain backscattering, we can substitute equations 2 and 3 into equation 4 and obtain an image which is a superposition of 4 individual images:

$$\begin{aligned} R(\mathbf{x}) = {} & R^{ff}(\mathbf{x}) + R^{bb}(\mathbf{x}) \\ & + R^{bf}(\mathbf{x}) + R^{fb}(\mathbf{x}). \end{aligned} \qquad (5)$$

Following the convention in Díaz and Sava (2012), the first superscript corresponds to the source wavefield and the second to the receiver wavefield. In this total image, two components (^{ff} and ^{bb}) provide an estimate of the reflectivity, and the other two components (^{fb} and ^{bf}) represent backscattering. This means that the backscattering is produced from the correlation of wavefields traveling in the same direction. For example, $R^{bf}(\mathbf{x})$ is produced when the backscattered source wavefield $u_s^b(\mathbf{x},t)$ resembles the forward scattered receiver wavefield $u_r^f(\mathbf{x},t)$, and $R^{fb}(\mathbf{x})$ is produced with the opposite combination of the propagating wavefields. Several authors (Yoon et al., 2004; Fei et al., 2010; Liu et al., 2011) use this wavefield directionality notion to keep only the components related to reflectivity in the image and to remove everything else. Here we use the directionality concept to keep the components that travel in the same direction during tomography.

2.2 Extended imaging condition

A generalized version of equation 4 can be used to understand the (kinematic) similarities between source and receiver wavefields. This concept is known as extended imaging (Rickett and Sava, 2002; Sava and Fomel, 2006; Sava and Vasconcelos, 2011). A general case of an extended image is defined as follows:

$$R(\mathbf{x},\boldsymbol{\lambda},\tau) = \sum_e \sum_t u_s(e,\mathbf{x}-\boldsymbol{\lambda},t-\tau) u_r(e,\mathbf{x}+\boldsymbol{\lambda},t+\tau), \qquad (6)$$

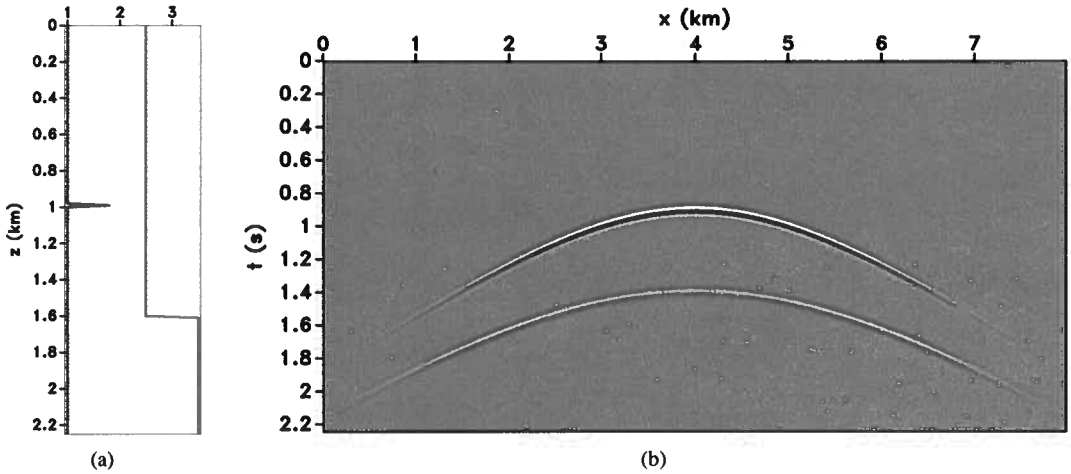

Figure 1. Synthetic experiment setup: (a) the density (spike function) model (g/cc) and the velocity (step function) model (km/s), and (b) the modeled data.

where $\boldsymbol{\lambda}$ and τ are space and time extensions of the cross-correlation, respectively. Extended images are commonly used to produce angle gathers (Sava and Fomel, 2003, 2006; Sava and Vlad, 2011) and for velocity estimation (Shen and Symes, 2008; Yang et al., 2012; Yang and Sava, 2011b).

In the presence of sharp models, we can substitute equations 2 and 3 into equation 6. By doing so, we can differentiate between the different components of the extended image, which is similar to what we do for conventional images:

$$R(\mathbf{x},\boldsymbol{\lambda},\tau) = R^{ff}(\mathbf{x},\boldsymbol{\lambda},\tau) + R^{bb}(\mathbf{x},\boldsymbol{\lambda},\tau) + R^{bf}(\mathbf{x},\boldsymbol{\lambda},\tau) + R^{fb}(\mathbf{x},\boldsymbol{\lambda},\tau). \quad (7)$$

The reflected data maps into the components ^{ff} and ^{bb}, whereas the backscattered energy maps into the ^{fb} and ^{bf} components. In the conventional image $R(\mathbf{x})$ (both backscattered and reflected energy) coexist above sharp interfaces, for example due to the presence of a salt body. The two components are usually separated based on the spectral content (the artifacts have low wavenumber content, whereas the reflectivity has high wavenumber content). This separation is normally done using some sort of high-pass filter, like a Laplacian (∇^2) operator (Youn and Zhou, 2001; Zhang and Sum, 2009) or by least-squares filtering (Guitton et al., 2007). The separation is not perfect in areas with similar spectral content. In the extended image space, however, the reflected and backscattered energy has unique mapping patterns (Díaz and Sava, 2012), which can be used to effectively separate both components (Kaelin and Carvajal, 2011).

Díaz and Sava (2012) show that the backscattered and reflected energy share the wavefield synchronization criterion. The spatial and temporal synchronization occurs above a sharp boundary for backscattered events, whereas the synchronization occurs at the position of the reflectors for reflected data. The synthetic model shown in Figure 1(a) illustrates the extended image kinematic sensitivity to model error. The data in Figure 1(b) show two events: the earlier one corresponding to a reflector in the density model (spike in Figure 1(a)), and the later one resulting from a sharp contrast in the velocity model (step function in Figure 1(a)). The third event in the data corresponds to an internal multiple generated between the density and velocity interfaces.

Figures 2(a), 2(b), and 2(c) show time-lag gathers for three different velocities. These gathers are generated using equation 6 with $\boldsymbol{\lambda} = \mathbf{0}$ after stacking over different experiments, i.e. shots in this case. We simulate a velocity error in the first layer and adjust the sharp boundary according to the migration velocity, for example a low velocity shifts the boundary upwards and a high velocity shifts the boundary downwards. The backscattering maps vertically in the three cases, however it deviates from $\tau = 0$ when the velocity is incorrect. The time delay error in the backscattering is the same to the one produced by the reflected energy at the sharp interface. Therefore, the backscattering provides information about the sharp interface at any place in the image above it.

Figures 3(a), 3(b), and 3(c) show the equivalent space-lag gather dependency with respect to the velocity error. Similar to the time-lag gathers, the space-lag gathers are generated after stacking the contribution from different experiments. The backscattering (mapping vertically in the gathers) spreads away from $\boldsymbol{\lambda} = \mathbf{0}$ with the velocity error, thus emulating the defocusing of the reflected data. Similarly to the time-lag gathers, the backscattering above the interface is the expression of the defocusing at the sharp boundary.

Since both reflected and backscattered data share similar velocity dependency, we conclude that we can design an inverse problem that optimizes both type of events simultaneously (Díaz and Sava, 2012). The following section details the velocity analysis procedure based on backscattering.

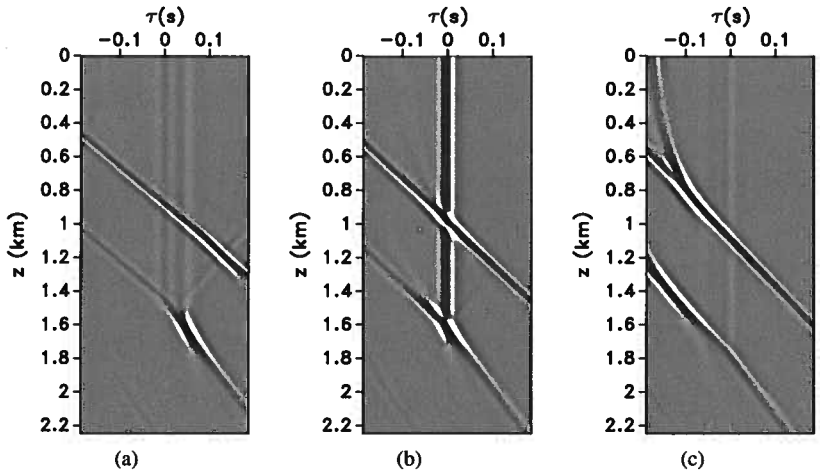

Figure 2. Time-lag gathers for (a) low, (b) correct and (c) high velocities.

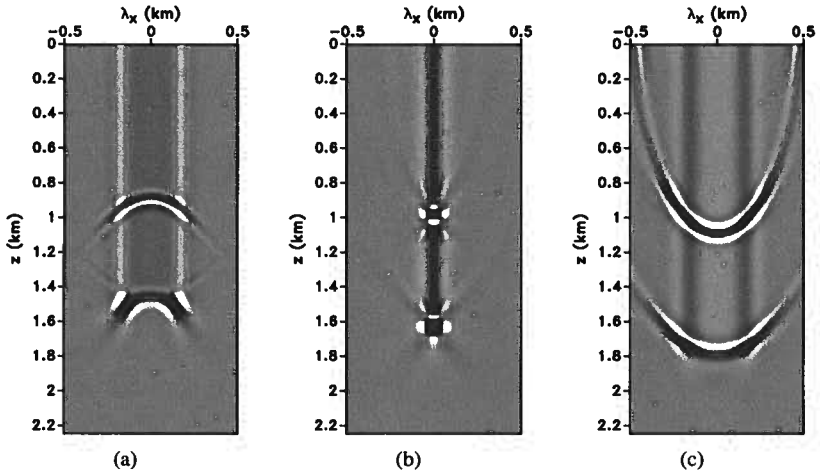

Figure 3. Space-lag gathers for (a) low, (b) correct and (c) high velocities.

3 WAVEFIELD TOMOGRAPHY WITH EXTENDED IMAGES

In order to analyze the velocity model error, we can make use of the semblance principle which seeks image consistency as a function of extended image parameters. Stork (1992) implements the idea using the consistency between common offset images. Symes and Carazzone (1991) exploit this concept using the differential semblance optimization (DSO) method. DSO can also be used to increase the flatness of angle gathers. Rickett and Sava (2002) and Sava and Fomel (2003) show that common angle gathers and extended images are related by a slant stacking operation. Therefore, these two type of common image gathers are equivalent for velocity analysis. Shen and Symes (2008) and Yang and Sava (2011a) use the consistency criterion in extended images to formulate a tomographic problem based on space-lag gathers or joint space and time-lag gathers, respectively.

3.1 Inversion with time-lag gathers

If the velocity is correct, the time-lag gathers (Sava and Fomel, 2006) show maximum focusing at zero lag. This observation derives from the fact that the source and receiver wavefields are synchronized at the reflector position. The velocity model can be improved by increasing the wavefield synchronization, which is equivalent to locating the events in the extended images as close as possible to $\tau = 0$. This can be done by minimizing the following objective function (OF):

$$J = \frac{1}{2} ||P(\tau)R(\mathbf{x},\tau)||^2 , \tag{8}$$

where $P(\tau) = |\tau|$ is an operator that penalizes the energy outside $\tau = 0$. Following the notation in Yang and Sava (2011a), we can express $R(\mathbf{x},\tau)$ as

$$R(\mathbf{x},\tau) = \sum_e \sum_t T(-\tau)u_s(e,\mathbf{x},t)T(+\tau)u_r(e,\mathbf{x},t), \tag{9}$$

where $T(\pm\tau)$ is a time-shift operator applied to the source or receiver wavefields. Note that this OF cannot drop to zero completely because in the time-lag gathers, there is always correlation energy for all values of τ. However, this OF is minimum when the velocity model is correct and most of the energy in the extended image locates at $\tau = 0$.

We compute the gradient of equation 8 using the Adjoint State Method (ASM) (Tarantola, 1984; Plessix, 2006). The adjoint source with respect to the source wavefield for an experiment e is

$$g_s(\mathbf{x}, e) = \sum_{\tau} T(-\tau)P^2(\tau)R(\mathbf{x}, \tau)T(-\tau)u_r(e, \mathbf{x}, t), \tag{10}$$

and the adjoint source with respect to the receiver wavefield is

$$g_r(\mathbf{x}, e) = \sum_{\tau} T(\tau)P^2(\tau)R(\mathbf{x}, \tau)T(\tau)u_s(e, \mathbf{x}, t). \tag{11}$$

We construct the adjoint state variables by injecting the adjoint sources at the gather positions and by extrapolating the wavefields using the adjoint modeling operators. The adjoint source wavefield $a_s(e, \mathbf{x}, t)$ is reconstructed backward in time, whereas the adjoint receiver wavefield $a_r(e, \mathbf{x}, t)$ is reconstructed forward in time. Using the state and adjoint state variables, the gradient with respect to the velocity model is

$$\nabla J(\mathbf{x}) = \frac{-2}{v^3(\mathbf{x})} \sum_e \sum_t \frac{\partial^2 u_s}{\partial t^2}(e, \mathbf{x}, t)a_s(e, \mathbf{x}, t) + \frac{\partial^2 u_r}{\partial t^2}(e, \mathbf{x}, t)a_r(e, \mathbf{x}, t), \tag{12}$$

where $\frac{-2}{v^3(\mathbf{x})}\frac{\partial^2}{\partial t^2}$ corresponds to the derivative of the modeling operator (equation 1) with respect to the velocity model.

In the gradient expression (equation 12) we expect to correlate state and adjoint state wavefields traveling in the same direction which implies that the gradient is smooth. However, if backscattering is present in the wavefield, we obtain cross-talk similar to that seen in RTM. The cross-talk in this case is generated by the correlation of wavefields traveling in the opposite direction. In order to attenuate the cross-talk, we can use a filter that preserves the components of wavefields traveling in the same direction and eliminates the wavefields traveling in opposite directions. We can find the direction of propagation using the approach of Yoon et al. (2004), which constructs the Poynting vectors $\mathbf{P}(e, \mathbf{x}, t)$ using the equation

$$\mathbf{P}(e, \mathbf{x}, t) \propto \frac{\partial u(e, \mathbf{x}, t)}{\partial t} \nabla u(e, \mathbf{x}, t), \tag{13}$$

where u can be either the source or the receiver wavefield. In practice we use the time-averaged Poynting vectors using a Gaussian smoothing over a small time window determined by the dominant period of the data

$$< \mathbf{P}(e, \mathbf{x}, t) >_t = \mathbf{P}(e, \mathbf{x}, t) * G(t). \tag{14}$$

Here, the symbol $*$ denotes convolution, and $G(t)$ is the Gaussian smoothing filter.

To keep just the wavefields components traveling in the same direction, we can compute a weighting function $W(\theta)$ with

$$\theta(\mathbf{x}, t) = \cos^{-1}\left(\frac{\mathbf{P}_s(\mathbf{x}, t) \cdot \mathbf{P}_r(\mathbf{x}, t)}{|\mathbf{P}_s(\mathbf{x}, t)||\mathbf{P}_r(\mathbf{x}, t)|}\right) \tag{15}$$

such that we preserve the wavefield cross-correlation for which $\mathbf{P}_s(\mathbf{x}, t) \cdot \mathbf{P}_r(\mathbf{x}, t) \approx 1$, i.e. when the direction of propagation is similar within a given tolerance. The weighting function can be designed using a cutoff angle, from which the function tapers off smoothly using a Gaussian function with standard deviation σ which defines the range from which the angles are accepted.

$$W(\theta, a, \sigma) = \begin{cases} 1 & : 0^\circ \leq \theta < a \\ e^{-(\theta - a)^2/(2\sigma^2)} & : a \leq \theta \leq 180^\circ. \end{cases} \tag{16}$$

Based on this filter, we change equation 12 to

$$\nabla J(\mathbf{x}) = \frac{-2}{v^3(\mathbf{x})} \sum_e \sum_t W(\theta)\frac{\partial^2 u_s}{\partial t^2}(e, \mathbf{x}, t)a_s(e, \mathbf{x}, t) + W(\theta)\frac{\partial^2 u_r}{\partial t^2}(e, \mathbf{x}, t)a_r(e, \mathbf{x}, t). \tag{17}$$

This new gradient avoids cross-talk and emphasizes wavefields traveling in the same direction.

Figures 4(a), 4(c), and 4(e) show the gradient constructed using equation 12 for low, correct, and high velocities, respectively. One can see that the intensity of the gradient with correct velocity is lower that obtained for either low or high velocities. One can also observe the cross-talk due to wavefields propagating in opposite directions which appears as reflectors in the gradient. The gradient is computed using equation 17 with a cutoff angle $a = 15^\circ$, Figures 4(b), 4(d), and 4(f) show the cross-talk significantly attenuated.

3.2 Inversion with space-lag gathers

We can also use the information contained in space-lag gathers (Rickett and Sava, 2002). If the velocity model is correct, then space-lag gathers focus at $\boldsymbol{\lambda} = \mathbf{0}$. If the velocity model is incorrect, the gathers contain defocused energy outside $\boldsymbol{\lambda} = \mathbf{0}$. This criterion is used by Shen and Symes (2008) and Yang and Sava (2011a) to formulate wavefield tomography using the OF

$$J = \frac{1}{2}\left|\left|P(\boldsymbol{\lambda})R(\mathbf{x}, \boldsymbol{\lambda})\right|\right|^2, \tag{18}$$

where $P(\boldsymbol{\lambda}) = |\boldsymbol{\lambda}|$ is a penalty operator. Even with correct velocity, this OF does not become zero due to the band-limited nature of the data and due to illumination effects (Yang et al., 2012). Nevertheless, this OF provides an effective criterion for velocity updating.

We compute the gradient of equation 18 using the same workflow as the one used for equation 8 (Yang and Sava, 2011a). The adjoint sources are defined as

$$g_s(\mathbf{x}, e) = \sum_{\boldsymbol{\lambda}} T(-\boldsymbol{\lambda})P^2(\boldsymbol{\lambda})R(\mathbf{x}, \boldsymbol{\lambda})T(-\boldsymbol{\lambda})u_r(e, \mathbf{x}, t) \tag{19}$$

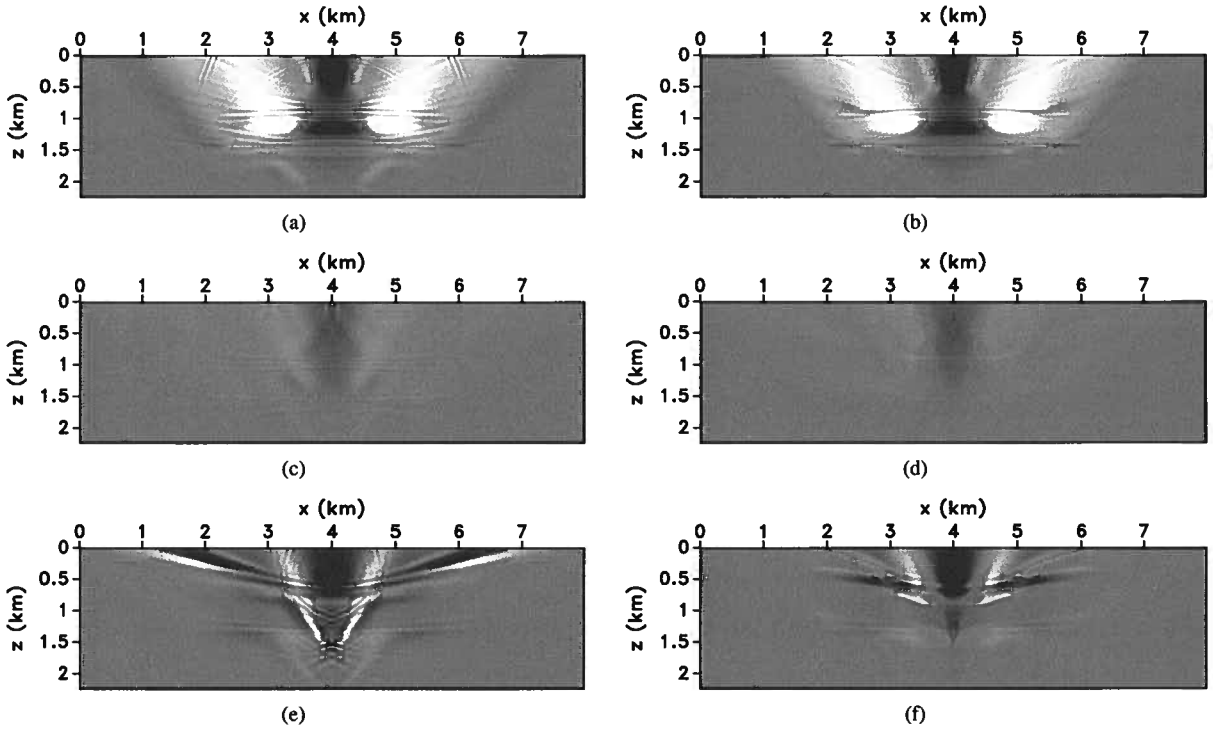

Figure 4. Gradients obtained using time-lag gathers for (a)-(b) low, (c)-(d) correct, and (e)-(f) high velocities. Gradients (a), (c), and (e) are constructed without filtering and (b), (d) and (f) with filtering.

for the source side, and

$$g_r(\mathbf{x}, e) = \sum_{\boldsymbol{\lambda}} T(+\boldsymbol{\lambda}) P^2(\boldsymbol{\lambda}) R(\mathbf{x}, \boldsymbol{\lambda}) T(+\boldsymbol{\lambda}) u_s(e, \mathbf{x}, t) \tag{20}$$

for the receiver side. Here $T(\pm\boldsymbol{\lambda})$ is a space shifting operator applied to the wavefields. The only difference between the time-lag and space-lag gather formulation is in the OF and in the computation of the adjoint sources. The gradient and adjoint wavefields are computed using the same wave-equation and background velocity model as in the case of thetime-lag gathers (equations 12 and 17).

Figures 5(a), 5(c), and 5(e) show the gradients for low, correct, and high velocity, respectively. To compute these gradients, we use the space-lag gathers shown in Figures 3(a), 3(b), and 3(c), respectively. As for the gradient constructed with time-lag gather, one can see that the energy in the space-lag gradient is proportional to the focusing error observed in the gathers. The gradients obtained using equation 12 also contain cross-talk similarly to the gradient constructed with time-lag gathers. If we apply the directional filtering during the gradient computation (equation 17), we obtain gradients with significantly lower cross-talk. Figures 5(b), 5(d), and 5(f) show the filtered gradients for the low, correct, and high velocity models, respectively.

4 EXAMPLES

In this section, we illustrate the use of the backscattering and reflected events on a modified version of the Sigsbee 2b model (Paffenholz et al., 2002). We focus on the small basin formed by the salt intrusion (Figure 6(a)). We simulate data for 61 shots evenly distributed on the surface, with a fixed receiver array at the surface, in order to test the effect of using a fast sediment velocity with an error increasing with depth (Figure 6(b)). After migrating the data with the fast sediment velocity, we interpret the top of salt (TOS) and place the salt bellow it as shown in Figure 6(c). Figure 6(d) shows the difference between Figure 6(c) and Figure 6(a), and indicates that overall the incorrect velocity is faster.

Figure 7(a) depicts the RTM image using the velocity in Figure 6(b), and show that the focusing of the TOS event degrades with depth and is not simple to interpret. Figure 7(b) shows evenly sampled space-lag gathers, which also indicate that the defocusing increases with depth. Figure 7(a) shows the RTM image obtained with the model after salt flooding (Figure 6(c)). One can see that the backscattering above the TOS event is not uniform and changes sign throughout the sediment section, thus indicating velocity or TOS interpretation error. Figure 7(b) shows space-lag gathers corresponding to the RTM image in Figure 7(c). Note that the backscattering (mapping vertically in the gathers) spreads away from $\boldsymbol{\lambda} = \mathbf{0}$, following the defocusing of the TOS reflector.

Figure 8(a) shows the gradient computed using the ve-

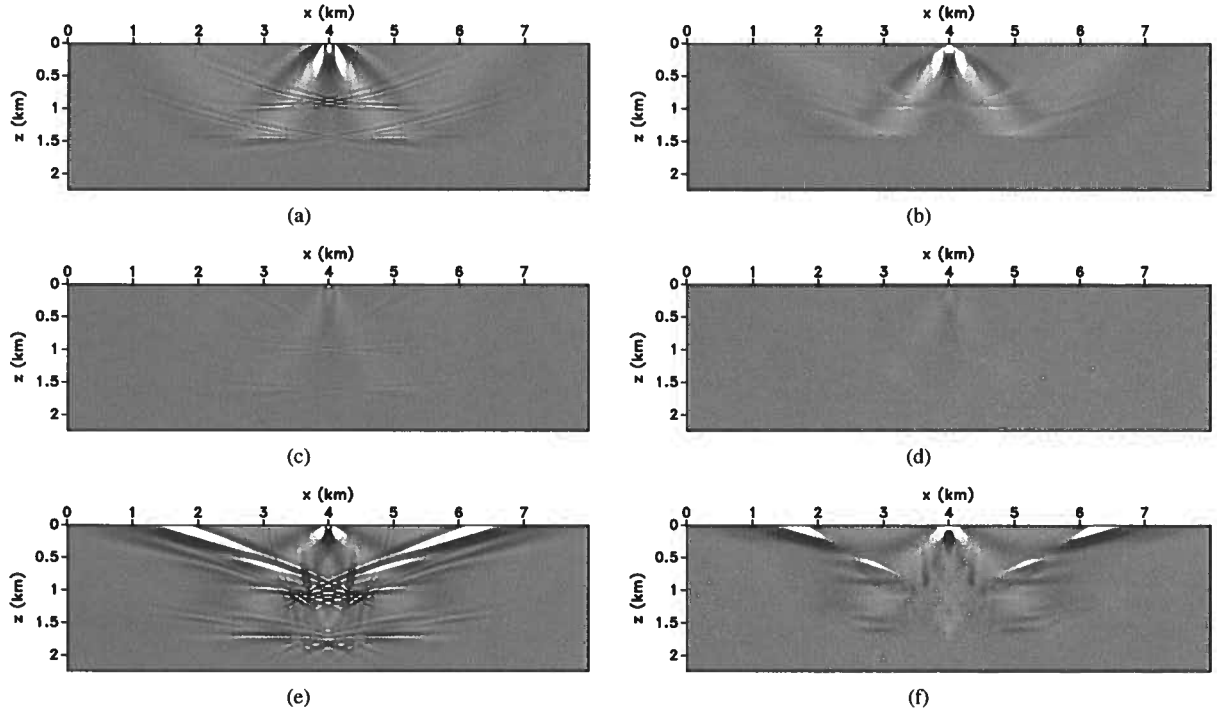

Figure 5. Gradients obtained using space-lag gathers for (a)-(b) low, (c)-(d) correct, and (e)-(f) high velocities. Gradients (a), (c), and (e) are constructed without filtering and (b), (d) and (f) with filtering.

locity in Figure 6(c). Figure 8(b) shows the filtered gradient, whereas Figure 8(c) shows the difference between the gradients in Figures 8(a)-8(b). One can see that the gradient energy is concentrated above the sharp boundary; therefore the update is correctly focused in the sediment basin, and the cross-talk is effectively removed by our filter using the Poynting vectors.

Since we use the top of salt for the tomography update, it is necessary to interpret the TOS event at each iteration. Interpretation of salt boundaries could be very difficult and time consuming, especially in complicated salt bodies with overhanging flanks (Ahmed et al., 2012). Since the sediment velocity changes at each iteration, the TOS also changes slowly with iteration. In practice, one could interpret the salt boundary in the first iteration and look for TOS changes in the vicinity of the previous solution, for example using automatic salt interpretation (Lomask et al., 2007; Halpert, 2011).

For comparison, we also compute a gradient using the fast sediment velocity shown in Figure 6(b) and the corresponding space-lag gathers in Figure 7(b). The gradient depicted in Figure 9(a) shows that some cross-talk is still present, despite the fact that strong sharp boundaries are not present in the model. We hypothesize that the cross-talk in the gradient is due to diving waves in the wavefields. The filtered gradient shown in Figure 9(a) and the difference shown in Figure 9(b) indicate that the filter effectively removes the cross-talk.

5 CONCLUSIONS

We demonstrate that it is possible to use RTM backscattered data in wavefield tomography. The RTM backscattering provides information about the wavefield synchronization and focusing of the sharp boundaries at any place in the image above the boundaries. As for RTM imaging, sharp models introduce cross-talk in wavefield tomography gradients, which appears as reflections instead of low wavenumber events as in the case of RTM images. We filter the cross-talk with an approach based on Poynting vectors to emphasise the wavefield components traveling in the same direction and to discard the wavefield components traveling in opposite directions. The purpose of this filter is exactly the opposite of the one proposed by Yoon et al. (2004) to attenuate the backscattering energy in RTM images.

We can use the backscattered information and sharp boundaries in the model to constrain the sediment velocity in the upper section. Using this information requires a dynamic model building work flow, with both the sediment and salt boundaries being updated at every iteration. Although we demonstrate the presence of cross-talk with extended images wavefield tomography, we assert that similar events exist in other two-way domain tomography methods, e.g. waveform inversion. Nevertheless, we conclude that sharp sediment-salt interfaces generate information useful for model updates.

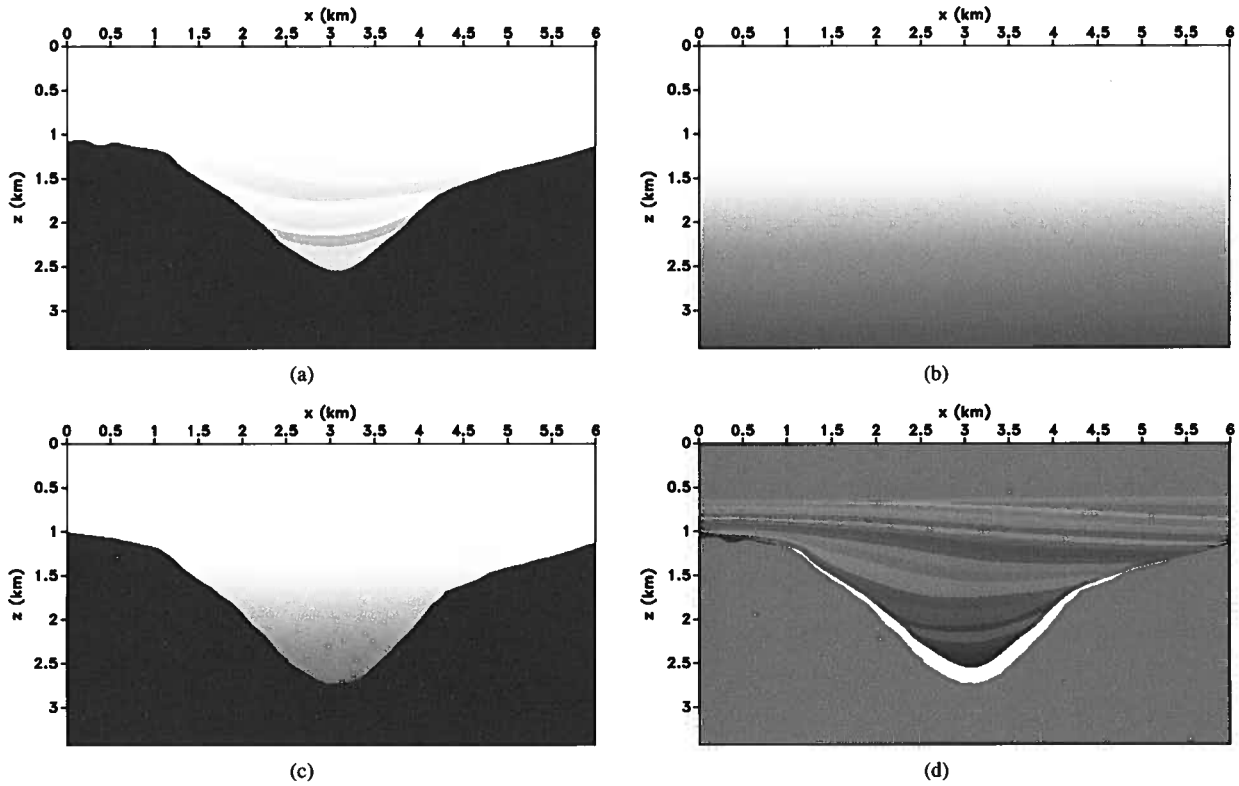

Figure 6. Salt model example: (a) true velocity model, (b) fast sediment flood velocity model, (c) fast sediment velocity with salt flood, and (c) the difference (c)-(a). In the difference, dark colors indicate positive difference and light colors indicate negative differences

6 ACKNOWLEDGMENTS

We would like to thank the sponsor companies of the Consortium Project on Seismic Inverse Methods for Complex Structures. The reproducible numeric examples in this paper use the Madagascar open-source software, freely available from http://www.ahay.org. We thank SMAART JV for the synthetic model. Esteban Díaz would like to thank to Natalya Patrikeeva and Tongning Yang for stimulating discussions about the Poynting vector and wavefield tomography, respectively.

REFERENCES

Ahmed, I., R. Faerber, C. Kumar, and F. Billette, 2012, Interactive velocity model validation (IVMV): SEG Technical Program Expanded Abstracts 2012, 1–5.

Baysal, E., D. D. Kosloff, and J. W. C. Sherwood, 1983, Reverse time migration: Geophysics, **48**, 1514–1524.

Claerbout, J. F., 1985, Imaging the earth's interior: Blackwell Scientific Publications, Inc.

Díaz, E., and P. Sava, 2012, Understanding the reverse time migration backscattering: noise or signal?: SEG Technical Program Expanded Abstracts 2012, 1–6.

Etgen, J., S. Gray, and Y. Zhang, 2009, An overview of depth imaging in exploration geophysics: Geophysics, **74**, WCA5–WCA17.

Fei, T. W., Y. Luo, and G. T. Schuster, 2010, De-blending reverse-time migration: SEG Technical Program Expanded Abstracts, **29**, 3130–3134.

Fletcher, R. F., P. Fowler, P. Kitchenside, and U. Albertin, 2005, Suppressing artifacts in prestack reverse time migration: SEG Technical Program Expanded Abstracts, **24**, 2049–2051.

Fliedner, M., and D. Bevc, 2008, Automated velocity model building with wavepath tomography: Geophysics, **73**, VE195–VE204.

Gray, S., J. Etgen, J. Dellinger, and D. Whitmore, 2001, Seismic migration problems and solutions: Geophysics, **66**, 1622–1640.

Guitton, A., B. Kaelin, and B. Biondi, 2007, Least-squares attenuation of reverse-time-migration artifacts: Geophysics, **72**, S19–S23.

Halpert, A. D., 2011, Model-building with image segmentation and fast image updates: 4035–4039.

Kaelin, B., and C. Carvajal, 2011, Eliminating imaging artifacts in RTM using pre-stack gathers: SEG Technical Program Expanded Abstracts, **30**, 3125–3129.

Liu, F., G. Zhang, S. A. Morton, and J. P. Leveille, 2011, An effective imaging condition for reverse-time migration using wavefield decomposition: Geophysics, **76**, S29–S39.

Lomask, J., R. Clapp, and B. Biondi, 2007, Application of image segmentation to tracking 3d salt boundaries: Geo-

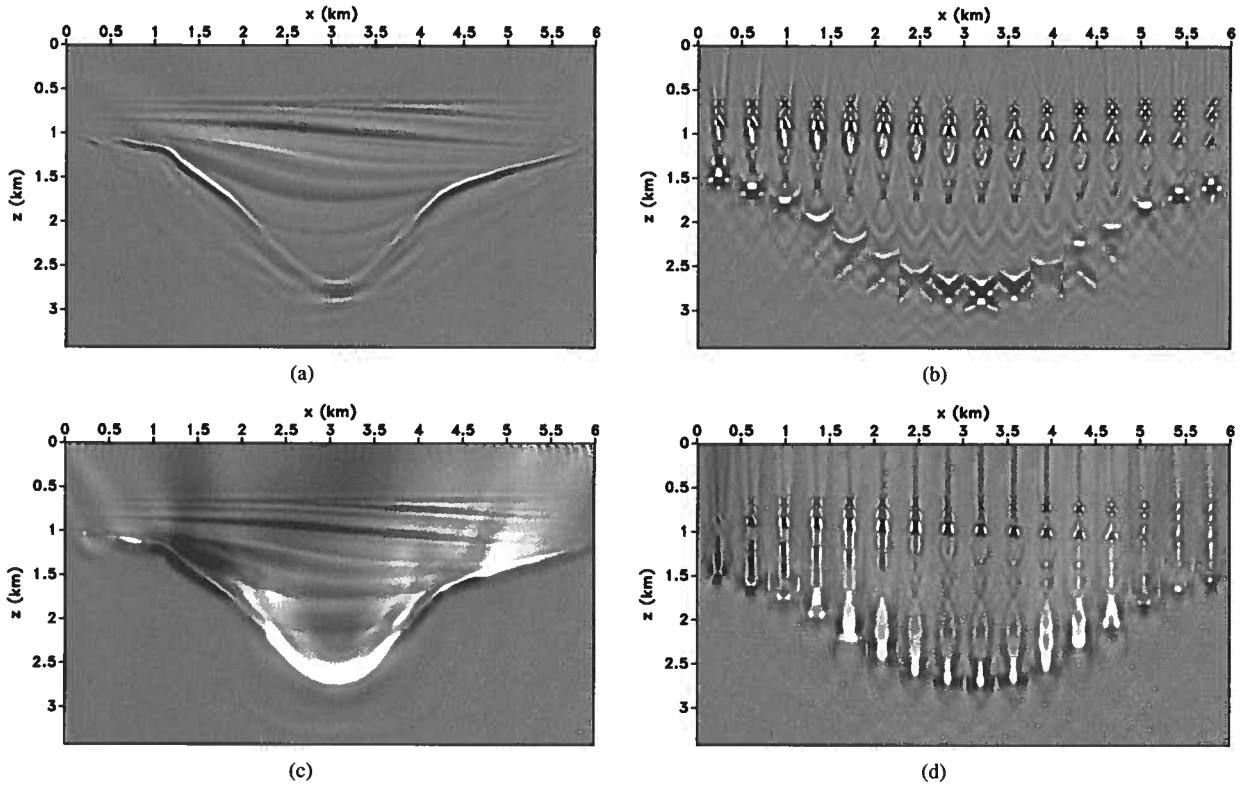

Figure 7. Imaging experiments using different velocities: (a) RTM and (b) space-lag gathers using fast sediment velocity from Figure 6(b), (c) RTM and (d) space-lag gathers using fast sediment velocity with salt flood from Figure 6(c).

physics, **72**, P47–P56.

McMechan, G. A., 1983, Migration by extrapolation of time-dependent boundary values: Geophysical Prospecting, **31**, 413–420.

Paffenholz, J., B. McLain, J. Zaske, and P. Keliher, 2002, Subsalt multiple attenuation and imaging: Observations from the Sigsbee 2B synthetic dataset: 72nd Annual International Meeting, SEG, Expanded Abstracts, 2122–2125.

Plessix, R.-E., 2006, A review of the adjoint-state method for computing the gradient of a functional with geophysical applications: Geophysical Journal International, **167**, 495–503.

Pratt, R. G., 1999, Seismic waveform inversion in the frequency domain, Part I: Theory and verification in a physical scale model: Geophysics, **64**, 888–901.

Rickett, J. E., and P. C. Sava, 2002, Offset and angle-domain common image-point gathers for shot-profile migration: Geophysics, **67**, 883–889.

Sava, P., and B. Biondi, 2004, Wave-equation migration velocity analysis - I: Theory: Geophysical Prospecting, **52**, 593–606.

Sava, P., and S. Fomel, 2006, Time-shift imaging condition in seismic migration: Geophysics, **71**, S209–S217.

Sava, P., and I. Vasconcelos, 2011, Extended imaging conditions for wave-equation migration: Geophysical Prospecting, **59**, 35–55.

Sava, P., and I. Vlad, 2011, Wide-azimuth angle gathers for wave-equation migration: Geophysics, **76**, S131–S141.

Sava, P. C., and S. Fomel, 2003, Angle-domain common-image gathers by wavefield continuation methods: Geophysics, **68**, 1065–1074.

Shen, P., and W. W. Symes, 2008, Automatic velocity analysis via shot profile migration: Geophysics, **73**, VE49–VE59.

Shen, P., W. W. Symes, and C. C. Stolk, 2003, Differential semblance velocity analysis by wave-equation migration: SEG Technical Program Expanded Abstracts, **22**, 2132–2135.

Stork, C., 1992, Reflection tomography in the postmigrated domain: Geophysics, **57**, 680–692.

Symes, W., and J. Carazzone, 1991, Velocity inversion by differential semblance optimization: Geophysics, **56**, 654–663.

Tarantola, A., 1984, Inversion of seismic reflection data in the acoustic approximation: Geophysics, **49**, 1259–1266.

Whitmore, N. D., 1983, Iterative depth migration by backward time propagation: SEG Technical Program Expanded Abstracts, **2**, 382–385.

Woodward, M., 1992, Wave-equation tomography: Geophysics, **57**, 15–26.

Yang, T., and P. Sava, 2010, Moveout analysis of wave-equation extended images: Geophysics, **75**, 151–161.

———, 2011a, Image-domain waveform tomography with

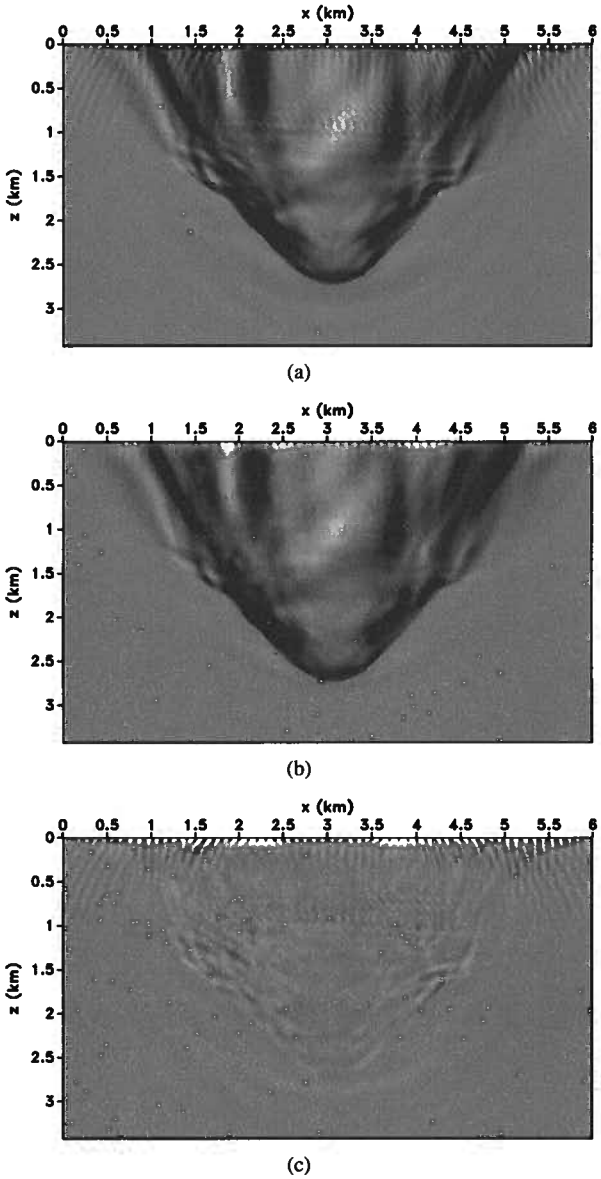

Figure 8. Gradients for salt model example using velocity in Figure 6(c): (a) gradient without filter, (b) gradient with directional filter, and (c) the difference.

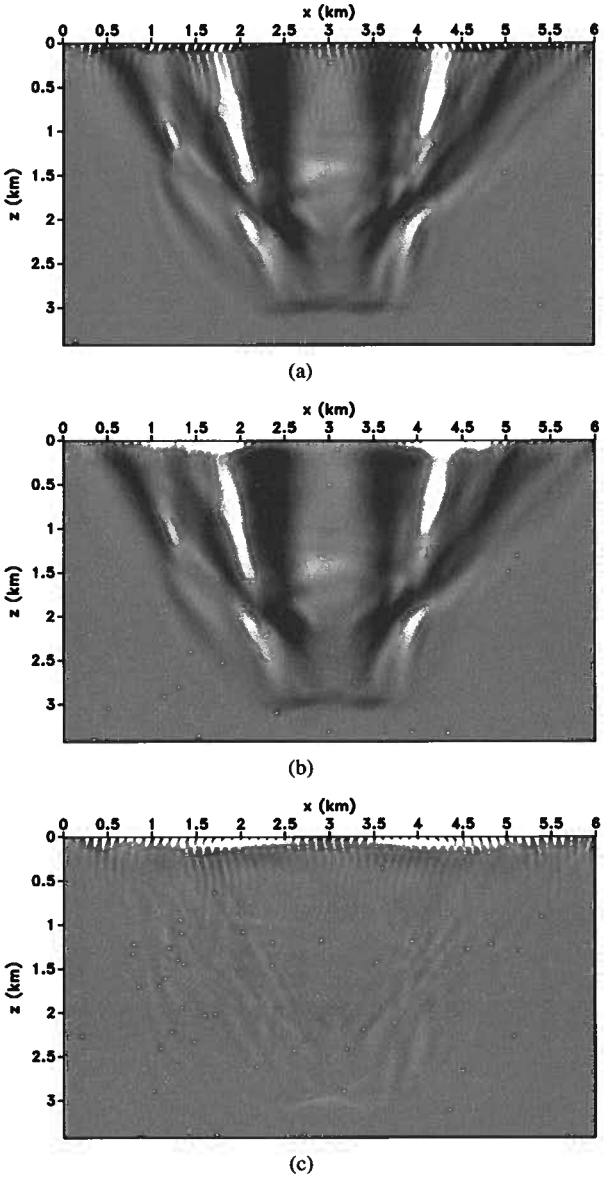

Figure 9. Gradients for salt model example using velocity in Figure 6(b): (a) gradient without filter, (b) gradient with directional filter, and (c) the difference.

two-way wave-equation: SEG Technical Program Expanded Abstracts 2011, **508**, 2591–2596.

———, 2011b, Wave-equation migration velocity analysis with time-shift imaging: Geophysical Prospecting, **59**, 635–650.

Yang, T., J. Shragge, and P. C. Sava, 2012, Illumination compensation for image-domain wavefield tomography: Submitted to Geophysics.

Yoon, K., K. J. Marfurt, and W. Starr, 2004, Challenges in reversetime migration: SEG Technical Program Expanded Abstracts, 1057–1060.

Youn, O. K., and H. Zhou, 2001, Depth imaging with multiples: Geophysics, **66**, 246–255.

Zhang, Y., and J. Sum, 2009, Practical issues in reverse time migration: true amplitude gathers, noise removal and harmonic source encoding: First Break, **27**, 53–59.

Separating traveltimes and amplitudes in waveform inversion

Simon Luo & Dave Hale
Center for Wave Phenomena, Colorado School of Mines, Golden, CO 80401, USA

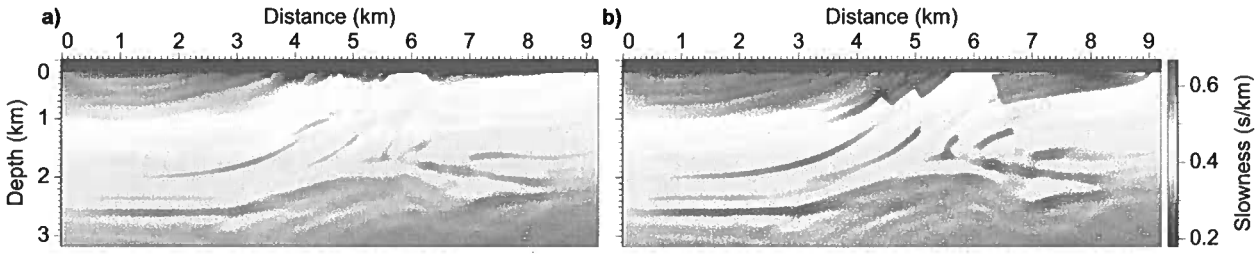

Figure 1. Slowness models computed with (a) conventional full waveform inversion and (b) full waveform inversion using an approximation of the data residual.

ABSTRACT

One difficulty in full waveform inversion is the requirement for an accurate initial model, which if not satisfied, can result in cycle skipping and convergence to local minima. Similarly, in least-squares migration, errors in the background model can lead to an incoherent, defocused image. These difficulties can be attributed in part to the fact that the data residual, the difference between simulated and observed data, contains error in both the smooth background model that affects traveltimes, as well as the rough reflectivity model that affects amplitudes. These two types of error are not treated equally in either full waveform inversion or in least-squares migration. To address this issue, we use an approximation of the data residual to separate traveltime and amplitude errors, and we show that the use of this approximation results in more accurate inversions for velocity in full waveform inversion, and better focused images in least-squares migration.

Key words: waveform inversion least-squares migration traveltime amplitude

1 INTRODUCTION

Iterative migration and inversion algorithms can produce high-resolution images and models of the subsurface. Such algorithms proceed by minimizing an objective function, e.g., a least-squares functional; and various methods exist for solving this optimization problem, including gradient descent and conjugate gradient methods, as well as Gauss-Newton, quasi-Newton, and full-Newton methods. Common to these methods is the computation of the gradient of the objective function with respect to model parameters, which is computed by applying a migration operator (Lailly, 1983; Tarantola, 1984) to a residual that depends on the choice of objective function. Clearly the choice of objective function is important, but from an algorithmic standpoint, the residual is the input to the computation of the gradient. So, it is interesting to investigate the influence of the residual in iterative migration and inversion algorithms.

In full waveform inversion (Lailly, 1983; Tarantola, 1984; Pratt et al., 1998) and least-squares migration (Nemeth et al., 1999; Dai, 2012), with a least-squares objective function, the residual is simply the data residual, i.e., the difference between simulated (modeled) and observed (recorded) data. As shown in Figure 1a, full waveform inversion is susceptible to cycle skipping and convergence to local minima, especially when the ini-

tial model is far from the true model, and simulated and observed data differ by more than one-half cycle. Least-squares migration faces a similar issue when the background velocity model used for migration contains errors, so that traveltimes in the simulated and observed data do not match. These issues arise partly from the fact that nonzero data residuals result from both traveltime and amplitude errors, but the different wavenumber components of the model responsible for these two types of error may be difficult to recover for any one inversion or migration algorithm. For example, least-squares migration inverts for a high-wavenumber reflectivity model; thus, it cannot recover the background model responsible for traveltime errors.

In this report, we use a simple approximation of the data residual when computing the gradient in least-squares migration and full waveform inversion. With this approximation, we can better separate traveltime errors, affected by the low-wavenumber component of the model, from amplitude errors, affected by the high-wavenumber component. We show that this separation can improve focusing and reflector continuity in migration images when the background model contains errors, and, as shown in Figure 1b, that it can also help mitigate cycle skipping and improve convergence in full waveform inversion.

2 LEAST-SQUARES MIGRATION

Migration can be described as the adjoint of a forward modeling operator applied to observed data (Claerbout, 1992). Migration produces a reflectivity image that approximates the true reflectivity insofar as the adjoint of the forward operator approximates the pseudoinverse. Thus, to obtain a more accurate reflectivity image, we require the pseudoinverse of the forward operator.

Least-squares migration (Nemeth et al., 1999; Østmo and Plessix, 2002; Plessix and Mulder, 2004; Kühl and Sacchi, 2003; Dai, 2012) can be described as the pseudoinverse of the forward operator applied to data. Direct application of the inverse operator requires the inverse of the Hessian matrix of second derivatives of an objective function with respect to model parameters, which is prohibitively expensive to compute for most practical-sized problems. Approximations of the inverse Hessian (Gray, 1997; Chavent and Plessix, 1999; Shin et al., 2001; Rickett, 2003; Guitton, 2004; Plessix and Mulder, 2004; Valenciano, 2008; Symes, 2008) are more feasible, and are often used to improve the quality of final migration images or to precondition iterative migration algorithms.

For least-squares migration, we assume a linear relation between data and model parameters. We separate the slowness model $s(\mathbf{x})$ into a smooth background model $s_0(\mathbf{x})$ and a rough reflectivity model

$$r(\mathbf{x}) = s(\mathbf{x})^2 - s_0(\mathbf{x})^2. \quad (1)$$

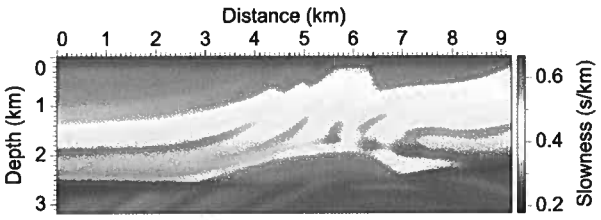

Figure 2. The background slowness model used in Born modeling and least-squares migration.

Then, assuming that wavefields satisfy the acoustic constant-density wave equation, we have, under the Born approximation, two forward modeling equations (Bleistein et al., 2001):

$$\left(s_0(\mathbf{x})^2 \frac{\partial^2}{\partial t^2} - \nabla^2\right) p_0(\mathbf{x}, t; \mathbf{x}_s) = f(t)\delta(\mathbf{x} - \mathbf{x}_s), \quad (2)$$

where $p_0(\mathbf{x}, t; \mathbf{x}_s)$ is the wavefield modeled in the smooth background for a point source with waveform $f(t)$ located at $\mathbf{x}_s$, and

$$\left(s_0(\mathbf{x})^2 \frac{\partial^2}{\partial t^2} - \nabla^2\right) p_1(\mathbf{x}, t; \mathbf{x}_s) = -r(\mathbf{x})\, \ddot{p}_0(\mathbf{x}, t; \mathbf{x}_s), \quad (3)$$

where $p_1(\mathbf{x}, t; \mathbf{x}_s)$ is the wavefield singly scattered by the reflectivity $r(\mathbf{x})$. In equation 3, the wavefield $p_1(\mathbf{x}, t; \mathbf{x}_s)$ is linear in the reflectivity $r(\mathbf{x})$. The solutions of equations 2 and 3 are, respectively,

$$p_0(\mathbf{x}, t; \mathbf{x}_s) = G_0(\mathbf{x}, t; \mathbf{x}_s) * f(t), \quad (4)$$

and

$$p_1(\mathbf{x}, t; \mathbf{x}_s) = -\int G_0(\mathbf{x}, t; \mathbf{x}') * r(\mathbf{x}')\, \ddot{p}_0(\mathbf{x}', t; \mathbf{x}_s)\, d\mathbf{x}', \quad (5)$$

where $G_0(\mathbf{x}, t; \mathbf{x}_s)$ is the Green's function satisfying equation 2 for $f(t) = \delta(t)$. Equation 5 is the Born modeling formula (Bleistein et al., 2001). Note that we do not compute $p_0(\mathbf{x}, t; \mathbf{x}_s)$ and $p_1(\mathbf{x}, t; \mathbf{x}_s)$ from equations 4 and 5, but instead use finite-difference approximations to solve equations 2 and 3.

Given observed data $\tilde{p}(\mathbf{x}_g, t; \mathbf{x}_s)$ recorded at receiver locations $\mathbf{x}_g$, we seek to invert for the reflectivity $r(\mathbf{x})$. We use a conjugate gradient method to minimize an objective function

$$J = \frac{1}{2} \sum_s \sum_g \int \left[p(\mathbf{x}_g, t; \mathbf{x}_s) - \tilde{p}(\mathbf{x}_g, t; \mathbf{x}_s)\right]^2 dt, \quad (6)$$

where $p(\mathbf{x}_g, t; \mathbf{x}_s)$ are the simulated data that depend on the model parameters. The gradient of the objective function in equation 6 with $p(\mathbf{x}_g, t; \mathbf{x}_s) \equiv p_1(\mathbf{x}_g, t; \mathbf{x}_s)$ is (Lailly, 1983; Tarantola, 1984; Plessix and Mulder, 2004)

$$\nabla_r J = -\sum_s \int \dot{p}_0(\mathbf{x}, t; \mathbf{x}_s) \dot{a}_0(\mathbf{x}, t; \mathbf{x}_s)\, dt, \quad (7)$$

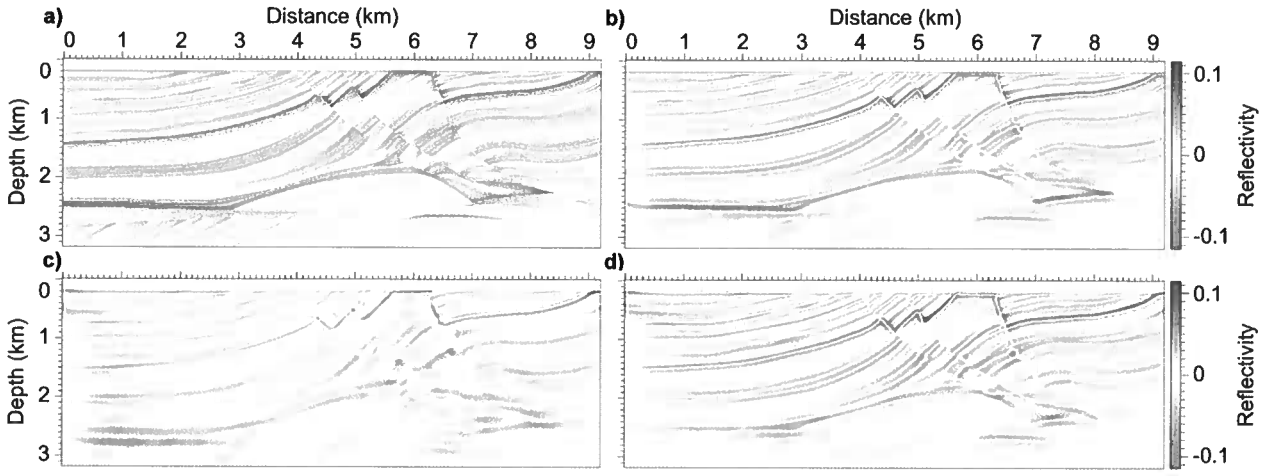

Figure 3. The (a) true reflectivity model, and reflectivity models computed using (b) least-squares migration for the true background slowness, (c) least-squares migration for the true background slowness scaled by 95%, and (d) least-squares migration using the amplitude residual (equation 11) for the true background slowness scaled by 95%.

where $a_0(\mathbf{x}, t; \mathbf{x}_s)$ is the adjoint state variable (Plessix, 2006; Symes, 2007) given by

$$a_0(\mathbf{x}, t; \mathbf{x}_s) = \sum_g G_0(\mathbf{x}, -t; \mathbf{x}_g) * \delta p(\mathbf{x}_g, t; \mathbf{x}_s), \quad (8)$$

where

$$\delta p(\mathbf{x}_g, t; \mathbf{x}_s) = p(\mathbf{x}_g, t; \mathbf{x}_s) - \tilde{p}(\mathbf{x}_g, t; \mathbf{x}_s), \quad (9)$$

are the data residuals. Thus, equation 7 corresponds to a migration of the residuals.

In migration, it is assumed that the smooth background model is correct, and hence that traveltimes in simulated data match those of observed data. If this assumption is satisfied, then any nonzero data residuals (equation 9) are due to differences in amplitude between simulated and observed data, and these differences in turn are due to errors in reflectivity. In this case, least-squares migration can recover an accurate reflectivity model. For example, Figure 3b shows the computed reflectivity model after 20 iterations of least-squares migration using the true background slowness model shown in Figure 2. The background slowness model shown in Figure 2 is obtained by smoothing the true slowness model (Figure 7a) with a two-sided exponential filter that approximates a Gaussian filter with a half-width of 100 m. The data used for migration are computed using 153 shots evenly spaced at the surface with receivers also at the surface, using a 10 Hz source function, which we assume is known. The reflectivity shown in Figure 3b matches well the true reflectivity shown in Figure 3a, because this is the ideal case in which the background slowness model used for migration is the true background slowness.

However, if the background model contains errors, then nonzero data residuals will result from both amplitude and traveltime errors in simulated data. Then, we should expect the image to be degraded, because least-squares migration inverts for reflectivity only. Reflectivity does not directly affect the kinematics of wave propagation, and thus least-squares migration cannot correct for traveltime errors. This degradation can be seen in Figure 3c, which shows the reflectivity model after 20 iterations of least-squares migration using an incorrect background slowness model, specifically, the true background slowness (Figure 2) scaled by 95%. Compared to the reflectivity computed for the true background slowness (Figure 3b), reflectors are misplaced and are generally less focused and less continuous as a result of traveltime errors in the simulated data.

The sensitivity of least-squares migration to errors in the background model has been noted by others (e.g., Dai et al., 2011; Yousefzadeh and Bancroft, 2012), and efforts have been made to reduce this sensitivity. For example, some authors use the flatness of common-image gathers as a regularization constraint in least-squares migration (Gerard Schuster, personal communication). Other approaches might involve data- or model-domain preconditioning to mitigate the effects of large traveltime errors.

We propose a simple approach, which is to modify the data residual used when computing the gradient of the objective function. Our goal in this modification is to distinguish terms in the residual due to amplitude errors from terms due to traveltime errors. With this goal in mind, we expand the observed data $\tilde{p}(\mathbf{x}_g, t; \mathbf{x}_s)$ about time $t + \tau$, where τ are the traveltime shifts between simulated and observed data:

$$\tilde{p}(\mathbf{x}_g, t; \mathbf{x}_s) = \tilde{p}(\mathbf{x}_g, t+\tau; \mathbf{x}_s) - \tau \dot{\tilde{p}}(\mathbf{x}_g, t+\tau; \mathbf{x}_s) + O(\tau^2). \quad (10)$$

Then, because we assume in migration that the background model affecting the kinematics of wave propa-

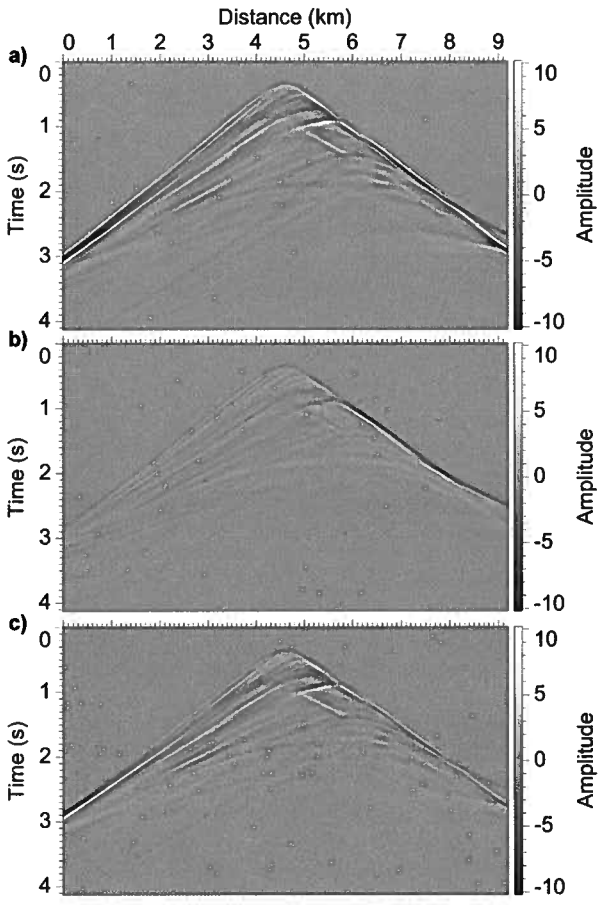

Figure 4. The (a) observed data computed using the true background slowness shown in Figure 2 and true reflectivity shown in Figure 3a for a source located at distance 4.6 km, (b) simulated data computed using the true background slowness scaled by 95% and reflectivity shown in Figure 3c, and (c) simulated data computed using the true background slowness scaled by 95% and reflectivity shown in Figure 3d. Note the similarity in amplitude between the observed data (a) and simulated data (c).

gation is known, i.e., that traveltime shifts τ are small, we drop $O(\tau)$ and higher terms in equation 10, and use

$$\delta p(\mathbf{x}_g, t; \mathbf{x}_s) \approx p(\mathbf{x}_g, t; \mathbf{x}_s) - \tilde{p}(\mathbf{x}_g, t + \tau; \mathbf{x}_s), \quad (11)$$

for the residual (instead of equation 9) when computing the gradient in least-squares migration. Equation 11 is a poor approximation when the traveltime shifts τ between simulated and observed data are large; however, note that if the traveltime shifts are estimated correctly, then any nonzero residuals in equation 11 are caused by errors in reflectivity. So, it is natural to use equation 11 in least-squares migration since we invert for (only) reflectivity.

We refer to equation 11 as the *amplitude residual*, as it ideally contains only amplitude errors. Computation of the amplitude residual requires estimating the traveltime shifts τ between simulated and observed data. For the examples in this report, we use dynamic warping (Hale, 2013) to estimate these shifts. Compared to local crosscorrelation, dynamic warping is less sensitive to cycle skipping, and estimated shifts are more accurate, especially when the shifts vary rapidly in time.

Figure 3d shows the reflectivity model after 20 iterations of least-squares migration using the amplitude residual (equation 11) to compute the gradient. Compared to the conventional least-squares migration image shown in Figure 3c, reflectors are more continuous and better focused. However, compared to the image for the true background slowness (Figure 3b), we see some discrepancies, most noticeably the mispositioning of reflectors in depth. This mispositioning is not surprising, because the incorrect background slowness model is never corrected in least-squares migration. Therefore, least-squares migration with an incorrect background model will result in misplaced reflectors, along with other migration artifacts. Nevertheless, with least-squares migration using the amplitude residual (Figure 3d), imaged reflectors are more continuous and better focused than for conventional least-squares migration (Figure 3c).

Finally, we compare data modeled using the different reflectivities shown in Figure 3, for a source located at distance 4.6 km. Figure 4a shows the observed data modeled using the true background slowness (Figure 2) and the true reflectivity (Figure 3a), Figure 4b shows the simulated data modeled using the true background slowness scaled by 95% and the reflectivity computed using least-squares migration (Figure 3c), and Figure 4c shows the simulated data modeled using the true background slowness scaled by 95% and the reflectivity computed using least-squares migration using the amplitude residual (Figure 3d). Compared with Figure 4b, the amplitudes in Figure 4c more closely match the amplitudes of the observed data (Figure 4a). However, large traveltime shifts remain between the observed data shown in Figure 4a and the simulated data shown in Figure 4c.

3 FULL WAVEFORM INVERSION

In full waveform inversion (Lailly, 1983; Tarantola, 1984; Pratt et al., 1998), we invert for slowness rather than reflectivity. For this reason, full waveform inversion can potentially recover both high- and low-wavenumber components of the slowness model, and thus can correct for both amplitude and traveltime errors between simulated and observed data.

As before, we solve the acoustic constant-density wave equation

$$\left(s(\mathbf{x})^2 \frac{\partial^2}{\partial t^2} - \nabla^2\right) p(\mathbf{x}, t; \mathbf{x}_s) = f(t)\delta(\mathbf{x} - \mathbf{x}_s), \quad (12)$$

to model the wavefield $p(\mathbf{x}, t; \mathbf{x}_s)$. Using the same least-

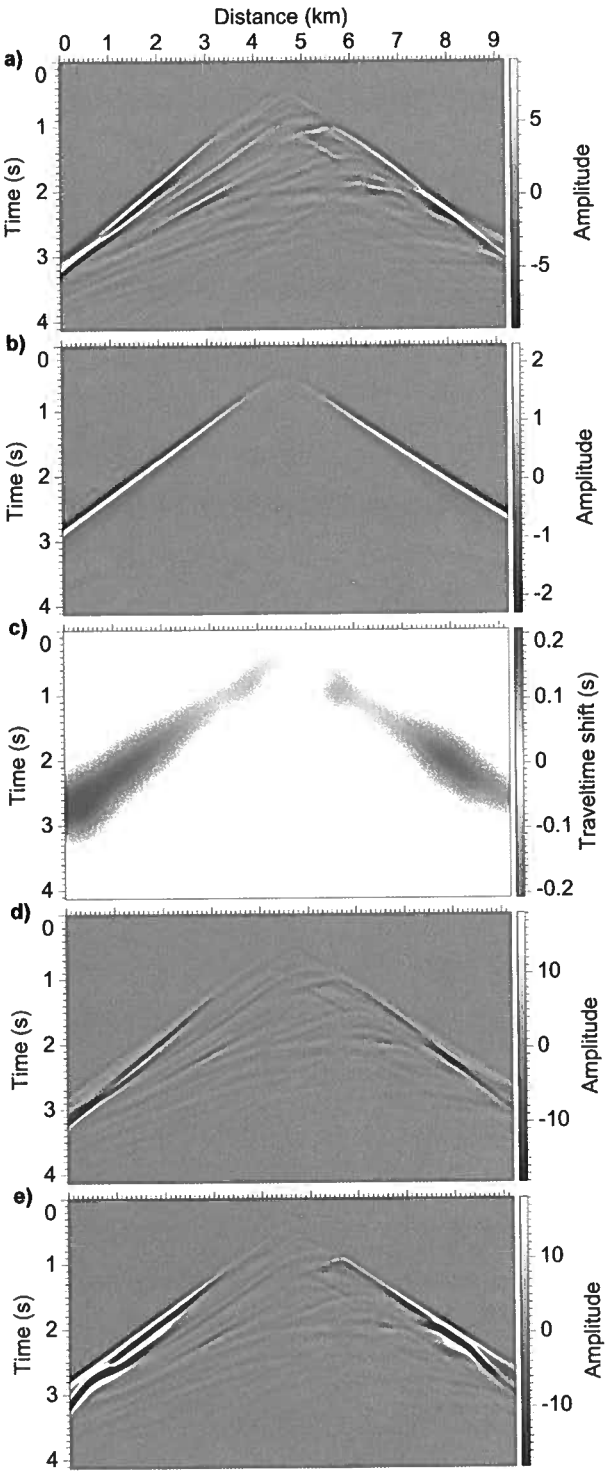

Figure 5. The (a) observed data computed using the true slowness model shown in Figure 7a for a source located at 4.6 km, (b) simulated data computed using the initial slowness model shown in Figure 7b, (c) estimated traveltime shifts between simulated and observed data, (d) data residual, and (e) combined residual.

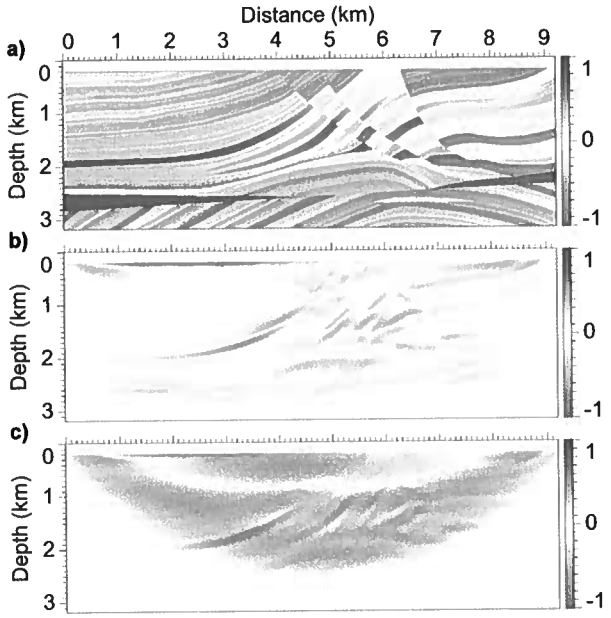

Figure 6. The (a) normalized difference between the initial and true models, (b) gradient for the first iteration of full waveform inversion, and (c) gradient for the first iteration of full waveform inversion using the combined residual (equation 14).

squares objective function (equation 6), the gradient is given by

$$\nabla_s J = -2\, s(\mathbf{x}) \sum_s \int \dot{p}(\mathbf{x}, t; \mathbf{x}_s) \dot{a}(\mathbf{x}, t; \mathbf{x}_s)\, dt, \qquad (13)$$

where $p(\mathbf{x}, t; \mathbf{x}_s)$ and $a(\mathbf{x}, t; \mathbf{x}_s)$ are defined analogously to equations 4 and 8 with $G_0(\mathbf{x}, t; \mathbf{x}_s)$ replaced by $G(\mathbf{x}, t; \mathbf{x}_s)$, the Green's function for equation 12, and likewise for the receiver-side Green's function.

Unlike in least-squares migration, in full waveform inversion we expect both amplitude and traveltime errors between simulated and observed data. For this reason, here we keep the $O(\tau)$ term in equation 10, and thus use

$$\begin{aligned} \delta p(\mathbf{x}_g, t; \mathbf{x}_s) \approx\ & p(\mathbf{x}_g, t; \mathbf{x}_s) \\ & -\tilde{p}(\mathbf{x}_g, t+\tau; \mathbf{x}_s) + \tau\, \dot{\tilde{p}}(\mathbf{x}_g, t+\tau; \mathbf{x}_s). \end{aligned} \qquad (14)$$

for the residual when computing the gradient in full waveform inversion. We refer to this residual (equation 14) as the *combined residual*, since it combines the amplitude residual (equation 11) with a traveltime-like residual.

An example of the combined residual is shown in Figure 5. The source function is a Ricker wavelet with 5 Hz peak frequency. Figure 5a shows the observed data modeled in the true slowness model shown in Figure 7a; Figure 5b shows the simulated data modeled in the initial slowness model shown in Figure 7b; Figure 5c shows the traveltimes shifts between simulated

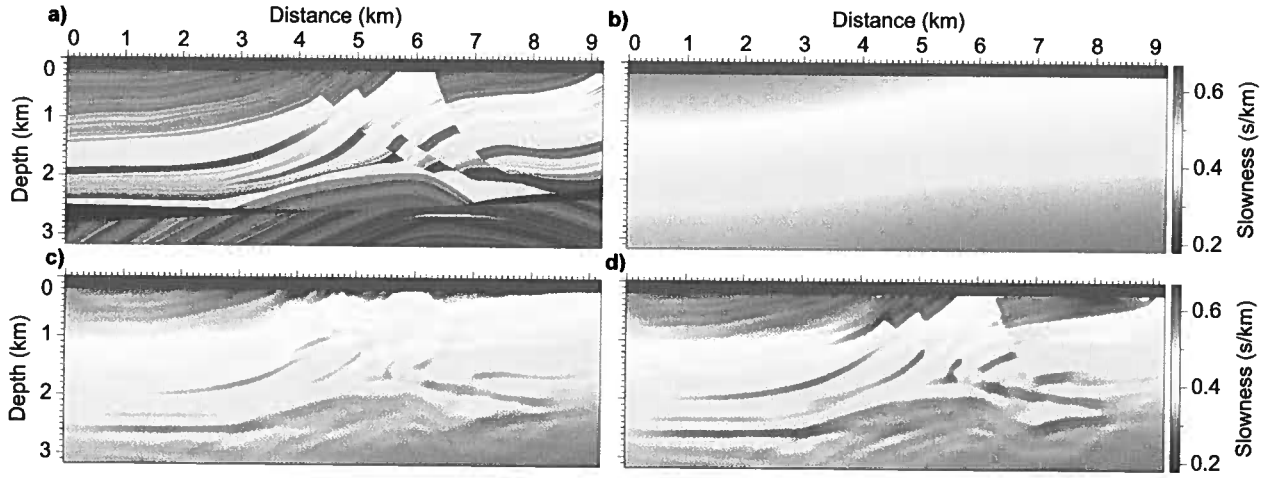

Figure 7. The (a) true slowness, (b) initial slowness, (c) slowness computed with conventional full waveform inversion, and (d) slowness computed with full waveform inversion using the combined residual (equation 14).

and observed data, estimated using dynamic warping; Figure 5d shows the data residual (equation 9); and Figure 5e shows the combined residual (equation 11). Note the similarity between Figures 5d and 5e, except for the early arrivals, which have larger amplitude in Figure 5e because of the large traveltime shifts between the first arrivals in the simulated and observed data. Despite this similarity, however, gradients computed using these two residuals show significant differences.

Gradients computed with 77 shots evenly spaced at the surface and with receivers also at the surface are shown in Figures 6b and 6c. Figure 6a shows the normalized difference between the initial slowness model shown in Figure 7b and the true slowness model shown in Figure 7a, and thus indicates the ideal gradient direction. Figure 6b shows the gradient for the first iteration of full waveform inversion computed using the data residual (Figure 5d), while Figure 6c shows the gradient for the first iteration computed using the combined residual (Figure 5e). Comparing Figures 6a and 6b, notice in some areas the difference in sign, which may result in slow convergence for full waveform inversion. Comparing Figures 6b and 6c, notice that the gradient computed using the combined residual contains more low-wavenumber information. When the initial model is far from the true model, as is the case for this example, the traveltime-like term in the combined residual will tend to dominate due to large traveltime shifts between simulated and observed data. As a result, the gradient will compensate mostly for traveltime errors, hence the low-wavenumber content in the gradient in Figure 6c. Once the kinematics are corrected and the traveltime shifts decrease, the amplitude residual will become more significant, and the gradient will begin to correct for amplitude errors caused by the high-wavenumber component of the model. In this way, the inversion tends to first update the low-wavenumber component of the model before updating the high-wavenumber component.

Figure 7 shows the results of the inversion. Figure 7a shows the true slowness model, which we seek to recover from the initial slowness shown in Figure 7b. Figure 7c shows the computed slowness model after 20 iterations of full waveform inversion, while Figure 7d shows the slowness model after 20 iterations of full waveform inversion using the combined residual (equation 14). Compared to Figure 7c, Figure 7d is closer to the true slowness, especially in shallow areas of the model. The improvement in Figure 7d is most noticeable in shallow areas because it is difficult to use reflection energy to update the low-wavenumber component of the model. To more effectively use reflection energy, one could alternately update the high- and low-wavenumber components of the model (Xu, 2012; Ma, 2012).

4 CONCLUSION

Using an approximation of the data residual, we are able to separate traveltime errors, due to an incorrect background model, from amplitude errors, due to an incorrect reflectivity model. We have demonstrated that the use of this approximation in computing the gradient of the objective function yields more coherent and better focused images in least-squares migration, and more accurate slowness models in full waveform inversion.

The result of using the amplitude residual in least-squares migration is a more focused reflectivity model (migration image), and forward modeling using this reflectivity model produces simulated data that match well the amplitudes of observed data, but not the traveltimes. These remaining traveltime errors indicate that the use of the amplitude residual in least-squares migration does not minimize the difference between simulated

and observed data. However, if our goal is to obtain a focused image, then perhaps minimizing that data difference is not the best approach.

In the case of full waveform inversion, using the combined residual results in a more accurate slowness model. This might suggest that, compared to the data residual, the combined residual minimizes an objective function that is more quadratic and contains fewer local minima. Also worth noting is that if there are no traveltime errors between simulated and observed data, then the combined residual equals the data residual. Thus, full waveform inversion using the combined residual could potentially achieve the same resolution as conventional full waveform inversion, in addition to being less susceptible to cycle skipping and local minima.

One remaining issue is that, because we approximated the data residual without considering the objective function, it is unclear what objective function is being minimized with either the amplitude residual or the combined residual. For small traveltime shifts, our approximation of the data residual is more valid, and the objective function could simply be the least-squares function. But for the examples shown, the traveltime shifts were relatively large. Nevertheless, the use of an approximation of the data residual improved the models computed using least-squares migration and full waveform inversion.

ACKNOWLEDGMENT

This research was supported by the sponsors of the Consortium Project on Seismic Inverse Methods for Complex Structures.

REFERENCES

Bleistein, N., J. K. Cohen, and J. W. Stockwell, Jr., 2001, Mathematics of multidimensional seismic imaging, migration, and inversion: Springer-Verlag New York, Inc.

Chavent, G., and R. Plessix, 1999, An optimal true-amplitude least-squares prestack depth-migration operator: Geophysics, **64**, 508–515.

Claerbout, J. F., 1992, Earth soundings analysis: Processing versus inversion: Blackwell Scientific Publications.

Dai, W., 2012, Multisource least-squares reverse time migration: PhD thesis, King Abdullah University of Science and Technology.

Dai, W., X. Wang, and G. T. Schuster, 2011, Least-squares migration of multisource data with a deblurring filter: Geophysics, **76**, R135–R146.

Gray, S., 1997, True amplitude migration: a comparison of three approaches: Geophysics, **62**, 929–936.

Guitton, A., 2004, Amplitude and kinematic corrections of migrated images for nonunitary imaging operators: Geophysics, **69**, 1017–1024.

Hale, D., 2013, Dynamic warping of seismic images: Geophysics, **78**, S105–S115.

Kühl, H., and M. D. Sacchi, 2003, Least-squares wave-equation migration for AVP/AVA inversion: Geophysics, **68**, 262–273.

Lailly, P., 1983, The seismic inverse problem as a sequence of before stack migration: Conference on Inverse Scattering: Theory and Applications, SIAM, 206–220.

Ma, Y., 2012, Waveform-based velocity estimation from reflection seismic data: PhD thesis, Colorado School of Mines.

Nemeth, T., C. Wu, and G. T. Schuster, 1999, Least-squares migration of incomplete reflection data: Geophysics, **64**, 208–221.

Østmo, S., and R.-E. Plessix, 2002, Finite-difference iterative migration by linearized waveform inversion in the frequency domain: 72nd Annual International Meeting, SEG, Expanded Abstracts.

Plessix, R.-E., 2006, A review of the adjoint-state method for computing the gradient of a functional with geophysical applications: Geophysical Journal International, **167**, 495–503.

Plessix, R.-E., and W. A. Mulder, 2004, Frequency-domain finite-difference amplitude-preserving migration: Geophysical Journal International, **157**, 975–987.

Pratt, G., C. Shin, and G. Hicks, 1998, Gauss-newton and full newton methods in frequency-space seismic waveform inversion: Geophysical Journal International, **113**, 341–462.

Rickett, J. E., 2003, Illumination-based normalization for wave-equation depth migration: Geophysics, **68**, 1371–1379.

Shin, C., S. Jang, and D. J. Min, 2001, Improved amplitude preservation for prestack depth migration by inverse scattering theory: Geophysical Prospecting, **49**, 592–606.

Symes, W. W., 2007, Reverse time migration with optimal checkpointing: Geophysics, **72**, SM213–SM221.

———, 2008, Approximate linearized inversion by optimal scaling of prestack depth migration: Geophysics, **73**, R23–R35.

Tarantola, A., 1984, Inversion of seismic reflection data in the acoustic approximation: Geophysics, **49**, 1259–1266.

Valenciano, A., 2008, Imaging by wave-equation inversion: PhD thesis, Stanford University.

Xu, S., 2012, Full waveform inversion for reflected seismic data: 74th EAGE Conference and Exhibition, Extended Abstracts.

Yousefzadeh, A., and J. C. Bancroft, 2012, Velocity evaluation using least squares prestack migration: 82nd Annual International Meeting, SEG, Expanded

Abstracts.

Image warping waveform tomography

Francesco Perrone and Paul Sava
Center for Wave Phenomena, Colorado School of Mines

ABSTRACT

Imaging the change in physical parameters in the subsurface requires an estimate of the long wavelength component of the same parameters in order to reconstruct the kinematics of the waves propagating in the subsurface. The model is unknown and must be estimated from the same data. One can try to reconstruct the method by matching the recorded data with modeled waveforms extrapolated in a trial model of the medium. Alternatively, assuming a trial model, one can obtain a set of images of the reflectors from a number of seismic experiments and match the locations of the imaged interfaces. Apparent displacements between migrated images contain information about the velocity model and can be used for velocity analysis. A number of methods are available to estimate the displacement between images; in this paper we compare penalized local correlations and image warping. We show that the image warping vector field is a more reliable tool for estimating displacements between migrated images and leads to a more robust velocity analysis procedure. Using image warping, we define an optimization problem for migration velocity analysis. We derive the expressions for the objective function using the adjoint-method and we also propose an alternative, simpler solution for the computation of the model update based on the estimated perturbation of the imaged reflectivity and demigration. The second approach has straightforward implementation and reduced computational cost compared to the adjoint-state method calculations. We also discuss the weakness of migration velocity analysis in the migrated-shot domain in the case of highly refractive media, when the Born modeling operator is far from being unitary and thus its adjoint operator (the migration operator) poorly approximates the inverse.

1 INTRODUCTION

Accurate propagation velocities in the subsurface are crucial in seismic imaging and exploration geophysics. A kinematically accurate velocity model allows us to correctly reconstruct Green functions and thus precisely image the subsurface discontinuities responsible for the data acquired at the surface or in boreholes. An accurate image of the geologic structure is key for planning drilling operations and for reducing hazards associated with drilling through faults. Seismic propagation velocities are sensitive to the stress conditions in the subsurface and carry information about the orientation of the principal stresses and overpressures (Carcione, 2007), which are both important for mitigating hazards during drilling operations and reducing risk in production.

In recent years, a main distinction has been drawn between methods that try to recover the velocity model by matching the recorded data with simulated synthetic wavefields modeled in a trial velocity model (Tarantola, 1984; Pratt, 1999; Sirgue and Pratt, 2004), and methods that focus on optimizing properties of the migrated images (Fowler, 1985; Faye and Jeannot, 1986; Al-Yahya, 1989; Chavent and Jacewitz, 1995; Biondi and Sava, 1999; Sava et al., 2005; Albertin et al., 2006). Full-waveform inversion is the name used to indicate techniques that operate in the data domain and focus on the minimization of some functional of the data residual. Migration velocity analysis, or image-domain tomography, identifies all methods that reconstruct the velocity model by analyzing the similarity between migrated images.

Full-waveform inversion is simple to implement, but it is very sensitive to every inconsistency between the recorded and modeled data. It requires an accurate parametrization of the physics of wave propagation, knowledge of the source signature, and a kinematically reliable starting model in order to converge to the global minimum of the objective function (Santosa and Symes, 1989; Kelly et al., 2010). Migration velocity analysis is not as sensitive to errors in the source signature and it is more robust against errors in the initial velocity model; it is characterized by an objective function which is convex over a wide range of model perturbations and thus intrinsically more suitable for gradient-based optimization procedures. Nonetheless, as it ignores the amplitude information in the data for inversion purposes, migration velocity analysis cannot achieve the high-resolution results that full-waveform inversion promises in the ideal scenario. Migration velocity analysis is conventionally used to produce a kinematically accurate model to initialize full-waveform inversion for refining the velocity with high-resolution details.

Image-domain tomography has advantages and disadvantages compared to the data-domain full-waveform inversion. In general, the image domain is more robust against errors in the velocity model. Full-waveform inversion needs a kinematically accurate initial guess of the model parameters in order to converge to geologically plausible models. Image-domain tomography recovers the long wavelength component of the model, which is responsible for the wave kinematics. Since it aims to match the observed data with simulated waveforms, full-waveform inversion is rather sensitive to the source signature; on the contrary, the image domain is insensitive to the source wavelet. On the other hand, the data-domain allows us to achieve higher resolution in the inversion result. Moreover, in extremely refractive media, single-shot migrated images can be contaminated by kinematic artifacts due to the fact that migration is just the adjoint, and not an inverse, of a modeling operator (Stolk and Symes, 2004). In this work, we are interested in the reconstruction of the long wavelength component of the model parameters and thus we focus on image-domain tomography.

This paper deals with the estimation of the velocity model using image warping. Perrone et al. (2012) show how the apparent displacement field estimated between two images can be used to measure velocity errors with a minimum number of migrated images. Perrone et al. (2012) also derive an approximation for the image perturbation based on the estimated displacement field and design a linearized wave-equation migration velocity analysis algorithm based on the method developed by Sava and Biondi (2004). The method presented in Perrone et al. (2012) relies on several approximations and linearizations: the wave-equation migration velocity analysis operator is obtained from the phase-shift continuation operator and several linearizations with respect to the wavefield and wavenumber (Born approximation). The entire inversion procedure stems from the particular form of the extrapolation operator that allows one to derive a linearized operator which links perturbation in the image space to perturbation in the model (slowness) parameters. Because of the strong assumption of a phase-shift continuation wave-extrapolator, this method cannot be applied to images obtained using different engines (for example, with reverse-time migration). Moreover, events that are not correctly handled by the extrapolation operator (for example, diving waves and overturning reflections) become noise for the inversion scheme.

In order to generalize the wave-equation migration velocity analysis method for nonlinear inversion, Perrone and Sava (2012) propose an image-domain wavefield tomography approach where the residual is computed from estimates of local shifts between migrated images. The shifts are obtained from penalized local correlations of images from nearby experiments. The gradient of the objective function is computed using the adjoint-state method and thus a local gradient-based nonlinear inversion scheme is implemented. The method presented in Perrone and Sava (2012) involves the solution of the full two-way wave equation and thus integrates reverse-time migration into the inversion procedure. The method shows weak points when reflectors are located near the acquisition surface (where the distance between the shot positions becomes an important illumination issue) and when several reflectors fall inside the same local window, thus biasing the computation of the local correlations through the crosstalk between the closely spaced events. In contrast, the displacement vector field appears to be a more stable and reliable measure of image variation: the displacement vectors can be computed using the algorithm developed by Hale (2007b) as an iterative procedure searching for the maximum of local correlations, thus leading to a smooth estimate of the displacement vectors.

In this paper, we extend the linearized wave-equation migration velocity analysis algorithm of Perrone et al. (2012) to incorporate a two-way extrapolation engine and to directly exploit the displacement field. The displacement vector field is used to estimate an image perturbation, then through single scattering Born modeling, the wavefield perturbation due to the image perturbation is computed. The correlation between the scattered and background wavefields represents the gradient of the objective function, which is the kernel for the model update. We compare the objective function based on the image perturbation with the objective function based on local image correlations (Perrone and Sava, 2012) and show that the displacement field leads to a robust objective function and model update. For comparison, we also derive the equations for the computation of the gradient of the objective function using the adjoint-state method and show that the greater complexity and computational cost does not produce a higher quality gradient.

2 THEORY

Perrone et al. (2012) introduce a measure of velocity error for migration velocity analysis exploiting the consistency between the orientation of the structural features in the image and the apparent displacement between two migrated images. The error measure $\mathcal{J}$ is the energy of the projection of the displacement vector $\mathbf{u}(\mathbf{x})$ onto the dip vector $\boldsymbol{\nu}(\mathbf{x})$

$$\mathcal{J}(m) = \frac{1}{2} \left\| \boldsymbol{\nu} \cdot \mathbf{u} \right\|^2, \tag{1}$$

where $m(\mathbf{x})$ represents the model parameter (slowness, slowness squared, or velocity) as a function of position $\mathbf{x}$. The dip vector $\boldsymbol{\nu}(\mathbf{x})$ is defined as the vector normal to the structure at position $\mathbf{x}$, and the displacement vector $\mathbf{u}(\mathbf{x})$ is also a function of the position vector $\mathbf{x}$. The dip vector $\boldsymbol{\nu}$ can be computed using the algorithm presented in Hale (2007a) and based on gradient square tensors (van Vliet and Verbeek, 1995). Displacement vectors $\mathbf{u}$ are obtained by iterative search of the maximum of local correlations and warping of the input images; the method, first applied to measuring the apparent shift between migrated images in 4D seismic processing, is described in detail in Hale (2007b).

Both the dip and the displacement vectors depend nonlinearly on the model parameters. The dip vector depends nonlinearly on the migrated image, since we need to compute the eigenvector associated with the largest eigenvalue of the gradient square tensor in order to obtain an estimate of the dip vector (van Vliet and Verbeek, 1995). The displacement vector

field is obtained by picking the correlation lag that maximizes the local correlation panels:

$$\mathbf{u}(\mathbf{x}) = \arg\max_{\boldsymbol{\lambda}} c(\mathbf{x}, \boldsymbol{\lambda}), \tag{2}$$

where $c(\mathbf{x}, \boldsymbol{\lambda}) = \int_{w(\mathbf{x})} R_i\left(\boldsymbol{\xi} - \frac{\boldsymbol{\lambda}}{2}\right) R_{i+1}\left(\boldsymbol{\xi} + \frac{\boldsymbol{\lambda}}{2}\right) d\boldsymbol{\xi}$ is the local correlation of two images $R_i = R_i(\mathbf{x})$ and $R_{i+1} = R_{i+1}(\mathbf{x})$, and $w(\mathbf{x})$ is are seamless overlapping windows. The arg max operator is not differentiable and thus we cannot compute the Frechét derivative with respect to the model parameters directly.

Perrone et al. (2012) show that, for optimization purposes, it is possible to substitute the dip vector field in equation 1 with the gradient of the migrated image, the latter being at every point parallel to the dip field and oriented toward the direction of maximum increase in the image amplitude. The objective function then becomes

$$\mathcal{J}(m) = \frac{1}{2}\|\nabla R \cdot \mathbf{u}\|^2. \tag{3}$$

Substituting the dip field with the image gradient has the advantage of introducing in equation 3 quantities (the gradient of the migrated images) that we can easily differentiate with respect to the model parameters using standard perturbation theory techniques and thus enable a gradient-based optimization algorithm.

In this paper, we discuss two possible approaches for minimizing equation 3. The first solution is to use the adjoint-state method (Lions, 1972; Fichtner et al., 2006) and can be considered the brute-force approach. The second solution is based on demigration of the residual $\nabla R \cdot \mathbf{u}$, which is interpreted as the mismatch between the updates of the small wavelengths of the model parameters obtained from adjacent shots. This second approach is related to the work of Xu et al. (2012), who follow a two-step, migration/demigration procedure to better condition FWI for reflection data. Another work on a similar path is the differential waveform inversion presented by Chauris and Plessix (2012) again in the framework of FWI. Here, we set up the problem in the image domain, i.e. in the framework of migration velocity analysis. The demigration approach reduces the computational cost and complexity with respect to the adjoint-state calculations and greatly simplifies the implementation and the physical interpretation of the method. Of course, since we are approximating the image difference with our image warping procedure and we are not constructing the exact gradient for the objective function in equation 3, we are introducing a systematic error in the procedure. The exact quantification of this error requires the comparison with the exact gradient obtained via the adjoint-state method.

2.1 Direct adjoint-state calculations for vector displacements

Let us consider equation 3; we can write the gradient of the objective function as follows:

$$\begin{aligned}\nabla_m \mathcal{J} &= \frac{\partial}{\partial m}\frac{1}{2}(\nabla R \cdot \mathbf{u})^2 \\ &= (\nabla R \cdot \mathbf{u})\left(\frac{\partial \nabla R}{\partial m} \cdot \mathbf{u} + \nabla R \cdot \frac{\partial \mathbf{u}}{\partial m}\right),\end{aligned} \tag{4}$$

in this paper $m(\mathbf{x})$ represents slowness squared. The gradient in equation 4 consists of two terms. The term $\frac{\partial \nabla R}{\partial m} \cdot \mathbf{u}$ involves a linear function of the image; the term $\nabla R \cdot \frac{\partial \mathbf{u}}{\partial m}$ involves a nonlinear function of the image, because the apparent displacement is estimated as the maximum argument of local image correlations (equation 2). Although lengthy, the adjoint-state calculations for the first part of the gradient are straightforward because of the linearity between ∇R and R; more complicated is the second term because the nonlinear and non differentiable arg max function does not allow an immediate application of the adjoint state method. Perrone and Sava (2012) avoid the complications of computing the differential of arg max by defining a measure of shifts through penalized local image correlations. The correlation operator is (bi)linear in the input images and allows one to derive directly the adjoint-state equation to compute the gradient with respect to the model parameters.

Using standard perturbation theory we can write

$$\begin{aligned}\mathcal{J} + \delta\mathcal{J} &= \frac{1}{2}\int (\nabla(R + \delta R) \cdot (\mathbf{u} + \delta\mathbf{u}))^2 \, d\mathbf{x} \\ &= \frac{1}{2}\int ((\nabla R + \nabla\delta R) \cdot (\mathbf{u} + \delta\mathbf{u}))^2 \, d\mathbf{x}.\end{aligned} \tag{5}$$

Expanding the products and identifying the terms that are linear in the perturbations in equation 5, we obtain

$$\begin{aligned}\delta\mathcal{J} &= \delta\mathcal{J}^{\nabla\delta R} + \delta\mathcal{J}^{\delta\mathbf{u}} \\ &= \int (\nabla R \cdot \mathbf{u})(\nabla\delta R \cdot \mathbf{u}) \, d\mathbf{x} \\ &+ \int (\nabla R \cdot \mathbf{u})(\nabla R \cdot \delta\mathbf{u}) \, d\mathbf{x}.\end{aligned} \tag{6}$$

The objective function perturbation in equation 6 consists of two terms: $\mathcal{J}^{\nabla\delta R}$ involves the perturbation of the image gradient, $\delta\mathcal{J}^{\delta\mathbf{u}}$ depends on the perturbation of the displacement. In the context of velocity analysis, the perturbations δR and $\delta\mathbf{u}$ depend on the the change in model parameters m. To derive an expression for the gradient of the objective function with respect to the model parameters, we need to relate the objective function perturbation to wavefield perturbations. Then, using standard adjoint-techniques, we can obtain the gradient of the objective function without actually computing the Frechét derivatives of the wavefield with respect to the model parameters (Fichtner et al., 2006). In the following, we analyze both terms $\delta\mathcal{J}^{\nabla\delta R}$ and $\delta\mathcal{J}^{\delta\mathbf{u}}$ and express them directly in terms of wavefield perturbations.

Let us start with $\delta\mathcal{J}^{\nabla\delta R}$. Since the ∇ operator is linear and the image R is a linear functional of the source and re-

ceiver wavefields, we can perturb the image with respect to the wavefields first and then apply the ∇ operator. The migrated image R is the zero-lag correlation in time of the source and receiver wavefields $u_s(\mathbf{x},t)$ and $u_r(\mathbf{x},t)$ (Claerbout, 1985):

$$R(\mathbf{x}) = \int u_s(\mathbf{x},t)\, u_r(\mathbf{x},t)\, dt. \tag{7}$$

By perturbing the source and receiver wavefields in equation 7 and collecting the terms that depend linearly on the perturbation, we obtain

$$\delta R = \int (u_s \delta u_r + \delta u_s u_r)\, dt, \tag{8}$$

where we drop the dependence on $\mathbf{x}$ and t to simplify the notation. The wavefield perturbations δu_s and δu_r in equation 8 can be easily computed using the demigration approach presented in (Xu et al., 2012) or using standard adjoint-state techniques. From the image perturbation δR is straightforward to compute the gradient by applying the operator ∇.

To link the second term in equation 6 to the perturbation of the source and receiver wavefields, we use the method of connective functions developed by Luo and Schuster (1991). Let us formally write the gradient of $\mathcal{J}^{\delta\mathbf{u}}$ with respect to the model parameters:

$$\nabla_m \mathcal{J}^{\delta\mathbf{u}} = (\nabla R \cdot \mathbf{u}) \left(\nabla R \cdot \frac{\partial \mathbf{u}}{\partial m} \right). \tag{9}$$

Notice that since we are analyzing only the changes of the apparent displacement field due to perturbations of the velocity model, we do not include in equation 9 the gradient of ∇R with respect to the model m. We want to explicitly link the displacement perturbation $\delta\mathbf{u}$ to the wavefield perturbation, then standard adjoint-state calculations allow us to avoid the computation of the Frechét derivatives of the wavefields and thus compute the gradient of the objective function in equation 3 efficiently.

By definition, the maximum of the local correlation is an extremum and thus the gradient with respect to the correlation lags must vanish for $\boldsymbol{\lambda} = \mathbf{u}$

$$\nabla_{\boldsymbol{\lambda}}\, c|_{\boldsymbol{\lambda}=\mathbf{u}} = \int_{w(\mathbf{x})} R_i(\boldsymbol{\xi})\, \nabla R_{i+1}(\boldsymbol{\xi}+\mathbf{u})\, d\boldsymbol{\xi} = 0. \tag{10}$$

Equation 10 implicitly connects the displacement vectors $\mathbf{u}$ with the model parameter m via the migrated images and the wave-equation. Thus, we define the connective function

$$F(\mathbf{x},\mathbf{u}) = \int_{w(\mathbf{x})} R_i(\boldsymbol{\xi})\, \nabla R_{i+1}(\boldsymbol{\xi}+\mathbf{u})\, d\boldsymbol{\xi} = 0 \tag{11}$$

Using equation 11 and following a derivation analogous to Luo and Schuster (1991), we rewrite the gradient of the displacement vectors with respect to the model parameters in equation 4 using the connective function $F(\mathbf{x},\mathbf{u})$

$$\nabla_m \mathcal{J}^{\delta\mathbf{u}} = (\nabla R \cdot \mathbf{u})\, \nabla R \cdot \left(\frac{\partial F}{\partial \mathbf{u}} \right)^{-1} \frac{\partial F}{\partial m}. \tag{12}$$

The derivative of the connective function with respect to the model parameters can be computed using adjoint-state techniques; the mathematical form of $F(\mathbf{x},\mathbf{u})$ involves only the migrated image and linear functions of the images, and thus, in principle, the derivative $\frac{\partial F}{\partial m}$ can be calculated using the adjoint-state method. The derivative $\frac{\partial F}{\partial \mathbf{u}}$ is the multidimensional generalization of the denominator in equation (7a) in Luo and Schuster (1991):

$$\frac{\partial F}{\partial \mathbf{u}} = \int R_i(\boldsymbol{\xi})\, \nabla\nabla R_{i+1}(\boldsymbol{\xi}+\mathbf{u})\, d\boldsymbol{\xi}, \tag{13}$$

where, in $2D$,

$$\nabla\nabla R_{i+1}(\boldsymbol{\xi}+\mathbf{u}) = \begin{bmatrix} \frac{\partial^2 R_{i+1}(\boldsymbol{\xi}+\mathbf{u})}{\partial z^2} & \frac{\partial^2 R_{i+1}(\boldsymbol{\xi}+\mathbf{u})}{\partial z \partial x} \\ \frac{\partial^2 R_{i+1}(\boldsymbol{\xi}+\mathbf{u})}{\partial x \partial z} & \frac{\partial^2 R_{i+1}(\boldsymbol{\xi}+\mathbf{u})}{\partial z^2} \end{bmatrix} \tag{14}$$

is a 2×2 tensor of second derivatives. Notice that since $\left(\frac{\partial F}{\partial \mathbf{u}}\right)^{-1}$ is a 2×2 matrix-valued function defined at every image point $\mathbf{x}$, and $\frac{\partial F}{\partial m}$ is a 2×1 vector-valued function at every point $\mathbf{x}$, their product is a 2×1 vector-valued function, and then the dot product with the spatial image gradient ∇R in equation 9 makes mathematical sense. The generalization to 3D is straightforward. This expression is similar to equations (6) and (7a) in (Luo and Schuster, 1991); the vectorial nature of the displacement field makes equation 12 tensorial.

The analysis of the differential of objective function in equation 3 with respect to the model parameters shows the mathematical complexity of implementing this solution for velocity analysis. Especially the multidimensional generalization of the procedure developed in Luo and Schuster (1991) poses a number of implementation challenges: in the time domain, we have one-dimensional shifts and equation (7a) in Luo and Schuster (1991) involves *scalar* functions; in the image domain, the shifts are vectors and we have to deal with *vector* and *matrix*-valued functions, which considerably increases the complexity of the gradient computation. Moreover, the data correlation used in Luo and Schuster (1991) is global over the entire seismic trace, intuitively that accounts for an average shift between the observed and simulated data. In the image domain, the global correlation of the migrated images has little physical sense (if any at all). The local correlation implementation increases the dimensionality of the problem and then the cost, and picking of specific location in the image is necessary for an efficient implementation.

In the next section, we show how to greatly simplify the computation of the update of the velocity model using the concept of image perturbation and the link between the image difference and the dot product $\nabla R \cdot \mathbf{u}$, as suggested in Perrone et al. (2012).

2.2 Adjoint-state method, demigration, and linearized inversion

The dot product between the gradient of the migrated image and the apparent displacement field between two images (equation 3) is a linear approximation of the image difference with respect to the displacement vector (Perrone et al., 2012). Compared to the image difference, equation 3 is less affected by amplitude differences due to the change of the shot location

and is less prone to cycle skipping problems because warping maps every event in one image to the corresponding event in the second image. The relation between image difference and the dot product of image gradient and displacement field can be used to set up a wavefield tomography procedure based on the image difference objective function, but more robust.

The adjoint-state calculations for the image difference objective function are well-known in the geophysics literature (Plessix, 2006). Although introduced as a regularization term for full-waveform inversion, the image-difference objective function represents a sensible functional for migration velocity analysis. Intuitively, all images from separate seismic experiments must be maximally similar to each-other when the velocity model is correct, and thus the energy of the first derivative along the shot dimension must be minimum. The major weak points of this approach are related to sensitivity to the acquisition geometry and cycle skipping in the image domain, as discussed in Perrone et al. (2012). Also, the kinematic artifacts due to the fact that the migration operator is the adjoint and not the inverse of the Born modeling operator limit any technique in the shot-image domain (Stolk and Symes, 2004).

The adjoint sources $g_{s_i}(\mathbf{x},t)$ and $g_{r_i}(\mathbf{x},t)$ for the image-difference objective function are straightforward to compute. They depend on the second derivative of the migrated images along the shot axis of the prestack image cube and the wavefields computed in the background model (Plessix, 2006):

$$g_{s_i} = (R_{i-1} - 2R_i + R_{i+1})\, u_{r_i} \quad (15)$$

$$g_{r_i} = (R_{i-1} - 2R_i + R_{i+1})\, u_{s_i}. \quad (16)$$

The functions in equation 15 are the force terms for the wavefield extrapolations

$$\mathcal{L}(m)\, a_{s_i} = g_{s_i} \quad (17)$$

$$\mathcal{L}(m)\, a_{r_i} = g_{r_i}, \quad (18)$$

where $a_{s_i}(\mathbf{x},t)$ and $a_{r_i}(\mathbf{x},t)$ are the adjoint wavefields. The adjoint sources generate the scattered fields due to the reflectivity perturbation represented by $(R_{i-1} - 2R_i + R_{i+1})$. These wavefields can also be interpreted as the *demigrated* reflectivity perturbation $(R_{i-1} - 2R_i + R_{i+1})$. The gradient of the objective function is then the zero-lag time correlation of the background and adjoint wavefields (Fichtner et al., 2006; Plessix, 2006).

By inspecting equation 15 and 16, we can immediately see the practical issues of implementing waveform tomography by minimizing the energy of the image difference. Amplitudes in the prestack images depend on the relative position between the shots, thus even when the velocity model is correct, uneven illumination of the subsurface may lead to spurious adjoint sources and gradients of the objective function. Even more important than illumination, cycle skipping may arise when the velocity model is severely inaccurate, because different images map the same structures at inconsistent positions in the subsurface.

We propose to replace the term $(R_{i-1} - 2R_i + R_{i+1})$ in the expression of the adjoint sources with an approximation derived from image warping. The apparent displacement field absorbs the amplitude differences due to the change in the shot position and, at the same time, removes the cycle skipping problem by warping one image into its neighbor. Let us indicate with $\mathbf{u}_{i-1}$ and $\mathbf{u}_i$ the apparent displacement field that warps R_{i-1} into R_i and R_i into R_{i+1}, respectively. We can construct approximations of the image differences by computing the dot product of the image gradient with the displacement fields. In order to guarantee symmetry with respect to the ith shot, we use R_i to construct the image perturbations

$$\Delta R_{i-1} = R_i - R_{i-1} \approx \nabla R_i \mathbf{u}_{i-1} \quad (19)$$

$$\Delta R_i = R_{i+1} - R_i \approx \nabla R_i \mathbf{u}_i. \quad (20)$$

Using the expressions in equations 19-20, we can approximate the second derivative along the shot axis as follows:

$$R_{i-1} - 2R_i + R_{i+1} \approx \Delta R_i - \Delta R_{i-1}, \quad (21)$$

which is robust against cycle skipping (only one image, R_i, enters the expression for the image perturbation), and it is less sensitive to illumination patterns because the amplitude effects are absorbed in the computation of the displacement fields.

3 NUMERICAL EXAMPLES

We test image warping wavefield tomography for different depths of the reflecting interface and compare it with the direct image difference tomography approach (Plessix, 2006) and local image correlation wavefield tomography (Perrone and Sava, 2012). We show that image warping wavefield tomography is more robust with respect to the depth of the reflector (i.e. the ratio between the source receiver offset and the depth of the reflector) and lead to more stable gradients for model update. We also show how the method fails to produce sensible gradients in highly refractive media, despite the fact that the objective function is able to identify the correct model. In this later case, the displacement estimation is stable but the artifacts in the migrated image produce noisy image gradients and thus lead to spurious scattered wavefields and artifacts in the gradient of the objective function. Finally, we test our method on the Marmousi model.

3.1 Horizontal reflector

Let us consider a flat horizontal reflector in a homogeneous velocity model. In the first case, the interface is at 2 km depth (Figure 1) and it is due to a density contrast. In order to measure errors in the velocity model, we analyze two nearby shots: the shot position of the first shot is $x = 3.8$ km and the distance between the shots is 200 m. We apply different homogeneous perturbations to the velocity model, we migrate the data and construct the image perturbations for the different models from the migrated images Figure 2. Figures 2(a), 2(c), and 2(e) show the migrated imaged for high, correct, and low velocities. The image perturbations for the different models computed as the inner product between the image gradient and the

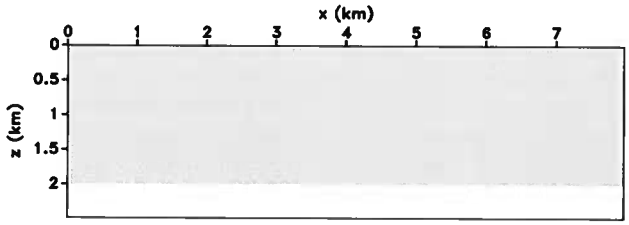

Figure 1. Horizontal reflector model. The interface is due to a density contrast in a constant velocity medium. The depth of the interface is large compared to the distance between the shot points.

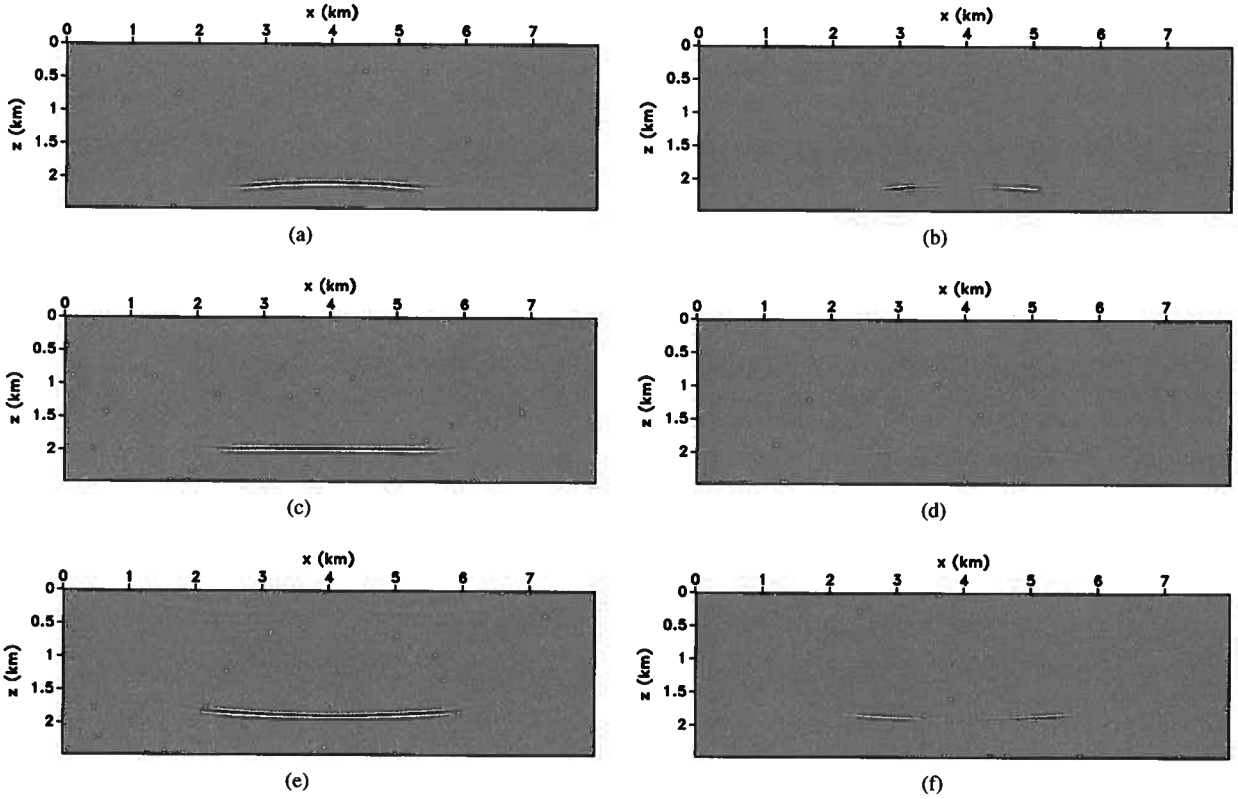

Figure 2. Migrated images using (a) high, (c) correct, and (e) low velocities. The perturbation with respect to the correct model is constant and homogeneous over the entire model. Image perturbations for (b) high , (d) correct, and (f) low velocities. The perturbation with respect to the correct model is constant and homogeneous over the entire model.

displacement vector field obtained by warping one image into the other are shown in Figures 2(b), 2(d), and2(f). Observe that the image perturbation is coherent when the velocity model is incorrect (Figures 2(b) and 2(f)), whereas it is practically weak random noise when the velocity model is correct (Figure 2(d)), except at the edges of the subsurface aperture. We obtain the sensitivity kernels and the objective function in Figures 3(a), 3(b), and 3(c) by correlating the background wavefields (used for migration) with the scattered wavefields excited by the interaction of the background wavefields with the reflectivity perturbation computed from equation 21. The gradient is smooth over the entire extent of the reflector when the velocity is incorrect and has negligible value when the model is correct. The objective function in Figure 12 is convex over the entire perturbation range and the global minimum clearly points at the correct model.

By comparison, Figures 4(a), 4(b), and 4(c) shows the gradients obtained for the same perturbations using the image-difference objective function. Notice the strong side lobes at the edges of the reflector, where we observe cycle skipping because the overlap between the images is not enough. The gradients are noisier than the ones obtained using image-warping, and also the objective function in Figure 4(d) shows a weak bias when the model is correct. Nonetheless, the gradients obtained using image warping in this example are comparable with the results reported in Perrone and Sava (2012) for the

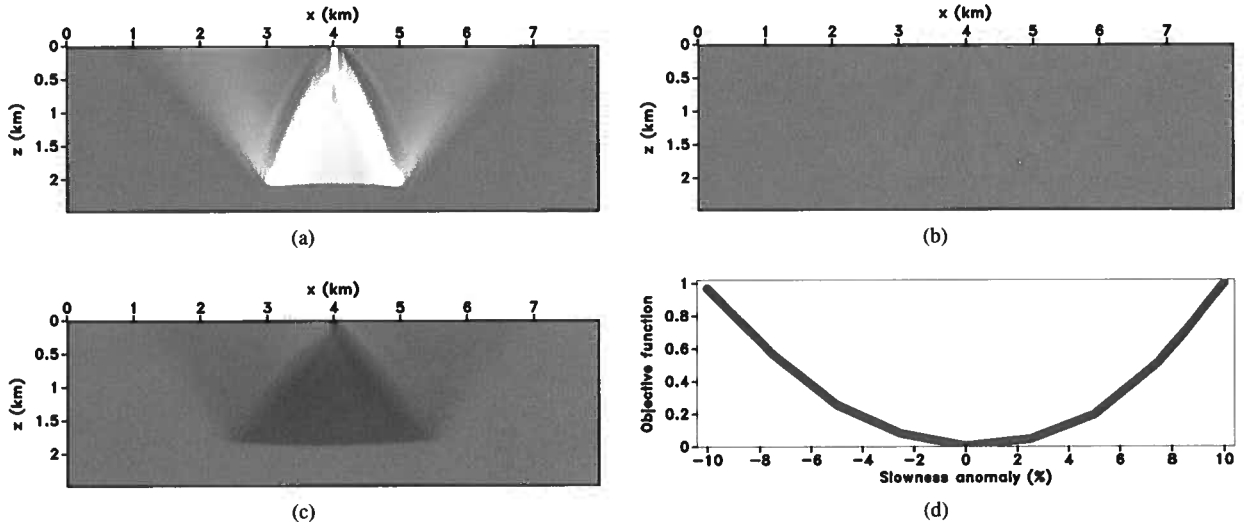

Figure 3. Sensitivity kernels obtained using *image warping* wavefield tomography for (a) high, (b) correct, and (c) low velocities. (d) Objective function for *image warping* wavefield tomography evaluated for a set of model perturbations and the *deep interface* in Figure 9(b). The minimum of the objective function indicates the correct model.

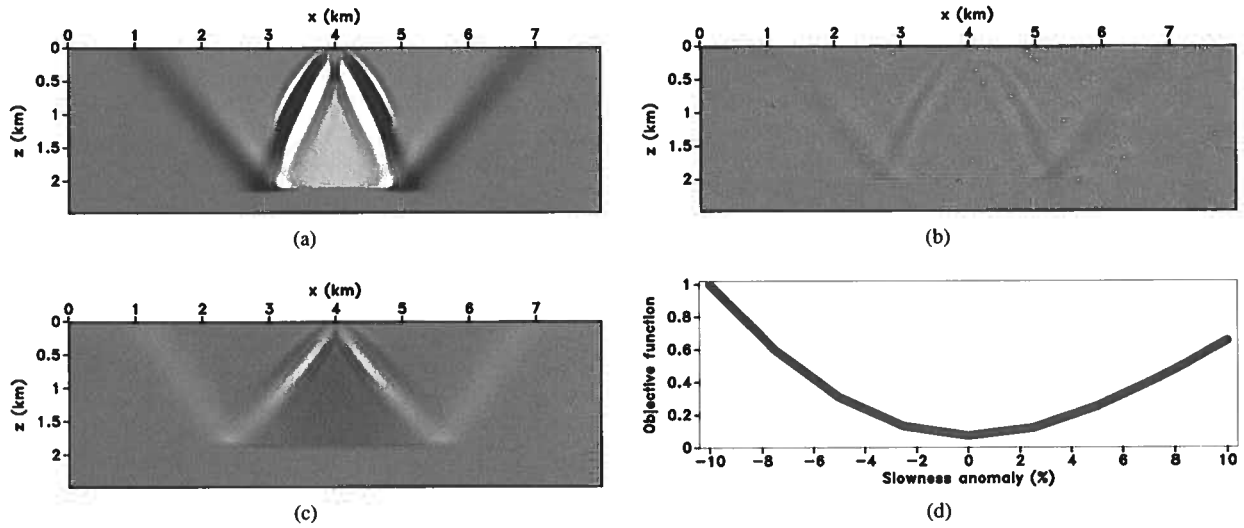

Figure 4. Sensitivity kernels obtained using *image difference* wavefield tomography for (a) high, (b) correct, and (c) low velocities. (d) Objective function for *image difference* wavefield tomography evaluated for a set of model perturbations and the *deep interface* in Figure 9(b).

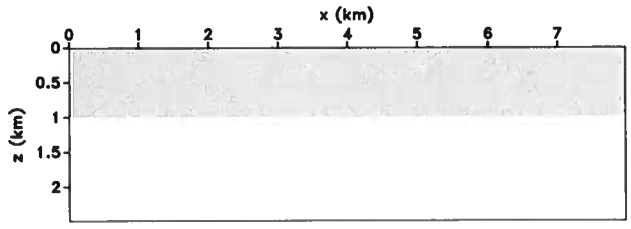

Figure 5. Horizontal reflector model. The interface is due to a density contrast in a constant velocity medium. The reflector is at half the depth of the model in Figure 1.

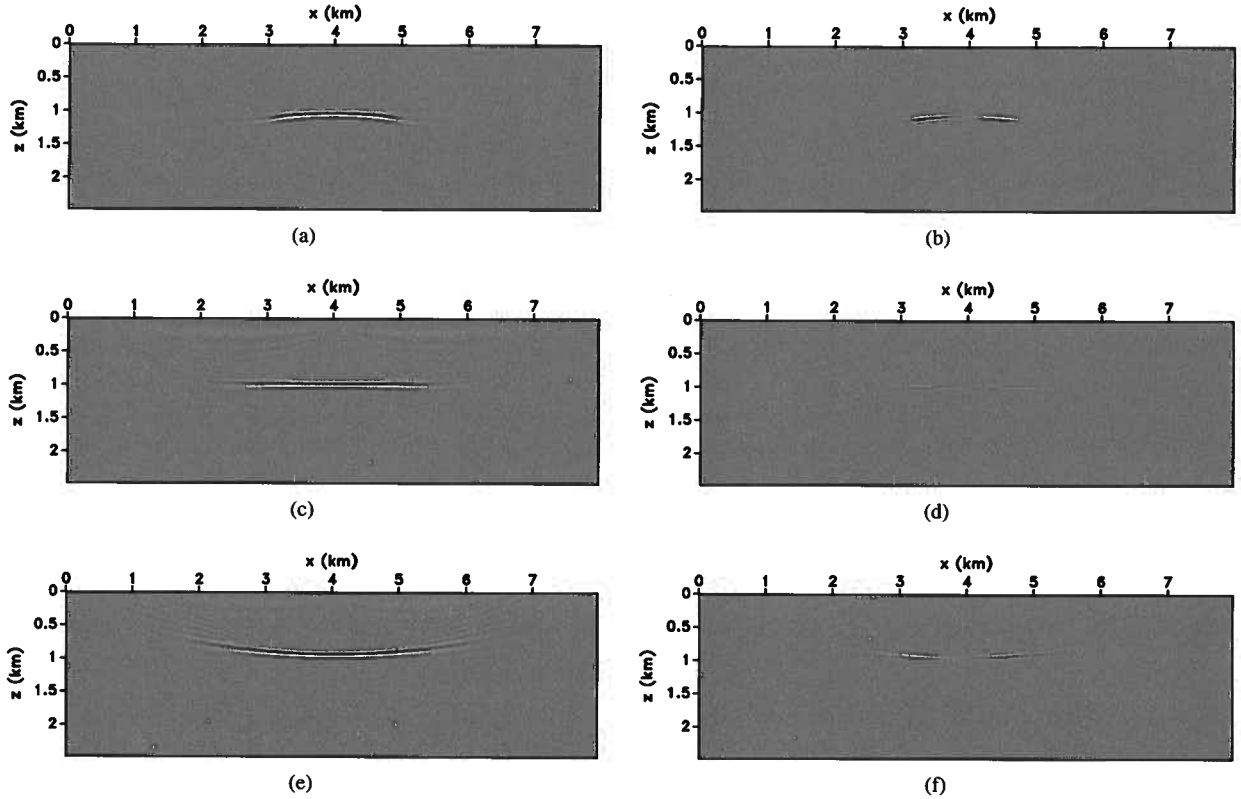

Figure 6. Migrated images of the shallow reflector using (a) high, (c) correct, and (e) low velocities. Image perturbations obtained using image warping for the shallow reflector and (b) high, (d) correct, and (f) low velocities. The perturbation with respect to the correct model is constant and homogeneous over the entire model.

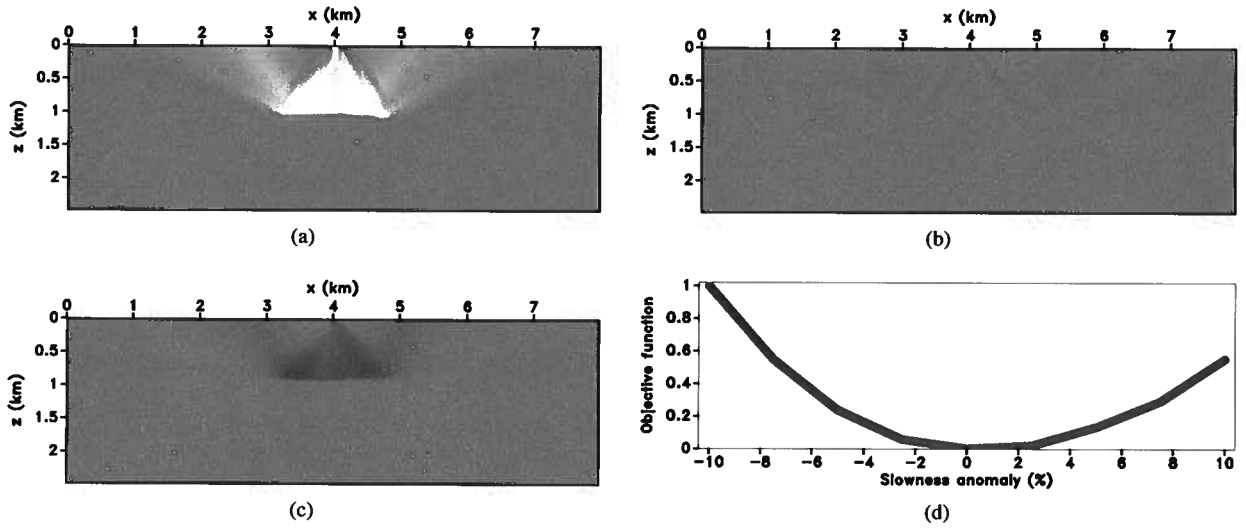

Figure 7. Sensitivity kernels obtained using *image warping* wavefield tomography for (a) high, (b) correct, and (c) low velocities. (d) Objective function for *image warping* wavefield tomography evaluated for a set of model perturbations and a *shallow interface*. As in the case of a deep reflector, the minimum of the objective function indicates the correct model.

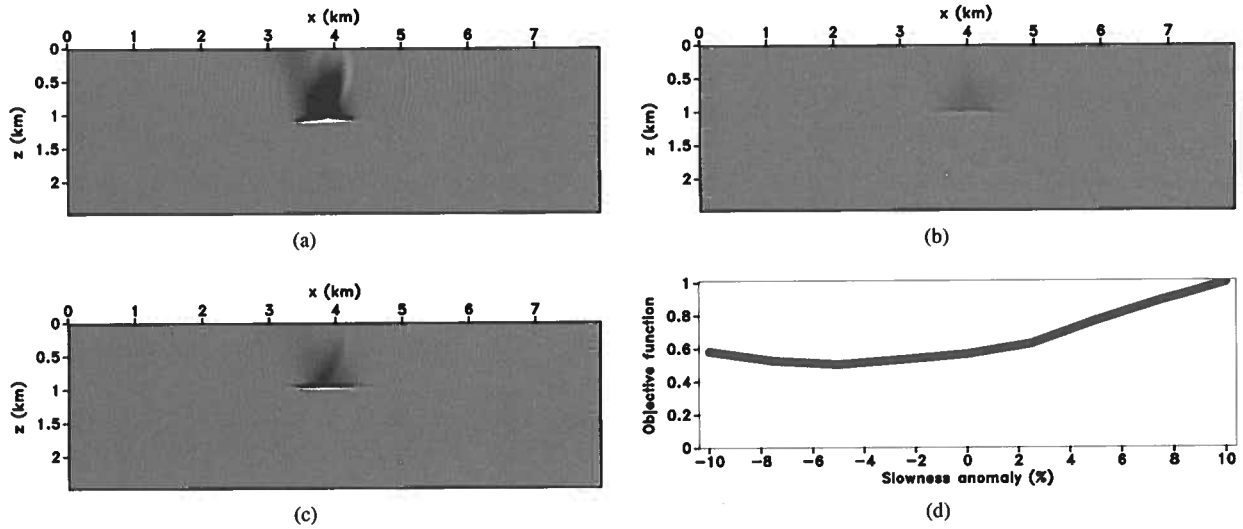

Figure 8. Sensitivity kernels obtained using *local image correlations* wavefield tomography for (a) high, (b) correct, and (c) low velocities. Notice that the kernels fail to recover the sign of the perturbation. (d) Objective function for *local image correlation* wavefield tomography evaluated for a set of model perturbations and a *shallow interface* in Figure 5. The objective function does not indicate correctly the correct model.

objective function employing local image correlations. Thus, the image warping and the penalized local image correlation are expected to perform similarly when the ratio between the depth of the reflector and the shot-point separation is large.

We also consider a shallower interface and compare the single scattering approach with the penalized local correlations. We consider the model in Figure 5 where the density interface is at 1 km depth. The model perturbations applied to the velocity field are the same used as in the previous case. The position of the first shot is again at $x = 3.8$ km and the shot separation is 200 m. The migrated images obtained using different perturbed velocity models are shown in Figures 6(a), 6(c), and 6(e). The lateral extent of the reflector that can now be imaged is smaller than in the previous case because of the shorter distance between acquisition surface and reflector. Figures 6(b), 6(d), and 6(f) shows the dot product of the migrated image with the estimated warping field in this second case. Again, the image perturbations are coherent when the migration model is incorrect (Figures 6(b) and 6(f)) and incoherent for the correct model (Figure 6(d)). Notice that the edges of the subsurface aperture impacts more severely the image perturbation when the reflector is shallow. The sensitivity kernels computed for the shallow reflector (Figures 7(a), 7(b), and 7(c)) show a good behavior, which is comparable with the case of the deep reflector. In Figure 7(d), the objective function is slightly less sensitive to positive perturbations probably because of both the vicinity of the interface to the acquisition surface and the smaller extent of the imaged reflector. Nonetheless, it maintains the convex shape seen in the preceding case and indicates the correct model (global minimum).

We also use the penalized local correlation approach presented in Perrone and Sava (2012) for this second case. The size of the local correlation window is 31 samples in both vertical and horizontal direction, which means the local window capture the overlapping part of the migrated images (the shot distance is 10 samples at the surface and the velocity model is constant). The computed gradients are shown in Figures 8(a), 8(b), and 8(c). Observe that we are not able to recover the correct sign of the perturbation. The separation between the migrated image is such that there is a poor overlap between the images, the values of the computed local correlation coefficients drop, and the estimated shift is strongly biased. The behavior of the objective function (Figure 8(d)) shows that for the case of shallow reflectors the penalized local correlations fail to measure the error in the velocity model.

3.2 Highly refractive model and migration failure

When the model is highly refractive, kinematic artifacts contaminate the single-experiment migrated images, even though the exact model is used to reconstruct the source and receiver wavefields (Stolk and Symes, 2004). This fact is due to the very nature of the migration operator, that is the adjoint of the Born modeling operator and not its inverse.

Figure 9 shows the velocity model and density model we use to study the behavior of image warping wavefield tomography in highly refractive media. The model contains a strong low velocity Gaussian anomaly, whose minimum value is 40% lower than the background 2 km/s velocity. The reflector is simulated by a density contrast. The data are generated using a 15 Hz Ricker wavelet and a staggered-grid finite-difference algorithm with absorbing boundary conditions on every side. The horizontal sampling is 20 m and the vertical sampling is 10 m.

The low velocity area in the model creates triplications of the wavefields. The shot-gather in Figure 10 shows the complexity of the wavefield recorded at the surface. The source is located at $x = 3$ km on the surface and receivers are at ev-

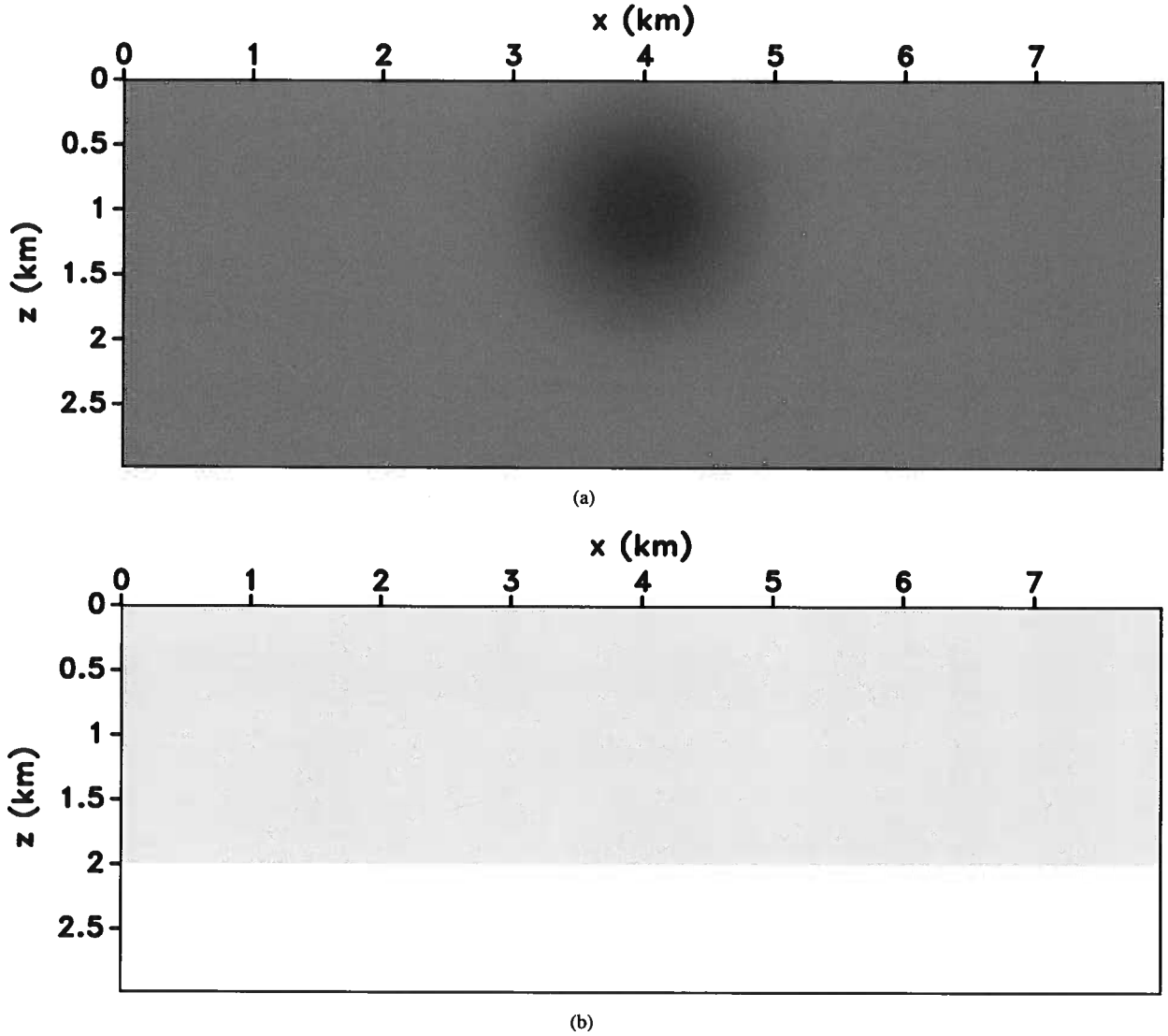

Figure 9. (a) Velocity model used to study the behavior of the inversion in highly refracting media. The low velocity anomaly is Gaussian-shaped and at its minimal value it is 40% smaller than the background 2 km/s background. (b) Density model used to generate reflections.

ery grid point at the surface. Figure 11(a) show the result of migrating the shot-gather in Figure 10 with the *exact* model. Notice that the image is contaminated at about $x = 5$ km with the kinematic artifacts described in Stolk and Symes (2004). These artifacts do not satisfy the relationship between dip field and displacement vector assumed in our inversion procedure. Moreover, since the migration operator is simply the adjoint, and not the inverse, of the Born modeling operator, the amplitudes of the image are corrupted as well. All these distortions affect the calculation of the sensitivity kernel. In Figure 11(b), we show the sensitivity kernel computed for the exact velocity model. Instead of having negligible amplitude, the sensitivity kernel is strong and totally spurious. A Possible solution to obtain kinematically correct images that are suitable for image warping is least-square migration (Nemeth et al., 1999) but would make the inversion procedure more computationally expensive.

Figure 12 shows the objective function obtained by perturbing the correct model with a Gaussian anomaly that progressively cancels out the low velocity zone. Interestingly, although the sensitivity kernel is inaccurate, the objective function is still able to measure the distance from the correct model. This indicates that although the velocity error measure is efficient, the linearizations used for computing the sensitivity kernels and model update can introduce strong errors.

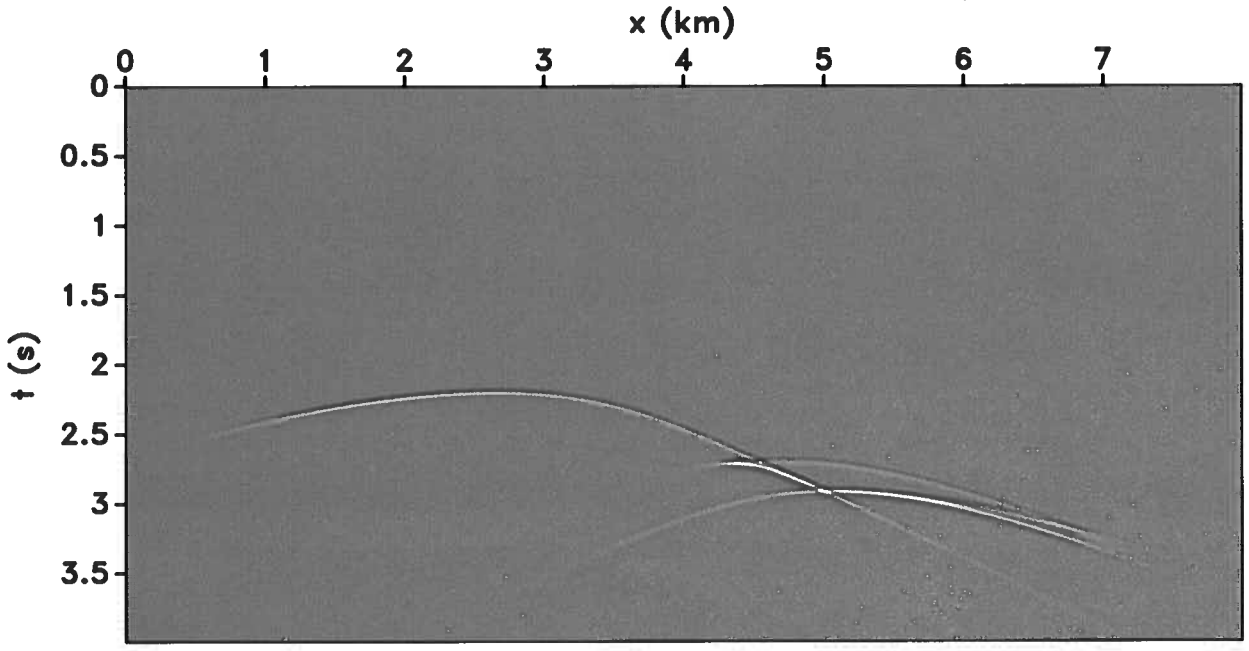

Figure 10. Shot-gather for a source at $x = 3$ km. Notice the complicated response of the medium due to the triplications of the wavefield passing through the low velocity anomaly.

3.3 Marmousi model

We also test our approach on the Marmousi model (Figure 13(a)). We model 100 shots separated by 80 m. The spatial sampling is 8 m in both the x and z direction. Receivers are located at every grid point on the surface. The data are modeled without free-surface multiples but internal multiples are present in the data. We assume that free-surface multiples can be effectively removed from the data using SRME (Verschuur, 1991). The Marmousi model represents a complex land-like scenario and it is characterized by multipathing and strong refractions. This complexity is exemplified by the raypaths calculated in a smoothed version of the correct model, Figure 13(b), for a shot at $x = 4.8$ km.

The initial model is obtained by filtering the exact Marmousi model with a triangular smoother with radius 120 samples vertically and 200 samples horizontally. The smooth model is then biased with a -0.4 km/s homogenous perturbation (Figure 14(a)). The migrated image obtained using this model is shown in Figure 14(b). The central part of the image is non interpretable and all reflectors are mispositioned and defocused; the deep and strong reflectors are shifted about 500 m upward because of the bias toward low velocities in the initial velocity model. The noise in the image is due to the strong errors in the migration model and the inconsistent imaging of the reflectors from different shots. Also, the internal multiples in the data are not imaged correctly since migration is based on single scattering (Born) assumptions.

The inversion reaches a floor after about 20 iterations and returns the velocity model in Figure 15(a) and the associated migrated image in Figure 15(b). In the final image, the reflectors are shifted toward their correct location. We improve the truncation of the sedimentary beds against the fault walls around $z = 1$ km and $x = 3.5$ km; the migration frowns in the original image, due to the discontinuities of the sediments at the fault locations, are corrected by the inversion procedure. Notice that the edges of the image are undercorrected with respect to the better illuminated part of the model. Illumination compensation using the energy of the source, receiver, or both wavefields can attenuate this problem. Because the image perturbation is related to the actual amplitude of the reflectors, the model update is naturally biased toward stronger, more coherent, and better illuminated interfaces. Illumination compensation can also help balancing the strength of the update between the sides of model, which are characterized by simple sedimentary structures, and the central part of the model, where the faults and discontinuities of the reflectors make the wavefields complicated and the wavefront less coherent.

The importance of regularization is described by Figure 15(c), which represent the image obtained after smoothing the model in Figure 15(a) using a triangular filter with radius 100 samples vertically and 400 samples horizontally. The smoothing homogenize the velocity models by spreading the update over a larger subsurface aperture, thus it effectively reduces the effects of uneven illumination. If we compare this image with Figure 13(a), we can observe that the position of the reflectors is quite accurate. The faulted portion of the model is not optimally imaged yet, but the kinematics of the wavefield has been clearly improved and, as a direct consequence, the migrated image improved as well. This result has been obtained in post-processing by smoothing the velocity

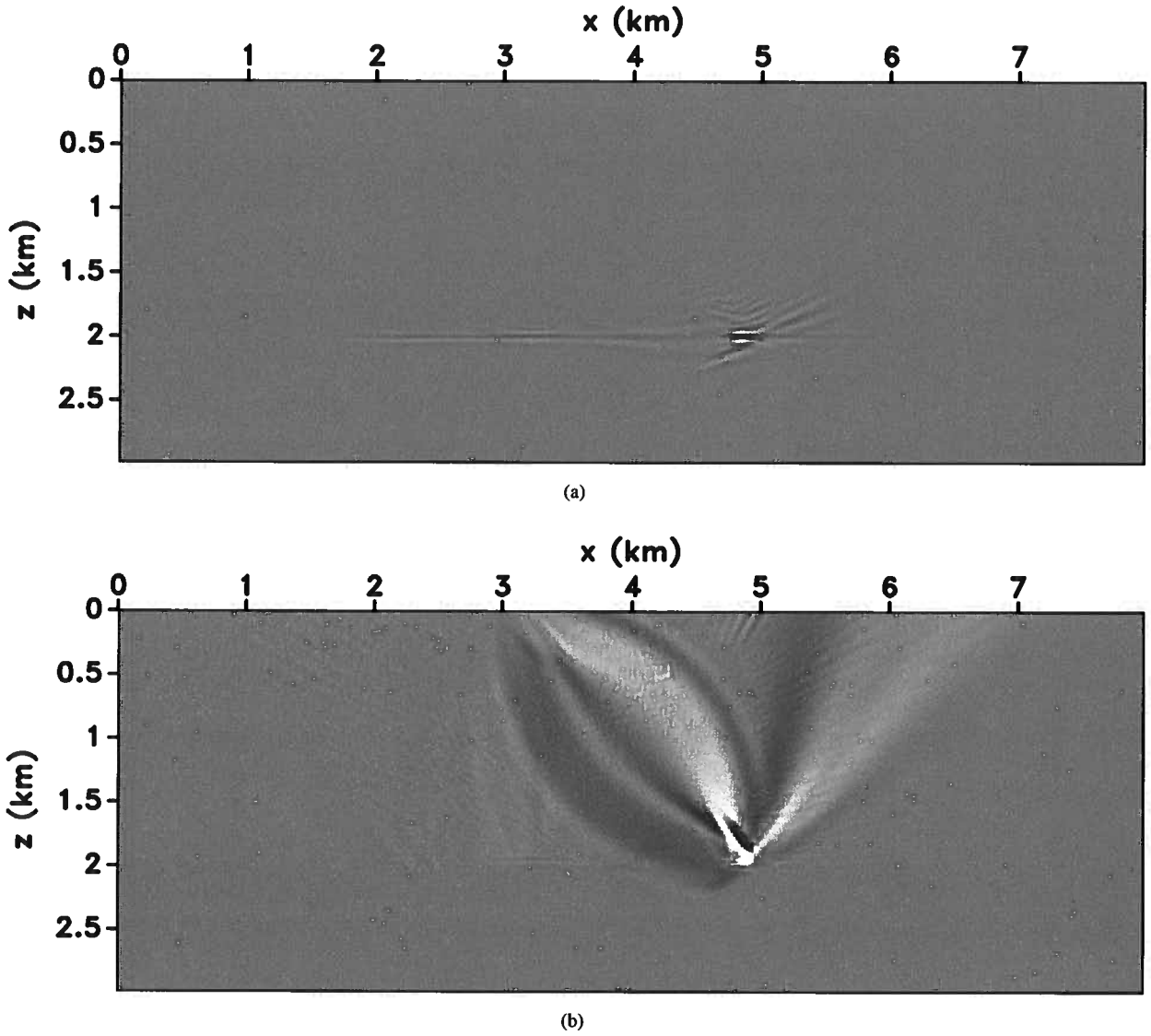

Figure 11. Migrated image obtained from the shot-gather in Figure 10 with the correct velocity model. Observe the distorted image of the reflectors and the artifacts introduced by the migration operator. (b) Sensitivity kernel obtained using image warping wavefield tomography for the correct velocity model. The kernel should be very small and incoherent because the model is actually correct; the spurious kernel is thus completely due to the artifacts in the image.

model obtained by inversion; smoothing corrects the uneven illumination and removes the abrupt changes in the velocity field that distort the image in Figure 15(b). We speculate that a careful illumination compensation and amplitude balancing in the computation of the gradient can achieve a similar result in a direct and automatic way.

4 DISCUSSION

The complete adjoint-state calculations for the objective function in equation 3 is computationally expensive and involved. We require not only the wavefields in the background medium but also their spatial derivatives. The warping field requires a dedicated procedure based on connective functions that link the warping vectors to the velocity model. From the point of the inversion, this step increases the dimensionality of the problem, as at every image point we have to consider the extra dimensions in which the warping vector is defined. Picking image point locations (Yang and Sava, 2010; Perrone and Sava, 2012) becomes crucial to reduce the dimensionality and thus the computational cost. In the method presented in this paper, no picking is necessary in order to construct the image perturbation that we use to construct the estimated scattered wavefields.

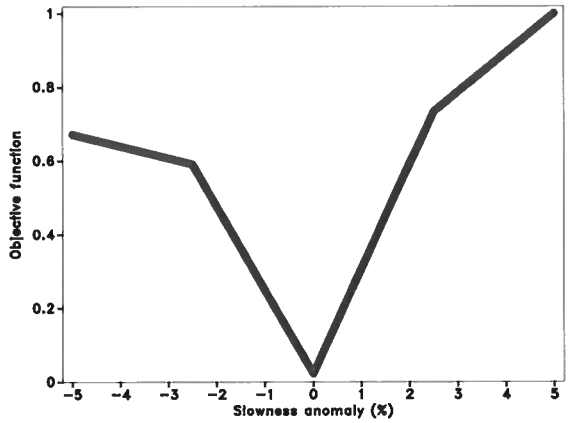

Figure 12. The objective function obtained by perturbing the model with a Gaussian anomaly having the same extent of the one in the correct model but with different amplitudes. Notice that the objective function correctly measures errors in the velocity model.

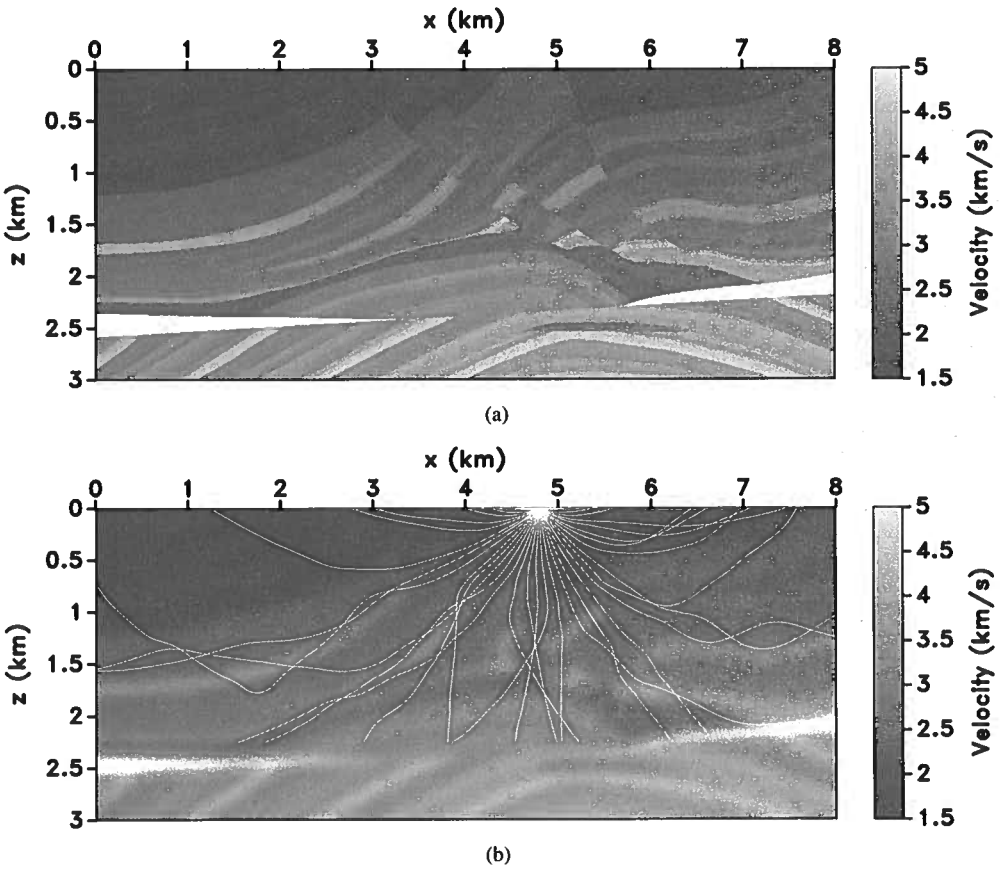

Figure 13. (a) Exact Marmousi velocity model. (b) Ray-tracing in a smooth version of the exact model for a shot at $x = 4.8$ km. The complex raypaths highlight the refractive behavior of the Marmousi model.

The image difference objective function presented in Plessix (2006) as a regularization term for full-waveform inversion is simple to implement and carries straightforward physical intuition about the action of the inversion. In media that are not highly refractive, the drawbacks related to the sensitivity to the amplitude patterns and potential cycle skipping can be effectively and efficiently handled using the apparent displacement field between migrated images and constructing robust approximations of the image difference. Estimating the displacement field and computing the image gra-

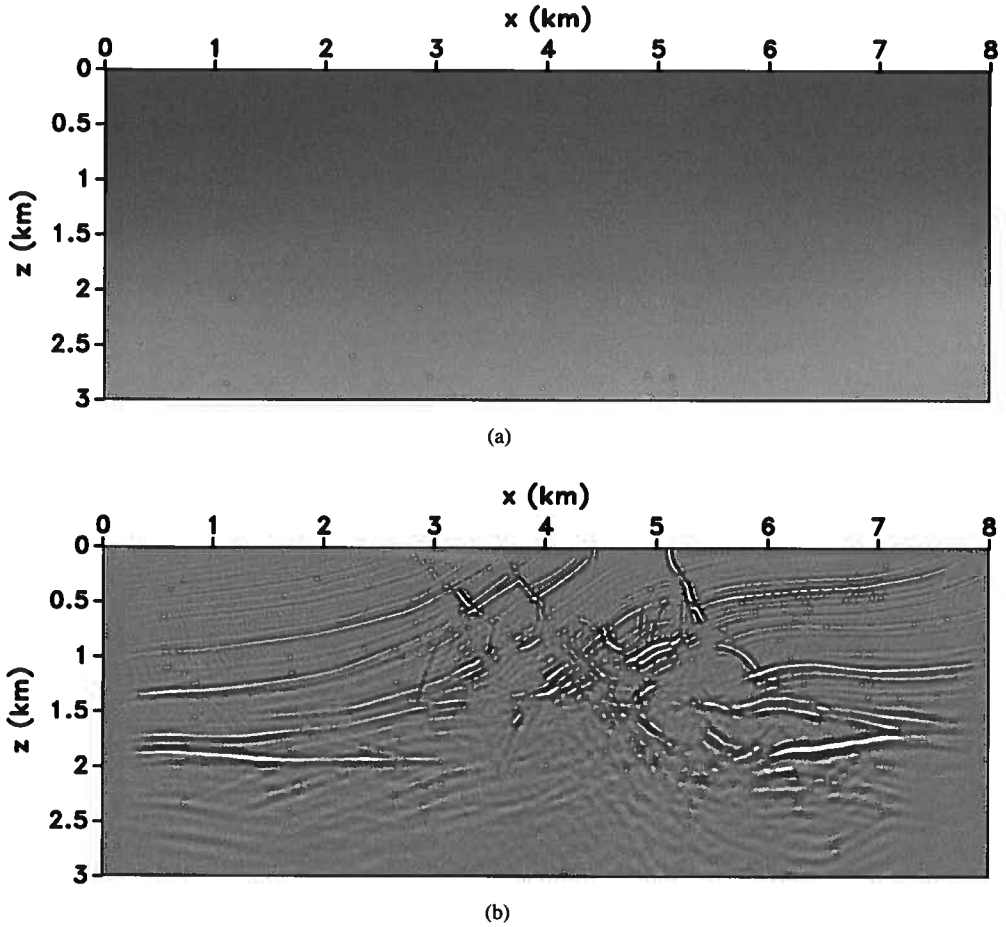

Figure 14. (a) The initial model represented by an incorrect $v(z)$ velocity. (b) The migrated image is distorted and not interpretable in the central part of the model. Observe the general upward shift of the image due to the bias in the velocity model.

dient have a negligible computational cost compared to migration. Moreover, we preserve the physical interpretation of the image perturbation that enters the expression of the adjoint sources, equation 15, which is useful for quality control and for quickly assessing the evolution of the inversion result. The residual evaluation is immediate and the calculation of the adjoint sources is straightforward compared to local correlation waveform tomography, where the computation of the adjoint-sources requires implementation of nonstationary convolutions of the input images with the penalty operators, and local scaling of the background wavefields. When compared to methods that require image-gathers or extended images, our method based on apparent displacement vectors appears easier to implement and less computationally demanding.

Computing the relative shift between two images in local seamless overlapping windows requires some degree of overlapping of the two migrated images. The quantity of interest to qualitatively characterize the distance between the two images in simple subsurface geometries is the ratio between the shot-point separation and the depth of the reflectors. The smaller this ratio, the greater the overlap between migrated images. When we estimate the shift between the migrated images using penalized local correlations, the extent of the local window constrains the domain in which the maximum of the correlation must be. When the separation between the shot is large and the local window is not wide enough to capture the position of the maximum of the local correlation, we introduce an error in the evaluation of the residuals. Notice that increasing the size of the local correlation window implies a decrease in resolution. Moreover, if other events (more reflectors) enter the local window and/or the reflector changes orientation in space, increasing the extent of the local window implies a drop in the values of the estimated correlation coefficients and thus a decrease in the quality of the estimated shifts. The displacement vector field is more robust than the penalized local correlations because of the iterative search and warping procedure used (Hale, 2007b) and thus it allows us to obtain high-quality velocity updates at shallow depths where the ratio between the shot distance and the depth of the reflector is relatively high.

The main drawback of performing inversion in the shot-migrated image domain is related to the nature of the migration operator and to the associated migration artifacts. In highly re-

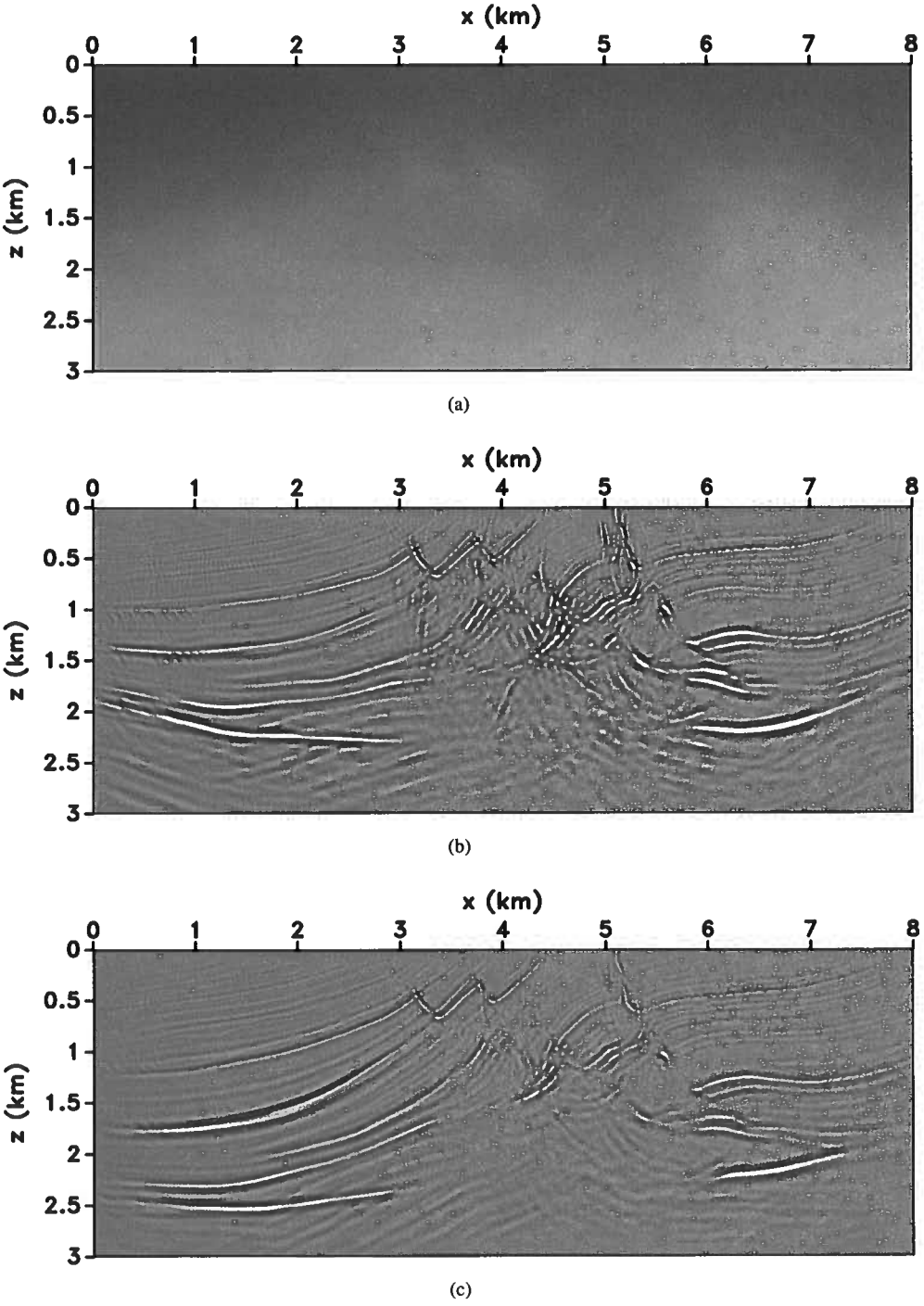

Figure 15. (a) Velocity model after 20 iteration of wavefield tomography and (b) corresponding migrated image. The reflectors shift toward their correct location, and the truncation of the beds against the fault walls improves. (c) Image obtained after smoothing the model in Figure 15(a) with a triangular filter with radius 100 vertically and 400 samples horizontally.

fractive media, triplications and multipathing between source and receiver produce artifacts in the migrated image (Stolk and Symes, 2004). The artifacts are due to the migration operator being the adjoint and not the inverse of the Born modeling operator; they have the same frequency content of the signal and, although the stack over experiments removes them from the final image, they severely contaminate the migrated images for individual shots. Since these kinematic artifacts do not satisfy the assumed relation between the directions of the image gradient and displacement vector field, they represent the principal source of noise for our method. Least-square migration may attenuate the artifacts in the reflectivity images but would increase the computational cost and time. The development of simpler and more cost effective methodologies to avoid the migration artifacts is currently a topic of research.

In complicated models, such as the Marmousi model, regularization plays an important role in balancing the strength of the update and removing the natural bias that comes from the uneven illumination and the complexity of the subsurface structures.

5 CONCLUSIONS

The image-difference objective function for wavefield tomography in the migrated-shot domain can be made more robust using image warping. Displacement fields warping a migrated image into the image obtained from a neighboring experiment absorbe amplitude differences due to the shift in source location and removes cycle skipping, because every reflector in one image is mapped into the corresponding event in the second image.

Our method is more effective than local image correlation wavefield tomography for shallow reflectors, i.e., when the ratio between the source separation and the depth of the reflector is high. However, kinematic artifacts contaminate the image in highly refractive media and destabilize the computation of the sensitivity kernel. Nonetheless, the objective function based on the warping relation between the images is able to measure the distance between different models, and to highlight the most coherent images, thus enabling local gradient-based optimization.

6 ACKNOWLEDGMENTS

This work was supported by the sponsors of the Consortium Project on Seismic Inverse Methods for Complex Structures. The reproducible numerical examples in this paper use the Madagascar open-source software package freely available from http://www.ahay.org and the Mines JTK freely available at https://github.com/dhale/jtk.

REFERENCES

Al-Yahya, K., 1989, Velocity analysis by iterative profile migration: Geophysics, **54**, P. 718–729.

Albertin, U., P. Sava, J. Etgen, and M. Maharramov, 2006, Adjoint wave-equation velocity analysis: Presented at the 74th Ann. Internat. Mtg., SEG.

Biondi, B., and P. Sava, 1999, Wave-equation migration velocity analysis: Presented at the 69th Ann. Internat. Mtg., SEG.

Carcione, J., 2007, Wave fields in real media wave propagation in anisotropic, anelastic, porous and electromagnetic media: Elsevier. Handbook of Geophysical Exploration.

Chauris, H., and R.-E. Plessix, 2012, Investigating the differential waveform inversion: Presented at the 74th EAGE Conference & Exhibition - Workshops, EAGE.

Chavent, G., and C. A. Jacewitz, 1995, Determination of background velocities by multiple migration fitting: Geophysics, **60**, 476–490.

Claerbout, J. F., 1985, Imaging the earth's interior: Blackwell Publishing.

Faye, J.-P., and J.-P. Jeannot, 1986, Prestack migration velocity analysis from focusing depth imaging: Presented at the 56th Ann. Internat. Mtg., Soc. of Expl. Geophys.

Fichtner, A., H.-P. Bunge, and H.Igel, 2006, The adjoint method in seismology I. theory: Physics of the Earth and Planetary Interiors, 86–104.

Fowler, P., 1985, Migration velocity analysis by optimization: Technical Report 44, Stanford Exploration Project.

Hale, D., 2007a, Local dip filtering with directional Laplacians: Technical Report CWP-567, Center for Wave Phenomena, Colorado School of Mines.

———, 2007b, A method for estimating apparent displacement vectors from time-lapse seismic data: Technical Report CWP-566, Center for Wave Phenomena, Colorado School of Mines.

Kelly, S., J. R. Martinez, B. Tsimelzon, and S. Crawley, 2010, A comparison of inversion results for two full-waveform methods that utilize the lowest frequencies in dual-sensor recordings: Presented at the 80th Ann. Internat. Mtg., Soc. of Expl. Geophys.

Lions, J., 1972, Nonhomogeneous boundary value problems and applications: Springer Verlag, Berlin.

Luo, Y., and G. T. Schuster, 1991, Wave-equation traveltime inversion: Geophysics, **56**, 645–653.

Nemeth, T., C. Wu, and G. T. Schuster, 1999, Least-squares migration of incomplete reflection data: Geophysics, **64**, 208–221.

Perrone, F., and P. Sava, 2012, Wavefield tomography based on local image correlation: Presented at the 74th Conference and Exhibition, EAGE.

Perrone, F., P. Sava, C. Andreoletti, and N. Bienati, 2012, Linearized wave-equation migration velocity analysis by image warping: Submitted to Geophysics.

Plessix, R.-E., 2006, A review of the adjoint-state method for computing the gradient of a functional with geophysical applications: Geophys. J. Int., **167**, 495–503.

Pratt, R. G., 1999, Seismic waveform inversion in the frequency domain, part 1: Theory and verification in a physical scale model: Geophysics, **64**, 888–901.

Santosa, F., and W. W. Symes, 1989, An analysis of least-

squares velocity inversion, *in* Geophysical Monograph no. 4: Soc. of Expl. Geophys.

Sava, P., and B. Biondi, 2004, Wave-equation migration velocity analysis. I. Theory: Geophysical Prospecting, **52**, 593–606.

Sava, P., B. Biondi, and J. Etgen, 2005, Wave-equation migration velocity analysis by focusing diffractions and reflections: Geophysics, **70**, U19–U27.

Sirgue, L., and R. Pratt, 2004, Efficient waveform inversion and imaging: A strategy for selecting temporal frequencies: Geophysics, **69**, 231–248.

Stolk, C. C., and W. W. Symes, 2004, Kinematic artifacts in prestack depth migration: Geophysics, **69**, 562–575.

Tarantola, A., 1984, Inversion of seismic reflection data in the acoustic approximation: Geophysics, **49**, 71–92.

van Vliet, L. J., and P. W. Verbeek, 1995, Estimators for orientation and anisotropy in digitalized images: Proceedings of the first annual conference of the Advanced School for Computing and Imaging, ASCI'95, 442–450.

Verschuur, D. J., 1991, Surface-related multiple elimination, an inversion approach: PhD thesis, Technische Univ., Delft (Netherlands).

Xu, S., D. Wang, F. Chen, and Y. Zhang, 2012, Full waveform inversion for reflected seismic data: Presented at the 74th Conference and Exhibition, EAGE.

Yang, T., and P. Sava, 2010, Wave-equation migration velocity analysis with extended common-image-point gathers: Presented at the 80th Ann. Internat. Mtg., Soc. of Expl. Geophys.

Gradient computation for elastic full-waveform inversion in 2D VTI media

Nishant Kamath & Ilya Tsvankin
Center for Wave Phenomena, Colorado School of Mines

ABSTRACT

Full-waveform inversion (FWI) has proved effective in significantly improving the spatial resolution of seismic models. However, it is implemented mostly for isotropic media and the applications to anisotropic models are often limited to acoustic approximations. In a previous publication, we introduced a methodology for performing FWI of multicomponent (PP and PS) reflection data from a stack of horizontal, homogeneous VTI (transversely isotropic with a vertical symmetry axis) layers. Taking into account both anisotropy and elasticity in the description of the reflected wavefield makes it possible to resolve the interval Thomsen parameters and constrain the depth scale of the model. Here, we develop a foundation for extending elastic FWI to laterally heterogeneous VTI media using the adjoint state method. The main focus is on deriving the gradients of the objective function with respect to the model parameters. To test the algorithm, we introduce Gaussian anomalies in the Thomsen parameters of a homogeneous VTI medium and study the influence of the size of the anomaly, the source-receiver configuration, and the source polarization on the gradients. The model update for FWI can be produced by an appropriate scaling of the gradient using the steepest descent or similar methods.

1 INTRODUCTION

Full-waveform inversion (FWI) is a technique for estimating subsurface properties by using entire seismic waveforms recorded at the surface or in a borehole. Depending on the problem and availability of forward-modeling algorithms, FWI can be performed in the time domain (Kolb et al., 1986; Gauthier, 1986; Mora, 1987; Bunks et al., 1995) or frequency domain (Song and Williamson, 1995; Song et al., 1995; Pratt, 1999; Pratt and Shipp, 1999). Evaluation of the gradient of the objective function is often based on the adjoint state method, as described in Tarantola (1984a), Fichtner et al. (2006), and Liu and Tromp (2006).

Köhn et al. (2012) discuss the influence of parameterization on elastic isotropic FWI and conclude that describing the model in terms of P- and S-wave velocities and density gives better results than using impedances. Liu and Tromp (2006) derive the gradients of the objective function for earthquake data with respect to the parameters (bulk and shear moduli, density, source location, and source function) of an elastic earth model. FWI has been extended to anisotropic media, but typically in the acoustic approximation (Plessix and Rynja, 2010; Gholami et al., 2011; Plessix and Cao, 2011; Shen, 2012). Such "anisotropic acoustic" algorithms, however, suffer from trade-offs between the model parameters. Elastic FWI of synthetic multicomponent surface seismic data (consisting of both diving waves and reflections) for VTI media is performed by Lee et al. (2010), but suboptimal parameterization in terms of the stiffness coefficients causes ambiguity in their results.

In our previous work (Kamath and Tsvankin, 2012; hereafter, referred to as Paper I), we invert multicomponent reflection data from a horizontally layered VTI model for the the interval Thomsen parameters – the P- and S-wave vertical velocities (V_{P0} and V_{S0}) and anisotropy parameters ϵ and δ. Including density as an unknown parameter makes the objective function highly nonlinear, thereby causing the algorithm to get trapped in local minima. Therefore, the densities in all layers are fixed at the correct values. Although PP-waves alone may be sufficient to resolve V_{P0}, V_{S0}, ϵ, and δ, stable parameter estimation for layers at depth requires employing long-offset data (with the spreadlength-to-depth ratio reaching at least two) or the addition of PS-waves. Inversion of multicomponent data benefits from using a multiscale approach, which helps reduce the sensitivity to the choice of the initial model (Bunks et al., 1995).

Here we build the foundation for extending FWI to laterally heterogeneous VTI media. The model is parameterized in terms of V_{P0}, V_{S0}, and the P-wave NMO ($V_{\mathrm{nmo},P}$) and horizontal ($V_{\mathrm{hor},P}$) velocities. To compute the gradient of the objective function, we adapt the results of Liu and Tromp (2006) obtained with the adjoint-state method. The algorithm is applied to VTI models with Gaussian anomalies in the Thomsen parameters inserted into a homogeneous background.

2 METHODOLOGY

2.1 Full-waveform inversion for VTI media

FWI in the time domain is designed to minimize the following objective function:

$$\mathcal{F} = \frac{1}{2}\sum_{r=1}^{N}\int_0^T \|\mathbf{u}(\mathbf{x}_r,t) - \mathbf{d}(\mathbf{x}_r,t)\|^2 dt\,, \qquad (1)$$

where N is the number of receivers, T is the trace length, $\mathbf{u}(\mathbf{x}_r,t)$ is the modeled displacement, and $\mathbf{d}(\mathbf{x}_r,t)$ is the observed displacement at receiver location $\mathbf{x}_r$. Since the relationship between the data and the model is nonlinear, the inversion is performed iteratively, and the model update at each iteration can be found as:

$$\Delta\mathbf{m} = [\mathbf{J^T J}]^{-1}\,\mathbf{J^T}\Delta\mathbf{d}, \qquad (2)$$

where $\mathbf{J}$ is the Fréchet derivative matrix obtained by perturbing each model parameter, $\mathbf{J^T J}$ is the approximate Hessian matrix, $\mathbf{T}$ denotes transposition, and $\Delta\mathbf{d}$ is the difference between the observed data and those computed for a trial model.

In Paper I, we use PP reflections or a combination of PP and PS events generated for a horizontally layered VTI model to invert for the interval parameters V_{P0}, V_{S0}, ϵ, and δ. For the purpose of inversion, it is convenient to use quantities that can be constrained by the data and have the same units. Hence, instead of ϵ and δ we invert for the P-wave NMO velocity ($V_{\mathrm{nmo},P} = V_{P0}\sqrt{1+2\delta}$) and the horizontal velocity ($V_{\mathrm{hor},P} = V_{P0}\sqrt{1+2\epsilon}$). If the number of layers (which is fixed during the inversion) is not large, it is possible to compute the Fréchet matrix and the approximate Hessian explicitly by perturbing each model parameter.

2.2 Inverse problem in 2D

In the case of laterally heterogeneous media, computation of the Fréchet derivatives becomes prohibitively expensive since it involves calculating as many forward models at each iteration as the number of parameters (typically defined on a grid). It is more practical to calculate the gradient ($\mathbf{J^T}\Delta\mathbf{d}$ in equation 2) of the objective function with the adoint state method, which has been widely used in FWI (Tarantola, 1984b; Plessix, 2006; Liu and Tromp, 2006; Fichtner et al., 2006). The model update, which is a scaled version of the gradient, is then calculated using steepest-descent or conjugate-gradient algorithms. Alternatively, either the so-called BFGS (Broyden-Fletcher-Goldfarb-Shanno) method or its limited-memory equivalent, the L-BFGS method (both are quasi-Newton techniques), can be employed to scale the gradient by the inverse of an approximate Hessian (Virieux and Operto, 2009).

The adjoint state method involves computing the so-called adjoint wavefield to obtain the gradient. Because the wave equation is self-adjoint, it can be solved for the adjoint wavefield with the data residuals treated as sources. The residuals at each time step are injected "backward in time" (i.e., starting from the last sample), which is commonly described as back-propagation of data residuals. For 2D multicomponent data, the vertical and horizontal displacement components of the data residuals should be injected into the medium simultaneously. The gradient is obtained by applying the imaging condition to the spatial derivatives of the forward and adjoint wavefields.

Here, we assume that the properties of the VTI medium vary in 2D and consider only in-plane polarized waves. Hence the model is described by four stiffness coefficients (written in the Voigt notation): C_{11}, C_{33}, C_{13}, and C_{55}. However, it is certain combinations of the stiffnesses that control traveltimes and amplitudes of seismic waves (Tsvankin, 2012). In particular, description of wave propagation and inversion of seismic data can be facilitated by employing Thomsen parameters and their simple combinations (e.g., the anellipticity coefficient η). Lee et al. (2010), who parameterize the VTI model in terms of the stiffnesses, are unable to resolve the coefficient C_{13}, likely because of the tradeoff between C_{13} and C_{55} in P-wave kinematic signatures. In Paper I we were able to constrain the relevant Thomsen parameters (V_{P0}, V_{S0}, ϵ, and δ), although the algorithm operated with the vertical, horizontal and NMO velocities. Here, we parameterize the model in terms of the squared velocities V_{P0}^2, V_{S0}^2, $V_{\mathrm{nmo},P}^2$, and $V_{\mathrm{hor},P}^2$. Squaring the velocities is a matter of convenience because it simplifies the gradient expressions.

The gradients of the objective function (equation 1) with respect to the elements of the stiffness tensor are derived in Appendix A using the results of Liu and Tromp (2006):

$$\frac{\partial\mathcal{F}}{\partial c_{ijkl}} = -\int_0^T \frac{\partial u_i}{\partial x_j}\frac{\partial\psi_k}{\partial x_l}\,\mathrm{d}t\,, \qquad (3)$$

where $\mathbf{u}$ and $\boldsymbol{\psi}$ are the forward and adjoint wavefields, respectively. Using the chain rule, we can find the gradient for the squared velocities V_n^2 (V_{P0}^2, V_{S0}^2, $V_{\mathrm{nmo},P}^2$, and $V_{\mathrm{hor},P}^2$):

$$\frac{\partial\mathcal{F}}{\partial V_n^2} = \sum_{ijkl}\frac{\partial\mathcal{F}}{\partial c_{ijkl}}\frac{\partial c_{ijkl}}{\partial V_n^2}. \qquad (4)$$

The stiffness coefficients are expressed in terms of the velocities in equations A18–A21. Combining equations 3, 4, and A18–A21 yields the gradients with respect to the squared velocities (equations A22– A25).

Here, FWI is implemented in the time domain, primarily because the finite-difference modeling software available to us performs time-domain computations. The multiscale approach described in Bunks et al. (1995) and Paper I helps reduce the nonlinearity of the objective function and ensure that each updated solution lies in the basin of convergence. At first, diving waves are employed to update the low-wavenumber component of the model and obtain a close approximation for traveltimes of the recorded arrivals. Reflection events can then be used to increase the vertical and lateral resolution of the inverted model. Application of this methodology to 2D synthetic data from heterogeneous VTI models will be discussed in a sequel paper.

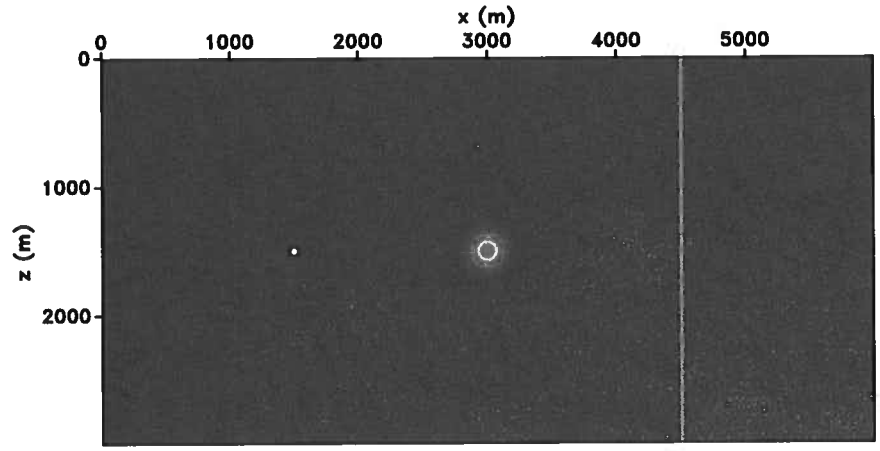

Figure 1. VTI model with a Gaussian anomaly (standard deviation $\sigma = 75$ m) in the anisotropy parameter ϵ. The background and maximum values of ϵ are 0.1 and 0.128, respectively. The other Thomsen parameters are spatially invariant: $V_{P0} = 3000\,\mathrm{m/s}$, $V_{S0} = 1500\,\mathrm{m/s}$, and $\delta = -0.1$. The white dot marks the source location and the white vertical line represents an array of receivers placed at each grid point (6.6 m apart).

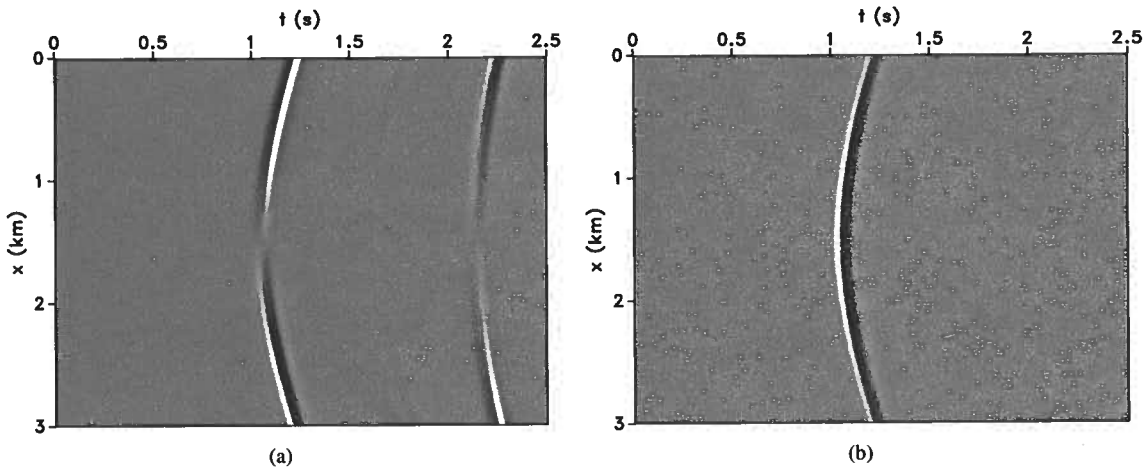

Figure 2. (a) Vertical and (b) horizontal displacements generated for the model in Figure 1.

3 GRADIENTS FOR GAUSSIAN ANOMALIES

Next, we perform tests for a simple synthetic model to verify the accuracy of the gradient computation. Because the initial stage of FWI involves diving waves, we compute the gradient for transmission experiments. The model includes Gaussian anomalies in the parameters V_{P0}, V_{S0}, ϵ, and δ inserted into a homogeneous VTI medium between a buried source and a vertical array of receivers (Figure 1). A point-displacement source with a peak frequency of 10 Hz polarized in the horizontal direction generates the data. The horizontal and vertical displacement components ("observed data") recorded by the receivers in the presence of the anomaly in ϵ are shown in Figure 2. Then the "modeled" data are generated in the background medium, and the adjoint source is obtained as the difference between the two wavefields (Figure 3).

The gradients with respect to the model parameters (squared velocities) for an anomaly in ϵ are calculated from equations A22–A25 (Figure 4). For the source-receiver geometry in Figure 1, waves travel close to the isotropy plane, and are influenced primarily by $V_{\mathrm{hor},P}$, which is a function of ϵ. Hence, the largest gradient is that for the velocity $V_{\mathrm{hor},P}$, which correctly identifies ϵ as the parameter that needs updating. However, the gradient with respect to V_{S0} is also significant, most likely because of the P-to-S conversion that takes place at the anomaly. The observed data include such conversions, while the wavefield modeled in the background medium does not. As a result, the obtained gradient resembles an "image" of the scatterer responsible for the conversion.

For a Gaussian anomaly with a larger radius (Figure 5), the gradient with respect to V_{S0} decreases (Figure 6), and there are fewer artifacts. This is likely due to the absence of the anomaly-induced PS conversions. In addition, the gradients for V_{P0} and $V_{\mathrm{nmo},P}$ are also small. In the presence of such a smooth anomaly in ϵ, we expect to see a change only

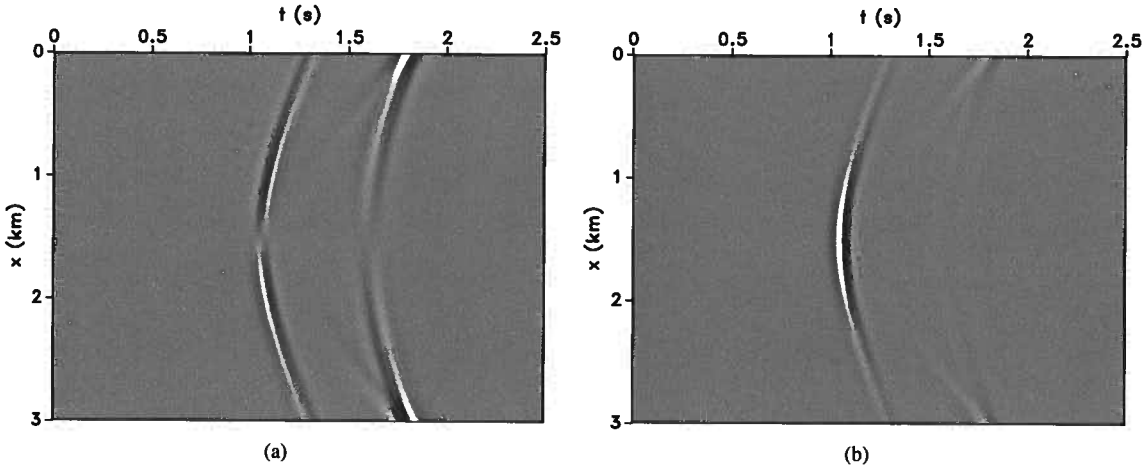

Figure 3. (a) Vertical and (b) horizontal components of the adjoint source for the model in Figure 1 obtained as the difference between the observed data from Figure 2 and the modeled data for the background medium (in the absence of the anomaly).

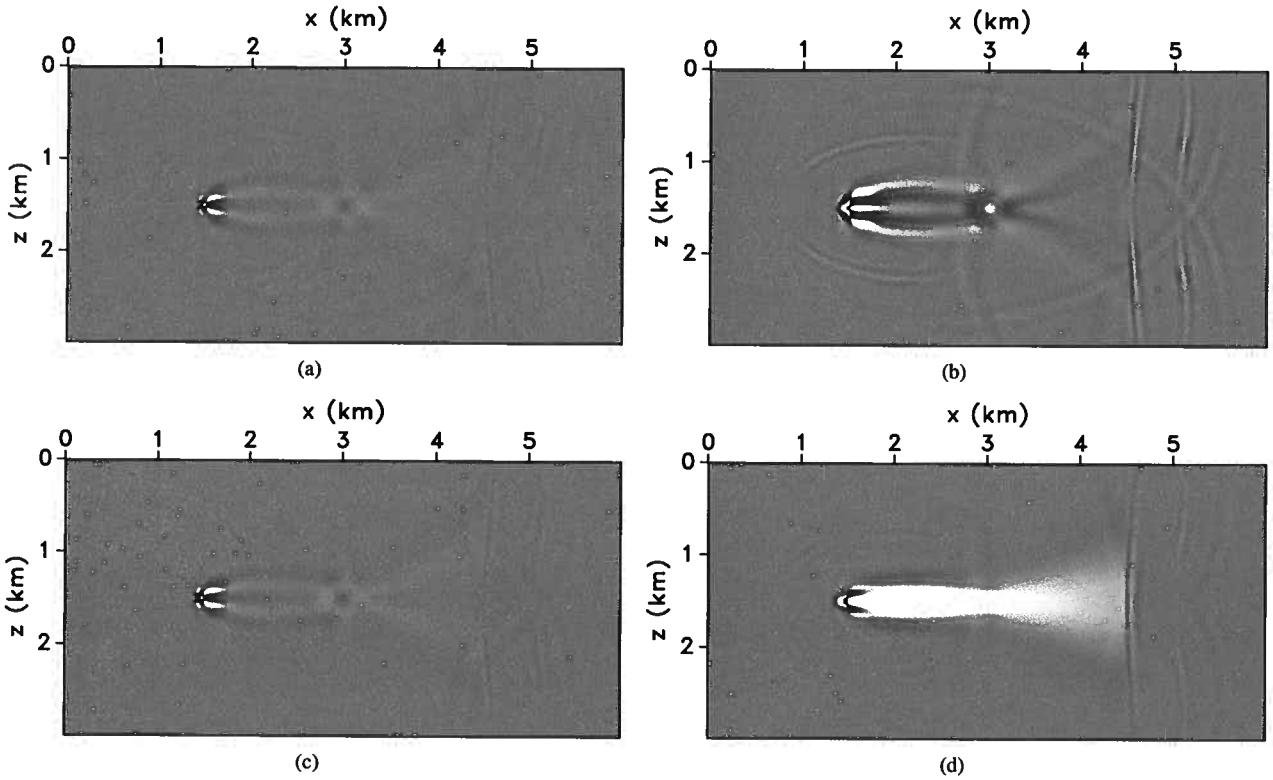

Figure 4. Gradients of the objective function (equation 1) with respect to (a) V_{P0}^2, (b) V_{S0}^2, (c) $V_{\mathrm{nmo},P}^2$, and (d) $V_{\mathrm{hor},P}^2$ for the model with an anomaly in ϵ (Figure 1). All four gradients here and on the plots below are plotted on the same scale.

in $V_{\mathrm{hor},P}$, which is indeed the case (Figure 6). As mentioned above, this is the desired result because $V_{\mathrm{hor},P}$ is the only parameter influenced by ϵ. All gradients in Figures 4 and 6 reach extremely large values at the source where the wavefield has the highest amplitude. This problem can be mitigated by applying an appropriate preconditioner (e.g., a Gaussian taper at the source). The large gradients along the horizontal raypath from the source indicate the nonuniqueness of the inverse problem for the configuration with a single source. Increasing the number of shots is likely to help focus the largest gradient values at the anomaly.

Similar tests performed for Gaussian anomalies in the pa-

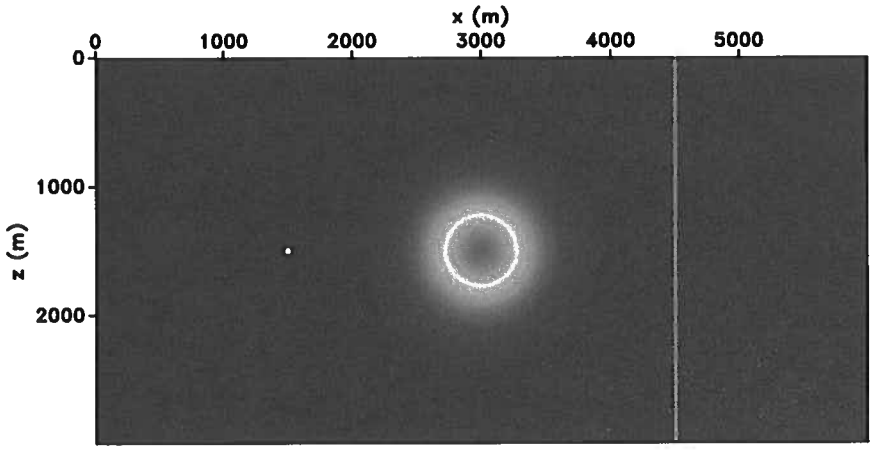

Figure 5. VTI model with a larger (in spatial extent) Gaussian anomaly in the anisotropy parameter ϵ. The standard deviation of the anomaly $\sigma = 300$ m. The background and maximum values of ϵ are 0.1 and 0.128, respectively. The other parameters are $V_{P0} = 3000\,\mathrm{m/s}$, $V_{S0} = 1500\,\mathrm{m/s}$, and $\delta = -0.1$.

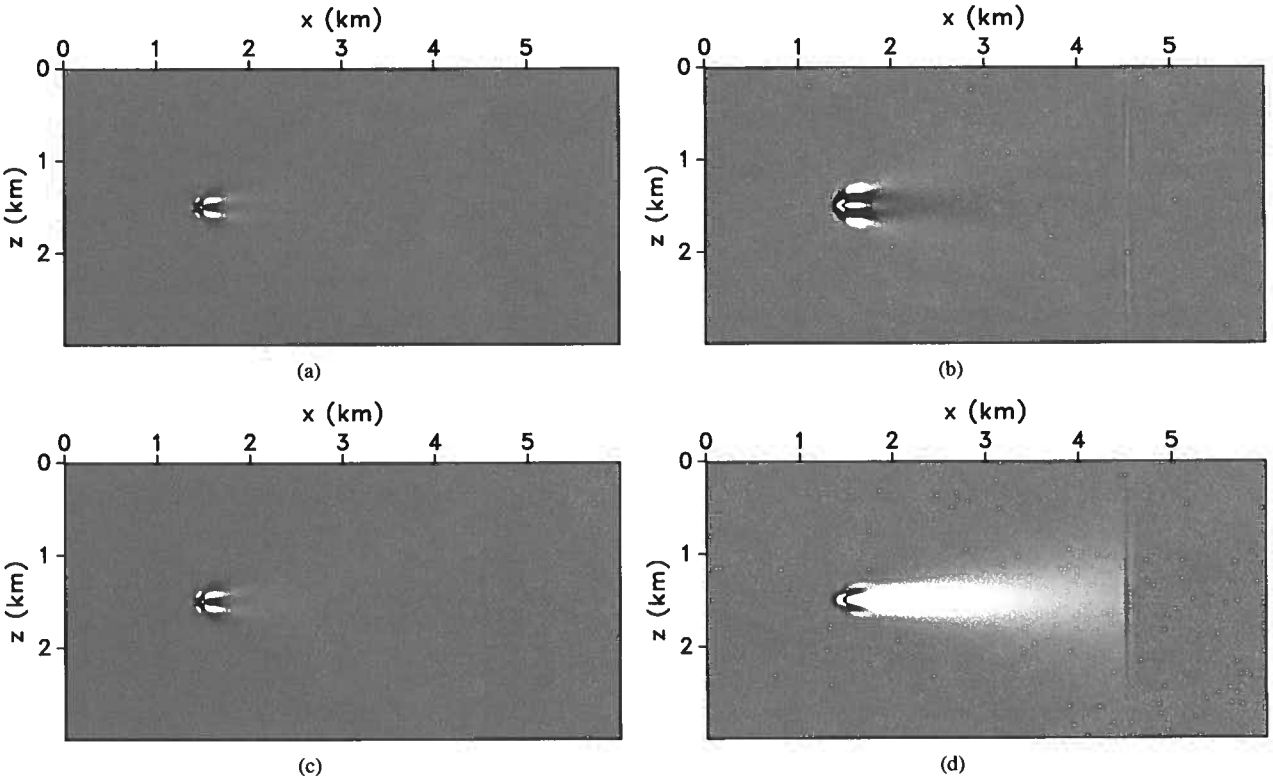

Figure 6. Gradients of the objective function with respect to (a) V_{P0}^2, (b) V_{S0}^2, (c) $V_{\mathrm{nmo},P}^2$, and (d) $V_{\mathrm{hor},P}^2$ for the model with an anomaly in ϵ from Figure 5.

rameter δ show that the gradients with respect to all four velocities are smaller compared to those obtained for the anomaly in ϵ.

Next we introduce an anomaly in the P-wave vertical velocity V_{P0} (Figure 7). As was the case for the model in Figure 5, there are no PS conversions because of the increased spatial extent of the anomaly. The largest gradient is the one with respect to the horizontal velocity (Figure 8), whereas the gradients with respect to V_{P0} and $V_{\mathrm{nmo},P}$ (which also depend on V_{P0}) are negligible. Although $V_{\mathrm{hor},P}$ depends on V_{P0}, updating the horizontal velocity without changing V_{P0} will result in an update in ϵ and steer the inversion away from recovering

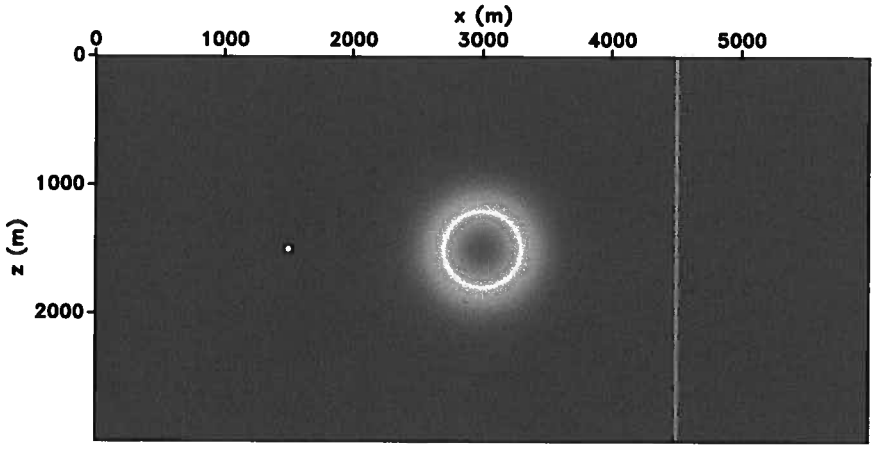

Figure 7. VTI model with a Gaussian anomaly in the P-wave vertical velocity V_{P0}. The background and maximum values of V_{P0} are 3000 m/s and 3140 m/s, respectively. The other parameters are $V_{S0} = 1500\,\mathrm{m/s}$, $\delta = -0.1$, and $\epsilon = 0.1$.

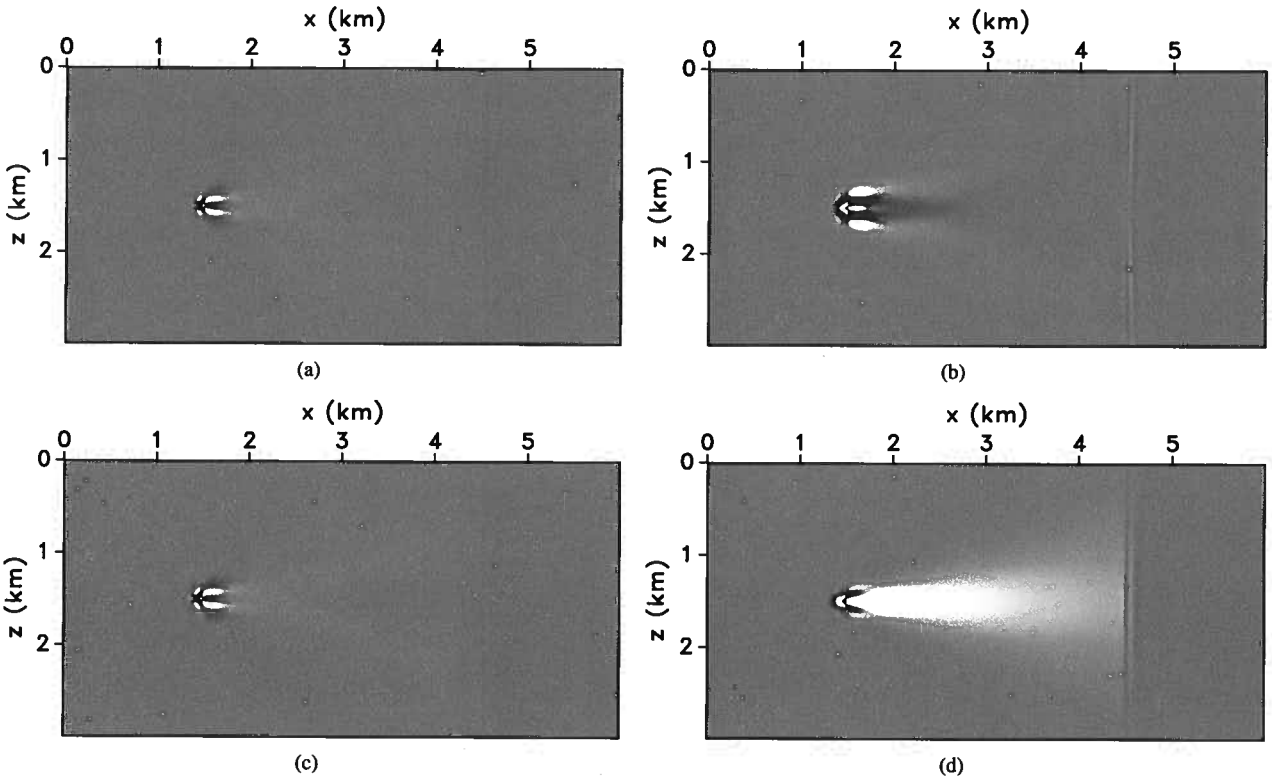

Figure 8. Gradients of the objective function with respect to (a) V_{P0}^2, (b) V_{S0}^2, (c) $V_{\mathrm{nmo},P}^2$, and (d) $V_{\mathrm{hor},P}^2$ for the model with an anomaly in V_{P0} from Figure 7.

the anomaly in V_{P0}. Increasing the number of sources, with a larger polar angle coverage, is likely to elevate the gradients with respect to all three velocities, and, potentially improve the convergence of the inversion algorithm.

When the source-receiver configuration is rotated by 90° (Figure 9) and the wave propagation is predominantly vertical, the largest gradient is the one with respect to V_{P0} (Figure 10). In principle, the gradients for V_{nmo} and $V_{\mathrm{hor},P}$ should not vanish, which would ensure that the parameters ϵ and δ do not get updated. As in the previous case, multiple shots with improved spatial coverage should increase the gradients for the NMO and horizontal velocities.

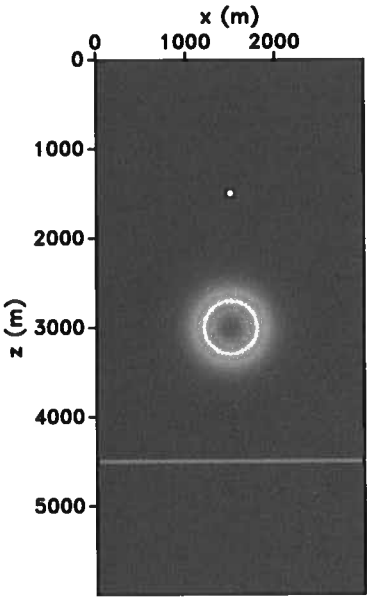

Figure 9. VTI model with a Gaussian anomaly ($\sigma = 300\,m$) in the P-wave vertical velocity V_{P0} and different source-receiver geometry. The source-receiver configuration from Figure 7 is rotated by 90°. The background and maximum values of V_{P0} are 3000 m/s and 3140 m/s, respectively. The other parameters are $V_{S0} = 1500$ m/s, $\delta = -0.1$, and $\epsilon = 0.1$.

The gradients for a Gaussian anomaly in V_{S0} and a horizontal receiver array (Figure 11) are displayed in Figure 12. As expected, the gradient with respect to V_{S0} is much larger than the other three. However, because the source is polarized in the vertical direction, the SV-wave amplitude vanishes along the symmetry axis and increases away from it. As a result, the gradient for V_{S0} reaches its maximum at oblique incidence angles near the symmetry axis.

4 CONCLUSIONS

One of the most important steps in performing FWI is calculation of the gradient of the objective function with respect to the model parameters. We discussed gradient computation for elastic multicomponent wavefields from 2D VTI media. The in-plane polarized waves (P and SV) are controlled by combinations of four stiffness coefficients: C_{11}, C_{13}, C_{33}, and C_{55}. The adjoint state method was employed to derive analytic expressions for the gradients of the least-squares objective function with respect to the stiffnesses. A more convenient parameterization, however, includes the squares of the P-wave vertical (V_{P0}), NMO ($V_{\mathrm{nmo},P}$), and horizontal ($V_{\mathrm{hor},P}$) velocities, and of the S-wave vertical velocity (V_{S0}).

After obtaining the gradients for V_{P0}^2, V_{S0}^2, $V_{\mathrm{nmo},P}^2$, and V_{hor}^2, we conducted numerical tests for Gaussian anomalies in the Thomsen parmeters V_{P0}, V_{S0}, ϵ, and δ embedded in a homogeneous VTI model. The gradients were computed for a single buried source and an array of receivers placed at each grid point along a straight line. If the spatial extent of the anomaly is small, it acts as a secondary source that generates P-to-S conversions. The obtained gradients in this case essentially represent images of the anomaly and their meaning requires further analysis.

For anomalies with a larger spatial extent, the converted waves are weak and there are fewer artifacts. The magnitude of the gradient with respect to each model parameter is governed by the source position and polarization, as well as the location and configuration of the receiver array. For example, an anomaly in V_{P0} produces a large gradient with respect to $V_{\mathrm{hor},P}$ when the wavefield propagates predominantly in the horizontal direction. The gradient for V_{P0}, however, is negligible, which would result in an undesired change in the parameter ϵ. However, for the same V_{P0} anomaly, but a different source-receiver geometry, when waves travel close to the vertical, the dominant gradient in the one with respect to V_{P0}. For the same source-receiver configuration with near-vertical wave propagation, an anomaly in the S-wave vertical velocity produces a large gradient with respect to V_{S0}. The maximum gradient, however, is observed at oblique incidence because the source polarization is vertical. Increasing the number of shots should improve illumination and result in gradients that are more consistent with the anomaly. Multiple shots are also expected to reduce the artifacts in the gradient fields.

The obtained gradients should be combined with an appropriate line-search technique to make meaningful model updates. In addition, it is necessary to investigate if the same step length can be used for all model parameters.

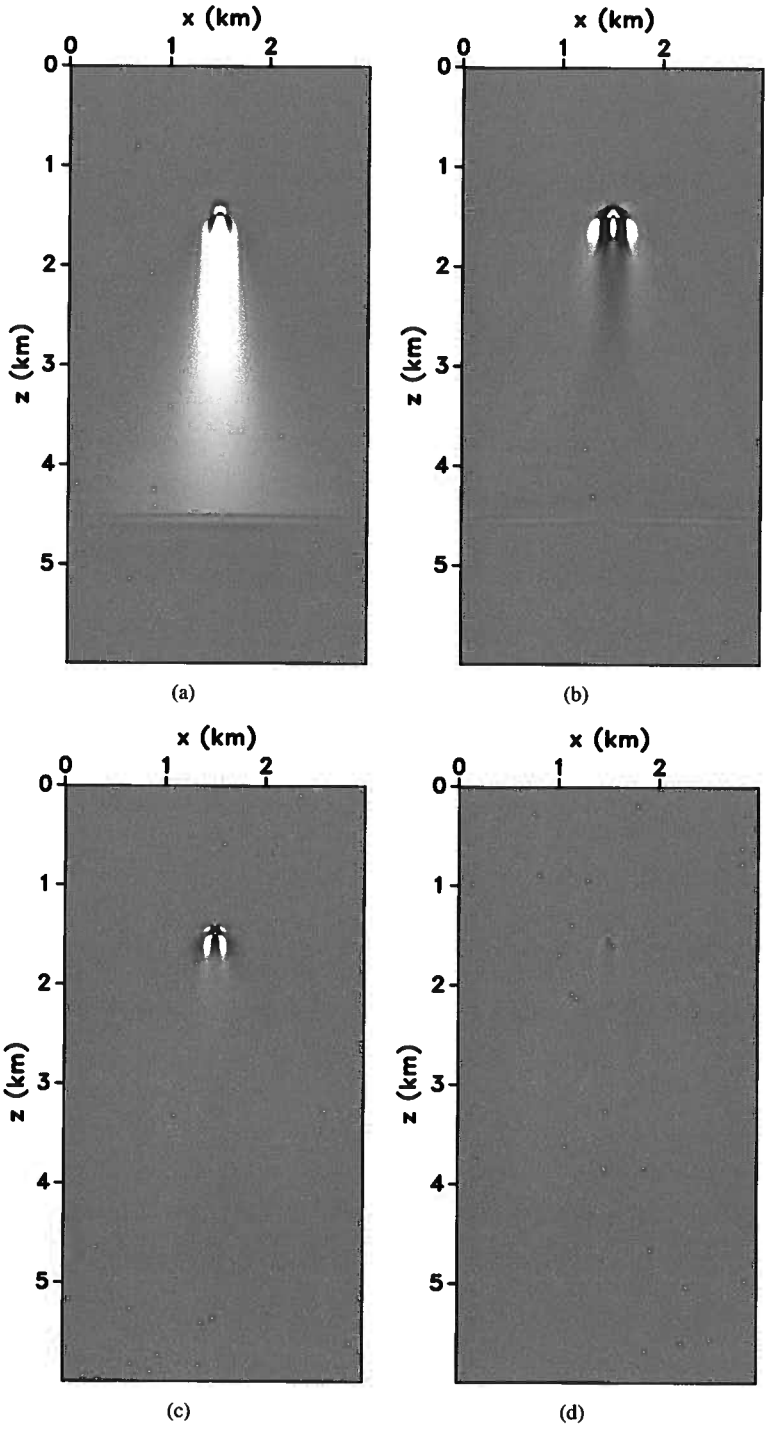

Figure 10. Gradients of the objective function with respect to (a) V_{P0}^2, (b) V_{S0}^2, (c) $V_{\mathrm{nmo},P}^2$, and (d) $V_{\mathrm{hor},P}^2$ for the model with an anomaly in V_{P0} from Figure 9.

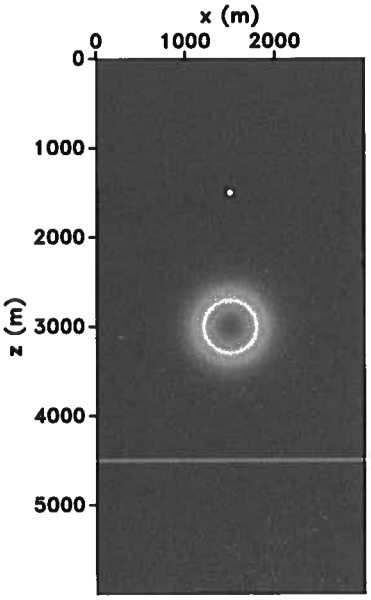

Figure 11. VTI model with a Gaussian anomaly ($\sigma = 300\,m$) in the S-wave vertical velocity V_{S0}. The background and maximum values of V_{S0} are 1500 m/s and 1640 m/s, respectively. The other parameters are $V_{P0} = 3000\,\mathrm{m/s}$, $\delta = -0.1$, and $\epsilon = 0.1$.

5 ACKNOWLEDGMENTS

We are grateful to the members of the A(nisotropy) and i(maging) teams at CWP and to Francesco Perrone, Esteban Diaz and Simon Luo (CWP), Daniel Köhn (University of Kiel), Ken Matson (Shell), and Jon Sheiman (contractor, Shell), for fruitful discussions. We would also like to thank John Stockwell (CWP) and Paul Martin (Dept. of Mathematics, CSM) for help with mathematical issues. This work was supported by the Consortium Project on Seismic Inverse Methods for Complex Structures at CWP and by the CIMMM Project of the Unconventional Natural Gas Institute at CSM. The reproducible numeric examples in this paper are generated with the Madagascar open-source software package freely available from http://www.ahay.org.

REFERENCES

Bunks, C., F. M. Saleck, S. Zaleski, and G. Chavent, 1995, Multiscale seismic waveform inversion: Geophysics, **60**, 1457–1473.

Fichtner, A., H.-P. Bunge, and H. Igel, 2006, The adjoint method in seismology: I. theory: Physics of the Earth and Planetary Interiors, **157**, 86 – 104.

Gauthier, O., 1986, Two-dimensional nonlinear inversion of seismic waveforms: Numerical results: Geophysics, **51**, 1387–1403.

Gholami, Y., R. Brossier, S. Operto, V. Prieux, A. Ribodetti, and J. Virieux, 2011, Two-dimensional acoustic anisotropic (VTI) full waveform inversion: The Valhall case study: SEG Technical Program Expanded Abstracts, **30**, 2543–2548.

Kamath, N., and I. Tsvankin, 2012, Full-waveform inversion of multicomponent data for layered VTI media: CWP Report, **706**, 11–19.

Köhn, D., D. De Nil, A. Kurzmann, A. Przebindowska, and T. Bohlen, 2012, On the influence of model parametrization in elastic full waveform tomography: Geophysical Journal International, **191**, 325–345.

Kolb, P., F. Collino, and P. Lailly, 1986, Pre-stack inversion of a 1-D medium: Proceedings of the IEEE, **74**, 498–508.

Lee, H., J. M. Koo, D. Min, B. Kwon, and H. S. Yoo, 2010, Frequency-domain elastic full waveform inversion for VTI media: Geophysical Journal International, **183**, 884–904.

Liu, Q., and J. Tromp, 2006, Finite-frequency kernels based on adjoint methods: Bulletin of the Seismological Society of America, **96**, 2383–2397.

Mora, P., 1987, Nonlinear two-dimensional elastic inversion of multioffset seismic data: Geophysics, **52**, 1211–1228.

Plessix, R., and Q. Cao, 2011, A parametrization study for surface seismic full waveform inversion in an acoustic vertical transversely isotropic medium: Geophysical Journal International, **185**, 539–556.

Plessix, R.-E., and H. Rynja, 2010, VTI full waveform inversion: a parameterization study with a narrow azimuth streamer data example: SEG Technical Program Expanded Abstracts, **29**, 962–966.

Plessix, R. ., 2006, A review of the adjointstate method for computing the gradient of a functional with geophysical applications: Geophysical Journal International, **167**, 495–503.

Pratt, R. G., 1999, Seismic waveform inversion in the frequency domain; part 1, theory and verification in a physical scale model: Geophysics, **64**, 888–901.

Pratt, R. G., and R. M. Shipp, 1999, Seismic waveform in-

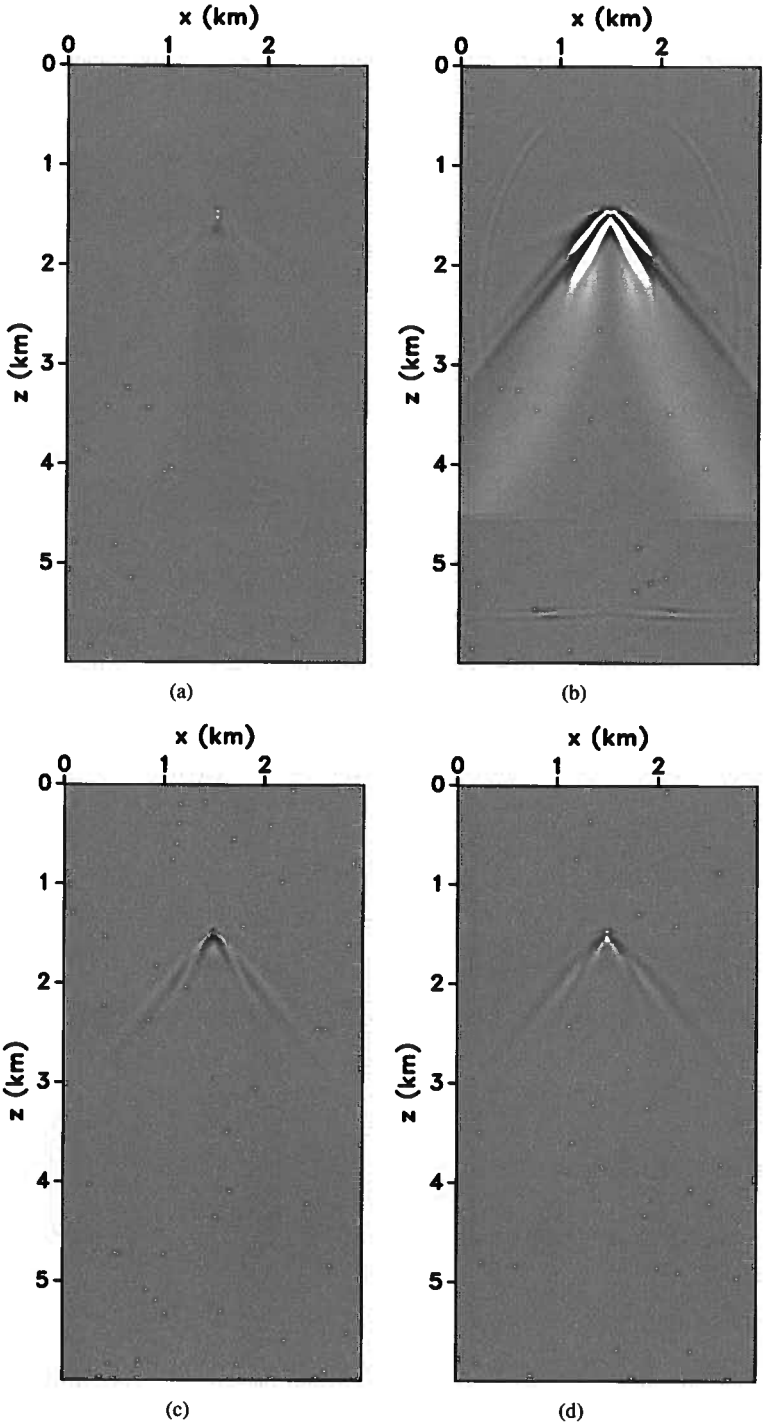

Figure 12. Gradients of the objective function with respect to (a) V_{P0}^2, (b) V_{S0}^2, (c) $V_{\mathrm{nmo},P}^2$, and (d) $V_{\mathrm{hor},P}^2$ for the model with an anomaly in V_{S0} from Figure 11.

version in the frequency domain; part 2; fault delineation in sediments using crosshole data: Geophysics, **64**, 902–914.
Shen, X., 2012, Early-arrival waveform inversion for near-surface velocity and anisotropic parameter: Parametrization study: SEG Technical Program Expanded Abstracts 2012, SEG, 1–5.
Song, Z., and P. R. Williamson, 1995, Frequency-domain acoustic-wave modeling and inversion of crosshole data; part 1, 2.5-D modeling method: Geophysics, **60**, 784–795.
Song, Z., P. R. Williamson, and R. G. Pratt, 1995, Frequency-domain acoustic-wave modeling and inversion of crosshole data; Part II — Inversion method, synthetic experiments and real-data results: Geophysics, **60**, 796–809.
Strang, G., 1991, Calculus: Wellesley-Cambridge Press.
Tarantola, A., 1984a, Inversion of seismic reflection data in the acoustic approximation: Geophysics, **49**, 1259–1266.
———, 1984b, Linearized inversion of seismic reflection data: Geophysical Prospecting, **32**, 998–1015.
Tsvankin, I., 2012, Seismic signatures and analysis of reflection data in anisotropic media, Third ed.: Society of Exploration Geophysicists.
Virieux, J., and S. Operto, 2009, An overview of full-waveform inversion in exploration geophysics: Geophysics, **74**, WCC1–26.

APPENDIX A: APPENDIX A: GRADIENT COMPUTATION FOR VTI MEDIA USING THE ADJOINT STATE METHOD

As discussed in Plessix (2006) and Liu and Tromp (2006), the objective function in equation 1 is minimized under the constraint that the modeled displacement $\mathbf{u}(\mathbf{x}_r, t)$ satisfies the elastic wave equation,

$$\rho \frac{\partial^2 u_i}{\partial t^2} - \frac{\partial}{\partial x_j}\left(c_{ijkl}\frac{\partial u_k}{\partial x_l}\right) = f_i\,, \tag{A1}$$

where ρ is the density, c_{ijkl} are components of the stiffness tensor and $\mathbf{f}$ is the body force per unit volume. All indices change from 1 to 3 and summation over repeated indices is implied. The displacement wavefield is subject to the initial conditions,

$$\mathbf{u}(\mathbf{x}, 0) = 0, \quad \frac{\partial \mathbf{u}(\mathbf{x}, 0)}{\partial t} = 0, \tag{A2}$$

and the radiation boundary condition,

$$\mathbf{u}(\mathbf{x}, t)|_{\mathbf{x}\to\infty} \to 0. \tag{A3}$$

The method of Lagrange multipliers (Strang, 1991) is used to define the Lagrangian Λ:

$$\Lambda = \frac{1}{2}\sum_r \int_0^T \|\mathbf{u}(\mathbf{x}_r, t) - \mathbf{d}(\mathbf{x}_r, t)\|^2 \mathrm{d}t - \int_0^T \int_\Omega \lambda_i \left[\rho \frac{\partial^2 u_i}{\partial t^2} - \frac{\partial}{\partial x_j}\left(c_{ijkl}\frac{\partial u_k}{\partial x_l}\right) - f_i\right] \mathrm{d}V\mathrm{d}t, \tag{A4}$$

where Ω is the domain of integration, $\partial\Omega$ is the surface of Ω, and $\boldsymbol{\lambda}(\mathbf{x}, t)$ is the vector Lagrange multiplier that needs to be determined. Note that when $\mathbf{u}(\mathbf{x}, t)$ satisfies the wave equation, the second term in the above equation disappears and Λ reduces to the objective function in equation 1. Each of the model parameters (c_{ijkl} in this case) and the state variable $\mathbf{u}$ are perturbed. After integration by parts and application of the Gauss divergence theorem, we obtain the change in the Lagrangian,

$$\begin{aligned}
\delta\Lambda = & \int_0^T \int_\Omega \sum_{r=1}^{N} \Big(u_i(\mathbf{x}, t) - d_i(\mathbf{x}, t)\Big)\delta(\mathbf{x} - \mathbf{x}_r)\delta u_i \,\mathrm{d}V\mathrm{d}t \\
& - \int_0^T \int_\Omega \delta c_{ijkl}\, \frac{\partial u_k}{\partial x_l}\, \frac{\partial \lambda_i}{\partial x_j}\, \mathrm{d}V\mathrm{d}t - \int_0^T \int_\Omega \left[\rho \frac{\partial^2 \lambda_i}{\partial t^2} - \frac{\partial}{\partial x_j}\left(c_{ijkl}\, \frac{\partial \lambda_k}{\partial x_l}\right)\right] \delta u_i \,\mathrm{d}V\mathrm{d}t \\
& - \int_\Omega \left[\rho \lambda_i \frac{\partial(\delta u_i)}{\partial t} - \rho\, \delta u_i\, \frac{\partial \lambda_i}{\partial t}\right]\Bigg|_0^T \mathrm{d}V \\
& + \int_0^T \int_{\partial\Omega} \lambda_i \left[\delta c_{ijkl}\, \frac{\partial u_k}{\partial x_l} + c_{ijkl}\, \frac{\partial(\delta u_k)}{\partial x_l}\right] n_j \,\mathrm{d}S\,\mathrm{d}t - \int_0^T \int_{\partial\Omega} \delta u_i\, c_{ijkl}\, \frac{\partial \lambda_k}{\partial x_l}\, n_j \,\mathrm{d}S\,\mathrm{d}t\,,
\end{aligned} \tag{A5}$$

where $\mathbf{n}$ is the vector normal to the surface $\partial\Omega$ and $r = 1, 2 \ldots$ N denotes the receivers. Perturbing $\mathbf{u}(\mathbf{x}, t)$ in equations A2 and A3 yields the initial and boundary conditions for $\delta\mathbf{u}(\mathbf{x}, t)$:

$$\delta\mathbf{u}(\mathbf{x}, 0) = 0, \quad \frac{\partial \delta\mathbf{u}(\mathbf{x}, t)}{\partial t} = 0, \quad \delta\mathbf{u}(\mathbf{x}, t)|_{\mathbf{x}\to\infty} \to 0. \tag{A6}$$

The wavefield $\boldsymbol{\lambda}$ is constrained by the 'final' conditions (i.e., those at time T),

$$\boldsymbol{\lambda}(\mathbf{x}, T) = \mathbf{0}, \quad \frac{\partial \boldsymbol{\lambda}(\mathbf{x}, T)}{\partial t} = \mathbf{0}, \tag{A7}$$

and the boundary condition,

$$\boldsymbol{\lambda}(\mathbf{x}, t)\,|_{\mathbf{x}\to\infty} \to 0. \tag{A8}$$

Equation A5 then reduces to

$$\delta\Lambda = \int_0^T \int_\Omega \sum_{r=1}^{N} \Big(u_i(\mathbf{x}, t) - d_i(\mathbf{x}, t)\Big)\delta(\mathbf{x} - \mathbf{x}_r)\delta u_i \,\mathrm{d}V\mathrm{d}t$$

$$-\int_0^T \int_\Omega \delta c_{ijkl} \frac{\partial u_k}{\partial x_l} \frac{\partial \lambda_i}{\partial x_j} \, \mathrm{d}V\mathrm{d}t - \int_0^T \int_\Omega \left[\rho \frac{\partial^2 \lambda_i}{\partial t^2} - \frac{\partial}{\partial x_j}\left(c_{ijkl} \frac{\partial \lambda_k}{\partial x_l}\right)\right] \delta u_i \, \mathrm{d}V\mathrm{d}t \, . \tag{A9}$$

According to Plessix (2006), the condition $\partial\Lambda/\partial\boldsymbol{\lambda} = 0$ leads to the "state equations" (in this case, the elastic wave equation); this can be verified from equation A4. The adjoint state equations are obtained by setting $\partial\Lambda/\partial\mathbf{u} = 0$. Taking the derivative in equation A9 gives the adjoint state equation,

$$\rho \frac{\partial^2 \lambda_i}{\partial t^2} - \frac{\partial}{\partial x_j}\left(c_{ijkl} \frac{\partial \lambda_k}{\partial x_l}\right) = \sum_{r=1}^{\mathrm{N}} \Big[u_i(\mathbf{x}_r, t) - d_i(\mathbf{x}_r, t)\Big], \tag{A10}$$

subject to the conditions at time T (equation A7) and boundary conditions (equation A8). In addition, $\partial\Lambda/\partial\mathbf{m} = \partial\mathcal{F}/\partial\mathbf{m}$, where $\mathbf{m}$ are the model parameters (Plessix, 2006). Hence, the change in the objective function $\delta\mathcal{F}$ caused by perturbations of the stiffness coefficients is given by:

$$\delta\mathcal{F} = -\int_0^T \int_\Omega \delta c_{ijkl} \frac{\partial u_i}{\partial x_j} \frac{\partial \lambda_k}{\partial u_l} \, \mathrm{d}V\mathrm{d}t \, . \tag{A11}$$

This is a general result for an anisotropic medium described by the complete stiffness tensor c_{ijkl}. Expressions for models with specific symmetries can be derived from equation A11 by substituting the appropriate stiffness tensors or matrices.

Note that the boundary conditions for $\mathbf{u}(\mathbf{x}, t)$ and $\boldsymbol{\lambda}(\mathbf{x}, t)$ can be modified to include a free surface where the tractions due to $\mathbf{u}$ and $\boldsymbol{\lambda}$ go to zero. However, the addition of the free surface causes complications in finite-difference modeling and produces surface multiples. Instead, we impose the radiation condition to create absoring boundaries on all sides of the model.

To simulate the Lagrange multiplier wavefield, it is convenient to define an "adjoint wavefield" ψ (Liu and Tromp, 2006):

$$\psi(\mathbf{x}, t) \equiv \boldsymbol{\lambda}(\mathbf{x}, T - t). \tag{A12}$$

The wavefield ψ satisfies the wave equation A10 but with the source function reversed in time:

$$\rho \frac{\partial^2 \psi_i}{\partial t^2} - \frac{\partial}{\partial x_j}\left(c_{ijkl} \frac{\partial \psi_k}{\partial x_l}\right) = \sum_{r=1}^{\mathrm{N}} \Big[u_i(\mathbf{x}_r, T - t) - d_i(\mathbf{x}_r, T - t)\Big] \, . \tag{A13}$$

The initial conditions for ψ (using equations A7 and A12) are as follows:

$$\psi(\mathbf{x}, 0) = 0, \quad \frac{\partial \psi(\mathbf{x}, 0)}{\partial t} = 0. \tag{A14}$$

The wavefield ψ also satisfies the radiation boundary condition:

$$\psi(\mathbf{x}, t)|_{\mathbf{x}\to\infty} \to 0. \tag{A15}$$

Note that defining the adjoint wavefield makes it possible to simulate the Lagrange multiplier wavefield (which starts at time T and propagates backward in time).

From equations A11 and A12, we can find the gradient of the objective function with respect to the stiffness coefficients:

$$\frac{\partial \mathcal{F}}{\partial c_{ijkl}} = -\int_0^T \frac{\partial u_i}{\partial x_j} \frac{\partial \psi_k}{\partial x_l} \, \mathrm{d}t. \tag{A16}$$

If, instead of c_{ijkl}, the model is described by parameters m_n, the gradient of $\mathcal{F}$ can be found from the chain rule:

$$\frac{\partial \mathcal{F}}{\partial m_n} = \sum_{ijkl} \frac{\partial \mathcal{F}}{\partial c_{ijkl}} \frac{\partial c_{ijkl}}{\partial m_n}. \tag{A17}$$

Here, we parameterize the model in terms of the squared velocities V_{P0}^2, V_{S0}^2, $V_{\mathrm{nmo},P}^2$, and $V_{\mathrm{hor},P}^2$. The stiffness coefficients (written in the two-index notation) represent the following functions of the velocities (Tsvankin, 2012):

$$C_{11} = \rho V_{\mathrm{hor},P}^2, \tag{A18}$$

$$C_{33} = \rho V_{P0}^2, \tag{A19}$$

$$C_{13} = \rho \sqrt{(V_{P0}^2 - V_{S0}^2)(V_{\mathrm{nmo},P}^2 - V_{S0}^2)} - \rho V_{S0}^2, \tag{A20}$$

$$C_{55} = \rho V_{S0}^2. \tag{A21}$$

Using equations A16, A17, and A18 – A21, we obtain the following gradients of the objective function with respect to V_n^2:

$$\frac{\partial \mathcal{F}}{\partial \left(V_{P0}^2\right)} = -\int_0^T \rho \left[\frac{\partial \psi_3}{\partial x_3}\frac{\partial u_3}{\partial x_3} + \frac{1}{2}\sqrt{\frac{V_{\mathrm{nmo},P}^2 - V_{S0}^2}{V_{P0}^2 - V_{S0}^2}} \left(\frac{\partial \psi_1}{\partial x_1}\frac{\partial u_3}{\partial x_3} + \frac{\partial \psi_3}{\partial x_3}\frac{\partial u_1}{\partial x_1} \right) \right] \mathrm{d}t, \tag{A22}$$

$$\frac{\partial \mathcal{F}}{\partial \left(V_{S0}^2\right)} = -\int_0^T \rho \left\{ \left[\frac{2V_{S0}^2 - V_{P0}^2 - V_{\mathrm{nmo},P}^2}{2\sqrt{(V_{\mathrm{nmo},P}^2 - V_{S0}^2)(V_{P0}^2 - V_{S0}^2)}} - 1 \right] \left(\frac{\partial \psi_1}{\partial x_1}\frac{\partial u_3}{\partial x_3} + \frac{\partial \psi_3}{\partial x_3}\frac{\partial u_1}{\partial x_1} \right) \right.$$

$$\left. + \left(\frac{\partial \psi_1}{\partial x_3} + \frac{\partial \psi_3}{\partial x_1} \right) \left(\frac{\partial u_1}{\partial x_3} + \frac{\partial u_3}{\partial x_1} \right) \right\} \mathrm{d}t, \tag{A23}$$

$$\frac{\partial \mathcal{F}}{\partial \left(V_{\mathrm{nmo},P}^2\right)} = -\int_0^T \frac{\rho}{2}\sqrt{\frac{V_{P0}^2 - V_{S0}^2}{V_{\mathrm{nmo},P}^2 - V_{S0}^2}} \left(\frac{\partial \psi_1}{\partial x_1}\frac{\partial u_3}{\partial x_3} + \frac{\partial \psi_3}{\partial x_3}\frac{\partial u_1}{\partial x_1} \right) \mathrm{d}t, \tag{A24}$$

$$\frac{\partial \mathcal{F}}{\partial \left(V_{\mathrm{hor},P}^2\right)} = -\int_0^T \rho \frac{\partial \psi_1}{\partial x_1}\frac{\partial u_1}{\partial x_1}\, \mathrm{d}t, \tag{A25}$$

Anisotropy signature in RTM extended images

Paul Sava[1] & Tariq Alkhalifah[2]
[1] *Center for Wave Phenomena, Colorado School of Mines*
[2] *King Abdullah University of Science and Technology*

ABSTRACT
Reverse-time migration can accurately image complex geologic structures in anisotropic media. Extended images at selected locations in the earth, i.e. at common-image-point gathers (CIPs), carry rich information to characterize the angle-dependent illumination and to provide measurements for migration velocity analysis. However, characterizing the anisotropy influence on such extended images is a challenge. Extended CIPs are cheap to evaluate, since they sample the image at sparse locations indicated by the presence of strong reflectors. Such gathers are also sensitive to velocity error which manifests itself through moveout as a function of space and time lags. Furthermore, inaccurate anisotropy leaves a distinctive signature in CIPs, which can be used to evaluate anisotropy through techniques similar to the ones used in conventional wavefield tomography. It, specifically, admits a "V"-shape residual moveout with the slope of the "V" flanks depending on the ellipticity anisotropic parameter η regardless of the complexity of the velocity model. It reflects the fourth-order nature of the anisotropy influence on moveout, as it manifests it self in this distinct signature in extended images after handling the velocity properly in the imaging process. Synthetic and real data observations support this assertion.

Key words: imaging, wave-equation, angle-domain, wide-azimuth, anisotropy

1 INTRODUCTION

Wave-equation depth migration is powerful and accurate for imaging complex geology, but its potential can only be achieved with high quality models of the earth (Gray et al., 2001). Imaging using reverse-time migration (Baysal et al., 1983; McMechan, 1983), addresses this challenge, although this technique is still fairly computationally intensive, especially in anisotropic media.

Imaging with reverse-time migration can be described as a sequence of two main steps. The first step consists of wavefield reconstruction from known quantities on the surface, i.e. the wavelet known at the source position, and the data known at the receiver positions. The wavefields are reconstructed everywhere in the medium as a solution of the wave-equation. This reconstruction makes use of an earth model which can be, for example, anisotropic. The second step represents an imaging condition, i.e. a procedure that identifies places in the subsurface where the reconstructed wavefields coincide. The imaging condition is often implemented by cross-correlation of the wavefields. A general imaging condition preserves in the output the space and time correlation lags, and thus it can be named an extended imaging condition for which the conventional cross-correlation is a special case.

Assuming that the wavefields are accurately reconstructed in the subsurface, the correlation maximizes at zero lag, both in space and in time. Accurate reconstruction implies not only that we use a correct earth model, but it also implies that the recorded data illuminates completely the subsurface in the area under investigation. Good illumination requires not only that we collect data with wide azimuth and long offsets, but it also means that the geologic structure does not obstruct our imaging target inside the earth through, for example, shadows caused by salt bodies.

Typically, the problem of large output can be addressed by analyzing subsets of the image. For example, we can consider common-image-gathers (CIGs), which are subsets of extended images constructed for various lags at fixed horizontal coordinates in the earth. For example, we can consider space-lag CIGs (Rickett and Sava, 2002) , or time-lag CIGs (Sava and Fomel, 2006) , which can be transformed into angle-gathers (Sava and Fomel, 2003) for easier analysis for even anisotropic media (Sava and Alkhalifah, 2012; Alkhalifah and Fomel, 2011). Alternatively, we can construct common-image-point-gathers (CIPs), which are subsets of extended images constructed for all lags at fixed coordinates in the image. The points where we construct the gathers can be identified automatically using image features, e.g. reflectivity strength, spatial coherency, etc. (Cullison and Sava, 2011) .

In anisotropic media, the extrapolation of the source and

receiver fields need to take anisotropy into account. This requires that we have access to proper anisotropic parameter description of the medium. For transversely isotropic (TI) media, this implies that we need to know the anisotropy model parameter, η, responsible for the anellipticity behavior of the phase velocity. This parameter, together with the normal moveout velocity described along the symmetry axis direction, enables us to perform accurate imaging in TI media (Alkhalifah et al., 2001). The axis of symmetry velocity, v_{p_z}, for a medium with vertical symmetry axis is mainly responsible for placing reflections at their accurate depth positions. Thus, for anisotropic media the key parameter for proper imaging and focussing is η. Ignoring η yields residual moveout in subsurface offsets and angle gathers (Alkhalifah and Fomel, 2011); it yields even more distinct features in extended images.

In this paper, we analyze the extended images in anisotropic media, and specifically transversely isotropic (TI) media. These extended images provide image point extensions as a function of space- and time-lags. Embedded in these lag sections is valuable image focusing information, which can be used to analyze the model accuracy used in the wavefield extrapolation. As a result, we use such lag sections to characterize the response of the extended images to ignoring anisotropy in RTM. We find that the anisotropy error leaves a distinctive signature in migrated extended images. We restrict our attention to the analysis of migrated images, and explore in detail the specific information provided by such images for anisotropic wavefield tomography.

2 THEORY

Conventional wavefield-based imaging consists of two major steps: the wavefield reconstruction and the imaging condition (Berkhout, 1982; Clærbout, 1985). The major driver for the accuracy of this technique are the source and receiver wavefields which depend on space $\mathbf{x} = \{x, y, z\}$ and time t. Wavefield reconstruction in tilted TI anisotropic medium, requires numeric solutions to a pseudo-acoustic wave-equation (Alkhalifah, 2000), e.g. the time-domain method of Fletcher et al. (2009) and Fowler et al. (2010), which consists of solving a system of second-order coupled equations:

$$\frac{\partial^2 p}{\partial t^2} = v_{p_x}^2 H_2[p] + v_{p_z}^2 H_1[q] \ , \tag{1}$$

$$\frac{\partial^2 q}{\partial t^2} = v_{p_n}^2 H_2[p] + v_{p_z}^2 H_1[q] \ . \tag{2}$$

Here, p and q are two wavefields depending on space $\mathbf{x}$ and time t, H_1 and H_2 are differential operators applied to the quantity in the square brackets Alternative formulations, e.g. Duveneck and Bakker (2011) and Zhang et al. (2011) provide expressions for stable extrapolation in more general cases, including TTI. The velocities v_{p_z}, v_{p_x}, and v_{p_n} are the vertical, horizontal and "NMO" velocities used to parametrize a generic TTI medium. If we describe the medium using the parameters introduced by Thomsen (2001), the velocities are related to the anisotropy parameters ϵ and δ by the relations $v_{p_n} = v_{p_z}\sqrt{1+2\delta}$ and $v_{p_x} = v_{p_z}\sqrt{1+2\epsilon}$. Thus, the quantities H_1 and H_2 depend on the medium parameters, as well as θ_a which describes the angle made by the TI symmetry axis with the vertical and ϕ_a the azimuth angle of the plane that contains the tilt.

A conventional imaging condition based on the reconstructed wavefields defines the image as the zero lag of the cross-correlation between the source and receiver wavefields (Clærbout, 1985). An extended imaging condition is a generalization of the conventional imaging condition in that it retains in the output image acquisition or illumination parameters. For example, we can generate image extensions by correlation of the wavefields shifted symmetrically in space (Rickett and Sava, 2002; Sava and Fomel, 2005) or in time (Sava and Fomel, 2006). This separation is simply the lag of the cross-correlation between the source and receiver wavefields (Sava and Vasconcelos, 2011):

$$R(\mathbf{x}, \boldsymbol{\lambda}, \tau) = \sum_{shots} \sum_{t} W_s(\mathbf{x} - \boldsymbol{\lambda}, t - \tau) \, W_r(\mathbf{x} + \boldsymbol{\lambda}, t + \tau) \ . \tag{3}$$

Here R represents the migrated image which depends on position $\mathbf{x}$, and the quantities $\boldsymbol{\lambda}$ and τ are cross-correlation lags in space and time, respectively. The source and receiver wavefields used for imaging, W_s and W_r are the main wavefields indicated by p in equations 1-2. The conventional imaging condition represents a special case of equation 3 for $\boldsymbol{\lambda} = 0$ and $\tau = 0$.

Various techniques have been proposed to convert the space- and time-lag extensions into reflection angles (Sava and Fomel, 2003, 2006; Sava and Vlad, 2011; Sava and Alkhalifah, 2012), thus facilitating amplitude and velocity analysis in complex geologic structures. In this paper, we do not follow this route, but instead concentrate on the interpretation of the moveout observed as a function of lags directly. A similar analysis can be done in the angle domain, but in this paper we disregard this possibility.

As indicated earlier, CIPs constructed using a correct earth model (and good subsurface illumination) reveal reflections as focused events at zero space- and time-lags. This shape has a straightforward physical interpretation. Following the discussion in Sava and Vlad (2011), the wavefield at a reflection point can be conceptually decomposed in planar components, each corresponding to a different propagation direction. We emphasize that we use the word "decomposition" only with a conceptual meaning, and not a practical one. Other researchers have proposed actual decomposition of the wavefields in elementary planar components with different directions, but we do not follow that path which is costlier and more difficult to implement in practice.

Nevertheless, the source and receiver wavefields at a reflection point where we construct a CIP gather behave as if they were strictly planar. Other planar components of the same non-planar wavefield exist, but they are located elsewhere in space, and thus do not contribute to the CIP under consideration. By simultaneously shifting the source and receiver wavefields in space and time, we obtain non-zero images only when the space- and time-lags are related to one-another by a rela-

tion which depends on the 3D angles of incidence and local material properties, (Sava and Vlad, 2011). It turns out that each direction of illumination is described in a CIP by a planar event in the $\lambda - \tau$ space. This observation is true both for isotropic and anisotropic media, but the physical interpretation is different: in isotropic media, the planar events identify directions corresponding to group angles, while in anisotropic media the planar events identify directions corresponding to phase angles, (Sava and Alkhalifah, 2012).

The most relevant property for velocity model building is that the planar events corresponding to different illumination directions overlap at zero space and time lag, i.e. at the origin of the extended space of each CIP. This is simply because we choose, by construction, points on reflectors, so ideally we form an image at zero lag from all propagation directions at the same place on the reflector. This is just a restatement of the semblance principle which says that the imaged geologic structure does not depend on the direction of illumination, assuming that the model used for wavefield reconstruction is correct. If the reconstruction is incorrect, then not all planar events in a CIP go through zero lag in space and time, thus indicating that not all illumination directions produce the image at the same depth. This information can be used for velocity analysis.

In anisotropic media, wavefield reconstruction depends on more than one parameter. For TI media, one simple way to describe the model parameters is through velocity v and the anisotropic parameter η. Reconstructed wavefields can be inaccurate due to inaccuracies in both parameters, so the effects observed in extended CIPs are simultaneously due to both. As for other domains, it is not trivial to differentiate between the effects of velocity and anisotropy error on the model. It is, nevertheless, interesting to understand how each parameter controls the observed moveout, which is a pre-requisite for tomography. Thus, we concentrate on the moveout due to anisotropy, assuming that the velocity has already been updated using other conventional methods. This is natural since the common velocity model building procedure starts with an isotropic assumption of the Earth.

Alkhalifah and Fomel (2011) show using anisotropic parameter continuation that the residual anisotropic response for post stack imaging in homogeneous media, and specifically residuals corresponding to the anisotropy parameter η, has a "V"-like shape. This response stems from the fourth-order nature of the η influence on travel-time as a function of offset. A residual reconstruction of such travel-time maps the fourth order influence to a mostly linear moveout, rather than a residual hyperbolic moveout, as shown in Figure 1. The slope of the V depends on the value of η, with negative η reverting its signature. A similar response characterizes the prestack case even in complex media.

The V-shape signature in the extended images exists regardless of the complexity of the background isotropic (or elliptically anisotropic) velocity model. Thus, such a behavior also characterizes the extended images for pre-stack data in complex anisotropic media. This is because the major wavefield complexities are compensated during the wavefield reconstruction in anisotropic media. Most of what remains are the influence of anisotropy which resembles the established behavior of poststack depth images. This property could be used to separate the effects of anisotropy from those of velocity, with applications to anisotropic earth model building.

3 EXAMPLES

The model for our first example, Figure 2(c), consists of a horizontal reflector in a 3D constant velocity model. Figures 2(a)-2(b) depict one snapshot of the wavefields for a source located on the surface in VTI and TTI models, respectively. The models are characterized by the parameters $\epsilon = 0.30$, $\delta = -0.10$ and, for the TTI model, by $\theta_a = 35^\circ$ and $\phi_a = 45^\circ$. Figures 3(a)-3(b) depict extended CIPs at $\{x, y, z\} = \{4, 4, 1\}$ km for many sources distributed uniformly on the surface and correct earth models. All CIPs show focusing at zero lags in space and time, thus indicating wavefield reconstruction with a correct earth model. However, the CIPs constructed with isotropic migration, Figures 3(c) and 3(d), are not focused, thus indicating that the CIPs are sensitive to anisotropy inaccuracy.

The next examples illustrate the behavior of the extended images as a function of anisotropy inaccuracy in constant and laterally heterogeneous models, respectively. The models are shown in Figures 4(a) and 6(a). The data, exemplified in Figures 4(b) and 6(b), are constructed with anisotropy characterized by parameter $\eta = 0.25$. Figures 7(a)-7(c) show the extended images for different shot locations obtained by reverse-time migration with the correct salt model. The figures indicate a dependency of the CIPs with the angle of illumination which can be exploited for angle decomposition. The summation for all shots leads to the CIP shown in Figure 7(e) which shows focusing of the image at zero space and time lags. This is due to the fact that all shots leave an imprint on the CIPs at zero space and time lags, but at different slopes which depend on the illumination angle, Figures 7(a)-7(c).

For incorrect η, the resulting response has an overall "V" shape similar to that seen for residual poststack migration. The slope of the "V" flanks, as illustrated in Figures 7(d)-7(f), depend on η. For η close to the correct value, the "V" energy tends to approach the apex, and for correct η it focuses at its apex, Figure 7(e). This general behavior is consistent regardless of the complexity of the medium, especially with respect to the portion of the signature that is near the apex. For comparison, Figures 5(d)-5(e) show extended gathers corresponding to the same values of η as in Figures 7(d)-7(e). Despite the fact that the background velocity model is significantly different, constant vs. salt, the CIPs are comparable, thus indicating that they are mainly influenced by the anisotropy parameters. Of course, for a varying η, such signatures reflect an effective value under the effective medium theory. This property can be exploited for anisotropic migration velocity analysis.

FInally, Figures 8(a)-8(b) illustrate the behavior of 3D anisotropic extended CIPs for a North Sea field dataset. Figure 8(a) shows the velocity model and Figure 8(b) shows the corresponding conventional image. Although the earth is

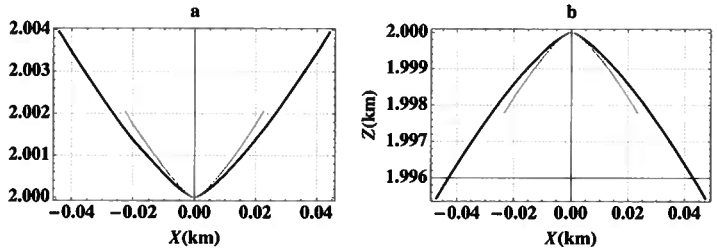

Figure 1. Image point defocusing corresponding to isotropic poststack migration with the correct velocity of 2 km/s in an anisotropic medium with (a) $\eta = 0.1$ (grey curve), $\eta = 0.2$ (black curve), (b) $\eta = -0.1$ (grey curve), and $\eta = -0.2$ (black curve).

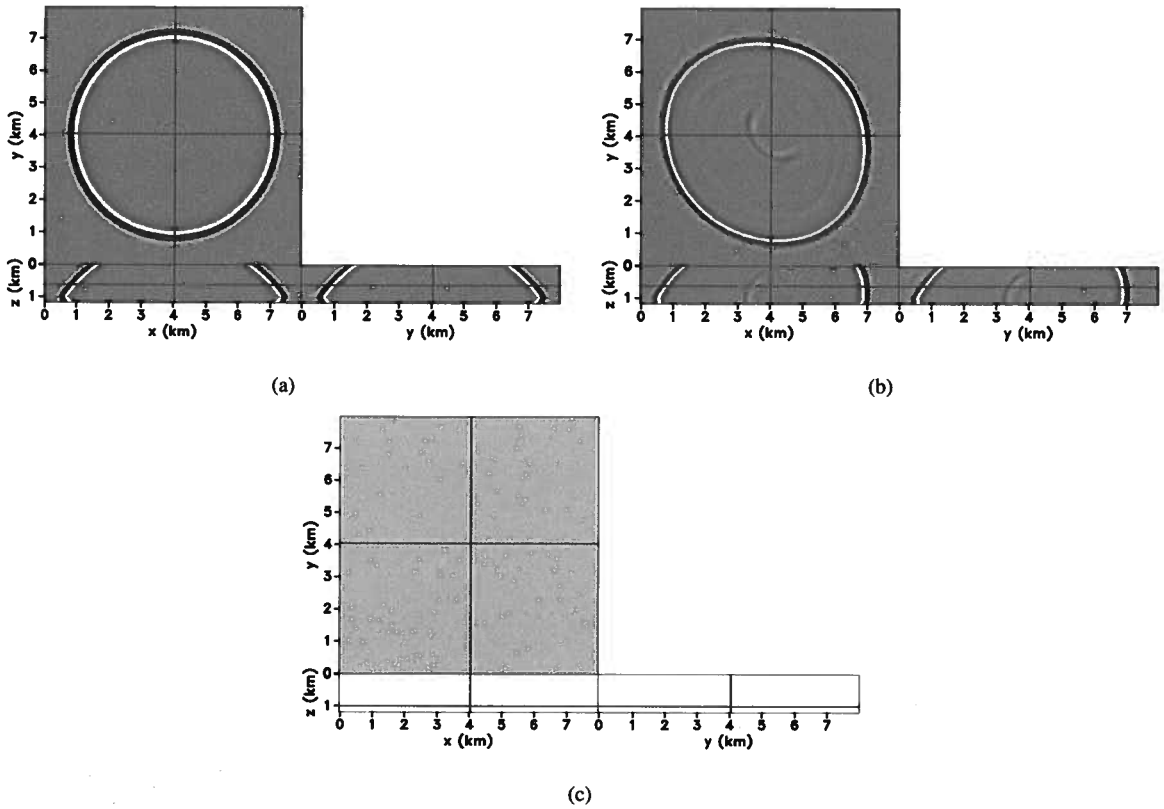

Figure 2. 3D model used to illustrate wide-azimuth extended images in anisotropic media. Panels (a) and (b) show the wavefields corresponding to a single source at $\{x, y\} = \{4, 4\}$ km for VTI and TTI media, respectively. The model (c) consists of a horizontal reflector in constant velocity.

known to be anisotropic in this region, the image shown in Figure 8(b) uses isotropic migration, and thus it is partially inaccurate.

Figure 9 shows the same image as the one shown in Figure 8(b), but in a perspective view and with three slices selected at a fixe inline, cross-line and depth, respectively. Overlain on the figure are also the locations of the CIPs constructed to analyze the accuracy of the image. CIPs are indicated by small ellipsoids instead of points, (Cullison and Sava, 2011). The flat ellipsoids represent the structure tensor constructed at each point, and the orientation of the ellipsoids in 3D space indicates the orientation of the reflectors at each position. We construct extended CIPs at each of these 5000 locations, which represents an enormous cost reduction relative to CIGs constructed for all depths at many regularly-spaced positions on the surface.

Figures 10(a)-10(b) depict different locations in the image, corresponding to CIPs automatically using the method discussed earlier.

In Figure 10(b), the CIP is selected in the middle of the image, therefore the inline illumination is good, although the cross-line aperture is more limited. In the inline direction, we observe the characteristic V, indicating that the model currently used for imaging is actually accurate, but the anisotropy is not accurate. The inline behavior should, in principle, repeat in the cross-line direction, although this is not what happens in this case due to the limited aperture. Partial illumination is also visible in Figure 10(b). In this case, we see a CIP located at the

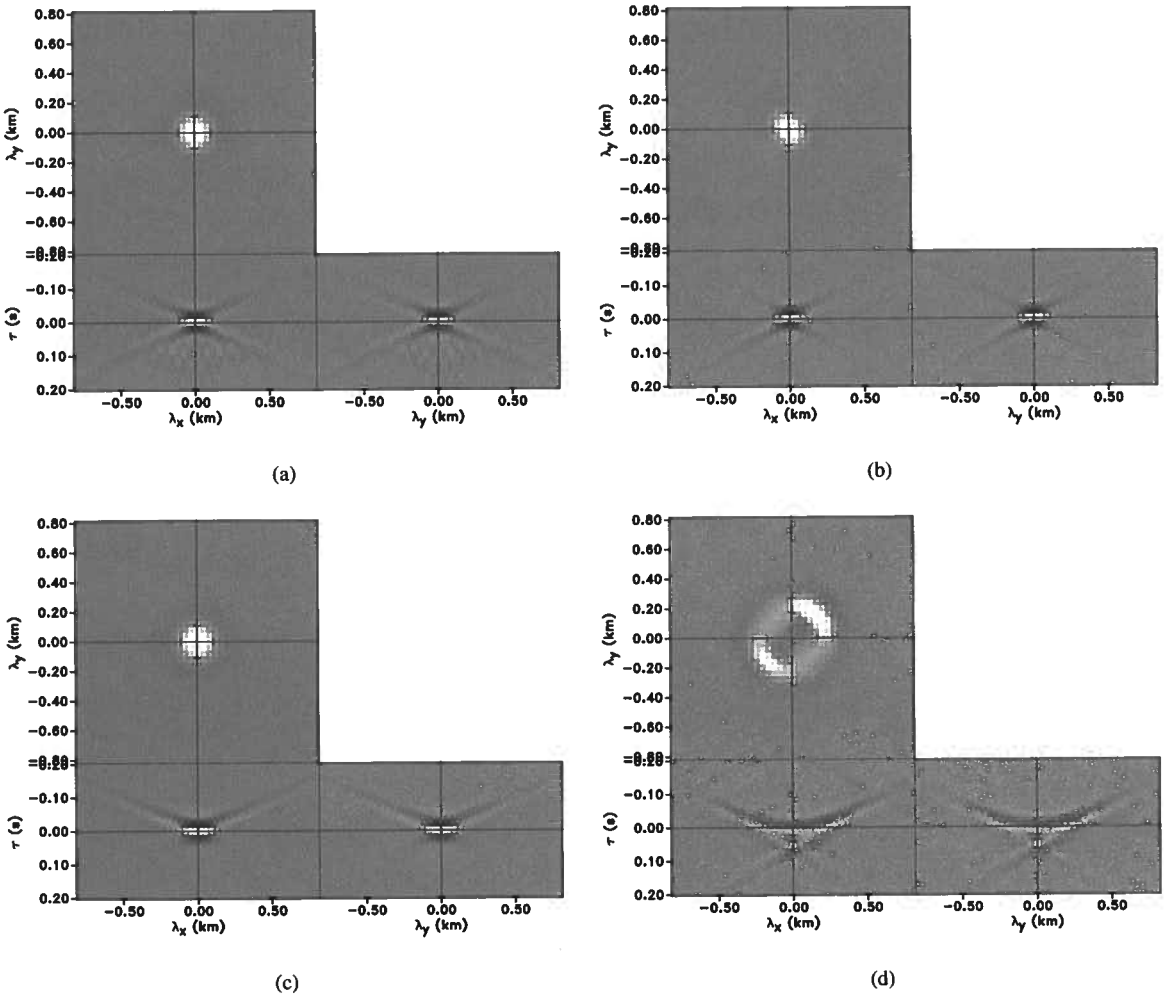

Figure 3. Extended CIPs at $\{x, y, z\} = \{4, 4, 1\}$ km for many sources distributed uniformly on the surface. The images are obtained by (a)-(b) isotropic migration, and (c)-(d) anisotropic migration of the VTI data (left) and TTI data (right).

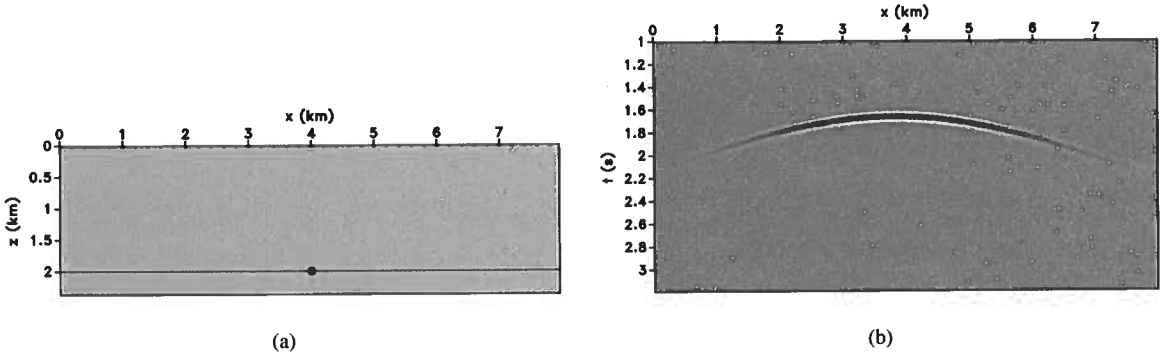

Figure 4. (a) 2D **constant model** used to study the dependence of the extended CIPs with anisotropy, and (b) one shot gather for a source located at $\{x, z\} = \{3.4, 0\}$ km. The earth model is anisotropic and characterized by parameter $\eta = 0.25$.

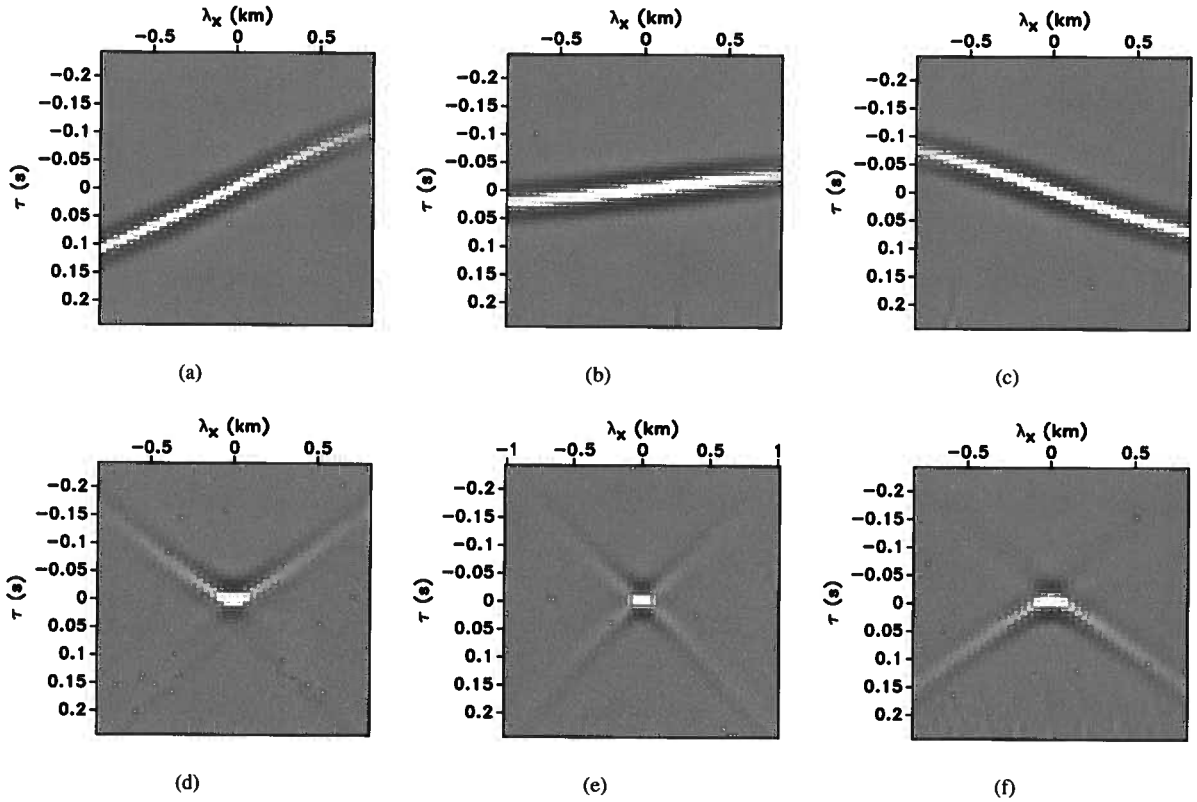

Figure 5. 2D extended CIPs at $\{x, z\} = \{4, 0\}$ km for the **constant model**, Figure 6(a). The extended images (a)-(c) correspond to individual shots at surface coordinates $x = \{3.2, 4.0, 4.8\}$ km and are obtained from wavefields reconstructed with the correct $\eta = 0.25$. The extended images (d)-(f) correspond to anisotropy characterized by parameter $\eta = \{0.15, 0.25, 0.35\}$.

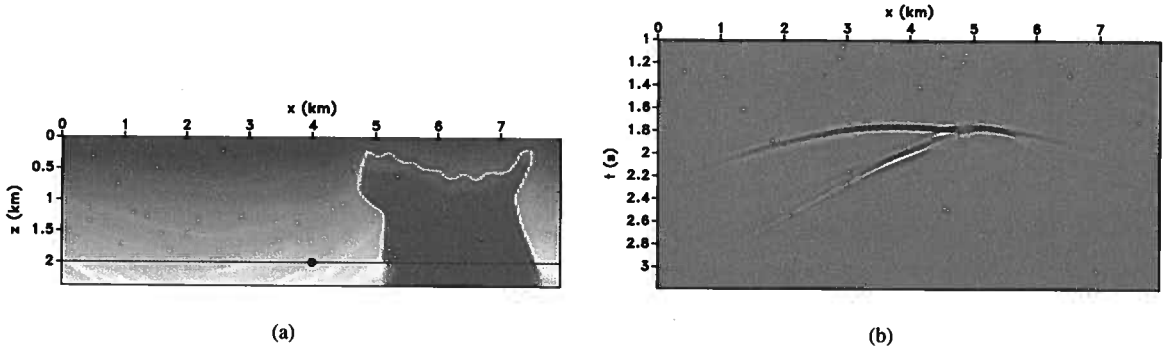

Figure 6. (a) 2D **salt model** used to study the dependence of the extended CIPs with anisotropy, and (b) one shot gather for a source located at $\{x, z\} = \{3.4, 0\}$ km. The earth model is anisotropic and characterized by parameter $\eta = 0.25$.

edge of the model, where the illumination is mainly from one side even in the inline direction.

4 CONCLUSIONS

The distinct anisotropic signatures, needed for parameter estimation, tend to get lost in the mist of the complexity of the velocity in the medium. Extended images preserve such signatures, which allows for direct anisotropy analysis. The slope of the residual moveout in extended CIPs mainly depends on η, which simplifies parameter estimation in anisotropic media. A comparison of extended images between simple and complex models supports our assertion.

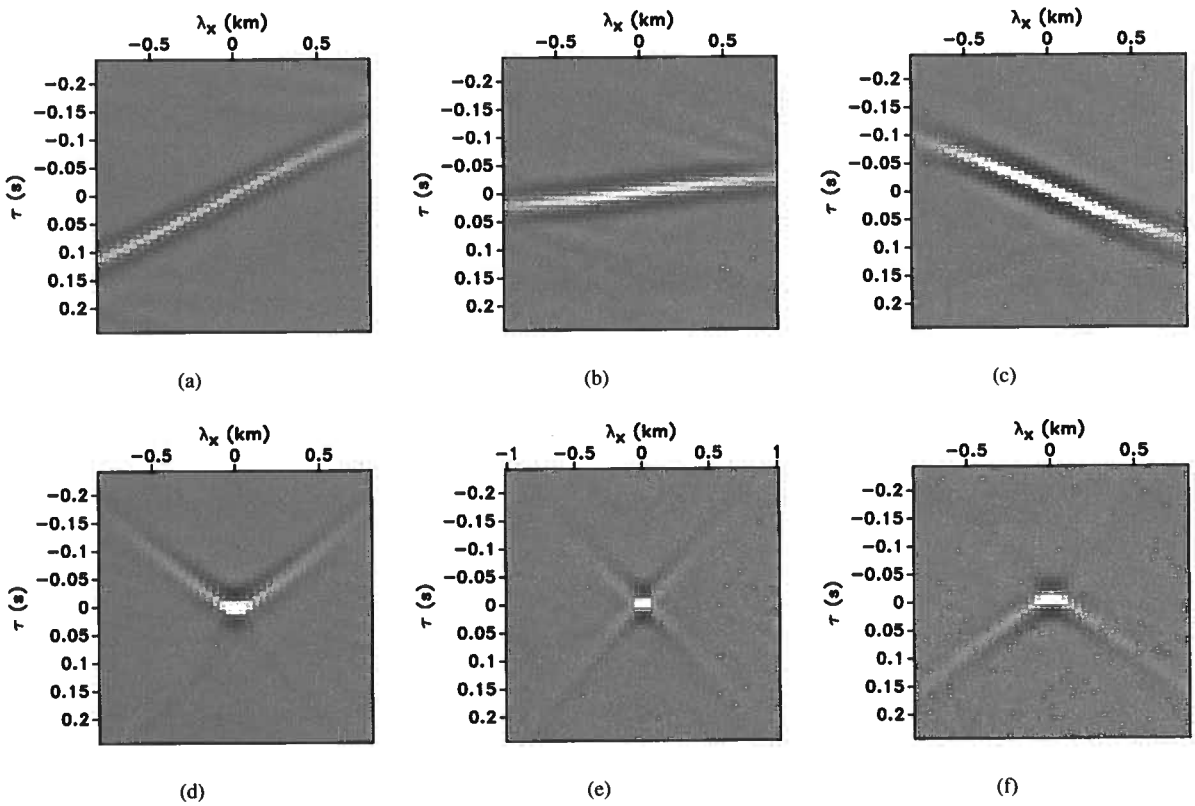

Figure 7. 2D extended CIPs at $\{x, z\} = \{4, 0\}$ km for the **salt model**, Figure 6(a). The extended images (a)-(c) correspond to individual shots at surface coordinates $x = \{3.2, 4.0, 4.8\}$ km and are obtained from wavefields reconstructed with the correct $\eta = 0.25$. The extended images (d)-(f) correspond to anisotropy characterized by parameter $\eta = \{0.15, 0.25, 0.35\}$.

5 ACKNOWLEDGMENTS

The authors would like to thank Statoil ASA and the Volve license partners, ExxonMobil E&P Norway and Bayerngas Norge, for the release of the Volve data. Partial funding for this research is provided by KACST. The reproducible numeric examples in this paper use the Madagascar open-source software package freely available from http://www.ahay.org.

REFERENCES

Alkhalifah, T., 2000, An acoustic wave equation for anisotropic media: Geophysics, **65**, 1239–1250.

Alkhalifah, T., and S. Fomel, 2011, The basic components of residual migration in VTI media using anisotropy continuation: J Petrol Explor Prod Technol, **1**, 17–22.

Alkhalifah, T., S. Fomel, and B. Biondi, 2001, The space-time domain: theory and modelling for anisotropic media: Geophysical Journal International, **144**, 105–113.

Baysal, E., D. D. Kosloff, and J. W. C. Sherwood, 1983, Reverse time migration: Geophysics, **48**, 1514–1524.

Berkhout, A. J., 1982, Imaging of acoustic energy by wave field extrapolation: Elsevier.

Clærbout, J. F., 1985, Imaging the Earth's interior: Blackwell Scientific Publications.

Cullison, T., and P. Sava, 2011, An image-guided method for automatically picking common-image-point gathers: Presented at the 81st Annual International Meeting, SEG, Expanded abstracts.

Duveneck, E., and P. M. Bakker, 2011, Stable P-wave modeling for reverse-time migration in tilted TI media: Geophysics, **76**, S65–S75.

Fletcher, R. P., X. Du, and P. J. Fowler, 2009, Reverse time migration in tilted transversely isotropic (TTI) media: Geophysics, **74**, WCA179–WCA187.

Fowler, P. J., X. Du, and R. P. Fletcher, 2010, Coupled equations for reverse time migration in transversely isotropic media: Geophysics, **75**, S11–S22.

Gray, S. H., J. Etgen, J. Dellinger, and D. Whitmore, 2001, Seismic migration problems and solutions: Geophysics, **66**, 1622–1640.

McMechan, G. A., 1983, Migration by extrapolation of time-dependent boundary values: Geophys. Prosp., **31**, 413–420.

Rickett, J., and P. Sava, 2002, Offset and angle-domain common image-point gathers for shot-profile migration: Geophysics, **67**, 883–889.

Sava, P., and T. Alkhalifah, 2012, Wide-azimuth angle gathers for anisotropic wave-equation migration: Geophysical

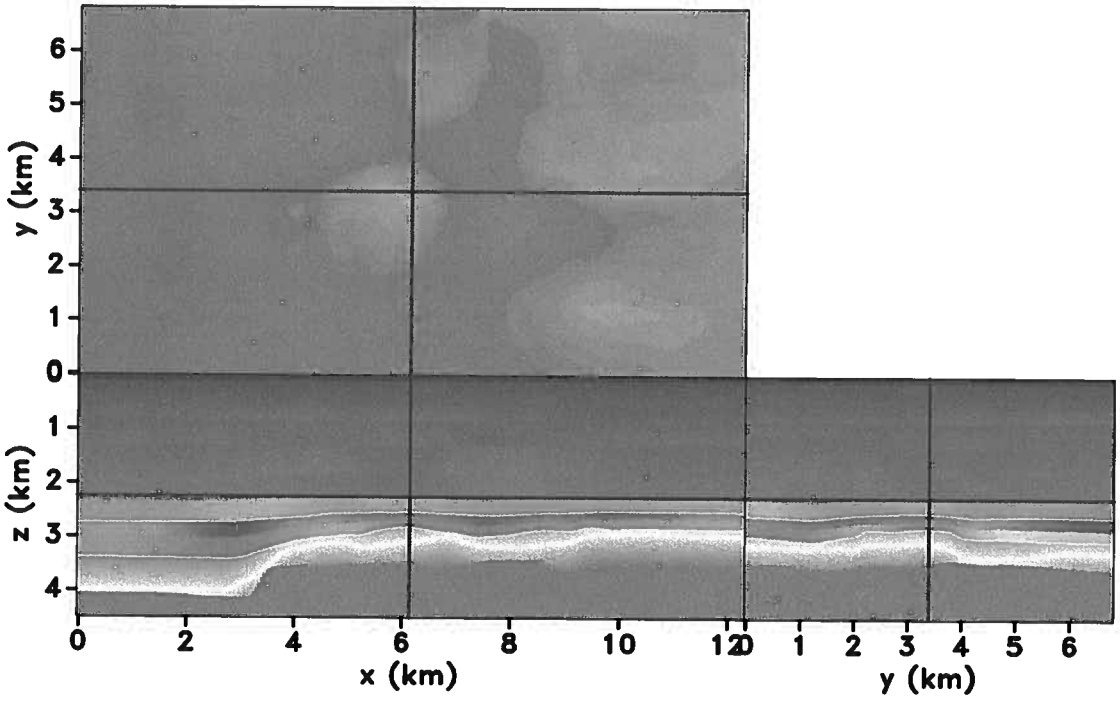

(a)

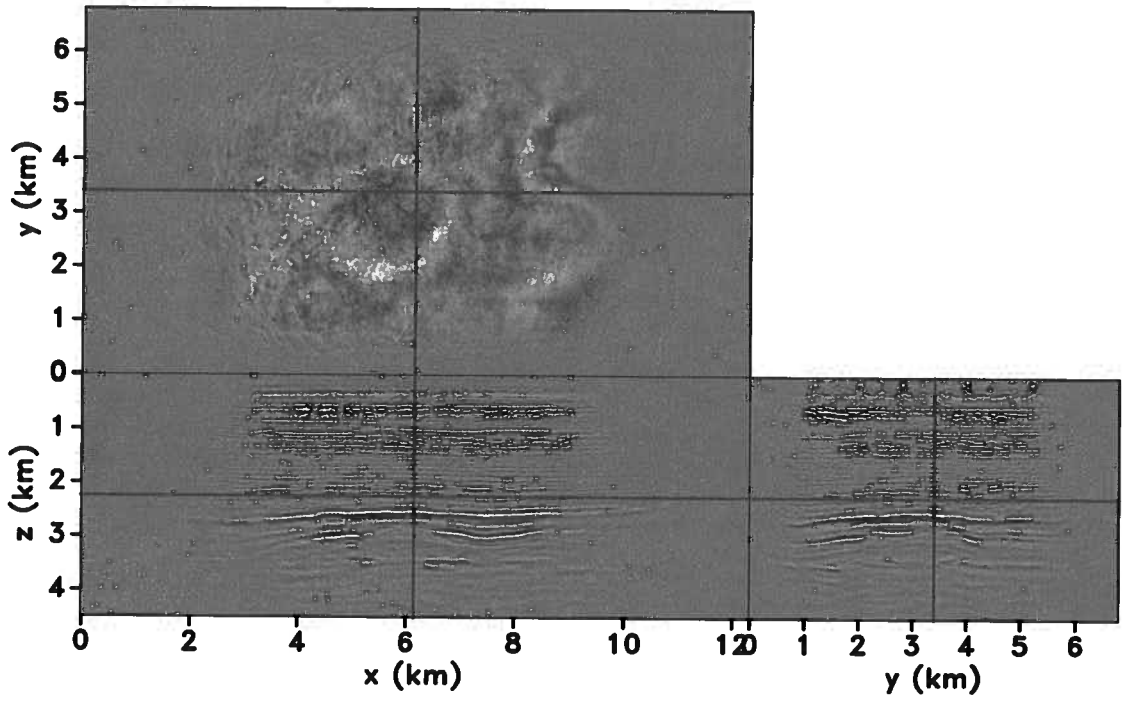

(b)

Figure 8. North Sea model: (a) P-wave velocity, and (b) isotropic image.

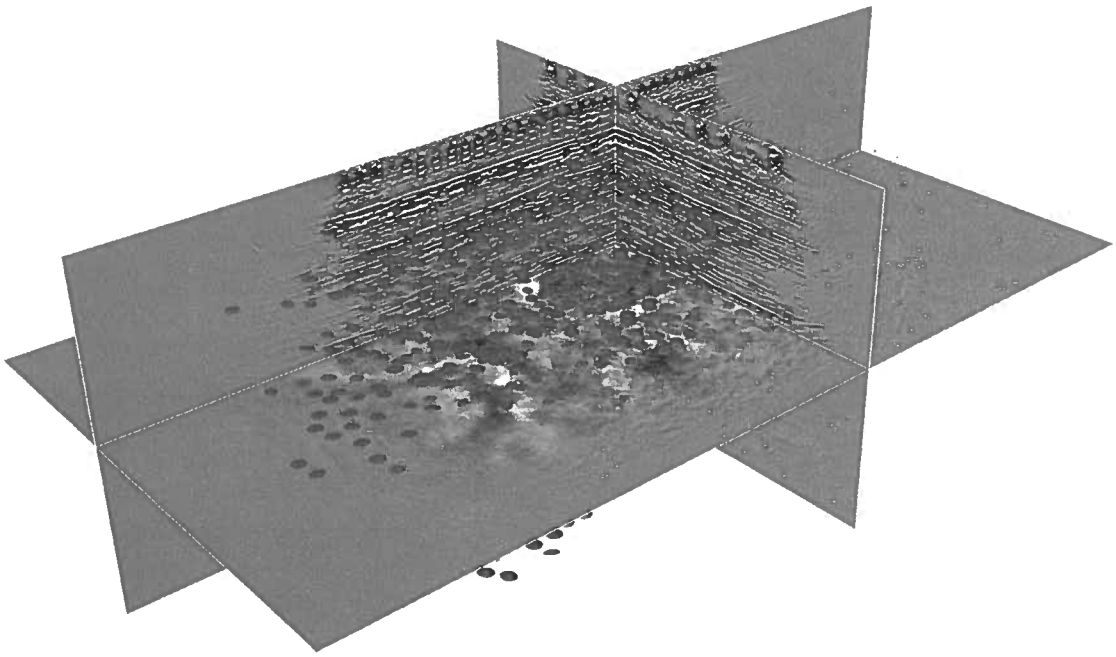

Figure 9. Image with the picked locations of the CIP gathers. The ellipsoids indicate the local slope and azimuth of the geologic structure.

Prospecting, in press.
Sava, P., and S. Fomel, 2003, Angle-domain common image gathers by wavefield continuation methods: Geophysics, **68**, 1065–1074.
———, 2005, Coordinate-independent angle-gathers for wave equation migration: 75th Annual International Meeting, SEG, Expanded Abstracts, 2052–2055.
———, 2006, Time-shift imaging condition in seismic migration: Geophysics, **71**, S209–S217.
Sava, P., and I. Vasconcelos, 2011, Extended imaging condition for wave-equation migration: Geophysical Prospecting, **59**, 35–55.
Sava, P., and I. Vlad, 2011, Wide-azimuth angle gathers for wave-equation migration: Geophysics, **76**, S131–S141.
Thomsen, L., 2001, Seismic anisotropy: Geophysics, **66**, 40–41.
Zhang, Y., H. Zhang, and G. Zhang, 2011, A stable TTI reverse time migration and its implementation: Geophysics, **76**, WA3–WA11.

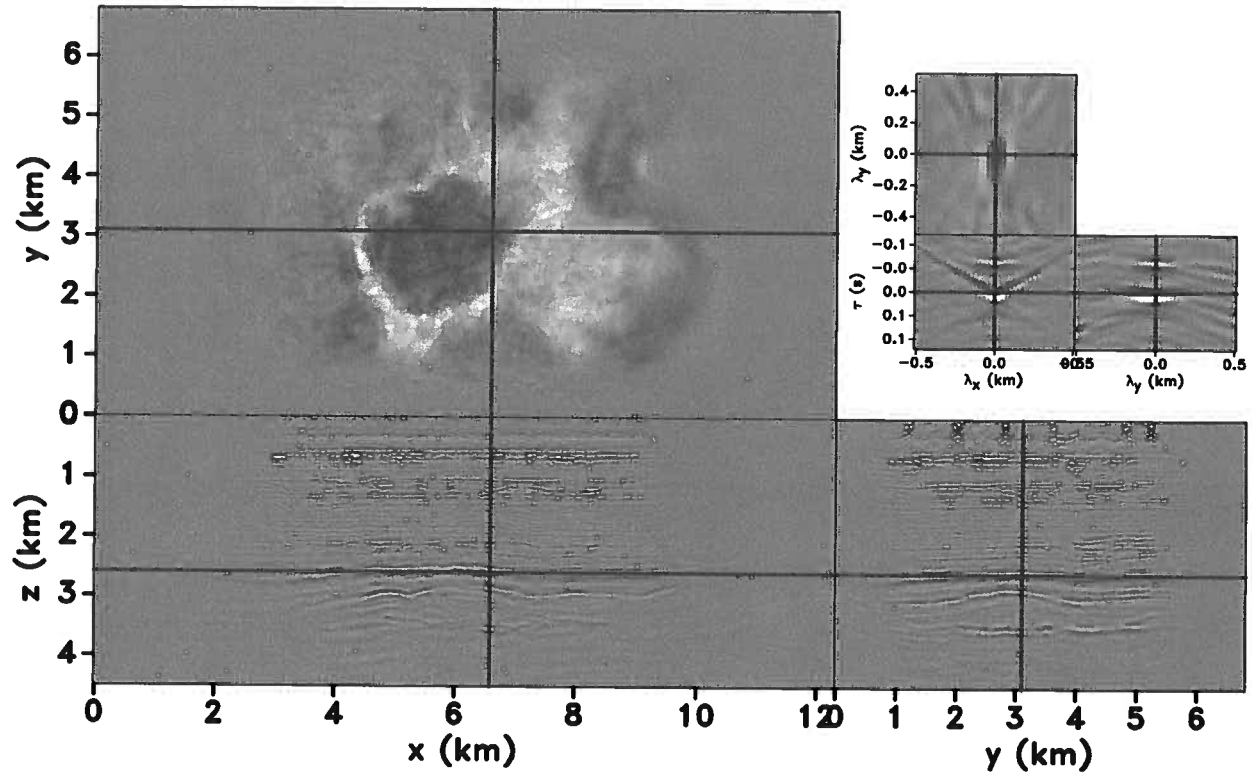

(a)

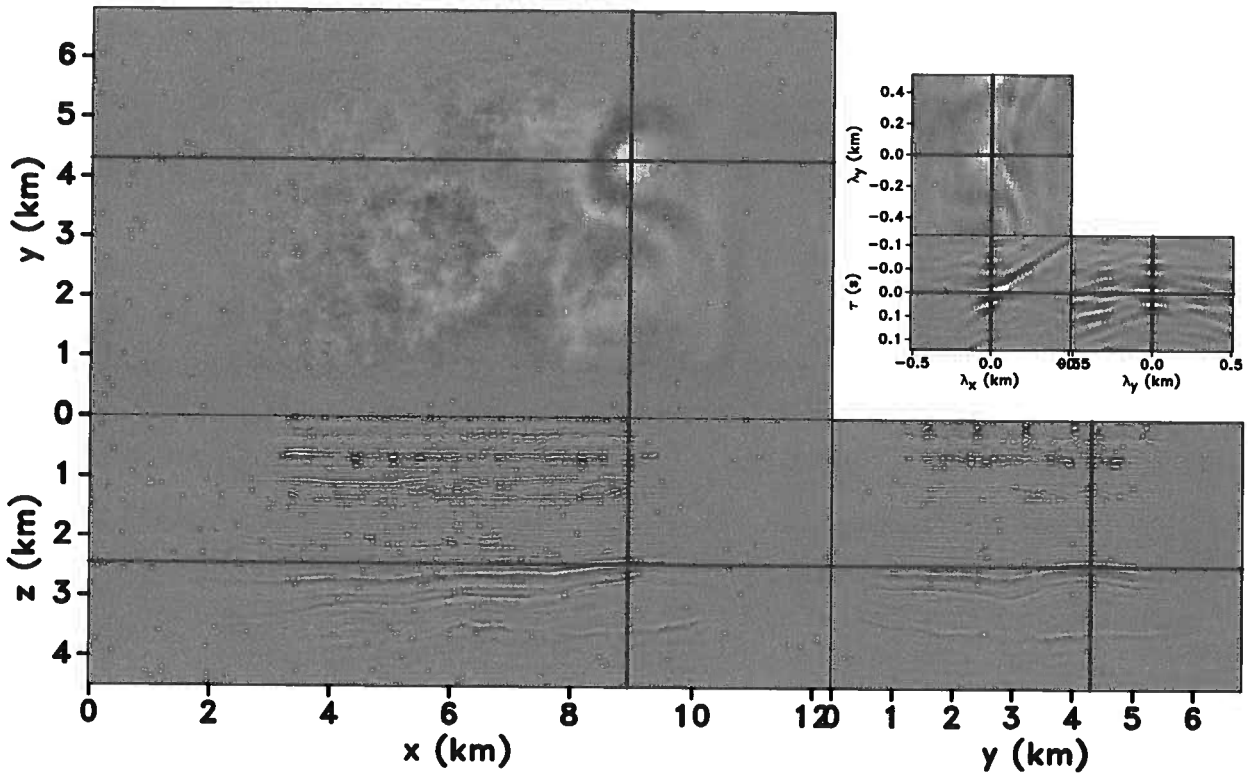

(b)

Figure 10. Conventional images with inset indicating the extended image at the coordinates marked by the intersecting lines.

Improving microseismic imaging: role of acquisition, velocity model, and imaging condition

Jyoti Behura[†], Farnoush Forghani[‡], & Farhad Bazargani[†]
[†] *Center for Wave Phenomena, Colorado School of Mines, Golden, Colorado*
[‡] *Center for Rock Abuse, Colorado School of Mines, Golden, Colorado; currently MicroSeismic Inc, Denver*

ABSTRACT
Surface microseismic data is being increasingly used in monitoring hydraulic-fracturing. Here, we suggest changes in the acquisition as well as processing stages to improve microseismic imaging and source characterization. Improved microseismic hypocenter imaging and reliable source mechanism estimation can be achieved by illuminating the hypocenter evenly from all directions. We introduce methodologies for designing optimized surface arrays for 2D and 3D acquisitions. Accurate microseismic imaging also requires the exact Green's function between the image point and the receivers. An inaccurate Green's function leads to poor focusing and numerous spurious microseismic hypocenters. We also introduce imaging conditions that can yield accurate source signatures even if they are extended in space and time. Such source signatures can yield the time history of fracture propagation in space and might be used to infer the time-varying slip along pre-existing fractures. These imaging conditions also reduce spurious events in the image. All conclusions are supported with numerical examples.

1 INTRODUCTION

Microseismic monitoring using surface arrays is becoming increasingly popular because of its reduced cost and increased aperture compared to borehole monitoring. Surface microseismic data is commonly acquired using a star-shaped array (Duncan & Eisner, 2010, Figure 1) or on a regular grid. These receivers can be placed on the surface or can be buried in the ground to improve the signal-to-noise ratio. Little attention is paid towards designing the array to optimize imaging using a fixed number of receivers. Therefore, optimizing a survey design can not only lead to better microseismic characterization but also result in cost savings. In fact, it is nowadays routine to perform illumination studies in order to design the best acquisition surveys in conventional reflection seismology. Here, we discuss how surface microseismic arrays can be designed to yield better hypocenter imaging.

Other important aspects of microseismic imaging involve the choice of imaging condition and the knowledge of the exact Green's functions between the image point and the receivers. The recorded data are imaged through a Kirchhoff-summation based algorithm (Gajewski *et al.*, 2007) or a reverse-time approach (McMechan, 1982; McMechan *et al.*, 1983; Fink *et al.*, 2000; Lu, 2002) with the primary aim being the location of microseismic hypocenters. Reverse-time imaging and Kirchhoff-summation based algorithms commonly use a smooth velocity model for imaging and therefore might not yield an accurate Green's function. We discuss the importance of an accurate subsurface model and its impact on imaging microseismic data.

Recent developments by Ulrich *et al.* (2013), Douma *et al.* (2013) and Bazargani & Snieder (2013) show that better temporal and spatial focusing can be achieved by designing optimal inverse-filters from the recorded data which are then back-propagated through a velocity model. Here, instead of optimizing the focusing of the microseismic data, we compute the source signature of the microseismic events. Imaging of microseismic data commonly refers to the reconstruction of the hypocenters of the microseismic sources. Therefore, microseismic images are usually displayed only as a function of the spatial axes. Microseismic sources, however, are functions of time as well. For example, it is most likely that the opening of a fracture is not instantaneous; instead different portions of the fracture likely open at different times resulting in a microseismic source extended both in space and time. Another example of such sources would be microseismic tremors that occur

Figure 1. Plan-view of star-shaped surface microseismic array. The blue lines represent the receiver arrays. Source: Duncan & Eisner (2010).

due to the slow slippage along a fault or fracture plane. Hence, by *microseismic imaging* we refer to the process of finding the microseismic source signature as a function of both space and time. By computing the source signatures as a function of time and space, we can infer the time history of fracture propagation in space and the time-dependent slip along natural fractures. Therefore, we introduce and analyze different imaging conditions that look for coherence in time as well as space between the computed Green's functions and the recorded data and test their effectiveness in imaging microseismic data. Our approach is particularly useful for microseismic sources that are extended in time and space.

2 SURFACE ACQUISITION

In order to obtain the best possible focus through imaging and also decipher the source radiation pattern accurately, one needs to sample the hypocenter evenly from all angles. In other words, the hypocenter must be evenly illuminated from all directions. If the microseismic source is imaged using plane waves evenly spaced in angle (Figure 2a), one can obtain an evenly illuminated image. However, neither a star-shaped surface array nor a regular-grid array would illuminate the hypocenter evenly from all directions. Instead, such receiver arrays will lead to the preferential illumination of certain angles (Figure 2b) thereby resulting in X-shaped hypocenter images. More importantly, such uneven angular sampling of the hypocenter might lead to an incorrect estimation of the source radiation pattern.

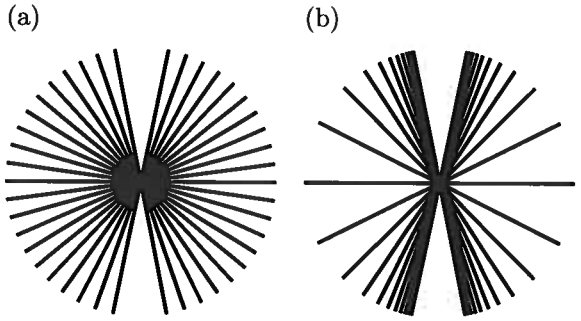

Figure 2. Hypocenter reconstruction using plane waves (a) evenly incident from all directions and (b) incident from receivers evenly spread along a line on the surface.

Figure 3. 2D surface array for optimized design (a) and conventional design (b). The optimized array is designed for a hypocentral depth of 1800 m, maximum offset of 6000 m and a constant velocity gradient of $\approx 1.3\ s^{-1}$.

2.1 Optimal design

Here, we suggest using a modified surface array designed with the aim of illuminating the microseismic hypocenters evenly from all directions. To design such an array one needs an approximate smooth velocity model of the subsurface, approximate center of the zone of microseismicity, maximum receiver offset, and the number of receivers. A practical solution would be to use a constant vertical velocity-gradient of the subsurface being monitored. Since most unconventional reservoirs undergoing hydraulic fracturing are fairly laterally-homogeneous, a well-log could be used to find the best-fit vertical velocity gradient. The mid-point of the hydraulically-fractured zone can be used for the center of the microseismicity-zone. By knowing the maximum offset and the number of receivers, one can shoot rays from the microseismicity-zone-center at equally-spaced (in angle) takeoff angles. The intersection of these rays with the surface determine the optimal locations of the surface receivers. For such simple velocity models, one can use analytic ray-path formulations for determining the location of the surface receivers; for more complicated models, one can use ray-tracing. Such a modified design was also proposed by Foulger & Julian (2011); Miller *et al.* (1998) with the above aim in mind (sampling the hypocenter evenly in angle). Miller *et al.* (1998) used ray-tracing to op-

(a)

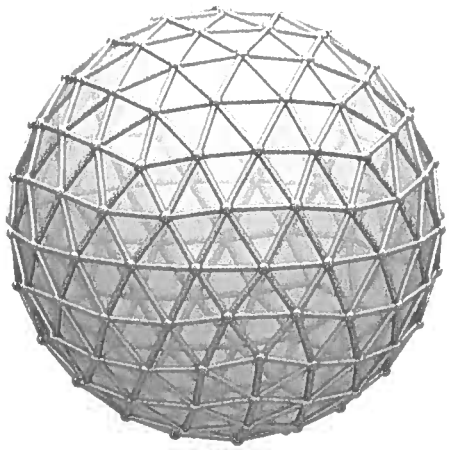

(b)

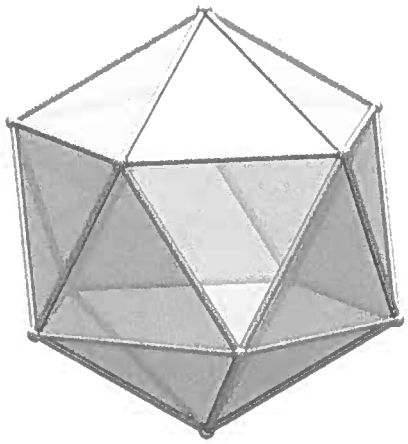

Figure 4. (a) Geodesic grid used in sampling the imaginary sphere surrounding the hypocenter. (b) Icosahedron that is divided to construct a geodesic grid. Source: Geodesic polyhedra, René K. Müller

timally place receiver stations on the surface to monitor a geothermal site.

The computation of these evenly-spaced (in takeoff angle) rays is straightforward in 2D where the polar angle at the hypocenter has to be divided into $n-1$ angular sectors with n being the number of surface receivers. An example of an optimal 2D surface receiver array is shown in Figure 3a; a conventional array (equally spaced on the surface) is also shown in Figure 3b for comparison. For 3D acquisition design, however, the computation of the equi-spaced takeoff angles is more involved because the whole sphere around the hypocenter needs to be evenly sampled (instead of the circular aperture in 2D).

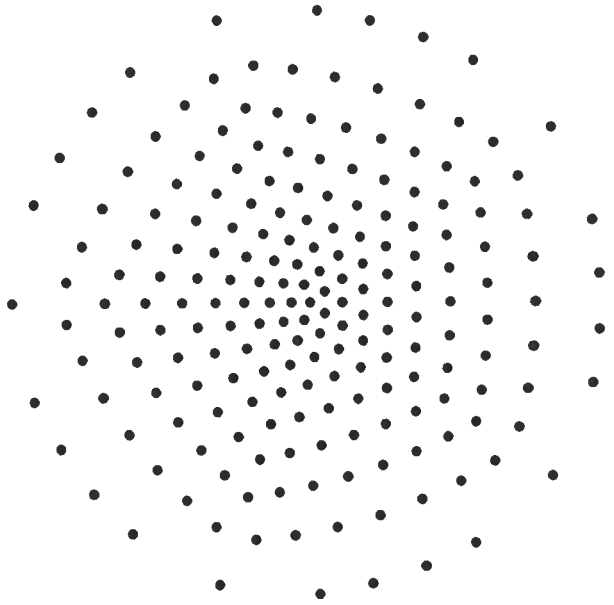

Figure 5. Plan view of the optimized surface acquisition in 3D. The optimized array is designed for a hypocentral depth of 1800 m, maximum offset of 6000 m and a constant velocity gradient of $\approx 1.3\ s^{-1}$.

Miller *et al.* (1998) and Foulger & Julian (2011) use the intersection points of the latitudes with the longitudes of a sphere to determine the azimuth and take-off angle of each ray. Their approach, however, will not sample the sphere evenly; it will lead to finer sampling of points near the poles and sparse-sampling of points close to the equator. Here, we use a geodesic grid (Figure 4a) to determine the azimuth and takeoff angles of the rays because the sphere surrounding the hypocenter is sampled evenly on a geodesic grid. Depending on the number of receivers, an icosahedron (Figure 4b) is divided evenly to yield a geodesic grid. The vertices of the geodesic grid yield the azimuth and takeoff angles of the rays. As described above, intersection of these rays (shot from the hypocenter at the computed azimuth and takeoff angles) with the surface determines the optimal locations of the receivers. An example of such an optimal 3D microseismic survey is shown in Figure 5. Note the marked difference in the optimal receiver pattern from that of a star-shaped array and a regular-grid array.

The instrumentation of borehole receiver strings prevents me from suggesting the above optimized receiver spacing for borehole acquisition. However, if multiple strings are used in monitoring microseismicity, one could still use the above optimization scheme to design a borehole acquisition geometry that illuminates the zone of microseismicity evenly from all directions.

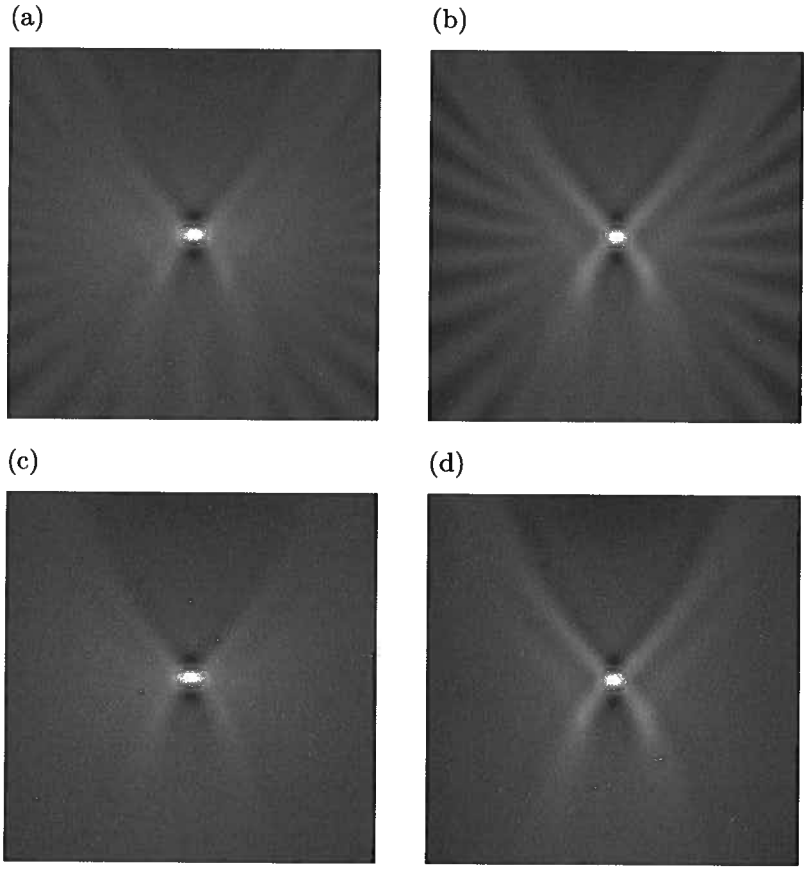

Figure 6. (a,b) Hypocenter images obtained using the optimized (Figure 3a) and the conventional (Figure 3b) 21-receiver array, respectively. (c,d) Images obtained from increased number of receivers (161).

2.2 Imaging

An acquisition design optimized to illuminate the hypocenter evenly from all directions should yield better images of the microseismic source. Images in Figures 6a and 6b are obtained using reverse-time imaging of the microseismic data acquired on an optimized array (Figure 3a) and a conventional array (Figure 3b), respectively. Note that the event focusing is better in Figure 6a than in Figure 6b. The individual plane waves forming the focus at the hypocenter are also visible. As expected, the plane waves in Figure 6a are evenly spaced in angle while in Figure 6b, they are unevenly spaced and concentrated at specific angles. Increasing the number of receivers increases the image quality (Figures 6c and 6d) for both acquisitions; however, the uneven illumination of the conventional acquisition still leads to an X-shaped image in Figure 6d. Note the similarity of Figures 6c and 6d to the plane-wave schematic in Figure 2a and 2b, respectively.

3 IMPORTANCE OF THE SUBSURFACE MODEL

Reverse-time imaging (McMechan, 1982; McMechan *et al.*, 1983; Lu, 2002) of microseismic data involves time-reversal of the data and their re-injection into a smooth velocity model. Following back-propagation, an imaging condition is applied which is usually some snapshot of the back-propagated wavefield at some time that is thought to be the initiation time of the microseismic source. Reverse-time imaging can, therefore, be written as

$$\begin{aligned}\mathcal{I}(\omega;\mathbf{x_s}) &= \left[\sum_{\mathbf{x_r}} d^*(\omega;\mathbf{x_r})G_s(\omega;\mathbf{x_s},\mathbf{x_r})\right]^* \\ &= \left[\sum_{\mathbf{x_r}} S^*(\omega;\mathbf{x_s})G^*(\omega;\mathbf{x_r},\mathbf{x_s})G_s(\omega;\mathbf{x_s},\mathbf{x_r})\right]^* \\ &= S(\omega;\mathbf{x_s})\left[\sum_{\mathbf{x_r}} G^*(\omega;\mathbf{x_r},\mathbf{x_s})G_s(\omega;\mathbf{x_s},\mathbf{x_r})\right]^* \end{aligned} \quad (1)$$

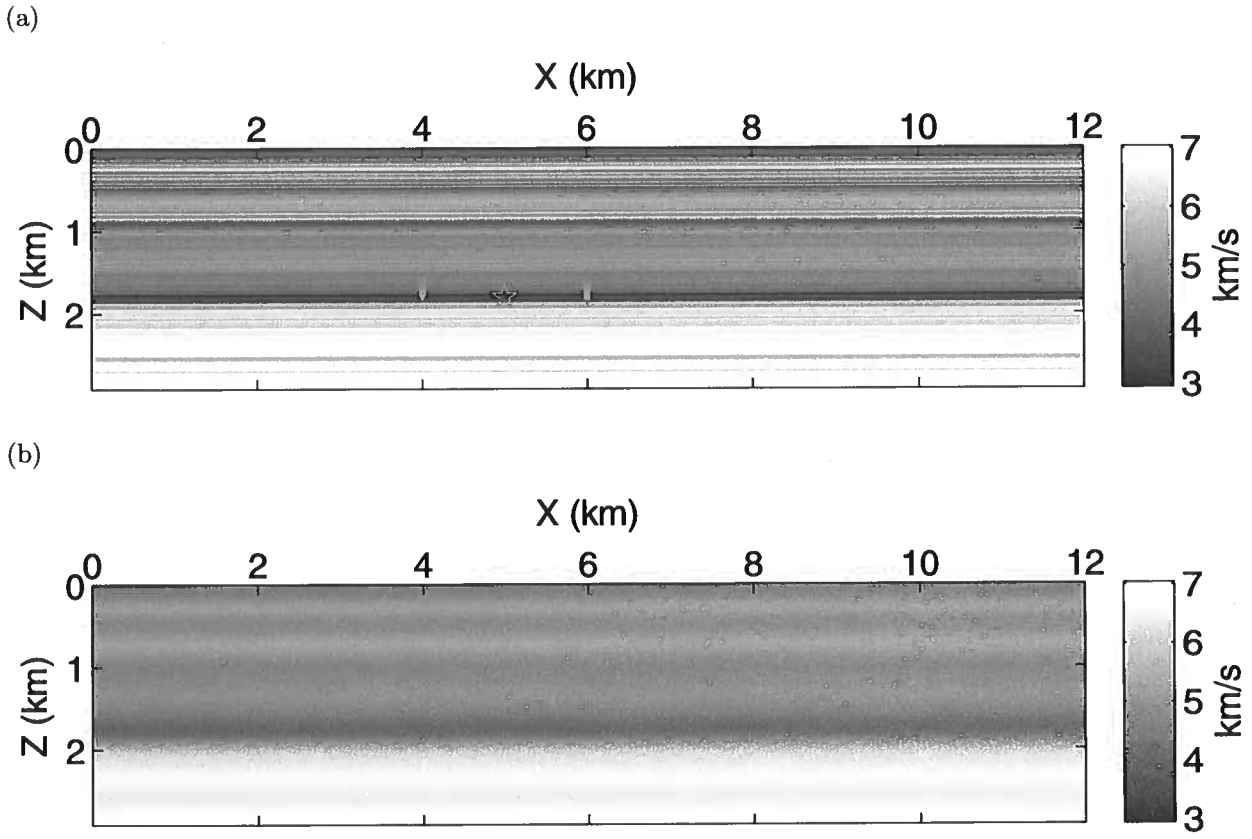

Figure 7. (a) The layer-cake velocity model used in generating borehole microseismic data. The pentagram represents the hypocenter of the microseismic source and the red triangles represent the borehole receivers. The borehole receivers are emplaced as two vertical receiver arrays. Each array comprises of 11 receivers evenly spaced at 20 m intervals. (b) Smoothed version of (a).

where $\mathcal{I}(\omega; \mathbf{x_s})$ is the image at image point $\mathbf{x_s}$, $\mathbf{x_r}$ represent the receiver coordinates, ω is the frequency, * represents complex conjugation, d is the microseismic data, G is the true Green's function, G_s is the Green's function computed during back-propagation in a smooth background velocity, and S is the source signature at image point $\mathbf{x_s}$.

Ideally we would like equation 1 to yield the true source signature at location $\mathbf{x_s}$ i.e. $\mathcal{I}(\omega; \mathbf{x_s}) = S(\omega; \mathbf{x_s})$. This means that in order to get the best possible image, G_s should be equal to G. This can be achieved by using the exact velocity (and density) model for back-propagation of the recorded data. For example, the well-log derived velocity (and density) could be used for back-propagation in laterally-homogeneous media. If a smooth model is used instead, the image (Figure 8a) could be substantially different from the true image (Figure 8b). In the absence of a detailed and accurate velocity model, an alternate approach suggested by Behura & Snieder (2013) could be used. It is noteworthy that even if the true Green's function is used in equation 1, reverse-time imaging will yield a source signature that is scaled by $\sum_{\mathbf{x_r}} |G|^2$; therefore, the image obtained using reverse-time imaging will not be accurate unless the subsurface velocity and density are actually slowly varying such that $|G|^2 = \delta$, where δ is the Kronecker delta.

4 IMAGING CONDITIONS

In order to obtain accurate source signatures of microseismic sources, we need to modify the imaging condition used in reverse-time imaging (equation 1). The microseismic data recorded at receiver $\mathbf{x_r}$ due to a source at some location $\mathbf{x_s}$ is given by

$$d(\omega; \mathbf{x_r}, \mathbf{x_s}) = S(\omega; \mathbf{x_s})\, G(\omega; \mathbf{x_r}, \mathbf{x_s}), \tag{2}$$

where ω is the frequency, $d(\omega; \mathbf{x_r}, \mathbf{x_s})$ is the data at receiver $\mathbf{x_r}$, $S(\omega; \mathbf{x_s})$ is the source signature at $\mathbf{x_s}$, and G is the Green's function between the source location $\mathbf{x_s}$ and the receiver location $\mathbf{x_r}$. Note that equation 2 is de-

(a)

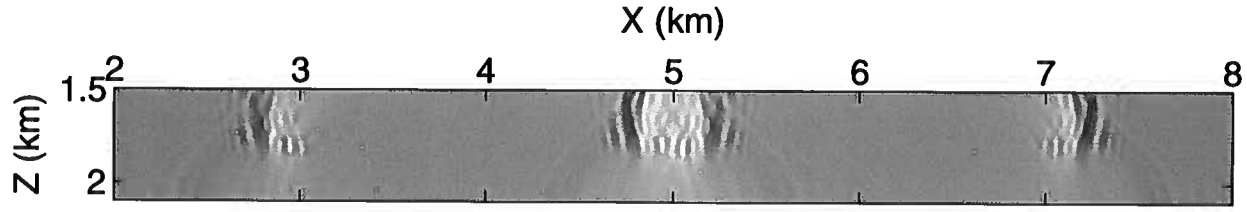

(b)

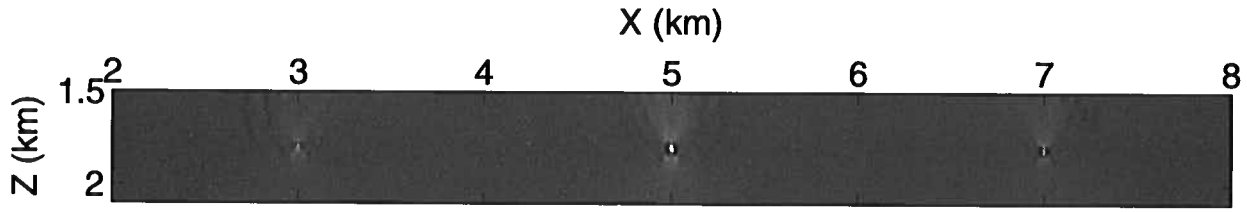

Figure 8. Reverse-time images of the microseismic source in Figure 7a using (a) the smoothed model (Figure 7b) and (b) the correct velocity model (Figure 7a).

fined only for a single microseismic source for simplicity; use of multiple sources will introduce undesirable cross-talk in the images. The source signature can then be computed from equation 2 using

$$S(\omega;\mathbf{x_s}) = \frac{d(\omega;\mathbf{x_r},\mathbf{x_s})}{G(\omega;\mathbf{x_r},\mathbf{x_s})}. \tag{3}$$

$S(\omega;\mathbf{x_s})$ in equation 3 is the source signature estimate using data from only a single receiver. In the case of multiple receivers, one can sum over the estimates from all the receivers:

$$S(\omega;\mathbf{x_s}) = \sum_{\mathbf{x_r}} \frac{d(\omega;\mathbf{x_r},\mathbf{x_s})}{G(\omega;\mathbf{x_r},\mathbf{x_s})}. \tag{4}$$

Equation 4 is a deconvolution operation followed by a summation over all the receivers. One needs to perform a stabilized deconvolution in equation 4 such as the water-level deconvolution (Aster *et al.*, 2012). Examples of the image resulting from the imaging condition 4 applied to the data in Figure 7a are shown in Figure 9a. Note that the above methodology is different from that of Ulrich *et al.* (2013) and Douma *et al.* (2013) who design inverse-fiters using deconvolution that improve the focusing of the time-reversed data in time and space.

To avoid the deconvolution operation, equation 4 can be modified to

$$S(\omega;\mathbf{x_s}) = \sum_{\mathbf{x_r}} d(\omega;\mathbf{x_r},\mathbf{x_s}) G^*(\omega;\mathbf{x_r},\mathbf{x_s}), \tag{5}$$

where * represents complex conjugation. Equation 5 represents a cross-correlation operation between d and G. Note that $|G|^2$ has been omitted going from equation 4 to equation 5 for stabilization purposes. Omission of $|G|^2$ will incorporate inaccuracies in the amplitude spectrum of the source signature; therefore, although imaging condition 5 might yield the correct phase of the microseismic source, its amplitude will be inaccurate unless $|G|^2 = \delta$. If a smooth velocity model is used for back-propagation, equation 5 becomes the cross-correlation imaging condition 1 used in reverse-time imaging. Figure 9b shows the image resulting from the cross-correlation imaging condition 5.

In the presence of multiple microseismic sources extended in space, imaging conditions 4 and 5 will result in cross-talk between the various sources and might yield degraded images. Also, in the above two imaging conditions (equation 4 and 5), the source signatures are computed for each receiver independently and then stacked. In other words, imaging conditions 4 and 5 use only the temporal coherence between the data recorded at a receiver with the computed Green's function. It might be possible to reduce cross-talk and improve imaging by exploiting spatial coherence in addition to temporal coherence. Hence, we modify equations 4 and 5 by performing a Fourier transform on the spatial receiver axis to obtain

$$S(\omega;\mathbf{x_s}) = \sum_{k_r} \frac{d(\omega;k_r,\mathbf{x_s})}{G(\omega;k_r,\mathbf{x_s})}, \tag{6}$$

and

$$S(\omega;\mathbf{x_s}) = \sum_{k_r} d(\omega;k_r,\mathbf{x_s})\, G^*(\omega;k_r,\mathbf{x_s}), \tag{7}$$

respectively; k_r is the wavenumber computed over the receiver coordinates. Images resulting from imaging conditions 6 and 7 are shown in Figures 9c and 9d, respectively.

Equation 2 can also be written as a linear system of algebraic equations

$$\mathbf{d} = \mathbf{GS}. \tag{8}$$

The least-squares solution (Aster *et al.*, 2012) for $\mathbf{S}$ from the equation 8 is given by

$$\mathbf{S}_{L_2} = (\overline{\mathbf{G}^T}\mathbf{G})^{-1}\overline{\mathbf{G}^T}\mathbf{d}, \tag{9}$$

where $\overline{\mathbf{G}^T}$ represents the conjugate transpose of $\mathbf{G}$. Equation 9 is solved for each frequency independently to obtain $S(\omega)$ at every image point of interest. [Note that the above inversion approach in equation 9 is different from that of Bazargani & Snieder (2013) who design injection sources (to be injected at the receiver locations) that optimally focus the microseismic event at a predefined time and space.] The image obtained from imaging condition 9 is shown in Figure 9e.

Note that the above imaging conditions result in images that are extended in time; images extended in space can be obtained by varying the image point $\mathbf{x_s}$. This is different from conventional imaging conditions where a zero-time imaging condition is applied to the back-propagated wavefield. Such an imaging condition assumes that we know the initiation time of the microseismic source and that the source is compact in time. However, as discussed above, microseismic sources can be extended both in space and time (for example, microseismic tremors); therefore, the imaging conditions introduced above should lead to a better characterization of microseismicity.

We also demonstrate the above imaging conditions on the Sigsbee model (Figure 10a). The microseismic survey comprises of 367 receivers spread on the surface at an equal spacing of 75 ft. Two microseismic sources (Figure 10a) are used for generating the data; the initiation times of the left- and the right-source are 0.096 s and 3.36 s, respectively. Also, the left source has a higher amplitude than the right source. For imaging, we use the smoothed velocity model shown in Figure 10b. The exact Green's functions necessary for imaging are generated using the algorithm of Behura & Snieder (2013). The resulting images obtained from the above five imaging conditions are shown in Figure 11. The images correspond to a depth of 5700 ft. All five imaging conditions reconstruct the source accurately at their correct times and spatial location. However, imaging condition 7 contains the least artifacts (Figure 11d). Overall, Figures 9 and 11 show that imaging conditions 6, 7, and 9 yield the best images while minimizing false positives.

5 DISCUSSION AND CONCLUSIONS

Microseismic imaging can be improved by evenly illuminating the hypocenters from all directions. The modified surface acquisition suggested here results in uniform sampling of microseismic hypocenters and better images as corroborated by synthetic examples.

The optimized surface acquisition design introduced has to be designed with a specific imaging zone in mind. Subsequently, microseismic hypocenters located far away from this imaging zone might not be optimally illuminated using the modified design. Still, most of the microseismicity is confined to the vicinity of the hydraulically-fractured zone which makes the optimized design useful.

The time-space imaging conditions discussed here yield good images and minimize spurious events on the image at the same time. These time-space imaging conditions exploit the similarity of the acquired data with the computed Green's function in both time and space. An accurate and detailed velocity model is also extremely important in imaging and reducing false positives in microseismic analysis.

ACKNOWLEDGMENTS

Mark Willis and Julie Shemeta were very helpful in clarifying many of our questions. Support for this work was provided by the Consortium Project on Seismic Inverse Methods for Complex Structures at Center for Wave Phenomena and by the sponsors of the Center for Rock Abuse.

References

Aster, R. C., Borchers, B., & Thurber, C. H. 2012. *Parameter Estimation and Inverse Problems.* 2 edn. Academic Press.

Bazargani, F., & Snieder, R. 2013. Optimal wave focusing. *CWP Project Review*, **769**, 249–258.

Behura, J., & Snieder, R. 2013. Imaging direct- as well as scattered-events in microseismic data using inverse scattering theory. *CWP Project Review*, **755**, 87–94.

Douma, J., Snieder, R., Fish, A., & Sava, P. 2013. Locating a microseismic event using deconvolution. *submitted to Geophysical Research Letters.*

Duncan, P., & Eisner, L. 2010. Reservoir characterization using surface microseismic monitoring. *Geophysics*, **75**(5), 75A139–75A146.

Fink, M., Cassereau, D., Derode, A., Prada, C., Roux, P., Tanter, M., J.-L.Thomas, & Wu, F. 2000. Time-reversed acoustics. *Reports on Progress in Physics*, **63**(12), 1933.

Foulger, G., & Julian, B. 2011. Earthquakes and errors: Methods for industrial applications. *Geophysics*, **76**(6), WC5–WC15.

Gajewski, D., Anikiev, D., Kashtan, B., Tessmer, E., & Vanelle, C. 2007. Localization of seismic events by diffraction stacking. *SEG Technical Program Expanded Abstracts*, 1287–1291.

Lu, R. 2002. *Time reversed acoustics and applications to earthquake location and salt dome ank imaging.* Ph.D. thesis, Massachusets Institute of Technology.

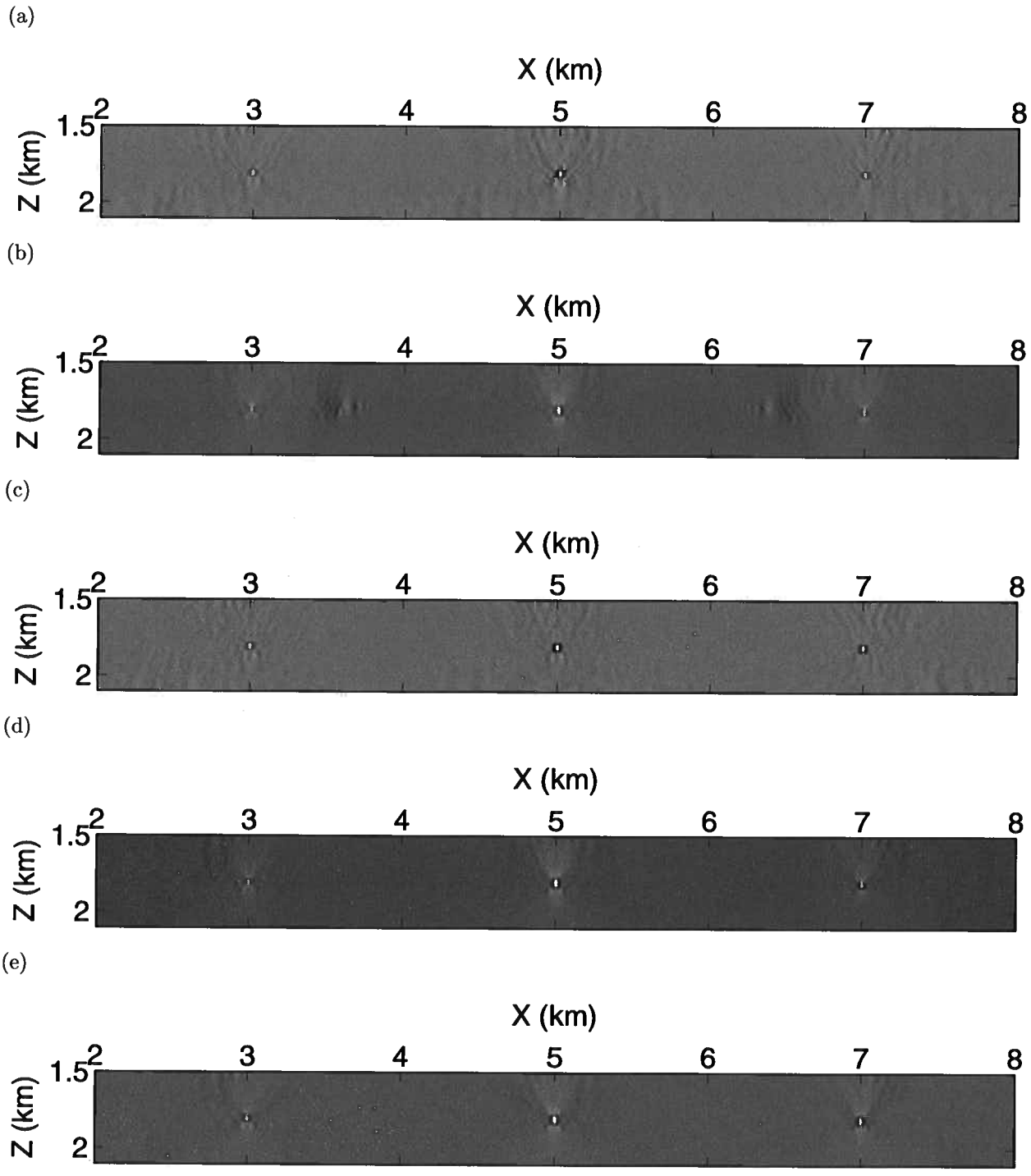

Figure 9. Images of the microseismic source in Figure 7a obtained using imaging condition 4 (a), 5 (b), 6 (c), 7 (d), and 9 (e).

McMechan, G. A. 1982. Determination of source parameters by wavefield extrapolation. *Geophysical Journal of the Royal Astronomical Society*, **71**, 613–628.

McMechan, G. A., Luetgert, J. H., & Mooney, W. D. 1983. Imaging of earthquake sources in Long Valley Caldera, California. *Bulletin of the Seismological Society of America*, **75**, 1005–1020.

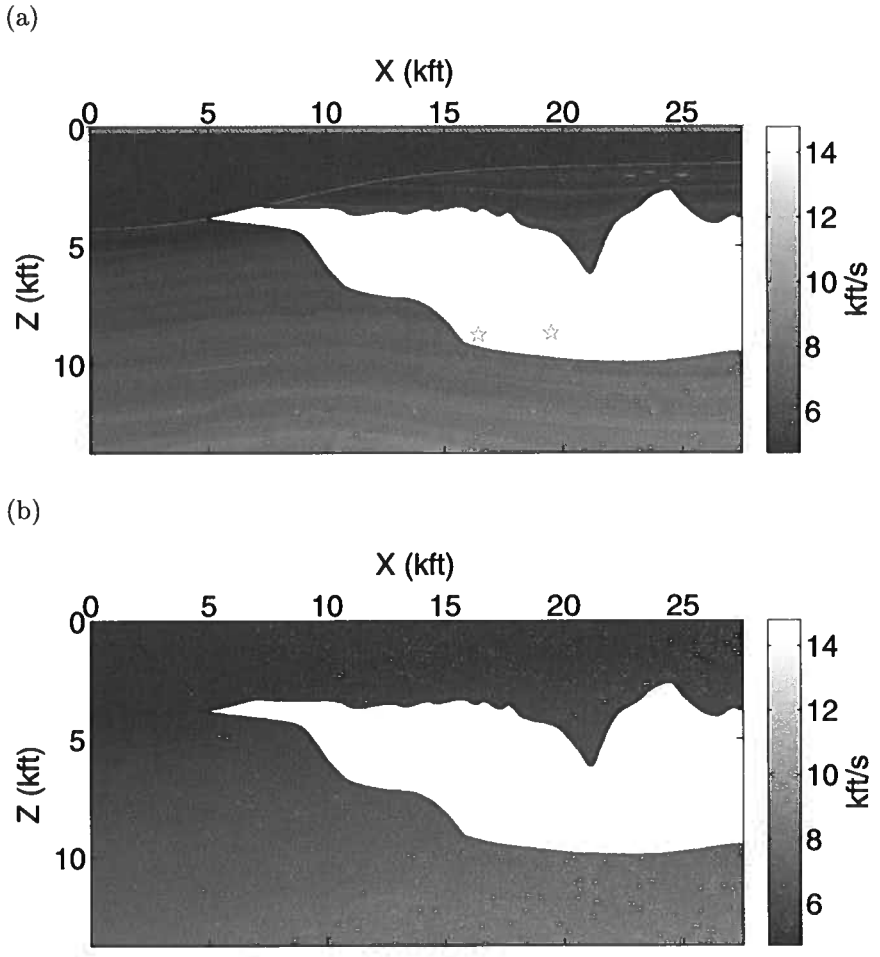

Figure 10. (a) The Sigsbee velocity model used in generating the microseismic data and the reflection seismic data. The two pentagrams represent the microseismic hypocenters and the red triangles represent the receivers. The initiation time of the two sources is There are a total of 367 receivers spread on the surface at an equal spacing of 75 ft. (b) The smooth model used in imaging.

Miller, A D, Julian, B R, & Foulger, G R. 1998. Three-dimensional seismic structure and moment tensors of non-double-couple earthquakes at the Hengill-Grensdalur volcanic complex, Iceland. *Geophysical Journal International*, **133**(2), 309–325.

Ulrich, T. J., Douma, J., Anderson, B. E., & Snieder, R. 2013. Improving time reversal focusing and source reconstruction through deconvolution. *submitted to the Journal of Applied Physics.*

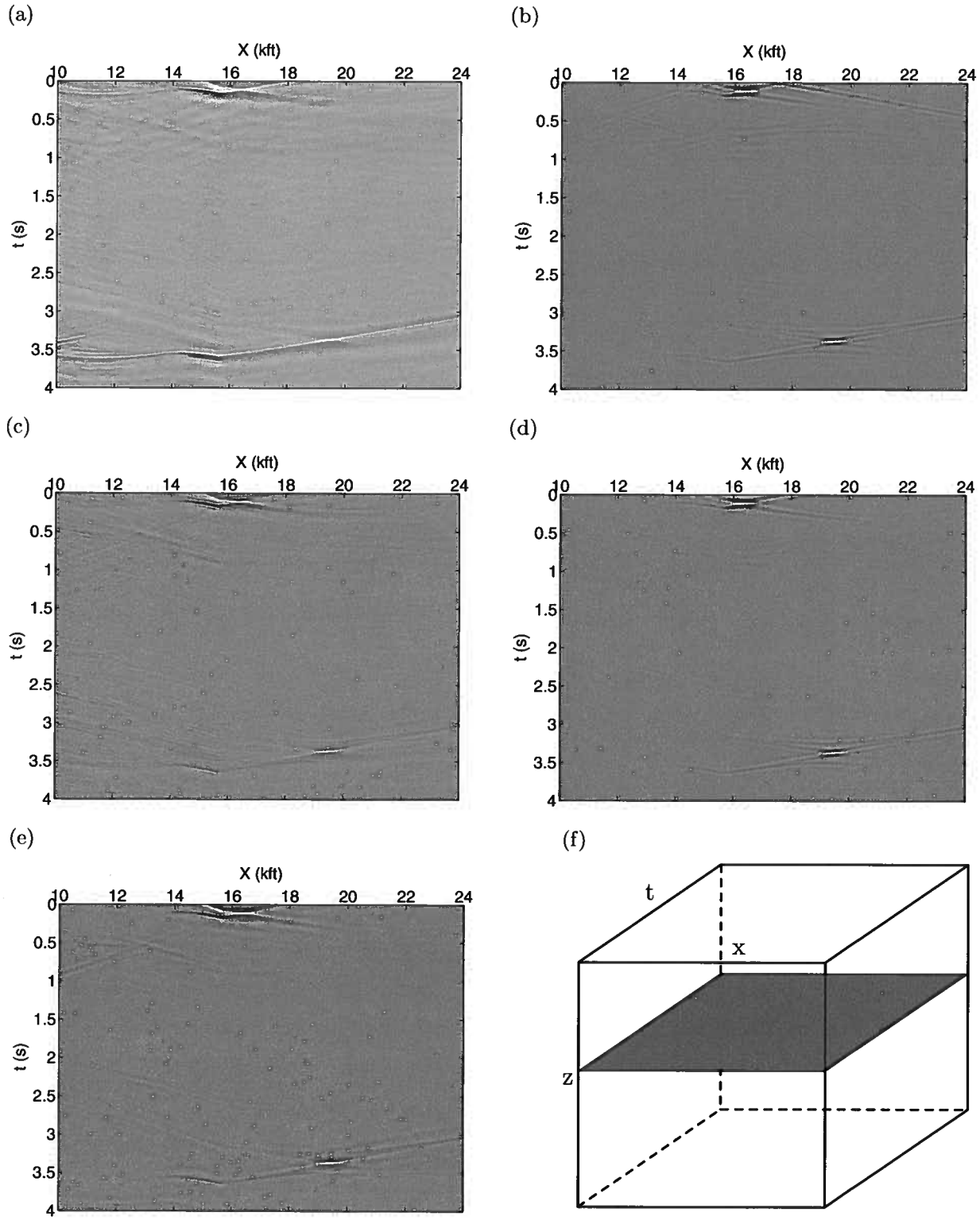

Figure 11. Images of the microseismic source in Figure 10a obtained using imaging condition 4 (a), 5 (b), 6 (c), 7 (d), and 9 (e). The images correspond to a depth of 5700 ft. (f) Depiction of the image slices displayed in (a)-(e).

Imaging direct- as well as scattered-events in microseismic data using inverse scattering theory

Jyoti Behura & Roel Snieder
Center for Wave Phenomena, Colorado School of Mines, Golden, Colorado

ABSTRACT

Similar to surface reflection data, microseismic data also contain multiply-scattered events. They are especially prevalent in borehole microseismic data because of low attenuation. These scattered events, if not imaged accurately, can lead to the spurious microseismic hypocenters. Here, we introduce an imaging algorithm that accurately images not only the primary arrivals but also the multiply scattered events. The algorithm uses the exact Green's function computed using an iterative scheme based on inverse-scattering theory. Extraction of the Green's function, however, requires surface reflection data and a background velocity model. Imaging of surface microseismic data involves computation of the Green's function between the image point and the surface receivers and the application of an imaging condition to the data. Borehole-microseismic-data imaging, however, requires two additional steps – first, computation of the Green's function between the borehole receivers and the surface and second, computation of the Green's function between the image point and the borehole receivers using seismic interferometry. Tests on synthetic data show that our imaging algorithm not only locates the microseismic hypocenters accurately but also substantially reduces the number of spurious events.

1 MULTIPLE ISSUES

As seismic waves propagate through the subsurface, they undergo scattering because of the presence of heterogeneities (in velocity and density). In reflection seismology, events undergoing more than one episode of scattering are commonly referred to as *multiples*. Since multiples can result in spurious reflectors on images, the common practice is to predict and suppress them prior to imaging. However, since multiples also contain information about the subsurface heterogeneities, there is an increased effort towards using them in imaging instead of just discarding them.

Data recorded by passive sensors and during active microseismic monitoring also contain singly- and multiply-scattered events in addition to the direct arrival. Such data are commonly used to locate the sources of these hydraulic-fracturing induced microseismic events and thus compute an estimate of the *stimulated reservoir volume* and the evolution and geometry of induced fractures. Kirchhoff migration (Gajewski *et al.*, 2007) and reverse-time imaging (McMechan, 1982; McMechan *et al.*, 1983) are the imaging algorithms commonly employed to locate the microseismic sources. Under Kirchhoff migration, the image at any location is computed by first computing the direct-arrival traveltime from the image point to the receivers and then stacking the recorded data along this traveltime-curve. In reverse-time imaging, the recorded data is reversed in time and then injected into a smooth estimate of the subsurface velocity. If the velocity model is accurate, the direct arrivals will focus at the correct microseismic hypocenters.

In the above imaging algorithms, the scattered arrivals, however, will also focus at times and locations that do not correspond to the true initiation time of the microseismicity and the true hypocenters, respectively. They will result in numerous *false positives* particularly for large reflection coefficients. Many of the unconventional reservoirs with underlying/overlying sand-shale sequences can aggravate this issue. Scattering can be problematic for borehole monitoring, in particular, because of the large magnitudes of the multiples. Unfortunately, such false positives will not only lead to an overestimation of the stimulated reservoir volume but also result in a poor correlation of microseismicity with production. An example of this is clearly evident in the work of Roundtree & Miskimins (2011) where a sandstone is hydraulically fractured in a controlled exper-

iment. The microseismic data, when imaged, resulted in numerous hypocenters *outside* the sandstone block (Jennifer Miskimins, personal communication).

1.1 Exact Green's function necessary

One possibility to addressing the above scattering issue in microseismic data is to predict and suppress the scattered events on data prior to imaging. Unfortunately, this requires the complete knowledge of the velocity and density model; no data-driven approaches exist for predicting multiples in microseismic data. A comparison of reverse-time imaging with smoothed versus true velocity model is shown in Behura *et al.* (2013). The alternative approach is to use all the data and image the scattered arrivals (along with the direct arrivals) such that they focus at the correct hypocenters. This approach necessitates either the detailed and accurate knowledge of the velocity (and density) model or the knowledge of the Green's function. It is extremely challenging to obtain detailed information of the subsurface velocity and density. Well-logs can provide such detailed models but only locally. Seismic-inversion-derived subsurface models most commonly depict only the low-wavenumber background.

1.2 Inverse-scattering theory to the rescue

Wapenaar *et al.* (2011) propose a methodology for reconstructing the 3D Green's function between any "virtual source" in the subsurface and any location on the surface using only surface reflection data and a background velocity model. Their proposal is the 3D extension of the 1D iterative algorithm of Rose (2002b,a) who shows that in layered media, it is possible to focus all the energy at a particular time (or depth if the velocity is known) by using a complicated source signature. Rose's algorithm was also implemented on 1D seismic data by Broggini & Snieder (2012) who again show that a 'virtual source' response can be generated from surface reflection data alone. The background velocity model is used to compute the direct arrivals between the "virtual source" and the surface which are subsequently fed into an iterative algorithm to compute the Green's function. Details of the 1D algorithm are given in Rose (2002b,a); Broggini & Snieder (2012); the 3D algorithm can be found in Wapenaar *et al.* (2011) with the derivation given in Wapenaar *et al.* (2013).

Here, we propose to use the above iterative algorithm to reconstruct Green's function between the subsurface image points and the surface and use them in imaging the direct as well as the scattered events in microseismic data. We also introduce a methodology to image borehole microseismic data by combining the computed Green's functions with seismic interferometry.

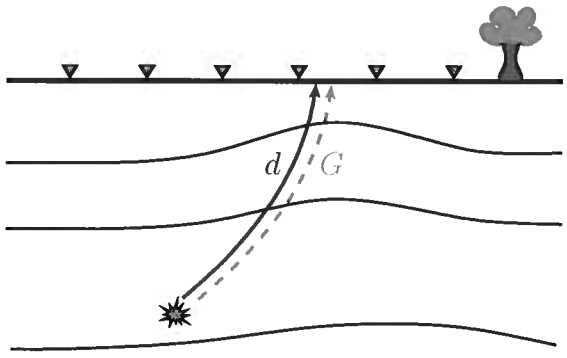

Figure 1. Schematic of the imaging algorithm applied to surface microseismic data. d represents the microseismic data recorded at the surface receivers (triangles) and G is the Green's function between any image point (denoted by the star) and the surface receivers obtained from the iterative algorithm.

2 SURFACE DATA IMAGING

The data recorded at a receiver $\mathbf{x_r}$ due to a source at some location $\mathbf{x}$ is given by

$$d(\omega; \mathbf{x_r}, \mathbf{x}) = S_{\mathbf{x}}(\omega)\, G(\omega; \mathbf{x_r}, \mathbf{x}), \tag{1}$$

where ω is the frequency, d is the data, $S_{\mathbf{x}}$ is the source signature at $\mathbf{x}$, and G is the Green's function. Note that $S_{\mathbf{x}}$ is not necessarily compact in time but can be complicated and of long duration. The source signature can therefore be computed by the application of an imaging condition to the data. A detailed description of the various imaging conditions used in microseismic imaging is given in Behura *et al.* (2013). Here, we use the 2D space-time cross-correlation imaging condition (Behura *et al.*, 2013):

$$S_{\mathbf{x}}(\omega) = \sum_{k_r} d(\omega, k_r)\, G^*(\omega, k_r), \tag{2}$$

where k_r is the wavenumber over the receiver coordinates and * represents complex-conjugation. Note that $S_{\mathbf{x}}$ obtained from equation 2 is a function of time which is different from the zero-time imaging condition commonly used in reverse-time imaging of microseismic data.

2.1 Sigsbee test

We test our imaging algorithm on the Sigsbee model (Figures 2) as it generates strong internal multiples. All the boundaries in the velocity model are absorbing.

The microseismic survey comprises of 367 receivers spread on the surface at an equal spacing of 75 ft. Two microseismic sources (Figure 2a) are used for generating the data; the initiation times of the left- and the right-source are 0.096 s and 3.36 s, respectively. Also, the left source has a higher amplitude than the right source.

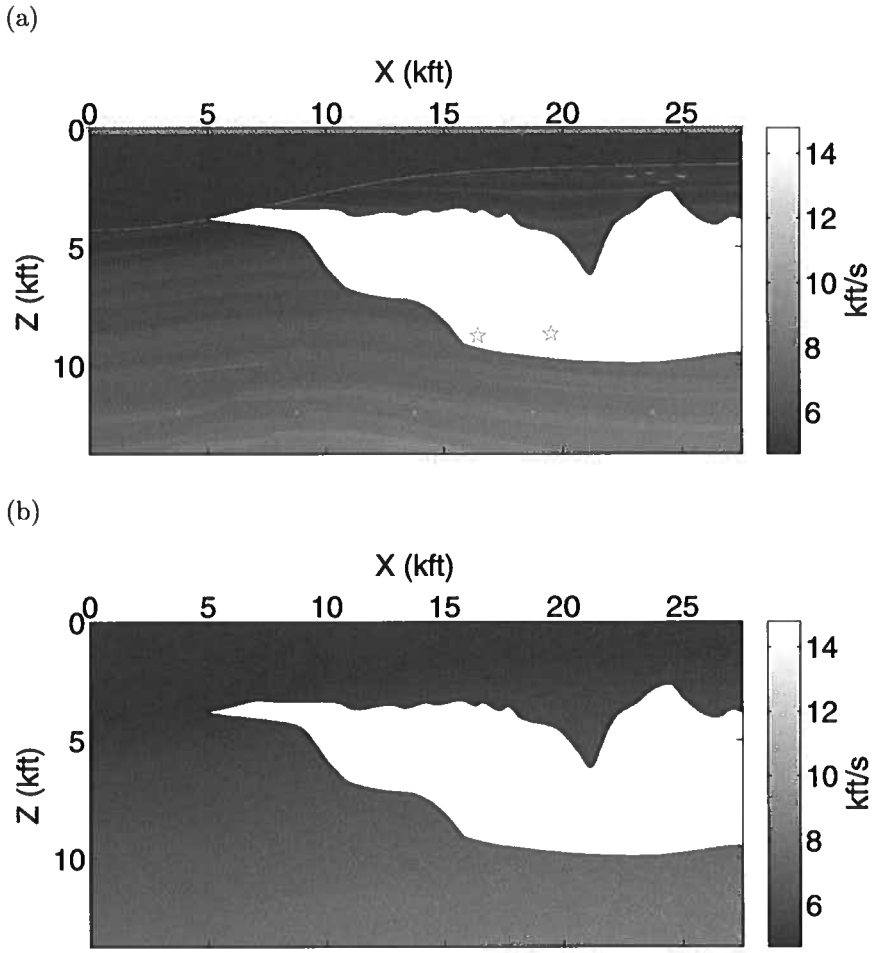

Figure 2. (a) The Sigsbee velocity model used in generating the microseismic data and the reflection seismic data. The two pentagons represent the microseismic hypocenters and the triangles represent the receivers. There are a total of 367 receivers spread on the surface at an equal spacing of 75 ft. (b) The smooth model used in imaging.

A fixed-spread receiver geometry is used for acquiring the surface reflection data; this spread coincides with the receiver geometry of the microseismic survey. Shot locations for the surface reflection data also coincide with the fixed-receiver spread. Thus, the surface reflection data comprises of 357 shot gathers, with each shot gather containing 367 traces.

Figure 3a shows the image of the two microseismic sources obtained using the imaging methodology introduced here. Behura *et al.* (2013) argue that the image of microseismic data should be displayed as a function of space as well as time because the sources can be extended in both space and time. The images in Figure 3 correspond to specific depth slices of the $z-x-t$ image cube. Note that both microseismic sources have been imaged at the correct time and also the right location; even the relative amplitudes of the two sources are preserved. More importantly, there are no spurious events in the image. The reverse-time image (Figure 3b), on the other hand, contains numerous events most of which are spurious. The left source is faintly visible, albeit its amplitude is much smaller than the spurious events; the right source is barely discernible. Some of these spurious events can be eliminated by smoothing the salt body; this will, however, lead to mis-positioning of the microseismic hypocenters (in time and space). Therefore, in the presence of multiples, reverse-time imaging can yield numerous false positives in identification of microseismic sources. For such data containing multiples, the inverse-scattering imaging method introduced here should be the algorithm of choice.

3 BOREHOLE DATA IMAGING

Like surface microseismic data, borehole data can also be imaged using the Green's function G_{ib} between the

(a)

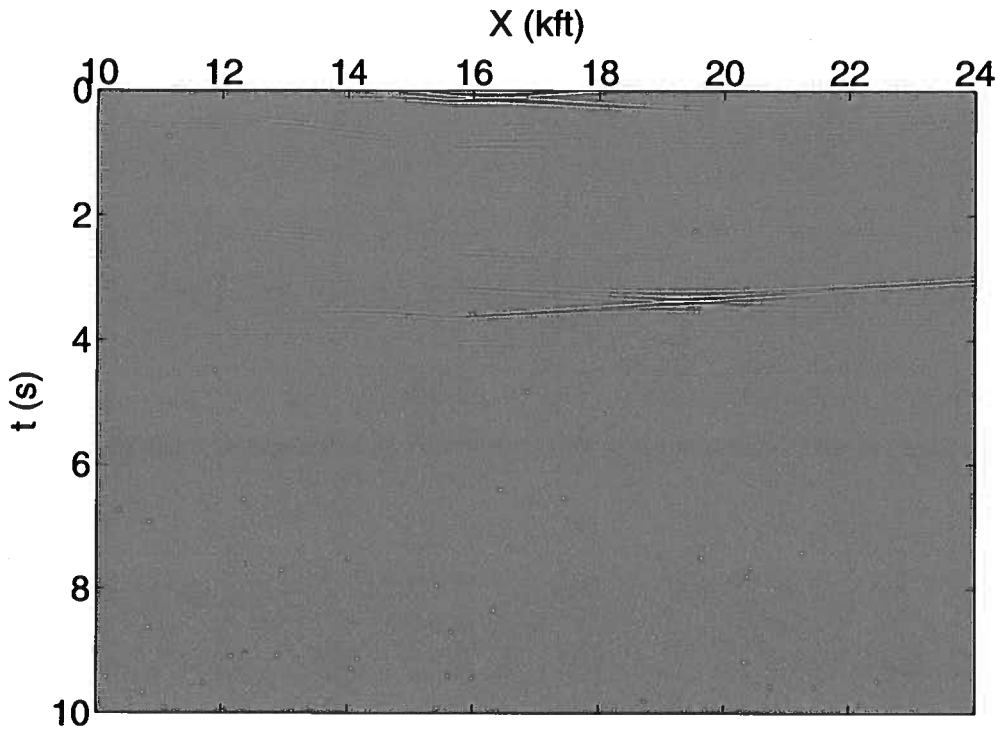

(b)

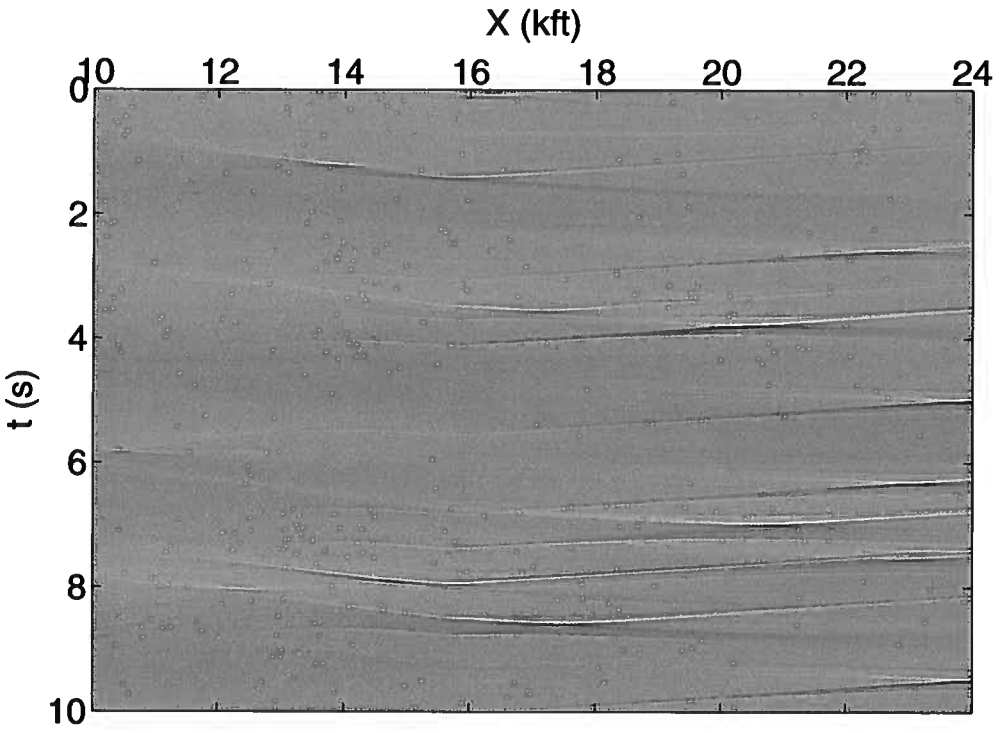

Figure 3. Images of the microseismic sources shown in Figure 2a obtained using the inverse-scattering-theory (a) and reverse-time imaging (b). The images correspond to a depth of 5700 ft. Two iterations were used in computing G using the iterative algorithm.

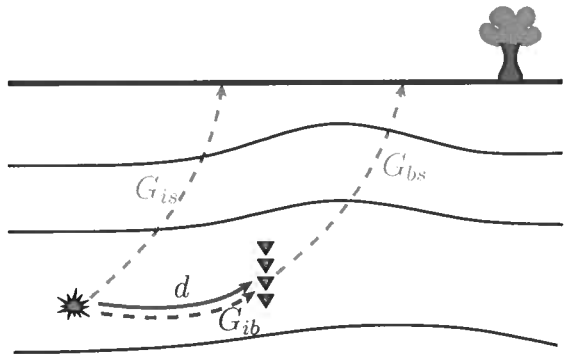

Figure 4. Schematic of the borehole microseismic data imaging algorithm based on Green's function retrieval using the iterative scheme. The triangles represent borehole receivers and the star is the microseismic hypocenter. d is the borehole microseismic data, G_{is} represents the Green's function between the image point and the surface, G_{bs} represents the Green's function between the borehole receivers and the surface, and G_{ib} is the Green's function between the image point and the borehole receivers. G_{is} and G_{bs} are computed from the surface reflection data using the iterative scheme, while G_{ib} is retrieved from G_{is} and G_{bs} using seismic interferometry.

image point and the borehole receivers. G_{ib}, however, cannot be directly computed using the iterative algorithm of Rose (2002b,a) because the borehole receivers are in the interior of the medium and because of the absence of reflection data with both shots and receivers in the borehole.. To compute G_{ib}, we use the following algorithm:

(i) compute G_{bs}, the Green's function between the borehole receivers and the surface receivers using the iterative algorithm

(ii) similarly, compute G_{is}, the Green's function between the image point and the surface receivers using the iterative algorithm

(iii) obtain G_{ib} from G_{is} and G_{bs} using seismic interferometry (Wapenaar & Fokkema, 2006) based either on cross-correlation, deconvolution, or multi-dimensional deconvolution (Wapenaar *et al.*, 2008).

Thereafter, we obtain the microseismic image by application of the following imaging condition to the data:

$$S_{\mathbf{x}}(\omega) = \sum_{k_r} d_{bh}(\omega, k_r)\, G^*_{ib}(\omega, k_r), \tag{3}$$

where d_{bh} is the borehole microseismic data and $S_{\mathbf{x}}$ is the source signature at $\mathbf{x}$.

3.1 Layer-cake test

We test the above borehole-microseismic-data imaging algorithm on a layer-cake velocity model (Figure 5a). The velocity model is constructed by extrapolating laterally a well-log velocity profile from Pennsylvania (Trenton Black River Project – Appalachian Basin).

Similar to the Sigsbee example above, all the boundaries are absorbing. The microseismic data is generated for a single source location shown in Figure 5a and recorded at the 22 borehole receivers (Figure 5a). The initiation time of the source is 0.2 s. The surface reflection data is acquired on a fixed-receiver spread with 461 receivers equally spaced at 25 m intervals. The shot points coincide with the receiver spread.

In order to perform imaging using our methodology, we compute G_{is}, G_{bs}, and G_{ib} as described above. Two iterations were used in computing G_{is} and G_{bs} using the iterative scheme. Thereafter, we apply imaging condition 3 on the borehole microseismic data. The recovered image for the true source depth level is shown in Figure 6a. Note that the focusing is better than that for reverse-time imaging (Figure 6b). In addition, the spurious events have been largely eliminated.

4 ROLE OF BACKGROUND VELOCITY

The background velocity model is used to compute the direct arrivals which are thereafter input into the iterative algorithm to calculate the Green's function Wapenaar *et al.* (2011). As suggested in (Wapenaar *et al.*, 2011), microseismic events visible on the data can also be substituted for direct arrivals. However, since we neither know the hypocenters of such events and nor are there microseismic sources everywhere, it is impractical to use visible events for direct arrivals.

A viable solution would be to use arrivals from perforation shots as direct arrivals because we already know the perforation locations. If the medium is laterally homogeneous (commonly true for unconventional reservoirs), one could use a well-log-derived velocity profile to compute direct arrivals for other image points from the perforation-shot events using upward/downward wavefield continuation. Such an approach would alleviate the need for a background velocity model.

As mentioned above, Green's function retrieval using the iterative algorithm of Rose (2002b,a); Wapenaar *et al.* (2011); Broggini & Snieder (2012) uses surface reflection data. Since the density information is already contained in the reflection data, the events corresponding to the scattered waves in the reconstructed Green's functions will have accurate amplitudes. This greater accuracy should further help in reducing false positives in microseismic imaging and also yield more accurate source signatures.

(a)

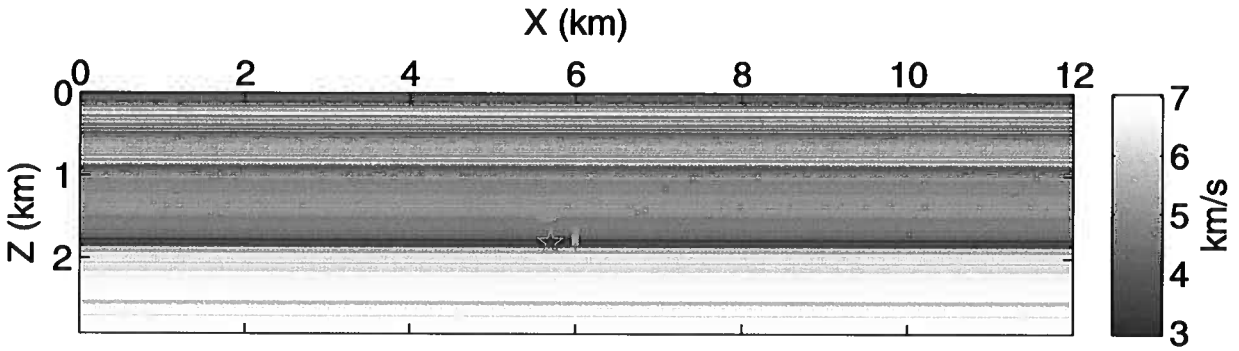

(b)

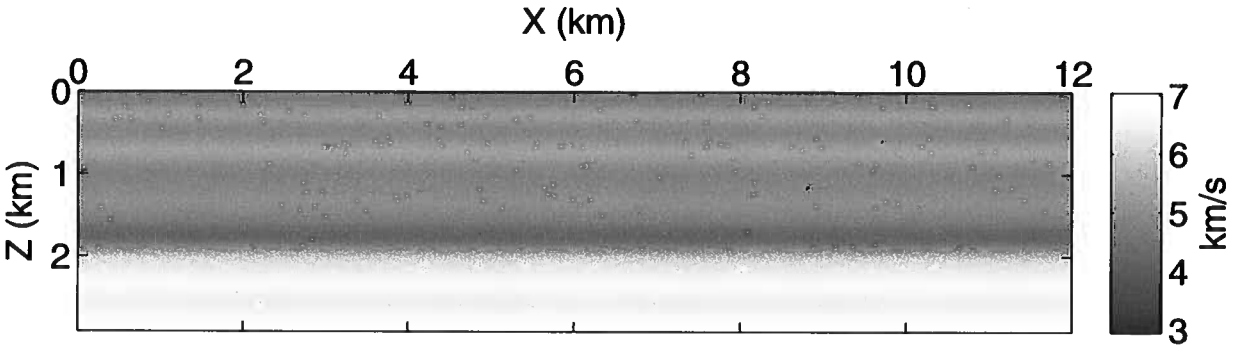

Figure 5. (a) The layer-cake velocity model used in generating borehole microseismic data and the surface reflection data. The pentagon represents the hypocenter of the microseismic source and the triangles represent the borehole receivers. The borehole receivers are emplaced as two separate arrays – one horizontal and the other vertical. Each array comprises of 11 receivers that are evenly spaced at 20 m intervals. (b) The smooth velocity model used in imaging.

5 DISCUSSION

Microseismic imaging using conventional imaging algorithms uses only the recorded data and a background velocity model. The imaging technique described here, however, needs surface reflection data in addition. Nonetheless, it is becoming common practice to acquire both surface reflection data and microseismic data for detailed characterization of unconventional plays. Moreover, the iterative algorithm requires an accurate knowledge of the source signature in the surface reflection data. The source function is known in many cases (e.g. vibroseis acquisition) or can be recorded in others (e.g. air-gun source). Where, the source signature is unknown, deterministic methods such as Virtual Real Source (Behura, 2007) should be used to compute it.

The iterative algorithm of Rose (2002b,a); Wapenaar *et al.* (2011); Broggini & Snieder (2012) can successfully recover the Green's function when all the scattering is in the interior of the medium. In the presence of a free-surface, however, the algorithm fails to compute the exact Green's function. Using a modified algorithm, Singh *et al.* (2013) show that the exact Green's function can be extracted even in the presence of free-surface reflections. This modified algorithm might be used for imaging microseismic data containing free-surface multiples.

The imaging algorithm introduced here is substantially more computationally intensive than conventional algorithms such as reverse-time imaging and Kirchhoff imaging. Computation of the direct arrivals is the primary driver of the cost. There are two strategies for computing the direct arrivals between the image points and the surface receivers. First – the direct arrivals for each image point can be computed on the fly while the code is being executed. The number of forward computations will equal the number of image points. This will require significant processor power but have minimal disk input-output costs. Second – since there are far fewer receivers than image points, one could compute the direct arrivals for all image points from each receiver location independently and then store them to the disk. Thus the number of forward computations will equal

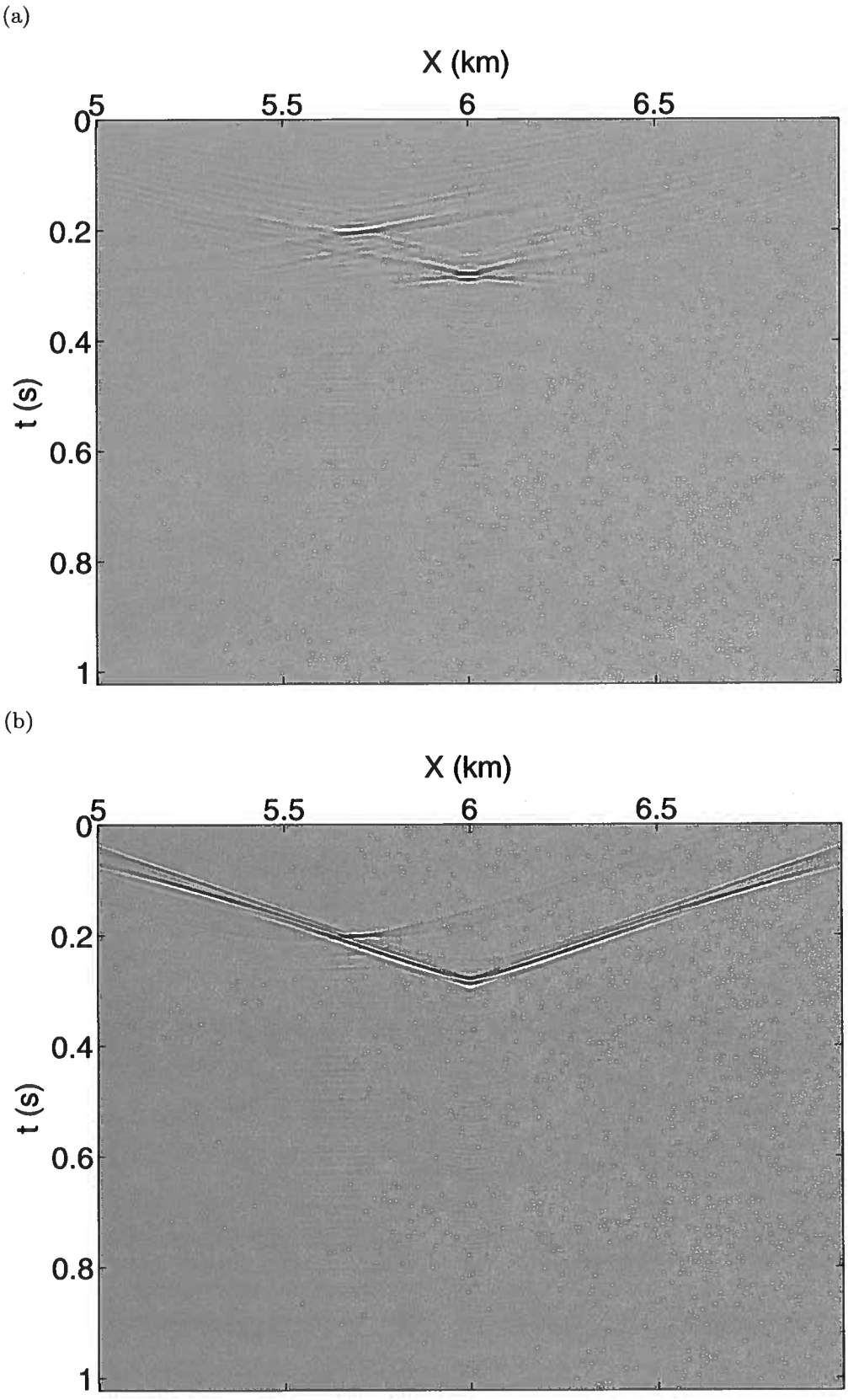

Figure 6. Images of the microseismic source shown in Figure 5a obtained using the inverse-scattering-theory based algorithm (a) and reverse-time imaging (b). The images correspond to the true depth of the microseismic hypocenter (1800 m). The event at t =0.3 s and x =6 km in (a) corresponds to the location of the vertical receiver array. The same event manifests as a linear moveout in (b).

the number of receivers. Because of reciprocity, one can then read the direct arrivals from the disk for each image point; this, however, involves substantial disk input-output operations. Based on the number of receivers versus the number of image points, one can choose either of the above two strategies.

The iterative algorithm of Rose (2002b,a); Wapenaar *et al.* (2011); Broggini & Snieder (2012) is applicable to only acoustic wave propagation. In the presence of strong shear waves in microseismic data (especially in borehole recordings), all imaging algorithms will fail to properly characterize the microseismicity. Therefore, shear waves should be suppressed in the data before imaging. Shear-wave suppression is more critical for borehole data and less so for surface acquisition because of the strong near-surface attenuation.

6 CONCLUSIONS

Imaging of microseismic data in the presence of multiples will result in numerous false positives i.e. identification of spurious microseismic hypocenters. In order to image such data accurately, we have developed an algorithm that uses exact Green's function derived using an iterative scheme based on inverse-scattering theory. Both surface- and borehole-microseismic data can be imaged using our approach. Tests on synthetic data show that our approach can reduce false positives significantly as well as improve the focusing of the microseismic hypocenters.

ACKNOWLEDGMENTS

We thank Farnoush Forghani and Satyan Singh for many discussions. Support for this work was provided by the Consortium Project on Seismic Inverse Methods for Complex Structures at Center for Wave Phenomena.

References

Behura, J. 2007. Virtual Real Source. *SEG Technical Program Expanded Abstracts*, 2693–2697.

Behura, J., Forghani, F., & Bazargani, F. 2013. Improving microseismic imaging: role of acquisition, velocity model, and imaging condition. *CWP Project Review*, **754**, 77–86.

Broggini, F., & Snieder, R. 2012. Connection of scattering principles: a visual and mathematical tour. *European Journal of Physics*, **33**(3), 593.

Gajewski, D., Anikiev, D., Kashtan, B., Tessmer, E., & Vanelle, C. 2007. Localization of seismic events by diffraction stacking. *SEG Technical Program Expanded Abstracts*, 1287–1291.

McMechan, G. A. 1982. Determination of source parameters by wavefield extrapolation. *Geophysical Journal of the Royal Astronomical Society*, **71**, 613–628.

McMechan, G. A., Luetgert, J. H., & Mooney, W. D. 1983. Imaging of earthquake sources in Long Valley Caldera, California. *Bulletin of the Seismological Society of America*, **75**, 1005–1020.

Rose, J. H. 2002a. *Time reversal, focusing and exact inverse scattering.* 1 edn. Springer-Verlag, Berlin. Pages 97–105.

Rose, J. H. 2002b. Single-sided autofocusing of sound in layered materials. *Inverse Problems*, **18**, 19231934.

Roundtree, R., & Miskimins, J. 2011. Experimental Validation of Microseismic Emissions from a Controlled Hydraulic Fracture in a Synthetic Layered Medium, SPE 140653. *In: SPE Journal.*

Singh, S., Snieder, R., & Behura, J. 2013. *Reconstruction of the exact Green's function in the presence of a free surface.*

Wapenaar, K., & Fokkema, J. 2006. Green's function representations for seismic interferometry. *Geophysics*, **71**(4), SI33–SI46.

Wapenaar, K., van der Neut, J., & Ruigrok, E. 2008. Passive seismic interferometry by multidimensional deconvolution. *Geophysics*, **73**(6), A51–A56.

Wapenaar, K., Broggini, F., & Snieder, R. 2011. A proposal for model–independent 3D wave field reconstruction from reflection data. *SEG Technical Program Expanded Abstracts*, **30**(1), 3788–3792.

Wapenaar, K., Broggini, F., Slob, E., & Snieder, R. 2013. Three-Dimensional Single-Sided Marchenko Inverse Scattering, Data-Driven Focusing, Green's Function Retrieval, and their Mutual Relations. *Phys. Rev. Lett.*, **110**(Feb), 084301.

Locating a microseismic event using deconvolution

Johannes Douma[1], Roel Snieder[1], Ashley Fish[1], and Paul Sava[1]
[1] *Center for Wave Phenomena, Colorado School of Mines, Golden, Colorado 80401*

ABSTRACT
We demonstrate a technique to enhance the ability of imaging the location of a microseismic event by improving both spatial and temporal focusing. The technique improves locating a microseismic event in a velocity model for which the interface boundaries are approximate but where it has the correct mean slowness. Our method designs a signal to be rebroadcasted from the receivers, using only the waves recorded at each receiver, such that the wave field has an optimal temporal focus at the source location. Additionally, this procedure leads to an improved spatial focus of the wave field. The numerical test shown include additive noise. This proposed technique only involves a simple preprocessing step to the recorded data and its cost is hence negligible compared to the total cost of microseismic imaging.

Key words: Microseismic, Time reversal, Deconvolution

1 INTRODUCTION

Microseismic events occur naturally or as a result of production or hydraulic stimulation (Duncan, 2005; Kendall et al., 2011). Clusters of microseismic events delineate faults and the formation of fractures and can indicate new or reactivating regions of failure. As hydraulic fracturing is becoming increasingly widespread, operators are aiming to monitor the induced events in order to characterize a reservoir. This has lead to a need from the industry to develop more accurate ways of locating and monitoring microseismic events (Foulger and Julian, 2012).

A standard processing method is based on picking arrival times of P and S waves. This process is, however, difficult when significant noise is present in the data and thus can require extensive user interaction (Bancroft et al., 2010; Bose et al., 2009; Hayles et al., 2011; Kummerow, 2010; Song et al., 2010). An alternative approach to locate events is by imaging the time reversed signal to focus microseismic signal at the source position (Artman et al., 2010; Lu and Willis, 2008; Lu, 2008; Steiner et al., 2008). The advantage of imaging the time reversed signal is that it does not require picking of arrival times, this is of particular importance for noisy data. In the imaging approach, one usually uses time reversal to focus the recorded waves at the source location in space and time (Artman et al., 2010).

If one time reverses the waves at every point in space, the wavefield will focus onto the original source location. If, however, the wavefield is sampled at only a limited number of locations, then it is not obvious that time reversal is the optimal way to focus energy on the original source. Much research has been carried out on focusing sparsely sampled wavefields (Aubry et al., 2001; Bertaix et al., 2004; Fink, 1997; Gallot et al., 2011; Jonsson et al., 2004; Larmat et al., 2010; Montaldo et al., 2004; Parvulescu, 1961; Roux and Fink, 2000; Tanter et al., 2001, 2000; Vignon et al., 2006). In this letter, we explore a simple extension to time reversal, based on deconvolution, as previously derived by Ulrich et al. (2012), to improve our imaging for locating a microseismic event. This method is a robust, though simplified, version of the inverse filter (Gallot et al., 2011; Tanter et al., 2000, 2001). It calculates a signal to be rebroadcast from the receiver such that the output at the focal location becomes an approximate delta function $\delta(t)$ and uses only the recorded signals at each receiver.

As with all imaging methods, reverse time imaging is unable to locate the microseismic event to a point location when the velocity model isn't the true velocity model or the aperture is poor; it causes the spatial image to defocus. We propagate the deconvolved waveforms through a smoothed version of the true slowness model. The local average of the slowness for this incorrect velocity model is equal to local average slowness of the true velocity model.

2 THEORY-DECONVOLUTION

Time reversal states that for a given recorded impulse response, a simple reversal in time of that signal followed by rebroadcasting the reversed signal from the receivers focuses an impulsive function $\delta(t)$ at the source location,

$$f(t) = \sum_i r_i(t) \star r_i(-t) \approx \delta(t) \tag{1}$$

where $\star$ denotes a convolution operator, $r_i(t)$ is the recorded impulse response at receiver i, and $r_i(-t)$ its time reversed counterpart. Equation (1) states that the autocorrelation of the recorded signal is ideally equal to a delta function. In practice, however, time reversal (TR) experiments are unable to recreate a true delta function focus as one or more conditions necessary to satisfy equation (1) are typically violated. For example, if attenuation is present in the medium, time reversal (TR) can not create a true delta function focus. Additionally, if the aperture is finite, TR experiments can not create a true delta function focus. Given these limitations, we introduce deconvolution to achieve a more impulsive focusing in time.

Let us assume that time reversal is not able to create a Dirac delta focus after rebroadcasting the time reversed impulse response. We aim to find a signal such that after rebroadcasting we get a temporal focus that is approximately equal to a Dirac delta function. Thus, we change equation (1) to

$$f(t) = \sum_i r_i(t) \star g_i(t) \approx \delta(t) \ , \tag{2}$$

where $f(t)$ is the back propagated signal at the source, $r_i(t)$ is the recorded impulse response at receiver i, and $g_i(t)$ is the signal that is back propagated to the source from receiver i. We determine the backpropogated signal $g_i(t)$ from the requirement that the right hand side of the equation (2) approximates a delta function as well as possible. In the frequency domain, this corresponds to the requirement,

$$\sum_i r_i(\omega) g_i(\omega) \approx 1 \ . \tag{3}$$

This condition defines the signal that optimizes the temporal focus at the source location. Equation (3), applied to each receiver states that

$$g_i(\omega) = \frac{1}{r_i(\omega)} \approx \frac{r_i^*(\omega)}{|r_i(\omega)|^2 + \epsilon}, \tag{4}$$

where $r(\omega)r^*(\omega) = |r(\omega)|^2$. We introduce a regularization parameter ϵ to stabilize the deconvolution that satisfies

$$\epsilon = \gamma \times mean(|r_i(\omega)|^2) \ . \tag{5}$$

where γ is a constant, which is sometimes referred to as the waterlevel parameter (Clayton and Wiggins, 1976), and the mean is calculated for each receiver over the frequencies for which the power spectrum differs significantly from zero. For small values of γ, the deconvolution may be sensitive to additive noise, whereas for larger values of γ the deconvolution reduces to time reversal. We choose the value of γ by maximizing the energy in a 80m by 80m region around the source. This process is similar to the time-domain procedure developed by Clayton and Wiggins (1976). We used a value of $\gamma = 0.272$ in all experiments shown. An inverse Fourier transform takes $g(\omega)$ back into the time domain. One can then directly rebroadcast $g(t)$ and does not have to apply a time reversal operation on $g(t)$.

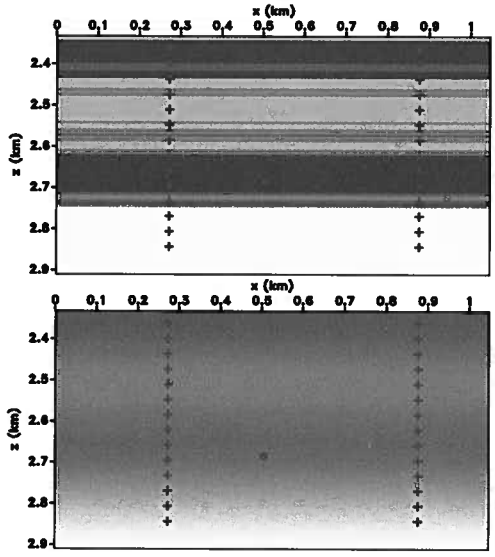

Figure 1. Velocity models of the numerical experiment. Top panel indicates the correct velocity model and represents the velocity model used to propagate the source wavefield through the medium. Bottom panel indicates the smoothed velocity model with correct mean slowness. This model is used for back propagation of the time reversed signal and optimized inverse signal. The plus symbols represent the receivers, the circular dot represents the source.

3 MICROSEISMIC EVENT LOCATING

The purpose of this study is to optimize microseismic event location using deconvolution. We use the velocity model shown in the top panel of Figure 1 to propagate the source wavefield to the receivers. The model consists of horizontally continuous layers whose velocities range from approximately 5 km/s to 6.6 km/s. In practice, one does not know the true velocity model. For this reason, we used the smoothed velocity model, shown in the bottom panel of Figure 1, for the back propagation. The velocity model is smoothed by using a two-dimensional triangle smoothing with a smoothing radius of .185 km in the z, and x direction (Fomel, 2007). This smoothed

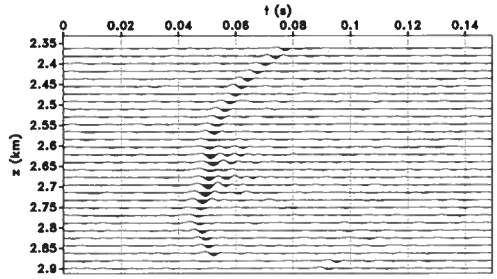

Figure 2. Wavefield excited by the source in figure 1 after propagation through the true velocity model (top panel of figure 1). Bandlimited noise is added to the data, the signal to noise ratio is .89

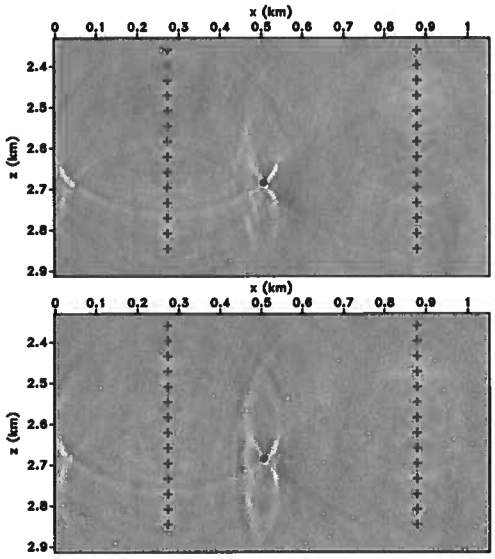

Figure 3. Wavefield $p(\mathbf{x}, t = 0)$ for deconvolution (top panel) and time reversal (bottom panel). The plus symbols represent the receivers, the circular dot represents the source. These images were created by back propagating the time reversed and inverse optimized signal through the incorrect velocity model (bottom panel of figure 1).

velocity model has the same mean slowness as the correct velocity model.

The location of the source is at $(x, z) = (0.51$ km, 2.68 km). The source wavelet is a Ricker wavelet with dominant frequency of 150 Hz. We use 56 receivers distributed over 2 vertical boreholes in our model. The x-locations of the receiver boreholes are 0.74 km and 0.88 km. The receivers range from a depth of 2.36 km to 2.86 km with a spacing of 18.5 m.

We find the focus time without knowing the triggering time. We do so by rebroadcasting our calculated inverse signal, producing an image every time step, and then calculate the energy of the spatial focus in a region around the source location until it reaches a maximum. In order to make the numerical simulation more realistic, we added noise to our recorded data at the receivers before running the time reversal or deconvolution process. Thus, both processes deal with the same noise. The additive noise only contains frequencies within the bandwidth of the data. The energy ratio of the signal to noise, defined as the ratio of the sum of the absolute values of the signal and noise squared, is equal to 0.89. The noise-contaminated data thus produced are shown in Figure 2.

As shown in Figure 3, deconvolution produces better spatial focusing than does time reversal. This allows one to find the location of the microseismic event with higher accuracy. This is possible because deconvolution suppresses the temporal sidelobes of the refocused signal and thus compresses more of the wave energy into the focus at the event time ($t = 0$). In order to compare the spatial focusing of each method, we show in figure 4(c) and (d) horizontal slices of the spatial image at the depth of the source at the time of the focus ($t = 0$). Figure 4(d) illustrates that deconvolution improves spatial focusing compared to simple time reversal (Figure 4(c)). We quantify this improved spatial focusing by computing the ratio of the energy near the focus and the total energy. Using a window centered at the source location with a width of 20 m, we calculated the energy of the focus. Dividing the energy of the focus by the total energy gives us the spatial energy ratio of the focus. Deconvolution yields a spatial energy ratio of 48% while time reversal has a spatial energy ratio of only 31%, which indicates quantitatively that deconvolution improves the spatial focus of a microseismic event.

We next consider temporal focusing. Figure 4(a) and (b) show improved temporal focusing for the deconvolution method compared to time reversal. We quantify the temporal focusing by computing the ratio of the energy near focus and the total energy. Using a window centered at $t = 0s$ with width of $.003s$, we calculated the energy of the temporal focus. Dividing this focused energy by the total energy gives us the temporal energy ratio of the focus. Deconvolution has a temporal energy ratio of 49% while time reversal has a temporal energy ratio of 40%. Thus, deconvolution improves temporal focusing.

In conclusion, deconvolution improves both temporal and spatial focusing for our model. This allows one to locate microseismic events with greater accuracy, even when the velocity model is not the true model and additive noise is present. Deconvolution improves spatial focusing even though the method we introduced is designed to improve temporal focus. It was shown by Ulrich et al. (2012) that improved temporal focusing improves spatial focusing for the spherically symmetric part of the focused wave field..

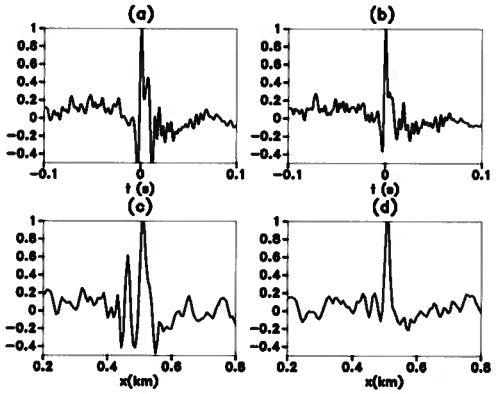

Figure 4. Temporal and spatial focused images produced by back propagating the calculated time reversed signals using time reversal and deconvolution for vertical borehole array. (a) Temporal focus at the source location obtained for time reversal, (b) Temporal focus at the source location obtained for deconvolution, (c) Horizontal cross section through the source depth at $t = 0$ obtained for time reversal, (d) Horizontal cross section through the source depth at $t = 0$ obtained for deconvolution.

4 IMPROVED TEMPORAL FOCUSING LEADS TO IMPROVED SPATIAL FOCUSING

In this section, we show that better temporal focusing implies better spatial focusing for the spherical average of the focus. We begin by first considering the wave field near its focal spot at $r = 0$ and consider the medium to be locally homogeneous in that region. The solution of the Helmholtz equation in an acoustic, homogeneous medium can be written as

$$p(r,\theta,\varphi,\omega) = \sum_{l=0}^{\infty} \sum_{m=-l}^{m=l} a_{lm} j_l(kr) Y_{lm}(\theta,\varphi) \,, \qquad (6)$$

see Table 8.2 of Arfken and Weber (2001). In this expression j_l denotes the spherical Bessel function, Y_{lm} the spherical harmonics, and $k = \omega/c$, where c is the wave speed. According to expressions (11.144) and (11.148) of Arfken and Weber (2001), $j_l(0) = 0$ for $l \geq 1$ and $j_0(0) = 1$. This means that at the focal point $r = 0$ only the terms $l = m = 0$ contribute. Using $Y_{00} = 1/\sqrt{4\pi}$ (Table 12.3 of Arfken and Weber (2001)), this means that at the focal point

$$p(r = 0,\theta,\varphi,\omega) = \frac{a_{00}}{\sqrt{4\pi}} \,. \qquad (7)$$

The properties of the wave field at the focal point thus only depend on the coefficient a_{00}. Since the $l = m = 0$ component of the spherical harmonics expansion gives the spherically symmetric component of the wave field, the properties of the wave field at the focal point can only bear a relation to the spherically symmetric component of the wave field. The properties of temporal focusing can thus be related to the spherically symmetric component of the spatial focusing only.

Because of this, we restrict ourselves to the spherically symmetric component ($l = m = 0$) of the wave field at the focal point. Using that $j_0(kr) = \sin(kr)/kr$, the spherically symmetric component of Eq. (6) is given by

$$p(r,\omega) = p_0 \, \frac{e^{-ikr} - e^{ikr}}{r} \,, \qquad (8)$$

with $p_0 = -a_{00}/(2ik\sqrt{4\pi})$. The coefficient p_0 depends on frequency. Using the Fourier convention $f(t) = \int p_0(\omega) e^{-i\omega t} d\omega$, and using that $k = \omega/c$, Eq. (8) corresponds, in the time domain, to

$$p(r,t) = \frac{f(t + r/c) - f(t - r/c)}{r} \,. \qquad (9)$$

In this equation, $f(t + r/c)$ denotes the wave that is incident on the focus, and $f(t - r/c)$ the outgoing wave once it has passed through the focus.The field at the focus follows by Taylor expanding $f(t \pm r/c)$ in r/c and taking the limit $r \to 0$, this gives

$$p(r = 0,t) = \frac{2}{c} f'(t) \,. \qquad (10)$$

In this expression and the following, the prime denotes the time derivative. Equation (10) states that the wave field at the focus is the time derivative of the incoming wave field and provides the temporal properties of the focus.

In order to get the spatial properties, we consider the wavefield near the focal point at time $t = 0$. Setting $t = 0$ in Eq. (9), gives

$$p(r, t = 0) = \frac{f(r/c) - f(-r/c)}{r} \,. \qquad (11)$$

Equation (11) states that the wave field at the time of focus is the difference between the incoming and outgoing wave and gives the spatial properties of the focus.

A improved temporal focus implies that $f'(t)$ is only nonzero for values of t close to $t = 0$. It follows from Eq. (11) that if that is the case, then $p(r, t = 0)$ is localized near $r = 0$. Note that if a constant was added to f when going from $f'(t)$ to $f(t)$, our conclusion would not change because the constant would be subtracted and cancelled out in Eq. (11).

5 CONCLUSION

We have introduced a method that improves temporal focusing of a microseismic event. The method can be beneficial for locating a microseismic event because it also improves spatial focusing compared to the standard time reversal method. We have shown how this techniques improves the locating for a microseismic event using synthetic data contaminated with additive noise.

The simplicity and robust nature of this method allows for a simple incorporation into existing reverse-time imaging methods. The cost of the deconvolution is minimal compared to running the finite difference model. Thus, it can be added as a preprocessing step without significant additional cost. Further research involves extending this method to elastic waves excited by a double couple source.

REFERENCES

Arfken, G., and H. Weber, 2001, Mathematical methods for physicists, 5th ed.: Harcourt.

Artman, B., I. Podladtchikov, and B. Witten, 2010, Source location using time-reverse imaging: Geophysical Prospecting, **58**, 861–873.

Aubry, J.-F., M. Tanter, J. Gerber, J.-L. Thomas, and M. Fink, 2001, Optimal focusing by spatio-temporal filter. II. Experiments. Application to focusing through absorbing and reverberating media: J. Acoust. Soc. Am., **110**, 48–58.

Bancroft, J. C., J. Wong, and L. Han, 2010, Sensitivity measurements for locating microseismic events: CSEG Recorder, 28–37.

Bertaix, V., J. Garson, N. Quieffin, S. Catheline, J. Derosny, and M. Fink, 2004, Time-reversal breaking of acoustic waves in a cavity: American Journal of Physics, **72**, 1308–1311.

Bose, S., H. Valero, Q. Liu, R. G. Shenoy, and A. Ounadjela, 2009, An Automatic Procedure to Detect Microseismic Events Embedded in High Noise: SEG Technical Program Expanded Abstracts, 1537–1541.

Clayton, R. W., and R. A. Wiggins, 1976, Source shape estimation and deconvolution of teleseismic body-waves: Geophys. J. Royal Astron. Soc., **47**, 151–177.

Duncan, P. M., 2005, Is there a future for passive seismic?: First Break, **23**, 111–115.

Fink, M., 1997, Time reversed acoustics: Physics Today, **50**, 34–40.

Fomel, S., 2007, Shaping regularization in geophysical-estimation problems: Geophysics, **72**, R29–R36.

Foulger, G. R., and B. R. Julian, 2012, Earthquakes and errors : Methods for industrial applications: Geophysics, **76**, WC5–WC15.

Gallot, T., S. Catheline, P. Roux, and M. Campillo, 2011, A passive inverse filter for Green's function retrieval: J. Acoust. Soc. Am., **131**, EL21–EL27.

Hayles, K., R. L. Horine, S. Checkles, J. P. Blangy, and H. Corporation, 2011, Comparison of microseismic results from the Bakken Formation processed by three different companies : Integration with surface seismic and pumping data: SEG Technical Program Expanded Abstracts, 1468–1472.

Jonsson, B. L. G., M. Gustafsson, V. H. Weston, and M. V. d. Hoop, 2004, Retrofocusing of acoustic wave fields by iterated time reversal: SIAM J. Appl. Math., **64**, 1954–1986.

Kendall, M., S. Maxwell, G. Foulger, L. Eisner, and Z. Lawrence, 2011, Special Section Microseismicity : Beyond dots in a box Introduction: Geophysics, **76**, WC1–WC33.

Kummerow, J., 2010, Using the value of the crosscorrelation coefficient to locate microseismic events: Geophysics, **75**, MA47–MA52.

Larmat, C., R. Guyer, and P. Johnson, 2010, Time-reversal methods in geophysics: Physics Today, **63**, 31–35.

Lu, R., a. T. N., and M. Willis, 2008, Locating Microseismic Events with Time Reversed Acoustics: A Synthetic Case Study: SEG Technical Program Expanded Abstracts, 1342–1346.

Lu, R., 2008, Time Reversed Acoustics and Applications to Earthquake Location and Salt Dome Flank Imaging: Massachusetts Institute of Technology. Earth Resources Laboratory.

Montaldo, G., M. Tanter, and M. Fink, 2004, Real time inverse filter focusing through iterative time reversal: J. Acoust. Soc. Am., **115**, 768–775.

Parvulescu, A., 1961, Signal detection in a multipath medium by M.E.S.S. processing: J. Acoust. Soc. Am., **33**, 1674–1674.

Roux, P., and M. Fink, 2000, Time reversal in a waveguide: study of the temporal and spatial focusing: J. Acoust. Soc. Am., **107**, 2418–2429.

Song, F., H. S. Kuleli, M. N. Toksöz, E. Ay, and H. Zhang, 2010, An improved method for hydrofracture-induced microseismic event detection and phase picking: Geophysics, **75**, A47–A52.

Steiner, B., E. H. Saenger, and S. M. Schmalholz, 2008, Time reverse modeling of low-frequency microtremors: Application to hydrocarbon reservoir localization: Geophysical Research Letters, **35**, L03307.

Tanter, M., J.-F. Aubry, J. Gerber, J.-L. Thomas, and M. Fink, 2001, Optimal focusing by spatio-temporal filter. I. Basic principles: J. Acoust. Soc. Am., **110**, 37–47.

Tanter, M., J.-L. Thomas, and M. Fink, 2000, Time reversal and the inverse filter: J. Acoust. Soc. Am., **108**, 223–234.

Ulrich, T., J. Douma, R. Snieder, and B. Anderson, 2012, Improving time reversal focusing and source reconstruction through deconvolution: J. Acoust. Soc. Am., Under Review.

Vignon, F., J.-F. Aubry, A. Saez, M. Tanter, D. Cassereau, G. Montaldo, and M. Fink, 2006, The Stokes relations linking time reversal and the inverse filter: J. Acoust. Soc. Am., **119**, 1335–1346.

Gradient computation for full-waveform inversion of microseismic data in VTI media

Oscar Jarillo Michel and Ilya Tsvankin
Center for Wave Phenomena, Colorado School of Mines

ABSTRACT

Source locations are usually estimated from microseismic data using kinematic techniques. Full-waveform inversion (FWI) can potentially provide more accurate source parameters along with an improved velocity model by incorporating information contained in the entire trace including the coda. Here, we address one of the key issues in implementing FWI for microseismic surveys — efficient calculation of the gradient of the objective function with respect to the model parameters. Application of the adjoint-state method helps obtain closed-form expressions for the gradients with respect to the source location and moment tensor. Computation of the forward and adjoint wavefields is performed with a finite-difference algorithm that handles elastic VTI (transversely isotropic with a vertical symmetry axis) models. Numerical examples illustrate the properties of the gradients for the wavefield from a moment-tensor source in homogeneous and layered VTI media.

Key words: full-waveform inversion, adjoint-state method, anisotropy, transverse isotropy, dislocation source, moment tensor

1 INTRODUCTION

Microseismicity has developed in recent years as an efficient technique for reservoir monitoring (Maxwell, 2010; Kendall et al., 2011). Microseismic experiments typically involve recording the seismic response to hydraulic fracturing of tight reservoirs, most often shales. The location of the induced microfractures, as well as the origin time of the corresponding seismic events can be inferred from the data acquired in an observation borehole or at the surface. Usually only a single borehole is available, but it is highly beneficial to record microseismic data in several boreholes.

Accurate location of microseismic events requires knowledge of the background velocity model. This initial model is usually obtained from sonic logs and traveltimes of the direct P- and S-waves excited by perforation shots and recorded by geophones deployed in a monitor borehole. Afterwards, the model can be updated using the traveltimes of microseismic events. Velocity analysis without adequately accounting for seismic anisotropy may lead to significant errors in event location. In particular, shales are known to be transversely isotropic and may become orthorhombic or possess an even lower symmetry due to fracturing (Tsvankin and Grechka, 2011; Tsvankin, 2012). Van Dok et al. (2011) highlight the sensitivity of estimated event locations to the anisotropy parameters of TI media. Grechka et al. (2011) demonstrate that anisotropic velocity models constructed while locating microseismic events provide more accurate source locations than those obtained with models based solely on sonic logs and perforation shots.

It is also important to study the source mechanism associated with microseismic events because it can reveal important information about the rupture process. Earthquake point sources are described by the second-rank symmetric seismic moment tensor M_{ij} with six independent elements. As discussed by Vavryčuk (2007), all components of the moment tensor for microseismic events can be retrieved from the amplitudes of P-waves recorded in three boreholes or from P- , SV-, and SH-wave amplitudes measured in two boreholes. For events located in the $[x_1, x_3]$-plane of a 2D azimuthally isotropic model, the in-plane polarized waves depend on the moment tensor elements M_{11}, M_{13}, and M_{33}, which can be found from P- and SV-waves recorded in a single borehole. Depending on the receiver geometry and distribution of sources, microseismic data potentially can help estimate the pertinent anisotropy parameters (Grechka and Duchkov, 2011) and the source location (Grechka et al., 2011).

Most existing methods of event location are based on kinematic inversion that replaces a seismic trace with the band-limited δ-functions corresponding to the direct arrivals, which restricts the resolution according to the Rayleigh criterion (i.e., two sources appear as one if the distance between them is

smaller than one-half of the predominant wavelength). Considering the increasing usage of back-projection techniques and the rich information content of microseismic data, improved results can be expected from full-waveform inversion (FWI). Indeed, FWI operates with the entire trace including scattered waves, so the results are not subject to the Rayleigh criterion. Hence, for typical wavelengths in downhole microseismic surveys, one can expect substantially reduced event-location errors. Another potential benefit of FWI is an improved accuracy of the velocity model.

FWI is used to build high-resolution velocity models from seismic data using phase and, sometimes, amplitude information (Tarantola, 1984; Gauthier et al., 1986; Mora, 1987; Pratt, 1999; Virieux and Operto, 2009). Recently FWI has been extended to elastic and anisotropic media (Lee et al., 2010; Kamath and Tsvankin, 2013), which makes it suitable for multicomponent reflection and microseismic data.

The objective function in FWI quantifies the difference between observed and predicted data in the time or frequency domain. Efficient inversion requires application of iterative optimization schemes such as the conjugate-gradient method, which involves calculation of the gradient of the objective function with respect to the model parameters. In principle, the gradient can be found from the Fréchet derivatives obtained by differentiating the wavefield with respect to each model parameter. However, if the number of unknowns is large, computation of the Fréchet derivatives becomes prohibitively expensive.

A computationally efficient alternative for computing the gradient and model updating without the Fréchet derivatives is the adjoint-state method (Plessix, 2006; Fichtner et al., 2006; Fichtner, 2009; Köhn, 2011). This method makes it possible to calculate the gradient using just two forward-modeling simulations: first to generate the forward wavefield, which yields the predicted data, and second to compute the adjoint wavefield.

There has been significant progress in applying adjoint methods to tomographic velocity analysis and source-parameter inversion in global seismology. Tromp et al. (2005) and Liu and Tromp (2006) employ an adjoint formulation based on the Lagrangian-multiplier method to derive the gradients for the P- and S- wave velocities in isotropic media. They also analyze the sensitivity (Fréchet) kernels for 2D and 3D velocity models. Kim et al. (2011) obtain gradient expressions for the source parameters using the adjoint-state method and implement conjugate-gradient inversion to estimate the moment tensor, location, and source time function for an earthquake in Southern California using a known isotropic velocity model. Morency and Mellors (2012) follow the same approach to evaluate the moment tensor and source location of a geothermal event.

Here, we discuss the gradient computation for full-waveform inversion of microseismic data. The current algorithm is designed to estimate only the source location and moment tensor from 2D microseismic experiments.

We start by describing elastic finite-difference modeling for dislocation-type sources in VTI media. The adjoint-state method is then employed for efficient gradient calculation by adapting to our problem the general expressions for the gradients obtained by Kim et al. (2011). Although we plan to estimate the interval Thomsen parameters of layered VTI media as well, the current formulation is limited to the gradients for the source parameters. The performance of the algorithm is illustrated by synthetic examples for homogeneous and layered VTI media which include the wavefields obtained by forward and adjoint finite-difference modeling and the gradients calculated for the source location and moment tensor.

2 FORWARD MODELING

2.1 Implementation

The wave equation for a homogeneous anisotropic medium can be written as (Tsvankin, 2012):

$$\rho \frac{\partial^2 u_i}{\partial t^2} - c_{ijkl} \frac{\partial^2 u_k}{x_j x_l} = f_i \,, \tag{1}$$

where $\mathbf{u}(\mathbf{x},t)$ is the displacement field, c_{ijkl} is the stiffness tensor ($i,j,k,l = 1,2,3$), $\rho(\mathbf{x})$ is density, $\mathbf{f}(t)$ is the body force, and t is time.

Dislocation-type sources are described by the seismic moment tensor,

$$\mathbf{M} = \begin{pmatrix} M_{11} & M_{12} & M_{13} \\ M_{21} & M_{22} & M_{23} \\ M_{31} & M_{32} & M_{23} \end{pmatrix} , \tag{2}$$

which can be incorporated into the source term of equation 1 by using the notion of equivalent force (Aki and Richards, 1980; Dahlen and Tromp, 1998):

$$\rho \frac{\partial^2 u_i}{\partial t^2} - c_{ijkl} \frac{\partial^2 u_k}{\partial x_j \partial x_l} = M_{ij} \frac{\partial[\delta(\mathbf{x}-\mathbf{x_s})]}{\partial x_j} S(t) \,, \tag{3}$$

where $\mathbf{x_s}$ is the source location, $S(t)$ is the source time function and $\delta(\mathbf{x}-\mathbf{x_s})$ is the spatial δ-function. A common numerical approach for solving equation 3 exactly is finite differences (FD) (e.g., Graves, 1996). To describe 2D dislocation-type sources in a FD algorithm, Coutant et al. (1995) develop a formulation based on stress discontinuities.

2.2 Modeling examples

We carry out forward modeling for gradient computation in VTI media with moment-tensor sources using the elastic finite-difference code `sfewe` in MADAGASCAR . The model is described by the Thomsen parameters (Thomsen, 1986; Tsvankin, 2012) — the P- and S-wave vertical velocities V_{P0} and V_{S0} and the anisotropy coefficients ε, δ, and γ. In the case of P- and SV-waves propagating in the $[x_1,x_3]$-plane, the wavefield is not influenced by γ. An important combination of Thomsen parameters is the coefficient $\sigma \equiv (V_{P0}/V_{S0})^2(\varepsilon-\delta)$,

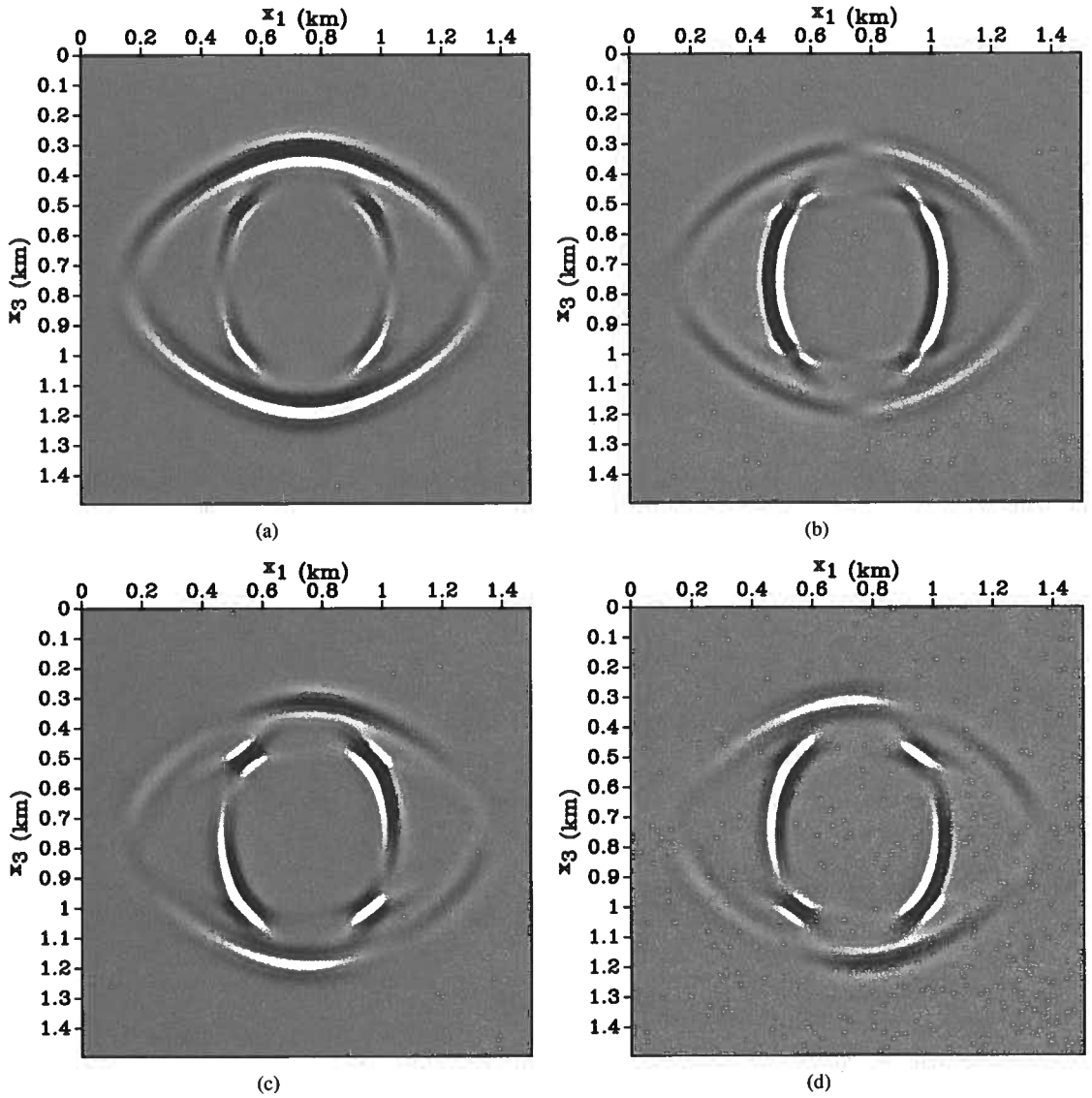

Figure 1. Vertical displacement generated by different moment-tensor sources in a homogeneous VTI medium. The medium parameters are $\rho = 2$ g/cm^3, $V_{P0} = 4047$ m/s, $V_{S0} = 2638$ m/s, $\varepsilon = 0.4$, and $\delta = 0$ ($\sigma = 0.94$). The source moment tensor is defined in the coordinate system rotated by the angle θ with respect to the horizontal (x_1) axis. The source parameters are: (a) $M_{11} = 4{\cdot}10^{10}$ Nm, $M_{13} = 0$, and $M_{33} = 4{\cdot}10^{10}$ Nm; (b) $M_{11} = 0$, $M_{13} = 4{\cdot}10^{10}$ Nm, $M_{33} = 0$, and $\theta = 0°$; (c) $M_{11} = 0$, $M_{13} = 4{\cdot}10^{10}$ Nm, $M_{33} = 0$, and $\theta = 45°$; and (d) $M_{11} = 0$, $M_{13} = 4{\cdot}10^{10}$ Nm, $M_{33} = 0$, and $\theta = 90°$.

which is largely responsible for the kinematic signatures of SV-waves in TI media.

The wavefields generated by explosive and dislocation-type sources in a homogeneous VTI medium are shown in Figure 1. The moment tensor is defined under the assumption that the medium around the source is locally isotropic. Due to the influence of anisotropy, a purely explosive source generates intensive S-waves in addition to P-waves (Figure 1 (a)). Figure 1 (b), (c), (d) display the wavefields excited by double-couple sources with different orientation (the corresponding rotation of the moment tensor is described in Appendix A). Rotation of the source causes pronounced changes in the radiation pattern of both P- and S-waves, which indicates the possibility of constraining the source orientation using FWI.

3 GRADIENTS FROM THE ADJOINT-STATE METHOD

3.1 Inverse problem

A mentioned above, the P- and SV-waves recorded in the $[x_1, x_3]$-plane depend on the components M_{11}, M_{13}, and M_{33} of the moment tensor. Originally, we invert just for these three

moment-tensor elements and the source coordinates x_1 and x_3 assuming that the velocity model and origin time are known.

The observed data $\mathbf{d}_{\text{obs}}$ and predicted data $\mathbf{d}_{\text{pre}}$ are produced by two forward simulations, where $\mathbf{d}_{\text{pre}}$ is obtained after modifying the source parameters used to generate $\mathbf{d}_{\text{obs}}$. In both cases, the elastic displacement field $\mathbf{u}(\mathbf{x}_s, \mathbf{x}_{r_n}, t)$ excited by a source located at $\mathbf{x}_s$ is recorded by N receivers located at $\mathbf{x}_{r_n}$ $(n = 1, 2, ..., N)$. Note that the source locations for the observed and predicted data may be different. The data residuals are measured by the least-squares objective function, which has to be minimized by the inversion algorithm:

$$\mathcal{F}(\mathbf{m}) = \frac{1}{2} \|\mathbf{d}_{\text{obs}} - \mathbf{d}_{\text{pre}}(\mathbf{m})\|^2 . \tag{4}$$

3.2 Application of the adjoint-state method

The objective function depends on the model parameters through the state variables, which represent the solution of the forward-modeling equations. In our case, the state variable is the elastic displacement field $\mathbf{u}(\mathbf{x}, t)$ generated by a microseismic source and governed by equation 3.

The conjugate-gradient method involves calculation of the model update at each iteration. The update direction is determined by the derivatives of the objective function with respect to the model parameters, $\partial \mathcal{F}(\mathbf{m})/\partial \mathbf{m}$. The adjoint-state method allows us to find this gradient for the entire set of model parameters in just two modeling simulations. However, because this method does not calculate the Fréchet derivatives, it is impossible to evaluate the sensitivity of the solution to measurement errors.

The adjoint-state method involves four main steps (Perrone and Sava, 2012):

(i) Computation of the state variable (forward wavefield).
(ii) Computation of the adjoint source.
(iii) Computation of the adjoint-state variable (adjoint wavefield).
(iv) Computation of the gradient of the objective function.

In addition to equation 3, the method requires solving the adjoint wave equation:

$$\rho \frac{\partial^2 u_i^\dagger}{\partial t^2} - c_{ijkl} \frac{\partial^2 u_k^\dagger}{\partial x_j \partial x_l} = \sum_{n=1}^{N} (\mathbf{d}_{\text{obs}} - \mathbf{d}_{\text{pre}})(T - t)\, \delta(\mathbf{x} - \mathbf{x}_{r_n}) , \tag{5}$$

where $\mathbf{u}^\dagger$ is called the adjoint wavefield. The so-called adjoint source on the right-hand side of equation 5 is obtained by differentiating the objective function $\mathcal{F}(\mathbf{m})$ with respect to the forward wavefield $\mathbf{u}$, and consists of the time-reversed data residuals. Therefore, the adjoint simulation can be carried out with the same modeling code by "injecting" the adjoint source at the receiver locations and then running the forward simulation.

The gradients of the objective function with respect to the moment-tensor elements and source coordinates can be found as (Kim et al., 2011):

$$\frac{\partial \mathcal{F}}{\partial M_{ij}} = \int_0^T \varepsilon_{ij}^\dagger(\mathbf{x}_s, t)\, S(T - t)\, \mathrm{d}t , \tag{6}$$

$$\frac{\partial \mathcal{F}}{\partial x_i} = \int_0^T \frac{\partial [\mathbf{M} : \boldsymbol{\varepsilon}^\dagger(\mathbf{x}_s, t)]}{\partial x_i} S(T - t)\, \mathrm{d}t , \tag{7}$$

where T is the recording time, $\boldsymbol{\varepsilon}^\dagger = \frac{1}{2}[\nabla \mathbf{u}^\dagger + (\nabla \mathbf{u}^\dagger)^{\mathrm{T}}]$ is defined as the adjoint stress tensor, and $\mathbf{M} : \boldsymbol{\varepsilon}^\dagger$ is the double inner product of the tensors $\mathbf{M}$ and $\boldsymbol{\varepsilon}^\dagger$. Equations 6 and 7 applied to the 2D problem yield the gradient vector $\mathbf{g}$ for the five source parameters:

$$\mathbf{g} = \left\{ \frac{\partial \mathcal{F}}{\partial M_{11}}, \frac{\partial \mathcal{F}}{\partial M_{13}}, \frac{\partial \mathcal{F}}{\partial M_{33}}, \frac{\partial \mathcal{F}}{\partial x_1}, \frac{\partial \mathcal{F}}{\partial x_3} \right\} . \tag{8}$$

It is interesting that in contrast to the gradients for velocity-related parameters (Liu and Tromp, 2006), which depend on the interaction between the forward and adjoint wavefields, equations 6 and 7 include only the adjoint wavefield. Therefore, there is no need to store the forward wavefield or to recalculate it during the adjoint simulation performed for computing the gradients.

In application of FWI to velocity analysis, the adjoint wavefield is supposed to "illuminate" the erroneous parts of the velocity model. Likewise, for the source-inversion problem, the adjoint wavefield should reveal the portion of the model that causes the differences between the observed and predicted data. The discrepancy, however, is attributed to errors in the source parameters. In principle, the number of sources in the adjoint problem is unrestricted. If the forward wavefield is excited by multiple sources, the adjoint wavefield may focus at each source location, and application of equations 6 and 7 is supposed to enhance the focusing.

4 NUMERICAL RESULTS

Next, we present the results of synthetic tests for a homogeneous VTI medium and a stack of three constant-density VTI layers, with the wavefield modeled using the FD code mentioned above.

In the first experiment (Figure 2), the observed and initial predicted data (Figures 3 and 4) are generated for a single microseismic event recorded in a vertical "borehole" by receivers located at each grid point. The large number of receivers helps to reduce artifacts due to the sparse receiver coverage. Whereas the observed field is generated by a double-couple source, the predicted field is computed with an explosive source. Next, the adjoint source "injected" at the receiver locations is used to compute the adjoint wavefield (Figure 5). This wavefield focuses at the time $t = 0.462$ s near the actual source, where the model perturbation is located. The focusing time corresponds to the raypath between the source and the receivers located at the end of the array.

After applying equations 6 and 7, we obtain the gradients for the five source parameters shown in Figure 6. As ex-

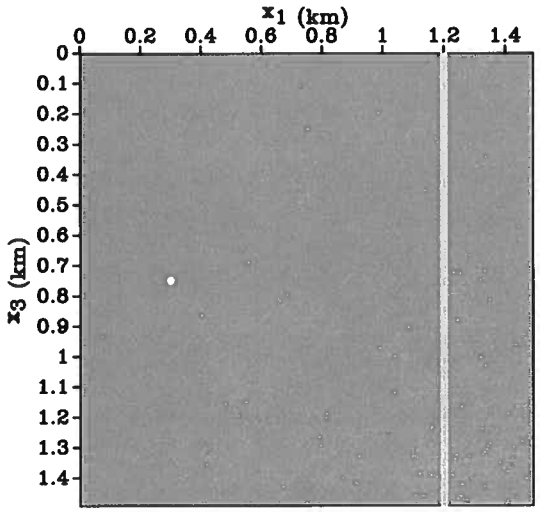

Figure 2. Source (white dot) and a vertical line of receivers at $x_1 = 1.2$ km embedded in a homogeneous VTI medium. The receivers are placed at each grid point (every 0.6 m). The medium parameters are $\rho = 2$ g/cm^3, $V_{P0} = 4047$ m/s, $V_{S0} = 2638$ m/s, $\varepsilon = 0.4$, and $\delta = 0$. The source is located at $x_1 = 0.3$ km, $x_3 = 0.75$ km.

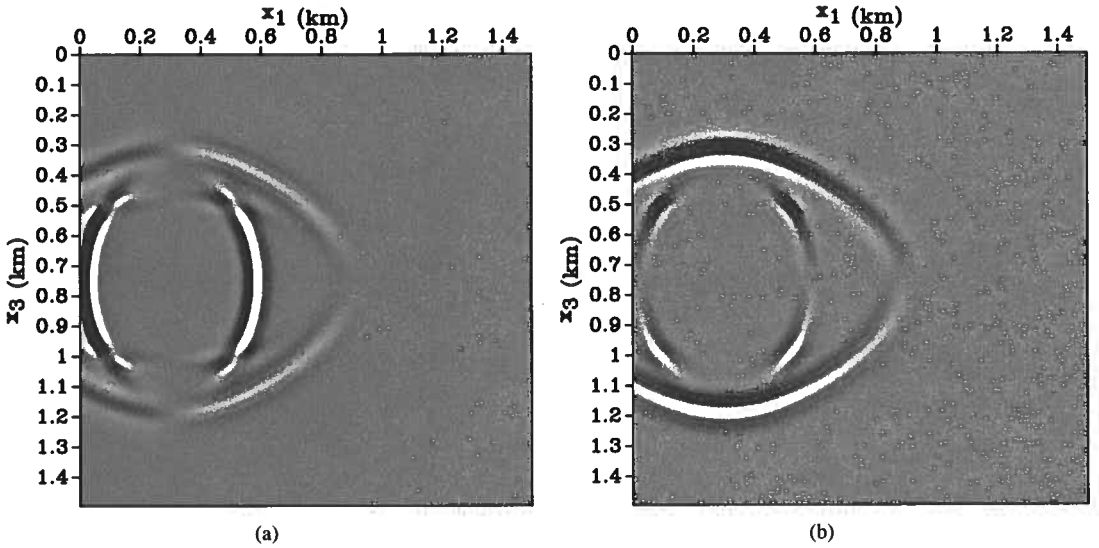

Figure 3. Snapshots of the vertical displacement for the model in Figure 2 at $t = 0.175$ s. (a) The observed wavefield produced by a double-couple source with $M_{11} = 0$, $M_{13} = 4{\cdot}10^{10}$ Nm, $M_{33} = 0$, and $\theta = 0°$. (b) The predicted wavefield from an explosive source with $M_{11} = 4{\cdot}10^{10}$ Nm, $M_{13} = 0$, and $M_{33} = 4{\cdot}10^{10}$ Nm.

pected, the major contribution to the gradients comes from the focusing of the adjoint wavefield near the source location. The additional anomalies are artifacts, likely due to the finite duration of the signal and limited number of sources and receivers (Fichtner et al., 2006). The significant magnitude of the gradients for x_1 and x_3 seems to be surprising because the locations of the observed and predicted sources coincide. However, the gradients for the source coordinates depend on the components of the moment tensor (equation 7), which produces the anomalies in Figure 6 (a), (b).

The second test is performed for the three-layer VTI model in Figure 7. The data are generated for a microseismic event occurring in the middle layer and recorded in a vertical "borehole". The gradients calculated using the forward and adjoint simulations are shown in Figure 8. As expected, layer boundaries create a number of reflected and mode-converted waves. However, the main contribution to the gradient still comes from the model perturbation at the source location.

For the third experiment, we keep the actual source at the same place as in the previous tests and use the homogeneous model from Figure 2. However, the initial predicted source is moved to a different location (Figure 9), which causes signifi-

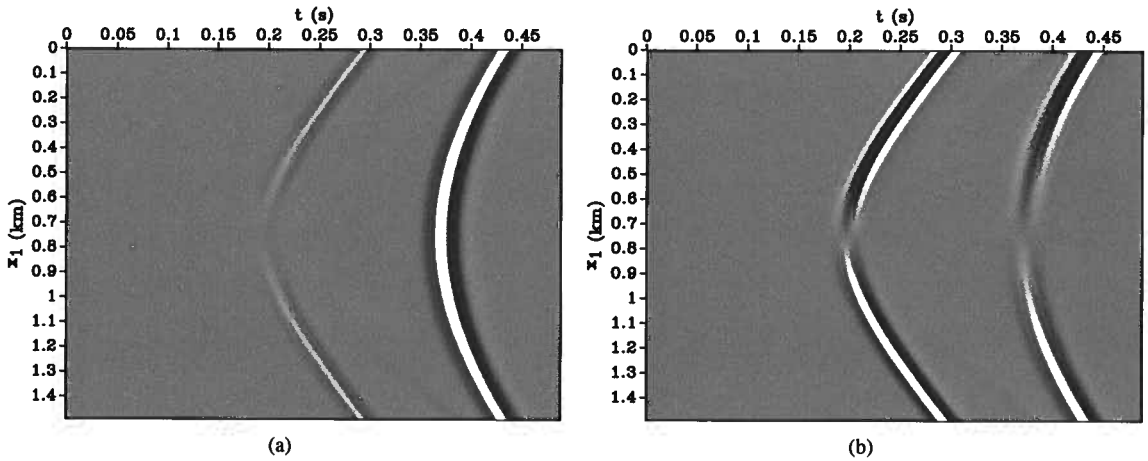

Figure 4. Vertical displacement of the (a) observed and (b) predicted data for the model in Figure 2 generated with the source parameters from Figure 3.

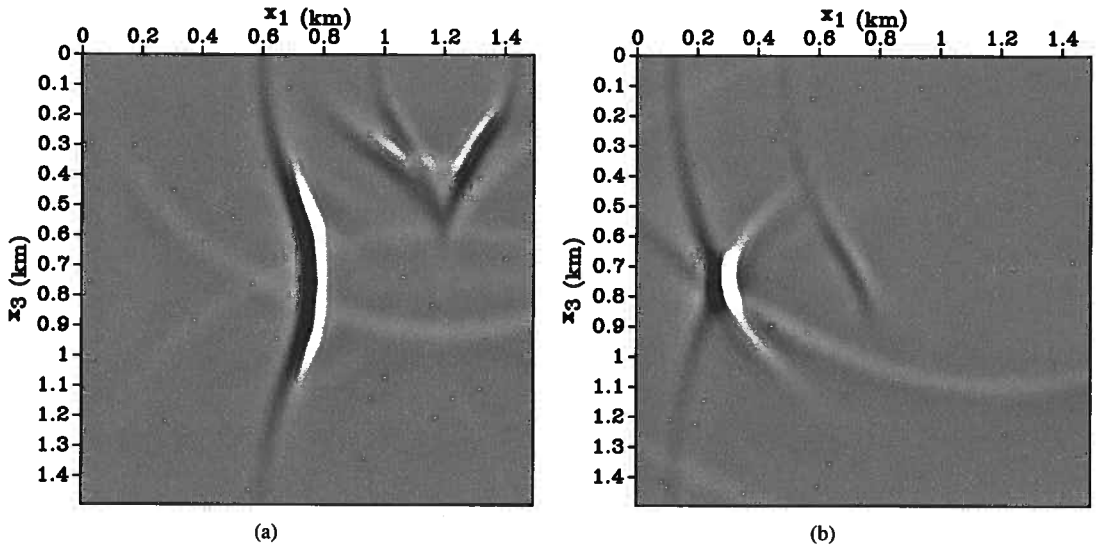

Figure 5. Snapshots of the vertical component of the adjoint wavefield for the model in Figure 2 at times (a) $t = 0.280$ s and (b) $t = 0.462$ s. The adjoint wavefield focuses at the actual source location on plot (b).

cant changes in the gradients (Figure 10). In particular, shifting the predicted source generates pronounced gradient contributions at both source locations. It is encouraging, however, that the largest gradients are observed near the predicted source. Although both sources have the same moment tensor, the gradients for M_{11}, M_{13}, and M_{13} do not vanish because the wavefield substantially changes with source location.

5 CONCLUSIONS

The adjoint-state method provides a computationally efficient way to calculate the gradients of the objective function. Here, we implemented adjoint-wavefield modeling and gradient computation of the FWI gradient for the source location and moment tensor using a known VTI velocity model.

Synthetic tests were carried out for a single source and a dense array of receivers in a vertical "borehole." The first experiment was performed for a trial source with a distorted moment tensor correctly positioned in a homogeneous VTI medium. The adjoint wavefield focuses near the source location, which identifies the perturbed area. Although the source position was not changed, the gradients for the source coordinates do not vanish because they depend on the moment-tensor elements. The gradients are contaminated by artifacts, which can be suppressed by adding receivers in another borehole or at the surface.

The second test was performed for a three-layer VTI

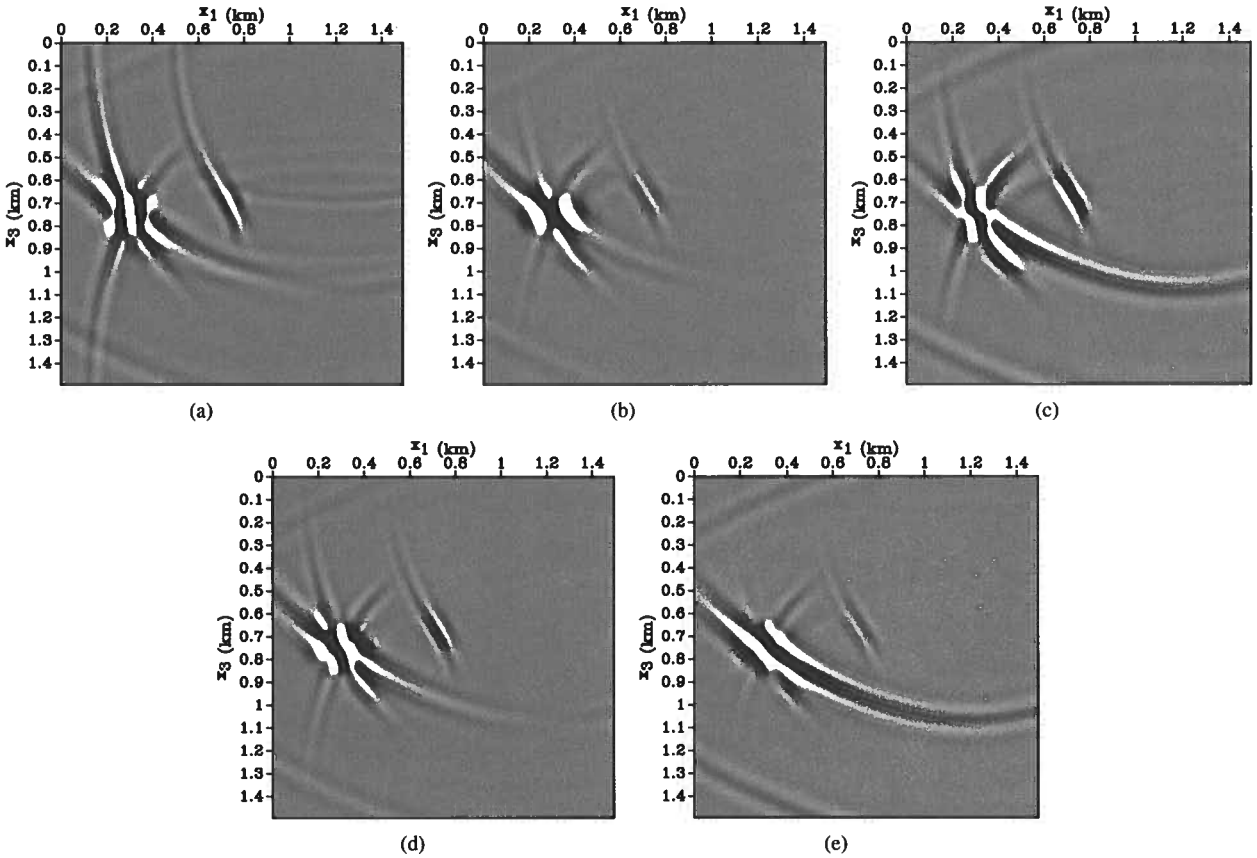

Figure 6. Gradients for the source parameters for the model in Figure 2: (a) M_{11}, (b) M_{13}, (c) M_{33}, (d) x_1, and (e) x_3.

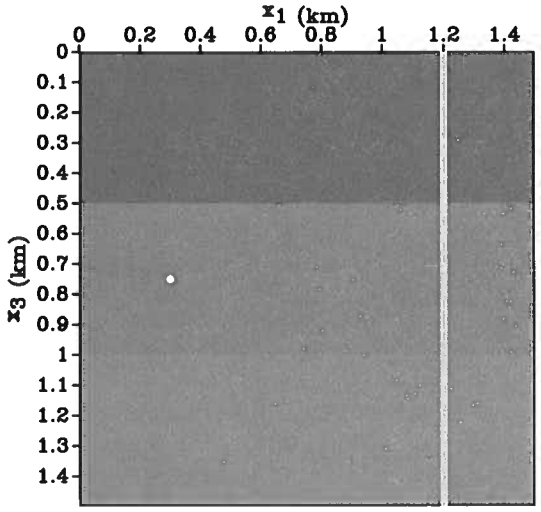

Figure 7. Three-layer VTI model used in the second experiment. The source-receiver geometry is the same as in Figure 2. The distance between receivers is 2.5 m. The parameters $\rho = 2$ kg/m^3, $\varepsilon = 0.4$, and $\delta = 0$ are the same in all three layers. The velocities in the first layer are $V_{P0} = 4047$ m/s and $V_{S0} = 2638$ m/s; for the second layer, $V_{P0} = 4169$ m/s and $V_{S0} = 2320$ m/s; for the third layer, $V_{P0} = 4693$ m/s and $V_{S0} = 2682$ m/s.

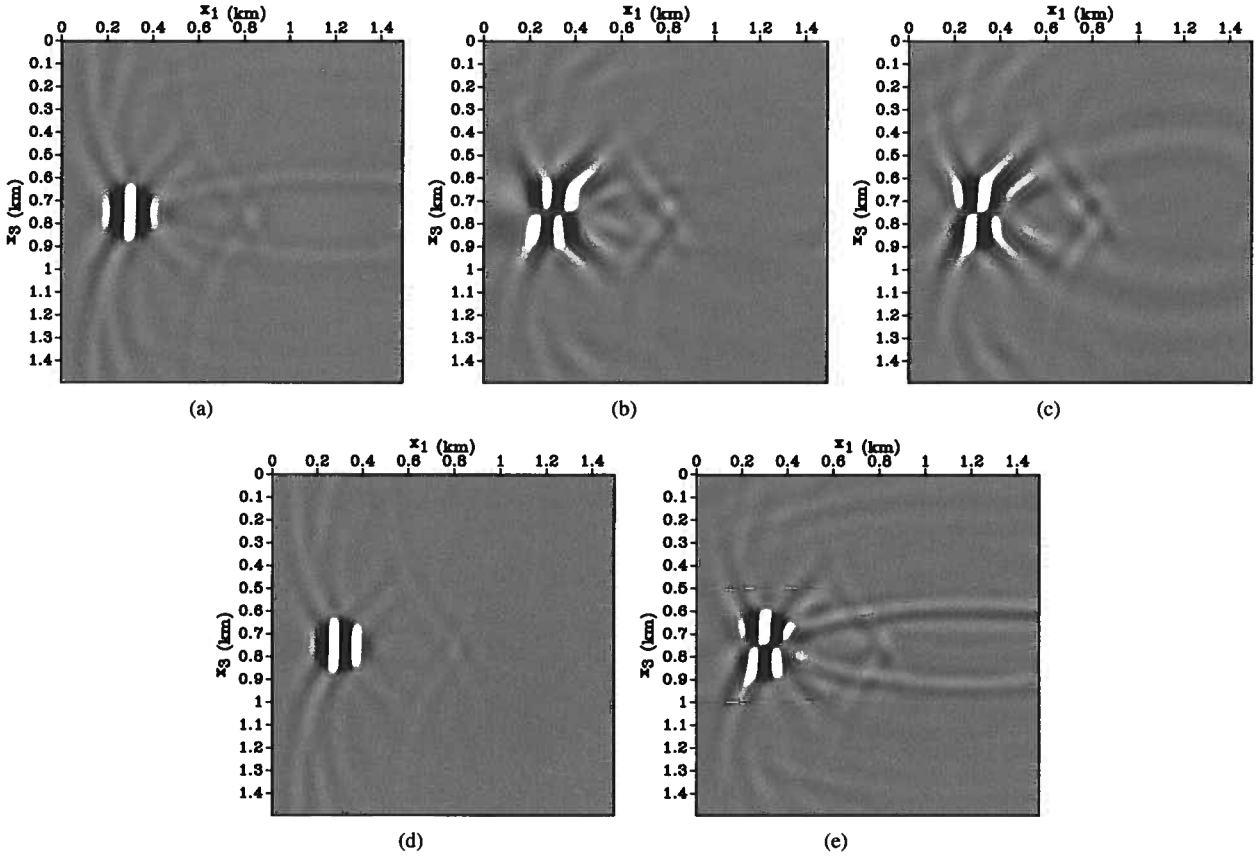

Figure 8. Gradients for the source parameters for the model in Figure 7: (a) M_{11}, (b) M_{13}, (c) M_{33}, (d) x_1, and (e) x_3.

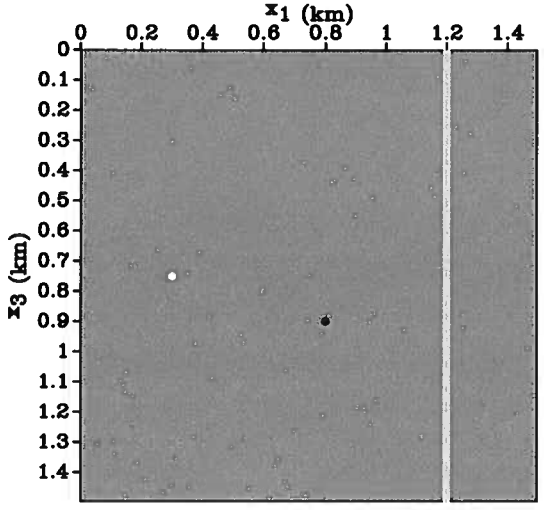

Figure 9. Actual source (white dot), predicted source (black dot) and a vertical line of receivers (spacing is 2.5 m) embedded in a homogeneous VTI medium. The medium parameters are the same as in Figure 2. The actual source is located at $x_1 = 0.3$ km, $x_3 = 0.75$ km and the predicted source is at $x_1 = 0.8$ km, $x_3 = 0.9$ km. The moment tensor for both sources corresponds to a horizontal ($\theta = 0$) double-couple with $M_{11} = 0$, $M_{13} = 4{\cdot}10^{10}$ Nm, and $M_{33} = 0$.

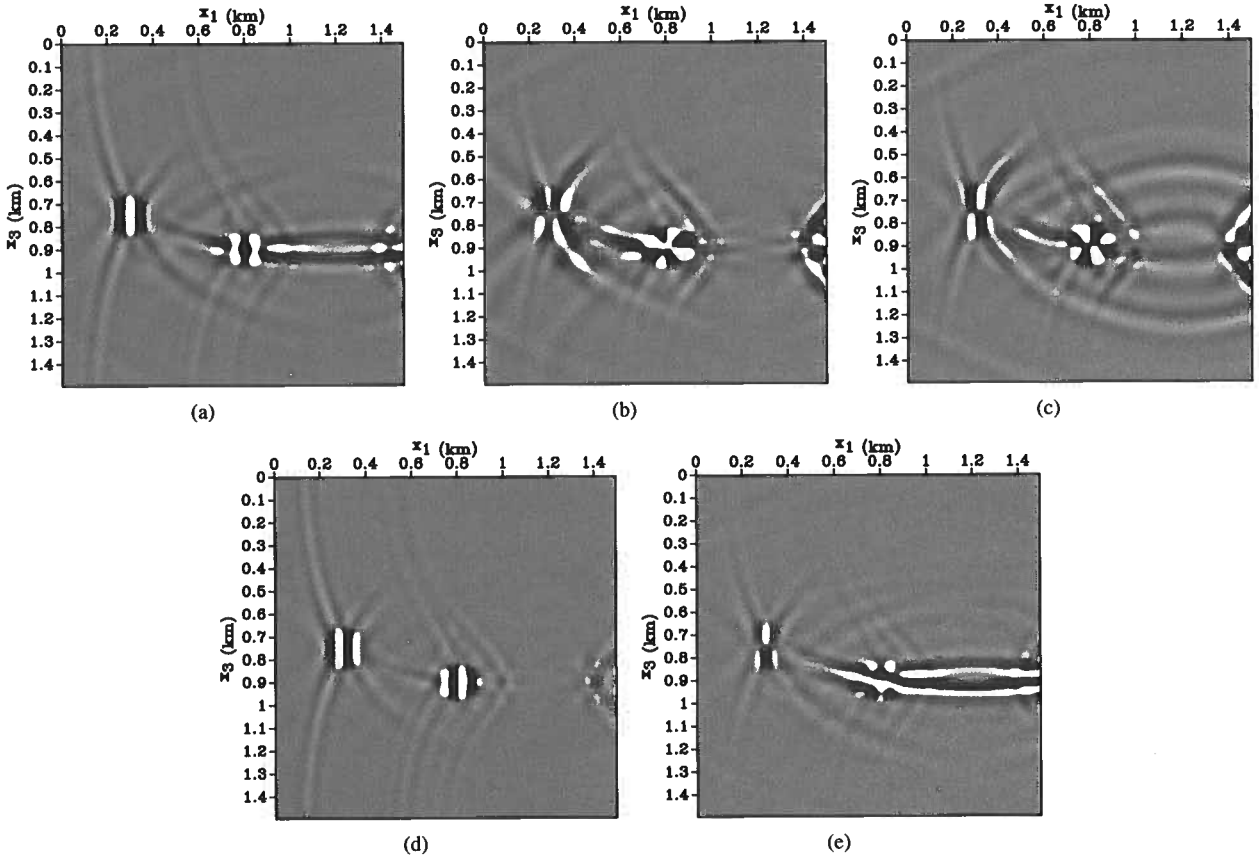

Figure 10. Gradients for the source parameters for the model in Figure 9: (a) M_{11}, (b) M_{13}, (c) M_{33}, (d) x_1, and (e) x_3.

model, which produces a number of reflected and converted waves. Although the gradients are more noisy, the anomaly at the source location is better focused due to the contribution of the additional events.

In the last test, the predicted wavefield was generated by a source with the correct moment tensor but erroneous location. The gradients for all source parameters, including the moment-tensor elements, exhibit pronounced anomalies, which are most intensive at the location of the trial source. These results indicate potential trade-offs between the source parameters in model updating using the conjugate-gradient method.

6 ACKNOWLEDGMENTS

We are grateful to Vladimir Grechka (Marathon Oil), who has generously provided valuable insights and feedback regarding various aspects of this work, and to Jeroen Tromp (Princeton University) for his advice on gradient calculation. We thank Esteban Díaz, Francesco Perrone, Nishant Kamath, and Steven Smith (all from CWP) for their technical assistance and help with the implementation of the adjoint problem. The numerical examples in this paper are produced with the MADAGASCAR open-source software package freely available at www.ahay.org. This work was supported by the Consortium Project on Seismic Inverse Methods for Complex Structures at the Center for Wave Phenomena (CWP).

APPENDIX A: 2D ROTATION OF THE MOMENT TENSOR

Dislocation-type events often occur along nonhorizontal fault planes. Here, we rotate the tensor **M** from the natural coordinate system associated with the fault to the $[x_1, x_3]$ coordinates.

The 2D rotation matrix **a** that produces a counterclockwise rotation is given by

$$\mathbf{a} = \begin{pmatrix} \cos\theta & -\sin\theta \\ \sin\theta & \cos\theta \end{pmatrix}. \tag{A1}$$

where θ is the angle between the x-axis in the natural coordinate system and the horizontal. The waves polarized in the $[x_1, x_3]$-plane are governed by the 2D moment tensor:

$$\mathbf{M} = \begin{pmatrix} M_{11} & M_{13} \\ M_{13} & M_{33} \end{pmatrix}. \tag{A2}$$

The moment tensor in the rotated coordinate system is then obtained as:

$$\mathbf{M}' = \mathbf{a}\mathbf{M}\mathbf{a}^{\mathrm{T}}, \tag{A3}$$

where $\mathbf{a}^{\mathrm{T}}$ is the transpose of $\mathbf{a}$. The explicit expressions for each element of the rotated moment tensor are:

$$M'_{11} = M_{11}\cos^2\theta - 2M_{13}\sin\theta\cos\theta + M_{33}\sin^2\theta, \tag{A4}$$

$$M'_{13} = M_{11}\sin\theta\cos\theta + M_{13}(\cos^2\theta - \sin^2\theta) - M_{33}\sin\theta\cos\theta, \tag{A5}$$

$$M'_{33} = M_{11}\sin^2\theta + 2M_{13}\sin\theta\cos\theta + M_{33}\cos^2\theta. \tag{A6}$$

Here, this rotation is used to obtain the predicted data for dislocation-type sources with different orientations.

REFERENCES

Aki, K., and P. G. Richards, 1980, Quantitative seismology theory and methods, volume I: W. H. Freeman and Company.

Coutant, O., J. Virieux, and A. Zollo, 1995, Numerical source implementation in a 2D finite difference scheme for wave propagation: Bulletin of the Seismological Society of America, **85**, 1507–1512.

Dahlen, F. A., and J. Tromp, 1998, Theoretical global seismology: Princeton University Press.

Fichtner, A., 2009, Full seismic waveform inversion for structural and source parameters: PhD thesis, Ludwig-Maximilians-Universität München.

Fichtner, A., H.-P. Bunge, and H. Igel, 2006, The adjoint method in seismology: I. Theory: Physics of the Earth and Planetary Interiors, **157**, 86–104.

Gauthier, O., J. Virieux, and A. Tarantola, 1986, Two-dimensional nonlinear inversion of seismic waveforms: Numerical results: Geophysics, **51**, 1387–1403.

Graves, R. W., 1996, Simulating seismic wave propagation in 3D elastic media using staggered-grid finite differences: Bulletin of the Seismological Society of America, **86**, 1091–1106.

Grechka, V., and A. Duchkov, 2011, Narrow-angle representations of the phase and group velocities and their applications in anisotropic velocity-model building for microseismic monitoring: Geophysics, **76**, WC127–WC142.

Grechka, V., P. Singh, and I. Das, 2011, Estimation of effective anisotropy simultaneously with locations of microseismic events: Geophysics, **76**, WC143–WC155.

Kamath, N., and I. Tsvankin, 2013, Full-waveform inversion of multicomponent data for horizontally layered VTI media: Geophysics.

Kendall, M., S. Maxwell, G. Foulger, L. Eisner, and Z. Lawrence, 2011, Microseismicity: Beyond dots in a box Introduction: Geophysics, **76**, WC1–WC3.

Kim, Y., Q. Liu, and J. Tromp, 2011, Adjoint centroid-moment tensor inversions: Geophysical Journal International, **186**, 264–278.

Köhn, D., 2011, Time domain 2D elastic full waveform tomography: PhD thesis, Christian-Albrechts-Universität zu Kiel.

Lee, H.-Y., J. M. Koo, D.-J. Min, B.-D. Kwon, and H. S. Yoo, 2010, Frequency-domain elastic full waveform inversion for VTI media: Geophysical Journal International, **183**, 884–904.

Liu, Q., and J. Tromp, 2006, Finite-frequency kernels based on adjoint methods: Bulletin of the Seismological Society of America, **96**, 2383–2397.

Maxwell, S., 2010, Microseismic: Growth born from success: The Leading Edge, **29**, 338–343.

Mora, P., 1987, Nonlinear two-dimensional elastic inversion of multioffset seismic data: Geophysics, **52**, 1211–1228.

Morency, C., and R. J. Mellors, 2012, Full moment tensor and source location inversion based on full waveform adjoint inversion: application at the Geysers geothermal field: SEG Technical Program Expanded Abstracts, 532, 1–5.

Perrone, F., and P. Sava, 2012, Wavefield tomography based on local image correlations: CWP Project Review Report, 51–76.

Plessix, R.-E., 2006, A review of the adjoint-state method for computing the gradient of a functional with geophysical applications: Geophysical Journal International, **167**, 495–503.

Pratt, R., 1999, Seismic waveform inversion in the frequency domain, Part 1: Theory and verification in a physical scale model: Geophysics, **64**, 888–901.

Tarantola, A., 1984, Inversion of seismic reflection data in the acoustic approximation: Geophysics, **49**, 1259–1266.

Thomsen, L., 1986, Weak elastic anisotropy: Geophysics, **51**, 1954–1966.

Tromp, J., C. Tape, and Q. Liu, 2005, Seismic tomography, adjoint methods, time reversal and banana-doughnut kernels: Geophysical Journal International, **160**, 195–216.

Tsvankin, I., 2012, Seismic signatures and analysis of reflection data in anisotropic media, third edition: Society of Exploration Geophysicists.

Tsvankin, I., and V. Grechka, 2011, Seismology of azimuthally anisotropic media and seismic fracture characterization: Society of Exploration Geophysicists.

Van Dok, R., B. Fuller, L. Engelbrecht, and M. Sterling, 2011, Seismic anisotropy in microseismic event location analysis: The Leading Edge, **30**, 766–770.

Vavryčuk, V., 2007, On the retrieval of moment tensors from borehole data: Geophysical Prospecting, **55**, 381 – 391.

Virieux, J., and S. Operto, 2009, An overview of full-waveform inversion in exploration geophysics: Geophysics, **74**, WCC1–WCC26.

Multiparameter TTI tomography: Application to synthetic and field data

Xiaoxiang Wang[1,2] & Ilya Tsvankin[2]
(1) Shell Exploration & Production Company, New Orleans, LA 70139
(2) Center for Wave Phenomena, Colorado School of Mines, Golden, Colorado 80401

ABSTRACT

Transversely isotropic models with a tilted symmetry axis (TTI media) are widely used in depth imaging of complex geologic structures. Here, we present a modification of a previously developed 2D P-wave tomographic algorithm for estimating heterogeneous TTI velocity fields and apply it to synthetic and field data. The symmetry-direction velocity V_{P0}, anisotropy parameters ϵ and δ, and symmetry-axis tilt ν are defined on a rectangular grid. To ensure stable reconstruction of the TTI parameters, reflection data are combined with walkaway VSP (vertical seismic profiling) traveltimes in joint tomographic inversion. To improve the convergence of the algorithm, we propose a three-stage model-updating procedure that gradually relaxes the constraints on the spatial variations of the anisotropy parameters, while the symmetry axis is kept orthogonal to the reflectors. Only at the final stage of the inversion the parameters V_{P0}, ϵ, and δ are updated on the same grid. We also incorporate geologic constraints into tomography by designing regularization terms that penalize parameter variations in the direction parallel to the interfaces. First, we examine the performance of the regularized joint tomography of reflection and VSP data for two sections of the BP TTI model that contain an anticline and a salt dome. All three TTI parameters in the shallow part of both sections (down to 5 km) are well-resolved by the proposed model-updating process. Then the algorithm is applied to a 2D section from 3D OBS (ocean bottom seismic) data acquired at Volve field in the North Sea. The inverted TTI model produces well-focused reflectors throughout the section and accurately positions the key horizons, which is confirmed by the available well markers.

Key words: reflection tomography, inversion, P-waves, prestack migration, velocity analysis, borehole data, transverse isotropy, TTI, case study

1 INTRODUCTION

Prestack depth imaging for complex geologic environments (including subsalt plays and fold-and-thrust belts) requires anisotropic velocity models such as transverse isotropy with a vertical (VTI) or tilted (TTI) axis of symmetry.* A stable velocity-analysis tool for prestack migration is reflection tomography in the migrated domain (Stork, 1992), which has been extended to heterogeneous TI media (Campbell et al., 2006; Woodward et al., 2008). A review of published migration velocity analysis (MVA) algorithms for TTI media can be found in our previous paper (Wang and Tsvankin, 2013; hereafter, referred to as Paper I).

P-wave velocity in TTI media is controlled by the velocity V_{P0} in the symmetry-axis direction, anisotropy parameters ϵ and δ, and the orientation of the symmetry axis (in 2D defined by the tilt ν from the vertical). Most current parameter-estimation techniques either rely on relatively simple model representation (e.g., layer- or block-based models employed by Behera and Tsvankin, 2009) or simplify the inversion by keeping the anisotropy parameters ϵ and δ fixed and updating only the symmetry-direction velocity V_{P0} on a grid (Huang et al., 2008, Charles et al., 2008). Because P-wave reflection traveltimes do not provide sufficient constraints for resolving all relevant TTI parameters, it is necessary to use additional information to reduce the nonuniqueness of the inverse problem (Morice et al., 2004, Tsvankin,

*This paper, which will be published in *Geophysics*, includes some material from the 2012 Project Review report by the authors.

2005, Bakulin et al., 2010b). However, there are few publications on such joint inversion of P-wave reflections and other data (e.g., VSP traveltimes) for anisotropic media.

Nonuniqueness of the inversion of reflection data can also be mitigated by regularization, which imposes a priori constraints on the estimated model (Engl et al., 1996). In Paper I, we employ Tikhonov (1963) regularization to smooth the velocity field with equal weights in the horizontal and vertical directions. Fomel (2007) develops so-called "shaping regularization" designed to steer velocity variations along geologic structures (e.g., layers). His mapping (shaping) operator is integrated into a conjugate-gradient iterative solver. Using the steering-filter preconditioner (Clapp et al., 2004) similar to shaping regularization, Bakulin et al. (2010c) perform joint tomographic inversion of horizontal and dipping P-wave reflection events and check-shot traveltimes for VTI media. They conclude that in the vicinity of the well it is possible to resolve the vertical variation of all three relevant parameters (V_{P0}, ϵ, and δ). In a case study, Bakulin et al. (2010a) compare several techniques for building VTI and TTI models using borehole-calibrated profiles of anisotropy parameters. They find that the TTI velocity field obtained by interpolation that conforms to several key horizons produces the smallest well misties and minimizes residual moveout in common-image gathers (CIGs).

In Paper I, we develop a 2D ray-based tomographic algorithm for iteratively updating the parameters V_{P0}, ϵ, and δ of TTI media defined on rectangular grids (the symmetry axis is set orthogonal to the imaged reflectors). Synthetic tests for models with a "quasi-factorized" TTI syncline (i.e., ϵ and δ are constant inside the TTI layer, while the tilt ν may vary spatially) and a TTI thrust sheet demonstrate that stable parameter estimation requires strong smoothness constraints or additional information from walkaway VSP traveltimes.

Here, we first introduce the objective function that includes the residual moveout in CIGs and the VSP traveltime misfit supplemented by regularization terms. The regularization is designed to smooth the parameters in the direction parallel to the interfaces, while allowing for more pronounced variations in the orthogonal direction. Next, we present a three-stage inversion methodology in which gridded tomography is preceded by two partial parameter-updating steps designed to stabilize the inversion. Then the tomographic algorithm is tested on two sections of the 2D TTI model devised by BP and a line from 3D OBS (ocean bottom seismic) data provided by Statoil.

2 METHODOLOGY

Basic elements of the tomographic algorithm employed here are described in Paper I. The residual moveout in common-image gathers produced by prestack Kirchhoff depth migration is minimized during iterative parameter updates. If walkaway VSP surveys (check shots represent zero-offset VSP data) are available, VSP traveltimes are computed for each trial model and included in the following objective function F:

$$F(\Delta\boldsymbol{\lambda}) = \|\boldsymbol{A}\,\Delta\boldsymbol{\lambda}-\boldsymbol{b}\|^2+\zeta_{\mathrm{VSP}}^2\|\boldsymbol{E}\,\Delta\boldsymbol{\lambda}-\boldsymbol{d}\|^2+R(\Delta\boldsymbol{\lambda})\,, \quad (1)$$

where $\Delta\boldsymbol{\lambda}$ is a vector composed of the parameter updates (ΔV_{P0}, $\Delta\epsilon$, and $\Delta\delta$) at each grid point, the elements of the matrix $\boldsymbol{A}$ are the traveltime derivatives with respect to the medium parameters at each grid point ($\boldsymbol{A}$ is computed analytically along the raypaths), $\boldsymbol{b}$ is a vector containing the residual moveout in CIGs, the matrix $\boldsymbol{E}$ includes VSP traveltime derivatives, and the vector $\boldsymbol{d}$ is the difference between the observed and calculated VSP traveltimes for each source-receiver pair. The regularization term R in equation 1 has the form:

$$R(\Delta\boldsymbol{\lambda}) = \zeta^2\|\Delta\boldsymbol{\lambda}\|^2+\zeta_1^2\|\boldsymbol{L}_1(\Delta\boldsymbol{\lambda}+\boldsymbol{\lambda}^0)\|^2 + \zeta_2^2\|\boldsymbol{L}_2(\Delta\boldsymbol{\lambda}+\boldsymbol{\lambda}^0)\|^2\,, \quad (2)$$

where $\zeta^2\|\Delta\boldsymbol{\lambda}\|^2$ restricts the magnitudes of parameter updates that have small derivatives in the matrices $\boldsymbol{A}$ and $\boldsymbol{E}$, $\boldsymbol{\lambda}^0$ is the vector of model parameters obtained in the previous iteration, the operators $\boldsymbol{L}_1$ and $\boldsymbol{L}_2$ are designed to make parameter variations more pronounced in the direction normal to the interfaces, and ζ, ζ_1, and ζ_2 are the regularization coefficients/weights. The choice of the weighting coefficients depends on the data volume, number of grid points, and desired strength of regularization. In 2D, the normal direction of a reflector is defined by the dip angle with the vertical, which is computed from the depth image using Madagascar program "sfdip." Then the symmetry-axis tilt ν at each grid point is set to be equal to the corresponding dip.

To construct the matrix $\boldsymbol{L}_1$, we first compute two components of the gradient $\nabla\lambda$ from a finite-difference approximation:

$$\lambda'(x) = \frac{\lambda(x+\mathrm{d}x)-\lambda(x-\mathrm{d}x)}{2\mathrm{d}x}+O[(\mathrm{d}x)^2]\,, \quad (3)$$

$$\lambda'(z) = \frac{\lambda(z+\mathrm{d}z)-\lambda(z-\mathrm{d}z)}{2\mathrm{d}z}+O[(\mathrm{d}z)^2]\,, \quad (4)$$

where λ is the parameter (V_{P0}, ϵ, or δ) at the grid point with the coordinates x and z, and $\mathrm{d}x$ and $\mathrm{d}z$ are the cell dimensions. Since the dip field yields the vector $\boldsymbol{n}$ orthogonal to reflectors, we minimize the norm of the cross-product $\|\boldsymbol{n}\times\nabla\lambda\|$ at all grid points, which is equivalent to aligning the direction of the largest parameter variation with $\boldsymbol{n}$ and restricting the variations along interfaces. More cells can be included by using a higher-order finite-difference approximation:

$$\lambda'(x) = [-\lambda(x+2\mathrm{d}x)+8\lambda(x+\mathrm{d}x)-8\lambda(x-\mathrm{d}x) + \lambda(x-2\mathrm{d}x)]/(12\mathrm{d}x)+O[(\mathrm{d}x)^4]\,, \quad (5)$$

$$\lambda'(z) = [-\lambda(z+2\mathrm{d}z)+8\lambda(z+\mathrm{d}z)-8\lambda(z-\mathrm{d}z) + \lambda(z-2\mathrm{d}z)]/(12\mathrm{d}z)+O[(\mathrm{d}z)^4]\,. \quad (6)$$

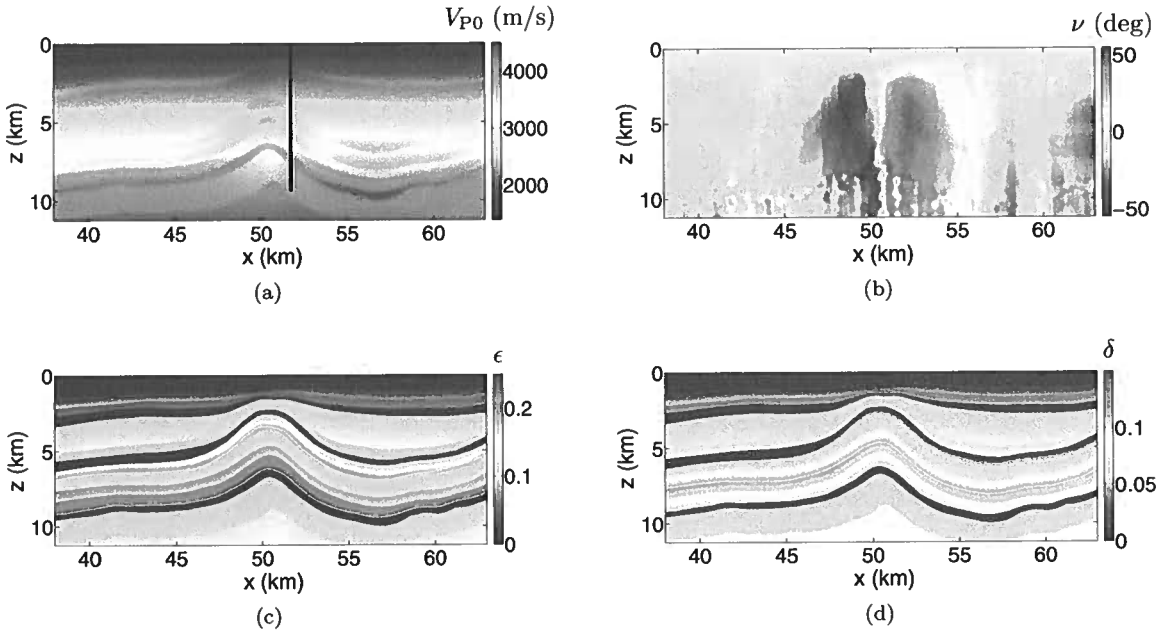

Figure 1. Section of the BP TTI model that includes an anticline (the grid size is 6.25 m × 6.25 m). The top water layer is isotropic with velocity 1492 m/s. (a) The symmetry-direction velocity V_{P0}. The black line marks a vertical "well" at $x = 51.4$ km. (b) The symmetry-axis tilt ν. The anisotropy parameters (c) ϵ and (d) δ.

Similarly, the operator $\boldsymbol{L}_2$ is built from the cross-product of $\boldsymbol{n}$ and the following two-component vector formed by second-order derivatives:

$$\lambda''(x) = \frac{\lambda(x+\mathrm{d}x) - 2\lambda(x) + \lambda(x-\mathrm{d}x)}{(\mathrm{d}x)^2}, \quad (7)$$

$$\lambda''(z) = \frac{\lambda(z+\mathrm{d}z) - 2\lambda(z) + \lambda(z-\mathrm{d}z)}{(\mathrm{d}z)^2}. \quad (8)$$

Then we minimize the norm of the cross-product to smooth the parameter variations in the direction parallel to the interfaces.

Defining the TTI parameters on a relatively small grid results in a large number of unknowns, and the Fréchet matrices $\boldsymbol{A}$ and $\boldsymbol{E}$ in equation 1 are sparse (i.e., only nonzero or relatively large elements are stored due to the limited computer memory). To solve such a large sparse linear system of equations in an efficient way, we employ a parallel direct sparse solver (PARDISO, Naumann and Schenk, 2011).

The anisotropic velocity field is iteratively updated starting from an initial model that may be obtained from stacking-velocity tomography at borehole locations (Wang and Tsvankin, 2010). In the first few iterations, the symmetry-direction velocity V_{P0} is typically inaccurate and simultaneous inversion for all TTI parameters may result in unacceptably large updates for ϵ and δ. If the anisotropy parameters are moderate (in the test below, $\epsilon < 0.25$ and $\delta < 0.15$), it is convenient to fix them temporarily at the initial values (typically small) and limit the updates to the velocity V_{P0}. When iterations no longer significantly reduce the data misfit, we move on to the second stage of parameter updating. At that stage, the model is divided into several layers based on the picked reflectors, and the anisotropy parameters are assumed to be spatially invariant within each layer. The velocity V_{P0} is then updated on a grid, while the inversion for ϵ and δ is layer-based. Such a "quasi-factorized" assumption is equivalent to strong smoothing of ϵ and δ and may help resolve all TTI parameters if V_{P0} is a linear function of the spatial coordinates and at least two distinct dips are available (Behera and Tsvankin, 2009). At the third and last stage of velocity analysis, the anisotropy parameters are updated on the same grid as that for V_{P0} to allow for more realistic treatment of heterogeneity. Still, because P-wave kinematics are less sensitive to anisotropy than to the symmetry-direction velocity, the ϵ- and δ-fields in equation 2 are typically regularized with larger weights.

3 BP ANTICLINE MODEL

First, we test the joint tomography of P-wave long-spread reflection data and walkaway VSP traveltimes on a section of the TTI model produced by BP. That section contains an anticline structure surrounded by gently dipping anisotropic layers. The velocity V_{P0} in the actual model is smoothly varying (Figure 1(a)), except for a small jump at the water bottom. The symmetry axis is set perpendicular to the interfaces (Fig-

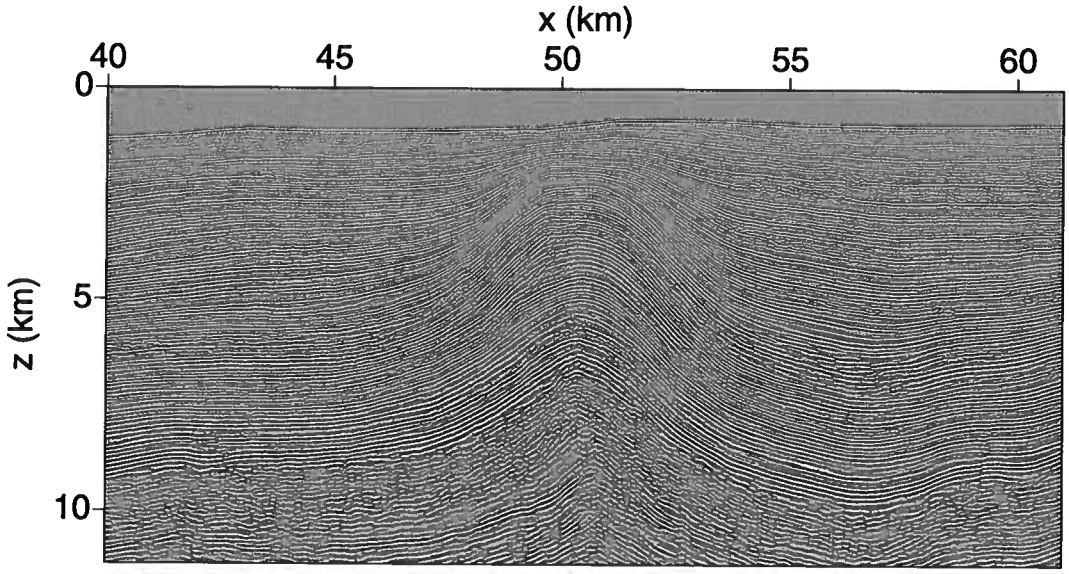

Figure 2. Depth image of the BP anticline model produced with the actual parameters from Figure 1.

ure 1(b)), and the anisotropy parameters ϵ and δ change from layer to layer. Note that the lateral variations of ϵ and δ are relatively weak compared to those of V_{P0} (Figure 1(c) and 1(d)). The depth image produced by Kirchhoff prestack depth migration with the actual velocity model is shown in Figure 2.

The tomographic algorithm is applied to CIGs from $x = 40$ km to 61 km with an interval of 150 m (the maximum offset is 10 km). Synthetic VSP data were generated by BP in a vertical "well" placed at location $x_{VSP} = 51.4$ km with 24 receivers spanning the interval from $z = 4756.25$ m to 5043.75 m every 12.5 m and 24 more receivers evenly placed between 7837.5 m and 8125 m. The VSP sources were located at the surface every 50 m from $x = 41.4$ km to 61.4 km (the maximum offset is also 10 km). In addition, check-shot traveltimes were recorded every 50 m from $z = 943.5$ m to 9493.75 m.

To build an initial model, we compute a 1D profile of V_{P0} from the check-shot traveltimes and then obtain the 2D velocity field (Figure 3(a)) by extrapolation that conforms to the picked interfaces. The initial model is isotropic, with both ϵ and δ set to zero. The exact position of the water bottom is assumed to be known, and the velocity of the water layer is fixed at the correct value. The noticeable residual moveout in the CIGs (Figure 3(b)) indicate that the velocity field contains significant errors.

Velocity analysis is performed using the three-stage parameter-estimation procedure described above, which operates with reflection and VSP data. First, we update only the velocity V_{P0} defined on a rectangular 200 m × 100 m grid, while keeping the model isotropic (i.e., $\epsilon = \delta = 0$). Then ϵ and δ are taken constant in each layer (delineated by the interfaces picked on the image) and updated simultaneously with V_{P0}. With this "quasi-factorized" TTI assumption, the inverted model (Figure 4) reduces the residual moveout in CIGs (Figure 5) and the VSP traveltime misfit.

However, the residual moveout in Figure 5 is not completely removed, mainly because the assumption about the anisotropy parameters does not conform to the actual ϵ- and δ- fields (Figures 1(c) and 1(d)). To allow for more realistic spatial variations, at the last stage of parameter updating we estimate the parameters ϵ and δ on the same grid as the one used for the velocity V_{P0}. However, because the trade-offs between the parameters may cause large errors in ϵ and δ defined on fine grids, the anisotropy parameters should be more tightly constrained, so the corresponding regularization coefficients are larger than those for V_{P0}.

After application of the joint tomography, the velocity V_{P0} above $z = 7$ km is relatively well-recovered with percentage errors in most areas smaller than 4% (Figure 6(a)). The spatial variations of ϵ and δ are partially resolved from the water bottom down to $z = 5$ km (Figure 6(c) and 6(d)). The coverage of VSP rays, however, becomes more sparse with depth. Also, the offset-to-depth ratio of P-wave reflections is insufficient to constrain the parameter ϵ below 7 km, although the maxi-

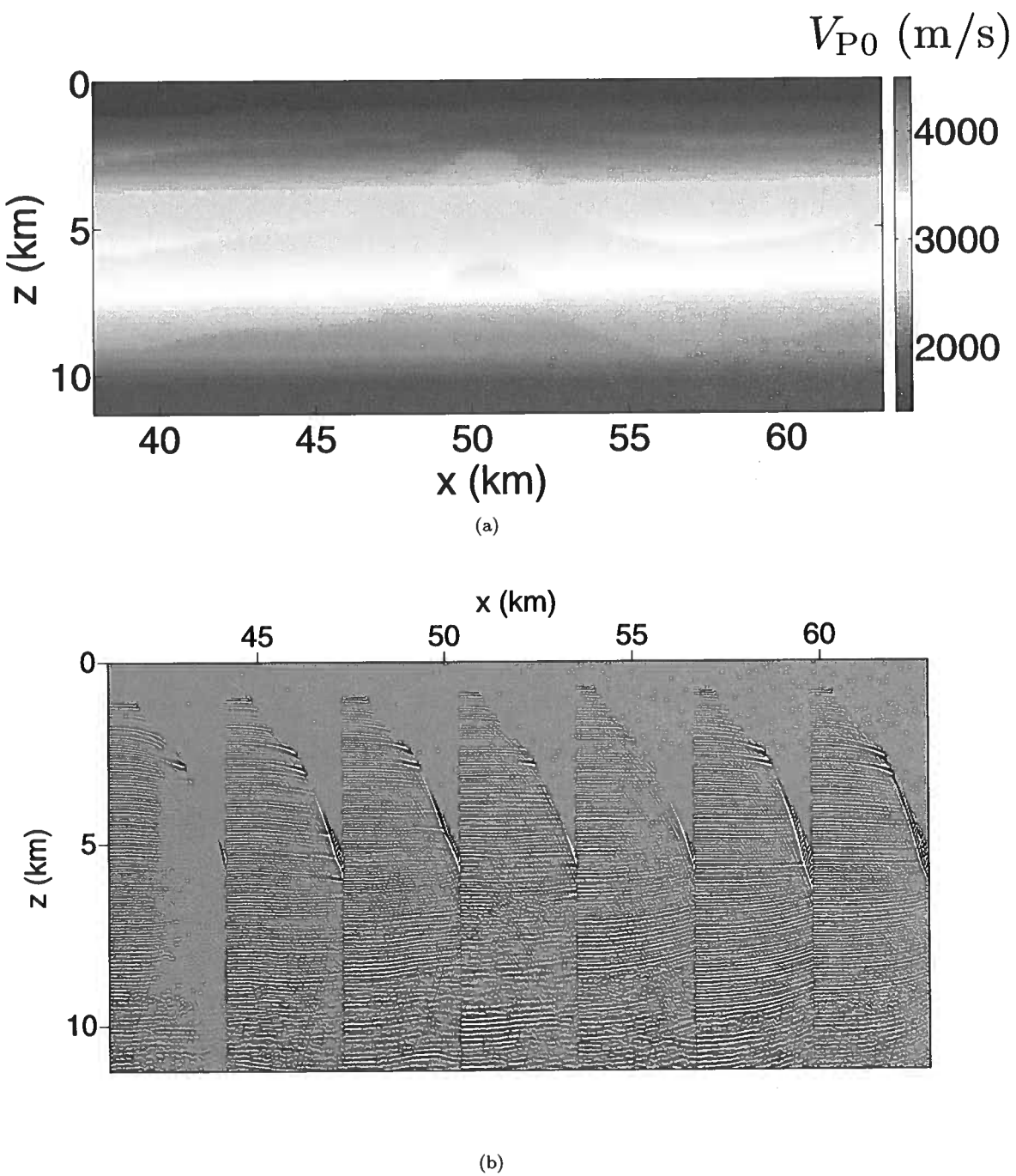

Figure 3. (a) Initial isotropic model with the velocity V_{P0} defined on a 200 m × 100 m grid. The velocity in the water is set to the correct value. (b) CIGs (displayed every 3 km from 41 km to 62 km) computed with the initial model from Figure 3(a).

mum offset reaches 10 km. Therefore, the accuracy in ϵ and δ decreases in the deep part of the section. Still, the final inverted model (Figure 6) practically removes the residual moveout in the CIGs (Figure 7(a), except for locations close to the left and right edges due to poor ray coverage), and the reflections are well focused (Figure 7(b)), especially those above $z = 7$ km. Comparison with several interfaces imaged using the actual model (Figure 2) shows that the reflectors are accurately positioned in depth, with the misties smaller than 40 m near the well.

An important parameter that influences the ac-

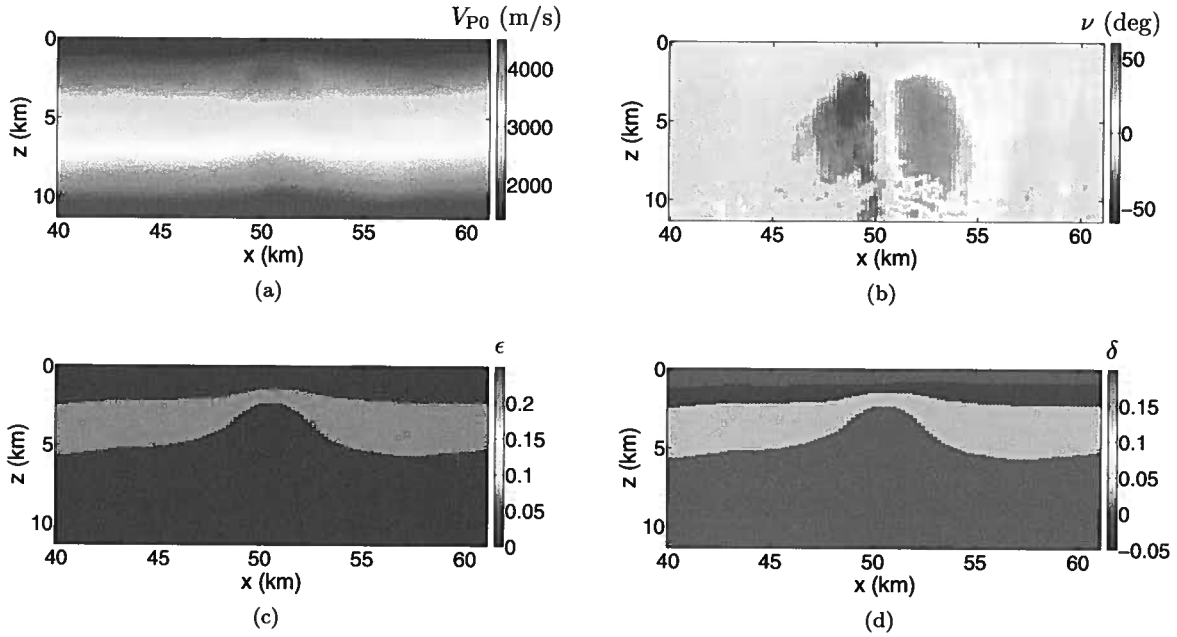

Figure 4. Anticline model from Figure 1 updated using the "quasi-factorized" TTI assumption. (a) The symmetry-direction velocity V_{P0} estimated on a 200 m × 100 m grid. (b) The tilt ν obtained by setting the symmetry axis perpendicular to the reflectors. The inverted interval parameters (c) ϵ and (d) δ, which are kept constant within each layer.

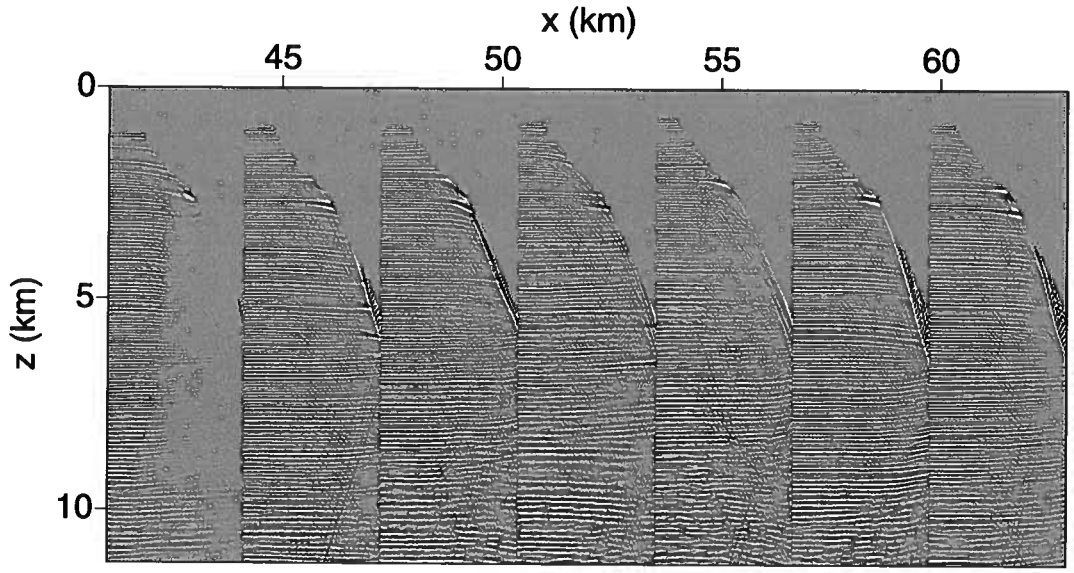

Figure 5. CIGs obtained with the "quasi-factorized" TTI model from Figure 4.

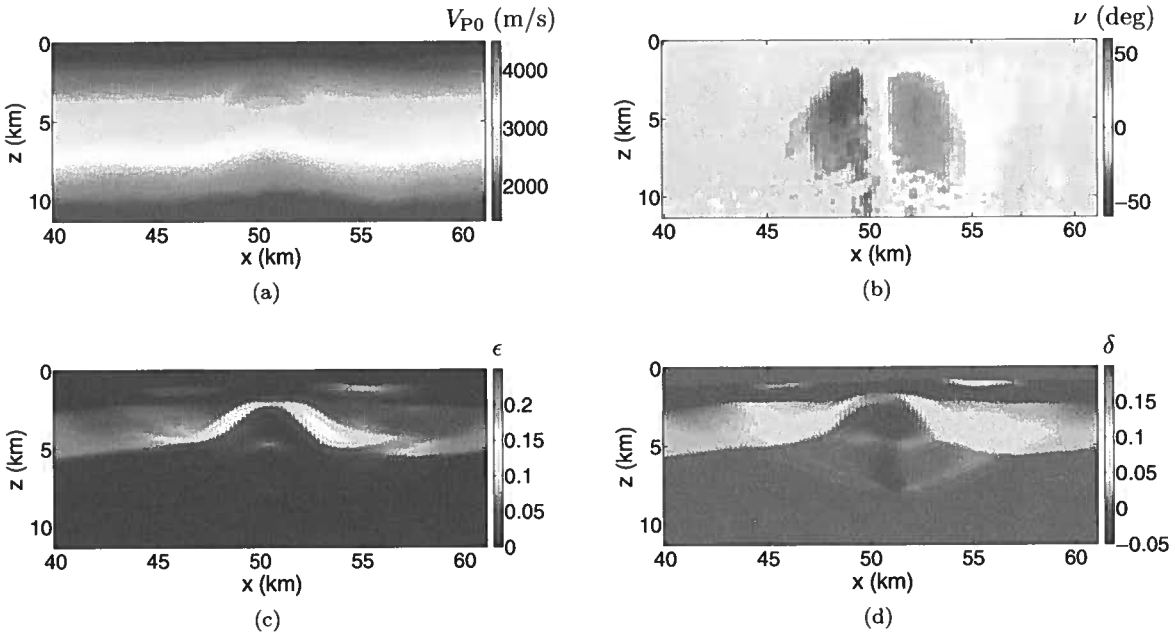

Figure 6. Inverted TTI parameters (a) V_{P0}, (c) ϵ, and (d) δ after the final iteration of tomography. (b) The symmetry-axis tilt ν computed from the depth image obtained before the final iteration. The parameters V_{P0}, ϵ, and δ are estimated on a 200 m × 100 m grid.

curacy of the reconstructed velocity model is the symmetry-axis tilt ν, which is computed directly from the depth image. Poorly constrained TTI parameters in the deep part of the model yield a distorted image, which produces large errors in the estimated values of ν. The obtained tilt field is used for the next iteration of tomography, which further distorts the other estimated TTI parameters. Therefore, without sufficient constraints from deep reflection events and VSP rays, the trade-offs between the tilt ν and the other TTI parameters increase the uncertainty in velocity analysis at depth.

4 BP SALT MODEL

Next, the joint tomography is applied to another section of the BP TTI model that includes a salt dome (Figure 8). The top of the salt and the flanks right beneath it produce strong reflections and are clearly imaged by Kirchhoff depth migration, but the deeper segments of the flanks are blurred even when the actual model is used (Figure 9). The image quality can be improved with a wavefield-based imaging algorithm, such as reverse time migration (RTM).

The maximum offset (10 km) and the source and receiver intervals (50 m) are the same as in the previous test. The CIGs used for MVA are computed every 150 m from $x = 16$ km to 46 km. The BP data set contains a vertical "well" at location $x_{\rm VSP} = 29.9$ km to the left of the salt body (Figure 8(a)). Two sets of evenly spaced 24 receivers (one between $z = 5275$ m and 5562.5 m and the other between $z = 8400$ m and 8687.5 m) were placed in the well to record a walkaway VSP survey. The maximum offset for the VSP data is also 10 km with a source interval of 50 m. The input data also include check-shot traveltimes obtained every 50 m from $z = 1743.75$ m to 9093.75 m.

During the inversion, the water layer and salt body are kept isotropic with the velocities fixed at the actual values. Also, the positions of the top and flanks of the salt dome are assumed to be known, and the update is performed only for the sedimentary formations around the salt body. Since ray tracing becomes unstable in the presence of sharp velocity contrasts, we apply 2D smoothing to the velocity model to find the raypaths crossing the salt and then calculate the traveltimes and their derivatives in the original (unsmoothed) model.

Similar to the previous test, an initial isotropic model (Figure 10(a)) is built using check-shot traveltimes and extrapolation along interfaces. Because the symmetry-direction velocity (and other parameters) is different on the two sides of the salt body, the residual moveout in the CIGs (Figure 10(b)) is larger to the right of the salt (i.e., further away from the well).

As in the first test, the joint tomography is performed using the three-stage parameter-estimation procedure. For the VSP sources to the left of the well, the corresponding rays pass through the relatively simple sedimentary section. The VSP rays originated to the

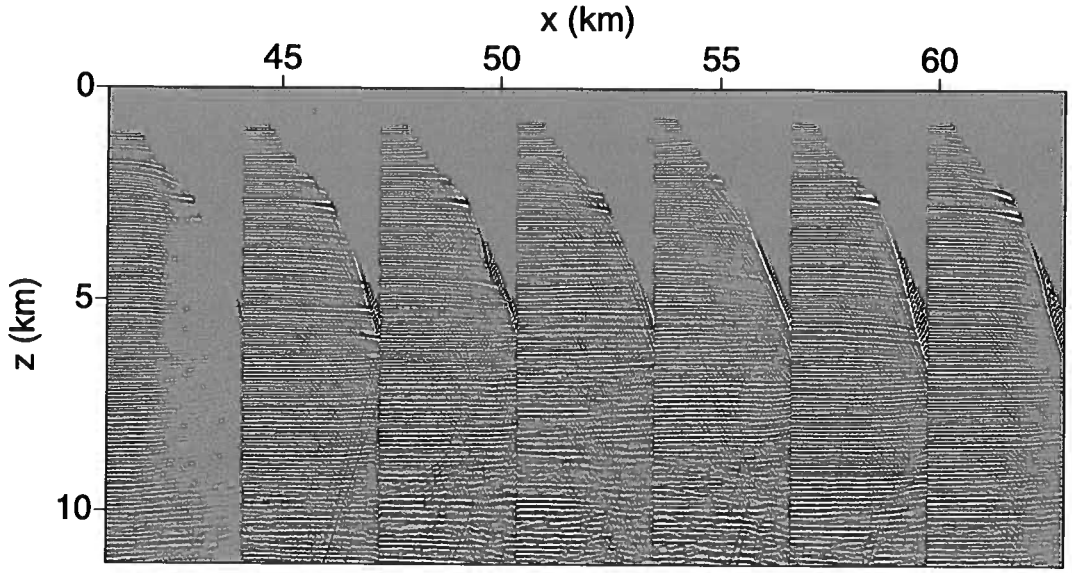

(a)

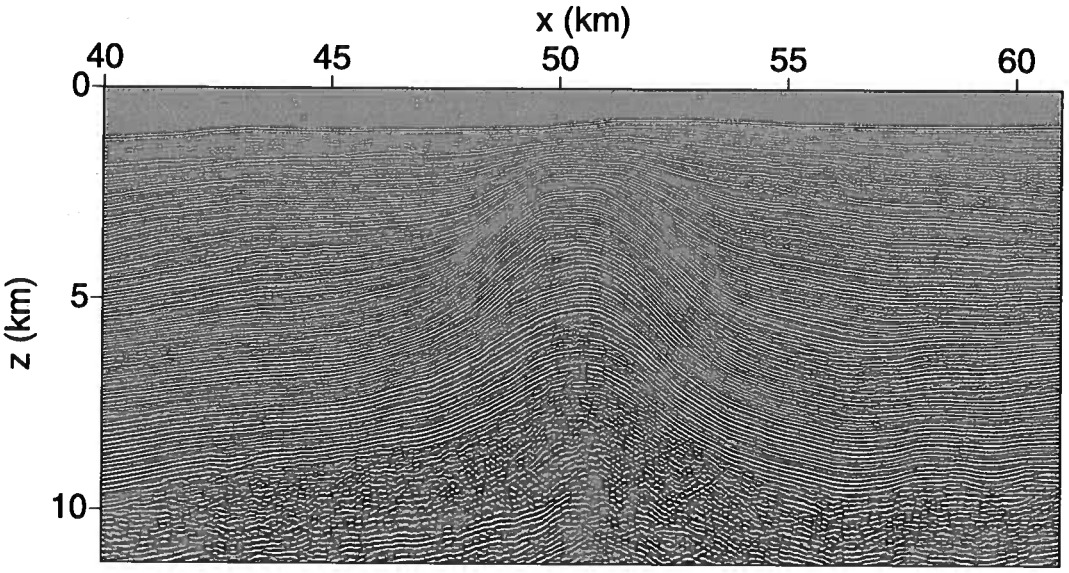

(b)

Figure 7. (a) CIGs and (b) the migrated section computed with the final inverted model from Figure 6.

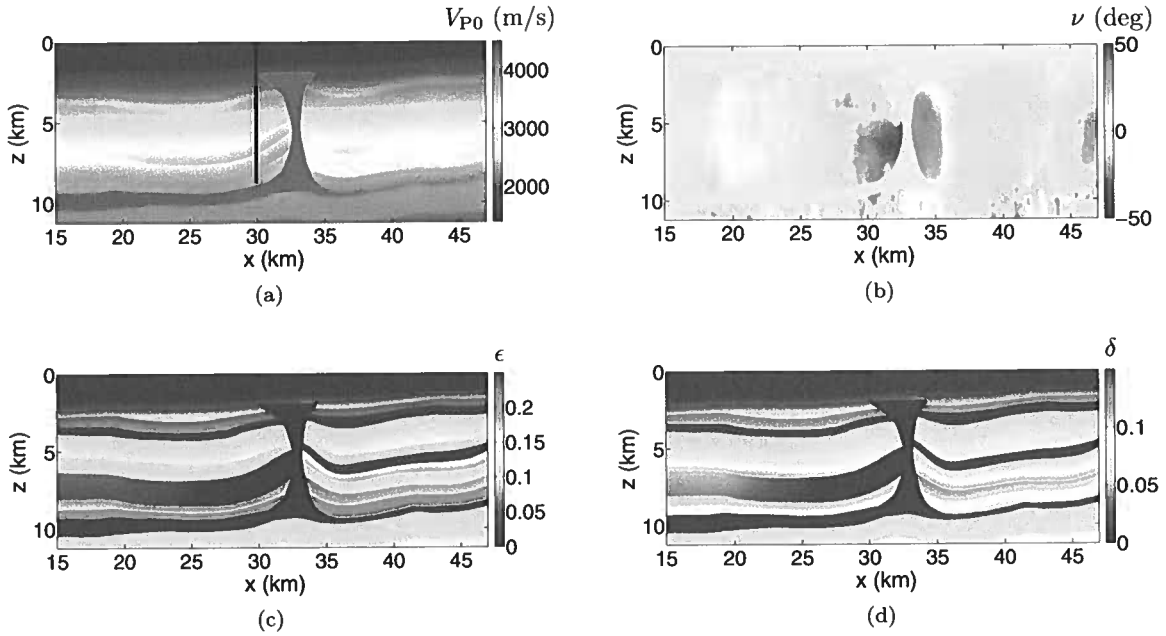

Figure 8. Section of the BP TTI model with a salt dome (the grid size is 6.25 m × 6.25 m). The top water layer and the salt body are isotropic with the P-wave velocity equal to 1492 m/s and 4350 m/s, respectively. (a) The symmetry-direction velocity V_{P0}. The vertical "well" at $x = 29.9$ km is marked by a black line. (b) The tilt of the symmetry axis, which is set orthogonal to the interfaces. The anisotropy parameters (c) ϵ and (d) δ.

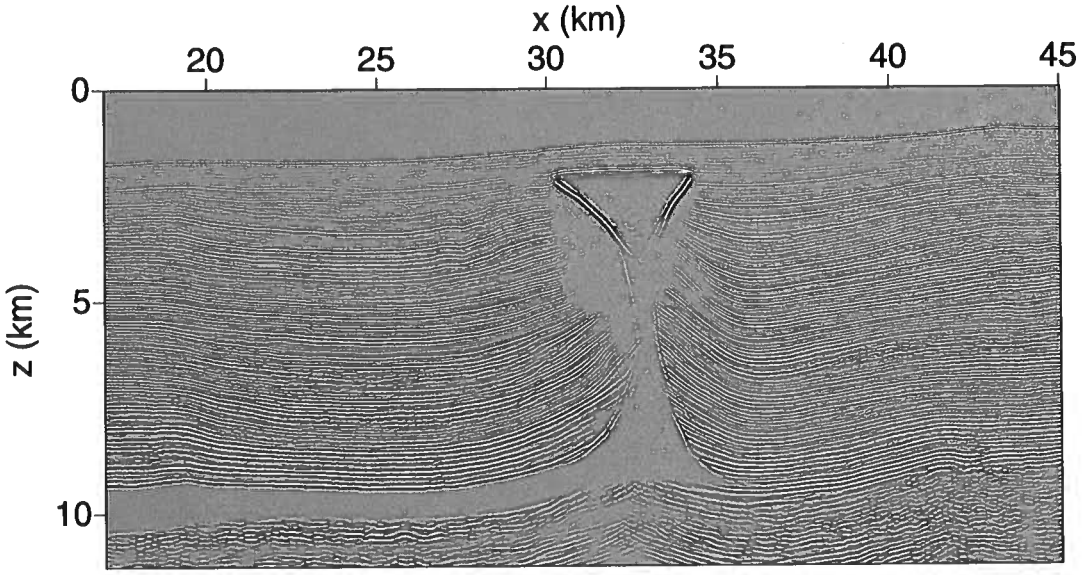

Figure 9. Depth image of the BP salt model produced with the actual parameters from Figure 8.

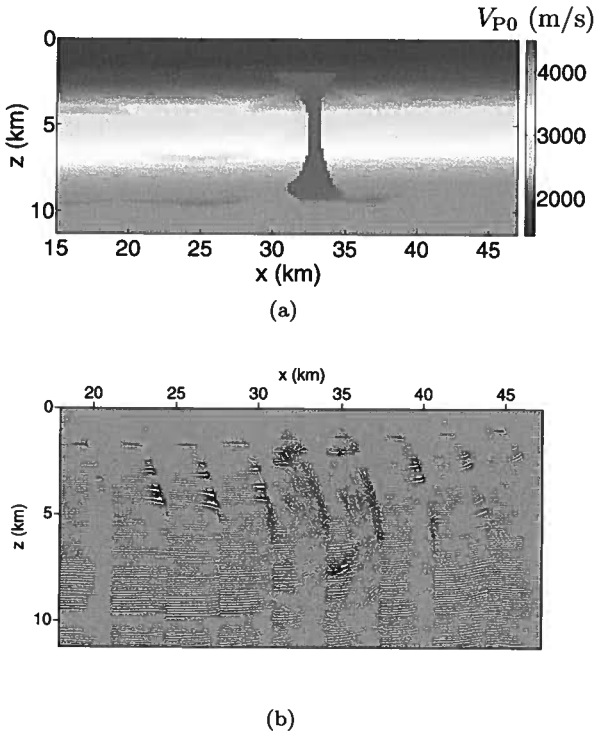

Figure 10. (a) Initial isotropic model with V_{P0} defined on a 200 m × 100 m grid. The P-wave velocities in the top water layer and salt body are set to the actual values. (b) CIGs (displayed every 3.25 km from 18 km to 44 km) computed with the initial model from Figure 10(a).

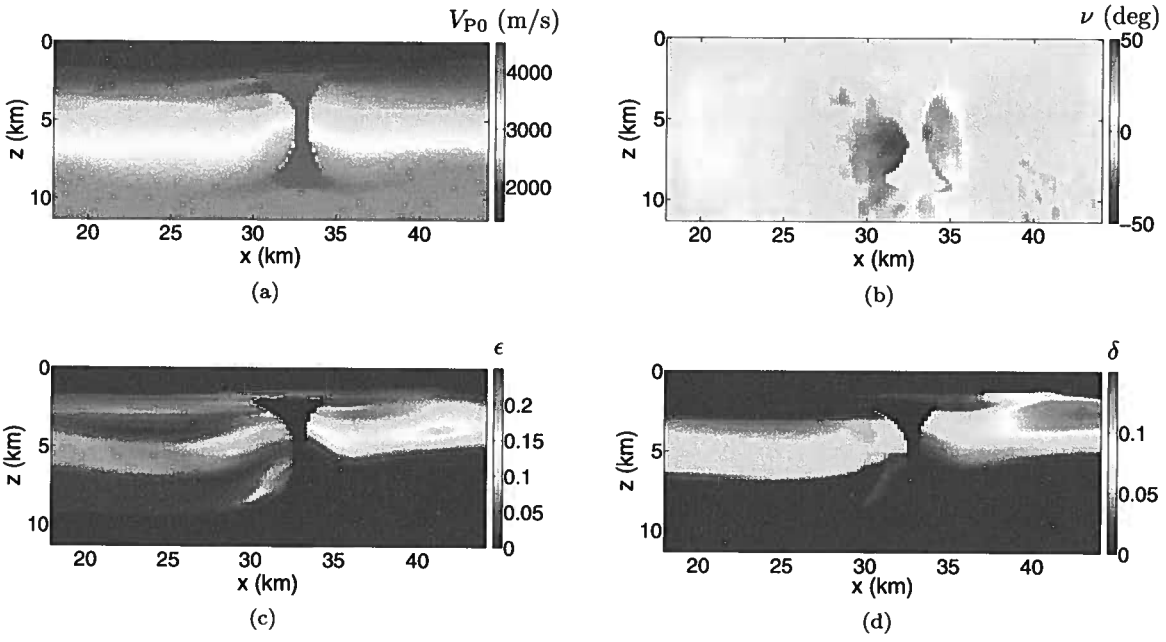

Figure 11. Inverted TTI parameters (a) V_{P0}, (c) ϵ, and (d) δ after the final iteration of joint tomography. (b) The symmetry-axis tilt ν computed from the depth image obtained before the final iteration. The parameters V_{P0}, ϵ, and δ are estimated on a 200 m × 100 m grid.

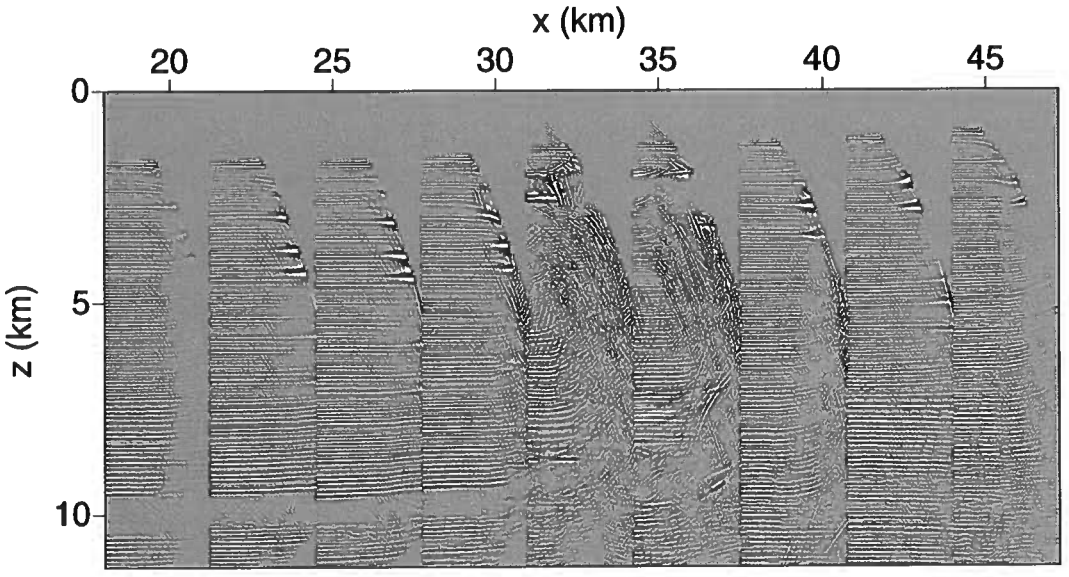

(a)

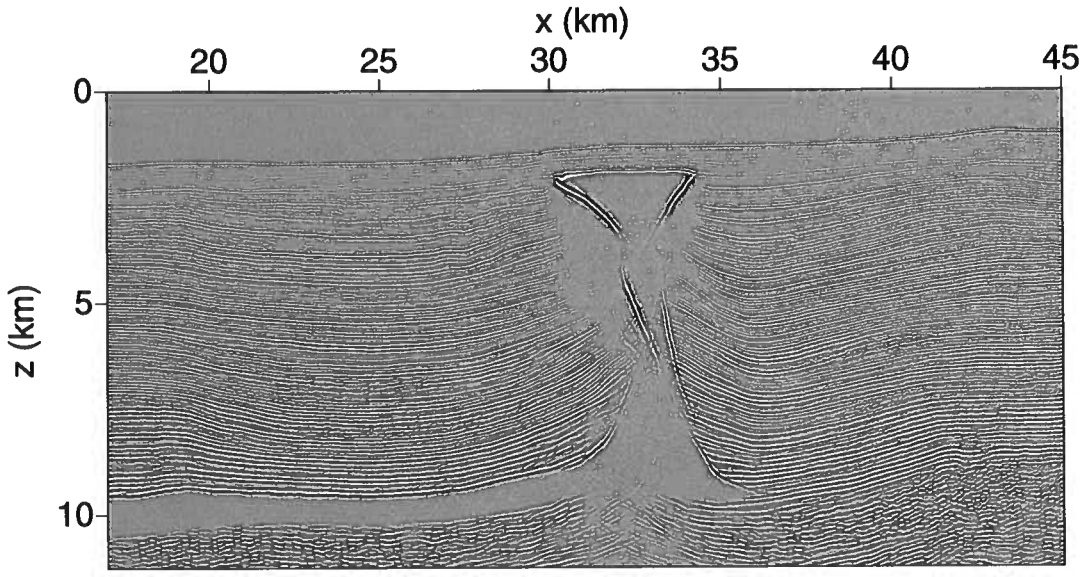

(b)

Figure 12. (a) CIGs and (b) the migrated section computed with the final inverted model from Figure 11.

right of the well, however, cross the high-velocity salt body, and errors in the velocity field near the salt boundaries may cause large perturbations of the ray trajectories. Therefore, we assign smaller weights in the objective function to the VSP traveltimes for the sources located to the right of the well. As a result, the anisotropic velocity field on the right side of the salt dome has to be determined mostly from the P-wave reflection data, which leads to larger uncertainty in the TTI parameters.

After all three parameters were updated on the same grid at the last stage of the updating procedure, the velocity V_{P0} (Figure 11(a)) above $z = 7$ km to the left of the salt body is relatively well-resolved (errors in most areas do not exceed 3%). However, the errors in V_{P0} on the right side of the section are higher because of the limited constraints from VSP data, as described above. The spatial variations of ϵ and δ are partially recovered from the water bottom down to $z = 5$ km (Figure 11(c) and 11(d)). Because of the smaller offset-to-depth ratio and poor coverage of VSP rays (especially for the right part of the model) at depth, the anisotropy parameters for most grid points below 5 km could not be updated.

Despite these problems, the final model flattens most CIGs (Figure 12(a)) and practically eliminates the VSP traveltime misfit. As a result, the migrated image (Figure 12(b)) reproduces the actual section with sufficient accuracy, except for the steep segments of the salt boundaries.

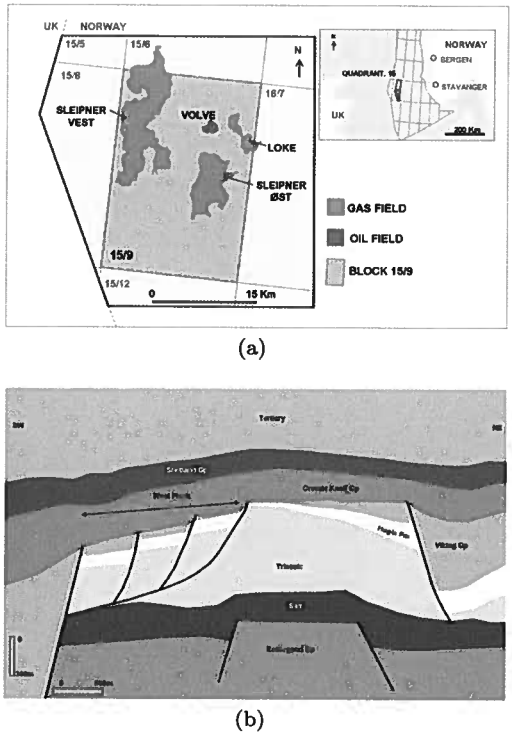

Figure 13. (a) Location of Volve field in the North Sea (figure courtesy of Statoil) and (b) a representative geologic cross-section of Volve field (after Akalin et al., 2010).

5 VOLVE OBS DATA

Volve field is located offshore Norway in the gas/condensate-rich Sleipner area of the North Sea (Figure 13(a)). It is a small oil field with a dome-shaped structure formed by the collapse of adjacent salt ridges during the Jurassic period (Szydlik et al., 2007). The reservoir in the Middle Jurassic Hugin sandstone formation is a structural trap bounded by faults which are mainly associated with salt tectonics (Figure 13(b)).

In 2002, a 3D ocean-bottom seismic (OBS) survey was acquired over a 12.3 km × 6.8 km area of the field (Figure 14). Six swaths of four-component (4C) data were recorded using inline shooting geometry. Each swath includes two 6 km-long cables placed on the seafloor (about 92 m below the water surface) with 400 m spacing (Figure 14), and a cable contains 240 receivers with an interval of 25 m. In each swath, flip-flop shooting was conducted along 25 dual source sail lines with 100 m separation. The sail line is 12 km long with a shot interval of 25 m (50 m between the flips).

The acquired 3D PP and PS data were preprocessed by Statoil. Preprocessing included noise suppression, multiple attenuation, and other standard steps described by Szydlik et al. (2007). Only traces with offsets less than 5 km were kept, and a layer-stripping technique was employed to construct a 3D VTI model

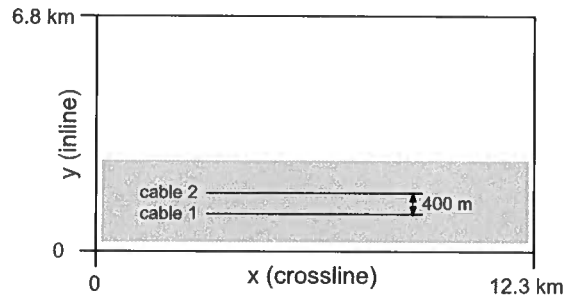

Figure 14. Geometry of the Volve 3D OBS survey. Two cables (black lines) are placed on the seafloor, and 25 sail lines parallel to the cables are shot with flip-flop sources in a 12 km × 2.4 km rectangular area (gray). After one swath of data is recorded, the cables and source lines are moved 800 m along the inline (y) direction.

for prestack depth imaging. The P- and S-wave vertical velocities V_{P0} and V_{S0} and the anisotropy parameters ϵ and δ in each layer (Figure 15; V_{S0} is not shown) were updated by flattening common-image gathers (Figure 16(a)), minimizing misties between seismic and well data, codepthing the key horizons on PP (Figure 16(b)) and PS migrated sections, and incorporating compressional sonic logs (Szydlik et al., 2007). However, com-

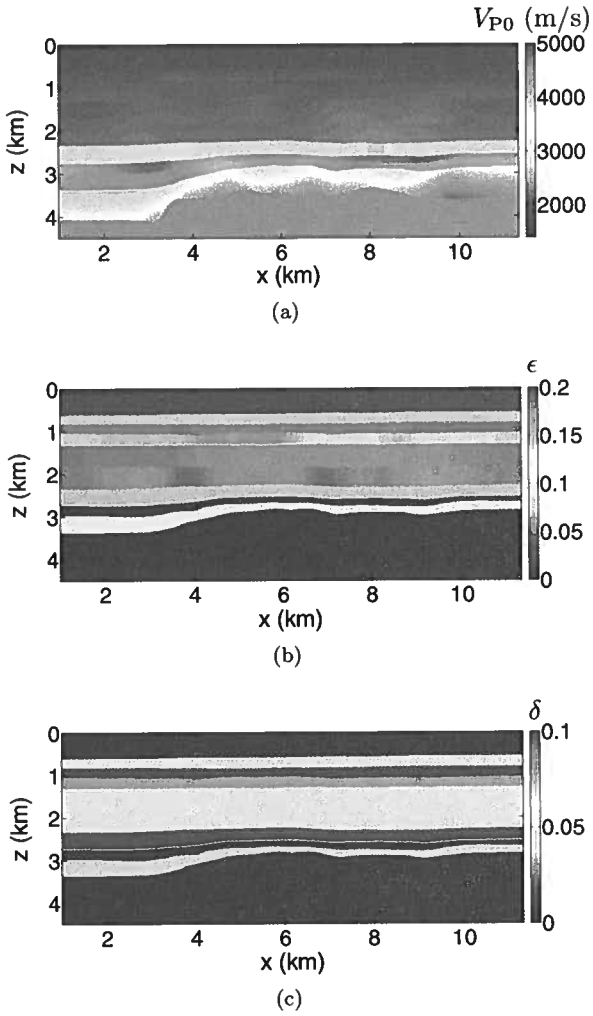

Figure 15. Cross-sections along the line with $y = 2.8$ km (Figure 14) of the 3D VTI model built by Statoil. (a) The P-wave vertical velocity V_{P0} and the anisotropy parameters (b) ϵ and (c) δ.

plete information about Statoil's VTI model-building process is not available to us.

Here, we use a 2D section from the 3D P-wave (vertical component) data recorded by the cable laid along $y = 2.8$ km (Figure 14). Two adjacent source lines ($y = 2.8 \pm 0.025$ km) provided 481 shots with a shot interval of 25 m. The tomographic MVA algorithm described above is applied to the CIGs from $x = 2.7$ km to 9.5 km with an interval of 50 m, under the assumption that out-of-plane propagation can be ignored. As before, the symmetry axis is assumed to be perpendicular to the interfaces; the parameters V_{P0}, ϵ, and δ are defined on a 100 m $\times$ 50 m grid.

There are two deviated wells (Figure 17) in the vicinity of the chosen line, and P-wave reflections are combined in the joint inversion with vertical check-shot (normal-incidence VSP) data recorded in the wells. Although the wells lie outside the vertical plane ($y =$ 2.8 km), only the x and z coordinates of the check shots are used to place each check-shot measurement. The provided data set also includes the well markers (i.e., depth measurements in the well) of several key horizons (e.g., the top and base of Utsira formation, top of Shetland Group, and base of Cretaceous). To evaluate the accuracy of velocity analysis, these well markers were compared with the migrated reflector depths (see below).

To build an initial model, the section is divided into eight layers based on key geologic horizons. The interval velocity V_{P0} in each layer is computed from the check-shot traveltimes in well 1, whose surface projection is closer to the chosen line than the projection of well 2 (Figure 17). Assuming the check-shot raypaths and the symmetry axis at the well to be vertical, the velocity is found as $V_{P0} = \Delta z/\Delta t$, where Δz is the depth interval, and Δt is the check-shot traveltime difference cor-

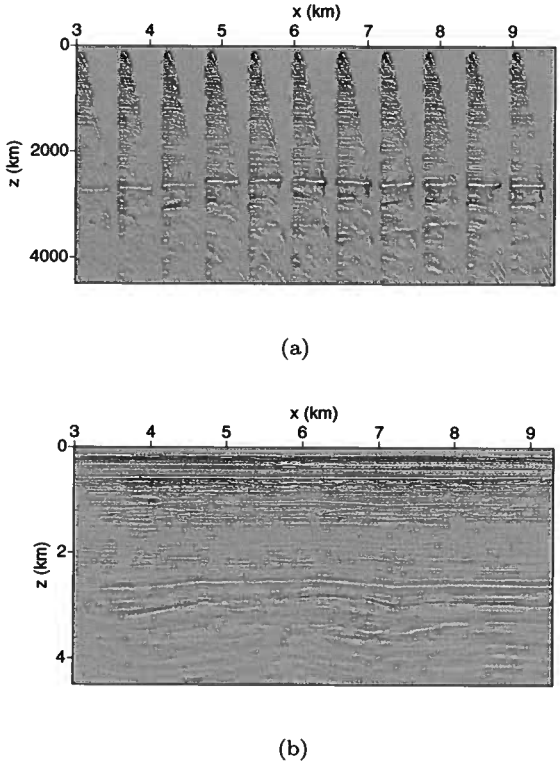

Figure 16. (a) CIGs (displayed every 0.6 km from 3 km to 9 km) and (b) the depth image produced by Kirchhoff prestack migration with the parameters from Figure 15.

responding to Δz. The interval NMO velocity ($V_{\rm nmo}$) and parameter η in each layer are estimated using nonhyperbolic moveout inversion (Tsvankin, 2005) applied to a CMP gather near the well. In combination with the velocity $V_{\rm P0}$ estimated along the well, $V_{\rm nmo}$ and η yield initial guesses for the parameters ϵ and δ at the well location.

Because of the limited offset-to-depth ratio (smaller than 1.2 for $z > 3$ km), the accuracy of the effective parameters η and ϵ estimated from nonhyperbolic moveout analysis decreases with depth. Also, the interval values of ϵ and δ may be strongly distorted by layer stripping in the bottom part of the section. Therefore, we have to assume the deeper layers to be isotropic and set ϵ and δ below 3 km to zero (Figures 18(b) and 18(c)). The initial TTI model (Figure 18) is obtained by extrapolating the 1D profiles of $V_{\rm P0}$, ϵ, and δ at well 1 along the picked interfaces. As expected, the CIGs obtained after Kirchhoff migration with the initial model exhibit noticeable residual moveout (Figure 19).

Using the same three-stage parameter-estimation procedure as in the synthetic tests, we gradually relax the constraints on the spatial variation of ϵ and δ, while updating $V_{\rm P0}$ at each grid point in all iterations and setting the symmetry axis orthogonal to the reflectors. Each iteration aims to simultaneously minimize the residual moveout in the CIGs and the check-shot traveltime misfit in both wells. In addition, the anisotropic velocity field is regularized by the structure-guided operators defined in equation 2.

The TTI model obtained after 10 iterations of tomography (Figure 20) yields relatively flat CIGs (Figure 21(a)). The remaining residual moveout in CIGs below $z = 3$ km is partially due to internal multiples that were not completely removed in the preprocessing. As mentioned above, the deeper part of the section ($z > 3$ km) is kept isotropic because of insufficient constraints on the anisotropy parameters provided by reflection data.

The average velocity $V_{\rm P0}$ (Figure 20(a)) in the Cretaceous Unit (approximately between $z = 2.5$ km and 3 km) is reduced after MVA to about 4300 m/s from its initial value 4500 m/s obtained from check shots. In the layer-based VTI model provided by Statoil (Figure 15(a)), $V_{\rm P0}$ in the Cretaceous Unit is larger, reaching 4900 m/s in some areas. Although the joint tomography used here minimizes the check-shot traveltime misfit in both wells and the structure-guided regularization helps propagate the borehole constraints along the interfaces, the depth scale of the section may not be sufficiently accurate. It is possible that the high velocity in the Cre-

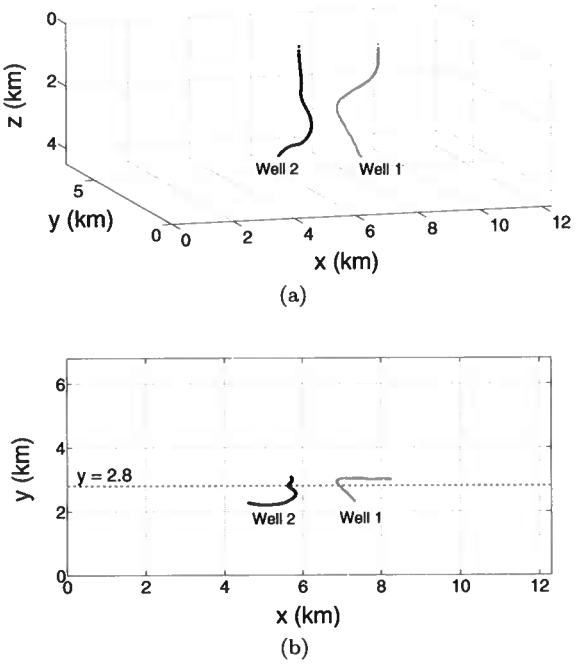

Figure 17. (a) Trajectories of two deviated wells near the line (y = 2.8 km, dashed) used for velocity analysis. (b) Well projections onto the horizontal surface. The maximum deviations (Δy) of the two wells from the vertical plane (y = 2.8 km) are 477 m and 603 m, respectively.

taceous Unit obtained by Statoil came from sonic logs or other information not available to us.

The inverted model helps image several reflectors in the Cretaceous Unit (Figure 22(a)), which are difficult to identify on the sections computed with both the initial model and Statoil's VTI model (Figure 22(b)). Also, some reflectors beneath the high-velocity Cretaceous Unit look more coherent than those imaged with Statoil's model (compare Figures 22(a) and 22(b)), which is important for structural interpretation of the reservoir. The key horizons on the final image (Figure 21(b)) are close to the well markers with the maximum mistie not exceeding 20 m, which confirms that the migrated section has an accurate depth scale near the wells.

There are several possible reasons for the above improvements. One is that the TTI model used here allows the symmetry-axis direction to vary spatially according to the reflector dips. Although the dips are gentle, such a model is more geologically plausible than VTI and should produce more accurate anisotropy parameters. In addition, our joint tomography simultaneously inverts for the TTI parameters defined at all grid points, which helps avoid error accumulation typical for layer stripping.

As any other 2D method, the algorithm applied here is based on the assumption that waves propagate in the vertical incidence plane. However, recorded events may correspond to out-of-plane reflection points; also, the check-shot raypaths in the nearby deviated wells lie outside the incidence plane. Moreover, the symmetry axis, even if it is orthogonal to dipping reflectors, may not be confined to the incidence plane. These 3D phenomena likely explain some remaining residual moveout in CIGs after application of the 2D TTI inversion. To construct a more robust TTI model and make use of the whole OBS data set, our tomographic algorithm should be extended to 3D and, preferably, wide-azimuth data. For the 3D algorithm, which has to ensure flattening CIGs along different azimuthal directions, the main challenge is the efficient construction of the Fréchet matrix in the objective function.

6 CONCLUSIONS

Although most migration techniques have been extended to TTI media, accurate reconstruction of the anisotropic velocity field remains a difficult problem. Previously we developed an efficient 2D tomographic algorithm for heterogeneous TTI models, with the parameters V_{P0}, ϵ, δ, and the symmetry-axis tilt ν defined on a rectangular (in most cases square) grid. While V_{P0}, ϵ, and δ are updated iteratively in the migrated domain, the tilt field is computed from the depth image by setting the symmetry axis perpendicular to the reflectors.

To resolve the TTI parameters in the presence of

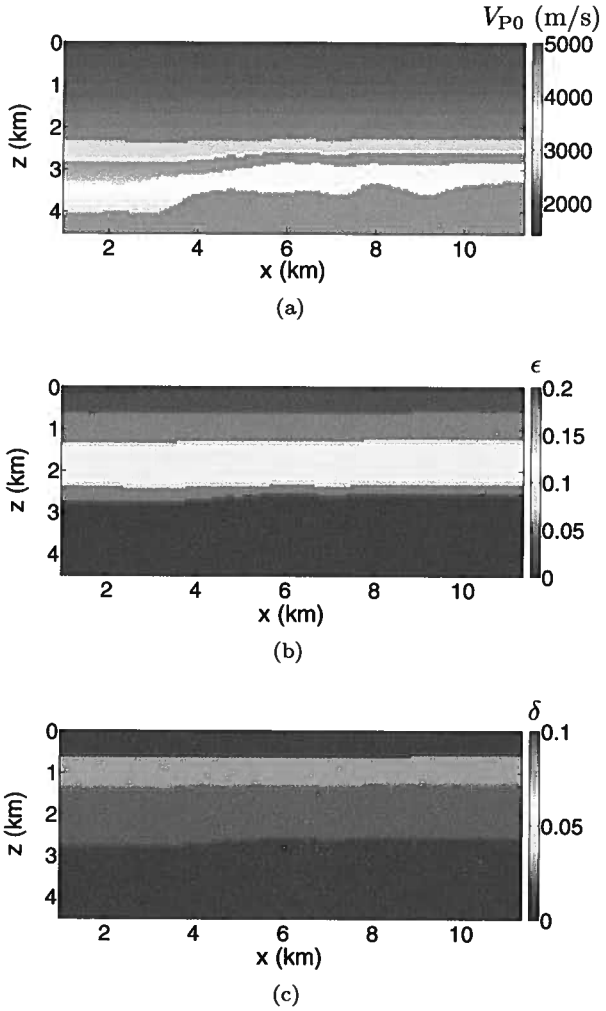

Figure 18. Initial TTI model for line $y = 2.8$ km. (a) The symmetry-direction velocity V_{P0} and the anisotropy parameters (b) ϵ and (c) δ. All three parameters are defined on a 100 m $\times$ 50 m grid.

spatial velocity variations, here we combined reflection data with walkaway VSP and check-shot traveltimes. Our tomographic algorithm also incorporates geologic constraints by appropriately designed regularization. The objective function includes regularization terms that allow for parameter variations across layers, but suppress them in the direction parallel to boundaries. Such structure-guided regularization also helps propagate along interfaces the most reliable parameter updates corresponding to large derivatives in the Fréchet matrix (e.g., those in the cells crossed by dense VSP rays).

To improve the convergence of the algorithm, we proposed a three-stage parameter-updating procedure. In the first several iterations, only the velocity V_{P0} is updated on a grid, while the anisotropy parameters ϵ and δ are fixed at their initial values. This operation eliminates potentially large distortions in ϵ and δ caused by the parameter trade-offs. At the second stage of the inversion, ϵ and δ are taken spatially invariant in each layer and updated together with the grid-based velocity V_{P0}. Finally, all three TTI parameters are estimated simultaneously on the grid with the constraints provided by the regularization terms described above.

First, the joint tomography of reflection and VSP data was tested on two sections of the BP TTI model, one with an anticline and the other with a salt dome. In both tests, a purely isotropic velocity field, which was obtained from check-shot traveltimes and extrapolated along the horizons, served as the initial model. With constraints from P-wave reflection and VSP data, the TTI parameters in the shallow part (above 5 km) of both sections are well resolved. However, the errors in ϵ and δ increase with depth due to the small offset-to-depth ratio and poor coverage of VSP rays. For the model with the salt dome, the anisotropic velocity field

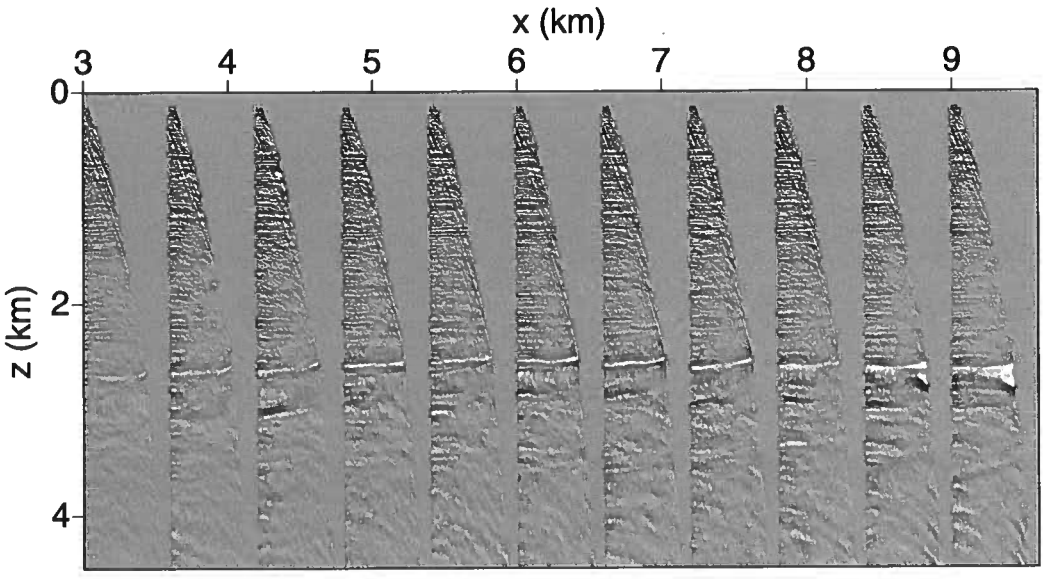

Figure 19. CIGs computed with the initial TTI model from Figure 18.

is recovered with higher accuracy to the left of the salt, where the inversion is tightly constrained by VSP data from a nearby well.

The tomographic algorithm was also applied to OBS data from Volve field in the North Sea. Iterative updating of V_{P0}, ϵ, and δ was performed by joint inversion of P-wave reflection and check-shot data with the structure-guided regularization. An initial anisotropic model was built by combining check-shot traveltimes with nonhyperbolic moveout analysis at the well locations. Then, the three-stage parameter-estimation procedure was employed to produce the final gridded TTI velocity field. The inverted TTI model made it possible to focus reflectors within and below the Cretaceous Unit and accurately position several key horizons in depth.

7 ACKNOWLEDGMENTS

We would like to thank Hemang Shah of BP for creating the TTI model and BP Exploration Operation Company Limited for generating the synthetic data set (`http://www.freeusp.org/2007_BP_Ani_Vel_Benchmark/`). We are grateful to Statoil ASA and the Volve license partners ExxonMobil E&P Norway and Bayerngas Norge for the release of the Volve data. The viewpoints about the Volve data set in this paper are of the authors and do not necessarily reflect the views of Statoil ASA and the Volve field license partners. Special thanks to Marianne Houbiers of Statoil for numerous helpful discussions of the Volve case study. This work was supported by the Consortium Project on Seismic Inverse Methods for Complex Structures at the Center for Wave Phenomena.

REFERENCES

Akalin, A., M. Thompson, J. Mispel, and E. Rundhovde, 2010, Volve - How close communication between the asset team and research was an enabler for field development: Petex Expanded Abstracts.

Bakulin, A., Y. Liu, O. Zdraveva, and K. Lyons, 2010a, Anisotropic model building with wells and horizons: Gulf of Mexico case study comparing different approaches: The Leading Edge, **29**, 1450–1460.

Bakulin, A., M. Woodward, D. Nichols, K. Osypov, and O. Zdraveva, 2010b, Building tilted transversely isotropic depth models using localized anisotropic tomography with well information: Geophysics, **75**, no. 4, D27–D36.

Bakulin, A., M. Woodward, O. Zdraveva, and D. Nichols, 2010c, Application of steering filters to localized anisotropic tomography with well data: 80th Annual International Meeting, SEG, Expanded Abstracts, 4286–4290.

Behera, L., and I. Tsvankin, 2009, Migration velocity analysis for tilted TI media: Geophysical Prospecting, **57**, 13–26.

Campbell, A., E. Evans, D. Judd, I. Jones, and S. Elam, 2006, Hybrid gridded tomography in the south-

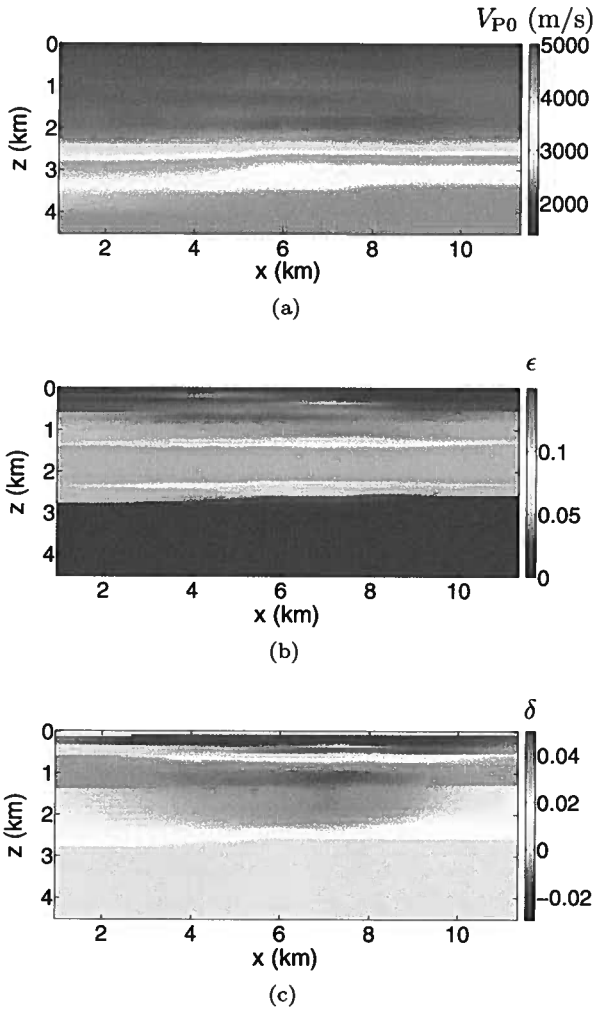

Figure 20. Inverted parameters (a) V_{P0}, (c) ϵ, and (d) δ after the final iteration of joint tomography.

ern North Sea: 76th Annual International Meeting, SEG, Expanded Abstracts, **25**, 2538–2541.

Charles, S., D. Mitchell, R. Holt, J. Lin, and J. Mathewson, 2008, Data-driven tomographic velocity analysis in tilted transversely isotropic media: A 3D case history from the Canadian Foothills: Geophysics, **73**, no. 5, VE261–VE268.

Clapp, R. G., B. L. Biondi, and J. F. Claerbout, 2004, Incorporating geologic information into reflection tomography: Geophysics, **69**, no. 2, 533–546.

Engl, H. W., M. Hanke, and A. Neubauer, 1996, Regularization of inverse problems: Kluwer Academic Publishers.

Fomel, S., 2007, Shaping regularization in geophysical-estimation problems: Geophysics, **72**, no. 2, R29–R36.

Huang, T., S. Xu, J. Wang, G. Ionescu, and M. Richardson, 2008, The benefit of TTI tomography for dual azimuth data in Gulf of Mexico: 78th Annual International Meeting, SEG, Expanded Abstracts, 222–226.

Morice, S., J.-C. Puech, and S. Leaney, 2004, Well-driven seismic: 3D data processing solutions from wireline logs and borehole seismic data: First Break, **22**, 61–66.

Naumann, U., and O. Schenk, 2011, Combinatorial Scientific Computing: Chapman & Hall/CRC Computational Science.

Stork, C., 1992, Reflection tomography in the postmigrated domain: Geophysics, **57**, 680–692.

Szydlik, T., P. Smith, S. Way, L. Aamodt, and C. Friedrich, 2007, 3D PP/PS prestack depth migration on the Volve field: First Break, **25**, 43–47.

Tikhonov, A. N., 1963, Solution of incorrectly formulated problems and the regularization method: Soviet Mathematical Doklady, **4**, 1035–1038.

Tsvankin, I., 2005, Seismic signatures and analysis of reflection data in anisotropic media, 2nd edition: Elsevier Science Publ. Co., Inc.

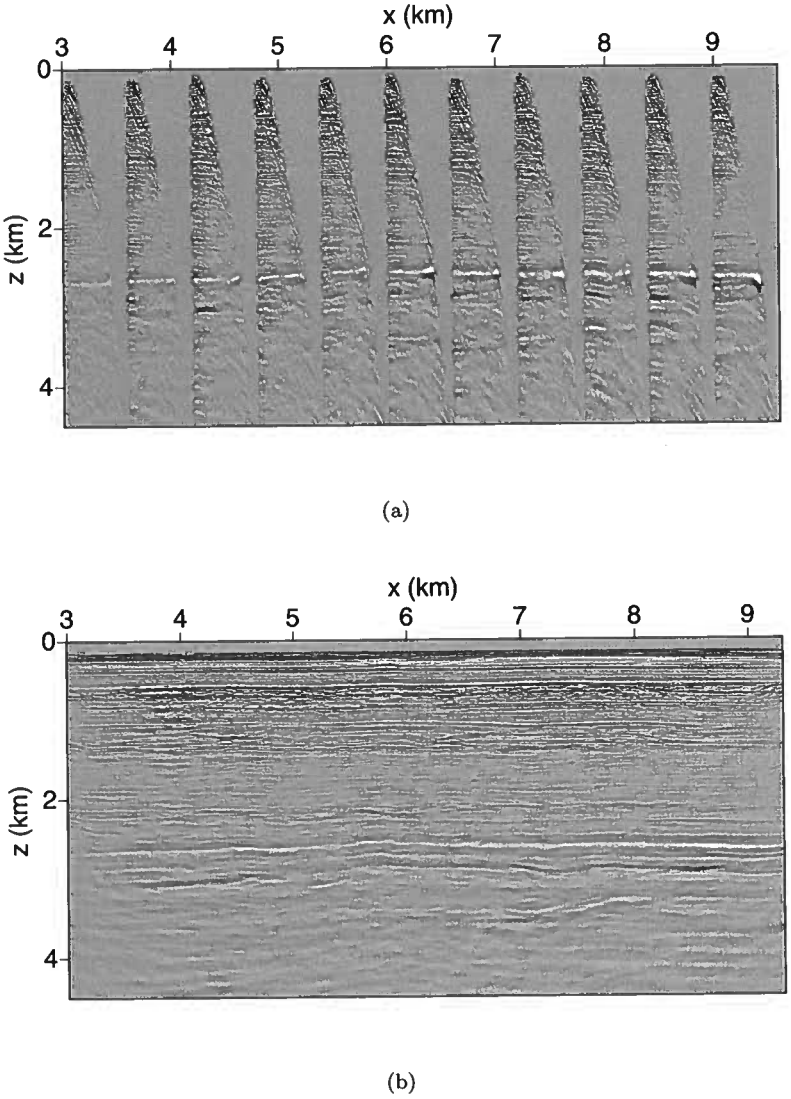

Figure 21. (a) CIGs and (b) the migrated section computed with the final inverted TTI model from Figure 20.

Wang, X., and I. Tsvankin, 2010, Stacking-velocity inversion with borehole constraints for tilted TI media: Geophysics, **75**, no. 5, D69–D77.

———, 2013, Ray-based gridded tomography for tilted transversely isotropic media: Geophysics, **78**, no. 1, C11–C23.

Woodward, M. J., D. Nichols, O. Zdraveva, P. Whitfield, and T. Johns, 2008, A decade of tomography: Geophysics, **73**, no. 5, VE5–VE11.

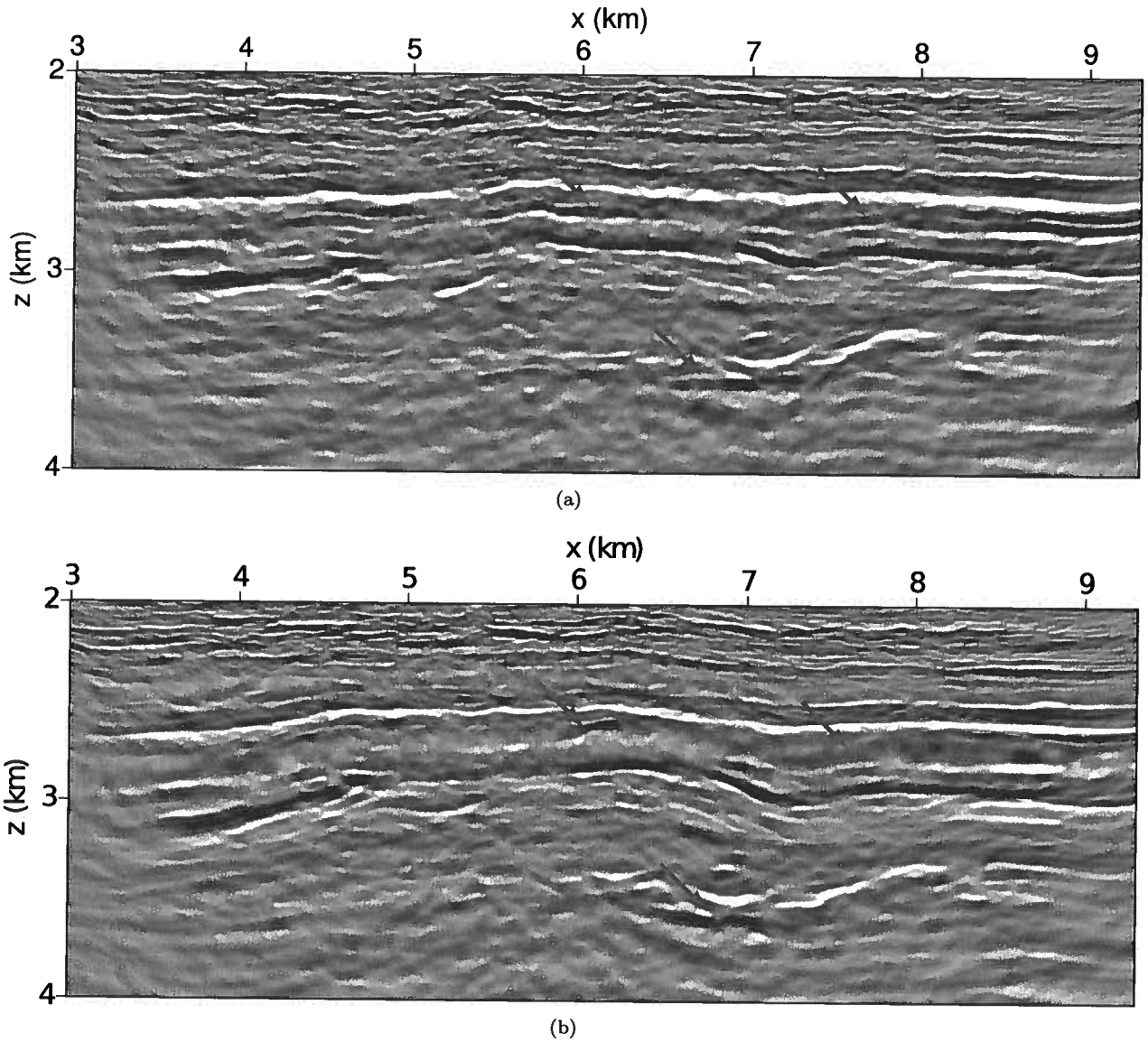

Figure 22. Segment of the migrated section between $z = 2$ km and 4 km computed with (a) the inverted model from Figure 20 and (b) the VTI model provided by Statoil (Figure 15).

Tomographic velocity analysis of PP- and PS-waves for VTI media: Field-data application

Pengfei Cai[1,2] & Ilya Tsvankin[1]

[1] *Center for Wave Phenomena, Colorado School of Mines, Golden, CO, USA*
[2] *CGG, 10300 Town Park Dr, Houston, TX, USA*

ABSTRACT

Mode-converted PS-waves can provide valuable information for anisotropic parameter estimation that cannot be obtained from compressional waves alone. In a previous paper, we developed an efficient tomographic methodology for 2D joint velocity analysis of PP and PS data from VTI (transversely isotropic with a vertical symmetry axis) media. The algorithm is designed to flatten image gathers of PP-waves as well as of pure SS reflections computed using the PP+PS=SS method. An important additional constraint is provided by codepthing of the migrated PP and SS sections. The model is divided into square cells, and the parameters V_{P0}, V_{S0}, ϵ, and δ are defined at each grid point. Here, this methodology is applied to multicomponent data recorded on a 2D line from an OBS (ocean bottom seismic) survey acquired at Volve field in the North Sea. Although the parameter-updating procedure did not include any borehole information, the VTI model obtained by joint tomography of the recorded PP-waves and constructed SS-waves produced generally well-focused PP and PS depth images. The depth consistency between the migrated PP and PS sections also corroborates the accuracy of the velocity-analysis algorithm.

Key words: velocity analysis, PS-waves, VTI, codepthing, OBS data

1 INTRODUCTION

Multicomponent data can improve reservoir imaging and provide useful information for lithology, fluid, and fracture characterization. For example, shear waves help in imaging of reservoirs beneath gas clouds, where P-waves suffer from high attenuation (Tsvankin, 2005).

PS-waves are usually more sensitive to anisotropy than P-waves and can be used to constrain not just the vertical shear-wave velocity but also the subset of the medium parameters responsible for P- and S-wave propagation. In particular, combining PP and PSV reflections in VTI media may help estimate all four pertinent Thomsen parameters – the P- and S-wave vertical velocities (V_{P0} and V_{S0}) and the anisotropy coefficients ϵ and δ (Tsvankin and Grechka, 2011).

Joint tomographic inversion of PP and PS data has been discussed in several publications (Stopin and Ehinger, 2001; Audebert et al., 1999; Broto et al., 2003; Foss et al., 2005). However, velocity analysis of mode convertions is hampered by the asymmetry of PS moveout (i.e., PS traveltimes generally do not stay the same when the source and receiver are interchanged) and polarity reversals of PS-waves.

The methodology proposed in our previous publication (Cai and Tsvankin, 2012) overcomes the problems caused by the moveout asymmetry of PS-waves and takes advantage of efficient MVA (migration velocity analysis) algorithms designed for pure modes. Instead of using PS-waves directly for parameter estimation, we employ the PP+PS=SS method of Grechka and Tsvankin (2002) to generate the traveltimes of the corresponding pure SS reflections, which have symmmetric moveout. Then the computed SS-waves are combined with the recorded PP-waves to build a 2D VTI velocity model. Our algorithm for updating the parameters V_{P0}, V_{S0}, ϵ, and δ is based on the gridded reflection tomography developed for P-waves by Wang and Tsvankin (2013). In addition to removing residual moveout in image gathers, the algorithm penalizes depth misties between the migrated PP and SS sections and regularizes the solution using a finite-difference approximation of the Laplacian operator.

Here, the methodology of Cai and Tsvankin (2012) is applied to OBS data from Volve field in the North Sea (courtesy of Statoil). We start by briefly describing the algorithm for joint tomographic inversion of PP and PS data, the geological setting of the field, and the acqusition parameters of the survey. Registration of the PP- and PS-waves on a 2D line from the survey produces five events used for computing the

traveltimes of the pure SS-waves. The VTI velocity model for the line is obtained by tomographic velocity analysis of the PP and SS data that includes codepthing of the five picked reflectors on the migrated PP and SS sections. Finally, the images of the recorded PP- and PS-waves are compared to those computed with the velocity model previously obtained by Statoil.

2 METHODOLOGY

The algorithm of Cai and Tsvankin (2012) operates with 2D PP and PS reflection data. The first processing step is event registration (correlation) followed by application of the PP+PS=SS method to construct the pure SS reflections with the correct kinematics. The velocity model is built by extending the P-wave MVA algorithm of Wang and Tsvankin (2013) to multicomponent (PP and SS) data. The parameters V_{P0}, V_{S0}, ϵ, and δ are defined on a grid by dividing the section into square cells. For purposes of migration velocity analysis, we apply prestack Kirchhoff depth migration to the recorded PP and constructed SS data. The initial model may be obtained from stacking-velocity tomography at borehole locations (Wang and Tsvankin, 2010) or nonhyperbolic moveout analysis (as done in the case study below).

The objective function used in the joint MVA of PP- and SS-waves is defined as follows:

$$F(\Delta\boldsymbol{\lambda}) = \mu_1||\mathbf{A}_P\,\Delta\boldsymbol{\lambda}+\mathbf{b}_P||^2+\mu_2||\mathbf{A}_S\,\Delta\boldsymbol{\lambda}+\mathbf{b}_S||^2 + \mu_3||\mathbf{D}\,\Delta\boldsymbol{\lambda}+\mathbf{y}||^2+\zeta||L\,\Delta\boldsymbol{\lambda}||^2, \quad (1)$$

where $\Delta\boldsymbol{\lambda}$ is the update of the vector $\boldsymbol{\lambda}$ of medium parameters, the matrices $\mathbf{A}_P$ and $\mathbf{A}_S$ include the derivatives of the PP and SS migrated depths with respect to the elements of $\boldsymbol{\lambda}$ (medium parameters), the vectors $\mathbf{b}_P$ and $\mathbf{b}_S$ characterize the residual moveout in PP- and SS-wave CIGs, the matrix $\mathbf{D}$ describes the differences between the derivatives of the PP and SS migrated depths with respect to the medium parameters, and the vector $\mathbf{y}$ contains the differences between the migrated depths on the PP and SS sections. Flattening PP and SS common-image gathers (CIGs) minimizes the first two terms ($||\mathbf{A}_P\Delta\boldsymbol{\lambda}+\mathbf{b}_P||^2$ and $||\mathbf{A}_S\Delta\boldsymbol{\lambda}+\mathbf{b}_S||^2$), and codepthing is achieved through minimizing the third term ($||\mathbf{D}\Delta\boldsymbol{\lambda}+\mathbf{y}||^2$). The regularization term ($||L\Delta\boldsymbol{\lambda}||$) helps stabilize the inversion. The coefficients μ_1, μ_2, μ_3 and ζ determine the weights of the corresponding terms.

The objective function is minimized by a least-squares algorithm. Since the VTI parameters are updated at each grid point, which makes the inversion time-consuming, we parallelize our algorithm. Common-image gathers for each reflector are computed on different cores, and flattening of PP and SS events is performed simultaneously.

3 APPLICATION TO FIELD DATA

3.1 Description of Volve field and OBS survey

Volve field is a Middle Jurassic oil reservoir located in the southern part of the Viking Graben in the gas/condensate-rich Sleipner area of the North Sea. It is a small dome-shaped structure formed by the collapse of adjacent salt ridges during the Jurassic (Szydlik et al., 2007). The reservoir is in the Middle Jurassic Hugin Sandstone Formation and the deposition was controlled by salt tectonics.

An ocean-bottom seismic (OBS) survey at Volve field was acquired in 2002 over a 12.3 km × 6.8 km area. It is comprised of six swaths of four-component (4C) data and each swath includes two 6 km-long cables placed on the seafloor. The cables have a 400 m spacing and move up 800 m after each swath. There are 240 receivers with an interval of 25 m on each cable. Dual-source flip-flop shooting gave a 25 m shot separation and 100 m separation between sail lines.

The PP and PS OBS data were preprocessed using a standard sequence including wavelet shaping, noise and multiple attenuation techniques (Szydlik et al., 2007). The VTI model produced by Statoil for prestack depth imaging is built using a layer-stripping approach. Each layer is updated by applying layer-based tomography and fitting check-shot data (Szydlik et al., 2007). The algorithm involves iterative flattening of common-image gathers and minimization of the misties between seismic and well data. However, complete information about the VTI model-building process employed by Statoil is unavailable to us.

3.2 Processing/inversion of PP and PS data

We use a 2D section from the 3D PP- and PS-wave data recorded by the cable laid along $y=2.8$ km. PP-waves from the same line were processed by Wang (2012), who built a TTI model using reflection tomography. Two adjacent source lines ($y=2.8\pm0.025$ km) include 481 shots with a shot interval of 25 m.

The joint MVA of PP- and PS-waves described above is applied to the CIGs from $x=3$ km to 9 km with an interval of 100 m. The initial model for the parameters V_{P0}, ϵ, and δ is taken from Wang (2012), who divided the section into eight layers based on key geologic horizons and applied nonhyperbolic moveout analysis in combination with check shots in two nearby wells. Since check-shot data for shear waves were not available, a smoothed version of the shear-wave vertical-velocity model provided by Statoil is used here as the initial V_{S0}-field. The parameters V_{P0}, V_{S0}, ϵ, and δ are defined on a 100 m × 50 m grid (Figure 1).

The PP and PS images migrated with the initial model are shown in Figure 2. There is a clearly visible mistie between the PP and PS sections for a reflector at a depth close to 2.5 km (top of the Cretaceous Unit); the depth of that reflector is smaller on the PS image. As expected, the CIGs of PP- and SS-waves obtained with the initial model parameters exhibit substantial residual moveout.

To apply the PP+PS=SS method, we registered (correlated) five events on the PP and PS stacked sections. For each of these five events pure shear data were constructed by convolving the computed SS traveltimes with a Ricker wavelet. The codepthing term in the objective function (equation 1) in-

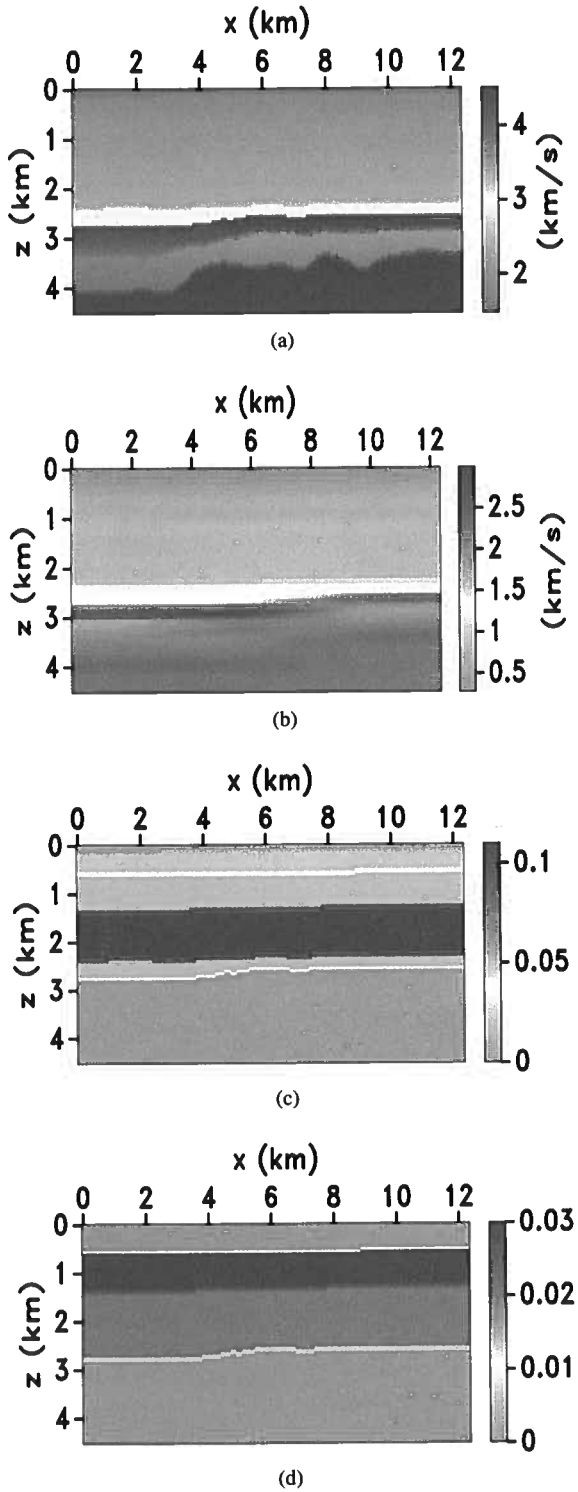

Figure 1. Initial VTI model for line y=2.8 km from the Volve survey. The vertical velocities (a) V_{P0} and (b) V_{S0} and the anisotropy parameters (c) ϵ and (d) δ.

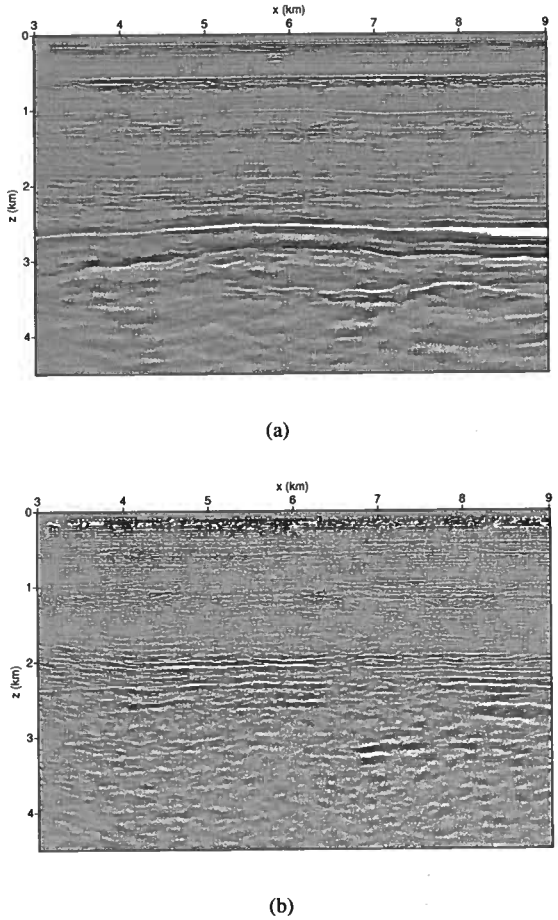

Figure 2. (a) PP- and (b) PS-wave images generated by Kirchhoff prestack depth migration with the initial model from Figure 1.

cludes the depths of these five reflectors on the PP and SS sections.

Because of the limited offset-to-depth ratio (smaller than 1.2 for z >3 km), the accuracy of the effective parameters η and ϵ estimated from nonhyperbolic moveout (i.e., long-spread CIGs) decreases with depth. Therefore, the deeper part of the section (z > 3 km) is kept isotropic during model updating. The VTI model obtained after eight iterations of joint MVA of PP- and PS-waves (Figure 3) yields relatively flat PP and SS CIGs and depth-consistent PP and SS images.

3.3 Images obtained with the inverted VTI model

The PS-wave depth image generated with the estimated VTI model is displayed in Figure 4. Compared with the section obtained using the initial model (Figure 2(b)), reflectors on the final image are better focused, especially at depths around 3 km (Cretaceous unit). However, the image quality below the Base Cretaceous unconformity is still lower than that for PP-waves (Figure 4(a)). This is probably because the deeper layers were

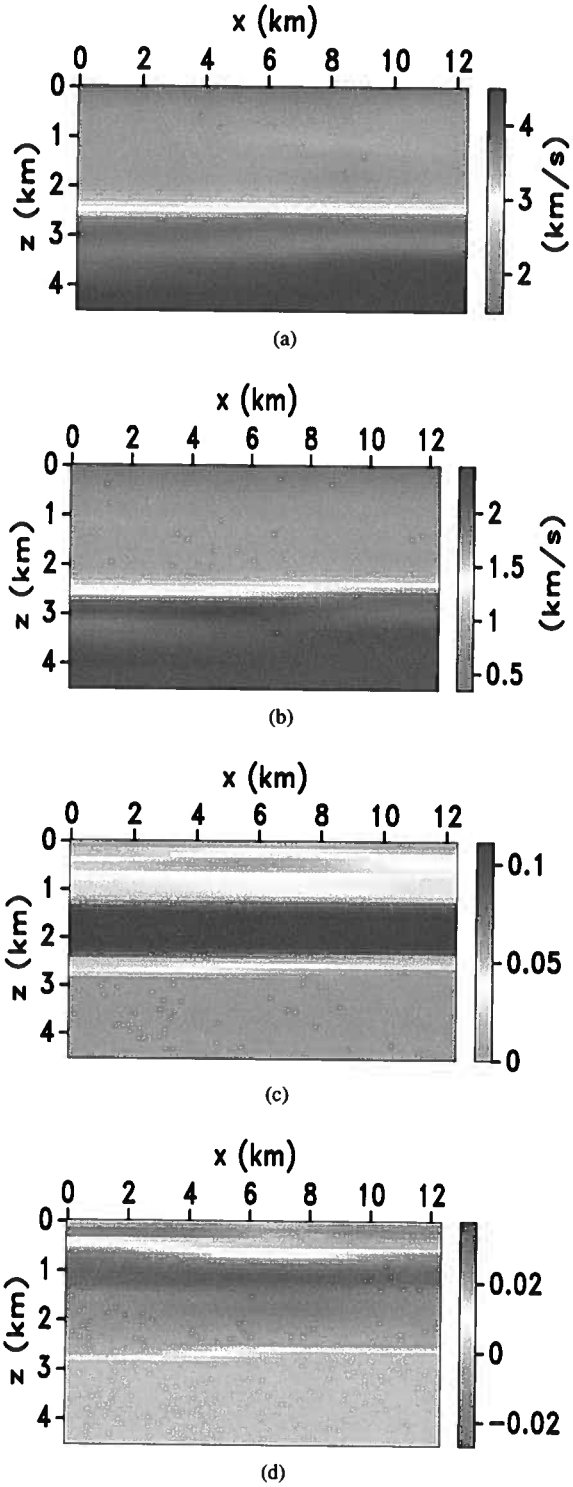

Figure 3. Estimated VTI model for line y=2.8 km from the Volve survey. The vertical velocities (a) V_{P0} and (b) V_{S0} and the anisotropy parameters (c) ϵ and (d) δ.

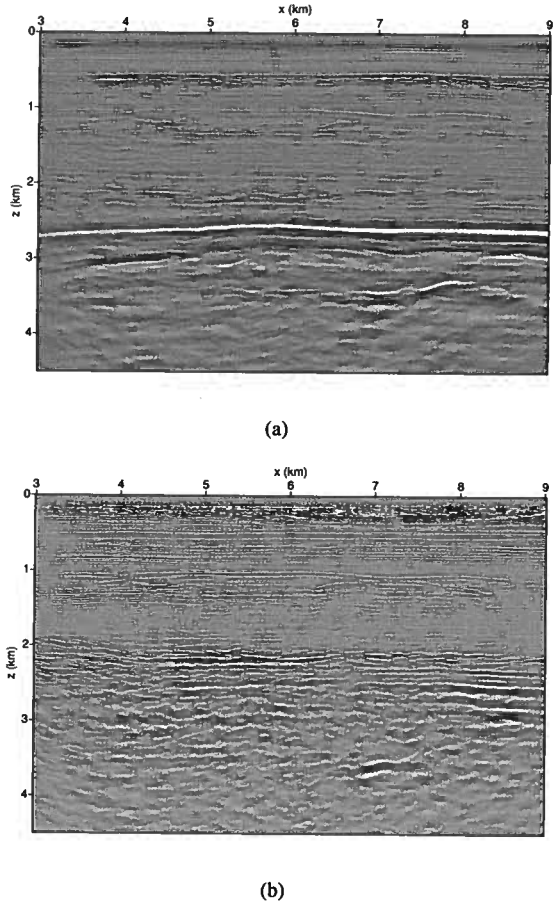

Figure 4. (a) PP- and (b) PS-wave depth images generated with the estimated model from Figure 3.

kept isotropic during MVA, and PS-waves are more sensitive to anisotropy than PP-waves.

The final PP image (Figure 4(a)) does not differ much from that obtained by Wang (2012) using P-wave tomography. However, the reflectors in the Cretaceous unit look somewhat less coherent than those imaged by Wang (2012). One possible reason is that we used a smaller number of reflectors in building the velocity model. Also, although the dips are gentle, the TTI model employed by Wang (2012) is more geologically plausible than VTI and may yield more accurate anisotropy parameters. It is likely that better PP and PS depth images can be obtained with a TTI model, but the current version of the algorithm does not allow for a tilt of the symmetry axis.

We were able to tie the PP depth image with the PS depth image down to Base Cretaceous unconformity (the deepest event used to generate SS data). These depth-consistent PP and PS images provide a robust estimate of the V_{P0}/V_{S0} ratio, which can be used for reservior characterization.

The final PP- and PS-wave images in Figure 4 are similar to those obtained with the VTI model provided by Statoil. It should be mentioned, however, that Statoil's parameter fields have a higher spatial resolution than the model in Figure

3 because our updating procedure operated only with reflection data. Clearly, there is still depth uncertainty in our images, which can be reduced by including borehole (e.g., VSP) information.

4 CONCLUSIONS

We carried out anisotropic processing of PP and PS data from Volve field in the North Sea using reflection tomography and Kirchhoff prestack depth migration. To avoid problems caused by the moveout asymmetry and other inherent features of mode conversions, PS-waves were replaced in velocity analysis with pure SS reflections generated by the PP+PS=SS method.

Registration (correlation) of the PP and PS sections helped identify five events that were used to compute the traveltimes of the corresponding SS-waves. Model updating was performed by flattening PP and SS image gathers and tying the five interfaces in depth on the migrated PP and SS images. The inverted sections of the parameters V_{P0}, V_{S0}, ϵ, and δ have a somewhat lower resolution than the corresponding sections obtained by Statoil with the help of borehole data. Nevertheless, the quality of the migrated images computed with our and Statoil's models is similar. The limited offset range of the survey did not allow us to estimate the anisotropy parameters below 3 km, which hampered the focusing of the deeper reflectors. It should be emphasized that the PP and PS sections are tied in depth down to the Base Cretaceous unconformity (the deepest event used to construct SS data).

Further improvement can be achieved by including walkaway VSP or other borehole data in the tomographic inversion and taking into account a possible tilt of the symmetry axis. On the whole, however, this case study demonstrates that combining PP-waves with mode conversions in anisotropic tomography results in depth-consistent PP and PS images, increases the accuracy of VTI velocity models, and provides estimates of the V_{P0}/V_{S0} ratio for lithology prediction and reservoir characterization.

5 ACKNOWLEDGMENTS

We would like to thank Statoil ASA and the Volve license partners ExxonMobil E&P Norway and Bayerngas Norge for the release of the Volve data. The viewpoints about the Volve data in this paper are of the authors and do not necessarily reflect the views of Statoil ASA and the Volve license partners. We also acknowledge the helpful suggestions of Marianne Houbiers of Statoil. We are grateful to our colleagues from the Center for Wave Phenomena (CWP) for valuable technical assistance. The support for this work was provided by the Consortium Project on Seismic Inverse Methods for Complex Structures at CWP.

REFERENCES

Audebert, F., P. Y. Granger, and A. Herrenschmidt, 1999, CCP-scan technique (1): True common conversion point sorting and converted wave velocity analysis solved by PP and PS Pre-Stack Depth Migration: SEG Technical Program Expanded Abstracts, **18**, 1186–1189.

Broto, K., A. Ehinger, J. H. Kommedal, and P. G. Folstad, 2003, Anisotropic traveltime tomography for depth consistent imaging of PP and PS data: The Leading Edge, 114–119.

Cai, P., and I. Tsvankin, 2012, Joint migration velocity analysis of PP- and PS- waves for VTI media: CWP Research Report (CWP-715).

Foss, S.-K., B. Ursin, and M. V. de Hoop, 2005, Depth-consistent reflection tomography using PP and PS seismic data: Geophysics, **70**, U51–U65.

Grechka, V., and I. Tsvankin, 2002, PP+PS=SS: Geophysics, **67**, 1961–1971.

Stopin, A., and A. Ehinger, 2001, Joint PP PS tomographic inversion of the Mahogany 2D 4-C OBC seismic data: SEG Technical Program Expanded Abstracts, **20**, 837–840.

Szydlik, T., P. Smith, S. Way, L. Aamodt, and C. Friedrich, 2007, 3d pp/ps prestack depth migration on the volve field: First Break, **25**, 43–47.

Tsvankin, I., 2005, Seismic signatures and analysis of reflection data in anisotropic media, 2nd ed.: Elsevier Science Publishing Company, Inc.

Tsvankin, I., and V. Grechka, 2011, Seismology of azimuthally anisotropic media and seismic fracture characterization: Society of Exploration Geophysicists.

Wang, X., 2012, Anisotropic velocity analysis of p-wave reflection and borehole data: PhD thesis, Colorado School of Mines.

Wang, X., and I. Tsvankin, 2010, Stacking-velocity inversion with borehole constraints for tilted TI media: Geophysics, **75**, D69–D77.

———, 2013, Ray-based gridded tomography for tilted transversely isotropic media: Geophysics, **78**, C11–C23.

Kirchhoff modeling for attenuative anisotropic media

Bharath Shekar & Ilya Tsvankin
Center for Wave Phenomena, Colorado School of Mines, Golden CO 80401

ABSTRACT
Seismic wave propagation in attenuative media can be efficiently modeled with ray-based methods. Here, we present a methodology to generate reflection data from attenuative anisotropic media using the Kirchhoff scattering integral and summation of Gaussian beams. Green's functions are computed in the reference elastic model by Gaussian-beam summation, and the influence of attenuation is incorporated as a perturbation along the central ray. The reflected wavefield is obtained by substituting the approximate Green's functions into the Kirchhoff scattering integral. Numerical examples for P-waves in transversely isotropic (TI) media with a horizontal reflector demonstrate the accuracy of the method.

Key words: attenuation, anisotropy, Kirchhoff modeling, Gaussian beams

Introduction

Attenuation analysis can provide seismic attributes sensitive to the physical properties of the subsurface. Reliable attenuation measurements have become feasible with acquisition of high-quality reflection and borehole data.

A prerequisite for estimating attenuation coefficients from seismic data is accurate and efficient modeling of wave propagation in attenuative media. The stiffness tensor in attenuative media is complex, which leads to amplitude decay along seismic rays and velocity dispersion. In the presence of attenuation, stress is obtained by convolving the time domain stiffness tensor (called the relaxation tensor) with the strain tensor (Carcione, 1990), which complicates time-domain finite-difference modeling of wave propagation. Further, to simulate a frequency-independent quality factor ("constant-Q" model, e.g., Kjartannson, 1979) it is essential to superimpose various relaxation mechanisms (Xu and McMechan, 1998; Ruud and Hestholm, 2005), thus increasing the cost of finite-difference modeling. The approach based on the Fourier pseudospectral method proposed by Carcione (2011) avoids the computation of relaxation functions, but it is restricted to viscoacoustic media. The reflectivity method (e.g., Schmidt and Tango, 1986) is limited to calculating exact synthetic seismograms for laterally homogeneous (elastic or attenuative) models with plane interfaces.

A computationally efficient alternative is ray tracing, which can generate asymptotic Green's functions in both elastic and attenuative models (Červený, 2001). So-called "complex" ray theory developed for attenuative models treats ray trajectories and parameters computed along the ray as complex quantities (Thomson, 1997; Hanyga and Seredyňska, 2000). However, numerical implementation of "complex" ray theory in seismic modeling is not straightforward. Ray tracing in the presence of attenuation can also be performed using perturbation methods, which involve computation of rays in a reference elastic medium with the influence of attenuation included as a perturbation along the ray (Gajewski and Pšenčik, 1992; Červený and Pšenčik, 2009; Shekar and Tsvankin, 2012).

Synthetic seismograms of reflected waves in heterogeneous media can be computed using the Kirchhoff scattering integral (Chapman, 2004). However, this method typically requires two-point ray tracing, which does not properly describe multivalued traveltimes (multipathing). Alternatively, the asymptotic Green's functions required in the Kirchhoff scattering integral can be generated by summation of Gaussian beams (Bleistein, 2008; Červený, 2001). Gaussian-beam summation can accurately handle multipathing and produce finite-frequency sensitivity kernels for amplitude inversion (Yomogida and Aki, 1987).

Here, we present an algorithm for computing 2.5D ray synthetic seismograms from attenuative anisotropic media. First, we describe the Kirchhoff scattering integral for purely elastic models and show how it should be modified in the presence of attenuation. Then we review the method of summation of Gaussian beams and its application to computation of the asymptotic "two-point" Green's functions in attenuative media. Finally, this methodology is implemented for TI media and its accuracy is illustrated with numerical examples.

Methodology

0.1 Kirchhoff scattering integral

For simplicity, here we describe the computation of synthetic seismograms for a single reflecting interface. Our treatment is restricted to P-waves and does not include P-to-S mode conversions. The sources and receivers are assumed to be distributed on the same surface, which lies above the reflector. Suppose the wavefield is excited by a point force located at $\mathbf{x}_s$ and aligned with the x_k-axis, and the receiver is located at $\mathbf{x}_r$. The nth component of the displacement field in the frequency domain is given by (Červený, 2001):

$$G_{nk}(\mathbf{x}_r,\mathbf{x}_s,\omega) = -\,i\,\omega \int_{\Sigma} \mathcal{W}_{iq}(\mathbf{x}') \times G_{in}(\mathbf{x}',\mathbf{x}_s,\omega)\, G_{qk}(\mathbf{x}',\mathbf{x}_r,\omega)\,\mathrm{d}\Sigma\,, \tag{1}$$

where $\mathbf{x}'$ are points on the scattering surface Σ, and the source- and receiver-side Green's functions, $G_{in}(\mathbf{x}',\mathbf{x}_s,\omega)$ and $G_{qk}(\mathbf{x}',\mathbf{x}_r,\omega)$, are computed for a smoothed medium. The weighting function $\mathcal{W}_{iq}(\mathbf{x}')$ is represented as:

$$\mathcal{W}_{iq}(\mathbf{x}') = a^{(1)}_{ijql}\,(n_j\,p^r_l - n_l\,p^s_j)\,(1+R)\,, \tag{2}$$

where $a^{(1)}_{ijql}$ is the local density-normalized stiffness tensor in the medium above the reflector, n_j is the normal to the reflector, $\mathbf{p}^s$ and $\mathbf{p}^r$ are the source- and receiver-side slowness vectors (respectively) at the scattering point, and R is the PP-wave reflection coefficient.

Equation 1 is valid for an arbitrary scattering surface, and all Green's functions have to be computed in 3D. However, if the medium properties do not vary in the x_2-direction, and the plane $[x_1, x_3]$ is a plane of symmetry, equation 1 can be represented in a 2.5D form. Then the surface integral in equation 1 can be reduced to a line integral by the method of stationary phase (Bleistein, 1984).

Here, we use the results of Bleistein (1986), who evaluates an integral similar to that in equation 1 by the stationary-phase method. The 2.5D version of equation 1 can be obtained as:

$$G_{nk}(\mathbf{x}_r,\mathbf{x}_s,\omega) = -\,i\sqrt{2\,\pi\,\omega}\int_{C,\,x_2=0} \frac{1}{\sigma}\,\mathcal{W}_{iq}(\mathbf{x}') \times G_{in}(\mathbf{x}',\mathbf{x}_s,\omega)\, G_{qk}(\mathbf{x}',\mathbf{x}_r,\omega)\,\mathrm{d}s, \tag{3}$$

where the Green's functions are defined in 2.5D, the scatterer is reduced to the curve C that lies in the $[x_1, x_3]$-plane, $\mathrm{d}s$ is an elementary arc-length along C, and function σ accounts for out-of-plane phenomena:

$$\sigma = \Big[\frac{\partial^2 T(\mathbf{x}',\mathbf{x}_s)}{\partial x_2^2} + \frac{\partial^2 T(\mathbf{x}',\mathbf{x}_r)}{\partial x_2^2}\Big]_{x_2=0}; \tag{4}$$

$T(\mathbf{x}',\mathbf{x}_s)$ is the traveltime from the scatterer to the source and $T(\mathbf{x}',\mathbf{x}_r)$ is the traveltime from the scatterer to the receiver. The second-order spatial derivatives of the traveltime functions may be calculated from dynamic ray tracing.

Equations 1-4 can be extended to attenuative media by making the stiffness tensor complex and replacing the elastic Green's functions with their viscoelastic counterparts. Although the reflection coefficient and slowness vector also become complex in attenuative media, we compute these quantities for the reference elastic medium. With the exception of anomalously high attenuation, plane-wave reflection coefficients are not significantly distorted by attenuation (Behura and Tsvankin, 2009). While the complex-valued slowness vectors at the reflector can somewhat alter the weighting function defined in equation 2, they do not significantly contribute to the displacement computed from equation 3 because attenuation is mostly a propagation phenomenon.

0.2 Asymptotic Green's function as a sum of Gaussian beams

Although the Green's functions in equation 3 can be computed by two-point ray tracing (Bulant, 1996), that method cannot accurately handle multipathing. A more rigorous approach to modeling asymptotic Green's functions involves summation of Gaussian beams (Červený, 2001). Here, we start with the computation of 2.5D elastic Green's functions and then describe the modifications needed for extending the methodology to attenuative media.

The Green's function $\mathbf{G}(\mathbf{x}',\mathbf{x}_s,\omega)$ can be found as the following sum of Gaussian beams (Červený, 2001):

$$\mathbf{G}(\mathbf{x}',\mathbf{x}_s,\omega) = \int \Phi(\gamma_1)\,\mathbf{u}_{GB}(R_0(\gamma_1))\,\mathrm{d}\gamma_1\,, \tag{5}$$

where $\mathbf{u}_{GB}(R_0(\gamma_1))$ represents a single Gaussian beam concentrated around a central ray $R_0(\gamma_1)$, $\Phi(\gamma_1)$ is a weighting function, and γ_1 is an initial value of a certain ray parameter (e.g., of the phase angle). Suppose that the ray $R_0(\gamma_1^0)$ illuminates a point close to $\mathbf{x}'$. The range of integration is then chosen to be symmetric over γ_1^0, and the Green's function is obtained by summation over a fan of beams that originate at the source location $\mathbf{x}_s$ and illuminate a region around $\mathbf{x}'$.

To evaluate the contribution of $\mathbf{u}_{GB}(R_0(\gamma_1))$ to $\mathbf{G}(\mathbf{x}',\mathbf{x}_s,\omega)$, we consider the point $\mathbf{x}''$ closest to $\mathbf{x}'$ on the central ray R_0. Then the contribution of $\mathbf{u}_{GB}(R_0(\gamma_1))$ to $\mathbf{G}(\mathbf{x}',\mathbf{x}_s,\omega)$ is (Červený and Pšenčík, 2010):

$$\mathbf{u}_{GB}(\mathbf{x}'',\mathbf{x}_s,\omega) = \frac{c(\mathbf{x}_s)}{c(\mathbf{x}'')}\,\mathbf{g}(\mathbf{x}'') \times \frac{1}{\sqrt{\det \tilde{\mathbf{W}}(\mathbf{x}'',\mathbf{x}_s)}}\,e^{-i\,\omega\,\tilde{T}(\mathbf{x}',\mathbf{x}_s)}\,, \tag{6}$$

where c is the phase velocity, $\mathbf{g}$ is the polarization vector,

and $\tilde{T}(\mathbf{x}', \mathbf{x}_s)$ is the complex traveltime:

$$\tilde{T}(\mathbf{x}', \mathbf{x}_s) = T(\mathbf{x}'', \mathbf{x}_s) + (\mathbf{x}' - \mathbf{x}'')^T \mathbf{p}(\mathbf{x}'') + \frac{1}{2}(\mathbf{x}' - \mathbf{x}'')^T \tilde{\mathbf{M}}^x (\mathbf{x}' - \mathbf{x}''), \quad (7)$$

where the superscripts "T" denotes the transpose, $\mathbf{p}$ is the slowness vector, and $\tilde{\mathbf{M}}^x$ is the complex-valued matrix of the second derivatives of the traveltime in the Cartesian coordinates. The matrix $\tilde{\mathbf{M}}^x$ is found by transforming the matrix $\tilde{\mathbf{M}}$ defined in Appendix A (equation 11) to the Cartesian coordinates (Červený and Pšenčik, 2010). The matrix $\tilde{\mathbf{W}}(\mathbf{x}'', \mathbf{x}_s)$ depends on the initial value $\tilde{\mathbf{M}}_0$ of the complex-valued matrix $\tilde{\mathbf{M}}$:

$$\tilde{\mathbf{W}}(\mathbf{x}'', \mathbf{x}_s) = \mathbf{Q}_1(\mathbf{x}'', \mathbf{x}_s) + \mathbf{Q}_2(\mathbf{x}'', \mathbf{x}_s)\,\tilde{\mathbf{M}}_0, \quad (8)$$

where the matrices $\mathbf{Q}_1$ and $\mathbf{Q}_2$ are computed by dynamic ray tracing in the ray-centered coordinates (see Appendix A). The matrix $\tilde{\mathbf{M}}_0$ is given by:

$$\tilde{\mathbf{M}}_0 = \frac{i}{l\,\omega^2}\,\mathbf{I}, \quad (9)$$

where $\mathbf{I}$ is the identity matrix, and l represents the beam width. In anisotropic media, the beam width can be chosen as (Alkhalifah, 1995):

$$l = \frac{V_{\text{avg}}}{f_{\text{min}}}, \quad (10)$$

where V_{avg} represents the average of the horizontal and vertical phase velocities over the entire model, and f_{min} is the minimum frequency of the source signal.

The weighting function $\Phi(\gamma_1)$ (equation 5) can be found from the matrices $\mathbf{Q}_2$, $\mathbf{M}$, and $\tilde{\mathbf{M}}$ (Červený, 2001):

$$\Phi(\gamma_1) = \sqrt{\frac{\omega}{2\pi}}\left|\det \mathbf{Q}_2(\mathbf{x}'', \mathbf{x}_s)\right| \times \sqrt{\det\left[\mathbf{M}(\mathbf{x}'', \mathbf{x}_s) - \tilde{\mathbf{M}}(\mathbf{x}'', \mathbf{x}_s)\right]}. \quad (11)$$

The real-valued matrices $\mathbf{Q}_2$ and $\mathbf{M}$ are computed by dynamic ray tracing with point-source initial conditions (Appendix A), and the complex-valued matrix $\tilde{\mathbf{M}}$ is computed from equation 11, Appendix A.

In attenuative media, equation 5 can be modified to obtain the viscoelastic Green's function $\mathbf{G}^{\text{att}}(\mathbf{x}', \mathbf{x}_s, \omega)$ (Červený, 1985):

$$\mathbf{G}^{\text{att}}(\mathbf{x}', \mathbf{x}_s, \omega) = \int \Phi(\gamma_1)\,\mathbf{u}^{\text{att}}_{GB}(R_0(\gamma_1))\,\mathrm{d}\gamma_1. \quad (12)$$

The weighting function $\Phi(\gamma_1)$ remains unchanged (equation 11), whereas the Gaussian-beam displacement $\mathbf{u}^{\text{att}}_{GB}(R_0)$ becomes

$$\mathbf{u}^{\text{att}}_{GB}(R_0(\gamma_1)) = \mathbf{u}_{GB}(R_0(\gamma_1))\,e^{-\omega\, t^*(\mathbf{x}', \mathbf{x}_s)}, \quad (13)$$

where $\mathbf{u}_{GB}(R_0(\gamma_1))$ is the Gaussian beam computed for the reference elastic medium. The real-valued quantity $t^*(\mathbf{x}', \mathbf{x}_s)$, called the "dissipation factor" (Gajewski and Pšenčik, 1992), accounts for the attenuation-induced amplitude decay along the central ray. The dissipation factor can be calculated using perturbation methods (Červený and Pšenčik, 2009; Shekar and Tsvankin, 2012).

0.3 Implementation

The reflected wavefields in attenuative heterogeneous media are calculated using equation 3 with the source-to-scatterer and scatterer-to-receiver Green's functions obtained from equation 6. The Gaussian beams (equation 7) are computed in the reference elastic medium with the dissipation factor found as a perturbation along the central ray (Červený and Pšenčik, 2009; Shekar and Tsvankin, 2012). The weighting function $\Phi(\gamma_1)$ for the summation of Gaussian beams is also calculated in the reference elastic medium. Likewise, the weighting functions σ and $\mathcal{W}_{iq}$ for the Kirchhoff integral (equation 3) are found from the quantities stored during the modeling of Gaussian beams in the elastic background. For TI models, the reflection coefficient R in equation 2 is obtained from the weak-contrast, weak-anisotropy approximation presented by Rüger (1997).

The outlined method involves a number of approximations. The Kirchhoff scattering integral itself is an asymptotic solution that ignores multiple scattering (Chapman, 2004). The method of summation of Gaussian beams is limited to computing asymptotic Green's functions in smooth media. The influence of attenuation is modeled using perturbation theory, which is valid for weakly-to-moderately dissipative media. Numerical examples illustrating the accuracy of the perturbation approach can be found in Shekar and Tsvankin (2012).

Numerical examples

First, we verify the accuracy of the Gaussian beam summation method in constructing the asymptotic Green's function. Figure 1 compares the displacements computed from perturbation ray theory (U_{ART}) and Gaussian beam summation (U_{GB}) for a homogeneous VTI model. Even though the medium is strongly dissipative with the P- and S-wave vertical quality factors equal to 10, perturbation theory is sufficiently accurate (Shekar and Tsvankin, 2012), and the two displacements are close to one another.

Next, we test the accuracy of the Kirchhoff scattering integral combined with the Gaussian beam summation method in generating reflection data. Table 1 displays the velocity and attenuation parameters for a laterally homogeneous VTI medium above a horizontal reflector. The exact reflected wavefield (Figure 2a) was generated using the reflectivity method (Mallick and Frazer, 1990). The data computed by the Kirchhoff scattering integral (Figure 2b) have a similar amplitude but

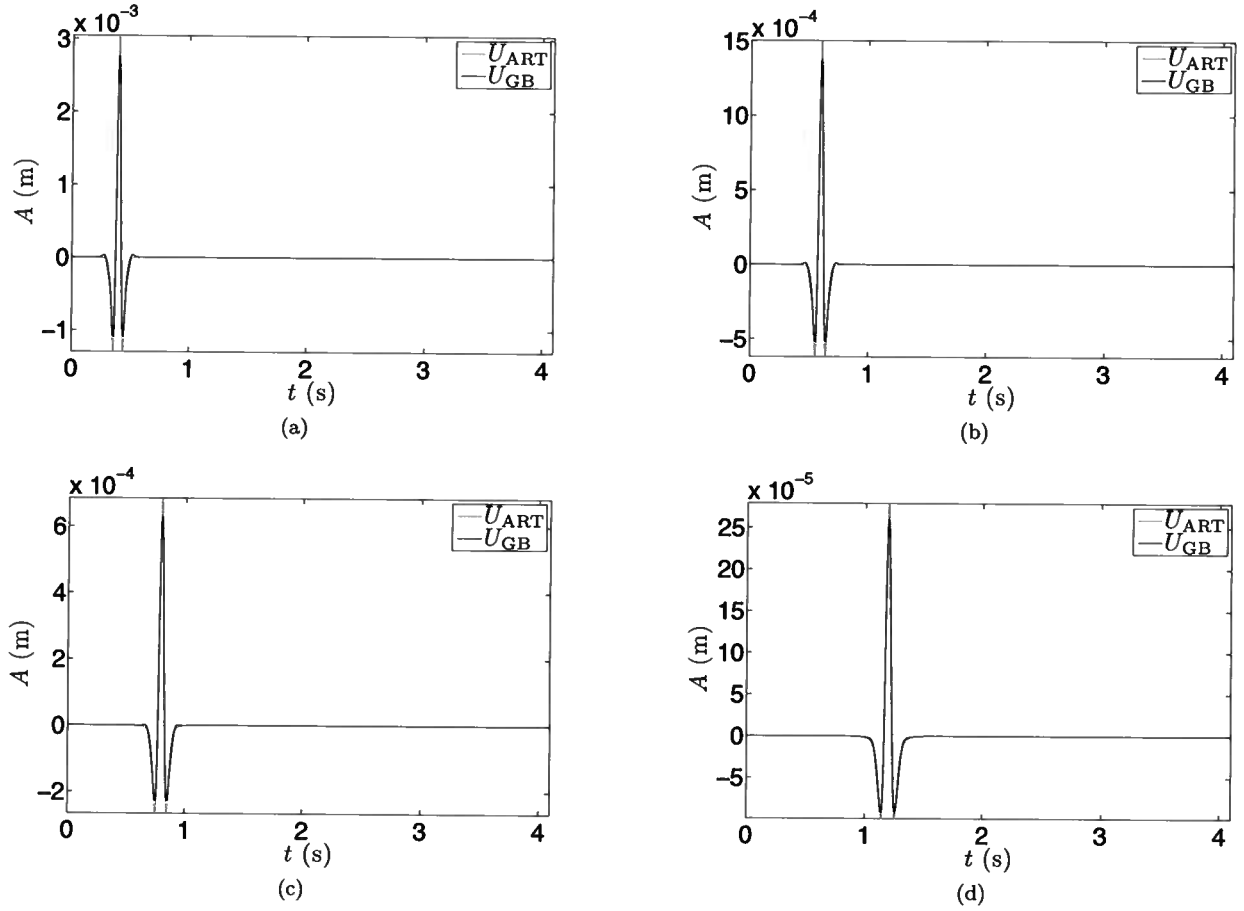

Figure 1. Comparison of the vertical displacement component computed using perturbation ray theory (U_{ART}, red line) and Gaussian-beam summation method (U_{GB}, black line) for group angles with the vertical of (a) 0°, (b) 30°, (c) 60°, and (d) 90°. The model is homogeneous VTI with the P-wave vertical velocity $V_{P0} = 2.0$ km/s, S-wave vertical velocity $V_{S0} = 1.0$ km/s, and anisotropy parameters $\epsilon = 0.4$ and $\delta = 0.25$. The P-wave vertical quality factor is $Q_{P0} = 10$, S-wave vertical quality factor $Q_{S0} = 10$, and the attenuation-anisotropy parameters (defined in Zhu and Tsvankin, 2006) are $\epsilon_Q = -0.45$ and $\delta_Q = -0.50$. The wavefield is excited by a vertical point force; the source signal is a Ricker wavelet with a central frequency of 10 Hz.

lower frequency content than the seismograms in Figure 2a because the Gaussian beam summation method yields finite-frequency Green's functions. The Kirchhoff scattering integral also produces spurious events near both ends of the receiver array, so these traces have been muted out.

Conclusions

We introduced a ray-based methodology for computing synthetic seismograms of reflected waves from attenuative anisotropic media. The wavefield is generated with the Kirchhoff scattering integral that includes 2.5D asymptotic Green's functions computed using Gaussian beam summation and perturbation theory.

The accuracy of the Gaussian-beam summation method in producing Green's functions was verified for highly attenuative TI media. We also compared the Kirchhoff scattering integral with the exact seismograms computed using the reflectivity method. The examples confirm that the proposed technique adequately models P-wave reflections even in the presence of strong anisotropic attenuation. However, the frequency content of the data produced by the Kirchhoff scattering integral is lower than that of the exact seismograms.

Acknowledgments

We are grateful to the members of the A(nisotropy)-Team of the Center for Wave Phenomena (CWP), Colorado School of Mines, for fruitful discussions. Support for this work was provided by the Consortium Project on Seismic Inverse Methods for Complex Structures at CWP.

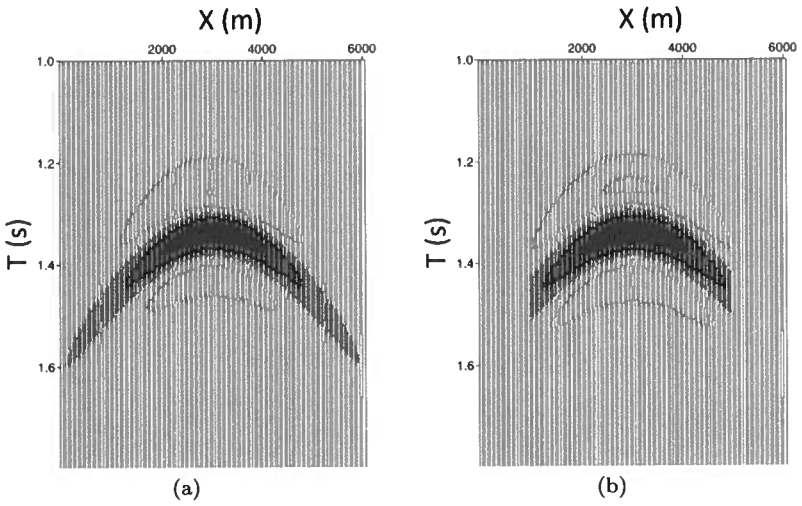

Figure 2. Vertical displacement for the model in Table 1 generated using (a) the reflectivity method and (b) the Kirchhoff scattering integral. The wavefield is excited and recorded on top of the model. The source is a vertical force at $X = 3.0$ km and the receivers are placed between $X = 0.5$ km and $X = 5.5$ km with a 50 m increment. The source signal is a Ricker wavelet with a central frequency of 10 Hz.

	Top layer	Bottom half-space
Thickness (km)	2.00	–
V_{P0} (km/s)	3.00	3.20
V_{S0} (km/s)	1.50	1.60
ϵ	0.20	0.10
δ	0.10	0.05
Q_{P0}	10	10
Q_{S0}	10	10
ϵ_Q	0.0	0.0
δ_Q	0.0	0.0

Table 1. Synthetic VTI model used to test the Kirchhoff scattering integral. The P-wave is reflected from a horizontal interface between the two media.

REFERENCES

Alkhalifah, T., 1995, Gaussian beam depth migration for anisotropic media: Geophysics, **60**, 1474–1484.

Bleistein, N., 1984, Mathematical Methods for Wave Phenomena: Academic Press.

———, 1986, Two-and-one-half dimensional in-plane wave propagation: Geophysical Prospecting, **34**, 686–703.

———, 2008, Seismic wavefields in layered isotropic media (course notes): CWP, Colorado School of Mines (http://www.cwp.mines.edu/norm/ShrtCrse).

Bulant, P., 1996, Amplitude and phase data inversion for phase velocity anomalies in the Pacific Ocean basin: Pure and Applied Geophysics, **148**, 421–447.

Carcione, J., 1990, Wave propagation in anisotropic linear viscoelastic media: theory and simulated wavefields: Geophysics Journal International, **101**, 739–750.

———, 2011, A generalization of the Fourier pseudospectral method: Geophysics, **76**.

Červený, V., 1985, Gaussian beam synthetic seismograms: Journal of Geophysics, **58**, 44–72.

———, 2001, Seismic ray theory: Cambridge University Press.

Červený, V., and L. Klimeš, 2010, Transformation relations for second-derivatives of traveltime in anisotropic media: Studia Geophysica et Geodaetica, **54**, 257–267.

Červený, V., and I. Pšenčik, 2009, Perturbation Hamiltonians in heterogeneous anisotropic weakly dissipative media: Geophysics Journal International, **178**, 939–949.

———, 2010, Gaussian beams in inhomogeneous anisotropic layered structures: Geophysics Journal International, **180**, 798–812.

Chapman, C., 2004, Fundamentals of Seismic Wave Propagation: Cambridge University Press.

Gajewski, D., and I. Pšenčik, 1992, Vector wavefield for weakly attenuating anisotropic media by the ray method: Geophysics, **57**, 27–38.

Hanyga, A., and M. Seredyńska, 2000, Ray tracing in elastic and viscoelastic media: Pure and Applied Geophysics, **157**, 679–717.

Kjartannson, E., 1979, Constant Q-Wave Propagation and Attenuation: Journal of Geophysical Research,

84, 4737–4748.

Mallick, S., and N. L. Frazer, 1990, Computation of Synthetic Seismograms for Stratified Azimuthally Anisotropic Media: Journal of Geophysical Research, **95**, 8513–8526.

Rüger, A., 1997, P-wave reflection coefficients for transversely isotropic models with vertical and horizontal axis of symmetry: Geophysics, **62**, 713–722.

Ruud, B. O., and S. Hestholm, 2005, Modeling seismic waves in orthorhombic, viscoelastic media by finite-differences: 75th Annual International Meeting, SEG, Expanded Abstracts.

Schmidt, H., and G. Tango, 1986, Efficient global matrix approach to the computation of synthetic seismograms: Geophysical Journal of the Royal Astronomical Society, **84**, 331–359.

Shekar, B., and I. Tsvankin, 2012, Attenuation analysis for heterogeneous transversely isotropic media: 82nd Annual International Meeting, SEG, Expanded Abstracts.

Thomson, C. J., 1997, Complex rays and wave packets for decaying signals in inhomogeneous, anisotropic and anelastic media: Studia Geophysica et Geodaetica, **41**, 345–381.

Xu, T., and G. A. McMechan, 1998, Efficient 3-D viscoelastic modeling with application to near-surface land seismic data: Geophysics, **63**, 601–612.

Yomogida, K., and K. Aki, 1987, Amplitude and phase data inversion for phase velocity anomalies in the Pacific Ocean basin: Geophysical Journal of the Royal Astronomical Society, **88**, 161–204.

Zhu, Y., and I. Tsvankin, 2006, Plane-wave propagation in attenuative transversely isotropic media: Geophysics, **71**, no.2, T17–T30.

Appendix A

Dynamic ray tracing and Gaussian beams in anisotropic media

In this section, we briefly review dynamic ray tracing in anisotropic media and introduce the quantities necessary for the construction of Gaussian beams.

The eikonal equation in elastic, anisotropic, heterogeneous media can be written as (Červený, 2001):

$$G(x_i, p_i) = 1\,, \tag{1}$$

where x_i are the spatial coordinates and p_i are the components of the slowness vector. The solutions of equation 1 represent the eigenvalues of the Christoffel equation:

$$\det\left[\Gamma_{ik} - G\,\delta_{ik}\right] = 0\,, \tag{2}$$

where $\Gamma_{ik} = a_{ijkl}\,p_j\,p_l$ are the components of the Christoffel matrix and a_{ijkl} form the density-normalized stiffness tensor.

The kinematic ray-tracing equations are given by (Červený, 2001):

$$\frac{\mathrm{d}x_i}{\mathrm{d}\tau} = \frac{1}{2}\frac{\partial G}{\partial p_i}\,, \tag{3}$$

$$\frac{\mathrm{d}p_i}{\mathrm{d}\tau} = -\frac{1}{2}\frac{\partial G}{\partial x_i}\,, \tag{4}$$

where τ represents the traveltime (eikonal) along the ray.

The dynamic ray tracing system in ray-centered coordinates can be represented as (Červený and Klimeš, 2010):

$$\begin{aligned}\frac{\mathrm{d}Q_{NI}}{\mathrm{d}\tau} &= A_{NM}\,Q_{MI} + B_{NM}\,P_{MI}\,,\\ \frac{\mathrm{d}P_{NI}}{\mathrm{d}\tau} &= -C_{NM}\,Q_{MI} - D_{NM}\,P_{MI}\,,\end{aligned} \tag{5}$$

where the indices N, M, and I vary from 1 to 2. Explicit expressions for matrices $\mathbf{A}$, $\mathbf{B}$, $\mathbf{C}$, and $\mathbf{D}$ can be found in Červený and Klimeš (2010). The matrices Q_{NI} and P_{NI} are defined as

$$Q_{NI} = \frac{\partial q_N}{\partial \gamma_I}\,, P_{NI} = \frac{\partial p_N}{\partial \gamma_I}\,,$$

where γ_I is a certain "ray parameter" (e.g., the initial phase angle of the ray), q_N are the coordinates tangent to the wavefront, and p_N denotes the slowness vector in the ray-centered coordinate system:

$$p_N = \frac{\partial \tau}{\partial q_N}\,. \tag{6}$$

The solution of system 5 for plane-wave initial conditions ($\mathbf{Q} = \mathbf{I}$, $\mathbf{P} = 0$; $\mathbf{I}$ is the identity matrix) is denoted by $\mathbf{Q}_1$ and $\mathbf{P}_1$, and for point-source initial conditions ($\mathbf{Q} = 0$, $\mathbf{P} = \mathbf{I}$) by $\mathbf{Q}_2$ and $\mathbf{P}_2$.

It is convenient to introduce the real-valued matrix $\mathbf{M}$ of the second-order traveltime derivatives:

$$\mathbf{M} = \mathbf{P}\,\mathbf{Q}^{-1}\,. \tag{7}$$

as discussed in the main text (equation 7), the matrix $\mathbf{M}$ is used for computing the paraxial traveltime. For point-source initial conditions, $\mathbf{M}$ is

$$\mathbf{M} = \mathbf{P}_2\,\mathbf{Q}_2^{-1}\,. \tag{8}$$

A Gaussian beam is a solution of system 5 with complex-valued initial conditions (Bleistein, 2008):

$$\mathbf{Q} = \frac{l\,\omega^2}{c_0}\,\mathbf{I}\,,\quad \tilde{\mathbf{P}} = \frac{i}{c_0}\,\mathbf{I}\,, \tag{9}$$

where l is the initial value of the beam width, ω is the angular frequency, and c_0 is the phase velocity at the take-off point. The matrix $\mathbf{M}$ becomes complex-valued:

$$\tilde{\mathbf{M}} = \left[\mathbf{P}_1 + \tilde{\mathbf{M}}_0\,\mathbf{P}_2\right]\left[\mathbf{Q}_1 + \tilde{\mathbf{M}}_0\,\mathbf{Q}_2\right]^{-1}\,, \tag{10}$$

where $\mathbf{P}_1$, $\mathbf{Q}_1$, $\mathbf{P}_2$, and $\mathbf{Q}_2$ are found by dynamic ray tracing. Since $\tilde{\mathbf{M}}$ is complex-valued, the traveltime is complex-valued, which leads to amplitude decay in the direction perpendicular to the central ray. The initial value of $\tilde{\mathbf{M}}$ is

$$\tilde{\mathbf{M}}_0 = \frac{i}{l\,\omega^2}\,\mathbf{I}\,. \tag{11}$$

Point-source radiation in attenuative anisotropic media

Bharath Shekar & Ilya Tsvankin
Center for Wave Phenomena, Colorado School of Mines, Golden CO 80401

ABSTRACT

Important insights into point-source radiation in attenuative anisotropic media can be gained by applying asymptotic methods. Here, we derive the asymptotic Green's function in homogeneous, attenuative, arbitrarily anisotropic media using the steepest-descent method. The saddle-point condition helps describe the behavior of the slowness and group-velocity vectors of the P-, S_1-, and S_2-waves in the far field. We test the accuracy of the asymptotic analysis by comparing it with the ray-perturbation method for P-waves in transversely isotropic media.

Key words: attenuation, anisotropy, aysmptotic analysis, inhomogeneity angle

Introduction

Velocity and attenuation anisotropy significantly influence the radiation pattern of seismic waves excited by a point source. A proper correction for the source directivity can help improve the robustness of AVO (amplitude variation with offset) and attenuation analysis. Point-source radiation in homogeneous anisotropic media has been mostly studied for nonattenuative materials using both asymptotic and numerical methods (e.g. Červený, 2001; Tsvankin, 2012; Gajewski 1993; Wang and Achenbach, 1994). Zhu (2006) presents an analytic and numerical study of point-source radiation in 2D homogeneous attenuative TI media. Vavryčuk (2007) derives the asymptotic Green's function for arbitrarily anisotropic, homogeneous, attenuative models by formally extending the results of Wang and Achenbach (1994).

In attenuative media, the Christoffel matrix becomes complex-valued because the stiffness tensor is complex. Although many results derived for elastic media can be generalized for attenuative media, there are several important differences. In asymptotic analysis for attenuative media, the saddle-point condition involves complex-valued slowness and group-velocity vectors, whose properties have to be clearly defined. Also, the expression for the eigenvalue of the complex Christoffel matrix in Vavryčuk (2007) is inaccurate, which distorts the analytic expression for the Green's function. Here, we present a rigorous derivation of the saddle-point condition and the eigenvalue of the complex Christoffel matrix.

We start by reviewing the definitions of the attenuation coefficient, group velocity, and other key signatures in attenuative media. Then the integral expression for the Green's function in homogeneous attenuative anisotropic media is evaluated by the steepest-descent method. The saddle-point condition is used to study the properties of the far-field P-wave. Finally, we compare the P-wave group velocity, polarization, and slowness vectors obtained from our asymptotic analysis for VTI (transversely isotropic with a vertical symmetry axis) media with those found from ray perturbation theory (Červený and Pšenčík, 2009).

Basic Definitions

In attenuative media, the wave vector is complex-valued (complex quantities are denoted by the tilde sign on top):

$$\begin{aligned}\tilde{\mathbf{k}} &= \mathbf{k}^R + i\,\mathbf{k}^I\,,\\ &= \omega(\mathbf{p}^R + i\,\mathbf{p}^I)\,,\end{aligned} \tag{1}$$

where $\mathbf{p}^R$ and $\mathbf{p}^I$ are the real-valued propagation and attenuation vectors, respectively, which form the slowness vector $\tilde{\mathbf{p}} = \mathbf{p}^R + i\,\mathbf{p}^I$. The orientations of $\mathbf{k}^R$ and $\mathbf{k}^I$ (or equivalently, of $\mathbf{p}^R$ and $\mathbf{p}^I$) can be different, and the angle between $\mathbf{k}^R$ and $\mathbf{k}^I$ is called the "inhomogeneity angle" ξ (Červený et al., 2008; Behura and Tsvankin, 2009; Tsvankin and Grechka, 2011). Plane waves satisfy the wave equation with arbitrary values of ξ, except for certain "forbidden directions" of $\mathbf{p}^I$ (Krebes and Le, 1994; Červený and Pšenčík, 2005; Carcione, 2007). Hence, the angle ξ is treated as a free parameter in plane-wave propagation (Behura and Tsvankin, 2009).

However, for waves excited by point-sources, the inhomogeneity angle is determined by medium properties and boundary conditions (Vavryčuk, 2007; Zhu, 2006). In reflection/transmission problems for plane waves, the inhomogeneity angle is constrained by Snell's law (Hearn and Krebes, 1990; Behura and Tsvankin, 2009).

Zhu and Tsvankin (2006) define the phase attenuation coefficient $\mathcal{A}$ as

$$\mathcal{A} = \frac{|\mathbf{k}^I|}{|\mathbf{k}^R|}. \tag{2}$$

The angle-dependent quality factor Q is given by

$$Q = \frac{1}{2\mathcal{A}}. \tag{3}$$

Červený and Pšenčik (2008) show that the group attenuation coefficient responsible for attenuation-related amplitude decay along seismic rays can be written as:

$$\mathcal{A}^{\mathrm{gr}} = \frac{\mathbf{p}^I \cdot \mathbf{F}^R}{\mathbf{p}^R \cdot \mathbf{F}^R}, \tag{4}$$

where $\mathbf{F}^R$ denotes the real part of the Poynting vector. The complex-valued Poynting vector characterizes the direction of energy flux, and its real part coincides with the group velocity vector:

$$F_i^R = \kappa\, \mathrm{Re}\big[\tilde{a}_{ijkl}\, \tilde{p}_l\, \tilde{g}_j^*\, \tilde{g}_l\big], \tag{5}$$

where κ is a constant, $\tilde{a}_{ijkl}$ are the complex-valued density-normalized stiffness coefficients, and $\tilde{g}_j$ are the components of the complex-valued polarization vector $\tilde{\mathbf{g}}$ that satisfies $\tilde{\mathbf{g}}^* \cdot \tilde{\mathbf{g}} = 1$; the asterisk "$*$" denotes the complex conjugate. Behura and Tsvankin (2009) prove that the group attenuation coefficient is practically independent of the inhomogeneity angle and coincides with the phase attenuation coefficient for $\xi = 0$, except for the vicinity of the forbidden directions. Similar results follow from the perturbation analysis presented by Červený and Pšenčik (2009).

Asymptotic Green's function in homogeneous attenuative anisotropic media

Here, we derive the asymptotic Green's function for P- and S-waves in a homogeneous, attenuative, arbitrarily anisotropic medium. The analysis is valid for all three wave modes (P, S_1, S_2), but breaks down in the vicinity of shear-wave singularities where the Christoffel equation has degenerate (coincident) eigenvalues.

The exact Green's function can be found from the wave equation as (Appendix A, equation 30):

$$G_{kn}(\mathbf{x}, \mathbf{x}^0, \omega) = \frac{i\omega}{(2\pi)^2} \int_{-\infty}^{\infty}\int_{-\infty}^{\infty} \Big[\frac{\tilde{S}_{kn}}{\partial[\det(\tilde{\mathbf{\Gamma}} - \mathbf{I})]/\partial p_3}\Big]_{p_3 = \tilde{p}_3^r} \times e^{-\omega R \tilde{\phi}}\, \mathrm{d}p_1\, \mathrm{d}p_2, \tag{6}$$

where

$$\tilde{\phi} = -i\,(p_1 \hat{x}_1 + p_2 \hat{x}_2 + \tilde{p}_3^r \hat{x}_3), \tag{7}$$

$R = \sqrt{[(x_1 - x_1^0)^2 + (x_2 - x_2^0)^2 + (x_3 - x_3^0)^2]}$ is the source-receiver distance, $\hat{x}_i$ is the unit vector in the source-receiver direction, p_j are the slowness components, $\tilde{\Gamma}_{ik} = \tilde{a}_{ijkl}\, p_j\, p_l$, and S_{kn} are the cofactors of the matrix $\tilde{\mathbf{\Gamma}} - \mathbf{I}$, $\mathbf{I}$ is the identity matrix. The solution of the equation $\det[\tilde{a}_{ijkl}\, p_j\, p_l - \delta_{ik}] = 0$ is denoted as $\tilde{p}_3^r = \tilde{p}_3(p_1, p_2)$.

The components of the slowness vector satisfy the following equation:

$$\det[\tilde{a}_{ijkl} p_j p_l - G\, \delta_{ik}] = 0, \tag{8}$$

where

$$G(p_i, x_i) = 1 \tag{9}$$

is the eigenvalue of the matrix $\tilde{\Gamma}_{ik} = \tilde{a}_{ijkl} p_j p_l$. Equations 8 or 9 represent the eikonal equation in anisotropic media (Červený, 2001). The eigenvector $\tilde{U}_i$ corresponding to the eigenvalue G is the polarization vector that satisfies the following equation:

$$\tilde{\Gamma}_{ik}\, \tilde{U}_k = G\, \tilde{U}_i. \tag{10}$$

If we assume that $\omega R/v$ (where v is a certain average of the group velocity) is a large parameter, G_{kn} (equation 6) can be evaluated by steepest-descent integration near the saddle point (Bleistein, 1984). The saddle-point condition is

$$\frac{\partial \tilde{\phi}}{\partial p_1} = \frac{\partial \tilde{\phi}}{\partial p_2} = 0, \tag{11}$$

i.e.,

$$\begin{aligned} \hat{x}_1 + \hat{x}_3 \Big[\frac{\partial \tilde{p}_3(p_1, p_2)}{\partial p_1}\Big]_{\tilde{p}_1^s, \tilde{p}_2^s} &= 0, \\ \hat{x}_2 + \hat{x}_3 \Big[\frac{\partial \tilde{p}_3(p_1, p_2)}{\partial p_2}\Big]_{\tilde{p}_1^s, \tilde{p}_2^s} &= 0, \end{aligned} \tag{12}$$

where $(\tilde{p}_1^s, \tilde{p}_2^s)$ denotes the saddle point. The partial derivatives in equation 12 can be calculated from the function G (equation 9) using the implicit function theorem (Courant, 1988). Then equation 12 becomes:

$$\begin{aligned} \hat{x}_1 \Big[\frac{\partial G}{\partial p_3}\Big]_{\tilde{p}_1^s, \tilde{p}_2^s} - \hat{x}_3 \Big[\frac{\partial G}{\partial p_1}\Big]_{\tilde{p}_1^s, \tilde{p}_2^s} &= 0, \\ \hat{x}_2 \Big[\frac{\partial G}{\partial p_3}\Big]_{\tilde{p}_1^s, \tilde{p}_2^s} - \hat{x}_3 \Big[\frac{\partial G}{\partial p_2}\Big]_{\tilde{p}_1^s, \tilde{p}_2^s} &= 0; \end{aligned} \tag{13}$$

$$\frac{\partial G}{\partial p_j} = \frac{\partial \tilde{\Gamma}_{ik}}{\partial p_j} \frac{\tilde{S}_{ik}}{\tilde{S}}. \tag{14}$$

The derivatives $\partial \tilde{\Gamma}_{ik}/\partial p_j$ and $\tilde{S}_{ik}/\tilde{S}$ can be found by substituting the complex-valued stiffness tensor in the definitions of $\partial \Gamma_{ik}/\partial p_j$ and S_{jk}/S given in Červený (1972). Since G is a homogeneous function of second degree in p_j, Euler's homogeneous function theorem yields:

$$p_j \frac{\partial G}{\partial p_j} = 2. \tag{15}$$

Next, we introduce the vector $\tilde{\mathbf{E}}$ as

$$\tilde{E}_j = \frac{1}{2}\frac{\partial G}{\partial p_j}. \tag{16}$$

In elastic media, equation 16 defines the components of the group-velocity vector. In attenuative media, $\tilde{\mathbf{E}}$ has been termed "energy velocity" (Vavryčuk, 2007), with its real part contributing to the traveltime and the imaginary part to energy dissipation. Since the unit vector in the source-receiver direction $\hat{\mathbf{x}}$ is real-valued, equation 13 implies that at the saddle point the vector $\tilde{\mathbf{E}} = \tilde{\beta}\,\hat{\mathbf{x}}$, where $\tilde{\beta}$ is a complex constant. Hence, the real and imaginary parts of the energy-velocity vector are parallel to the vector connecting the source and the receiver (i.e., $\mathrm{Re}\,[\tilde{\mathbf{E}}] \parallel \hat{\mathbf{x}}$ and $\mathrm{Im}\,[\tilde{\mathbf{E}}] \parallel \hat{\mathbf{x}}$).

Evaluating the integral in equation 6 by the method of steepest descent (Bleistein, 2012), we find:

$$G_{kn}(\mathbf{x},\mathbf{x}^0,\omega) = \frac{i}{(2\pi)}\frac{1}{\sqrt{\det\tilde{\boldsymbol{\Phi}}''}} \times \frac{\tilde{S}_{kn}}{\partial[\det(\tilde{\boldsymbol{\Gamma}}-\mathbf{I})]/\partial p_3}\exp(-\omega R\tilde{\phi}), \tag{17}$$

where all quantities are obtained at $(\tilde{p}_1^s,\ \tilde{p}_2^s,\ \tilde{p}_3^r)$, and $\tilde{\boldsymbol{\Phi}}''$ is the Hessian matrix of the partial derivatives of $\tilde{\phi}$ with respect to p_1 and p_2. The matrix $\tilde{\boldsymbol{\Phi}}''$ can be computed from equation 8 using the implicit function theorem. The phase function at the saddle point can be found from equations 7, 13, and 15:

$$\tilde{\phi} = -\frac{i}{\sqrt{E_j^2}}. \tag{18}$$

In the next section, we show that the real part of E_j contributes to the traveltime and the imaginary part to attenuation. For 2D VTI media, equation 17 reduces to the expression for the Green's function derived by Zhu (2006).

Although the asymptotic analysis carried out above is similar to that presented by Vavryčuk (2007), we proved (rather than assumed) that at the saddle point the real and imaginary parts of the "energy-velocity" vector are parallel to each other. To derive expressions for the "energy-velocity" vector and the Gaussian curvature of the slowness surface (which is related to the Hessian matrix obtained by the steepest-descent method), Vavryčuk (2007) uses the following expression for the eigenvalue G:

$$G = \tilde{a}_{ijkl}\,p_j\,p_l\,\tilde{U}_i\,\tilde{U}_k, \tag{19}$$

where $\mathbf{U}$ is the polarization vector (equation 10). Equation 19, however, is not valid for complex symmetric matrices (Horn and Johnson, 1990). Instead, we employed the implicit function theorem to evaluate the "energy-velocity" vector and the Hessian matrix.

Model	1	2	3	4
V_{P0} (km/s)	3.00	3.00	3.00	3.00
V_{S0} (km/s)	1.50	1.50	1.50	1.50
ϵ	0.10	0.40	0.40	0.40
δ	0.005	0.25	0.25	0.25
Q_{P0}	100	100	10	100
Q_{S0}	60	60	10	10
ϵ_Q	-0.20	0.45	0	0
δ_Q	-0.10	-0.50	0	0

Table 1. Homogeneous TI models with anisotropic velocity and attenuation functions. The parameters V_{P0} and V_{S0} are the vertical P- and S-wave vertical velocities, Q_{P0} and Q_{S0} are the vertical P-wave and S-wave quality factors, and ϵ_Q and δ_Q are the attenuation-anisotropy parameters defined in Zhu and Tsvankin (2006).

Numerical Examples

In this section, the analytic results presented above are used to study the behavior of the inhomogeneity angle and the group-velocity and polarization vectors in homogeneous, attenuative VTI media. Table 1 shows the parameters of the velocity and attenuation functions for four VTI models defined in Zhu (2006).

First, we analyze the energy-velocity vector defined in equation 16. Červený et al. (2008) demonstrate that the perturbed group velocity $\tilde{\mathcal{U}}$ in attenuative media is given by

$$\tilde{\mathcal{U}}_i = \left(1 - i\,\mathcal{A}\right)\mathcal{U}_i, \tag{20}$$

where $\mathcal{U}$ is the group-velocity vector in the reference elastic medium and $\mathcal{A}$ is the phase attenuation coefficient computed for a zero inhomogeneity angle in the phase direction that corresponds to the given group direction. The complex-valued energy-velocity vector $\tilde{\mathbf{E}}$ is compared with the perturbed group velocity $\tilde{\mathcal{U}}$ in Figure 1. Both the real and imaginary parts of the vectors coincide, so our solution for $\tilde{\mathbf{E}}$ accurately describes both the traveltime and attenuation along the ray.

Equation 8 and the saddle-point condition (equation 13) can be used to compute the complex-valued slowness vector $\tilde{\mathbf{p}}$ and, hence, the corresponding inhomogeneity angle. For the purpose of numerical computations, it is convenient to parametrize $\tilde{\mathbf{p}}$ in the following way (Červený and Pšenčik, 2005):

$$\tilde{\mathbf{p}} = \tilde{\sigma}\,\mathbf{n} + i\,D\,\mathbf{m}, \tag{21}$$

where the vector $\mathbf{n}$ specifies the phase direction and $\mathbf{m}$ is chosen to be perpendicular to $\mathbf{n}$ (i.e., $\mathbf{n}\cdot\mathbf{m} = 0$).

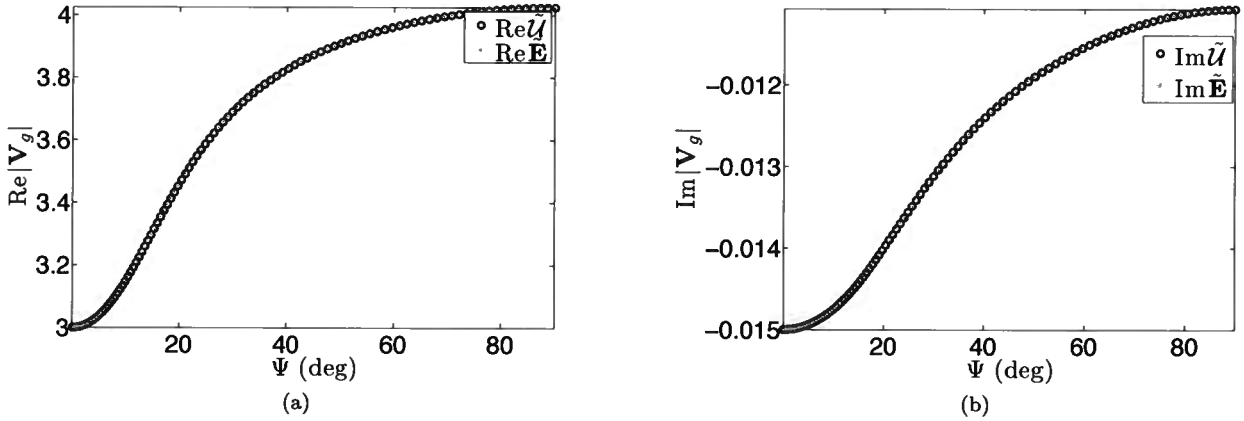

Figure 1. Comparison of the magnitudes of the energy-velocity vector $\tilde{\mathbf{E}}$ (equation 16) and perturbed P-wave group velocity vector $\tilde{\mathcal{U}}$ (equation 20) for model 2 from Table 1. The magnitudes of (a) real and (b) imaginary parts of $|\tilde{\mathcal{U}}|$ and $|\tilde{\mathbf{E}}|$; Ψ is the group angle with the vertical.

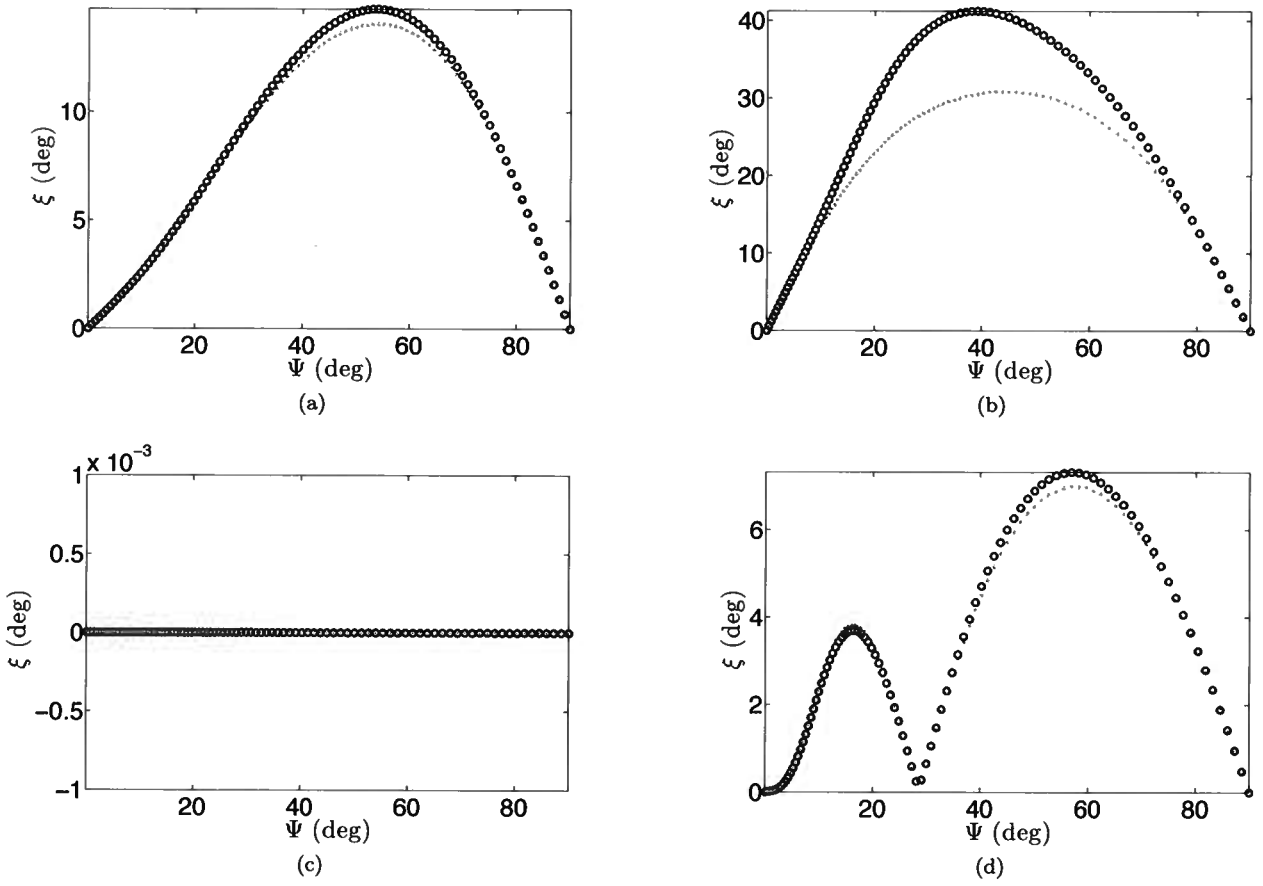

Figure 2. Inhomogeneity angle ξ computed from the asymptotic analysis in this paper (red stars) and ray perturbation theory (black circles) for models (a) 1, (b) 2, (c) 3, and (d) 4.

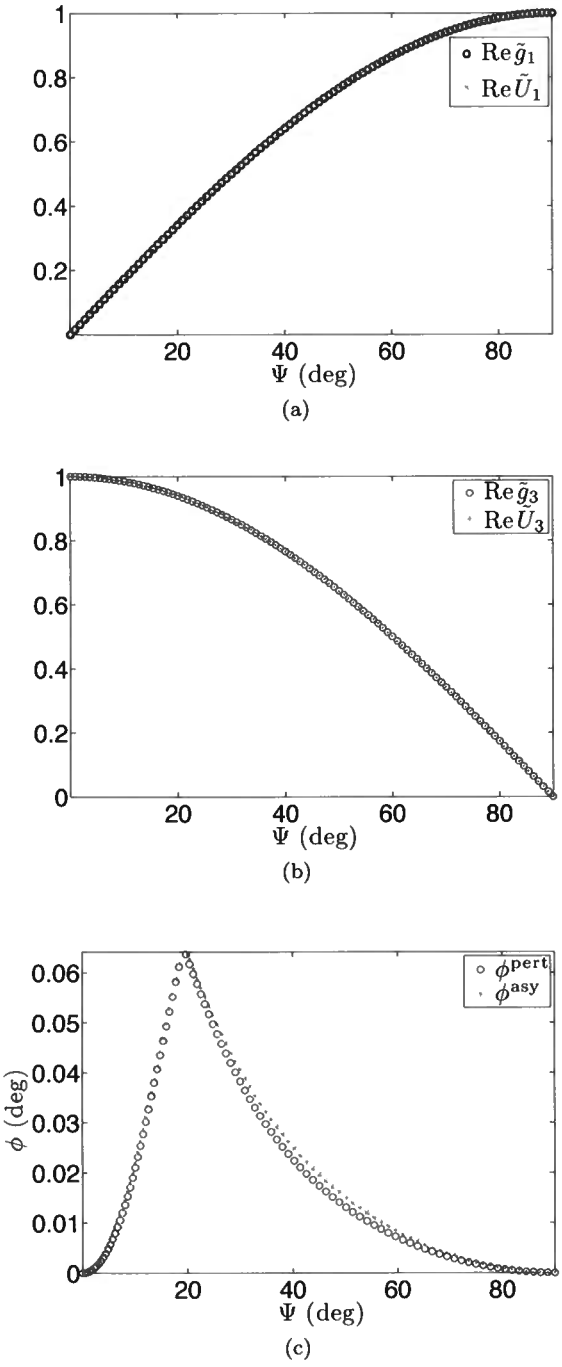

Figure 3. Comparison of the complex-valued polarization vectors $\tilde{\mathbf{U}}$ and $\tilde{\mathbf{g}}$ for model 2. The (a) X-component and (b) Z-component of the real parts of $\tilde{\mathbf{U}}$ and $\tilde{\mathbf{g}}$. (c) The phase of $\tilde{\mathbf{U}}$ (ϕ^{asym}) and $\tilde{\mathbf{g}}$ (ϕ^{pert}).

The quantity D is called the inhomogeneity parameter (Červený and Pšenčik, 2005). In our examples with VTI models, we can assume that $\mathbf{n}$ is confined to the $[x_1, x_3]$-plane, and we can choose $\mathbf{m}$ to lie in the same plane. To find the parameters $\tilde{\sigma}$ and D corresponding to the saddle point, we solve the constrained optimization problem:

$$\text{Minimize} \left|\left| \frac{\tilde{\mathbf{E}}}{\sqrt{\tilde{E}_j^2}} - \hat{\mathbf{x}} \right|\right|_2^2, \quad \text{subject to } G = 1. \qquad (22)$$

Therefore, the objective function is the difference between the orientation of $\tilde{\mathbf{E}}$ and $\hat{\mathbf{x}}$ (equation 13), with equation 8 serving as a constraint.

Figure 2 compares the inhomogeneity angle ξ computed from our asymptotic analysis and the ray-perturbation approach (see Appendix B, equation 10). The values of ξ obtained by the two methods are close to one another for models 1, 3, and 4. The discrepancy for model 2 can be expected because P-wave attenuation for that model is strongly anisotropic. Indeed, the perturbation method assumes the magnitude of attenuation and attenuation anisotropy to be small. Although model 3 has substantial attenuation and an anisotropic velocity function, the inhomogeneity angle for that model vanishes because the quality-factor components Q_{ij} are identical (see Appendix B).

The polarization vector $\tilde{\mathbf{U}}$ for the plane wave that corresponds to the saddle-point condition can be computed from equation 10. Using ray perturbation theory, an approximate polarization vector $\tilde{\mathbf{g}}$ can be obtained from equation 6. Figure 3 shows the real parts and phases of the complex-valued vectors $\tilde{\mathbf{U}}$ and $\tilde{\mathbf{g}}$ for model 2. While the real parts practically coincide, there is a small difference between the phase terms. Clearly, our analysis accurately describes the direction of the P-wave particle motion. The imaginary parts of $\tilde{\mathbf{U}}$ and $\tilde{\mathbf{g}}$ vanish for model 3 because the attenuation function is isotropic.

Conclusions

We presented a rigorous derivation of the Green's function in homogeneous, attenuative, arbitrarily anisotropic media using the steepest-descent method. Application of the saddle-point condition helps identify the plane wave that makes the most significant contribution to the displacement field of each mode. Our results make it possible to evaluate the inhomogeneity angle and describe the behavior of the group-velocity vector in the high-frequency approximation.

P-wave signatures obtained from our asymptotic analysis for TI media were compared with the same quantities computed by ray perturbation theory. The asymptotic energy-velocity vector is close to the perturbed group-velocity vector and, therefore, correctly predicts the traveltime and attenuation along the ray.

The inhomogeneity angles computed from the saddle-point condition and perturbation theory differ only for strongly attenuative models. The polarization vector is complex, and both the real and imaginary parts are well-described by our asymptotic expressions.

Acknowledgments

We are grateful to the members of the A(nisotropy)-Team of the Center for Wave Phenomena (CWP), Colorado School of Mines, for fruitful discussions. Colin Thomson (Schlumberger), Paul Martin (CSM), and Matthew Reynolds (CU Boulder) provided valuable help with asymptotic analysis and linear algebra. This work was supported by the Consortium Project on Seismic Inverse Methods for Complex Structures at CWP.

REFERENCES

Aki, K., and P. G. Richards, 1980, Quantitative Seismology: Theory and Methods, Volume I: W.H. Freeman and Company.

Behura, J., and I. Tsvankin, 2009, Role of the inhomogeneity angle in anisotropic attenuation analysis: Geophysics, **74**, no. 5, WB177–WB191.

Bleistein, N., 1984, Mathematical Methods for Wave Phenomena: Academic Press.

———, 2012, Saddle point contribution for an n-fold complex-valued integral: CWP Research Report 741.

Carcione, J., 2007, Wave Fields in Real Media. Theory and numerical simulation of wave propagation in anisotropic, anelastic, porous and electromagnetic media.: Elsevier.

Červený, V., 1972, Seismic rays and ray intensities in inhomogeneous anisotropic media: Geophysical Journal of the Royal Astronomical Society, **29**.

———, 2001, Seismic ray theory: Cambridge University Press.

Červený, V., L. Klimeš, and I. Pšenčik, 2008, Attenuation vector in heterogeneous, weakly dissipative, anisotropic media: Geophysics Journal International, **175**, 346–355.

Červený, V., and I. Pšenčik, 2005, Plane waves in viscoelastic anisotropic media – I. Theory: Geophysics Journal International, **161**, 197–212.

———, 2008, Quality factor Q in dissipative anisotropic media: Geophysics, **73**, T63–T75.

———, 2009, Perturbation Hamiltonians in heterogeneous anisotropic weakly dissipative media: Geophysics Journal International, **178**, 939–949.

Courant, R., 1988, Differential and Integral Calculus: Wiley-Interscience, **2**.

Gajewski, D., 1993, Radiation from point sources in general anisotropic media: Geophysics Journal International, **113**, 299–317.

Hearn, D. J., and E. S. Krebes, 1990, On computing ray-synthetic seismograms for anelastic media using complex rays: Geophysics, **55**, 422–432.

Horn, R. A., and C. R. Johnson, 1990, Matrix Analysis: Cambridge University Press.

Klimeš, L., 2002, Second-order and higher-order perturbations of travel time in isotropic and anisotropic media: Studia Geophysica et Geodaetica, **46**, 213–248.

Krebes, E. S., and L. H. T. Le, 1994, Inhomogeneous plane waves and cylindrical waves in anisotropic anelastic media: Journal of Geophysical Research, **99**, 899–919.

Tsvankin, I., 1995, Seismic wavefields in layered isotropic media (course notes): Samizdat Press (http://samizdat.mines.edu/).

———, 2012, Seismic signatures and analysis of reflection data in anisotropic media, third ed.: Society of Exploration Geophysicists.

Tsvankin, I., and V. Grechka, 2011, Seismology of azimuthally anisotropic media and seismic fracture characterization: SEG.

Vavryčuk, V., 2007, Asymptotic Green's function in homogeneous anisotropic viscoelastic media: Proceedings of The Royal Astronomical Society, **463**, 2689–2707.

Wang, C. Y., and J. D. Achenbach, 1994, Elastodynamic fundamental solutions for anisotropic solids: Geophysics Journal International, **118**, 384–392.

Zhu, Y., 2006, Seismic wave propagation in attenuative anisotropic media: PhD thesis, Colorado School of Mines.

Zhu, Y., and I. Tsvankin, 2006, Plane-wave propagation in attenuative transversely isotropic media: Geophysics, **71**, no.2, T17–T30.

Appendix A

Exact Green's function for attenuative anisotropic media

The wave equation in the frequency-wavenumber domain for a homogeneous, attenuative, anisotropic medium can be written as (Zhu, 2006):

$$(\tilde{a}_{ijkl}(\omega)k_j k_l - \omega^2\delta_{ik})\,\tilde{U}_k(\mathbf{k},\omega) = \tilde{f}_i(\mathbf{k},\omega), \tag{23}$$

where ω is the frequency, $\tilde{a}_{ijkl}$ are the components of the density-normalized stiffness tensor, k_j are the wavenumbers, $\tilde{\mathbf{U}}$ is the displacement vector, and $\tilde{f}(\mathbf{k},\omega)$ is the body force per unit volume (source). All indices vary from 1 to 3.

The frequency-domain displacement can be found as the Fourier integral:

$$\tilde{u}_k(\mathbf{x},\omega) = \frac{1}{(2\pi)^3}\int_{-\infty}^{\infty}\int_{-\infty}^{\infty}\int_{-\infty}^{\infty}\tilde{U}_k(k,\omega)\,e^{ik_j x_j}\,\mathrm{d}\mathbf{k}, \tag{24}$$

where

$$\tilde{U}_k(k,\omega) = \frac{\tilde{B}_{ki}\,\tilde{f}_i(k_j,\omega)}{\det\tilde{\mathbf{D}}} \tag{25}$$

and $\mathrm{d}\mathbf{k} = \mathrm{d}k_1\,\mathrm{d}k_2\,\mathrm{d}k_3$. The matrix $\tilde{\mathbf{D}}$ ($\tilde{D}_{ki} = \tilde{a}_{ijkl}k_j k_l - \omega^2\delta_{ik}$) with cofactors $\tilde{B}_{ki}$ is closely related to the Christoffel matrix. The source in equation 25 can be defined as a point impulsive force applied at location $\mathbf{x}_0$ parallel to the x_n-axis:

$$\tilde{f}_i(\omega,k_j) = \delta_{in}\,e^{-i\,k_j\,x_j^0}. \tag{26}$$

The particle displacement from this source is the Green's function:

$$G_{kn}(\mathbf{x},\mathbf{x}^0,\omega) = \frac{1}{(2\pi)^3}\int_{-\infty}^{\infty}\int_{-\infty}^{\infty}\int_{-\infty}^{\infty}\frac{\tilde{B}_{ki}\,\delta_{in}}{\det\tilde{\mathbf{D}}}\,e^{ik_j(x_j-x_j^0)}\,\mathrm{d}\mathbf{k}. \tag{27}$$

The integral over k_3 in equation 27 can be extended into the complex plane $\tilde{k}_3 = \mathrm{Re}\,k_3 + i\,\mathrm{Im}\,k_3$. The closed contour includes the real axis and a semicircle with an infinitely large radius in the upper half-plane. The integral can then be evaluated by the residue theorem (i.e., by computing the residues at the poles), as described in Aki and Richards (1980) and Tsvankin (1995). The poles correspond to the roots of the following equation for k_3:

$$\det\tilde{\mathbf{D}} = \det[\tilde{a}_{ijkl}k_j k_l - \omega^2\delta_{ik}] = 0. \tag{28}$$

Equation 28 is a sixth-order polynomial in k_3 that can have at most six distinct roots that correspond to up- and downgoing P-, S_1- and S_2-waves.

In nonattenuative media, the roots of k_3 lie on the real k_3-axis, and the integral can be evaluated by introducing small attenuation, moving the roots into the complex plane, and applying the residue theorem (Tsvankin, 1995). Alternatively, the integral over k_3 can be evaluated using Cauchy's principal value (Bleistein, 1984). In the presence of attenuation, the roots of equation 28 lie in the complex plane. The pole $\tilde{k}_3^r = \tilde{k}_3(k_1,k_2)$, which corresponds to a certain mode (e.g., P-waves) and is located inside the integration contour, yields the residue for that mode. The integral over k_3 in equation 24 reduces to the residue at the pole, and the Green's function becomes:

$$G_{kn}(\mathbf{x},\mathbf{x}^0,\omega) = \frac{i}{(2\pi)^2}\int_{-\infty}^{\infty}\int_{-\infty}^{\infty}\Big[\frac{\tilde{B}_{kn}}{\partial(\det\tilde{\mathbf{D}})/\partial k_3}\Big]_{k_3=\tilde{k}_3^r} \times e^{i\left[k_1(x_1-x_1^0)+k_2(x_2-x_2^0)+\tilde{k}_3^r(x_3-x_3^0)\right]}\,\mathrm{d}k_1\,\mathrm{d}k_2. \tag{29}$$

Substituting $k_j = \omega\,p_j$, where p_j denotes the components of the slowness vector, yields $\det\tilde{\mathbf{D}} = \omega^6\det(\tilde{\Gamma}_{ik} - \delta_{ik})$, where $\tilde{\Gamma}_{ik} = a_{ijkl}p_j p_l$. The cofactors of $\tilde{\mathbf{\Gamma}} - \mathbf{I}$ ($\mathbf{I}$ is the identity matrix) are denoted by S_{kn}, and $B_{kn} = \omega^4 S_{kn}$. Equation 29 can then be written as

$$G_{kn}(\mathbf{x},\mathbf{x}^0,\omega) = \frac{i\omega}{(2\pi)^2}\int_{-\infty}^{\infty}\int_{-\infty}^{\infty}\Big[\frac{\tilde{S}_{kn}}{\partial[\det(\tilde{\mathbf{\Gamma}}-\mathbf{I})]/\partial p_3}\Big]_{p_3=\tilde{p}_3^r} \times e^{i\left[p_1(x_1-x_1^0)+p_2(x_2-x_2^0)+\tilde{p}_3^r(x_3-x_3^0)\right]}\,\mathrm{d}p_1\,\mathrm{d}p_2. \tag{30}$$

Appendix B

Perturbation analysis for anisotropic attenuative media

In this section, we present approximate expressions for the propagation and attenuation vectors (and, hence, the inhomogeneity angle) in homogeneous, attenuative, anisotropic media using the method of perturbation Hamiltonians introduced by Červený and Pšenčik (2009). We also derive the conditions under which the inhomogeneity angle vanishes.

In their methodology, Červený and Pšenčik (2009) treat the traveltime as a complex-valued quantity, with the real part contributing to the phase and the imaginary part to the dissipation along the ray. The complex-valued traveltime and traveltime gradients can be computed as a perturbation of the corresponding real-valued quantities found along the ray. The density-normalized stiffness tensor is given by $\tilde{a}_{ijkl} = a^R_{ijkl} - i\, a^I_{ijkl}$, with the real part corresponding to the reference nonattenuative medium, and the imaginary part to the perturbation that makes the medium viscoelastic.

We consider the linear perturbation Hamiltonian $\mathcal{H}(\mathbf{x}, \mathbf{p}, \alpha)$ defined in Červený and Pšenčik (2009):

$$\mathcal{H}(\mathbf{x}, \mathbf{p}, \alpha) = \mathcal{H}^0(\mathbf{x}, \mathbf{p}) + \alpha\, \Delta\mathcal{H}(\mathbf{x}, \mathbf{p}), \tag{1}$$

with

$$\Delta\mathcal{H}(\mathbf{x}, \mathbf{p}) = \tilde{\mathcal{H}}(\mathbf{x}, \mathbf{p}) - \mathcal{H}^0(\mathbf{x}, \mathbf{p}), \tag{2}$$

where $\mathcal{H}^0$ and $\tilde{\mathcal{H}}$ correspond to the (elastic) reference and (viscoelastic) perturbed medium, respectively, $\mathbf{p}$ is the slowness vector, and α is the perturbation parameter. The reference Hamiltonian $\mathcal{H}^0$ can be expressed through the slowness ($\mathbf{p}$) and polarization ($\mathbf{g}$) vectors computed for the reference medium:

$$\mathcal{H}^0(\mathbf{x}, \mathbf{p}) = \frac{1}{N} \left[a^R_{ijkl}\, p_j\, p_l\, g_i\, g_k \right]^{N/2}, \tag{3}$$

where N is an integer. The polarization vector $\mathbf{g}$ satisfies the equation

$$\Gamma_{ik}\, g_k = [a^R_{ijkl}\, p_j\, p_l]\, g_k = \lambda\, g_i, \tag{4}$$

where λ represents the eigenvalue of the Christoffel matrix for the mode of interest. The perturbed Hamiltonian $\tilde{\mathcal{H}}$ is given by

$$\tilde{\mathcal{H}}(x_m, p_n) = \frac{1}{N} \left[\tilde{a}_{ijkl}\, p_j\, p_l\, \tilde{g}_i\, \tilde{g}_k \right]^{N/2}, \tag{5}$$

where the complex polarization vector $\tilde{\mathbf{g}}$ is computed as the eigenvector of the complex Christoffel matrix $\tilde{\Gamma}_{ik}$:

$$\tilde{\Gamma}_{ik}\, \tilde{g}_k = [\tilde{a}_{ijkl}\, p_j\, p_l]\, \tilde{g}_k = (\lambda + \Delta\lambda)\, g_i, \tag{6}$$

where λ is the eigenvalue that corresponds to the reference elastic medium and $\Delta\lambda$ is the perturbation of λ. The slowness vector $\mathbf{p}$ in equations 5 – 6 corresponds to the reference elastic medium and is real-valued.

The traveltime gradient, which corresponds to the perturbation Hamiltonian defined in equation 5, can be expanded in the perturbation parameter α (Červený and Pšenčik, 2009):

$$\frac{\partial \tau}{\partial x_i} \approx \frac{\partial \tau^0}{\partial x_i} + \alpha \left[\frac{\partial^2 \tau}{\partial x_i\, \partial \alpha} \right]_{\alpha=0} + \cdots, \tag{7}$$

where $\partial\tau^0/\partial x_i = p^0_i$ is computed in the reference medium. An approximation for the the traveltime gradient in attenuative media can be obtained by substituting $\alpha = 1$ and retaining the first two terms of the expansion in equation 7. Then the real part of the traveltime gradient corresponds to $\mathbf{p}^R$ and the imaginary part to $\mathbf{p}^I$:

$$p^R_i = \mathrm{Re}\left[\frac{\partial \tau}{\partial x_i} \right] \approx p^0_i + \mathrm{Re}\left[\frac{\partial^2 \tau}{\partial x_i\, \partial \alpha} \right]_{\alpha=0}, \tag{8}$$

$$p^I_i = \mathrm{Im}\left[\frac{\partial \tau}{\partial x_i} \right] \approx \mathrm{Im}\left[\frac{\partial^2 \tau}{\partial x_i\, \partial \alpha} \right]_{\alpha=0}. \tag{9}$$

The inhomogeneity angle can be computed from

$$\cos\xi = \frac{\mathbf{p}^I \cdot \mathbf{p}^R}{|\mathbf{p}^I|\, |\mathbf{p}^R|}. \tag{10}$$

The second-order partial derivative in equation 7 is evaluated using quadratures along the reference rays. Detailed derivations and the methodology can be found in Klimeš (2002) and Červený and Pšenčik (2009). Here, we will only

provide the expressions corresponding to the perturbation Hamiltonian defined in equation 1 for a homogeneous medium. The relevant expressions are

$$\frac{\partial^2 \tau}{\partial x_i \, \partial \alpha} = \tilde{T}_k(\alpha) \, [Q_{ki}^{\text{ray}}]^{-1}, \tag{11}$$

with the vector $T_k(\alpha)$ given by

$$\tilde{T}_K(\alpha) = \tilde{T}_K^0(\alpha) + \tau \, \tilde{\mathcal{W}}_i \, P_{iK}^{\text{ray}}, \quad K = 1, 2, \tag{12}$$

$$\tilde{\mathcal{W}}_i = \Big(\frac{\partial \tilde{\mathcal{H}}}{\partial p_i} - \frac{\partial \mathcal{H}^0}{\partial p_i} \Big), \tag{13}$$

$$\tilde{T}_3(\alpha) = \mathcal{H}^0 - \tilde{\mathcal{H}}. \tag{14}$$

The upper-case index "K" changes from 1 to 2, and the lower-case index "k" from 1 to 3. The real-valued matrices Q_{ik}^{ray} (not to be confused with the quality-factor matrix) and P_{ik}^{ray} are computed during dynamic ray tracing in the reference elastic medium. They are defined as:

$$\begin{aligned} Q_{ik}^{\text{ray}} &= \frac{\partial x_i}{\partial \gamma_k}, \\ P_{ik}^{\text{ray}} &= \frac{\partial p_i^0}{\partial \gamma_k}; \end{aligned} \tag{15}$$

γ_k denotes a certain "ray parameter" (e.g. the initial phase angle or the traveltime along the ray). In equation 12, $\tilde{T}_K^0(\alpha) = 0$ for a point source, however, for plane-wave propagation the values of $\tilde{T}_K^0(\alpha)$ (initial conditions) may be chosen arbitrarily (Klimeš, 2002).

We now derive the conditions under which the inhomogeneity angle vanishes in homogeneous media. Substituting equations 3 and 5 into equation 13 yields:

$$\tilde{\mathcal{W}}_i = \tilde{a}_{ijkl} \, p_k \, \tilde{g}_j \, \tilde{g}_l - a_{ijkl}^R \, p_k \, g_j \, g_l. \tag{16}$$

For weakly dissipative media, we can use the approximation $\tilde{\mathbf{g}} \approx \mathbf{g}$ and reduce equation 16 to

$$\tilde{\mathcal{W}}_i = -i \, a_{ijkl}^I \, p_k \, g_j \, g_l. \tag{17}$$

For the special case of identical Q components (i.e., $a_{ijkl}^I = a_{ijkl}^R / Q$), we have

$$\tilde{\mathcal{W}}_i = -i \, \frac{a_{ijkl}^R}{Q} \, p_k \, g_j \, g_l = -i \, \frac{\mathcal{U}_i}{Q}, \tag{18}$$

where $\mathcal{U}_i$ are the components of the group-velocity vector in the reference elastic medium. Substituting equation 18 into equation 12, we obtain

$$\tilde{T}_{K\alpha}(\gamma_3) = -i \, (\gamma_3 - \gamma_3^0) \, \frac{\mathcal{U}_i}{Q} \, P_{iK}^{\text{ray}} = 0, \quad K = 1, 2, \tag{19}$$

because the group-velocity vector is orthogonal to the first two columns of the matrix $\mathbf{P}^{\text{ray}}$, i.e., $\mathcal{U}_i \, P_{iK} = 0$ (Červený, 2001). Then, equations 8 and 9 for $\mathbf{p}^R$ and $\mathbf{p}^I$ take the form:

$$p_i^R = p_i^0 + \text{Re} \, [\tilde{T}_{3\alpha}] \, p_i^0, \tag{20}$$

and

$$p_i^I = \text{Im} \, [\tilde{T}_{3\alpha}] \, p_i^0, \tag{21}$$

where $p_i^0 = [Q_{3i}^{\text{ray}}]^{-1}$ (Červený, 2001). From equations 20 and 21, it follows that $\mathbf{p}^R$ is parallel to $\mathbf{p}^I$. Hence, the inhomogeneity angle vanishes in the case of identical Q components, i.e., when the attenuation coefficients of all three wave-modes are isotropic. Note that the velocity function may still be anisotropic. Further, the inhomogeneity angle also vanishes for isotropic velocity and attenuation functions. This can be proved by substituting the expressions for the Hamiltonian in isotropic media into equation 16.

CWP-746

Inversion of multicomponent seismic time shifts for reservoir pressure and length: A feasibility study

Steven Smith[1] and Ilya Tsvankin[2]
Colorado School of Mines, Center for Wave Phenomena, Golden Colorado

(1) email: SteveSmithCSM@aol.com
(2) email: ilya@mines.edu

ABSTRACT

Pressure drops associated with reservoir production generate excess stress and strain that cause traveltime shifts of reflected waves. Here, we invert time shifts of P-, S-, and PS-waves measured between baseline and monitor surveys for pressure reduction and reservoir length. The inversion results can be used to estimate compaction-induced stress and strain changes around the reservoir. We implement a hybrid inversion algorithm that incorporates elements of gradient, global/genetic, and nearest-neighbor methods, and permits exploration of the parameter space while simultaneously following local misfit gradients. Our synthetic examples indicate that optimal estimates of reservoir pressure from P-wave data can be obtained using the reflections from the reservoir top. For S-waves, time shifts from the top of the reservoir can be inverted for pressure if the noise level is low. However, if noise contamination is significant, it is preferable to use S-wave data (or combined shifts of all three modes) from reflectors beneath the reservoir. Reservoir length can be estimated using the time shifts of any mode from the reservoir top or deeper reflectors. Numerical testing shows that a potentially serious source of error in the inversion is a distortion in the strain-sensitivity coefficients which govern the magnitude of stiffness changes. We conclude by illustrating the differences between the actual strain field and those corresponding to the best-case inversion results obtained using P- and S- wave data. This feasibility study suggests which wave types and reflector locations may provide the most accurate estimates of reservoir parameters from compaction-induced time shifts.

Key words: geomechanics, seismic modeling, inversion, stress-induced anisotropy, converted waves, shear waves, time-lapse, compacting reservoir, transverse isotropy, VTI

INTRODUCTION

Pressure variations inside a petroleum reservoir influence drilling and production decisions throughout the life of the field. Inversion for the pressure distribution in multicompartment reservoir models permits identification of depleted zones and isolated compartments sealed off by geologic formations (Greaves and Fulp, 1987; Landrø, 2001; Lumley, 2001; Calvert, 2005; Hodgson et al., 2007; Wikel, 2008). Pressure inversion may also identify regions of elevated stress and strain where existing wells may fail, or additional drilling should be avoided.

Most existing publications on modeling and estimation of production-induced strains and time shifts have focused on vertical strain formulations (Hatchell and Bourne, 2005; Janssen et al., 2006; Roste, 2007; Hodg-

son et al., 2007; Staples et al., 2007; De Gennaro et al., 2008). However, several studies have shown that modeling of triaxial strains/stresses is necessary because shear strains contribute significantly to stiffness perturbations and, thus, time shifts (Schutjens et al., 2004; Sayers and Schutjens, 2007; Herwanger, 2008; Fuck et al., 2009; Sayers, 2010; Fuck et al., 2011; Smith and Tsvankin, 2012).

Time shifts and reservoir pressure estimated from seismic data can be highly dependent on processing methods, geomechanical model, and the quality of the recorded waveforms. A process known as "cross equalization" (Rickett and Lumley, 1998, 2001) is typically applied to field data for the purpose of making them suitable for time-lapse inversion. Time-shift computation from synthetic data still requires post-processing of the modeled reflected wavefields designed to suppress artifacts caused by interfering arrivals (Smith and Tsvankin, 2012).

Using geomechanical modeling and time-shift analysis, Fuck et al. (2009) demonstrated that it is essential to account for triaxial stress and stress-induced anisotropy in describing offset-dependent P-wave time shifts. Smith and Tsvankin (2012) extended time-shift modeling to multicomponent data and studied the variation of P-, S-, and PS-wave time shifts with reservoir pressure and reflector depth (here, by S-waves we mean the SV-mode). Because stress-induced anisotropy is close to elliptical, the velocity of SV-waves and of the SV-leg of PS-waves is almost independent of direction. Large compaction-induced strains inside the reservoir generate S-wave time shifts for deep reflectors that are 2-3 times larger than those for P-waves. A sensitivity study by Smith and Tsvankin (2013) demonstrates that S-wave time shifts for reflectors beneath the reservoir become nonlinear in pressure for relatively large stiffness changes corresponding to pressure reductions exceeding approximately 10%. Their results suggest that time shifts of shear-wave reflections may be large enough to invert for reservoir pressure when P-wave shifts (which are smaller) are obfuscated by noise.

Here, we present integrated 2D geomechanical/seismic inversion of compaction-induced time shifts obtained from multicomponent seismic data generated for simple, single-compartment reservoir models. The reservoir is embedded in a homogeneous, isotropic background medium that becomes heterogeneous and anisotropic after the pressure reduction. The time shifts are estimated using P-, S-, and PS-wave reflections from three interfaces around the reservoir. Our inversion algorithm combines global and gradient techniques with the goal of both exploring the error space and ensuring convergence toward a global minimum. Inversion for reservoir pressure and length is performed for each mode (P, S, PS) separately, as well as for the combination of time shifts of all three wave types. We also examine the differences between the strain field of the reference reservoir and those of the best inverted models.

THEORETICAL BACKGROUND

Geomechanical and time-shift modeling

The far-field stress and strain fields of a subsurface inclusion undergoing pressure or thermal changes (Hu, 1989; Downs and Faux, 1995) can be expressed through the Green's function. A closed-form equation describing the pressure-dependent vertical strain in a half-space with a free surface is given by McCann and Wilts (1951) and Mindlin and Cheng (1950). In what has become a standard method, Hodgson et al. (2007) invert time shifts for the vertical strain ϵ_{zz} using the "R-factor" equation of Hatchell and Bourne (2005):

$$\frac{\Delta t}{t} = (1 + R)\,\epsilon_{zz}\ , \tag{1}$$

where Δt is the estimated P-wave time shift, t is the P-wave traveltime, and R is a coefficient empirically determined from field-survey time-shift measurements. Then pressure reductions can be estimated from ϵ_{zz} by incrementally updating rock-physics and geologic properties with the help of well logs and seismic data.

However, rocks both inside and outside a producing reservoir are subject to varying combinations of vertical and horizontal stress (e.g. Herwanger, 2008), indicating the need to account for triaxial stress/strain. A numerical example showing the equivalence of time shifts produced by single-compartment and two-compartment reservoirs of identical dimensions is given in Smith and Tsvankin (2013), who model a complete compaction-induced strain tensor.

Here, we invert for reservoir pressure and length using time shifts estimated from coupled geomechanical and seismic modeling (Smith and Tsvankin, 2012). The strain field around the compacting reservoir of Figure 1 is computed with triaxial, plane-strain finite-element modeling (COMSOL AB, 2008). The section is composed of a homogeneous unstressed material, and the effective pressure of the region designated as the reservoir is given by

$$P_{\text{eff}} = P_{\text{c}} - \alpha\, P_{\text{fluid}} = P_{\text{c}} - \alpha\,(\xi P^{\circ}_{\text{fluid}})\ , \tag{2}$$

where P_{c} is the confining pressure of the overburden column, P_{fliud} is the pressure of the fluid in the pore space, and P°_{fliud} is the initial fluid pressure. The coefficient ξ is is responsible for reservoir depressurization, and α is an effective stress coefficient describing the response of the aggregate fluid and rock matrix.

Pore-pressure ($P_{\text{p}} = P_{\text{fluid}}$) reduction within the reservoir block (Figure 1) results in an anisotropic velocity field due to the excess stress and strain. The resulting 2D model is transversely isotropic with a tilted axis of symmetry (TTI) (Tsvankin, 2005; Fuck et al.,

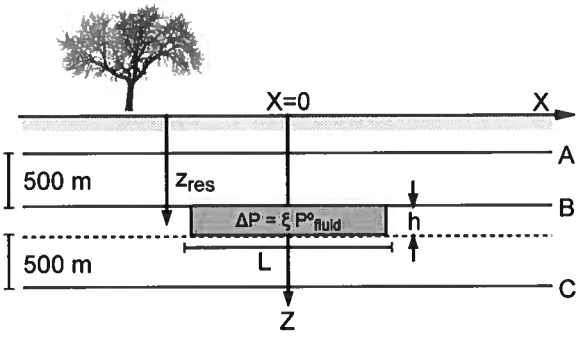

Figure 1. Compacting reservoir and reflectors (marked A, B, and C) used to measure traveltime shifts. ΔP is the change in the initial reservoir fluid pressure given in equation 2. The reservoir is at a depth of 1.5 km, and measures 2.1 km in length (L), and 0.1 km in thickness (h). The reservoir is embedded in a homogeneous medium with density $\rho = 2140$ kg/m^3, velocities $V_P = 2300$ m/s and $V_S = 1640$ m/s and the third-order stiffness coefficients $C_{111} = -13,904$ GPa, $C_{112} = 533$ GPa, and $C_{155} = 481$ GPa (Sarkar et al., 2003).

2011). The coefficient α can change with reservoir properties, making equation 2 nonlinear in pressure for large compaction/porosity changes. However, for the range of effective pressures in this study, α is approximately constant (Hornby, 1996). The depressurization of the reservoir compartment and fluid type are assumed to be uniform, and the reservoir material is taken to be homogeneous. We do not consider large production-induced changes of bulk moduli, which can occur when gas bubbles out of pore fluids (i.e., the pressure drops below the "bubble-point") (Batzle and Han, 2009), or the replacement of oil by water.

Strain-induced changes in the second-order stiffnesses c_{ijkl}, which serve as input to seismic modeling, are computed using the so-called nonlinear theory of elasticity (Hearmon, 1953; Thurston and Brugger, 1964; Fuck et al., 2009):

$$c_{ijkl} = c^o_{ijkl} + \frac{\partial c_{ijkl}}{\partial e_{mn}} \Delta e_{mn} = c^o_{ijkl} + c_{ijklmn} \Delta e_{mn} \ , \quad (3)$$

where c^o_{ijkl} is the stiffness tensor of the background (unperturbed) medium, c_{ijklmn} is the sixth-order "strain-sensitivity" tensor and Δe_{mn} is the excess strain tensor. Index pairs of the tensor c_{ijklmn} can be contracted into single indices changing from 1 to 6 using Voigt notation (e.g., Tsvankin, 2005), which results in the matrix $C_{\alpha\beta\gamma}$.

We employ a 2D elastic finite-difference code (Sava et al., 2010) to generate multicomponent P-, S- and PS-wave data for baseline ($\Delta P = 0$) and monitor ($\Delta P > 0$) surveys. Reflectors measuring one grid point in thickness are inserted into the model as density anomalies (for details, see Smith and Tsvankin, 2012).

Time shifts for P-waves are estimated using the vertical (Z) displacement component, while those for S(SV)- and PS-wave data are estimated on the horizontal (X) component. Shot gathers from baseline and monitor surveys are windowed and FK-filtered to isolate the arrivals of interest, and crosscorrelated trace-by-trace to measure the time shifts. The data are smoothed to remove spurious or sharp/high-frequency variations in the time-shift curves. The smoothing represents a form of regularization that improves inversion stability while sacrificing a degree of fit to the data (Aster et al., 2005). This process produces smooth time-shift curves for P-, S-, and PS-waves as a function of the lateral coordinate at reflectors A, B, and C (Figure 1). Similar post-processing including resampling/interpolation, filtering, stacking, amplitude matching, etc. (referred to as cross-equalization) would be applied to field data prior to time-shift estimation (Rickett and Lumley, 1998, 2001; Magnesan et al., 2005).

INVERSION METHODOLOGY

Properties of multicomponent time shifts

Time shifts are estimated from synthetic data generated for the depressurized reference reservoir in Figure 1. Figure 2 shows time shifts of P-, S-, and PS-waves for a fluid-pressure drop of 20% with the source located above the reservoir center. The spatial patterns of compaction-induced time shifts remain consistent over a range of pressure drops, and reflectors A, B, and C are positioned to sample these distributions for inversion purposes. Compaction-induced strains in the reservoir volume are 1-2 orders of magnitude larger than those in the surrounding medium (Smith and Tsvankin, 2012). The resulting velocity increases inside the reservoir cause time shifts to change from lags in the overburden to leads beneath the reservoir. Therefore, the reservoir essentially behaves like a high-velocity lens for all wave types.

P-wave time shifts (Figure 2a) exhibit pronounced offset variations around the reservoir due to the stress-induced anisotropy. While SV-wave anisotropy is weak, shear-wave time shifts from reflection points beneath the reservoir are 2-3 times larger than those of P-waves (Figure 2b). PS-wave time-shift trends (Figure 2c) depend on the reflection (conversion) point, and for reflectors beneath the reservoir are governed by the combination of P-wave lags in the overburden and larger S-wave leads accumulated inside the reservoir. For reflectors in the overburden, S-wave leads practically cancel P-wave lags, and time shifts of PS-waves are generally small (Smith and Tsvankin, 2012). Variations in these time-shift patterns occur with source location, and the proximity of the reservoir to the free surface.

Multicompartment reservoirs exhibit time-shift distributions similar to those in Figure 2, but with strain and time-shift perturbations caused by the inter-compartment pressure differences or variations in shape

(Smith and Tsvankin, 2012; Smith and Tsvankin, 2013). The results for a single-compartment reservoir presented here highlight the general properties of time shifts of different wave types for a wide range of reflector depths. Making the model more complicated by introducing a multicompartment reservoir or a heterogeneous background would result in a loss of generality, making the results specific to a certain geologic section.

Model properties and inversion constraints

As in our previous publications, the reservoir is comprised of and embedded in a homogeneous material with the properties of Berea sandstone (Figure 1). The effective stress coefficient α for the reservoir is 0.85 (equation 2). Velocities are reduced by 10% from the laboratory values to account for the difference between static and dynamic stiffnesses in low-porosity rocks (Yale and Jamieson, 1994).

For geomechanical modeling, the reservoir is located in a finite-element mesh measuring 20 km × 10 km, which allows us to obtain stress, strain, and displacement close to those for a half-space. The pressure reduction in the reference (actual) reservoir is 17.5%, with pressure drops of the inversion models constrained to be between 10% and 20% ($0.8P^{\circ}_{\text{fluid}} \le P_{\text{fluid}} \le 0.9P^{\circ}_{\text{fluid}}$, with the actual value $0.825P^{\circ}_{\text{fluid}}$). The reservoir length is varied between 1.5 and 2.5 km; the actual value $L =$ 2.1 km. Such ranges are not considered unrealistic because the reservoir pressure and length typically can be estimated from well pressure at depth and seismic images, respectively. Due to the high computational cost of forward modeling and post-processing, it is currently impractical to run inversions for a wider range of these parameters.

Objective function

Both the reference reservoir and trial inversion models are depressurized from an initial zero-stress/strain state. Misfits (objective functions) for P-, S-, and PS-wave time shifts Δt for a trial reservoir model computed as the L2-norm,

$$\mu = \sqrt{\sum_{k=1}^{N} \left(\Delta t_k^{\text{ref}} - \Delta t_k\right)^2}\,, \tag{4}$$

where Δt^{ref} are the time shifts for the reference reservoir, and $k = 1, 2, ..., N$ are the individual traces in the shot record. For both the baseline and monitor surveys we use a single source located above the center of the reservoir (Figure 2). Time-shift trends for sources displaced with respect to the reservoir center are discussed in Smith and Tsvankin (2012). In principle, the methodology employed here can be implemented for multiple shot records and reflector/wave type combinations.

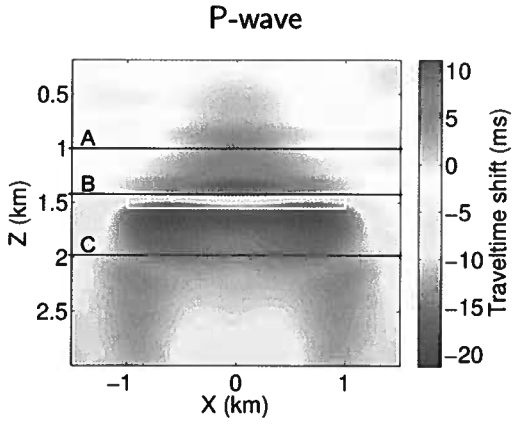

(a)

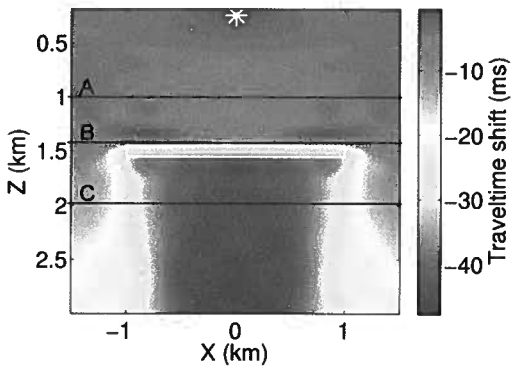

(b)

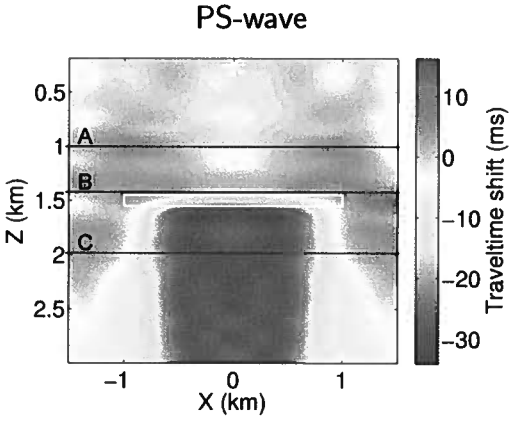

(c)

Figure 2. Typical two-way time-shift distributions for (a) P-waves, (b) S-waves, and (c) PS-waves measured using 22 reflectors around the reservoir (white box) from Figure 1 (Smith and Tsvankin, 2012). The time shifts correspond to hypothetical specular reflection points at each (X,Z) location in the subsurface. Positive shifts indicate lags where monitor survey reflections arrive later than the baseline events; negative shifts are leads. Source location is indicated by the white asterisk at the top.

The joint misfit for all three wave types (P, S, PS) is the L2-norm of the individual wave-type misfits,

$$\mu_{\text{joint}} = \sqrt{\mu_{\text{P}}^2 + \mu_{\text{S}}^2 + \mu_{\text{PS}}^2} \,. \tag{5}$$

Misfits discussed below have not been normalized to facilitate comparison of results for different wave types at specific reflectors. The smoothing of time shifts in post-processing amounts to an unspecified regularization term added to equation 4.

To evaluate the stability of the inversion algorithm, time shifts for the reference reservoir are contaminated by Gaussian noise with standard deviations of 5 ms and 10 ms (we also present results for noise-free data). This noise corresponds to moderate (5 ms), and significant (10 ms) levels of time-shift errors with respect to the P-wave shifts in Figure 2a. Although average noise of 10 ms may be comparable to P-wave time shifts measured in the field, it amounts to about 50% of the P-wave shifts directly beneath the reservoir, and only 25% of the S-wave shifts below the reservoir. While low levels of noise can mask and smooth out only short-length features in the time-shift curves, too much noise can distort time-shift behavior at all scales. The influence of noise on misfit characteristics is discussed in Appendix B.

Inversion algorithm

While here we invert for reservoir pressure drop and length, potentially it may be possible to simultaneously estimate other reservoir parameters (i.e., the elastic properties, effective stress coefficient, etc.), or the pressure distribution in several compartments. In fact, the methods described here can be applied to more complicated reservoir geometries by employing multicompartment modeling. Obviously, this could greatly expand the parameter space and complicate the inversion.

As mentioned above, changes in time shifts with respect to pressure-induced stiffness perturbations are generally nonlinear (Smith and Tsvankin, 2013). Time shifts become increasingly nonlinear for shorter reservoirs with large stress/strain anomalies at the corners. Therefore, we have devised a hybrid inversion technique (Appendix A) that combines the convergence characteristics of a gradient algorithm with the ability of global inversion to identify and avoid local minima.

Our method is based on the "nearest neighbor" algorithm of Sambridge (1999) that samples the parameter space, dividing the objective function into so-called Voronoi cells. Nearest neighbor selects a subset of minimum-misfit models to update, and divides those cells by inserting new models via a random walk or Gibbs-sampler within the cell. This procedure helps obtain a discrete (compartmentalized) estimate of the misfit but it does not give any gradient information. Thus, model updates may be located up-gradient from local or global minima, reducing the rate of convergence. To update the existing set of inversion models, our algorithm estimates the local gradient using some of the minimum-misfit models. The global portion of the algorithm is designed to fill unsampled voids in the parameter space, preventing the search from getting trapped in local minima. Therefore, multiple gradient-trackers can simultaneously converge toward local minima or, if found, the global minimum.

Evolution of the misfit surface

Figure 3a-e demonstrates the ability of the algorithm to reconstruct the structure of the misfit surface (2D slice in multiparameter inversions), while converging to local/global minima. The surfaces are interpolated using the misfits for all forward models run through the current iteration. Figure 3f shows how the objective function that includes joint-wave type misfits (equation 5) from reflector C changes during five inversion iterations. Gaussian noise with a standard deviation of 5 ms was added to the time shifts of the reference reservoir.

Four initial models (black circles in Figure 3a) were placed in the parameter space using a pseudo-regular distribution, which ensures that they are not equidistant from one another. Thus, the step sizes of all the initial-model updates are different, and the parameter space is well-sampled prior to the next iteration. At each iteration, a single minimum-misfit model was used for gradient estimation and model updates (see Appendix A). In addition to updated models inserted near the current low-misfit models, ten "exploration" models per iteration were added to better sample the parameter space. The maximum number of computed models was set to 100.

By the third iteration (Figure 3c), the general structure of the misfit surface is reasonably well-defined by the exploration models. The normalized joint misfit drops by approximately 25% in only five iterations (Figure 3f), resulting in an inverted pressure drop of 16.5% and reservoir length of 2.19 km (both are reasonably close to the actual values). Additional misfit reductions can be achieved by adjusting the termination conditions (Appendix A). Increasing the number of minimum-misfit/gradient-estimation models will further reduce the minimum misfit and improve the rate of convergence.

ANALYSIS OF NUMERICAL RESULTS

For the entire set of inversion results, the reference reservoir parameters and constraints are the same as those in Figure 3. While only one minimum-misfit model was used for gradient tracking in the joint-misfit inversions, two gradient trackers were employed for the P-, S-, and PS-wave inversions to increase convergence rates and resolve multiple minima. The maximum number of allowed forward models for the individual modes was

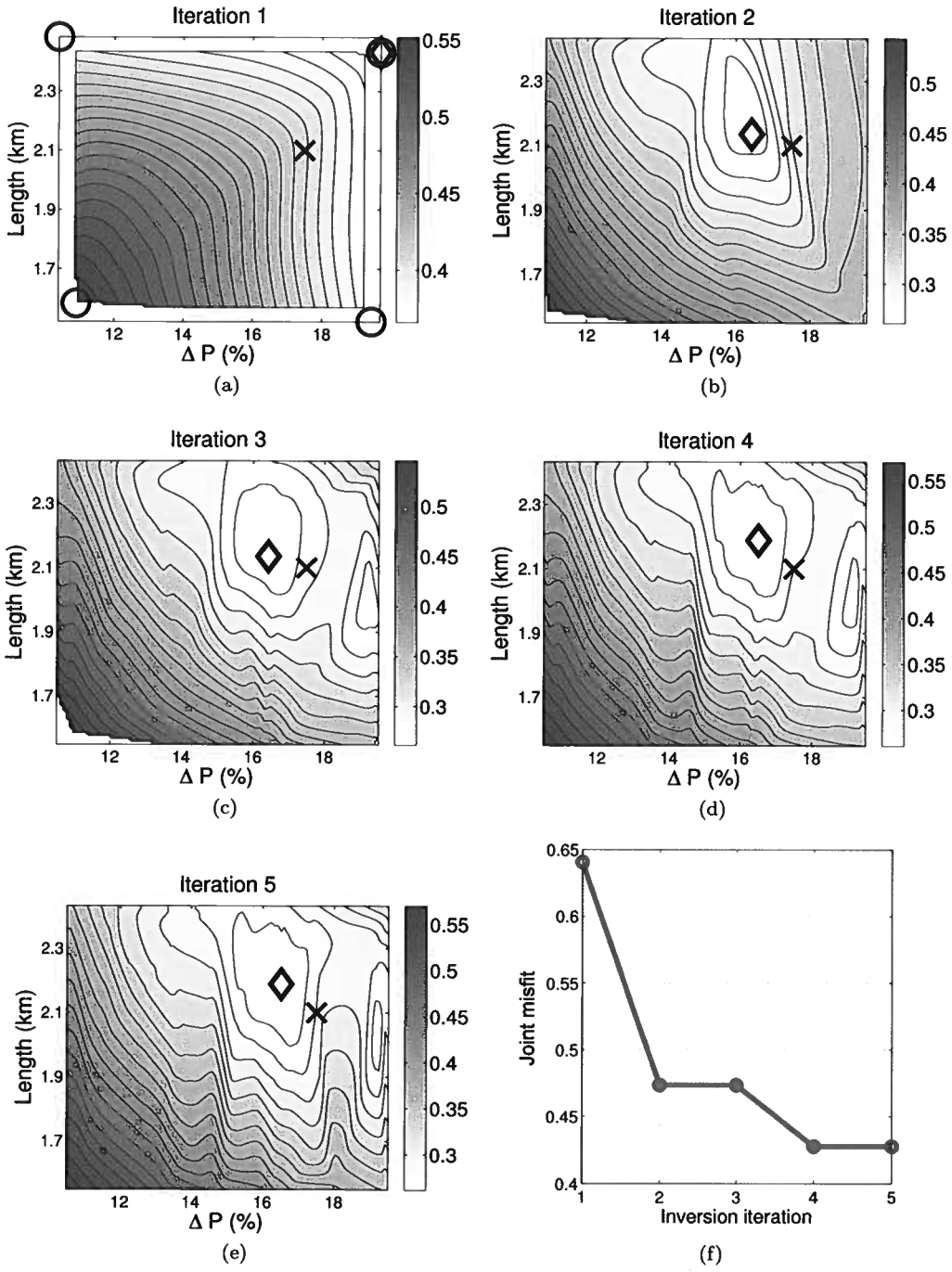

Figure 3. Evolution of misfit surfaces for the inversion of joint-misfit data (equation 5) from reflector C. Plot (a) shows the locations of the initial inversion models (circles). Five iterations (a-e) were completed employing 57 forward models. The normalized minimum joint misfit (f) falls by approximately 25%, and the sub-tolerance change in misfit between iterations 4 and 5 terminated the inversion. Reference reservoir time shifts were contaminated with Gaussian noise having a standard deviation of 5 ms. The surfaces are interpolated between the misfit values for all models computed through the specified iteration. The reference reservoir pressure drop and length (marked by the cross) are 17.5% and 2.1 km, respectively. The location of the minimum-misfit model at each iteration is marked by a diamond, with a final solution (plot e) of $\Delta P = 16.5\%$ and $L = 2.19$ km.

also increased from 100 to 200. A minimum of 80 forward models and three iterations were required before tolerance-based termination was permitted.

Inverted pressure and length

All pressure-inversion results arranged by wave type are displayed in Figure 4. Because P-wave time shifts in the overburden are small (Figure 2a), they are easily masked by noise. Thus, P-wave inversion for reflector A is successful only for noise-free data (Figure 4a). However, the magnitude of the P-wave shifts accumulated in the overburden increases with depth and reaches maximum values at the top of the reservoir (reflector B). Further, these elevated P-wave shifts extend laterally across the entire reservoir (Figure 2a). Consequently, inversion of P-wave shifts for reflector B yields accurate pressure estimates even for 10 ms noise. P-wave time-shift magnitudes are largest immediately beneath the reservoir due to elevated strains inside it (Figure 2a; see Smith and Tsvankin, 2013) but decrease to 6-8 ms at reflector C (Figure 5a). Thus, P-wave time shifts for reflector C with 5 ms noise still retain the trend of the noise-free data (Figure 5b). That pattern, however, is severely distorted by 10 ms noise (Figure 5c), which results in a large null space in the inversion for ΔP and L (Figure 5d, see Appendix B). Therefore, the accurate pressure estimate obtained from P-wave data for reflector C with $\sigma_{\text{noise}} = 10$ ms should be considered fortuitous. In general, inversion for any reflector may be possible when the standard deviation of the noise does not exceed the range of the time-shift variation.

The conclusions drawn for the P-wave time shifts for reflector C also apply to the S-wave shifts for reflectors A and B, which do not exceed 9 ms in magnitude (Figures 2b and 4b). In contrast, the higher-magnitude S-wave time-shift curve for reflector C retains a distinct trend even after contamination with 10 ms noise (Figure 5e), and the misfit surface possesses a well-defined global minimum (Figure 5f). Because time shifts of PS-waves above the reservoir are mostly controlled by P-wave lags, low-noise PS results for reflector A are similar to those for P-waves. The low-noise PS-wave shifts (Figure 2c) from reflector B and those from reflector C with all noise levels give acceptable (albeit 3-6% too low) estimations of ΔP (Figure 4c).

Noise-free joint-misfit (P, S, and PS) inversions for all reflectors produce accurate pressure values (±3% of the reference ΔP). The best results using joint misfits for noisy data are achieved at the reservoir top, with ΔP estimates for reflector C being somewhat inferior (Figure 4d).

Inverted reservoir length for P-, S-, and PS-waves (and their combination) from all reflectors is shown in Figure 6. Due to the pronounced variations of time shifts beneath the reservoir with length, accurate inversion results for L (±0.1 km of the actual value) are obtained for all wave types and noise levels at reflector C. As discussed above, P-wave time shifts at reflector A are masked by 5 ms noise, and practically obliterated by 10 ms noise (Figure 6a). Thus, similar to the inversion for ΔP, the seemingly accurate estimates of L for high-noise (10 ms) P- and PS-wave shifts for reflector A should be considered fortuitous. The P-wave time-shift magnitude increases near the reservoir top, and the length is well-constrained by the P-wave reflections from interface B for all levels of noise. Optimal estimates of length from S- and PS-waves are obtained for reflectors B (except for data with $\sigma_{\text{noise}} = 10$ ms) and C.

Perturbations in the strain-sensitivity coefficients

There are few available measurements of the third-order stiffnesses C_{111} and C_{112}, and most published values correspond to dry core samples at room temperature. Also, stress applied in the laboratory typically is not triaxial. Hence, laboratory experiments cannot reproduce in situ conditions, and the third-order stiffnesses will likely vary with temperature and saturation. Figure 7 displays the inversion results obtained with the stiffnesses C_{111} and C_{112} perturbed by ±20%. In agreement with the sensitivity study of Smith and Tsvankin (2013), a 20% increase in C_{111} causes a 15-20% reduction in the inverted pressure (see the cluster on the left of plot). Inverted pressures for C_{111} reduced by 20% are approximately 15% higher. The perturbations of the coefficient C_{112}, whose magnitude is relatively small, have negligible influence on the inversion. The estimated length is less sensitive to errors in C_{111} than is pressure, with almost all results falling within ±5% of the actual value.

Accuracy in reconstructing the strain field

In Figure 8, we illustrate the differences in the horizontal, vertical, and shear strains between the reference reservoir and the models corresponding to the best-case S- and P-wave inversions. In identifying the best inversion models, we consider only the results for noise-contaminated data. The strain fields have been smoothed to remove numerical singularities at the sharp corners of the reservoir, and reveal the nearby field structure where wells may be located or planned. Although the maximum strain differences reach about 20%, the average strains for the inverted models deviate from the reference values by only 1-2%.

Interestingly, the model obtained from P-wave inversion (Figure 8g,h,i) provides a better approximation for the strain field than that derived from S-waves (Figure 8d,e,f). For both models the largest vertical-strain differences are inside the reservoir and near the endcaps, whereas the most significant differences in the horizontal and shear strain are observed at the endcaps. It should

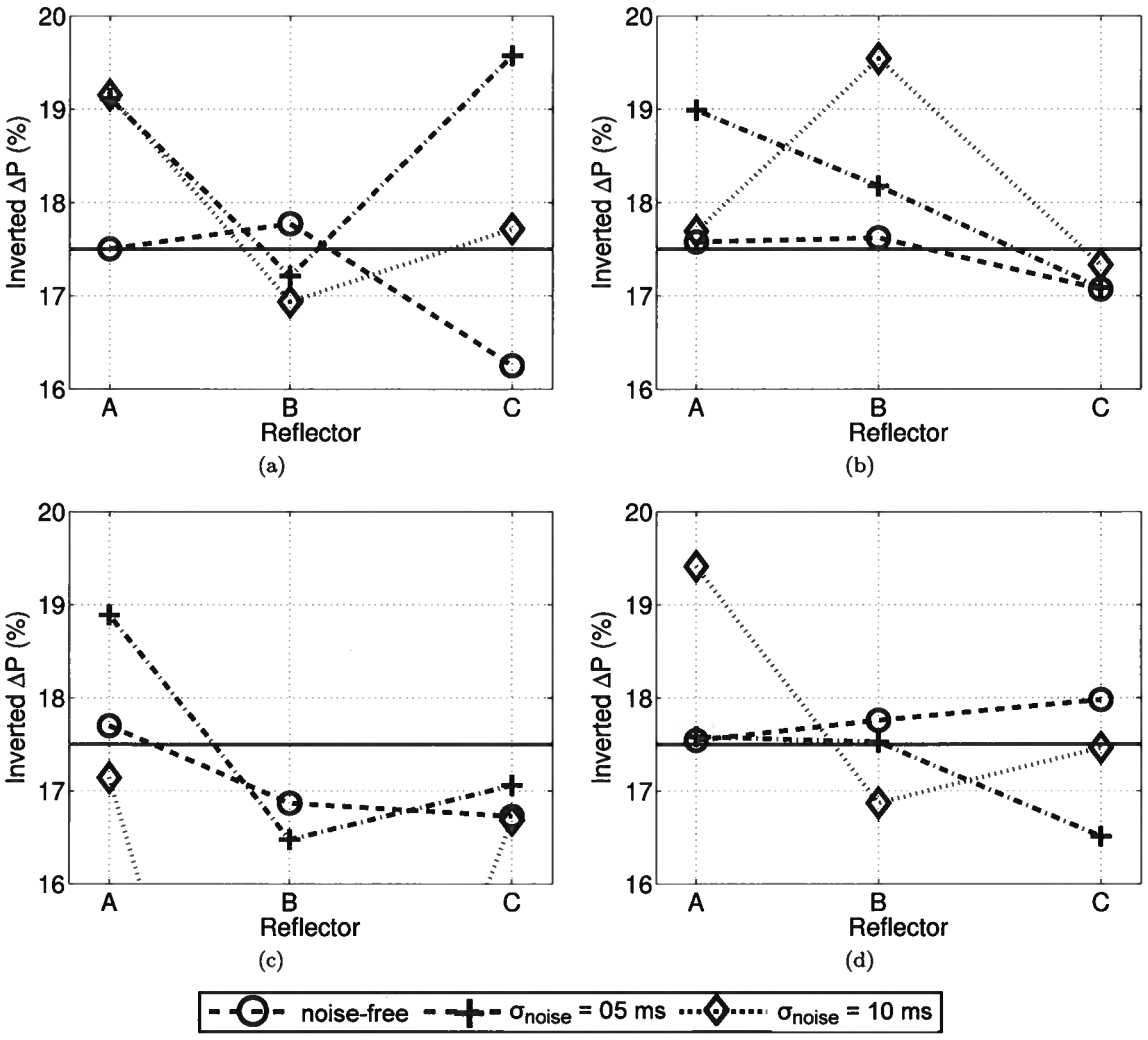

Figure 4. Inverted reservoir pressure drop using time-shift misfits of (a) P-waves, (b) S-waves, (c) PS-waves, and (d) the combination of all three modes (joint misfits). The actual reservoir pressure drop is 17.5%, and is marked by the solid line. Plot legends indicate the standard deviation of Gaussian noise added to the time shifts of the reference reservoir. The inverted $\Delta P = 10.4\%$ for PS-waves from reflector B with $\sigma_{\text{noise}} = 10$ ms is located outside the plot.

be emphasized that the best-case S- and P-wave models have close values of the pressure drop (differing by 2.5%). Hence, the errors in the estimated strains are confined to the vicinity of the reservoir, where the strain field is quite sensitive to small changes in reservoir pressure.

DISCUSSION

The results shown here may be considered optimistic compared to those that may be obtained by applying this method to field data. First, we use a known, simple model geometry consisting of a single-compartment reservoir with flat boundaries embedded in an initially homogeneous background, so the compaction produces well-understood stress and strain fields of low complexity. Second, when generating seismic data and computing time shifts for inversion, we have the ability to place strong reflectors at locations of our choosing. Consequently, we generate high signal-to-noise reflections and clean time-shift data (except where arrivals interfere). Hence, the inverse problem discussed here is better conditioned than that for typical field sets, although we did study the influence of noise on the inversion results.

For example, when dealing with field seismic data, only sections of reflectors may be available for time-shift measurements. In that case, employing joint misfits (i.e., equation 5) for multiple reflectors and arrivals (P, S, PS) may be necessary. Note that while we have used only a

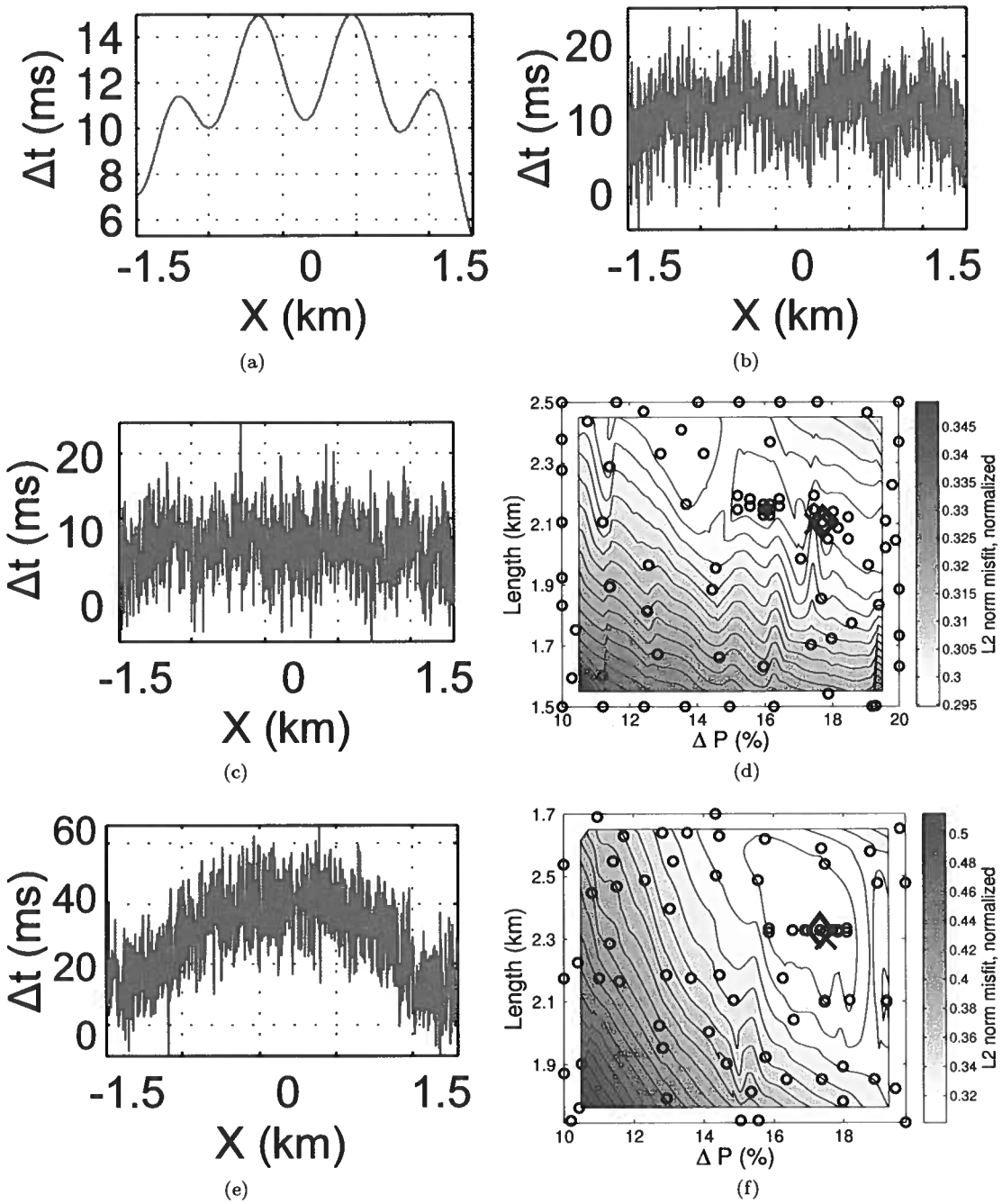

Figure 5. Measured P-wave time shifts vs offset $[\Delta t(x)]$ from reflector C for (a) noise-free data (Figure 2a), (b) $\sigma_{\text{noise}} = 5$ ms, and (c) $\sigma_{\text{noise}} = 10$ ms. (d) The misfit surface for P-waves from reflector C with $\sigma_{\text{noise}} = 10$ ms; the actual parameters are marked by the cross, and inverted parameters by the diamond. (e) S-wave time shifts from reflector C with $\sigma_{\text{noise}} = 10$ ms (Figure 2b), and (f) the misfit surface for the S-wave shifts from plot (e).

single shot record for each reflector, improved results should be expected for multiple sources located both above and to the side of the reservoir.

The P-wave time shifts for our models are larger than than those published in the literature for field time-lapse data. Modifications to the modeling process such as adding a pressure-dependent effective stress coefficient α (equation 2) will reduce changes in the stiff-

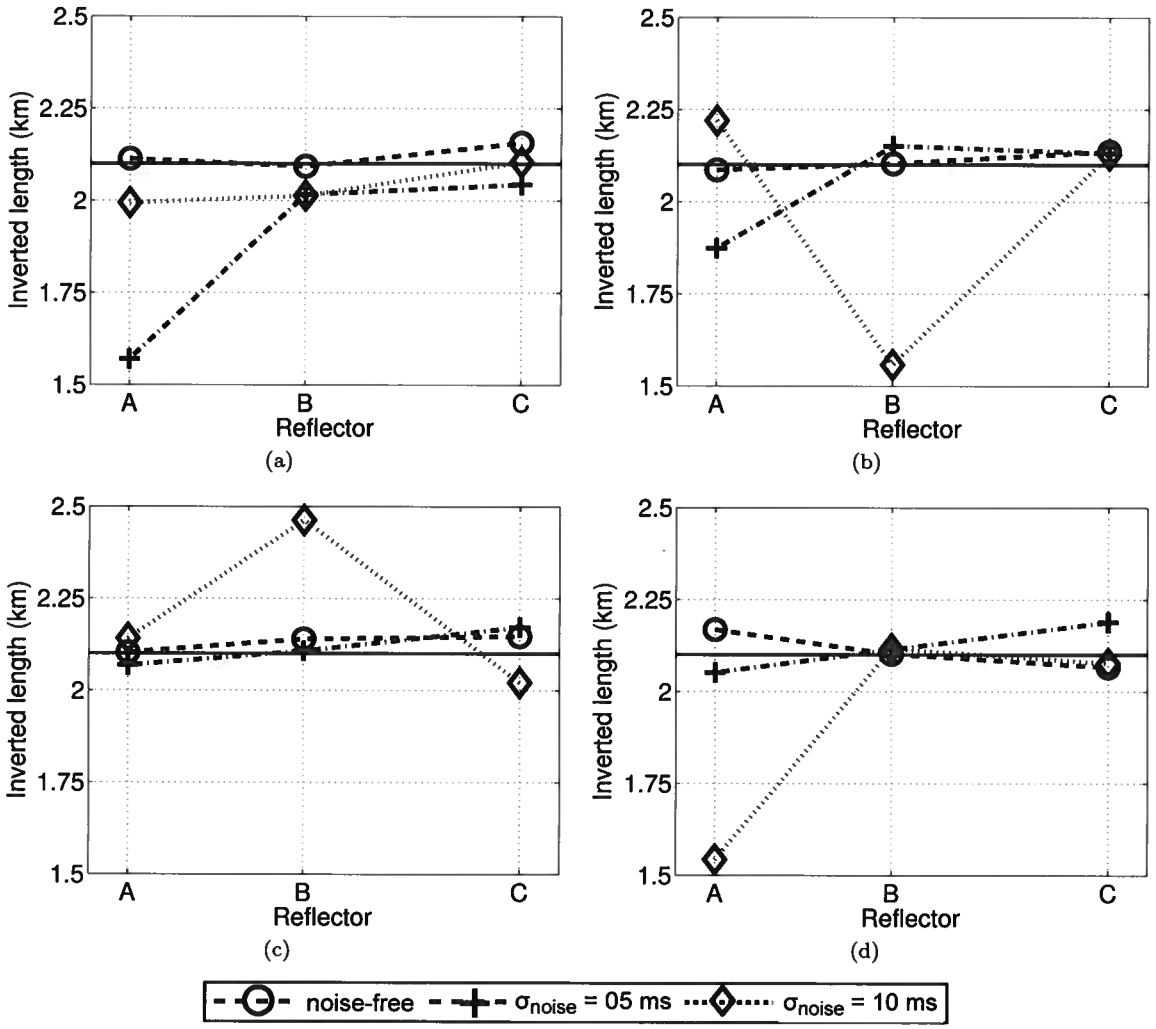

Figure 6. Reservoir length (L) estimated from time-shift misfits of (a) P-waves, (b) S-waves, (c) PS-waves, and (d) the combination of all three modes. The actual reservoir length (2.1 km) is marked by the solid line.

nesses, and thus the overall time-shift magnitudes (Figure 2). Further, the strain-sensitivity coefficients used here (Sarkar et al., 2003) were measured at room temperature on dry rock, and are likely to be different from in situ values. Adjusting the geomechanical modeling to incorporate in situ reservoir rock physics should reduce the modeled strains and time shifts. However, the spatial patterns of time shifts around the reservoir (Figure 2) will remain essentially the same, as will the time-shift variations with wave type. For example, the P-wave shift pattern of Figure 2a is similar to the lower-magnitude time shifts measured for the Shearwater North Sea reservoir (Staples et al., 2007). Thus, the dependence of the inversion results on the input data and signal-to-noise ratio is adequately addressed by the presented study.

CONCLUSIONS

We applied a hybrid global/gradient algorithm to evaluate the feasibility of inverting compaction-induced time shifts of P-, S-, and PS-waves for reservoir pressure and length. The time shifts were measured for three reflectors around a single-compartment reservoir embedded in an initially homogeneous, isotropic medium. The hybrid inversion algorithm presented here extends the "nearest-neighbor" method by estimating the local gradient at a subset of low-misfit models in the parameter space. This makes the developed technique applicable to more complicated inverse problems, including those for multicompartment reservoirs.

Our numerical analysis helps identify the reflector locations and wave types that should be used to invert for the reservoir parameters for different levels of noise.

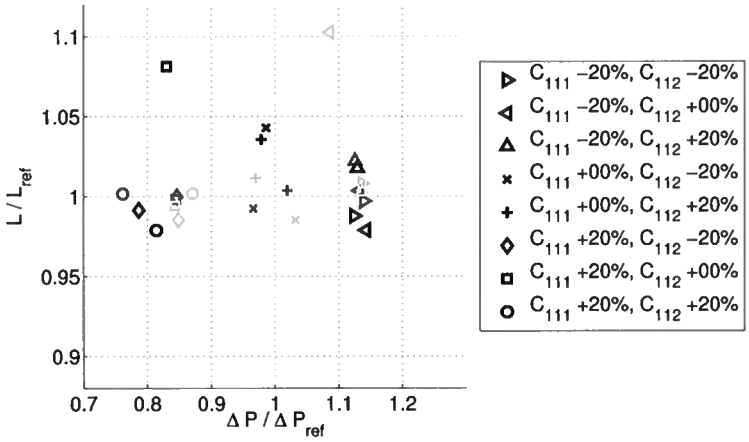

Figure 7. Inversion results obtained with distorted third-order stiffnesses C_{111} and C_{112}. Each coefficient was perturbed by $\pm 20\%$, as shown in the legend. The time shifts for the reference reservoir were obtained with the correct values of C_{111} and C_{112}. Inversions were performed using noise-free joint misfits (equation 5) from each reflector (black markers - reflector A, blue markers - reflector B, and green markers - reflector C).

Reflectors in the overburden generate small time shifts that are suitable for inversion only when the data are essentially noise-free. The magnitude and lateral extent of time shifts increase near the reservoir, making it possible to invert even noisy P-wave reflections from the reservoir top for pressure changes. The most accurate pressure estimates for noise-contaminated S-and PS-wave data are obtained using reflections from interfaces beneath the reservoir, where the shear-wave time shifts reach their maximum values. Reservoir length is well-constrained by the time shifts of all modes from the reservoir top (except for high-noise S and PS data) and from reflectors beneath the reservoir. It should be also noted that inversion of reflections from deep interfaces typically requires computing fewer forward models. Inversion of joint (P, S, PS) time shifts using models with $\pm 20\%$ errors in the strain-sensitivity coefficients resulted in comparable distortions in the pressure drop, but insignificant errors in reservoir length.

The results of this work can be used to model expected strain and stress changes around the depressurizing reservoir. The maximum differences between the strain values computed for the reference reservoir and the best inverted models are limited to about 20% of the reference strain.

ACKNOWLEDGMENTS

We are grateful to Rodrigo Fuck (CWP, now HRT-Brazil), Mike Batzle (CSM/CRA), Roel Snieder (CWP), Jyoti Behura (CWP), Matt Reynolds (Applied Math, University of Colorado) and Ritu Sarker (CSM/CRA, now Shell) for discussions, comments, and suggestions, and to Jeff Godwin (CWP, now Transform Software) and John Stockwell (CWP) for technical assistance. The paper by McCann and Wilts (1951) was made available via Stephanie Spika and the City of Long Beach Public Library. This work was supported by the Consortium Project on Seismic Inverse Methods for Complex Structures at CWP.

APPENDIX A: INVERSION ALGORITHM

Because time shifts are generally nonlinear in pressure (Smith and Tsvankin, 2013), we have developed a hybrid inversion algorithm that combines the advantages of global and gradient methods. Gradient inversion algorithms (Gaussian, Levenberg-Marquardt, conjugate gradient, etc.; see Gubbins, 2004; Aster et al., 2005) require the inversion to begin with a model close to the global minimum (true solution). However, the structure of the misfit function is unknown, and may be complicated. Also, gradient algorithms typically need several forward models per iteration to compute the gradient and curvature (Jacobian, Hessian) of the objective function and estimate the update step size in the parameter space. Misfit data for all generated models typically are not retained, and cannot be used in later iterations.

The gradient portion of our algorithm is based on the "nearest neighbor" method of Sambridge (1999). The inversion begins with a regular distribution of initial models in parameter space that have been randomly perturbed to assure that they are neither equidistant to each other or the center of the parameter space (Figure 3a). At each iteration the algorithm computes the misfit for each forward model and selects a subset of minimum-misfit models to update. Nearest-neighbor method divides parameter space into Voronoi cells and updates

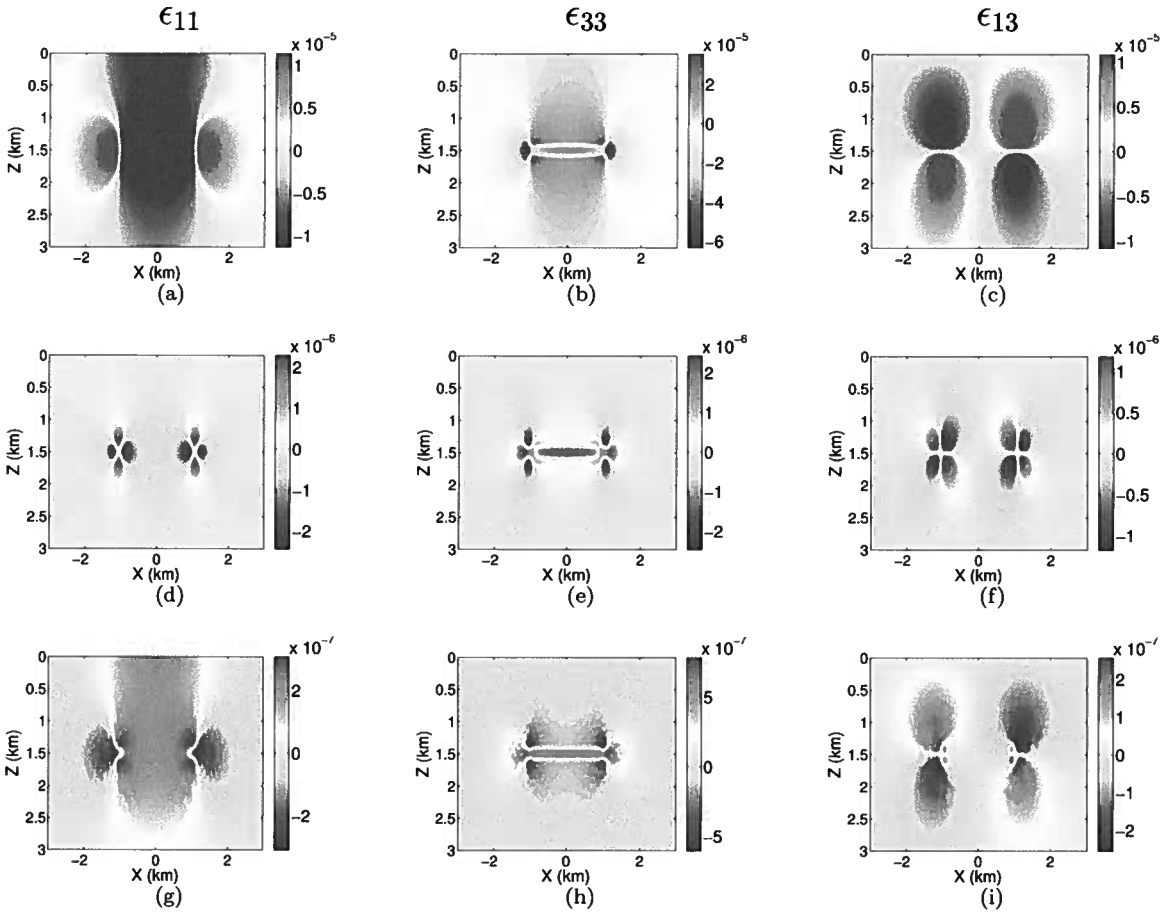

Figure 8. Comparison of the strain fields for the actual and inverted models. (a,d,g) The horizontal strain ϵ_{11}; (b,e,h); the vertical strain ϵ_{33}; (c,f,i) the shear strain ϵ_{13}. The strains for the reference reservoir ($\Delta P = 17.5\%$, L = 2.1 km) are shown in the top row (a,d,c). The strain differences (i.e., the difference between the actual strain field and that for an inverted model) for the "best-case" S-wave and P-wave inversions are shown in the third (d,e,f), and fourth rows (g,h,i), respectively. Both best-case inversions were carried out for reflector C with 10 ms noise. The maximum percentage differences in the strain components for S-waves (d,e,f) are $\epsilon_{11} = 21\%$, $\epsilon_{33} = 4\%$, $\epsilon_{13} = 11\%$, while those for P-waves (g,h,i) are $\epsilon_{11} = 3\%$, $\epsilon_{33} = 1\%$, and $\epsilon_{13} = 2\%$.

minimum-misfit models using a Gibbs's sampler or random walk in each cell. In contrast, our algorithm estimates local gradients of the objective function in the region around the minimum-misfit subset, and places updated models along the gradient direction.

Figure 9 illustrates the method used for estimating the local gradient for the designated N_c minimum-misfit models in the parameter space (equations 4 or 5). Each of these N_c models (point M in Figure 9) is assumed to reside in a local minimum of the misfit surface, and that assumption must be tested using the K nearest models in the K-dimensional parameter space (points N and Q in Figure 9). If the K nearest models possess larger misfits, the direction of the gradient is estimated as the sum of the vectors between the minimum-misfit model and those neighbors. Model updates are inserted in the direction of the estimated gradient; one is located up-gradient, and one down-gradient. At least one additional model is added orthogonal to the gradient, should the current model reside at a saddle point. In the two-parameter inversions shown here, four update models were added at each iteration (two parallel and two orthogonal to the gradient) near the current misfit model. Each of the N_u update models is inserted at one-half the distance to the nearest model used to estimate the gradient direction, thus sampling the local parameter space around the N_c minimum-misfit models. Should none of the updated models possess a lower misfit, their data are simply incorporated into the gradient estimation at the next iteration. This results in a sequence of updates that converges down-gradient toward the local minima (see Figure 10a).

Note that computing Jacobians and Hessians is not required, and the method is computationally simple enough so that one can run many simultaneous gradient-tracking updates (i.e., gradient trackers). Further, this

technique reduces convergence time compared to that of a standard global algorithm because models located in basins of convergence descend along the gradient in a systematic fashion (Figure 10a, also see Appendix B).

Global inversion algorithms (Monte-Carlo, Metropolis, genetic; see Sen and Stoffa, 1995) can explore the entire parameter space and avoid local minima, but typically require many more models than gradient techniques. Here, the goals are to sample parameter space efficiently to delineate the structure of the objective function, and differentiate between local and global minima. In addition to the $N_c * N_u$ gradient estimation/tracking models, N_e "exploration" models are inserted into parameter space. The exploration models are sequentially inserted into voids in the parameter space. These voids are identified by locations having the most common value of an N-dimensional potential function of the form $\sum_{i=1}^{N} 1/|\mathbf{r}|^{\gamma}$, where $|\mathbf{r}|$ is the distance from the ith model in the current set, and γ is a constant. If a smaller misfit value occurs at one of the exploration models, that model is incorporated into the subset of N_c convergence/update models, and gradient estimation/tracking shifts to that region of parameter space. Therefore, estimating and tracking the local gradient moves the search toward a local minimum, while the global/exploration models potentially make it possible to find the global minimum. As the inversion progresses, data from all computed forward models are saved in memory, which helps build the misfit surface by interpolation (Figures 10a,b and 3).

The inversion is typically terminated when changes in the user-specified misfit value fall below a specified tolerance level. It is necessary to specify a minimum and maximum number of iterations (or models) run before terminating the inversion. In some cases, the inversion halts when the total number of iterations or forward models passes a limit specified by the user. However, should the algorithm become trapped in one or more local minima, the user may increase the number of exploratory models per iteration (N_e), the number of gradient trackers (N_c), the minimum or maximum number of models to be run before termination, or all of these parameters.

In the examples shown here, the algorithm is implemented in a 2D parameter space, but the extension to higher-dimension parameter sets is straightforward. While not done here, interpolating the N-dimensional misfit surface may allow for an additional, and potentially more accurate update model to be placed in parameter space at the minimum of the interpolated misfit function. This provides an estimate of the global minimum, and placing a model there may increase the rate of convergence.

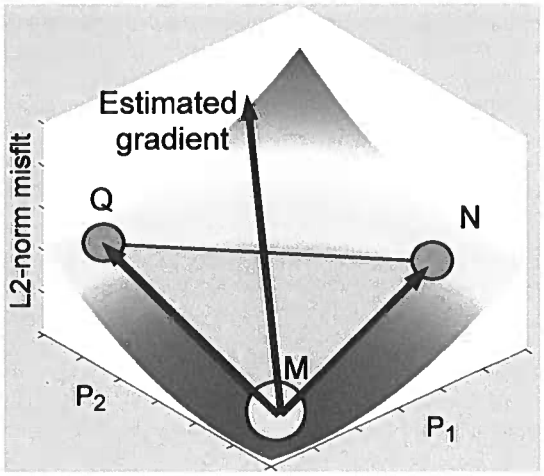

Figure 9. Local gradient estimation using nearest models in a two-dimensional ($K = 2$) parameter space $[P_1, P_2]$. Each minimum-misfit model (point M) is assumed to be in a local minimum. The gradient direction is estimated by summing the vectors **MN** and **MQ**, where N and Q are the nearest models. If the misfits at N and Q are greater than that at M, new models are placed along and orthogonal to the estimated gradient vector at distances equal to $\pm(1/2)\min(|\mathbf{MN}|, |\mathbf{MQ}|)$.

APPENDIX B: MISFIT SURFACES AND THE PERFORMANCE OF THE INVERSION ALGORITHM

The misfit curve in Figure 3f illustrates the convergence characteristics of the hybrid algorithm. It is typical for the misfit to drop substantially in the first iteration when the misfit surface is simple and smooth. As the gradient-tracking part of the algorithm reduces the step-size over iterations, misfit functions generate traditional "L-shaped" curves. However, the global portion of the algorithm may locate new local minima in the parameter space, or a gradient-tracker may turn down a sharp slope. In this case, the misfit curve experiences a significant drop (e.g., between iterations 3 and 4 in Figure 3f).

An example of the gradient-tracking behavior of the algorithm is clearly seen in Figure 10a where a series of models descends the misfit surface toward the actual $\Delta P = 17.5\%$. The misfit surface is interpolated using the entire set of inversion models (black circles) from the current and all prior iterations (no models are chosen/interpolated from the misfit surface). Note that the parameter space is well-sampled by the global portion of the algorithm.

It is useful to study the misfit surfaces to gauge how well a multiparameter inversion is conditioned, and determine whether or not the algorithm converges toward the global minimum. Figure 10a shows a "bowl-shaped" misfit surface computed using noise-free P-wave time shifts from reflector A. The addition of noise to the time

shifts for the reference reservoir not only increases the misfit magnitude, but also smoothes the misfit surface by flattening the data's power spectrum. This reduces the complexity of the misfit surface (improves conditioning) and allows the gradient portion of the algorithm to perform more efficiently. However, as the noise level increases, coherent/desired data become masked and the misfit surfaces become over-smoothed (Figure 10b). This flattens out local minima, creates an extended null space, and causes the inversion for noisy data from shallow reflectors to fail. In over-smoothed, failed inversions, the minimum misfit is typically located away from the actual solution at the edges of the parameter space (diamond marker), as the global portion of the algorithm has not located any additional minima with a lower misfit.

A well-sampled parameter space with a complex misfit surface indicates poor conditioning, and the true solution cannot be found without employing the global portion of the algorithm. An example is given in Figure 10c, which corresponds to the best inversion result for PS-waves. Although there is a well-defined basin of attraction, the misfit surface is generally complicated, and there is the potential for multiple local minima. This requires a global algorithm to locate the neighborhood of the actual model.

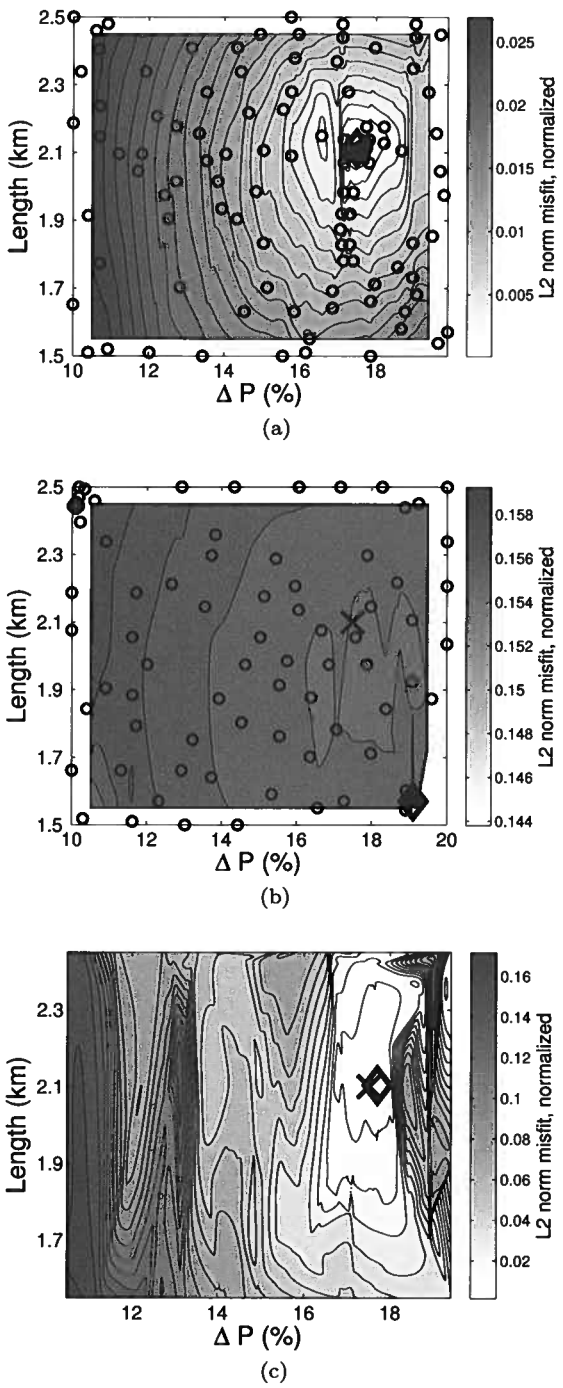

Figure 10. (a,b) Misfit (objective function) surfaces, with inversion models marked by circles, for different levels of noise added to the reference-reservoir time shifts. The misfits are computed for P-wave time shifts from reflector A (a) without noise and (b) with $\sigma_{\text{noise}} = 5$ ms. The actual parameters are marked by crosses, while diamonds mark the final inversion results. Black circles mark all forward models used in the inversion. (c) The misfit surface for the best-case PS-wave inversion (using noise-free shifts from reflector A). While this PS-result is accurate (cross and diamond overlap), the misfit surface is complicated enough to require the use of a global inversion algorithm.

References

Aster, R. C., B. Borchers, and C. Thurber, 2005, Parameter estimation and inverse problems: Academic Press.

Batzle, M., and D. Han, 2009, Rock and fluid properties: Seismic rock physics. SEG Continuing Education Series, Denver Geophysical Society.

Calvert, R., 2005, Insights and methods for 4D reservoir monitoring and characterization: Distinguished Instructor Short Course, Society of Exploration Geophysicists.

COMSOL AB, 2008, COMSOL Multiphysics. COMSOL AB, http://www.comsol.com/.

De Gennaro, S., A. Onaisi, A. Grandi, L. Ben-Brahim, and V. Neillo, 2008, 4D reservoir geomechanics: a case study from the HP/HT reservoirs of the Elgin and Franklin fields: First Break, **26**, 53–59.

Downs, J., and D. A. Faux, 1995, Calculation of strain distributions in multiple-quantum-well strained-layer structures: Journal of Applied Physics, **77**, no. 6, 2444–2447.

Fuck, R. F., A. Bakulin, and I. Tsvankin, 2009, Theory of traveltime shifts around compacting reservoirs: 3D solutions for heterogeneous anisotropic media: Geophysics, **74**, no. 1, D25–D36.

Fuck, R. F., I. Tsvankin, and A. Bakulin, 2011, Influence of background heterogeneity on traveltime shifts for compacting reservoirs: Geophysical Prospecting, **59**, no. 1, 78–89.

Greaves, R. J., and T. J. Fulp, 1987, Three-dimensional seismic monitoring of an enhanced oil recovery process: Geophysics, **52**, no. 9, 1175–1187.

Gubbins, D., 2004, Time series analysis and inverse theory for geophysicists: Cambridge University Press.

Hatchell, P., and S. Bourne, 2005, Rocks under strain: Strain-induced time-lapse time shifts are observed for depleting reservoirs: The Leading Edge, **24**, no. 12, 1222–1225.

Hearmon, R., 1953, 'Third-Order' elastic coefficients: Acta Crystalographia, **6**, 331–340.

Herwanger, J., 2008, R we there yet?: 70th Annual International Meeting, EAGE, Expanded Abstracts.

Hodgson, N., C. MacBeth, L. Duranti, J. Rickett, and K. Niheil, 2007, Inverting for reservoir pressure change using time-lapse time strain: Application to Genesis Field, Gulf of Mexico: The Leading Edge, **26**, no. 5, 649.

Hornby, B. E., 1996, Experimental investigation of effective stress principles for sedimentary rocks: SEG Technical Program Expanded Abstracts, 1707–1710.

Hu, S. M., 1989, Stress from a parallelepipedic thermal inclusion in a semispace: Journal of Applied Physics, **66**, no. 6, 2741–2743.

Janssen, A. L., B. A. Smith, and G. W. Byerley, 2006, Measuring velocity sensitivity to production-induced strain at the Ekofisk field using time-lapse time-shifts and compaction logs: SEG Technical Program Expanded Abstracts.

Landrø, M., 2001, Discrimination between pressure and fluid saturation changes from time lapse data: Geophysics, **66**, no. 3, 836–844.

Lumley, D., 2001, Time-lapse seismic reservoir monitoring: Geophysics, **66**, no. 1, 50–53.

Magnesan, M., S. Depagne, K. Nixon, B. Regel, J. Opich, G. Rogers, and T. Hudson, 2005, Seismic processing for time-lapse study: Genesis field, Gulf of Mexico: The Leading Edge, **24**, no. 4, 364–373.

McCann, G. D., and C. H. Wilts, 1951, A mathematical analysis of the subsidence in the Long Beach-San Pedro area: Technical report, Caltech.

Mindlin, R. D., and D. H. Cheng, 1950, Nuclei of strain in the semi-infinite solid: Journal of Applied Physics, **21**, 926–930.

Rickett, J., and D. Lumley, 1998, A cross-equalization processing flow for off-the-shelf 4d seismic data: SEG Technical Program Expanded Abstracts, **17**, doi:10.1190/1.1820252.

———, 2001, Cross-equalization data processing for time-lapse seismic reservoir monitoring: A case study from the Gulf of Mexico: Geophysics, **66**, no. 4, 1015–1025, doi:10.1190/1.1487049.

Roste, T., 2007, Monitoring overburden and reservoir changes from prestack time-lapse seismic data - applications to chalk fields: PhD thesis, Norwegian University of Science and Technology.

Sambridge, M., 1999, Geophysical inversion with a neighbourhood algorithm - I. searching a parameter space: Geophysical Journal International, **138**, 479–494.

Sarkar, D., A. Bakulin, and R. L. Kranz, 2003, Anisotropic inversion of seismic data for stressed media: Theory and a physical modeling study on Berea sandstone: Geophysics, **68**, no. 2, 690–704.

Sava, P., J. Yan, and J. Godwin, 2010, SFEWE elastic finite difference wave-propagation development code for the Madagascar seismic software collection: http://www.reproducability.org.

Sayers, C. M., 2010, Geophysics under stress: Geomechanical applications of seismic and borehole acoustic waves. Number 13 *in* Distinguished Instructor Short Course: Society of Exploration Geophysicists.

Sayers, C. M., and P. M. Schutjens, 2007, An introduction to reservoir geomechanics: The Leading Edge, **26**, no. 5, 597–601.

Schutjens, P. M. T. M., T. H. Hanssen, M. H. H. Hettema, J. Merour, P. de Bree, J. W. A. Coremans, and G. Helliesen, 2004, Compaction-induced porosity/permeability reduction in sandstone reservoirs: data and model for elasticity-dominated deformation: SPE Reservoir Evaluation & Engineering, SPE 88441, 202–216.

Sen, M. K., and P. L. Stoffa, 1995, Global optimization methods in geophysical inversion, volume **4** *of* Advances in Exploration Geophysics: Elsevier Science.

Smith, S., and I. Tsvankin, 2012, Modeling and analysis of compaction-induced traveltime shifts for multicomponent seismic data: Geophysics, **77**, no. 6, T221–T237.

Smith, S., and I. Tsvankin, 2013, Sensitivity of compaction-induced multicomponent seismic time shifts to variations in reservoir properties: Submitted to Geophysics.

Staples, R., J. Ita, R. Burrel, and R. Nash, 2007, Monitoring pressure depletion and improving geomechanical models of the Shearwater field using 4D seismic: The Leading Edge, 636–642.

Thurston, R. N., and K. Brugger, 1964, Third-order elastic constants and the velocity of small amplitude elastic waves in homogeneously stressed media: Physical Review, **133**, A1604–A1610.

Tsvankin, I., 2005, Seismic signatures and analysis of reflection data in anisotropic media, 2nd ed.: Elsevier Science.

Wikel, K. R., 2008, Three-dimensional geomechanical modeling of a tight gas reservoir, Rulison Field, Colorado: Master's thesis, Reservoir Characterization Project, Colorado School of Mines.

Yale, D. P., and W. H. Jamieson, 1994, Static and dynamic mechanical properties of carbonates, *in* Nelson, P.P., and S.E. Laubach, *eds.*, Rock Mechanics, Models, and Measurements Challenges from Industry, Proceedings of the 1st North American Rock Mechanics Symposium, 463–471. Balkema. ISBN 9054103858.

Shot-domain 4D time-lapse seismic velocity analysis using apparent image displacements

Francesco Perrone and Paul Sava
Center for Wave Phenomena, Colorado School of Mines

ABSTRACT

Hydrocarbon production modifies the stress conditions in the subsurface and changes the model parameters previously estimated from the prospect. The capability to remotely monitor the changes in the reservoir using seismic data has strategic importance since it allows us to infer fluid movement and evolution of stress conditions, which are key factors to enhance recovery and reduce uncertainty and risk during production. A model of the subsurface parameters is necessary to reconstruct the seismic waves traveling through the medium and thus correctly image reflectors in the subsurface. Geomechanical changes in the subsurface can be measured by changes of seismic images obtained from the recorded data of multiple time-lapse surveys. In this work, we estimate changes of subsurface model parameters using the apparent shifts between migrated images obtained by 4D time-lapse seismic surveys. We assume that the shift between the time-lapse images of the same reflectors is completely due to the perturbation of the model parameters, and we use the image from the first (baseline) survey as a reference to estimate this perturbation. The apparent shifts are measured using penalized local correlations in the image domain, and they are exploited using wavefield tomography with an objective function minimized using the adjoint-state method. Our time-lapse monitoring method is efficient due to the fact that inversion can be conducted for pairs of seismic experiments, which eliminates the need to construct costly gathers. Since relatively small amounts of data are needed, our method can be used to invert for model changes at short intervals, thus increasing the resolution of 4D monitoring.

1 INTRODUCTION

Production of a hydrocarbon reservoir changes the physical parameters of the subsurface. Oil and/or gas extraction modifies the bulk modulus of the rocks and affects the geomechanics of the area. Stress changes induced by hydrocarbon production represent a key issue for constructing a geomechanical model of the reservoir. Monitoring these changes using remote sensing techniques is crucial for the oil and gas industry to design wells, predict recovery, and mitigate hazards and risk (Lumley, 2001).

Seismic waves are sensitive to the elastic properties of the subsurface. The propagation velocities of the elastic waves are directly related to to the stress state in the subsurface (Aki and Richards, 2002). By repeated seismic surveys over a reservoir at the various production stages, we can track changes in the propagation velocity in the subsurface and reconstruct the perturbation with respect to an initial model. This analysis exploits the sensitivity of the seismic waves to the elastic parameters of the subsurface. Inversion maps the changes in the recorded waveforms into a perturbation of the velocity model, which can then be related to stresses in the subsurface for geomechanical applications.

Time-lapse analysis is usually performed in the time domain (Hatchell and Bourne, 2005) and assumes small perturbations with respect to the background (baseline) model. Great care must be taken to match the baseline and monitor survey, a process called cross-equalization (Rickett and Lumley, 2001), in order to remove from the data all the differences that are not related to changes in the model parameters (e.g., differences in acquisition geometry). Similarly, time-lapse analysis can be done in the image domain, which is less sensitive to differences in the acquisition geometries and thus more robust against repeatability issues than the data domain. Shragge and Lumley (2012) propose a linearized inversion approach in the depth-domain based on the wave-equation migration velocity analysis algorithm developed by Sava and Biondi (2004). Shragge et al. (2012) apply the methodology developed by Yang and Sava (2011) to 4D seismic monitoring and uses the adjoint-state method (Fichtner et al., 2006), which removes the linearity assumptions. By operating directly in the depth domain without linearity assumptions, this inversion can handle strong errors in the velocity model.

Wave-equation MVA (Sava and Biondi, 2004) and image-domain waveform tomography (Yang and Sava, 2011) require complete aperture to correctly construct the image perturbation that drives the tomographic procedure and to evaluate fo-

cusing in the subsurface, respectively. The requirements for the acquisition geometry can be relaxed using the approach proposed by Yang and Sava (2012); nonetheless, a large aperture is necessary for resolution purposes. We advocate the use of local image correlations (Hale, 2007) to measure the relative displacement between shot-migrated images and then use the inversion technique of Perrone and Sava (2012) to evaluate a model update following production. Local image correlations allow us to estimate the velocity model errors shot by shot. The image-domain approach is robust against repeatability issues, such as errors in the shot and receiver positions, and the adjoint-state method allows us to implement a nonlinear inversion procedure, which is effective for large and complex model updates.

2 THEORY

Perrone and Sava (2012) restate the semblance principle considering locally coherent events in the image domain: the velocity model is correct when the images from different neighboring experiments show conformal features, that is, when the dips of the reflectors in the two images are point-wise consistent. This criterium can be applied to migration velocity analysis using local image correlations to evaluate the relative movement of the two images with respect to their structural dips. We can use the same idea for 4D time-lapse seismic and compare the images obtained from the baseline and monitor survey. In this case, we measure shifts of the monitor image with respect to the baseline, which represents the reference. The shift is measured along the normal to the reflector (in the dip direction).

We set an optimization problem by defining the objective function

$$\mathcal{J}(m) = \frac{1}{2} \| \sum_{\boldsymbol{\lambda}} \mathcal{P}(\mathbf{x}, \boldsymbol{\lambda})\, c(\mathbf{x}, \boldsymbol{\lambda}) \|^2_{\mathbf{x}}, \tag{1}$$

where $c(\mathbf{x}, \boldsymbol{\lambda}) = \int_{w(\mathbf{x})} R_{bsl}\left(\boldsymbol{\xi} - \frac{\boldsymbol{\lambda}}{2}\right) R_{mon}\left(\boldsymbol{\xi} + \frac{\boldsymbol{\lambda}}{2}\right) d\boldsymbol{\xi}$ is the local correlation of the baseline image $R_{bsl}(\mathbf{x})$ and the monitor image $R_{mon}(\mathbf{x})$, and $\mathcal{P}(\mathbf{x}, \boldsymbol{\lambda})$ is a penalty operator that highlights features which are related to velocity errors. The correlations are computed in local seamless overlapping windows $w(\mathbf{x})$, and the variable $m(\mathbf{x})$ denotes the model, which is slowness squared in our implementation to simplify the expression of the gradient of the objective function. When the velocity model is correct, the two images are perfectly aligned and the residual $\sum_{\boldsymbol{\lambda}} \mathcal{P}(\mathbf{x}, \boldsymbol{\lambda})\, c(\mathbf{x}, \boldsymbol{\lambda})$, a proxy for the relative displacement, is at minimum.

While we assume that the shifts between the migrated baseline and monitor survey are related to the errors in the velocity model, this is not necessarily true since changes in the stress conditions can cause compaction of the reservoir and lead to subsidence, that is physical movement of all the reflectors above the reservoir. Although subsidence up to 12 m due to hydrocarbon production has been observed and reported in the literature (for example, in the Ekofisk field in the North Sea), shifts in the subsurface are usually negligible compared to the wavelength of the seismic signal (typically these movements can be in the order of a meter between the top and bottom of the reservoir (Hatchell and Bourne, 2005)); it is thus safe to assume that the estimated shifts in the reflector positions are due to changes in the migration model and not to changes of the positions of the interfaces. This is especially true when monitor surveys are performed at short intervals, as advocated in this paper.

We compute the gradient of the objective function in equation 1 using the adjoint-state method (Fichtner et al., 2006). The migrated images are defined as the zero-lag time-correlation of the source and receiver wavefield $u_s(\mathbf{x}, t)$ and $u_r(\mathbf{x}, t)$, which are extrapolated in a model $m(\mathbf{x})$ of the subsurface. The wavefields are computed by solving the wave-equations

$$\mathcal{L}(m)\, u_s = f_s,\ \mathcal{L}(m)\, u_r = f_r, \tag{2}$$

where $\mathcal{L}(m) = m\,\partial_{tt} - \nabla^2$ is the d'Alambert operator, $f_s(\mathbf{x}_s, t)$ and $f_r(\mathbf{x}_r, t)$ are the source and the seismic reflected data, respectively, and $\mathbf{x}_s$ and $\mathbf{x}_r$ indicate the source and receiver positions. In this formulation, $m(\mathbf{x})$ represents slowness squared and since $\mathcal{L}(m)$ is linear in m, this choice simplifies the expression of the gradient of the objective function (Fichtner et al., 2006). The gradient of the objective function is

$$\nabla_m \mathcal{J} = \int (\ddot{u_s} a_s + \ddot{u_r} a_r) dt, \tag{3}$$

where the adjoint wavefields $a_s(\mathbf{x}, t)$ and $a_r(\mathbf{x}, t)$ are solutions to the wave-equations

$$\mathcal{L}^\dagger(m)\, a_s = g_s,\ \mathcal{L}^\dagger(m)\, a_r = g_r. \tag{4}$$

$\mathcal{L}^\dagger(m)$ is the adjoint of the d'Alambert operator, and the adjoint sources $g_s(\mathbf{x}, t) = \nabla_{u_s} \mathcal{J}$ and $g_r(\mathbf{x}, t) = \nabla_{u_r} \mathcal{J}$ are given by the Frechét derivatives of the objective function with respect to the background wavefields. The double dot indicates the second derivative with respect to time.

From the perspective of time-lapse analysis, the gradient $\nabla_m \mathcal{J}$ indicates which parts of the model must change in order to reduce the mismatch between the baseline and monitor migrated images. Through inversion, we can localize the areas in the model that experienced a perturbation in physical parameters and eventually relate that perturbation to geomechanical effects, such as stress changes induced by the reservoir production.

3 SENSITIVITY TESTS

We run a set of sensitivity tests to verify the behavior of the gradient computation in presence of anomalies with different signs and different sources of noise for time lapse monitoring. We verify that the gradient computation is stable when the source wavelet used for imaging is phase shifted with respect to the correct one: we use a minimum phase wavelet to image data obtained using a zero-phase wavelet. We simulate a non-repeatable survey by perturbing the positions of both sources and receivers, and we check the gradient is not

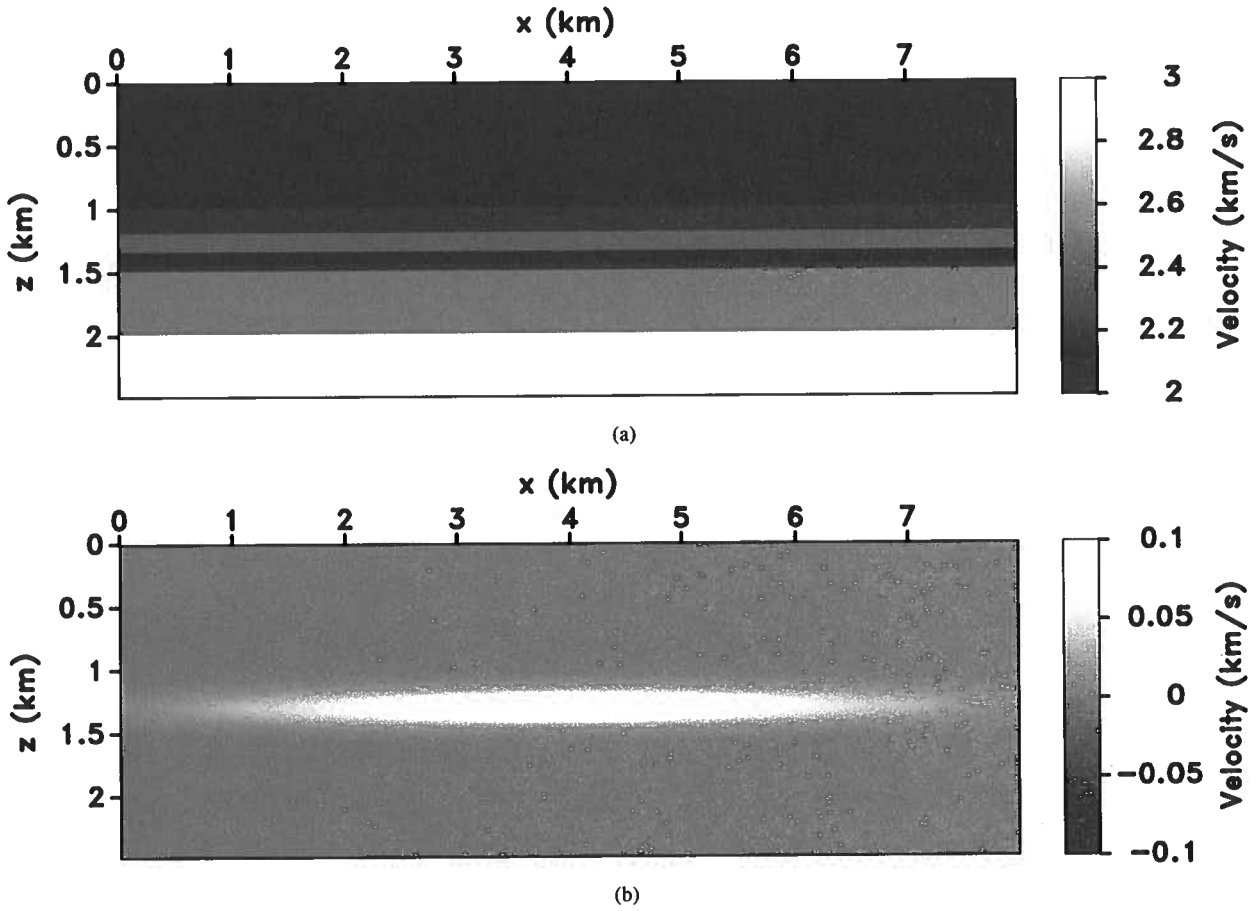

Figure 1. (a) Velocity model used to generate the data and (b) the model perturbation.

affected by source repeatability. Finally, we test the robustness of our method for errors in the baseline velocity model, and we verify that we are able to recover the relative perturbation between the baseline and monitor model.

3.1 Sensitivity to velocity variations

We generate full-acoustic finite-difference data using the velocity model in Figure 1(a). Figure 1(b) represents the velocity model perturbation due to a change in the physical parameters of the medium. The anomaly is confined to a layer and may be caused by fluid substitution or stress changes due to compaction. From an imaging perspective, these different physical phenomena translate into changes in the wave propagation velocities. The anomaly has a maximum amplitude of 0.1 km/s, which corresponds to about 5% of the background value. The vertical and horizontal sampling is 10 m and 20 m, respectively. The source function is a 15 Hz Ricker wavelet. Absorbing boundary conditions are applied so that no surface-related multiples are present in the data. We smooth the model vertically with a 10-sample triangular filter to obtain the baseline migration model.

We test the sensitivity of the algorithm to different values of the perturbation. By computing the gradient of equation 1 with the adjoint-state method from the monitor images computed using the models in Figure 2, we obtain the kernels in Figure 3. Notice that the signs of the kernels reflect the signs of the anomaly.

In a real case, the size of the anomaly would depend on the geology and geomechanics of the subsurface and also on the production activity. The link between seismic velocities and pressure in the reservoir is nonlinear, and thus it is difficult to give bounds on the minimum and maximum size of the anomaly that can be observed in the field. Also, the evolution of the anomaly as a function of time depends on the geomechanics of the area and the production activities, and these pieces of information are necessary to schedule repeated acquisition to monitor the 4D time-lapse effects.

3.2 Sensitivity to wavelet accuracy

We test the robustness of the methodology to small changes of the wavelet used for imaging. Wavelet estimation is a key step in data domain inversion techniques, but it is also quite

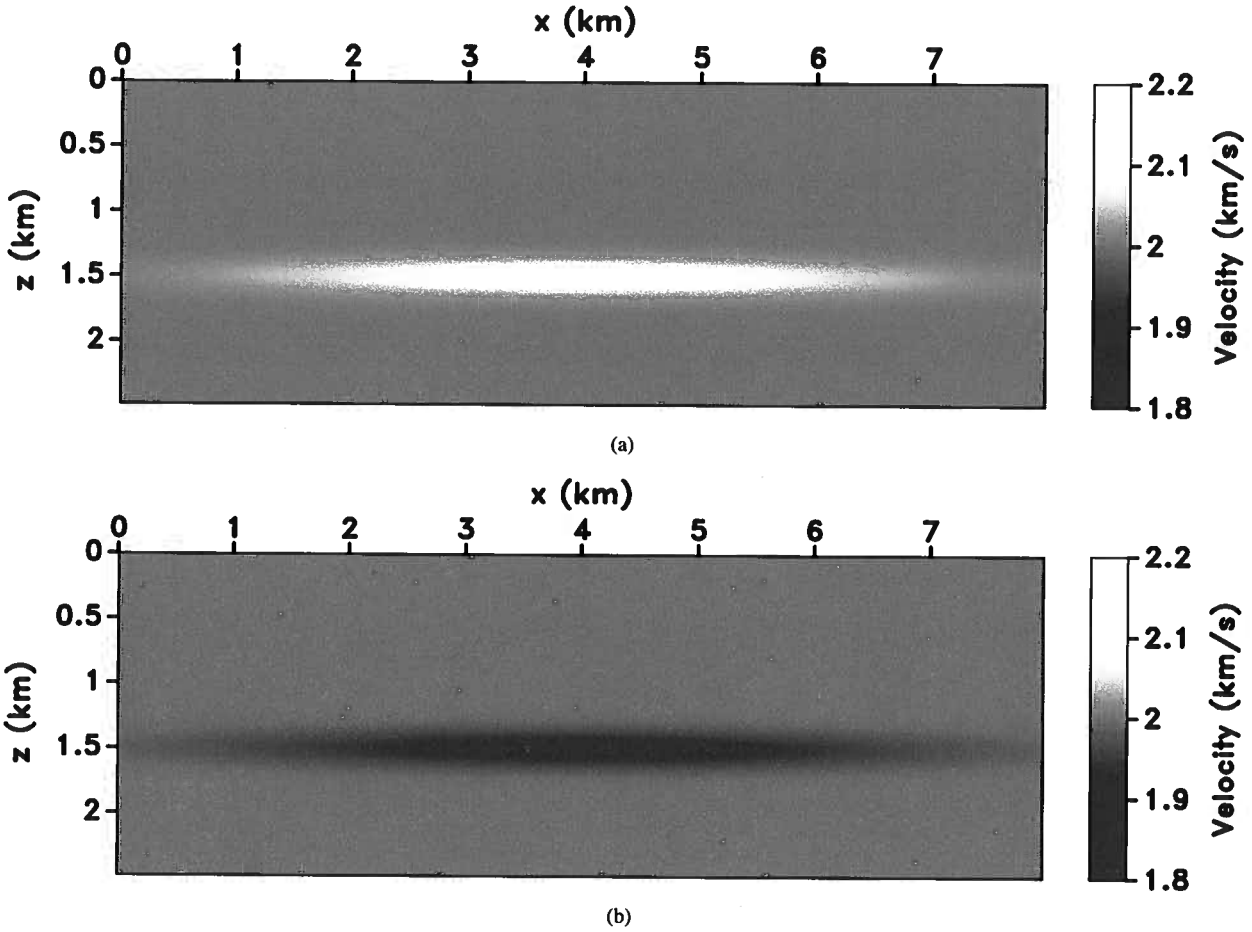

Figure 2. Velocity models with (a) positive and (b) negative anomaly with respect to a constant 2 km/s background velocity.

important when we want to estimate shifts between images of different surveys. Keeping fixed the migration velocity model, we can shift the position of the peak and trough of the wavelet superimposed on the imaged reflector by simply applying a phase-shift to the source wavelet. These shifts are unrelated to errors in the velocity model and can bias the estimate of the apparent shift between baseline and monitor image and then influence the computation of the gradient of the objective function.

Figure 4 shows (a) the wavelet used to generate the baseline and (b) the monitor data. The baseline wavelet is obtained by bandpassing the original 15 Hz Ricker wavelet using a zero-phase filter with cut-off frenquecy 15 Hz. The monitor wavelet is obtained by filtering the original Ricker wavelet in the same frequency band but using a minimum phase-filter instead. The minimum-phase filter introduces a phase shift in the wavelet that can be clearly observed in Figure 4(b).

We migrate the data with the baseline wavelet in Figure 4(a) and the two models in Figure 2. The computed gradients in Figure 5 show that for this simple case, the algorithm is robust against errors between a zero-phase and a minimum-phase source wavelet. The image shift due to errors in the source wavelet adds to the shift due to velocity errors. It is possible that the model error is small and the phase error dominates the image shift. In this latter case, the gradient would be biased. A thorough study of these possible scenarios is necessary to assess the trade-off between different sources of image displacement.

3.3 Sensitivity to survey positioning errors

Repeatability is one of the major problems in 4D time-lapse seismic processing because it is practically impossible to reproduce the same acquisition conditions over multiple surveys, and this inconsistency translates directly into differences in the acquired data that are not associated with 4D effects. We test the robustness of our inversion procedure to non-repeatability issues by randomly perturbing the positions of the source and receivers used to model the monitor data with respect to the baseline survey. The source position in the baseline survey is at $x = 3.9$ km. We record data at 100 locations evenly spaced 20 m apart starting from the source position. Figure 6 shows the baseline data, the monitor data, and their difference. Notice that the earliest events at 1.2 s and 1.3 s in the data do

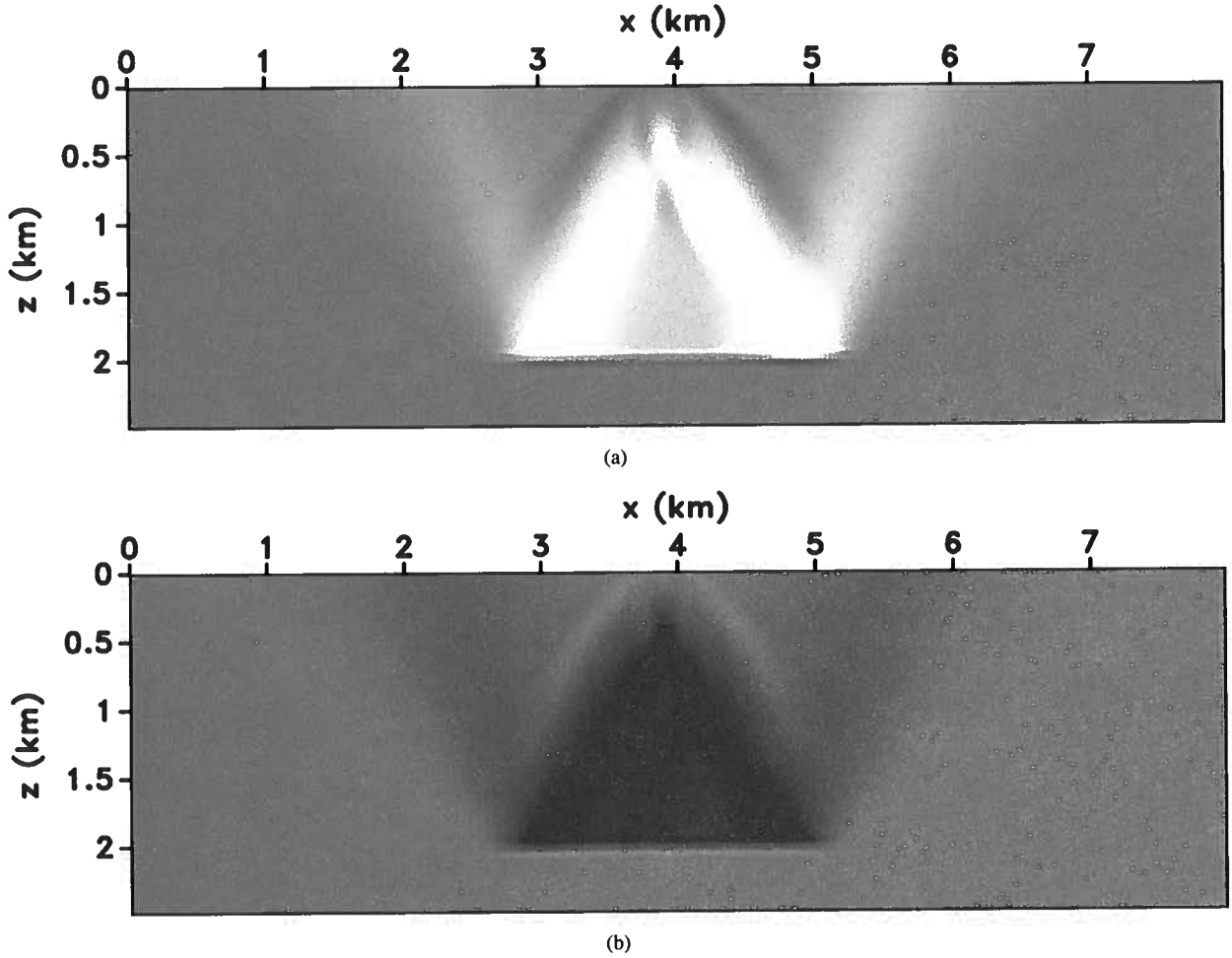

Figure 3. Gradients obtained for (a) the positive and (b) the negative anomaly in Figure 2.

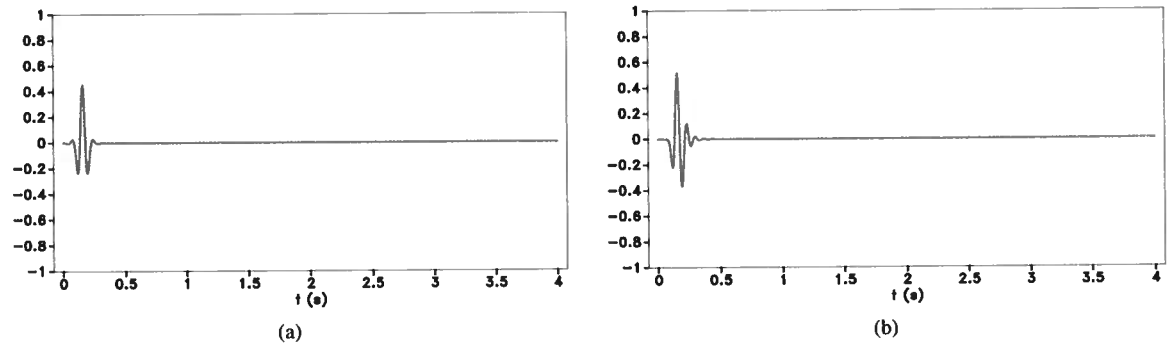

Figure 4. Wavelet for (a) the baseline and (b) the monitor survey.

not cancel because of the error in the shot position. From visual inspection, it is impossible to assess the quality of the baseline model for the monitor image; nonetheless the penalized local correlations highlight the shifts between the two images (Figure 7). Observe that the shallow reflector at 1 km depth is not affected by the anomaly, and our shift estimate correctly returns a near zero value at that location. We compute the gradient using the adjoint-state method and after 60 steepest-descent iterations, we obtain the estimated perturbation shown in Figure 8. Because of the limited aperture of the

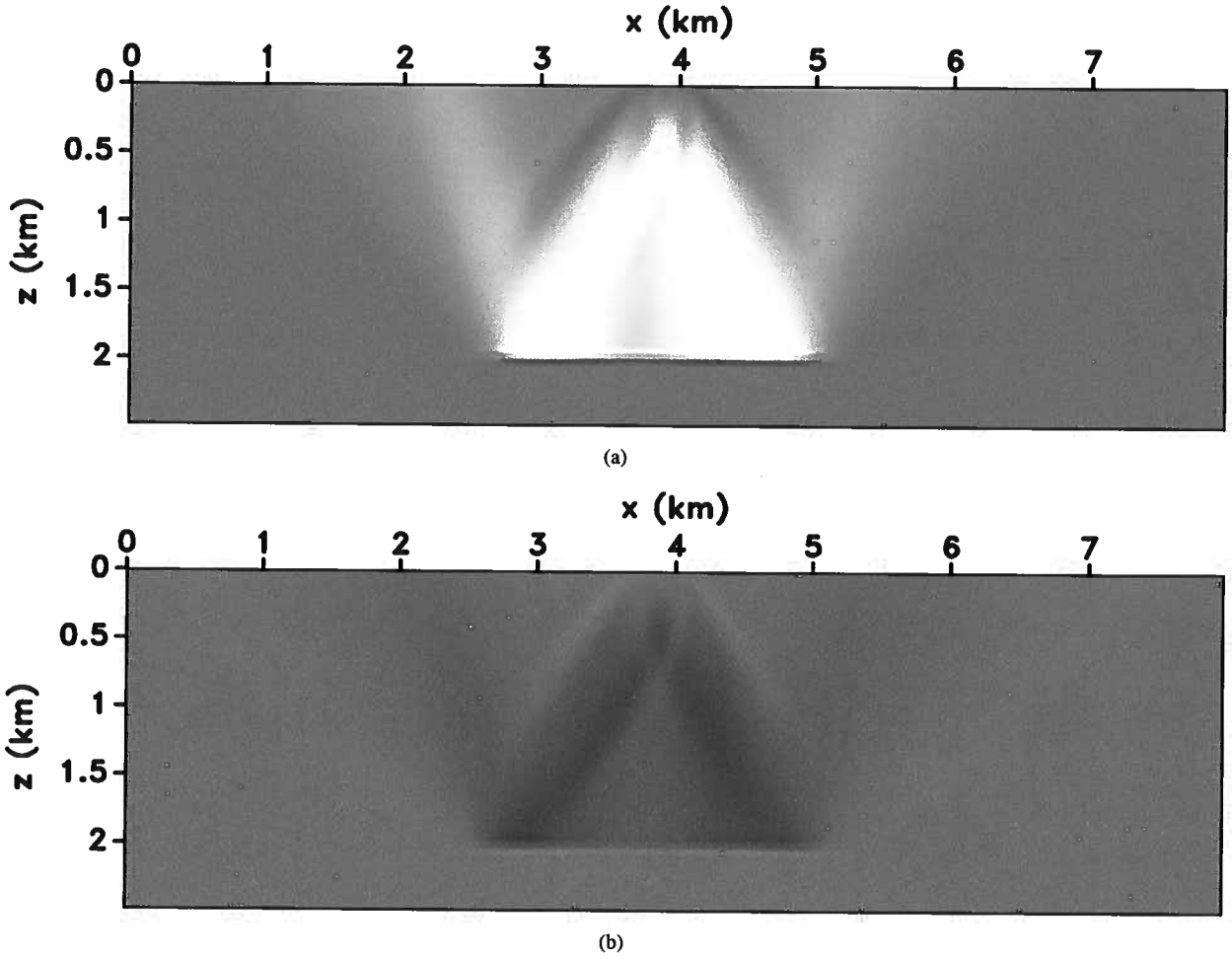

Figure 5. Gradients obtained using the minimum phase-wavelet to image zero-phase data for (a) the positive and (b) the negative anomaly in Figure 2.

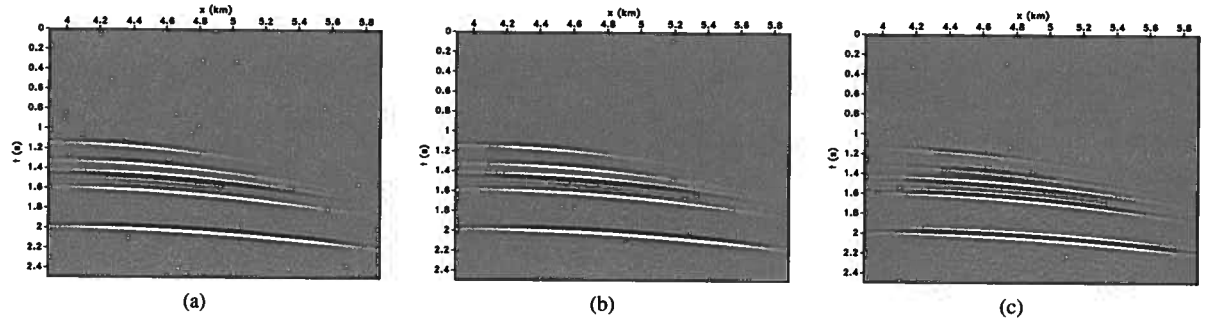

Figure 6. (a) Baseline data, (b) monitor data, and (c) data difference. Notice that because of the positioning error the events above the anomaly (at at 1.2 s and 1.3 s) do not cancel.

survey, only a portion of the anomaly is reconstructed, but the anomaly is building up in the correct layer.

3.4 Sensitivity to baseline model accuracy

Since we measure the displacement of the monitor with respect to the baseline image, we actually estimate the relative error between the monitor and baseline model. This allows us

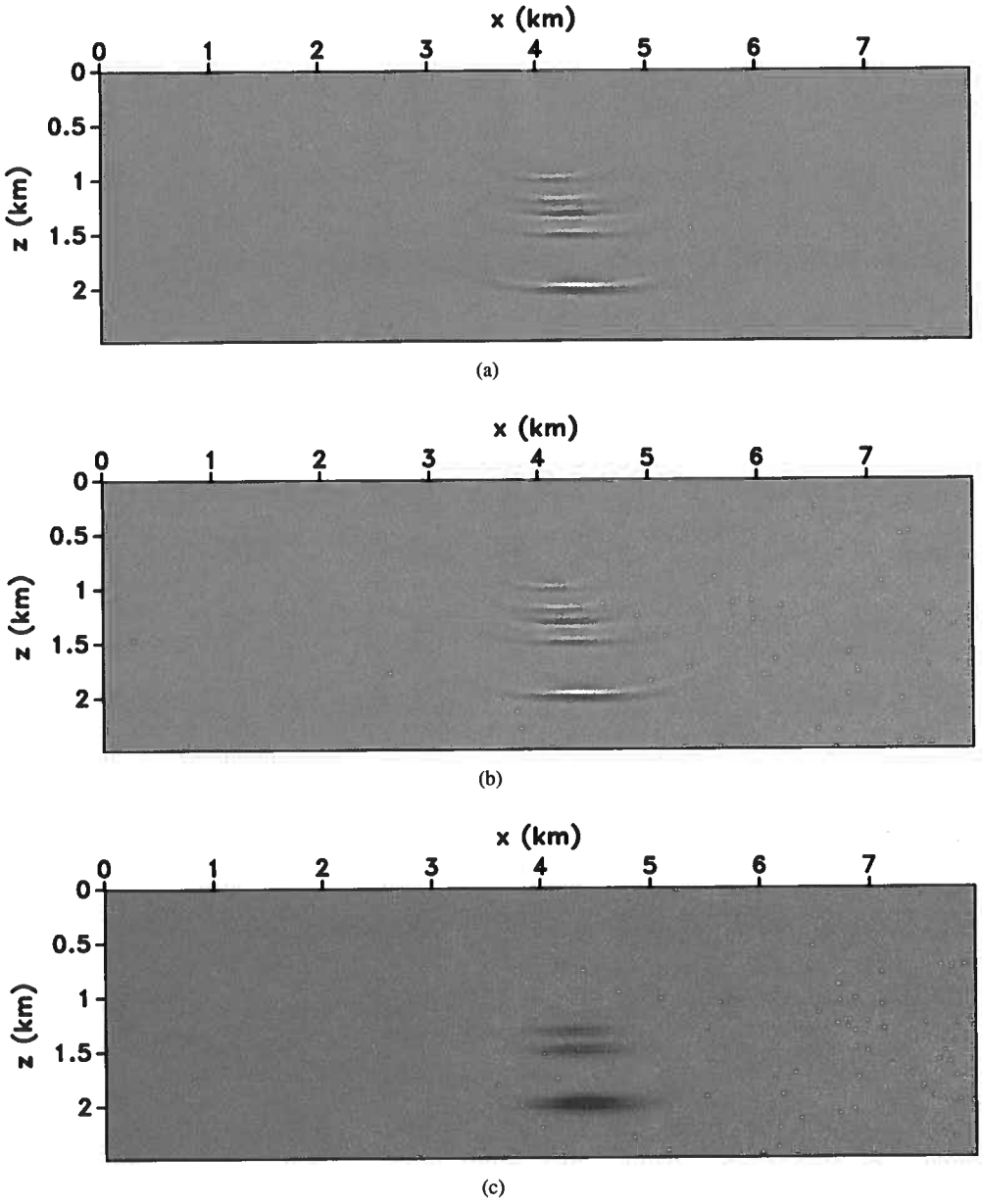

Figure 7. (a) Baseline image, (b) monitor image obtained using the baseline velocity model, and (c) relative shifts between the two images. Black indicates positive (downward) shifts and white represents negative (upward) shifts. The baseline migration model is kinematically accurate and the error is due only to 4D effects in the monitor survey.

to use a somewhat incorrect baseline model and still reconstruct the 4D changes between surveys. Figure 9 shows the baseline image, monitor image, and their relative shift if the baseline velocity model is 5% faster than the model used in Figure 7. The interfaces in both migrated images Figure 9(a) and 9(b) are mispositioned because of the bias in the baseline model. Nonetheless, the shifts only depend on the relative error between the baseline and monitor model, Figure 14(a).The result of the inversion is analogous to the case of correct baseline model, although slightly shifted in depth because of the bias in the baseline model (Figure 10).

4 SYNTHETIC RESERVOIR DEPLETION MODEL

When a reservoir is produced, the depletion causes geomechanical effects both inside and outside the reservoir. Because of the drop in pore pressure, the reservoir rock compacts and the effective stress (and seismic velocity) increases; outside

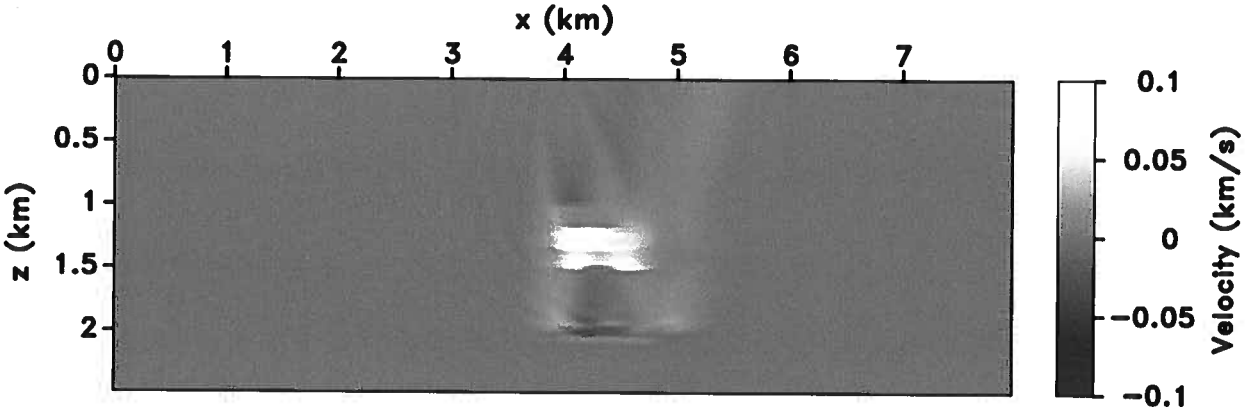

Figure 8. Estimated perturbation after 60 tomographic iterations with a correct baseline velocity model.

the reservoir the rock is strained and the seismic velocity decreases. This observed phenomenon can be analyzed using time-shifts (Hatchell and Bourne, 2005; Hale et al., 2008; Smith and Tsvankin, 2012) and describes the complex changes in subsurface stress conditions caused by oil and gas production.

In order to test our velocity estimation procedure in a more realistic scenario, we use a geomechanical model designed by Smith and Tsvankin (2012) to obtain the model parameters for a reservoir under depletion. We generate data with acoustic finite-differences using density reflectors at various depths and with absorbing boundary conditions on each side of the model (Figure 11(a)). The initial velocity model is homogenous and equal to 2.07 km/s velocity. Figure 11(b) shows the model of the reservoir undergoing a 15% depletion. Observe the complex pattern of the velocity anomaly outside the reservoir. The velocity model perturbation inside the reservoir is about $+15\%$ with respect to the baseline model. Figure 12 shows the data obtained for the baseline and monitor surveys. Observe the internal multiples arriving after 2.5 s and following the strong deeper reflection. From visual inspection, it is difficult to notice any shift in the waveform. However, because of the opposite sign of the velocity anomaly, the early arrivals (around 1.2 s) are delayed and the late waveforms (after 1.5 s) are advanced in time.

Our inversion experiment uses a single shot gather with the source located at $x = 1.5$ km and with a streamer 3.2 km long. The length of the cable is about the same as the lateral extent of the reservoir. The streamer carries 300 evenly spaced receivers and the receiver spacing is 8 m. The gradient of the objective function is smoothed using a triangular filter with radius 2 samples vertically and 5 samples horizontally. The model is updated using a steepest descent algorithm. We implement regularization through triangular smoothing. The smoothing procedure acts as regularization in the inversion by removing spurious high wavenumber sidelobes in the gradient. More sophisticated and structure oriented regularization approaches can be used for more complex subsurface scenarios.

Figure 13 shows the true perturbation and the result of our single-shot inversion after 60 tomographic iterations. Because of the limited aperture of the acquired data, the wavefields are not sensitive to the complete extent of the anomaly. Nonetheless, the imaged portion of the model allows us to constrain the size and location of the anomaly. Notice that the inversion is able to recover the weaker perturbation outside the reservoir of opposite sign with respect to the perturbation within the reservoir, and observe that we are also able to correctly image the left side of the anomaly thus correctly constraining its lateral extent.

Figure 14 shows the shifts between the baseline and monitor migrated images before and after inversion. Black indicated a downward shift whereas white indicate an upward whift. Before inversion the shallower and deeper reflectors are shifted in opposite direction because of the different sign of the anomaly inside and outside the reservoir (see Figure 13(a)). After inversion the reflectors are better aligned and the shifts for all reflectors approach zero. Inversion warps the monitor image into the baseline image and returns the velocity anomaly that corrects the shifts of the imaged interfaces.

5 DISCUSSION

The change of physical properties (such as wave propagation velocity) due to reservoir production leads to apparent shifts in the migrated images obtained from repeated time-lapse seismic surveys of the field. Because the velocity model used in migration is calibrated on the baseline survey, the monitor survey reflectors are slightly mispositioned since we are not taking into account the perturbation of the model due to the production of the field. By matching the baseline and monitor migrated images for single shots, we can translate the apparent image shift into a model perturbation. This approach is fully shot-based since the basic building blocks of the inversion procedure are the single-shot migrated images. This feature is advantageous in a real production scenario when it is difficult to repeat a complete survey because of physical obstructions in the field (such as platforms) which can cause big illumination

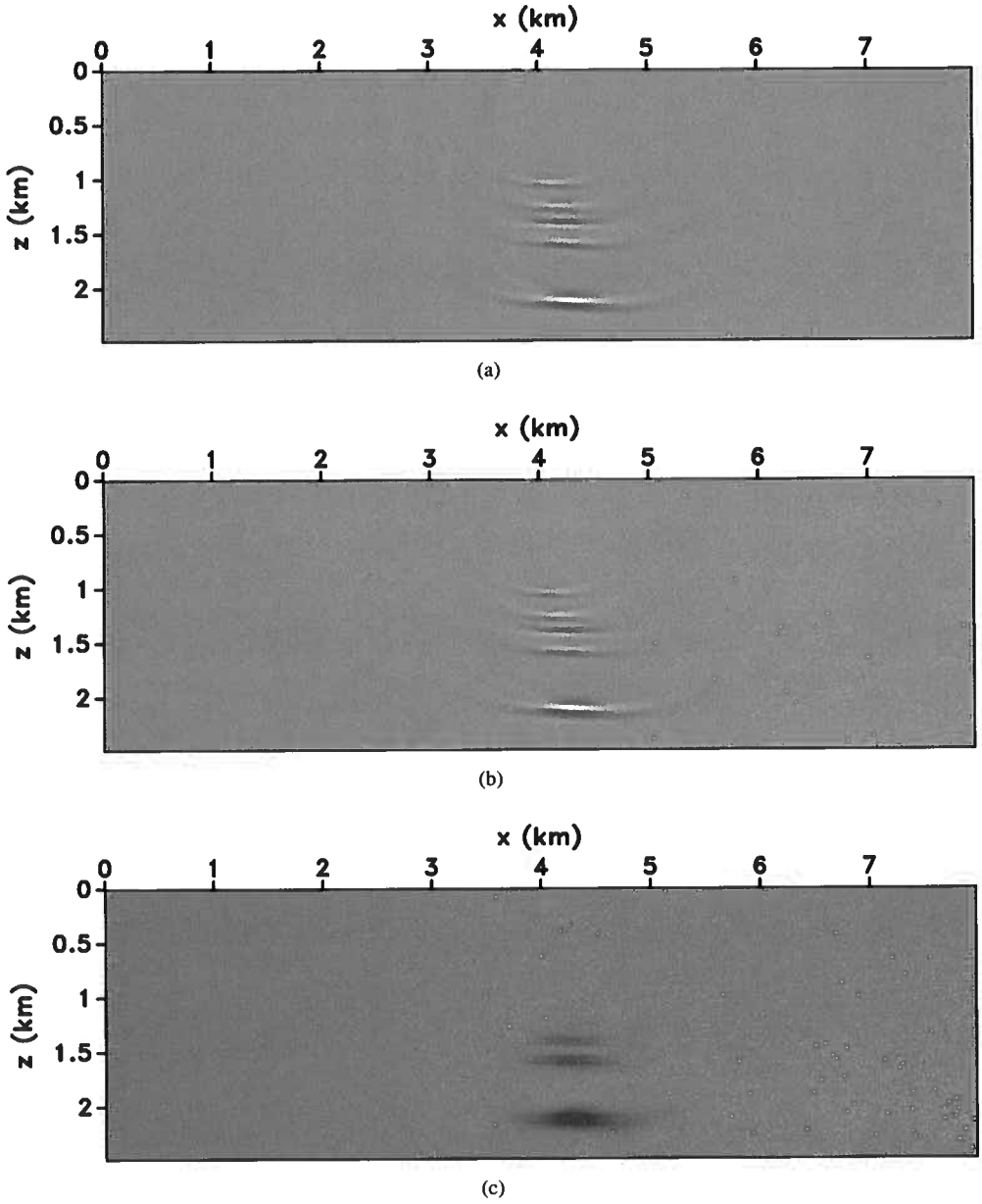

Figure 9. (a) Baseline image, (b) monitor image obtained using the baseline velocity model, (c) relative shifts between the two images. Black indicates positive (downward) shifts and white represents negative (upward) shifts. Here, the migration velocity model is 5% faster than the correct one.

holes in the images. Conducting a complete survey over a producing field is also costly because production must be stopped during acquisition in order to reduce the noise in the seismic data. Our technique addresses this practical problem and can potentially allow for fast and frequent surveys over a producing reservoir.

The advantage of our technique over methods based on wavefield focusing (Girard and Vasconcelos, 2010; Shragge et al., 2012) comes from the reduced implementation cost (no extended images are needed) and the robustness against poor illumination. By analyzing single-shot migrated images, we are automatically taking into account the illumination pattern of those experiments; on the contrary, focusing measures require full aperture or point-spread function compensation to equalize the complex illumination patterns due to the geologic structures and/or acquisition geometry. In this work, we recover a portion of the anomaly from a *single* migrated shot, which would be impossible using any technique based on focusing.

In general, velocity anomalies due to reservoir stimula-

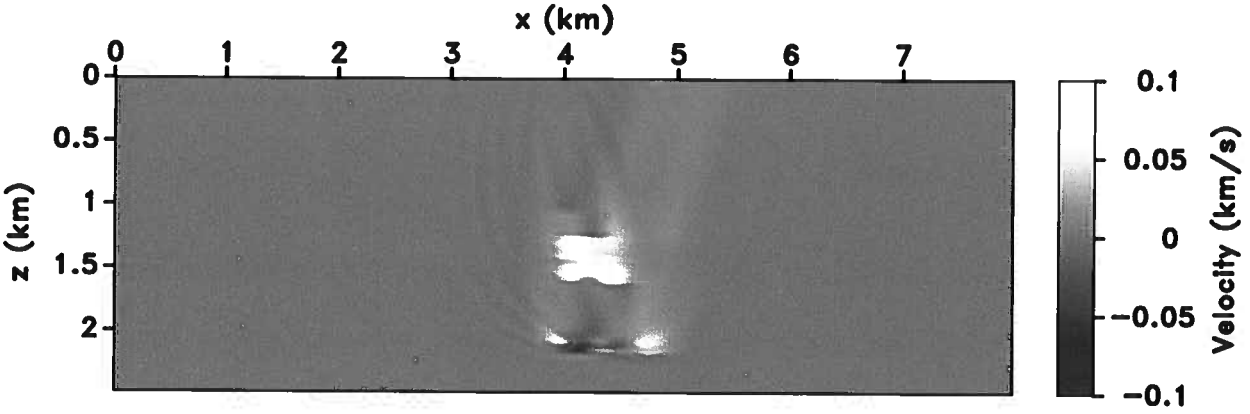

Figure 10. Estimated perturbation after 60 tomographic iterations with an incorrect baseline velocity model.

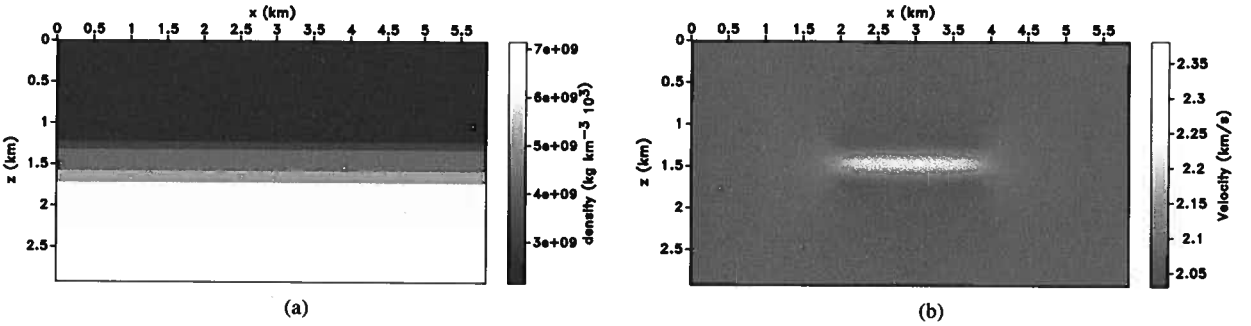

Figure 11. (a) Density model used to simulate the reflecting interfaces. (b) Velocity model of the depleted reservoir. The original model is homogenous with 2.07 km/s velocity. Observe the characteristic shape of the anomaly with increasing velocity inside the reservoir (because of compaction) and decreasing velocity outside the reservoir (because of strain).

tion or production are small relative to the velocity error in the initial stages of model building. Moreover, the baseline velocity model should already be calibrated and thus be expected to produce a high-quality migrated image. Therefore, our technique based on apparent image shifts is more robust for time-lapse seismic monitoring than for the original migration velocity analysis, when we match a set of inaccurate images.

6 CONCLUSIONS

Local correlations evaluated in the image domain allow us to assess the quality of the velocity model from a limited number of migrated images. In 4D seismic applications, we can quickly estimate a perturbation of the migration model by comparing shot images from baseline and monitor surveys. In the image domain, we measure the consistency and similarity of locally coherent events, like the local dip of the reflectors; these features are weakly sensitive to differences in the acquisition geometry and make our approach more robust against survey repeatability issues as compared to alternative strategies in the data domain. The method is able to recover the relative error in the model and does not require separate velocity analysis for baseline and monitor surveys in order to estimate the differences between the models inverted independently.

7 ACKNOWLEDGMENTS

We would like to thank Jyoti Behura for interesting discussions about 4D time-lapse seismic and for encouraging FP to look into this problem. This work was supported by the sponsors of the Consortium Project on Seismic Inverse Methods for Complex Structures. The reproducible numerical examples in this paper use the Madagascar open-source software package freely available from http://www.ahay.org and the Mines JTK freely available at https://github.com/dhale/jtk.

REFERENCES

Aki, K., and P. G. Richards, 2002, Quantitative seismology: University Science Books.

Fichtner, A., H.-P. Bunge, and H.Igel, 2006, The adjoint method in seismology I. theory: Physics of the Earth and Planetary Interiors, 86–104.

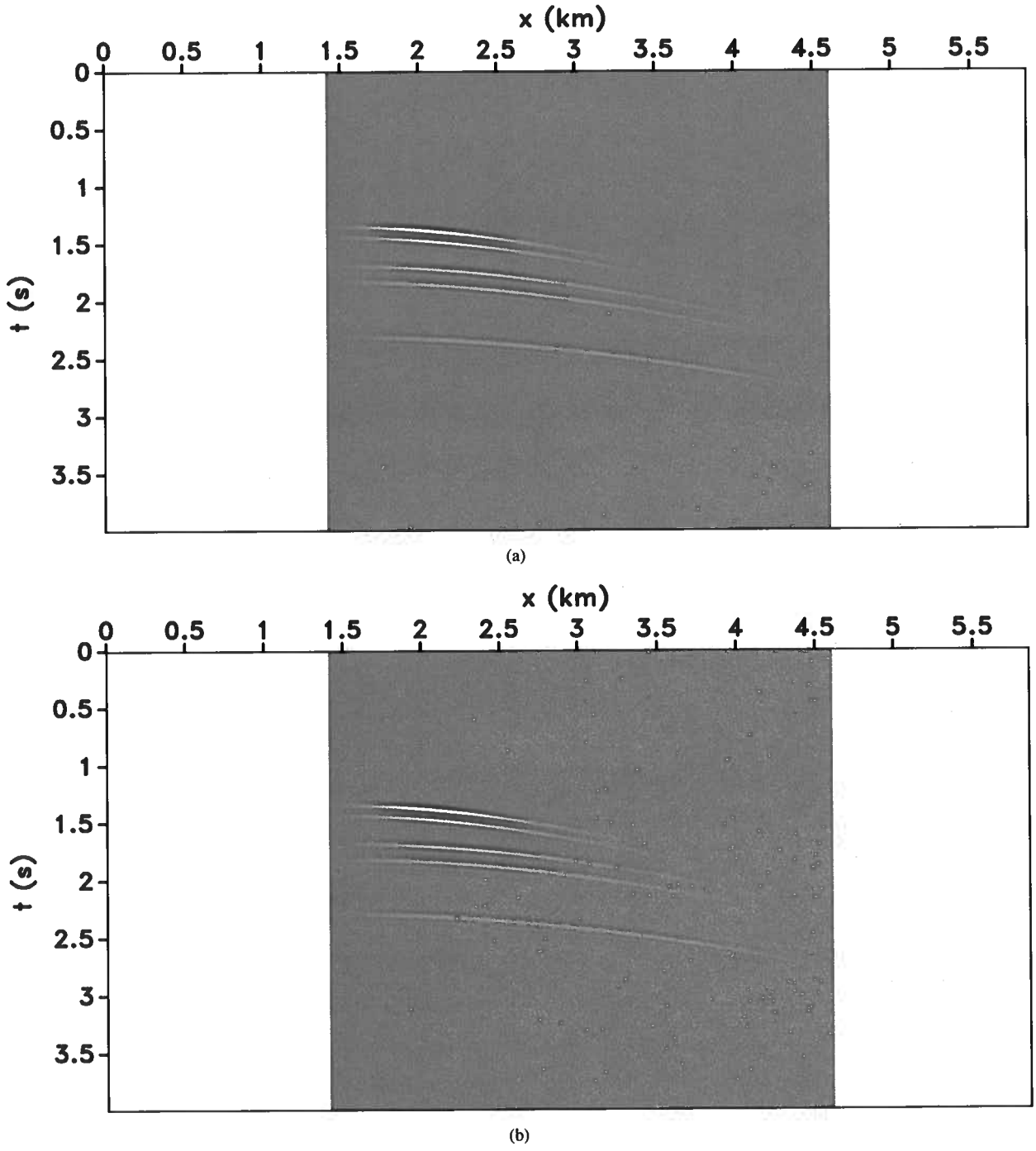

Figure 12. (a) Baseline data and (b) monitor data simulated in the depleted reservoir. By inspection, it is impossible to observe any perturbation in the arrival times.

Girard, A., and I. Vasconcelos, 2010, Image-domain time-lapse inversion with extended images: Presented at the 80th Ann. Internat. Mtg., Soc. of Expl. Geophys.

Hale, D., 2007, A method for estimating apparent displacement vectors from time-lapse seismic data: Technical Report CWP-566, Center for Wave Phenomena, Colorado School of Mines.

Hale, D., B. Cox, and P. J. Hatchell, 2008, Apparent horizontal displacements in time-lapse seismic images: Presented at the SEG Technical Program Expanded Abstracts, SEG.

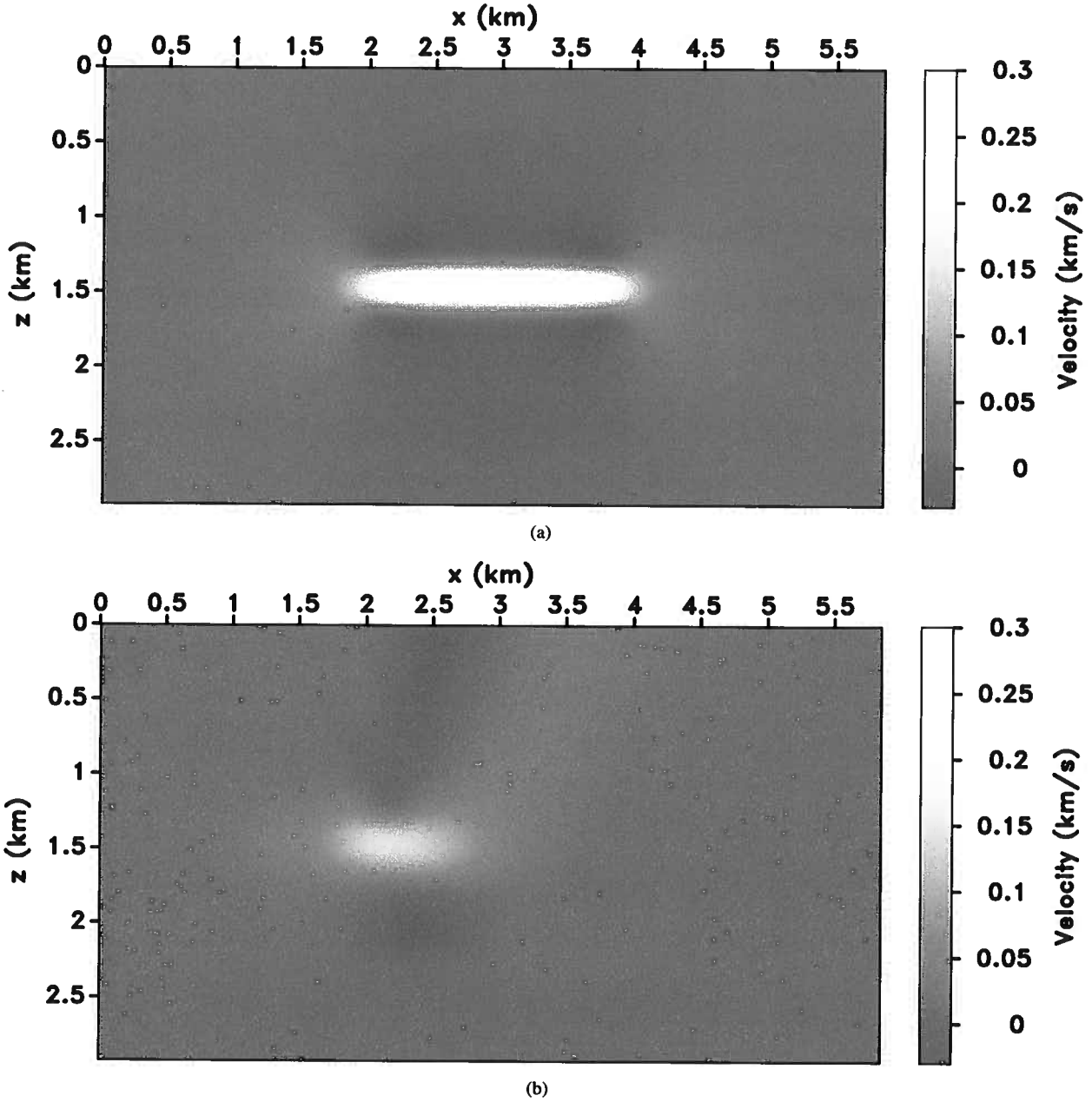

Figure 13. (a) Real time-lapse model perturbation and (b) inverted perturbation after 60 iterations of wavefield tomography. Notice that we are able to correctly image the anomaly and also constrain its lateral extent at about $x = 2$ km.

Hatchell, P. J., and S. J. Bourne, 2005, Measuring reservoir compaction using time-lapse timeshifts: Presented at the 75th Ann. Internat. Mtg., Soc. of Expl. Geophys.

Lumley, D. E., 2001, Time-lapse seismic reservoir monitoring: Geophysics, **66**, 50–53.

Perrone, F., and P. Sava, 2012, Wavefield tomography based on local image correlation: Presented at the 74th Conference and Exhibition, EAGE.

Rickett, J. E., and D. E. Lumley, 2001, Cross-equalization data processing for time-lapse seismic reservoir monitoring: A case study from the Gulf of Mexico: Geophysics, **66**.

Sava, P., and B. Biondi, 2004, Wave-equation migration velocity analysis. I. Theory: Geophysical Prospecting, **52**, 593–606.

Shragge, J. C., and D. E. Lumley, 2012, 4D seismic wave-equation depth migration velocity analysis: Presented at the 74th Conference and Exhibition, EAGE.

Shragge, J. C., T. Yang, and P. Sava, 2012, Time-lapse image-

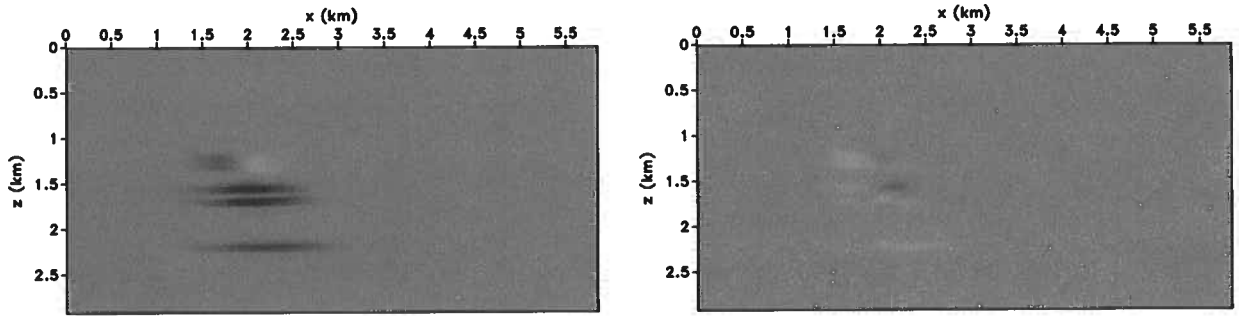

Figure 14. (a) Initial estimated shifts and (b) estimated shifts after 60 iterations of wavefield tomography. Black indicates positive (downward) shifts and white represents negative (upward) shifts. Inversion matches the baseline and monitor images and reduces the shifts between them.

domain velocity analysis using adjoint-state methods: Presented at the SEG Technical Program Expanded Abstracts, Soc. of Expl. Geophys.

Smith, S. S., and I. Tsvankin, 2012, Modeling and analysis of compaction-induced traveltime shifts for multicomponent seismic data: Geophysics, **77**, T221–T237.

Yang, T., and P. Sava, 2011, Image-domain waveform tomography with two-way wave-equation: Presented at the 81th Ann. Internat. Mtg., Soc. of Expl. Geophys.

——, 2012, Illumination compensation for image-domain wavefield tomography: Presented at the 74th Conference and Exhibition, EAGE.

Time-lapse monitoring of velocity changes in Utah

Chinaemerem Kanu [1], Roel Snieder[1] and Kristine Pankow[2]
Center for Wave Phenomena, Geophysics Department, Colorado School of Mines, Golden, CO, USA[1],
University of Utah, Seismograph Stations [2].

ABSTRACT
The Wasatch fault region is an actively deforming region characterized by prominent seismicity and has the potential for large magnitude events in the near future. The present day deformation of the region, which extends into the Basin and Range, motivates the need for continuous monitoring of the region. One of these continuous monitoring is a time-lapse characterization of velocity properties of the region. In this study we monitor time-lapse velocity changes within Utah and eastern Nevada using coda waves generated by explosive events. This monitoring characterizes velocity changes within the region from June to September of 2007. We observe, both temporally and spatially, variable velocity changes within the monitored region, with a maximum path-average velocity changes of 0.2%. This suggests a significant change in the velocity within the region given the short monitoring duration and provides enormous implications to the characterization of the deformation within the region.

Key words: time-lapse monitoring, coda wave interferometry

1 INTRODUCTION

Coda wave interferometry is an effective tool to monitor time-lapse changes within a medium, especially for weak changes within the medium (Snieder et al., 2002). Coda wave interferometry allows us to extract subsurface changes from scattered seismic waves generated from repeated sources. With identical sources and negligible noise, differences within the seismic coda (such as time shift and amplitude decay) provide information about the changes within the monitored medium through which the coda wave travels. Due to the redundancy in the coda waves and possibly increased illumination of the subsurface by the scattered waves, the sensitivity of the scattered waves to perturbations within the subsurface usually increases with increasing travel time. This sensitivity of the multiply scattered waves has allowed for monitoring weak changes in velocity, in the order of 0.1% (Snieder, 2006). Coda wave interferometry has successfully been used to monitor velocity changes along fault regions (Schaff and Beroza, 2004; Poupinet et al., 1984), detect in situ velocity changes due to stress changes in mining sites (Grt et al., 2006), characterize near-surface velocity changes (Nakata and Snieder, 2012), monitor temporal changes within volcanic regions (Matsumoto et al., 2001), and detect far-field stress-induced velocity changes (such as solid earth tide) (Spane, 2002).

The monitored region in this study covers western and central Utah, eastern Nevada, and the southern part of Idaho. Some of the notable features within this region include most of the Wasatch fault region, the north-western Colorado plateaus, the eastern part of the Great Basin, and the southern Rocky Mountain region (Prodeul, 1970) (figure 1). The Great Salt Lake and the Wasatch front are situated in the eastern section of the monitored region. The Wasatch fault system is a 370-km normal fault system (Armstrong et al., 2004) cutting across Utah from the north to the southern part of Utah. The fault defines the eastern boundary of the Basin and Range province of western North America. With a northward striking direction and a dip range of 45^0-60^0 toward the west, the Wasatch fault characterizes a broad area of active deformation which consists of more than 10 segments, and the regions connecting the fault segments are characterized by gaps in seismicity (Simpson and Richards, 1981; Gori and Hays, 1992). The Wasatch fault separates the Wasatch Range to the east and Salt Lake Basin to the west. The Wasatch range consists of the Rocky Mountains characterized by late Paleozoic and Mesozoic rocks (Hunt, 1956). To the west of the fault is the Salt Lake Basin which is an extension of the Basin and Range. Unlike the Wasatch range, this section of the western US is actively deforming which has been attributed to a variety of factors including crustal shearing due to the north-

western relative movement of the Pacific Plate (Wise, 1963; Hamilton and Myers, 1966) and the elevated heat characteristics of the Western US (Eaton, 1982). Some places within the Salt Lake Basin consist of soft sediments which are more than 1-km deep (Roten et al., 2011). The soft sediments are potentially susceptible to both near-field and far-field stress loadings.

In this study, we monitor temporal velocity changes within the crustal sub-surface around the Wasatch fault region. We use coda waves generated by time-lapse active sources conducted in the summer of 2007. These coda waves were recorded by the equally spaced US-Array stations which cover most of the Wasatch fault cutting across Utah. In the following section, we describe in detail the data processing routine we use in this study. In sections 3 and 4 we present the results from the time-lapse monitoring of the Wasatch fault region and interpretation of the results, respectively. Section 5 both concludes and discusses the assumptions we made in this study.

2 DATA PROCESSING

We process coda signals generated by 10 rocket motor explosions, occurring between June 4 and September 10 2007, which were surface rocket explosions at the Utah Test and Training Range (UTTR) of Hill Air Force Base, Utah (Stump et al., 2007). Each of the explosions was carried out at the same location with latitude and longitude of N41.141^o and W112.9065^o, respectively. These explosions are identical. The similarity in the source properties of the monitoring signals prevents errors in the estimated fractional velocity changes due to changes in the properties of the sources (such as shift in source location or source mechanism) generating the coda signals (Weaver et al., 2011; Kanu et al., 2013). The onset times of the explosions are given in Table 1. The blast signals were recorded on the USArray transportable array (TA) shown in Figure 1 and the TA consists of 54 stations surrounding the blast location (red star) shown in Figure 1.

2.1 Processing of blast doublets for velocity changes

In this study we process three (N-S, E-W and vertical) components of the recorded explosive signals. Figure 2 shows an example of the three-component blast signals. The signals in figure 2 are unfiltered having an amplitude spectrum shown in Figure 3. We use a 1-5Hz frequency band in this time-lapse monitoring and the blast signal for the 1-5Hz frequency band is given in Figure 4.

In this time-lapse study we use the coda section of the signals (i.e. the section of the signal with exponential amplitude decay) (Figure 5). The onset time of the

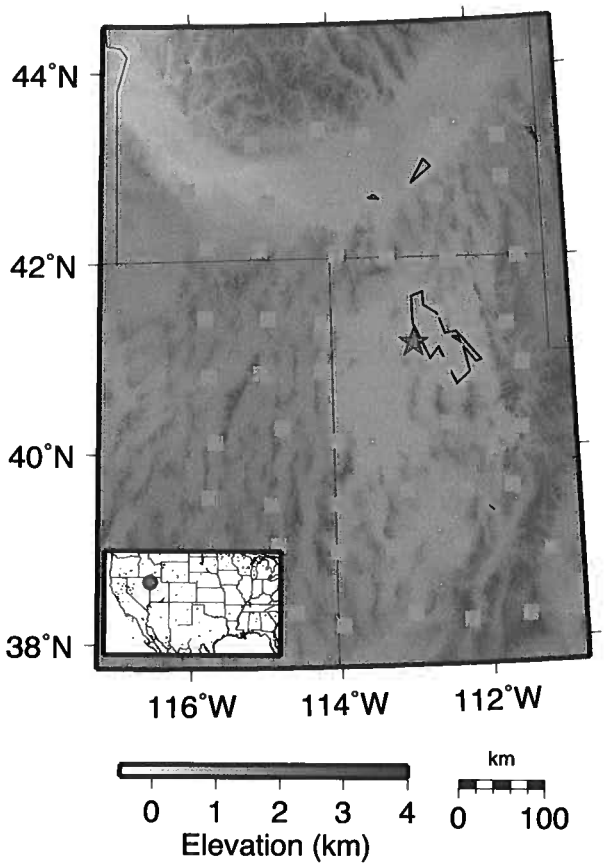

Figure 1. USArray transportable array given by the green squares. The locations of the stations are given relative to the blast location (red star).

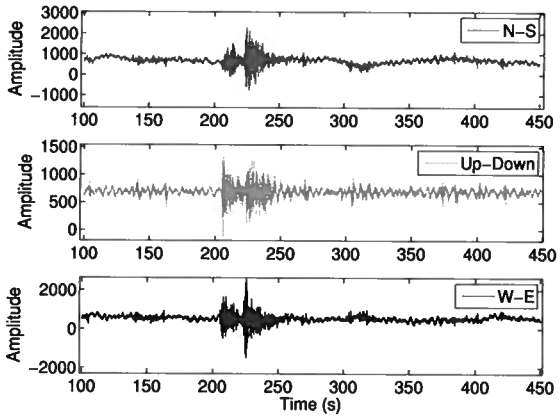

Figure 2. Typical recordings of the blast events. The three components, N-S (blue), Vertical (red) and the E-W (black) are all used in the time-lapse analysis.

Table 1. Descriptions for the blast events used in this studies.

Event (Data name)	Month	Day	Hour	Minutes	Seconds
Reference (20070604)	06	04	19	52	21.22
Signal 1 (20070611)	06	11	19	49	24.10
Signal 2 (20070626)	06	26	19	43	19.78
Signal 3 (20070709)	07	09	21	38	37.13
Signal 4 (20070716)	07	16	17	33	31.13
Signal 5 (20070801)	08	01	20	01	24.26
Signal 6 (20070806)	08	06	–	–	–
Signal 7 (20070813)	08	13	19	38	30.56
Signal 8 (20070827)	08	27	20	43	11.45
Signal 9 (20070910)	09	10	17	33	01.56

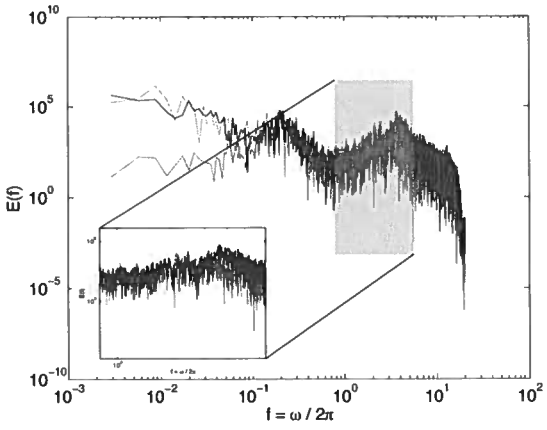

Figure 3. Typical amplitude spectrum of the blast events. The three components, N-S (blue), Vertical (red) and the E-W (black) are all used in the time-lapse analysis. The gray rectangle bounds the used frequency range.

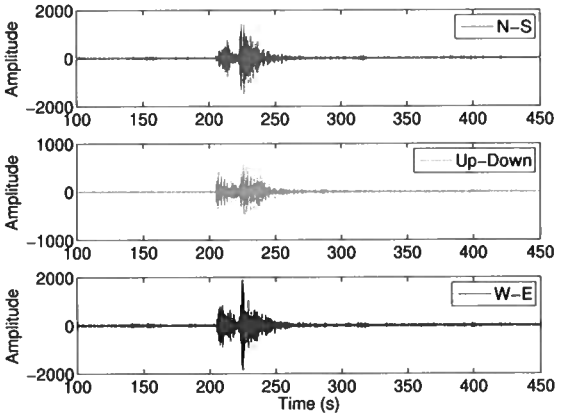

Figure 4. Typical recordings of the blast events (filtered) bandpass filtered between 1-5Hz. The three components, N-S (blue), Vertical (red) and the E-W (black) are all used in the time-lapse analysis.

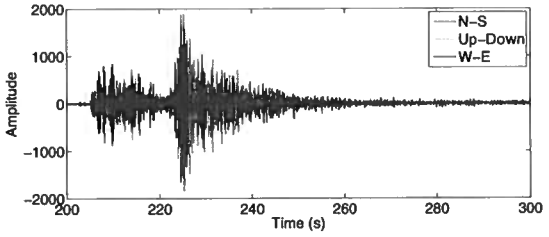

Figure 5. The coda section of the blast signals. The three components, N-S (blue), Vertical (red) and the E-W (black) are all used in the time-lapse analysis. The gray rectangle bounds the coda section of the signal

coda section after the S-waves varies between stations. We filter the signals between 1-5Hz. We also normalize each signal with its maximum amplitude and resampled each of the signals from a time interval δt of 0.025s to 0.001s. The resampling increases the resolution of the estimated velocity changes. The data is processed using three signal referencing cases. Case 1 consists of comparing each of the recorded signals to the first blast signal (Signal 20070604 - Table 1). In Case 2, each signal is compared to the previous signal (in time). For Case 3, we use only the signals from 08/01/2007 to 09/10/2007. Each of the signals in this Case is compared to the blast signal on 08/01/2007 (Signal 20070801 - Table 1). The purpose for these three cases is to check for consistency in our estimate of velocity change.

To extract the fractional velocity change from the time-lapse data, we use the stretching method (Hadziioannou et al., 2009). However rather than using the maximum correlation as the misfit function for the time-lapse misfit, we use the L_2 norm as the misfit function (Kanu et al., 2013). We initialize the time of the signals to the onset times of the explosive events in order

to apply the stretching algorithm. A doublet consists of time-lapse signals from two explosive events. The source properties of the explosive signals are the same; therefore any difference in the signals results from either changes along the propagation path of the signals or differences in noise properties of the signals. The major challenge we encountered while analyzing this explosive data was accounting for missing data. In some cases the data were either missing one of the components or all three of the components. We only used explosive signals that are recorded on all three components of the stations. Table 2 shows the stations with their missing data.

Because of the presence of noise in the data and because the noise becomes prominent with increasing coda time, we only use the codas where the correlation of the early part of the coda is greater than 0.75 and the correlation of the end of the coda is greater than 0.5 (similarity criterion). This section of the coda is submitted to the stretching algorithm. In cases where this criterion is not met, we assign zero to the relative velocity change and its error. We compute the error associated with the estimated velocity change using the method of Kanu et al. (2013) (equation 14).

The fractional velocity changes estimated in Cases 1 and 3 are cumulative velocity changes from the reference signals. However in Case 2, the changes estimated are interval velocity changes for each monitored time period. In order to express the estimated velocity changes of Case 2 in a way that is consistent with the other two cases, we sum the estimated velocity changes and their associated error values using the following equations:

$$\left\langle \frac{\delta \hat{V}}{V} \right\rangle_j = \sum_{i=1}^{j} \left\langle \frac{\delta \hat{V}}{V} \right\rangle_i, \tag{1}$$

and

$$e_j = \sqrt{\sum_{i=1}^{j} e_i^2}, \tag{2}$$

where $\left\langle \hat{\delta V/V} \right\rangle$ is the estimated average velocity change, e is the error of the relative velocity change, and i and j denote the time intervals we are monitoring with values 1 to 9.

3 TIME-LAPSE VELOCITY CHANGE

3.1 Average velocity changes

Figure 6 shows the cumulative estimates of the average relative velocity changes for Case 1, Case 2 and Case 3. We compute the average velocity change using all the monitoring stations with non-zero estimated velocity change. In Case 2, we have zero velocity changes in the first two time periods (doublets) because the time-lapse doublets do not meet our similarity criteria in the data processing (section 3.1). This inability to meet our criteria is because the signal resulting from the explosion of June 11 (Signal 20070611 - Table 1) is different from the rest of the signals due to the presence of noise. In Case 3 only signals after August 1 are processed, and the reference signal for the estimation of velocity change in Case 3 is the signal of August 1 (Signal 20070801 - Table 1). Each of these cases show significant velocity changes between June 4 and July 9. However the subsequent estimated velocity changes ($\delta V/V(\%)$) for both Cases 1 and 2 are below the error-level while in Case 3 these estimated velocity changes are well above the error values. The error values are standard deviations of the estimated velocity changes.

Comparison of the estimated velocity changes from all three cases reveals that the estimated velocity changes for each of the components follow a consistent trend. The average velocity increases within the monitored region from the June 4 to June 26. This increase in velocity remains fairly constant until August 1 after which the average velocity decreases. The reduction in velocity occurs between August 1 and 6. As is indicated in Case 3, the average velocity remains constant between the August 6 and 13. After the August 13, the average velocities increases and decreases for the following time periods: August 13 to 27 and August 27 to September 10, respectively.

Table 2. The stations with missing data and their missing data

USArray Station	Missing Data
L15	20070604 20070611 20070626 20070709
L16	20070604 20070611 20070626 20070709
M16	20070604 20070611 20070626 20070709
N16	20070604 20070611 20070626 20070709
O15	20070604 20070611 20070626
O16	20070604 20070611 20070626

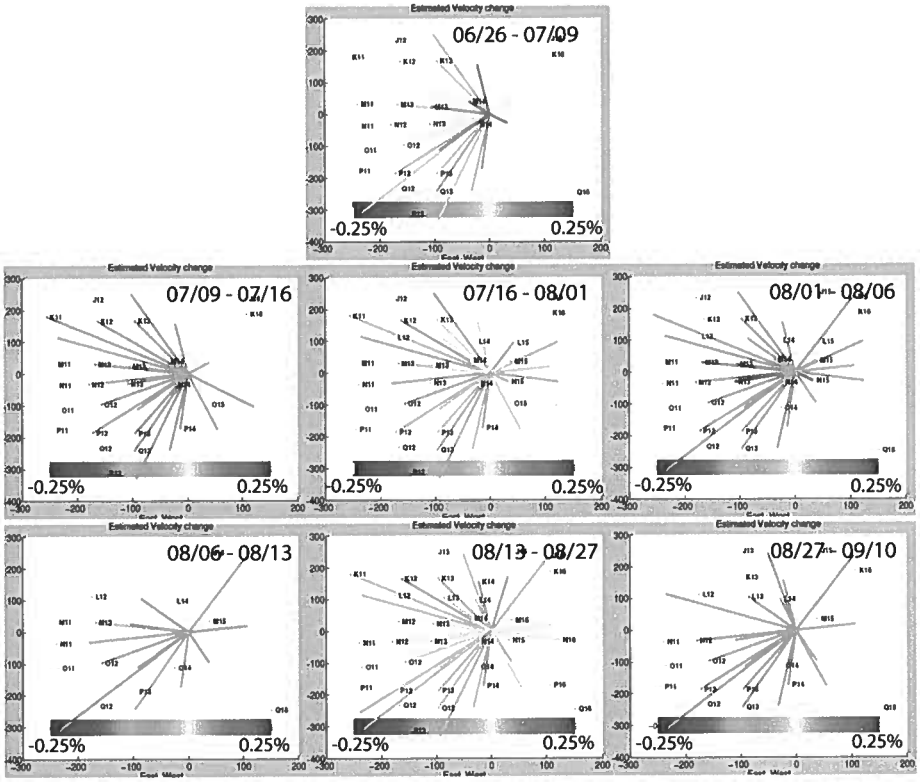

Figure 7. Percentage velocity changes estimated from the 9 blast doublets using vertical component of the stations. The first two doublets have missing estimates. The red points are the surface stations. The source location is the point where are the colored lines meet. The color lines are the estimated percentage velocity changes for each source-receiver pair. The velocity changes are estimated from the vertical component of the coda wave generated by the blast.

3.2 Spatial distribution of velocity change

Figure 7 shows a trend in velocity change similar to what is observed in the average velocity changes computed using all the stations. These average changes are the estimated velocity changes in Case 2 for each time-lapse period. The first two time-lapse periods (06/04/2007 - 06/11/2007 and 06/11/2007 - 06/26/2007) are missing due to presence of noise in signal 20070611 (Table 1). Figure 7, shows the spatial distribution of the velocity changes as changes seem to vary with source-receiver pairs; and the region of dominant velocity changes also varies from one time period to the other.

The estimated velocity changes generally decrease with increasing source-receiver distance (Figure 8). The dependence of the estimated velocity change on the source-receiver distance explains the high error levels in the average of the estimated velocity change shown in section 3.1. The spread in the velocity changes estimated at the stations is not due to random error but due to variations in the estimated velocity change with the source-receiver distance. The spatial distribution of the velocity changes and the dependence of the velocity change on the source-receiver distance might suggest that the velocity changes in the medium are localized. During some of the time intervals shown in Figure 8, the estimated velocity changes are distributed over broad values of velocity changes for the same source-receiver distance (for example, for period 07/16/2007 - 08/01/2007 at the source-receiver distance of 100km). This might be an indication of lateral variation of the velocity change within the monitored region.

3.3 Parameter Estimation:

The travel time shifts (and therefore the estimated velocity changes) depend on the magnitude of the subsurface velocity change Δv, the volume of the velocity change ΔV, the diffusion coefficient D of the scattered wave intensity (Pacheco and Snieder, 2005), and the source-receiver distance R. Assuming a uniform lateral velocity change which extends to the earth's free surface (Figure 9), we can formulate the parametric dependence of the estimated relative velocity change $\langle \epsilon \rangle$ as follows:

$$\langle \epsilon \rangle = F(\Delta v/v, h, D, \mathbf{r}), \tag{3}$$

where h is the depth extent of the velocity change.

The function F can be found from the theory of

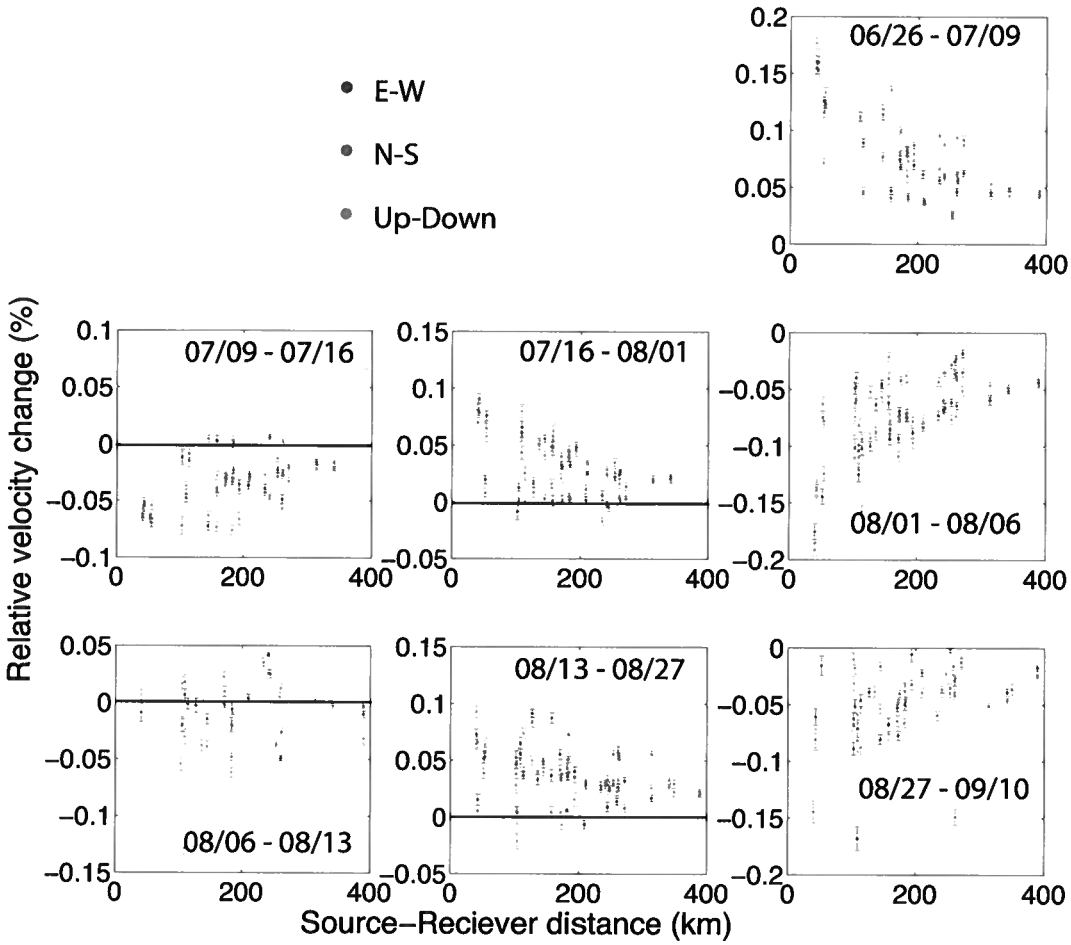

Figure 8. The relative velocity change estimated for each of the time periods as a function of source-receiver distance. The first two periods (06/04 - 06/11 and 06/11 - 06/26) have missing measurements due to the quality of the data at the period. The black horizontal line corresponds to zero velocity change.

Pacheco and Snieder (2005), which relates the estimated relative velocity change $\langle\epsilon\rangle$ to the model parameters $(\Delta v/v, h, D, \mathbf{r})$ as follows:

$$\langle\epsilon(t)\rangle t = \int_V K(\mathbf{r}, t; D)\frac{\Delta v}{v}(\mathbf{r})\,\mathrm{d}V. \tag{4}$$

The estimated relative velocity change seems to depend directly on the parameter ζ, which is defined as

$$\zeta = \frac{h}{D}\frac{\Delta v}{v}. \tag{5}$$

Figure 10 shows the apparent (estimated) velocity changes using the source-receiver distance of station J13 for values of ζ from 0 to 0.1 using equation (4). These values of ζ correspond to values of $\Delta v/v$, h, and D ranging from 0-10%, 0-10km, 1-10x10^3m/s^2, respectively. Figure 10 suggests that the three parameters - the magnitude of the subsurface velocity change Δv, the depth of the velocity change h, and the diffusion coefficient D - only influence the estimated velocity change through the combination that defines ζ in equation 5. The diffusion coefficient, however, shows a weaker trade-off with the other two parameter, the magnitude of subsurface velocity change $\Delta v/v$ and the depth of velocity change h. Station J13 is chosen arbitrarily because the trade-off of the three model parameters applies to all the stations.

The strong trade-off between the $\Delta v/v$ and h suggests that determining each of these parameters independently will be difficult. According to equation (A12) in Appendix A, we can use a power law relation to describe the estimated velocity changes (Figure 11) as:

$$\langle\epsilon\rangle = aR^b, \tag{6}$$

where $a = 3\frac{h}{\pi}\frac{\Delta v}{v}\Sigma$ and b = -1 (See Appendix A). Σ is a dimensionless constant of the monitored region. Table 3 gives the estimated parameters for the fitting solutions of the estimated velocity changes, the qualities of the fitting solutions in the adjusted R squared (a measure of regression) values, and the inverted values of $h\Delta v/v$. We

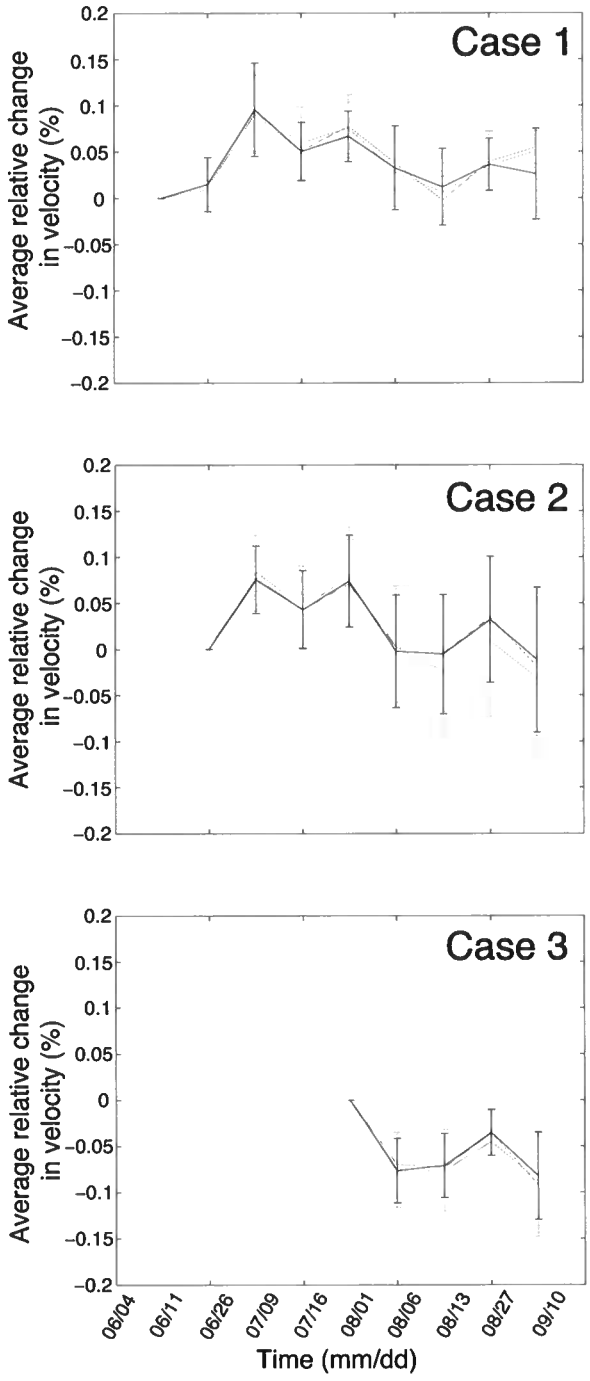

Figure 6. The cumulative relative velocity changes expressed in percentages for N-S (red), Vertical (green) and the E-W (black) components. Here the average is computed using all the stations in TA. Missing first two estimates in Case 2 is due to influence of noise in the signal of June 11. Missing first five estimates in Case 3 is because only signals from 1^{st} of August is processed in Case 3.

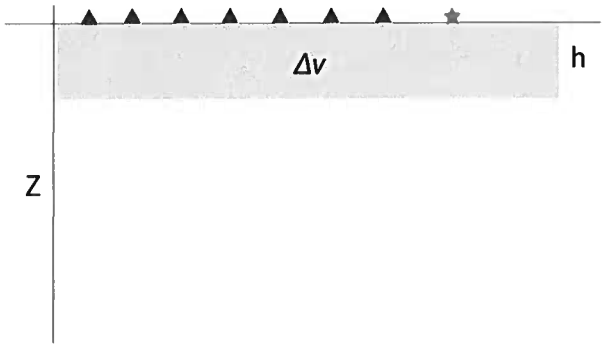

Figure 9. Schematic description of the layer of near-surface fractional velocity change. The red star is the source and the black triangles are the receivers.

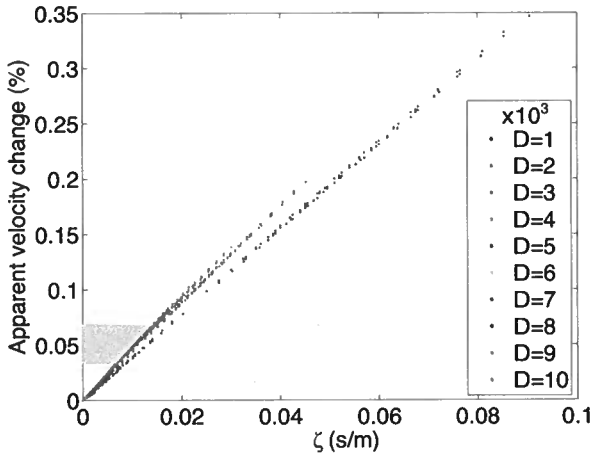

Figure 10. Dependence of the estimated velocity change on the dimensionless parameter ζ. The definition of ζ is given in equation 5. The green region corresponds to the range of velocity changes estimated with station J13.

use the weighted nonlinear least-squares method with the inverse of the estimated errors as weights. We ignore estimated velocity changes less than 0.02% for period 07/16-08/01 in the fitted solution, because the values do not fit the power law relation. Using the diffusion model of scattered intensity in the 3D semi-infinite medium we can only invert for values of $h\Delta v/v$ from the estimated velocity changes. Based on the surface layer model, the inverted $h\Delta v/v$ values are in the order of $1\%km$, which implies that the percentage velocity change is of the order 1% over a depth in the order of $1km$. These values seem large for a region such as Utah with negligible precipitation and given that the durations of the monitoring are on about 2 weekly basis.

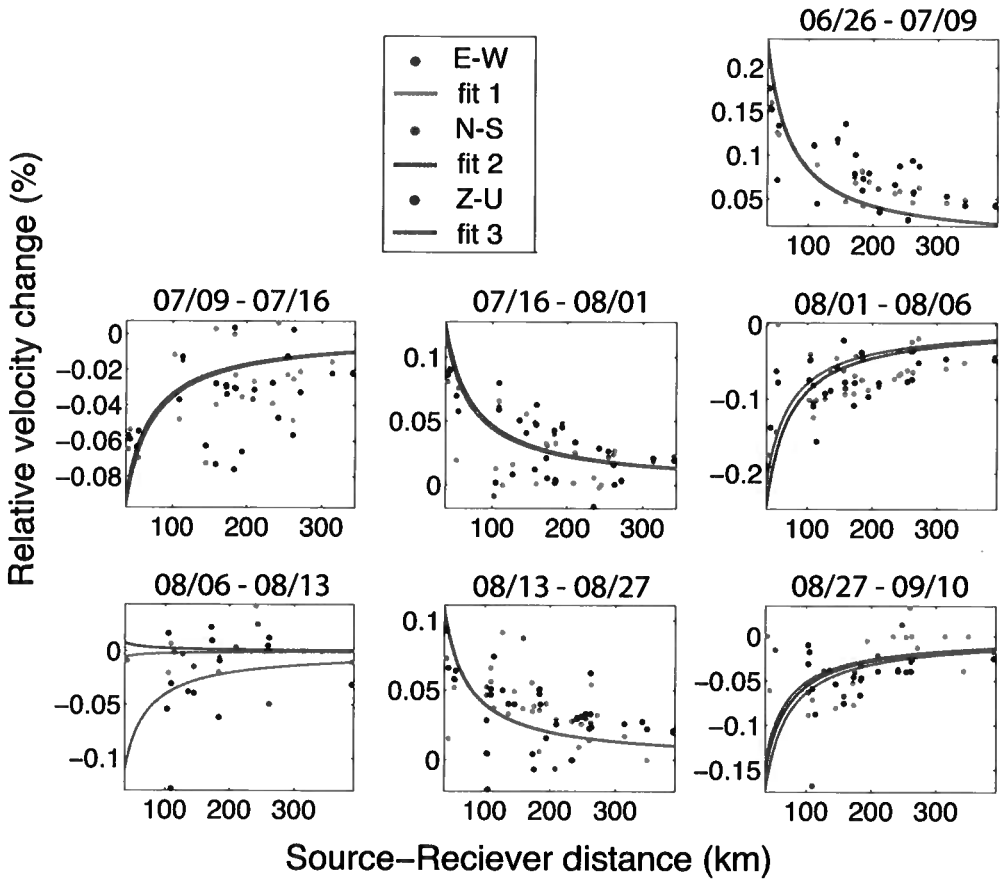

Figure 11. Power law fitting of the estimated velocity changes in Utah Wasatch fault region. Fit 1, 2, and 3 are the fitting solutions for the estimated velocity changes of E-W, N-S, and Z-U components, respectively.

4 CAUSES FOR THE VELOCITY CHANGES

4.1 Rainfall and groundwater level

Utah is a region that receives little precipitation. Figure 12 shows the amount of precipitation observed within the time period we are monitoring using the following two stations: Salt Lake County Government Center (N40.7284 W111.8877) (Figure 12.1A and 12.2A) and Magna Station (N40.7109 W112.1002) (Figure 12.1B and 12.2B). The figures show that the amount of precipitation is small (amounting to a cumulative precipitation of less than 2 inches) during the monitored period. This may explain why there is negligible relation between the precipitation and estimated velocity changes.

The groundwater level can vary temporally, not only due to precipitation but also to stress loading resulting from large earthquakes (Montgomery and Manga, 2003) and solid earth tides (Spane, 2002). Figure 13 shows the cumulative groundwater subsidence over the monitored period in this study. The recording wells of the groundwater subsidence are shown in Figure 14. Figure 13 shows that the cumulative groundwater subsidence generally increases and decreases with the average estimated velocity change. However, the maximum cumulative groundwater subsidence is less than 10m. This amount of groundwater subsidence is unlikely to totally explain the observed velocity changes.

4.2 Local seismicity

Figure 15 shows the peak horizontal acceleration (PHA) due to local seismicity and the estimated velocity changes. We compute peak horizontal acceleration using the PHA relationship with event magnitude proposed by *Campbell* (1981) based on world-wide data (equation 7):

$$\ln PHA(g) = -4.141+0.868M-1.09\ln[R+0.606\exp(0.7M)], \quad (7)$$

where M is the event magnitude, R is the distance to the fault rupture location in km, and g is the accelera-

Table 3. Estimated model parameters using the inverse R relation.

Event period	a $(\%km)$	Adjusted R^2	$h\frac{\Delta v}{v}$ $(\%km)$
Period 1 (06/04-06/11)	-	-	-
Period 2 (06/11-06/26)	-	-	-
Period 3 (06/26-07/09)			
E-W	8.272 ±0.6536	0.3448	1.9144 ±0.1514
N-S	8.223 ±0.6651	0.3593	1.9030 ±0.1541
Z-U	8.450 ±1.1125	-0.3393	1.9556 ±0.2576
Period 4 (07/09-07/16)			
E-W	-3.382 ±0.3990	0.2096	-0.7827 ±0.0924
N-S	-3.342 ±0.4005	0.2440	-0.7734 ±0.0927
Z-U	-3.574 ±0.5839	0.2823	-0.8271 ±0.1352
Period 5 (07/16-08/01)			
E-W	4.677 ±0.3941	0.4538	1.0824 ±0.0913
N-S	4.677 ±0.3941	0.4538	1.0824 ±0.0913
Z-U	4.382 ±0.4513	0.2150	1.0141 ±0.1045
Period 6 (08/01-08/06)			
E-W	-9.001 ±0.6926	0.09855	-2.0831 ±0.1605
N-S	-8.932 ±0.7020	0.1131	-2.0671 ±0.1626
Z-U	-7.889 ±0.8625	-0.0293	-1.8258 ±0.1997
Period 7 (08/06-08/13)			
E-W	-0.2111 ±7.7143	-0.07994	-0.0489 ±1.7853
N-S	0.2761 ±9.6735	-0.2961	0.0639 ±2.2387
Z-U	-4.062 ±33.2908	-0.05158	-0.9401 ±7.7045
Period 8 (08/13-08/27)			
E-W	4.003 ±0.5133	-0.3547	0.9264 ±0.1188
N-S	3.937 ±0.4923	-0.4684	0.9111 ±0.1140
Z-U	4.019 ±0.4722	0.06362	0.9301 ±0.1093
Period 9 (08/27-09/10)			
E-W	-5.143 ±0.9411	0.118	-1.1902 ±0.2178
N-S	-5.602 ±1.1110	0.1414	-1.2965 ±0.2572
Z-U	-6.328 ±3.2270	-0.355	-1.4645 ±0.7469

tion due to gravity. We compute the PHA values using magnitude and hypocenter parameters of the detected seismic events during the monitored time period for station L11A. Station L11A is selected arbitrarily.

The following durations have anomalous PHA events: 06/04/2007 - 06/11/2007, 06/26/2007 - 07/09/2007, 08/01/2007 - 08/06/2007, 08/13/2007 - 08/27/2007, and 08/27/2007 - 09/10/2007. Among these time periods, only the following time periods – 06/04/2007 - 06/11/2007, 06/26/2007 - 07/09/2007 and 08/01/2007 - 08/06/2007 – have the anomalous PHA events occurring near the end of the period. Apart from the period 06/04/2007 - 06/11/2007 – in which we do not have the estimate of velocity change – these three periods correspond to periods with highest velocity changes (Figure 14). However, the periods 06/26/2007 - 07/09/2007 and 08/01/2007 - 08/06/2007 with anomalous PHAs show different signs in the velocity changes. To make a closer comparison of the PHA and velocity changes, we might need to incorporate the local site effects of the monitored region into the PHA computation and compute the spatial PHA across the monitored region.

The effect of the local seismicity is expected to be constrained near the Wasatch fault which is situated in the eastern section of the monitored region. This section of the monitored region is close to the source location and might in part explain the source-receiver dependence of the estimated velocity change.

4.3 Crustal deformation

A critical assumption we made in the estimation of $h\Delta v/v$ is that the velocity changes are uniformly limited to a surface layer, which may be unrealistic. The monitored region covers the eastern flank of the Basin and Range, which has been shown to have elevated heat characteristics (Eaton, 1982) that might be responsible

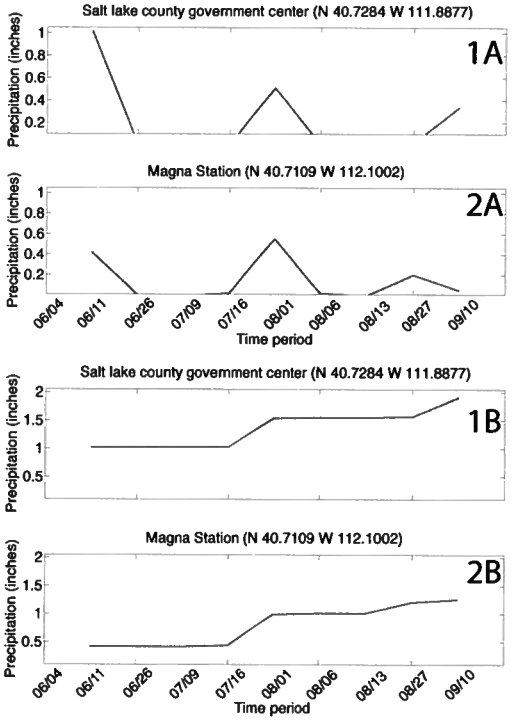

Figure 12. Precipitation recorded during the time period monitored in this study. A. The amount of precipitation per period and B. The cumulative amount of precipitation. 1. Salt lake county government center station and 2. Magna station.

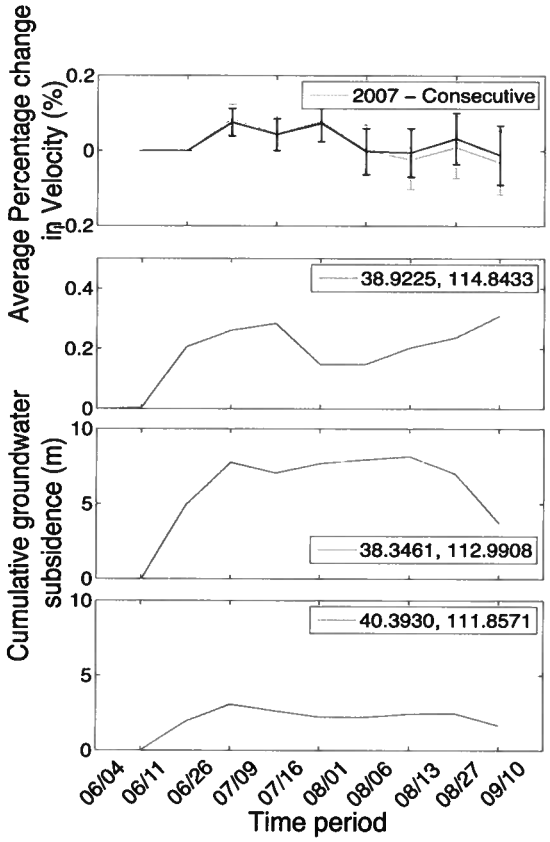

Figure 13. Groundwater level in meters from the land surface.

for broad active deformation in the region. A tectonic deformation of the region will induce velocity changes within the crust; however, these velocity changes will be deeper, broader and more gradual than the changes due to other physical mechanisms such as changes in groundwater level or regional seismicity. Because of the broad and gradual properties of the crustal deformation-induced velocity changes, we expect larger values of h (volume of change) and lower fractional velocity changes $\Delta v/v$. With a larger value in h, crustal deformation due to stress changes or elevated heat deep within the crust might explain, at least in part, the inverted values of $h\Delta v/v$ of an order of $1\%km$, however, discerning the depth profile of the observed velocity changes is challenging using the coda waves and the surface receivers.

5 DISCUSSIONS AND CONCLUSIONS

The estimated velocity changes and the inverted values of $h\Delta v/v$ suggest that the Wasatch front and, in extension, the eastern flank of the Basin and Range, are undergoing small but significant velocity changes within a short period of time. We observe path-averaged velocity changes that depend on the distance between the monitoring source and receivers. The magnitude of the estimated average velocity change varies from one time-lapse period to the other. The maximum of the absolute value of the estimated velocity change is 0.2%. To resolve the magnitude of the localized velocity change and the location of the observed velocity changes using the coda waves, we need to make some assumptions about the monitored region. In this study, to resolve the magnitude of the velocity changes and the region of change, we have made the following simplifying assumptions:

First, we assume that the coda waves we use for the time-lapse monitoring are described using the diffusion approximation of multiply scattered waves. This approximation is usually an over-simplification of the scattered waves especially in the early part of the coda. This approximation is likely to result in an overestimation of the inverted values of $h\Delta v/v$. Also we assume a uniform diffusion model for the monitored area defined by an average diffusivity constant. This diffusivity constant is related to the distance between source and receivers using the diffusion model of the recorded intensities. If the average diffusivity constant is unchar-

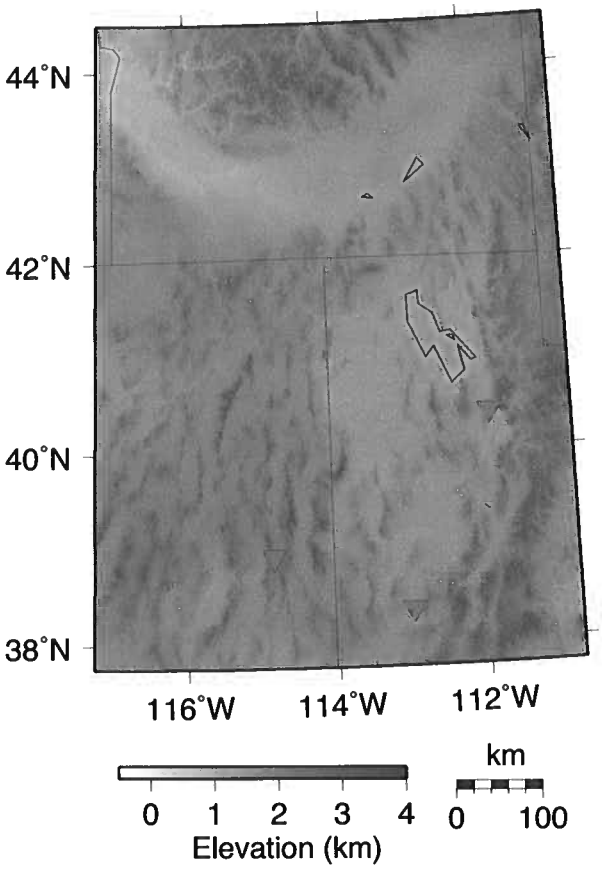

Figure 14. Groundwater monitoring stations. The red triangle are the locations of the groundwater subsidence wells used in Figure 13.

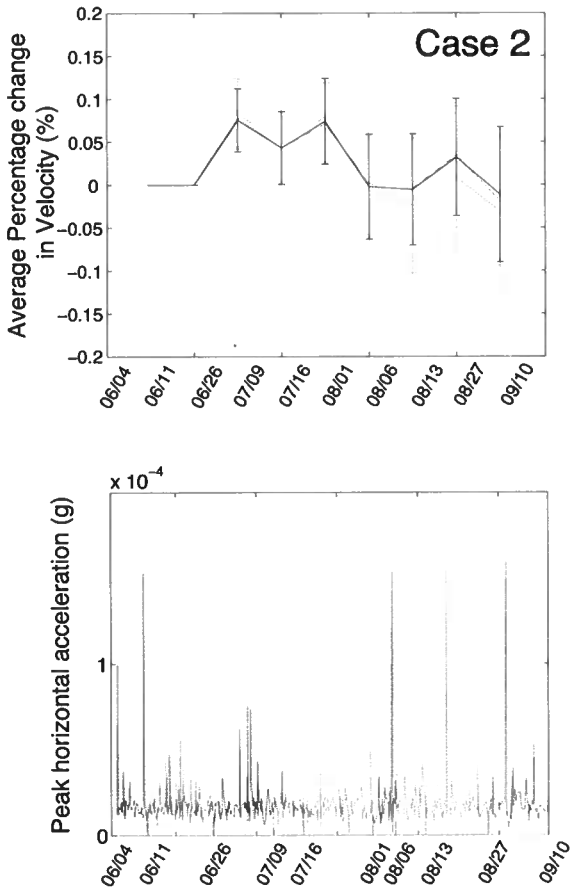

Figure 15. Peak horizontal acceleration (PHA) estimated from the local seismicity that occurred during the monitored period. The PHA are estimated using relationship between PHA and the magnitude of an earthquake in equation 7.

acteristic of the variation of the diffusion property of the monitored region, the inverted $h\Delta v/v$ will also be erroneous.

Second, we use a semi-infinite 3D subsurface with a fully reflecting free surface to invert for $h\Delta v/v$. The fully reflecting free surface may be a fair approximation of the free surface, but we ignore the presence of Moho discontinuity. This boundary will change the magnitude of the sensitivity kernel (equation A2) of the coda because the crustal thickness is much less than the source-receiver distance of the estimated velocity changes. Keller et al. (1975) suggest that the crustal Great Basin-Colorado Plateau transition has a thickness of about $25km$ with a crustal thickness of 30km for the Basin and Range (Gilbert and Sheehan, 2004). Assuming an absorbing boundary at the crust-upper mantle interface will likely increase the magnitude of the sensitivity kernel (equation A2) (Rossetto et al., 2011). This will result in a reduction of the value of the inverted $h\Delta v/v$.

Third, we made a 2D approximation of the equation A1 in equation A6. This is a valid approximation for $h/R \ll 1$. Therefore, the inverted $h\Delta v/v$ represents the true $h\Delta v/v$ within the subsurface if the velocity changes are restricted to the near surface. If the observed velocity changes result from a deeper region of the subsurface, then the true values of $h\Delta v/v$ might deviate from the inverted values. Because of the large values of R (several hundred kms), the h/R approximation is not likely to significantly affect the inverted values of $h\Delta v/v$.

Fourth, due to the extent of the monitored region, the recorded explosive signals are expected to generate surface waves. The surface waves can arrive within the coda wave time window especially for short source-receiver distances. In the recorded explosive signals, the surface waves mostly arrive after the coda waves, however the relative arrival times of the coda wave and the surface wave are dependent on the source-receiver distances and the surface wave can contaminate the coda signal. In this study we have restricted the velocity changes analysis to the coda wave. However the presence of surface wave or surface dominated scattered waves will increase the sensitivity of the scattered waves to lo-

calized velocity change. This will result to lower values of $h\Delta v/v$. Therefore the inverted $h\Delta v/v$ values can be considered as the upper limit of the real $h\Delta v/v$ changes within the monitored region.

Finally, we assume a uniform lateral velocity change in a layer of velocity change across the monitored region. The reality is that the velocity changes are localized in space both laterally and in depth. The inverted $h\Delta v/v$ can be seen as the average $h\Delta v/v$ of the true $h\Delta v/v$ within the monitored region. This means that in some areas of the monitored region the true changes will be higher or lower than the inverted values.

The above assumptions notwithstanding, the estimated velocity changes suggest that the crust underneath the region around Wasatch fault is undergoing a significant velocity change within a short period of time. These velocity changes will have significant implications for the characterization of both the seismicity and deformation of the region. It would be useful to discern if these velocity changes are seasonal, i.e., if they might be linked to seasonal loadings (such as tides and precipitations) in both near- and far-fields.

ACKNOWLEDGMENTS

We are grateful for the financial support of the Department of Energy (DOE) through grant DE-EE0002758.

APPENDIX A: ANALYTICAL APPROXIMATION OF EQUATION 4:

The timeshift $\langle\tau(t)\rangle$ extracted from repeating coda (assuming the diffusion model) can be related to the localized velocity changes by the model of Pacheco and Snieder (2005) as

$$-\frac{\langle\tau(t)\rangle}{t} = \langle\epsilon(t)\rangle = \int_V \frac{K(\mathbf{s},\mathbf{x_o},\mathbf{r},t)}{t}\frac{\Delta v}{v}(\mathbf{x_o})\,\mathrm{d}V, \tag{A1}$$

where V in the integration volume and $\mathbf{s}$, $\mathbf{x_o}$, and $\mathbf{r}$ are the source, arbitrary, and receiver locations, respectively. The sensitivity kernel $K(\mathbf{s},\mathbf{x_o},\mathbf{r},t)$ is

$$K(\mathbf{s},\mathbf{x_o},\mathbf{r},t) = \frac{\int_0^t P(\mathbf{s},\mathbf{x_o},t')P(\mathbf{x_o},\mathbf{r},t-t')\,\mathrm{d}t'}{P(\mathbf{s},\mathbf{r},t)}, \tag{A2}$$

and $P(\mathbf{x_1},\mathbf{x_2},t)$ is the normalized intensity recorded at a receiver location x_2 due to a source at x_1. Using the diffusion approximation for the normalized intensity in a 3D semi-infinite inhomogenous medium with a full reflecting surface boundary and where the source and receivers are located on the boundary, the normalized intensity is

$$P(R,t) = \frac{2}{(4\pi Dt)^{3/2}}\exp\left(-\frac{R^2}{4Dt}\right). \tag{A3}$$

Then the sensitivity kernel $K(\mathbf{s},\mathbf{x_o},\mathbf{r},t)$ in a 3D medium with a full reflecting surface boundary is given by (Rossetto et al., 2011)

$$K(\mathbf{s},\mathbf{x_o},\mathbf{r},t) = \frac{1}{2\pi D}\exp\left(\frac{R^2-(r+s)^2}{4Dt}\right)\left(\frac{1}{s}+\frac{1}{r}\right), \tag{A4}$$

where R is the source-receiver distance, and r and s are distances from the receiver and source to x_o, respectively. Therefore from equation (A1),

$$-\frac{\langle\tau(t)\rangle}{\langle t\rangle} = \langle\epsilon(t)\rangle =$$

$$\int_x\int_y\int_0^h \frac{1}{2\pi D\langle t\rangle}\exp\left(\frac{R^2-(r+s)^2}{4D\langle t\rangle}\right)\left(\frac{1}{s}+\frac{1}{r}\right)\frac{\Delta v}{v}(\mathbf{x_o})\,\mathrm{d}z\,\mathrm{d}y\,\mathrm{d}x. \tag{A5}$$

Assuming $h/R << 1$ and that the fractional velocity change is constrained to the near surface slab such that $\frac{\Delta v}{v}(\mathbf{x_o}) = \frac{\Delta v}{v}$, then

$$-\frac{\langle\tau(t)\rangle}{\langle t\rangle} = \langle\epsilon(t)\rangle \simeq h\frac{\Delta v}{v}\int_x\int_y \frac{1}{2\pi D\langle t\rangle}\exp\left(\frac{R^2-(r+s)^2}{4D\langle t\rangle}\right)\left(\frac{1}{s}+\frac{1}{r}\right)\mathrm{d}y\,\mathrm{d}x. \tag{A6}$$

The travel time $\langle t\rangle$ associated with the estimated average velocity $\langle\epsilon(t)\rangle$ is

$$\langle t\rangle = \frac{\int_{t'} w(t)t\,\mathrm{d}t'}{\int_{t'} w(t)\,\mathrm{d}t'}, \tag{A7}$$

where $w(t)$ is the intensity of the scattered waves. Because the intensity is higher in the early part of the coda rather than in the later, then the weighted average time $\langle t\rangle$ lies close to the peak of the intensity. At the intensity peak,

$$\frac{\partial P(R,t)}{\partial t} = 0. \tag{A8}$$

Based on equation (A3), $R^2/6D\langle t\rangle = 1$.

To express the variables as dimensionless quantities, let $x' = x/\sqrt{6D\langle t\rangle}$, $y' = y/\sqrt{6D\langle t\rangle}$, $R' = R/\sqrt{6D\langle t\rangle} = 1$, $r' = r/\sqrt{6D\langle t\rangle}$, and $s' = s/\sqrt{6D\langle t\rangle}$. Then,

$$-\frac{\langle\tau(t)\rangle}{\langle t\rangle} = \langle\epsilon(t)\rangle \simeq \frac{h}{\pi}\frac{\Delta v}{v}\sqrt{\frac{3}{2D\langle t\rangle}}\int_{x'}\int_{y'}\exp\left(\frac{3}{2}\left(1-(r'+s')^2\right)\right)\left(\frac{1}{s'}+\frac{1}{r'}\right)\mathrm{d}y'\,\mathrm{d}x'. \tag{A9}$$

Let

$$\int_{x'}\int_{y'}\exp\left(\frac{3}{2}\left(1-(r'+s')^2\right)\right)\left(\frac{1}{s'}+\frac{1}{r'}\right)\mathrm{d}y'\,\mathrm{d}x' = \Sigma. \tag{A10}$$

Therefore,

$$-\frac{\langle\tau(t)\rangle}{\langle t\rangle} = \langle\epsilon(t)\rangle \simeq \frac{h}{\pi}\frac{\Delta v}{v}\sqrt{\frac{3}{2D\langle t\rangle}}\Sigma. \tag{A11}$$

Using $R^2/6D\langle t\rangle = 1$, equation A11 follows that

$$-\frac{\langle \tau(t)\rangle}{\langle t\rangle} = \langle \epsilon(t)\rangle \simeq 3\frac{h}{\pi}\frac{\Delta v}{v}\frac{1}{R}\Sigma. \tag{A12}$$

Equation (A12) allows for a parametric description of the apparent velocity change $\langle \epsilon(t)\rangle$ in terms of the model parameters h, $\frac{\Delta v}{v}$, and R. Σ is a constant dimensionless parameter and is equal to 4.52 ± 0.02. The error in Σ is a numerical error.

REFERENCES

Armstrong, P. A., A. R. Taylor, and T. A. Ehlers, 2004, Is the Wasatch fault footwall (Utah, United States) segmented over million-year time scales?: Geology, **32**, no. 5.

Eaton, G. P., 1982, The Basin and Range Province: Origin and tectonic significance: Annual Review of Earth and Planetary Sciences, **10**, 409.

Gilbert, H. J. and A. F. Sheehan, 2004, Images of crustal variations in the intermountain west: Journal of Geophysical Research: Solid Earth, **109**.

Gori, P. L. and W. W. Hays, 1992, Assessment of regional earthquake hazards and risk along the Wasatch Front, Utah: U.S. Geological Survey Professional Paper, U.S. Government Printing Office.

Grêt, A., R. Snieder, and U. Özbay, 2006, Monitoring in situ stress changes in a mining environment with coda wave interferometry: Geophysical Journal International, **167**, 504–508.

Hadziioannou, C., E. Larose, O. Coutant, P. Roux, and M. Campillo, 2009, Stability of monitoring weak changes in multiply scattering media with ambient noise correlation: Laboratory experiments: Journal of the Acoustical Society of America, **125**, 3688–3695.

Hamilton, W. and W. B. Myers, 1966, Cenozoic tectonics of the western United States: Rev. Geophys., **5**, 509–549.

Hunt, C. B., 1956, Cenozoic geology of the Colorado Plateau, volume **279**: Geological Survey Professional Paper, U.S. Government Printing Office.

Kanu, C., R. Snieder, and D. O'Connell, 2013, Estimation of velocity change using repeating earthquakes with dierent locations and focal mechanisms.: Journal of Geophysical Research, **Under Review**.

Keller, G. R., R. B. Smith, and L. W. Braile, 1975, Crustal structure along the Great Basin-Colorado Plateau Transition from seismic refraction studies: Journal of Geophysical Research, **80**, 1093–1098.

Matsumoto, S., K. Obara, K. Yoshimoto, T. Saito, A. Ito, and A. Hasegawa, 2001, Temporal change in P-wave scatterer distribution associated with the M6.1 earthquake near Iwate volcano, northeastern Japan: Geophysical Journal International, **145**, 48–58.

Montgomery, D. R. and M. Manga, 2003, Streamflow and water well responses to earthquakes: Science (New York, N.Y.), **300**, 2047–2049. PMID: 12829774.

Nakata, N. and R. Snieder, 2012, Estimating near-surface shear wave velocities in Japan by applying seismic interferometry to KiK-net data: Journal of Geophysical Research: Solid Earth, **117**.

Pacheco, C. and R. Snieder, 2005, Time-lapse travel time change of multiply scattered acoustic waves: The Journal of the Acoustical Society of America, **118**, 1300–1310.

Poupinet, G., W. L. Ellsworth, and J. Frechet, 1984, Monitoring velocity variations in the crust using earthquake doublets: An application to the Calaveras fault, California: Journal of Geophysical Research, **89**, 5719–5731.

Rossetto, V., L. Margerin, T. Planès, and E. Larose, 2011, Locating a weak change using diffuse waves: Theoretical approach and inversion procedure: Journal of Applied Physics, **109**, 903–911.

Roten, D., K. B. Olsen, J. C. Pechmann, V. M. Cruz-Atienza, and H. Magistrale, 2011, 3D simulations of M 7 earthquakes on the Wasatch fault, Utah, Part I: Long-Period (0-1 Hz) ground motion: Bulletin of the Seismological Society of America, **101**, 2045–2063.

Schaff, D. P. and G. C. Beroza, 2004, Coseismic and postseismic velocity changes measured by repeating earthquakes: Journal of Geophysical Research: Solid Earth, **109**.

Simpson, D. W. and P. G. Richards, 1981, Earthquake prediction: An international review: American Geophysical Union.

Snieder, R., 2006, The theory of coda wave interferometry: Pure and Applied Geophysics, **163**, 455–473.

Snieder, R., A. Grêt, H. Douma, and J. Scales, 2002, Coda wave interferometry for estimating nonlinear behavior in seismic velocity: Science, **295**, 2253 –2255.

Spane, F. A., 2002, Considering barometric pressure in groundwater flow investigations: Water Resources Research, **38**, 1–18.

Stump, B., R. Burlacu, C. Hayward, K. Pankow, S. Nava, J. Bonner, S. Hock, D. Whiteman, A. Fisher, T. S. Kim, R. Kubacki, M. Leidig, J. Britton, D. Drobeck, P. ONeill, K. Jensen, K. Whipp, G. Johnson, P. Roberson, R. Read, R. Brogan, and S. Masters, 2007, Seismic and Infrasonic energy generation and propagation at local and regional distances: Phase IDivine Strake Experiment: Air Force Research Laboratory report, **AFRL-RV-HA-TR-2007-1188**.

Weaver, R. L., C. Hadziioannou, E. Larose, and M. Campillo, 2011, On the precision of noise correlation interferometry: Geophysical Journal International, **185**, 1384–1392.

Wise, D. U., 1963, An outrageous hypothesis for the tectonic pattern of the North American Cordillera: Geological Society of America Bulletin, **74**, 357–362.

Smooth dynamic warping

Dave Hale and Stefan Compton
Center for Wave Phenomena, Colorado School of Mines, Golden CO 80401, USA

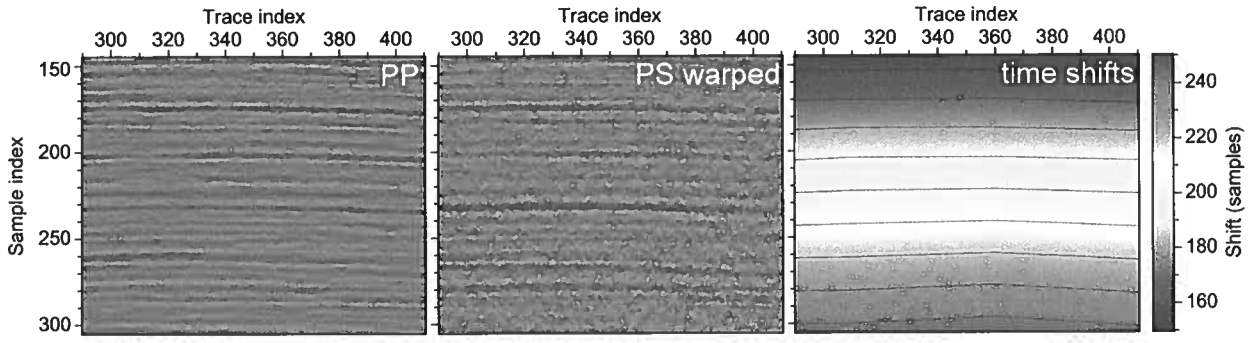

Figure 1. Subsets of a PP image and a corresponding PS image warped using time shifts estimated automatically by smooth dynamic warping. Contour lines (at 10-sample intervals) highlight the smoothness of the estimated time shifts.

ABSTRACT
Dynamic time warping is a simple classic method for aligning two sampled functions of time. The sequence of time shifts computed by this method are a globally optimal solution to a non-linear optimization problem with linear inequality constraints that may be directly related to subsurface properties. In applications to seismic traces, the time shifts may increase or decrease rapidly in time (and space). However, when related to integrals of subsurface parameters, such variations in time shifts are often smooth. A new method for smooth dynamic warping exploits this inherent smoothness to increase the accuracy of time shift estimates, especially where differences between seismic traces to be aligned are not limited to time shifts. The new method requires only a few simple modifications to the classic method, and can be easily extended to multidimensional image warping as well. In an application to registration of PP and PS images, we used smooth dynamic warping to compute times shifts that vary smoothly in both time and space, and are significantly more accurate than those computed using the classic method.

Key words: seismic image dynamic warping

1 INTRODUCTION

Dynamic image warping is a method for shifting features in one image to align them with corresponding features in another image. In applications to seismic images, the shifts are often in time or depth, and the correspondence is rarely exact.

Figure 1 illustrates one example, the registration of PP and PS seismic images. Here we have warped a PS image to align reflections with those in a PP image. The time shifts, while increasing rapidly with time, vary smoothly in time and space. We computed these time shifts using a new method for *smooth dynamic warping* proposed in this paper.

Clearly, differences between the PP and PS images in Figure 1 are not limited to time shifts. Other differences include noise, which is most apparent in the PS image, as well as differences in reflection amplitudes and waveforms related to differences in PP and PS reflection coefficients.

The PP and warped PS images shown in Figure 1 are subsets of the PP and (not yet warped) PS images shown in Figure 2. The images are displayed with different vertical scales so that reflections in the PP image are visually and approximately aligned with corresponding reflections in the PS image. The time shifts shown in Figure 1 are a subset of the time shifts we computed from the entire PP and PS images shown in Figures 2a and 2c.

Again, differences in noise and reflection amplitudes and waveforms are apparent in the PP and PS images. We compensated somewhat for amplitude differences by applying a time-variable gain to each trace in the PP and PS images. This gain normalizes amplitudes within seamlessly overlapping windows so that the rms amplitude within each window is one. Because the windows approximate a Gaussian with half-width 100 samples, the applied gain varies slowly with time.

Remaining differences complicate our estimation of time shifts. Yet we often estimate time differences, as in this example, because (1) they are related to subsurface properties, such as the ratio of P-wave and S-wave velocities V_P/V_S, and (2) after compensating for differences in reflection times, we can more readily analyze differences in reflection waveforms. So it is important that we estimate time shifts using methods that are accurate in the presence of noise and other such differences.

Several authors, including Gaiser (1996), Fomel et al. (2003), Nickel and Sonneland (2004), Fomel et al. (2005), and Liang and Hale (2012) have described methods for registration of PP and PS images and the corresponding estimation of V_P/V_S ratios. For this and similar problems, the dynamic warping method (Sakoe and Chiba, 1978; Anderson and Gaby, 1983; Hale, 2013) has two important advantages. First, dynamic warping honors specified bounds on time shifts and on the rate at which time shifts may vary with time. Second, using the computational method of dynamic programming, dynamic warping finds a globally optimal solution to an error minimization problem that may have many local minima.

The first advantage is important because the constraints are often related to geophysical parameters. For example, because $V_P \geq V_S$, we know that PS reflection time is never less than the corresponding PP reflection time, and that the differences between PS and PP reflection times can never decrease with time.

The second advantage improves the accuracy of dynamic warping in the presence of noise and reflection waveform differences. Such differences, which are unrelated to time shifts, imply that we often want a locally sub-optimal but globally optimal image registration.

In this paper we propose an improved method for *smooth dynamic warping* that enables control of a trade-off between accuracy and resolution of estimated *time strains*, changes in time shifts with time. The trade-off is important because estimates of time strain may correspond directly to subsurface parameters, such as V_P/V_S ratios. In addition, this new warping method improves robustness in the presence of noise and other differences, while requiring significantly less computer memory in applications to 2D and 3D images.

We first describe a basic dynamic time warping algorithm that is equivalent to one developed by Sakoe and Chiba (1978), but is most similar to one developed by Hale (2013). We then describe our improved algorithm, and extend the improvement to image warping, in which we compute shifts that are smooth in all sampled image dimensions (time and space), as illustrated in Figure 1. Throughout this paper we use the registration of PP and PS images shown in Figure 2 as just one example of the application of our improved method for smooth dynamic warping. The improvements extend to other applications as well.

2 DYNAMIC TIME WARPING

The problem in dynamic warping is to find a sequence of time shifts $u[0:n_i-1] \equiv \{u[0],u[1],\ldots,u[n_i-1]\}$ that aligns two sequences (time series) f and g so that

$$f[i] \approx g[i+u[i]], \quad i=0,1,\ldots,n_i-1 \tag{1}$$

More precisely, dynamic time warping computes time shifts

$$u[0:n_i-1] \equiv \underset{l[0:n_i-1]}{\arg\min} \sum_{i=0}^{n_i-1} e[i,l[i]] \tag{2}$$

subject to constraints

$$u_l \leq u[i] \leq u_u, \quad r_l \leq u[i]-u[i-1] \leq r_u, \tag{3}$$

where

$$e[i,l] \equiv (f[i]-g[i+l])^2. \tag{4}$$

In the inequality constraints 3, u_l and u_u are lower and upper bounds on shifts $u[i]$, and r_l and r_u are lower and upper bounds on time strain, the rate at which time shifts change with time sample index i. As noted above, these lower and upper bounds may sometimes be related to bounds on geophysical parameters.

The 2D array $e[i,l]$ contains *alignment errors* computed for all sample indices i and lag indices l. These alignment errors could be computed in alternative ways. For example, we could use an absolute value of differences instead of the square of differences in equation 4; we used the latter to obtain all of the results shown in this paper.

The bounds $[u_l,u_u]$ on shifts $u[i]$ imply that we must compute $e[i,l]$ only for lags l that satisfy $u_l \leq l \leq u_u$. For simplicity in array indexing, we instead use the bounds $0 \leq l \leq n_l-1$, where $n_l = 1+u_u-u_l$ is the number of lags l for which we compute $e[i,l]$. In practice, if $u_l \neq 0$, then we simply add u_l to l on the right-hand side of equation 4 as we compute alignment

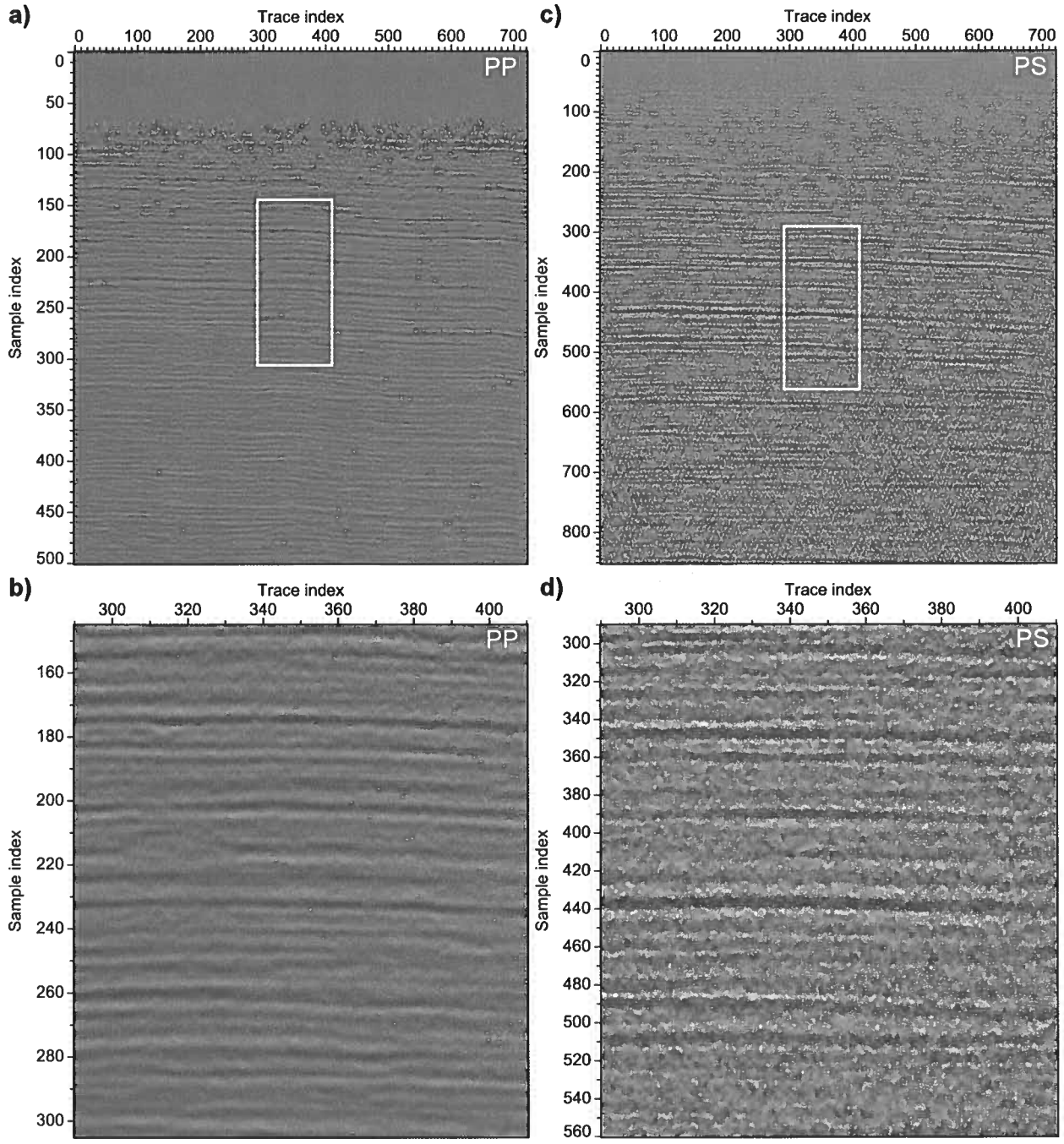

Figure 2. PP (a) and PS (c) images to be aligned, with subsets (b and d) corresponding to the white rectangles. The vertical scales for the PS images are different from those for the corresponding PP images, and were chosen to approximately align reflections in the two images.

errors. If we let f denote one trace from the PP image in Figure 2a and g denote a corresponding trace from the PS image in Figure 2c, then the lower bound on shift is in fact $u_l = 0$ because, as noted above, PS reflections never appear before corresponding PP reflections.

It is important to recognize that the sequence of shifts u defined by equation 2 is the globally optimal solution to a non-linear least-squares problem with linear inequality constraints 3. In practice, the oscillatory nature of seismograms represented by the sequences f and

g causes this minimization problem to have many local minima. As noted above, the ability to find the globally optimal solution to this problem is a key advantage of the dynamic warping method, when compared with alternative methods.

Given a 2D array of alignment errors $e[i,l]$ and bounds on strain r_l and r_u, we compute the optimal shifts $u[i]$ using a dynamic programming algorithm. This algorithm has four phases, which are highlighted in the pseudocode for Algorithm 1.

Algorithm 1 Find shifts $u[i]$

```
 1: procedure FINDSHIFTS(r_l, r_u, e, u)
 2:     for l = 0 to n_l − 1                          ▷ initialize
 3:         d[0, l] = e[0, l]
 4:     for i = 1 to n_i − 1                          ▷ accumulate
 5:         for l = 0 to n_l − 1
 6:             d_l = ∞
 7:             q_l = max(⌈r_l⌉, l − n_l + 1)
 8:             q_u = min(⌊r_u⌋, l)
 9:             for q = q_l to q_u
10:                 d_q = d[i − 1, l − q] + e[i, l]
11:                 if d_q < d_l
12:                     d_l = d_q
13:                     m_l = q
14:             d[i, l] = d_l
15:             m[i, l] = m_l
16:     i = n_i − 1                                   ▷ minimize d
17:     d_i = ∞
18:     for l = 0 to n_l − 1
19:         if d[i, l] < d_i
20:             d_i = d[i, l]
21:             u[i] = l
22:     while i > 0                                   ▷ backtrack
23:         u[i − 1] = u[i] − m[i, u[i]]
24:         i = i − 1
```

Lines 2–3 initialize the first column, the one for sample index $i = 0$, of a 2D array of *accumulated errors* $d[i,l]$.

Lines 4–15 perform a non-linear accumulation of alignment errors $e[i,l]$, and store the accumulated errors in $d[i,l]$. The accumulation is recursive, in that we compute accumulated errors for sample index i from those for sample index $i-1$. Also, while accumulating, we record in a separate 2D array $m[i,l]$ the lags l for the accumulated errors $d[i-1,l]$ used to compute $d[i,l]$. We think of the array $m[i,l]$ as recording the *error minimizing moves* that are made while accumulating. These moves are constrained by the bounds $[r_l, r_u]$; $\lceil r_l \rceil$ in line 7 denotes the smallest integer not less than r_l, and $\lfloor r_u \rfloor$ in line 8 denotes the largest integer not greater than r_u. Accumulation, the most costly of the four phases, ends with the computation of the last column of accumulated errors $d[n_i - 1, l]$.

Lines 16–21 then search this last column for the lag l that minimizes $d[n_i - 1, l]$. This lag is the optimal shift $u[i]$ for sample index $i = n_i - 1$. The accumulated error $d[n_i - 1, u[n_i - 1]]$ is the minimized sum in equation 2.

Finally, lines 22–24 use the moves recorded in $m[i,l]$ to backtrack, computing the optimal shift $u[n_i - 2]$ from $u[n_i - 1]$, $u[n_i - 3]$ from $u[n_i - 2]$, and so on, until finally computing $u[0]$ from $u[1]$.

Our improved Algorithm 2 is similar, but differs from Algorithm 1 in two ways.

Algorithm 2 Find subsampled shifts $u_i[j] \equiv u[i[j]]$

```
 1: procedure FINDSHIFTSI(r_l, r_u, e, i, u_i)
 2:     for l = 0 to n_l − 1                          ▷ initialize
 3:         d[0, l] = e[0, l]
 4:     for j = 1 to n_j − 1                          ▷ accumulate
 5:         h = i[j] − i[j − 1]
 6:         for l = 0 to n_l − 1
 7:             d_l = ∞
 8:             q_l = max(⌈h r_l⌉, l − n_l + 1)
 9:             q_u = min(⌊h r_u⌋, l)
10:             for q = q_l to q_u
11:                 d_q = d[j − 1, l − q]
12:                 for p = 0 to h − 1
13:                     d_q = d_q + e[i[j] − p, l − pq/h]
14:                 if d_q < d_l
15:                     d_l = d_q
16:                     m_l = q
17:             d[j, l] = d_l
18:             m[j, l] = m_l
19:     j = n_j − 1                                   ▷ minimize d
20:     d_j = ∞
21:     for l = 0 to n_l − 1
22:         if d[j, l] < d_j
23:             d_j = d[j, l]
24:             u_i[j] = l
25:     while j > 0                                   ▷ backtrack
26:         u_i[j − 1] = u_i[j] − m[j, u_i[j]]
27:         j = j − 1
```

The first difference is that Algorithm 2 computes shifts $u_i[j] \equiv u[i[j]]$ for only a subset of sample indices $i[0 : n_j - 1] \equiv \{i[0], i[1], \ldots, i[n_j - 1]\}$. Note that an array of indices i in this subset must be specified as input to the procedure in Algorithm 2. To compute shifts $u[i]$ for all sample indices i, we must later interpolate the subsampled shifts $u_i[j] \equiv u[i[j]]$ computed by Algorithm 2.

The second difference lies in the accumulation step, where lines 11–13 in Algorithm 2 have replaced line 10 in Algorithm 1. The additional inner loop **for** $p = 0$ **to** $h-1$ accumulates $h = i[j] - i[j-1]$ (line 5) alignment errors $e[i,l]$. Lines 4–18 compute and store accumulated errors $d[j,l]$ and moves $m[j,l]$ corresponding to the indices $i[j]$ in the subset $i[0 : n_j - 1]$.

Figure 3 illustrates how subsampling in Algorithm 2 can produce smoother sequences of shifts. This figure

shows a closeup view of shifts $u[i]$ computed from $e[i,l]$ obtained by averaging alignment errors for all traces in the PP and PS images shown in Figure 2. For this example, we chose strain limits $r_l = 0$ and $r_u = 2$, so that with $h = 1$ only three values of strain $u[i] - u[i-1]$ are possible: 0, 1, or 2. In other words, as we increase the sample index i, shift $u[i]$ must either remain the same or increase by one or two lags. This restriction explains the rough sequence of shifts for $h = 1$ shown in Figure 3a.

In contrast, for the same strain limits, subsampling with $h = 50$ yields 51 possible values of strain and the smooth sequence of shifts shown in Figure 3a. These shifts were obtained by interpolating subsampled shifts $u_i[j] \equiv u[i[j]]$ computed using Algorithm 2.

Figures 3b and 3c show computational stencils used for $h = 1$ and $h = 5$, again for strain limits $r_l = 0$ and $r_u = 2$. Lines 8 and 9 of Algorithm 2 determine which previously accumulated errors are accessed when computing the accumulated error $d[j,l]$ set in line 17. For $h = 1$ (Figure 3b), Algorithm 2 will access only three previously accumulated errors, $d[j-1,l]$, $d[j-1,l-1]$, and $d[j-1,l-2]$, as it computes $d[j,l]$.

For $h = 5$ (Figure 3c), Algorithm 2 will access 11 previously accumulated errors (corresponding to 11 different lags l), and for each of them it will sum $h = 5$ alignment errors $e[i,l]$, as it determines which change in shift minimizes accumulated error $d[j,l]$.

Note that the expression $l - pq/h$ in line 13 of Algorithm 2 may not have an integer value. For some sample indices i, the lines representing the computational stencil shown in Figure 3c lie between two integer lag indices l. This means that interpolation of alignment errors $e[i,l]$ for non-integer lags l is required in line 13. In practice, we find that linear interpolation or simply choosing the alignment error $e[i,l]$ for the nearest integer lag l is sufficient.

When the spacing between consecutive subsample indices $i[j]$ is $h = 1$ (so that $i[j] = j$ and $n_j = n_i$), then Algorithm 2 is equivalent to Algorithm 1. The ability in Algorithm 2 to sample shifts with larger subsampling intervals enables us to increase accuracy in estimated time strains (and shifts), by sacrificing temporal resolution of those same strains.

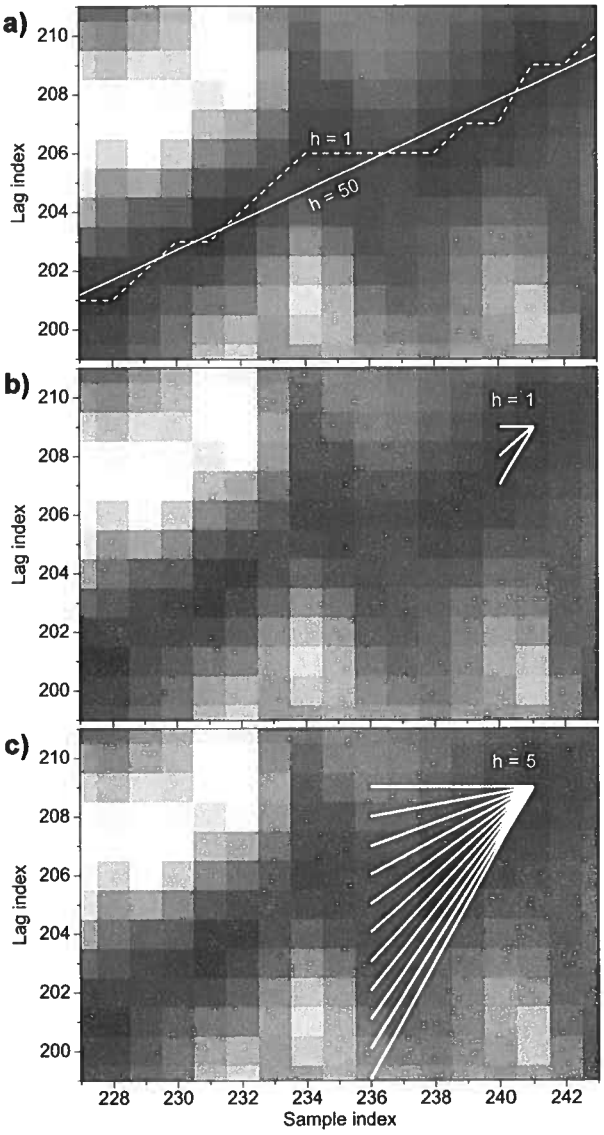

Figure 3. Closeup views of alignment errors $e[i,l]$ and shifts $u[i]$ (a) computed without subsampling ($h = 1$) and with subsampling by a factor of $h = 50$. For strain limits $0 \leq u[i] - u[i-1] \leq 2$, the computational stencil for $h = 1$ (b) can represent only two changes in lag; at each sample, lag must either remain constant or increase by one or two. In contrast, the stencil for $h = 5$ (c) represents 10 changes in lag, and a stencil for $h = 50$ (not shown) represents 100 changes in lag.

3 ACCURACY VERSUS RESOLUTION

Such a trade-off between accuracy and resolution is common in signal processing, and is unavoidable when estimating time shifts from two time series.

Figure 4 illustrates this trade-off for shifts $u[i]$ estimated from the PP and PS images of Figure 2. In Figure 4a, the sequence of shifts $u[i]$ is the globally optimal solution to the optimization problem of equations 2–4. We computed these shifts from alignment errors $e[i,l]$ using Algorithm 2 for $h = 1$.

Figures 4b and 4c show smoother sequences of shifts $u[i]$ computed using the same algorithm for $h = 50$ and $h = 100$, respectively. With Algorithm 2, we first computed subsampled shifts $u[i[j]]$ at the highlighted points, and then interpolated those shifts using piecewise-cubic polynomials to obtain finely sampled shifts $u[i]$. We used polynomials that preserve monotonicity (Fritsch and Carlson, 1980) to ensure that $u[i] - u[i-1] \geq 0$, as required by the strain constraints for PP-PS image registration. A simpler alternative, one more consistent

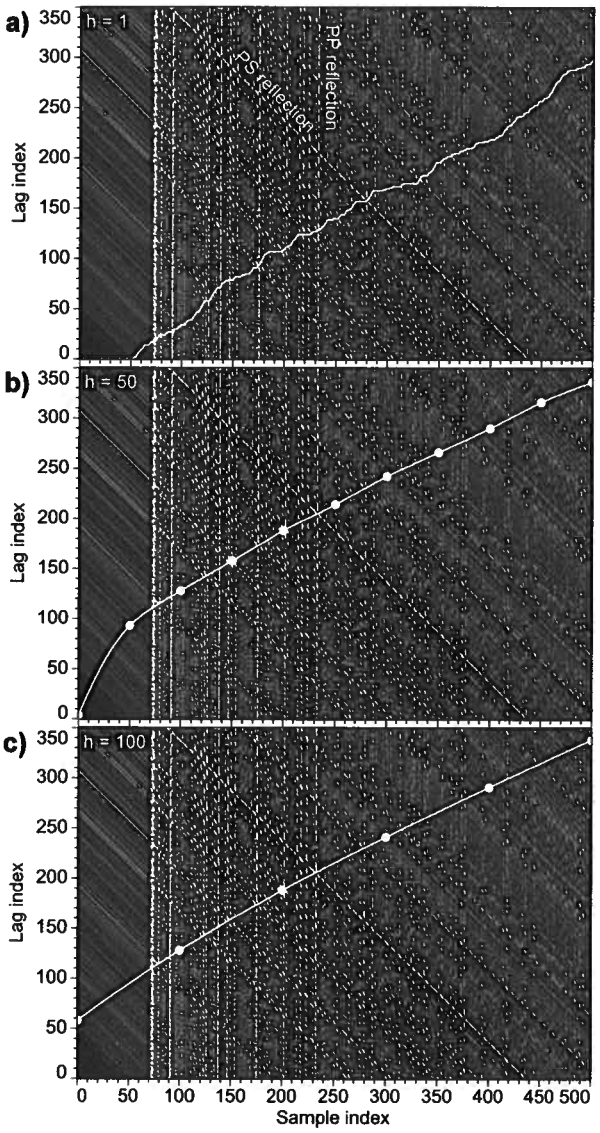

Figure 4. Alignment errors and shifts computed without subsampling (a) and with subsampling by factors of $h = 50$ (b) and $h = 100$ (c). Subsampled shifts are both smoother and more accurate, and cannot be computed by simply smoothing the shifts obtained without subsampling ($h = 1$). In the background images of alignment errors, white vertical features correspond to reflections in the PP image, and diagonal features correspond to (shifted) reflections in the PS image.

with the accumulation of alignment errors along linear paths like those shown in Figure 3c, would be piecewise-linear interpolation.

The sequence of shifts $u[i]$ obtained without subsampling for $h = 1$ exhibit much more detail than those obtained with subsampling for either $h = 50$ or $h = 100$. In other words, for $h = 1$, changes in time shifts with time are well-resolved. However, in this example the shifts obtained for $h = 1$ are useless. We show below that the shifts obtained for $h = 50$ are much more accurate. Moreover, the shifts computed for $h = 50$ cannot be obtained by simply smoothing the shifts computed for $h = 1$.

For $h = 100$ (Figure 4c) Algorithm 2 computes shifts for only six samples. Except near sample index $i = 0$, the interpolated shifts $u[i]$ well approximate those computed for $h = 50$.

To demonstrate that the shifts $u[i]$ computed for $h = 50$ are more accurate than those for $h = 1$, Figure 5 shows closeup views of results obtained for three different arrays of alignment errors $e[i, l]$. Figures 5a–c show averages of 1 (no averaging), 5, and 721 alignment errors computed from pairs of traces in the PP and PS images in Figure 2. Figures 5d–f show the same alignment errors with shifts computed for $h = 1$ and $h = 50$.

Figure 5a shows a closeup view of alignment errors $e[i, l]$ computed from only the middle pair of traces in the PP and PS images. Because differences between traces in the PP and PS images are not limited to time shifts, a unique path of minimum error is not apparent in this 2D array, and the shifts computed for $h = 1$ and $h = 50$ differ significantly, as shown in Figure 5d.

Recall that we can compute a 2D array of alignment errors $e[i, l]$ from each pair of corresponding traces in the PP and PS images. By averaging alignment errors computed for the five pairs of traces nearest the middle of these images, we obtain the results shown in Figures 5b and 5e. Again, the shifts computed for $h = 1$ and $h = 50$ differ significantly, but in this case the shifts for $h = 50$ are more accurate.

We know this because of the results shown in Figures 5c and 5f, which were obtained by averaging alignment errors for all 721 pairs of traces in the PP and PS images. In Figure 5c, the path of minimum error is obvious, and shifts computed using both $h = 1$ and $h = 50$ are well-aligned with this path, which we may assume corresponds to a lateral average of the correct relationship between PP and PS reflection times.

Although the path of minimum error is clearly apparent in Figure 5c, other nearly parallel paths with small error are apparent as well. These other paths are caused by cycle skipping, subtracting one cycle of a reflection waveform in the PS image from a different cycle of the corresponding waveform in the PP image. Recall that one of the advantages of the dynamic warping algorithm is that it will always find the globally optimal and constrained path that minimizes the sum of alignment errors, and will never be trapped in nearby local minima caused by cycle skipping.

While more accurate, shifts $u[i]$ for $h = 1$ shown in Figure 5f are still not as smooth as those for $h = 50$. In fact, the alignment errors and shifts shown in Figure 3a are closeup views of those shown in Figure 5f. Again, the roughness of shifts for $h = 1$ is due to coarse sampling of only three values (0,1 or 2) of time strain

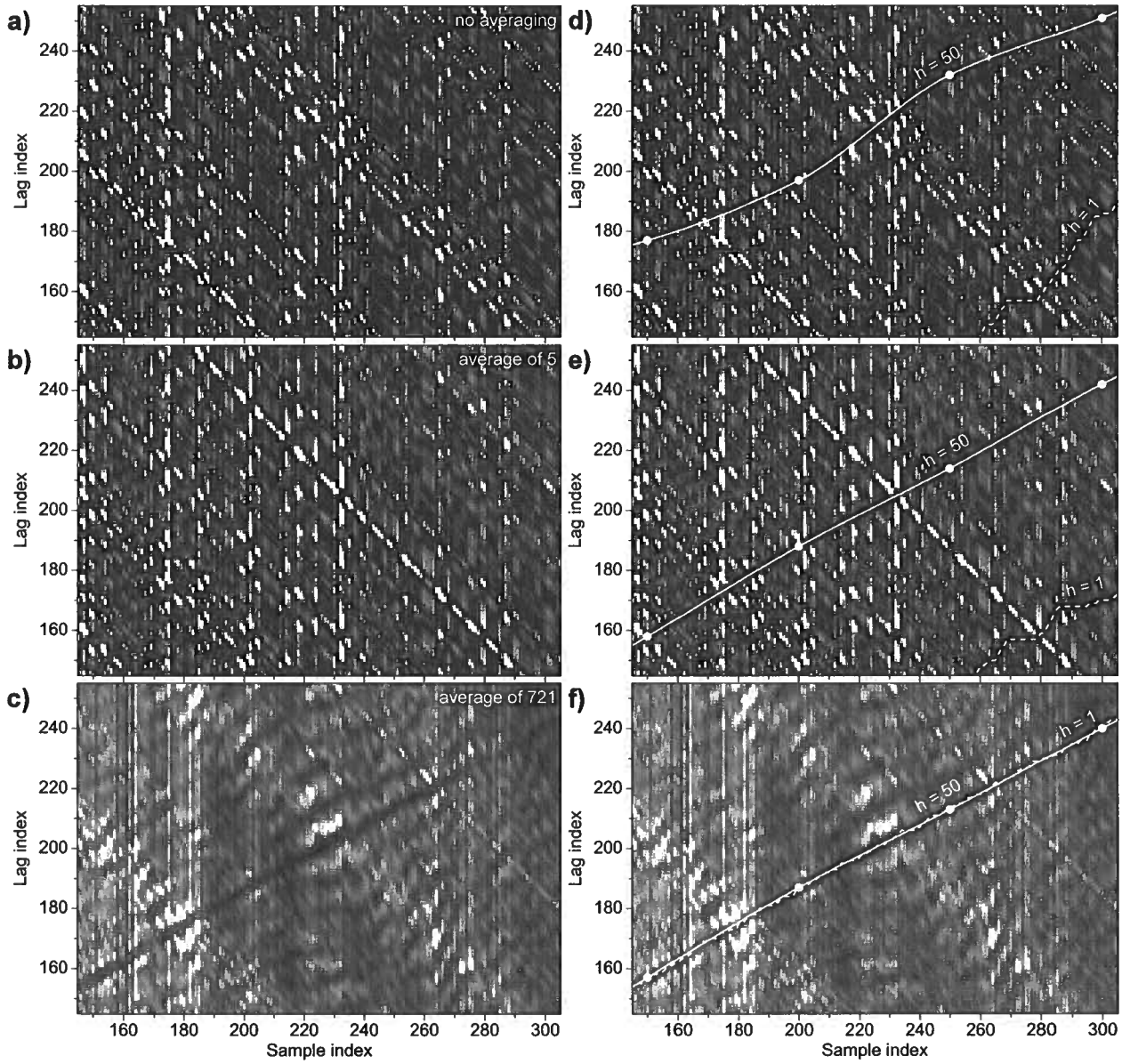

Figure 5. Closeup views of alignment errors $e[i,l]$ obtained from a single pair of PP and PS traces (a) and by averaging alignment errors computed for 5 (b) and all 721 (c) pairs of traces, displayed with (a, b and c) and without (d, e and f) shifts $u[i]$ computed for $h = 1$ and $h = 50$. In this example, the correct shifts (lags) are most apparent in (c), because lateral variation in shifts is small. With subsampling ($h = 50$) the correct shifts can be found by averaging alignment errors computed for only 5 pairs of traces (b and e).

$u[i] - u[i-1]$. The smoothness of shifts for $h = 50$ is due to a much finer sampling of 101 values of time strain. Such fine sampling may be useful in this application to PP-PS image registration, because a value of time strain corresponds directly to a value for

$$\frac{V_P}{V_S} = 1 + 2(u[i] - u[i-1]). \tag{5}$$

For sample indices i in the closeup view shown in Figure 3a, we observe that $V_P/V_S \approx 2$, but this value corresponds to none of the three time strains sampled for $h = 1$.

The results shown in Figure 5 demonstrate an improvement in accuracy that comes from computing subsampled shifts as in Algorithm 2. This improvement is due to the fact that, in this application, the correct shifts are smooth, because they are directly related to the integral of a subsurface property, V_P/V_S. This inherent smoothness implies that shifts $u[i]$ can be subsampled

without aliasing, and then later reconstructed with interpolation.

The results of Figure 5 also demonstrate the difficulty in estimating time shifts from time series that have differences unrelated to time shifts, such as noise and reflection waveform differences. Using just one pair of PP and PS traces (Figures 5a and 5d) it may be impossible to obtain an accurate estimate of the correct shifts $u[i]$. In this example, lateral averaging of alignment errors computed from many pairs of PP and PS traces helps to improve accuracy, but only because lateral variations in time shifts are small. However, while small, lateral variations can be significant, as shown below. By accounting for these variations we can further improve the accuracy of smooth dynamic warping.

4 SMOOTH IMAGE WARPING

We do this using the method for dynamic image warping proposed by Hale (2013). In that method, we first recognize that lines 4–14 of Algorithm 1 perform a recursive non-linear smoothing of alignment errors $e[i,l]$. We then repeatedly apply this smoothing filter — top-to-bottom, bottom-to-top, left-to-right, right-to-left, and so on, for all image dimensions — to alignment errors computed for all pairs of traces in two images. The result is a multi-dimensional array of alignment errors that have been smoothed both vertically and horizontally. Finally, we apply Algorithm 1 once more to the smoothed alignment errors to obtain shifts that vary both vertically and horizontally.

To extend this method to Algorithm 2, we recognize that lines 4–17 of this algorithm perform both a *smoothing and subsampling* of alignment errors. Accumulation of alignment errors e along linear paths like those shown in Figure 3c is equivalent to a smoothing filter, a form of anti-alias filter that enables accumulated alignment errors d to be subsampled. Let $\tilde{e}_f$ denote a 2D array of these forward-accumulated and subsampled errors, the values d stored in line 17 of Algorithm 2. We can apply the same filter in the opposite direction to obtain a different 2D array $\tilde{e}_r$ of reverse-accumulated and subsampled errors. Finally, we can construct symmetrically smoothed and subsampled alignment errors

$$\tilde{e}[j,l] = \tilde{e}_f[j,l] + \tilde{e}_r[j,l] - e[i[j],l]. \qquad (6)$$

Each $\tilde{e}[j,l]$ is a sum along piecewise linear paths (Figure 3c) of alignment errors $e[i,l]$. In equation 6, $\tilde{e}_f[j,l]$ is the forward sum for sample indices 0 to $i[j]]$, $\tilde{e}_r[j,l]$ is the reverse sum for sample indices $i[j]$ to $n_i - 1$, and subtraction of $e[i[j],l]$ prevents this value from being included twice in the sum $\tilde{e}[j,l]$.

By repeating this smoothing and subsampling process for each array of alignment errors $e[i,l]$ (i.e., for all pairs of traces in two images), we obtain a collection of arrays of smoothed and subsampled alignment errors $\tilde{e}[j,l]$. In typical applications, the number of samples n_j after smoothing and subsampling will be much smaller (say, by a factor of $h = 50$) than the number of samples n_i input to this process. This means that we will typically be able to keep the entire collection of $\tilde{e}[j,l]$ in fast computer memory, as we apply the same smoothing and subsampling process along other (horizontal) image dimensions.

Finally, as in Hale (2013), we apply a simple dynamic warping (with no further subsampling) to the smoothed and subsampled alignment errors $\tilde{e}$ to obtain shifts u that are subsampled in all image dimensions. We then interpolate these coarsely sampled shifts to obtain smoothly varying shifts for every image sample.

We applied this method (using bilinear interpolation) for smooth dynamic image warping to the PP and PS images shown in Figure 2 to obtain the time shifts shown in Figure 1. We used these time- and laterally-varying time shifts to warp the PS image.

To illustrate the significance of the lateral variation, in Figure 6 we compare PS images after both 1D and 2D warping. We performed 1D warping using time shifts computed from the average of alignment errors of all 721 pairs of traces in the PP and PS images. These shifts were computed for $h = 50$ and are identical to those displayed in Figure 5f.

Figure 6a shows a subset of the PS image after 1D warping, and Figure 6b shows the sample-by-sample differences between this warped PS image and the PP image subset shown in Figure 2b. The images shown in Figures 6c and 6d show comparable results obtained for 2D warping.

While differences between the warped PS images in Figures 6a and 6c may be difficult to see, reflections in the latter appear at slightly earlier times near the middle of the image, consistent with the upward bend in the contours of constant time shift apparent in Figure 1.

This slight lateral variation in time shifts explains the differences apparent in Figures 6b and 6d. After 2D warping, significant differences remain between the warped PS image and the PP image, but the differences are weaker and are less spatially correlated than for 1D warping. These differences suggest that the time shifts computed with smooth dynamic 2D warping are more accurate than those for 1D warping.

5 CONCLUSION

With a simple modification to the dynamic time warping algorithm, we enable a trade-off between accuracy and resolution in estimates of time strains. Our improved dynamic warping algorithm computes smoothly varying shifts by smoothly interpolating shifts that have been coarsely subsampled. While decreasing our ability to resolve rapid variations in time strains, this coarse subsampling increases the accuracy with which smooth time shifts can be estimated.

In registration of PP and PS images (and in other

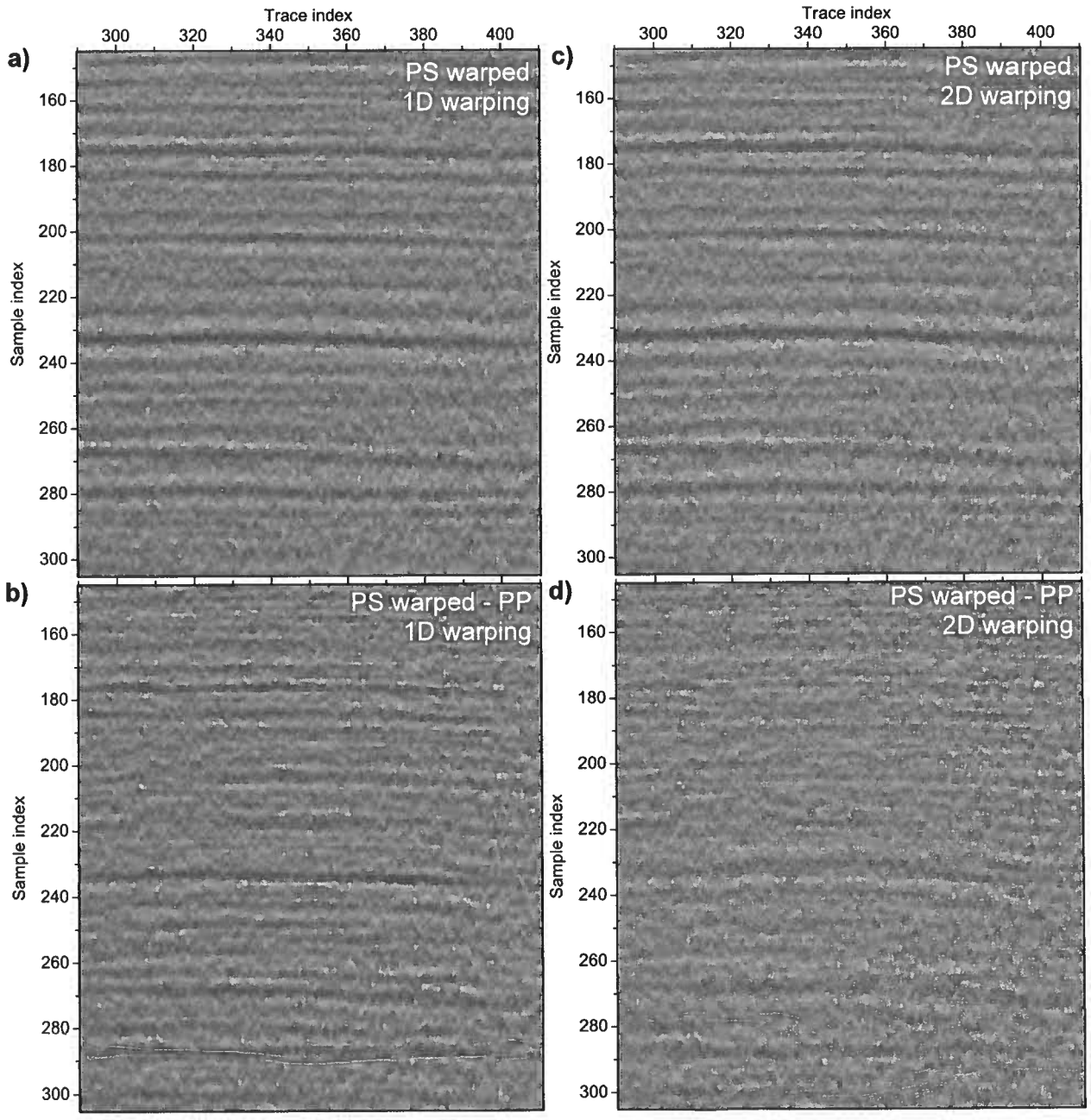

Figure 6. Subsets of the PS image after 1D (a) and 2D (c) warping. For 1D warping (a), shifts were subsampled vertically by a factor of $h = 50$. For 2D warping (c), shifts were subsampled by the same factor both vertically and horizontally. Corresponding sample-by-sample differences (b and d) indicate that 2D warping more accurately aligns the PS image with the PP image.

applications not discussed in this paper), smooth dynamic warping has enabled us to significantly improve the accuracy of time shift estimates, especially where differences between sequences or images to be aligned cannot be attributed entirely to time shifts. In a separate report, we use smooth dynamic warping to estimate V_P/V_S ratios that correspond directly to time strains computed using smooth dynamic warping of 3D images.

The only disadvantage we have found in smooth dynamic warping is an increase in computation cost that is proportional to h, the nominal subsampling interval. The computational complexity of simple dynamic warping via Algorithm 1 is $O(n_i \times n_l)$. The computational complexity of smooth dynamic warping via Algo-

rithm 2 is $O(n_i \times n_l \times h)$. In practice we have found this increase in cost to be worthwhile, especially for multidimensional image warping, in which subsampling of smoothed alignment errors quickly reduces computational cost as smoothing and subsampling are performed for each image dimension.

ACKNOWLEDGMENT

We thank sponsor companies of the Consortium Project on Seismic Inverse Methods for Complex Structures, whose support made this research possible. The seismic PP and PS images shown in Figure 2 were provided courtesy of Sinopec.

REFERENCES

Anderson, K., and J. Gaby, 1983, Dynamic waveform matching: Information Sciences, **31**, 221–242.

Fomel, S., M. Backus, M. DeAngelo, P. Murray, and B. Hardage, 2003, Multicomponent seismic data registration for subsurface characterization in the shallow Gulf of Mexico: Offshore Technology Conference, Expanded Abstracts, 15117.

Fomel, S., M. Backus, K. Fouad, B. Hardage, and G. Winters, 2005, A multistep approach to multicomponent seismic image registration with application to a West Texas carbonate reservoir study: 75th Annual International Meeting, SEG, Expanded Abstracts, 1018–1021.

Fritsch, F., and R. Carlson, 1980, Monotone piecewise cubic interpolation: SIAM Journal on Numerical Analysis, **17**, 238–246.

Gaiser, J., 1996, Multicomponent V_P/V_S correlation analysis: Geophysics, **61**, 1137–1149.

Hale, D., 2013, Dynamic warping of seismic images: Geophysics, **78**, S105–S115.

Liang, L., and D. Hale, 2012, Automatic registration of PP and PS images using dynamic image warping: CWP Report 724.

Nickel, M., and L. Sonneland, 2004, Automated PS to PP event registration and estimation of a high-resolution $V_P - V_S$ ratio volume: 74th Annual International Meeting, SEG, Expanded Abstracts, 869–872.

Sakoe, H., and S. Chiba, 1978, Dynamic programming algorithm optimization for spoken word recognition: IEEE Transactions on Acoustics, Speech, and Signal Processing, **26**, 43–49.

Estimating V_p/V_s ratios using smooth dynamic image warping

Stefan Compton & Dave Hale
Center for Wave Phenomena, Colorado School of Mines, Golden CO 80401, USA

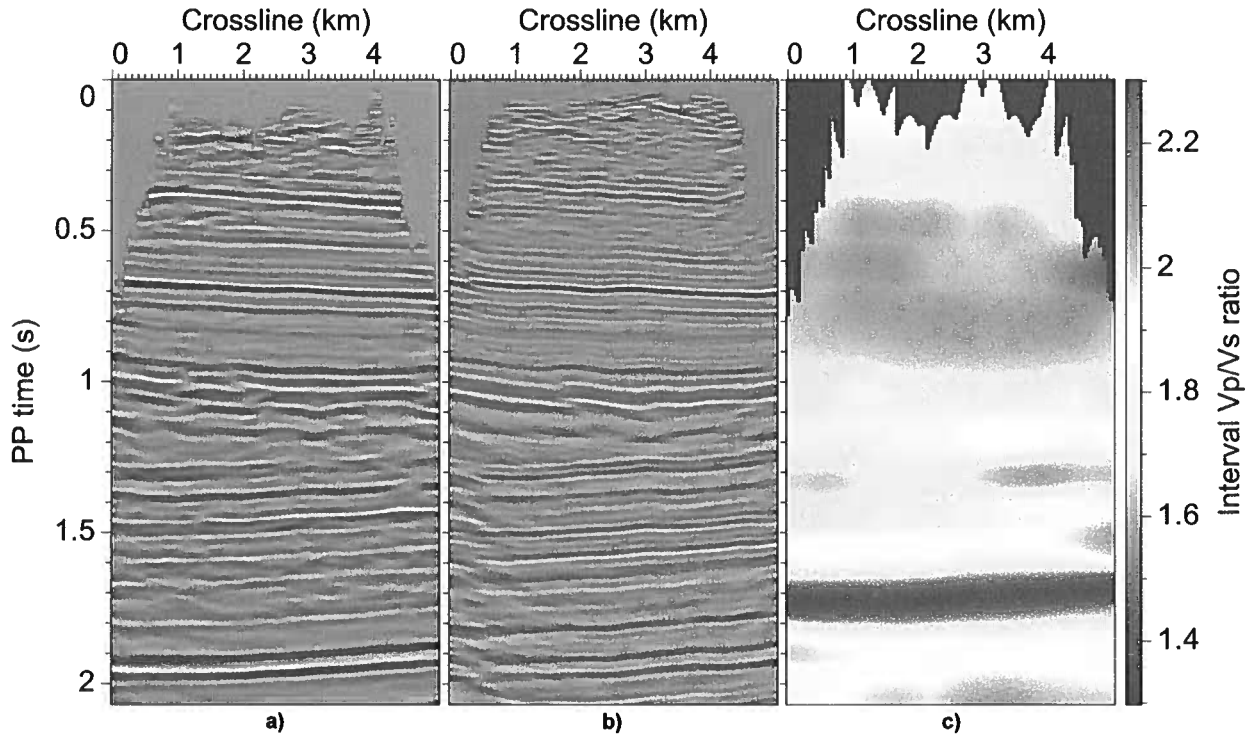

Figure 1. PP image (a) and PS image (b) after automatic registration to PP time, with interval V_p/V_s ratios (c) estimated from time shifts that align the two images. The time shifts were computed from 3D PP and PS images using smooth dynamic image warping (Hale and Compton, 2013).

ABSTRACT
Interval V_p/V_s ratios can be estimated from derivatives of vertical shifts that align reflections in PP and PS images. This alignment, however, is nontrivial because features in PS images are not simply time-shifted versions of features in PP images. To align PP and PS images we use a smooth dynamic image warping algorithm that can be accurate with respect to problems unrelated to time shifts, such as differences in noise and reflection waveforms. To optimize accuracy of estimated time shifts and V_p/V_s ratios, we automatically construct a coarse lattice of points located on reflections with high amplitudes, and then estimate time shifts at only those points. By adjusting the coarseness of the lattice, we trade off resolution of changes in V_p/V_s with increased accuracy in V_p/V_s estimates. By processing 3D PP and PS images we learned that our estimates of V_p/V_s cannot be obtained by simply smoothing estimates obtained using other methods.

Key words: seismic image dynamic image warping V_p/V_s ratio

1 INTRODUCTION

Converted-wave seismic data can be used in exploration geophysics to aid in estimation of petrophysical properties and reservoir characterization. Joint PP and PS analysis has applications in structural imaging, lithology estimation, anisotropy analysis, fluid description, and reservoir monitoring (Stewart et al., 2003). Because traveltimes for events in PP images and corresponding events in converted PS images differ, a crucial first step in analysis is the alignment, or registration, of these events.

The vertical shifts that align PP and PS images can be used to quantify the ratio of P- and S-wave velocities (V_p/V_s), an important attribute that is the target of much P-S analysis (Stewart et al., 2003). However, PP and PS image registration is complicated by differences in noise and reflection waveforms between the two images, and thus this registration is often done manually. Many techniques have nevertheless been developed to automate the registration process and to estimate V_p/V_s ratios (Gaiser, 1996; Fomel and Backus, 2003; Nickel and Sonneland, 2004; Yuan et al., 2008; Liang and Hale, 2012).

Liang and Hale (2012) used dynamic image warping (Hale, 2013) for this purpose. Dynamic image warping computes vertical time shifts that align events in PP and PS images; these shifts are a globally optimal solution of a minimization problem with many possible local minima. The dynamic warping algorithm satisfies bounds on time shifts and satisfies constraints for how rapidly time shifts vary. The method discussed here improves estimates of vertical time shifts, using a modified dynamic warping algorithm, *smooth dynamic warping* (Hale and Compton, 2013).

This new algorithm estimates changes in time shifts more accurately than the previous dynamic warping method. For PP and PS image registration, time shifts are related to integrals of V_p/V_s ratios, and thus, are often smoothly varying. Under the assumptions that time shifts vary smoothly and that alignment of image features can be achieved by vertical time shifts alone, we show in application to 3D PP and PS images that smooth dynamic warping is a robust and accurate method for automatic image registration and estimation of V_p/V_s ratios.

2 THEORY

We can use dynamic image warping to find corresponding events in PP and PS images, and this correspondence can be represented by time shifts. These time shifts enable image registration, the alignment of events in PP and PS images, while also providing estimates of V_p/V_s ratios.

2.1 Traveltime Relations

Let t_{pp} denote the PP traveltime for a reflector apparent in a PP image, and t_{ps} denote the PS traveltime for the same reflector in the corresponding PS image. For each t_{pp}, we have a corresponding t_{ps} defined by the function

$$t_{ps}(t_{pp}) = t_{pp} + u(t_{pp}), \tag{1}$$

where $u(t_{pp})$ denotes the time shift, which varies with t_{pp}.

The time shift $u(t_{pp})$ is related to the ratio V_p/V_s of P- and S-wave velocities. For an infinitesimal interval dz of depth z, the P- and S-wave velocities are

$$V_p = 2\frac{dz}{dt_{pp}}, \quad V_s = 2\frac{dz}{dt_{ss}}, \tag{2}$$

where t_{ss} denotes the SS time corresponding to the PP time t_{pp}. The factors of 2 are necessary because t_{pp} and t_{ss} are two-way traveltimes; the infinitesimal time intervals dt_{pp} and dt_{ss} are the times required for P- and S-waves to travel twice through the depth interval dz. From these definitions of interval velocities we define the interval V_p/V_s ratio by

$$\gamma_i(t_{pp}) \equiv \frac{V_p}{V_s} = \frac{dt_{ss}}{dt_{pp}}. \tag{3}$$

The time t_{ss} is that at which we would observe a reflector in an SS image, if we had one. If we instead have a converted-wave PS image, we must express the interval V_p/V_s ratio $\gamma_i(t_{pp})$ in terms of the time $t_{ps}(t_{pp})$ or, equivalently, the time-shift function $u(t_{pp})$. To do this, we recall that PS time is the average of PP and SS times

$$t_{ps}(t_{pp}) = \frac{t_{pp} + t_{ss}(t_{pp})}{2}. \tag{4}$$

Substituting this expression into equation 3, we obtain

$$\gamma_i(t_{pp}) = 2\frac{dt_{ps}}{dt_{pp}} - 1. \tag{5}$$

Then, using equation 1, we have

$$\gamma_i(t_{pp}) = 1 + 2\frac{du(t_{pp})}{dt_{pp}}. \tag{6}$$

2.2 Constraints on Time Shifts

One of the most attractive features of dynamic warping is that it computes a globally optimal shift function $u(t_{pp})$, while satisfying specified bounds on both the values and derivatives of this function. Let u_l and u_u denote lower and upper bounds on the shifts, so that

$$u_l \le u(t_{pp}) \le u_u. \tag{7}$$

To specify a lower bound u_l, we may use the fact that $V_p \ge V_s$, which implies that $t_{ps} \ge t_{pp}$ and that all shifts $u(t_{pp})$ must be non-negative, so that the lower bound is $u_l = 0$. Indeed, at the surface, where $t_{pp} = t_{ps} = 0$, we should theoretically find that $u(0) = 0$. In

practice, we might relax this lower bound to permit negative shifts because uncertainties in near-surface variations of V_p and V_s may lead to inconsistencies in datums and statics corrections used to obtain PP and PS images. However, near the surface we are also likely to find ratios $V_p/V_s \gg 1$, so that shifts $u(t_{pp})$ will increase rapidly with time t_{pp}, and therefore quickly become positive. For all examples shown in this paper, we use the lower bound $u_l = 0$.

We estimate the upper bound u_u from an estimate of the average V_p/V_s ratio and a maximum time of interest. Analogous to equation 5, the average V_p/V_s ratio is

$$\gamma_a(t_{pp}) = 2\frac{t_{ps}}{t_{pp}} - 1. \tag{8}$$

Therefore, if T_{ps} is the maximum time of interest in a PS image, then the corresponding time in the PP image is

$$T_{pp} = \frac{2T_{ps}}{1 + \gamma_a(T_{pp})}. \tag{9}$$

Note that T_{pp} is not the maximum recording time in the PP image. Rather, T_{pp} is the maximum time in the PP image for which a corresponding event of interest appears in the PS image at the maximum PS time, T_{ps}. We will ignore times $t_{pp} > T_{pp}$ in the PP image for which there are no corresponding events of interest in the PS image.

If we could solve equation 9 for T_{pp}, then we could simply compute the upper bound on shift as $u_u = T_{ps} - T_{pp}$. Although we are unlikely to know the function $\gamma_a(t_{pp})$ until after we have estimated time shifts $u(t_{pp})$ a precise upper bound u_u is unnecessary. In practice, we need only ensure that we do not set this bound too low, so that the correct shifts $u(t_{pp})$ will not exceed u_u. This requirement means that we should generally overestimate the average V_p/V_s ratio $\gamma_a(T_{pp})$ at the maximum PP time T_{pp}. We find that $\gamma_a(T_{pp}) \approx 2$, so that $u_u \approx T_{ps}/3$ is often a safe choice.

In addition to bounds on estimated time shifts $u(t_{pp})$, dynamic warping also honors bounds on derivatives of the estimated shift function $u(t_{pp})$, which are directly related to bounds on interval V_p/V_s ratios $\gamma_i(t_{pp})$ according to equation 6. Specifically, if r_l and r_u denote lower and upper bounds such that

$$r_l \le \frac{du(t_{pp})}{dt_{pp}} \le r_u, \tag{10}$$

then r_l and r_u correspond to lower and upper bounds on interval V_p/V_s, γ_{iMin} and γ_{iMax}, from which we compute

$$r_l = \frac{\gamma_{iMin} - 1}{2} \tag{11}$$

$$r_u = \frac{\gamma_{iMax} - 1}{2}. \tag{12}$$

Because $\gamma_i \ge 1$, a safe lower bound is $r_l = 0$. The upper bound r_u depends on the maximum interval V_p/V_s ratio γ_{iMax}. Because this ratio is seldom known in advance, an overestimate should generally be used.

2.3 3D Dynamic Image Warping

When warping 3D images, the time shifts u are a function of PP time t_{pp}, inline coordinate x, and crossline coordinate y. To simplify notation, we henceforth replace t_{pp} with t.

Let $f(x,y,t)$ denote the PP image and $g(x,y,t)$ denote the PS image. Then, dynamic warping computes the time-shift function $u(x,y,t)$ such that

$$f(x,y,t) \approx g(x,y,t + u(x,y,t)). \tag{13}$$

Specifically,

$$u = \arg\min_s \int_0^{T_{pp}} e(x,y,t;s)dt, \tag{14}$$

where $s \equiv s(x,y,t)$, and

$$e(x,y,t;s) \equiv [(f(x,y,t) - g(x,y,t+s)]^2 \tag{15}$$

are the alignment errors of squared differences between $f(x,y,t)$ and $g(x,y,t)$ for all possible shifts $s(x,y,t)$. The alignment errors need not be *squared* differences, but this is the measure used for all examples shown in this report.

The shifts $u = u(x,y,t)$ computed in dynamic warping are a globally optimal constrained solution to this non-linear minimization problem. In 3D image warping, values and partial derivatives of the shifts $u(x,y,t)$ are constrained by

$$u_l \le u(x,y,t) \le u_u \tag{16}$$

and

$$r_{lx} \le \frac{\partial u(x,y,t)}{\partial x} \le r_{ux}, \tag{17}$$

$$r_{ly} \le \frac{\partial u(x,y,t)}{\partial y} \le r_{uy}, \tag{18}$$

$$r_{lt} \le \frac{\partial u(x,y,t)}{\partial t} \le r_{ut}. \tag{19}$$

Recall that $\partial u(x,y,t)/\partial t$ is directly related to the interval V_p/V_s ratio γ_i(x,y,t) given by equation 6. Therefore, the bounds r_{lt} and r_{ut} are those given by equations 11 and 12, respectively.

Whereas the time shifts $u(x,y,t)$ can never decrease with increasing time t, they may decrease or increase with increasing x or y coordinates. The bounds r_{lx}, r_{ly}, r_{ux}, and r_{uy} control rates at which the time shifts $u(x,y,t)$ may vary laterally. These bounds are important, because they are related to the rates at which corresponding estimates of V_p/V_s ratios $\gamma_i(x,y,t)$ can vary laterally. In practice, we do not know in advance what these rates will be, so we typically begin with loose bounds on lateral variations and tighten them as necessary to reduce suspicious oscillations in estimated V_p/V_s ratios.

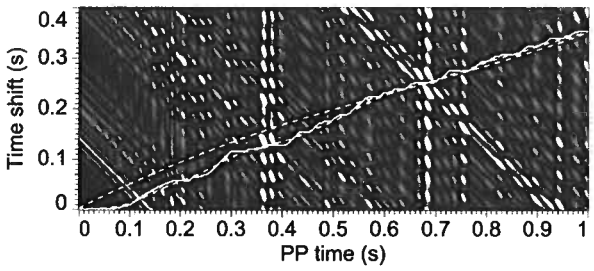

Figure 2. Alignment errors computed from a single trace from the PP and PS images shown in Figures 1a and 1b. Here, only the alignment errors for times 0 to 1 second are shown. Overlaid curves are the 1D time shifts u for this trace, extracted from the 3D time shifts $u(x,y,t)$ computed from two different dynamic image warping algorithms. The solid white curve shows rough time shifts computed from DIW (Hale, 2013) and the dashed blue curve shows these shifts after smoothing. The dashed yellow curve shows the computed time shifts from SDIW (Hale and Compton, 2013) with a minimum subsampling interval of 100 ms.

3 SMOOTH DYNAMIC IMAGE WARPING

In practical applications, $f(x,y,t)$ and $g(x,y,t)$ are sampled functions in time and space. In the dynamic image warping (DIW) algorithm described by Hale (2013), the computed time shifts $u(x,y,t)$ are sequences of integer shifts. DIW is used by Liang and Hale (2012) to register PP and PS images and to estimate V_p/V_s ratios. Because the shifts are integers, the number of possible shift derivatives is small; thus from equation 6, the number of possible computed $\gamma_i(x,y,t)$ values is correspondingly small. Therefore, an important step in Liang and Hale's (2012) application is to smooth the optimally computed sequences of integer shifts to increase the number of possible changes in shift before estimating interval V_p/V_s.

Since time shifts are related to the integral of V_p/V_s, we expect that $u(x,y,t)$ be a smooth function compared to $\gamma_i(t_{pp})$; however, estimating V_p/V_s by smoothing a rough sequence of integer shifts might be inaccurate. Instead, we use a smooth dynamic image warping (SDIW) algorithm (Hale and Compton, 2013) that directly computes a smooth and more accurate time-shift function $u(x,y,t)$. SDIW is a modification to DIW that increases the accuracy of computed changes in time shift by computing time shifts only at subsampled locations in time and space.

Figure 2 shows the alignment errors (equation 15) for a single pair of traces in the PP and PS images from Figure 1. Overlaid on the alignment errors are time-shift curves extracted from the 3D DIW and SDIW algorithms. For a more detailed comparison, these curves and the alignment errors are shown for only a 1 second time interval.

The solid white curve in Figure 2 shows the time shifts computed from DIW. Note the roughness of the white curve, which results from the fact that DIW computes time shifts at every time sample. In fact, the white time-shift curve contains only two slopes, 0 and 1. These slopes correspond to the bounds r_{lt} and r_{ut} from equation 19, and thus $\gamma_{iMin} = 1$ and $\gamma_{iMax} = 3$ from equations 11 and 12 respectively. Not only are these the bounds on $\gamma_i(t)$, but from equation 6 we know that these are the only two possible values of $\gamma_i(t)$ we can compute. Hence, the motivation to smooth these shifts, as Liang and Hale (2012) do, is to obtain more estimates of interval V_p/V_s. The dashed blue curve in Figure 2 shows the white time-shift curve after smoothing.

The yellow curve in Figure 2 shows the interpolated time shifts computed from SDIW. For SDIW, time shifts are computed only at specific subsampled locations and then are interpolated at all other locations. The subsampled locations correspond to high-amplitude reflectors in the PP image that, in this example, are a minimum of 100 ms apart. This selection process will be discussed in a subsequent section.

Note the large difference beween the yellow and blue curves between 0 and 0.6 s. To see that the yellow curve in Figure 2 is more accurate, compare the PP image (Figure 3a) with the warped PS image using smoothed DIW time shifts (Figure 3b), and the warped PS image using SDIW time shifts (Figure 3c). Recall that the curves overlaid on alignment errors in Figure 2 were extracted from 3D shift functions $u(x,y,t)$. The location of those alignment errors corresponds to the vertical black lines in the inline and crossline sections of Figure 3.

The events at 0.7 s are well aligned in both Figures 3b and 3c, and we can see in Figure 2 that the yellow and blue curves are consistent at this time. However, a large discrepancy between the two shift functions can be seen at 0.38 s in the alignment errors in Figure 2, and correspondingly in the time slices in Figures 3b and 3c, which show time 0.38 s. The warped PS image in Figure 3c is a better match to the PP image in Figure 3a, indicating that the yellow curve is in fact more accurate.

This increase in accuracy with SDIW is achieved by sacrificing temporal resolution of changes in time shifts. When images are not simply shifted versions of one another, as is the case for PP and PS image registration, we trade resolution of changes in time shifts for more accurate estimates of those changes by subsampling with SDIW. The subsampling greatly increases the number of possible changes in shift, and, as was shown in Figures 2 and 3, increases the accuracy of estimated time shifts. The white curve in Figure 2 shows that trying to resolve changes in time shifts at every image sample results in misalignment of image features; furthermore, the correct time-shift function cannot be obtained by smoothing the white curve.

Figures 4a and 4b show the interval V_p/V_s ratios estimated from DIW time shifts and SDIW time shifts

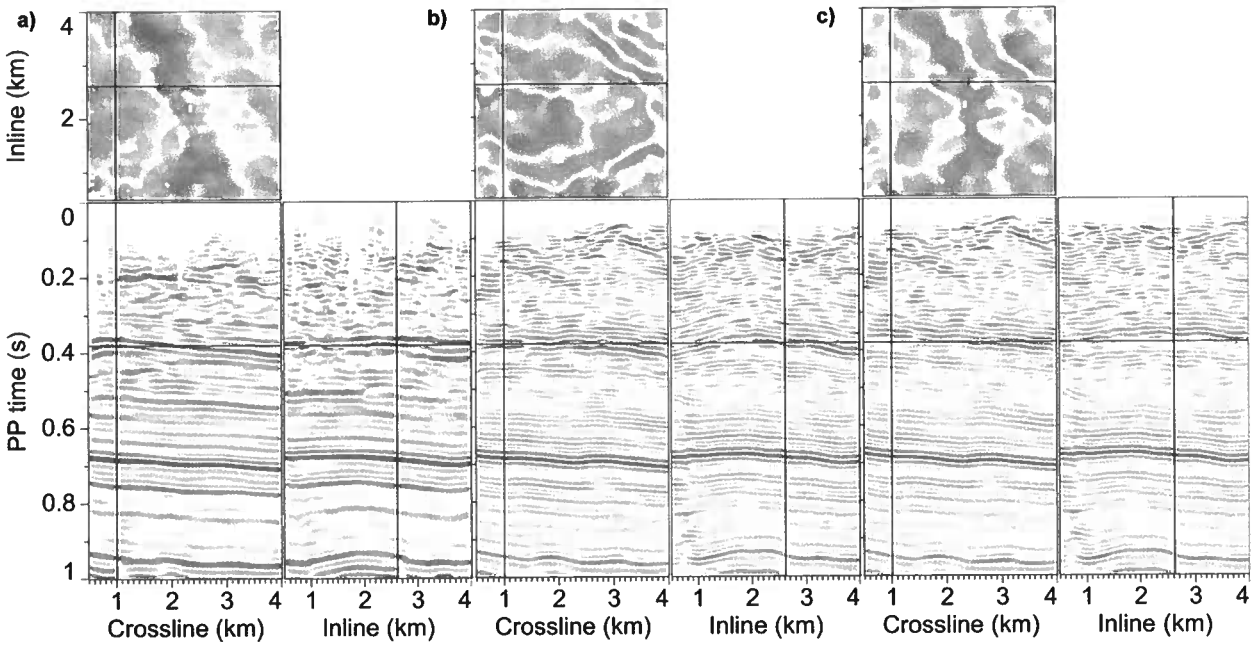

Figure 3. Slices through three 3D volumes with the same PP time interval shown in the alignment errors of Figure 2. The location for those alignment errors corresponds to the vertical black lines in the inline and crossline sections. Compare the PP image (a) with the warped PS image obtained using smoothed DIW time shifts (b) and that obtained using SDIW time shifts (c). The strong events at 0.7 s are well aligned in each case, but the time slice through the event at 0.38 s shows that time shifts computed using smooth dynamic image warping are more accurate. The differences in time shifts can be seen clearly in Figure 2.

respectively. The two images exhibit some similar trends of high or low V_p/V_s; Figure 4a, however, shows a high level of detail that is unwarranted given the resolution of seismic reflections and differences in noise and reflection waveforms between the PP and PS images.

While subsampling shifts improves accuracy, it also improves efficiency. For image warping we smooth alignment errors in all three image dimensions, and the output of this smoothing is subsampled in each dimension (Hale and Compton, 2013). Alignment errors $e(x, y, t; s)$ are smoothed and subsampled as they are computed for all pairs of traces in the 3D PP and PS images. This subsampling dramatically reduces memory requirements and increases the speed of 3D image warping.

4 COARSE SAMPLING LOCATIONS

Coarse sampling improves the accuracy of computed shifts, but the placement of the coarse lattice of sample points affects the accuracy as well. As distance between coarse samples increases, so does the smoothness of shifts. One simple approach is to use a regular grid parameterized by a coarse sampling interval in each dimension. We examine this approach for a 1D example where we compute time shifts $u(t)$ using smooth dynamic time warping, and focus only on subsampling the PP recording time.

Figure 5a shows alignment errors computed from a single pair of traces from the 3D PP and PS images shown in Figure 1. In Figure 5b the blue curve represents the time shifts $u(t)$ after interpolation and the blue dots represent the coarse sample locations where time shifts were computed. In this example we specified a coarse interval of 160 ms and computed sample locations that are regularly (not uniformly) spaced. The computed spacing is slightly variable to include the first and last time samples; however, all intervals are greater than or equal to the specified interval of 160 ms.

In Figure 5, note that strong events in the PP trace (Figure 5c) appear as predominantly vertical features with high error (white) in the array of alignment errors. The diagonally crossing features with high error correspond to strong events in the PS image. We can estimate shifts best at the locations where these strong events occur. However, by selecting coarse sample locations on a regular grid, as shown by the blue dots in Figure 5b, strong events are sampled only when they happen to coincide with our specified coarse sampling interval. Rather than select coarse samples on a regular

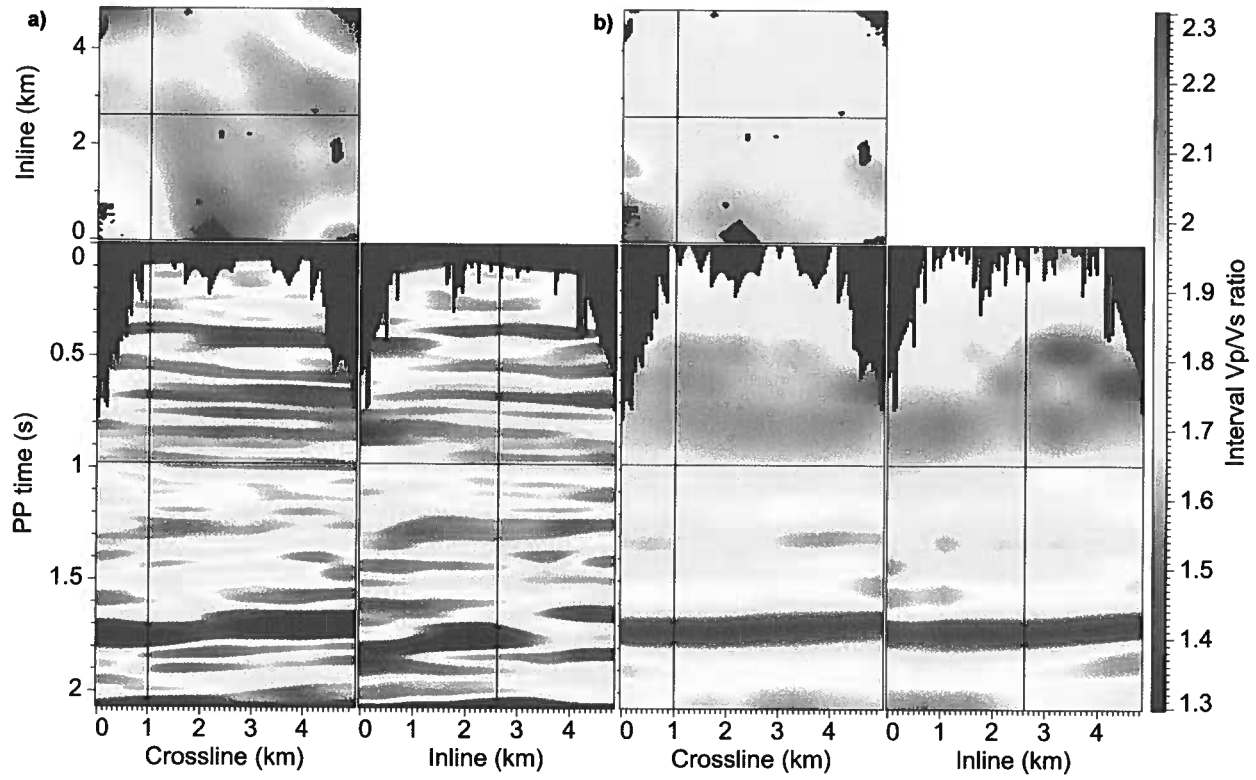

Figure 4. Interval V_p/V_s ratios estimated from smoothed DIW time shifts (a) and those estimated from SDIW time shifts(b). The V_p/V_s ratios from smoothed DIW time shifts exhibit fine details, but those smoothed shifts are less accurate, as shown in Figures 2 and 3, than shifts estimated using SDIW.

grid, we should instead select coarse sample locations to coincide with high-amplitude events in the PP trace.

Figure 5c shows the PP trace $f(t)$ in black and overlaid in red is the envelope of the PP trace computed as

$$a(t) = \sqrt{f^2(t) + \hat{f}^2(t)}, \tag{20}$$

where $\hat{f}(t)$ is the Hilbert transform of $f(t)$. Our approach to improve the coarse sample locations is to use the envelope $a(t)$ to preferentially select locations with the highest amplitudes, while also satisfying a specified minimum interval parameter. We search for coarse grid points in descending order of envelope amplitudes in $a(t)$. A coarse sample is chosen when its location is at a distance greater than or equal to the specified minimum interval from all previously selected coarse samples. As with the regular-grid scheme, we include the endpoints of the original sampled grid.

The yellow squares in Figure 5b represent the coarse sample locations where time shifts were computed along the yellow time shift curve. These squares were preferentially selected to correspond with locations of strong events, while maintaining a minimum separation interval of 100 ms. We reduce the minimum interval used for the regular grid (160 ms) in order to include some of the highest amplitude events that are within that interval of one another. In this example, we have selected the same number of subsamples for the regular grid and the reflector-aligned grid.

The time-shift curves shown in Figure 5b for each grid are quite similar from 0 to 1.6 s except for a large discrepancy around 1.2 s. The blue dot indicates that a time shift was computed for that location, but there is no corresponding yellow square nearby. From both the alignment errors and the envelope of the PP trace in Figure 5c we see that there are weak events at and around 1.2 s; therefore, we have little confidence in the accuracy of the computed time shift at the blue dot. After 1.6 s, the two curves are quite different, with a fairly dramatic change in shift at approximately 1.6 s. The slope decreases, but the locations of the blue dots are such that this change in slope cannot be captured. The fact that these two computed time-shift curves have significant differences confirms that we cannot accurately register PP and PS events using a single pair of traces. However, from 3D time shifts and warping results not

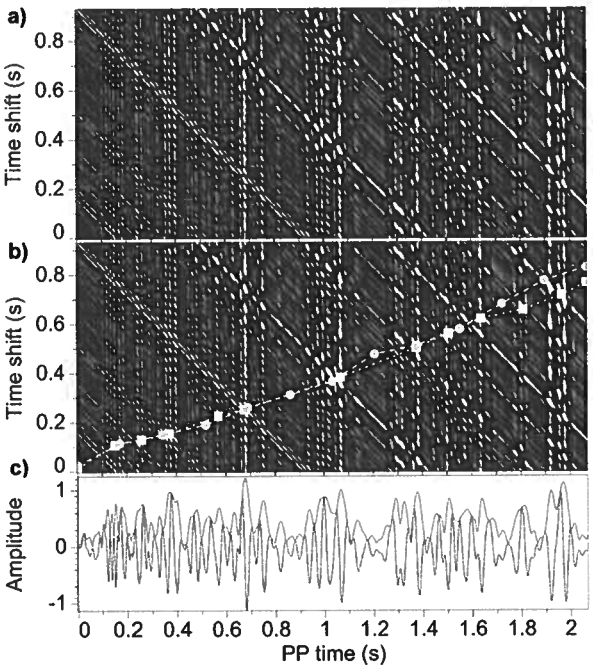

Figure 5. Alignment errors (a) computed from a single trace from the PP and PS images shown in Figure 1, with time shifts (b) computed from 1D smooth dynamic time warping using two different subsampling grids. A regular-interval coarse grid was used for the blue curve, with subsampling locations represented by blue dots, and a reflector-aligned grid was used for the yellow curve with subsampling locations represented by yellow squares. The PP trace (c) overlaid with the envelope of the trace shows that strong PP events correlate with strong vertical features in the alignment errors above.

shown here, the yellow curve corresponds to the correct shifts, even in the 1D case. This fact confirms that the optimal placing of coarse sample locations improves shift estimates.

When smoothing and subsampling alignment errors in 3D, we require the same number of coarse-grid time samples for all coarse inline and crossline sample locations. Therefore, we wish to select the highest amplitudes that are consistent throughout the image, i.e., the strongest reflectors. We cannot directly use the method described above because reflectors in seismic images are generally not horizontal, but when seismic images are not structurally complex, we can make reflectors horizontal using seismic image flattening (Parks et al., 2008; Parks, 2010).

Figure 6a shows the PP image, which is structurally simple but contains dipping reflectors. Therefore, we compute a volume of shifts (Figure 6b) that flatten image features so that a constant time in the flattened image (Figure 6c) corresponds to a single seismic horizon. In this flattened image space we can stack the envelopes of all image traces:

$$a_s(t) = \sum_{m=0}^{M-1} \sum_{n=0}^{N-1} a_{nm}(t), \tag{21}$$

where M and N are the number of inline and crossline samples, respectively. Now, we can search for times corresponding to the strongest reflection events in the flattened 3D image and compute a coarse lattice of points in all three dimensions, indicated by the red dots in Figure 6c. We then map the coordinates of these lattice points from the flattened space to the original image space to obtain a reflector-aligned 3D lattice on which to compute time shifts using smooth dynamic image warping.

We compare a simple regular-interval grid, defined by coarse interval parameters in each dimension, shown in Figure 7a, with the reflector-aligned coarse grid in Figure 7b. Both grids have the same nearly uniform sampling in the inline and crossline directions. Time shifts are estimated only at locations of coarse samples, and we improve the accuracy of these estimates by aligning the coarse grid with strong reflectors. Interval V_p/V_s ratios estimated from the regular-interval grid and the reflector-aligned grid are shown in Figures 7c and 7d, respectively. Note the step in V_p/V_s at 1.7 and 1.8 s for the layers in the crossline slice of Figure 7c. This step is a compensation for the regular-interval coarse grid sampling right through a dipping reflector with a consistently low V_p/V_s throughout the image. This layer is seen in Figure 7d where the coarse grid points are aligned with reflectors in the image.

Note that this automated approach to picking sample locations is independent of our smooth image warping algorithm. Thus, a more interpretive approach of selecting specific reflection events interactively could be used instead, especially for a more complex image that might be more difficult to flatten.

5 INTERPOLATION

The smooth dynamic warping algorithm computes time shifts only at specified subsampled locations to improve accuracy, but we ultimately need time shifts at every image location to align PP and PS images. Therefore, time shifts at all image locations not sampled by the smooth dynamic image warping algorithm are interpolated from the computed coarse lattice of time shifts.

For the 3D examples shown here, we do this interpolation in two steps. The interpolation is first done laterally using bilinear interpolation. With bilinear interpolation we ensure that the bounds on shifts u_l and u_u and our assumption of monotonically increasing time shifts are satisfied. For vertical interpolation of our time shifts, we need to consider the effect on the V_p/V_s ratios we are trying to estimate.

As described by Hale and Compton (2013), the

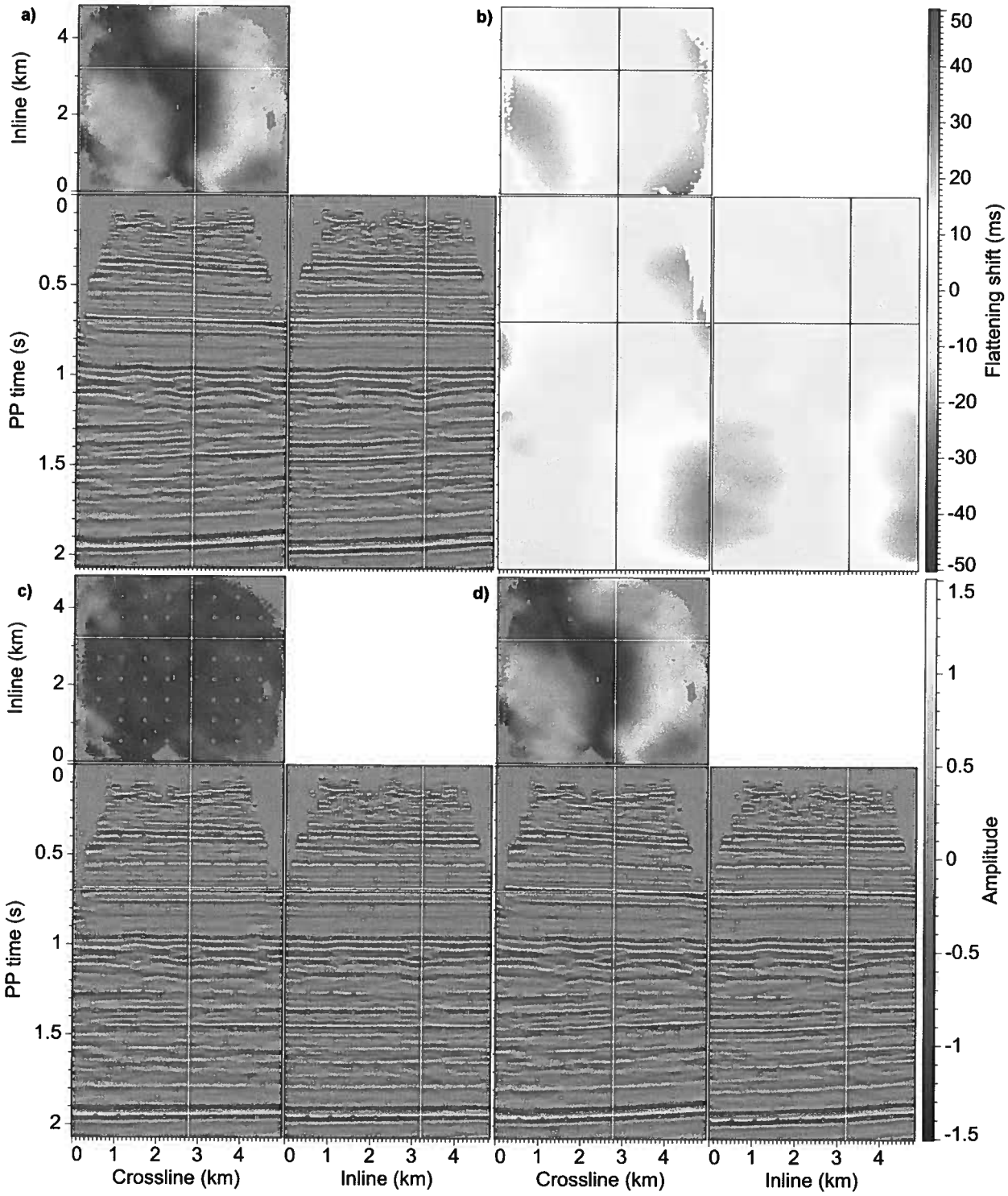

Figure 6. The PP image (a) and time shifts (b) used to flatten the image so that constant time corresponds to a single seismic horizon. After flattening (c), we find the strongest reflection events in the image by stacking the envelopes of all traces. The coarse lattice of points on the flattened image (c) is shown by the red dots. This lattice can be mapped back to the original (unflattened) coordinates space to obtain a coarse lattice of points that is aligned with dipping reflectors (d). We use this lattice in smooth dynamic image warping to compute time shifts at locations with strong reflectors in the PP image.

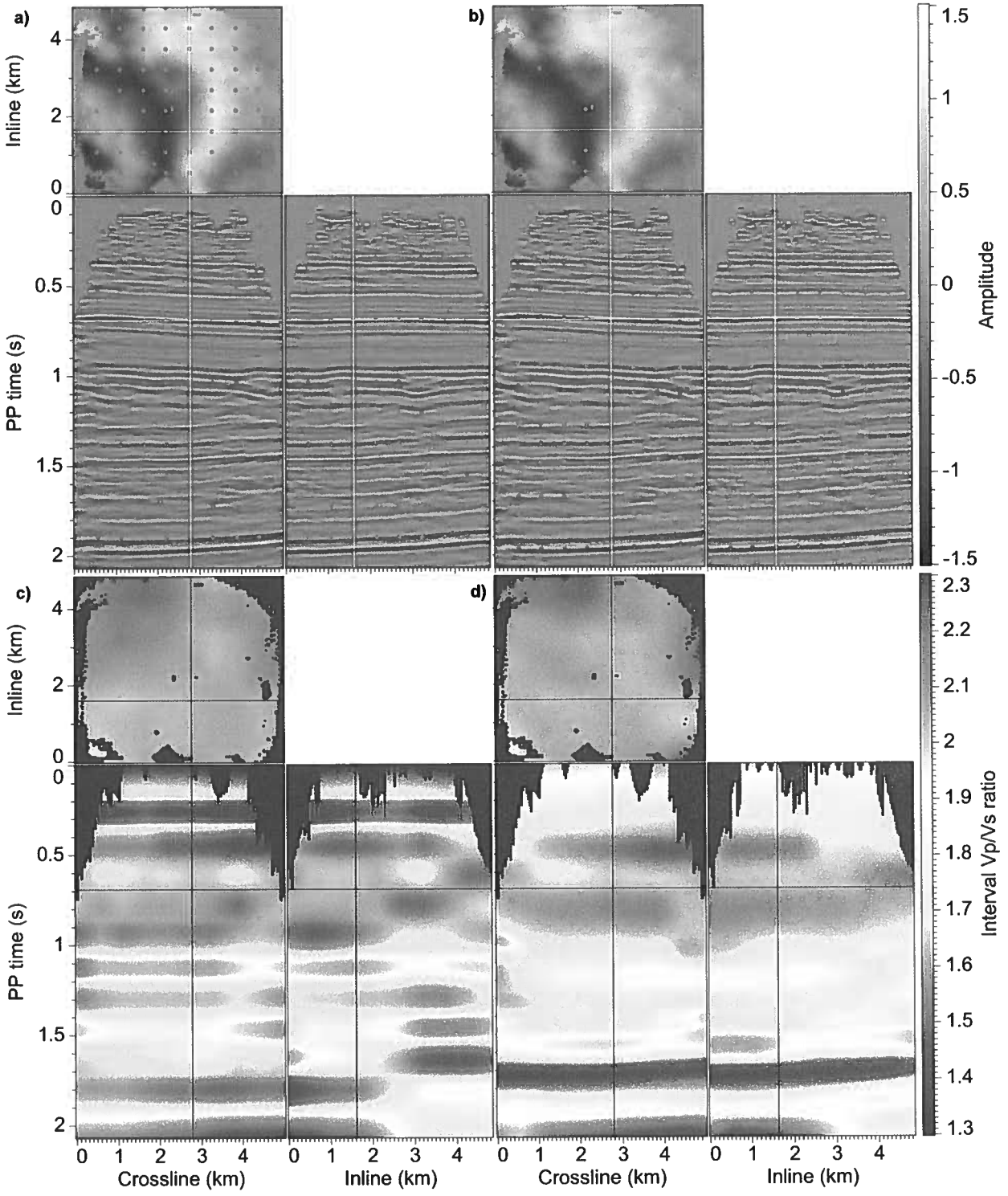

Figure 7. The regular-interval coarse grid (a) indicated by the red dots has minimum intervals of 500 m in the inline and crossline directions and 160 ms in time. The reflector-aligned coarse lattice of points (b) has the same minimum intervals of 500 m in the inline and crossline directions, but with coarse samples that follow strong reflectors in the PP image, and are also a minimum of 100 ms apart. The grid points in the regular-interval grid cross strong reflectors horizontally. This effect is seen in the interval V_p/V_s ratios (c), most notably with the two layers centered at 1.7 and 1.8 s, where stepping indicates a compensation for the low interval V_p/V_s clearly seen in the V_p/V_s ratios estimated from the reflector-aligned grid (d). In the reflector-aligned coarse lattice, intervals are consistent with strong reflectors, and thus, we generally see interval V_p/V_s defined between strong reflectors.

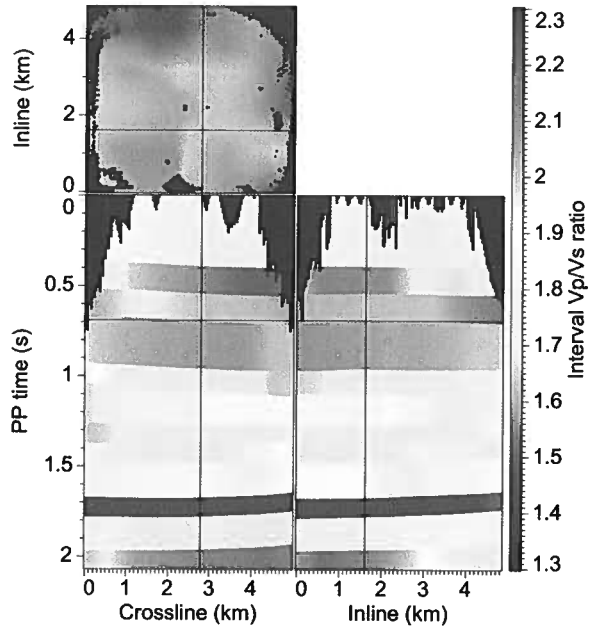

Figure 8. Interval V_p/V_s estimates when time shifts are linearly interpolated.

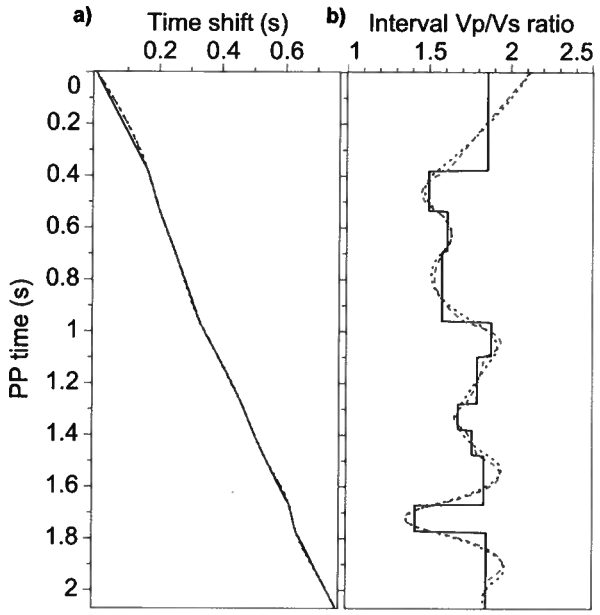

Figure 9. Computed time shifts $u(t)$ (a) extracted from 3D time shifts $u(x, y, t)$ and the corresponding estimates of $\gamma_i(t)$ (b). The three different curves represent three different methods of interpolating time shifts: linear (black), cubic monotonic (red), and cubic spline (blue).

smooth dynamic image warping algorithm accumulates alignment errors at coarse sample locations along piecewise-linear segments of minimum error. Thus, the most consistent approach for interpolating time shifts is linear interpolation. Figure 8 shows the estimated interval V_p/V_s ratios when time shifts are linearly interpolated. Compare this result with Figure 7d, showing the same image slices, where V_p/V_s ratios were computed after cubic monotonic interpolation of time shifts. Both results were obtained from computed shifts at coarse sample locations shown in Figure 7b.

The V_p/V_s ratios in Figure 8 are piecewise-constant between subsampled time locations and are more precise than estimates in Figure 7d. We computed time shifts only at coarse sample locations, and thus truly know changes in shift only between these locations. When smoother estimates of V_p/V_s than those shown in Figure 8 are required, we can interpolate time shifts using a smoother method. However, smoother V_p/V_s ratios will be inconsistent with the method we used to compute time shifts.

Figures 9a and 9b show respectively, the time shifts $u(t)$ extracted from the 3D time shifts $u(x, y, t)$, and the corresponding estimated V_p/V_s ratios. The three curves in each image show results from three methods of interpolation. The black curves show linearly interpolated time shifts and the corresponding piecewise-constant V_p/V_s ratios. The other two interpolation methods use piecewise-cubic polynomials. The red time shift curve was interpolated from polynomials that preserve monotonicity, while the blue curve was interpolated from the classic cubic spline with continuous first and second derivatives.

Linear interpolation is the only method that guarantees time shifts will be both monotonic and bounded by $[r_{lt}, r_{ut}]$. Monotonicity is still guaranteed for the red time shift curve, but the bounds $[r_{lt}, r_{ut}]$ are no longer satisfied. At 1.7 s, the red curve extends beyond the lower bound $r_{lt} = 1.4$ used in this example. This overshoot occurs because the first derivatives of this interpolated curve must be continuous. Cubic spline interpolation is shown for completeness, but this method is worse still. Overshoot with this method will generally be more severe than with piecewise-cubic monotonic interpolation to satisfy continuity of first and second derivatives. For this method we can guarantee neither monotonicity of interpolated time shifts nor derivatives within the bounds $[r_{lt}, r_{ut}]$, and in fact, it is possible to estimate $V_p/V_s < 1$, but for the example shown in Figure 9b this does not occur.

If we expect that interval V_p/V_s ratios are continuous, then cubic monotonic interpolation might be satisfactory. Otherwise, the piecewise-constant V_p/V_s ratios shown in Figure 8 are the most accurate estimates we can obtain from our estimates of time shifts.

6 CONCLUSION

We showed that the smooth dynamic image warping algorithm can be used to directly compute smooth time shifts that register 3D PP and PS images with increased accuracy compared to similar methods. This algorithm computes time shifts on a coarse lattice of sample locations in the PP image, from which we interpolated time shifts at all original image sample locations. We aligned the coarse lattice with strong reflectors in the PP image, further increasing the accuracy of the computed changes in time shifts, and thus the estimated V_p/V_s ratios.

Our computed V_p/V_s ratios do not exhibit fine details shown in similar methods because of an inherent trade-off between accuracy and resolution with the SDIW algorithm. We showed that trying to resolve changes in time shifts at every image location with the DIW algorithm was less accurate. Furthermore, smoothing those rough time shifts in order to estimate V_p/V_s ratios did not improve accuracy and is not equivalent to the globally optimal time shifts computed by the smooth dynamic image warping algorithm. Because of inevitable differences in noise and reflection waveforms between PP and PS images, obtaining fine temporal resolution of changes in time shifts is not feasible from the alignment of seismic reflections alone.

Smooth dynamic image warping provides a robust method for PP and PS image registration and enables constraints on both the time shifts and derivatives of the time shifts to be related to geophysical properties. The upper bound on time shift can be computed from an estimate of the average V_p/V_s ratio at the maximum PP time of interest, and this upper bound need not be known precisely. Constraints on the derivatives of time shifts can be computed from expected minimum and maximum interval V_p/V_s ratios.

Lastly, the smooth dynamic image warping algorithm improves computational efficiency and dramatically reduces memory requirements, a significant advancement for 3D image warping.

ACKNOWLEDGMENTS

This work was funded by sponsor companies of the Consortium Project on Seismic Inverse Methods for Complex Structures. The seismic data used in this report is licensed and provided courtesy of Geokinetics Inc. and Geophysical Pursuit, Inc. This work benefited from several helpful conversations with James Gaiser.

REFERENCES

Fomel, S., and M. M. Backus, 2003, Multicomponent seismic data registration by least squares: SEG Expanded Abstracts.

Gaiser, J. E., 1996, Multicomponent vp/vs correlation analysis: Geophysics, **61**, 1137–1149.

Hale, D., 2013, Dynamic warping of seismic images: Geophysics, **78(2)**, 105–115.

Hale, D., and S. Compton, 2013, Smooth dynamic warping: CWP Report, 0.

Liang, L., and D. Hale, 2012, Automatic registration of pp and ps images using dynamic image warping: CWP Report, 724.

Nickel, M., and L. Sonneland, 2004, Automated ps to pp event registration and estimation of a high-resolution vp-vs ratio volume: SEG Expanded Abstracts.

Parks, D., 2010, Seismic image flattening as a linear inverse problem: Master's thesis, Colorado School of Mines.

Parks, D., W. Harlan, and D. Hale, 2008, Defining regions in seismic images by flattening: CWP Report, 592.

Stewart, R. R., J. E. Gaiser, R. J. Brown, and D. C. Lawton, 2003, Converted-wave seismic exploration: Applications: Geophysics, **68**, 40–57.

Yuan, J. J., G. Nathan, A. Calvert, and R. Bloor, 2008, Automated c-wave registration by simulated annealing: SEG Expanded Abstracts.

Extracting horizons and sequence boundaries from 3D seismic images

Xinming Wu & Dave Hale
Center for Wave Phenomena, Colorado School of Mines, Golden, CO 80401, USA

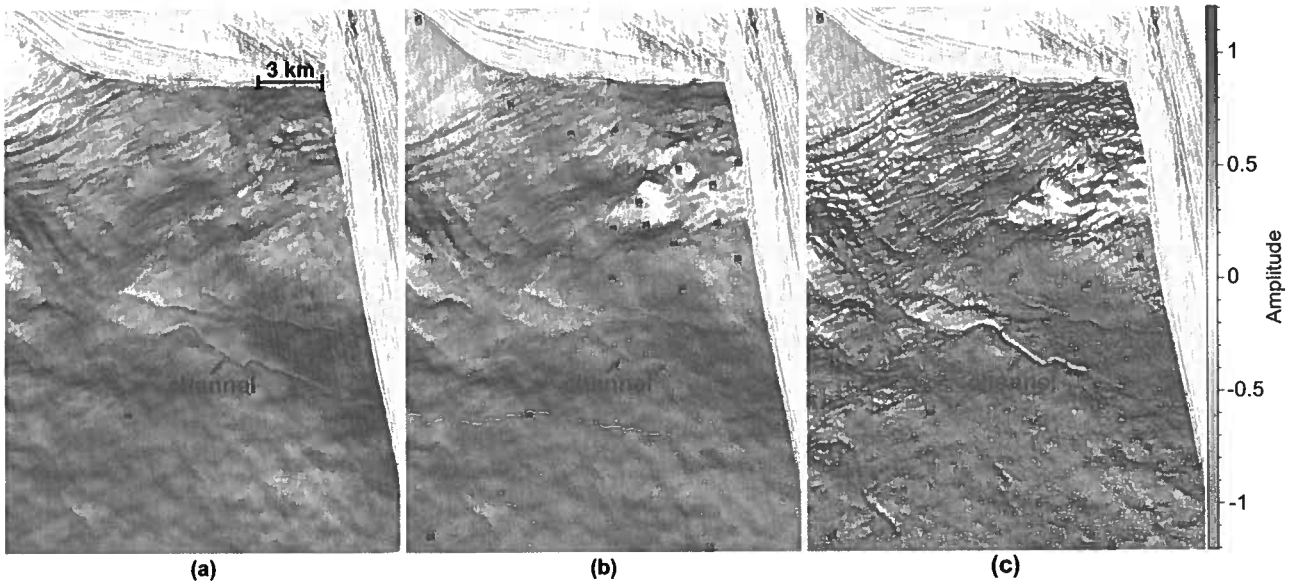

Figure 1. A 3D view of the amplitude-colored seismic horizons (blue, green and red curves in Figure 6) that are extracted using (a) one control point, (b) 25 control points, and (c) 25 control points with refinement using our active-surface method.

ABSTRACT
Horizons and sequence boundaries are important geologically significant surfaces that can be extracted from seismic images. Many automatic methods have been developed to extract horizons, but these methods usually have difficulty extracting horizons that terminate at angular unconformities or sequence boundaries. Using sequence boundaries as constraints is one way to solve this problem, but there exists no automatic method for sequence-boundary extraction. We first introduce a globally optimal method to efficiently extract a horizon from a seismic image. We then use scattered control points as constraints to enable our horizon-extraction method to extract sequence boundaries. Finally, we propose an active-surface method to refine the globally optimized horizons to align with amplitude peaks or troughs and thereby reveal more geologic details.

Key words: horizon sequence boundary control point active surface

1 INTRODUCTION

In 3D seismic images, primary seismic reflectors coincide with geologic interfaces such as stratal surfaces and unconformities with sufficient velocity-density contrasts. A stratal surface is a primary bedding or ancient depositional surface representing a geologically synchronous surface, while an unconformity is a non-depositional or erosional surface separating older strata below from

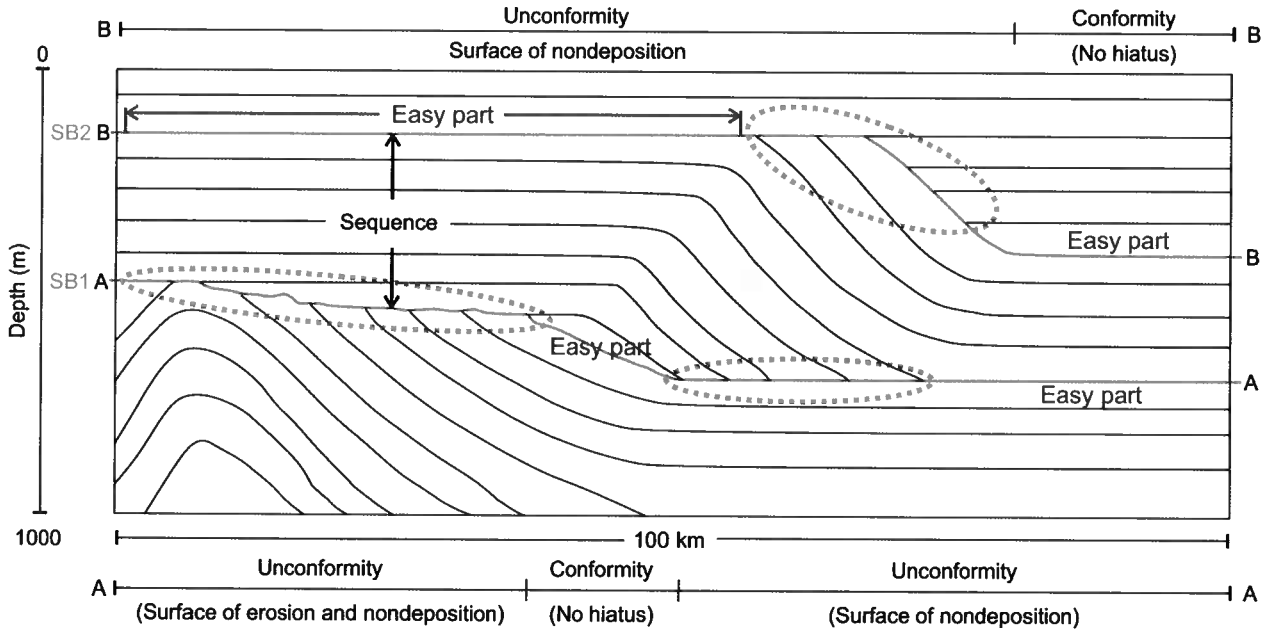

Figure 2. A synthetic sequence stratigraphic model (modified from Mitchum et al. (1977)) containing horizons (black curves) and sequence boundaries (heavy red curves). Ellipses highlight angular unconformities while the easy parts denote conformities and paraconformities.

younger strata above and thus represents a significant gap in geologic time (Vail et al., 1977). Therefore, by tracking or extracting surfaces throughout a 3D seismic image along amplitude peaks or troughs of seismic reflectors, we are able to identify geologically significant surfaces such as horizons and sequence boundaries.

Geologically, horizons (e.g., the black curves in Figure 2) refer to those reflectors representing stratal surfaces. Color-coding of horizons based on amplitude (Figure 1) or other attributes can help reveal ancient depositional environments and geomorphic features (Posamentier et al., 2007). Sequence boundaries (red curves in Figure 2) coinciding with angular unconformities (highlighted by dashed magenta ellipses in Figure 2) can also be extracted along the seismic reflectors, but these represent geologically time-variable surfaces. Sequence boundaries are important in seismic stratigraphic interpretation to define depositional sequences (Mitchum et al., 1977).

One can manually pick horizons and sequence boundaries from 3D seismic images, but this is usually a time-consuming task. To make the process more efficient, methods have been developed to extract horizons automatically. These automated methods, however, cannot extract sequence boundaries, and most fail where horizons terminate at an angular unconformity or sequence boundary.

1.1 Horizon extraction

Automated horizon-extraction methods can be generally classified into three categories. The first is amplitude-based, and extracts horizons by searching the peaks or troughs of seismic reflectors. Coherence or correlation between neighboring traces is usually used to constrain this searching process. Horizons extracted using these methods are helpful for revealing geologic details because they are locally optimal and are thus sensitive to local and small-scale geologic structures. These methods, however, are usually sensitive to noise and limited to simple geology (Hoyes and Cheret, 2011). In addition, they have difficulty extracting horizons that terminate at an angular unconformity or sequence boundary because they do not know how to grow a horizon where truncations, downlaps, onlaps, and toplaps occur.

The second category uses dips (Lomask et al., 2006; Parks et al., 2010) or normal vectors (Luo and Hale, 2012) estimated from seismic reflectors to globally flatten or unfold entire 3D seismic images. These methods obtain all horizons in a seismic image simultaneously and they are more robust for noisy data. However, horizons extracted using these methods are usually smooth and therefore lack detailed geologic structures. In addition, the dips or seismic normal vectors are estimated using locally averaged features of seismic reflectors. While this averaging improves their robustness in noisy data, it degrades their ability to resolute geologic details. These methods also fail to extract horizons that terminate at a sequence boundary because plane-wave de-

struction filters (Claerbout, 1992; Fomel, 2002) or structure tensors (van Vliet and Verbeek, 1995; Fehmers and Höcker, 2003) they use are unable to provide accurate dips or normal vectors at locations where multiple orientations exist in seismic images.

The third category is similar to the second in that it flattens an entire 3D seismic image, but without use of dips or normal vectors. Instead, it uses a relative geologic time (RGT) volume generated by unwrapping a corresponding seismic instantaneous phase image (Stark, 2005; Wu and Zhong, 2012). When globally optimized methods are used to compute an RGT result, these methods yield smooth horizons. Therefore, these methods have similar disadvantages to those of the second category. Wu and Zhong (2012) discuss handling of unconformities by manually interpreting sequence boundaries that serve as constraints. However, the problem remains of how to handle unconformities automatically.

1.2 Sequence boundary extraction

All of the horizon-extraction methods discussed above share the common difficulty in extracting horizons that terminate at an angular unconformity or sequence boundary. One way to solve this problem is to first extract all possible sequence boundaries in a seismic image and then use them as constraints while extracting other horizons. Extracting sequence boundaries would have the added benefit of helping to define depositional sequences. Despite definite benefits in extracting sequence boundaries, however, no method has yet been developed to accomplish this automatically. In manual interpretation of a sequence boundary, interpreters usually first look for angular unconformities (highlighted by magenta dashed ellipses in Figure 2) that imply the presence of sequence boundaries (heavy red curves in Figure 2), and then track the angular unconformities and correlative conformable parts (the easy parts in Figure 2) throughout the seismic image. Angular unconformities in seismic images are landmarks for interpreters who manually pick sequence boundaries; however, they are challenges for automatic methods as discussed above.

1.3 This paper

This paper describes methods for automatically extracting sequence boundaries and horizons in seismic images complicated by noise or chaotic reflectors, and for combining both the orientations and amplitudes of reflectors to obtain globally and locally optimized surfaces.

We first introduce a horizon-extraction method that uses estimated seismic normal vectors. This method uses one control point to indicate the horizon (which contains this point) we want to extract and to initialize a horizontal surface passing through this control point. This initial surface, of course, is inconsistent with the horizon we want to extract. But it is deformed to a different surface whose normal vectors match the seismic normal vectors. Similar to the second category of methods, our method efficiently extracts a globally optimized horizon from a seismic image.

We then discuss the use of control points that constrain our horizon-extraction method to extract sequence boundaries from seismic images. For a sequence boundary, denoted by the red heavy curves in Figure 2, our horizon-extraction method works well for the conformable parts (the easy part in Figure 2), because we can accurately estimate seismic normal vectors for these parts using structure tensors. But the estimated normal vectors at the angular unconformities (highlighted by ellipses in Figure 2) of the sequence boundary are usually not accurate enough to correctly locate the surface at the sequence boundary. We therefore insert several control points at angular unconformities and elsewhere, if necessary. Using a small number of control points, our method can reliably extract a sequence boundary, as well as horizon surfaces where a seismic image is contaminated by noise or where reflectors are chaotic.

Finally, we introduce an *active-surface method* that uses seismic amplitudes to further refine our globally optimized horizon (Figure 1b) to obtain a locally optimized horizon (Figure 1c) with more geologic detail. The active-surface method is similar to the snake or active-contour method proposed by Kass et al. (1988). In contrast to the closed contour used in the snake method, our extracted horizon is an active open surface. Our active-surface method directly uses seismic amplitudes to generate an external force that attracts a horizon to the nearest peaks or troughs in amplitude.

2 HORIZON EXTRACTION FROM SEISMIC NORMAL VECTOR FIELDS

The slopes or normal vectors of seismic reflectors can be used to automatically compute shifts that flatten (Lomask et al., 2006; Parks et al., 2010; Luo and Hale, 2012) a seismic image. Then any seismic horizon can be easily extracted from those shifts. Here we describe a similar method for extracting a single seismic horizon using a seismic normal vector field.

Using structure tensors (van Vliet and Verbeek, 1995; Fehmers and Höcker, 2003), we first compute a field of unit normal vectors $\mathbf{n} = [n_x\ n_y\ n_z]^T$ that are locally perpendicular to seismic reflectors (Luo and Hale, 2012). We then assume a surface $z = f(x,y)$ that was initially horizontal at some specified depth (or time). If we define the surface implicitly by

$$U(x,y,z) = z - f(x,y) = 0, \tag{1}$$

then normal vectors for the surface can be computed as

$$\mathbf{n}_s = \frac{\nabla U(x,y,z)}{\|\nabla U(x,y,z)\|} = \alpha \begin{bmatrix} -f_x \\ -f_y \\ 1 \end{bmatrix}, \tag{2}$$

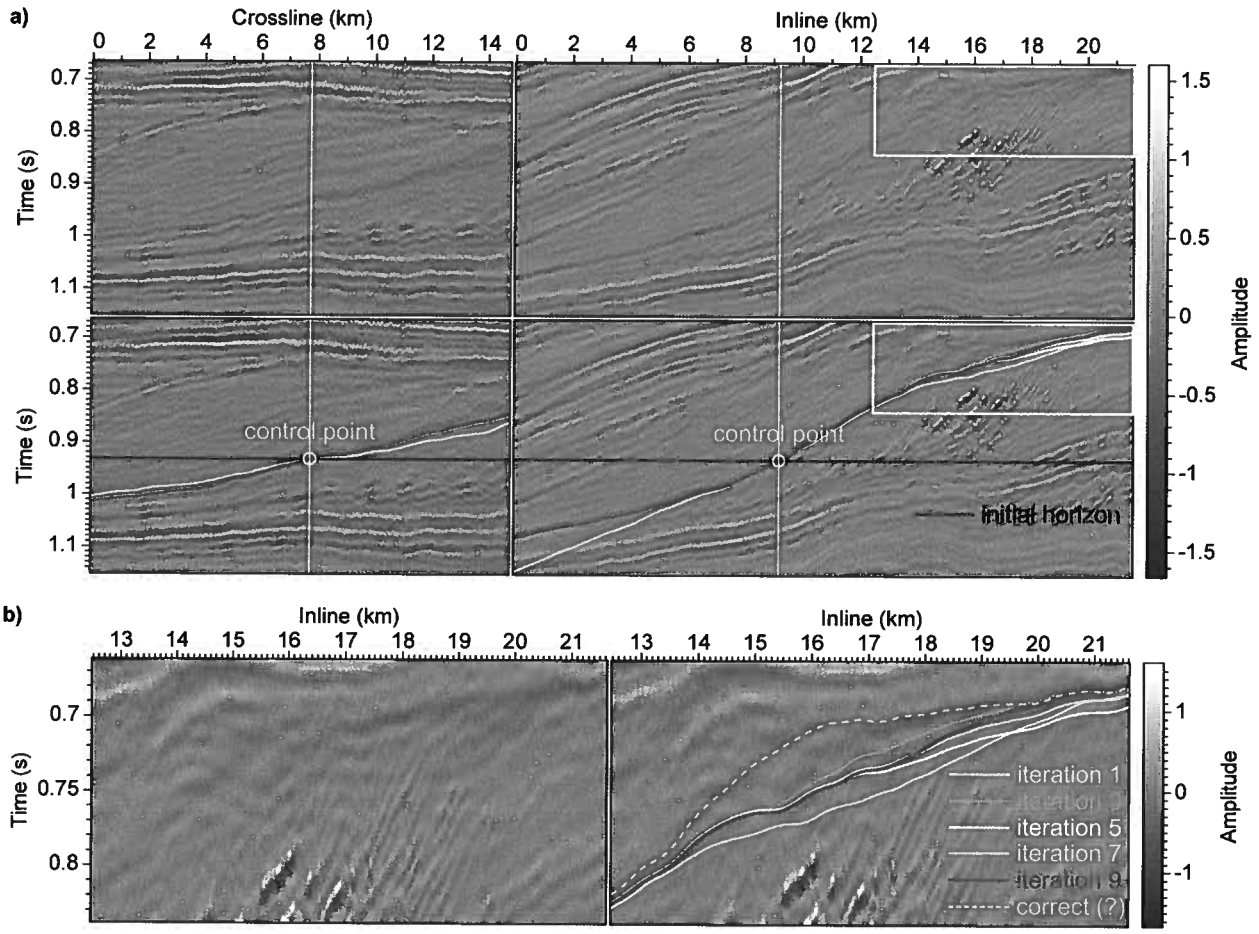

Figure 3. Seismic sections (a) and subsections (b) that intersect with a sequence boundary. The initially horizontal surface (black curve) passes through one control point and is updated iteratively using seismic normal vectors. The dashed green curve denotes the sequence boundary extracted using 26 control points.

where $f_x \equiv \partial f(x,y)/\partial x$, $f_y \equiv \partial f(x,y)/\partial y$, and α is a scale factor to normalize $\mathbf{n}_s$ as unit vectors.

To extract a seismic horizon, we seek to find a surface whose normal vectors $\mathbf{n}_s$ equal the seismic normal vectors $\mathbf{n}$ at corresponding points in the 3D seismic image:

$$\alpha \begin{bmatrix} -f_x \\ -f_y \\ 1 \end{bmatrix} = \begin{bmatrix} n_x \\ n_y \\ n_z \end{bmatrix}. \tag{3}$$

Therefore, setting $\alpha = n_z$, we solve the following inverse-gradient problem to extract the horizon surface $z = f(x,y)$,

$$\begin{bmatrix} f_x \\ f_y \end{bmatrix} = \begin{bmatrix} p \\ q \end{bmatrix}, \tag{4}$$

where $p = -n_x/n_z$ and $q = -n_y/n_z$ are reflector slopes in the x and y directions, respectively. To solve this inverse gradient problem, a common scheme is to minimize the following least-squares cost function (e.g., Horn and Brooks, 1986; Frankot et al., 1988; Horn, 1990; Farnebäck et al., 2007):

$$E = \int\int_{\Omega} [|f_x - p|^2 + |f_y - q|^2] dxdy. \tag{5}$$

Inspired by Wei and Klette (2002), we modify this cost function by adding a term related to surface curvature:

$$\begin{aligned} E = &\int\int_{\Omega} \frac{1}{2}(|f_x - p|^2 + |f_y - q|^2) dxdy \\ &+ \frac{\mu}{2} \int\int_{\Omega} (|f_{xx}|^2 + 2|f_{xy}|^2 + |f_{yy}|^2) dxdy. \end{aligned} \tag{6}$$

This second term is used to improve the robustness of the method for noisy or chaotic seismic reflectors. The value $\mu \geq 0$ weights this surface-curvature term.

To minimize the above cost function E, we use calculus of variations to obtain the Euler-Lagrange equation:

$$\Delta f - \mu \Delta^2 f = \nabla \cdot \mathbf{g}, \tag{7}$$

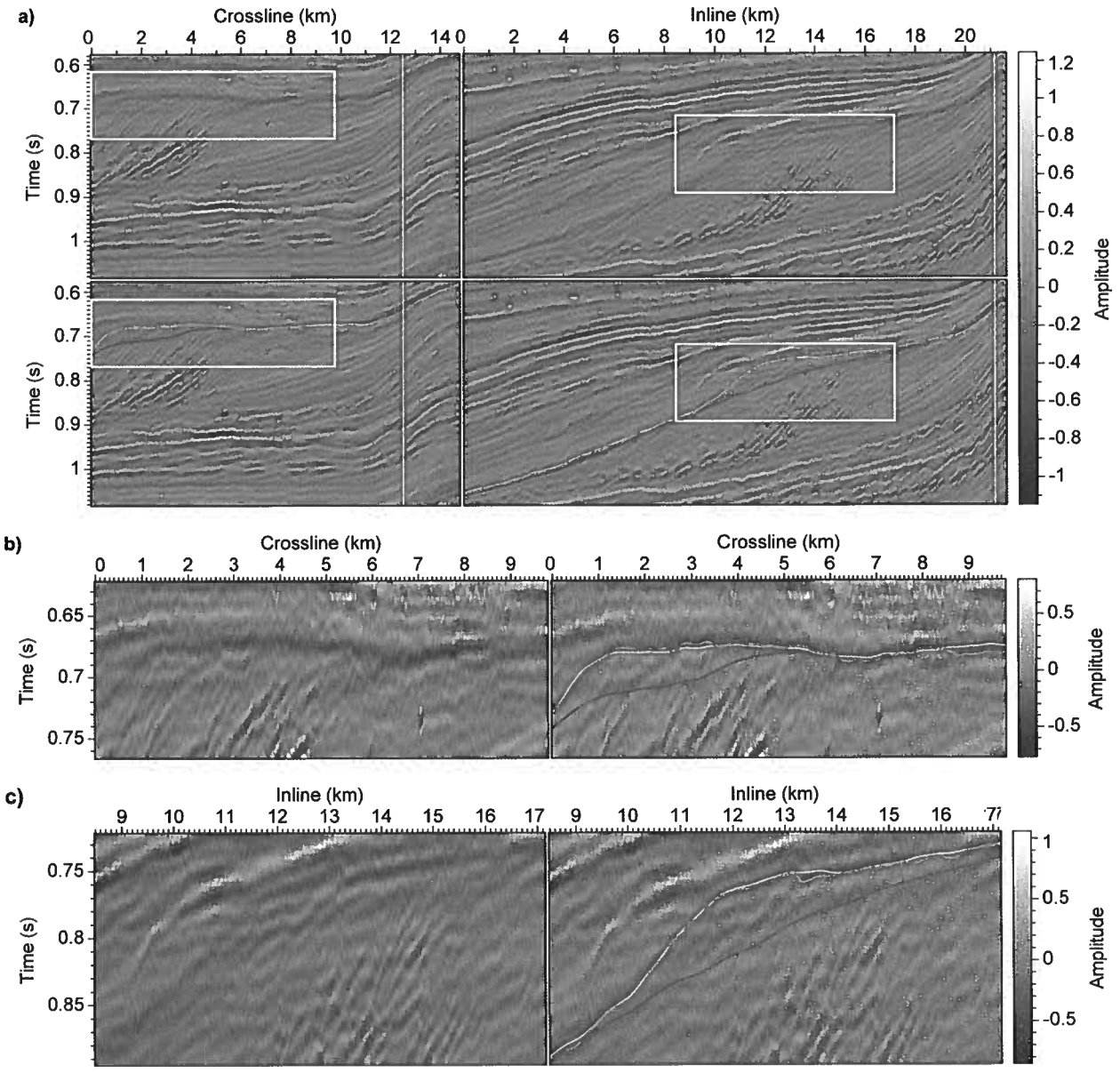

Figure 4. Seismic sections (a) and subsections (b) and (c) corresponding to the white and yellow rectangles, respectively, that intersect with an extracted sequence boundary (the one shown in Figure 3) using one control point (blue curve), 26 control points (green curve), and after refining (red curve) using our active-surface method.

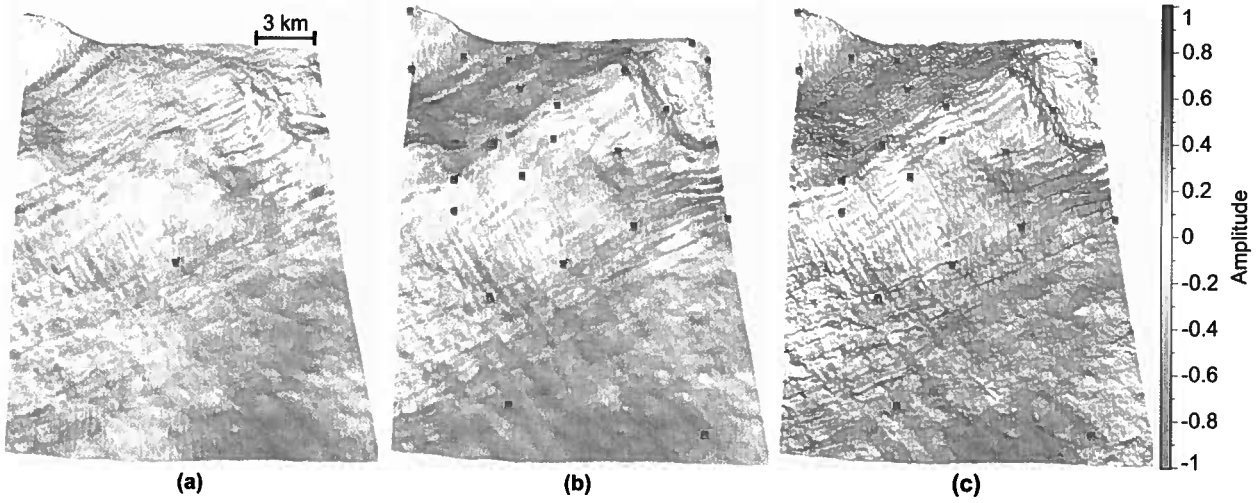

Figure 5. A 3D view of the amplitude-colored sequence boundaries (blue, green and red curves in Figure 4) that are extracted using (a) one control point, (b) 26 control points, and (c) 26 control points with refinement using our active-surface method.

where $\mathbf{g} = [p\ q]^T$ is a vector of reflector slopes, $\Delta f = f_{xx} + f_{yy}$, and $\Delta^2 f = f_{xxxx} + 2f_{xxyy} + f_{yyyy}$. By solving this equation, we can update the surface $z = f(x, y)$ so that its normal vectors $\mathbf{n}_s$ match the seismic normal vectors $\mathbf{n}$ at the current locations of the surface.

Therefore, given an initially horizontal surface (black curves in Figure 3) that is inconsistent with any seismic reflector, our method iteratively reduces the difference between the normal vectors of the surface $\mathbf{n}_s$ and the seismic normal vectors $\mathbf{n}$ at surface locations (x, y, z) to obtain a seismic horizon surface (blue curves in Figure 3).

In Figure 3, using only one control point to indicate which horizon we want to extract, our method deforms the initially horizontal surface to the more nearly correct seismic horizon (blue curves in Figure 3) after 9 iterations. However, in the subsections shown in Figure 3b, we observe that this method fails to deform the surface to the location of the angular unconformity (green dashed curve in Figure 3b). Extracting such a sequence boundary or unconformity is an important but difficult problem for automatic seismic interpretation. Using structure tensors, we fail to estimate the correct normal vector field at an unconformity, but instead compute a smoothed one that yields the incorrect horizon surface shown in Figure 3b. In the next section, we will describe a method to correctly extract a sequence boundary using 26 control points.

3 HORIZON CORRECTION USING CONTROL POINTS

In the previous section we described a seismic horizon-extraction method based on seismic normal vectors. Near unconformities, or in areas the image is noisy, the estimated normal vector field is not reliable enough to extract a correct horizon, sequence boundary, or unconformity. In such cases, instead of using a fully automatic method, we might manually interpret the seismic image to obtain a more geologically reasonable surface. However, we need not manually interpret the entire horizon. Using a small number of control points, we interpolate a correction for an updating surface described in section 2 to efficiently extract a accurate sequence boundary or horizon in a noisy image.

Suppose we have a set of n control points $(x_i, y_i, z_i), i = 1, 2, \ldots, n$ that are not all collinear. we can impose constraints in our horizon extraction using the method described by Horovitz and Kiryati (2004). In each iteration of horizon updating as described in section 2, we first compute an updated horizon $z = f(x, y)$ using seismic normal vectors, and then use the thin-plate spline interpolation method to interpolate a correction surface $z_c = c(x, y)$ by using the depth difference $z_i - f(x_i, y_i)$ between the control points and the updated horizon. The horizon is then corrected using the interpolated correction field, before the next iteration.

3.1 Thin-plate spline interpolation

Thin-plate spline interpolation is a classic method for interpolation of scattered data to yield a smooth function $c(x, y)$ that minimizes the integral

$$I(c) = \int\int_{\Omega} (|c_{xx}|^2 + 2|c_{xy}|^2 + |c_{yy}|^2) dx dy, \quad (8)$$

while satisfying the interpolation conditions

$$c(x_i, y_i) = z_i,\ i = 1, 2, \ldots, n. \quad (9)$$

Duchon (1977) shows that the interpolating function $c(x, y)$ has the form

$$c(x,y) = a_0 + a_1 x + a_2 y + \sum_{i=1}^{n} w_i \phi(r_i), \quad (10)$$

where r_i is the distance between the i-th control point (x_i, y_i) and $(x, y) \in \Omega$; a_0, a_1 and a_2 are the coefficients of the planar term in $c(x, y)$; and

$$\phi(r) = r^2 log(r),\ 0 < r < \infty. \quad (11)$$

The coefficients w_i satisfy

$$\sum_{i=1}^{n} w_i = 0,\ \sum_{i=1}^{n} w_i x_i = 0,\ \sum_{i=1}^{n} w_i y_i = 0. \quad (12)$$

From the correction values known at the control points,

$$c(x_i, y_i) = z_i - f(x_i, y_i), \quad (13)$$

we can compute the coefficients in equation 10 by solving the system of linear equations:

$$\begin{bmatrix} \mathbf{K} & \mathbf{P} \\ \mathbf{P}^T & \mathbf{O} \end{bmatrix} [\mathbf{W} | a_0\ a_1\ a_2]^T = [\mathbf{C} | 0\ 0\ 0]^T, \quad (14)$$

where

$$\mathbf{K} = [\phi(r_{ij})]_{n \times n},\ r_{ij} = |(x_i, y_i) - (x_j, y_j)|, \quad (15)$$

$$\mathbf{P} = \begin{bmatrix} 1 & x_1 & y_1 \\ 1 & x_2 & y_2 \\ \vdots & \vdots & \vdots \\ 1 & x_n & y_n \end{bmatrix}_{n \times 3}, \quad \mathbf{O} = \begin{bmatrix} 0 & 0 & 0 \\ 0 & 0 & 0 \\ 0 & 0 & 0 \end{bmatrix}_{3 \times 3}, \quad (16)$$

$$\mathbf{W} = [w_1\ w_2\ \ldots\ w_n]_{1 \times n}, \quad (17)$$

and

$$\mathbf{C} = [c(x_1, y_1)\ \ c(x_2, y_2)\ \ \ldots\ \ c(x_n, y_n)]_{1 \times n}. \quad (18)$$

With the coefficients $[\mathbf{W}\ a_0\ a_1\ a_2]$, we can use equation 10 to interpolate correction values $c(x, y)$ at every (x, y) for which the surface is defined. The updated horizon $f(x, y)$ using seismic normal vectors is then

$$f_c(x,y) = f(x,y) + c(x,y). \quad (19)$$

This corrected horizon $f_c(x, y)$, which now honors the control points, is then used for the next iteration.

3.2 Results using control points

When the normal vectors estimated using structure tensors are inaccurate (e.g., near unconformities, noisy data, and chaotic reflectors), the use of control points helps to extract a more reliable horizon or sequence boundary.

As shown in Figure 3, when we extract the sequence boundary passing through the control point (green circle in Figure 3a), the surface we extract (blue curves in Figure 3) matches well with reflectors in the conformable areas (left-side section and the left part of the right-side section in Figure 3a) where normal vectors can be estimated accurately. However, the extracted surface (blue curves) at the unconformity area (Figure 3b) is deflected from the corrected position (dashed green curve in Figure 3b) because estimated normal vectors at that area are inaccurate. Using 26 control points (green points in Figure 5b), we compute a more accurate sequence boundary (dashed green curve in Figure 3b). Figure 4 shows two different seismic sections that intersect with the sequence boundary extracted by using one control point (blue curves), 26 control points (green curves), and further refined (red curves) using the active-surface method discussed below. We observe that the sequence boundary extracted using 26 control points correctly follows the unconformity while the one using only one control point does not. Figure 5 shows the extracted sequence-boundary surface colored with amplitudes. Amplitude values for 26 control points (Figure 5b) are more uniform than for one control point (Figure 5a).

Moreover, with use of more control points, an initially horizontal surface converges more quickly to a seismic reflector. For example, it takes nine iterations to converge (blue curves in Figure 4) using one control point but only five iterations to converge (green curves in Figure 4) using 26 control points.

4 HORIZON REFINEMENT USING ACTIVE-SURFACE METHOD

Horizons extracted using amplitude-based methods are often locally correct but are sensitive to noise and usually accurate for only simple geology (Hoyes and Cheret, 2011). Our horizon-extraction method and other methods that use orientations (Lomask et al., 2006; Parks et al., 2010; Luo and Hale, 2012) estimated from seismic images are more robust for noisy data and can extract globally optimal horizons. Because of the global optimization and use of orientations estimated from locally averaged structures, these methods, however, might smooth out some subtle geologic structures or details that can be important in geologic interpretations. To reveal more subtle geologic structures or events in a horizon, we developed an active-surface method to refine extracted horizons.

4.1 Active surface

The active-snake or active-contour model, first introduced by Kass et al. (1988), is a powerful method for detecting closed boundary curves in 2D image segmentations. The active snake method is based on energy-minimizing spline curves influenced by internal forces and external image forces. The external image forces

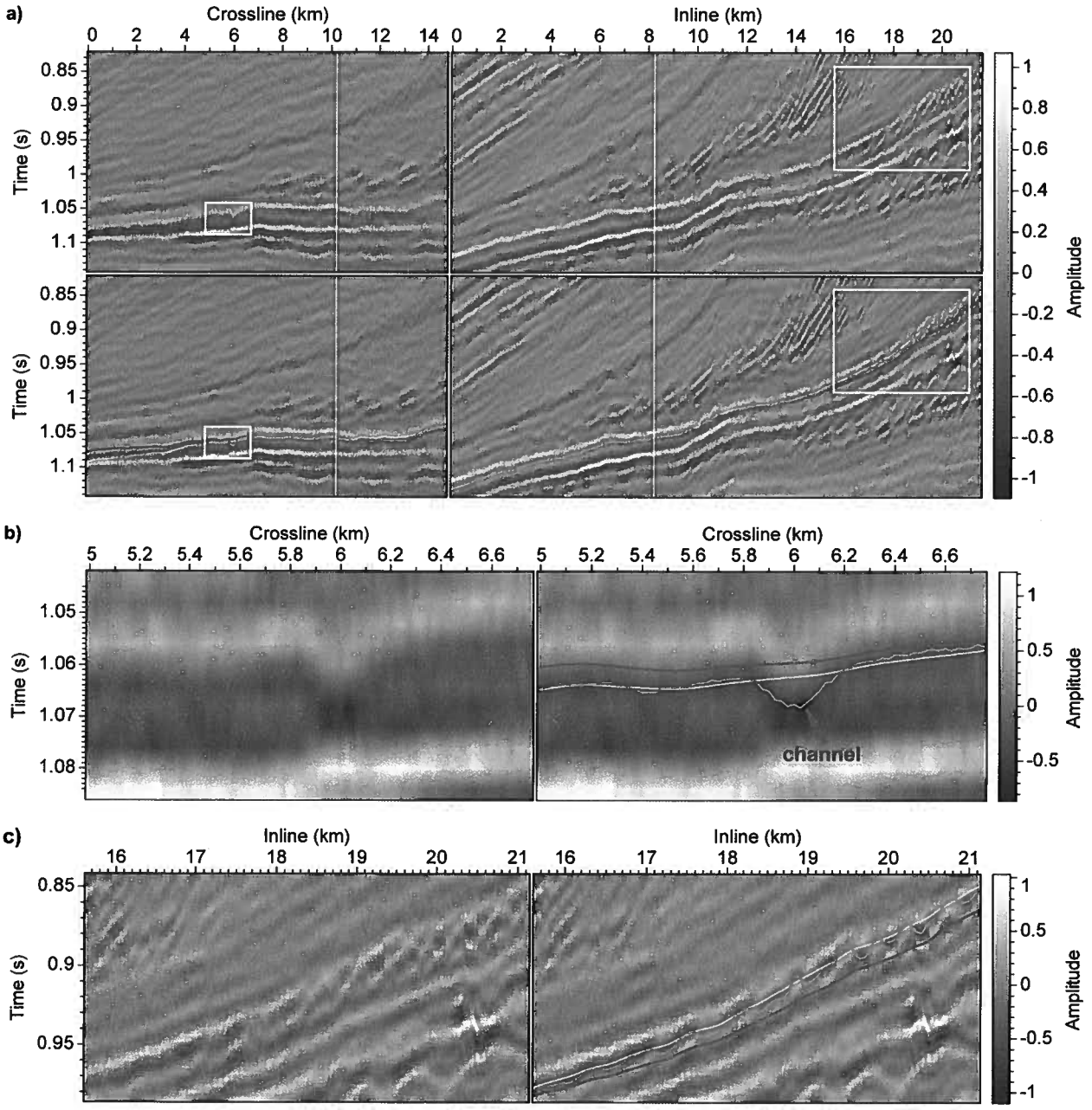

Figure 6. Seismic sections (a) and subsections (b) and (c) corresponding to the white and yellow rectangles, respectively, that intersect with an extracted seismic horizon (the one shown in Figure 1) using one control point (blue curve), 25 control points (green curve), and after refining (red curve) using our active-surface method.

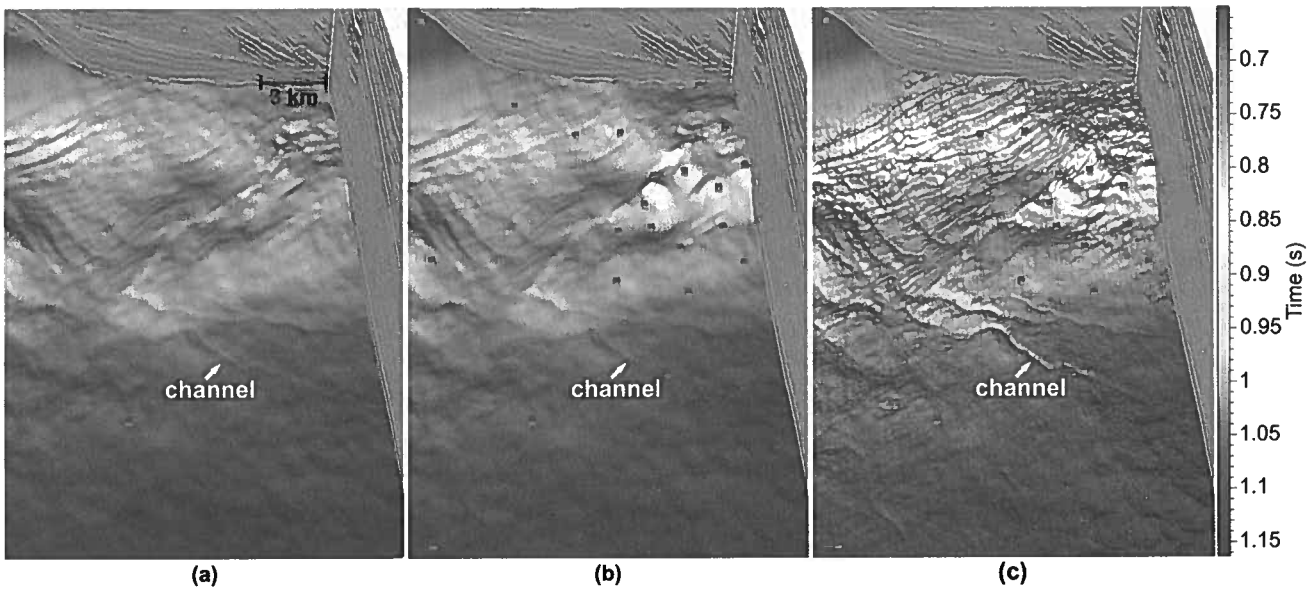

Figure 7. A 3D view of the time-colored horizons (blue, green and red curves in Figure 6) that are extracted using (a) one control point, (b) 25 control points, and (c) 25 control points with refinement using our active-surface method.

pull an initial contour to nearby edges in the 2D image, while the internal forces preserve the original shape and smoothness of the contour. Chopra and Marfurt (2008) suggest that the active-snake or active-contour method might be used to detect channels and other stratigraphic features. In this paper, we discuss an active surface which is an open surface that deforms vertically to align with nearby peaks or troughs in seismic amplitude.

Using seismic normal vectors, control points, and the methods described above, we obtain a globally optimized horizon that is consistent with reflector structure is not necessarily aligned with seismic peaks or troughs. We seek to deform the extracted horizon $z = f(x, y)$ to be aligned with the seismic peaks or troughs. Considering the horizon as an active surface, we define the energy of the active surface using an internal energy term E_{int} and an external energy term E_{ext}:

$$E(f, A) = \beta E_{int}(f) + E_{ext}(A), \tag{20}$$

where A is a 3D seismic image and β builds a trade-off between the internal and external energy terms. By minimizing this energy function, we can align the horizon with nearby seismic peaks or troughs.

The internal energy of the active surface is defined by its bending energy using the surface curvature approximation shown in equation 6 and 8:

$$E_{int}(f) = \int\int_{\Omega} \frac{1}{2}(|f_{xx}|^2 + 2|f_{xy}|^2 + |f_{yy}|^2)dxdy. \tag{21}$$

The external energy of the active surface is defined by its position in a seismic image:

$$E_{ext}(A) = \int\int_{\Omega} \pm A(x, y, f(x, y))dudv. \tag{22}$$

To align the horizon $z = f(x, y)$ with seismic troughs we simply use the seismic amplitude $A(x, y, f(x, y))$; to align with seismic peaks we use $-A(x, y, f(x, y))$.

Assume we want the horizon to be aligned with seismic troughs. Then the total energy of the active surface is

$$E(f, A) = \int\int_{\Omega} [\frac{\beta}{2}(|f_{xx}|^2 + 2|f_{xy}|^2 + |f_{yy}|^2) + A(x, y, f(x, y))]dxdy. \tag{23}$$

We consider only the vertical deformation of the active surface; then we can use calculus of variations to equalize the minimization of the above energy function by solving the Euler-Lagrange equation:

$$\beta\Delta^2 f + \frac{\partial A}{\partial z}|_{z=f(x,y)} = 0. \tag{24}$$

By solving this equation, an extracted horizon can be further refined to align with nearby seismic troughs.

4.2 Results for the active-surface method

In Figure 6, observe that the extracted horizon (green curves) using 25 control points is closer the seismic troughs than the one (blue curves) using only one control point, but both horizons are locally smooth and are not aligned with troughs in Figures 6b and 6c. Because these horizons are extracted using a globally optimal method and normal vectors estimated from averaged reflector structures, we obtain smooth horizon surfaces as shown in Figures 7a and 7b. Even though local amplitude variations indicate small geologic structures in horizons shown in Figures 1a and 1b, the shapes of those

small geologic structures cannot be seen in the horizons (Figures 7a and 7b, Figures 1a and 1b).

After applying our active-surface method to the globally optimized horizons (green curves in Figures 4 and 6), we obtain refined horizons (red curves in Figures 4 and 6) that are well aligned with troughs in seismic amplitude, as expected. In the 3D visualizations of the refined horizons (Figures 1c, 5c and 7c), we see many subtle geologic structures that cannot be seen in the unrefined horizons (Figures 1a and 1b, 5a and 5b, 7a and 7b). For example, channel structures appearing in a seismic image can be difficult to detect using just seismic normal vectors estimated from structure tensors. Therefore, globally optimized horizons extracted using normal vectors, but without using the active-surface method, fail to detect the incised valley of a subtle channel appearing in Figure 6b and marked in Figures 1 and 7. Although we observe some amplitude variations that indicate the existence of a channel in the globally optimized horizons (Figures 1a and 1b), the incised valley structure of the channel is not apparent. After refinement using the active-surface method, we clearly see the cross-section of the incised channel in the horizon (red curve in Figure 6b). The incised valley structure and shape of the channel are readily and continuously apparent in both the time- (Figure 7c) and amplitude-colored (1c) horizons.

5 CONCLUSION

We have developed methods to extract globally optimal horizons using seismic normal vectors, to extract sequence boundaries using control points, and to refine extracted horizons to align with seismic peaks or troughs using an active-surface method. Our horizon-extraction method is flexible for extracting any horizon we choose in a seismic image by using one control point that indicates the chosen horizon. When we sparsely define control points at angular unconformities, the horizon-extraction method can be improved to extract sequence boundaries. Of course, we can also choose control points in complicated areas with noise or chaotic reflectors to extract more reliable horizons in such areas. Using the active-surface method, extracted horizons can be aligned with seismic peaks or troughs to reveal more geologic detail.

Our methods can be further improved. Firstly, instead of using a small-dip approximation for surface curvatures, as in all the methods we describe here, we can use a more accurate one. Secondly, the step of horizon refinement using active-surface methods was separated from the step of horizon extraction using normal vectors; we can combine the two steps together to extract a horizon that honors both seismic amplitudes and orientations. Thirdly, our methods extract single horizons or sequence boundaries from a seismic image one at a time, but processing an entire seismic image is perhaps more useful, and we should modify our method to do this. Finally, we use control points to allow our method to avoid difficulties in horizon extraction at angular unconformities. However, estimating accurate normal vectors at angular unconformities is a preferable solution to this problem and would enable a completely automatic method for sequence-boundary extraction.

ACKNOWLEDGMENTS

We thank the sponsor companies of the Consortium Project on Seismic Inverse Methods for Complex Structures, whose support made this research possible. The 3D seismic images shown in this paper were provided by dGB Earth Sciences. Thanks to Ken Larner and Diane Witters for reviewing and revising this paper. Xinming thanks all C-team members and Luming Liang for their help with Java and Mines Java Toolkit (JTK) during his research.

REFERENCES

Chopra, S., and K. J. Marfurt, 2008, Emerging and future trends in seismic attributes: The Leading Edge, **27**, 298–318.

Claerbout, J. F., 1992, Earth soundings analysis: Processing versus inversion: Blackwell Science.

Duchon, J., 1977, Splines minimizing rotation-invariant semi-norms in sobolev spaces: Constructive Theory of Functions of Several Variables, Springer Berlin Heidelberg, 85–100.

Farnebäck, G., J. Rydell, T. Ebbers, M. Andersson, and H. Knutsson, 2007, Efficient computation of the inverse gradient on irregular domains: 2007 IEEE 11th International Conference on Computuer Vision, Vols 1-6, IEEE, 2710–2717.

Fomel, S., 2002, Applications of plane-wave destruction filter: Geophysics, **67**, 1946–1960.

Frankot, R. T., R. Chellappa, and S. Member, 1988, A method for enforcing integrability in shape from shading algorithms: IEEE Transactions on Pattern Analysis and Machine Intelligence, **10**, 439–451.

Horn, B. K. P., 1990, Height and gradient from shading: International Journal of Computer Vision, **5**, 37–75.

Horn, B. K. P., and M. J. Brooks, 1986, The variational approach to shape from shading: Computer Vision, Graphics, and Image Processing, **33**, 174–208.

Horovitz, I., and N. Kiryati, 2004, Depth from gradient fields and control points: bias correction in photometric stereo: Image and Vision Computing, **22**, 681–694.

Hoyes, J., and T. Cheret, 2011, A review of global interpretation methods for automated 3D horizon picking: The Leading Edge, **30**, 38–47.

Kass, M., A. Witkin, and D. Terzopoulos, 1988,

Snakes: Active contour models: International Journal of Computer Vision, **1**, 321–331.

Lomask, J., A. Guitton, S. Fomel, J. Claerbout, and A. A. Valenciano, 2006, Flattening without picking: Geophysics, **71**, 13–20.

Luo, S., and D. Hale, 2012, Unfaulting and unfolding 3D seismic images: CWP Report 722.

Fehmers, G. C., and C. Höcker, 2003, Fast structural interpretation with structure-oriented filtering: Geophysics, **68**, 1286–1293.

Mitchum, R. M., P. R. V. Jr., and S. Thompson, 1977, Seismic stratigraphy and global changes of sea level: Part 2. the depositional sequence as a basic Unit for stratigraphic analysis: Section 2. application of seismic reflection configuration to stratigraphic interpretation: M 26: Seismic Stratigraphy-Applications to Hydrocarbon Exploration, AAPG Memoirs, 53–62.

Parks, D., C. S. of Mines. Dept. of Mathematical, and C. Sciences, 2010, Seismic image flattening as a linear inverse problem: Colorado School of Mines.

Posamentier, H., R. Davies, J. Cartwright, and L. Wood, 2007, Seismic geomorphology - an overview: in: R.J. Davies, H.W. Posamentier, L.J. Wood, J.A. Cartwright (Eds.), Seismic Geomorphology, Geological Society of London Special Publication, 1–14.

Stark, T. J., 2005, Generating a seismic Wheeler volume: 75th Ann. Internat. Mtg., Soc. of Expl. Geophys., 782–785.

Vail, P. R., R. G. Todd, and J. B. Sangree, 1977, Seismic stratigraphy and global changes of sea level: Part 5. chronostratigraphic significance of seismic reflections: Section 2. application of seismic reflection configuration to stratigraphic interpretation: M 26: Seismic Stratigraphy-Applications to Hydrocarbon Exploration, AAPG Memoirs, 99–116.

van Vliet, L. J., and P. W. Verbeek, 1995, Estimators for orientation and anisotropy in digitized images: ASCI95, Proc. First Annual Conference of the Advanced School for Computing and Imaging (Heijen, NL, May 16-18), ASCI, 442–450.

Wei, T., and R. Klette, 2002, Height from gradient using surface curvature and area constraints: In 3rd Indian Conference on Computer Vision, Graphics and Image Processing, Ahmedabad, 204–210.

Wu, X., and G. Zhong, 2012, Generating a relative geologic time volume by 3D graph-cut phase unwrapping method with horizon and unconformity constraints: Geophysics, **77**, 21–34.

Relationship between one-sided and two-sided Green's function representations

Filippo Broggini[1], Kees Wapenaar[2], Roel Snieder[1], & Evert Slob[2]
[1] *Center for Wave Phenomena, Colorado School of Mines, Golden CO 80401, USA*
[2] *Department of Geoscience and Engineering, Delft University of Technology, 2600 GA Delft, The Netherlands*

ABSTRACT
The Green's function, defined as the response recorded at the acquisition surface for a source located in the interior of the subsurface, is a combination of the downgoing and upgoing wave fields needed to reconstruct an image of the discontinuities inside the earth. Two-sided Green's function representations require measurement on the full boundary enclosing the domain of interest and allow us to retrieve the Green's function originating from any location inside the medium. Practical constraints usually prevent the placement of receivers at depth inside the earth; hence standard imaging techniques need to apply approximations to two-sided Green's function representations to construct an image of the subsurface. Recently-developed one-sided representations need data acquired on only one side of the boundary enclosing the region of interest. They present a practical advantage because they remove the physical constraints of having receivers at depth; hence one-sided representations do not require the approximations needed by two-sided techniques. In this paper, we show the connection between one-sided and two-sided Green's function representations.

Key words: Greens function representations, Marchenko equations, seismic interferometry, one-sided integral equations, two-sided integral equations

1 INTRODUCTION

Green's function representations requiring measurement on a closed boundary surrounding an inhomogeneous medium allow us to retrieve the Green's function originating from any location inside the medium itself (Aki and Richards, 2002). Techniques based on these representations can be used to create an image of structures present inside the earth. Unfortunately, because of practical constraints, we are unable to place receivers along a closed boundary inside the earth. Since measurements are not available on the full closed boundary, standard imaging techniques need to apply approximations to two-sided Green's function representations to construct an image of the subsurface. Because these equations require measurements on a closed boundary, we refer to these equations as *two-sided* integral equations.

Pioneering work of Rose has shown the connection between one-dimensional autofocusing and the Marchenko equation (Rose, 2001, 2002a; Aktosun and Rose, 2002; Rose, 2002b). We have extended this connection to one-dimensional Green's function retrieval by combining the time-reversed focusing wave field with its reflection response (Broggini and Snieder, 2012; Broggini et al., 2012b). Wapenaar et al. (2012, 2013a,b), and Broggini et al. (2012a) introduce an integral equation that allows one to reconstruct from reflection data at the surface the Green's function propagating from a location inside a medium to receivers located at the acquisition surface. Because reflection data are needed on only one side of the medium, we refer to this equation as *one-sided* integral equation. Following an insight by Lamb (1980), Wapenaar et al. (2013a) show that a *focusing solution* of the source-free wave equation is required to prove the validity of the one-sided integral equation and, additionally, discuss an iterative scheme to solve it.

The techniques introduced by one-side integral equations are elegant, but their derivations, based on the Marchenko equations, restrict their application to a limited number of problems. Here we show that tech-

niques based on one-side representations can be derived from well-known integral equations for Green's function retrieval, known as seismic interferometry in the geophysical community (Bakulin and Calvert, 2006; Wapenaar and Fokkema, 2006; Schuster, 2009). Since these two-sided equations are applicable to a wide range of problems (Lobkis and Weaver, 2001; Larose et al., 2006), one-sided techniques can, in principle, be extended to a large class of problems as well. In this paper, we present a derivation valid for acoustic waves in lossless media.

2 TWO-SIDED INTEGRAL EQUATION FOR GREEN'S FUNCTION RETRIEVAL

We introduce the Green's function $G(\mathbf{x},\mathbf{x}_B,t)$ as a solution to the wave equation $LG=-\rho\delta(\mathbf{x}-\mathbf{x}_B)\frac{\partial\delta(t)}{\partial t}$, with $L=\rho\nabla\cdot(\rho^{-1}\nabla)-c^{-2}\frac{\partial^2}{\partial t^2}$. The mass density and the velocity are denoted by $\rho(\mathbf{x})$ and $c(\mathbf{x})$, respectively. Following de Hoop (1995), the Green's function $G(\mathbf{x},\mathbf{x}_B,t)$ corresponds to the acoustic pressure measured at $\mathbf{x}$ due to an impulsive point source of volume injection rate at $\mathbf{x}_B$. We define the spatial coordinate $\mathbf{x}$ as $\mathbf{x}=(\mathbf{x}_H,x_3)$, where $\mathbf{x}_H=(x_1,x_2)$ is the horizontal coordinate vector and x_3 the vertical coordinate. The positive direction of the x_3-axis points downward. The Green's function $G(\mathbf{x},\mathbf{x}_B,t)$ can be decomposed in its downgoing $G^+(\mathbf{x},\mathbf{x}_B,t)$ and upgoing $G^-(\mathbf{x},\mathbf{x}_B,t)$ components. In this paper, these two wave fields are pressure-normalized (Ursin et al., 2012). Using the Fourier convention $f(\mathbf{x},\omega)=\int_{-\infty}^{+\infty}f(\mathbf{x},t)\exp(-j\omega t)dt$, the frequency domain Green's function $G(\mathbf{x},\mathbf{x}_B,\omega)$ obeys the equation $LG=-j\omega\rho\delta(\mathbf{x}-\mathbf{x}_B)$, with $L=\rho\nabla\cdot(\rho^{-1}\nabla)+\omega^2/c^2$. Here, j is the imaginary unit and ω denotes the angular frequency. To keep a simple notation, we use the same symbol for the time-domain version of a function as for its frequency-domain counterpart.

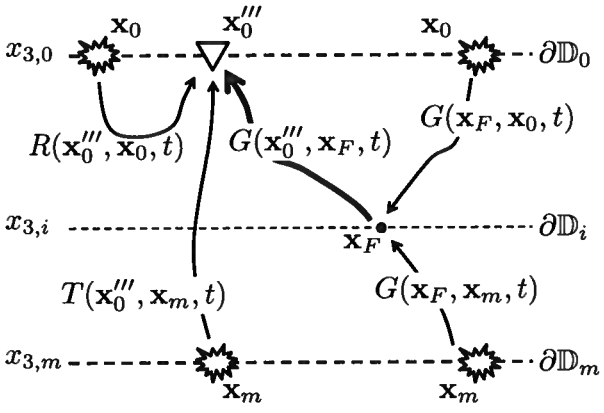

Figure 1. Definition of the variables used in equation (3).

Our starting point is the acoustic representation of Green's functions in the frequency domain given by equation (18) in Wapenaar and Fokkema (2006):

$$\begin{aligned}&\chi_{\mathbb{D}}(\mathbf{x}_A)G(\mathbf{x}_A,\mathbf{x}_B,\omega)+\chi_{\mathbb{D}}(\mathbf{x}_B)G^*(\mathbf{x}_B,\mathbf{x}_A,\omega)\\&=\oint_{\partial\mathbb{D}}\frac{-1}{j\omega\rho(\mathbf{x})}\left\{G^*(\mathbf{x},\mathbf{x}_A,\omega)\partial_iG(\mathbf{x},\mathbf{x}_B,\omega)\right.\\&\quad\left.-\partial_iG^*(\mathbf{x},\mathbf{x}_A,\omega)G(\mathbf{x},\mathbf{x}_B,\omega)\right\}n_i\mathrm{d}^2\mathbf{x},\end{aligned}\tag{1}$$

where $*$ indicates complex-conjugation and $\chi_{\mathbb{D}}(\mathbf{x})$ is the characteristic function for the domain $\mathbb{D}$, defined as

$$\chi_{\mathbb{D}}(\mathbf{x})=\begin{cases}1 & \text{for } \mathbf{x}\in\mathbb{D}\\ \frac{1}{2} & \text{for } \mathbf{x}\in\partial\mathbb{D}\\ 0 & \text{for } \mathbf{x}\in\mathbb{R}^3\in\setminus\{\mathbb{D}\cup\partial\mathbb{D}\}.\end{cases}\tag{2}$$

In equation (1), ∂_i denotes the partial derivative in the x_i-direction (Einstein's summation convention applies for repeated subscripts) and it acts on $\mathbf{x}$ which corresponds to a receiver location. The term $\frac{-1}{j\omega\rho(\mathbf{x})}\partial_iG(\mathbf{x},\mathbf{x}_B,\omega)$ in equation (1) corresponds to the particle velocity recorded at $\mathbf{x}$ due to a monopole source located at $\mathbf{x}_B$. We consider an inhomogeneous lossless medium $\mathbb{D}$ enclosed by the boundary $\partial\mathbb{D}$ with outward point normal vector $\mathbf{n}=(n_1,n_2,n_3)$.

By infinitely extending the sides of the domain $\mathbb{D}$, we can replace the closed surface integral over $\partial\mathbb{D}$ by an integral over two horizontal boundaries $\partial\mathbb{D}_0$ and $\partial\mathbb{D}_m$ at depth $x_3=x_{3,0}$ and $x_3=x_{3,m}$, respectively, as shown in Figure 1. For this reason, we define equation (1) as a two-sided integral equation. In the following, the upper half-space $x_3<x_{3,0}$ and the lower half-space $x_3>x_{3,m}$ are homogeneous and their medium parameters do not have to be the same. The boundaries $\partial\mathbb{D}_0$ and $\partial\mathbb{D}_m$ do not correspond with physical interfaces; hence they do not cause reflection of acoustic waves. With this configuration, the partial derivative ∂_i (acting on $\mathbf{x}$) is along the vertical direction x_3. Next, we take $\mathbf{x}_A$ to be a point $\mathbf{x}_F$ in the interior of $\mathbb{D}$ and take $\mathbf{x}_B$ to be the position $\mathbf{x}_0'''$ of a receiver located just above the surface $\partial\mathbb{D}_0$; see Figure 1, where $\mathbf{x}_0'''=(\mathbf{x}_H,x_3)$. The second term on the left-hand side of equation (1) disappears because $\chi_{\mathbb{D}}(\mathbf{x}_0''')=0$ when $\mathbf{x}_0'''$ is outside $\mathbb{D}$. These substitutions reduce expression (1) to

$$\begin{aligned}&G(\mathbf{x}_F,\mathbf{x}_0''',\omega)\\&=\int_{\partial\mathbb{D}_0\cup\partial\mathbb{D}_m}\frac{-1}{j\omega\rho(\mathbf{x})}\left\{G^*(\mathbf{x},\mathbf{x}_F,\omega)\partial_iG(\mathbf{x},\mathbf{x}_0''',\omega)\right.\\&\quad\left.-\partial_iG^*(\mathbf{x},\mathbf{x}_F,\omega)G(\mathbf{x},\mathbf{x}_0''',\omega)\right\}n_i\mathrm{d}^2\mathbf{x}\\&\equiv I_{\partial\mathbb{D}_0}+I_{\partial\mathbb{D}_m}.\end{aligned}\tag{3}$$

$I_{\partial\mathbb{D}_0}$ and $I_{\partial\mathbb{D}_m}$ correspond to the integrals over the top $\partial\mathbb{D}_0$ and bottom $\partial\mathbb{D}_m$ boundaries, respectively.

We want to reduce the two terms inside the integral in equation (3) to a single term. To achieve this, we have to analyze separately the integral over the top and bottom boundaries because $\mathbf{x}_0'''$ and $\mathbf{x}_F$ are on different sides with respect to $\partial\mathbb{D}_0$, while they are on the same side with respect to $\partial\mathbb{D}_m$. First, we focus on the integral

over the top boundary $\partial\mathbb{D}_0$,

$$I_{\partial\mathbb{D}_0} = \int_{\partial\mathbb{D}_0} \frac{1}{j\omega\rho(\mathbf{x})} \left\{G^*(\mathbf{x},\mathbf{x}_F,\omega)\partial_3 G(\mathbf{x},\mathbf{x}_0''',\omega) - \partial_3 G^*(\mathbf{x},\mathbf{x}_F,\omega)G(\mathbf{x},\mathbf{x}_0''',\omega)\right\} \mathrm{d}^2\mathbf{x}, \quad (4)$$

where we used that $\partial_i n_i = -\partial_3$ (n_3 points upward at $\partial\mathbb{D}_0$, while x_3 points downward). According to Appendix B.3 of Wapenaar and Berkhout (1989), we can rewrite equation (4) (for the integral over $\partial\mathbb{D}_0$) as

$$I_{\partial\mathbb{D}_0} = \int_{\partial\mathbb{D}_0} \frac{2}{j\omega\rho(\mathbf{x})} \left\{G^+(\mathbf{x},\mathbf{x}_F,\omega)\right\}^* \partial_3 G^+(\mathbf{x},\mathbf{x}_0''',\omega)\mathrm{d}^2\mathbf{x} + \int_{\partial\mathbb{D}_0} \frac{2}{j\omega\rho(\mathbf{x})} \left\{G^-(\mathbf{x},\mathbf{x}_F,\omega)\right\}^* \partial_3 G^-(\mathbf{x},\mathbf{x}_0''',\omega)\mathrm{d}^2\mathbf{x}, \quad (5)$$

where $G = G^+ + G^-$. Note that equation (5) is not exact because the evanescent waves are neglected at the boundary $\partial\mathbb{D}_0$. Furthermore, because the medium above $\partial\mathbb{D}_0$ is homogeneous, the downgoing component of $G(\mathbf{x},\mathbf{x}_F,\omega)$ is equal to zero; hence $G(\mathbf{x},\mathbf{x}_F,\omega) = G^-(\mathbf{x},\mathbf{x}_F,\omega)$. This yields

$$I_{\partial\mathbb{D}_0} = \int_{\partial\mathbb{D}_0} \frac{2}{j\omega\rho(\mathbf{x})} \left\{G^-(\mathbf{x},\mathbf{x}_F,\omega)\right\}^* \partial_3 G^-(\mathbf{x},\mathbf{x}_0''',\omega)\mathrm{d}^2\mathbf{x}. \quad (6)$$

The term $\frac{-1}{j\omega\rho(\mathbf{x})}\partial_3 G^-(\mathbf{x},\mathbf{x}_0''',\omega)$ in equation (6) corresponds to the vertical component of the particle velocity of the upgoing field recorded at $\mathbf{x}$ due to a monopole source located at $\mathbf{x}_0'''$ just above the boundary $\partial\mathbb{D}_0$, or, via reciprocity, to the acoustic pressure recorded at $\mathbf{x}_0'''$ due to a downward radiating dipole source located at $\mathbf{x}$. Since we deal with pressure-normalized wave fields, we use the last definition and define the reflection response as

$$R(\mathbf{x}_0''',\mathbf{x},\omega) = \frac{2}{j\omega\rho(\mathbf{x})}\partial_3 G^-(\mathbf{x},\mathbf{x}_0''',\omega). \quad (7)$$

Wapenaar et al. (2012) use the same definition for $R(\mathbf{x}_0''',\mathbf{x},\omega)$. The reflection response is acquired in a seismic experiment where sources and receivers are both located along the acquisition surface at $x_3 = x_{3,0}$. Using this, we rewrite equation (6) as

$$I_{\partial\mathbb{D}_0} = \int_{\partial\mathbb{D}_0} R(\mathbf{x}_0''',\mathbf{x},\omega)G^*(\mathbf{x},\mathbf{x}_F,\omega)\mathrm{d}^2\mathbf{x}, \quad (8)$$

where $G(\mathbf{x},\mathbf{x}_F,\omega) = G^-(\mathbf{x},\mathbf{x}_F,\omega)$.

Next, we analyze the integral over the bottom boundary $\partial\mathbb{D}_m$ in equation (3):

$$I_{\partial\mathbb{D}_m} = \int_{\partial\mathbb{D}_m} \frac{-1}{j\omega\rho(\mathbf{x})} \left\{G^*(\mathbf{x},\mathbf{x}_F,\omega)\partial_3 G(\mathbf{x},\mathbf{x}_0''',\omega) - \partial_3 G^*(\mathbf{x},\mathbf{x}_F,\omega)G(\mathbf{x},\mathbf{x}_0''',\omega)\right\} \mathrm{d}^2\mathbf{x}, \quad (9)$$

where we used that $\partial_i n_i = +\partial_3$ (n_3 points downward at $\partial\mathbb{D}_m$, while x_3 also points downward). As previously mentioned, $\mathbf{x}_0'''$ and $\mathbf{x}_F$ are on the same side with respect to $\partial\mathbb{D}_m$; hence, we can use the same arguments given by Wapenaar and Fokkema (2006) to reduce the integral over $\partial\mathbb{D}_m$ to a single term. This yields

$$I_{\partial\mathbb{D}_m} = -\int_{\partial\mathbb{D}_m} \frac{2}{j\omega\rho(\mathbf{x})} \left\{G^+(\mathbf{x},\mathbf{x}_F,\omega)\right\}^* \partial_3 G^+(\mathbf{x},\mathbf{x}_0''',\omega)\mathrm{d}^2\mathbf{x}. \quad (10)$$

We define the pressure-normalized transmission response as

$$T(\mathbf{x}_0''',\mathbf{x},\omega) = -\frac{2}{j\omega\rho(\mathbf{x})}\partial_3 G^+(\mathbf{x},\mathbf{x}_0''',\omega) \quad (11)$$

and rewrite equation (10) as

$$I_{\partial\mathbb{D}_m} = \int_{\partial\mathbb{D}_m} T(\mathbf{x}_0''',\mathbf{x},\omega)G^*(\mathbf{x},\mathbf{x}_F,\omega)\mathrm{d}^2\mathbf{x}, \quad (12)$$

where $G(\mathbf{x},\mathbf{x}_F,\omega) = G^+(\mathbf{x},\mathbf{x}_F,\omega)$. We finally combine equations (8) and (12) to obtain

$$G(\mathbf{x}_0''',\mathbf{x}_F,\omega) = \int_{\partial\mathbb{D}_0} R(\mathbf{x}_0''',\mathbf{x},\omega)G^*(\mathbf{x}_F,\mathbf{x},\omega)\mathrm{d}^2\mathbf{x} + \int_{\partial\mathbb{D}_m} T(\mathbf{x}_0''',\mathbf{x},\omega)G^*(\mathbf{x}_F,\mathbf{x},\omega)\mathrm{d}^2\mathbf{x}, \quad (13)$$

where we have used the source-receiver reciprocity relation $G(\mathbf{x},\mathbf{x}_F,\omega) = G(\mathbf{x}_F,\mathbf{x},\omega)$. Note that, if R and T are known, we could solve this equation to retrieve the unknown wave field G (but the trivial solution $G = 0$ would also be a valid solution).

Equation (13) is the starting point to derive the relationship with the one-sided integral equation given by Wapenaar et al. (2012, 2013a,b). In the time domain, equation (13) corresponds to

$$G(\mathbf{x}_0''',\mathbf{x}_F,t) = \int_{\partial\mathbb{D}_0} \mathrm{d}^2\mathbf{x} \int_{-\infty}^{+\infty} R(\mathbf{x}_0''',\mathbf{x},t-t')G(\mathbf{x}_F,\mathbf{x},-t')dt' + \int_{\partial\mathbb{D}_m} \mathrm{d}^2\mathbf{x} \int_{-\infty}^{+\infty} T(\mathbf{x}_0''',\mathbf{x},t-t')G(\mathbf{x}_F,\mathbf{x},-t')dt'. \quad (14)$$

3 RELATIONSHIPS BETWEEN GREEN'S FUNCTIONS AND FOCUSING SOLUTION

In the domain $\mathbb{D}$ enclosed by the boundaries $\partial\mathbb{D}_0$ and $\partial\mathbb{D}_m$, we consider three independent acoustic states: the Green's function $G(\mathbf{x},\mathbf{x}_0''',\omega)$ due to an impulsive point source of volume injection rate at $\mathbf{x}_0'''$ (just above $\partial\mathbb{D}_0$), the Green's function due to a similar source at $\mathbf{x}_m$ (just below $\partial\mathbb{D}_m$), and the *focusing solution* $f_1(\mathbf{x},\mathbf{x}_i',\omega)$. This particular wave field $f_1(\mathbf{x},\mathbf{x}_i',\omega)$ is defined anywhere as the wave field that focuses at the location $\mathbf{x}_i'$ in the interior of $\mathbb{D}$. The domain $\mathbb{D}$ is source-free for all states, and the medium parameters are identical between the boundary $\partial\mathbb{D}_0$ and the depth level $\partial\mathbb{D}_i$, where $\partial\mathbb{D}_i$ is an arbitrary depth level between $\partial\mathbb{D}_0$ and $\partial\mathbb{D}_m$. For this

situation, the reciprocity theorems of the convolution-type and correlation-type are (Fokkema and van den Berg, 1993), respectively,

$$\int_{\partial\mathbb{D}_0} \frac{2}{j\omega\rho(\mathbf{x}_0)} \{(\partial_3 f_1)G - f_1(\partial_3 G)\}\, \mathrm{d}^2\mathbf{x}_0 = \int_{\partial\mathbb{D}_i} \frac{2}{j\omega\rho(\mathbf{x}_i)} \{(\partial_3 f_1)G - f_1(\partial_3 G)\}\, \mathrm{d}^2\mathbf{x}_i, \quad (15)$$

$$\int_{\partial\mathbb{D}_0} \frac{2}{j\omega\rho(\mathbf{x}_0)} \{(\partial_3 f_1)^* G - f_1^*(\partial_3 G)\}\, \mathrm{d}^2\mathbf{x}_0 = \int_{\partial\mathbb{D}_i} \frac{2}{j\omega\rho(\mathbf{x}_i)} \{(\partial_3 f_1)^* G - f_1^*(\partial_3 G)\}\, \mathrm{d}^2\mathbf{x}_i. \quad (16)$$

Substituting $f_1 = f_1^+ + f_1^-$ and $G = G^+ + G^-$ into equations (15) and (16) and following the derivation in Appendix B.3 of Wapenaar and Berkhout (1989), we obtain

$$-\int_{\partial\mathbb{D}_0} \frac{2}{j\omega\rho(\mathbf{x}_0)} \{f_1^+(\partial_3 G^-) + f_1^-(\partial_3 G^+)\}\, \mathrm{d}^2\mathbf{x}_0 = \int_{\partial\mathbb{D}_i} \frac{2}{j\omega\rho(\mathbf{x}_i)} \{(\partial_3 f_1^+)G^- + (\partial_3 f_1^-)G^+\}\, \mathrm{d}^2\mathbf{x}_i, \quad (17)$$

$$-\int_{\partial\mathbb{D}_0} \frac{2}{j\omega\rho(\mathbf{x}_0)} \{(f_1^+)^*(\partial_3 G^+) + (f_1^-)^*(\partial_3 G^-)\}\, \mathrm{d}^2\mathbf{x}_0 = \int_{\partial\mathbb{D}_i} \frac{2}{j\omega\rho(\mathbf{x}_i)} \{(\partial_3 f_1^+)^* G^+ + (\partial_3 f_1^-)^* G^-\}\, \mathrm{d}^2\mathbf{x}_i, \quad (18)$$

where in equation (18) the evanescent wave field is neglected.

Figure 2 shows the three different states to which we apply equations (17) and (18). State A1 is defined in the actual medium between the boundaries $\partial\mathbb{D}_0$ and $\partial\mathbb{D}_m$, and a source is located at $\mathbf{x}_0'''$, just above $\partial\mathbb{D}_0$. The downgoing and upgoing Green's function at $\mathbf{x}_0 \in \partial\mathbb{D}_0$ are

$$\frac{2}{j\omega\rho(\mathbf{x}_0)} \partial_3 G^+(\mathbf{x}, \mathbf{x}_0''', \omega)|_{x_3=x_{3,0}} = -\delta(\mathbf{x}_H - \mathbf{x}_H'''), \quad (19)$$

$$\frac{2}{j\omega\rho(\mathbf{x}_0)} \partial_3 G^-(\mathbf{x}, \mathbf{x}_0''', \omega)|_{x_3=x_{3,0}} = R(\mathbf{x}_0''', \mathbf{x}_0, \omega). \quad (20)$$

Like state A1, state A2 is also defined in the actual medium, but now we have a source located at $\mathbf{x}_m$, just below $\partial\mathbb{D}_m$. The downgoing and upgoing Green's function at $\mathbf{x}_0 \in \partial\mathbb{D}_0$ are

$$\frac{2}{j\omega\rho(\mathbf{x}_0)} \partial_3 G^+(\mathbf{x}, \mathbf{x}_m, \omega)|_{x_3=x_{3,0}} = 0, \quad (21)$$

$$\frac{2}{j\omega\rho(\mathbf{x}_0)} \partial_3 G^-(\mathbf{x}, \mathbf{x}_m, \omega)|_{x_3=x_{3,0}} = T(\mathbf{x}_m, \mathbf{x}_0, \omega). \quad (22)$$

State B1 is defined in a reference medium where the medium parameters are identical to the actual medium between the boundary $\partial\mathbb{D}_0$ and the depth level $\partial\mathbb{D}_i$. Below $\partial\mathbb{D}_i$, state B1 is composed of a reflection-free half-space. The focusing solution f_1 is defined in this reference medium and its dowgoing and upgoing components at $\mathbf{x}_i' \in \partial\mathbb{D}_i$ are

$$\frac{2}{j\omega\rho(\mathbf{x}_i)} \partial_3 f_1^+(\mathbf{x}, \mathbf{x}_i', \omega)|_{x_3=x_{3,i}} = -\delta(\mathbf{x}_H - \mathbf{x}_H'), \quad (23)$$

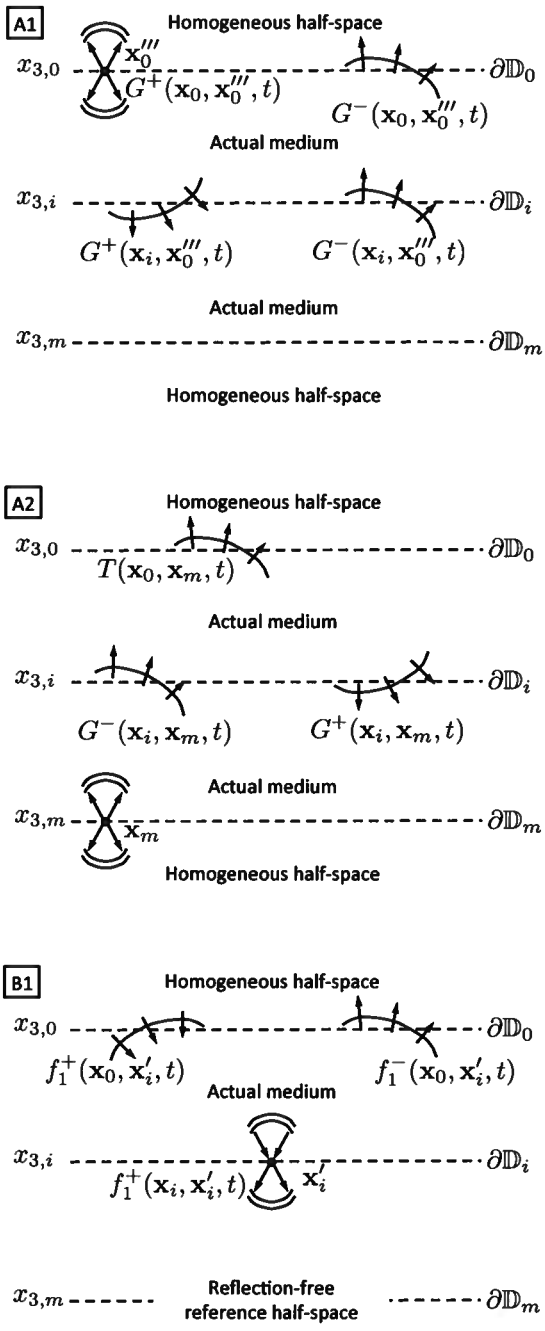

Figure 2. States for reciprocity theorems. Top - State A1: Green's function with a source at $\mathbf{x}_0'''$ just above $\partial\mathbb{D}_0$. Middle - State A2: Green's function with a source at $\mathbf{x}_m$ just below $\partial\mathbb{D}_m$. Bottom - State B1: focusing solution f_1 with a focal point at $\mathbf{x}_i'$ at depth level $\partial\mathbb{D}_i$.

$$\frac{2}{j\omega\rho(\mathbf{x}_i)}\partial_3 f_1^-(\mathbf{x},\mathbf{x}_i',\omega)|_{x_3=x_{3,i}}=0. \tag{24}$$

Substituting equations (19-20) and (23-24) into equations (17-18) gives

$$\begin{aligned} &G^-(\mathbf{x}_i',\mathbf{x}_0''',\omega) \\ &=\int_{\partial\mathbb{D}_0} R(\mathbf{x}_0''',\mathbf{x}_0,\omega) f_1^+(\mathbf{x}_0,\mathbf{x}_i',\omega)\mathrm{d}^2\mathbf{x}_0 \\ &-f_1^-(\mathbf{x}_0''',\mathbf{x}_i',\omega), \end{aligned} \tag{25}$$

and

$$\begin{aligned} &G^+(\mathbf{x}_i',\mathbf{x}_0''',\omega) \\ &=-\int_{\partial\mathbb{D}_0} R(\mathbf{x}_0''',\mathbf{x}_0,\omega)\left\{f_1^-(\mathbf{x}_0,\mathbf{x}_i',\omega)\right\}^*\mathrm{d}^2\mathbf{x}_0 \\ &+\left\{f_1^+(\mathbf{x}_0''',\mathbf{x}_i',\omega)\right\}^*. \end{aligned} \tag{26}$$

Adding these expressions yields

$$\begin{aligned} &G(\mathbf{x}_i',\mathbf{x}_0''',\omega) \\ &=\int_{\partial\mathbb{D}_0} R(\mathbf{x}_0''',\mathbf{x}_0,\omega) f_2(\mathbf{x}_i',\mathbf{x}_0,\omega)\mathrm{d}^2\mathbf{x}_0 \\ &+\left\{f_2(\mathbf{x}_i',\mathbf{x}_0''',\omega)\right\}^*, \end{aligned} \tag{27}$$

where we defined a second focusing solution $f_2(\mathbf{x}_i',\mathbf{x}_0''',\omega) = f_1^+(\mathbf{x}_0''',\mathbf{x}_i',\omega) - \left\{f_1^-(\mathbf{x}_0''',\mathbf{x}_i',\omega)\right\}^*$. The focusing solution f_2 has a focal point at $\mathbf{x}_0'''$ (Wapenaar et al., 2013a), as shown in Figure 3. Substituting equations (21-24) into equations (17-18) gives

$$\begin{aligned} &G^-(\mathbf{x}_i',\mathbf{x}_m,\omega) \\ &=\int_{\partial\mathbb{D}_0} T(\mathbf{x}_m,\mathbf{x}_0,\omega) f_1^+(\mathbf{x}_0,\mathbf{x}_i',\omega),\mathrm{d}^2\mathbf{x}_0 \end{aligned} \tag{28}$$

and

$$\begin{aligned} &G^+(\mathbf{x}_i',\mathbf{x}_m,\omega) \\ &=-\int_{\partial\mathbb{D}_0} T(\mathbf{x}_m,\mathbf{x}_0,\omega)\left\{f_1^-(\mathbf{x}_0,\mathbf{x}_i',\omega)\right\}^*\mathrm{d}^2\mathbf{x}_0. \end{aligned} \tag{29}$$

Adding these last two expressions yields

$$\begin{aligned} &G(\mathbf{x}_i',\mathbf{x}_m,\omega) \\ &=\int_{\partial\mathbb{D}_0} T(\mathbf{x}_m,\mathbf{x}_0,\omega) f_2(\mathbf{x}_i',\mathbf{x}_0,\omega)\mathrm{d}^2\mathbf{x}_0. \end{aligned} \tag{30}$$

4 COMPARISON BETWEEN THE INTEGRAL EQUATIONS

In this section, we show the consistency between two-sided, i.e. equation (13), and one-sided Green's function representations. Substituting equations (27) and (30) into equation (13) gives

$$\begin{aligned} &G(\mathbf{x}_0''',\mathbf{x}_F,\omega) \\ &=\int_{\partial\mathbb{D}_0}\mathrm{d}^2\mathbf{x}_0 R(\mathbf{x}_0''',\mathbf{x}_0,\omega) \\ &\times\int_{\partial\mathbb{D}_0}\left\{R(\mathbf{x}_0,\mathbf{x}_0'',\omega)\right\}^*\left\{f_2(\mathbf{x}_F,\mathbf{x}_0'',\omega)\right\}^*\mathrm{d}^2\mathbf{x}_0'' \\ &+\int_{\partial\mathbb{D}_0} R(\mathbf{x}_0''',\mathbf{x}_0,\omega) f_2(\mathbf{x}_F,\mathbf{x}_0,\omega)\mathrm{d}^2\mathbf{x}_0 \\ &+\underbrace{\int_{\partial\mathbb{D}_m}\mathrm{d}^2\mathbf{x}_m T(\mathbf{x}_0''',\mathbf{x}_m,\omega)}_{\mathrm{T1}} \\ &\underbrace{\times\int_{\partial\mathbb{D}_0}\left\{T(\mathbf{x}_m,\mathbf{x}_0'',\omega)\right\}^*\left\{f_2(\mathbf{x}_F,\mathbf{x}_0'',\omega)\right\}^*\mathrm{d}^2\mathbf{x}_0''}_{\mathrm{T1}}. \end{aligned} \tag{31}$$

Now, we focus on term T1 of equation (31) and we reorder its terms:

$$\begin{aligned} &\int_{\partial\mathbb{D}_0}\mathrm{d}^2\mathbf{x}_0''\left\{f_2(\mathbf{x}_F,\mathbf{x}_0'',\omega)\right\}^* \\ &\times\int_{\partial\mathbb{D}_m}\left\{T(\mathbf{x}_m,\mathbf{x}_0'',\omega)\right\}^* T(\mathbf{x}_0''',\mathbf{x}_m,\omega)\mathrm{d}^2\mathbf{x}_m. \end{aligned} \tag{32}$$

Wapenaar et al. (2004) derives a relationship between flux-normalized reflection and transmission responses for a domain $\mathbb{D}$ enclosed by boundaries $\partial\mathbb{D}_0$ and $\partial\mathbb{D}_m$. In the Appendix, we derive a similar relationship for pressure-normalized reflection and transmission responses, equation (A-14); its expression is:

$$\begin{aligned} &\int_{\partial\mathbb{D}_m}\mathrm{d}^2\mathbf{x}_m\left\{T(\mathbf{x}_m,\mathbf{x}_0'',\omega)\right\}^* T(\mathbf{x}_0''',\mathbf{x}_m,\omega) \\ &=\delta(\mathbf{x}_H''-\mathbf{x}_H''') \\ &-\int_{\partial\mathbb{D}_0}\mathrm{d}^2\mathbf{x}_0 R(\mathbf{x}_0''',\mathbf{x}_0,\omega)\left\{R(\mathbf{x}_0,\mathbf{x}_0'',\omega)\right\}^*. \end{aligned} \tag{33}$$

Note that equation (33) shows the unitarity of the scattering matrix (Rodberg and Thaler, 1967). Then, we use

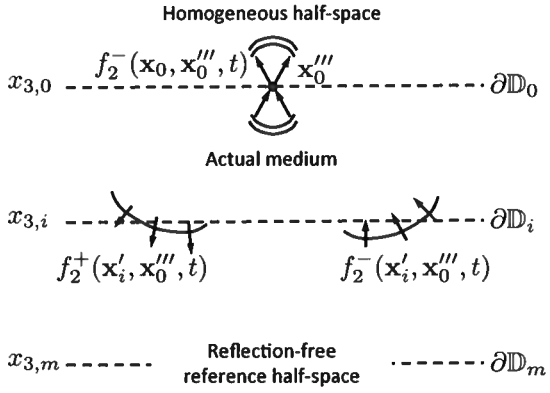

Figure 3. Focusing solution f_2 with a focal point at $\mathbf{x}_0'''$ at the depth level $\partial\mathbb{D}_0$.

equation (33) to rewrite term T1 as defined in expression (32):

$$\begin{aligned}&\left\{f_2(\mathbf{x}_F,\mathbf{x}_0''',\omega)\right\}^* \\ &-\int_{\partial\mathbb{D}_0}\mathrm{d}^2\mathbf{x}_0''\left\{f_2(\mathbf{x}_F,\mathbf{x}_0'',\omega)\right\}^* \\ &\times\int_{\partial\mathbb{D}_0}R(\mathbf{x}_0''',\mathbf{x}_0,\omega)\left\{R(\mathbf{x}_0,\mathbf{x}_0'',\omega)\right\}^*\mathrm{d}^2\mathbf{x}_0.\end{aligned}\tag{34}$$

Finally, we insert expression (34) into equation (31) to give

$$\begin{aligned}&G(\mathbf{x}_0''',\mathbf{x}_F,\omega) \\ &=\underbrace{\int_{\partial\mathbb{D}_0}\mathrm{d}^2\mathbf{x}_0R(\mathbf{x}_0''',\mathbf{x}_0,\omega)}_{\mathrm{T1}} \\ &\underbrace{\times\int_{\partial\mathbb{D}_0}\left\{R(\mathbf{x}_0,\mathbf{x}_0'',\omega)\right\}^*\left\{f_2(\mathbf{x}_F,\mathbf{x}_0'',\omega)\right\}^*\mathrm{d}^2\mathbf{x}_0''}_{\mathrm{T1}} \\ &+\int_{\partial\mathbb{D}_0}\mathrm{d}^2\mathbf{x}_0R(\mathbf{x}_0''',\mathbf{x}_0,\omega)f_2(\mathbf{x}_F,\mathbf{x}_0,\omega) \\ &+\left\{f_2(\mathbf{x}_F,\mathbf{x}_0''',\omega)\right\}^* \\ &\underbrace{-\int_{\partial\mathbb{D}_0}\mathrm{d}^2\mathbf{x}_0''\left\{f_2(\mathbf{x}_F,\mathbf{x}_0'',\omega)\right\}^*}_{\mathrm{T3}} \\ &\underbrace{\times\int_{\partial\mathbb{D}_0}R(\mathbf{x}_0''',\mathbf{x}_0,\omega)\left\{R^+(\mathbf{x}_0,\mathbf{x}_0'',\omega)\right\}^*\mathrm{d}^2\mathbf{x}_0}_{\mathrm{T3}}.\end{aligned}\tag{35}$$

The terms T1 and T3 in equation (35) cancel each other; hence equation (35) becomes

$$\begin{aligned}&G(\mathbf{x}_0''',\mathbf{x}_F,\omega) \\ &=\int_{\partial\mathbb{D}_0}R^+(\mathbf{x}_0''',\mathbf{x}_0,\omega)f_2(\mathbf{x}_F,\mathbf{x}_0,\omega)\mathrm{d}^2\mathbf{x}_0 \\ &+\left\{f_2(\mathbf{x}_F,\mathbf{x}_0''',\omega)\right\}^*.\end{aligned}\tag{36}$$

This one-sided Green's function representation is the key result of our paper. This expression shows that the two-sided and one-sided integral equations for the Green's function retrieval lead to equivalent results. Wapenaar et al. (2013a) use a causality argument to solve equation (36) in the time domain for the focusing solution f_2. Once f_2 is known, it can be used to retrieve $G(\mathbf{x}_0''',\mathbf{x}_F,\omega)$. Note that equation (36) is equivalent to equation (27) which is an intermediate step needed to show the consistency between the two-sided integral equation equation (13) and the one-sided equation (36). Alternative derivations based on the unitarity relation (Rodberg and Thaler, 1967) need further investigation, which is beyond the scope of this paper.

5 CONCLUSION

We have shown the connection between one- and two-sided integral equations for Green's function retrieval. Representations based on one-sided equations are more recent and present a practical advantage because they remove the physical constraints of having receivers and sources at depth; hence, they do not require approximations that are needed because measurements are unavailable at depth. On the other hand, methods requiring data on a closed boundary (two-sided) present well-known applications. For these reasons, their connection can introduce mutual benefits to the different representations.

ACKNOWLEDGMENTS

We thank Ken Larner for his constructive comments. This work was supported by the sponsors of the Consortium Project on Seismic Inverse Methods for Complex Structures at the Center for Wave Phenomena and the Netherlands Research Centre for Integrated Solid Earth Science (ISES).

REFERENCES

Aki, K., and P. G. Richards, 2002, Quantitative seismology, 2nd ed.: University Science Books.

Aktosun, T., and J. H. Rose, 2002, Wave focusing on the line: Journal of Mathematical Physics, **43**, 3717–3745.

Bakulin, A., and R. Calvert, 2006, The virtual source method: Theory and case study: Geophysics, **71**, SI139–SI150.

Broggini, F., and R. Snieder, 2012, Connection of scattering principles: a visual and mathematical tour: European Journal of Physics, **33**, 593–613.

Broggini, F., R. Snieder, and K. Wapenaar, 2012a, Creating a virtual source inside a medium from reflection data: numerical examples for laterally-varying velocity models, spatially-extended virtual sources, and inaccurate direct arrivals: SEG Technical Program Expanded Abstracts, **710**, 1–5.

———, 2012b, Focusing the wavefield inside an unknown 1D medium - Beyond seismic interferometry: Geophysics, **77**, A25–A28.

de Hoop, A. T., 1995, Handbook of radiation and scattering of waves: Academic Press.

Fokkema, J. T., and P. M. van den Berg, 1993, Seismic Applications of Acoustic Reciprocity: Elsevier.

Lamb, G. L., 1980, Elements of soliton theory: Wiley-Interscience.

Larose, E., O. Lobkis, and R. Weaver, 2006, Passive correlation imaging of a buried scatterer (L): Journal of the Acoustical Society of America, **119**, 3549–3552.

Lobkis, O., and R. Weaver, 2001, On the emergence of the Green's function in the correlations of a diffuse field: Journal of the Acoustical Society of America, **110**, 3011–3017.

Rodberg, L. S., and R. M. Thaler, 1967, Introduction to the Quantum Theory of Scattering: Academic Press.

Rose, J. H., 2001, "Single-sided" focusing of the time-dependent Schrödinger equation: Phys. Rev. A, **65**, 012707.

———, 2002a, Single-sided autofocusing of sound in layered materials: Inverse Problems, **18**, 1923–1934.

———, 2002b, Time Reversal, Focusing and Exact Inverse Scattering, *in* Imaging of Complex Media with Acoustic and Seismic Waves: Springer, 97–106.

Schuster, G. T., 2009, Seismic Interferometry: Cambridge University Press.

Ursin, B., O. Pedersen, and B. Arntsen, 2012, Flux-normalized wavefield decomposition and migration of seismic data: Geophysics, **77**, S83–S92.

Wapenaar, K., and A. J. Berkhout, 1989, Elastic wave field extrapolation: Redatuming of single- and multi-component seismic data: Elsevier.

Wapenaar, K., F. Broggini, E. Slob, and R. Snieder, 2013a, Three-Dimensional Single-Sided Marchenko Inverse Scattering, Data-Driven Focusing, Green's Function Retrieval, and their Mutual Relations: Phys. Rev. Lett., **110**, 084301.

Wapenaar, K., F. Broggini, and R. Snieder, 2012, Creating a virtual source inside a medium from reflection data: heuristic derivation and stationary-phase analysis: Geophysical Journal International, **190**, 1020–1024.

Wapenaar, K., and J. Fokkema, 2006, Green's function representations for seismic interferometry: Geophysics, **71**, SI33–SI46.

Wapenaar, K., E. Slob, F. Broggini, R. Snieder, J. Thorbecke, and J. van der Neut, 2013b, Data-driven Green's function retrieval from reflection data: Theory and example: EAGE Expanded Abstracts.

Wapenaar, K., J. Thorbecke, and D. Draganov, 2004, Relations between reflection and transmission responses of three-dimensional inhomogeneous media: Geophysical Journal International, **156**, 179–194.

APPENDIX: RELATIONSHIP BETWEEN PRESSURE-NORMALIZED REFLECTION AND TRANSMISSION RESPONSES

In this appendix, we derive a Green's function representation of the correlation-type for one-way (down- and up-going) fields and a relationship between pressure-normalized reflection and transmission responses measured on the top and bottom boundaries. We start from a two-way reciprocity theorem of the correlation-type:

$$\int_{\partial\mathbb{D}_0}\Big\{[G_3^{p,f}(\mathbf{x}_0,\mathbf{x}_0'',\omega)]^*G_3^{v,q}(\mathbf{x}_0,\mathbf{x}_0''',\omega)+[G_{3,3}^{v,f}(\mathbf{x}_0,\mathbf{x}_0'',\omega)]^*G^{p,q}(\mathbf{x}_0,\mathbf{x}_0''',\omega)\Big\}\,\mathrm{d}^2\mathbf{x}_0 \tag{A-1}$$
$$=\int_{\partial\mathbb{D}_m}\Big\{[G_3^{p,f}(\mathbf{x}_m,\mathbf{x}_0'',\omega)]^*G_3^{v,q}(\mathbf{x}_m,\mathbf{x}_0''',\omega)+[G_{3,3}^{v,f}(\mathbf{x}_m,\mathbf{x}_0'',\omega)]^*G^{p,q}(\mathbf{x}_m,\mathbf{x}_0''',\omega)\Big\}\,\mathrm{d}^2\mathbf{x}_m,$$

where the superscripts p and v characterize the Green's function as a pressure or velocity, respectively. The superscripts q and f specify if the source is a point source of volume injection rate (monopole) or a point source of force (dipole), respectively. The subscript 3 indicates the vertical component of the velocity or the vertical component of the point source force. We then rewrite $G_{3,3}^{v,f}(\mathbf{x},\mathbf{x}_0'',\omega)$ as

$$G_{3,3}^{v,f}(\mathbf{x},\mathbf{x}_0'',\omega)=-\frac{1}{j\omega\rho(\mathbf{x})}\frac{\partial G_3^{p,f}(\mathbf{x},\mathbf{x}_0'',\omega)}{\partial x_3}+\frac{1}{j\omega\rho(\mathbf{x})}\delta(\mathbf{x}-\mathbf{x}''), \tag{A-2}$$

and insert it into equation (A-1) to obtain

$$\int_{\partial\mathbb{D}_0}\Big\{[G_3^{p,f}(\mathbf{x}_0,\mathbf{x}_0'',\omega)]^*G_3^{v,q}(\mathbf{x}_0,\mathbf{x}_0''',\omega)-\frac{1}{j\omega\rho(\mathbf{x}_0)}[\frac{\partial G_3^{p,f}(\mathbf{x}_0,\mathbf{x}_0'',\omega)}{\partial x_3}]^*G^{p,q}(\mathbf{x}_0,\mathbf{x}_0''',\omega)\Big\}\,\mathrm{d}^2\mathbf{x}_0 \tag{A-3}$$
$$=\int_{\partial\mathbb{D}_m}\Big\{[G_3^{p,f}(\mathbf{x}_m,\mathbf{x}_0'',\omega)]^*G_3^{v,q}(\mathbf{x}_m,\mathbf{x}_0''',\omega)+\frac{1}{j\omega\rho(\mathbf{x}_m)}[\frac{\partial G_3^{p,f}(\mathbf{x}_m,\mathbf{x}_0'',\omega)}{\partial x_3}]^*G^{p,q}(\mathbf{x}_m,\mathbf{x}_0''',\omega)\Big\}\,\mathrm{d}^2\mathbf{x}_m.$$

Now, we focus on $\partial\mathbb{D}_0$ and the result for $\partial\mathbb{D}_m$ follows from a similar reasoning. In the following, we assume that the medium parameters are laterally invariant at $\partial\mathbb{D}_0$. We use $G=G^+ + G^-$ and apply Parseval's theorem (Wapenaar and Berkhout, 1989, equation B-27) to equation (A-3), this gives

$$\int_{\partial\mathbb{D}_0}\Big\{([G_3^{p,f+}(\chi_0,\mathbf{x}_0'',\omega)]^*+[G_3^{p,f-}(\chi_0,\mathbf{x}_0'',\omega)]^*)[G_3^{v,q+}(\chi_0,\mathbf{x}_0''',\omega)+G_3^{v,q-}(\chi_0,\mathbf{x}_0''',\omega)] \tag{A-4}$$
$$-\frac{1}{j\omega\rho(x_{3,0})}(jk_3[G_3^{p,f+}(\chi_0,\mathbf{x}_0'',\omega)]^*-jk_3[G_3^{p,f-}(\chi_0,\mathbf{x}_0'',\omega)]^*)[G^{p,q+}(\chi_0,\mathbf{x}_0''',\omega)+G^{p,q-}(\chi_0,\mathbf{x}_0''',\omega)]\Big\}\,\mathrm{d}^2\chi_0,$$

where $\chi_0\equiv(k_1,k_2,x_3)$ and $\left(\frac{\partial G^\pm}{\partial x_3}\right)^*=\pm jk_3(G^\pm)^*$ (Wapenaar and Berkhout, 1989, equation B-29c). We reorder the terms in expression (A-4) and obtain

$$\int_{\partial\mathbb{D}_0}\Big\{([G_3^{p,f+}(\chi_0,\mathbf{x}_0'',\omega)]^*+[G_3^{p,f-}(\chi_0,\mathbf{x}_0'',\omega)]^*)[G_3^{v,q+}(\chi_0,\mathbf{x}_0''',\omega)+G_3^{v,q-}(\chi_0,\mathbf{x}_0''',\omega)] \tag{A-5}$$
$$-([G_3^{p,f+}(\chi_0,\mathbf{x}_0'',\omega)]^*-[G_3^{p,f-}(\chi_0,\mathbf{x}_0'',\omega)]^*)\frac{1}{j\omega\rho(x_{3,0})}[jk_3G^{p,q+}(\chi_0,\mathbf{x}_0''',\omega)+jk_3G^{p,q-}(\chi_0,\mathbf{x}_0''',\omega)]\Big\}\,\mathrm{d}^2\chi_0.$$

Then, we use $\mp jk_3(G^\pm)^*=\frac{\partial G^\pm}{\partial x_3}$ (Wapenaar and Berkhout, 1989, equation B-29b) and apply Parsevel's theorem to expression (A-5), yielding

$$\int_{\partial\mathbb{D}_0}\Big\{([G_3^{p,f+}(\mathbf{x}_0,\mathbf{x}_0'',\omega)]^*+[G_3^{p,f-}(\mathbf{x}_0,\mathbf{x}_0'',\omega)]^*)[G_3^{v,q+}(\mathbf{x}_0,\mathbf{x}_0''',\omega)+G_3^{v,q-}(\mathbf{x}_0,\mathbf{x}_0''',\omega)] \tag{A-6}$$
$$-([G_3^{p,f+}(\mathbf{x}_0,\mathbf{x}_0'',\omega)]^*-[G_3^{p,f-}(\mathbf{x}_0,\mathbf{x}_0'',\omega)]^*)\frac{1}{j\omega\rho(\mathbf{x}_0)}[-\frac{\partial G^{p,q+}(\mathbf{x}_0,\mathbf{x}_0''',\omega)}{\partial x_3}+\frac{\partial G^{p,q-}(\mathbf{x}_0,\mathbf{x}_0''',\omega)}{\partial x_3}]\Big\}\,\mathrm{d}^2\mathbf{x}_0,$$

where the medium parameters are now laterally varying. Using the relation

$$G_3^{v,q}(\mathbf{x},\mathbf{x}_0''',\omega)=-\frac{1}{j\omega\rho(\mathbf{x})}\frac{\partial G^{p,q}(\mathbf{x},\mathbf{x}_0''',\omega)}{\partial x_3}, \tag{A-7}$$

we rewrite expression (A-6) as

$$\int_{\partial\mathbb{D}_0}\Big\{([G_3^{p,f+}(\mathbf{x}_0,\mathbf{x}_0'',\omega)]^*+[G_3^{p,f-}(\mathbf{x}_0,\mathbf{x}_0'',\omega)]^*)[G_3^{v,q+}(\mathbf{x}_0,\mathbf{x}_0''',\omega)+G_3^{v,q-}(\mathbf{x}_0,\mathbf{x}_0''',\omega)] \tag{A-8}$$
$$-([G_3^{p,f+}(\mathbf{x}_0,\mathbf{x}_0'',\omega)]^*-[G_3^{p,f-}(\mathbf{x}_0,\mathbf{x}_0'',\omega)]^*)[G_3^{v,q+}(\mathbf{x}_0,\mathbf{x}_0''',\omega)-G_3^{v,q-}(\mathbf{x}_0,\mathbf{x}_0''',\omega)]\Big\}\,\mathrm{d}^2\mathbf{x}_0.$$

In expression (A-8), the terms containing Green's functions propagating in the same directions (e.g. $[G_3^{p,f+}]^* G_3^{v,q+}$) cancel; hence we obtain

$$2\int_{\partial\mathbb{D}_0}\Big\{[G_3^{p,f+}(\mathbf{x}_0,\mathbf{x}_0'',\omega)]^* G_3^{v,q+}(\mathbf{x}_0,\mathbf{x}_0''',\omega) - [G_3^{p,f-}(\mathbf{x}_0,\mathbf{x}_0'',\omega)]^* G_3^{v,q-}(\mathbf{x}_0,\mathbf{x}_0''',\omega)\Big\}\,\mathrm{d}^2\mathbf{x}_0 \tag{A-9}$$
$$= 2\int_{\partial\mathbb{D}_m}\Big\{[G_3^{p,f+}(\mathbf{x}_m,\mathbf{x}_0'',\omega)]^* G_3^{v,q+}(\mathbf{x}_m,\mathbf{x}_0''',\omega) + [G_3^{p,f-}(\mathbf{x}_m,\mathbf{x}_0'',\omega)]^* G_3^{v,q-}(\mathbf{x}_m,\mathbf{x}_0''',\omega)\Big\}\,\mathrm{d}^2\mathbf{x}_m,$$

where we assumed that the evanescent waves can be neglected. This is a one-way reciprocity theorem of the correlation-type.

We define two acoustic states that will be used in the one-way reciprocity theorem, defined by equation (A-9), to derive a relationship between the pressure-normalized reflection and transmission responses measured on $\partial\mathbb{D}_0$ and $\partial\mathbb{D}_m$. Both states are defined in the actual medium between the boundaries $\partial\mathbb{D}_0$ and $\partial\mathbb{D}_m$, as in state A1 in Figure 2. We choose an impulsive point source of volume injection rate at $\mathbf{x}'''$, just above $\partial\mathbb{D}_0$, and define state C1 as

$$\mathbf{x}\in\partial\mathbb{D}_0 = \begin{cases} G_3^{v,q+}(\mathbf{x}_0,\mathbf{x}_0''',\omega) = -G_3^{p,f+}(\mathbf{x}_0''',\mathbf{x}_0,\omega) = -\delta(\mathbf{x}_H-\mathbf{x}_H'''), \\ G_3^{v,q-}(\mathbf{x}_0,\mathbf{x}_0''',\omega) = -G_3^{p,f-}(\mathbf{x}_0''',\mathbf{x}_0,\omega) = -R(\mathbf{x}_0''',\mathbf{x}_0,\omega), \end{cases} \tag{A-10}$$

$$\mathbf{x}\in\partial\mathbb{D}_m = \begin{cases} G_3^{v,q+}(\mathbf{x}_m,\mathbf{x}_0''',\omega) = -G_3^{p,f+}(\mathbf{x}_0''',\mathbf{x}_m,\omega) = -T(\mathbf{x}_0''',\mathbf{x}_m,\omega), \\ G_3^{v,q-}(\mathbf{x}_m,\mathbf{x}_0''',\omega) = 0. \end{cases} \tag{A-11}$$

For state D1, we choose a point source of force at $\mathbf{x}''$, just above $\partial\mathbb{D}_0$:

$$\mathbf{x}\in\partial\mathbb{D}_0 = \begin{cases} G_3^{p,f+}(\mathbf{x}_0,\mathbf{x}_0'',\omega) = \delta(\mathbf{x}_H-\mathbf{x}_H''), \\ G_3^{p,f-}(\mathbf{x}_0,\mathbf{x}_0'',\omega) = R(\mathbf{x}_0,\mathbf{x}_0'',\omega), \end{cases} \tag{A-12}$$

$$\mathbf{x}\in\partial\mathbb{D}_m = \begin{cases} G_3^{p,f+}(\mathbf{x}_m,\mathbf{x}_0'',\omega) = T(\mathbf{x}_m,\mathbf{x}_0'',\omega), \\ G_3^{p,f-}(\mathbf{x}_0,\mathbf{x}_0'',\omega) = 0. \end{cases} \tag{A-13}$$

Now, we plug these expressions into equation (A-9) and obtain

$$\int_{\partial\mathbb{D}_m}[T(\mathbf{x}_m,\mathbf{x}_0'',\omega)]^* T(\mathbf{x}_0,\mathbf{x}_m,\omega)\mathrm{d}^2\mathbf{x}_m \tag{A-14}$$
$$= \delta(\mathbf{x}_H''-\mathbf{x}_H'') - \int_{\partial\mathbb{D}_0}[R(\mathbf{x}_0,\mathbf{x}_0'',\omega)]^* R(\mathbf{x}_0''',\mathbf{x}_0,\omega)\mathrm{d}^2\mathbf{x}_0. \tag{A-15}$$

This is the pressure-normalized version of equation (20) in Wapenaar et al. (2004).

Three-dimensional single-sided Marchenko inverse scattering, data-driven focusing, Green's function retrieval, and their mutual relations

Kees Wapenaar[1], Filippo Broggini[2], Evert Slob[1], & Roel Snieder[2]
[1] *Department of Geoscience and Engineering, Delft University of Technology, 2600 GA Delft, The Netherlands*
[2] *Center for Wave Phenomena, Colorado School of Mines, Golden CO 80401, USA*

ABSTRACT
The 1D Marchenko equation forms the basis for inverse scattering problems in which the scattering object is accessible from one side only. Here we derive a 3D Marchenko equation which relates the single-sided reflection response of a 3D inhomogeneous medium to a field inside the medium. We show that this equation is solved by a 3D iterative data-driven focusing method, which yields the 3D Green's function with its virtual source inside the medium. The 3D single-sided Marchenko equation and its iterative solution method form the basis for imaging of 3D strongly scattering inhomogeneous media that are accessible from one side only.

Key words: data-driven focusing, Green's function retrieval, Marchenko equations

1 INTRODUCTION

Inverse scattering is the problem of determining a medium perturbation (or in quantum mechanics a potential) from an acoustic, electromagnetic or quantum-mechanical wave field, scattered by this perturbation (or potential). One particular approach to 1D inverse scattering makes use of the Marchenko equation. This is an exact integral equation which relates the reflection response, measured at one side of the perturbation, to the field inside the medium (Lamb, 1980; Burridge, 1980). Rose (2001) shows that solving the Marchenko equation is equivalent to designing a wave field which, when emitted from one side of the perturbation into the inhomogeneous medium, focuses inside the medium. He proposes an iterative scheme to design the focusing wave field, which only requires the reflection response at one side of the perturbation as input. This "autofocusing" method solves the Marchenko equation and, subsequently, the 1D inverse scattering problem. Broggini and Snieder (2012) show that the focusing wave field and its response can be combined in a specific way to yield the 1D medium's Green's function, with its virtual source at the focal point inside the medium.

The question arises whether the discussed concepts of single-sided Marchenko inverse scattering, autofocusing, Green's function retrieval and their mutual relations (Broggini and Snieder, 2012) can be extended from one to three dimensions. A 3D extension of the Marchenko equation is the so-called Newton-Marchenko (NM) equation (Newton, 1982; Budreck and Rose, 1990). 3D inverse scattering based on the NM equation requires omnidirectional reflection and transmission measurements. Hence, despite the fact that the NM equation is very useful for this class of inverse problems, it is not applicable to single-sided reflection measurements. Prada et al. (1991) pioneered 3D single-sided autofocusing, but their method is limited to focusing waves onto the strongest scatterers and does not account for multiple scattering.

We derive a 3D version of the Marchenko equation which relates the single-sided scalar reflection response of a 3D inhomogeneous medium to the field inside the medium. Next we briefly review a new 3D data-driven focusing method (Wapenaar et al., 2012) and show that this method solves the 3D single-sided Marchenko equation. We also show that a specific combination of the 3D focusing wave field and its reflection response gives the 3D Green's function, with its virtual source at the fo-

cal point inside the medium. Unlike in other data-driven Green's function retrieval methods (Weaver and Lobkis, 2001; Campillo and Paul, 2003; Wapenaar et al., 2004; Schuster, 2009), no receiver is needed at the position of the virtual source.

2 FUNDAMENTAL SOLUTIONS

In the derivation of the 1D Marchenko equation, so-called "fundamental solutions" of the source-free Schrödinger equation play an essential role (Lamb, 1980). For the situation of a localized potential $u(x)$, the fundamental solutions $f_1(x,t)$ and $f_2(x,t)$ of the Schrödinger equation are those solutions that reduce to impulsive outgoing waves for $x \to \infty$ and $x \to -\infty$, respectively. Here we extend the fundamental solutions to 3D. We define the spatial coordinate vector $\mathbf{x}$ as $\mathbf{x} = (\mathbf{x}_H, x_3)$, in which $\mathbf{x}_H = (x_1, x_2)$ is the horizontal coordinate vector and x_3 the vertical coordinate; the positive x_3-axis is pointing downward. Coordinates at a constant depth level $x_3 = x_{3,i}$ are denoted as $\mathbf{x}_i = (\mathbf{x}_H, x_{3,i})$ and time is denoted by t. Consider an inhomogeneous lossless medium between transparent boundaries $\partial\mathbb{D}_0$ and $\partial\mathbb{D}_m$ at depth levels $x_3 = x_{3,0}$ and $x_3 = x_{3,m}$, respectively. The domain enclosed by $\partial\mathbb{D}_0$ and $\partial\mathbb{D}_m$ is denoted as $\mathbb{D}$. The upper half-space $x_3 < x_{3,0}$ and the lower half-space $x_3 > x_{3,m}$ are homogeneous. A fundamental solution $f_1(\mathbf{x},t)$ of the scalar wave equation consists in the upper half-space of a downgoing field $f_1^+(\mathbf{x},t)$ and an upgoing field $f_1^-(\mathbf{x},t)$, with $f_1^+(\mathbf{x},t)$ shaped such that $f_1(\mathbf{x},t)$ focuses at $\mathbf{x}'_m = (\mathbf{x}'_H, x_{3,m})$ at $t = 0$, and continues as an impulsive diverging downgoing field $f_1^+(\mathbf{x},t)$ into the lower half-space. The focal point $\mathbf{x}'_m$ is a variable at $\partial\mathbb{D}_m$ and will from here onward be included in the argument list, hence $f_1(\mathbf{x},t)$ becomes $f_1(\mathbf{x},\mathbf{x}'_m,t)$ (Fig 1(a)). Similarly, the fundamental solution $f_2(\mathbf{x},\mathbf{x}''_0,t)$ focuses at $\mathbf{x}''_0 = (\mathbf{x}''_H, x_{3,0})$ at $t = 0$, and continues as an impulsive diverging upgoing field $f_2^-(\mathbf{x},\mathbf{x}''_0,t)$ into the upper half-space (Fig 1(b)). The temporal Fourier transform of a time-dependent function $u(t)$ is defined as $u(\omega) = \int_{-\infty}^{\infty} u(t)\exp(i\omega t)\mathrm{d}t$, where ω is the angular frequency and i the imaginary unit. To keep the notation simple, the same symbol is used for time- and frequency-domain functions (here u). In the frequency domain, the aforementioned focusing conditions for f_1 and f_2 are $f_1(\mathbf{x}_m,\mathbf{x}'_m,\omega) = \delta(\mathbf{x}_H - \mathbf{x}'_H)$ and $f_2(\mathbf{x}_0,\mathbf{x}''_0,\omega) = \delta(\mathbf{x}_H - \mathbf{x}''_H)$. Throughout this paper we ignore evanescent waves, hence, headwaves, turning waves etc. are excluded from the following analysis. Moreover, $\delta(\mathbf{x}_H)$ should be interpreted as a spatially bandlimited delta function (because it lacks the wavenumber components of the evanescent field).

The two fundamental solutions are mutually related. The relation can be rigorously derived from reciprocity theorems for flux-normalized downgoing and upgoing wave fields (Wapenaar et al., 2004). Here we present a short, more intuitive, derivation. In the upper half-space the upgoing field f_1^- can be seen as the response to a distribution of Huygens sources along $\partial\mathbb{D}_0$, weighted by f_1^- at $\partial\mathbb{D}_0$. Since f_2 focuses at $\partial\mathbb{D}_0$ (Fig1(b)) and emits impulsive upward propagating waves into the upper half-space, f_2 at $\partial\mathbb{D}_0$ provides the Huygens sources. Similarly, the downgoing field f_1^+ in the upper half-space can be seen as the acausal response to time-reversed Huygens sources (or Huygens sinks) f_2^*, weighted by f_1^+ at $\partial\mathbb{D}_0$ (the asterisk denotes complex conjugation). Hence, for $f_1 = f_1^+ + f_1^-$ we have in the upper half-space

$$\begin{aligned} f_1(\mathbf{x},\mathbf{x}'_m,\omega) &= \int_{\partial\mathbb{D}_0} f_2(\mathbf{x},\mathbf{x}''_0,\omega) f_1^-(\mathbf{x}''_0,\mathbf{x}'_m,\omega)\mathrm{d}\mathbf{x}''_0 \\ &+ \int_{\partial\mathbb{D}_0} f_2^*(\mathbf{x},\mathbf{x}''_0,\omega) f_1^+(\mathbf{x}''_0,\mathbf{x}'_m,\omega)\mathrm{d}\mathbf{x}''_0. \end{aligned} \quad (1)$$

Recall that $\mathbf{x}''_0 = (\mathbf{x}''_H, x_{3,0})$, hence, the integrations take place at $\partial\mathbb{D}_0$ along the horizontal coordinate vector $\mathbf{x}''_H$. Since f_1 and f_2 are solutions of one-and-the-same source-free wave equation for all $\mathbf{x} \in \mathbb{R}^3$, equation (1) not only holds in the upper half-space but throughout space. In a similar way, f_2 can be expressed in terms of f_1 and f_1^*.

The downgoing and upgoing constituents of f_1 at $\partial\mathbb{D}_0$ are related via the reflection response $R(\mathbf{x}_0,\mathbf{x}''_0,\omega)$ of the inhomogeneous medium in $\mathbb{D}$, according to

$$f_1^-(\mathbf{x}_0,\mathbf{x}'_m,\omega) = \int_{\partial\mathbb{D}_0} R(\mathbf{x}_0,\mathbf{x}''_0,\omega) f_1^+(\mathbf{x}''_0,\mathbf{x}'_m,\omega)\mathrm{d}\mathbf{x}''_0. \quad (2)$$

Similarly, the downgoing field at $\partial\mathbb{D}_m$ is related to the downgoing field at $\partial\mathbb{D}_0$ via the transmission response $T(\mathbf{x}_m,\mathbf{x}''_0,\omega)$. Because the downgoing wave field focuses at $\mathbf{x}'_m = (\mathbf{x}'_H, x_{3,m})$, this gives

$$\delta(\mathbf{x}_H - \mathbf{x}'_H) = \int_{\partial\mathbb{D}_0} T(\mathbf{x}_m,\mathbf{x}''_0,\omega) f_1^+(\mathbf{x}''_0,\mathbf{x}'_m,\omega)\mathrm{d}\mathbf{x}''_0. \quad (3)$$

We introduce the inverse of $f_1^+(\mathbf{x}_0,\mathbf{x}'_m,\omega)$ via $\int_{\partial\mathbb{D}_m} f_1^+(\mathbf{x}_0,\mathbf{x}'_m,\omega)\{f_1^+(\mathbf{x}''_0,\mathbf{x}'_m,\omega)\}^{\mathrm{inv}}\mathrm{d}\mathbf{x}'_m = \delta(\mathbf{x}_H - \mathbf{x}''_H)$. Applying this inverse to both sides of equation (3) gives $\{f_1^+(\mathbf{x}''_0,\mathbf{x}_m,\omega)\}^{\mathrm{inv}} = T(\mathbf{x}_m,\mathbf{x}''_0,\omega)$. Applying $T(\mathbf{x}'_m,\mathbf{x}''_0,\omega)$ to both sides of equation (1) gives, using equation (2),

$$\begin{aligned} &\int_{\partial\mathbb{D}_m} f_1(\mathbf{x},\mathbf{x}'_m,\omega) T(\mathbf{x}'_m,\mathbf{x}''_0,\omega)\mathrm{d}\mathbf{x}'_m \\ &= \int_{\partial\mathbb{D}_0} f_2(\mathbf{x},\mathbf{x}'_0,\omega) R(\mathbf{x}'_0,\mathbf{x}''_0,\omega)\mathrm{d}\mathbf{x}'_0 \\ &+ f_2^*(\mathbf{x},\mathbf{x}''_0,\omega). \end{aligned} \quad (4)$$

In the following we show that the left-hand side of equation (4) is equal to the Green's function $G(\mathbf{x},\mathbf{x}''_0,\omega)$ and we use the right-hand side to derive the 3D Marchenko equation.

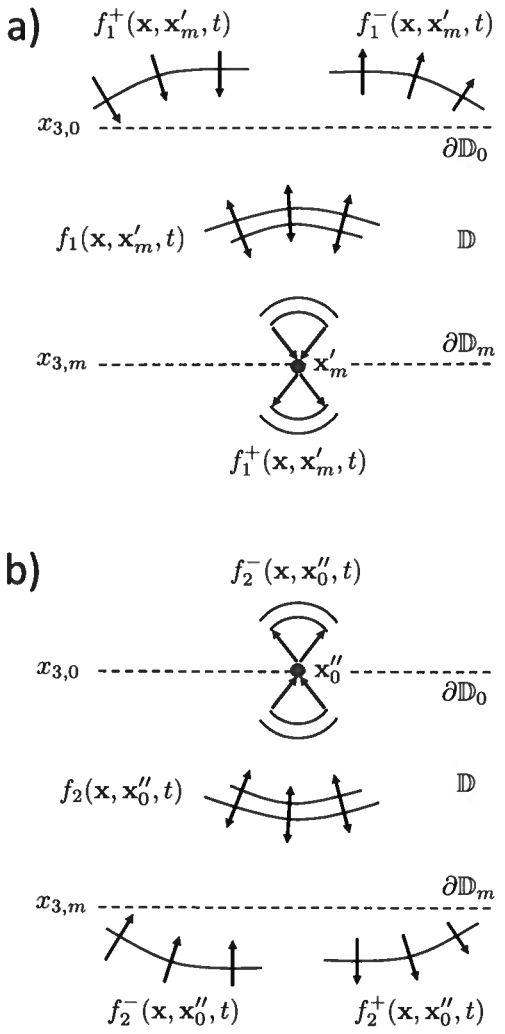

Figure 1. *Fundamental solutions of the 3D wave equation.*

3 GREEN'S FUNCTION

We define an internal boundary $\partial\mathbb{D}_i$ at depth level $x_{3,i}$, anywhere between $x_{3,0}$ and $x_{3,m}$, and analyze the Green's function $G(\mathbf{x}_i, \mathbf{x}''_0, \omega)$. The downgoing and upgoing constituents, G^+ and G^-, are related via (Wapenaar et al., 2008)

$$G^-(\mathbf{x}'_i, \mathbf{x}''_0, \omega) = \int_{\partial\mathbb{D}_i} R(\mathbf{x}'_i, \mathbf{x}_i, \omega) G^+(\mathbf{x}_i, \mathbf{x}''_0, \omega) \mathrm{d}\mathbf{x}_i. \tag{5}$$

This equation resembles equation (2), but because $\partial\mathbb{D}_i$ is an internal boundary it is less trivial. $R(\mathbf{x}'_i, \mathbf{x}_i, \omega)$ is the reflection response of a truncated medium (consisting of the actual medium below $\partial\mathbb{D}_i$ and a scattering-free half-space above $\partial\mathbb{D}_i$), whereas the Green's function is defined in the actual medium. Using a similar derivation as in Wapenaar et al. (2008), we also obtain

$$\int_{\partial\mathbb{D}_i} T(\mathbf{x}'_m, \mathbf{x}_i, \omega) G^+(\mathbf{x}_i, \mathbf{x}''_0, \omega) \mathrm{d}\mathbf{x}_i = T(\mathbf{x}'_m, \mathbf{x}''_0, \omega), \tag{6}$$

where $T(\mathbf{x}'_m, \mathbf{x}_i, \omega)$ is the transmission response of the truncated medium. Similar as above we have $\{f_1^+(\mathbf{x}_i, \mathbf{x}'_m, \omega)\}^{\mathrm{inv}} = T(\mathbf{x}'_m, \mathbf{x}_i, \omega)$. Substituting this in the left-hand side of equation (6) and applying f_1^+ to both sides gives

$$G^+(\mathbf{x}_i, \mathbf{x}''_0, \omega) = \int_{\partial\mathbb{D}_m} f_1^+(\mathbf{x}_i, \mathbf{x}'_m, \omega) T(\mathbf{x}'_m, \mathbf{x}''_0, \omega) \mathrm{d}\mathbf{x}'_m. \tag{7}$$

Applying the reflection response R to both sides of equation (7) gives, using equation (5) for $G^\pm$ and $f_1^\pm$,

$$G^-(\mathbf{x}_i, \mathbf{x}''_0, \omega) = \int_{\partial\mathbb{D}_m} f_1^-(\mathbf{x}_i, \mathbf{x}'_m, \omega) T(\mathbf{x}'_m, \mathbf{x}''_0, \omega) \mathrm{d}\mathbf{x}'_m. \tag{8}$$

Summing equations (7) and (8) and dropping the subscript i confirms that the left-hand side of equation (4) is equal to the Green's function $G(\mathbf{x}, \mathbf{x}''_0, \omega)$ for $\mathbf{x} \in \mathbb{D}$.

4 3D MARCHENKO EQUATION

We transform equation (4), with the left-hand side replaced by $G(\mathbf{x}, \mathbf{x}''_0, \omega)$, to the time domain, which gives

$$\begin{aligned} &G(\mathbf{x}, \mathbf{x}''_0, t) \\ &= \int_{\partial\mathbb{D}_0} \mathrm{d}\mathbf{x}'_0 \int_{-\infty}^{\infty} f_2(\mathbf{x}, \mathbf{x}'_0, t') R(\mathbf{x}'_0, \mathbf{x}''_0, t - t') \mathrm{d}t' \\ &+ f_2(\mathbf{x}, \mathbf{x}''_0, -t). \end{aligned} \tag{9}$$

Let $t_\mathrm{d}(\mathbf{x}, \mathbf{x}''_0)$ denote the traveltime of the first arrival between $\mathbf{x}''_0 \in \partial\mathbb{D}_0$ and $\mathbf{x} \in \mathbb{D}$. By evaluating equation (9) only for $t < t_\mathrm{d}(\mathbf{x}, \mathbf{x}''_0)$, the left-hand side can be replaced by zero. Equation (9) (with 0 on the left-hand side) only constrains f_2 up to a multiplicative constant and therefore an ansatz will be made for the form of this function. In the 1D derivation (Lamb, 1980), $f_2(x, t)$ is defined as a delta pulse traveling in the negative x-direction, followed by a scattering coda caused by the potential $u(x)$. Moreover, the incident field is shaped such that the scattering coda vanishes beyond the scattering region, leaving only the delta pulse for $x \to -\infty$. Analogous to the 1D situation, the ansatz for $f_2(\mathbf{x}, \mathbf{x}''_0, t)$ is a superposition of a direct wave and a scattering coda, according to

$$\begin{aligned} &f_2(\mathbf{x}, \mathbf{x}''_0, t) \\ &= \{T_\mathrm{d}(\mathbf{x}, \mathbf{x}''_0, t)\}^{\mathrm{inv}} + \theta(t + t_\mathrm{d}(\mathbf{x}, \mathbf{x}''_0)) M(\mathbf{x}, \mathbf{x}''_0, t). \end{aligned} \tag{10}$$

Here $\{T_\mathrm{d}(\mathbf{x}, \mathbf{x}''_0, t)\}^{\mathrm{inv}}$ is the inverse of the direct arrival of the transmission response, which focuses at $\mathbf{x}''_0$; its traveltime is $-t_\mathrm{d}(\mathbf{x}, \mathbf{x}''_0)$. In practice it will often suffice to approximate $\{T_\mathrm{d}(\mathbf{x}, \mathbf{x}''_0, t)\}^{\mathrm{inv}}$ by the time-reversal $T_\mathrm{d}(\mathbf{x}, \mathbf{x}''_0, -t)$, or even by $\delta(t + t_\mathrm{d}(\mathbf{x}, \mathbf{x}''_0))$. $M(\mathbf{x}, \mathbf{x}''_0, t)$ is the coda following the direct arrival. It is the result of scattering taking place in the inhomogeneous

medium in $\mathbb{D}$. The coda is assumed to be causal, i.e., $M(\mathbf{x},\mathbf{x}_0'',t)=0$ for $t<-t_\mathrm{d}(\mathbf{x},\mathbf{x}_0'')$. This causality is expressed by multiplying the coda with the Heaviside function $\theta(t+t_\mathrm{d}(\mathbf{x},\mathbf{x}_0''))$ in equation (10). Note that the ansatz limits the validity of what follows to configurations for which the ansatz holds true. For example, it holds in layered media with moderately curved interfaces as long as $|\mathbf{x}_\mathrm{H}-\mathbf{x}_\mathrm{H}''|$ is not too large (to avoid occurence of turning waves, headwaves etc.). The conditions underlying the ansatz need further investigation, which is beyond the scope of this paper. Substituting equation (10) into (9) (with 0 on the left-hand side) yields

$$\begin{aligned}0 &= \int_{\partial\mathbb{D}_0}\mathrm{d}\mathbf{x}_0'\int_{-\infty}^{\infty}\{T_\mathrm{d}(\mathbf{x},\mathbf{x}_0',t')\}^{\mathrm{inv}}R(\mathbf{x}_0',\mathbf{x}_0'',t-t')\mathrm{d}t'\\ &+\int_{\partial\mathbb{D}_0}\mathrm{d}\mathbf{x}_0'\int_{-t_\mathrm{d}(\mathbf{x},\mathbf{x}_0')}^{\infty}M(\mathbf{x},\mathbf{x}_0',t')R(\mathbf{x}_0',\mathbf{x}_0'',t-t')\mathrm{d}t'\\ &+M(\mathbf{x},\mathbf{x}_0'',-t),\end{aligned}\tag{11}$$

with $\mathbf{x}\in\mathbb{D}$ and $t<t_\mathrm{d}(\mathbf{x},\mathbf{x}_0'')$. This is the 3D single-sided Marchenko equation. Next we show that it can be solved with an iterative 3D data-driven focusing scheme.

5 3D DATA-DRIVEN FOCUSING

Inspired by the work of Rose (2001), the authors proposed an iterative scheme to design a downgoing wave field $p^+(\mathbf{x}_0,t)$ at $\partial\mathbb{D}_0$ that focuses at $t=0$ at a focal point $\mathbf{x}_\mathrm{F}\in\mathbb{D}$ (and at $\mathbf{x}_\mathrm{F}$ only) (Wapenaar et al., 2012). The initial estimate $p_0^+(\mathbf{x}_0,t)$ is defined as $p_0^+(\mathbf{x}_0,t)=\{T_\mathrm{d}(\mathbf{x}_0,\mathbf{x}_\mathrm{F},t)\}^{\mathrm{inv}}$. When emitted from $\partial\mathbb{D}_0$ into the inhomogeneous medium, this field not only focuses at $\mathbf{x}_\mathrm{F}$, but it also causes ghost images at $t=0$. These ghost images can be cancelled by updating the incident field, which causes new ghost images, which again need to be cancelled, etc. The following iterative scheme accomplishes this task (Wapenaar et al., 2012)

$$\begin{aligned}&p_k^+(\mathbf{x}_0',\mathbf{x}_\mathrm{F},t)\\ &\quad=\{T_\mathrm{d}(\mathbf{x}_0',\mathbf{x}_\mathrm{F},t)\}^{\mathrm{inv}}\\ &\quad-\theta(t+t_\mathrm{d}(\mathbf{x}_0',\mathbf{x}_\mathrm{F}))p_{k-1}^-(\mathbf{x}_0',\mathbf{x}_\mathrm{F},-t),\end{aligned}\tag{12}$$

$$\begin{aligned}&p_k^-(\mathbf{x}_0'',\mathbf{x}_\mathrm{F},t)\\ &=\int_{\partial\mathbb{D}_0}\mathrm{d}\mathbf{x}_0'\int_{-\infty}^{\infty}R(\mathbf{x}_0'',\mathbf{x}_0',t-t')p_k^+(\mathbf{x}_0',\mathbf{x}_\mathrm{F},t')\mathrm{d}t'.\end{aligned}\tag{13}$$

Here $p_k^+(\mathbf{x}_0',\mathbf{x}_\mathrm{F},t)$ is the kth iteration of the downgoing wave field, intended to focus at $\mathbf{x}_\mathrm{F}$, whereas $p_k^-(\mathbf{x}_0'',\mathbf{x}_\mathrm{F},t)$ is its upgoing reflection response. The scheme starts for $k=0$, with $p_{-1}^-(\mathbf{x}_0',\mathbf{x}_\mathrm{F},-t)=0$. Unlike the 1D scheme of Rose, which only needs the reflection response as input, this 3D scheme requires the reflection response $R(\mathbf{x}_0'',\mathbf{x}_0',t)$ and the direct transmission response $T_\mathrm{d}(\mathbf{x}_0',\mathbf{x}_\mathrm{F},t)$. The reflection response is measured at the boundary $\partial\mathbb{D}_0$. The transmission response mainly requires an estimate of the direct arrival time $t_\mathrm{d}(\mathbf{x}_0',\mathbf{x}_\mathrm{F})$, for which no detailed information about the medium is required: a smooth background model suffices to compute the direct transmission response $T_\mathrm{d}(\mathbf{x}_0',\mathbf{x}_\mathrm{F},t)$. Note that estimating the background model is state-of-the-art methodology in geophysical imaging (Harlan et al., 2008). All information about the scattering properties of the medium comes from the measured reflection response. This is why we call the scheme of equations (13) and (14) "data-driven focusing".

Assuming the scheme converges, the final result is denoted by dropping the subscripts $k-1$ and k. Substituting equation (13) into equation (14), using source-receiver reciprocity for the reflection and transmission responses, gives for $t<t_\mathrm{d}(\mathbf{x}_\mathrm{F},\mathbf{x}_0'')$ the 3D Marchenko equation (11), with $M(\mathbf{x}_\mathrm{F},\mathbf{x}_0'',-t)=-p^-(\mathbf{x}_0'',\mathbf{x}_\mathrm{F},t)$. Hence, the iterative 3D data-driven focusing scheme of equations (13) and (14) solves the 3D Marchenko equation.

6 3D GREEN'S FUNCTION RETRIEVAL

Here we generalize the approach of Broggini and Snieder (2012) to retrieve the 3D Green's function. Comparison of equation (10) with equation (13) (without the subscripts $k-1$ and k) gives $f_2(\mathbf{x}_\mathrm{F},\mathbf{x}_0',t)=p^+(\mathbf{x}_0',\mathbf{x}_\mathrm{F},t)$. Substituting this into equation (9), using equation (14) and source-receiver reciprocity for the Green's function, gives (dropping the primes)

$$G(\mathbf{x}_0,\mathbf{x}_\mathrm{F},t)=p^+(\mathbf{x}_0,\mathbf{x}_\mathrm{F},-t)+p^-(\mathbf{x}_0,\mathbf{x}_\mathrm{F},t).\tag{14}$$

This shows that a combination of the focusing wave field p^+ and its response p^- yields the Green's function with its virtual source at the position of the focal point inside the medium. Unlike in other Green's function retrieval methods (Weaver and Lobkis, 2001; Campillo and Paul, 2003; Wapenaar et al., 2004; Schuster, 2009), no physical receiver is required at the position of the virtual source. The method is illustrated with a 2D numerical example. Figure 2(a) shows an inhomogeneous medium (the colors represent the propagation velocity c). The yellow dot represents the virtual source position $\mathbf{x}_\mathrm{F}$ and the yellow triangles represent 23 receiver positions $\mathbf{x}_0$ at the surface. Figure 2(b) shows the direct transmission response $T_\mathrm{d}(\mathbf{x}_0,\mathbf{x}_\mathrm{F},t)$ for all 23 receiver positions, modeled in a smoothed version of the medium. This direct field is used in the iterative scheme of equations (13) and (14), together with the reflection response at the surface (not shown). Figure 2(c) shows the Green's function $G(\mathbf{x}_0,\mathbf{x}_\mathrm{F},t)$ obtained from equation (14) (black dashed traces), overlain on the directly modeled Green's function (red traces). All traces have been multiplied by $\exp(2t)$ to emphasize the scattering coda. Note that this coda is very well recovered.

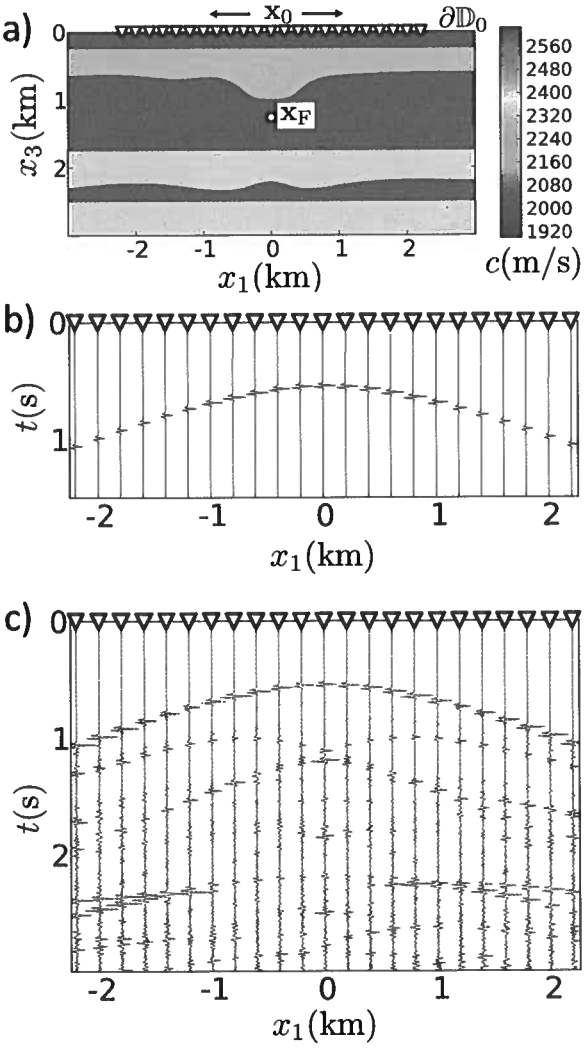

Figure 2. *Numerical example.*

7 CONCLUDING REMARKS

We have derived a 3D version of the Marchenko equation, which relates the single-sided 3D reflection response of an inhomogeneous medium to a field inside the medium. In the derivation we assumed scalar waves in a lossless medium, ignored evanescent waves and further assumed that the scattering coda of the fundamental solution follows the inverse of the direct arrival of the transmission response. These conditions imply some restrictions that need further investigation. For those situations in which the conditions are fulfilled, we showed that the 3D single-sided Marchenko equation is solved by an iterative data-driven focusing scheme. This scheme requires the 3D reflection response at one side of the medium and an estimate of the direct arrival of the transmission response. It is, in fact, through the arrival time of direct arrivals that one specifies the location of the focal point. We also showed that a combination of the focusing wave field and its reflection response gives the 3D Green's function with its virtual source located at the focal point. Because no physical receiver is needed at the position of the focal point, the focal point can be chosen anywhere inside the medium. This gives the possibility to obtain Green's functions with virtual sources throughout the medium, which can be used for imaging of objects that are accessible from one side only. The methodology will be of particular interest for situations in which the target image is blurred by multiple scattering. The next challenge is to extend the method to vector wave fields. We foresee applications in many areas, ranging from non-destructive inspection of construction materials to seismological reflection imaging and monitoring of structures and processes in the earth's interior.

ACKNOWLEDGEMENTS

We thank Jan Thorbecke and Joost van der Neut for their contributiuons to the numerical experiment.

REFERENCES

Broggini, F. and Snieder, R., Eur. J. Phys. **33**, 593 (2012).

Budreck, D. E. and Rose, J. H., Inverse Problems **6**, 331 (1990).

Burridge, R., Wave Motion **2**, 305 (1980).

Campillo, M. and Paul, A., Science **299**, 547 (2003).

Harlan, W. S., Langan, R. T., and Nemeth, T., Geophysics **73**, VE1 (2008).

Lamb, G. L., *Elements of soliton theory* (John Wiley and Sons, Inc., New York, 1980).

Newton, R. G., J. Math. Phys. **23**, 594 (1982).

Prada, C., Wu, F., and Fink, M., J. Acoust. Soc. Am. **90**, 1119 (1991).

Rose, J. H., Phys. Rev. A **65**, 012707 (2001).

Schuster, G. T., *Seismic interferometry* (Cambridge University Press, 2009).

Wapenaar, K., Thorbecke, J., and Draganov, D., Geophys. J. Int. **156**, 179 (2004).

Wapenaar, K., Broggini, F., and Snieder, R., Geophys. J. Int. **190**, 1020 (2012).

Wapenaar, K., Slob, E., and Snieder, R., Geophys. Prosp. **56**, 419 (2008).

Weaver, R. L. and Lobkis, O. I., Phys. Rev. Lett. **87**, 134301 (2001).

CWP-769

Optimal wave focusing

Farhad Bazargani and Roel Snieder
Center for Wave Phenomena, Colorado School of Mines, Golden, CO 80401, USA

ABSTRACT
Focusing waves inside a medium has applications in various science and engineering fields, e.g., in medical imaging, ultrasound therapy, noninvasive surgery, nondestructive evaluation, and geophysics in areas such as imaging and focusing microseismic events. The goal in focusing is to concentrate the wave energy at a specific time and location inside a medium. Various techniques have been devised and used to achieve this goal. Time-reversal (TR) is a well-researched method that has been used routinely to focus acoustic and seismic waves. Here, we propose a new technique wherein wave focusing is cast as an optimization problem. The objective is to study the possibility of improving upon the performance of the existing focusing methods.

Key words: wave focusing, optimization, time-reversal, imaging, microseismic

1 INTRODUCTION

The objective in wave focusing is to determine the waveforms that, when transmitted through a medium, create a wavefield that concentrates at a specific time and location. Wave focusing is conceptually related to the problem of imaging, and hence finds important applications in areas such as exploration geophysics.

Several methods for focusing have been devised, including those based on inverse scattering (Haddadin and Ebbini, 1998; Broggini et al., 2012; Behura et al., 2012), phase conjugation (Parvulescu, 1961), and time-reversal (Fink, 1997). Time-reversal (TR) is a well-established focusing technique that is robust and effective in heterogeneous media. The method relies on the time-reversal invariance of the wave operator and spatial reciprocity (Fink et al., 2002; Snieder, 2004).

A time-reversal mirror (TRM) is an array of transducers, each capable of detecting and recording, time-reversing (last-in first-out), and retransmitting signals into the medium. The TR process consists of two basic steps (Figure 1). In the first, the wavefield generated at a source in the medium is recorded using a closed TRM surrounding the source. In the second step, the recorded waveforms are time-reversed, retransmitted through the medium, and propagated back to refocus approximately at the original source location. In a dissipative medium, time-reversal invariance is not satisfied. Spatial reciprocity alone, nevertheless, explains the robustness and efficiency of the TR process in many applications involving dissipative media (Fink, 2006).

TR focusing methods have now been implemented in a variety of physical scenarios. TR can be done in both physical and numerical (back-propagation) experiments. In both, one deals with propagation of a time-reversed field, but the propagation is real in a physical problem and simulated in a back-propagation numerical problem (Fink, 2006). Applications involving physical TR problems include medical imaging (Robert and Fink, 2008), lithotripsy, underwater acoustics, and nondestructive testing (Fink, 1997; Larmat et al., 2010).

TR back-propagation methods are applied in key areas of geophysics on both global and exploration scales. In global seismology, TR techniques are used for studying earthquake source mechanism and evolution, event location, explosion monitoring, and environmental applications of geophysics (Lu, 2002; Larmat et al., 2006, 2010). In exploration seismology, TR focusing is used in microseismic event location (Lu and Willis, 2008; McMechan, 1982; Xuan and Sava, 2010), fracking and reservoir monitoring (Shapiro, 2008), salt-flank imaging and redatuming seismic data (Lu, 2002), and migration (Berkhout, 1997). Reversed time migration, one of the most successful imaging techniques in exploration seismology, consists of three basic steps; time-reversal of the recorded data, propagation of source and receiver wavefields, and implementation of an imaging condition (McMechan, 1983; Schuster, 2002).

Despite these broad applications, the TR process has important theoretical limitations. In theory, for a broadband pulse emitted by an ideal point source, the returning field refocuses on a spot with dimensions on

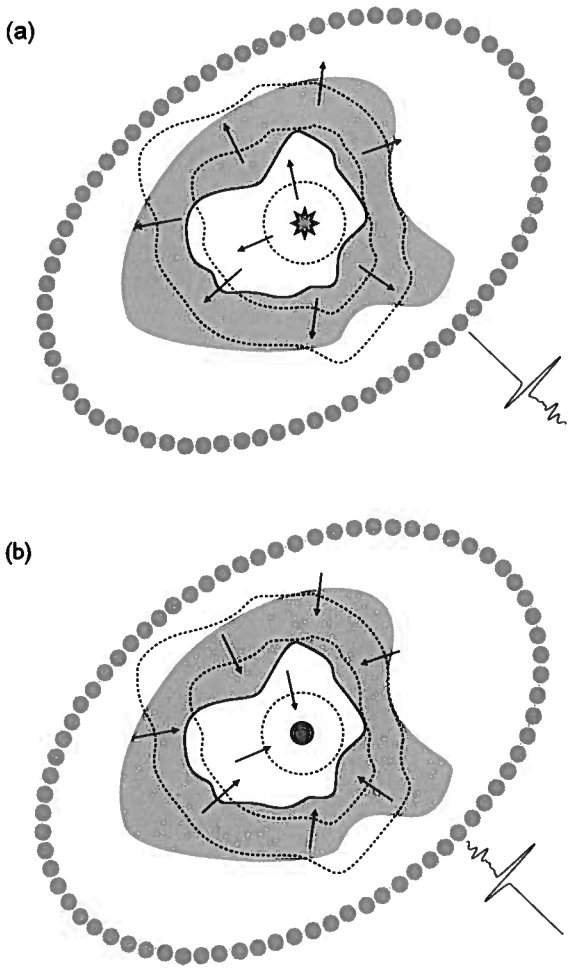

Figure 1. Illustration of a time-reversal experiment. (a) Forward propagation step: waves excited by a source travel through the complex medium and are recorded at stations marked as circles. (b) Back-propagation step: the recorded signals are reversed in time and re-emitted into the medium at the corresponding stations. The waves then propagate through the medium and converge on the original source location. Figure from (Lu, 2002).

the order of the smallest wavelength (Abbe diffraction limit). This is because evanescent waves containing source details smaller than the involved wavelengths cannot be sensed in the far-field. Therefore, this information is lost and causes the resolution of the process to be bounded by the diffraction limit (Fink, 1997).

TR focusing also has several practical limitations. From the experimental point of view, it is not possible to record and retransmit the wavefield everywhere on a surface that fully encloses the source. In practice, the wavefield is sampled at spatially sparse locations. Also, it is often not practical to surround the area of interest with a full-aperture TRM, so a finite-aperture TRM is used instead. This imperfect acquisition causes an increase in the dimension of the point-spread function (Fink, 2006). Another problem is that in real applications of TR-focusing, the media are dissipative and time-reversal invariance of the wave equation does not hold valid in dissipative media. As shown by Fink (2006), however, even in a dissipative medium, the TR process always maximizes the output amplitude received at the source at the focal time although it does not impose any constraints on the field around the focus. For example, side lobes can be observed around the source.

Several studies have been devoted to investigate these limitations and alleviate their effect to improve the TR procedure. Tanter et al. (2000, 2001), Aubry et al. (2001), and Montaldo et al. (2003) present the spatio-temporal inverse-filter method, a new focusing technique based on the inverse of the wave propagator between a source and elements in a TRM. For a lossless medium, the inverse filter method yields the same result as that of the TR method, but in the presence of attenuation, the spatio-temporal inverse filter methods are more effective than is the TR method.

Research on the connection between medium complexity and the size of the focal spot has shown a direct relationship between complexity of medium and resolution in TR focusing; the more complicated the medium between the source and the TRM, the sharper the focus (Blomgren et al., 2002; Fink, 2008; Vellekoop et al., 2010). This is because a finite-aperture TRM acts as an antenna that uses complex environments to appear wider than it actually is, resulting in a focusing capability that is less dependent on the TRM aperture. In media made of random distribution of sub-wavelength scatterers, a time-reversed wave field can interact with the random medium to regenerate not only the propagating but also evanescent waves required to refocus below the diffraction limit (super-resolution). Schuster et al. (2012) demonstrate a method that uses evanescent waves generated by scatterers in the near-field region of seismic sources to achieve super-resolution.

In this paper, we propose an alternative approach to wave focusing wherein the problem is cast as an optimization problem. As discussed above, the mainstream focusing methods currently in use are not optimal for real problems because of imperfect acquisition, attenuation, and the diffraction limit. The motivation for this research is to improve upon the existing techniques especially where such techniques do not perform optimally in dealing with the inherent and unavoidable limitations encountered in real focusing problems. In section 2, we lay out the theoretical foundation of the new focusing method and then,in section 3, compare our approach with other common focusing techniques. Section 4 is devoted to a numerical wave focusing experiment that demonstrates the implementation of the proposed method. We also provide a comparison of the

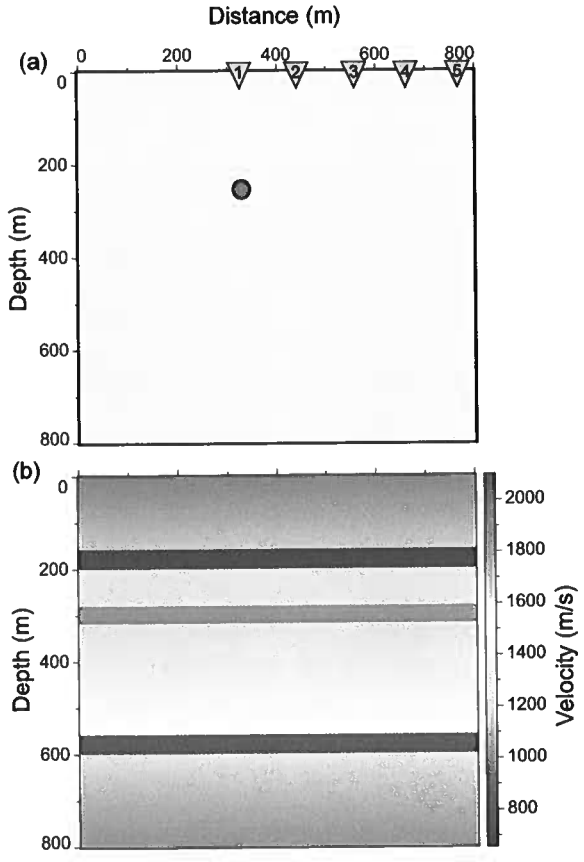

Figure 2. Configuration of the synthetic experiment (a) showing the locations of the sources (yellow triangles) and focusing target (red circle), and the assumed acoustic velocity model (b) for the medium.

focus achieved by the proposed method with the outcome of other focusing methods. Finally, in section 5, we discuss applications of the method in areas such as seismic imaging and microseismic event location, and elaborate on issues associated with each particular application.

2 FOCUSING AS AN OPTIMIZATION PROBLEM

Consider N sources at distinct locations $\mathbf{r}_i$ wherein each source is capable of transmitting predefined signals. The objective is to design signals such that, upon transmission, focuses optimally at a specific time and location inside the medium. Each source must work in concert with the others by injecting a signal that is tailored in amplitude and shape according to the specific medium, source geometry, and focusing target in order to achieve the best spatio-temporal focus.

If we denote the signal injected by the source at $\mathbf{r}_i$ as $a_i(t)$, then the superposed wavefield recorded at an arbitrary location $\mathbf{r}$ inside the medium is

$$u(\mathbf{r},t) = \sum_{i=1}^{N} a_i(t) * g(\mathbf{r},\mathbf{r}_i,t), \tag{1}$$

where $*$ is the convolution operator, and $g(\mathbf{r},\mathbf{r}_i,t)$ is the impulse response (Green's function) recorded at location $\mathbf{r}$ and corresponding to an impulsive source at location $\mathbf{r}_i$. Note that if the velocity of the medium is known, these Green's functions can be computed.

Convolution in the time domain corresponds to multiplication in the frequency domain. Therefore, considering the problem in the frequency domain, each frequency component of the wavefield u in equation 1 can be restated as a weighted sum of the corresponding frequency component $G(\mathbf{r},\mathbf{r}_i,\omega)$ of the Green's functions

$$u(\mathbf{r},\omega) = \sum_{i=1}^{N} a_i(\omega)\, G(\mathbf{r},\mathbf{r}_i,\omega), \tag{2}$$

where the weights $a_i(\omega)$ are the Fourier components of the injected signals.

The problem can now be restated as how to optimally determine the weights $a_i(\omega)$ in equation 2 so that the superposed field u in the time domain focuses at a desired location of focus $\mathbf{r}_f$ and at a desired time of focus (usually taken to be $t_f = 0$). Put another way, the goal is to have $u(\mathbf{r},t)$ as close as possible to $\delta(\mathbf{r}-\mathbf{r}_f)\delta(t)$, where δ denotes the Dirac delta function. In the frequency domain, this amounts to making each $u(\mathbf{r},\omega)$ as close as possible to $\delta(\mathbf{r}-\mathbf{r}_f)$. This goal can be achieved, for example, by minimizing an objective function defined as

$$J = \int |u(\mathbf{r},\omega) - \delta(\mathbf{r}-\mathbf{r}_f)|^2 d\mathbf{r}. \tag{3}$$

This condition is known as the *deltaness criterion* in the context of the method of Backus and Gilbert (BG) in inverse theory (Backus and Gilbert, 1968). A good description of this method is provided by Aki and Richards (1980) and Aster et al. (2012). Inserting equation 2 in objective function 3 and minimizing with respect to each $a_i(\omega)$ gives a linear system of equations of the form

$$\Gamma \mathbf{a} = \mathbf{g}^*, \tag{4}$$

where Γ is the $N \times N$ Gram matrix (Parker, 1994) with elements defined as

$$\Gamma_{ij} = \int G(\mathbf{r},\mathbf{r}_i,\omega)\, G^*(\mathbf{r},\mathbf{r}_j,\omega)\, d\mathbf{r}, \qquad i,j = 1,2,...,N, \tag{5}$$

$\mathbf{g}$ is an $N \times 1$ vector with components

$$\mathbf{g}_i = G(\mathbf{r}_f,\mathbf{r}_i,\omega), \qquad i = 1,2,...,N, \tag{6}$$

and the symbol $*$ denotes complex conjugate.

The linear system in 4 can be solved for the $N \times 1$ vector $\mathbf{a}$ for each frequency. These $\mathbf{a}_i(\omega)$ vectors consti-

tute the Fourier coefficients for the signals that must be transmitted by each source at $\mathbf{r}_i$ to achieve an optimal focus at $\mathbf{r}_f$.

3 COMPARISON WITH OTHER TECHNIQUES

The Backus and Gilbert (BG) focusing method, introduced in section 2, is closely related to other techniques commonly in use. As explained below, particular choices of the Gram matrix Γ in equation 4 can reduce the BG method to other methods such as time-reversal or the deconvolution method presented by Ulrich et al. (2012).

First, we discuss the connection between the BG method and the TR method: Replacing Γ in equation 4 by the identity matrix I gives

$$\mathbf{a} = \mathbf{g}^*. \tag{7}$$

As before, this equation gives each frequency component of the vector $\mathbf{a}$. Now, since complex conjugation in the frequency domain is equivalent to time-reversal in the time domain, the new system of equations 7 describes exactly the same process as time-reversal in the time domain. Replacing Γ by the identity matrix amounts to cancelling the cross-talk between sources and having each source work independently to inject time-reversed Green's functions.

Next, we discuss the connection between the BG method and the deconvolution method: Setting the off-diagonal elements of Γ in equation 4 equal to zero ($\Gamma_{i,j} = 0$ for $i \neq j$), and solving the system of equations for $\mathbf{a}$, gives

$$a_i(\omega) = \frac{G^*(\mathbf{r}_f, \mathbf{r}_i, \omega)}{\int G(\mathbf{r}, \mathbf{r}_i, \omega)\, G^*(\mathbf{r}, \mathbf{r}_i, \omega)\, d\mathbf{r}}, \quad i = 1, 2, ..., N. \tag{8}$$

In the deconvolution method (Ulrich et al., 2012), the same frequency components of the signals to be back-propagated for focusing are computed as

$$a_i(\omega) = \frac{G^*(\mathbf{r}_f, \mathbf{r}_i, \omega)}{G(\mathbf{r}_f, \mathbf{r}_i, \omega)\, G^*(\mathbf{r}_f, \mathbf{r}_i, \omega) + \epsilon}, \quad i = 1, 2, ..., N, \tag{9}$$

where ϵ is a regularization term, on the order of $|G(\mathbf{r}_f, \mathbf{r}_i, \omega)|^2$, added for stability of the solution. Notice the similarity between equations 8 and 9; both equations have the same numerator on the right hand side, the denominators are similar except for the integration over the spatial element in equation 8 and the regularization term ϵ in equation 9.

Based on the discussions above, we can say that, compared to the TR and deconvolution techniques, the BG method provides a more general solution to the wave-focusing problem. In other words, TR and deconvolution methods are special cases of the more-general BG method with particular choices of Γ. The elements

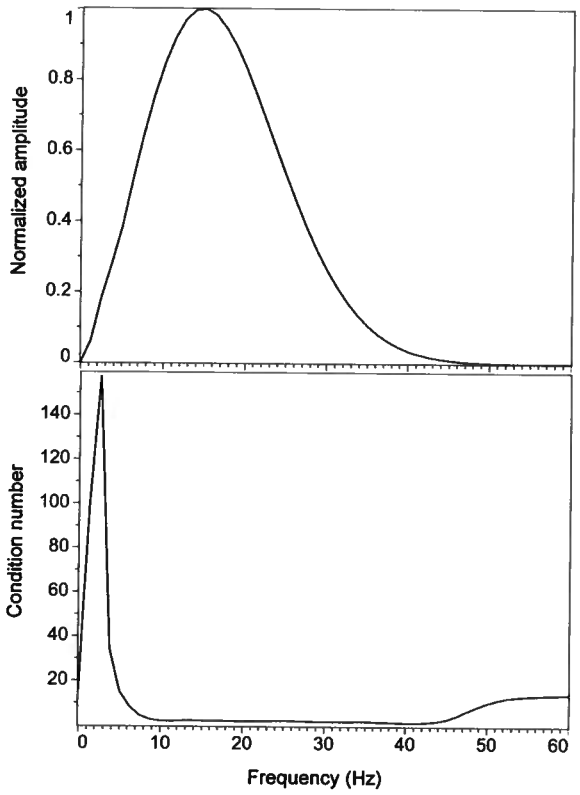

Figure 3. Amplitude spectrum (a) of the Ricker wavelet used as the source in the numerical experiment, and condition number (b) of the Gram matrix Γ as a function of frequency.

of the Gram matrix Γ hold crucial information about the configuration of the wave-focusing experiment, i.e., the relative positions of the sources with respect to the propagation medium and the focusing target. Each element plays a role in determining how the sources must work in tandem to inject the signals that achieve the optimum focusing at the target. The off-diagonal elements in Γ adjust the signal emitted by each source with respect to other sources.

4 SYNTHETIC DATA EXPERIMENT

To test the ideas presented above, we perform a numerical focusing experiment where we apply the BG method to focus wavefields at a target and compare the result with the focus achieve by other techniques such as TR, deconvolution, and TR with spectral whitening. TR with spectral whitening is a simple method for boosting the weak frequencies of a signal by dividing the components of the frequency band by their magnitudes ($a(\omega) \rightarrow a(\omega)/|a(\omega)|$) such that the resulting spectrum is flattened (whitened).

The configuration of the numerical experiment is

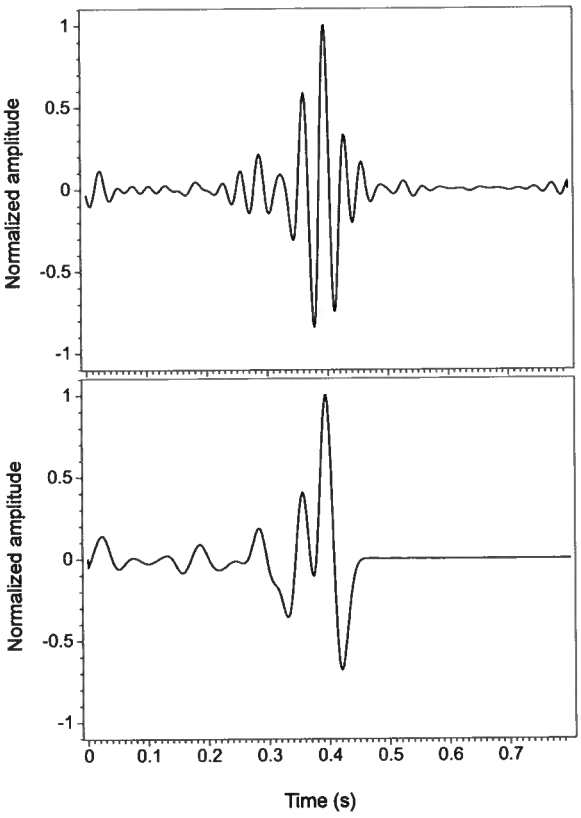

Figure 4. Signals required to be injected by source 2 shown in Figure 2 computed by (a) the proposed focusing method, and (b) time-reversal method.

shown in Figure 2a. The triangles represent the injection points (sources), the locations where the signals are emitted and numerically propagated to focus at the target, denoted by the red circle. The velocity model used for wave propagation is a 2D model (Figure 2b) consisting of a linearly varying background and three layers of low- and high-velocity contrasts inserted in the background. Wave propagation is simulated using an explicit finite-difference approximation of the 2D acoustic isotropic wave equation with absorbing boundary condition.

To form the Gram matrix Γ according to equation 4, we require an approximation of the impulse response of the medium $g(\mathbf{r}, \mathbf{r}_i, t)$. To compute the impulse response, at each injection point we inject a bandlimited Ricker wavelet with peak frequency of 16 Hz (Figure 3a) and forward propagate the wavefield in time. These wavefields are then transformed to the frequency domain and used in equation 5 to compute the elements of the 5×5 matrix Γ for each frequency. At this point, the right-hand side of equation 4 is also known because $\mathbf{g}_i = G(\mathbf{r}_f, \mathbf{r}_i, \omega) = G(\mathbf{r}, \mathbf{r}_i, \omega)|_{\mathbf{r}=\mathbf{r}_f}$.

Solving equation 4 for each frequency gives the Fourier coefficients $\mathbf{a}(\omega)$ of the signals that, upon injection, create wavefields that optimally focus at the target. Figure 4a shows one such signal computed for injection point 2. The signal, of the same injection point computed using the TR method, is shown in Figure 4b for comparison. Note the higher frequency content of the optimally computed signal (Figure 4a) compared to the time reversed signal (Figure 4b). Also, note the presence of noncausal energy between 0.45 s and 0.8 s (energy at times prior to the first arrival in the original recorded signal) in the optimally computed signal in Figure 4a.

To compare the effectiveness of the different wave-focusing methods, Figures 5a, b, c, and d show snapshots of the wavefield associated with the BG, TR, deconvolution, and TR with spectral whitening, respectively. As is evident in these snapshots, the BG method has outperformed the other methods in achieving a more concentrated spatial focus in this synthetic experiment.

5 DISCUSSION

5.1 Alternative deltaness criteria

The deltaness criterion defined as minimizing objective function 3 is not the only and probably not the best option. Other formulations of the deltaness criterion have been suggested and used in the inverse theory literature (Backus and Gilbert, 1968; Aki and Richards, 1980; Parker, 1994; Aster et al., 2012).

The focused fields shown in Figure 5 illustrate a possible motivation for trying other deltaness criteria. Even though our method shows a better spatial focus in Figure 5a compared to TR in Figure 5b, energy is present around the focus in the side lobes.

To reduce this side energy, we can use an objective function in which energy at distances farther away from the focusing target is penalized. One such objective function suggested by (Backus and Gilbert, 1968) is

$$W = \int (\mathbf{r} - \mathbf{r}_f)^2 \, |u(\mathbf{r}, \omega)|^2 \, d\mathbf{r}, \tag{10}$$

subject to the constraint

$$\int |u(\mathbf{r}, \omega)| \, d\mathbf{r} = 1, \tag{11}$$

where the weight factor $(\mathbf{r} - \mathbf{r}_f)^2$ in the integrand of expression 10 is responsible for penalizing the side energy. Note that depending on the specific requirements of a wave focusing problem, other weight factors can also be used. Minimizing the energy in the side lobes could be essential for some applications of wave focusing, e.g., in imaging. In other applications such as microseismic event location it might not be as important.

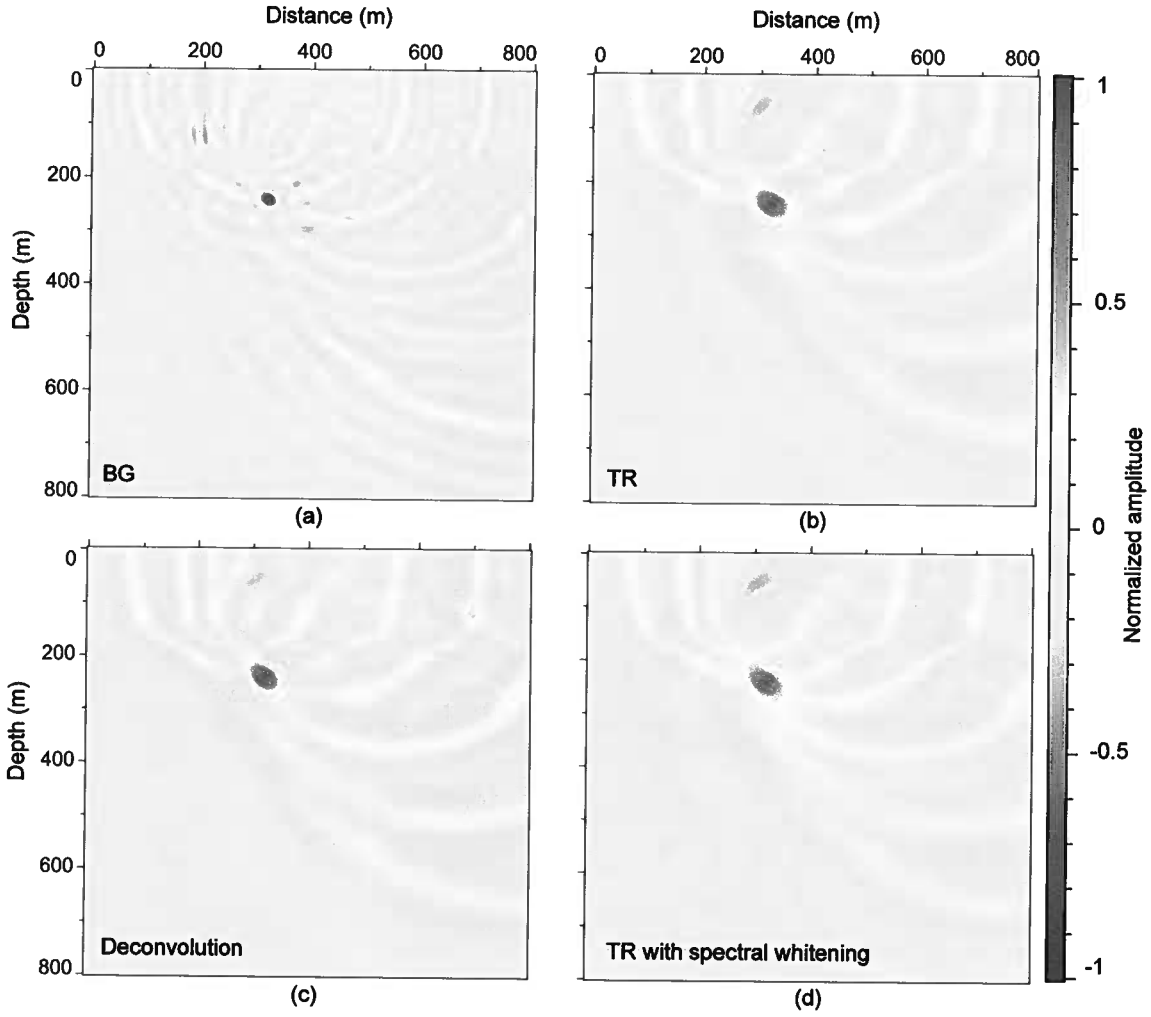

Figure 5. Results of the numerical focusing experiment of section 4 using noise-free data. The plots show the snapshots of propagating wavefields at the time of focus for (a) BG (the proposed method), (b) time-reversal, (c) deconvolution , and (d) time-reversal with spectral whitening.

5.2 Application in imaging

The Backus and Gilbert method presented in this paper to enhance focusing can also be used to enhance reverse-time-migration (RTM) imaging. Here, we show how the two ideas are connected and propose a method to combine them.

In the space-time domain, RTM is formulated as

$$\mathbf{m}_{mig}(\mathbf{r}) = \int [g(\mathbf{r}_g, \mathbf{r}, -t) * d(\mathbf{r}_g, \mathbf{r}_s, t)] \otimes_{t=0} [w(t) * g(\mathbf{r}, \mathbf{r}_s, t)]\, dg, \qquad (12)$$

where subscripts s and g stand for source and receiver, respectively, $\otimes|_{t=0}$ denotes the zero-lag cross-correlation, $\mathbf{m}_{mig}(\mathbf{r})$ represents the reflectivity distribution perturbed from the background medium, $g(\mathbf{r}, \mathbf{r}_s, t)$ denotes the Greens function for a specified background medium with a source at $\mathbf{r}_s$ and a receiver at $\mathbf{r}$, and $d(\mathbf{r}_g, \mathbf{r}_s, t)$ is the reflected wave recorded by the geophone at $\mathbf{r}_g$ due to a source with wavelet $w(t)$ shot at $\mathbf{r}_s$. The integration is over the data-space geophone variable denoted by $\mathbf{r}_g$.

By rearranging equation 12, Schuster (2002) introduces generalized diffraction-stack migration as an alternative implementation and interpretation of RTM. In generalized diffraction-stack migration, the migration image $\mathbf{m}_{mig}(\mathbf{r})$ can be interpreted as the zero-lag cross-correlation of the shot gather data $d(\mathbf{r}_g, \mathbf{r}_s, t)$ with a focusing kernel defined as

$$f(\mathbf{r}_s, \mathbf{r}, \mathbf{r}_g, t) = g(\mathbf{r}_g, \mathbf{r}, t) * w(t) * g(\mathbf{r}, \mathbf{r}_s, t). \qquad (13)$$

We show in Appendix A that, using a method similar to that described in section 2, we can optimize the focusing kernel 13 for each shot and for specific targets

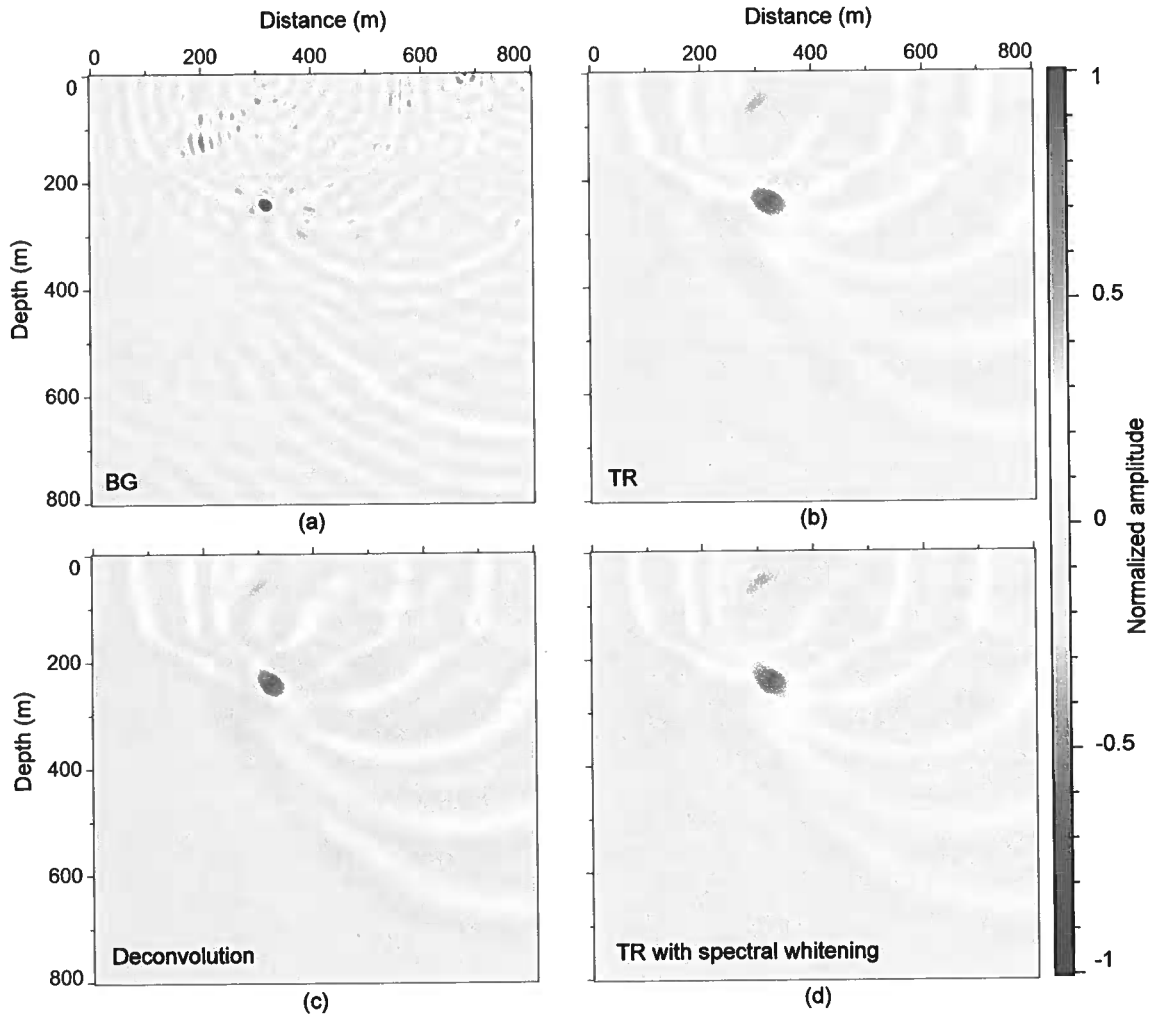

Figure 6. Same results as in Figure 5 for the same data plus bandlimited noise to simulate a microseismic location experiment. The plots show the snapshots of propagating wavefields at the time of focus for (a) BG (the proposed method), (b) time-reversal, (c) deconvolution, and (d) time-reversal with spectral whitening.

in the image. Using an optimized focusing kernel in implementation of the generalized diffraction-stack migration could enhance the resolution of the migration image and reduce the acquisition foot print in the image.

Least-Squares Migration (Nemeth et al., 1999) is an effective imaging method that deals with imaging problems resulting from imperfect acquisition. In this respect, one interesting question to address is how the proposed optimized generalized-diffraction stack migration scheme compares with the least-squares migration.

5.3 Application in microseismic event location

Locating seismic sources is an important problem in earthquake seismology and microseismic monitoring (Rentsch et al., 2007). Techniques based on time-reversal focusing are commonly used in seismology for event location (Larmat et al., 2010). Therefore, the effectiveness of such techniques is bounded by the same issues that limit the efficacy of TR focusing, i.e., diffraction limit, attenuation, and imperfect acquisition.

For this reason, the BG methodology proposed to enhance TR focusing can be particularly useful in source-location applications. For example, note that $g(\mathbf{r}_f, \mathbf{r}_i, \omega)$ in equation 6 is the impulse response of a source at $\mathbf{r}_i$ recorded at $\mathbf{r}_f$, and reciprocity implies that $g(\mathbf{r}_f, \mathbf{r}_i, \omega) = g(\mathbf{r}_i, \mathbf{r}_f, \omega)$. In the context of seismic event location, the Green's function $g(\mathbf{r}_i, \mathbf{r}_f, t)$ represents the microseismic or earthquake data recorded in the field at each receiver location.

The presence of noise in field data is an important matter that needs careful attention in applying BG focusing to event location. With noisy data, equation 4

must be modified as

$$\Gamma \mathbf{a} = \mathbf{g}^* + \boldsymbol{\eta}, \tag{14}$$

where $\boldsymbol{\eta}$ denotes the noise vector. In this case, Γ must be computed according to equation 5 using a velocity model, which is ideally accurate, and $\mathbf{g}$ represents the data measured in the field, so it does not need the velocity model. Even when the velocity model is not accurate, using the Γ matrix computed based on this inaccurate velocity is better than ignoring it altogether as is done the case in time-reversal. The stability of the solution $\mathbf{a}$ in equation 14 depends on the condition number of the Gram matrix Γ, which itself depends on the configuration of the receivers (injection points) and the medium.

Figure 3b shows the condition number of Γ as functions of frequency for the synthetic example of section 4. For the particular configuration and velocity model of this experiment, Γ is well-conditioned for most frequencies in the signal bandwidth (see Figure 3b). Only at the low and high ends of the signal bandwidth, where the amplitude of the frequencies approach zero, does the condition number of Γ increase. Therefore, here, the system of equations 14 is relatively stable and robust in the presence noise (for this particular experiment). In general, however, a combination of some sort of regularization and alternative deltaness criteria (section 5.1) might be used to stabilize equation 14.

We repeat the synthetic experiments of section 4 for data contaminated with bandlimited white noise with an rms signal-to-noise ratio of 5. The added noise in these experiments has the same bandwidth as the data. For real experiments, such as microseismic monitoring, a signal-to-noise ratio of 5 is rather high, but note that, in such experiments, the number of receivers is usually significantly larger than the number used in our synthetic example and this increase in the number of receivers improves the overall signal-to-noise ratio. Figures 6a, b, c, and d show snapshots of the focused wavefields produced by BG, TR, deconvolution, and TR with spectral whitening, respectively.

Comparison of the focused wavefields created by different focusing methods using noise-free and noisy data in Figures 5 and 6 reveals that the BG method can focus just as well in the presence of noise. Although, other methods are less sensitive to noise. Note the increase of side lobe energy in the result of BG focusing in Figure 6a compared to Figure 5a. The other three methods have produced almost the same focusing results for data with and without noise.

Another important consideration related to applying the BG focusing method to microseismic event location is the source mechanism. In the numerical examples shown in this paper, we have assumed a point source with an isotropic radiation pattern. The source mechanism for a microseismic event is, however, a double couple with its characteristic radiation pattern for both P and S waves. Therefore, it is more appropriate to use a deltaness criterion that takes assumed features of the source mechanism for microseismic events into account. The BG focusing technique can also be used for determining the optimal way to process and combine all different components of recorded microseismic data in order to achieve more accurate results in microseismic monitoring.

6 CONCLUSION

The ability of time-reversal (TR) methods to focus wave fields inside heterogeneous media is bounded by limitations caused by imperfect acquisition, attenuation, and the diffraction limit. To go beyond these limitations, we present a solution by formulating wave focusing as an optimization problem. Solving this optimization problem gives the needed signals for transmission to the medium to get the best focus. These signals are optimized for the configuration of the injection points, velocity of the medium, and the focusing target.

Our numerical tests show that the Backus and Gilbert (BG) approach is capable of achieving a significantly more compact focus compared to that of other common focusing techniques (e.g., TR, deconvolution, and TR with spectral whitening) but it can be more sensitive to noise.

The BG methodology can find application in key areas of geophysics. The resolution of RTM imaging can be enhanced by optimizing the focusing kernel of RTM. Another important application is improving the precision of earthquake or microseismic event location. Although the basic concepts of BG focusing are presented in this paper, certain modifications might be required on a case-by-case basis to customize the method for different applications.

7 ACKNOWLEDGEMENTS

We thank Simon Luo for the wave propagation code used to produce the results in this paper, and Diane Witters and Ken Larner for instructions on revision and editing. The software used to produce the results in the paper was written in Java with the use of libraries in the Mines Java Toolkit. This research was supported by the sponsors of the Center for Wave Phenomena at the Colorado School of Mines.

REFERENCES

Aki, K., and P. Richards, 1980, Quantitative seismology theory and methods: Freeman and Company.

Aster, R., B. Borchers, and C. Thurber, 2012, Parameter estimation and inverse problems second edition: Academic Press.

Aubry, J. F., M. Tanter, J. Gerber, J. L. Thomas, and M. Fink, 2001, Optimal focusing by spatio-temporal inverse filter. ii. experiments. application to focusing through absorbing and reverberating media: The Journal of the Acoustical Society of America, **110**, 48–58.

Backus, G., and F. Gilbert, 1968, The resolving power of gross earth data: Geophysical Journal of the Royal Astronomical Society, **16**, 169–205.

Behura, J., K. Wapenaar, and R. Snieder, 2012, Newton-marchenko-rose imaging: Image reconstruction based on inverse scattering theory: Technical Report CWP-720, Center for Wave Phenomena, Colorado School of Mines.

Berkhout, A., 1997, Pushing the limits of seismic imaging, part i: Prestack migration in terms of double dynamic focusing: Geophysics, **62**, 937–954.

Blomgren, P., G. Papanicolaou, and H. Zhao, 2002, Super-resolution in time-reversal acoustics: The Journal of the Acoustical Society of America, **111**, 230–248.

Broggini, F., R. Snieder, and K. Wapenaar, 2012, Focusing the wavefield inside an unknown 1d medium: Beyond seismic interferometry: Geophysics, **77**, A25–A28.

Fink, M., 1997, Time-reversed acoustics: Physics Today, **50**, 30–34.

———, 2006, Time-reversal acoustics in complex environments: Geophysics, **71**, 151–164.

———, 2008, Time-reversal waves and super resolution: Journal of Physics:Conference Series, **124**, 1–29.

Fink, M., W. Kuperman, J. Montagner, and A. Tourin, 2002, Imaging of complex media with acoustic and seismic waves: Springer-Verlag.

Haddadin, O., and E. S. Ebbini, 1998, Ultrasonic focusing through inhomogeneous media by application of the inverse scattering problem: Journal of the Acoustical Society of America, **104**, 313–325.

Larmat, C., R. A. Guyer, and P. A. Johnson, 2010, Time-reversal methods in geophysics: Physics Today, **63**, 31–35.

Larmat, C., J. Montagner, M. Fink, and Y. Capdeville, 2006, Time-reversal imaging of seismic sources and application to the great sumatra earthquake: Geophysical Research Letters, **33**, L19312.

Lu, R., 2002, Time reversed acoustics and applications to earthquake location and salt dome flank imaging: PhD Thesis, Massachusetts Institute of Technology.

Lu, R., and M. E. Willis, 2008, Locating microseismic events with time reversed acoustics: A synthetic case study: SEG Technical Program Expanded Abstracts, 1342–1346.

McMechan, G. A., 1982, Determination of source parameters by wavefield extrapolation: Geophysical Journal of the Royal Astronomical Society, **71**, 613–628.

———, 1983, Migration by extrapolation of time-dependent boundary values: Geophysical Prospecting, **31**, 413–420.

Montaldo, G., M. Tanter, and M. Fink, 2003, Real time inverse filter focusing through iterative time reversal: The Journal of the Acoustical Society of America, **115**, 768–775.

Nemeth, T., C. Wu, and J. T. Schuster, 1999, Least-squares migration of incomplete reflection data: Geophysics, **64**, 208–221.

Parker, R., 1994, Geophysical inverse theory: Princeton University Press.

Parvulescu, A., 1961, Signal detection in a multipath medium by m.e.s.s. processing: The Journal of the Acoustical Society of America, **33**, 1674.

Rentsch, S., S. Buske, S. Luth, and A. Shapiro, 2007, Fast location of seismicity: A migration-type approach with application to hydraulic-fracturing data: Geophysics, **72**, S33–S40.

Robert, J., and M. Fink, 2008, Greens function estimation in speckle using the decomposition of the time reversal operator: Application to aberration correction in medical imaging: The Journal of the Acoustical Society of America, **123**, 866–877.

Schuster, J. T., 2002, Reverse-time migration = generalized diffraction stack migration: 72nd Annual International Meeting, SEG, Expanded Abstracts, 1280–1283.

Schuster, J. T., S. Hanafy, and Y. Huang, 2012, Theory and feasibility tests for a seismic scanning tunnelling macroscope: Geophysical Journal International, **190**, 1593–1606.

Shapiro, S. A., 2008, Microseismicity a tool for reservoir characterization: EAEG.

Snieder, R., 2004, A guided tour of mathematical methods for the physical sciences, 2nd ed.: Cambridge Univ. Press.

Tanter, C., J. L. Thomas, and M. Fink, 2000, Time reversal and inverse filter: Journal of the Acoustical Society of America, **108**, 223–234.

Tanter, M., J. F. Aubry, J. Gerber, J. Thomas, and M. Fink, 2001, Optimal focusing by spatio-temporal inverse filter. i. basic principles: The Journal of the Acoustical Society of America, **110**, 37–47.

Ulrich, T., B. Anderson, C. Le Bas, P.-Y. Payan, J. Douma, and R. Snieder, 2012, Improving time reversal focusing through deconvolution: 20 questions: Proc. of Meetings on Acoustics, **16**, 045015.

Vellekoop, I., A. Lagendijk, and A. Mosk, 2010, Exploiting disorder for perfect focusing: Nature Photonics, **4**, 320–322.

Xuan, R., and P. Sava, 2010, Probabilistic microearthquake location for reservoir monitoring: Geophysics, **75**, MA9–MA26.

APPENDIX A: OPTIMIZATION OF THE RTM FOCUSING KERNEL

We use the Backus and Gilbert method to optimize the RTM focusing kernel (see section 5.2) for each receiver in a shot gather for a specific target in the model space.

For weak scattering, the scattered data recorded at receiver location $\mathbf{r}_g$ with a source at $\mathbf{r}_s$ can be written in the frequency domain in terms of the Born approximation to the Lippmann-Schwinger equation (Schuster, 2002):

$$d(\mathbf{r}_g, \mathbf{r}_s) = \int G(\mathbf{r}_g, \mathbf{r})\, W\, G(\mathbf{r}, \mathbf{r}_s)\, \mathbf{m}(\mathbf{r})\, d\mathbf{r}, \qquad \text{(A1)}$$

where $G(\mathbf{r}_g, \mathbf{r})$ is the Green's function for the Helmholtz equation for a specified background medium with a source at $\mathbf{r}$ and receiver at $\mathbf{r}_g$, $G(\mathbf{r}, \mathbf{r}_s)$ is the Green's function for the same medium with a source at $\mathbf{r}_s$ and receiver at $\mathbf{r}$, $\mathbf{m}(\mathbf{r})$ represents the reflectivity distribution perturbed from the background, and W represents the source wavelet function. The integration is over the model space.

Using RTM equation 12 written in the frequency domain for N geophones at locations $\mathbf{r}_{g_i}$ where $i = 1, 2, ..., N$, the reflectivity value at a target location $\mathbf{r}_f$ can be expressed as a weighted sum of data

$$\mathbf{m}_{mig}(\mathbf{r}_f) = \sum_{i=1}^{N} a_i\, d(\mathbf{r}_{g_i}, \mathbf{r}_s), \qquad \text{(A2)}$$

where the complex weights a_i are

$$a_i = G^*(\mathbf{r}_{g_i}, \mathbf{r}_f)\, W^*\, G^*(\mathbf{r}_f, \mathbf{r}_s), \quad i = 1, 2, ..., N. \qquad \text{(A3)}$$

Note that a_i in A3 is the complex conjugate of the RTM focusing kernel defined in equation 13.

Inserting $d(\mathbf{r}_g, \mathbf{r}_s)$ from A1 into A2 and changing the order of integration and summation gives

$$\mathbf{m}_{mig}(\mathbf{r}_f) = \int [\sum_{i=1}^{N} a_i\, G(\mathbf{r}_{g_i}, \mathbf{r})\, W\, G(\mathbf{r}, \mathbf{r}_s)]\, \mathbf{m}(\mathbf{r})\, d\mathbf{r}. \qquad \text{(A4)}$$

The bracketed factor in A4 is an averaging kernel that we would ideally like to closely approximate a Dirac delta function with spatial support at $\mathbf{r}_f$, i.e.,

$$\sum_{i=1}^{N} a_i\, G(\mathbf{r}_{g_i}, \mathbf{r})\, W\, G(\mathbf{r}, \mathbf{r}_s) \rightarrow \delta(\mathbf{r} - \mathbf{r}_f). \qquad \text{(A5)}$$

Our goal here is to determine new coefficients a_i' (instead of a_i defined in A3) such that the deltaness criterion A5 is satisfied as closely as possible. This goal can be achieved, for example, by minimizing an objective function of the form

$$J = \int |\sum_{i=1}^{N} a_i'\, G(\mathbf{r}_{g_i}, \mathbf{r})\, W\, G(\mathbf{r}, \mathbf{r}_s) - \delta(\mathbf{r} - \mathbf{r}_f)|^2 d\mathbf{r}, \qquad \text{(A6)}$$

where the integration is carried out over the model space.

Minimizing A6 gives a linear system of the form

$$\Gamma \mathbf{a}' = \mathbf{a}, \qquad \text{(A7)}$$

where Γ is an $N \times N$ matrix with elements

$$\Gamma_{ij} = \int G(\mathbf{r}_{g_i}, \mathbf{r})\, G^*(\mathbf{r}_{g_j}, \mathbf{r})\, G(\mathbf{r}, \mathbf{r}_s)\, G^*(\mathbf{r}, \mathbf{r}_s)\, d\mathbf{r}, \quad i, j = 1, 2..., N, \qquad \text{(A8)}$$

and $\mathbf{a}$ is an $N \times 1$ vector with elements defined in A3.

Solving equation A7 gives the $N \times 1$ vector $\mathbf{a}'$ of optimized kernels that can be used as enhanced migration focusing kernels in generalized diffraction-stack migration.

3D synthetic aperture and steering for controlled-source electromagnetics

Allison Knaak[1], Roel Snieder[1], Yuanzhong Fan[2], & David Ramirez-Mejia[2]

[1] *Center for Wave Phenomena, Colorado School of Mines, Golden, CO, USA*
[2] *Shell International Exploration & Production, Houston, TX, USA*

ABSTRACT

Controlled-source electromagnetics (CSEM) is a geophysical electromagnetic method used to detect hydrocarbon reservoirs in marine settings. Used mainly as a derisking tool by the industry, the applicability of CSEM is limited by the size of the target, low-spatial resolution, and depth of the reservoir. Synthetic aperture, a technique that increases the size of the source by combining multiple individual sources, has been applied to CSEM fields to increase the detectability of hydrocarbon reservoirs. We apply synthetic aperture to a 3D synthetic CSEM field with a 2D source distribution to evaluate the benefits of the technique. The 2D source allows for steering in the inline and crossline directions. We present an optimized beamforming of the 2D source which increases the detectability of the reservoir. With only a portion of three towlines spaced 2km apart, we enhance the anomaly from the target by 80%. We also demonstrate the benefits of using the Poynting vector to view CSEM fields in 3D. Synthetic aperture, beamforming, and Poynting vectors are tools that will increase the amount of information gained from CSEM survey data.

Key words: synthetic aperture, steering, CSEM

1 INTRODUCTION

Controlled-source electromagnetics (CSEM) is a geophysical electromagnetic method used for detecting hydrocarbon reservoirs in marine settings. First developed in academia in the 1970s, a CSEM survey involves towing a horizontal antenna just above the seafloor, where electromagnetic receivers are placed. The oil industry has used CSEM for almost two decades as a derisking tool in the exploration of hydrocarbon reservoirs (Constable and Srnka, 2007; Edwards, 2005; Constable, 2010). CSEM is often used in conjunction with other geophysical methods such as seismic but it has limitations that prevent it from gaining more widespread use in industry. The limitations come from the fact that the electromagnetic field in CSEM is a predominantly diffusive field. For the reservoir to be detectable, the lateral extent of the reservoir must be large enough compared to the depth of burial, and enough of the weak signal from the reservoir must reach the receivers (Constable and Srnka, 2007; Fan et al., 2010). Also compared to seismic methods, the spatial resolution of CSEM is low (Constable, 2010).

These drawbacks prompted an investigation of how to improve the signal received from the reservoir through synthetic aperture, a method developed for radar and sonar that constructs a larger virtual source by using the interference of fields created by different sources (Barber, 1985; Bellettini and Pinto, 2002). Fan et al. (2010) demonstrate for a 1D array of sources that the wave-based concept of synthetic aperture sources can also be applied to CSEM fields and that it can be used to improve the detectability of reservoirs. The similarities in the frequency-domain expressions of diffusive and wave fields show that a diffusive field at a single frequency does have a specific direction of propagation (Fan et al., 2010). Synthetic aperture allows for the use of beamforming, a technique used to create a directional transmission from a source or sensor array (see Van Veen and Buckley, 1988). One can apply the basic principles of phase shifts and addition to electromagnetic fields to

change the direction in which the energy moves. The shifts create constructive and destructive interference between the energy propagating in the field which, with a CSEM field, can increase the illumination of the reservoir (Fan et al., 2012). Manipulating diffusive fields by using interference is not necessarily new; physicists have previously used the interference of diffusive fields for a variety of applications (Yodh and Chance, 1995; Wang and Mandelis, 1999). Fan et al. (2010) applied the concepts of synthetic aperture and beamforming to CSEM fields with one line of sources. They demonstrated the advantages of synthetic aperture steering and focusing to CSEM fields; the main improvement is to the detectability of targets shallower and deeper than the typical range of depths for CSEM.

In this paper, we introduce the concept of 3D synthetic aperture for electromagnetic fields; the source distribution is expanded from sources along a line to 2D with multiple parallel lines allowing the fields to be steered in 3D. We also briefly discuss a visualization tool to view 3D electromagnetic fields.

2 MATHEMATICAL BASIS

Fan et al. (2010) first applied synthetic aperture to controlled-source electromagnetic fields with one line of sources. Synthetic aperture was used earlier for radar, sonar, medical imaging, and other applications (Barber, 1985; Bellettini and Pinto, 2002; Jensen et al., 2006). One reason synthetic aperture, a wave-based concept, has not been previously applied to CSEM fields is that it was assumed diffusive fields could not be steered because they have no direction of propagation (Mandelis, 2000). Fan et al. (2010) showed that the 3D scalar diffusion equation has a plane wave solution at a single frequency with a defined direction of propagation which allows the direction of the field to be manipulated by synthetic aperture. The equation for synthetic aperture is given by

$$S(\mathbf{r},\omega) = \iint\limits_{sources} e^{-A(\mathbf{s})} e^{-i\Delta\Psi(\mathbf{s})} F(\mathbf{r},\mathbf{s},\omega) d\mathbf{s}, \quad (1)$$

where, for each source $\mathbf{s}$, $\Delta\Psi$ is a phase shift and A is an energy compensation coefficient. $F(\mathbf{r},\mathbf{s},\omega)$ is a general field; it could any component the electric or magnetic field at receiver $\mathbf{r}$ and source $\mathbf{s}$. For a plane wave synthetic aperture source, the field is steered by applying a phase shift and energy compensation terms defined by

$$\Delta\Psi(\mathbf{s}) = k(\hat{\mathbf{n}} \cdot \boldsymbol{\Delta}\mathbf{s}) \quad (2)$$

$$\hat{\mathbf{n}} = \begin{pmatrix} \cos\varphi \sin\theta \\ \sin\varphi \sin\theta \\ \cos\theta \end{pmatrix} \quad (3)$$

$$A(\mathbf{s}) = k(\boldsymbol{\Delta}\mathbf{s} \cdot \mathbf{a}) \quad (4)$$

The shift $\Delta\Psi(\mathbf{s})$ is a function of the wavenumber, the steering angle $\hat{\mathbf{n}}$, and a location vector $\boldsymbol{\Delta}\mathbf{s}$. The unit vector $\hat{\mathbf{n}}$ in equation 3 defines the steering direction of the phase shift which is controlled by angles θ and φ. The dip of the direction of the steering angle, represented by θ, is measured with respect to the vertical. The angle φ represents the azimuthal direction. The quantity $\boldsymbol{\Delta}\mathbf{s} = \mathbf{s_n} - \mathbf{s_1}$ is the relative location of an individual source $\mathbf{s_n}$ and the source defined to be at the bottom left corner of the survey footprint $\mathbf{s_1}$. The energy compensation term $A(\mathbf{s})$ in equation 4 is the dot product of the distances in $\boldsymbol{\Delta}\mathbf{s}$ and the vector $\mathbf{a}$ which is composed of $[a_i \ a_c \ a_d]$. These three values define the weighting components for the inline direction, crossline direction, and depth, respectively.

In a traditional CSEM survey one tows a source along parallel lines (inline direction) over receivers on the seafloor; the source and receiver geometry in the examples in this paper follow the traditional design (Constable and Srnka, 2007). The exponential weighting (equation 4) equalizes the amplitudes and creates interference needed to steer diffusive fields; other methods of weighting exist (Fan et al., 2012). For a homogeneous medium, the phase shift and energy compensation term are set to be equal because the decay of the field is proportional to the phase shift, and the attenuation coefficient in equation 1 is equal to the wave number (Fan et al., 2011). For a realistic CSEM field, the background is heterogeneous and the phase shift and energy compensation terms are not equal. In this case, the energy compensation term accounts for the diffusive loss, decreases the background field to create a window to view the secondary field, and equalizes the interfering fields to create destructive interference (Fan et al., 2011, 2012).

The proper choice for the energy compensation term and the phase shift for a CSEM field are determined by maximizing a quantity of the CSEM field that indicates the presence of a reservoir. For this paper, we choose to use the ratio of the absolute value of the inline component of the electric field with and without the reservoir; we call this value the *detectability ratio*. This measure is commonly used in industry to quantify the anomaly from hydrocarbon reservoirs (Constable and Srnka, 2007). In future research, we will investigate other types of metrics for the quality of the synthetic aperture source. The optimization of the steering parameters of the synthetic aperture source finds the values of four parameters: θ, ϕ, a_i, a_c that control steering. The a_d component of the weighting term is not included because the depth component of $\boldsymbol{\Delta}\mathbf{s}$ is zero for this survey; if sources in a survey are located at different depth then this term becomes relevant. We selected a range for each variable and combinations of the parameters were put into the steering equation until the combination was found that produced the maximum average detectability ratio between the inline component of the electric

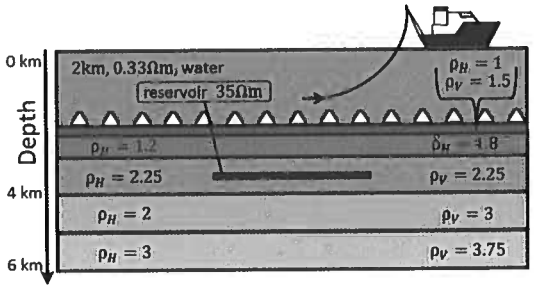

Figure 1. The model used to create the synthetic CSEM data. The values of ρ_H and ρ_V are the resistivity of the layer in the horizontal and vertical direction respectively given in Ohm-meters.

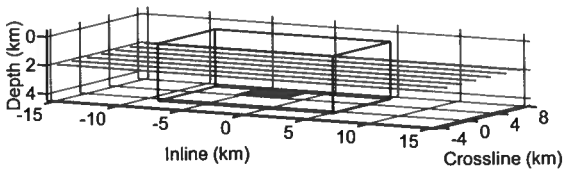

Figure 2. The geometry of the CSEM survey for the synthetic data. The seven tow lines are shown as black lines. The reservoir is the black rectangle. The coverage of the sampling points is outlined by the 3D box.

field with a reservoir and the field without a reservoir. The outcome from the steering and optimization is discussed in the next section.

3 NUMERICAL EXAMPLES

We use synthetic controlled-source electromagnetic fields to demonstrate the benefits of steering with 3D synthetic aperture. We computed a synthetic dataset using a code from the CEMI group at University of Utah (Hursán and Zhdanov, 2002). The synthetic data contains all three components of both the electric and magnetic fields. The model contains seven towlines 2km apart and 15km long over a 4km x 4km x 50m reservoir located at 3.5km depth. All of the parameters are within the ranges for a typical CSEM survey. The source is a 300m horizontal dipole with a frequency of 0.2Hz. The resistivity of the earth model varies with depth and direction; the model is shown in Figure 1. The reservoir has a resistance of 35Ωm. Because of the large water depth (2km), the airwave is weak at the acquisition level (sea bottom). The fields are sampled at points on the seafloor and at several depths in the subsurface. The sampling points in the subsurface give information about the flow of energy around and near the reservoir. The points span -7km to 7km in the inline direction and -4km to 4km in the crossline direction spaced every 250m. In depth, the sample points range from 0km to 4km and occur at a sampling interval of 200m. Figure 2 displays the survey geometry.

We create a 2D synthetic aperture source to demonstrate inline and crossline steering. The source extends from -6.6km to -1.8km in the inline direction and is 4km wide in the crossline direction. The individual sources are sparsely spaced in the crossline direction, 2km apart, and more densely spaced in the inline direction, 300m apart. The choice of location of the 2D source region is offset from the reservoir to test the strength of the inline and crossline steering. The optimization discussed above finds the optimum steering angles θ and φ and two components of the energy compensation terms a_i and a_c. For these examples, the range of the steering angles θ and ϕ is from zero to $\pi/2$. The range for the energy compensation terms, a_i and a_c is zero to one. The increase in the detectability of the reservoir needs to occur over an area, not just a single point, to ensure the signal is recorded by a receiver placed in the region of interest. We include this spatial requirement by defining an area where we would expect to find the anomaly from the reservoir. We use the detectability ratio of a single source located in the middle of our proposed 2D source to determine the area of expected increased anomaly. Then the detectability ratio in the defined area is averaged and the maximum average detectability ratio defines the best steering. We defined the area of expected increased anomaly to be 0km to 4km in the inline and crossline direction for this synthetic model (the dashed box in Figure 3).

The maximum average detectability ratio in that area results in these values for the specified 2D source: $\theta = 64°$, $\varphi = 83°$, $a_i = 0.125$, $a_c = 0.875$. The steering angles are reasonable for the geometry of the source relative to the reservoir in that the steered source sends the energy down and toward the energy. Figure 3 depicts the detectability ratio of the inline electric field with and without the reservoir at the sea floor for a single source (panel a), an unsteered 2D synthetic aperture source (panel b), and a steered 2D synthetic aperture source (panel c). The average detectability ratio between the field with and without the reservoir for a single source (located at -4.5km in the inline direction and -2km in the crossline direction) in the area we expect the anomaly is 1.11 meaning there is a 11% anomaly from the presence of the reservoir. After we apply synthetic aperture to the 2D source the average detectability ratio becomes 1.19. When the 2D synthetic aperture source is steered with the parameters found by the optimization, the average detectability ratio becomes 2.06. This corresponds to a 100% anomaly from the reservoir. From combining and steering sources from parts of three towlines, we increased the detectability of the reservoir from a small indication of its presence to a level where its existence is certain. The maximum of the average ratio between

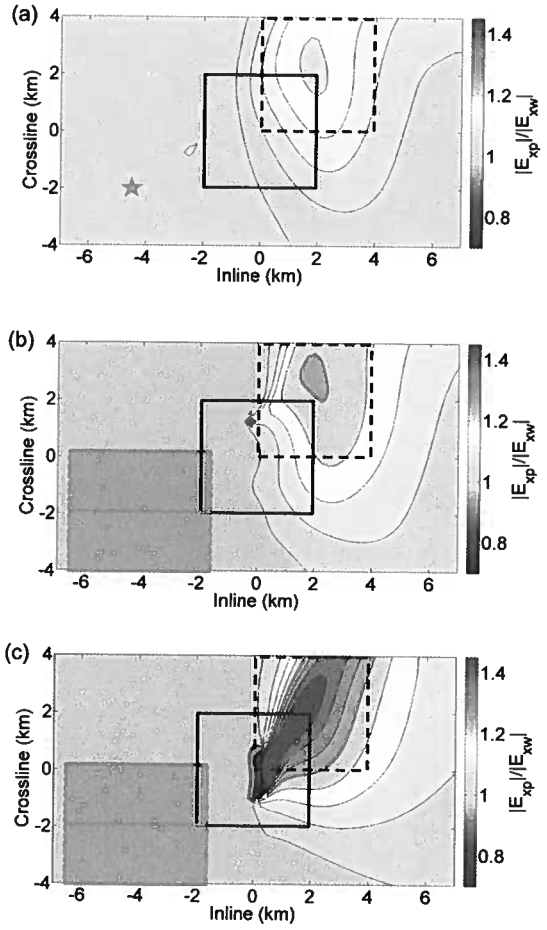

Figure 3. The ratio of the absolute value of the inline electric component for a single source (panel a), a 2D synthetic aperture source (panel b), and a steered 2D synthetic aperture source (panel c). All three images depict the response at receivers located on the ocean floor. The footprint of the reservoir is outlined in black and the source is outlined in red. The area of expected reservoir anomaly is shown as the dashed black box.

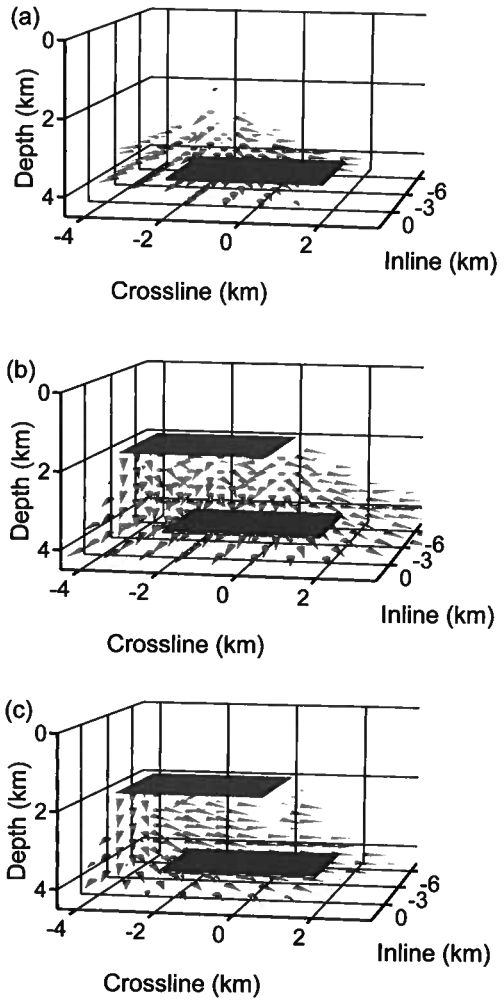

Figure 4. The normalized, time-averaged Poynting vectors with z-component greater than zero for a single source (panel a), a 2D synthetic aperture source (panel b), and a steered 2D synthetic aperture source (panel c). The Poynting vectors from the 2km water layer (including the airwave) have been removed for clarity. All three images depict the footprint of the reservoir in black and the source in blue.

the inline electrical component with and without the reservoir is not the only choice for a measure of the improvement obtained with steering. Future research will focus on developing a more robust optimization scheme possibly including more parameters such as number of sources and placement of sources. Maximizing the average ratio of the inline electric component with and without the reservoir demonstrates the increases in detectability that synthetic aperture can achieve.

4 VISUALIZING STEERED FIELDS IN 3D

To visualize the impact the steering has on the direction of the energy transport, we use the Poynting vector. The most common way to visualize electric and magnetic field is through magnitude and phase plots but these lack the capability to show the direction the field is propagating (Constable, 2010). The Poynting vector measures the direction in which the energy flux of the electromagnetic field is traveling; it is an effective way to examine how an electromagnetic field propagates (Fan et al., 2012). The energy flux density of the electromagnetic field is given by

$$\mathbf{P} = \mathbf{E} \times \mathbf{H}, \tag{5}$$

where $\mathbf{E}$ is the electric field and $\mathbf{H}$ is the magnetic field (Jackson, 1999). For frequency domain fields, the Poynt-

ing vectors must be averaged over time to eliminate the oscillation of the source. The time-averaged Poynting vector is given by (Jackson, 1999)

$$\bar{\mathbf{P}} = 1/2Re(\mathbf{E} \times \mathbf{H}^*). \quad (6)$$

The synthetic CSEM dataset presented in this paper is sampled in three dimensions which enables the Poynting vector of the field to be viewed in 3D as well. The resulting Poynting vector field is too dense to view all of the vectors at once. It is more demonstrative to show the downward propagating field from the source. Figure 4 shows the Poynting vectors with z-component greater than zero for a single source, the 2D synthetic aperture source, and the steered 2D synthetic aperture source. The Poynting vectors from the 2km water layer, which includes the airwave, are not shown to make the subsurface interactions of the field visible. The message of Figure 4 is the difference in direction of the Poynting vectors from the steered source when compared to the other sources. The steered source shifts the energy towards the reservoir in the crossline direction (panel c) while the energy of the single source (panel a) and unsteered 2D synthetic aperture source (panel b) radiate downward and away from the reservoir. Our ability to steer in the crossline direction, shown in Figure 3c, is promising because even though the towlines are sparsely spaced, 2km apart in the crossline direction, we are still able to achieve coherent steering of the energy with just three towlines. The Poynting vectors show an organization in the crossline direction that is not present in the vectors of the other sources. These vectors may assist in refining the optimization by defining the change in the direction of the energy propagating through the reservoir. The Poynting vector is a useful tool to view all parts of the electromagnetic energy propagating through the earth.

5 CONCLUSION

The synthetic aperture technique offers a way to address some of the limitations of CSEM without requiring any changes in acquisition. Applying the technique to synthetic CSEM data demonstrates the possible increase to the detectability of hydrocarbon reservoirs. Steering the fields in both the inline and crossline directions sends more energy toward the reservoir rather than propagating out symmetrically. The implementation of these techniques increases the amount of information gleaned from data acquired from the CSEM survey, making CSEM a more valuable tool for industry. Research is ongoing to optimize the synthetic aperture source and to investigate the implications of synthetic aperture to the design of CSEM surveys.

ACKNOWLEDGMENTS

We are grateful for the financial support from the Shell Gamechanger Program of Shell Research, and thank Shell International Exploration & Production for the permission to publish this work.

References

Barber, B. C., 1985, Review article. theory of digital imaging from orbital synthetic-aperture radar: International Journal of Remote Sensing, **6**, 1009–1057.

Bellettini, A., and M. A. Pinto, 2002, Theoretical accuracy of synthetic aperture sonar micronavigation using a displaced phase-center antenna: IEEE Journal of Oceanic Engineering, **27**, 780–789.

Constable, S., 2010, Ten years of marine CSEM for hydrocarbon exploration: Geophysics, **75**, A67–A81.

Constable, S., and L. J. Srnka, 2007, An introduction to marine controlled-source electromagnetic methods for hydrocarbon exploration: Geophysics, **72**, WA3–WA12.

Edwards, N., 2005, Marine controlled source electromagnetics: Principles, methodologies, future commercial applications: Surveys in Geophysics, **26**, 675–700.

Fan, Y., R. Snieder, E. Slob, J. Hunziker, and J. Singer, 2011, Steering and focusing diffusive fields using synthetic aperture: EPL (Europhysics Letters), **95**, 34006.

Fan, Y., R. Snieder, E. Slob, J. Hunziker, J. Singer, J. Sheiman, and M. Rosenquist, 2010, Synthetic aperture controlled source electromagnetics: Geophysical Research Letters, **37**, L13305.

———, 2012, Increasing the sensitivity of controlled-source electromagnetics with synthetic aperture: Geophysics, **77**, E135–E145.

Hursán, G., and M. Zhdanov, 2002, INTEM3D: www.cemi.utah.edu/soft/index.

Jackson, J. D., 1999, Classical electrodynamics: Wiley.

Jensen, J. A., S. I. Nikolov, K. L. Gammelmark, and M. H. Pedersen, 2006, Synthetic aperture ultrasound imaging: Ultrasonics, **44**, e5–e15.

Mandelis, A., 2000, Diffusion waves and their uses: Physics Today, **53, 8**, 29–34.

Van Veen, B., and K. Buckley, 1988, Beamforming: a versatile approach to spatial filtering: IEEE ASSP Magazine, **5**, 4–24.

Wang, C., and A. Mandelis, 1999, Purely thermal-wave photopyroelectric interferometry: Journal of Applied Physics, **85**, 8366–8377.

Yodh, A., and B. Chance, 1995, Spectroscopy and imaging with diffusing light: Physics Today, **48, 3**, 34–40.

Synthetic aperture Green's function retrieval

Roel Snieder[1], and Kaoru Sawazaki[2]

(1) Center for Wave Phenomena, Colorado School of Mines, Golden CO 80401, email rsnieder@mines.edu
(2) National Research Institute for Earth Science and Disaster Prevention Tsukuba, Japan

ABSTRACT

The cross correlation of noise at two receivers has been used extensively to determine the waves propagating between receivers. This method presumes that noise is incident with equal energy from all directions. In applications when noise is incident from one direction, this leads, in general, to biased estimates of the waves propagating between these receives. We present a method to obtain the true wave velocity from noise propagating in one unknown direction by using three receivers that are not located on a line. Raising the normalized cross correlations of noise recorded at pairs of receivers to appropriately chosen powers is equivalent to projecting the relative location of receivers onto all azimuths over a full circle. By averaging over these azimuths one can retrieve the wave velocity between the receivers and the direction of the propagating noise.

1 INTRODUCTION

The extraction of the earth response from cross correlation of recorded noise has rapidly developed over the last decade. The literature on this topic is extensive, and has been summarized in review papers (Larose et al., 2006; Curtis et al., 2006; Wapenaar et al., 2010a,b; Ritzwoller et al., 2011; Snieder and Larose, 2013), a special issue (Campillo et al., 2011), and books (Wapenaar et al., 2008; Schuster, 2009). The principle that the system response, or Green's function, can be extracted from noise is based on the concept of equipartitioning which states that the noise is either equally distributed over all modes of the system (Lobkis and Weaver, 2001), or that it propagates with equal strength in all directions of propagation (Weaver and Lobkis, 2005). In practice the noise is excited by localized sources, such as storms at the oceans (Stehly et al., 2006), industrial sources (Miyazawa et al., 2008), a concrete dam (O'Connell, 2007), or other sources (Mulargia and Castellaro, 2008; Mulargia, 2012), which violates equipartitioning.

To illustrate the impact of strongly directional noise on Green's function retrieval, we consider the situation where the noise consists of one plane wave with complex spectrum $S(\omega)$ that propagates in the direction of a unit vector $\hat{\mathbf{n}}$ with wave number $k = \omega/c$:

$$u(\mathbf{r},\omega) = S(\omega)e^{ik\hat{\mathbf{n}}\cdot\mathbf{r}} \,, \tag{1}$$

where ω is the angular frequency and c the wave velocity. The cross correlation $\tilde{C}_{12}(\omega)$ of the noise recorded by receivers at locations $\mathbf{r}_1$ and $\mathbf{r}_2$ is given by

$$\tilde{C}_{12}(\omega) = \langle u(\mathbf{r}_1,\omega)u^*(\mathbf{r}_2,\omega)\rangle = \langle |S(\omega)|^2\rangle e^{ik\hat{\mathbf{n}}\cdot(\mathbf{r}_1-\mathbf{r}_2)} \,, \tag{2}$$

where the asterisk denotes complex conjugation, and $\langle\cdots\rangle$ the expectation value. This corresponds to a wave that arrives at time $t_{estimated} = \hat{\mathbf{n}}\cdot(\mathbf{r}_1-\mathbf{r}_2)/c$ instead of the true arrival time $t_{true} = |\mathbf{r}_1-\mathbf{r}_2|/c$. Since $\hat{\mathbf{n}}\cdot(\mathbf{r}_1-\mathbf{r}_2) < |\mathbf{r}_1-\mathbf{r}_2|$ the estimated arrival time is too short, and as a result the estimated velocity is too high. If we knew the direction of wave propagation $\hat{\mathbf{n}}$ we could correct for the bias, but in general this direction is not known.

Several solutions have been proposed to correct for the directional characteristics of noise. The first approach consists of directional filtering of the noise with an array to select the noise that propagates in the desired direction (Curtis and Halliday, 2010). Another approach consists of extracting the coda waves first from cross correlation, and to correlate these coda waves again (Stehly et al., 2008). In this work we present an alternative procedure to extract the correct waves propagating between two receivers when the waves come in from one unknown direction. This procedure is built on the idea that the relative locations between three stations can be projected onto an arbitrary direction. By performing this operation for each direction and integrating over all directions, one can retrieve the wavenumber and direction of propagation of the wave field. We present the theory in section 2 and show a numerical simulation in section 3.

2 THEORY

Consider the geometry of figure 1 with stations at locations $\mathbf{r}_1$, $\mathbf{r}_2$, and $\mathbf{r}_3$. We denote the relative locations of

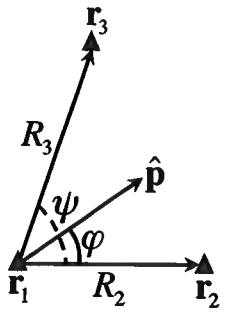

Figure 1. The location of the stations at $\mathbf{r}_1$, $\mathbf{r}_2$ and $\mathbf{r}_3$, the definition of the interstation vectors $\mathbf{R}_2$ and $\mathbf{R}_3$, the angle ψ between these vectors, and the polarization vector $\hat{\mathbf{p}}$ at azimuth φ.

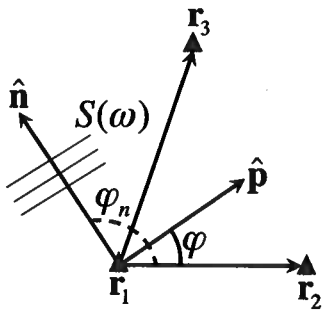

Figure 2. Geometry of figure 1 and the propagation direction $\hat{\mathbf{n}}$ of the propagating noise at azimuth φ_n.

stations 2 and 3 with respect to station 1 by $\mathbf{R}_2 = \mathbf{r}_2 - \mathbf{r}_1$ and $\mathbf{R}_3 = \mathbf{r}_3 - \mathbf{r}_1$, respectively. We denote the angle between these vectors by ψ, see figure 1. The normalized cross correlation of the noise recorded at receivers 2 and 3 with the recorded noise at receiver 1 is defined as $C_{12}(\omega) = \tilde{C}_{12}/|\tilde{C}_{12}|$. With this definition the normalized cross correlation for the noise in expression (1) is given by

$$C_{12}(\omega) = \frac{\langle u(\mathbf{r}_2,\omega)u^*(\mathbf{r}_1,\omega)\rangle}{\langle |u(\mathbf{r}_2,\omega)||u(\mathbf{r}_1,\omega)|\rangle} = e^{ik\hat{\mathbf{n}}\cdot\mathbf{R}_2} ,$$
$$C_{13}(\omega) = \frac{\langle u(\mathbf{r}_3,\omega)u^*(\mathbf{r}_1,\omega)\rangle}{\langle |u(\mathbf{r}_3,\omega)||u(\mathbf{r}_1,\omega)|\rangle} = e^{ik\hat{\mathbf{n}}\cdot\mathbf{R}_3} . \tag{3}$$

Note that in general $\langle fg^*\rangle/\langle |fg|\rangle \neq \langle fg^*/|fg|\rangle$, hence the normalized cross correlation is not the same as the cross coherence.

We define a unit vector $\hat{\mathbf{p}}(\varphi)$ such that it has an azimuth φ relative to the vector $\mathbf{R}_2$, see figure 1. The angle φ can be chosen at will, and in the following we integrate over all values of φ. We assume that the three stations are not located along a line. In that case the vectors $\mathbf{R}_2$ and $\mathbf{R}_3$ are independent, and we can write $\hat{\mathbf{p}}(\varphi)$ as a linear superposition of the vectors $\mathbf{R}_2$ and $\mathbf{R}_3$:

$$R_0\,\hat{\mathbf{p}}(\varphi) = a(\varphi)\mathbf{R}_2 + b(\varphi)\mathbf{R}_3 . \tag{4}$$

The prefactor R_0 ensures that the coefficients $a(\varphi)$ and $b(\varphi)$ are dimensionless. In practice on chooses a value R_0 that is comparable to R_2 and R_3. In the following we suppress in the notation the dependence of the coefficients $a(\varphi)$ and $b(\varphi)$ on the angle φ. Taking the dot product of expression (4) with the vectors $\mathbf{R}_2$ and $\mathbf{R}_3$, respectively, gives using the geometry sketched in figure 1,

$$aR_2 + bR_3\cos\psi = R_0\cos\varphi ,$$
$$aR_2\cos\psi + bR_3 = R_0\cos(\varphi - \psi) . \tag{5}$$

This system of equations has the solution

$$a = \frac{R_0}{R_2}\,\frac{\sin(\psi-\varphi)}{\sin\psi} , \quad b = \frac{R_0}{R_3}\,\frac{\sin\varphi}{\sin\psi} . \tag{6}$$

We next raise C_{12} to the power a and C_{13} to the power b, with expression (3) this gives

$$C_{12}^a C_{13}^b = e^{ik\hat{\mathbf{n}}\cdot(a\mathbf{R}_2 + b\mathbf{R}_3)} = e^{ikR_0\hat{\mathbf{n}}\cdot\hat{\mathbf{p}}(\varphi)} , \tag{7}$$

where equation (4) is used in the last identity. The right hand side has the same phase as would have been measured by the cross coherence of the wave at two stations with separation $R_0\hat{\mathbf{p}}(\varphi)$. We denote the azimuth of the propagating wave with φ_n, see figure 2, so that equation (7) reduces to

$$C_{12}^a C_{13}^b = e^{ikR_0\cos(\varphi-\varphi_n)} , \tag{8}$$

If we knew the direct of propagation φ_n, we could align the unit vector $\hat{\mathbf{p}}$ with this direction by choosing $\varphi = \varphi_n$ and obtain an unbiased estimate of the velocity c. Since we don't know the direction of propagation, we average equation (8) over all angles φ. Restoring the φ-dependence of the coefficients a and b then gives

$$\frac{1}{2\pi}\int_0^{2\pi} C_{12}^{a(\varphi)} C_{13}^{b(\varphi)} d\varphi = \frac{1}{2\pi}\int_0^{2\pi} e^{ikR_0\cos(\varphi-\varphi_n)} d\varphi . \tag{9}$$

Replacing the integration variable $\varphi \rightarrow \varphi + \varphi_n$ yields

$$\frac{1}{2\pi}\int_0^{2\pi} C_{12}^{a(\varphi)} C_{13}^{b(\varphi)} d\varphi = \frac{1}{2\pi}\int_0^{2\pi} e^{ikR_0\cos\varphi} d\varphi$$
$$= J_0(kR_0) , \tag{10}$$

where expression (11.30c) of Arfken and Weber (2001) is used the last identity. Note that expression (10) is independent of the unknown direction φ_n in which the wave propagates.

This approach is similar to the theory derived by Aki (1957) who achieved the angular integration by assuming that uncorrelated noise comes in from all directions with equal amplitude. His ideas formed the basis of what later became known as the SPAC method (Chávez-Garcia and Luzón, 2005; Asten, 2006). One can compute the right hand side of (10) as a function of frequency and tune $k(\omega)$ to fit the measurements. Alternatively one can write the Bessel function as a sum

of Hankel functions and get the sum of the causal and acausal Green's function (equations (19.40) and (19.41) of Snieder (2004)).

3 NUMERICAL EXAMPLE

We present a numerical example using the geometry shown in the top left panel of figure 3. The origin is chosen at the location of sensor 1. The x-axis is aligned with $\mathbf{R}_2$. The stations 2 and 3 are at a distance $R_2 = 20$ km, $R_3 = 30.4$ km, and $\psi = 80.5°$. The top panels are computed for random noise propagating with a velocity $c = 3$ km/s coming in at an azimuth $\varphi_n = 130°$, as shown by the red arrow in panel 3a. The noise has a white spectrum containing frequencies between 0 and 5 Hz. In the example we rather arbitrarily used that $R_0 = 19.73$ km. Panel 3b shows the waveforms of expression (8) after a Fourier transform to the time domain, using $R_0 = 19.7$ km. The dependence of the retrieved waveform in the top right panel show a wave arriving with the dependence $\cos(\varphi - \varphi_n)$ predicted by expression (8). The maximum travel time is obtained for $\varphi = 130°$, which corresponds to the direction of the incoming noise. Panel 3c shows that upon integration over φ one obtains causal and anti-causal waves arriving at times $\pm R_0/c = \pm 6.58$ s. The red curve gives the theoretical superposition of waves coming in from all directions. Note that the extracted waveforms are determined by the angles $\varphi = 130°$ and $\varphi = 310°$ where the travel time is stationary. Panel 3a shows the result of integration over φ in the frequency domain. This gives the Bessel function $J_0(kR_0)$ as predicted by expression (10).

The middle panels 3 show the same as the top panels, except that a number of incoming waves, indicated by the red arrows in panel 3d are incident on the receivers. The spread in the direction of the incoming waves is $\pm 5°$. Panel 3d shows that for low wave numbers the Bessel function is reproduced well, but for larger wave numbers the Bessel function is not reproduced. This is reflected in panels 3ef where the high-frequency components of the waves are not reconstructed.

When two noise trains travel in the same direction they behave as one noise train propagating in the same direction. In appendix A we address the question how large the directional difference between two noise trains can be so that they can be treated as propagating in the same direction as measured by the cross correlation. We derive that this is the case when the angle θ between the direction of propagation of the two noise trains satisfies

$$kR_0\,\theta^2 < \frac{\pi}{2}\,. \tag{11}$$

In this example, the waves deviate 5° from the main direction of propagation, to that the angle between the different directions of propagation is 10°. For this angle and the employed parameters, criterion (11) gives $k < 2.6$ km^{-1}. It is close to this wavenumber that the extracted curve in figure 3e deviates from the Bessel function. The lower panels in figure 3 are for a spread of $\pm 10°$ in incoming waves. Now the Bessel function in panel 3g is only reconstructed for the lowest wave numbers. For a difference in propagation of 20°, criterion (11) predicts that only wave numbers $k < 0.7$ km^{-1} are accurately retrieved. This agrees well with the simulation in panel 3g. Since only the lowest wave numbers are retrieved in this case, only the low frequency components or the waves are obtained in panel 3i.

4 DISCUSSION

The theory presented here make it possible to extract the wavenumber and direction of propagation from directional noise. The central idea is that the relative distance between three receivers can be projected onto a vector with arbitrary direction. This projection can be carried out by raising the normalized cross correlations between the stations to prescribed powers. By doing this for all possible directions, and by integrating over these directions, one obtains the wavenumber and direction of propagation of the noise.

The projection of the correlation onto an arbitrary direction is equivalent to placing two receivers at an arbitrary azimuth with respect to each other. The real receivers are, of course, at fixed locations, hence it is as if one creates an array of two receivers that can rotate over an arbitrary angle. The technique thus creates a synthetic rotating aperture to extract the Green's function, hence the name *synthetic aperture Green's function retrieval.*

The concept is based on the assumption that one plane wave propagates through the region of the three receivers. The numerical simulation of section 3 shows that the theory breaks down when this assumption is violated. The criterion (11) predicts how large an angle between propagating noise components can be handled. There are, however, situations where noise is being generated by a single localized source. Examples of such sources include localized industrial activities (Miyazawa et al., 2008), drill bit noise (Poletto and Miranda, 2004), seismic noise generated by a concrete dam (O'Connell, 2007), and, earthquakes.

REFERENCES

Aki, K., 1957, Space and time spectra of stationary stochastic waves with special reference to microtremors: Bull. of the Earthquake Res. Inst., **35**, 415–456.

Arfken, G., and H. Weber, 2001, Mathematical methods for physicists, 5th ed.: Harcourt.

Asten, M., 2006, On bias and noise in passive seismic

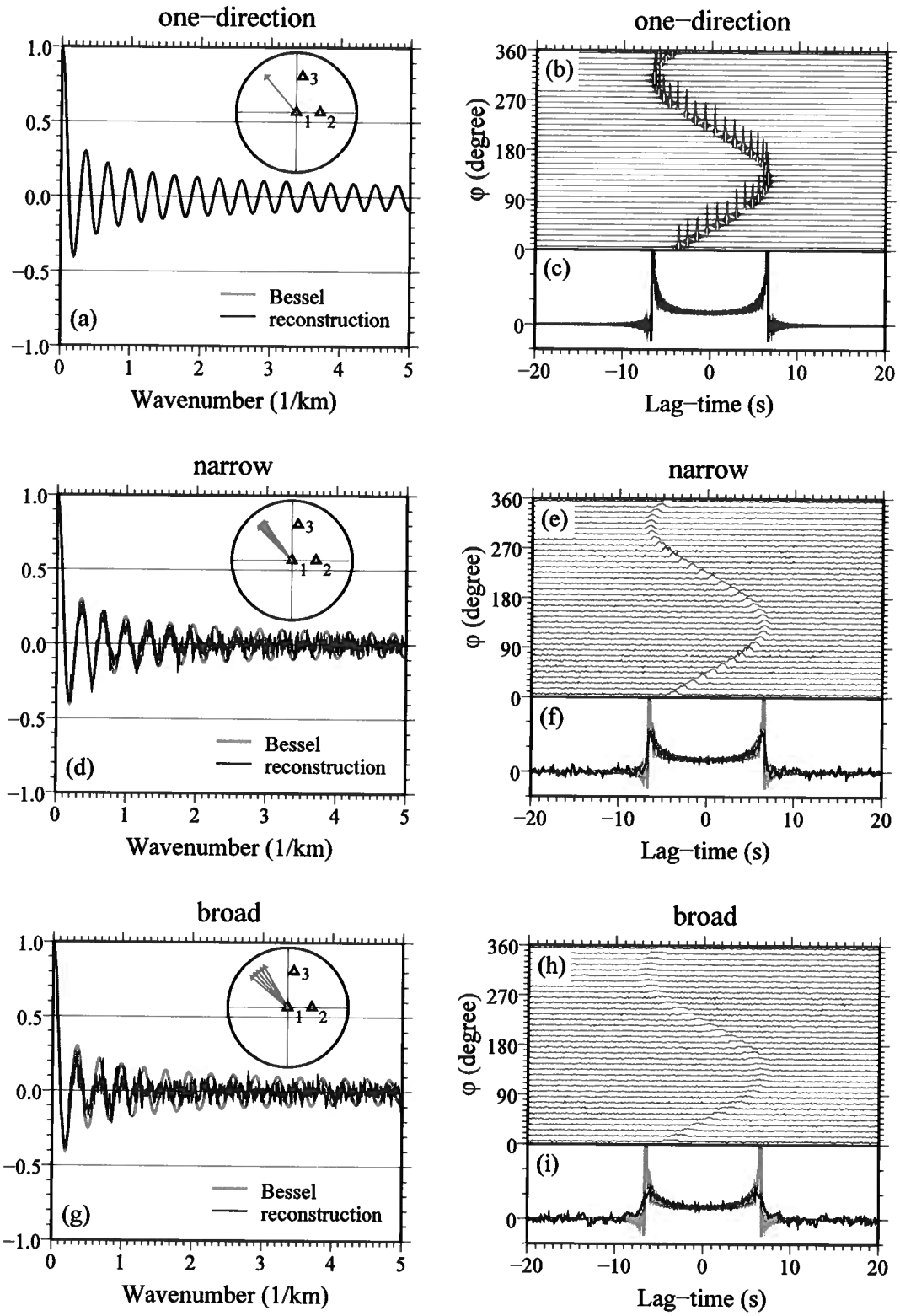

Figure 3. Left panels, the Bessel function $J_0(kR_0)$ (red line) and its reconstruction (black line). the inset in the top right corner gives the directs of the propagating noise (red arrows). Upper right panels, the extracted waves in the time domain as a function of φ, and it's sum over azimuth (black lines in bottom right panels). The red lines in panels c, e, and h, denote the superposition of waves coming in from all directions. Top panels are for one incoming wave, middle panels for waves with a range in azimuth of $\pm 5°$, and bottom panels for waves with a range in azimuth of $\pm 10°$.

data from finite circular array data processed using SPAC methods: Geophysics, **71**, V153–V162.
Campillo, M., H. Sato, N. Shapiro, and R. van der Hilst, 2011, New developments on imaging and monitoring with seismic noise: Comptes Rendus Geoscience, **343**, 487–495.
Chávez-Garcia, F., and F. Luzón, 2005, On the correlation of seismic microtremors: J. Geophys. Res., **110**, B11313, doi:10.1029/2005JB003686.
Curtis, A., P. Gerstoft, H. Sato, R. Snieder, and K. Wapenaar, 2006, Seismic interferometry – turning noise into signal: The Leading Edge, **25**, 1082–1092.
Curtis, A., and D. Halliday, 2010, Directional balancing for seismic and general wavefield interferometry: Geophysics, **75**, SA1–SA14.
Larose, E., L. Margerin, A. Derode, B. van Tiggelen, M. Campillo, N. Shapiro, A. Paul, L. Stehly, and M. Tanter, 2006, Correlation of random wavefields: an interdisciplinary review: Geophysics, **71**, SI11–SI21.
Lobkis, O., and R. Weaver, 2001, On the emergence of the Green's function in the correlations of a diffuse field: J. Acoust. Soc. Am., **110**, 3011–3017.
Miyazawa, M., R. Snieder, and A. Venkataraman, 2008, Application of seismic interferometry to extract P and S wave propagation and observation of shear wave splitting from noise data at Cold Lake, Alberta, Canada: Geophysics, **73**, D35–D40.
Mulargia, F., 2012, The seismic noise wavefield is not diffuse: J. Acoust. Soc. Am., **131**, 2853–2858.
Mulargia, F., and S. Castellaro, 2008, Passive imaging in nondiffusive acoustic wavefields: Phys. Rev. Lett., **100**, 218501.
O'Connell, D. R. H., 2007, Concrete dams as seismic imaging sources: Geophys. Res. Lett., **34**, L20307, doi:10.1029/2007GL031219.
Poletto, F., and F. Miranda, 2004, Seismic while drilling, fundamentals to drill-bit seismic for exploration, *in* Handbook of Geophysical Exploration: Elsevier.
Ritzwoller, M., F.-C. Lin, and W. Shen, 2011, Ambient noise tomography with a large seismic arrays: Comptes Rendus Geoscience, **343**, 558–570.
Schuster, G., 2009, Seismic interferometry: Cambridge Univ. Press.
Snieder, R., 2004, A guided tour of mathematical methods for the physical sciences, 2nd ed.: Cambridge Univ. Press.
Snieder, R., and E. Larose, 2013, Extracting the earth response from noise measurements: Ann. Rev. Earth Planet. Sci., **in press**.
Stehly, L., M. Campillo, B. Froment, and R. Weaver, 2008, Reconstructing Green's function by correlation of the coda of the correlation (C3) of ambient seismic noise: J. Geophys. Res., **113**, B11306.
Stehly, L., M. Campillo, and N. Shapiro, 2006, A study of seismic noise from long-range correlation properties: J. Geophys. Res., **111**, B10306.

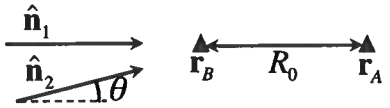

Figure A1. Definition of geometric variables for two incoming waves at a relative azimuth θ.

Wapenaar, K., D. Draganov, and J. Robertsson, eds., 2008, Seismic interferometry: History and present status: Society of Exploration Geophysics, volume **26** *of* SEG Geophysics Reprints Series.
Wapenaar, K., D. Draganov, R. Snieder, X. Campman, and A. Verdel, 2010a, Tutorial on seismic interferometry. Part 1: Basic principles and applications: Geophysics, **75**, 75A195–75A209.
Wapenaar, K., E. Slob, R. Snieder, and A. Curtis, 2010b, Tutorial on seismic interferometry. Part 2: Underlying theory: Geophysics, **75**, 75A211–75A227.
Weaver, R., and O. Lobkis, 2005, Fluctuations in diffuse field-field correlations and the emergence of the Green's function in open systems: J. Acoust. Soc. Am., **117**, 3432–3439.

APPENDIX A: WHEN ARE TWO WAVES DIFFERENT, AS MEASURED BY THE CORRELATION?

When are two waves different as seen by the correlation? Consider the geometry in figure A1 where two receivers are separated over a distance R_0 along the x-axis. One wave comes in along the x-axis, and the second waves comes in as a small angle θ relative to the first wave. The total wave field is given by

$$u(\mathbf{r},\omega) = S_1(\omega)e^{ikx} + S_2(\omega)e^{ik(x\cos\theta + y\sin\theta)}\,, \qquad \text{(A1)}$$

where y is the coordinate perpendicular to the x-axis. Assuming that the two incoming waves are uncorrelated ($\langle S_1 S_2\rangle = 0$), the cross correlation of the waves recorded at receivers A and B is given by

$$C_{AB} = \langle u_A u_B^*\rangle = |S_1|^2 e^{ikR_0} + |S_2|^2 e^{ikR_0\cos\theta}\,, \qquad \text{(A2)}$$

where we used that the receivers are located on the x-axis. The two waves contribute coherently to the cross correlation when the phase difference of the two terms in the right hand side is small compared to a cycle. Assuming that the phase difference must be less than $\pi/4$, this gives the criterion $(kR_0 - kR_0\cos\theta) \leq \pi/4$. For small values of θ this criterion reduces to expression (11).

A practical approach to prediction of internal multiples and ghosts

Jyoti Behura[†] & Farnoush Forghani[‡]
[†] *Center for Wave Phenomena, Colorado School of Mines, Golden, Colorado*
[‡] *Center for Rock Abuse, Colorado School of Mines, Golden, Colorado*

ABSTRACT
Existing methods of internal multiple prediction are either computationally expensive or not automated. Here, based on stationary phase arguments, we introduce a method for predicting internal multiples that is not only fully automated but also computationally inexpensive. The procedure is completely data driven and requires no velocity information or reflector identification. An additional advantage of the proposed method is that it can also be used to predict source- and receiver-ghosts. The method, however, is limited to gently-dipping reflectors. Through synthetic examples and field data, we demonstrate the effectiveness of our methodology.

1 INTRODUCTION

In most stages of seismic data processing, it is assumed that the data is devoid of multiply scattered energy and contains only primaries. For example, the contribution of multiples to semblance panels (for velocity analysis) might result in erroneous picking of velocities. More importantly, most imaging algorithms are based on the Born approximation (single scattering). If not suppressed, the multiples might show up as spurious events in the image or even interfere with the primaries resulting in a degraded image.

Suppressing surface-related multiples using SRME (Verschuur *et al.*, 1992) is a standard practice now. Internal-multiple suppression, on the other hand, is not prevalent either because it is not fully automated or is computationally expensive. Berkhout & Verschuur (1997) proposed an iterative algorithm that includes extrapolating the shot records to a reflecting boundary responsible for the generation of the internal multiples. On similar lines, Jakubowicz (1998) proposed isolating the primary events on data followed by a convolution and deconvolution process to predict the internal multiples. The above two methods are not computationally intensive but are not fully automated. The inverse scattering approach of Weglein *et al.* (1997) and ten Kroode (2002) overcomes the above drawback and can also predict all possible internal multiples. The method, however, is computationally expensive.

In marine acquisition, since sources and receivers lie under the water surface, the air-water interface acts as a mirror. So the source would have a mirror source (ghost) above the surface; the same argument applies for the receiver as well. The source- and receiver-ghosts act as filters on the data with zeros at many frequencies. Such notch filters result in poor data quality by limiting the usable bandwidth of the data.

Existing methods of source- and receiver-ghosts suppression are primarily confined to the acquisition stage. Ziolkowski (1971) suggested recording at two different depths so as to fill in the zeros in the spectra. Similar recommendations have been made by others including Ghosh (2000). Such an acquisition is termed as over/under streamer acquisition (Moldoveanu *et al.*, 2007). The extreme case of all hydrophones having different depths was recently proposed by Soubaras & Whiting (2011). Ghosts could also be attenuated using dual-sensors (pressure and velocity) in a streamer (Carlson *et al.*, 2007).

Here, we introduce a practical approach to predict internal multiples with the primary aim of making the process computationally tractable as well as automatic. We also demonstrate how the proposed method could also be used to predict source- and receiver-ghosts.

2 INTERNAL MULTIPLES

As proposed by Jakubowicz (1998), any first-order internal multiple can be represented as a combination of three primaries. For example, in Figure 1a, the internal multiple $\mathcal{M}(\omega; x_A, x_E)$ is given by a convolution of primaries $\mathcal{P}_{ABG}$ and $\mathcal{P}_{FDE}$ followed by a deconvolution with the third primary $\mathcal{P}_{FCG}$. To automate the process,

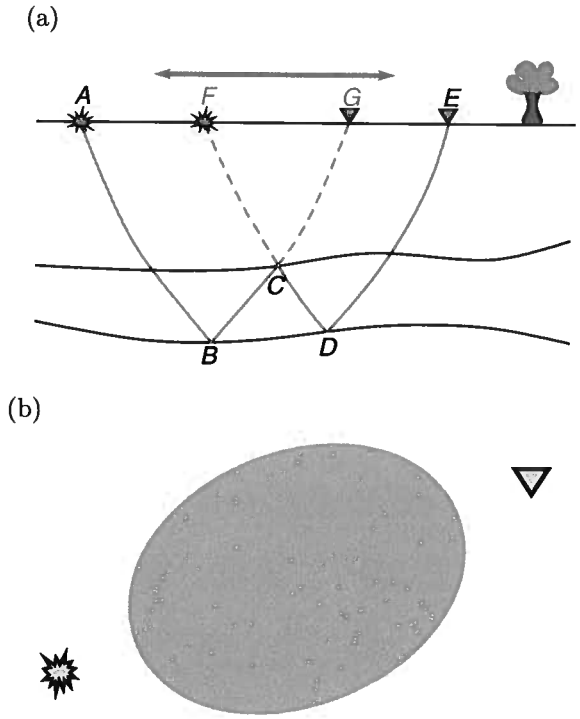

Figure 1. (a) Illustration of the computation of the internal multiple for a 2D acquisition. The summation zone (two-sided arrow) spans between the source at x_A and the receiver at x_E. The dashed red line denotes the primary that is common to the two other primaries and needs to be deconvolved in equation 1. (b) Plan view of a 3D surface-seismic acquisition. The grey area represents the proposed summation zone for a given source-receiver pair.

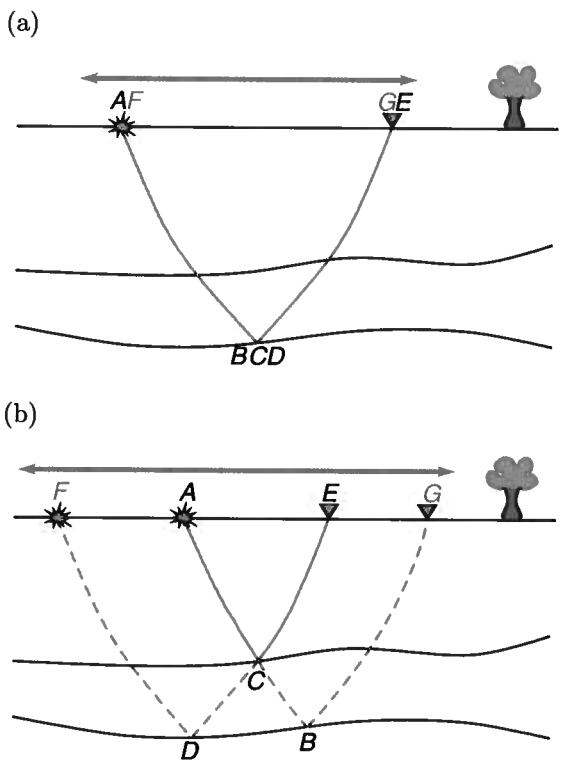

Figure 2. (a,b) Illustration depicting the need for limiting the zone of stationary phase integration to the interior of points A and E.

we replace the windowed primaries (Jakubowicz, 1998) with the full Green's function between the source and receiver. In practice, the internal multiple is obtained by following dual-summation over the locations of F and G:

$$\mathcal{M}(\omega; x_A, x_E) = \sum_{x_F} \sum_{x_G} \frac{\mathcal{U}(\omega; x_A, x_G)\mathcal{U}(\omega; x_F, x_E)}{\mathcal{U}(\omega; x_F, x_G)}, \quad (1)$$

where x represents the coordinate location, $\mathcal{U}$ is the recording between any source and receiver and ω is the frequency. Equation 1 predicts all orders of internal multiples at the same time. The above procedure is akin to seismic interferometry (Lobkis & Weaver, 2001; Wapenaar & Fokkema, 2006) that retrieves the Green's function between a virtual source and a receiver. The maximum contribution to the summation 1 comes from the stationary points at x_F and x_G. Note that the source signature inherent in $\mathcal{U}$ is retained in $\mathcal{M}$ because of the deconvolution operation in equation 1.

To predict only multiples, we limit the summation over locations x_F and x_G to a specific spatial location and aperture. It is crucial that points x_F and x_G lie in between the source at x_A and the receiver at x_E. If F and G lie outside this region (Figure 2b) or are close the points A and E (Figure 2a), respectively, then $\mathcal{M}(\omega; x_A, x_E)$ would contain primaries in addition to multiples. For example, in the special case of F coinciding with A and G coinciding with E, equation 1 would reduce to $\mathcal{M}(\omega; x_A, x_E) = \mathcal{U}(\omega; x_A, x_G)$, i.e. the 'predicted multiple' would be the Green's function between source at x_A and receiver at x_E and contain all primaries and multiples. A significant advantage of limiting the summation to a small aperture (determined by the source and receiver locations) is the reduction in computational cost. Summing over all possible locations of F and G would not only be prohibitively expensive, but also would not yield the internal multiples. In 3D, the summation can be carried over all surface points in a region (grey area in Figure 1b) that would likely contain the stationary points F and G. In the inverse scattering approach (Weglein *et al.*, 1997; ten Kroode, 2002), on the other hand, the summation is over all possible locations of F and G which adds to its computational cost.

The above modifications (using the Green's function in equation 1 and limiting the region of summation), however, result in other drawbacks and limitations. Usage of the full Green's function in equation 1

results in spurious events that have been extensively studied in seismic interferometry (Snieder *et al.*, 2006; Forghani & Snieder, 2010). However, since there is no stationary phase contribution to the spurious events, including more traces into the summation can suppress these events. Another drawback is that the near-offset prediction would not be accurate because of the proximity of F and G to A and E, respectively and also because of the limited number of traces going into the summation in equation 1. The limitation imposed on the region of summation assumes that the stationary points x_F and x_G lie in between x_A and x_G. This might not be the case for complicated geology and steeply dipping reflectors. For example, in Figure 2, since G lies outside the zone of integration (between x_A and x_E), the internal multiple would not be predicted accurately. So the method proposed here would work well for gently dipping layers and non-complicated subsurfaces. This is the primary limitation of our methodology compared to the methods of Berkhout & Verschuur (1997); Jakubowicz (1998); Weglein *et al.* (1997); ten Kroode (2002).

Synthetic examples: The synthetic test demonstrated here is that for a 1D velocity model comprising of 3 layers. A shot gather for this test is shown in Figure 3a. The predicted internal multiples are shown in Figure 3b. As explained above, the near-offset prediction is not accurate; however, the mid- and far-offsets clearly show the first- and second-order internal multiples.

3 GHOSTS

The geometry of a source+receiver ghost (Figure 4) is similar to that of an internal multiple (Figure 1a). So the same algorithm, that is used for predicting internal multiples, can be exploited for predicting source+receiver ghosts. The source+receiver ghost $g(\omega; x_A, x_G)$ between the source at x_A and the receiver at x_G is given by the dual-summation:

$$g(\omega; x_A, x_G) = \sum_{x_C} \sum_{x_E} \frac{\mathcal{U}(\omega; x_A, x_E)\mathcal{U}(\omega; x_C, x_G)}{\mathcal{U}(\omega; x_C, x_E)}. \quad (2)$$

Viking Graben data: The above ghost-prediction algorithm is tested on a 2D seismic line from North Sea, acquired over the Viking Graben (Keys & Foster, 1998). The shallow seafloor results in strong source and receiver ghosts. The data also contains strong reverberations most likely because of guided waves in the subsurface. A set of common-offset gathers from the field data and the predicted ghosts is shown in Figure 5. The common-offset sections (Figures **??** and **??**) are dominated by a few mono-frequency signals. In addition to the presence of guided waves, note the presence of surface-related and internal multiples in Figures **??** and **??**.

4 CONCLUDING REMARKS

Although not presented here, prediction of internal multiples should be followed by an adaptive subtraction method that eliminates these multiples from the data. The predicted ghosts could be suppressed in a similar fashion or using deconvolution techniques. Also, some interpretation of the predicted multiples might be necessary because of the generation of spurious events during the interferometry process. Additional processing steps might also be adopted to suppress these artifacts. The zone of summation (aperture) is an important variable in the algorithm. Too small an aperture would not predict any multiples and too large an aperture might lead to the presence of primaries in the prediction. Depending on the complexity of the subsurface, a few tests might be necessary to find this parameter.

The ability to predict internal multiples and ghosts using one single algorithm makes our methodology versatile and powerful. Although our method is limited to gently dipping interfaces, it should be applicable in numerous fields, especially in many onshore unconventional plays.

ACKNOWLEDGMENTS

We thank the developers/maintainers of freeDDS (http://www.freeusp.org/DDS). Discussions with Imtiaz Ahmed, Bruce Ver West, Roel Snieder, and John Etgen were extremely useful. John Stockwell helped us obtain the Viking Graben data. Support for this work was provided by the Consortium Project on Seismic Inverse Methods for Complex Structures at CWP and by the sponsors of the Center for Rock Abuse.

References

Berkhout, A. J., & Verschuur, D. J. 1997. Estimation of multiple scattering by iterative inversion, Part I: Theoretical considerations. *Geophysics*, **62**(5), 1586–1595.

Carlson, D., Söllner, W., Tabti, H., Brox, E., & Widmaier, M. 2007. Increased resolution of seismic data from a dual-sensor streamer cable. *SEG Technical Program Expanded Abstracts*, **26**(1), 994–998.

Forghani, F., & Snieder, R. 2010. Underestimation of body waves and feasibility of surface-wave reconstruction by seismic interferometry. *The Leading Edge*, **29**(7), 790–794.

Ghosh, S. K. 2000. Deconvolving the ghost effect of the water surface in marine seismics. *Geophysics*, **65**(6), 1831–1836.

Jakubowicz, H. 1998. Wave equation prediction and removal of interbed multiples. *SEG Technical Program Expanded Abstracts*, **17**(1), 1527–1530.

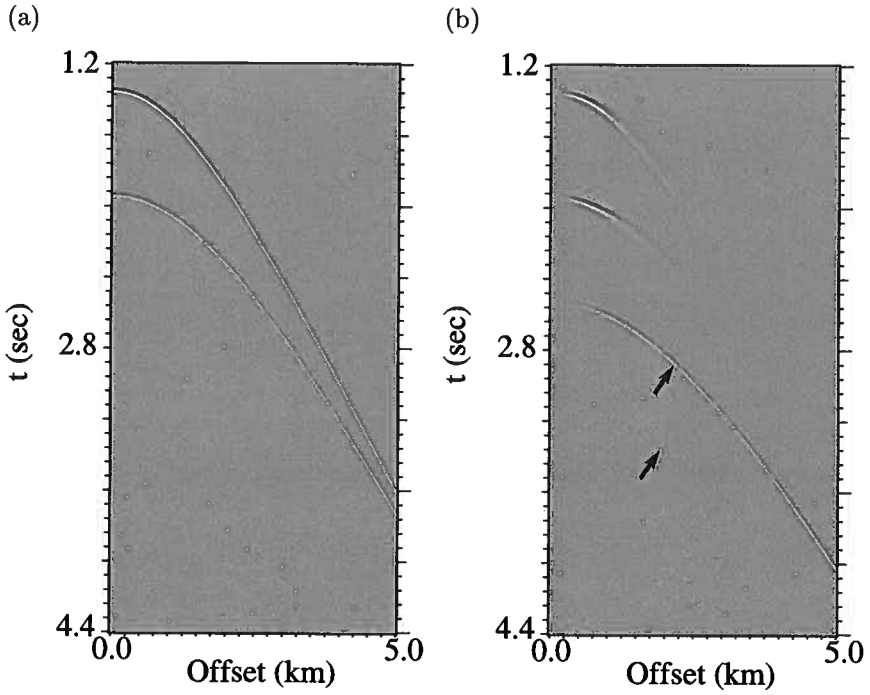

Figure 3. Shot-gather (a) and predicted internal multiples (b) for a layer-cake subsurface (three layers). The figures have been scaled to their respective maximum values. The internal multiples are too weak (compared to the primaries) to be seen in (a). An aperture equal to half the offset and centered about the mid-point was used in the prediction process. The arrows point to the predicted internal multiples.

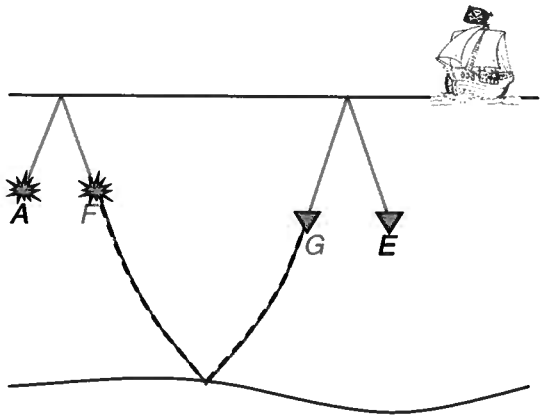

Figure 4. Illustration of the geometry behind source+receiver ghost computation.

Keys, R. G., & Foster, D. J. (eds). 1998. *Comparison of seismic inversion methods on a single real data set.* Tulsa: Society of Exploration Geophysicists.

Lobkis, O.I., & Weaver, R.L. 2001. On the emergence of the Green's function in the correlations of a diffuse field. *Journal of Acoustical Society of America*, **110**, 3011–3017.

Moldoveanu, N., Combee, L., Egan, M., Hampson, G., Sydora, L., & Abriel, W. 2007. Over/under towed-streamer acquisition: A method to extend seismic bandwidth to both higher and lower frequencies. *The Leading Edge*, **26**(1), 41–58.

Snieder, R., Wapenaar, K., & Larner, K. 2006. Spurious multiples in seismic interferometry of primaries. *Geophysics*, **71**(4), SI111–SI124.

Soubaras, R., & Whiting, P. 2011. Variable depth streamer — The new broadband acquisition system. *SEG Technical Program Expanded Abstracts*, **30**(1), 4349–4353.

ten Kroode, Fons. 2002. Prediction of internal multiples. *Wave Motion*, **35**(4), 315 – 338.

Verschuur, D. J., Berkhout, A. J., & Wapenaar, C. P. A. 1992. Adaptive surface-related multiple elimination. *Geophysics*, **57**(9), 1166–1177.

Wapenaar, K., & Fokkema, J. 2006. Green's function representations for seismic interferometry. *Geophysics*, **71**(4), SI33–SI46.

Weglein, A. B., Gasparotto, F. A., Carvalho, P. M., & Stolt, R. H. 1997. An inverse-scattering series method for attenuating multiples in seismic reflection data. *Geophysics*, **62**(6), 1975–1989.

Ziolkowski, A. 1971. Design of a Marine Seismic Re-

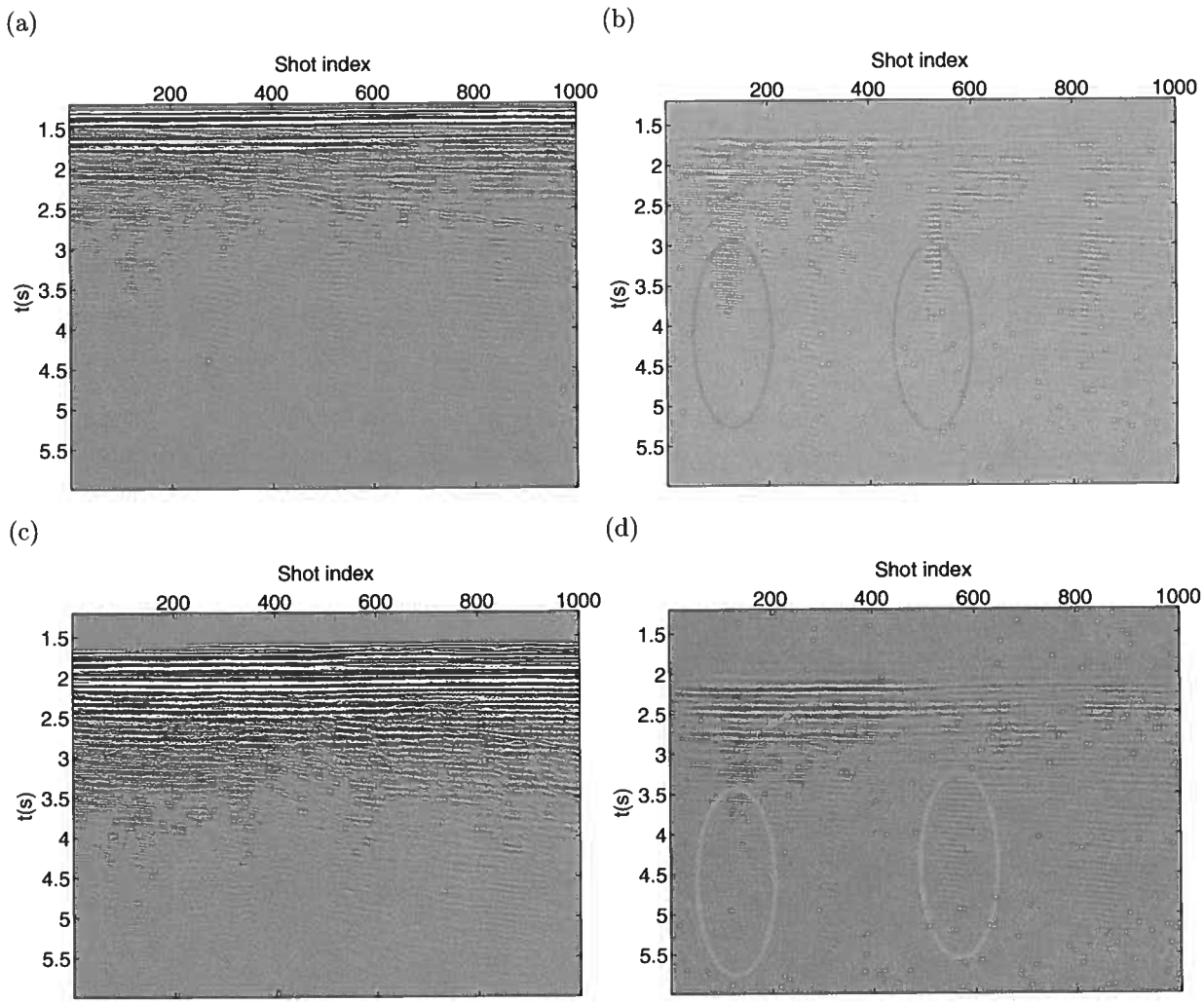

Figure 5. Mid (a) and far (c) common-offset sections of the Viking Graben data and corresponding predicted source+receiver ghost in (b) and (d), respectively. The arrow points to an interval containing internal multiples. The ovals highlight guided waves.

flection Profiling System using Air Guns as a Sound Source. *Geophysical Journal of the Royal Astronomical Society*, **23**(5), 499–530.

Retrieval of local surface wave velocities from traffic noise - an example from the La Barge basin (Wyoming)

Michael Behm[1], Roel Snieder[1] & Garrett M. Leahy[2]
[1] *Center for Wave Phenomena, Geophysics Department, Colorado School of Mines, Golden, CO*
[2] *Deptartment of Geology and Geophysics, Yale University, New Haven, CT*

ABSTRACT
In regions where active source seismic exploration is constrained by limitations of energy penetration and recovery, cost and logistical concerns, or regulatory restrictions, analysis of natural source seismic data may provide an alternative. In this study, we investigate the feasibility of using locally-generated seismic noise in the 2 - 6 Hz band to obtain a subsurface model via interferometric analysis. We apply this technique to 3-component data recorded during the La Barge Passive Seismic Experiment, a local deployment in south-western Wyoming that recorded continuous seismic data between November 2008 and June 2009. We find traffic noise from a nearby state road to be the dominant source of surface waves recorded on the array, and observe surface wave arrivals associated with this source up to distances of 5 kilometres. The orientation of the road with respect to the deployment ensures a large number of stationary points, leading to clear observations on both inline and cross-line virtual source - receiver pairs. This results in a large number of usable interferograms, which in turn enables the application of standard active source processing methods like signal processing, common offset stacking and travel time inversion. We investigate the dependency of the interferograms on the amount of data, on a range of processing parameters, and on the choice of the interferometry algorithm. The obtained interferograms exhibit a high signal to noise ratio on all three components. Rotation of the horizontal components to the radial/transverse direction facilitates the separation of Rayleigh and Love waves. Though the narrow frequency spectrum of the surface waves prevents the inversion for depth-dependent shear wave velocities, we are able to map the arrival times of the surface waves to laterally varying group and phase velocities for both Rayleigh and Love waves. Our results correlate well with the geologic structure. We outline a scheme for obtaining localized surface wave velocities from local noise sources, and show how the processing of passive data benefits from the combination with well-established exploration seismology methods. We highlight the differences to interferometry applied to crustal scale data and conclude with recommendations for similar deployments.

Key words: seismic interferometry, surface waves, three-component, near surface

1 INTRODUCTION

Passive seismology is gaining increased interest in the subsurface imaging community. Applications range from monitoring subsurface fluid injection and fault mapping to imaging basin-scale tectonic features. For imaging problems, the methodologies used so far typically draw heavily from methods established in the field of crustal seismology (e.g., teleseimic inversion, interferometry, receiver functions), and there is a natural focus on medium- to large-scale structures. In terms of scale and geologic variability, the different settings of local targets require modified processing schemes and may require choices of parameters that deviate strongly from the standards in global and regional studies. In particular, there is much interest in ambient noise, or daylight imaging techniques, in which local structure

allow identifying the noise source. The interferograms are inverted for shallow surface wave velocities in section 4, and section 5 concludes with the most important insights and recommendations for further deployments and studies.

2 DATA

Analysis of the raw data focuses on the calculation of the power spectral densities (PSD) to get an initial estimate of the exploitable frequency content. We find signals over a wide frequency range, sometimes up to the Nyquist frequency (50 Hz). Figure 3 gives an example of the two stations L11 and L29 where the latter one is at a close proximity to the road. L11 shows the onset of an unknown noise activity at 12:30 local time. The pronounced noise bursts at station L29 are attributed to passing cars or trucks, but their high-frequency contributions decay quickly with the distance to the road. The earths microseism, peaking between 0.05-0.5 Hz (e.g., Webb 1998) can be clearly seen on all stations. These signals are excited by interactions between ocean waves and the ocean floor. Our investigation shows a broad variation on both spatial and temporal scales, though a complete and detailed analysis of the spectral characteristics of the entire data set is beyond the scope of this paper. The uniform instrumentation allows for a direct comparison of the PSD (Figure 2) for the entire observation period of 7 months. The coloured circles in Figure 2 represent the average PSD of the vertical component of each station. These values are obtained as follows: At first, the averages of the PSD within certain frequency bins (0.001 0.1, 0.1 0.3, 0.3 1, 1 5, 5 10, 10 20, 20 40 Hz) are calculated for each 24 hour interval within the entire observation period. In each frequency bin, averaging is performed a second time over all 24 hour intervals and these double-averaged PSDs are then normalized to the maximum and minimum of all stations. Finally, the shown values in Figure 2 are calculated by averaging these normalized values over all frequency bins. Low values indicate a weak surface response, and we find a clear large-scale correlation with surface geology since stations east of the Hogsback thrust show higher values. Outliers like the high values at two stations west of the thrust can be correlated with local machinery (e.g. pumping pads). Similar results are obtained for the horizontal components. If we further restrict the data to time windows which include surface and body waves from regional and global earthquakes only, we derive the same pattern. We therefore interpret these values as indicators for local attenuation due to the near-surface geological structure. A detailed treatment is beyond the scope of this study, but we conclude that some stations will be more affected by attenuation and thus might anticipate interferograms of lower quality west of the Hogsback thrust.

3 PROCESSING

3.1 The virtual source method and the stationary phase principle

In seismology, Greens function represents the impulse response of the earth. The virtual source method (Bakulin and Calvert, 2006) aims to derive Greens function between two receiver stations by transforming one station into a (virtual) seismic source. It is assumed that one or more (real) sources radiate seismic energy which is recorded by a set of receivers. As our study is based on seismic noise of initially unknown origin, we refer to those real sources as noise sources in the following. The noise sources are assumed to be located outside the deployment. In case of ambient noise studies (e.g. Wapenaar and Fokkema (2006)) and continuous recording, the timing and location of the noise sources dont have to be known. By correlating the trace $y_A(t)$ at receiver A (the virtual source) with the trace $y_B(t)$ at receiver B, the interferogram $g_{AB}(t)$ between the two instruments is obtained:

$$g_{AB}(t) = y_B(t) \star y_A(-t) \tag{1}$$

Note that we consider the traces, and thus the Greens function, as time series of discrete samples which are represented as vectors. In equation (1), the star sign denotes convolution which is equivalent to correlation with the reversed time series. For many reasons (e.g. source signature, instrument noise, attenuation, scattering phenomena, measurement of displacement instead of stress; Snieder (2007); Halliday and Curtis (2008); Tsai (2011)), the obtained interferogram $g_{AB}(t)$ is only an approximation to the actual Green's function, and therefore an estimate of the impulse response of the earth. Thus Greens functions recovered by interferometry might be considered as empirical Green's functions. Correlation results in both positive (causal) and negative (acausal) time lags. The character of the causal and acausal parts of the interferogram gives evidence on the noise sources: symmetry hints towards evenly distributed noise sources, while a stronger causal (or acausal) part indicates a dominance of noise sources closer to receiver A (or B) (Paul, 2005; Stehly et al., 2006).

As correlation in the time domain is equivalent to convolution with the reversed time-series, equation (1) can be stated in the Fourier domain as

$$g_{AB}(f) = y_B(f) \cdot \overline{y_A(f)} \tag{2}$$

Interferometry can also be approached in the Fourier domain by deconvolution (Snieder and Safak, 2006; Vasconcelos and Snieder, 2008; Wapenaar et al., 2010b)

$$g_{AB}(f) = \frac{y_B(f)}{y_A(f)} \tag{3}$$

which transforms to

$$g_{AB}(\mathrm{f}) = \frac{y_B(\mathrm{f}) \cdot \overline{y_A(\mathrm{f})}}{\|y_A(\mathrm{f})\|^2} \tag{4}$$

A modification to equation (4) leads to interferometry by cross-coherence (Aki, 1957; Wapenaar et al., 2010b; Prieto et al., 2009):

$$g_{AB}(\mathrm{f}) = \frac{y_B(\mathrm{f}) \cdot \overline{y_A(\mathrm{f})}}{\|y_A(\mathrm{f})\| \cdot \|y_B(\mathrm{f})\|} \tag{5}$$

Equations (2), (4), (5) are, apart from the denominator, identical, which in the two latter cases comprise the amplitude spectra of the seismic data. If the amplitude spectra are flat (unlikely in practice), the interferograms obtained by all three methods are of identical shape and recover identical empirical Greens functions. If not, each of the different Greens function recovery methods will result in different estimates of the impulse response of the earth. The performance of these three techniques is examined in more detail in section 3.3. The stationary phase principle (Snieder, 2004; Snieder et al., 2006) is of great importance to seismic interferometry. Translated to ray theory, it states that the dominant contribution to the reconstructed Greens function comes from ray paths which are identical prior to the arrival at the receivers. Wapenaar et al. (2010a) show that these paths are equivalent to rays which are parallel at the source. In case of a homogeneous half space, the stationary phase region (location of the noise sources which satisfy the stationary phase principle) for surface waves is simply the outward extension of the line which connects the receiver and the virtual source. In practice, seismic waves comprise finite frequencies and the ray path is replaced by the Fresnel zone (or finite-frequency kernel). Further, we may expect a multitude of noise sources distributed all over and around the investigated area. In this case, the stationary phase principle ensures a kinematically correct empirical Greens function if the noise sources are of equal strength, and are distributed evenly around the virtual source - receiver pair. Only then will contributions from noise sources outside the stationary phase region cancel. The dominant contribution from oscillatory integrals where the phase varies much more rapidly than the amplitude comes from the integration points where the phase is stationary (section 6.5 of Bender and Orszag (1978) or section 2.7 of Bleistein (1984)). For interferometric applications this implies that the dominant sources are those at the stationary phase points, provided the source strength varies over distance much more slowly than the phase of the interferometric integral does. The stationary phase principle is usually valid in global seismology because the dominant noise sources (ocean waves, strong earthquakes) are ubiquitous. At smaller scales, the noise sources may be concentrated at certain locations (e.g., cultural noise, roads, trees) and thus the results must be evaluated carefully with respect to a possible violation of the requirement that noise sources are evenly distributed. Coherent signals of noise sources may be expected to be of very small amplitude. Stacking of individual interferograms is commonly applied to enhance information from ambient noise data. This increases the signal-to-noise (S/N) ratio of the interferograms by down-weighting non-coherent seismic energy. Alternatively, correlation of the entire time series at once would be possible, but computation is more efficient and practical when the continuous recordings are cut into short time windows. Correlation is then performed for each time window, and the resulting individual interferograms are stacked into a final interferogram. The total amount of input data and the length of the time windows depend on the virtual source - receiver distance, the sub-surface structure (attenuation), the location, type and strength of the noise sources, and on computational considerations. For the testing of processing parameters and methods (sections 3.2 and 3.3), we use 5 days of vertical component data (December 1st to December 5th of 2008) and cut them into 10 s time windows. A more exhaustive analysis of the time window length and the overall amount of data is presented in section 3.4.

(Note that the term noise is used throughout with two different meanings: Prior to interferometry, it describes the ambient seismic energy which is radiated by the actual (real) sources. This noise is turned into a signal by interferometry, which creates a virtual seismic trace. Consequently, the S/N ratio of this trace (the interferogram) is high when the amount of ambient noise is high.)

3.2 Pre-Processing

Prior to correlation, the data are subjected to a sequence of processing steps. Bensen et al. (2007) describe the data processing which is commonly applied to global-scale data (frequency filtering, temporal normalization, spectral whitening). We essentially follow their methodology, but with some minor modifications as discussed below. The raw data indicate a broad spectrum (Figure 3) which ranges from below the Earths microseism (0.07 and 0.13 Hz, respectively) to the Nyquyist frequency (50 Hz), but only spatially coherent signals will provide useful interferograms.

Exploration industry is interested in broadening the frequency content of seismic data towards the lower end of the spectrum to obtain improved starting models for full waveform inversion. For interferometric applications, the low frequency threshold depends on the noise source, on the local subsurface structure, and on the receiver spacing and aperture of the array. If the wavelength is large in comparison to the virtual source-receiver distance (e.g. earthquake surface waves), the correlation resembles a zero-lag peak. The same accounts for waves which arrive simultaneously at the re-

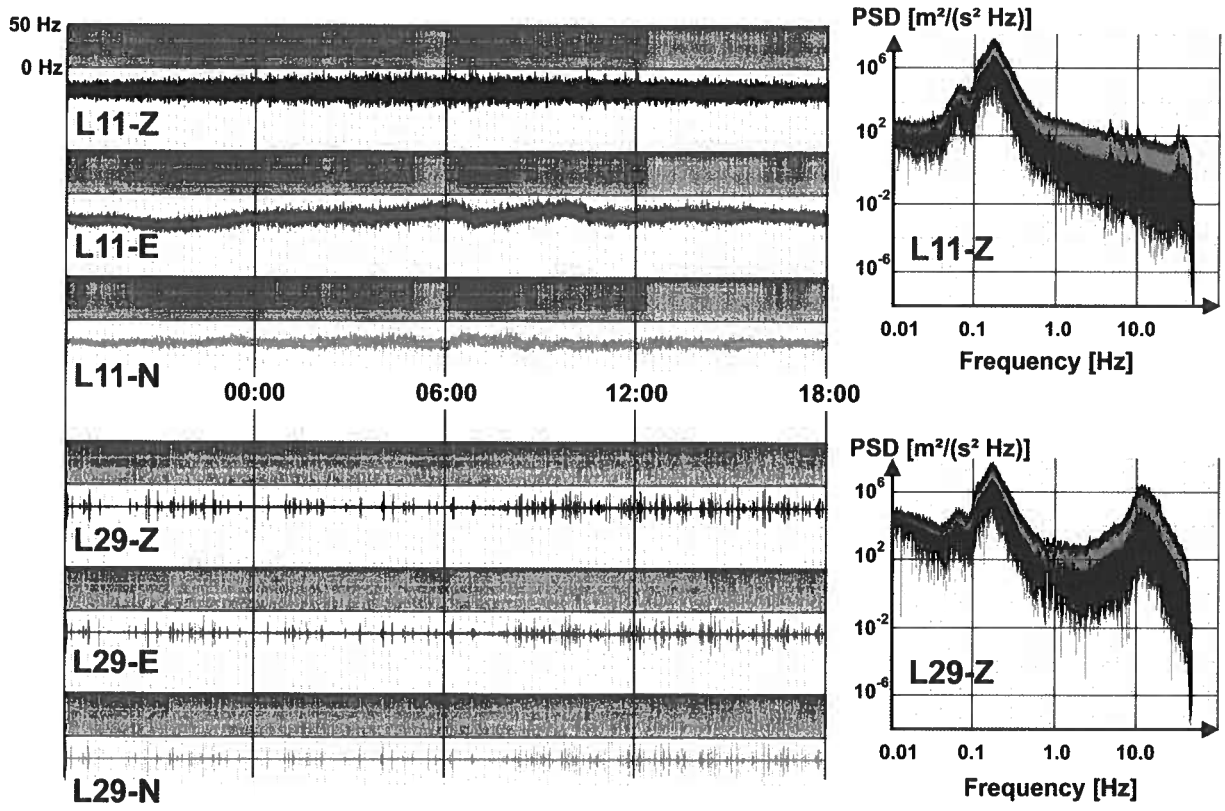

Figure 3. Data, spectrograms and power spectral densities (PSD) of the stations L11 and L29. The 24 h long data series start at November 29th, 2008 at 18:00 local time. The red curve in the PSD plots is a running average over 10 samples.

ceivers, e.g. vertical-incidence body waves from teleseismic earthquakes. Thus we exclude data which comprise surface and body waves from regional and global earthquakes, based on a catalogue by C. Byriol (pers. comm. 2011). Tests with different high-pass filters showed that a strong zero-lag arrival emerges if frequencies lower than 2 Hz are included. This may indicate that some earthquake energy is still remnant in the data set. Low-frequency oscillations of the basin, possibly excited by earthquake originated waves (Rial, 1989), may also contribute. Because of their consideration we conclude that a high-pass filter of 2 Hz is required for further processing. With respect to the expected velocities of surface waves, 2 Hz are roughly equivalent to a wavelength range from 750 to 2000 meters. The high-frequency end of the spectral component that can be used is examined by different low-pass filters applied to the input data. Figures 4a,c show interferograms obtained from correlation in the time domain applied to data band pass-filtered with different upper corner frequencies (20 Hz, 40 Hz). Both results appear noisy and do not give much additional insight into subsurface structure. We further detect spurious energy over the entire frequency band (e.g. the zero-lag peak). This results from spectral whitening (see below) which, though applied after band pass filtering, is automatically performed from the lowest to the Nyquist frequency. Analogously to active-source processing, we thus apply a band pass filter after interferometry (post-stack filtering, Figures 4b,d). It shows that the interferograms do not comprise coherent signals with frequencies higher than 5 Hz, no matter which low-pass filter is applied to the data. Note that the post-stack band pass filter becomes obsolete if spectral whitening is performed over the same frequency range only as the pre-stack band pass filter. This depends however on the actual implementation of the whitening algorithm. In our case, all shown interferograms are band pass-filtered from 2 to 6 Hz.

Though the stationary phase principle requires noise sources of equal strength, this is not generally the case; we therefore apply temporal normalization to the input data. Bensen et al. (2007) compare different algorithms, and we additionally test the performance of automatic gain control (AGC). The running-mean normalization by Bensen et al. (2007) is similar to AGC, but is based on the absolute amplitudes instead of the squared amplitudes. We find the difference of one-bit normalization, running-mean normalization, and AGC to be minor. We chose the AGC with a window length of 0.1 s. One-bit normalization has the dis-

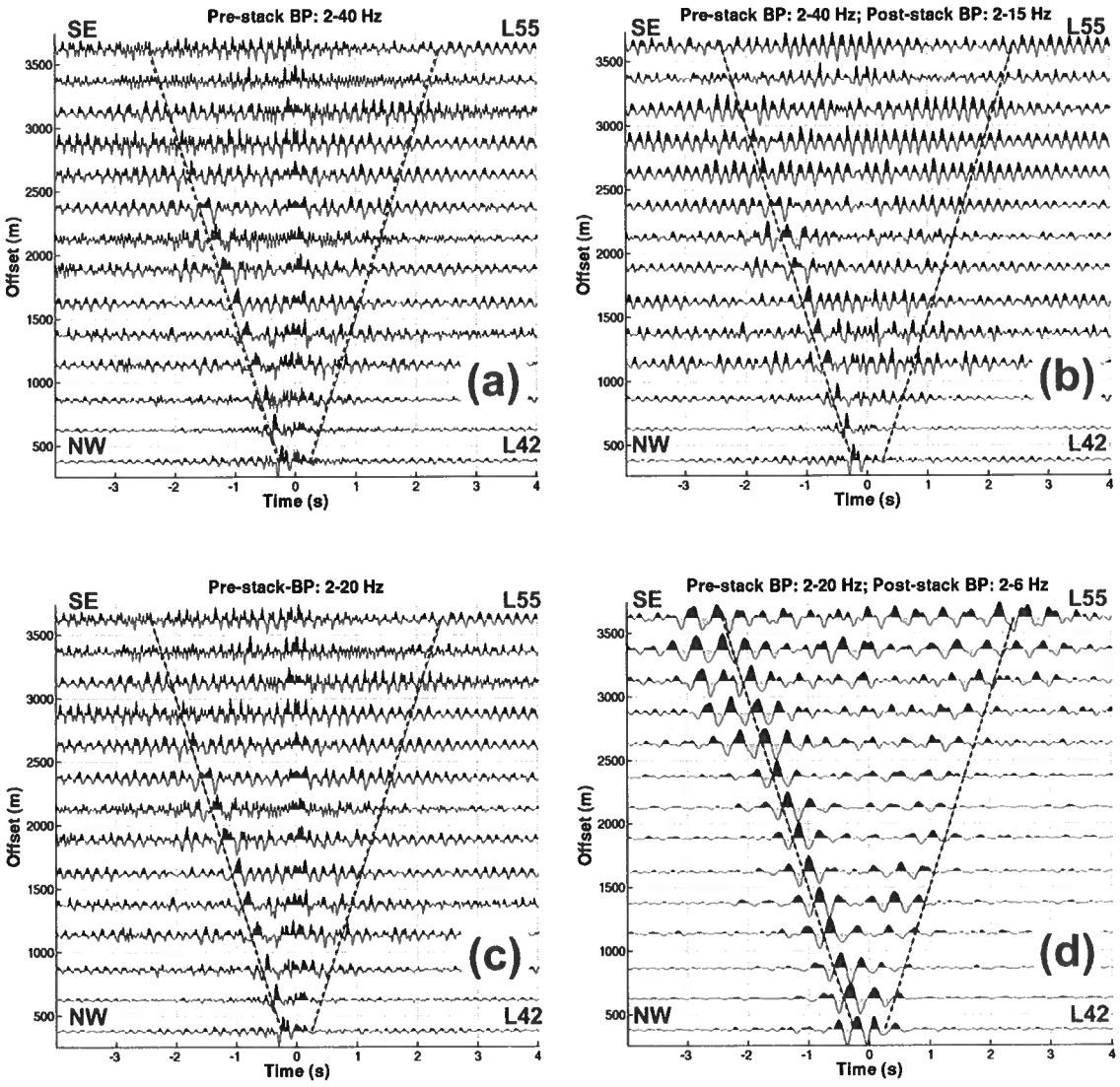

Figure 4. Comparison of different pre- and post-processing band pass filters for virtual source L22 and receivers along segment 3. The broken lines indicate linear move-outs for a velocity of 1500 m/s. NW and SE refer to the geographic directions. See text for details.

advantage of not being commutative with respect to rotation of the horizontal components, which is needed for the transformation to radial and transverse components (cf. section 3.5). Spectral whitening aims at normalizing the amplitude spectrum of the input data, thus boosting low-amplitude frequency components and collapsing monochromatic signals. The latter is of importance in industrial settings, since industrial machinery (e.g., drill rigs, pumps) operate at discrete frequencies (e.g. Poletto and Miranda (2004). Total whitening may be performed by normalizing the amplitude spectra at all frequencies. User-controlled whitening is achieved when the amplitude spectra is divided by a smoothed version of itself (Bensen et al., 2007). A strong smoothing filter (smoothing over large frequency intervals) has little effect compared to weak smoothing (smoothing over small frequency intervals). We prefer user-controlled smoothing since total whitening results in slightly more spiky interferograms. Tests show that the optimum smoothing length with regard to the S/N ratio of the interferograms is 0.1 Hz. Like one-bit normalization, total whitening is also not compatible with the transformation to radial and transverse components (section 3.5). Because spectral whitening introduces incoherent high-frequency artefacts, post-processing (after interferometry) always included a band-pass filter of 2 to 6 Hz and

weighted smoothing in the time domain with a window length of 0.3 s. The linear move-out of the arrivals is a prominent feature and an indication for surface waves (Figure 4d).

3.3 Comparison of different algorithms

As outlined in section 3.1, the three different interferometry algorithms (correlation, deconvolution, cross-coherence) are identical if the amplitude spectra of the input data are flat. The flatness depends on the whitening operator (section 3.2), and as we chose user-controlled whitening, different results are expected. It is noted that both deconvolution and cross-coherence intrinsically whiten the data by spectral division, although the whitening operator (the denominator in equations 3-5) varies with virtual source and receiver stations. E.g., spectral notches which are stronger at the receiver station than at the virtual source will not be completely removed. For these reasons, and for simplicity and consistency, we apply all three methods on a uniform, pre-whitened data set. The comparison is shown in Figures 5 and 6. For short offsets (less than 2 km; Figure 5), the results are similar. At medium offsets (2 to 4 km; Figure 6), the correlation interferograms are generally more noisy, in particular if whitening is weak. This difference to deconvolution and cross-coherence might be explained by the additional spectral division (equations 3-5), which additionally equalizes the receiver and virtual source amplitude spectrum. Cross-coherence, and in particular deconvolution, exhibit a pronounced zero-lag peak at medium offsets, which is slightly enhanced in the case of weak whitening. A similar behaviour is observed at offsets larger than 4 km. In case of weak whitening and correlation, monochromatic signals persist in the interferograms. Ultimately, theoretical equivalence results in the fact that the choice of method will be determined by the character of the dataset of interest, and the preference and expertise of the analyst. In this case, we find that the best results are achieved with strong whitening (smoothing over 0.1 Hz wide frequency intervals) and by the use of cross-coherence. Consequently, all following computations are performed with this combination.

3.4 Influence of the window length and number of input data

In case of continuous recordings and unknown noise sources, the choice for the amount of input data is important. Depending on the available data and computing resources, different strategies can be imagined. In the case of a short, temporary deployment, overlapping time windows may be used to increase the probability of correlating signals from noise sources (Seats et al., 2012). For our data set, we regard the 7 months of data to be sufficiently long and therefore use adjacent time windows, and restrict the analysis to the number and length of the time windows. The wave forms in Figures 4 6 are based on 10 s long time windows from a 5 day period. In a first test, the 5 day period is extended to 10 days, 15 days, 20 days, and 35 days, and also is decreased to one day. In case of short to medium offsets and low attenuation, there is no direct correlation of the S/N ratio of the interferogram with the length of the observation period. Instead it turns out that the interferograms from the individual 5 day periods differ significantly which indicates varying strength of the noise source within these time frames. The same effect is observed at large offsets and/or stations located in regions of stronger geological attenuation (e.g., section 1). In order to improve the S/N ratio, a possible strategy would be the selection and stacking of interferograms from periods with higher S/N ratio. The second test is a variation of the length of the time windows (10 s, 20 s, 60 s, 120 s). Longer time windows provide clearer surface wave arrivals, and in particular the zero-lag peak (section 3.3) is minimized. A possible explanation for both observations is the dissection of long coherent signals by cutting the input data into short time windows. The zero-lag peaks, which are considered as artefacts from remnant unwanted energy (e.g., high-frequency body waves of earthquakes not included in the used catalogue, section 3.2), are down weighted by improved correlation of longer time series. With regard to these tests, all following computations are performed for 120 s long time windows from a 5 day period (December 1st to December 5th, 2008).

3.5 Horizontal component processing

As the horizontal component data (east E, north N) are of similar quality as the vertical (Z) component data, we also calculate interferograms for the horizontal components. On average, initial tests show clear arrivals at the (N)-interferograms, and a lower S/N ratio at the (E)-interferograms. Further, most of the (N)-interferograms exhibit significantly higher apparent velocities which might indicate the presence of faster Love waves. We analyze this by the transformation of the horizontal (E,N) components into the radial and transverse (R,T) components. The radial direction is defined as the virtual source - receiver azimuth , and the transverse direction points 90 degrees clockwise to the radial direction. In case of a layered structure, the radial component (R) and the vertical component (Z) should highlight the Rayleigh wave, while the Love wave should be present on the transverse (T) component only. Surface waves reconstructed by interferometry suffer the loss of their original particle motion due to the correlation process, thus the 90 phase shift between the vertical and horizontal components of the Rayleigh wave cannot be observed on. Nonetheless, Rayleigh and Love waves can be separated by their different velocities. Lin et al. (2008) ana-

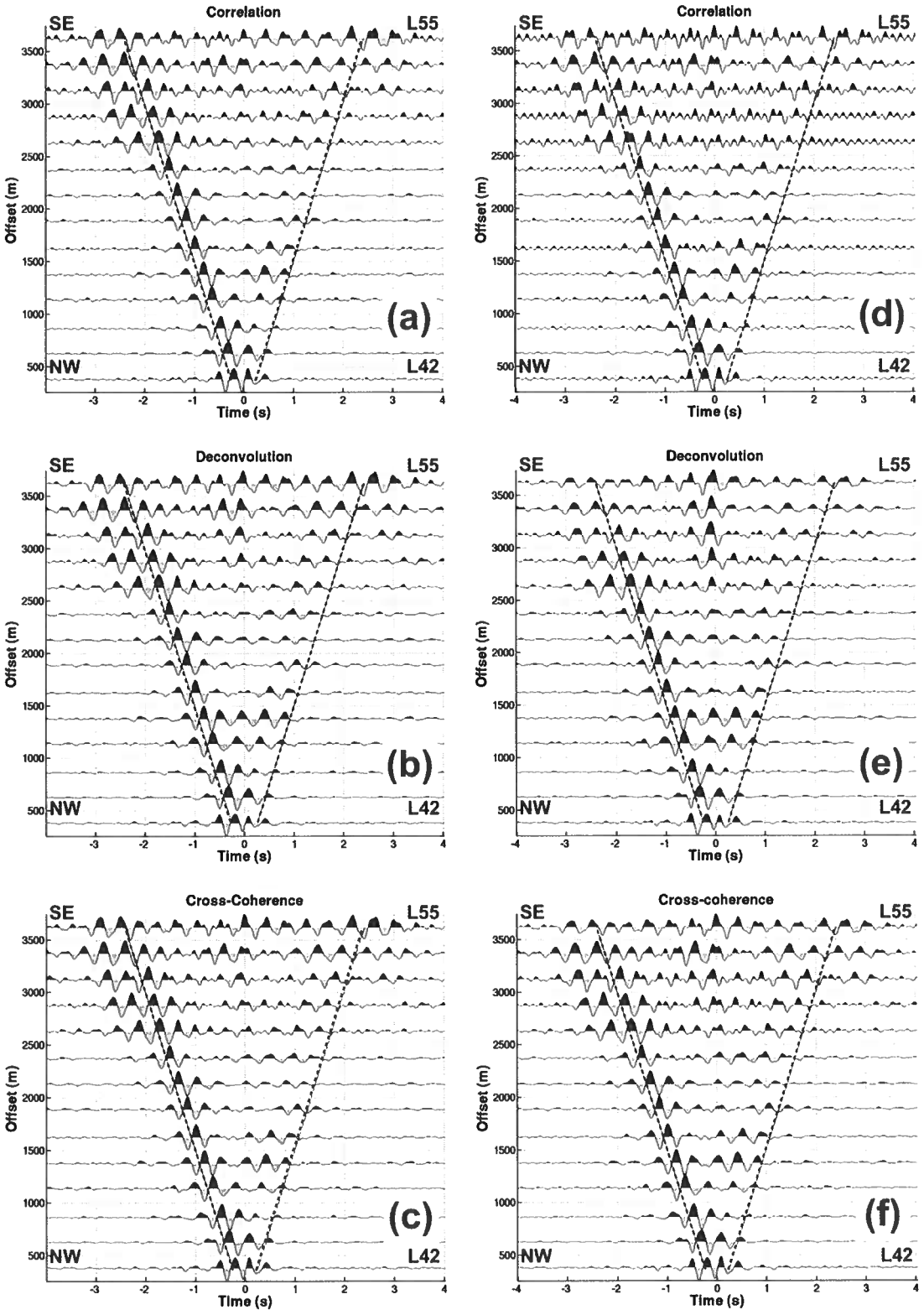

Figure 5. Comparison of different pre- and post-processing band pass filters for virtual source L22 and receivers along segment 3. The broken lines indicate linear move-outs for a velocity of 1500 m/s. NW and SE refer to the geographic directions. See text for details.

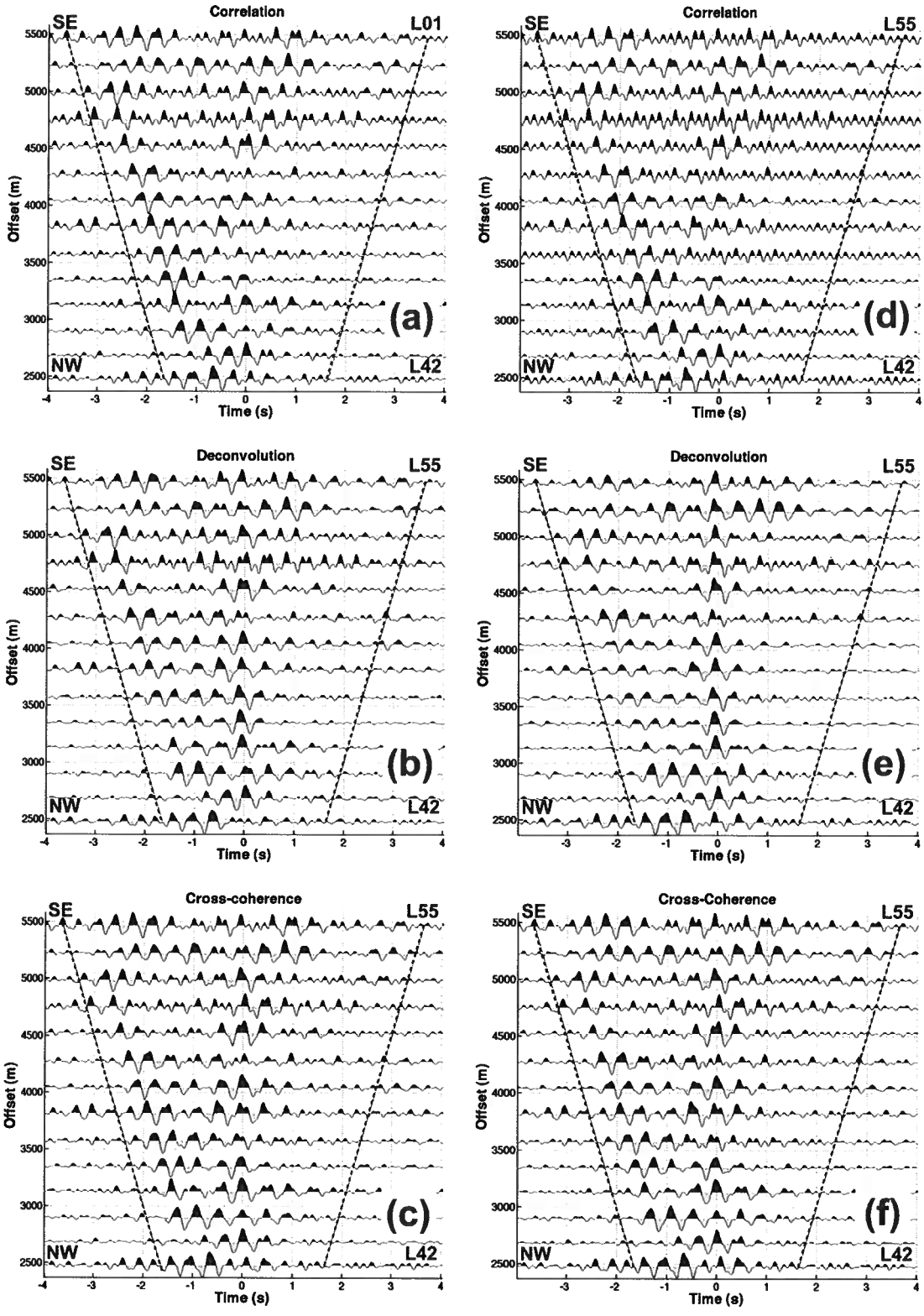

Figure 6. Comparison of correlation (a,d), deconvolution (b,e), and cross-coherence (c,f) for virtual source L22 and receivers along segment 3 (short to medium offsets). The left/right columns (a-c/d-e) are based on strongly/weakly whitened data (smoothing interval 0.1 Hz / 1 Hz). The broken lines indicate linear move-outs for a velocity of 1500 m/s.

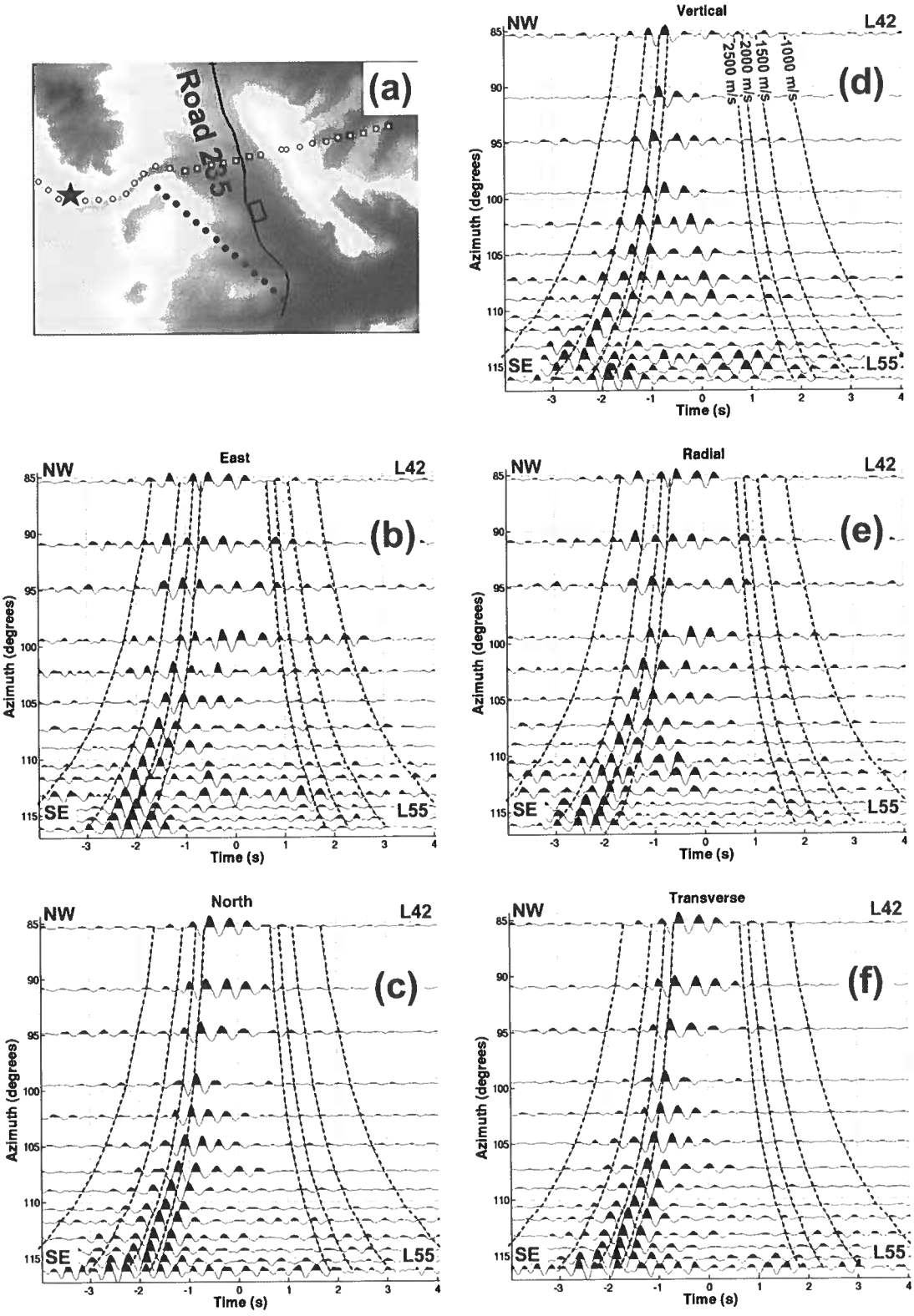

Figure 7. Transformation of the east (b) and north (c) components to radial (e) and transverse (f) components for virtual source L16 (star in (a)) and receivers along segment 3 (black dots in (a)). Trace spacing is proportional to the virtual source receiver azimuth. The broken lines indicate linear move-outs for different velocities. The azimuth is counted positive in clockwise direction starting from the north axis.

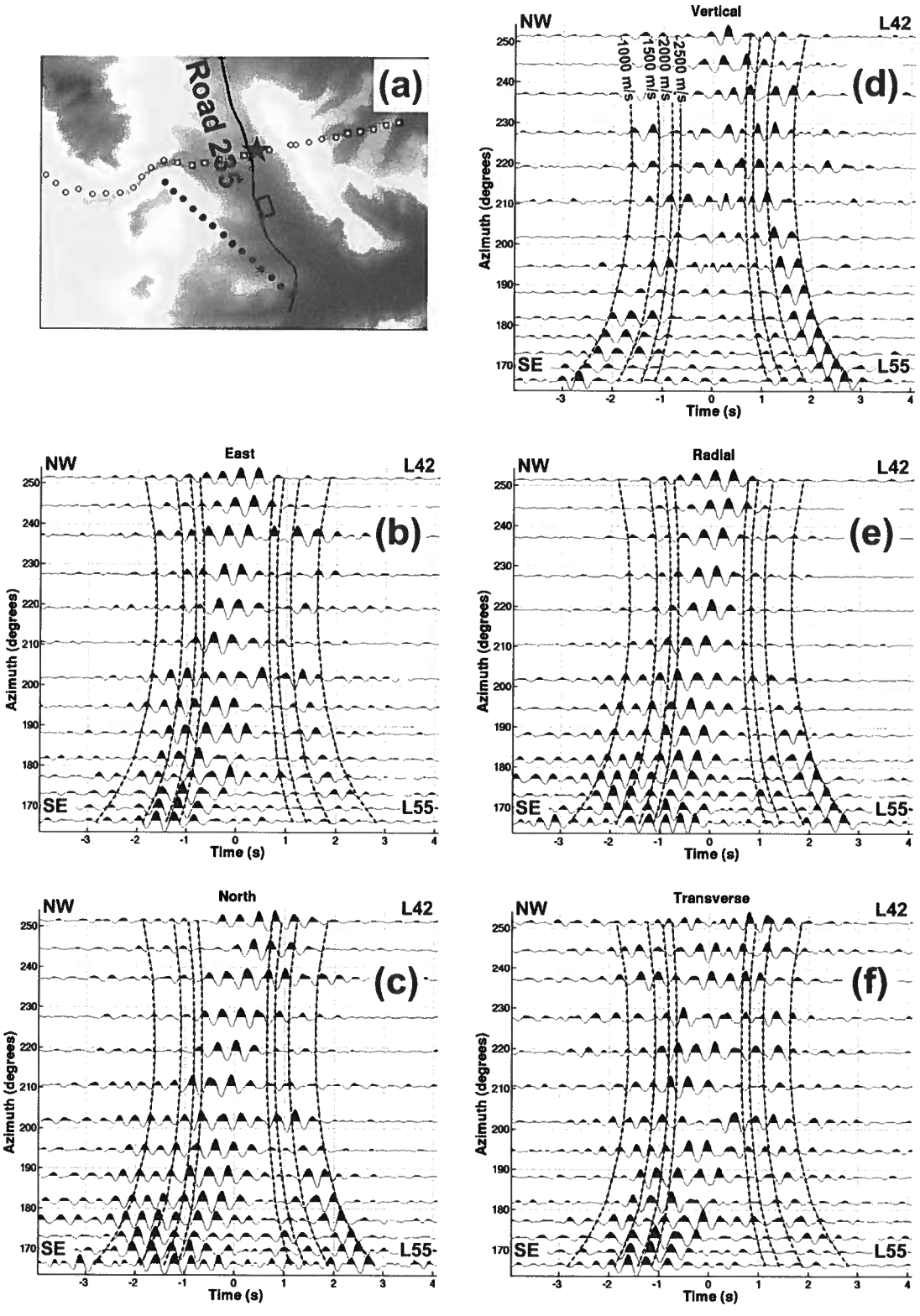

Figure 8. Transformation of the east (b) and north (c) components to radial (e) and transverse (f) components for virtual source L30 (star in (a)) and receivers along segment 3 (black dots in (a)). Trace spacing is proportional to the source receiver azimuth. The broken lines indicate linear move-outs for different velocities.

lyzed the radial and transverse parts of crustal seismology interferograms and were able to demonstrate that the T-component has a higher S/N ratio than the R-component, and that the Love wave is clearly present on the T-component. Subsequently they derived Rayleigh wave velocities from Z-component readings, and Love wave velocities from the T-components. We might expect the same, but have to consider that the scale of local velocity variations with respect to the wavelength is different than in crustal seismology. Local wave front curvatures at the stations will be larger, and Love and Rayleigh waves will be partially projected on both the (R) and (T) components. Consequently, the wave separation by (R,T) transformation is less effective. Additionally, due to the short offsets Rayleigh and Love waves are more likely to interfere which hampers their separation. Pre-processing becomes an issue in case of (R,T) transformation. Ideally, one would perform the rotation of the raw data first, and then do the pre-processing and finally applying interferometry. This is not practical with a 3D deployment because for each virtual source the azimuth depends on the receiver in question and pre-processing must be performed for each virtual source - receiver combination with an according multiplicative effect on the computational expense. Like Lin et al. (2008), we overcome this by choosing pre-processing operators which are commutative with the rotation operator such that pre-processing has to be applied to the horizontal component raw data (e(t), n(t)) only once. Band-pass filtering and whitening can be regarded as convolution operators in the time domain. Commutativity is achieved if the convolution operators for both components are identical, which is the case for a band-pass filter with constant corner frequencies. In case of user-controlled whitening (section 3.2), a practical solution is achieved by averaging the smoothed amplitude spectra of both components. Temporal normalization (AGC) is approached in a similar way. AGC can be formulated as an element-wise multiplication of the raw data series (e(t), n(t)) with series of normalizing factors ($g_e(t)$, $g_n(t)$). Again, commutativity is satisfied when $g_e(t)$ and $g_n(t)$ are identical. As the normalizing factors depend on the data, we calculate both $g_e(t)$ and $g_n(t)$, and chose the smaller one for each sample. 1-bit normalization cannot be adapted in a similar fashion, and thus it is not commutative with rotation. With regard to their subsequent workflow, Lin et al. (2008) applied interferometry on the pre-processed data, and finally rotated the interferograms. For reasons related to data handling, we switch this order and perform the rotation of the pre-processed data before applying interferometry. The parameters for the pre-processing steps (band-pass corner frequencies, AGC window length, and whitening smoothing length) for the horizontal components are identical to the ones used for vertical-component processing. A comparison of all five components (Z,N,E,R,T) is shown in Figures 7 and 8, where the spacing of the traces is proportional to their virtual source-receiver azimuth. Figure 7 gives an example where the virtual source is west of the receivers, and the state road is east of the receivers. We expect that this road is the dominant noise source (cf. section 3.6) which is also illustrated by the appearance of waves in the acausal part only. Therefore the faster Love waves would not only be expected on the T-component (Figure 7f), but also mainly on the N-component (Figure 7c) at W-E oriented azimuths. Due to the sine and cosine functions in the rotation operator, the contribution of the N-component still is twice as large as from the E-component (Figure 7b) at an azimuth of 115, which explains the overall similarity of the T- and N-components (Figures 7c,f). Comparing the Z-, R- and T-components, the latter ones feature a higher apparent velocity which is interpreted as the Love wave. Figure 8 shows that Love and Rayleigh waves might also be associated with different excitations. As the virtual source and the southernmost receivers are located close to the road, both causal and acausal signals may be expected at these receivers. This is the case for the Z- and R-components (Figures 8d,e), but the causal signals are missing at the T-component (Figure 8f). We therefore conclude that stronger Love waves are generated at the southern part of the road.

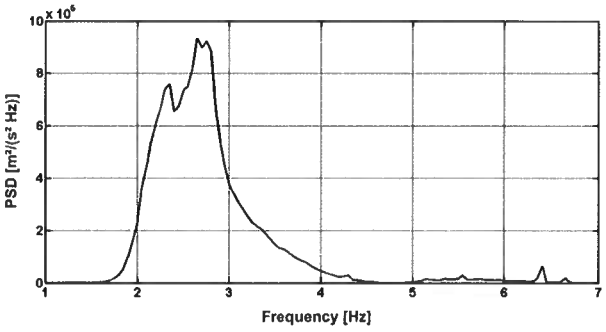

Figure 9. Stacked power spectral density of all obtained interferograms. See text for details.

3.6 Results

Splitting the 5-day interval (December 1st to December 5th, 2008) into 120 s long windows at 50 Hz results in 3600 data sections for each of the three components. For 2,916 virtual source-receiver pairs, the total number of all calculated individual interferograms amounts to approximately 31,000,000. In this section we draw conclusions on the obtained final interferograms, in particular with respect to the frequency content and the noise source. Due to the large number of interferograms, emphasis is laid upon exemplary and summative illustrations. Overall, the comparison between the three components suggests the presence of both Rayleigh and

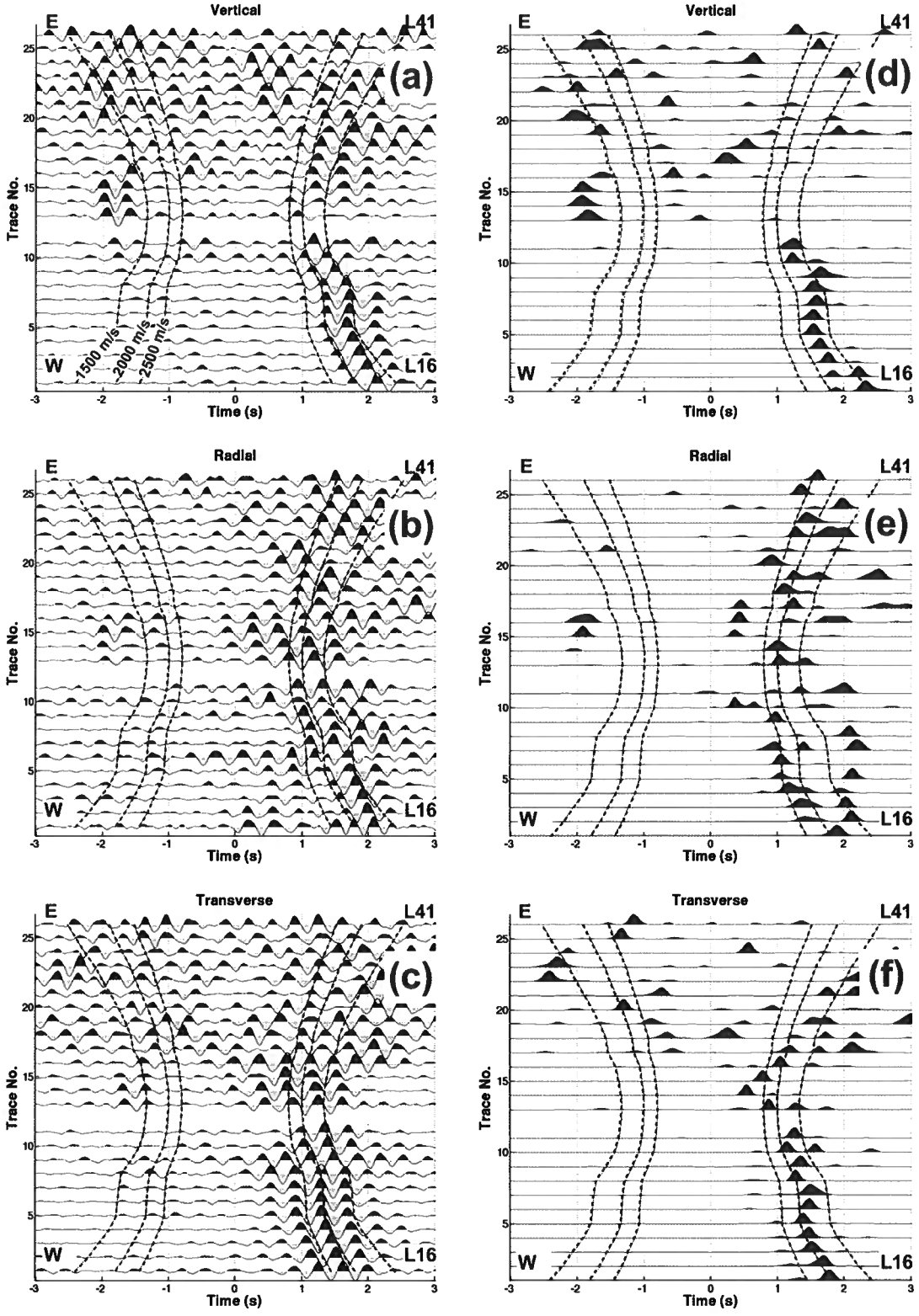

Figure 10. Interferograms of the vertical (a,d), radial (b,e), and transverse (c,f) components for virtual source L51 along segment 2. The trace spacing is equidistant. The right column (d-f) shows the application of the Hilbert transform. The broken lines indicate linear move-outs for different velocities.

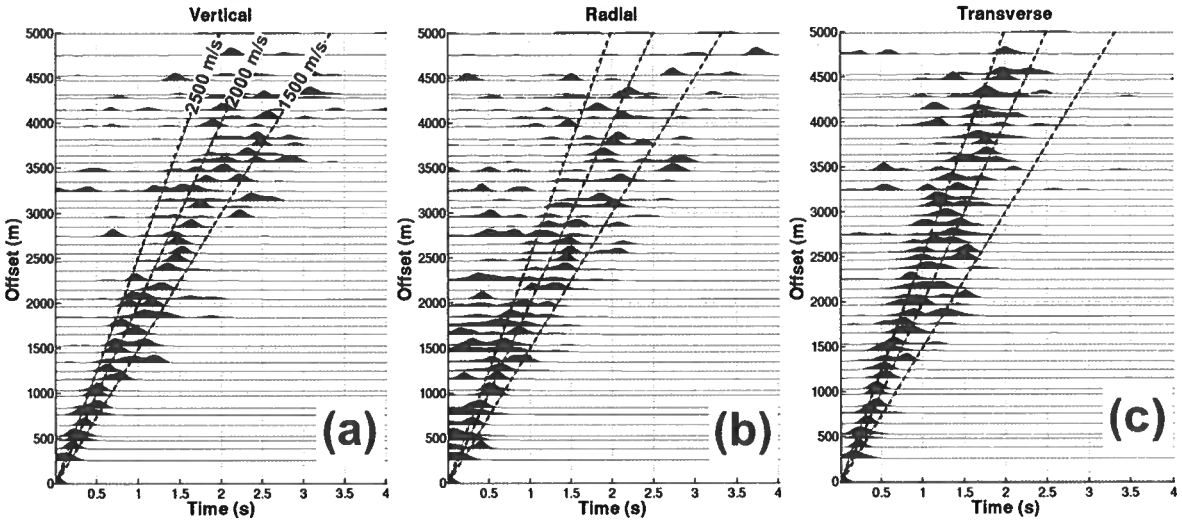

Figure 11. Common offset stacking applied to a subset of Hilbert-transformed interferograms (see text for details). The broken lines indicate linear move-outs for different velocities. (a,b,c,): Vertical, radial, and transverse component data, respectively.

Love waves due to their different apparent velocities. Surface waves appear clearer on Z- and T-components than on R-components. The derived waveforms have a strong amplitude and high S/N ratio. Nevertheless, the arrivals are not always characterized by one pronounced peak, but often by a sequence of two, three, or more peaks of similar amplitude (e.g. Figures 5 - 8). This is a consequence of the narrow frequency spectrum (Figure 9). A closer inspection shows that the maxima at 2.3 Hz and 2.8 Hz are differently pronounced on the vertical and horizontal components. Thus they are related to a slightly varying frequency response of the vertical and horizontal component instruments. Overall, the narrow band prevents the extraction of dispersion properties (cf. section 4). Frequency-wave number analysis is hampered by the limited spatial sampling and could only be used to get rough and approximate phase velocities, which however can also be obtained from the interferograms in the time domain. The individual peaks in the interferograms can be correlated, but the true onset of the arrivals is not always clear. Thus the envelope function (modulus of the analytical signal) is applied in order to reduce the wavelet to a single peak. The envelope function is additionally raised to its 5th power to enhance the strongest amplitude, which mostly corresponds to the surface wave arrival (Figure 10). This procedure retains the kinematic properties of the observed wave, and the transformed wavelet now represents group velocities instead of phase velocities. The envelope calculation of the horizontal components may be flawed at short offsets, where Love and Rayleigh waves are superimposed. Also, non-stationary contributions will result in inaccuracies, but overall the analyst can pick arrivals much more consistently than prior to the envelope calculation. To obtain a more representative picture of the investigated area, we stack a sub-set of the final interferograms into offset bins with a size of 100 m. Due to local velocity variations, we have to expect to mix phases with different arrival times in each bin and thus velocity information deduced from the stacks must be interpreted with caution. The data subset is defined by the stations L12-L31 and L42-L55, which feature interferograms with the clearest appearance. Since the move-out and the spacing of the stations are too large with respect to the wavelength, we stack the Hilbert transformed data. The results for all three components are shown in Figure 11. Arrivals on the T-component have a higher apparent velocity, and these arrivals can be observed over longer offsets. Z- and R-component arrivals appear rather similar, with an overall lower S/N ratio of the R-components. This observation is also made by Lin et al. (2008), although they analyzed data on a global scale. The higher S/N ratio on the Z-component in comparison to the R-component may be related to the subsurface structure (e.g. Boore and Toksoez (1969)). Overall, the common offset stacks strengthen the assumption that both Rayleigh and Love waves are observed. Overall we obtain a substantial set of useful interferograms, both on inline and cross-line virtual source receiver pairs, which indicate a wide distribution of stationary source points. The examples shown so far feature a pronounced difference of the causal and acausal parts. This is observed throughout the area, where on average the acausal part dominates. Note that the westernmost stations (L01 - L11) exhibit a lower S/N ratio. For virtual sources located west of the state road, receivers at and

east of the mesa (L32 - L41) show only little coherent energy, and observed surface waves often arrive with unreasonably high velocities. The latter observation could be explained by the existence of a dominant noise source located in-between virtual sources and receivers. Altogether, there is strong evidence for a dominant noise source in the eastern part of the deployment, and we conclude that traffic from the state road 235 excites the majority of the observed surface waves. The observed variability of the quality of the interferograms with respect to the used time frame (section 3.4) might also be explained by irregular traffic activity. With respect to the geometry of the deployment, the north-south oriented road provides a large number of stationary source points. Lak et al. (2011) analyze the frequency response of roads to traffic. They take into account the construction of the road, the type of the vehicle, and the soil structure. They focused on the near-field effect (2 to 64 m) and concluded that the resulting spectrum mainly depends on the eigenfrequencies of the vehicles which range from 2 to 15 Hz. Since the offsets in our study are much larger, we expect to observe only the lower end of this spectrum.

4 INVERSION

The inversion of surface waves for depth-dependent shear wave velocities is a standard procedure for global surface wave data. The frequency-time analysis method (FTAN; Dziewonski et al. (1969)) makes use of the dispersion characteristics of surface waves and is commonly applied to Rayleigh waves (Bensen et al. (2007), and references therein), and also to Love waves (Lin et al., 2008). FTAN provides dispersion curves for group velocities for a single source receiver combination. The surface wave velocity - frequency relation is inverted for an average shear wave velocity - depth relation between the source and receiver. We also applied FTAN to the interferograms, but due to the limited bandwidth in conjunction with the lateral geologic variability we did not derive meaningful dispersion curves. On the other hand, we derive a substantial number of useful interferograms on both inline and cross-line virtual source receiver combinations. The envelope calculation facilitates consistent manual picking of surface wave arrival times. Consequently, these arrival times can be inverted for laterally varying group velocities by a tomographic approach similar to the simultaneous iterative reconstruction technique (SIRT; e.g. van der Sluis and van der Horst (1987)). Modifications of the SIRT method for lateral velocity modelling are given by Iwasaki (2002), Song et al. (2004), and Behm et al. (2007). We parameterize the surface velocities at grid points with a lateral spacing of 250 m. Surface wave paths are approximated by straight rays between the virtual source and the receiver. We are aware that these simplifications may introduce artefacts in the obtained models, but we consider them to be of equal or minor effect in comparison to the accuracy of travel time picking. If the surface velocity at a grid point is expressed as the slowness s, the travel time t for a specific ray is calculated from:

$$t = \sum_{i=1}^{N} l_i \cdot \sum_{j=1}^{M} \lambda_j \cdot s_j \qquad (6)$$

The ray is split into N segments of equal length l_i, where N is the ratio of the total ray length (offset) to the grid point spacing (250 m). The corresponding slowness for each segment is represented by the second summation term in equation (6), and it is interpolated from the slownesses s_j at the neighbouring grid points. λ_j is a factor which decreases with the distance between the ray segment midpoint and the j-th grid point. The number M of contributing grid points is defined by a maximum distance of 375 m. The λ_j are calculated from a distance-dependent Gaussian function to guarantee smooth behaviour for the velocity interpolation, and they are normalized such that their sum is 1. For all observed travel times t_{obs}, a set of linear equations is established and solved for the unknown slownesses s_j at the grid points. Travel time residuals to an initial model are calculated, and singular value decomposition (SVD) is used for the inversion. The trade-off between the RMS error of the travel time residuals and the variance of the derived velocity map is controlled by a cut-off value for the eigenvalues and additional smoothing of the obtained slowness improvements. At this stage we focus on the large-scale structure of the region which is more sensitive to systematic mispicks (e.g., following a wrong phase) than to slightly inaccurate travel time readings. Correlation-based travel time picking improves the accuracy of individual picks, but nonetheless a visual control is necessary to check for systematic mispicks. We therefore chose to pick travel times manually. Travel times are only picked if the phases can be clearly correlated over at least two adjacent stations. Additional quality criteria are the S/N ratio and a realistic apparent velocity (1000 - 3000 m/s). Those envelope travel times (Figure 12) are inverted for group velocities, where vertical-component data provide Rayleigh wave velocities and transverse-component data provide Love wave velocities. We chose constant velocity initial models, and calculate the velocities from the slope of the regression lines in Figure 12. Picks are limited to traces with offsets between 0.3 and 5 km. The inversion statistics are summarized in Table 1.

The lower number of T-component travel times reflects the uncertainty of picking the horizontal component, which we attribute to the imperfect separation of Love and Rayleigh waves. This is also the reason why we don't include the R-component data in the inversion for Rayleigh wave velocities. Phase velocities are associated with the interferograms prior to the Hilbert transform. As outlined before, the true onset of the phases (the

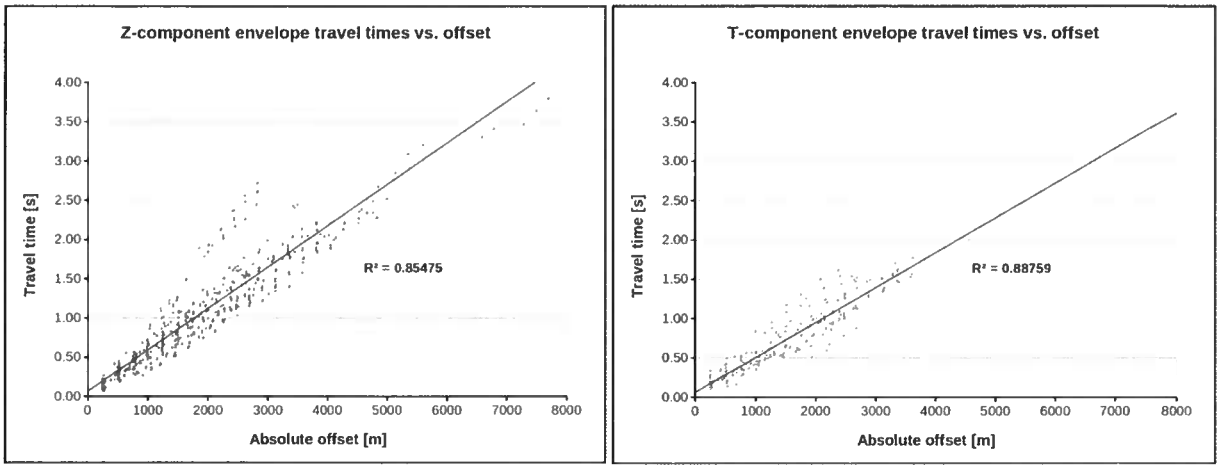

Figure 12. Picked surface wave travel times vs. offset for Hilbert-transformed interferograms of the Z- and the T-components. The slopes of the regression lines correspond to 1880 m/s and 2250 m/s, respectively. The zero-offset times are in the order of +0.05 s and are attributed to the entire post-processing steps including the Hilbert transform. They are subtracted from the travel times prior to the inversion.

Type	no. of travel time picks	initial velocity [m/s]	Travel time residual RMS prior to inversion [s]	Travel time residual RMS after inversion [s]	avg. / std.dev / min / max of the velocities after inversion [m/s]
Z-comp.	634	1880	0.272	0.117	1757 / 325 / 1104 / 2373
T-comp.	247	2250	0.154	0.109	2179 / 256 / 1545 / 2618

Table 1. Table 2: Statistics and results for the inversion of envelope travel times.

absolute travel time) is difficult to determine at most occasions, but the phases can be clearly correlated over adjacent traces. Thus the travel time difference between two adjacent traces can be estimated with comparably high accuracy, and equation (6) is reformulated to express travel time differences. In this case, the initial model is of great importance due to the relative nature of the input data, and we chose the result from the group velocity inversions as initial models. Due to the effective absence of dispersion as a consequence of the limited bandwidth, we do not expect a large systematic disparity between group and phase velocities. Instead, we anticipate more localized velocity information and a larger coverage by the additional use of phase travel time differences. The RMS error of travel time residuals does not significantly change after the inversion, and in case of the Z-component it even slightly increases (Table 2). On the other hand, this error is considerably smaller than the RMS error of the absolute travel times (Table 1), and the results change only locally (Figure 13). This implies that the limited bandwidth of the data effectively results in identical group- and phase velocities. The additional use of phase travel time differences provides improved coverage and confirms the large-scale structure of the group velocity model, but local changes to the velocity model may be regarded as possible inversion artefacts. In whole, all four inversions correlate with surface geology. The carbonates west of the Hogsback thrust are represented by higher velocities than the clay and silt stones in the east. We estimate the depth sensitivity by the vertical eigenfunction of the surface waves (e.g., Stein and Wysession (2003)). The amplitude A of a Love wave as a function of depth z is proportional to

$$A \sim e^{-k_x \cdot r \cdot z} \tag{7}$$

where k_x is the horizontal wave number and r is given by

$$r = \sqrt{1 - \frac{c^2}{\beta^2}} \tag{8}$$

c is the phase velocity of the surface wave and is the shear-wave velocity of the bottom layer. Based on our results and previous investigation of the area, we assume a frequency of 2.5 Hz, an average Love wave velocity (c) of 2100 m/s, and a bottom layer shear-wave velocity (β) of 3000 m/s, and evaluate equation (7). A(z) decays to

Type	no. of travel time picks	Travel time residual RMS prior to inversion [s]	Travel time residual RMS after inversion [s]	avg. / std.dev / min / max of the velocities after inversion [m/s]
Z-comp.	643	0.046	0.052	1809 / 369 / 1122 / 2624
T-comp.	465	0.027	0.026	2107 / 261 / 1636 / 2619

Table 2. Table 1: Statistics and results for the inversion of travel time differences.

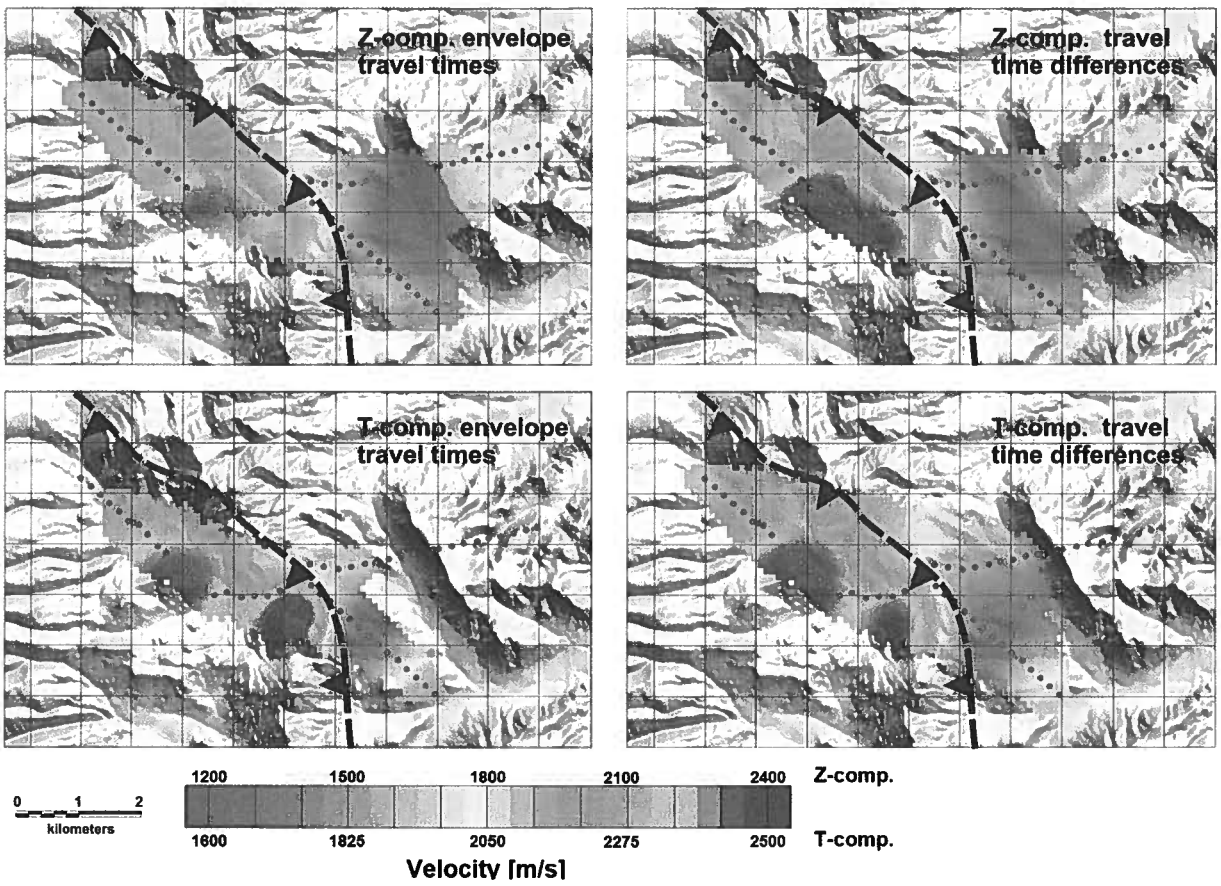

Figure 13. Results from travel time inversion. Z- and T-component travel times are related to Rayleigh and Love wave velocities, respectively. Envelope travel times represent the Hilbert transformed interferograms and group velocities, while the travel time differences from the original interferograms reflect phase velocities. See text for details. Note the different colour scaling for Z- and T-components. Varying coverage results from picking different virtual source receiver combinations.

a third of its maximum value at a depth of 206 meters, which is approximately a quarter of the wavelength and we use this value as a rough estimate of the depth sensitivity of the surface waves. This estimation is in agreement with layer depth calculation based on Rayleigh and Love wave velocities (e.g. Shearer (1999)). Both estimations depend on several assumptions, in particular on the poorly known bottom layer shear wave velocities, but we conclude that the observed surface waves represent average velocities from the upper 100 to 300 meters. We finally calculate the ratio of the Love and Rayleigh wave velocities (Figure 14). Due to the overall indifference of group and phase velocities, we chose the latter one because of their larger coverage. The average ratio is 1.18, and the variations correlate again with surface geology with the region east of the thrust having higher values.

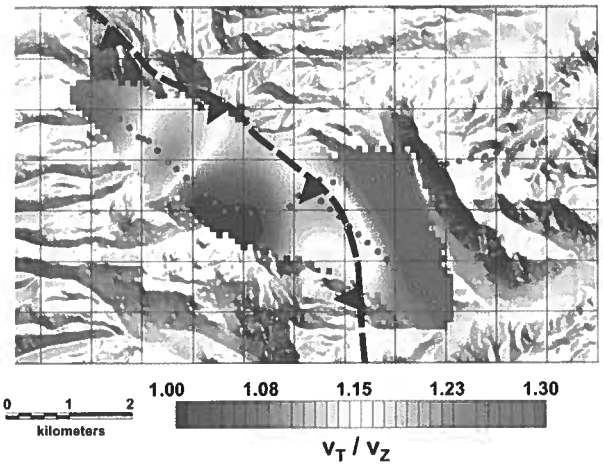

Figure 14. Ratio of Love and Rayleigh wave velocities.

5 CONCLUSIONS

We successfully applied interferometry to passive seismology data from a local deployment in an industrial setting. Well-established methods from the global seismology community were adapted to the needs for local studies. Traffic noise from a state highway was the main source of the extracted surface waves. The orientation of the road with respect to the deployment results in a high number of stationary points, thus enabling a large coverage. Stacking of five days of data is sufficient to retrieve surface waves up to 5 kilometres of distance. Longer observation periods do not necessarily lead to better results. The S/N ratio of the interferograms is proportional to the length of the windows which are used to calculate the correlations, and we find a length of 120 seconds sufficient for our purposes. The performance of different interferometry algorithms depends on the pre-processing. Cross-coherence is regarded as the most flexible method with respect to the input data, and provides robust results in this study. Both the vertical and horizontal components are of similar quality, and can be used to discriminate between Love and Rayleigh waves. The limited band width prevents the calculation of depth-dependent shear wave velocities, but the high number of usable interferograms allow for inversion for laterally varying Love and Rayleigh wave velocities. These velocities correlate well with surface geology and represent the few upper hundred meters of the subsurface. An important lesson is the relatively low amount of needed input data in areas with traffic noise. If and how the depth-sensitivity of locally excited surface waves can be increased poses an important research question. From a practical point of view, the spectral character of the noise source ultimately determines the ability to obtain dispersion curves and therefore depth dependent structure. Ideally, a noise source spanning a sufficiently wide frequency range (perhaps from 0.5 to 10 Hz) will provide sufficient frequency coverage to obtain robust geologic models for more sophisticated imaging applications. In a frequency limited scenario (such as ours), the models may still be useful for calculation of near-surface shear wave statics from surface wave velocities and large scale geologic characterization.

ACKNOWLEDGMENTS

ExxonMobil provided funding of this study. We thank Mike Mooney (CSM), Berk Byriol (University of Arizona), Kyle Lewallen and Jelena Tomic (ExxonMobil) for discussion and administrative support. IRIS data management centre was used to access waveform data. Kees Wapenaar and two anonymous reviewers helped to improve the manuscript by their detailed and thoughtful comments. Data analysis was done with the software package Seismon (Mertl and Hausmann, 2009), to which interferometry processing tools have been added.

REFERENCES

Aki, K., 1957, Space and time spectra of stationary stochastic waves, with special reference to microtremors: Bulletin of the Earthquake Research Institute, **35**, 415–457.

Bakulin, A., and R. Calvert, 2006, The virtual source method: Theory and case study: Geophysics, **71**, SI139.

Behm, M., E. Brückl, W. Chwatal, and H. Thybo, 2007, Application of stacking and inversion techniques to three-dimensional wide-angle reflection and refraction seismic data of the Eastern Alps: Geophysical Journal International, **170**, 275–298.

Bender, C., and S. Orszag, 1978, Advanced Mathematical Methods for Scientists and Engineers: McGraw-Hill.

Bensen, G. D., M. H. Ritzwoller, M. P. Barmin, a. L. Levshin, F. Lin, M. P. Moschetti, N. M. Shapiro, and Y. Yang, 2007, Processing seismic ambient noise data to obtain reliable broad-band surface wave dispersion measurements: Geophysical Journal International, **169**, 1239–1260.

Bleistein, N., 1984, Mathematical Methods for Wave Phenomena: Academic Press.

Boore, D., and M. Toksoez, 1969, Rayleigh wave particle motion and crustal structure: Bulletin of the Seismological Society of America, **59**, 331–346.

Bussat, S., and S. Kugler, 2009, Feasibility of Offshore Ambient-Noise Surface-Wave Tomography on a Reservoir Scale: SEG Expanded Abstract, 1627–1631.

Draganov, D., X. Campman, J. Thorbecke, A. Verdel, and K. Wapenaar, 2009, Reflection images from ambient seismic noise: Geophysics, **74**, 63–67.

Dziewonski, A., S. Bloch, and M. Landisman, 1969, A technique for the analysis of transient seismic signals:

Bulletin of the Seismological Society of America, **59**, 427–444.

Forghani, F., and R. Snieder, 2010, Underestimation of body waves and feasibility of surface-wave reconstruction by seismic interferometry: The Leading Edge, **29**, 790–794.

Halliday, D., and C. Curtis, 2008, Seismic interferometry, surface waves and source distribution: Geophysical Journal International, **175**, 1067–1087.

Iwasaki, T., 2002, Extended time-term method for identifying lateral structural variations from seismic refraction data: Earth Planets Space, **54**, 663–677.

Lak, M., G. Degrande, and G. Lombaert, 2011, The effect of road unevenness on the dynamic vehicle response and ground-borne vibrations due to road traffic: Soil Dynamics and Earthquake Engineering, **31**, 1357–1377.

Lin, F.-C., M. P. Moschetti, and M. H. Ritzwoller, 2008, Surface wave tomography of the western United States from ambient seismic noise: Rayleigh and Love wave phase velocity maps: Geophysical Journal International, **173**, 281–298.

Mertl, S., and H. Hausmann, 2009, Seismon - a flexible seismic processing software: Geophysical Research Abstracts, EGU, EGU2009–4266.

O'Connell, D. R. H., 2007, Concrete dams as seismic imaging sources: Geophysical Research Letters, **34**, 4–8.

Paul, A., 2005, Empirical synthesis of time-asymmetrical Green functions from the correlation of coda waves: Journal of Geophysical Research, **110**, 1–13.

Picozzi, M., S. Parolai, D. Bindi, and a. Strollo, 2009, Characterization of shallow geology by high-frequency seismic noise tomography: Geophysical Journal International, **176**, 164–174.

Poletto, F., and F. Miranda, 2004, Seismic while drilling: Fundamentals to drill-bit seismic for exploration. Handbook of Geophysical Exploration (35): Pergamon Press.

Prieto, G., J. Lawrence, and G. Beroza, 2009, Anelastic Earth Structure from the Coherency of the Ambient Seismic Field: Journal of Geophysical Research, **114**, B07303.

Rial, J., 1989, Seismic wave resonances in 3-D sedimentary basins: Geophysical Journal International, **99**, 81–90.

Ridder, S. D., and J. Dellinger, 2011, Ambient seismic noise eikonal tomography for near-surface imaging at Valhall: The Leading Edge, **30**, 1–7.

Saltzer, R., G. M. Leahy, J. Schmedes, J. Roth, and E.-M. Rumpfhuber, 2011, Earthquakes A naturally occurring source of low frequency data: SEG Expanded Abstract, SEG, 3689–3693.

Seats, K., J. Lawrence, and G. Prieto, 2012, Improved ambient noise cross correlation functions using Welch's method: Geophysical Journal International, **188**, 513–523.

Shearer, P., 1999, Introduction to seismology: Cambridge Universitz Press.

Snieder, R., 2004, Extracting the Greens function from the correlation of coda waves: A derivation based on stationary phase: Physical Review E, **69**.

———, 2007, Extracting the Green's function of attenuating heterogeneous acoustic media from uncorrelated waves: Journal of the Acoustical Society of America, **121**, 2637–2643.

Snieder, R., and E. Safak, 2006, Extracting the Building Response Using Seismic Interferometry: Theory and Application to the Millikan Library in Pasadena, California: Bulletin of the Seismological Society of America, **96**, 586–598.

Snieder, R., K. Wapenaar, and K. Larner, 2006, Spurious multiples in seismic interferometry of primaries: Geophysics, **71**, SI111–SI124.

Song, L.-P., M. Koch, K. Koch, and J. Schlittenhardt, 2004, 2-D anisotropic Pn-velocity tomography underneath Germany using regional traveltimes: Geophysical Journal International, **157**, 645–663.

Stehly, L., M. Campillo, and N. M. Shapiro, 2006, A study of the seismic noise from its long-range correlation properties: Journal of Geophysical Research, **111**, B10306.

Stein, S., and M. Wysession, 2003, An introduction to seismology, earthquakes, and earth structure: Blackwell Publishing.

Tsai, V., 2011, Understanding the amplitudes of noise correlation measurements: Journal of Geophysical Research, **116**, B09311.

van der Sluis, A., and H. van der Horst, 1987, Numerical solution of large, sparse linear algebraic systems arising from tomographic problems, *in* Seismic Tomography: Hingham, 49–83.

Vasconcelos, I., and R. Snieder, 2008, Interferometry by deconvolution, Part 1 Theory for acoustic waves and numerical examples: Geophysics, **73**.

Wapenaar, K., D. Draganov, R. Snieder, X. Campman, and A. Verdel, 2010a, Tutorial on seismic interferometry: Part 1 Basic principles and applications: Geophysics, **75**, 75A195–75A209.

Wapenaar, K., and J. Fokkema, 2006, Greens function representations for seismic interferometry: Geophysics, **71**, SI33–SI46.

Wapenaar, K., E. Slob, R. Snieder, and A. Curtis, 2010b, Tutorial on seismic interferometry: Part 2 Underlying theory and advances: Geophysics, **75**, A211–A227.

Blind deconvolution of multichannel recordings by linearized inversion in the spectral domain

Michael Behm
Center for Wave Phenomena, Geophysics Department, Colorado School of Mines, Golden, CO

ABSTRACT
Blind deconvolution aims at recovering both the source wavelet and the Green's function (e.g. reflectivity series) from a recorded seismic trace. A multitude of algorithms exist which tackle this ill-posed problem by different approaches. Making assumptions on the phase spectra of the source wavelet and/or the statistical distribution of the reflectivity series are useful for single traces. The nature of closely spaced multichannel recordings enables a better estimation of a common source wavelet and thus increases the confidence of the results. This approach has been exploited in the past, although different types of assumptions are used for a variety of algorithms. I introduce a new method for simultaneous reconstruction of arbitrary source wavelets and local vertical reflectivity series from teleseismic earthquakes. It is considered that closely spaced receivers record vertically incident earthquake body waves and their surface related multiples which comprise the unknown reflectivity series. By assuming a common source wavelet for all receivers, the observation of several events results in a set of convolution equations relating the unknown source wavelets and unknown reflectivity series to the observed seismic trace. The overdetermined system of equations is linearized and solved by conventional inversion algorithms in the spectral domain. Synthetic tests indicate a better performance of the introduced method than conventional deconvolution in the presence of white noise, which is attributed to the constraint of a common model for all observations. Application to field data from a local deployment allows imaging a basement reflector from teleseismic body waves, although the data are contaminated with strong coherent noise. From a practical point of view, the presented method is potentially well suited for local and regional large-scale imaging from multichannel passive seismic data.

Key words: deconvolution, reflectivity structure, inversion

1 INTRODUCTION

Blind deconvolution is a term coined in signal processing theory and aims at reconstructing both the unknown source wavelet w(t) and the unknown transfer function r(t) from the observed convolution z(t)=r(t) $\star$ w(t). It is obvious that assumptions on either w(t), r(t), or both, have to be made to derive a solution. Conventional deconvolution might be regarded as a special case of blind deconvolution since an estimate of w(t) can be obtained from the autocorrelation of z(t) in case r(t) is white. Since the autocorrelation provides the amplitude spectra only, premises on the phase spectra of w(t) (e.g. minimum-phase) have to be made. Wiggins (1978) introduced the minimum entropy deconvolution method based on kurtosis maximization of the transfer function. Minimum entropy deconvolution does not rely on the minimum-phase assumption, but requires a broad-band source wavelet. To circumvent the broad-band pre-condition, even more advanced statistical approaches have emerged in the field of electrical engineering (Cadzow and Li, 1995) as well as in seismic exploration (van der Baan and Pham, 2008). In earthquake seismology, multichannel recordings are often utilized to obtain an estimate of the source wavelet by simply averaging the recordings. If the source wavelet of an earthquake is stationary with respect to the receiver array aperture, the average wavelet of all receivers can be deconvolved from the individual recordings to obtain r(t). This method is used to image lateral sub-surface

variations on basin scale (e.g. Yang et al. (2012)) and on crustal scale (e.g. Tseng and Chen (2006)). Simultaneous least-squares deconvolution of several seismic events (Gurrola et al., 1995) is an alternative approach. Based on the theory of homomorphic systems, multichannel recordings can be transformed into the log-spectral domain where averaging leads to an improved estimate of the source wavelet (Otis and Smith, 1977). This approach has been used in exploration seismology (Tria et al., 2007) as well as in earthquake seismology (Bostock and Sacchi, 1997). The latter study makes uses of multisource and multichannel recordings to sharpen later teleseismic arrivals (e.g., reflections from the mantle-core boundary). Bostock (2004) revisits these concepts in a more elaborate framework which includes the evaluation of three-component recordings to get more insight into the crustal structure on the receiver side. From a technical point of view, many of the aforementioned studies focus on the reconstruction of the source wavelet in the spectral (or log-spectral) domain which in turn is deconvolved from the data. In contrast, Kaaresen and Taxt (1995) introduce a method for multichannel data and sparse reflectivity which estimates w(t) and r(t) by a quasi-simultaneous, iterative scheme in the time domain.

Although by far not exhaustive, the list of cited studies illustrates that blind deconvolution finds its application in both exploration and earthquake seismology. Bridging the gap between these two fields is further facilitated by the industrys growing attention for passive seismology and broad-band data. In particular the interest in the low frequency spectrum of seismic data is mainly driven by the need for robust initial velocity models for full waveform inversion (Sirgue and Pratt, 2004; Denes et al., 2009). Passive seismology is well suited to provide those low frequency data due to the instrument specifications and the wide range of possible sources (e.g. cultural noise, regional and global seismicity). Passive seismic methods might also be employed to get a large-scale image of unexplored terrain without utilizing active sources. I introduce a new blind deconvolution method for imaging local vertical reflectivity series from teleseismic events which were recorded on a passive array in south-western Wyoming. The data were acquired in academia-industry cooperation to investigate the feasibility of passive seismology for large-scale subsurface characterization. Therefore, the presented study also aims to contribute to the aforementioned topics.

2 METHOD

A set of N seismic events is recorded on an array comprising M receivers. Those receivers are closely spaced, such that the source wavelet $w_n(t)$ of each event is invariant with respect to the receiver location. It is further assumed that the incoming wave is a vertically incident plain wave. While the latter constraint is satisfied by teleseismic events with epicentral distances greater than 30 degrees in case of small array aperture (<100 km), the validity of the wavelet invariance assumption mainly depends on two factors. These are the size of the Fresnel zone, and the size and magnitude of the impedance discontinuities along the ray path between the source location and the maximum imaging depth at the receiver side. If the spatial extent of these velocity discontinuities is large in comparison to the array aperture, the source wavelets at each individual station are affected by the same transmission coefficients and are identical at each receiver. The local vertical reflectivity series at each receiver station is denoted by $r_m(t)$, and the duration of $r_m(t)$ corresponds to the aforementioned maximum possible imaging depth. The observed seismic trace $z_{nm}(t)$ is associated with the n-th event recorded at station m. It is modeled by the superposition of the incoming wave $w_n(t)$ and its convolution with $r_m(t)$ after the reflection at the free surface:

$$\begin{aligned} z_{nm}(t) &= s(w_n(t), r_m(t)) + noise(t) \\ &= w_n(t) - r_m(t) \star w_n(t) + noise(t) \end{aligned} \quad (1)$$

In equation (1), the star sign denotes convolution. Taking the superposition of the wavelet and the convolution term instead of convolution only is of crucial importance when the duration of the wavelet is equal or larger than the zero-offset two-way travel times of the expected reflections (or in other words, when the weaker reflectivity responses are buried beneath the strong source wavelet; Figure 1). The negative sign of the convolution term in equation (1) results from the reflection coefficient at the free surface (-1) and the desire for using the convention nomenclature for reflectivity, where positive impedance contrasts are described by positive reflection coefficients. While all statements so far have been made with P-waves in mind, they are also valid for S-waves where the free surface reflection coefficient is +1, and positive impedance contrasts are characterized by negative reflection coefficients (Aki and Richards, 2009). It should be noted that $w_n(t)$ does not represent the exact source-time function of the earthquake, because it is imprinted by all transmission coefficients between the source and the receiver. To fulfill the aforementioned invariance assumption for the source wavelet, it is required that the product of the transmission coefficients between the imaging depth and the receiver surface is constant over all receivers. This is guaranteed if the targeted discontinuities extend throughout the imaging area, and if the impedance contrast constant along this discontinuities is constant. Further, equation (1) is only valid if both the surface and the discontinuities are subhorizontal.

In the spectral domain, equation (1) becomes the complex-valued equation

$$\begin{aligned} Z_{nm}(f) &= S(W_n(f), R_m(f)) + Noise(f) \\ &= W_n(f) - R_m(f) \cdot W_n(f) + Noise(f) \end{aligned} \quad (2a)$$

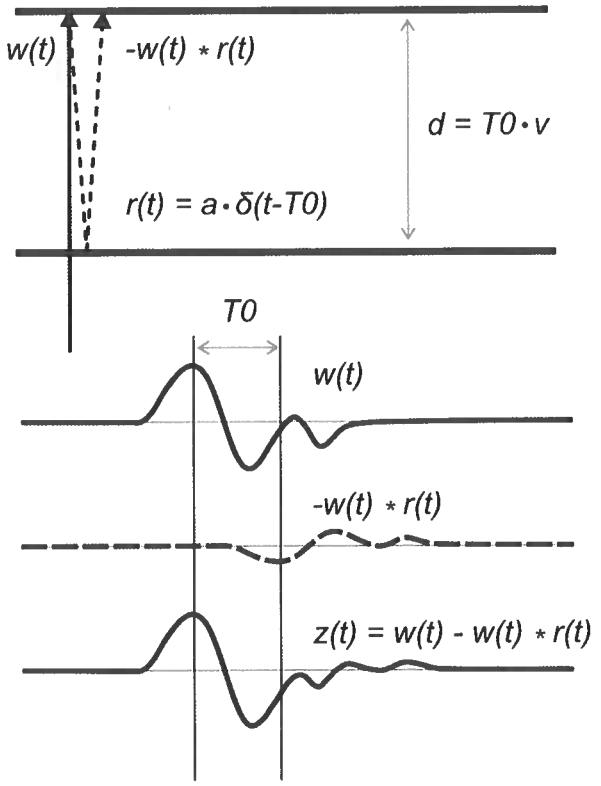

Figure 1. Superposition of a low-frequency vertically incident planar wave w(t) and its convolution with the near-surface reflectivity series after the reflection at the free surface. Note that the relatively weak reflection in the recording z(t) at time T0 is hidden by the stronger source wavelet. v: velocity above the reflector; d, T0 and a: depth, two-way travel time and reflection coefficient of the reflector; δ: Delta-function. The star sign denotes convolution.

In the following, the frequency (f) is dropped from the notation for simplicity. The function $S(W_n,R_m)$ in (2a) is explicitly rewritten in terms of real and imaginary parts:

$$S^R(W_n, R_m) = W_n^R - W_n^R \cdot R_m^R + W_n^I \cdot R_m^I \qquad (2b)$$

$$S^I(W_n, R_m) = W_n^I - W_n^R \cdot R_m^I - W_n^I \cdot R_m^R \qquad (2c)$$

where the superscripts (^{R}, ^{I}) indicate real and imaginary parts, respectively. If the noise is neglected, 2 x N x M observations (Z_{nm}^R, Z_{nm}^I) and 2 x (N + M) unknowns (W_n^R, W_n^I, R_m^R, R_m^I) are derived for each frequency component (f). If either N or M is larger than 2, these equations become (over-)determined and are solved by linearization with respect to the unknowns (e.g., Rawlinson and Sambridge (1998)). Starting from an initial model (W_{n0}^R, W_{n0}^I, R_{m0}^R, R_{m0}^I), the linearization is described by

$$\Delta S_{nm}^R = Z_{nm}^R - S^R(W_{n0}^R, W_{n0}^I, R_{m0}^R, R_{m0}^I) \qquad (3a)$$

$$\Delta S_{nm}^I = Z_{nm}^I - S^I(W_{n0}^R, W_{n0}^I, R_{m0}^R, R_{m0}^I) \qquad (3b)$$

$$\Delta S_{nm}^R = \frac{\partial S^R}{\partial W_n^R} \cdot \Delta W_n^R + \frac{\partial S^R}{\partial W_n^I} \cdot \Delta W_n^I + \frac{\partial S^R}{\partial R_m^R} \cdot \Delta R_m^R + \frac{\partial S^R}{\partial R_m^I} \cdot \Delta R_m^I \qquad (3c)$$

$$\Delta S_{nm}^I = \frac{\partial S^I}{\partial W_n^R} \cdot \Delta W_n^R + \frac{\partial S^I}{\partial W_n^I} \cdot \Delta W_n^I + \frac{\partial S^I}{\partial R_m^R} \cdot \Delta R_m^R + \frac{\partial S^I}{\partial R_m^I} \cdot \Delta R_m^I \qquad (3d)$$

Note that the noise iis now regarded as those part of the data Z_{nm} which cannot be fitted by the model S. The partial derivatives in (3c,d) are given by

$$\frac{\partial S^R}{\partial W_n^R} = 1 - R_m^R, \quad \frac{\partial S^R}{\partial W_n^I} = R_m^I, \quad \frac{\partial S^R}{\partial R_m^R} = -W_n^R, \quad \frac{\partial S^R}{\partial R_m^I} = W_n^I \qquad (4a)$$

$$\frac{\partial S^I}{\partial W_n^R} = -R_m^I, \quad \frac{\partial S^I}{\partial W_n^I} = 1 - R_m^R, \quad \frac{\partial S^I}{\partial R_m^R} = -W_n^I, \quad \frac{\partial S^I}{\partial R_m^I} = -W_n^R \qquad (4b)$$

Adopting a conventional nomenclature, these linearized equations are formulated in matrix notation as:

$$\mathbf{B} \cdot \mathbf{x} = \mathbf{y}, \qquad (5)$$

where $\mathbf{x}$ is the vector of model parameter updates (ΔW_n^R,ΔW_n^I ,ΔR_m^R, ΔR_m^I), $\mathbf{y}$ comprises the reduced observations (ΔS_{nm}^R, ΔS_{nm}^I; 3a,b) and $\mathbf{B}$ contains the partial derivatives (4). Both $\mathbf{y}$ and $\mathbf{B}$ are evaluated at the initial model (W_{n0}^R,W_{n0}^I,R_{m0}^R,R_{m0}^I). Continuity constraints on the reflectivity series ($\mathbf{C}$, $\mathbf{\Delta}\phi$, $\mathbf{\Delta}\tau$; see next page) are appended in form of additional rows to $\mathbf{B}$ and $\mathbf{y}$, such that (5) becomes

$$\begin{bmatrix} \mathbf{B} \\ \mathbf{C} \end{bmatrix} \cdot \mathbf{x} = \begin{bmatrix} \mathbf{y} \\ -\mathbf{\Delta}\tau \\ -\mathbf{\Delta}\phi \end{bmatrix} = \mathbf{D} \cdot \mathbf{x} = \mathbf{y}' \qquad (6)$$

Equation (6) is solved for $\mathbf{x}$ by the least-squares solution:

$$\mathbf{x} = (\mathbf{D}^\mathbf{T} \cdot \mathbf{D}^{-1}) \cdot \mathbf{D}^\mathbf{T} \cdot \mathbf{y}' \qquad (7)$$

Although $\mathbf{D}^\mathbf{T} \cdot \mathbf{D}$ is over-determined, the inverse in (7) may be ill posed and is calculated by spectral decomposition. By allowing only large singular values and corresponding singular vectors to contribute to the solution, spectral decomposition minimizes the projection

of noise on the model in case of poorly conditioned systems. The columns of $\mathbf{B}$ are weighted to account for a possible numerical discrepancy between the source amplitude spectra and the reflectivity series spectra. Additionally, manually chosen weighting factors are introduced to determine the relative importance of source wavelets and reflectivity series. Due to the nonlinearity of equation (2), the updates are damped by a factor β (<1) prior to their addition to the initial model:

$$\begin{bmatrix} \mathbf{W}^R \\ \mathbf{W}^I \\ \mathbf{R}^R \\ \mathbf{R}^I \end{bmatrix} = \begin{bmatrix} \mathbf{W}_0^R \\ \mathbf{W}_0^I \\ \mathbf{R}_0^R \\ \mathbf{R}_0^I \end{bmatrix} + \beta \cdot \mathbf{x} \tag{8}$$

($\mathbf{W}^R$, $\mathbf{W}^I$, $\mathbf{R}^R$ and $\mathbf{R}^I$) in equation (8) are column vectors comprising the Fourier coefficients of all source wavelets and reflectivity series for a single frequency component. The choice of β depends on the data. Finally, the initial model is replaced by the updated model, and the entire procedure is iterated starting from equations (3) until convergence is achieved.

Stabilization of inversion can be achieved by adding additional constraints on the model parameters. E.g., asking for a smooth model by setting the second spatial derivative of the velocity to zero is common practice in travel time tomography and full waveform inversion. The model parameters in this study are the spectra of source wavelets and reflectivity series, and the inversion is performed independently for each frequency component. With respect to the assumptions on the method, lateral continuity along a reflector is regarded as a more useful constraint than its smoothness. Lateral continuity is expressed by setting the difference of the reflectivity series between adjacent stations to zero. For each station pair, two continuity constraints for the real and imaginary parts of the Fourier coefficients ($\mathbf{R}^R$, $\mathbf{R}^I$) are derived. It is reasonable to treat amplitude spectra and phase spectra independently, since the first one represents the reflection coefficient and the latter one the associated two-way travel time of a reflector. By expressing the amplitude τ and the phase ϕ through the unknowns (real and imaginary parts), the continuity equations between two stations (A, B) are formulated by

$$\Delta\tau_{AB} = \tau_A - \tau_B = \sqrt{(R_A^R + R_A^I)^2} - \sqrt{(R_A^R + R_A^I)^2} = 0 \tag{9a}$$

$$\Delta\phi_{AB} = \phi_A - \phi_B = tan^{-1}\left(\frac{R_A^I}{R_A^R}\right) - tan^{-1}\left(\frac{R_B^I}{R_B^R}\right) \tag{9b}$$

The indices (A, B) are replaced by the corresponding m, and M stations result in M x (M - 1) independent continuity equations (9a, b). Their linearization leads to the matrix formulation

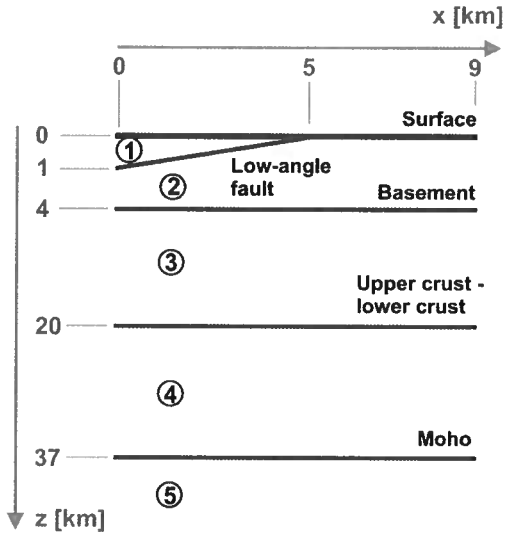

Figure 2. Schematic of the subsurface model used for calculation of synthetic reflectivity data (not to scale). Encircled numbers refer to the layers in table 1.

$$\mathbf{C} \cdot \mathbf{x} = \begin{bmatrix} -\Delta\tau \\ -\Delta\phi \end{bmatrix} \tag{10}$$

Note that $\mathbf{x}$ in equation (10) contains the real and imaginary parts of the reflectivity series (ΔR_m^R,ΔR_m^I) only, but not the source wavelets as in equation (5). The partial derivatives in $\mathbf{C}$ calculate as:

$$\begin{aligned} \frac{\partial\Delta\tau_{AB}}{\partial R_A^R} &= \frac{R_A^R}{\tau_A}, & \frac{\partial\Delta\tau_{AB}}{\partial R_A^I} &= \frac{R_A^I}{\tau_A}, \\ \frac{\partial\Delta\tau_{AB}}{\partial R_B^R} &= \frac{-R_B^R}{\tau_B}, & \frac{\partial\Delta\tau_{AB}}{\partial R_B^I} &= \frac{-R_B^I}{\tau_B} \end{aligned} \tag{11a}$$

$$\begin{aligned} \frac{\partial\Delta\phi_{AB}}{\partial R_A^R} &= \frac{-R_A^I}{\tau_A}, & \frac{\partial\Delta\phi_{AB}}{\partial R_A^I} &= \frac{R_A^R}{\tau_A}, \\ \frac{\partial\Delta\phi_{AB}}{\partial R_B^R} &= \frac{-R_B^I}{\tau_B}, & \frac{\partial\Delta\phi_{AB}}{\partial R_B^I} &= \frac{-R_B^R}{\tau_B} \end{aligned} \tag{11b}$$

The coefficients of $\mathbf{C}$ and the misfits ($\Delta\tau$, $\Delta\phi$) are evaluated at each iteration step. The rows of $\mathbf{C}$ are individually weighted by their interstation distance, and manually chosen weights control the importance of the amplitude continuity versus the phase continuity. After padding the source wavelets columns in $\mathbf{C}$ and the source wavelet rows of $\mathbf{x}$ with zeros, equations (10) are appended to $\mathbf{B}$ and $\mathbf{y}$ prior to the calculation of the inverse (equations 5 - 6).

Layer	Description	Upper - lower interface	Vp [km/s]	Vs [km/s]	Density [g/ccm]	Vertical extent (top / bottom) [km]
1	High-Velocity Layer (Carbonates)	Surface - low-angle fault	5.0	2.5	2.5	0 / 1-0
2	Sediment (Shale)	Surface/low-angle fault - basement	4.0	1.96	2.3	1-0 / 4
3	Upper crust (Granite)	Basement - crustal interface	6.3	3.7	2.8	4 / 20
4	Lower crust	Crustal interface - Moho	6.5	3.71	2.85	20 / 37
5	Mantle	Moho	8.0	4.45	3.3	37

Table 1. Parameters of the synthetic model (Figure 2).

Reflection / Transmission	From layer 1	From layer 2	From layer 3	From layer 4	From layer 5
To layer 1	–	0.15/0.85	–	–	–
To layer 2	-0.15/1.15	–	-0.31/1.31	–	–
To layer 3	–	0.31/0.69	–	-0.02/1.02	–
To layer 4	–	–	0.02/0.98	–	-0.18/1.18
To layer 4	–	–	–	0.18/0.82	–

Table 2. Vertical incidence reflection/transmission coefficients for the synthetic model (Figure 2).

3 SYNTHETIC TESTS

The applicability of the outlined methodology is tested on a synthetic data set. A 2D reflectivity model is based on the expected subsurface structure of the region where the field data (cf. section 4) were acquired (Leahy et al., 2012; Gans, 2011). It comprises a 9 km long section with 5 distinct layers (Figure 2, Table 1). With the exception of the low-angle fault, which separates layer 1 from layer 2, all interfaces are horizontal. Transmission and reflection coefficients between the layers are calculated for vertical incidence P-waves (Aki and Richards, 2009) and are summarized in Table 2. Fifty-five receivers are distributed along the 9 km long section. For each receiver, a reflectivity model r(t) is obtained by multiplication of the according reflection and transmission coefficients for the down- and upgoing waves and conversion to vertical two-way travel times. These total reflectivity coefficients calculate as -0.15, 0.30, 0.02 and 0.16 for the low-angle fault, the basement, the upper/lower crust boundary and the Moho at the left side of the section where the low-angle fault is present. The corresponding numbers at the right side, where the low-angle fault does not exist, are almost identical (0.31, 0.02 and 0.16 for the basement, the upper/lower crust boundary, and the Moho). Five source wavelets w(t) are calculated by applying different Butterworth filters to a spike (Ryan, 1994), and synthetic observation data z(t) for each wavelet are derived by evaluating equation (1). The Butterworth filter is chosen for its flexibility in creating minimum- and mixed-phase spectra which also characterize real earthquake wavelets. The used frequency content ranges from 0.3 to 1.8 Hz. Those values where selected to resemble the real data set (cf. section 4). White noise is added to z(t) in the frequency range 0.2 - 2 Hz, where the signal-to-noise (S/N) ratio is specified as the ratio of the maximum absolute amplitude of w(t) to the maximum range of the uniform noise distribution. The used wavelets and examples of synthetic data are shown in Figure 3. The synthetic data illustrate the two major challenges that are (i) the burial of shallow reflections beneath the source wavelet and (ii) the weak reflection signatures in presence of noise. If the source wavelet is of more complex shape (e.g., wavelet no. 2), these difficulties aggravate. A multitude of inver-

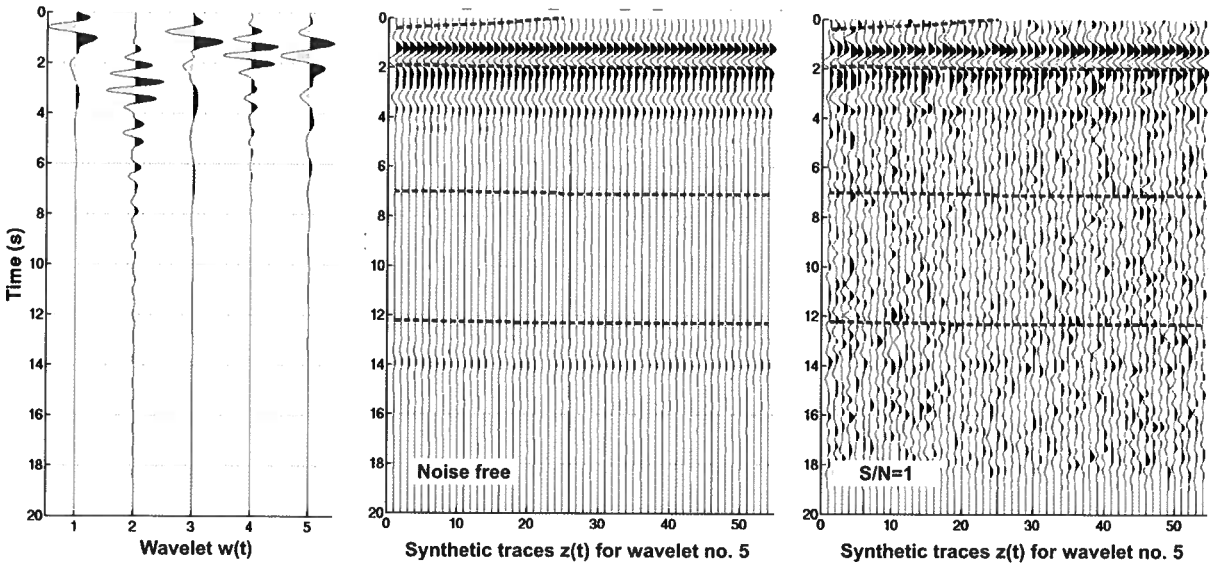

Figure 3. Five different source wavelets and resulting synthetic data for source wavelet no. 5. Dashed black lines indicate the vertical two-way travel times associated with the reflectors (fault, basement, upper/lower crust boundary, Moho) shown in Figure 2.

sions of this synthetic data set is performed in to gain a better understanding of the inversion parameters. Five source wavelets and 55 stations result in 275 observed traces versus 60 unknown source wavelets and reflectivity series. The exact onset of a wavelet is usually hard to define on real data, but it is not need to be known since the phase spectra is part of the solution. The initial reflectivity is zero at all stations, and the initial source wavelets are calculated as the average wavelet of the first 6 seconds of each event. Apart from noise-free data, two additional data sets with S/N ratios of 2.0 and 1.0, respectively, are also inverted. For comparison, conventional single-trace deconvolution including stacking over all events is also applied to the data. The estimated source wavelet for deconvolution is identical to the initial source wavelet for blind deconvolution. In the following, I summarize the most important findings of the synthetic tests.

The number of used singular values and singular vectors depend on the signal-to-noise ratio, but also on the weight of the continuity constraints. In more or less all inversions, the damping factor β (equation 8) must be kept small (0.1 - 0.2) to guarantee stability, which indicates a strong degree of nonlinearity. Accordingly, a large number of iterations (30 - 50) are necessary to achieve convergence. A crucial parameter is the relative weight of the source wavelet and the reflectivity series (Figure 4). Although the effect of strong vs. weak weighting has not much effect on the estimation of the source wavelet itself (Figures 4d, e), there is a pronounced difference in the obtained reflectivity series (Figures 4a, b). The overall ringy character of the reflectivity solution shown in Figure 4b possibly expresses a compensation for spurious small amplitudes in the corresponding source wavelet solution (Figure 4e). On the other hand, only the result from strong source wavelet weighting (Figure 4b) indicates the reflection from the low-angle fault. Thus there is no obvious best choice for this parameter, and I take this as another expression of strong nonlinearity. The true, initial and obtained source wavelets are very similar in general, which possibly results from the strong amplitude of the incoming wave in comparison to the reflected waves. Conventional deconvolution applied to the noise-free data set (Figure 4c) provides a result similar to blind deconvolution with weak source wavelet weighting (Figure 4a). However, more artifacts appear in the uppermost section (0 - 1 s) since the deconvolution does not take the superposition of the incoming and reflected waves into account. The weak reflectivity contrast at the upper/lower crust boundary is not resolved adequately with any of the methods. It is also noted that the polarity of the reflectors is correctly reconstructed. Fig. 5 illustrates results from the inversion of the data set with a signal-to-noise ratio of 1. There is a clear improvement when the continuity constraints are enforced (Figure 5b vs. Figure 5a). In opposite, conventional deconvolution (Figure 5c) performs poorly in reconstructing the reflectivity series. The low-angle fault is not recovered reliably in any of the inversions nor deconvolutions. A second suite of tests was run on synthetic data sets based on more complicated source wavelets (e.g., longer coda). As expected, the recovery of the reflectivity structure degrades with the complexity of the source wavelets, in

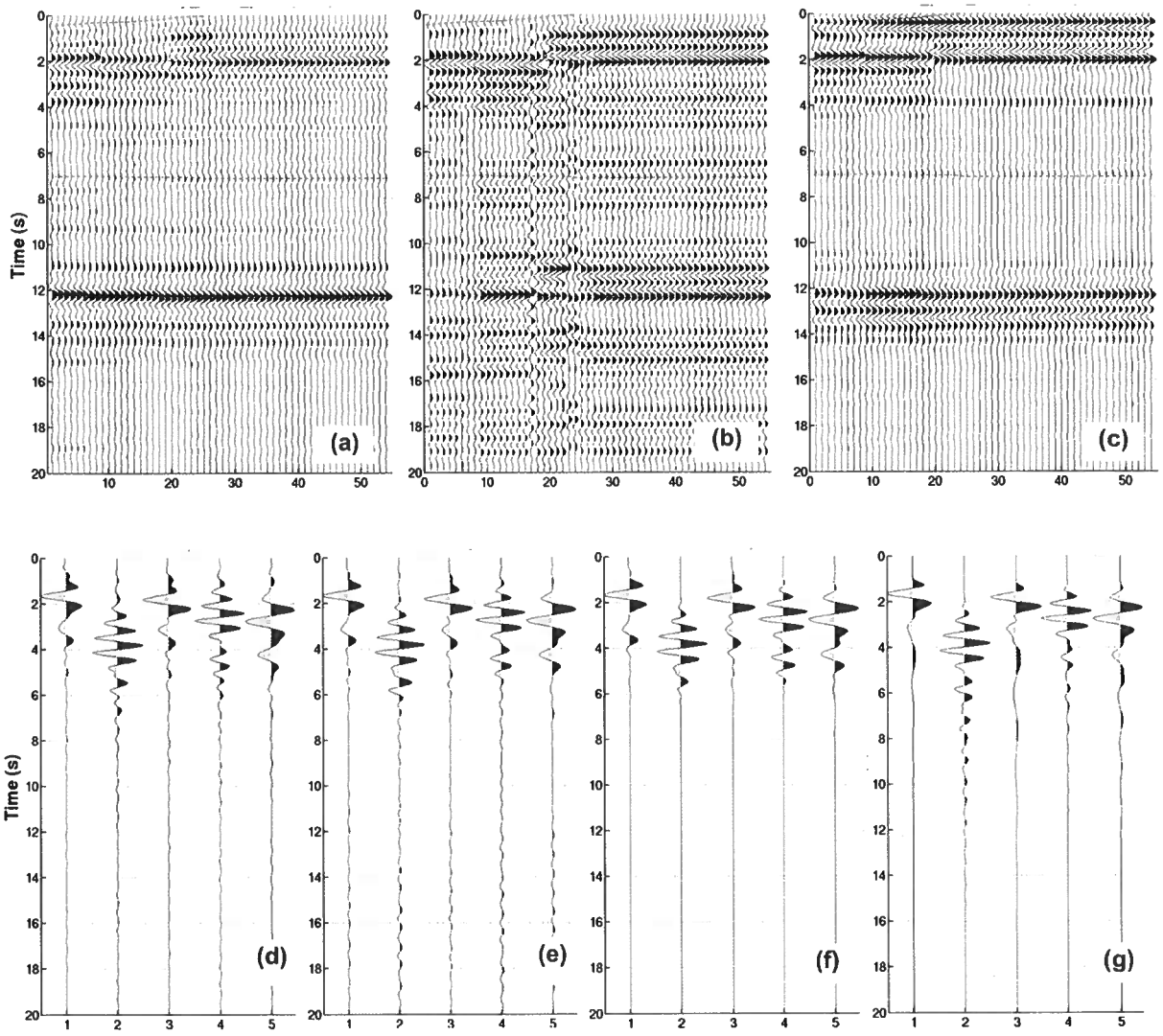

Figure 4. Estimated reflectivity time series and source wavelets from noise-free synthetic data: Reflectivity series (a) and source wavelets (d) for weak (0.1) relative source wavelet weighting. Reflectivity series (b) and source wavelets (e) for strong (1.0) relative source wavelet weighting. Note the spurious amplitudes at later times (T >12 s) in (e). (c) Reflectivity series obtained by deconvolution (reversed polarity). (f) Initial source wavelets for inversion and deconvolution. (g) True source wavelet used for generation of synthetic data. All traces are bandpass filtered in the range of 0.5 - 2 Hz. Dashed grey lines indicate vertical two-way travel times associated with the reflectors in the synthetic model.

particular in combination with a low signal-to-noise ratio. In this case, the continuity constraints become more important, and blind deconvolution performs far superior to standard deconvolution.

4 APPLICATION TO FIELD DATA

The La Barge seismic experiment is an industry-academia cooperation and aims at evaluating the use low-frequency passive seismic data for local sub-surface characterization (Saltzer et al., 2011). From November 2008 to June 2009, fifty-five 3-component broadband instruments (Guralp CMG 3T, natural period 120 s) were continuously recording over an active oil/gas production site in Wyoming (Figure 6). The site is located in the La Barge region in the Green River Basin. On a local scale, the dominant structural feature is the low-angle Hogsback thrust which separates claystones and siltstones in the east from an approximately 1 km thick carbonate sequence in the west. The instruments were deployed at the surface with a very narrow station spacing of 250 m, and the sample interval was 10 milliseconds. Data from the La Barge seismic experiment were

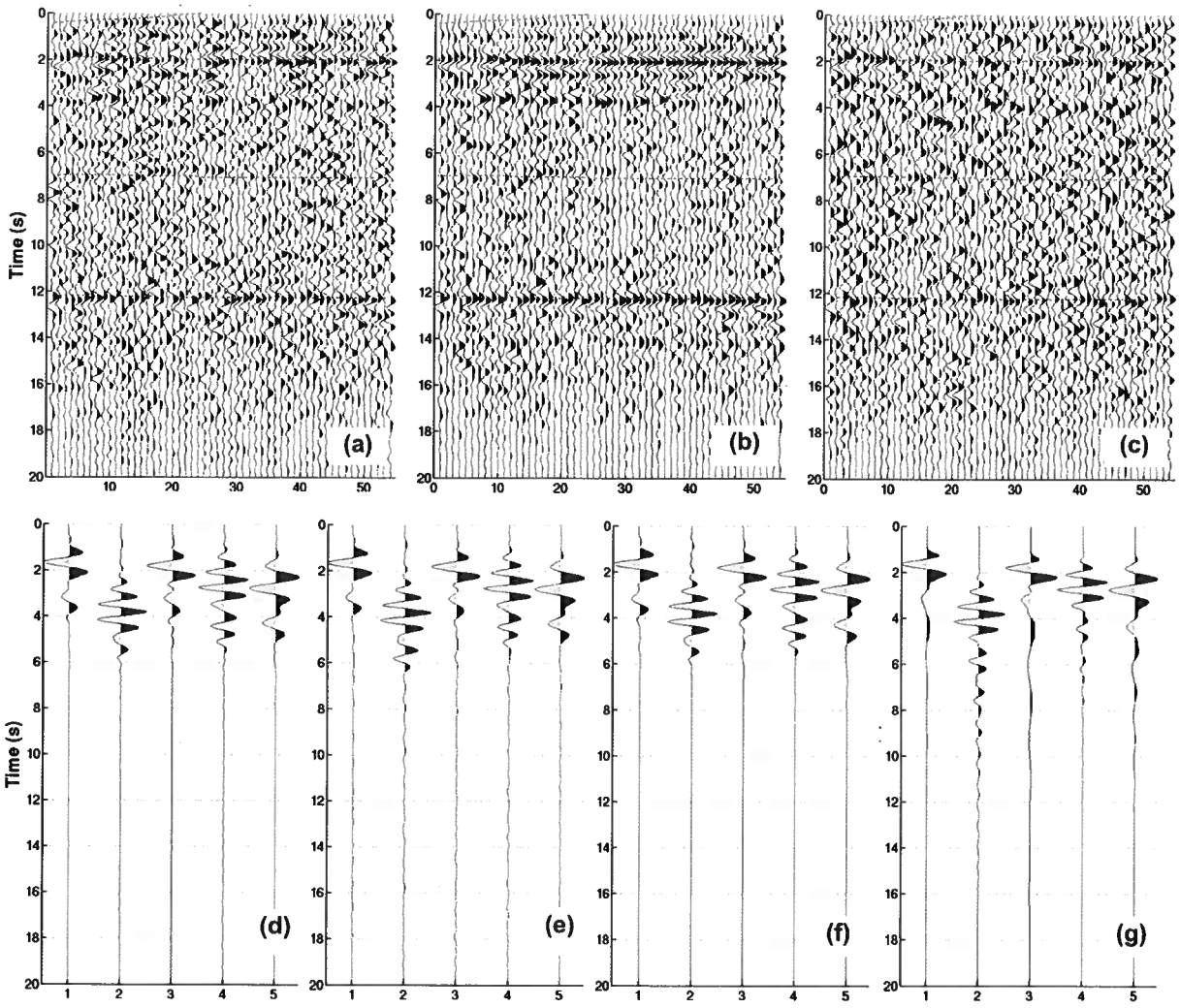

Figure 5. Estimated reflectivity time series and source wavelets from synthetic data with an S/N ratio of 1: Reflectivity series (a) and source wavelets (d) from inversion without applying continuity constraints. Reflectivity series (b) and source wavelets (e) from inversion with enforced reflectivity constraints. (c) Reflectivity series obtained by deconvolution (reversed polarity). (f) Initial source wavelets for inversion and deconvolution. (g) True source wavelet used for generation of synthetic data. All traces are bandpass filtered in the range of 0.5 - 2 Hz.

subject to several other studies. Gans (2011) calculated P-to-S receiver functions for illumination of the entire crust and uppermost mantle and found remarkable variations on a very small spatial scale. Leahy et al. (2012) were able to derive comparably high-resolution receiver function images of the shallow crust by exploiting the upper frequency range of teleseismic events. Biryol et al. (2013) retrieved velocity models of the shallow crust by finite-frequency travel time inversion of regional seismic events. Behm et al. (2013) used traffic noise from a nearby road to obtain local surface wave velocities. While all the applied methods have their origin in earthquake seismology, the novelty of most of these studies is their focus on the uppermost part of the crust (<5 km depth).

4.1 Teleseismic events

Due to the long recording interval, a large number of teleseismic events were collected. The assumption of vertical incidence implies the use of events with an epicentral distance greater than 25 degrees, which in turn requires magnitudes greater than 5.5 for a clear observation. The strength of a particular teleseismic phase depends on the source mechanism and on the geologic structure at the source location. A well defined wavelet may only be obtained if different phases of a single event

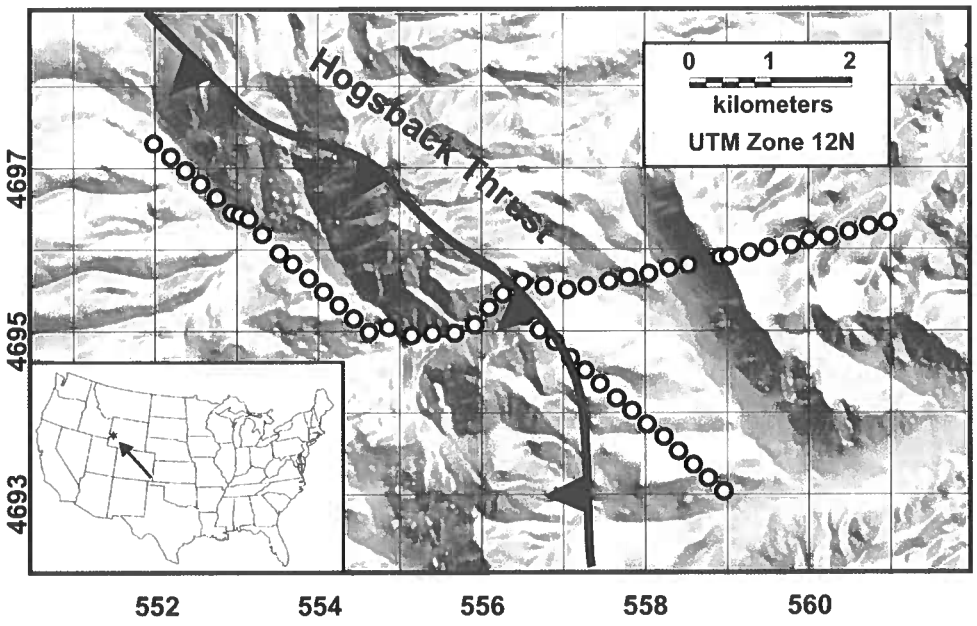

Figure 6. Location of the 55 broadband stations of the La Barge Passive Seismic Experiment. The Hogsback thrust separates carbonates in the west from claystones and siltstones in the east.

No.	Usage	Date/Time	Mag.	Distance [deg.]	BAZ [deg.]	Long. [deg.]	Lat. [deg.]	Depth [km]
1	pP	2008-11-04 / 18:35:45	6.3	95.0	251.7	168.47	-17.14	205
2	P,pP	2008-11-21 / 07:05:35	6.1	96.0	263.6	159.55	-8.95	263
3	pP	2009-03-15 / 08:19:05	5.7	67.4	137.6	-70.36	-14.45	189
4	pP	2009-03-20 / 12:26:03	5.5	89.9	240.5	-179.38	-21.48	622
5	P	2009-04-18 / 02:03:53	5.8	94.0	234.1	-177.45	-28.92	65
6	pP	2009-04-18 / 19:17:59	6.6	65.8	311.1	151.43	46.01	35
7	P	2009-04-21 / 05:26:12	6.2	61.1	314.0	155.01	50.83	152
8	P	2009-05-22 / 00:24:21	5.5	33.1	143.4	-90.74	13.88	69
9	P	2009-05-22 / 19:24:19	5.6	26.2	153.8	-98.46	18.11	62

Table 3. Used teleseismic events and phases for the application of blind deconvolution. P: direct arrival. pP: source-side surface reflection. BAZ: Receiver Event azimuth.

(e.g. direct arrival (P), reflection from the outer core (PcP), source-side surface reflection (pP), midpoint surface reflection (PP)) are well separated in time. The degree of separation depends on the focal mechanism, on the distance and on the depth of the event. As some of these factors may be poorly known and/or weakly constrained, a visual inspection of a range of pre-selected event gathers is still necessary. The final selection criteria are the requirements of a short duration pulse of the source wavelet and the absence of later phases within a time range according to the investigation depth. I use both direct arrivals (P) and source-side surface reflections (pP) of 9 different events as source wavelets (Table 3). These wavelets have main frequencies between 0.4 and 1.2 Hz.

4.2 Data and pre-processing

As this study focuses on P-waves, only vertical component data are used subsequently. The data are band-

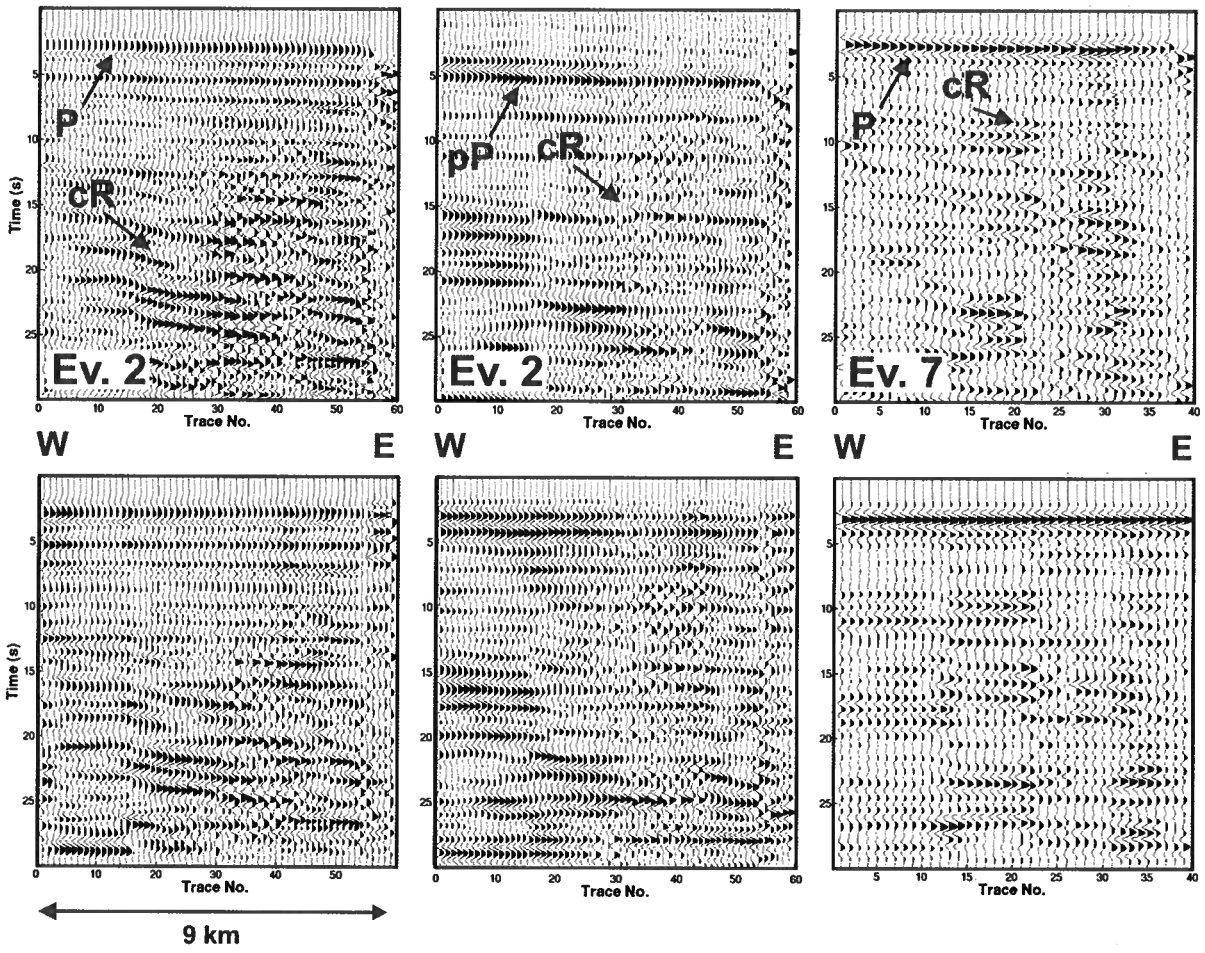

Figure 7. Examples of vertical component data used for the inversion (events 2 and 8, Table 3). P and pP refer to the teleseismic phases (P: direct arrival, pP: source-side surface reflection). Upper row: Band-pass filtered (0.6 - 4 Hz) event gathers. Time zero is approximately 2 seconds prior to the onset of the phase at the westernmost station. The time delay of the easternmost stations is due to their larger distances to the array. Note the converted surface waves ("cR") arriving at times greater than 8 seconds. Lower row: Corresponding time-aligned and singular-value decomposed event gathers which are the input data for inversion and deconvolution.

pass filtered between 0.6 - 4 Hz, and they are cut to a length of 30 seconds, starting one second prior to the earliest onset of the used phase (Figure 7, upper row). The traces are then aligned by their difference in arrival time to the receiver with the earliest onset. Arrival time picking is done manually, since the estimation of the reflectivity series is not significantly flawed by small inaccuracies with respect to the used frequency range. The same accounts for the calculation of the initial source wavelet from the aligned traces. To avoid numerical issues in the inversion due to different magnitudes, all event gathers are normalized to their maximum amplitude. An analysis of the entire data set suggests the presence of strong converted surface waves associated with the majority of the events (phase "cR" in Figure 7). Conversions from incident teleseismic body waves to Rayleigh waves are attributed to lateral Moho variations or rugged topography (e.g. Neele and Snieder (1991)). Their directionality indicates an origin in the west to northwest of the deployment, and their arrival times suggests conversion distances greater than 30 kilometers. The southern part of the Wyoming Mountain Range is located in this area and it is interpreted to account for the conversions, which occur as early as 6 seconds after the onset of the body waves. As reflections from the lower crust and the Moho are expected to arrive between 8 and 14 seconds, the superposition of the converted surface waves poses an additional challenge. Singular value decomposition (SVD) of a wave field is a practical way to attenuate or enforce laterally coherent features of event gathers (Freire and Ulrychs, 1988). By choosing a limited range of the largest singular values

and corresponding singular vectors, laterally coherent signals are amplified at the expense of dipping phases and high-frequency noise. The choice of the range of singular values is somewhat subjective, and selecting too few singular values might result in suppressing laterally varying subsurface structures. Tests showed that in case of the P-phase the inclusion of the upper 15% of the singular values and singular vectors provides a significant improvement of the inversion result without degrading the main structural features of the inverted reflectivity series. The corresponding number for the pP-phase is 40%.

4.3 Inversion and results

Inversions are carried out for P and pP data (Table 3), and the results are shown in Figure 8. Inversion parameters (Table 4) are chosen based on the insights from the synthetic tests. I further use conventional deconvolution as well as results from teleseismic travel time inversion (Biryol et al., 2013) and receiver function analysis (Gans, 2011; Leahy et al., 2012) to validate my findings.

All inversions derive a continuous reflector with positive polarity at a time of approximately 2 seconds. The arrival times are slightly less in the western part. The results from the pP data (Figure 8c) are shifted by about 0.3 seconds compared to P data. This shift might be related to the lower frequency of the pP wavelets, and should be subject to further analysis. Enforcement of the continuity constraints (Figure 8b) facilitates the recovery of a reflector at about 14 s in the P dataset. The result obtained from conventional deconvolution (Figure 8d) appears noisier overall, and coherent later arrivals are more difficult to interpret. The inversion from P data with enforced continuity constraints (Figure 8b) is converted to depth with a 1D velocity depth-model based on the aforementioned studies (Figure 9). The shallow reflector at approximately 4 km depth correlates well with the basement transition from low-velocity sandstones to high-velocity carbonates and granites. The small but significant apparent rise of the reflector in its western part is attributed to the uppermost thin sheet of carbonates prevailing only west of and above the low-angle Hogsback thrust. The higher velocities of the carbonates are not included in the 1D velocity model and result in an apparent shallower reflector. The Hogsback thrust itself cannot be deduced reliably from the inversion, but a pronounced lateral change of the reflectivity is observed in the according depth range. Gans (2011) interpreted a seismic discontinuity at ca. 15 km depth but this is not indicated by the blind deconvolution inversion. The reason for this disagreement is not entirely clear, but it might be due to a combination of weak P-wave impedance contrast and superposition of converted surface waves in the blind deconvolution data. The reflections from ca. 40-42 km depth correlate well with the Moho depth range given by Gans (2011). The strong apparent dip (8 degrees) towards the west is surprising, but Gans (2011) also found the Moho depths to be about 2 km deeper west of the Hogsback thrust than in the eastern part of the array. Considering the small array aperture, the enforced continuity constraints might smear an abrupt lateral change into a dipping structure. Lateral velocity changes above the Moho may also partly explain the apparent dip.

5 DISCUSSION

I start with comparing the presented inversion scheme to conventional deconvolution. The main difference is that the reflectivity series now is described by a model with which all observations must comply, while conventional (single-trace) deconvolution derives a new model for each seismic event. This drawback might be overcome by stacking deconvolved traces for several events, but there still is a strong sensitivity on noise. Modeling by inversion provides a more natural way to minimize the influence of white noise, although coherent noise over several traces (e.g. surface waves arriving at oblique angles, or later arriving vertical-incidence waves) can be projected into the reflectivity model. The simultaneous estimation of the wavelet and the reflectivity series is considered as an advantage over methods which calculate the wavelet only prior to the reflectivity series. As with any inversion, constraints on the model and the determination (weights) of the unknowns can be incorporated in a flexible and natural way. The superposition with the source wavelet is an important modification to the conventional deconvolution model in case of shallow structures, in particular when the S/N-ratio is low (e.g. Figures 4, 5). Application to both synthetic and real data shows that the inversion scheme is more stable than conventional deconvolution. White noise is handled well by the inversion, while coherent noise over several traces presents a challenge, and such signals must be eliminated by pre-processing. If the cause of the coherent noise is well known, it may also be modeled and estimated in the inversion. The assumption of vertical incidence presents a severe constraint to the method. Teleseismic events with epicentral distances greater than 25 degrees and thus large magnitudes are required, and the need for clear and well-defined source wavelets imposes a strong selection criterion. In practice, it implies a long observation period to collect a sufficient number of events. In this study, the frequency range of the teleseismic phases is confined to the range of 0.4 to 1.2 Hz which limits the resolution capabilities. However, no special efforts were made to exploit the higher frequency range (5 - 10 Hz) of earthquake body waves (e.g. Leahy et al. (2012). Advanced pre-processing in future studies should also focus on this aspect. The assumption of a stationary source wavelet restricts the lateral extent of the deployment in general, but the actual aperture depends on the specific subsurface characteristics of a

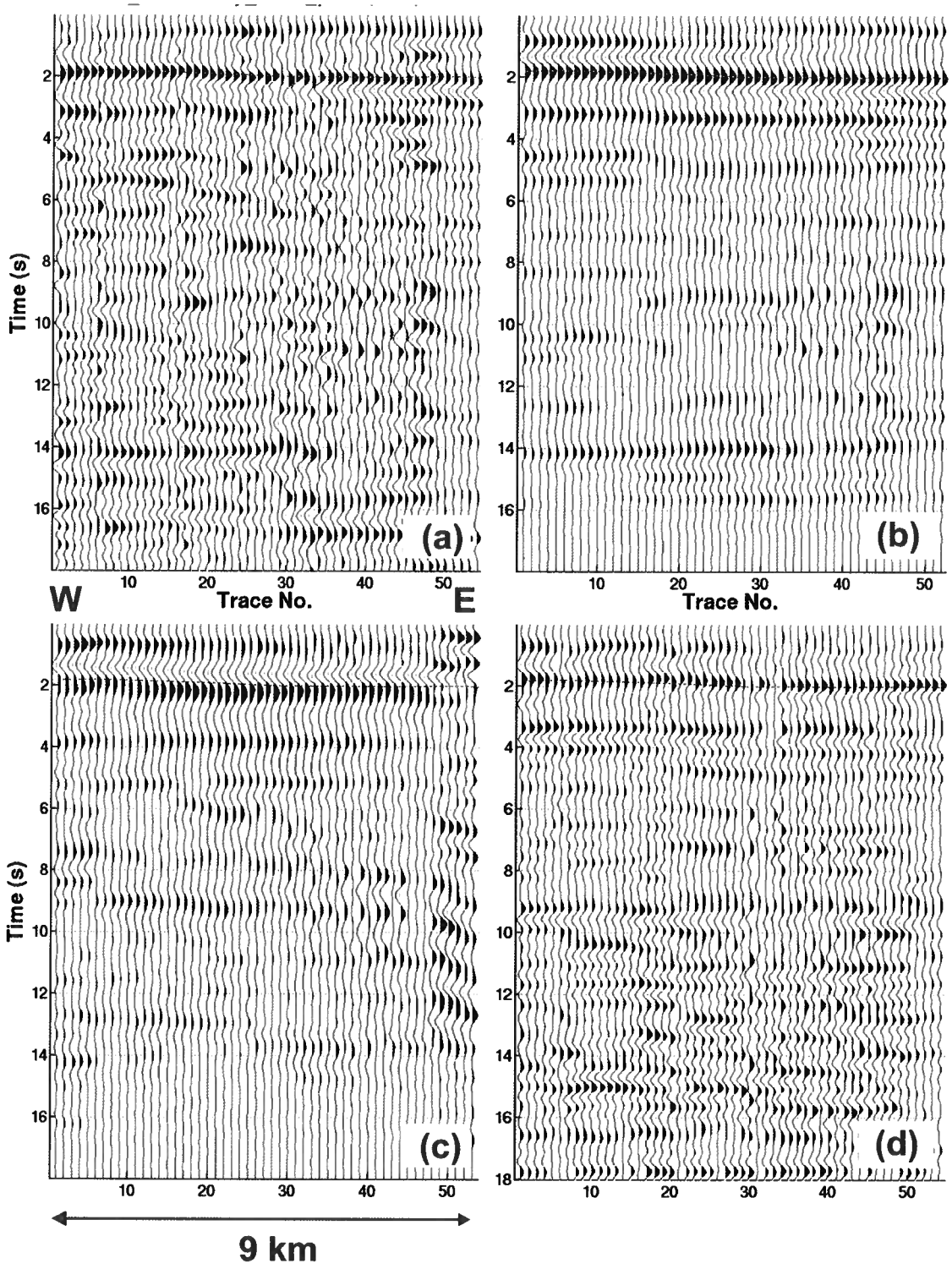

Figure 8. Reflectivity series obtained from the La Barge data. (a) Reflectivity series from P phases without applying continuity constraints. (b) Reflectivity series from P phases with enforced continuity constraints. (c) Reflectivity series from pP phases without applying continuity constraints. (d) Conventional deconvolution of P wavelets. The dashed grey line depicts the maximum amplitude of the shallow reflector in (b), and it is superimposed on the other panels for comparison. See text for details.

	Used phase / no. of events	SVD ratio α	Damping factor β / no. of iterations	Source weight	Initial source wavelet length [s]	Continuity constraints
Fig. 8a	P / 5	0.04	0.1 / 50	0.10	4.0	No
Fig. 8b	P / 5	0.002	0.1 / 50	0.15	4.0	Yes
Fig. 8c	pP / 5	0.15	0.1 / 50	0.10	5.3	No

Table 4. Parameter used for the inversion results shown in Fig. 8. The SVD ratio α describes the threshold for singular values and vectors. Only those singular values, whose ratio to the largest singular value are higher than α, are used in the inversion.

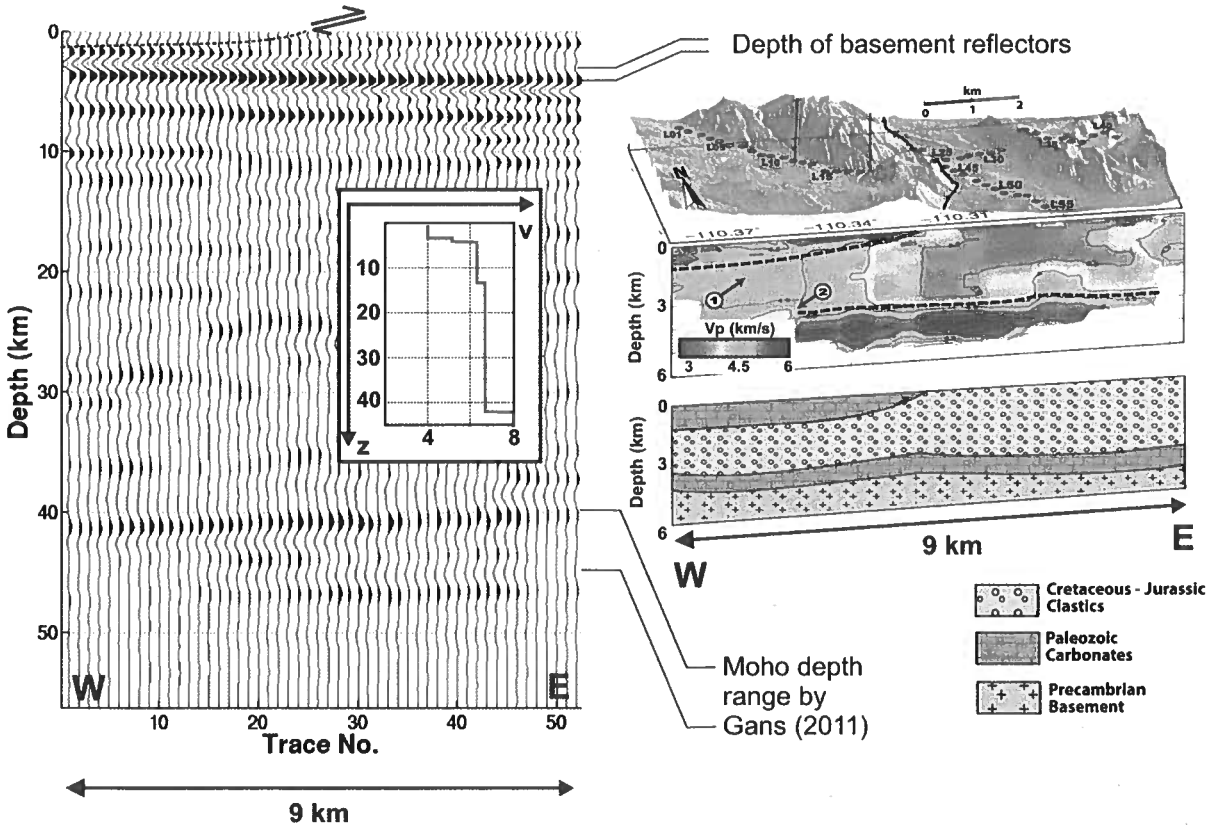

Figure 9. Depth converted seismic image from Figure 8b. The 1D velocity-depth model is based on previous studies (Gans, 2011; Leahy et al., 2012; Biryol et al., 2013). The cartoon including the geological section and the velocity model is taken from Biryol et al. (2013). The dashed black line in the seismic images indicates the Hogsback thrust as known from surface geology and active source seismic investigations. See text for details.

region in question. A laterally homogenous medium is more advantageous, and applications to other data sets will help to obtain a better understanding of the scale range of the method. The multichannel approach is not limited to specific deployment geometry and thus well suited for common passive seismic experiments on a local scale. Larger recording arrays may be targeted by allowing the source wavelet to vary spatially through interpolation, but this remains a subject to further studies. The presented scheme can be used to supplement conventional receiver function methods due to the similar type of input data, but it does not require three-component observations. However, structural information on the shear-wave reflectivity might be additionally obtained by evaluating shear body waves on the horizontal components. With respect to the targeted depth range and resolution capabilities, low-frequency geophones might be used in future deployments to sub-

stitute for costly broadband stations. The focus of the presented study is the inversion for local and shallow reflectivity series, and the inversion parameters are chosen in such a way to derive a realistic subsurface model. This comes at the expense of projecting noise into the source wavelets. Future research should be dedicated to the applicability of the method for exact source wavelet reconstruction (e.g., by assuming realistic initial reflectivity models or advanced pre-processing).

6 CONCLUSION

With respect to the initial question on the applicability for exploration seismology, the outlined method presents a potentially useful technique for local large-scale subsurface characterization from passive seismic data. Shallow to intermediate and deep crustal structures can be imaged from a comparably low number of (well-suited) teleseismic earthquakes. As with any inversion technique, the results are sensitive to inversion parameters and the input data. Nonetheless, synthetic and real data examples indicate improved performance in comparison to conventional deconvolution which is attributed to a common model for all observations. Further studies, and in particular applications to other datasets will help to develop a better understanding of the merits and practical limitations of the method.

ACKNOWLEDGMENTS

ExxonMobil funded this study. I thank Roel Snieder for discussion and helpful comments on the paper. Berk Biryol (University of Arizona) kindly provided his cartoons for Figure 9.

REFERENCES

Aki, K., and P. G. Richards, 2009, Quantitative seismology, 2 ed.: University Science Books.

Behm, M., G. M. Leahy, and R. Snieder, 2013, Retrieval of local surface wave velocities from traffic noise - an example from the La barge basin (Wyoming): Geophysical Prospecting, **accepted**.

Biryol, C., G. M. Leahy, G. Zandt, and S. Beck, 2013, Imaging the shallow crust with local and regional earthquake tomography: Journal of Geophysical Research, **accepted**.

Bostock, M. G., 2004, Green's functions, source signatures, and the normalization of teleseismic wave fields: Journal of Geophysical Research, **109**, B03303.

Bostock, M. G., and M. D. Sacchi, 1997, Deconvolution of Teleseismic Recordings for Mantle Structure: Geophysical Journal International, 143–152.

Cadzow, J. A., and X. Li, 1995, Blind deconvolution: Digital Signal Processing, **5**, 3–20.

Denes, V., E. Starr, and J. Kapoor, 2009, Developing Earth models with full waveform inversion: The Leading Edge, **28**, 432–435.

Freire, S. L. M., and T. J. Ulrychs, 1988, Application of singular value decomposition to vertical seismic profiling: Geophysics, **53**, 778–785.

Gans, C. R., 2011, Investigations of the crust and upper mantle of modern and ancient subduction zones, using Pn tomography and seismic receiver functions: Phd thesis, University of Arizona.

Gurrola, H., G. Baker, and J. Minster, 1995, Simultaneous time-domain deconvolution with application to the computation of receiver functions: Geophysical Journal International, **120**, 537–549.

Kaaresen, K. F., and T. Taxt, 1995, Multichannel blind deconvolution of seismic signals: Geophysics, **63**, 2093–2107.

Leahy, G. M., R. L. Saltzer, and J. Schmedes, 2012, Imaging the shallow crust with teleseismic receiver functions: Geophysical Journal International, **191**, 627–636.

Neele, F., and R. Snieder, 1991, Are long-period body wave coda caused by lateral heterogeneity?: Geophysical Journal International, **107**, 131–153.

Otis, R., and R. Smith, 1977, Homomorphic deconvolution by log spectral averaging: Geophysics, **42**, 1146–1157.

Rawlinson, N., and M. Sambridge, 1998, Seismic traveltime tomography of the crust and lithosphere: Advances in Geophysics, **46**, 81–197.

Ryan, H., 1994, A Choice of Wavelets: CSEG Recorder, 24–25.

Saltzer, R., G. M. Leahy, J. Schmedes, J. Roth, and E.-M. Rumpfhuber, 2011, Earthquakes A naturally occurring source of low frequency data: SEG Expanded Abstract, SEG, 3689–3693.

Sirgue, L., and R. Pratt, 2004, Efficient waveform inversion and imaging: A strategy for selecting temporal frequencies: Geophysics, **69**, 231–248.

Tria, M., M. V. D. Baan, A. Larue, and J. I. Mars, 2007, Wavelet Estimation and Blind Deconvolution of Realistic Synthetic Seismic Data by Log Spectral Averaging: SEG Expanded Abstract, 1982–1986.

Tseng, T.-L., and W.-P. Chen, 2006, Probing the Southern Indian Shield with P-wave Receiver-Function Profiles: Bulletin of the Seismological Society of America, **96**, 328–333.

van der Baan, M., and D.-T. Pham, 2008, Robust wavelet estimation and blind deconvolution of noisy surface seismics: Geophysics, **73**, V37–V46.

Wiggins, R., 1978, Minimum entropy deconvolution: Geoexploration, **16**, 21–35.

Yang, Z., A. F. Sheehan, W. L. Yeck, K. C. Miller, E. A. Erslev, L. L. Worthington, and S. H. Harder, 2012, Imaging Basin Structure with Teleseismic Virtual Source Reflection Profiles: Geophysical Research Letters, **39**, L02303.

Body-wave interferometry using multi-dimensional deconvolution after wavefield decomposition at free surface

Nori Nakata[1] and Roel Snieder[1]

[1] *Center for Wave Phenomena, Geophysics Department, Colorado School of Mines*

ABSTRACT

Passive seismic methods using earthquakes can be applied for extracting body waves and obtaining information of subsurface structure. To analyze earthquake data, one traditionally uses receiver functions, tomography, and seismic interferometry. In this study, we retrieve reflected body waves by applying seismic interferometry to the recorded ground motion from a cluster of earthquakes. We employ upgoing/downgoing P/S wavefield decomposition, time windows, time reversal, and multi-dimensional deconvolution to improve the quality of the extraction of reflected body waves with seismic interferometry. The wavefield separation and seismic interferometry based on multi-dimensional deconvolution (MDD) allow us to reconstruct PP, PS, SP, and SS reflected waves without unwanted crosstalk between P and S waves. From earthquake data, we obtain PP, PS, and SS reflected plane waves that reflect off the same reflector, and estimate P- and S-wave velocities.

Key words: Seismic interferometry; Body wave; Wavefield decomposition; Multi-dimensional deconvolution

1 INTRODUCTION

Body waves obtained from earthquakes (especially teleseismic events) have been used for imaging deep structure (e.g., Bostock and Sacchi, 1997; Bostock and Rondenay, 1999; Baig et al., 2005; Dasgupta and Nowack, 2006; Behm, 2013). The receiver function is one technique to obtain information of subsurface structure by estimating travel-time differences between P and PS converted waves (e.g., Langston, 1979; Li et al., 2000; Assumpção et al., 2002). Seismic interferometry (Aki, 1957; Claerbout, 1968; Wapenaar, 2004) is also used for analyses of passive seismic waves including earthquake records. One can apply seismic interferometry to body waves generated by earthquakes and obtain images of subsurface structure (e.g., Abe et al., 2007; Tonegawa et al., 2009; Ruigrok et al., 2010; Ruigrok and Wapenaar, 2012). Abe et al. (2007) found that the image obtained from seismic interferometry has higher resolution than retrieved from receiver functions, but seismic interferometry creates pseudo events, which can be suppressed by averaging over many earthquakes. Higher resolution Green's functions are also obtained by estimating and deconvolving source functions from earthquake data recorded by a receiver array (Bostock, 2004). The target for most seismic interferometry studies is deep structure, but a few studies create images in shallow zones (Ryberg, 2011; Yang et al., 2012). Seismic interferometry has been developed for analyzing data trace by trace, and Wapenaar et al. (2008a,b) improve seismic interferometry by using multi-dimensional deconvolution (MDD). Although MDD interferometry requires one to separate wavefields depending on the direction of wave propagation and to solve an inverse problem, MDD overcomes several limitations (e.g., attenuation, complicated incident waves, and source distribution) of trace-by-trace interferometry (see section 4.3).

In this study, we apply trace-by-trace and MDD seismic interferometry to earthquake data to reconstruct direct and reflected plane waves. We first propose a technique of wavefield decomposition at the free surface. Using this decomposition, we can separate observed two-component wavefields into upgoing/downgoing P/S wavefields, which is necessary for MDD interferometry, and show why this is an improvement over seismic interferometry. Next, we introduce earthquake data observed over the LaBarge field in Wyoming. Then we show a mathematical description of seismic interferometry and improvement of interferometric wavefields by applying different techniques to the earthquake data.

2 UPGOING/DOWNGOING AND P/S WAVEFIELD DECOMPOSITION

A number of studies propose different techniques for wavefield separation: using, for example, dual sensors (Loewenthal and Robinson, 2000), Helmholtz decomposition (Robertsson and Muyzert, 1999; Robertsson and Curtis, 2002), over/under

Table 1. Notations of physical parameters and wavefields.

Notation	Description	Relationship with other parameters
ω	Angular frequency[1]	
α	P-wave velocity at the layer below the free surface	
β	S-wave velocity at the layer below the free surface	
ρ	Density	
σ_{ij}	Stress in the ij component	
μ	Lame's parameters	$\mu = \beta^2\rho$
λ		$\lambda = (\alpha^2 - 2\beta^2)\rho$
θ_p	Angle of the P incident wave with respect to the free surface	
θ_s	Angle of the S incident wave with respect to the free surface	
k	Horizontal wavenumber	$k = \omega \sin\theta_p/\alpha = \omega \sin\theta_s/\beta$
ν_p	Vertical wavenumber for P wave	$\nu_p = \omega\cos\theta_p/\alpha = \sqrt{\omega^2/\alpha^2 - k^2}$
ν_s	Vertical wavenumber for S wave	$\nu_s = \omega\cos\theta_s/\beta = \sqrt{\omega^2/\beta^2 - k^2}$
u_z	Vertical component of the displacement of observed wavefields	
u_x	Horizontal component of the displacement of observed wavefields	
$\boldsymbol{U_p}$	Vector displacement of upgoing P waves	
$\boldsymbol{D_p}$	Vector displacement of downgoing P waves	
$\boldsymbol{U_s}$	Vector displacement of upgoing S waves	
$\boldsymbol{D_s}$	Vector displacement of downgoing S waves	
U_p	Scalar displacement of upgoing P waves at the free surface	
D_p	Scalar displacement of downgoing P waves at the free surface	
U_s	Scalar displacement of upgoing S waves at the free surface	
D_s	Scalar displacement of downgoing S waves at the free surface	
U_p^d	Direct upgoing P waves	
U_p^r	Surface-related reflected upgoing P waves	$U_p = U_p^d + U_p^r$
G	Green's function	

[1] We consider that the angular frequency is positive; therefore wavenumbers are also positive. For negative frequencies, we compute complex conjugate of a function in positive frequencies.

towed-streamer acquisition (Moldoveanu et al., 2007), and two steps of acoustic and elastic decomposition (Schalkwijk et al., 2003). Wavefield separation improves interferometric gathers to focus on target reflections (Mehta et al., 2007; Vasconcelos et al., 2008; van der Neut and Bakulin, 2009). When receivers are embedded in a medium (e.g., ocean-bottom sensors and borehole sensors), direct and reflected waves come from quasi-opposite directions. Therefore with decomposition, one can suppress some spurious multiples caused by crosstalk of direct-direct and reflected-reflected waves generated during the process of seismic interferometry (Snieder et al., 2006b; Mehta et al., 2007). Because receivers are deployed at the free surface in our data, we cannot suppress the spurious multiples by separating wavefields based on the direction of wave propagation. We employ time windows to reduce the spurious multiples (Bakulin and Calvert, 2006), and apply wavefield decomposition for separating direction of wave propagation, which is necessary for MDD (Wapenaar et al., 2011b), and for suppressing crosstalk of P and S waves.

We decompose wavefields into upgoing/downgoing P/S waves using the stress-free boundary condition at the free surface (similar to Wapenaar et al., 1990). Table 1 shows the notation used in this study, and Figure 1 defines the positive directions of x, z, and each wavefield. Let us consider the reflection at the free surface within the vertical plane in which the wave propagates. The goal of this wavefield decomposition is to independently compute U_p, D_p, U_s, and D_s from observed data. We assume that a layer below the free surface is laterally homogeneous, which means α and β are constant at the near surface. Based on the theory in Aki and Richards (2002,Table 5.1), the displacements of upgoing/downgoing P/S waves in the space-time domain using the Fourier convention $f(x,t) = (1/2\pi)^2 \iint_{-\infty}^{\infty} F(k,\omega)e^{i(kx-\omega t)}dkd\omega$ are

$$
\begin{aligned}
\boldsymbol{U_p}(x,z,t) &= \left(\frac{1}{2\pi}\right)^2 \iint_{-\infty}^{\infty} U_p(k,\omega)\frac{\alpha}{\omega}\begin{pmatrix} k \\ -\nu_p \end{pmatrix} e^{i(kx-\nu_p z-\omega t)}dkd\omega, \\
\boldsymbol{D_p}(x,z,t) &= \left(\frac{1}{2\pi}\right)^2 \iint_{-\infty}^{\infty} D_p(k,\omega)\frac{\alpha}{\omega}\begin{pmatrix} k \\ \nu_p \end{pmatrix} e^{i(kx+\nu_p z-\omega t)}dkd\omega, \\
\boldsymbol{U_s}(x,z,t) &= \left(\frac{1}{2\pi}\right)^2 \iint_{-\infty}^{\infty} U_s(k,\omega)\frac{\beta}{\omega}\begin{pmatrix} \nu_s \\ k \end{pmatrix} e^{i(kx-\nu_s z-\omega t)}dkd\omega, \\
\boldsymbol{D_s}(x,z,t) &= \left(\frac{1}{2\pi}\right)^2 \iint_{-\infty}^{\infty} D_s(k,\omega)\frac{\beta}{\omega}\begin{pmatrix} \nu_s \\ -k \end{pmatrix} e^{i(kx+\nu_s z-\omega t)}dkd\omega,
\end{aligned}
\tag{1}
$$

where the subscript s denotes SV waves. Since the scalar displacements are composed of constant amplitudes of upgoing waves and reflection coefficients at the free surface (see Table 5.1 in Aki and Richards, 2002), these scalar displacements are functions of wavenumber and frequency but not of depth. In

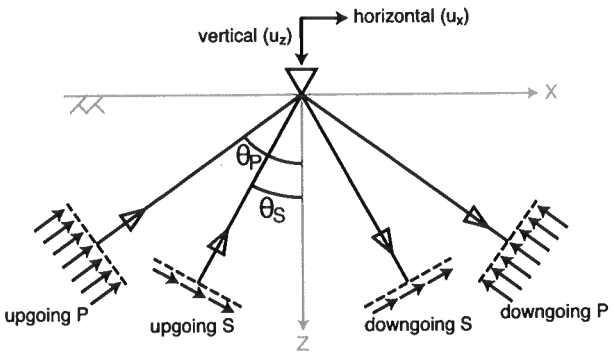

Figure 1. Plane-wave reflection system and coordinates for the wavefield decomposition in section 2. The horizontal gray line shows the free surface (indicated by ⩘), and the downward triangle on the line is a receiver. The black arrows near the receiver define the positive directions of observed records. The dashed lines illustrate portions of plane waves of upgoing/downgoing P/S waves. The black arrows near the dashed lines describe the positive directions of each vector wavefield. Solid black lines connected to dashed lines indicate the ray paths of each wavefield, and the triangles on the solid lines the direction of propagation. The angles θ_P and θ_S are the angles of incidence for P and S waves, respectively.

the wavenumber-frequency domain, expression 1 is written as

$$\begin{aligned}
\boldsymbol{U}_p(k,z,\omega) &= U_p(k,\omega)\frac{\alpha}{\omega}\begin{pmatrix} k \\ -\nu_p \end{pmatrix} e^{-i\nu_p z},\\
\boldsymbol{D}_p(k,z,\omega) &= D_p(k,\omega)\frac{\alpha}{\omega}\begin{pmatrix} k \\ \nu_p \end{pmatrix} e^{i\nu_p z},\\
\boldsymbol{U}_s(k,z,\omega) &= U_s(k,\omega)\frac{\beta}{\omega}\begin{pmatrix} \nu_s \\ k \end{pmatrix} e^{-i\nu_s z},\\
\boldsymbol{D}_s(k,z,\omega) &= D_s(k,\omega)\frac{\beta}{\omega}\begin{pmatrix} \nu_s \\ -k \end{pmatrix} e^{i\nu_s z}. \qquad (2)
\end{aligned}$$

The horizontal and vertical components of the displacement are, in the wavenumber-frequency domain, given by

$$\begin{aligned}
u_x(k,z,\omega) =& U_p(k,\omega)\frac{\alpha k}{\omega}e^{-i\nu_p z} + D_p(k,\omega)\frac{\alpha k}{\omega}e^{i\nu_p z}\\
&+ U_s(k,\omega)\frac{\beta\nu_s}{\omega}e^{-i\nu_s z} + D_s(k,\omega)\frac{\beta\nu_s}{\omega}e^{i\nu_s z}, \qquad (3)\\
u_z(k,z,\omega) =& U_p(k,\omega)\frac{-\alpha\nu_p}{\omega}e^{-i\nu_p z} + D_p(k,\omega)\frac{\alpha\nu_p}{\omega}e^{i\nu_p z}\\
&+ U_s(k,\omega)\frac{\beta k}{\omega}e^{-i\nu_s z} + D_s(k,\omega)\frac{-\beta k}{\omega}e^{i\nu_s z}. \qquad (4)
\end{aligned}$$

When receivers are located at the free surface ($z = 0$), expressions 3 and 4 simplify to

$$\begin{aligned}
u_x(k,0,\omega) =& \frac{1}{\omega}\left\{\alpha k\left(U_p(k,\omega) + D_p(k,\omega)\right)\right.\\
&\left.+\beta\nu_s\left(U_s(k,\omega) + D_s(k,\omega)\right)\right\}, \qquad (5)\\
u_z(k,0,\omega) =& \frac{1}{\omega}\left\{-\alpha\nu_p\left(U_p(k,\omega) - D_p(k,\omega)\right)\right.\\
&\left.+\beta k\left(U_s(k,\omega) - D_s(k,\omega)\right)\right\}. \qquad (6)
\end{aligned}$$

Because the stress condition at the free surface is

$$\sigma_{xz} = 0 \rightarrow \frac{\partial u_x}{\partial z} + \frac{\partial u_z}{\partial x} = 0, \qquad (7)$$

$$\sigma_{zz} = 0 \rightarrow \lambda\left(\frac{\partial u_x}{\partial x} + \frac{\partial u_z}{\partial z}\right) + 2\mu\frac{\partial u_z}{\partial z} = 0, \qquad (8)$$

the scalar displacements satisfy

$$\begin{aligned}
&2\alpha k\nu_p\left\{U_p(k,\omega) - D_p(k,\omega)\right\}\\
&\qquad -\beta\left(k^2 - \nu_s^2\right)\left\{U_s(k,\omega) - D_s(k,\omega)\right\} = 0, \qquad (9)\\
&\alpha\left(\lambda k^2 + \lambda\nu_p^2 + 2\mu\nu_p^2\right)\left\{U_p(k,\omega) + D_p(k,\omega)\right\}\\
&\qquad - 2\beta\mu k\nu_s\left\{U_s(k,\omega) + D_s(k,\omega)\right\} = 0, \qquad (10)
\end{aligned}$$

where we inserted equations 3–4 into equations 7–8. To solve four unknowns (U_p, D_p, U_s, and D_s), we have four equations (equations 5, 6, 9, and 10); therefore we can compute scalar wavefields:

$$\begin{aligned}
U_p(k,\omega) &= \frac{\beta^2 k}{\alpha\omega}u_x(k,0,\omega) - \frac{\omega^2 - 2\beta^2k^2}{2\alpha\omega\nu_p}u_z(k,0,\omega),\\
D_p(k,\omega) &= \frac{\beta^2 k}{\alpha\omega}u_x(k,0,\omega) + \frac{\omega^2 - 2\beta^2k^2}{2\alpha\omega\nu_p}u_z(k,0,\omega),\\
U_s(k,\omega) &= \frac{\omega^2 - 2\beta^2k^2}{2\beta\omega\nu_s}u_x(k,0,\omega) + \frac{\beta k}{\omega}u_z(k,0,\omega),\\
D_s(k,\omega) &= \frac{\omega^2 - 2\beta^2k^2}{2\beta\omega\nu_s}u_x(k,0,\omega) - \frac{\beta k}{\omega}u_z(k,0,\omega). \qquad (11)
\end{aligned}$$

Finally, we apply inverse Fourier transforms to expression 11 to obtain upgoing/downgoing P/S waves in the space-time domain.

If we knew k, θ_p, or θ_s, we could solve equation 11 with one receiver in the space-time domain; however the estimation is difficult because incoming waves are composed of a variety of angles of incidence. Therefore for this decomposition, we need a receiver array for the Fourier transform, which decomposes the wavefields into the different wavenumber components k, and the assumption, in which velocities just below the free surface in the region of this array are constant (laterally homogeneous in the near surface). In expression 11, u_x and u_z are observed after a double Fourier transform, k and ω are given in the wavenumber-frequency domain, and ν_p and ν_s can be computed in the wavenumber-frequency domain when α and β are given (Table 1). In conclusion, when we assume α and β, we can compute U_p, D_p, U_s, and D_s using equation 11.

To estimate velocities, we use the fact that U_p and U_s do not include direct S and P waves, respectively. If we use correct velocities, the amplitudes of U_s around the arrival time of direct P waves are small and those of U_p around the time of direct S waves are also small. Therefore, we can estimate α and β by minimizing amplitudes around arrival times of direct P waves in U_s and of direct S waves in U_p. Note that because U_s only depends on β (see equation 11), the estimation of β from U_s and then α from U_p is computationally easier.

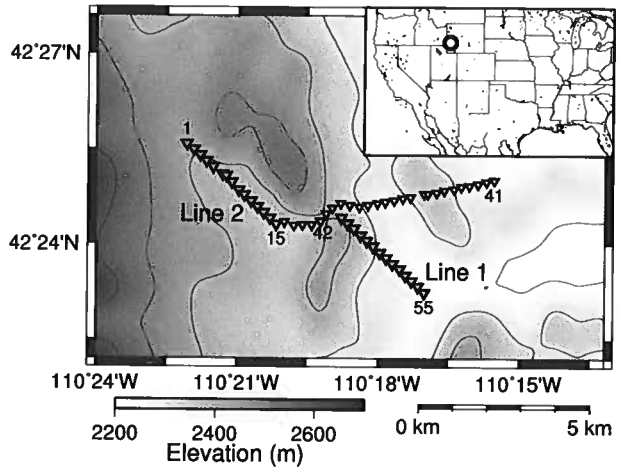

Figure 2. Geometry of receivers (triangles). We use records observed at the receivers shown by red triangles for this study. Survey lines 1 and 2 contain receivers 1–15 and 42–55, respectively. The circle on the top-right map shows the location of magnified area. The gray scale illustrates topography.

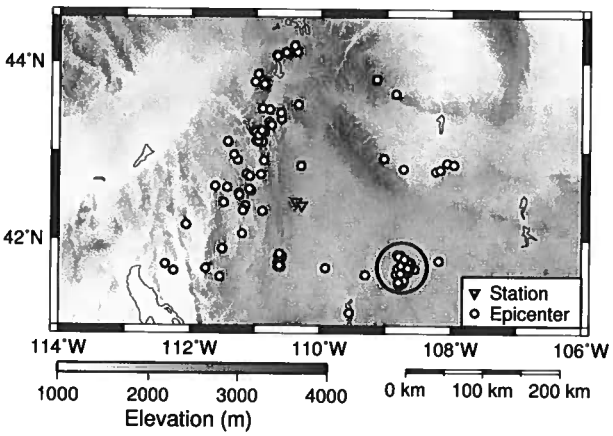

Figure 3. Geometry of earthquakes (yellow dots) and receivers (red triangles). We use an earthquake swarm (embraced by black circle) for the interferometry study. Triangles indicate the locations of receivers No. 1 and 55. The gray scale illustrates topography.

3 EARTHQUAKE DATA

3.1 Data set and previous studies

We analyze local earthquake data recorded at the LaBarge field in Wyoming (Figure 2) to extract subsurface information using seismic interferometry. A dense receiver network, which contained 55 three-component broadband seismometers with a 250-m average receiver interval, recorded more than 200 earthquakes (Figure 3) during a continuous recording period (November 2008–June 2009). With the dense receiver geometry, we have an opportunity to obtain relatively shallow structural information ($\lesssim$ 5 km). Most of the earthquakes are not listed in the earthquake catalog provided by the U.S Geological Survey (USGS) due to their small sizes; however, we expect that the magnitudes and depths of observed earthquakes are smaller than 2 and shallower than 10 km, respectively, based on the information from a few earthquakes in the catalog. Using this data set, several studies obtain images or velocities of the subsurface in the survey area. Leahy et al. (2012) apply receiver function to teleseismic events to image the subsurface. Schmedes et al. (2012) and Biryol et al. (2013) apply earthquake tomography to teleseismic and local earthquake data, respectively. Behm et al. (2013) apply seismic interferometry to reconstruct surface waves using ambient-noise data and obtain Rayleigh- and Love-wave velocities. From teleseismic data, Behm (2013) obtains vertical-incident reflected waves by employing blind deconvolution based on a multichannel analysis.

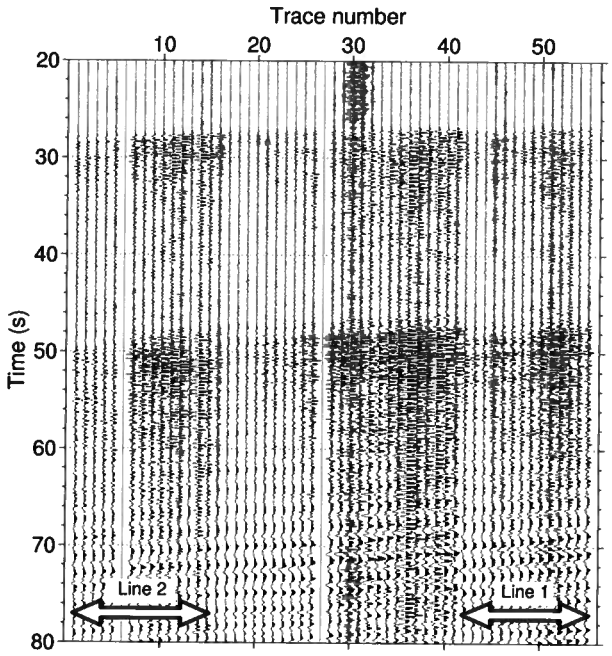

Figure 4. Example of observed records from an earthquake in the North-South horizontal component after applying a bandpass filter, 0.4–0.5–7–9 Hz. Time 0 s is the origin time of the earthquake. Trace numbers correspond with the receiver numbers in Figure 2. The white arrows show the receivers used for survey lines 1 and 2.

3.2 Observed data

Because the wavefield decomposition in section 2 is valid for the wave propagation in a vertical plane, we restrict ourselves to hypocenters and receivers near that vertical plane. We use a cluster of earthquakes (represented by the black circle in Figure 3), which contains about 100 earthquakes and produces quasi-plane waves with nearly the same angles of incidence. This cluster of earthquakes is roughly 180 km away from the stations and located on the extensions of survey lines 1 and 2 in Figure 2. Therefore in this study, we use this cluster of

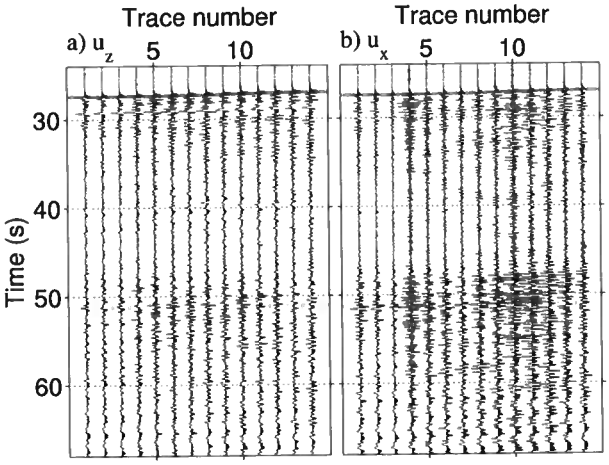

Figure 5. Space-interpolated observed record in (a) vertical and (b) radial components in line 1 (after rotating the horizontal components in the radial direction) from the same earthquake used in Figure 4. Trace number is assigned after the space interpolation, and traces 1–14 correspond to traces 42–55 in Figure 4. We apply the same bandpass filter used in Figure 4 to waveforms in all panels. The pink and yellow lines indicate the picked arrival times for direct P and S waves, respectively. Amplitudes are normalized separately at each panel.

earthquakes and receivers of survey lines 1 and 2 (the red triangles in Figure 2) to reconstruct direct and reflected plane waves with seismic interferometry.

Figure 4 shows sample observed wavefields excited by one earthquake. Direct P waves arrive around 28 s, S waves around 50 s, and surface waves around 70 s. Wavefields at traces 29-30 are contaminated by traffic noise which is generated from a road close to these receivers. The high-energy waveforms contain frequencies up to 7 Hz. Because the aperture of the receiver array is small, we cannot estimate seismic phases of each arrival wave from the curvature of travel times in Figure 4. The possible seismic phases of incoming waves are direct waves (Pg,Sg), reflected waves from the outer side of the Moho (PmP, SmS), and diving waves through the upper mantle (Pn,Sn). Note that we can apply seismic interferometry to any type of phases and we do not have to specify the seismic phases although some studies use specific seismic phases to confine the angle of incident waves (Ruigrok et al., 2010; Ruigrok and Wapenaar, 2012). In this study, we estimate the travel times of each seismic phase to validate our interferometric wavefields, where we evaluate whether the reconstructed waves with seismic interferometry are reflected waves or later phases. To estimate travel times of each phase, we construct a three-dimensional (3D) local model based on Gans (2011) that includes crustal inhomogeneity and perform 3D ray tracing with the program ANRAY (Pšenčík, 1998). According to the ray tracing, travel-time differences are small for Pn/Pg as well as Sn/Sg, and PmP/SmS arrive 0.7/1.2 s later than Pn/Sn. Amplitudes of Pg/Sg are smaller than Pn/Sn and PmP/SmS. Although both travel times and, in particular, amplitudes still depend on the subsurface model, we conclude that the observed first arrivals are most likely Pn/Sn or PmP/SmS since their amplitudes are stronger.

3.3 Wavefield decomposition

To apply wavefield decomposition in the wavenumber-frequency domain using equation 11, we need traces at uniform spatial intervals. Therefore, we interpolate the observed data in space using a spline interpolation before the decomposition. Note that the receiver intervals in survey lines 1 and 2 are almost uniform and the interpolated distances are small. Figure 5 shows the interpolated wavefields after rotating the horizontal components in the radial direction (the same direction as the receiver array).

Figure 6 shows the particle motion around the P- and S-wave arrival times. We compute the angles of incident P and S waves by ray tracing with a velocity model based on Gans (2011) (shallow) and Kennett and Engdahl (1991) (deep); the angles of incidence in survey line 1 are 35° and 18 ° for P and S waves, respectively (the blue lines in Figure 6). The particle motions around P-wave arrivals correspond to the angle of incidence estimated by ray tracing, but the particle motions around S-wave arrivals do not. This anomalous particle motion for the S-wave arrivals may be caused by the fact that S waves overlap with the P-wave coda, the S-wave arrival time is less clear than the P-wave time (see Figure 5), and the subsurface may create strong PS converted waves (which we discuss later). Note that in both P and S waves, the particle motions do not have to perfectly align to the angle of incidence estimated by ray tracing because the incoming waves are not perfect plane waves.

Wavefield decomposition shown in equation 11 requires P- and S-wave velocities. We do not need to know the angle of incidence for the wavefield decomposition because we solve equation 11 in the wavenumber-frequency domain. To estimate velocities, we employ the method proposed in section 2 and minimize upgoing P-wave amplitude around S-wave arrival times as well as upgoing S-wave amplitude around P-wave arrival times. Figure 7 shows upgoing/downgoing P/S waves decomposed from waves in Figure 5 with estimated P- and S-wave velocities, which are 3.5 and 1.2 km/s, respectively. Based on these velocities, and an angle of 35° of the P incident wave, the reflection coefficients at the free surface are -0.905 (P$\acute{\text{P}}$), 0.665 (P$\acute{\text{S}}$), 0.273 (S$\acute{\text{P}}$), and 0.905 (S$\acute{\text{S}}$) (Aki and Richards, 2002). In Figure 7a, the amplitudes in the pink/blue time intervals are larger than the yellow/green time intervals. In contrast in Figure 7b, amplitude differences between the pink/blue and yellow/green time intervals are not clear, which implies that the wavefields include strong PS converted waves in the pink/blue time interval. Since we normalize the amplitudes in Figure 7 for each panel separately, we cannot directly compare the amplitudes between panels.

Figures 8 and 9 show comparisons of wavefields and particle motions between upgoing P and S waves. In Figure 8a, because direct P waves (at around 27–27.5 s) exist only in the upgoing P wavefields, we successfully separate observed waves into upgoing P and S waves (also see the top row of

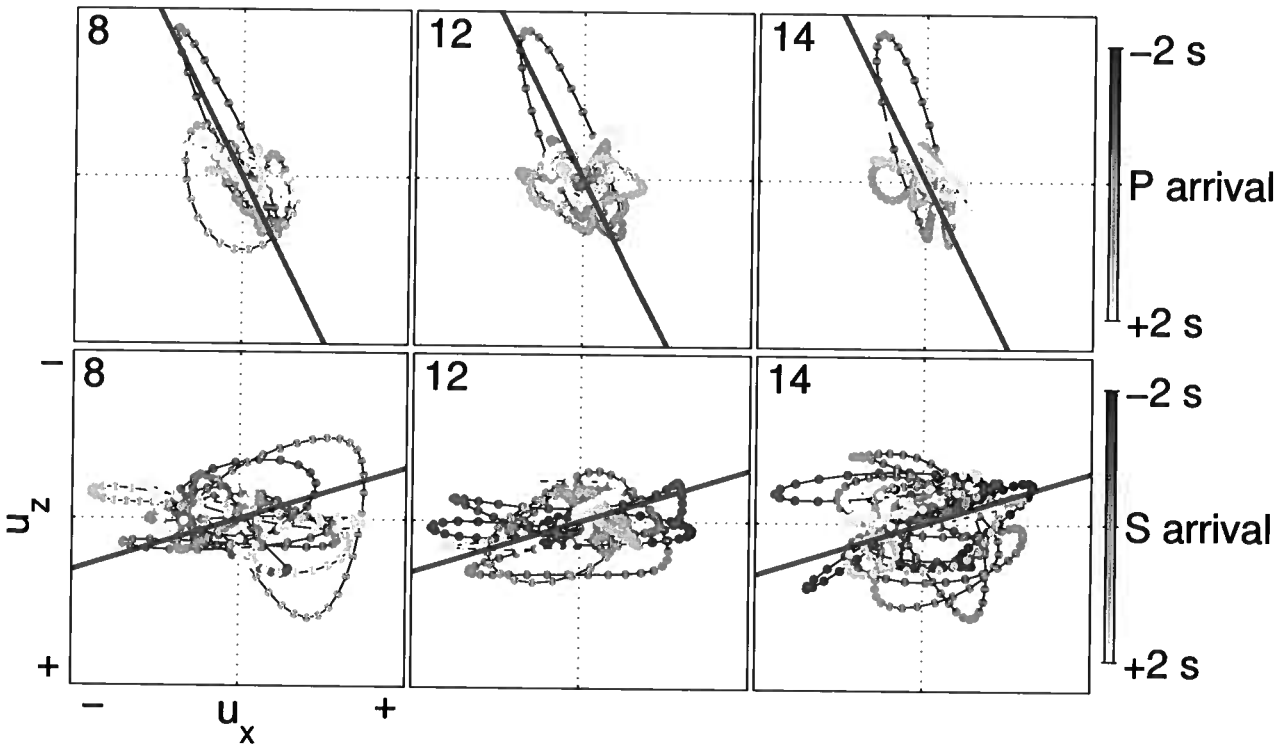

Figure 6. Particle motion of observed wavefields in the vertical and radial components (Figures 5) at around (top row) P- and (bottom row) S-wave arrivals after applying the same bandpass filter used in Figure 4. Red (0 s in the color bar) indicates the times at the pink line for P waves and the yellow line for S waves in Figure 5. Blue lines illustrate the particle motion based on the angle of incidence estimated by ray tracing. Top-left numbers at each panel describe trace numbers of each motion.

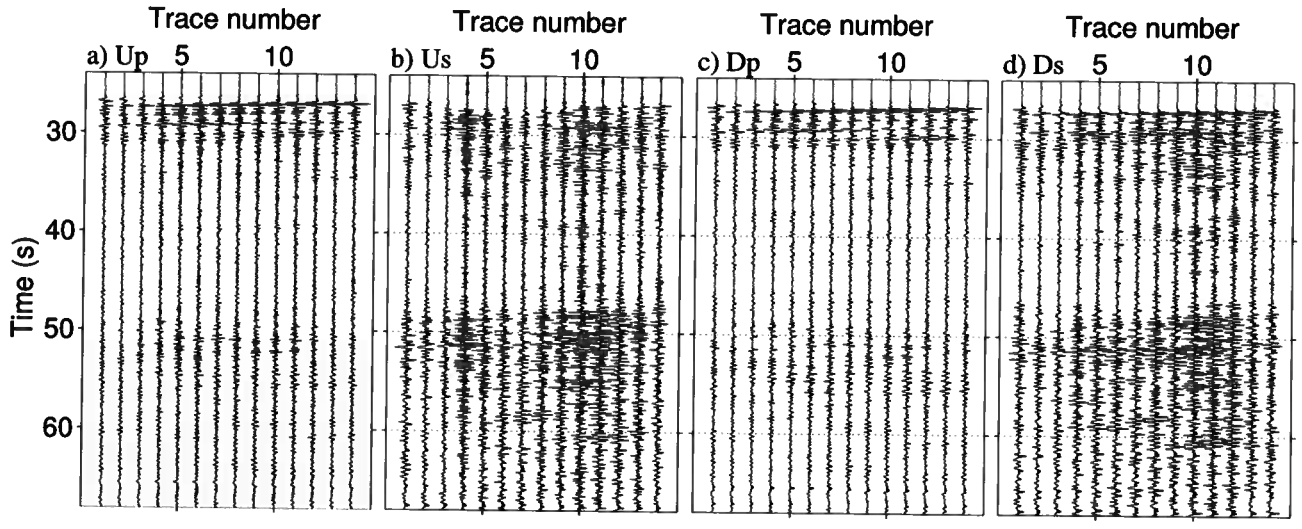

Figure 7. Upgoing/downgoing P/S waves after applying wavefield decomposition (equation 11) to the wavefields in Figure 5. We employ the same bandpass filter used in Figure 4 in all panels. The colors in panel (a) indicate the time windows we use in this study to separate direct (pink for P and yellow for S) and reflected waves (blue for P and green for S). The arrival times represented by the pink/yellow lines in Figure 5 locate the interfaces between pink/yellow and blue/green, respectively. Amplitudes are normalized separately at each panel.

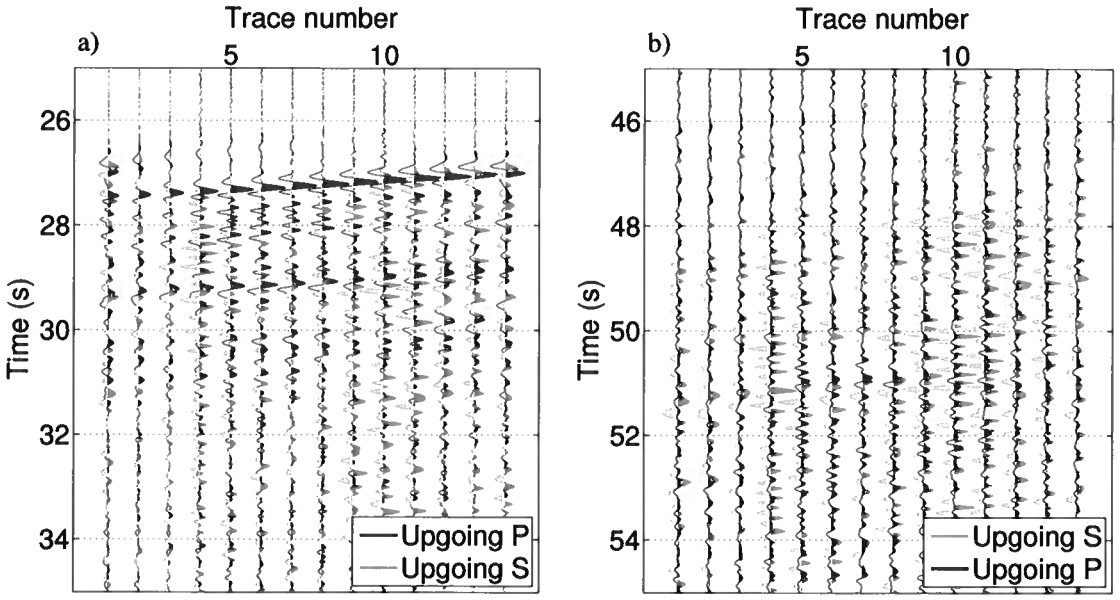

Figure 8. Comparison between upgoing P and S wavefields in Figures 7a and 7b at around (a) P-wave and (b) S-wave arrival times. Although in both panels upgoing P and S waves are shown in black and red, respectively, we change the order of wavefields; upgoing P is behind in panel (a) and upgoing S is behind in panel (b). Amplitude ratios between upgoing P/S waves are preserved.

Figure 9). Strong upgoing S waves appearing just after the direct P waves in Figure 8a indicate that the observed waveforms include strong PS converted waves. Since Figure 8b is mostly red, upgoing S wavefields are dominant in this time interval, which implies that we can also separate wavefields in this interval. The particle motions in the bottom row of Figure 9 move along the horizontal blue lines, which denote that upgoing S wavefields are dominant in this interval. The anomalous particle motion in trace 14, which is at the edge of the array, may be caused by the space-wavenumber Fourier transform; therefore, we only use traces 3–12 for interferometry.

4 APPLICATION OF SEISMIC INTERFEROMETRY TO EARTHQUAKE DATA

We introduce a mathematical description of seismic interferometry related to this study while assuming 2D wave propagation and show reconstructed waveforms from the earthquake data. More information on seismic interferometry is given by Snieder et al. (2009), Wapenaar et al. (2010a,b), and Wapenaar et al. (2011b), who summarize trace-by-trace and multidimensional interferometry. In this section, all equations are written in the space-frequency domain.

4.1 Trace-by-trace deconvolution

For trace-by-trace deconvolution interferometry, we compute deconvolution for each pair of traces at each earthquake. This method works well in the case of 1D wave propagation (Snieder and Şafak, 2006; Nakata and Snieder, 2012) and can be applied to higher dimensions (e.g., Vasconcelos and Snieder, 2008b).

4.1.1 Deconvolution without wavefield decomposition

Deconvolution applied to the waveforms from one earthquake recorded by the vertical component of receivers A and B is given by

$$DI_{zz}(B,A) = \frac{u_z(B)}{u_z(A)} \approx \frac{u_z(B)u_z^*(A)}{|u_z(A)|^2 + \epsilon\langle|u_z(A)|^2\rangle}, \qquad (12)$$

where ϵ is a regularization parameter (Clayton and Wiggins, 1976), the asterisk denotes the complex conjugate, and $\langle\cdots\rangle$ indicates the average power spectrum. In deconvolution interferometry, the receiver at the denominator in equation 12 (receiver A) behaves as a virtual source (Vasconcelos and Snieder, 2008a). We can compute deconvolution for all combinations of the vertical and horizontal components, and each combination corresponds to different types of wave propagation between receivers A and B. For simplicity, we show only one combination in equation 12. In the 1D case, $DI_{zz}(B,A)$ is equivalent to the wave propagation from receiver A to receiver B (Snieder et al., 2006a). In the 2D and 3D cases, we average $DI_{zz}(B,A)$ over many sources around the receivers to reconstruct the wave propagation (Vasconcelos and Snieder, 2008a). Because u_z includes both P and S waves (equation 5), $DI_{zz}(B,A)$ contains crosstalk between P and S waves.

In Figure 10, we apply trace-by-trace deconvolution to observed wavefields shown in Figure 5 (equation 12). Receiver A in equation 12 is at offset 0 km (virtual source). The deconvolved wavefields in Figure 10 are contaminated by noise

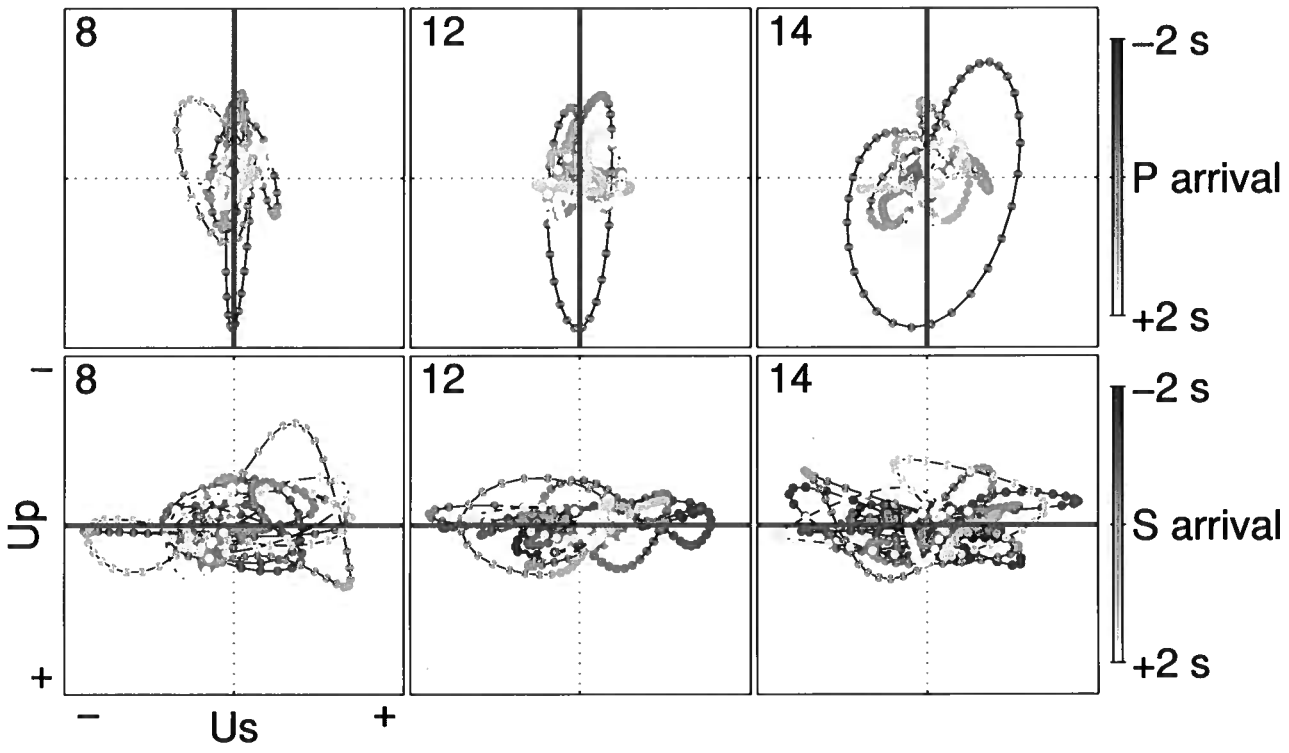

Figure 9. Particle motion of upgoing P and S wavefields at around (top row) P- and (bottom row) S-wave arrivals after applying the same bandpass filter used in Figure 4. Red (0 s in the color bar) indicates the times at the pink line for P wave and the yellow line for S waves in Figure 5. Blue lines illustrate the ideal particle motion of P (top row) and S (bottom row) waves in the case when wavefields are perfectly separated and no converted waves are generated. Top-left numbers at each panel describe trace numbers of each motion. Note that in contrast to Figure 6, the axes denote the upgoing P- and S-wave components.

around the zero-lag time; hence, trace-by-trace deconvolution using neither wavefield decomposition nor time windowing does not provide useful information about the subsurface.

4.1.2 *Direct-wave reconstruction*

To improve interferometric wavefields, we decompose u_x and u_z into U_p, D_p, U_s, and D_s (Figure 7) using equation 11 before applying seismic interferometry. We represent the wavefield U_p at receiver B (the red triangle in Figure 11) with the wavefield U_p at receiver A (the blue triangle in Figure 11) as

$$U_p(B) = G_p U_p(A), \tag{13}$$

where we assume that all wavefields recorded at receiver B are also recorded at receiver A. The Green's function G_P accounts for the propagation of the direct waves from receiver A to receiver B (when the waves are plane waves, the Green's function relates to the distance h_d in Figure 11). Deconvolving equation 13 with $U_p(A)$ gives G_p:

$$\frac{U_p(B)}{U_p(A)} = G_p. \tag{14}$$

In practice, for computing this deconvolution, we use a regularization parameter introduced in equation 12.

We apply trace-by-trace deconvolution (equation 14), where we compute $U_p(B)/U_p(A)$ and $U_s(B)/U_s(A)$, to decomposed wavefields obtained from each earthquake and average over all earthquakes used (Figure 12). The solid lines show the dips which maximize the amplitudes of slant-stacked waveforms. These dips depend on the angles of incidence and the wave velocities. Based on the angles of incidence estimated by ray tracing (35° for P waves and 18° for S waves), the P- and S-wave velocities are 4.2 km/s and 1.5 km/s, respectively. These velocities are average velocities over ray paths of the direct waves (h_d in Figure 11). We also apply this deconvolution to survey line 2 (dashed lines in Figure 12). The dips in line 2 are flatter than in line 1, which corresponds to the high-velocity layer under line 2 (Leahy et al., 2012). Note that without wavefield separation, we cannot clearly reconstruct direct waves (compare Figure 10 with Figure 12).

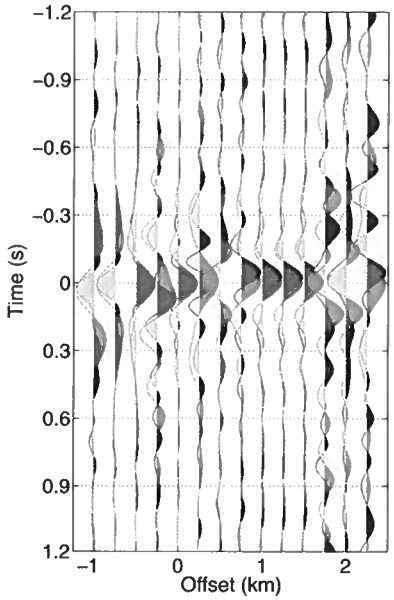

Figure 10. Wavefields at line 1 obtained by applying trace-by-trace deconvolution to observed vertical (black) and radial (red) components (equation 12). We apply a bandpass filter 0.4–0.5–7–9 Hz to wavefields in the vertical component and 0.4–0.5–4–6 Hz to wavefields in the radial component. Offset 0 km is the location of the virtual source.

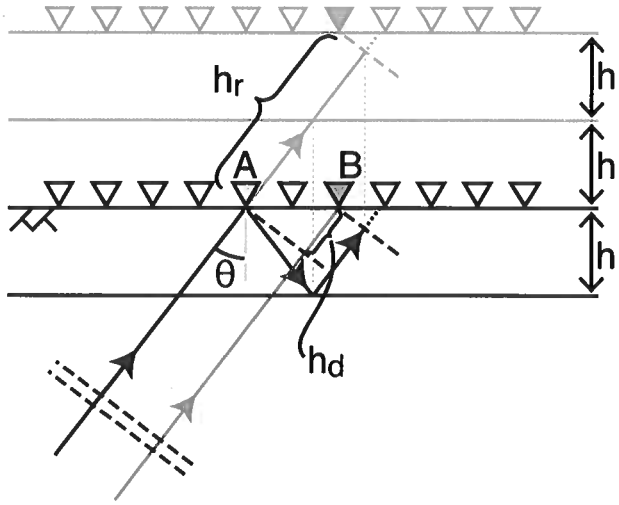

Figure 11. Schematic plane-wave propagation. Receivers (triangles) are deployed at the free surface (indicated by ⩘), and a plane wave (the black arrow at lower-left) propagates with angle θ of the incidence. Dashed lines, all of which are parallel, indicate the portions of plane waves. The red arrow illustrates the ray path for the different portion of the same plane wave as the black arrow. The model contains one horizontal layer and a half space below the layer. The thickness of the layer is h. Gray lines and receivers show unfolded imaginary layers and receivers to understand reflected plane waves based on Snell's law. Distance h_d corresponds with the difference of the travel distance between direct upgoing waves to receivers A and B, and h_r is the travel distance of the reflected waves from A to B. We do not show converted waves in this figure.

4.1.3 Reflected-wave reconstruction

Equation 13 indicates the relationship between upgoing waves recorded at different receivers. Next, we reconstruct the reflected waves using upgoing and downgoing waves. Surface-related reflected upgoing P waves at receiver B are given by

$$U_p^r(B) = G_{pp}D_p(A) + G_{ps}D_s(A), \tag{15}$$

where G_{pp} and G_{ps} are the P-P and P-S reflected Green's function representing the wave propagation from receiver A to receiver B (Figure 13). In this study, we use time windows to separate direct and reflected waves. Equation 15 after deconvolving with $D_p(A)$ is given as

$$\frac{U_p^r(B)}{D_p(A)} = G_{pp} + G_{ps}\frac{D_s(A)}{D_p(A)}. \tag{16}$$

Although we obtain the P-P reflected Green's function (G_{pp}) using equation 16, the deconvolved wavefield ($U_p^r(B)/D_p(A)$) is contaminated by crosstalk of downgoing P and S waves. Note that we compute $U_p^r(B)/D_p(A)$ to obtain G_{pp}, and $G_{ps}D_s(A)/D_p(A)$ in equation 16 is an unwanted wave created by crosstalk. Therefore in the elastic-wave case, we cannot obtain pure (no crosstalk) reflected Green's function with trace-by-trace deconvolution.

To focus on the first surface-related multiples, which are the most coherent reflected waves, we use only direct downgoing P waves:

$$\frac{U_p^r(B)}{D_p^d(A)} = G_{pp} + G_{ps}\frac{D_s(A)}{D_p^d(A)}, \tag{17}$$

where we cannot apply a time window to D_s because this wavefield is contained in U_p^r. Reflected waves are less coherent between traces than direct waves due to multiple scattering. Therefore, when we show a virtual-shot gather (i.e., we fix receiver A and change receiver B), which we use in this study, the gather created by equation 17 has little coherency between traces. To improve the coherency between traces in the virtual-shot gather, we use time reversal. Under time reversal, $G \rightarrow G^*$, $U \rightarrow D$, and $D \rightarrow U$; as a result, we rewrite equation 15 to

$$D_p(B) = G_{pp}^* U_p^r(A) + G_{ps}^* U_s^r(A) \tag{18}$$

and equation 17 to

$$\frac{D_p^d(B)}{U_p^r(A)} = G_{pp}^* + G_{ps}^*\frac{U_s^r(A)}{U_p^r(A)}. \tag{19}$$

Because the direct downgoing P waves D_p^d is more coherent than the reflected upgoing P waves U_p^d, expression 19 gives more coherent virtual-shot gathers than expression 17.

We compute equation 19 to obtain reflected waves while applying time windows for separating direct and reflected waves. We independently create time windows for each earthquake, and the time windows shown in Figure 7a are the windows for the earthquake in Figure 7. Figure 14 shows all P/S combinations of the trace-by-trace deconvolved waveforms after averaging over all earthquakes used. In Figures 14a and

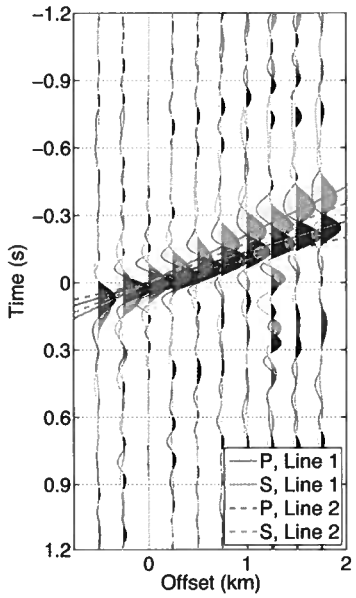

Figure 12. Wavefields in survey line 1 obtained by applying trace-by-trace deconvolution to upgoing P (black) and S (red) waves (equation 14). The solid lines show the dip of P (black) and S (red) plane waves in survey line 1, and the dashed lines in survey line 2. We apply the same bandpass filters used in Figure 10. Offset 0 km is the location of the virtual source.

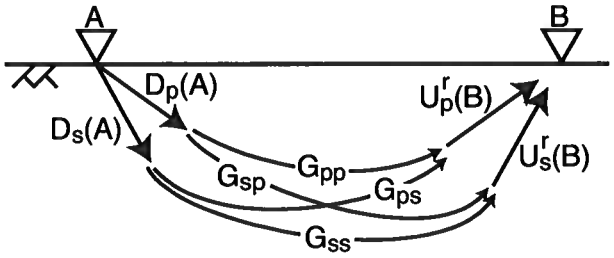

Figure 13. Relationship of upgoing/downgoing P/S wavefields and Green's functions between receivers *A* and *B*. The free surface is indicated by ⩘. The direction of arrows represents the direction of causality. Upgoing waves are reflected waves (direct upgoing waves are not shown).

14b, we employ the pink/blue time windows shown in Figure 7a (modified for each earthquake), respectively. Similarly, in Figures 14c and 14d, we use the yellow/green time windows shown in Figure 7a (modified for each earthquake). To avoid truncation of waves, we apply cosine tapers at the edge of each time window. In Figure 14, offset 0 km is the location of the virtual source, which excites a quasi-plane wave at time 0 s. Although each panel in Figure 14 aims to show the target reflected Green's function (e.g., G_{pp} for Figure 14a), each panel includes unwanted crosstalk caused by the last term in equation 19. Evaluating the amount of crosstalk is difficult, but we expect that the energy of SP reflected waves should be smaller than other reflected waves in the estimated angle of incidence (Aki and Richards, 2002). For example in the assumption of horizontal layers, when the P and S velocities in the first/second layers are 3.5/5.0 and 1.2/2.2 km/s (modified after Leahy et al., 2012) and the angle of P-wave incidence is 35°, the reflection coefficients at the interface are 0.189 (P̀Ṕ), -0.135 (P̀Ś), -0.055(S̀Ṕ), and -0.162 (S̀Ś). Almost no P-wave energy is present in Figure 8b, which also indicates that G_{sp} is small. However, the amplitudes in Figure 14c are greater than those in Figure 14d, which might be caused by the crosstalk between upgoing waves in equation 19.

The right-most trace at each panel in Figure 14 shows slant-stacked wavefields, where the dip for stacking (the red lines in Figure 14) is chosen to maximize the peak amplitude of stacked waveforms. Since the dips are related to the wave velocities and the angles of incidence, the dips in Figures 14a and 14b as well as those in Figures 14c and 14d are almost the same. Stacked waveforms in Figure 14 are noisy and difficult to interpret.

4.2 Trace-by-trace crosscoherence

Because normalization in the frequency domain improves the signal-to-noise ratio of interferometric wavefields (Nakata et al., 2011), we apply the normalization before deconvolving waveforms, which is so-called crosscoherence interferometry. We normalize equation 18 with the amplitude of $D_p(B)$:

$$\frac{D_p(B)}{|D_p(B)|} = G^*_{pp}\frac{U^r_p(A)}{|D_p(B)|} + G^*_{ps}\frac{U^r_s(A)}{|D_p(B)|}. \tag{20}$$

By deconvolving equation 20 with $U^r_p(A)/|D_p(B)|$, we obtain the form of crosscoherence interferometry:

$$\begin{aligned}\frac{D_p(B)}{|D_p(B)|}\frac{|U^r_p(A)|}{U^r_p(A)} &= \frac{D_p(B)U^{r*}_p(A)}{|D_p(B)||U^r_p(A)|} \\ &= \frac{|U^r_p(A)|}{|D_p(B)|}\left\{G^*_{pp} + G^*_{ps}\frac{U^r_s(A)}{U^r_p(A)}\right\},\end{aligned} \tag{21}$$

where $|U^r_p(A)|/|D_p(B)|$ is considered as an amplification term. Note that we still have crosstalk in equation 21 ($G^*_{ps}U^r_s(A)/U^r_p(A)$). Similar to equation 17, we focus on the first surface-related multiples in equation 21 and compute

$$\frac{D^d_p(B)U^{r*}_p(A)}{|D^d_p(B)||U^r_p(A)|} = \frac{|U^r_p(A)|}{|D^d_p(B)|}\left\{G^*_{pp} + G^*_{ps}\frac{U^r_s(A)}{U^r_p(A)}\right\}. \tag{22}$$

In practice, we use a regularization parameter to compute trace-by-trace crosscoherence (Nakata et al., 2013):

$$\frac{D^d_p(B)U^{r*}_p(A)}{|D^d_p(B)||U^r_p(A)|} = \frac{D^d_p(B)U^{r*}_p(A)}{|D^d_p(B)||U^r_p(A)| + \epsilon\langle|D^d_p(B)||U^r_p(A)|\rangle}. \tag{23}$$

When we apply trace-by-trace crosscoherence interferometry to earthquake data, we can suppress noise and compensate amplitude balance among traces (equation 22) as shown by Nakata et al. (2011) (Figure 15). Figure 15 shows more coherent waves than Figure 14 with the noise in traces around

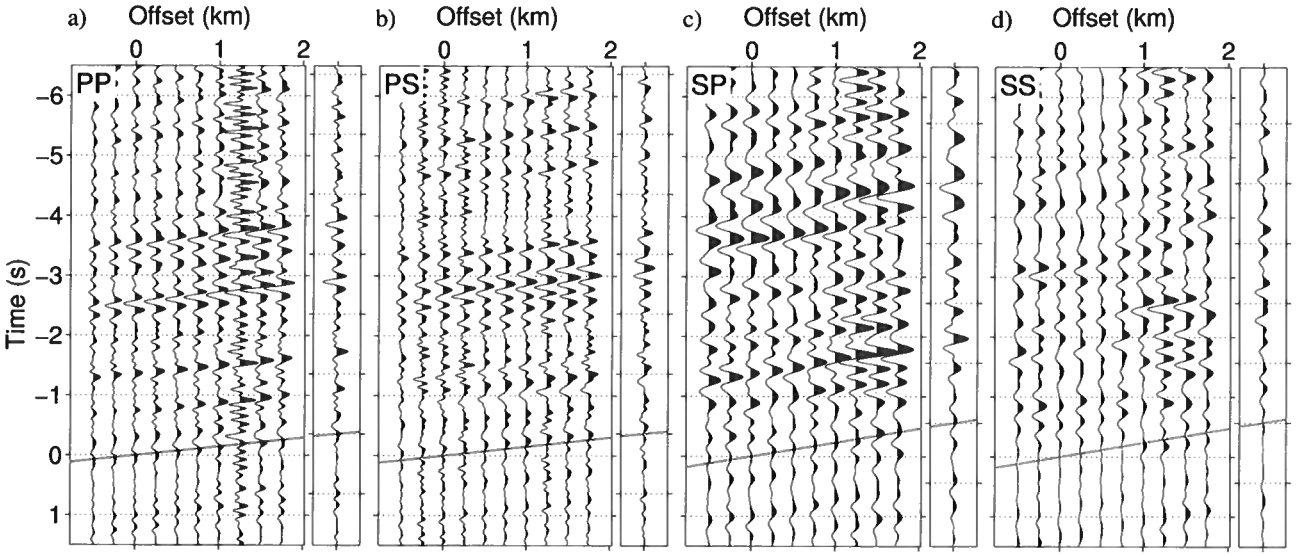

Figure 14. Reflected plane waves retrieved by trace-by-trace deconvolution after time windowing. We compute (a) $D_p^d(B)/U_p^r(A)$ ($\approx G_{pp}^*$), (b) $D_p^d(B)/U_s^r(A)$ ($\approx G_{ps}^*$), (c) $D_s^d(B)/U_p^r(A)$ ($\approx G_{sp}^*$), and (d) $D_s^d(B)/U_s^r(A)$ ($\approx G_{ss}^*$). We apply bandpass filters with (a,b) 0.4–0.5–7–9 Hz and (c,d) 0.4–0.5–4–6 Hz. Red lines indicate the dip for slant stacking, and the rightmost trace at each panel is the stacked trace. The reference trace for the deconvolution is the trace at offset 0 km (virtual source). The amplitudes in panels (c,d) are multiplied by a factor 2.5 compared with those in panels (a,b), and the amplitudes in panels (a,b) are the same .

offset 1–1.5 km being suppressed. One criterion to evaluate the quality of the interferometric wavefields is given by using causality. Because we employ time reversal and apply time windows, the wavefields after applying interferometry should contain waves only for $t < 0$, and waves for $t > 0$ are noise. Comparing Figures 14 and 15, the amplitudes in the causal time in Figure 15 are smaller than in Figure 14, which indicates that the wavefields constructed by trace-by-trace cross-coherence have the higher signal-to-noise ratio than trace-by-trace deconvolution. Although crosscoherence improves the signal-to-noise ratio, the waveforms in Figure 15 include unwanted crosstalk as indicated in equation 22. For example, a negative-amplitude wave exists at 4.6 s in both stacked waveforms of Figures 15c and 15d, which may be caused by the crosstalk because SP and SS waves rarely arrive at the same time.

4.3 Multi-dimensional deconvolution

In trace-by-trace interferometry, we solve the Green's functions of P and S reflected waves at each pair of traces for each combination of P/S waves separately. In MDD interferometry, we solve the Green's functions of all components for all traces simultaneously. From equation 18 and the similar notation for S waves, we obtain

$$\begin{pmatrix} D_p \\ D_s \end{pmatrix} = \begin{pmatrix} G_{pp}^* & G_{ps}^* \\ G_{sp}^* & G_{ss}^* \end{pmatrix} \begin{pmatrix} U_p^r \\ U_s^r \end{pmatrix}, \tag{24}$$

where each wavefield includes all traces (see Figure 13 to understand equation 24 schematically). Confining only direct downgoing waves (similar to equation 17), we obtain

$$\begin{pmatrix} D_p^d \\ D_s^d \end{pmatrix} = \begin{pmatrix} G_{pp}^* & G_{ps}^* \\ G_{sp}^* & G_{ss}^* \end{pmatrix} \begin{pmatrix} U_p^r \\ U_s^r \end{pmatrix}. \tag{25}$$

To solve equation 25, we first right-multiply $(U_p^{r*} \;\; U_s^{r*})$ (Wapenaar et al., 2011b):

$$\begin{pmatrix} D_P^d U_P^{r*} & D_P^d U_S^{r*} \\ D_S^d U_P^{r*} & D_S^d U_S^{r*} \end{pmatrix} = \begin{pmatrix} G_{PP}^* & G_{PS}^* \\ G_{SP}^* & G_{SS}^* \end{pmatrix} \begin{pmatrix} U_P^r U_P^{r*} & U_P^r U_S^{r*} \\ U_S^r U_P^{r*} & U_S^r U_S^{r*} \end{pmatrix} \tag{26}$$

and then add a damping parameter $\epsilon \boldsymbol{I}$ to equation 26 to obtain a stable inverse matrix (van der Neut et al., 2011b):

$$\begin{pmatrix} D_P^d U_P^{r*} & D_P^d U_S^{r*} \\ D_S^d U_P^{r*} & D_S^d U_S^{r*} \end{pmatrix} \left\{ \begin{pmatrix} U_P^r U_P^{r*} & U_P^r U_S^{r*} \\ U_S^r U_P^{r*} & U_S^r U_S^{r*} \end{pmatrix} + \epsilon \boldsymbol{I} \right\}^{-1} = \begin{pmatrix} G_{PP}^* & G_{PS}^* \\ G_{SP}^* & G_{SS}^* \end{pmatrix}. \tag{27}$$

Employing equation 27, we can retrieve the Green's matrix from upgoing/downgoing P/S wavefields.

Because MDD treats the reconstruction of the Green's function as an inverse problem, MDD has several advantages compared with trace-by-trace interferometry. MDD can be applied to passive seismic data generated by uneven distributed sources in a dissipative medium (but MDD requires even distributed receivers) (van der Neut et al., 2011b; Wapenaar et al., 2011a,b). Snieder et al. (2009) suggest that one can retrieve Green's functions without estimating source spectra by using MDD. This method also removes complicated overburden without requiring a velocity model when receivers are embedded inside a medium (van der Neut et al., 2011a,b). Note that

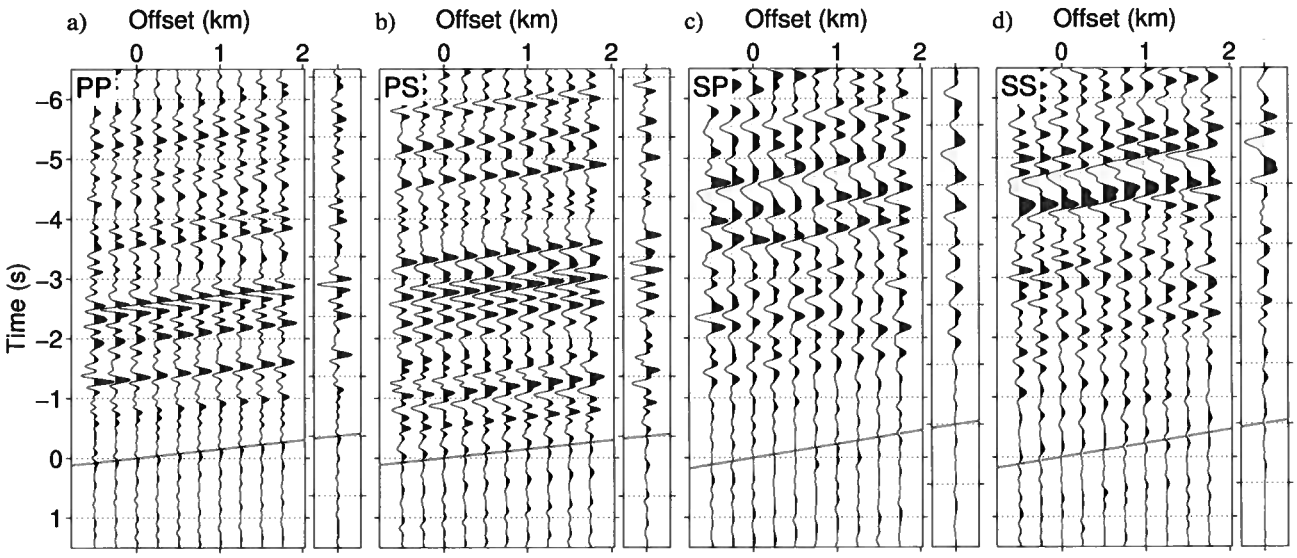

Figure 15. Reflected plane waves retrieved by trace-by-trace crosscoherence after time windowing. We compute (a) $D_p^d(B)U_p^{r*}(A)/|D_p^d(B)||U_p^r(A)|$ ($\approx G_{pp}^*$), (b) $D_p^d(B)U_s^{r*}(A)/|D_p^d(B)||U_s^r(A)|$ ($\approx G_{ps}^*$), (c) $D_s^d(B)U_p^{r*}(A)/|D_s^d(B)||U_p^r(A)|$ ($\approx G_{sp}^*$), and (d) $D_s^d(B)U_s^{r*}(A)/|D_s^d(B)||U_s^r(A)|$ ($\approx G_{ss}^*$). We apply the same bandpass filters as used in Figure 14. Red lines indicate the dip for slant stacking, and the rightmost trace at each panel is the stacked trace. The reference trace for the interferometry is the trace at offset 0 km (virtual source). The amplitudes in panels (c,d) are multiplied by a factor 2.5 compared with those in panels (a,b), and the amplitudes in panels (a,b) are the same.

by comparing equations 19 and 27, MDD retrieves the Green's functions without unwanted crosstalk when we separate P and S waves.

Figure 16 shows wavefields reconstructed by MDD interferometry (expression 27). The amplitudes of causal waves are weaker than those in Figures 14 and 15, which indicates that based on the criterion of causality the quality of wavefields produced by MDD is better than trace-by-trace interferometry. Wavefields in Figure 16 do not include unwanted crosstalk, which contaminates waveforms in Figures 14 and 15, because MDD solves the inverse problem (equation 27). As shown in Figure 8b, SP converted waves are weak (compare Figure 16c with the other panels in Figure 16). Also, the slant-stacked wavefields in Figures 16c and 16d are much dissimilar than the SP and SS waveforms in Figures 15c and 15d obtained by trace-by-trace crosscoherence. This is an indication that MDD successfully eliminate the crosstalk that contaminates Figures 15c and 15d.

Leahy et al. (2012) show that a reflector exists at about 3.8 km depth. The waves pointed by three arrows in Figure 16 are reflected waves from the reflector; their arrival times are 1.38 s (PP), 2.66 s (PS), and 4.10 s (SS). We do not pick the SP reflected wave because it is weak and noisy. Since these arrivals are much larger than the estimated travel-time differences between Pn/Sn and PmP/SmS, which are 0.7 s and 1.2 s, the reconstructed waves are reflected waves but not later direct arrivals. The arrival times of these reflected waves highlighted by the arrows in Figure 16 are dependent. Using the arrival times of the PP and SS reflected waves, the arrival time of the PS reflected wave should be 2.74 s, which is a 3% discrepancy ($\approx (2.74 - 2.66)/2.66$) from the observed time in Figure 16b. When we assume that the reflector is flat, the average P and S velocities over the raypaths of the reflected waves (h_r in Figure 11) are 4.5 km/s and 1.7 km/s, respectively, with the angles of incidence we estimated.

5 DISCUSSION OF VELOCITIES

The estimated velocities (4.2 and 1.5 km/s from direct waves and 4.5 and 1.7 km/s from reflected waves) and velocities used for the wavefield decomposition (3.5 and 1.2 km/s) are different. These differences indicate the depth variation of velocities. Gans (2011) and Leahy et al. (2012) show that the velocities in the region of survey line 1 monotonically increase with depth. The velocities estimated from direct (from Figure 12) and reflected waves (from Figure 16) are the average velocities over the distances h_d and h_r in Figure 11. Based on the estimated angles of incidence and the depth of the reflector, the velocities from the reflected waves include the information of deeper structure. Therefore, the fact that the estimated velocities from reflected waves are faster than those from direct waves is consistent with previous studies. The velocities used for decomposition are theoretically the velocities at the surface but practically the average velocities over a medium with some thickness depending on the wavelength we used. Since the velocities used for decomposition are slower than the velocities estimated from direct waves, the decomposition is sensitive for the velocities in the shallower structure than the distance $h_d \cos(\theta)$ in Figure 11 for the used frequency range.

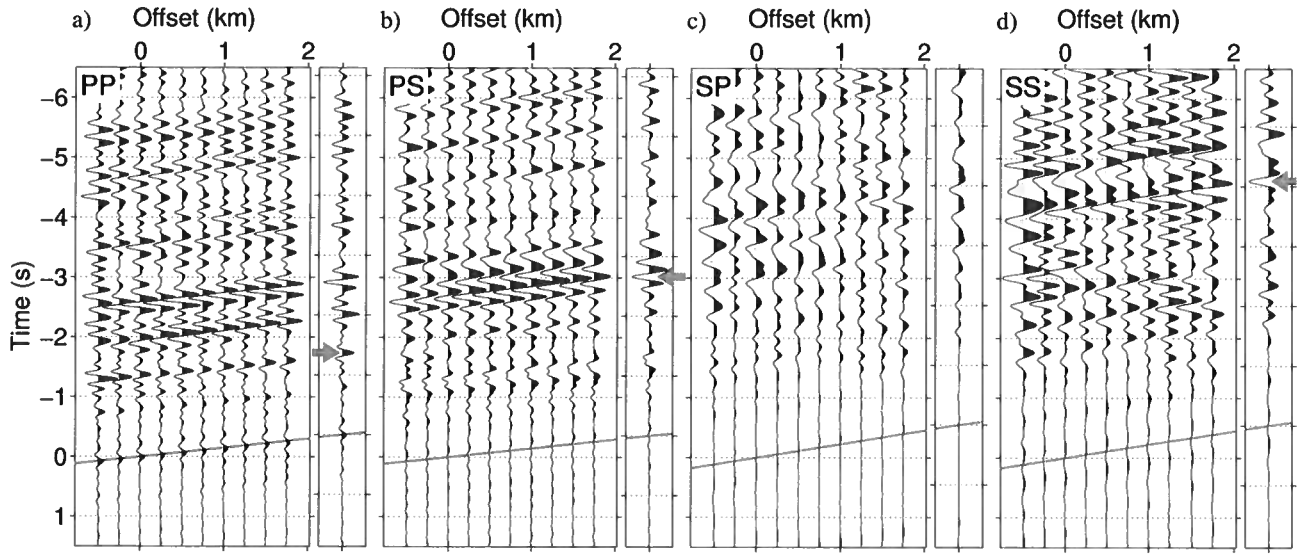

Figure 16. Reflected plane waves retrieved by multi-dimensional deconvolution after time windowing. (a) G^{*}_{pp}, (b) G^{*}_{ps}, (c) G^{*}_{sp}, and (d) G^{*}_{ss}. We apply the same bandpass filters as used in Figure 14. Red lines indicate the dip for slant stacking, and the rightmost trace at each panel is the stacked trace. The red arrows on the rightmost traces in panels (a,b,d) point at the waves that we interpret. The reference trace for the interferometry is the trace at offset 0 km (virtual source). The amplitudes in panels (c,d) are multiplied by a factor 2.5 compared with those in panels (a,b), and the amplitudes in panels (a,b) are the same.

6 CONCLUSION

We apply seismic interferometry to plane waves excited by a cluster of earthquakes and obtain subsurface information. To improve the quality of interferometric wavefields, we employ several techniques such as upgoing/downgoing P/S wavefield decomposition, time windowing to separate direct and reflected waves, time reversal, and multi-dimensional analysis. The wavefield decomposition proposed here works well when the medium has no or weak lateral heterogeneity. For trace-by-trace interferometry, wavefield decomposition enhances coherency of interferometric wavefields between traces. We retrieve the Green's matrix without unwanted crosstalk of P and S waves with MDD interferometry. Although MDD interferometry requires wavefield separation, the computed waveforms follow causality and have the highest signal-to-noise ratio compared with trace-by-trace interferometry. The difference between the velocities estimated from direct waves and reflected waves retrieved by seismic interferometry is evidence of the depth variation of the velocities.

ACKNOWLEDGMENTS

We are grateful to sponsor companies of the Consortium Project on Seismic Inverse Methods for Complex Structures at the Center for Wave Phenomena. We thank the IRIS data management center and Exxonmobil to provide the earthquake data, and USGS for managing the earthquake catalog. Figures 2 and 3 are produced by using the Generic Mapping Tools (GMT: http://gmt.soest.hawaii.edu, last accessed March 2013). We are grateful to Filippo Broggini for providing a code to implement MDD interferometry and Diane Witters for her professional help in preparing this manuscript.

REFERENCES

Abe, S., E. Kurashimo, H. Sato, N. Hirata, T. Iwasaki, and T. Kawanaka, 2007, Interferometric seismic imaging of crustal structure using scattered teleseismic waves: Geophys. Res. Lett., **34**, L19305.

Aki, K., 1957, Space and time spectra of stationary stochastic waves, with special reference to microtremors: Bull. Earthq. Res. Inst., **35**, 415–456.

Aki, K., and P. G. Richards, 2002, Quantitative Seismology, 2 ed.: Univ. Science Books.

Assumpção, M., D. James, and A. Snoke, 2002, Crustal thicknesses in se brazilian shield by receiver function analysis: Implications for isostatic compensation: J. Geophys. Res., **107**, ESE2–1–2–15.

Baig, A. M., M. G. Bostock, and J. P. Mercier, 2005, Spectral reconstruction of teleseismic P Green's functions: J. Geophys. Res., **110**, B08306.

Bakulin, A., and R. Calvert, 2006, The virtual source method: Theory and case study: Geophysics, **71**, S1139–S1150.

Behm, M., 2013, Blind deconvolution of multichannel recordings by linearlized inversion in the spectral domain: CWP report, **774**, 299–312.

Behm, M., R. Snieder, and G. Leahy, 2013, Retrieval of local surface velocities from traffic noise – an example from

the LaBarge basin (Wyoming): Geophys. Prospect. (submitted).

Biryol, C. B., G. M. Leahy, G. Zandt, and S. L. Beck, 2013, Imaging the shallow crust with local and regional earthquake tomography: J. Geophys. Res. (in press).

Bostock, M. G., 2004, Green's functions, source signatures, and the normalization of teleseismic wave fields: J. Geophys. Res., **109**, B03303.

Bostock, M. G., and S. Rondenay, 1999, Migration of scattered teleseismic body waves: Geophys. J. Int., **137**, 732–746.

Bostock, M. G., and M. D. Sacchi, 1997, Deconvolution of teleseismic recordings for mantle structure: Geophys. J. Int., **129**, 143–152.

Claerbout, J. F., 1968, Synthesis of a layered medium from its acoustic transmission response: Geophysics, **33**, 264–269.

Clayton, R. W., and R. A. Wiggins, 1976, Source shape estimation and deconvolution of teleseismic bodywaves: Geophys. J. R. astr. Soc., **47**, 151–177.

Dasgupta, S., and R. L. Nowack, 2006, Deconvolution of three-component teleseismic P waves using the autocorrelation of the P to SV scattered waves: Bull. Seismol. Soc. Am., **96**, 1827–1835.

Gans, C. R., 2011, Investigations of the crust and upper mantle of modern and ancient subduction zones, using Pn tomography and seismic receiver functions: PhD thesis, The university of Arizona.

Kennett, B. L. N., and E. R. Engdahl, 1991, Traveltimes for global earthquake location and phase identification: Geophys. J. Int., **105**, 429–465.

Langston, C. A., 1979, Structure under Mount Rainier, Washington, inferred from teleseismic body waves: J. Geophys. Res., **84**, 4749–4762.

Leahy, G. M., R. L. Saltzer, and J. Schmedes, 2012, Imaging the shallow crust with teleseismic receiver functions: Geophys. J. Int., **191**, 627–636.

Li, X., S. V. Sobolev, R. Kind, X. Yuan, and C. Estabrook, 2000, A detailed receiver function image of the upper mantle discontinuities in the japan subduction zone: Earth Planet. Sci. Lett., **183**, 527–541.

Loewenthal, D., and E. A. Robinson, 2000, On unified dual fields and Einstein deconvolution: Geophysics, **65**, 293–303.

Mehta, K., A. Bakulin, J. Sheiman, R. Calvert, and R. Snieder, 2007, Improving the virtual source method by wavefield separation: Geophysics, **72**, V79–V86.

Moldoveanu, N., L. Combee, M. Egan, G. Hampson, L. Sydora, and W. Abriel, 2007, Over/under towed-streamer acquisition: A method to extend seismic bandwidth to both higher and lower frequencies: The Leading Edge, **26**, 41–58.

Nakata, N., and R. Snieder, 2012, Estimating near-surface shear-wave velocities in Japan by applying seismic interferometry to KiK-net data: J. Geophys. Res., **117**, B01308.

Nakata, N., R. Snieder, S. Kuroda, S. Ito, T. Aizawa, and T. Kunimi, 2013, Monitoring a building using deconvolution interferometry. I: Earthquake-data analysis: Bull. Seismol. Soc. Am. (in press).

Nakata, N., R. Snieder, T. Tsuji, K. Larner, and T. Matsuoka, 2011, Shear-wave imaging from traffic noise using seismic interferometry by cross-coherence: Geophysics, **76**, SA97–SA106.

Pšenčík, I., 1998, Package anray, version 4.10: Technical Report Report 7, 403-404, Department of Geophysics, Charles University Prague.

Robertsson, J. O. A., and A. Curtis, 2002, Wavefields separation using densely deployed three-component single-sensor groups in land surface-seismic recordings: Geophysics, **67**, 1624–1633.

Robertsson, J. O. A., and E. Muyzert, 1999, Wavefield separation using a volume distribution of three componenet recordings: Geophys. Res. Lett., **26**, 2821–2824.

Ruigrok, E., X. Campman, D. Draganov, and K. Wapenaar, 2010, High-resolution lithospheric imaging with seismic interferometry: Geophys. J. Int., **183**, 339–357.

Ruigrok, E., and K. Wapenaar, 2012, Global-phase seismic interferometry unveils P-wave reflectivity below the Himalayas and Tibet: Geophys. Res. Lett., **39**, L11303.

Ryberg, T., 2011, Body wave observations from corss-correlations of ambient seismic noise: A case study from the Karoo, RSA: Geophys. Res. Lett., **38**, L13311.

Schalkwijk, K. M., C. P. A. Wapenaar, and D. J. Verschuur, 2003, Adaptive decomposition of multicomponent ocean-bottom seismic data into downgoing and upgoing P- and S-waves: Geophysics, **68**, 1091–1102.

Schmedes, J., J. B. Roth, R. L. Saltzer, and G. M. Leahy, 2012, Imaging the shallow crust using teleseismic tomography: Bull. Seismol. Soc. Am., **102**, 1276–1282.

Snieder, R., and E. Şafak, 2006, Extracting the building response using seismic interferometry: Theory and application to the Millikan Library in Pasadena, California: Bull. Seismol. Soc. Am., **96**, 586–598.

Snieder, R., M. Miyazawa, E. Slob, I. Vasconcelos, and K. Wapenaar, 2009, A comparison of strategies for seismic interferometry: Surveys in Geophysics, **30**, 503–523.

Snieder, R., J. Sheiman, and R. Calvert, 2006a, Equivalence of the virtual-source method and wave-field deconvolution in seismic interferometry: Phys. Rev. E, **73**, 066620.

Snieder, R., K. Wapenaar, and K. Larner, 2006b, Spurious multiples in seismic interferometry of primaries: Geophysics, **71**, SI111–SI124.

Tonegawa, T., K. Nishida, T. Watanabe, and K. Shiomi, 2009, Seismic interferometry of teleseismic S-wave coda retrieval of body waves: an application to the Philippine Sea slab underneath the Japanese Islands: Geophys. J. Int., **178**, 1574–1586.

van der Neut, J., and A. Bakulin, 2009, Estimating and correcting the amplitude radiation pattern of a virtual source: Geophysics, **74**, SI27–SI36.

van der Neut, J., M. Tatanova, J. Thorbecke, E. Slob, and K. Wapenaar, 2011a, Deghosting, demultiple, and deblurring in controlled-source seismic interferometry: International Journal of Geophysics, **2011**, 870819.

van der Neut, J., J. Thorbecke, K. Mehta, E. Slob, and K.

Wapenaar, 2011b, Controlled-source interferometric redatuming by crosscorrelation and multidimensional deconvolution in elastic media: Geophysics, **76**, SA63–SA76.

Vasconcelos, I., and R. Snieder, 2008a, Interferometry by deconvolution, Part 1 - Theory for acoustic waves and numerical examples: Geophysics, **73**, S115–S128.

———, 2008b, Interferometry by deconvolution: Part 2 - Theory for elastic waves and application to drill-bit seismic imaging: Geophysics, **73**, S129–S141.

Vasconcelos, I., R. Snieder, and B. Hornby, 2008, Imaging internal multiples from subsalt VSP data - Examples of target-oriented interferometry: Geophysics, **73**, S157–S168.

Wapenaar, C. P. A., P. Herrmann, D. J. Verschuur, and A. J. Berkhout, 1990, Decomposition of multicomponent seismic data into primary P- and S-wave responses: Geophys. Prospect., **38**, 633–661.

Wapenaar, K., 2004, Retrieving the elastodynamic Green's function of an arbitrary inhomogeneous medium by cross correlation: Phys. Rev. Lett., **93**, 254–301.

Wapenaar, K., D. Draganov, R. Snieder, X. Campman, and A. Verdel, 2010a, Tutorial on seismic interferometry: Part 1 - Basic principles and applications: Geophysics, **75**, 75A195–75A209.

Wapenaar, K., E. Ruigrok, J. van der Neut, and D. Draganov, 2011a, Improved surface-wave retrieval from ambient seismic noise by multi-dimensional deconvolution: Geophys. Res. Lett., **38**, L01313.

Wapenaar, K., E. Slob, and R. Snieder, 2008a, Seismic and electromagnetic controlled-source interferometry in dissipative media: Geophys. Prospect., **56**, 419–434.

Wapenaar, K., E. Slob, R. Snieder, and A. Curtis, 2010b, Tutorial on seismic interferometry: Part 2 – Underlying theory and new advances: Geophysics, **75**, 75A211–75A227.

Wapenaar, K., J. van der Neut, and E. Ruigrok, 2008b, Passive seismic interferometry by multidimensional deconvolution: Geophysics, **73**, A51–A56.

Wapenaar, K., J. van der Neut, E. Ruigrok, D. Draganov, J. Hunziker, E. Slob, J. Thorbecke, and R. Snieder, 2011b, Seismic interferometry by crosscorrelation and by multidimensional deconvolution: a systematic comparison: Geophys. J. Int., **185**, 1335–1364.

Yang, Z., A. F. Sheehan, W. L. Yeck, K. C. Miller, E. A. Erslev, L. L. Worthington, and S. H. Harder, 2012, Imaging basin structure with teleseismic virtual source reflection profiles: Geophys. Res. Lett., **39**, L02303.

Extracting the earth response from noise measurements

Roel Snieder[1] and Eric Larose[2]

(1) Center for Wave Phenomena, Colorado School of Mines, Golden CO 80401, rsnieder@mines.edu
(2) Institut des Sciences de la Terre, CNRS & Université de Grenoble, BP53, 38041 GRENOBLE Cedex 9, France

ABSTRACT

Recent research has shown that noise can be turned from a nuisance into a useful seismic source. In seismology and other fields in science and engineering, the estimation of the system response from noise measurements has proven to be powerful technique. To convey the essence of the method, we first treat the simplest case of a homogeneous medium to show how noise measurements can be used to estimate waves that propagate between sensors. We provide an overview of research in physics that dates back more than 100 years that shows that random field fluctuations contain information about the system response. This principle has found extensive use in surface wave seismology, but can also be applied to the estimation of body waves. Because noise provides a continuous illumination of the subsurface, the extracted response in ideally suited for time-lapse monitoring. We present examples of the softening of soil after the 2011 Tohoku-oki earthquake, the detection of a precursor to a landslide, and monitoring the lunar soil.

1 INTRODUCTION

The retrieval of the response of a system, such as the Earth, from recorded noise is a field that has gone through an explosive growth over the last decade. Traditionally, seismologists use point sources, such as earthquakes or controlled sources, to probe Earth's interior. The response to such sources that are localized in space and are temporally impulsive is called the *impulse response*, or *Green's function*. We show in this review how the impulse response can be inferred from noise measurements. The ability to use ambient noise as a seismic source has changed many aspects of seismology. At the meeting of the American Geophysical Union one can now hear seismologists make statements such as "we carefully removed data that are contaminated by earthquakes." This is a sure sign that something new has happened in seismology.

The technique of extraction the impulse response from noise measurements is known under different names that include *Green's function extraction*, *Green function retrieval*, and *seismic interferometry*. This field has been the topic of review articles (Larose et al. 2006a, Curtis et al. 2006, Galetti & Curtis 2012), tutorials (Wapenaar et al. 2010ab), special issues of journals (Song 2010, Campillo et al. 2011), collection of reprints (Wapenaar et al. 2008), and a textbook (Schuster 2009). In this review we restrict ourselves to solid Earth seismology, but important contributions to Green's function extraction have been made in a variety of other fields that include helioseismology (Duvall et al. 1993, Rickett & Claerbout 2000), ultrasound (Weaver & Lobkis 2001, Weaver & Lobkis 2003ab, Malcolm et al. 2004, van Wijk 2006, Larose et al. 2006b), infrasound (Haney 2009), ocean acoustics (Roux et al. 2004, Sabra et al. 2005c, Roux et al., 2011), engineering (Sabra et al. 2008, Duroux et al. 2010), structural engineering (Snieder & Şafak 2006, Snieder et al. 2006, Kohler et al. 2007, Prieto et al. 2010), and medical diagnostics (Sabra et al. 2007, Gallot et al. 2011).

This overview contains the following elements. In section 2 we show the essence of Green's function extraction for the simplest example of acoustic waves in a homogeneous medium. The principle of extracting the system response from noise goes back more than a century, and we present an overview of developments in physics in section 3. The next section features a historical overview of developments in seismology. Retrieving body waves has proven to be much more difficult than extracting surface waves, we discuss this discrepancy in section 5. A particularly promising application of Green's function retrieval is monitoring because one can get the Earth response on a quasi-continuous basis (section 6), and we show examples of time-lapse monitoring of the softening of the soil by an earthquake, the detection of a precursor to a landslide, and temporal changes in the lunar response.

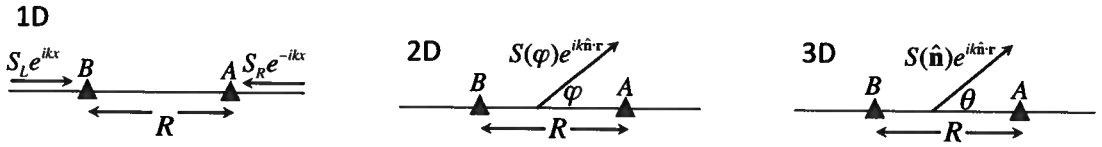

Figure 1. Two receivers A and B separated over a distance R in 1 dimension (left panel), 2 dimensions (middle panel), and 3 dimensions (right panel).

2 SIMPLEST CASE, WAVE PROPAGATION IN A HOMOGENEOUS MEDIUM

We first explain the principle of the extraction of the wave response from noise for the simplest case of a homogenous medium in one, two, or three dimensions (figure 1). In all cases we consider receivers A and B that are separated over a distance R, and carry out the analysis in the frequency domain where the wave number at angular frequency ω is denoted by k.

We focus first on one dimension, as shown in the left panel of figure 1. The receiver B is at $x = 0$ and receiver A at $x = R$. Random waves with spectrum S_L are incident from the left and waves with spectrum S_R are incident from the right. The total wave field is given by $u(x) = S_L e^{ikx} + S_R e^{-ikx}$. The waves recorded at the two receivers are thus given by

$$u_A = S_L e^{ikR} + S_R e^{-ikR} \ , \ u_B = S_L + S_R \ . \qquad (1)$$

Correlation of these signals corresponds in the frequency domain to the product $u_A u_B^*$, where the asterisk denotes complex conjugation (equation (15.52) of Snieder, 2004b). The spectra of the incident waves are random variables, and we denote the expectation value by angled brackets $\langle \cdots \rangle$. When the noise incident from the left and the right is uncorrelated, and has the same power spectrum, then

$$\langle |S_L|^2 \rangle = \langle |S_R|^2 \rangle = \langle |S|^2 \rangle \text{ and } \langle S_L S_R^* \rangle = \langle S_L^* S_R \rangle = 0 \ . \qquad (2)$$

Under these assumptions the expectation value $\langle u_A u_B^* \rangle$ of the cross correlation recorded at the two stations reduces to

$$\langle u_A u_B^* \rangle = \langle |S|^2 \rangle \left(e^{ikR} + e^{-ikR} \right) \ . \qquad (3)$$

The Green's function of a one-dimensional homogenous medium is given by $G_{1D}(R,\omega) = (-i/2k)\exp(ikR)$ (Snieder 2004b). Using this in expression (3) gives

$$\langle u_A u_B^* \rangle = 2ik \langle |S|^2 \rangle \left(G_{1D}(R,\omega) - G_{1D}^*(R,\omega) \right) \ . \qquad (4)$$

This means that if one knows the power spectrum of the noise, one can obtain the difference $G - G^*$ of the Green's function and its complex conjugate by the cross correlation of field fluctuations. Note that one does need to know the amplitude spectrum of the noise, but it's phase spectrum needs not be known. The difference $G(R,\omega) - G^*(R,\omega)$ corresponds in the time domain to $G(R,t) - G(R,-t)$. The Green's function is causal, hence $G(R,t)$ is nonzero only for positive time $t > 0$ and $G(R,-t)$ is only nonzero for $t < 0$. By parsing these two solutions one can retrieve the full Green's function.

We next consider the case of a homogeneous medium in two dimensions, see the middle panel of figure 1. The receivers are at locations $\mathbf{r}_B = (0,0)$ and $\mathbf{r}_A = (R,0)$, respectively. A superposition of plane waves $e^{ik\hat{\mathbf{n}}\cdot\mathbf{r}}$ with random spectrum $S(\varphi)$ propagating in the direction $\hat{\mathbf{n}} = (\cos\varphi, \sin\varphi)$ strikes the two receivers. The total wave field recorded at the receivers is given by

$$u_A = \int_0^{2\pi} S(\varphi) e^{ikR\cos\varphi} d\varphi \ , \ u_B = \int_0^{2\pi} S(\varphi') d\varphi' \ . \qquad (5)$$

When the plane waves coming in from different directions are uncorrelated and have a power spectrum independent of the angle of incidence, $\langle S(\varphi) S^*(\varphi') \rangle = |S|^2 \delta(\varphi - \varphi')$, hence the average cross correlation is given by

$$\langle u_A u_B^* \rangle = |S|^2 \int_0^{2\pi} e^{ikR\cos\varphi} d\varphi \ . \qquad (6)$$

We show in appendix A that this integral is equal to

$$\langle u_A u_B^* \rangle = 4i\pi |S|^2 \left(G_{2D}(R,\omega) - G_{2D}^*(R,\omega) \right) \ , \qquad (7)$$

where $G_{2D}(R,\omega)$ is the Green's function in a homogeneous 2D medium. Note that this expression has the same form as equation (3) for one dimension. A time-domain version of this derivation has been given by Roux et al. (2005b). For completeness we show in appendix A that for a homogeneous medium in three dimensions

$$\langle u_A u_B^* \rangle = 8i\pi |S|^2 \left(G_{3D}(R,\omega) - G_{3D}^*(R,\omega) \right) \ , \qquad (8)$$

with $G_{3D}(R,\omega) = -\exp(ikR)/(4\pi R)$.

We first illustrate with a data example that the Green's function in 2D indeed follows from cross-correlation of recorded noise. Figure 2, from Lin et al. (2009), shows the cross correlation of noise recorded at stations of US-Array for two different lag times. Shown is the cross correlation of noise at a master station (marked with an asterisk) with noise recorded at all other stations (shown as triangles) after interpolating the result on a regular grid. The noise that was used is excited by waves in the ocean (Webb 1998), this noise is most pronounced for periods between 5 and 10 s. Figure 2 shows a spherical wavefront that emanates from the master station. This wavefront propagates with the velocity of the fundamental-mode Rayleigh wave. The

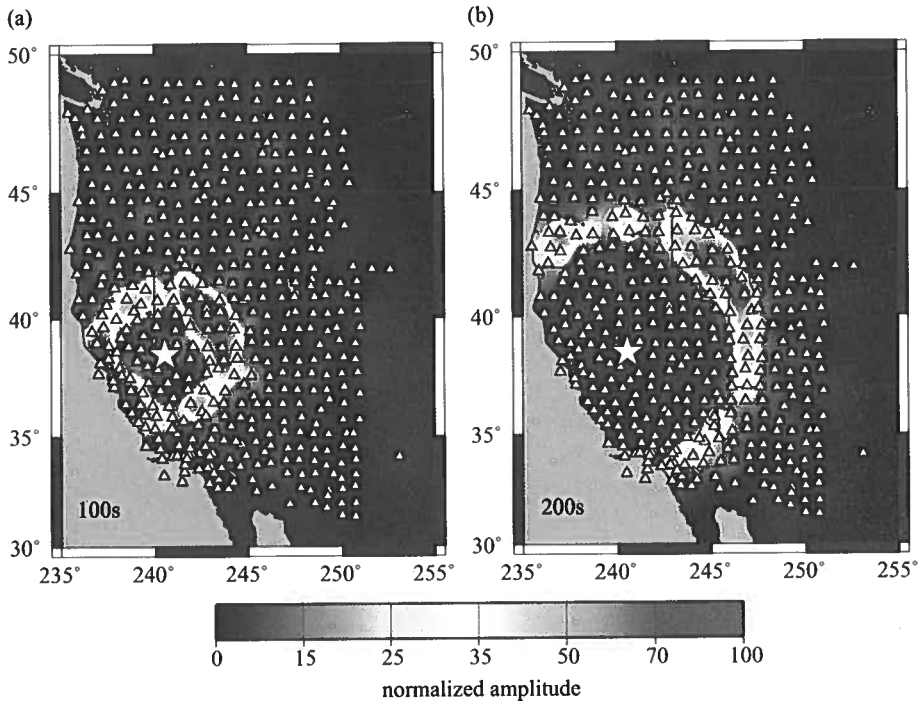

Figure 2. The cross-correlation at the station marked with the asterisk with all other stations of US-Array (triangles) for a lapse time of 100 s (left panel) and 200 s (right panel). This results in surface waves that emanate from the station marked with the asterisk.

master station acts as if a source is present. Since there is no physical source at the master station, this station acts as a *virtual source* (Bakulin & Calvert 2006).

Note that there is no magic in Green's function extraction from noise in the sense that one can only retrieve a wave that propagates between receivers by data processing of recorded noise if there is a physical wave that propagates between receivers. An ideal point source would give a spherical wavefront with constant amplitude, see equation (7), but the wavefronts in figure 2 show variations in amplitude. These variations are due to variations in the strength of the incoming oceanic noise as a function of azimuth. Studies using arrays have shown that oceanic noise is mostly generated by storms in the oceans (Schulte-Pelkum et al. 2004, Gerstoft et al. 2006, Stehly et al. 2006). Because of the localized nature of storms the oceanic noise is, in practice, not isotropic.

Fortunately the fact that the noise is in reality not isotropic is not necessarily a problem. We illustrate this with the cartoon in figure 3. Consider first the noise source S. The travel time of a wave propagating between the receivers is denoted by t_{AB}, while the travel times of waves from a source S to receivers A and B are denoted by t_{SA} and t_{SB}, respectively. Cross correlation corresponds to taking the time difference of the signals that are analyzed, hence the noise generated by source S gives, after cross correlation, a wave arriving at

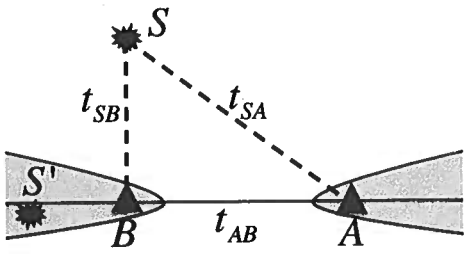

Figure 3. The stations A and B in two dimensions and the stationary phase regions for sources (shaded grey areas).

time $t_{SA} - t_{SB}$. In general, $t_{SA} - t_{SB} \neq t_{AB}$, hence the contribution of source S does not correspond to a wave propagating between the receivers. As a consequence the contribution of source S should vanish upon integration over all sources. So how is a wave arriving at time t_{AB} generated? Consider the noise source S' on the left. This source launches a wave that first propagates to B and then continues to receiver A. The cross correlation of this wave recorded at the two receivers gives a wave arriving at the correct time: $t_{AB} = t_{S'A} - t_{S'B}$. There is a mathematical reason why in the end the noise source S' gives the correct contribution to the retrieval while the noise source S does not contribute. Consider first source S'. When we change the location of this source a little bit, the travel time difference of the waves travel-

ing to both receivers does not change. This means that source S' is at a *stationary phase position.* In contrast, when the location of S is moved, the travel time difference $t_{SA} - t_{SB}$ varies to first order in the location of the source position. The source S thus is not at a stationary position. When integrating oscillatory functions, the dominant contribution comes from stationary phase positions (Bleistein & Handelsman 1975, Bleistein 1984, Snieder 2004b). This means that upon integrating over all sources, the dominant contribution comes from sources in the grey areas of figure 3, this area is also called the *coherency zone* (Larose 2006) or the *end-fire lobes* (Roux et al. 2004). Sources in this zone launch waves in the right direction to propagate between the receivers and lead to the extraction of G_{AB} (Snieder 2004a). For inhomogeneous media it has also been shown using the equations of kinematic and dynamic ray tracing that the sources that lie in stationary phase regions dominate in the extraction of the Green's function (Snieder et al. 2006). In general, the stationary phase regions launch waves along the same rays that propagate to the two receivers (appendix A of Wapenaar et al. 2010a). For each reflected wave there also is a stationary phase region that gives the dominant contribution to the extraction of the reflected wave by cross correlation (Snieder et al. 2006).

3 THE BROADER PICTURE; HISTORY OF THE FLUCTUATION-RESPONSE THEOREM

The principle of extracting the response of a system form noise goes back more that century to the seminal paper of Einstein (1906) on Brownian motion. Consider first the left panel of figure 4, which shows a heavy particle, such as a smoke particle, that is suspended in air. The particle is bombarded by air molecules, and as a result the smoke particle moves in a random way. Its motion is described by a diffusion constant D that characterizes the Brownian motion. The motion of the particle depends, of course, on the kinetic energy of the air molecules, and the diffusion constant is proportional to the thermal energy $k_B T$ of the air, where k_B is the constant of Stefan-Boltzmann. The right panel of figure 4 shows the same smoke particle suspended in air, but now the particle is kicked by a force $\mathbf{F}$. As a result the particles moves, but is slowed down by the viscosity γ of the air. Einstein (1906) established the relation between the diffusion constant and the viscosity. The diffusion constant characterizes the response of the smoke particle to a random forcing, while the viscosity measures the response of the particle to an external force. Implicitly the viscosity determines the Green's function of the motion of the smoke particle, hence the work of Einstein established the connection between the response of a system to a random excitation and its Green's function.

Johnson (1928) carried out measurements of the voltage fluctuations of resistors and found that the voltage fluctuations of a resistor satisfy

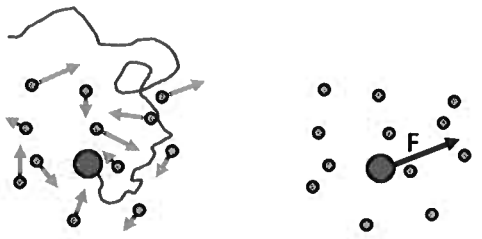

Figure 4. Left panel: when gas molecules bombard a heavy particle, the particle executes a Brownian motion characterized by a diffusion constant D. Right panel: When the same smoke particle is kicked, it slows down because of the viscosity γ of the air.

$$\langle V^2/R \rangle \sim k_B T \,, \tag{9}$$

where V denotes voltage, R electrical resistance, k_B Boltmann's constant, and T absolute temperature. Nyquist (1928) explained this proportionality from the principle of thermal equilibrium. Thermal fluctuations cause voltage fluctuations that result in a current $I = V/R$. The associated power dissipation in the resistor is given by $P = VI = V^2/R$. Expression (9) thus captures the balance between the power dissipated in the resister and the thermal energy. In statistical mechanics it is the thermal energy that leads to field fluctuations. It was after the second world war that general proofs were given that the response of a general quantum mechanical system to an impulsive excitation – the Green's function – is proportional to the cross correlation of field fluctuations caused by thermal noise (Callen & Welton 1951, Greene & Callen 1951). This principle was later formalized by Kubo (1966) as the *fluctuation dissipation theorem.* Tatarskii (1987) recognized that the distinction between a system and its noise is artificial, and considered the fluctuation dissipation theorem by dividing the whole physical system as the system of interest, e.g. the smoke particle, and the rest of the world. Rytov et al. (1989) give a comprehensive treatment of fluctuations of electromagnetic fields and their relation to the electromagnetic response of a system.

There exists a general connection between the fluctuations in a system in thermal equilibrium and its response (Le Bellac et al. 2004). Suppose one has a thermodynamic system characterized with variables A_i that each are associated with conjugate variables λ_i that act as control parameters. As shown in appendix B, the expectation values of A_i satisfy

$$\frac{\partial \langle A_i \rangle}{\partial \lambda_j} = \langle (A_i - \langle A_i \rangle)(A_j - \langle A_j \rangle) \rangle \,. \tag{10}$$

The left hand side gives the change in the expectation value $\langle A_i \rangle$ as the control parameter λ_j is varied. This derivative denotes the response of the system to a perturbation. The right hand side of equation (10) gives

the covariance of the variables A_i and A_j. This quantity characterizes the fluctuations of the system. Expression (10) thus relates the response of the system to the fluctuations of the system, for this reason expression is known as the *fluctuation response theorem* (Le Bellac et al. 2004). The retrieval of the system response thus follows from general thermodynamic principles. The value of the thermal excitation is, however, very small compared to the energy of macroscopic motion in the Earth. At a temperature of 300 K, the thermal energy is $k_B T = 4 \times 10^{-21}$ J, which is, for example, negligible compared to the energy of dropping a weight of 1 gram from 1 m height ($mgh = 10^{-2}$ J). This implies that ones needs macroscopic, non-thermal sources to explain the retrieval of the Earth response from recorded noise.

The retrieval of the Green's function of a general system from cross correlation of field fluctuations has been derived for general systems using derivations that do not rely on thermodynamic arguments (Wapenaar et al. 2006, Snieder et al. 2007, Weaver 2008, Gouédard et al. 2008). Green's function extraction form field fluctuations can be applied to diffusion problems (Snieder 2006), and the principle even holds for potential field problems (Slob et al. 2010, Snieder et al. 2010). In the latter application the Green's function is static, but can still be retrieved from the correlation of field fluctuations caused by time-dependent sources. For electric problems, theory requires that such sources are electric dipoles, which is fortunate because fluctuations in a system do not create charges (monopoles), but a charge separation creates an electric dipole. Random electric bursts have been observed to be caused by fluid flow through rock samples (Haas & Revil 2009).

4 HISTORY IN SEISMOLOGY

Many of the discoveries in seismology were made by Keiiti Aki and Jon Clearbout, who were often several decades ahead of their time. Aki (1957) proposed to use ambient noise to extract surface waves propagating in the near surface. Instead of cross correlation he used the cross coherence of signals u_A and u_B that is defined as

$$H_{AB}(\omega) = \left\langle \frac{u_A(\omega) u_B^*(\omega)}{|u_A(\omega)||u_B(\omega)|} \right\rangle . \qquad (11)$$

Because of the employed normalization with the amplitude spectrum, this measure corrects for fluctuations in amplitude. When waves are incident with equal power from all directions, the cross coherence gives the surface wave Green's function. This follows the same steps as those taken in the derivation of expression (7).

Claerbout (1968) studied the relation between the reflection response and transmission response of a one-dimensional layered acoustic medium. The transmission coefficient of a wave propagating vertically upward through such a stack of layers is denoted by T, while the reflection coefficient of a wave that propagates downward is denoted by R, see figure 5. Clearbout (1968) showed that these coefficients are, in the frequency domain, related by

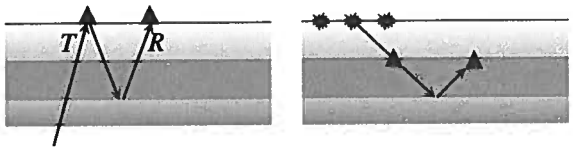

Figure 5. Left panel: definition of the transmission coefficient T and reflection coefficient R. The reflection coefficients accounts for the total reflection response of the stack of layers. Right panel: extracting the body waves that propagate between buried receivers (triangles) that are excited by sources at the surface.

$$1 + R(\omega) + R^*(\omega) = T(\omega) T^*(\omega) . \qquad (12)$$

This equation is exact and contains all internal multiples in the stack of layers. Consider waves with complex spectrum $S(\omega)$ that are incident from below on the stack of layers. The transmitted wave recorded at the surface is then given by $u(\omega) = T(\omega) S(\omega)$. Inserting this in expression (12) gives

$$1 + R(\omega) + R^*(\omega) = \frac{1}{|S(\omega)|^2} \langle u(\omega) u^*(\omega) \rangle , \qquad (13)$$

this expression relates the reflected waves to the average cross correlation of transmitted waves. Note that one only needs to know the power spectrum of the incident waves, but that the phase spectrum needs not be known. This was the earliest example of retrieving the reflection response from the cross correlation of waves with an unknown phase spectrum. Scherbaum (1987) extended the analysis of Claerbout (1968) to SH waves with nonzero angle of incidence.

Trampert et al. (1993) deconvolved earthquake recordings taken in a borehole with measurements at the surface. Instead of correlation or cross coherence they used the following measure

$$D_{AB}(\omega) = \left\langle \frac{u_A(\omega)}{u_B(\omega)} \right\rangle . \qquad (14)$$

They showed that this gives the wave that travels from the borehole sensor to the surface sensor, and the wave reflected by the free surface that propagates from the surface to the borehole sensor (left panel of figure 6). They applied this to the ground motion due to an earthquake in the Rhine Graben, the resulting deconvolved waveforms are shown in the right panel of figure 6. The wave at negative times propagates from the borehole sensor to the surface sensor, and the wave for positive time is the reflected wave that propagates downward to the borehole sensor. The travel times are identical, as they should be, but the amplitudes are different. This is due to attenuation losses, and the amplitude ratio of these waves can be used to estimate the quality factor

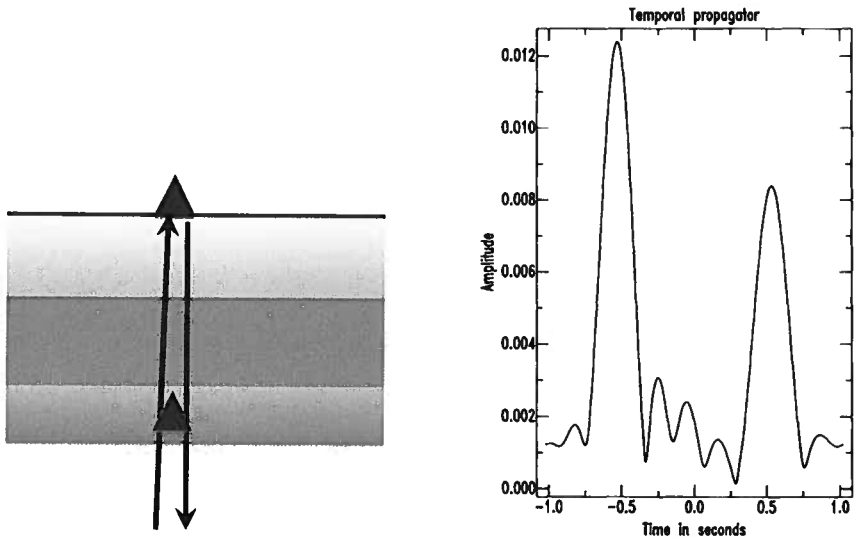

Figure 6. Left panel: geometry of waves propagating up and down a borehole. Right panel: deconvolution of waves recorded in the borehole with those recorded at the surface for an earthquake in the Rhine Graben recorded at a distance of 43 km (Trampert et al., 1993).

Q. Since the two waves are recorded at the same seismometer, this estimation is not contaminated by uncertainties in instrument calibration or instrument coupling. This technique has later been applied to measurements taken with arrays in boreholes (Mehta et al. 2007bc) and to the vibrations of buildings (Snieder & Şafak 2006, Snieder et al. 2006, Kohler et al. 2007, Prieto et al. 2010).

It was the work of Lobkis & Weaver (2001) that gave the field much visibility in seismology. They provided a beautiful derivation showing that cross correlation of recorded noise leads to the Green's function. Their derivation was based on normal-mode theory, a language that is natural for seismologists. Lobkis & Weaver (2001) also presented ultrasound measurements taken on a irregularly shaped aluminum block that beautifully confirmed their theory. In subsequent papers they showed additional laboratory measurements that confirmed the ability to extract the Green's function from field fluctuations (Weaver & Lobkis 2001, 2003ab). They also extended their earlier derivation based on normal modes for closed systems to open systems where uncorrelated noise in incident from all directions (Weaver & Lobkis 2005).

Campillo & Paul (2003) applied the concept of Green's function retrieval to coda waves of earthquakes at the western margin in Central America, recorded at stations in Mexico. They showed that by this procedure one can extract the surface waves that propagated between the two stations. In fact, they showed experimentally that they could retrieve all components of the Green's tensor for surface waves by cross correlation the coda recorded at different components at the two stations, a result that was later explained theoretically (Snieder 2004a).

Several subsequent studies confirmed that the fundamental mode surface waves could successfully be extracted (Shapiro & Campillo 2004, Paul et al. 2005). The surface wave noise appeared to be strongest for periods between 5 and 10 seconds, which is the frequency band of the dominant noise generated in the oceans (Webb 1998), but it was shown that surface waves could be extracted for periods as large as several tens of seconds (Shapiro & Campillo 2004) and even for the Earth's hum with a period of about 200 s (Nishida et al. 2009). One of the spectacular successes of seismic interferometry was that the surface waves could be extracted so robustly. With the advent of dense arrays, such as US Array, this could be used to extract the surface waves that propagate between each pair of sensors. This provided an unprecedented illumination for surface wave tomography. This was applied first to stations in Southern California (Shapiro et al. 2005, Sabra et al. 2005b). Surface waves at the periods of microseismic noise (5-10 s) sample the upper 30 kilometers, hence these noise studies revolutionized tomography of the Earth's crust as evidenced by an explosive growth in the number of crustal studies based on surface waves extracted from noise (e.g. Yao et al. 2006, Lin et al. 2008, Yang & Ritzwoller 2008; Ekström et al. 2009, Li et al. 2009, Moschetti et al. 2010). A comprehensive overview of this field is given by Ritzwoller et al. (2011). Surface waves extracted from noise have also been used for lower frequencies to determine global Earth structure (Nishida et al. 2011), and at higher frequencies with the purpose of imaging the shear velocity near surface (Halliday et al. 2008a, Bussat & Kugler 2011, de Rid-

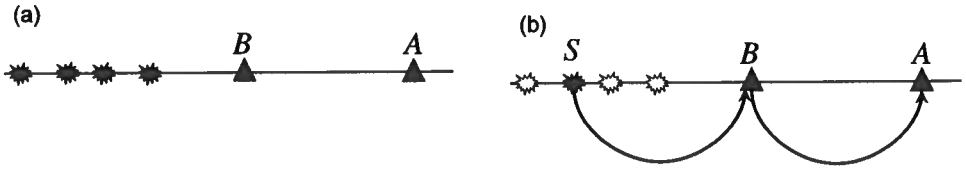

Figure 7. Left panel: for surface waves, sources can be located anywhere on the receiver line. Right panel: for body wave only the source S gives the body that propagated between the receivers.

der & Dellinger 2011). The dominance of surface waves in the response estimated from noise cross correlations has been used to suppress surface waves in exploration seismology (Halliday et al. 2008b, Xue et al. 2009).

Recent studies have used the cross coherence, as originally proposed by Aki (1957) to estimate attenuation (Prieto et al. 2009, Lawrence & Prieto 2011). For non-attenuating media it suffices to have noise sources on a closed surface surrounding the receivers, but in the presence of attenuation noise must be present throughout the medium with a strength proportional to the local attenuation (Roux 2005b, Snieder 2007). Tsai (2011) gives a detailed overview of the sources used for Green's function extraction in the presence or absence of attenuation.

Earthquake signals are usually much stronger than recorded noise, this is why earthquakes used to be the seismic source used to probe deep Earth structure. It is important to suppress the large contributions of earthquake signals to the cross correlation because these signals violate the requirement that noise sources are distributed around the receivers. An effective way of suppressing such large amplitude signals is one-bit filtering (Larose et al. 2004), where the signal is replaced by +1 if the amplitude is positive and by -1 if the amplitude is negative. Perhaps surprisingly this drastic filtering produces dispersive surface waves that with a waveform similar to surface waves excited by earthquakes (Shapiro & Campillo 2004). Bensen et al. (2007) give a comprehensive overview and comparison of methods to suppress bursts of energy.

Apart form surface waves, it is possible to extract refracted waves from recorded noise (Mikesell et al. 2009, Mikesell & van Wijk 2011). Interferometric techniques have also been used to increase the signal to noise ratio of refracted waves (Mallison et al. 2011, Bharadwaj et al. 2012) and to extract waves diffracted by the core to measure deep mantle structure (Ruigrok et al. 2012).

5 INCREASING ILLUMINATION WITH BODY WAVES

Extracting body waves from noise measurements has proven to be much more difficult. Low-frequency P waves (Roux et al. 2005a) and Moho-reflected body waves have been extracted from cross correlation of noise (Zhan et al. 2010, Poli et al. 2012). Noise generated by hurricance Katrina has led to extraction of P-waves (Gerstoft et al. 2006), and several studies have shown that oceanic noise does generate P-waves (Gerstoft et al. 2008, Zhang et al. 2009). Cross correlation of noise in exploration seismology has led to reflected P-waves (Draganov et al. 2007, 2009) and S-waves (Nakata et al. 2011). In all of these studies, the extracted body waves were of much lower quality than the surface waves extracted from noise. For this reason, the extraction of body waves from noise has not taken the prominent place in seismology that surface wave interferometry has taken.

Figure 7 illustrates why it is more difficult to extract body waves from noise than it is to retrieve surface waves. The left panel is relevant for the retrieval of surface waves. Any source, marked with a star, on the receiver line launches waves that first propagate to receiver B, and then to receiver A. The cross correlation of these waves gives the surface wave that propagates between these receivers, no matter where the noise source is exactly located on the line through the receivers. The situation for the retrieval of body waves is different. The right panel of figure 7 shows a diving body wave that propagates from B to A. Receiver B does not radiate a body wave, of course, so the only way this body wave can propagate between the receivers is that a noise source S marked with a black star is located at just the right distance so that it launches body waves that upon reflection by the free surface propagate as the diving wave from B to A. The noise sources indicated by the white stars do not launch such waves, and hence they do not contribute to the extraction of the body wave. The requirements for the presence of noise sources for the retrieval of body waves are thus more stringent than for the retrieval of surface waves. Halliday & Curtis (2008) show that for the retrieval of higher mode surface waves ones needs a more extensive distribution of noise sources than for the fundamental mode. Theory has shown that the convergence of the correlations toward the Green function (or impulse response) is slower in 3D (bulk waves) than in 2D (Larose et al. 2008). Since noise is not generated everywhere along the Earth's surface it has proven to be more difficult to extract body waves than it is to retrieve surface waves (Forghani & Snieder 2010).

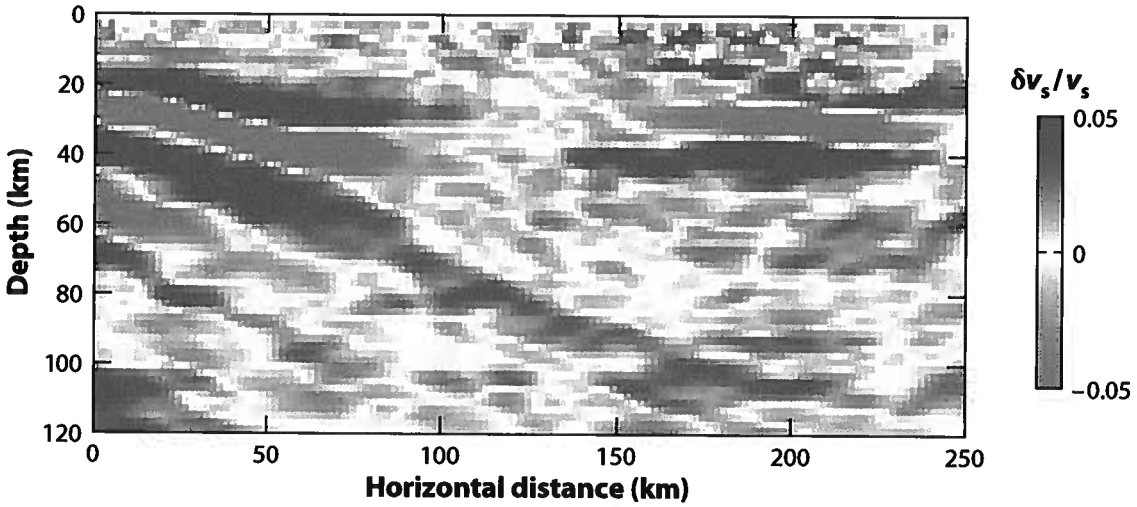

Figure 8. Image created from reflected waves retrieved from teleseismic body waves (Bostock et al. 2002).

There are two ways out of this conundrum. The first way is to use downhole sensors (right panel of figure 5). Using downhole sensors with either controlled surface sources (Bakulin & Calvert 2006, Bakulin et al. 2007) or random noise (Miyazawa et al. 2008) has led to the *virtual source method* in exploration seismology that retrieve body waves that propagate between sensors. This method removes the imprint of a complicated overburden, and allows for an illumination of the subsurface that could not be obtained otherwise. This has been used, for example, to illuminate the flanks of salt domes from sensors in a vertical borehole (Xiao et al. 2006, Hornby & Yu 2007) and to eliminate waves reflected at the Earth's surface (Mehta et al. 2007a). Gerry Schuster, in particular, has pionered interferometric methods to increase illumination of the subsurface (Schuster et al. 2004, Schuster 2005, Schuster 2009)

The second way to retrieve body waves is to use sources that launch waves upward towards sensors at the surface, as shown in the left panel of figure 5. The body waves reflected by the free surface can then be used to probe Earth's interior. This principle has been applied using teleseismic body waves as illumination (Bostock 1997, Bostock 1999, Bostock et al. 2002, Kumar & Bostock 1997). Although their method is based on the concept of Claerbout (1968) to convert transmission data into reflection data, they used multichannel deconvolution in their implementation rather than correlation. Figure 8 shows an image of the Cascadia subduction zone obtained from this principle. The subducting slab and the base of the crust are clearly visible.

Body waves have also been successfully extracted by using earthquakes that illuminate a borehole sensor and the surface from below, an early example from Trampert et al (1993) of this principle is shown in figure 6. This principle has been applied to detect time-lapse changes in the near surface by Sawazaki et al. (2009). Nakata & Snieder (2011) applied deconvolution of earthquake signals recorded in borehole sensors and surface sensors at Kik-net stations. This gives the S-waves that propagate between sensors. Figure 9 shows the S-wave thus extracted at a seismic station in Fukushima, Japan. The S-wave thus extracted from different earthquakes is highly stable. Note that during the Tohoku-oki event (magenta trace) the S-wave is strongly delayed, which indicates a softening of the soil by the shaking. In the two months after the Tohoku-oki event the extracted shear waves still have a residual delay, corresponding to a reduction of the shear modulus. In the next section, we further investigate the possibility to use repetitive noise-based correlation imaging to track temporal changes of the subsurface.

6 TIME-LAPSE MONITORING OF THE NEAR SURFACE

The continuous presence of noise makes it possible to extract the Earth response on a quasi-continuous basis. In practice, the reason that the Earth response cannot be retrieved continuously is that one needs to time average the cross correlation over a certain period of time (Larose et al. 2008). Depending on the periods used this can be a few hours (e.g. Miyazawa et al. 2008) to several months (Shapiro & Campillo 2004). This makes it possible to detect time-lapse changes on the scale of at least this averaging period. An interesting point is that the noise sources do not necessarily need to be perfectly distributed to monitor the medium changes (Hadziioannou et al. 2009). In other words, noise-based time-lapse monitoring requires less restrictive conditions than noise-based imaging.

Early examples of time-lapse studies were based on

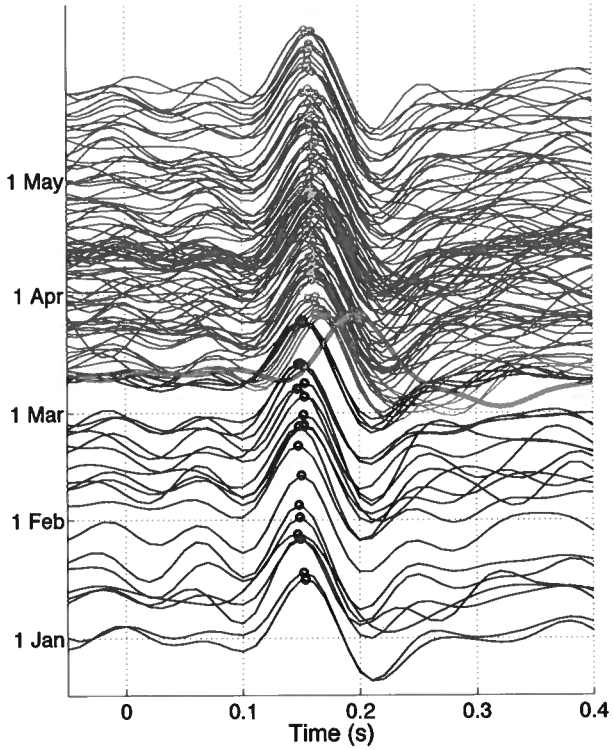

Figure 9. The waveform recorded for different earthquakes at the surface in station FKSH18 (Fukishima) deconvolved with the waves recorded in a borehole 100 m deep before the Tohoku-oki event (black traces), on the day of the event (red traces), and after the event (blue traces). The deconvolved waves for the Tohoku-oki event are shown in magenta.

the auto correlation of recorded noise. The auto correlation gives the waves that propagate from a sensor into the medium, and then back propagate to that sensor. It is not clear whether these reflected waves are body waves or surface waves, hence it is not obvious which part of the subsurface is sampled by these waves. Sens-Schönfelder & Wegler (2006) used this technique to detect time-lapse changes at a volcano, Mt. Merapi in Indonesia, and discovered that the time-lapse changes they found correlate well with precipitation. This is an indication that the waves extracted by auto correlation of noise recorded at the surface sample the near surface. Signals extracted from ambient noise or complicated earthquake recordings have been used in several studies to show that the subsurface velocity is reduced after earthquakes in Japan (Wegler & Sens-Schönfelder 2007, Ohmi et al. 2008, Yamada et al. 2010; Nakata & Snieder 2012), at Parkfield (Brenguier et al. 2008), and after the Sumatra earthquake (Xu & Song 2009). Cross-correlation of noise has been used to monitor changes in Mount St. Helens (Sabra et al. 2006). The prospect of detecting precursors to natural disasters is of particular interest (Brenguier et al. 2008b). The earth response extracted with interferometric techniques from noise or earthquakes has shown that the shear velocity in the near surface displays a seasonal cycle (Meier et al. 2010, Nakata & Snieder, 2012).

6.1 Monitoring of a landslide

The characterization of landslides, along with their failure prediction, is of critical importance for society. In most cases, failure is associated with hydrogeological features. Unfortunately, the converse does not hold: an increase of moisture and/or water table level does not necessarily trigger slope failure. As seismic waves are sensitive to the mechanical properties of the material they traverse, they are useful to monitor the evolution of the rigidity (and rheology) of the slope. Ambient noise correlation is promising, as it is quasi continuous and does not rely on reproducible controlled source.

Mainsant et al. (2012) studied a clay-rich landslide located in the Swiss Alps, next to the Diablerets ski resort and along the road leading to the highly frequented Le Pillon pass. The purpose of the seismic noise correlation experiment was to monitor the failure of this slope, which occurred between August 18 and August 20, 2010, following significant cumulative rainfall in July. The geometry of the experiment is depicted in figure 10. The landslide is of moderate size; it is 100 m in height, has a length of 300 m, and 20 to 40 m of lateral extension. It was equipped with two seismic sensors located on each side of the landslide on stable ground. Both sensors were connected to the same recording system for continuous data logging. The records were studied in the 4-25 Hz frequency range, which corresponds to Rayleigh wave penetration depths ranging from a few meters to a few tens of meters, thus probing the active shallow layers of the landslide. From direct observations during the field experiments, two main sources of ambient noise were identified in this frequency band: the wind in the trees and the traffic along the road at the foot of the landslide. While the noise from both sources may be variable in time, the important feature for monitoring is that their locations are stable (Hadziioannou et al. 2009).

The 24-hour cross-correlations were calculated and averaged each day. Correlations were subsequently filtered in a narrow 10-14 Hz frequency band before analyzing the relative velocity change. In the case of a homogeneous velocity change δv, all the waveforms constituting the correlograms are extended in time by a factor $-\delta v/v$. The relative velocity change between subsequent days was measured with the stretching technique (Sens-Schönfelder & Wegler 2006, Hadziioannou et al. 2009)

Variation of velocity versus time is displayed on Figure 11, along with the daily precipitation. From the beginning of April to the middle of July 2010, the apparent Rayleigh wave velocity was relatively stable: observed velocity fluctuations are smaller than 1%. From mid-May to mid-July, rainfall increased the wa-

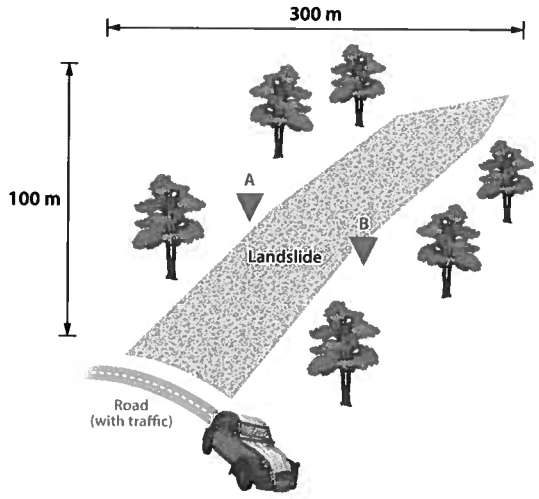

Figure 10. Location of seismometers (triangles) and landslide area (brown).

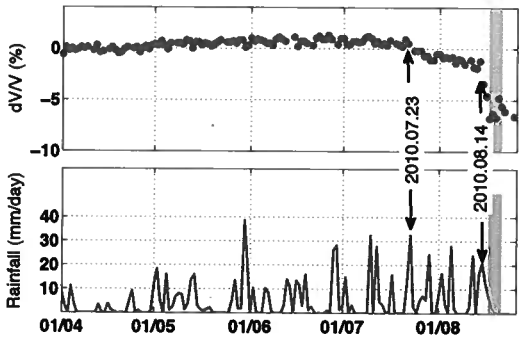

Figure 11. Relative velocity change (top panel), and precipitation (bottom panel) as a function of time. The landslide occurred in the time interval marked with the grey bar.

ter content of the soil. On July 24, after a short rainfall event, the apparent Rayleigh wave velocity underwent a gradual decrease of 2% over 20 days. On August 15, after a series of intense precipitation events and related increases in the water table, the apparent velocity dropped by 7% in only four days. While losing its rigidity, the creeping material reached its stability limit and the slope failed, with a composite earthslide-earthflow event. This catastrophic event occurred between August 18th and 20th, as indicated by the grey bar in Figure 11. From ambient noise measurements and processing, it was thus possible to observe a significant drop (7%) in Rayleigh wave velocity a few days before the event, after an initial gentler decrease (2%). The observed significant drop in seismic velocity prior to slope failure suggests that time-dependent variation in this parameter can be a valuable precursor to landslide failure.

6.2 Extracting the lunar response

The ambient noise on the earth is primarily controlled by the oceanic activity below 1 Hz, and by the weather and the human activity above. Imagine now a seismic experiment where all those sources would be deactivated. What would the noise correlations resemble to? Would they still provide information on the subsoil? Of course, such an experiment is not possible at the Earth, but it can be carried out on the Moon. During the Apollo era, seismic devices were operated continuously during a significant amount of time to test the noise-based imaging and monitoring techniques. The set of data collected by the Apollo 17 mission is of particular interest.

The Apollo 17 Lunar Seismic Profiling Experiment (LSPE) was deployed on Dec. 14, 1972 at a distance of about 180 m W-NW of the lunar module. Four geophones, labeled G1 to G4, were deployed in a triangular array (Figure 12a) and recorded the vertical ground velocity in the frequency range from 3 to 30 Hz during the landing mission in 1972 and then again continuously from August 1976 to April 1977. The geophones were simultaneously connected to the central station where the seismic signals were digitized and telemetered to the Earth. The cross-correlations between all pairs of geophones were computed, a procedure that gave the direct Rayleigh wave propagating in the lunar regolith (Figure 12b). From the dispersion properties of the Rayleigh wave, it was possible to determine the shear-wave velocity profile of the first ten meters of the superficial lunar regolith (Figure 12c). More details on the experiment and data-processing are given by Larose et al. (2005).

As the seismic noise was almost continuously excited, it was also possible to process correlations on a 24h period basis. The comparison between each daily correlation and the correlation averaged over the whole period of interest allowed to measure the relative velocity variations (Sens-Schönfelder & Larose 2008). These variations are related to the thermal heating of the sun. During the lunar day, the surface temperature increases by more than $250°C$. The heat then slowly diffuses at depth, and the elastic moduli subsequently decrease, which results in a decrease in apparent Rayleigh wave velocity (Figure 13). Conversely, during the lunar night, the temperature decreases and the seismic velocity increases. Variations of energy inflow due to changes in the sun-moon distance are reflected by the variations in the incident solar flux (blue line in Figure 13). This experiment demonstrates that it is possible to evaluate the change of temperature in the lunar soil from the correlation of ambient seismic noise. These experiments demonstrate not only that we can reconstruct direct waves between passive sensors with ambient noise, but also that we can take advantage of reconstructed multiply scattered waves to monitor very weak changes in a complex natural environment.

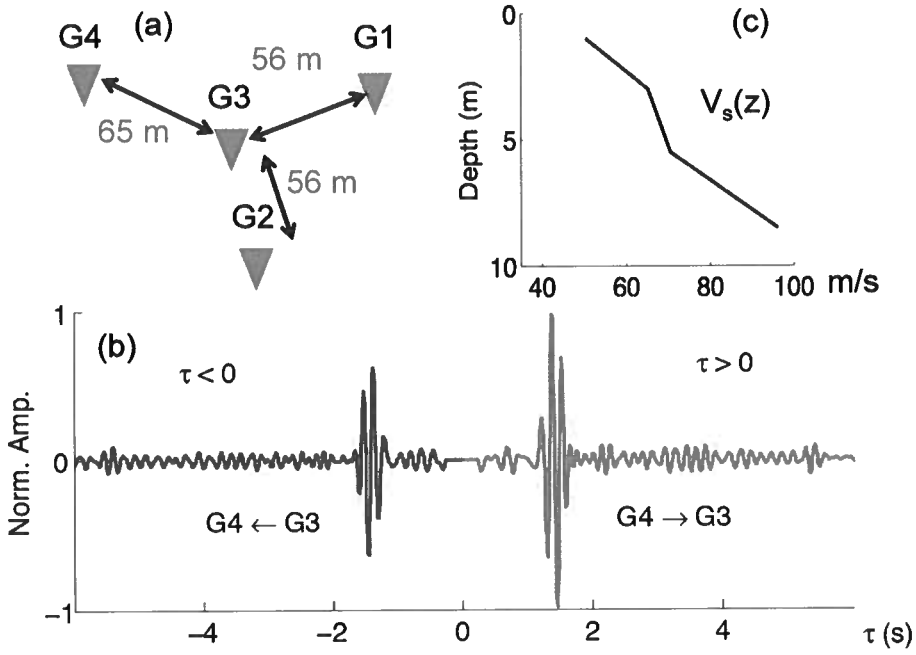

Figure 12. a) Configuration of the four geophones spread in a triangle shape array at the Apollo 17 landing site. b) example of positive ambient noise correlations between geophones 3 and 4. The pulse around 1.5s is the direct Rayleigh between the geophones. c) The shear-wave velocity profile of the subsoil under the sensors inferred from the dispersion of Rayleigh waves.

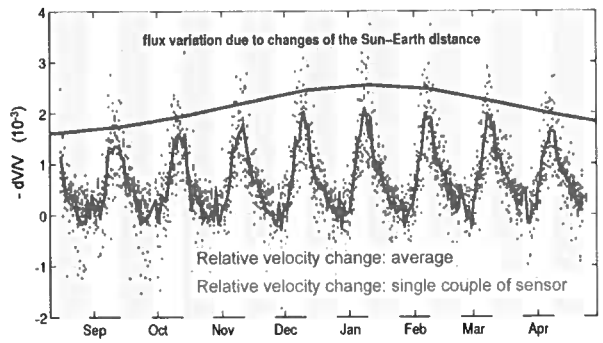

Figure 13. Relative velocity variations ($\delta v/v$) versus time, obtained on the moon from august 1976 to may 1977. Gray points indicate experimental measurements. The red line indicates the average of $\delta v/v$ over all available couples of sensors. The blue line is linearly proportional to the sun-earth distance. Note the negative sign of the $\delta v/v$ on the vertical axis.

7 CONCLUSION

The field of seismic interferometry is still rapidly progressing, and this review can not do justice to all developments that are taking place. Multiple schemes for extracting the Earth response are being exploited. In this review we have mentioned the use of correlation, deconvolution (Vasconcelos & Snieder 2008ab), and cross-coherence. In addition to these methods, two other approaches have been proposed. In multi-dimensional deconvolution (Wapenaar et al. 2008, 2011, van der Neut et al. 2011) one decomposes a recorded elastic or electromagnetic wave field into upgoing and downgoing fields and solves for the reflectivity by solving a linear system of equations. Slob & Wapenaar (2007) proposed convolution interferometry, a technique that is appropriate when the receivers are on opposite sides of a surface that contains the noise sources. The merits and drawbacks of different approaches are discussed by Snieder et al. (2009). Nakata et al. (2011) compare the statistical properties of cross correlation, deconvolution, and cross-coherence. In general, a straightforward cross correlation or deconvolution does not optimally focus energy onto the receiver that acts as a virtual source. When noise is recorded on an array, the formalism of multi-dimensional deconvolution can be used to optimize the focusing of noise on the receiver that acts as a virtual source (van der Neut & Bakulin 2009, Wapenaar & van der Neut 2010, Wapenaar et al. 2011).

Seismic interferometry has been used for a number of unexpected applications. Recorded ambient oceanic noise has been used for the localization of stations and calibration of their clocks (Sabra et al. 2005c), and to correct for the time drift of seismic stations (Stehly et al. 2007). We have shown examples that receivers can act as a virtual source, but one can also turn seismic

sources into virtual receivers (Curtis et al. 2009). It also is possible to retrieve the waves propagating between sources from measurements of the energy flux (Snieder et al. 2012). Seismic noise has also been used to locate earthquakes (Barmin et al. 2011). Correlation of coda waves that are themselves obtained from cross correlation can be used to compensate for deficiencies in the illumination by ambient noise (Stehly et al. 2008, Froment et al. 2011). A method relying on fiducial stations has been developed to determine the wave that propagate between seismic sensors that were never deployed at the same time (Ma & Beroza 2012), and as shown by Curtis et al. (2012), seismic interferometry can even be used to reconstruct data that were never recorded!

REFERENCES

Aki, K., 1957, Space and time spectra of stationary stochastic waves with special reference to microtremors: Bull. of the Earthquake Res. Inst., **35**, 415–456.

Arfken, G., and H. Weber, 2001, Mathematical methods for physicists, 5th ed.: Harcourt.

Bakulin, A., and R. Calvert, 2006, The virtual source method: Theory and case study: Geophysics, **71**, SI139–SI150.

Bakulin, A., A. Mateeva, K. Mehta, P. Jorgensen, J. Ferrandis, I. Sinha Herhold, and J. Lopez, 2007, Virtual source applications to imaging and reservoir monitoring: The Leading Edge, **26**, 732–740.

Barmin, M., A. Levshin, Y. Yang, and M. Ritzwoller, 2011, Epicentral location based on Rayleigh wave empirical Green's functions from ambient seismic noise: Geophys. J. Int., **184**, 869–884.

Bensen, G., M. Ritzwoller, M. Barmin, A. Levshin, F. Lin, M. Moschetti, N. Shapiro, and Y. Yang, 2007, Processing seismic ambient noise data to obtain reliable broad-band surface wave dispersion measurements: Geophys. J. Int., **169**, 1239–1260.

Bharadwaj, P., G. Schuster, I. Mallison, and W. Dai, 2012, Theory of supervirtual refraction interferometry: Geophys. J. Int., **188**, 263–273.

Bleistein, N., 1984, Mathematical methods for wave phenomena: Academic Press.

Bleistein, N., and R. Handelsman, 1975, Asymptotic expansions of integrals: Dover.

Bostock, M., 1999, Seismic imaging of lithospheric discontinuities and continental evolution, *in* Composition, deep structure and evolution of continents: Elsevier, 1–16.

Bostock, M., R. Hyndman, S. Rondenay, and S. Peacock, 2002, An inverted continental Moho and serpentinization of the forearc mantle: Nature, **417**, 536–538.

Bostock, M., and M. Sacchi, 1997, Deconvolution of teleseismic recordings for mantle structure: Geophys. J. Int., **129**, 143–152.

Brenguier, F., M. Campillo, C. Hadziioannou, N. Shapiro, and E. Larose, 2008a, Postseismic relaxation along the San Andreas Fault at Parkfield from continuous seismological observations: Science, **321**, 1478–1481.

Brenguier, F., N. Shapiro, M. Campillo, V. Ferrazzini, Z. Duputel, O. Coutant, and A. Nercessian, 2008b, Towards forecasting volcanic eruptions using seismic noise: Nature Geoscience, **1**, 126 – 130.

Bussat, S., and S. Kugler, 2011, Offshore ambient noise surface-wave tomography above 0.1 Hz and its applications: The Leading Edge, **30**, 514–524.

Callen, H., and T. Welton, 1951, Irreversibility and generalized noise: Phys. Rev., **83**, 34–40.

Campillo, M., and A. Paul, 2003, Long-range correlations in the diffuse seismic coda: Science, **299**, 547–549.

Campillo, M., H. Sato, N. Shapiro, and R. van der Hilst, 2011, New developments on imaging and monitoring with seismic noise: Compter Rendus Geoscience, **343**, 487–495.

Claerbout, J., 1968, Synthesis of a layered medium from its acoustic transmission response: Geophysics, **33**, 264–269.

Curtis, A., E. Behr, Y. Entwhistle, E. Galetti, J. Townend, and S. Bannister, 2012, The benefit of hindsight in observational science: Retrospective seismological observations: Earth. Planet. Sci. Lett., **345-348**, 212–220.

Curtis, A., P. Gerstoft, H. Sato, R. Snieder, and K. Wapenaar, 2006, Seismic interferometry – turning noise into signal: The Leading Edge, **25**, 1082–1092.

Curtis, A., H. Nicolson, D. Halliday, J. Trampert, and B. Baptie, 2009, Virtual seismometers in the subsurface of the Earth from seismic interferometry: Nature Geoscience, **2**, 700–704.

de Ridder, S., and J. Dellinger, 2011, Ambient noise eikonal tomography for near-surface imaging at Valhall: The Leading Edge, **30**, 506–512.

Draganov, D., X. Campman, J. Thorbecke, A. Verdel, and K. Wapenaar, 2009, Reflection images from ambient seismic noise: Geophysics, **74**, A63–A67.

Draganov, D., K. Wapenaar, W. Mulder, J. Singer, and A. Verdel, 2007, Retrieval of reflections from seismic background-noise measurements: Geophys. Res. Lett., **34**, L04305.

Duroux, A., K. Sabra, J. Ayers, and M. Ruzzene, 2010, Extracting guided waves from cross-correlations of elastic diffuse fields: Applications to remote structural health monitoring: J. Acoust. Soc. Am., **127**, 204–215.

Duvall, T. L., S. M. Jefferies, J. W. Harvey, and M. A. Pomerantz, 1993, Time-distance helioseismology: Nature, **362**, 430–432.

Einstein, A., 1906, Zur Theorie der Brownschen Bewegung: Annalen der Physik, **19**, 371–381.

Ekström, G., G. Abers, and S. Webb, 2009, Determi-

nation of surface-wave phase velocities across usarray from noise and Aki's spectral formulation: Geophys. Res. Lett., **36**, L18301.

Forghani, F., and R. Snieder, 2010, Underestimation of body waves and feasibility of surface-wave reconstruction by seismic interferometry: The Leading Edge, **29**, 790–794.

Froment, B., M. Campillo, and P. Roux, 2011, Reconstructing the Green's function through iteration of correlations: Contes Rendus Geoscience, **343**, 623–632.

Galetti, E., and A. Curtis, 2012, Generalised receiver functions and seismic interferometry: Tectonophysics, **532-535**, 1–26.

Gallot, T., S. Catheline, P. Roux, J. Brum, N. Benech, and C. Negreira, 2011, Passive elastography: Shear wave tomography from physiological noise correlation in soft tissues: IEEE trans. Ultrason., Ferroelect., Freq. Contr., **58**, 1122–1126.

Gerstoft, P., M. Fehler, and K. Sabra, 2006, When Katrina hit California: Geophys. Res. Lett., **33**, L17308.

Gerstoft, P., P. Shearer, N. Harmon, and J. Zhang, 2008, Global P, PP, and PKP wave microseisms observed from distant storms: Geophys. Res. Lett., **35**, L23306.

Gouédard, P., L. Stehly, F. Brenguier, M. Campillo, Y. Colin de Verdière, E. Larose, L. Margerin, P. Roux, F. Sánchez-Sesma, N. Shapiro, and R. Weaver, 2008, Cross-correlation of random fields: mathematical approach and applications: Geophys. Prosp., **56**, 375–393.

Greene, R., and H. Callen, 1951, On the formulation of thermodynamic fluctuation theory: Phys. Rev., **83**, 1231–1235.

Haas, A., and A. Revil, 2009, Electrical burst signature of pore-scale displacements: Water Resources Res., **45**, W10202.

Hadziioannou, C., E. Larose, O. Coutant, P. Roux, and M. Campillo, 2009, Stability of monitoring weak changes in multiply scattering media with ambient noise correlation: Laboratory experiments: J. Acoust. Soc. Am., **125**, 3688–3695.

Halliday, D., and A. Curtis, 2008, Seismic interferometry, surface waves and source distribution: Geophys. J. Int., **175**, 1067–1087.

Halliday, D., A. Curtis, and E. Kragh, 2008a, Seismic surface waves in a suburban enviroment: active and passive interferometric methods: The Leading Edge, **27**, 210–218.

Halliday, D., A. Curtis, J. Robertsson, and D.-J. van Manen, 2008b, Interferometric surface-wave isolation and removal: Geophysics, **72**, A69–A73.

Haney, M., 2009, Infrasonic ambient noise interferometry from correlations of microbaroms: Geophys. Res. Lett., **36**, L19808.

Hornby, B., and J. Yu, 2007, Interferometric imaging of a salt flank using walkaway VSP data: The Leading Edge, **26**, 760–763.

Johnson, J., 1928, Thermal agitation of electricity in conductors: Phys. Rev., **32**, 97–109.

Kohler, M., T. Heaton, and S. Bradford, 2007, Propagating waves in the steel, moment-frame Factor building recorded during earthquakes: Bull. Seismol. Soc Am., **97**, 1334–1345.

Kubo, R., 1966, The fluctuation-dissipation theorem: Rep. Prog. Phys., **29**, 255–284.

Kumar, M., and M. Bostock, 2006, Transmission to reflection transformation of teleseismic wavefields: J. Geophys. Res., **111**, B08306.

Larose, E., 2006, Mesoscopics of ulstrasound and seismic waves: applications to passive imaging: Ann. Phys. Fr., **31**, 1–126.

Larose, E., A. Derode, M. Campillo, and M. Fink, 2004, Imaging from one-bit correlations of wideband diffuse wave fields: J. Appl. Phys., **95**, 8393–8399.

Larose, E., A. Khan, Y. Nakamura, and M. Campillo, 2005, Lunar subsurface investigated from correlation of seismic noise: Geophys. Res. Lett., **32**, L16201.

Larose, E., L. Margerin, A. Derode, B. van Tiggelen, M. Campillo, N. Shapiro, A. Paul, L. Stehly, and M. Tanter, 2006, Correlation of random wavefields: an interdisciplinary review: Geophysics, **71**, SI11–SI21.

Larose, E., G. Montaldo, A. Derode, and M. Campillo, 2006b, Passive imaging of localized reflectors and interfaces in open media: Appl. Phys. Lett., **88**, 104103.

Larose, E., P. Roux, M. Campillo, and A. Derode, 2008, Fluctuations of correlations and Greens function reconstruction: role of scattering: J. Appl. Phys., **103**, 114907.

Lawrence, J., and G. Prieto, 2011, Attenuation tomography of the western United States from ambient seismic noise: J. Geophys. Res., **116**, B06302.

Le Bellac, M., F. Mortessagne, and G. Batrouni, 2004, Equilibrium and non-equilibrium statistical thermodynamics: Cambridge Univ. Press.

Li, H., W. Su, and Z. Wang, C.Y.and Huang, 2009, Ambient noise rayleigh wave tomography in western Sichuan and eastern Tibet: Earth Planet. Sci. Lett., **282**, 201–211.

Lin, F., M. Moschetti, and M. Ritzwoller, 2008, Surface wave tomography of the western United States from ambient noise: Rayleigh and Love wave phase velocity maps: Geophys. J. Int., **173**, 281–298.

Lin, F., M. Ritzwoller, and R. Snieder, 2009, Eikonal tomography: surface wave tomography by phase front tracking across a regional broad-band seismic array: Geophys. J. Int., **177**, 1091–1110.

Lobkis, O., and R. Weaver, 2001, On the emergence of the Green's function in the correlations of a diffuse field: J. Acoust. Soc. Am., **110**, 3011–3017.

Ma, S., and G. Beroza, 2012, Ambient-field Green's function from asynchronous seismic observations: J. Geophys. Res., **39**, L06301.

Mainsant, G., E. Larose, Brönnimann, D. Jongmans,

C. Michoud, and M. Jaboyedoff, 2012, Ambient seismic noise monitoring of a clay landslide: toward failure prediction: J. Geophys. Res., **117**, F01030.

Malcolm, A., J. Scales, and B. van Tiggelen, 2004, Extracting the Green's function from diffuse, equipartitioned waves: Phys. Rev. E, **70**, 015601.

Mallison, I., P. Bharadwaj, G. Schuster, and J. Jakubowicz, 2011, Enhanced refractor imaging by supervirtual interferometry: The Leading Edge, **30**, 546–550.

Mehta, K., A. Bakulin, J. Sheiman, R. Calvert, and R. Snieder, 2007a, Improving the virtual source method by wavefield separation: Geophysics, **72**, V79–V86.

Mehta, K., R. Snieder, and V. Graizer, 2007b, Downhole receiver function: a case study: Bull. Seismol. Soc. Am., **97**, 1396–1403.

———, 2007c, Extraction of near-surface properties for lossy layered medium using propagator matrix: Geophys. J. Int., **168**, 271–280.

Meier, U., S. N.M., and F. Brenguier, 2010, Detecting seasonal variations in seismic velocities within Los Angeles basin from correlations of ambient seismic noise: Geophys. J. Int., **181**, 985–996.

Mikesell, D., and K. van Wijk, 2011, Seismic refraction interferometry with a semblance analysis on the cross-correlation gathering: Geophysics, **76**, SA77–SA82.

Mikesell, S., K. Van Wijk, A. Calvert, and M. Haney, 2009, The virtual refraction: useful spurious energy in seismic interferometry: Geophysics, **74**, A13–A17.

Miyazawa, M., R. Snieder, and A. Venkataraman, 2008, Application of seismic interferometry to extract P and S wave propagation and observation of shear wave splitting from noise data at Cold Lake, Canada: Geophysics, **73**, D35–D40.

Moschetti, M., M. Ritzwoller, F. Lin, and Y. Yang, 2010, Seismic evidence for widespread western-US deep-crustal deformation caused by extension: Nature, **464**, 885–889.

Nakata, N., and R. Snieder, 2011, Near-surface weakening in Japan after the 2011 Tohoku-Oki earthquake: Geophys. Res. Lett., **38**, L17302.

———, 2012, Estimating near-surface shear-wave velocities in Japan by applying seismic interferometry to KiK-net data: J. Geophys. Res., **117**, B01308.

Nakata, N., R. Snieder, T. Tsuji, K. Larner, and T. Matsuoka, 2011, Shear wave imaging from traffic noise using seismic interferometry by cross-coherence: Geophysics, **76**, SA97–SA106.

Nishida, K., J.-P. Montagner, and H. Kawakatsu, 2009, Global surface wave tomography using seismic hum: Science, **326**, 112.

Nyquist, H., 1928, Thermal agitation of electric charge in conductors: Phys. Rev., **32**, 110–113.

Ohmi, S., K. Hirahara, H. Wada, and K. Ito, 2008, Temporal variations of crustal structure in the the source region of the 2007 Noto Hanto Earthquake, central Japan, with passive image interferometry: Earth Planets Space, **60**, 1069–1074.

Paul, A., M. Campillo, L. Margerin, E. Larose, and A. Derode, 2005, Empirical synthesis of time-asymmetrical Green functions from the correlation of coda waves: J. Geophys. Res., **110**, B08302.

Poli, P., H. Perdersen, M. Campillo, and P. W. Group, 2012, Emergence of body waves from cross-correlation of short period seismic noise: Geophys. J. Int., **188**, 549–558.

Prieto, G., J. Lawrence, and G. Beroza, 2009, Anelastic earth structure from the coherency of the ambient seismic field: J. Geophys. Res., **114**, B07303.

Prieto, G., J. Lawrence, A. Chung, and M. Kohler, 2010, Impulse response of civil structures from ambient noise analysis: Bull. Seismol. Soc. Am., **100**, 2322–2328.

Rickett, J., and J. Claerbout, 2000, Calculation of the sun's acoustic impulse response by multidimensional spectral factorization: Solar Physics, **192**, 203–210.

Ritzwoller, M., F.-C. Lin, and W. Shen, 2011, Ambient noise tomography with a large seismic array: Comptes Rendus Geoscience, **343**, 558–570.

Roux, P., W. Kuperman, and N. Group, 2004, Extracting coherent wave fronts from acoustic ambient noise in the ocean: J. Acoust. Soc. Am., **116**, 1995–2003.

Roux, P., W. Kuperman, and K. Sabra, 2011, Ocean acoustic noise and passive coherent array processing: Contes Rendus Geoscience, **343**, 533–547.

Roux, P., K. Sabra, P. Gerstoft, and W. Kuperman, 2005a, P-waves from cross correlation of seismic noise: Geophys. Res. Lett., **32**, L19303.

Roux, P., K. Sabra, W. Kuperman, and A. Roux, 2005b, Ambient noise cross correlation in free space: Theoretical approach: J. Acoust. Soc. Am., **117**, 79–84.

Ruigrok, E., D. Mikesell, and K. van Wijk, 2012, Scanning for velocity anomalies in the crust and mantle with diffractions from the core-mantle boundary: Geophys. Res. Lett., **39**, L11301.

Rytov, S., Y. Kravtsov, and V. Tatarskii, 1989, Principles of statistical radiophysics. vol. 3, elements of random fields: Springer.

Sabra, K., S. Conti, P. Roux, and W. Kuperman, 2007, Passive in-vivo elastography from skeletal muscle noise: Appl. Phys. Lett., **90**, 194101.

Sabra, K., P. Gerstoft, P. Roux, W. Kuperman, and M. Fehler, 2005a, Extracting time-domain Green's function estimates from ambient seismic noise: Geophys. Res. Lett., **32**, L03310.

———, 2005b, Surface wave tomography from microseisms in Southern California: Geophys. Res. Lett., **32**, L14311.

Sabra, K., P. Roux, P. Gerstoft, W. Kuperman, and M. Fehler, 2006, Extracting coherent coda arrivals from cross-correlations of long period seismic waves during the Mount St. Helens 2004 eruption: J. Geophys. Res., **33**, L06313.

Sabra, K., P. Roux, A. Thode, G. D'Spain, and W. Hodgkiss, 2005b, Using ocean ambient noise for array self-localization and self-synchronization: IEEE J. of Oceanic Eng., **30**, 338–347.

Sabra, K., A. Srivastava, F. di Scalea, I. Bartoli, P. Rizzo, and S. Conti, 2008, Structural health monitoring by extraction of coherent guided waves from diffuse fields: J. Acoust. Soc. Am., **123**, EL8–EL13.

Sawazaki, K., H. Sato, H. Nakahara, and T. Nishimura, 2009, Time-lapse changes of seismic velocity in the shallow ground caused by strong ground motion shock of the 2000 Western-Tottori earthquake, Japan, as revealed from coda deconvolution analysis: Bull. Seismol. Soc. Am., **99**, 352–366.

Scherbaum, F., 1987, Levinson inversion of earthquake geometry SH-transmission seismograms in the presence of noise: Geophys. Prosp., **35**, 787–802.

Schulte-Pelkum, V., P. Earle, and F. Vernon, 2004, Strong directivity of ocean-generated seismic noise: Geochemistry, Geophysics, Geosystems, **5**, Q03004.

Schuster, G., 2005, Fermat's interferometric priciple for target-oriented traveltime tomography: Geophysics, **70**, U47–U50.

———, 2009, Seismic interferometry: Cambridge Univ. Press.

Schuster, G., J. Yu, J. Sheng, and J. Rickett, 2004, Interferometric/daylight seismic imaging: Geophys. J. Int., **157**, 838–852.

Sens-Schönfelder, C., and Larose, 2008, Temporal changes in the lunar soil from correlation of diffuse vibrations: Phys. Rev E, **78**, 045601.

Sens-Schönfelder, C., and U. Wegler, 2006, Passive image interferometry and seasonal variations at Merapi volcano, Indonesia: Geophys. Res. Lett., **33**, L21302.

Shapiro, N., and M. Campillo, 2004, Emergence of broadband Rayleigh waves from correlations of the ambient seismic noise: Geophys. Res. Lett., **31**, L07614.

Shapiro, N., M. Campillo, L. Stehly, and M. Ritzwoller, 2005, High-resolution surface-wave tomography from ambient seismic noise: Science, **307**, 1615–1618.

Slob, E., R. Snieder, and A. Revil, 2010, Retrieving electric resistivity data from self-potential measurements by cross-correlation: Geophys. Res. Lett., **37**, L04308.

Slob, E., and K. Wapenaar, 2007, GPR without a source: Cross-correlation and cross-convolution methods: IEEE Trans. on Geosc. and Remote Sensing, **45**, 2501–2510.

Snieder, R., 2004a, Extracting the Green's function from the correlation of coda waves: A derivation based on stationary phase: Phys. Rev. E, **69**, 046610.

———, 2004b, A guided tour of mathematical methods for the physical sciences, 2nd ed.: Cambridge Univ. Press.

———, 2006, Retrieving the Green's function of the diffusion equation from the response to a random forcing: Phys. Rev. E, **74**, 046620.

———, 2007, Extracting the Green's function of attenuating heterogeneous acoustic media from uncorrelated waves: J. Acoust. Soc. Am., **121**, 2637–2643.

Snieder, R., and E. Şafak, 2006, Extracting the building response using seismic interferometry; theory and application to the Millikan library in Pasadena, California: Bull. Seismol. Soc. Am., **96**, 586–598.

Snieder, R., H. Douma, and I. Vasconcelos, 2012, Extracting the Green's function from measurements of the energy flux: J. Acoust. Soc. Am., **131**, EL309–EL315.

Snieder, R., M. Miyazawa, E. Slob, I. Vasconcelos, and K. Wapenaar, 2009, A comparison of strategies for seismic interferometry: Surveys in Geophysics, **30**, 503–523.

Snieder, R., J. Sheiman, and R. Calvert, 2006a, Equivalence of the virtual source method and wavefield deconvolution in seismic interferometry: Phys. Rev. E, **73**, 066620.

Snieder, R., E. Slob, and K. Wapenaar, 2010, Lagrangian Green's function extraction, with applications to potential fields, diffusion, and acoustic waves: New J. Phys., **12**, 063013.

Snieder, R., K. Wapenaar, and K. Larner, 2006b, Spurious multiples in seismic interferometry of primaries: Geophysics, **71**, SI111–SI124.

Snieder, R., K. Wapenaar, and U. Wegler, 2007, Unified Green's function retrieval by cross-correlation; connection with energy principles: Phys. Rev. E, **75**, 036103.

Song, X., 2010, Preface to the special issue on ambient noise seismology: Earthquake Science, **23**, 395–396.

Stehly, L., M. Campillo, B. Froment, and R. Weaver, 2008, Reconstructing Green's function by correlation of the coda of the correlation (C3) of ambient seismic noise: J. Geophys. Res., **113**, B11306.

Stehly, L., M. Campillo, and N. Shapiro, 2006, A study of seismic noise from long-range correlation properties: J. Geophys. Res., **111**, B10306.

———, 2007, Traveltime measurements from noise correlation: stability and detection of instrumental timeshifts: Geophys. J. Int., **171**, 223–230.

Tatarskii, V., 1987, Example of the description of dissipative processes in terms of reversible dynamic equations and some comments on the fluctuation dissipation theorem: Sov. Phys. Usp., **30**, 134–152.

Trampert, J., M. Cara, and M. Frogneux, 1993, *SH* propagator matrix and Q_s estimates from borehole- and surface-recorded earthquake data: Geophys. J. Int., **112**, 290–299.

Tsai, V., 2011, Understanding the amplitudes of noise correlation measurements: J. Geophys. Res., **116**, B09311.

van der Neut, J., and A. Bakulin, 2009, Estimating and correcting the amplitude radiation pattern of a virtual source: Geophysics, **74**, SI27–SI36.

van der Neut, J., J. Thorbecke, K. Mehta, E. Slob, and K. Wapenaar, 2011, Controlled-source interferometric redatuming by crosscorrelation and multidimensional deconvolution in elastic media: Geophysics, **76**, SA63–SA76.

van Wijk, K., 2006, On estimating the impulse response between receivers in a controlled ultrasonic experiment: Geophysics, **71**, SI79–SI84.

Vasconcelos, I., and R. Snieder, 2008a, Interferometry by deconvolution, Part 1 theory for acoustic waves and numerical examples: Geophysics, **73**, S115–S128.

———, 2008b, Interferometry by deconvolution: Part 2 theory for elastic waves and application to drill-bit seismic imaging: Geophysics, **73**, S129–S141.

Wapenaar, K., D. Draganov, and J. Robertsson, eds., 2008a, Seismic interferometry: History and present status: Society of Exploration Geophysics, volume **26** *of* SEG Geophysics Reprints Series.

Wapenaar, K., D. Draganov, R. Snieder, X. Campman, and A. Verdel, 2010a, Tutorial on seismic interferometry. Part 1: Basic principles and applications: Geophysics, **75**, 75A195–75A209.

Wapenaar, K., E. Ruigrok, J. van der Neut, and D. Draganov, 2011a, Improved surface-wave retrieval from ambient seismic noise by multi-dimensional deconvolution: Geophys. Res. Lett., **38**, L01313.

Wapenaar, K., E. Slob, and R. Snieder, 2006, Unified Green's function retrieval by cross-correlation: Phys. Rev. Lett., **97**, 234301.

———, 2008b, Seismic and electromagnetic controlled-source interferometry in dissipative media: Geophys. Prosp., **56**, 419–434.

Wapenaar, K., E. Slob, R. Snieder, and A. Curtis, 2010b, Tutorial on seismic interferometry. Part 2: Underlying theory: Geophysics, **75**, 75A211–75A227.

Wapenaar, K., and J. van der Neut, 2010, A representation for Green's function retrieval by multidimensional deconvolution: J. Acoust. Soc. Am., **128**, EL366–EL371.

Wapenaar, K., J. van der Neut, E. Ruigrok, D. Draganov, J. Hunziker, E. Slob, J. Thorbecke, and R. Snieder, 2011b, Seismic interferometry by crosscorrelation and by mutidimensional deconvolution: a systematic comparison: Geophys. J. Int., **185**, 1335–1364.

Weaver, R., 2008, Ward identities and the retrieval of Green's functions in the correlations of a diffuse field: Wave Motion, **45**, 596–604.

Weaver, R., and O. Lobkis, 2001, Ultrasonics without a source: Thermal fluctuation correlations at MHz frequencies: Phys. Rev. Lett., **87**, 134301.

———, 2003a, On the emergence of the Green's function in the correlations of a diffuse field: pulse-echo using thermal phonons: Ultrasonics, **40**, 435–439.

———, 2003b, Elastic wave thermal fluctuations, ultrasonic waveforms by correlation of thermal phonons: J. Acoust. Soc. Am., **113**, 2611–2621.

———, 2005, Fluctuations in diffuse field-field correlations and the emergence of the Green's function in open systems: J. Acoust. Soc. Am., **117**, 3432–3439.

Webb, S., 1998, Broadband seismology and noise under the ocean: Rev. Geophys., **36**, 105–142.

Wegler, U., and C. Sens-Schönfelder, 2007, Fault zone monitoring with passive image interferometry: Geophys. J. Int., **168**, 1029–1033.

Xiao, X., M. Zhou, and G. Schuster, 2006, Salt-flank deliniation by interferometric imaging of transmitted P to S waves: Geophysics, **71**, SI197–SI207.

Xu, Z., and X. Song, 2009, Temporal changes of surface wave velocity associated with major Sumatra earthquakes from ambient noise correlation: Proc. Natl. Ac. Sci., **106**, 14207–14212.

Xue, Y., S. Dong, and G. Schuster, 2009, Interferometric prediction and subtraction of surface waves with a nonlinear local filter: Geophysics, **74**, SI1–SI8.

Yamada, M., J. Mori, and S. Ohmi, 2010, Temporal changes of subsurface velocities during strong shaking as seen from seismic interferometry: J. Geophys. Res., **115**, B03302.

Yang, Y., and M. Ritzwoller, 2008, Teleseismic surface wave tomography in the western US using the transportable array component of USArray: Geophys. Res. Let., **5**, L04308.

Yao, H., R. van der Hilst, and M. de Hoop, 2006, Surface-wave array tomography in SE Tibet from ambient seismic noise and two- station analysis - I. Phase velocity maps: Geophys. J. Int., **166**, 732–744.

Zhan, Z., S. Ni., D. Helmberger, and R. Clayton, 2010, Retrieval of Moho-reflected shear wave arrivals from seismic noise: Geophys. J. Int., **182**, 408–420.

Zhang, J., P. Gerstoft, and P. Shearer, 2009, High-frequency P-wave seismic noise driven by ocean winds: Geophys. Res. Lett., **36**, L09302.

APPENDIX A: DERIVATION OF EXPRESSIONS (7) AND (8)

Using the integral representation theorem of the Bessel function (expression (11.30c) of Arfken & Weber (2001)), $2\pi J_0(\xi) = \int_0^{2\pi} exp(i\xi\cos\varphi)d\varphi$, with J_0 the Bessel function of order zero. The Bessel function can be decomposed into the Hankel function of the first and second kind using $J_0(kR) = (1/2)\left(H_0^{(1)}(kR) + H_0^{(2)}(kR)\right) = (1/2)\left(H_0^{(1)}(kR) + H_0^{(1)*}(kR)\right)$, where expressions (11.85) and (11.86) of Arfken & Weber (2001) have been used. These results reduce equation (6) to

$$\langle u_A u_B^* \rangle = \pi |S|^2 \left(H_0^{(1)}(kR) + H_0^{(1)*}(kR)\right) . \quad \text{(A1)}$$

The Green's function for wave propagation in a 2D homogeneous medium is given by $G_{2D}(R) =$

$(-i/4)H_0^{(1)}(kR)$ (expression (19.43) of Snieder 2004b). Inserting this in equation (A1) gives expression (7).

The derivation is actually simpler in 3D, the geometry of this problem is shown in the right panel of figure 1. Following similar steps as those leading to equation (6) give for this case

$$\langle u_A u_B^* \rangle = |S|^2 \int_0^{\pi} \int_0^{2\pi} e^{ikR\cos\theta} d\varphi \sin\theta d\theta \,, \qquad \text{(A2)}$$

where θ now is the angle between the direction on wave propagation of the plane waves and the line between the receivers (now the z-axis). Note that instead of the integration over the unit circle in expression (6) we now integrate over the unit sphere that describes the directions of the incoming waves. The integration over φ gives a multiplication with 2π, and the integration over θ is given by $\int_0^{\pi} e^{ikR\cos\theta} \sin\theta d\theta = \int_{-1}^{1} e^{ikRu} du = \left(e^{ikR} - e^{-ikR}\right)/(ikR)$. Inserting these results into equation (A2) gives equation (8).

APPENDIX B: DERIVATION OF THE FLUCTUATION RESPONSE THEOREM (10)

The expectation value of a parameter $f(A_i)$ is given by (Le Bellac et al. 2004)

$$\langle f(A_i) \rangle = \frac{Tr\left(f(A_i)\exp\left(\sum_k \lambda_k A_k\right)\right)}{Tr\left(\exp\left(\sum_k \lambda_k A_k\right)\right)} \,, \qquad \text{(B1)}$$

where Tr denotes the trace, defined as a sum over all degrees of freedom. With this definition the expectation value of A_i is given by

$$\begin{aligned} \langle A_i \rangle &= \frac{Tr\left(A_i \exp\left(\sum_k \lambda_k A_k\right)\right)}{Tr\left(\exp\left(\sum_k \lambda_k A_k\right)\right)} \\ &= \frac{Tr\left(\dfrac{\partial}{\partial\lambda_i}\exp\left(\sum_k \lambda_k A_k\right)\right)}{Tr\left(\exp\left(\sum_k \lambda_k A_k\right)\right)} = \frac{1}{Z}\frac{\partial Z}{\partial \lambda_i} \,. \end{aligned} \qquad \text{(B2)}$$

where the partition function Z is defined by

$$Z = Tr\left(\exp\left(\sum_k \lambda_k A_k\right)\right) \,. \qquad \text{(B3)}$$

Differentiating equation (B2) with respect to λ_j gives

$$\frac{\partial \langle A_i \rangle}{\partial \lambda_j} = \frac{1}{Z}\frac{\partial^2 Z}{\partial\lambda_i \partial\lambda_j} - \frac{1}{Z^2}\frac{\partial Z}{\partial\lambda_i}\frac{\partial Z}{\partial\lambda_j} \,. \qquad \text{(B4)}$$

It follows from expression (B2) that the last term is equal to $\langle A_i \rangle \langle A_j \rangle$. The first term in the right hand side follows from the identities

$$\begin{aligned} \frac{\partial^2 Z}{\partial\lambda_i \partial\lambda_j} &= \frac{\partial^2}{\partial\lambda_i\partial\lambda_j} Tr\left(\exp\sum_k \lambda_k A_k\right) \\ &= Tr\left(A_i A_j \exp\sum_k \lambda_k A_k\right) = \langle A_i A_j \rangle Z \,, \end{aligned} \qquad \text{(B5)}$$

where expressions (B1) and (B3) are used in the last identity. Using these results reduces equation (B4) to

$$\frac{\partial \langle A_i \rangle}{\partial \lambda_j} = \langle A_i A_j \rangle - \langle A_i \rangle \langle A_j \rangle \,. \qquad \text{(B6)}$$

With the identity $\langle A_i A_j \rangle - \langle A_i \rangle \langle A_j \rangle = \langle (A_i - \langle A_i \rangle)(A_j - \langle A_j \rangle) \rangle$, this gives equation (10).

Monitoring a building using deconvolution interferometry. I: Earthquake-data analysis

Nori Nakata[1], Roel Snieder[1], Seiichiro Kuroda[2], Shunichiro Ito[3], Takao Aizawa[3], & Takashi Kunimi[4]

[1] *Center for Wave Phenomena, Geophysics Department, Colorado School of Mines*
[2] *National Institute for Rural Engineering*
[3] *Suncoh Consultants Co., Ltd.*
[4] *Akebono Brake Industry*

ABSTRACT

For health monitoring of a building, we need to separate the response of the building to an earthquake from the imprint of soil-structure coupling and from wave propagation below the base of the building. Seismic interferometry based on deconvolution, where we deconvolve the wave elds recorded at different oors, is a technique to extract this building response and hence estimate velocity of the wave which propagates inside the building. Deconvolution interferometry also allows us to estimate the damping factor of the building. Compared with other interferometry techniques, such as crosscorrelation and crosscoherence interferometry, deconvolution interferometry is the most suitable technique to monitor a building using earthquake records. For deconvolution interferometry, we deconvolve the wave elds recorded at all levels with the waves recorded at a target receiver inside the building. This receiver behaves as a virtual source, and we retrieve the response of a cut-off building, a short building which is cut off at the virtual source. Because the cut-off building is independent from the structure below the virtual source, the technique might be useful for estimating local structure and local damage. We apply deconvolution interferometry to 17 earthquakes recorded during two weeks at a building in Fukushima, Japan and estimate time-lapse changes in velocity and normal-mode frequency. As shown in a previous study, the change in velocity correlates with the change in normal-mode frequency. We compute the velocities from both traveling waves and the fundamental mode using coda-wave interferometry. These velocities have a negative correlation with the maximum acceleration of the observed earthquake records.

Key words: time-lapse monitoring, seismic interferometry, deconvolution, earthquake, building

1 INTRODUCTION

The response of a building to an earthquake has been studied since the early 1900s [e.g., *Biot*, 1933; *Sezawa and Kanai*, 1935; *Carder*, 1936]. We can estimate the frequencies of the fundamental and higher modes of buildings using ambient and forced vibration experiments (Trifunac, 1972; Ivanović et al., 2000; Kohler et al., 2005; Clinton et al., 2006; Michel et al., 2008). Due to the shaking caused by major earthquakes, the frequencies of normal modes decrease (Trifunac et al., 2001a; Kohler et al., 2005); the reduction is mostly temporary (a few minutes) and healing occurs with time, but some reduction is permanent (Clinton et al., 2006), who found more than 20% temporal reduction and 4% permanent reduction in the fundamental frequency of the motion of the Millikan Library located at the California Institute of Technology after the 1987 M6.1 Whittier Narrows earthquake. The reduction in the frequency logarithmically correlates with the maximum acceleration of observed records (Clinton et al., 2006). Precipitation, strong wind, temperature, reinforcement, and

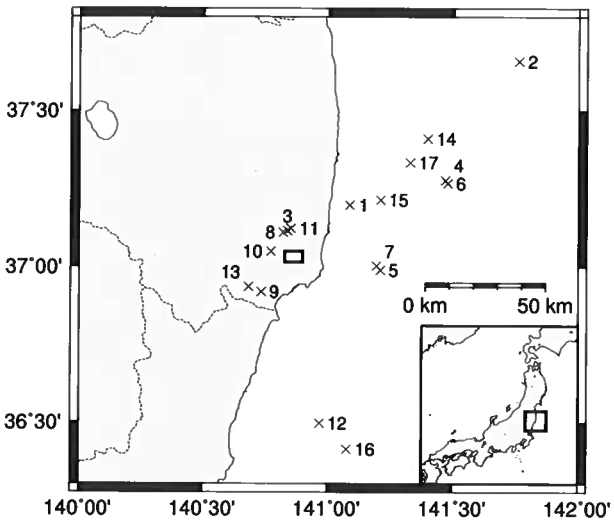

Figure 1. The building (rectangle, not to scale) and epicenters of earthquakes used (crosses). Numbers beside of crosses correspond to the sequencial numbers in Table 1. The lower-right map indicates the location of the magnified area.

heavy weight loaded in a building also change the frequencies of normal modes (Kohler et al., 2005; Clinton et al., 2006). Because these frequencies are related to both the building itself and the soil-structure coupling, we have to consider soil-structure interactions (Şafak, 1995) and nonlinearities in the response of the foundation soil (Trifunac et al., 2001a,b). Normal-mode frequencies estimated from observed records are, therefore, not suitable for health monitoring of a building in isolation of its environment (Todorovska and Trifunac, 2008b).

Snieder and Şafak (2006) show that one can estimate an impulse response independent from the soil-structure coupling and the complicated wave propagation (e.g., attenuation and scattering) below the bottom receiver by using seismic interferometry based on deconvolution. Seismic interferometry is a technique to extract the Green's function which accounts for the wave propagation between receivers (Lobkis and Weaver, 2001; Derode et al., 2003; Snieder, 2004; Paul et al., 2005; Snieder et al., 2006b; Wapenaar and Fokkema, 2006). Seismic interferometry can be based on crosscorrelation, deconvolution, and crosscoherence (Snieder et al., 2009; Wapenaar et al., 2010). Deconvolution interferometry is a useful technique for monitoring structures especially in one dimension (Nakata and Snieder, 2011, 2012a,b). Because deconvolution interferometry changes the boundary condition at the base of the building, we are able to extract the pure response of the building regardless of its coupling to the subsurface (Snieder and Şafak, 2006; Snieder et al., 2006a).

Deconvolution interferometry has been applied to earthquake records observed in a building to retrieve the velocity of traveling waves and attenuation of the building (Oyunchimeg and Kawakami, 2003; Snieder and Şafak, 2006; Kohler et al., 2007; Todorovska and Trifunac, 2008a,b) (some studies call the method *impulse response function* or *normalized input-output minimization*). Todorovska and Trifunac (2008b) use 11 earthquakes occurring over a period of 24 years to monitor the fundamental frequency of a building after applying deconvolution interferometry. The fundamental frequencies they estimated from the interferometry are always higher than the frequencies obtained from the observed records because the frequencies computed from the observed records are affected by both the building itself and soil-building coupling, while the frequencies estimated using the interferometry are only related to the building itself. Oyunchimeg and Kawakami (2003) apply short-time moving-window seismic interferometry to an earthquake record to estimate the velocity reduction of a building during an earthquake. Prieto et al. (2010) apply deconvolution interferometry to ambient vibrations after normalizing amplitudes per frequency using the multitaper method (Thomson, 1982) to estimate the traveling-wave velocity and damping factor.

In this study, we apply deconvolution interferometry to 17 earthquakes observed at a building in Japan over a period of two weeks and monitor the changes in velocity of the building. This study is based on the work of Snieder and Şafak (2006); furthermore, we extend the deconvolution interferometry as proposed by Snieder and Şafak (2006) to deconvolution with the waveforms recorded at an arbitrary receiver, compare this with crosscorrelation and crosscoherence interferometry, and use interferometry for monitoring a building in Japan. First, we introduce our data: geometry of receivers, locations of the building and epicenters of earthquakes used, observed waveforms, and shapes of the normal modes extracted from observed records. We also introduce the equations of interferometry based on deconvolution, crosscorrelation, and crosscoherence. We further indicate the deconvolved waveforms obtained from one earthquake and estimate a velocity as well as a quality factor (Q). Next, we apply deconvolution interferometry to all observed earthquakes and monitor the change in velocity of the building using coda-wave interferometry (Snieder et al., 2002). In a companion paper, we apply the interferometry to ambient vibrations.

2 BUILDING AND EARTHQUAKES

The building (rectangle in Figure 1) in which we recorded vibrations is located in the Fukushima prefecture, Japan. Continuous seismic vibrations were recorded by Suncoh Consultants Co., Ltd. for two weeks using 10 microelectromechanical-systems (MEMS) accelerometers, which were developed by Akebono Brake Industry Co., Ltd., and 17 earthquakes were observed during the two weeks (Table 1 and Figure 1). In this

Table 1. Origin times, magnitudes, and hypocenter locations of recorded earthquakes estimated by the Japan Meteorological Agency (JMA). The earthquakes are numbered sequentially according to their origin times. Maximum acceleration is the observed maximum amplitude of the MEMS accelerometers at the first floor in the 120 s following the origin time of each earthquake.

No.	Origin time	M_{JMA}	Latitude	Longitude	Depth (km)	Maximum acceleration (m/s^2)
1	5/31/11 16:12:20.2	3.9	37.1983	141.0900	32	0.145
2	6/1/11 01:41:19.6	4.2	37.6583	141.7617	44	0.088
3	6/1/11 06:23:27.2	3.4	37.1167	140.8400	7	0.061
4	6/3/11 21:44:38.7	4.2	37.2783	141.4683	36	0.040
5	6/4/11 01:00:14.1	5.5	36.9900	141.2100	30	1.923
6	6/4/11 09:03:33.7	4.3	37.2683	141.4783	36	0.147
7	6/4/11 10:41:10.0	4.1	37.0033	141.1933	28	0.083
8	6/5/11 17:32:38.9	3.5	37.1117	140.8217	7	0.281
9	6/5/11 19:46:06.3	3.9	36.9200	140.7333	14	0.175
10	6/5/11 20:16:37.0	4.4	37.0500	140.7717	11	0.843
11	6/7/11 03:11:55.9	2.6	37.1233	140.8540	5	0.020
12	6/9/11 19:38:32.9	5.7	36.4967	140.9700	13	0.358
13	6/11/11 00:40:55.4	3.9	36.9367	140.6833	11	0.075
14	6/11/11 01:41:19.6	3.9	37.4117	141.3983	46	0.087
15	6/12/11 05:08:58.4	4.5	37.2150	141.2100	21	0.153
16	6/12/11 17:09:45.4	4.6	36.4117	141.0800	47	0.270
17	6/13/11 05:59:35.1	4.4	37.3350	141.3283	33	0.180

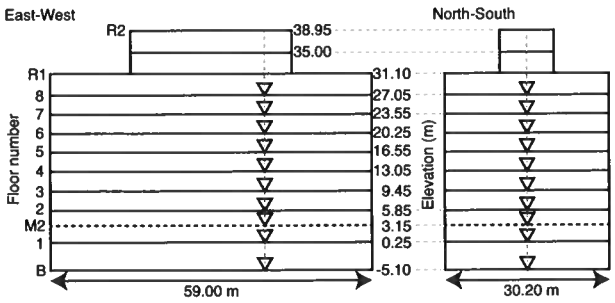

Figure 2. The (left) EW and (right) NS vertical cross sections of the building and the positions of receivers (triangles). Elevations denote the height of each floor from ground level. We put receivers on stairs 0.19 m below each floor except for the basement (on the floor) and the first floor (0.38 m below). Receiver M2 is located between the first and second floors. Horizontal-receiver components are aligned with the EW and NS directions.

study, we focus on processing of the earthquake records, and we analyze ambient vibrations in the companion paper. The building includes eight stories, a basement, and a penthouse (Figure 2). We installed receivers on the stairs, located 20 m from the east side and at the center between the north and south sides. The sampling interval of the records is 1 ms, and the receivers have three components. Here, we use two horizontal components which are aligned with the east-west (EW) and north-south (NS) directions.

Figures 3a–3d illustrate the observed waveforms and their power spectra of earthquake No. 5, which gives the greatest acceleration to the building. Figures 3e and 3f show the spectrogram of the motion at the fourth floor computed with the continuous-wavelet transform (Torrence and Compo, 1998). Higher frequencies quickly attenuate and the fundamental mode is dominant for later times in Figures 3e and 3f. The frequency of the fundamental mode in the EW component (1.17 Hz) is higher than the frequency in the NS component (0.97 Hz) because the EW side of the building is longer than the NS side. Both components have large amplitudes at around 0.5 Hz between 14 and 21 s. Since the 0.5-Hz component is localized in time (Figure 3e and 3f), it corresponds to a surface wave that moves the entire building. However, because the frequency of the surface wave is less than that of the fundamental mode of the building, it does not excite waves that propagate within the building.

Figure 4 illustrates the shapes of the normal-mode displacement computed from the real part of the Fourier spectra at different floors. We calculate displacement from acceleration using numerical integration (Schiff and Bogdanoff, 1967). Just as for the fundamental mode, the frequencies of overtones in the EW component are also higher than those in the NS component. Although the displacements of both components in mode 1 (the fundamental mode) are almost the same, the NS-component displacement is larger than that of the EW component in modes 2 and 3. The amplitude of mode 1 is much larger than the amplitudes of other modes.

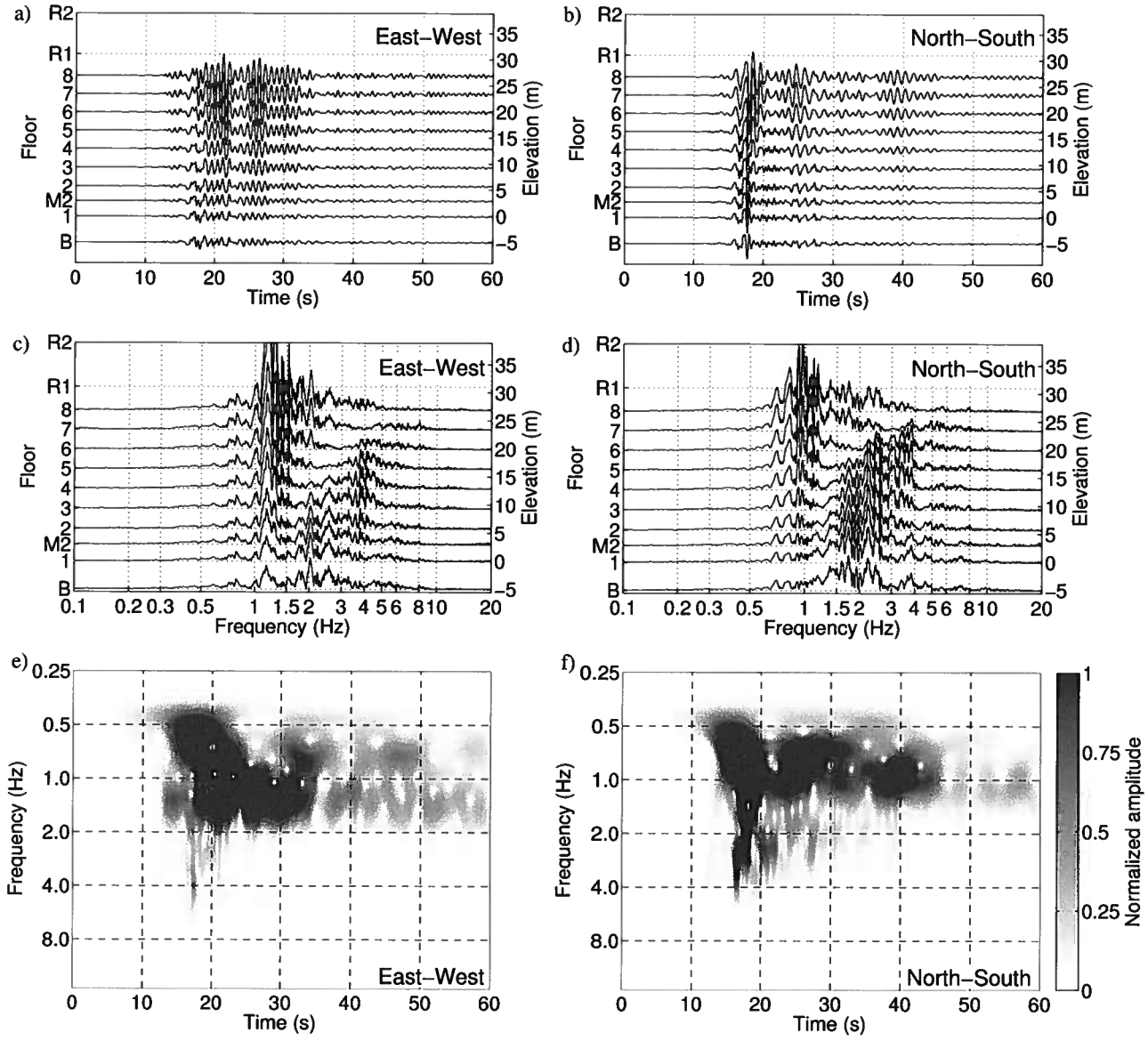

Figure 3. Unfiltered waveforms of earthquake No. 5 recorded at the building in (a) the EW component and (b) the NS component, and (c, d) their power spectra. (e, f) Spectrogram computed with continuous-wavelet transformed waveforms recorded at the fourth floor. Time 0 s represents the origin time of the earthquake. We preserve relative amplitudes of the EW and NS components.

3 DECONVOLUTION WITH AN ARBITRARY RECEIVER

By deconvolving observed earthquake records, we obtain the impulse response of a building (Oyunchimeg and Kawakami, 2003; Snieder and Şafak, 2006; Kohler et al., 2007; Todorovska and Trifunac, 2008a). When the height of the building is H, the recorded signal of an earthquake in the frequency domain at an arbitrary receiver at height z is given by Snieder and Şafak (2006):

$$u(z) = \sum_{m=0}^{\infty} S(\omega) R^m(\omega) \{ e^{ik(2mH+z)} e^{-\gamma|k|(2mH+z)} + e^{ik(2(m+1)H-z)} e^{-\gamma|k|(2(m+1)H-z)} \} = \frac{S(\omega)\{ e^{ikz} e^{-\gamma|k|z} + e^{ik(2H-z)} e^{-\gamma|k|(2H-z)} \}}{1 - R(\omega) e^{2ikH} e^{-2\gamma|k|H}}, \quad (1)$$

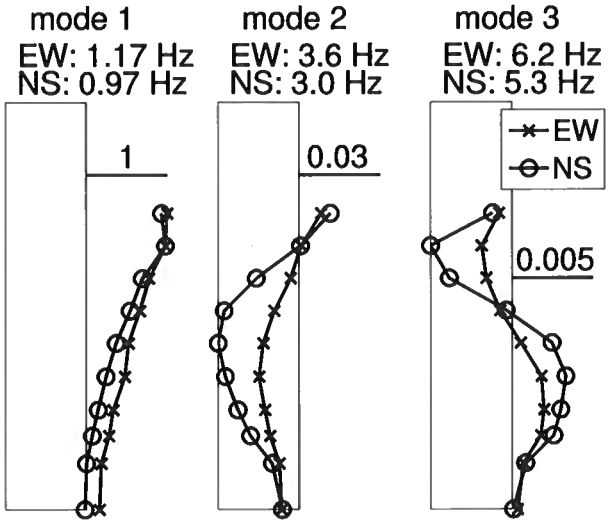

Figure 4. Displacement of the first three horizontal normal modes for earthquake No. 5 estimated from the real part of the Fourier spectra at different floors. Each mark indicates the displacement of a receiver. The center frequency of each mode is shown at the top of each panel. Black horizontal lines and the numbers on the lines show the amplitude ratio among modes, and the box depicts the height of the building (R2 in Figure 2). The zero displacement is at the right side of each box.

where $S(\omega)$ is the incoming waveform to the base of the building, $R(\omega)$ the reflection coefficient related to the coupling of the ground and the base of the building, k the wavenumber, γ the attenuation coefficient, and i the imaginary unit. We use the absolute value of wavenumbers in the damping terms because the waves attenuate regardless of whether the wavenumber is positive or negative. In expression 1, we assume the wave vertically propagates in the building (one-dimensional propagation) with constant amplitude and wavenumber, and without internal reflections. The constant wavenumber implies that we assume constant velocity c because $k = \omega/c$. The incoming waveform $S(\omega)$ includes the source signature of the earthquake and the effect of propagation such as attenuation and scattering along the path from the hypocenter of the earthquake to the base of the building. The attenuation coefficient γ is defined as

$$\gamma = \frac{1}{2Q}, \tag{2}$$

with Q the quality factor (Aki and Richards, 2002).

For $m = 0$ in the first line in expression 1, the first term $S(\omega)e^{ikz}e^{-\gamma|k|z}$ indicates the incoming upgoing wave and the second term $S(\omega)e^{ik(2H-z)}e^{-\gamma|k|(2H-z)}$ the downgoing wave, which is reflected off the top of the building. The index m represents the number of reverberations between the base and top of the building.

As we deconvolve a waveform recorded by a receiver at z with a waveform observed by another receiver at z_a, from expression 1 we obtain

$$\begin{aligned} D(z, z_a, \omega) =& \frac{u(z)}{u(z_a)} \\ =& \frac{S(\omega)\{e^{ikz}e^{-\gamma|k|z} + e^{ik(2H-z)}e^{-\gamma|k|(2H-z)}\}}{S(\omega)\{e^{ikz_a}e^{-\gamma|k|z_a} + e^{ik(2H-z_a)}e^{-\gamma|k|(2H-z_a)}\}} \\ =& \sum_{n=0}^{\infty}(-1)^n \left\{e^{ik(2n(H-z_a)+z-z_a)}e^{-\gamma|k|(2n(H-z_a)+z-z_a)}\right. \\ & \left. + e^{ik(2n(H-z_a)+2H-z-z_a)}e^{-\gamma|k|(2n(H-z_a)+2H-z-z_a)}\right\}, \end{aligned} \tag{3}$$

where we use a Taylor expansion in the last equality. In equation 3, the receiver at z_a behaves as a virtual source. Equation 3 may be unstable because of the spectral devision. In practice we use a regularization parameter ϵ (Yilmaz, 2001,Section 2.3):

$$D(z, z_a, \omega) = \frac{u(z)}{u(z_a)} \approx \frac{u(z)u^*(z_a)}{|u(z_a)|^2 + \epsilon\langle|u(z_a)|^2\rangle}, \tag{4}$$

where $*$ is a complex conjugate and $\langle|u(z_a)|^2\rangle$ the average power spectrum of $u(z_a)$. In this study we use $\epsilon = 1\%$.

Note that these deconvolved waves are independent of the incoming waveform $S(\omega)$ and the ground coupling $R(\omega)$. When we consider substitutions $S(\omega) \to 1$, $R(\omega) \to -1$, $H \to H - z_a$, and $z \to z - z_a$, equation 1 reduces to equation 3. These conditions indicate the physical properties of the deconvolved waveforms: impulse response ($S(\omega) \to 1$), perfect reflection at the virtual source ($R(\omega) \to -1$), and a small building ($H \to H - z_a$ and $z \to z - z_a$) as we discuss later.

When $z > z_a$, equation 3 describes a wave that is excited at z_a and reverberates between z_a and the top of the building. Using a normal-mode analysis (equation A4 in Appendix A), the fundamental mode of equation 3 in the time domain is given by

$$D(z, z_a, t) = \frac{4\pi c}{H - z_a}e^{-\gamma\omega_0 t}\sin(\omega_0 t)\cos\left(\omega_0\frac{H - z}{c}\right), \tag{5}$$

where $\omega_0 = \pi c/\{2(H - z_a)\}$. The period of the fundamental mode is, thus,

$$T_0 = \frac{4(H - z_a)}{c}, \tag{6}$$

which corresponds to the period of the fundamental mode of the building that is cut off at z_a (cut-off building: Figure 5a). According to equation 3 the polarity change resulting from reflection at z_a is given by $(-1)^n$, the reflection coefficient at the virtual source is -1. Therefore, the cut-off building is only sensitive to the properties of the building above z_a, and the reconstructed wave motion in the cut-off building has the potential to estimate local structure and local damage instead of structure and damage for the entire building.

When $z < z_a$ and $n = 0$ in equation 3, we

obtain two waves: an acausal upgoing wave from z to z_a ($e^{ik(z-z_a)}e^{-\gamma|k|(z-z_a)}$) and a causal downgoing wave from z_a to z ($e^{ik(2H-z-z_a)}e^{-\gamma|k|(2H-z-z_a)}$). Waves for $n \geq 1$ in equation 3 account for the reverberations between z_a and the top of the building. Because $D(z_a, z_a, \omega) = 1$, the deconvolved waveforms at z_a is a delta function in the time domain ($D(z_a, z_a, t) = \delta(t)$); hence $D(z_a, z_a, t) = 0$ for $t \neq 0$ (clamped boundary condition (Snieder et al., 2006a, 2009)). The upgoing and downgoing waves interfere destructively at z_a.

Although we assume, for simplicity, a constant velocity in equation 1, we can apply deconvolution interferometry to wavefields observed at a building with smoothly varying velocities. When the velocity c varies with height, the local wavenumber does so as well, and using the WKBJ approximation for the phase, expression 1 generalizes to

$$u(z) = \frac{U}{1 - R(\omega)\exp\left(2i\int_0^H k(z)dz\right)\exp\left(-2\gamma\int_0^H |k(z)|dz\right)} \tag{7}$$

with

$$\begin{aligned} U =& S(\omega)\left[\exp\left(i\int_0^z k(z)dz\right)\exp\left(-\gamma\int_0^z |k(z)|dz\right)\right. \\ &+ \exp\left\{i\left(\int_0^H k(z)dz + \int_z^H k(z)dz\right)\right\} \\ &\left.\times \exp\left\{-\gamma\left(\int_0^H |k(z)|dz + \int_z^H |k(z)|dz\right)\right\}\right], \end{aligned}$$

and equation 3 generalizes in this case to

$$\begin{aligned} D(z, z_a, \omega) =& \sum_{n=0}^{\infty}(-1)^n \\ &\times \left[\exp\left\{i\left(2n\int_{z_a}^H k(z)dz + \int_{z_a}^z k(z)dz\right)\right\}\right. \\ &\times \exp\left\{-\gamma\left(2n\int_{z_a}^H |k(z)|dz + \int_{z_a}^z |k(z)|dz\right)\right\} \\ &+ \exp\left\{i\left((2n+1)\int_{z_a}^H k(z)dz + \int_z^H k(z)dz\right)\right\} \\ &\left.\times \exp\left\{-\gamma\left((2n+1)\int_{z_a}^H |k(z)|dz + \int_z^H |k(z)|dz\right)\right\}\right]. \end{aligned} \tag{8}$$

As for equation 3, equation 8 represents the waves in a cut-off building at z_a, and the period of the fundamental mode of the cut-off building depends on the slowness averaged between z_a and H. Note that when $z > z_a$, $D(z, z_a, \omega)$ in equation 8 is only related to $k(z)$ above z_a.

When z_a is at the first floor ($z_a = 0$) or at the top of the building ($z_a = H$), equation 3 corresponds to equations 26 or 21 in Snieder and Şafak (2006), respectively, which we rewrite here as

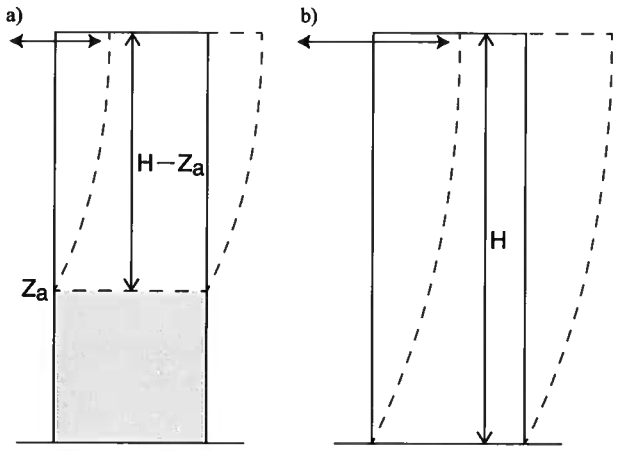

Figure 5. Schematic shapes of the fundamental mode retrieved by using seismic interferometry. (a) Fundamental mode retrieved by deconvolving wavefields with a motion recorded at z_a (equation 3). (b) Fundamental mode retrieved by deconvolving wavefields with a motion recorded at the first floor (equation 9).

$$\begin{aligned} D(z, 0, \omega) =& \sum_{n=0}^{\infty}(-1)^n \times \left\{e^{ik(2nH+z)}e^{-\gamma|k|(2nH+z)}\right. \\ &\left. + e^{ik(2(n+1)H-z)}e^{-\gamma|k|(2(n+1)H-z)}\right\}, \end{aligned} \tag{9}$$

$$D(z, H, \omega) = \frac{1}{2}\left\{e^{ik(H-z)}e^{-\gamma|k|(H-z)} + e^{-ik(H-z)}e^{\gamma|k|(H-z)}\right\}. \tag{10}$$

Figure 5b illustrates a schematic shape of the fundamental mode as given in equation 9. The period of the mode in equation 9 is related to the structure of the entire building as if the building were placed on a rigid subsurface (i.e., the reflection coefficient at the base is -1). When we put a receiver at the top floor (8 in Figure 2) of a building instead of the rooftop (R_1 or R_2 in Figure 2), we theoretically do not obtain the response in equation 10 because the traveling waves reflect at the top of the building rather than at the top floor. In this case, the deconvolved response follows equation 3. This difference may be insignificant when the wavelength of the traveling waves is much longer than the distance between the top floor and the top of the building.

4 CROSSCORRELATION AND CROSSCOHERENCE INTERFEROMETRY

In the previous section, we focused on seismic interferometry based on deconvolution. Let us consider seismic interferometry based on crosscorrelation [e.g., *Schuster et al.*, 2004] and crosscoherence [e.g., *Nakata et al.*, 2011]; these two methods are the widest-applied technique and the earliest application (Aki, 1957), respectively.

4.1 Crosscorrelation

From equation 1, the crosscorrelation of $u(z)$ and $u(z_a)$ is

$$\begin{aligned} C(z, z_a, \omega) &= u(z)u^*(z_a) \\ &= |S(\omega)|^2 \frac{\left\{e^{ikz}e^{-\gamma|k|z} + e^{ik(2H-z)}e^{-\gamma|k|(2H-z)}\right\}\left\{e^{-ikz_a}e^{-\gamma|k|z_a} + e^{-ik(2H-z_a)}e^{-\gamma|k|(2H-z_a)}\right\}}{1 - R(\omega)e^{2ikH}e^{-2\gamma|k|H} - R^*(\omega)e^{-2ikH}e^{-2\gamma|k|H} + |R(\omega)|^2e^{-4\gamma|k|H}}. \end{aligned} \tag{11}$$

In contrast to the deconvolution (equation 3), equation 11 depends on the incoming wave $S(\omega)$ and the ground coupling $R(\omega)$, and does not create a clamped boundary condition ($C(z_a, z_a, \omega) \neq 1$). Because of the presence of the reflection coefficient $R(\omega)$ and the power spectrum $|S(\omega)|^2$, it is much more complicated to estimate the properties (e.g., traveling-wave velocity and attenuation) of the building from crosscorrelation than from deconvolution.
When $z_a = 0$ and $z_a = H$, equation 11 reduces to

$$C(z, 0, \omega) = |S(\omega)|^2 \frac{e^{ikz}e^{-\gamma|k|z} + e^{-ikz}e^{-\gamma|k|(4H-z)} + e^{ik(2H-z)}e^{-\gamma|k|(2H-z)} + e^{-ik(2H-z)}e^{-\gamma|k|(2H+z)}}{1 - R(\omega)e^{2ikH}e^{-2\gamma|k|H} - R^*(\omega)e^{-2ikH}e^{-2\gamma|k|H} + |R(\omega)|^2e^{-4\gamma|k|H}}, \tag{12}$$

$$C(z, H, \omega) = 2\,|S(\omega)|^2 \frac{e^{-2\gamma|k|H}\left\{e^{ik(H-z)}e^{-\gamma|k|(H-z)} + e^{-ik(H-z)}e^{\gamma|k|(H-z)}\right\}}{1 - R(\omega)e^{2ikH}e^{-2\gamma|k|H} - R^*(\omega)e^{-2ikH}e^{-2\gamma|k|H} + |R(\omega)|^2e^{-4\gamma|k|H}}, \tag{13}$$

respectively. If $R(\omega) = 0$ (no reflection at the base), equation 13 is, apart from the prefactor $2|S(\omega)|^2e^{-2\gamma|k|H}$, the same as equation 10.

4.2 Crosscoherence

Crosscoherence is defined as frequency-normalized crosscorrelation:

$$\begin{aligned} CH(z, z_a, \omega) &= \frac{u(z)u^*(z_a)}{|u(z)||u(z_a)|} \\ &\approx \frac{u(z)u^*(z_a)}{|u(z)||u(z_a)| + \epsilon'\langle|u(z)||u(z_a)|\rangle} \end{aligned} \tag{14}$$

Similar to equation 4, we use a regularization parameter ϵ' in the last equality in practice. In this study, we use $\epsilon' = 0.1\%$. For mathematical interpretation, using Taylor expansions of $\sqrt{1+X}$ and $1/\sqrt{1+X}$ for $X < 1$, the crosscoherence between $u(z)$ and $u(z_a)$ is given by

$$\begin{aligned} CH(z, z_a, \omega) &= \frac{u(z)u^*(z_a)}{|u(z)||u(z_a)|} = \frac{u(z)u^*(z_a)}{\sqrt{u(z)u^*(z)}\sqrt{u(z_a)u^*(z_a)}} = \frac{\sqrt{u(z)}\sqrt{u^*(z_a)}}{\sqrt{u^*(z)}\sqrt{u(z_a)}} \\ &= \sqrt{\frac{\left\{e^{ikz}e^{-\gamma|k|z} + e^{ik(2H-z)}e^{-\gamma|k\,(2H-z)}\right\}\left\{e^{-ikz_a}e^{-\gamma|k|z_a} + e^{-ik(2H-z_a)}e^{-\gamma|k|(2H-z_a)}\right\}}{\left\{e^{-ikz}e^{-\gamma|k|z} + e^{-ik(2H-z)}e^{-\gamma|k|(2H-z)}\right\}\left\{e^{ikz_a}e^{-\gamma|k|z_a} + e^{ik(2H-z_a)}e^{-\gamma|k|(2H-z_a)}\right\}}} \\ &= e^{ik(z-z_a)} \times \left[1 + \frac{1}{2}\sum_{n=1}^{\infty}\left\{\frac{e^{2ink(H-z)}e^{-2n\gamma|k|(H-z)}}{n!}A_{n-1}\right\}\right]\left[1 + \frac{1}{2}\sum_{n=1}^{\infty}\left\{\frac{e^{-2ink(H-z_a)}e^{-2n\gamma|k|(H-z_a)}}{n!}A_{n-1}\right\}\right] \\ &\quad \times \left[1 + \sum_{n=1}^{\infty}\left\{\frac{e^{-2ink(H-z)}e^{-2n\gamma|k|(H-z)}}{n!}A_n\right\}\right]\left[1 + \sum_{n=1}^{\infty}\left\{\frac{e^{2ink(H-z_a)}e^{-2n\gamma|k|(H-z_a)}}{n!}A_n\right\}\right], \end{aligned} \tag{15}$$

where $A_0 = 1$ and $A_n = (2n-1)!!/(-2)^n$. As for deconvolution interferometry, equation 15 does not depend on $S(\omega)$ and $R(\omega)$. For a complex number $z = re^{i\phi}$, the square root is defined as $\sqrt{z} = \sqrt{r}e^{i\phi/2}$. Furthermore, the waveforms of crosscoherence interferometry satisfies a clamped boundary condition at $z = z_a$ ($CH(z_a, z_a, \omega) = 1$, hence $CH(z_a, z_a, t) = \delta(t)$, and $CH(z_a, z_a, t) = 0$ for $t \neq 0$).
For $z_a = 0$ and $z_a = H$, equation 15 simplifies to

$$CH(z,0,\omega) = e^{ikz} \times \left[1 + \frac{1}{2}\sum_{n=1}^{\infty}\left\{\frac{e^{2ink(H-z)}e^{-2n\gamma|k|(H-z)}}{n!}A_{n-1}\right\}\right] \times \left[1 + \frac{1}{2}\sum_{n=1}^{\infty}\left\{\frac{e^{-2inkH}e^{-2n\gamma|k|H}}{n!}A_{n-1}\right\}\right]$$
$$\times \left[1 + \sum_{n=1}^{\infty}\left\{\frac{e^{-2ink(H-z)}e^{-2n\gamma|k|(H-z)}}{n!}A_{n}\right\}\right] \times \left[1 + \sum_{n=1}^{\infty}\left\{\frac{e^{2inkH}e^{-2n\gamma|k|H}}{n!}A_{n}\right\}\right], \quad (16)$$

$$CH(z,H,\omega) = e^{ik(z-H)} \times \left[1 + \frac{1}{2}\sum_{n=1}^{\infty}\left\{\frac{e^{2ink(H-z)}e^{-2n\gamma|k|(H-z)}}{n!}A_{n-1}\right\}\right] \times \left[1 + \sum_{n=1}^{\infty}\left\{\frac{e^{-2ink(H-z)}e^{-2n\gamma|k|(H-z)}}{n!}A_{n}\right\}\right], \quad (17)$$

respectively. Note that because of the complexity of crosscoherence interferometry, equations 15–17 contain pseudo events which propagate at slower velocities than the true velocity of the building. For example, equation 16 can be expanded into

$$\begin{aligned}
&CH(z,0,\omega)\\
&= e^{ikz}\left\{1 - \frac{1}{4}e^{-4\gamma|k|(H-z)} - \frac{1}{4}e^{-4\gamma|k|H}\right\} + \frac{1}{4}e^{-ikz}e^{-2\gamma|k|(2H-z)} + \frac{1}{4}e^{3ikz}e^{-2\gamma|k|(2H-z)}\\
&- \frac{1}{2}e^{-ik(2H-3z)}e^{-2\gamma|k|(H-z)} - \frac{1}{2}e^{ik(2H+z)}e^{-2\gamma|k|H} + \frac{1}{2}e^{ik(2H-z)}e^{-2\gamma|k|(H-z)} + \frac{1}{2}e^{-ik(2H-z)}e^{-2\gamma|k|H}\\
&+ \frac{3}{8}e^{-ik(4H-5z)}e^{-4\gamma|k|(H-z)} - \frac{1}{8}e^{-ik(4H-z)}e^{-4\gamma|k|H} - \frac{1}{4}e^{ik(4H-z)}e^{-2\gamma|k|(2H-z)} - \frac{1}{4}e^{-ik(4H-3z)}e^{-2\gamma|k|(2H-z)}\\
&+ \frac{3}{8}e^{-ik(4H-z)}e^{-4\gamma|k|H} - \frac{1}{8}e^{ik(4H-3z)}e^{-4\gamma|k|(H-z)} + O(e^{-6\gamma|k|(H-z)}). \quad (18)
\end{aligned}$$

The terms $e^{3ikz}e^{-2\gamma|k|(2H-z)}/4$ and $-e^{-ik(2H-3z)}e^{-2\gamma|k|(H-z)}/2$ indicate waves that propagate at one third of the true velocity, and the term $3e^{-ik(4H-5z)}e^{-4\gamma|k|(H-z)}/8$ at one fifth. These unphysical waves complicate the estimation of the velocity of traveling waves by applying crosscoherence interferometry to earthquake data.

4.3 Comparison of deconvolution, crosscorrelation, and crosscoherence

Each type of interferometry has different properties (e.g., amplitude or complexity). It follows from expressions 4, 11, and 14 that in the frequency domain the phases obtained by interferometry based on deconvolution, crosscorrelation, and crosscoherence are the same. The spectral amplitude is different, though, and this leads to different waveforms in the time domain. We list in Table 2 the amplitudes of the first four causal waves propagating at the true velocity of the building for observed record, deconvolution, crosscorrelation, and crosscoherence (equations 1, 9, 12, and 16, respectively). For crosscorrelation interferometry, we calculate the amplitudes of the traveling waves in Appendix B using Taylor expansions. Although the amplitudes of crosscorrelation are complicated due to the reflection coefficient $R(\omega)$ and the power spectrum $|S(\omega)|^2$, the ratios of amplitudes for each pair of traveling waves are the same as those for observed records. The amplitudes of the waveforms obtained by crosscoherence are independent of incoming waveform $S(\omega)$ and reflection coefficient $R(\omega)$, but the ratio of amplitudes varies between each pair of traveling waves. Therefore, estimating attenuation of the building using crosscoherence interferometry is problematic. Since the amplitudes of the deconvolved waveforms are independent of $S(\omega)$ and $R(\omega)$ and depend exponentially on the traveled distance, deconvolution interferometry can be used to estimate attenuation of the building.

We numerically compute synthetic waveforms excited at 0 m by an impulsive source ($S(\omega) = 1$) based on equation 1 shown in Figure 6a. In the computation, we use the following parameters: $H = 100$ m, $R(\omega) = 0.5$, $Q = 3000$, and $c = 200$ m/s. In applying seismic interferometry, we compute deconvolution ($\{u(z)u^*(0)\} / \{|u(0)|^2 + \epsilon\langle|u(0)|^2\rangle\}$: Figure 6b), crosscorrelation ($u(z)u^*(0)$: Figure 6c), and crosscoherence ($\{u(z)u^*(0)\} / \{|u(z)||u(0)| + \epsilon'\langle|u(z)||u(0)|\rangle\}$: Figure 6d), where $\epsilon = 1\%$ and $\epsilon' = 0.1\%$, using the synthetic waveforms shown in Figure 6a. In Figures 6b–6d, the virtual source is at $z = 0$ m. Deconvolved waveforms (Figure 6b) arrive at the same time as the waves in the synthetic records, but the polarization is reversed when the wave is reflected at $z = 0$ m due to the clamped boundary condition. In crosscorrelation interferometry (Figure 6c), the causal waves arrive at the same time as the waves in the synthetic records (Figure 6a), and the acausal waves are kinematically identical to the time-reversed causal waves. Although for simplicity we use $S(\omega) = 1$ in Figure 6, the in-

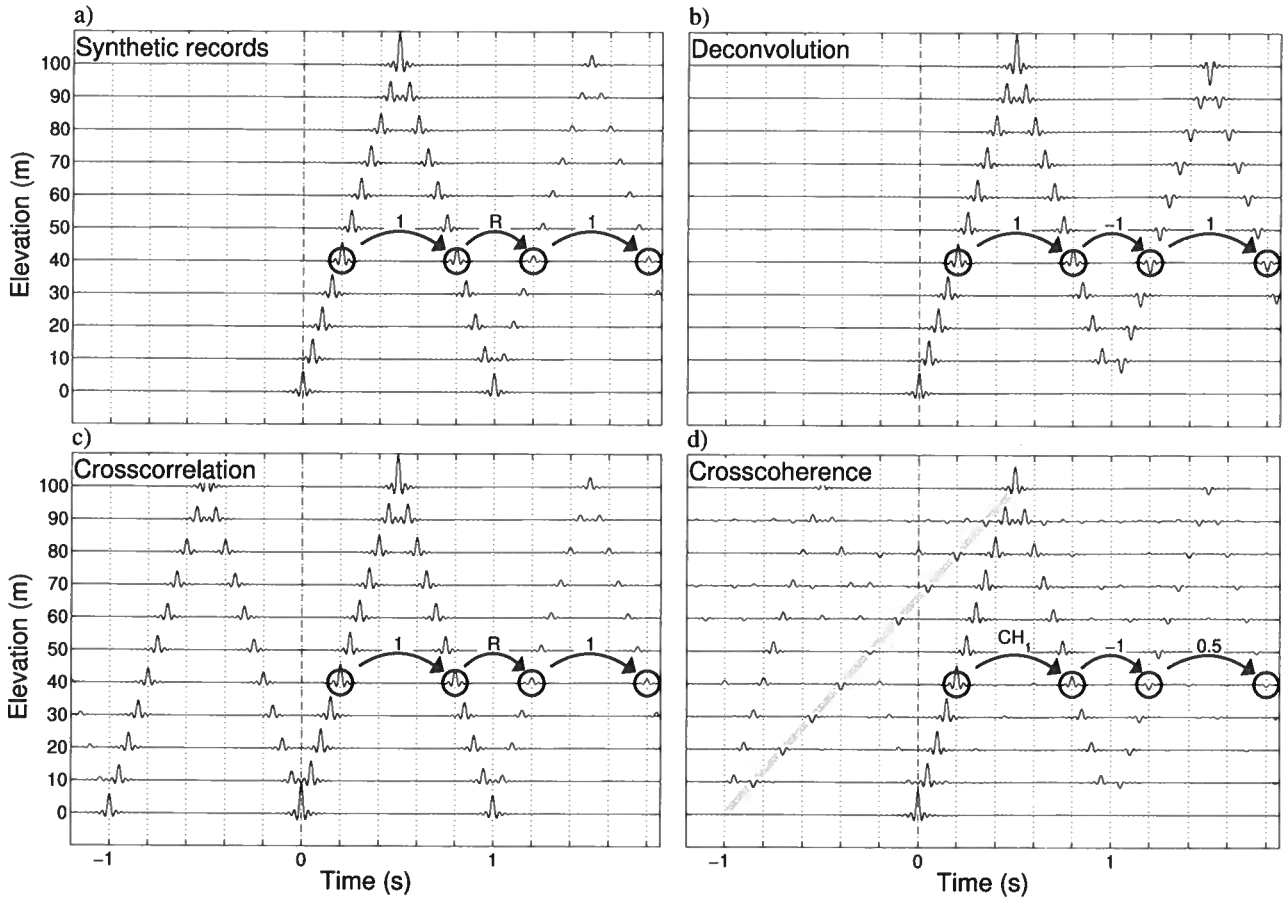

Figure 6. (a) Synthetic waveforms based on equation 1. We numerically calculate waveforms with an impulse response ($S(\omega) = 1$) at $t = 0$ s at 0 m, $R(\omega) = 0.5$, $Q = 3000$, $H = 100$ m, and $c = 200$ m/s. Interferometric waveforms by computing deconvolution (panel b: equation 9), crosscorrelation (panel c: equation 12), and crosscoherence (panel d: equation 16) using waveforms shown in panel (a). The virtual source for interferometry is at the 0-m receiver. We apply a bandpass filter 0.5-1-30-40 Hz after computing each waveform. The circles in each panel highlight four waves which are discussed in the main text. The numbers near each arrow indicate the ratio of the amplitude difference between two waves highlighted by the circles apart from the attenuation expected from the traveling distance at the correct velocity. To estimate the ratio of amplitude in panel (d), we ignore wavefields which attenuate faster than $e^{-6\gamma|k|(H-z)}$, and $CH_1 = 2/(4 - e^{-4\gamma|k|(H-z)} - e^{-4\gamma|k|H})$ where $z = 40$ m. Amplitudes in each panel are normalized by the amplitude of the first highlighted wave (at t=0.2 s). The gray line in panel (d) shows the wave which propagates at 66.67 m/s.

coming wave complicates the crosscorrelated waveforms when we use real earthquake data, and picking the arrival times of the traveling waves may be difficult in that case. Crosscoherence interferometry creates traveling waves which propagate at slower velocities than true velocity $c = 200$ m/s. In Figure 6d, the gray line highlights the wave $-e^{-ik(2H-3z)}e^{-2\gamma|k|(H-z)}/2$, which travels with one third of the true wave speed (66.7 m/s). To estimate the velocity of the traveling waves, therefore, deconvolution interferometry is useful.

We highlight the amplitudes of the waves in Figure 6 with the circles. A comparison of Figures 6a and 6b shows that the ratios of the amplitudes of the synthetic records and deconvolved waves within the first two circles are the same, but the ratios in the second and third circles are different. The reflection coefficient at 0 m of the synthetic records is $R(\omega)$ while the reflection coefficient of waves obtained by deconvolution interferometry is -1; see the numbers next to the arrows in Figures 6a and 6b. The difference between the reflection coefficients implies that deconvolved waveforms are independent from the ground coupling, and the decay of amplitudes of the waves are only related to the attenuation of the building. The ratios of the amplitudes of the waves highlighted by the circles in crosscorrelation interferometry are the same as those in the synthetic records; see the numbers next to the arrows in Figures 6a and 6c. Hence, both the building and the soil-structure cou-

Table 2. Amplitudes of traveling waves obtained from observed records and computed by seismic interferometry based on deconvolution, crosscorrelation, and crosscoherence for $z_a = 0$ (equations 1, 9, 12, and 16). We compute the amplitudes of crosscorrelation interferometry in Appendix B. For crosscoherence interferometry we ignore wavefields which attenuate faster than $e^{-6\gamma|k|(H-z)}$.

Phase	Observed record	Deconvolution	Crosscorrelation	Crosscoherence
e^{ikz}	$S(\omega)e^{-\gamma\|k\|z}$	$e^{-\gamma\|k\|z}$	C_1	$1-\frac{1}{4}e^{-4\gamma\|k\|(H-z)}-\frac{1}{4}e^{-4\gamma\|k\|H}$
$e^{ik(2H-z)}$	$S(\omega)e^{-\gamma\|k\|(2H-z)}$	$e^{-\gamma\|k\|(2H-z)}$	C_2	$\frac{1}{2}e^{-2\gamma\|k\|(H-z)}$
$e^{ik(2H+z)}$	$S(\omega)R(\omega)e^{-\gamma\|k\|(2H+z)}$	$-e^{-\gamma\|k\|(2H+z)}$	C_3	$-\frac{1}{2}e^{-2\gamma\|k\|H}$
$e^{ik(4H-z)}$	$S(\omega)R(\omega)e^{-\gamma\|k\|(4H-z)}$	$-e^{-\gamma\|k\|(4H-z)}$	C_4	$-\frac{1}{4}e^{-2\gamma\|k\|(2H-z)}$

$$C_1 = |S(\omega)|^2 e^{-\gamma|k|z}\left\{1+R(\omega)e^{-4\gamma|k|H}\right\}\left\{\sum_{n=0}^{\infty}|R(\omega)|^{2n}e^{-4n\gamma|k|H}\right\}$$

$$C_2 = |S(\omega)|^2 e^{-\gamma|k|(2H-z)}\left\{1+R(\omega)e^{-4\gamma|k|H}\right\}\left\{\sum_{n=0}^{\infty}|R(\omega)|^{2n}e^{-4n\gamma|k|H}\right\}$$

$$C_3 = |S(\omega)|^2 R(\omega)e^{-\gamma|k|(2H+z)}\left\{1+R(\omega)e^{-4\gamma|k|H}\right\}\left\{\sum_{n=0}^{\infty}|R(\omega)|^{2n}e^{-4n\gamma|k|H}\right\}$$

$$C_4 = |S(\omega)|^2 R(\omega)e^{-\gamma|k|(4H-z)}\left\{1+R(\omega)e^{-4\gamma|k|H}\right\}\left\{\sum_{n=0}^{\infty}|R(\omega)|^{2n}e^{-4n\gamma|k|H}\right\}$$

pling influence the amplitudes of crosscorrelated waveforms. In crosscoherence interferometry (Figure 6d), the ratios of the amplitudes of the waves within the circles are different from either synthetic records or deconvolution interferometry. When we consider the amplitudes of each interferometry, deconvolution interferometry is useful for estimating the attenuation of the building.

Based on equations 11–18, Table 2, and Figure 6, we conclude that deconvolution interferometry is suitable for application to earthquake records to estimate the velocity and attenuation of the building. Crosscorrelated waveforms depend on the incoming wave $S(\omega)$ and the ground coupling $R(\omega)$. Crosscoherence interferometry creates pseudo events, and the decay of amplitudes of waveforms reconstructed by crosscoherence is not exponentially depending on the traveled distances. Therefore, these types of interferometry are not appropriate to estimate velocity and attenuation.

Snieder et al. (2006a) show that the wavefields obtained from deconvolution interferometry satisfy the same wave equation as the wavefield of the real building for an external source. Using this idea, we explain why crosscoherence interferometry creates unphysical events. Following Snieder et al. (2006a), we denote the linear differential operator that defines the wave propagation by $L(z)$ (e.g., for the one-dimensional wave equation $L(z) = d^2/dz^2 + \omega^2/c^2(z)$). The operator acts on the space variable z. For an internal source at z_0, the wavefield $u(z)$ (equation 1) satisfies $L(z)u(z) = F(z_0)$ where F is the excitation at z_0. For an external source, on the other hand, $u(z)$ satisfies $L(z)u(z) = 0$; this homogeneous equation applies to earthquake data. Applying the operator $L(z)$ to equations 3, 11, and 14, respectively, gives

$$L(z)D(z,z_a,\omega) = L(z)\frac{u(z)}{u(z_a)} = \frac{1}{u(z_a)}L(z)u(z) = 0, \tag{19}$$

$$L(z)C(z,z_a,\omega) = L(z)u(z)u^*(z_a) = \{L(z)u(z)\}u^*(z_a) = 0, \tag{20}$$

$$L(z)CH(z,z_a,\omega) = L(z)\frac{u(z)u^*(z_a)}{|u(z)||u(z_a)|} = \frac{u^*(z_a)}{|u(z_a)|}L(z)\left(\frac{u(z)}{|u(z)|}\right) \neq 0 \tag{21}$$

where we used that $L(z)$ acts on the z-coordinate only. Crosscoherence interferometry (equation 21) does not produce a wavefield that satisfies the wave equation of the real building, but deconvolution and crosscorrelation interferometry do satisfy the wave equation. Equation 21 shows that crosscoherence interferometry creates unphysical internal sources that complicate wavefields obtained from crosscoherence.

5 DECONVOLVED WAVEFORMS GENERATED FROM AN EARTHQUAKE

As an illustration of the data analysis, we first show the application of deconvolution interferometry to the records of earthquake No. 5. We first estimate whether the reflection point of the traveling wave is at R1 or R2 because the building has a penthouse (Figure 2). Figure 7 shows waveforms deconvolved by the motion recorded at the first floor (equation 9) for the EW and NS components. We apply a 0.4-0.5-45-50 Hz sine-squared bandpass filter to the deconvolved waveforms. Because the physical property at the basement is different from the

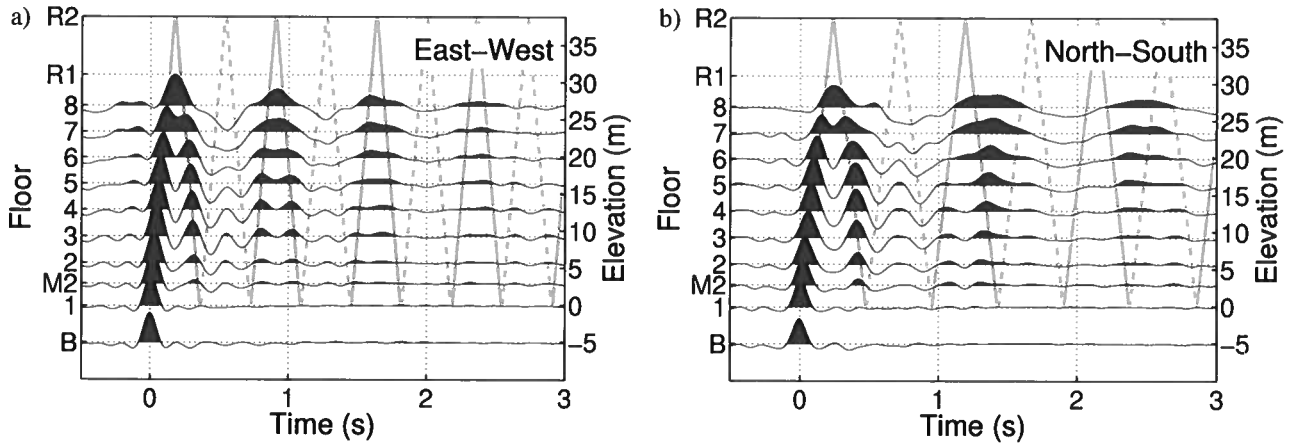

Figure 7. Deconvolved waveforms, in which the virtual source is at the first floor, of earthquake No. 5 after applying a bandpass filter 0.4-0.5-45-50 Hz in the (a) EW and (b) NS components. Gray lines indicate the arrival time of traveling waves with the velocity that is estimated from the least-squares fitting of the first upgoing and downgoing waves. We repeat the gray lines after the second traveling waves based on equation 9. Solid gray lines highlight the waves in the positive polarization and dashed gray lines the waves in the negative polarization.

other floors, we do not deconvolve with the motion in the basement in this study. During the first several hundred milliseconds in Figure 7, the waveforms depict a traveling wave excited at the first floor at $t = 0$ s. The wave is reflected off the top of the building and propagates down, and then reflects again at the first floor with the opposite polarization because the reflection coefficient of the deconvolved waves at the first floor is equal to -1 (according to equation 9). While reverberating between the first floor and the top of the building, higher frequencies attenuate and the fundamental mode is dominant for later times.

To estimate the velocity of the traveling wave and the location of the reflection point, we compute the travel-time curve using a least-squares fitting of the picked travel times on the first upgoing and downgoing waves at each floor (the first two solid gray lines in Figure 7). For picking the travel times, we seek the maximum amplitude time in each traveling wave. We repeatedly draw the reverberating travel-wave paths based on equation 9 using the velocity estimated from the first upgoing and downgoing waves (in Figure 7). To avoid large uncertainties, we use the picked travel times between floors one through five in the EW component and between floors one through six in the NS component because at these floors the positive amplitudes of the upgoing and downgoing waves do not overlap. Both travel-time curves in the EW and NS components indicate that the waves reflect off the top of the penthouse (R2), and the velocity is 214 ± 9 m/s in the EW direction and 158 ± 7 m/s in the NS direction, respectively, where the uncertainties are one standard deviation of measurements. Because the NS side is shorter, the velocity in the NS component is slower. The deconvolved waveforms in the NS component show large deviation from expected arrival times shown in the gray lines in Figure 7b, which indicates that the frequency dispersion in the NS component is larger than in the EW component. In the following, we focus on the EW-component analysis.

In Appendix C, we apply crosscorrelation and crosscoherence interferometry to records in the EW component. Because of the power spectrum of the incoming wave, we cannot obtain traveling waves using crosscorrelation interferometry (Figure C1c). We can estimate the velocity of traveling waves from the waveforms created by crosscoherence interferometry, but cannot estimate attenuation because the fundamental mode is not reconstructed (Figure C1d).

Next, we deconvolve the wavefields with the motion recorded by the receiver at the fourth floor (Figure 8), where the fourth-floor receiver behaves as a virtual source and satisfies a clamped boundary condition; then we apply the same bandpass filter as used in Figure 7. We can interpret waveforms in Figure 8 in two ways, which are explained using Figures 8a and 8b. We obtain upgoing and downgoing waves, which interfere at the fourth floor. At the circle in Figure 8a, the upgoing wave from the bottom and downgoing wave from the top cancel, and the deconvolved waveform at the fourth floor vanishes for nonzero time, which is due to the fact that the waveform at the virtual source is a band-limited delta function.

The fourth floor also behaves as the reflection point with reflection coefficient -1 (equation 3), which means we can separate the building to two parts: above and

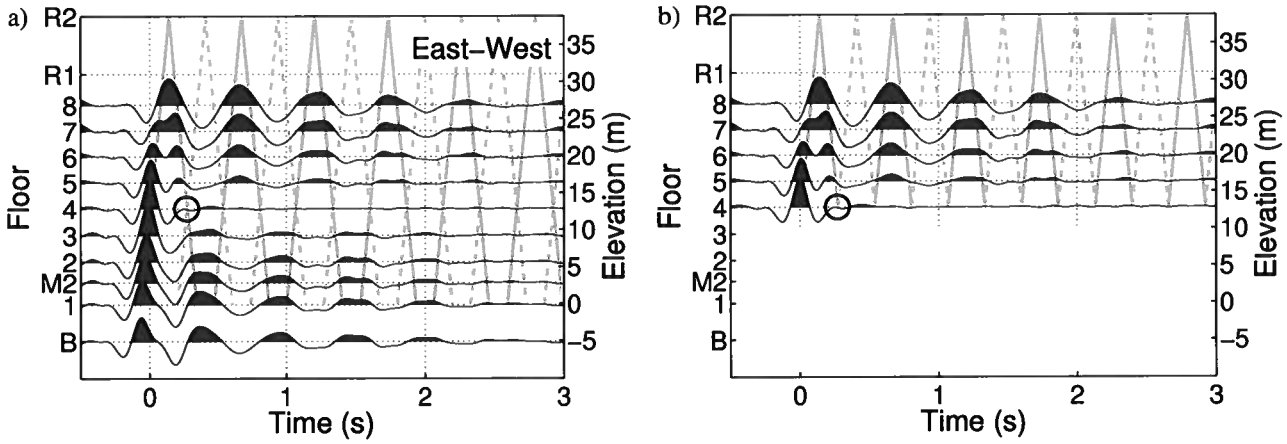

Figure 8. (a) Deconvolved waveforms, in which the virtual source is at the fourth floor, of earthquake No. 5 after applying a bandpass filter 0.4-0.5-45-50 Hz in the EW component. The gray lines indicate the travel paths expected from the velocity 195 m/s and equation 3. Solid gray lines highlight the waves in the positive polarization and dashed gray lines the waves in the negative polarization. The circle indicates the point where the positive and negative polarization waves cancel. (b) The same waveforms shown in panel (a) but omitting deconvolved waveforms lower than the fourth floor. When we focus on the cut-off building above the fourth floor, the reflection coefficient at the circle is -1.

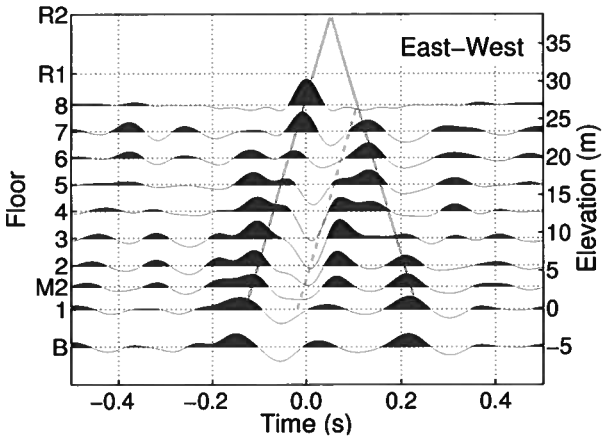

Figure 9. Deconvolved waveforms, in which the virtual source is at the eighth floor, of earthquake No. 5 after applying a bandpass filter 0.4-0.5-12-16 Hz in the EW component. The gray lines show the travel time of the waves propagating at 210 m/s. The positions of the lines are estimated from equation 3. The thick lines have positive polarization and the dashed line negative polarization.

below the virtual source. Figure 8b shows the building above the virtual source. At the circle in Figure 8b, the downgoing wave with positive polarization from the top is perfectly reflected as the negative-polarization upgoing wave. Since we obtain an upgoing wave from the virtual source and reverberations between the fourth floor and the top of the building, this example of interferometry creates the response of a cut-off building that is independent from the structure below the fourth floor (see equation 3 and Figure 8b). Similar to Figure 7, the fundamental mode for the cut-off building (equation 3 and Figure 5a) is dominant for later times in Figure 8b. Note the similarity between Figures 7a and 8b; both figures show traveling waves and fundamental mode. The period of the normal mode in Figure 8b is shorter than in Figure 7a as is expected from equation 6. Interestingly, because the cut-off building is independent from the structure below the fourth floor, this fictitious building is useful for detecting local structure and local damage of the building.

Applying a least-squares fit of the travel times of the first upgoing wave at the first to fourth floors ($n = 0$ and $0 \leq z \leq z_a$ in equation 3), we obtain the velocity of traveling waves to be 195 ± 25 m/s. To avoid large uncertainties, we use the travel times at the first to fourth floors to estimate the velocity. At these floors, the upgoing waves are well separated from the downgoing waves. For the cut-off building, by estimating the velocity from the deconvolved waveforms at the floors only below or above the virtual source, we can obtain the velocity which is only related to the structure below or above the virtual source because the virtual source satisfies the clamped boundary conditions. The structure between the first and fourth floors (below the virtual source) contributes to the estimation of this velocity. This is the main reason why the mean velocities estimated from Figures 7 and 8 differ, but this discrepancy is not statistically significant.

We apply deconvolution interferometry to the mo-

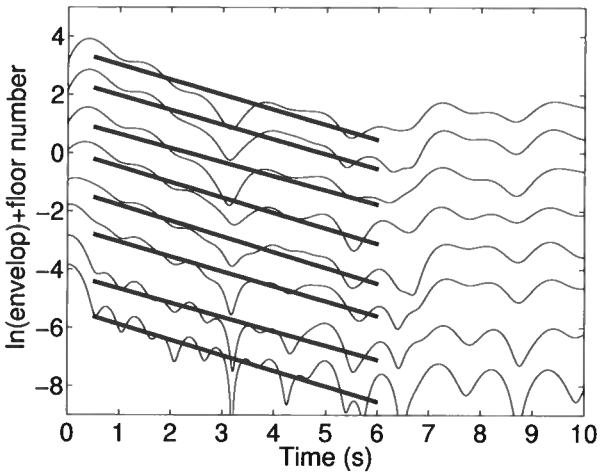

Figure 10. Natural logarithm of the envelopes (thin line) and linear fitting using the least-squares method (thick line). We show envelopes at only the middle-second to eighth floors because the first floor is a virtual source and the basement floor has a different physical condition.

tion recorded by the receiver at the eighth floor, which is the highest receiver in the building (Figure 9). Snieder and Şafak (2006) found that this procedure gives only one pair of upgoing and downgoing waves; however, since the eighth-floor receiver is about 12 m below the top of the building (R2), the deconvolved waveforms in Figure 9 satisfy equation 3 instead of equation 10. In Figure 9, we apply a 0.4-0.5-12-16 Hz sine-squared bandpass filter to deconvolved waveforms. Because the quality of the data is not enough to accurately pick travel times, we cannot estimate the wave velocity from Figure 9. The gray lines in Figure 9 indicate the arrival time of the traveling waves at 210 m/s as inferred from Figure 7a.

From the resonant waves in Figures 7 and 8, we can estimate Q following the method proposed by Snieder and Şafak (2006). Figure 10 shows the logarithmic envelopes of the deconvolved waveforms in Figure 7a at each floor except the basement and the first floor (thin lines), and their least-squares linear fits (thick lines). Because we use the waveforms deconvolved with the first floor, the estimated Q is for the entire building. We assume Q is constant in the entire building because the wavelength in the frequency range used is much longer than the height of the building (the resonant frequency is 1.17 Hz). In Figure 10, the average slope of the fitting lines indicates that $Q^{-1} = 0.098$ based on the fundamenta-mode frequency 1.17 Hz.

6 MONITORING A BUILDING USING 17 EARTHQUAKES

Using the 17 earthquakes recorded in the two weeks (Table 1 and Figure 2), we monitor the change in the shear-wave velocity of the building. Figure 11 illustrates the waveforms which are deconvolved by the wave recorded at the first floor of each earthquake (left panel) and the power spectra of the deconvolved waveforms (right panel). The virtual source is at the first floor (similar to Figure 7a). The frequency component around 1.5 Hz shows the fundamental mode and around 5 Hz the first overtone. From the bottom to top traces for each earthquake, the traces are aligned from the first to eighth floors, and the waves propagating between the bottom and the top are visible. Comparing the fundamental-mode waves for later times among earthquakes, we can roughly estimate changes in velocity from a visual inspection, e.g., the velocities in earthquakes 5, 8, 10, and 12 are slower. The earthquakes, which show slower velocity, indicate lower normal-mode frequencies as shown by Todorovska and Trifunac (2008b). The ratio of the reductions in velocity and frequency are almost the same.

The amplitude of each resonant wave provides an estimate of attenuation. For example, the attenuation is strong for earthquake No. 5 because the amplitude of the fundamental mode fades away at around 2.5 s. For some earthquakes, although the fundamental mode is dominant at later times, deconvolved waveforms still show upgoing and downgoing waves (e.g., at 2.5 s of earthquake No. 15), which implies either that the attenuation at higher frequency is relatively weak at the time these earthquakes occurred, or that the overtones are strongly excited. We estimate the velocity of traveling waves using the method that is the same as for Figure 7a (the black symbols in Figure 12). The black marks in Figure 12b illustrate a negative correlation between the velocities and the maximum acceleration of observed records.

To estimate velocities, we also apply coda-wave interferometry as developed by Snieder et al. (2002) to deconvolved waveforms. Coda-wave interferometry allows us to estimate a relative velocity change from two waveforms by computing crosscorrelation. Coda-wave interferometry has been applied to multiplets [e.g., *Poupinet et al.*, 1984; *Snieder and Vrijlandt*, 2005] and to waveforms which are obtained by seismic interferometry [e.g., *Sens-Schönfelder and Wegler*, 2006]. By using coda-wave interferometry, we estimate velocities from the deconvolved waves between 1-3 s in Figure 11. The waves in the time interval are mostly the fundamental mode. We choose earthquake No. 5 as a reference and estimate the relative velocity for each earthquake from the reference earthquake. In coda-wave interferometry, we stretch and interpolate one waveform and compute a correlation coefficient (CC) with a reference waveform (u_{ref}) in the time domain (Figure 13) (Lobkis

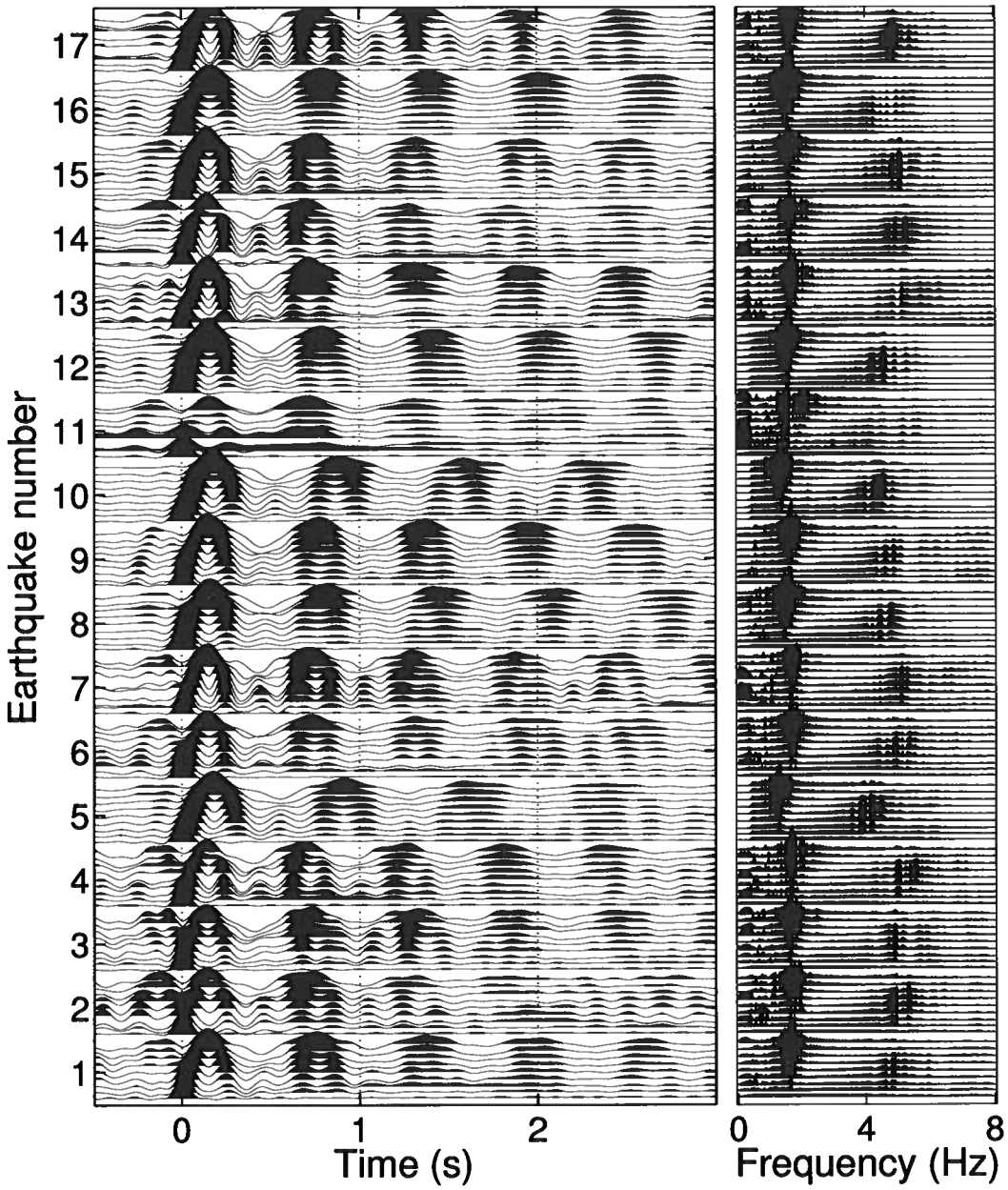

Figure 11. The waveforms of each earthquake in the EW component after deconvolution with the waves recorded on the first floor in the time domain (left panel), and the power spectra of the waveforms (right panel). We apply a bandpass filter 0.4-0.5-45-50 Hz. We show the traces from the first floor to the eighth floor in each earthquake.

and Weaver, 2003; Hadziioannou et al., 2009; Weaver et al., 2011):

$$CC(\alpha) = \frac{\int_{t_1}^{t_2} u(t(1-\alpha))u_{ref}(t)dt}{\sqrt{\int_{t_1}^{t_2} u^2(t(1-\alpha))dt \int_{t_1}^{t_2} u_{ref}^2(t)dt}}, \quad (22)$$

where t_1 and t_2 denote the time window, and in this study we use 1-3 s. At the maximum of $CC(\alpha)$,

$$\alpha = \frac{v - v_{ref}}{v_{ref}}, \quad (23)$$

where v and v_{ref} are the velocities at each earthquake and the reference earthquake, respectively. For comput-

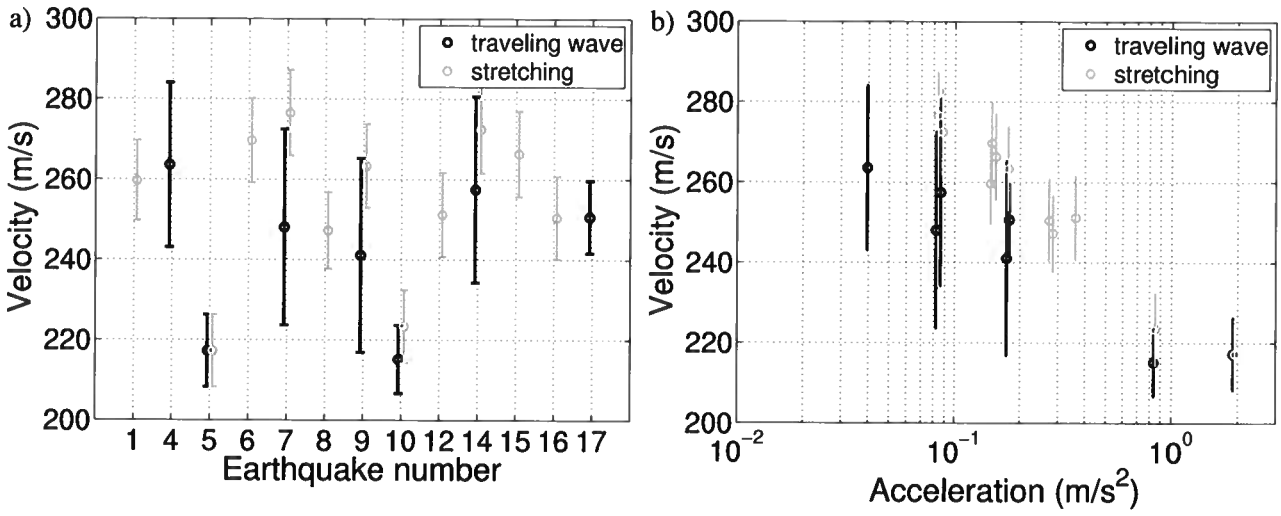

Figure 12. (a) Velocities estimated from traveling waves (black) and by coda-wave interferometry using the stretching method (gray) of each earthquake. The error bars of the velocities estimated from traveling waves (black) are one standard deviation of individual arrival times, and the bars in the stretching method are calculated by $\sqrt{\sigma_5^2 + \sigma_{\delta v}^2}$. We illustrate only velocities which have smaller than 10% velocity uncertainty (for traveling waves) or are estimated from more than three traces which have a correlation coefficient greater than 0.9 (for the stretching method). (b) Crossplot of estimated velocities with maximum acceleration observed at the first floor.

ing CC, we apply the same bandpass filter as for Figure 11, and the waves are mostly the fundamental mode.

Note that even though we use the waves between 1-3 s for applying coda-wave interferometry, the origin time for stretching is at time 0 s. The gray symbols in Figure 12 are the velocities estimated by coda-wave interferometry using the stretching method. Because we use earthquake No. 5 as a reference (u_{ref}), the estimated velocities of each earthquake using the stretching method (the gray symbols in Figure 12) are the relative velocities with respect to the velocity of earthquake No. 5. Therefore, the velocities estimated from traveling waves and by the stretching method in earthquake No. 5 are, by definition, the same. The standard deviation of the velocity change (the gray bars in Figure 12) for each earthquake is estimated by $\sqrt{\sigma_5^2 + \sigma_{\delta v}^2}$, where σ_5 is the standard deviation of the velocity measurements estimated from traveling waves at different floors in earthquake No. 5, and $\sigma_{\delta v}$ is the standard deviation of the relative velocity measurements between each earthquake and earthquake No. 5 estimated by the stretching method at different floors. The gray symbols in Figure 12b indicate that the velocities obtained by the stretching method also have a negative correlation with the acceleration, but the slope is steeper than that for the traveling waves. Since the waves in 1-3 s are mostly fundamental mode and the main difference between the traveling waves and the fundamental mode is the frequency (the traveling waves contain higher frequencies than the fundamental mode), the difference in slopes indicates dispersion. The steeper slope of the gray symbols in Figure 12b indicates that the imprint of acceleration is stronger for lower frequencies than for higher frequencies.

7 CONCLUSION

We obtain impulse responses of the building and their changes in velocity by applying deconvolution interferometry to 17 earthquake records. We estimate the reflection point of the traveling wave, which is at the top of the penthouse, from the deconvolved waveforms. Since the shape of the ground plan of the building is rectangular, the velocities of the traveling wave in two orthogonal horizontal components are different. According to the properties of deconvolution, the responses are independent from the soil-structure coupling and the effect of wave propagation below the bottom receiver. Because the cut-off building is independent of the structure below the virtual source, one might be able to use the cut-off building to investigate local structure and local damage. Crosscorrelation interferometry cannot separate the building response from the soil-building coupling and the wave propagation below the virtual source. Crosscoherence interferometry produces unphysical wavefields propagating at slower velocity than the true wave speed of the real building, and the attenuation of the waveforms obtained from crosscoherence do not correspond to the travel distance of the waves. Hence, in contrast to deconvolution interferometry, these types of interferometry are not appropriate

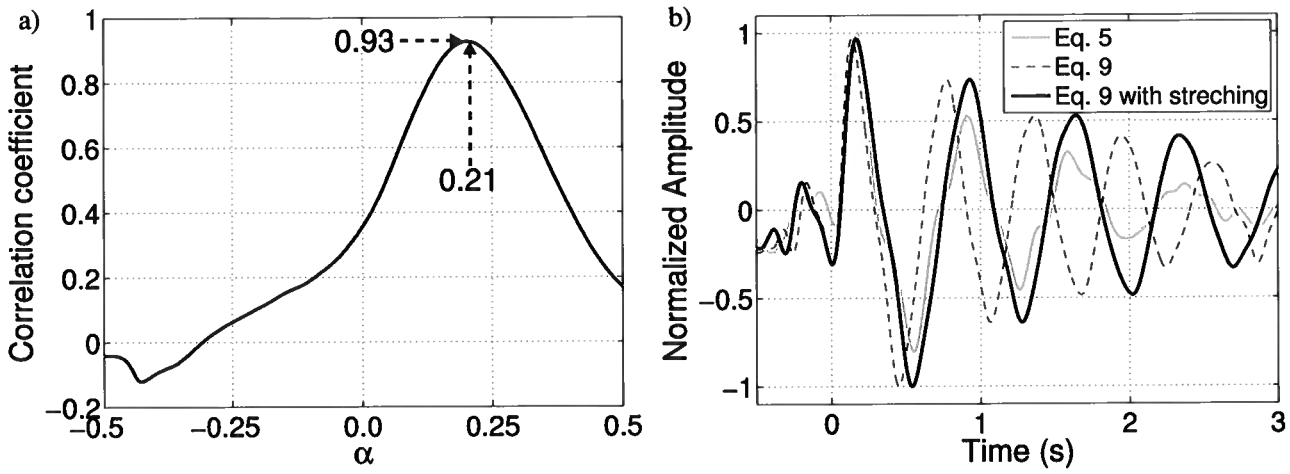

Figure 13. (a) Correlation coefficient (CC) as a function of α (equation 22) between deconvolved waveforms computed from earthquakes No. 5 and No. 9 at the eighth floor. Dashed arrows point to the maximum CC value and its value of α. For computing CC, we use only the waveforms from 1.0 s to 3.0 s. (b) Deconvolved waveforms at the eighth floor of earthquakes No. 5, No. 9, and No. 9 with stretching for $\alpha = 0.21$ (see panel (a)).

for applying to earthquake records for estimating velocities and attenuation of buildings. We estimate velocities from both traveling waves and the fundamental mode of deconvolved waveforms. The velocities estimated from each earthquake and maximum acceleration have a negative correlation.

ACKNOWLEDGMENTS

We thank sponsor companies of the Consortium Project on Seismic Inverse Methods for Complex Structures. We thank JMA for providing the earthquake catalog. We are grateful to Diane Witters for her help in preparing this manuscript.

REFERENCES

Aki, K., 1957, Space and time spectra of stationary stochastic waves, with special reference to microtremors: Bull. Earthq. Res. Inst., **35**, 415–456.

Aki, K., and P. G. Richards, 2002, Quantitative Seismology, 2 ed.: Univ. Science Books.

Biot, M., 1933, Theory of elastic systems vibrating under transient impulse with an application to earthquake-proof buildings: Proc. Natl. Acad. Sci., **19**, 262–268.

Carder, D. S., 1936, Observed vibrations of buildings: Bull. Seismol. Soc. Am., **26**, 245–277.

Clinton, J. F., S. C. Bradford, T. H. Heaton, and J. Favela, 2006, The observed wander of the natural frequencies in a structure: Bull. Seismol. Soc. Am., **96**, 237–257.

Şafak, E., 1995, Detection and identification of soil-structure interraction in buildings from vibration recordings: J. Struct. Eng., **121**, 899–906.

Derode, A., E. Larose, M. Campillo, and M. Fink, 2003, How to estimate the Green's function of a heterogeneous medium between two passive sensors? Application to acoustic waves: Applied Physics Letters, **83**, 3054–3056.

Hadziioannou, C., E. Larose, O. Coutant, P. Roux, and M. Campillo, 2009, Satability of monitoring weak changes in multiply scattering media with ambient noise correlation: Laboratory experiments: J. Acoust. Soc. Am., **125**, 3688–3695.

Ivanović, S. S., M. D. Trifunac, and M. I. Todorovska, 2000, Ambient vibration tests of structures–a review: ISET J. Earthq. Tech, **37**, 165–197.

Kohler, M. D., P. M. Davis, and E. Şafak, 2005, Earthquake and ambient vibration monitoring of the steel-frame UCLA Factor building: Earthquake Spectra, **21**, 715–736.

Kohler, M. D., T. H. Heaton, and S. C. Bradford, 2007, Propagating waves in the steel, moment-frame Factor building recorded during earthquakes: Bull. Seismol. Soc. Am., **97**, 1334–1345.

Lobkis, O. I., and R. L. Weaver, 2001, On the emergence of the Green's function in the correlations of a diffuse field: J. Acoust. Soc. Am., **110**, 3011–3017.

———, 2003, Coda-wave interferometry in finite solids: Recovery of P-to-S conversion rates in an elastodynamic billiard: Phys. Rev. Lett., **90**, 254302.

Michel, C., P. Guéguen, and P.-Y. Bard, 2008, Dynamic parameters of structures extracted from ambient vibration measurements: An aid for the seismic vulnerability assessment of existing buildings in mod-

erate seismic hazard regions: Soil Dyn. Earthquake Eng., **28**, 593–604.

Nakata, N., and R. Snieder, 2011, Near-surface weakening in Japan after the 2011 Tohoku-Oki earthquake: Geophys. Res. Lett., **38**, L17302.

———, 2012a, Estimating near-surface shear-wave velocities in Japan by applying seismic interferometry to KiK-net data: J. Geophys. Res., **117**, B01308.

———, 2012b, Time-lapse change in anisotropy in Japan's near surface after the 2011 Tohoku-Oki earthquake: Geophys. Res. Lett., **39**, L11313.

Nakata, N., R. Snieder, T. Tsuji, K. Larner, and T. Matsuoka, 2011, Shear-wave imaging from traffic noise using seismic interferometry by cross-coherence: Geophysics, **76**, SA97–SA106.

Oyunchimeg, M., and H. Kawakami, 2003, A new method for propagation analysis of earthquake waves in damaged buildings: evolutionary normalized input-output minimization (NIOM): J. Asian. Archit. Build., **2**, 9–16.

Paul, A., M. Campillo, L. Margerin, and E. Larose, 2005, Empirical synthesis of time-asymmetrical Green functions from the correlation of coda waves: J. Geophys. Res., **110**, B08302.

Poupinet, G., W. L. Ellsworth, and J. Frechet, 1984, Monitoring velocity variations in the crust using earthquake doublets: An application to the Calaveras fault, California: J. Geophys. Res., **89**, 5719–5731.

Prieto, G. A., J. F. Lawrence, A. I. Chung, and M. D. Kohler, 2010, Impulse response of civil structures from ambient noise analysis: Bull. Seismol. Soc. Am., **100**, 2322–2328.

Schiff, A., and J. L. Bogdanoff, 1967, Analysis of current methods of interpreting strong-motion accelerograms: Bull. Seismol. Soc. Am., **57**, 857–874.

Schuster, G. T., J. Yu, J. Sheng, and J. Rickett, 2004, Interferometric/daylight seismic imaging: Geophys. J. Int., **157**, 838–852.

Sens-Schönfelder, C., and U. Wegler, 2006, Passive image interferometry and seasonal variations of seismic velocities at Merapi Volcano, Indonesia: Geophys. Res. Lett., **33**, L21302.

Sezawa, K., and K. Kanai, 1935, Energy dissipation in seismic vibrations of actual buildings: Bull. Earthq. Res. Inst., **13**, 925–941.

Snieder, R., 2004, Extracting the Green's function from the correlation of coda waves: A derivation based on stationary phase: Phys. Rev. E, **69**, 046610.

Snieder, R., and E. Şafak, 2006, Extracting the building response using seismic interferometry: Theory and application to the Millikan Library in Pasadena, California: Bull. Seismol. Soc. Am., **96**, 586–598.

Snieder, R., A. Grêt, H. Douma, and J. Scales, 2002, Coda wave interferometry for estimating nonlinear behavior in seismic velocity: Science, **295**, 2253–2255.

Snieder, R., M. Miyazawa, E. Slob, I. Vasconcelos, and K. Wapenaar, 2009, A comparison of strategies for seismic interferometry: Surveys in Geophysics, **30**, 503–523.

Snieder, R., J. Sheiman, and R. Calvert, 2006a, Equivalence of the virtual-source method and wave-field deconvolution in seismic interferometry: Phys. Rev. E, **73**, 066620.

Snieder, R., and M. Vrijlandt, 2005, Constraining the source separation with coda wave interferometry: Theory and application to earthquake doublets in the Hayward fault, California: J. Geophys. Res., **110**, B04301.

Snieder, R., K. Wapenaar, and K. Larner, 2006b, Spurious multiples in seismic interferometry of primaries: Geophysics, **71**, SI111–SI124.

Thomson, D. J., 1982, Spectrum estimation and harmonic analysis: Proc. of the IEEE, **70**, 1055–1096.

Todorovska, M. I., and M. D. Trifunac, 2008a, Earthquake damage detection in the Imperial Country Services Building III: Analysis of wave travel times via impulse response functions: Soil Dyn. Earthquake Eng., **28**, 387–404.

———, 2008b, Impulse response analysis of the Van Nuys 7-story hotel during 11 earthquakes and earthquake damage detection: Struct. Control Health Monit., **15**, 90–116.

Torrence, C., and G. P. Compo, 1998, A practical guide to wavelet analysis: Bull. Am. Meteorol. Soc., **79**, 61–78.

Trifunac, M. D., 1972, Comparisons between ambient and forced vibration experiments: Earthquake Eng. and Structural Dynamics, **1**, 133–150.

Trifunac, M. D., S. S. Ivanović, and M. I. Todorovska, 2001a, Apparent periods of a building. I: Fourier analysis: J. Struct. Eng., **127**, 517–526.

———, 2001b, Apparent periods of a building. II: Time-frequency analysis: J. Struct. Eng., **127**, 527–537.

Wapenaar, K., D. Draganov, R. Snieder, X. Campman, and A. Verdel, 2010, Tutorial on seismic interferometry: Part 1 - Basic principles and applications: Geophysics, **75**, 75A195–75A209.

Wapenaar, K., and J. Fokkema, 2006, Green's function representations for seismic interferometry: Geophysics, **71**, SI33–SI46.

Weaver, R. L., C. Hadziioannou, E. Larose, and M. Campillo, 2011, On the precision of noise correlation interferometry: Geophys. J. Int., **185**, 1384–1392.

Yilmaz, O., 2001, Seismic data analysis, 2 ed.: Society Of Exploration Geophysicists, volume **10** *of* Investigations in Geophysics.

APPENDIX A: NORMAL-MODE ANALYSIS OF DECONVOLUTION INTERFEROMETRY

In equation 3, we analyze the deconvolution interferometry based on superposition of traveling waves using a Taylor expansion. Here, we analyze equation 3 based on summation of normal-mode waves while using contour integration as following the procedure proposed by Snieder and Şafak (2006). Applying the inverse Fourier transform to $D(z, z_a, \omega)$ and using the relationship $k = \omega/c$, the deconvolved response in the time domain is given by

$$D(z, z_a, t) = \int_{-\infty}^{\infty} \frac{e^{-i\omega\left(t-\frac{z}{c}\right)} e^{-\gamma|\omega|\frac{z}{c}} + e^{-i\omega\left(t-\frac{2H-z}{c}\right)} e^{-\gamma|\omega|\frac{2H-z}{c}}}{e^{i\omega\frac{z_a}{c}} e^{-\gamma|\omega|\frac{z_a}{c}} + e^{i\omega\frac{2H-z_a}{c}} e^{-\gamma|\omega|\frac{2H-z_a}{c}}} d\omega. \tag{A1}$$

For $t > (2H - z)/c$, the locations of poles ($\omega_\dagger$) of the integrand in equation A1 are

$$\omega_\dagger = \omega_l(\pm 1 - i\gamma), \ (l = 0, 1, 2, \cdots) \tag{A2}$$

where the normal-mode frequencies are given by

$$\omega_l = \frac{\left(l + \frac{1}{2}\right)\pi c}{H - z_a} \tag{A3}$$

Using the residue theorem, equation A1 can be written as the summation of normal-mode wavefields:

$$D(z, z_a, t) = \frac{4\pi c}{H - z_a} \sum_{l=0}^{\infty} (-1)^l e^{-\gamma\omega_l t} \sin(\omega_l t) \cos\left(\omega_l \frac{H - z}{c}\right). \tag{A4}$$

APPENDIX B: AMPLITUDE OF CROSSCORRELATION INTERFEROMETRY

In this appendix, we compute the amplitude of the crosscorrelated waveforms in equation 12. Using Taylor expansions, we rewrite the equation 12 as

$$\begin{aligned} C(z, 0, \omega) = |S(\omega)|^2 &\left\{ e^{ikz} e^{-\gamma|k|z} + e^{-ikz} e^{-\gamma|k|(4H-z)} + e^{ik(2H-z)} e^{-\gamma|k|(2H-z)} + e^{-ik(2H-z)} e^{-\gamma|k|(2H+z)} \right\} \\ &\times \left\{ \sum_{n=0}^{\infty} (R(\omega))^n e^{2inkH} e^{-2n\gamma|k|H} \right\} \left\{ \sum_{m=0}^{\infty} (R^*(\omega))^m e^{-2imkH} e^{-2m\gamma|k|H} \right\}. \end{aligned} \tag{B1}$$

Here, we only focus on the waves with phases e^{ikz}, $e^{ik(2H-z)}$, $e^{ik(2H+z)}$, and $e^{ik(4H-z)}$, and define their amplitudes as C_1, C_2, C_3, and C_4, respectively. From equation B1, C_1 is obtained by

$$\begin{aligned} C_1 e^{ikz} = |S(\omega)|^2 &\left[e^{ikz} e^{-\gamma|k|z} \sum_{n=0}^{\infty} \left\{ (R(\omega))^n e^{2inkH} e^{-2n\gamma|k|H} (R^*(\omega))^n e^{-2inkH} e^{-2n\gamma|k|H} \right\} \right. \\ &\left. + e^{-ik(2H-z)} e^{-\gamma|k|(2H+z)} \sum_{n=0}^{\infty} \left\{ (R(\omega))^{n+1} e^{2i(n+1)kH} e^{-2(n+1)\gamma|k|H} (R^*(\omega))^n e^{-2inkH} e^{-2n\gamma|k|H} \right\} \right] \\ C_1 = |S(\omega)|^2 &\, e^{-\gamma|k|z} \left\{ 1 + R(\omega) e^{-4\gamma|k|H} \right\} \left\{ \sum_{n=0}^{\infty} |R(\omega)|^{2n} e^{-4n\gamma|k|H} \right\}. \end{aligned} \tag{B2}$$

Similar to expression B2, we obtain C_2, C_3, and C_4 as

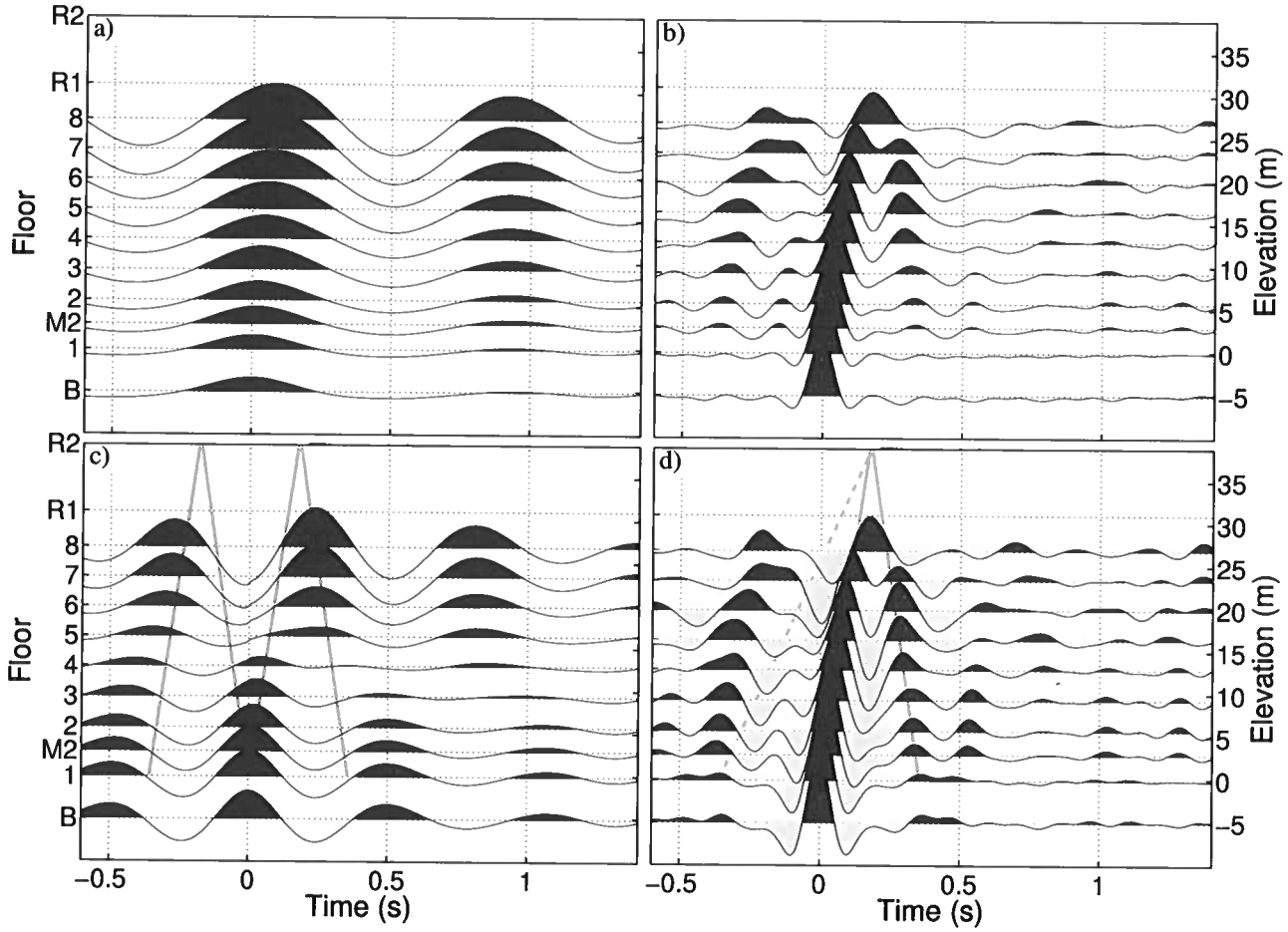

Figure C1. Waveforms obtained by applying (a,c) crosscorrelation and (b,d) crosscoherence interferometry, in which the virtual source is at the first floor, to the records of earthquake No. 5 in the EW component. These waveforms are applied bandpass filters (a,b) 0.4-0.5-45-50 Hz, (c) 1.3-1.6-45-50 Hz, and (d) 1.4-2-45-50 Hz. Note that the bandpass filter for panels (a) and (b) is the same filter as for Figure 7. The amplitude scales in each panel are different. The solid gray lines in panel (c) and (d) are the positive-polarity traveling waves with the velocity estimated from Figure 7a based on equations 12 and 16. The dashed gray line in panel (d) indicates the wave that propagates at one third of the velocity of Figure 7a.

$$C_2 = |S(\omega)|^2 e^{-\gamma|k|(2H-z)} \left\{1 + R(\omega)e^{-4\gamma|k|H}\right\} \left\{\sum_{n=0}^{\infty} |R(\omega)|^{2n} e^{-4n\gamma|k|H}\right\}, \tag{B3}$$

$$C_3 = |S(\omega)|^2 R(\omega) e^{-\gamma|k|(2H+z)} \left\{1 + R(\omega)e^{-4\gamma|k|H}\right\} \left\{\sum_{n=0}^{\infty} |R(\omega)|^{2n} e^{-4n\gamma|k|H}\right\}, \tag{B4}$$

$$C_4 = |S(\omega)|^2 R(\omega) e^{-\gamma|k|(4H-z)} \left\{1 + R(\omega)e^{-4\gamma|k|H}\right\} \left\{\sum_{n=0}^{\infty} |R(\omega)|^{2n} e^{-4n\gamma|k|H}\right\}. \tag{B5}$$

Appendix C: Applying crosscorrelation and crosscoherence interferometry to real data

In Figure C1, we apply crosscorrelation and crosscoherence interferometry to real data to draw similar figures as Figure 7a. When we use the same bandpass filter as for Figure 7, crosscorrelation interferometry enhances the fundamental-mode frequency, and only the fundamental mode is visible (Figure C1a). This is caused by the power spectrum of the incoming wave (equation 12). When we cut the fundamental-mode frequency, the first-

higher mode is dominant in the crosscorrelated waveforms (Figure C1c). Therefore, we cannot estimate the velocity of traveling waves.

Figure C1b illustrates upgoing and downgoing waves from $t = 0$ s, and the waves propagate at the same velocity as the traveling waves reconstructed by deconvolution interferometry (Figure 7a). However, these propagating waves may be affected by the wave which propagates at slower velocities. The fundamental mode is not clear in Figure C1b. This is due to the spectral ratio used in crosscoherence interferometry, as a result the amplitude in later times is much smaller than the amplitude of deconvolution interferometry (Table 2). Because of the frequency we used, the wave propagating with slower velocity is not clear (the dashed gray line in Figure C1d). The negative amplitudes around the dashed line might be related to the wave with slower velocity.

Monitoring a building using deconvolution interferometry. II: Ambient-vibration analysis

Nori Nakata[1] and Roel Snieder[1]

[1] *Center for Wave Phenomena, Geophysics Department, Colorado School of Mines*

ABSTRACT

Application of deconvolution interferometry to earthquake data recorded inside a building is a powerful technique for monitoring parameters of the building, such as velocities of traveling waves, frequencies of normal modes, and intrinsic attenuation. In this study, we apply interferometry to ambient-vibration data, instead of using earthquake data, to monitor a building. The time continuity of ambient vibrations is useful for temporal monitoring. We show that because multiple sources simultaneously excite vibrations inside the building, the deconvolved waveforms obtained from ambient vibrations are non-zero for both positive and negative times, unlike the purely causal waveforms obtained from earthquake data. We develop a string model to qualitatively interpret the deconvolved waveforms. Using the synthetic waveforms, we nd that the traveling waves obtained from ambient vibrations propagate with the correct velocity of the building, and the amplitude decay of the deconvolved waveforms depends on both intrinsic attenuation and ground coupling. The velocities estimated from ambient vibrations are more stable than those computed from earthquake data. Since the acceleration of the observed earthquake records varies depending on the strength of the earthquakes and the distance from the hypocenter, the velocities estimated from earthquake data vary because of the nonlinear response of the building. From ambient vibrations, we extract the wave velocity due to the linear response of the building.

Key words: time-lapse monitoring, deconvolution interferometry, ambient noise, building, normal mode

1 INTRODUCTION

Spectral analysis using forced vibrations and/or earthquakes is a common technique to estimate frequencies of normal modes, mode shapes, and viscous damping parameters of a building (Kanai and Yoshizawa, 1961; Trifunac, 1972; Trifunac et al., 2001a,b; Clinton et al., 2006). These parameters are useful for risk assessment and for estimating the response of a building to earthquakes (Michel et al., 2008). The sources listed above are sometimes inappropriate to use for temporal monitoring a building because of the lack of data continuity. Ambient vibrations, caused by sources within the building, are more suitable for monitoring a building because of the quasi-continuous nature of these vibrations (Trifunac, 1972; Ivanović et al., 2000). In this study we use seismic interferometry to analyze ambient vibrations recorded inside a building in the Fukushima prefecture in Japan.

Using seismic interferometry, we can reconstruct waves that propagate from one receiver to another. Seismic interferometry was invented by Aki (1957) and Claerbout (1968), and has been well-developed over the last decade [e.g., *Lobkis and Weaver*, 2001; *Derode et al.*, 2003; *Snieder*, 2004b; *Wapenaar*, 2004; *Schuster*, 2009; *Snieder et al.*, 2009; *Tsai*, 2011]. One can apply seismic interferometry to active sources [e.g., *Bakulin and Calvert*, 2006; *Wegler et al.*, 2006; *Mehta et al.*, 2008; *van der Neut et al.*, 2011] or to earthquake data [e.g., *Sawazaki et al.*, 2009; *Yamada et al.*, 2010; *Nakata and Snieder*, 2011, 2012a,b]. These latter studies used interferometry for monitoring purposes. One can also apply interferometry to noise caused by production [e.g., *Miyazawa et al.*, 2008], drilling [e.g., *Vasconcelos and Snieder*, 2008a,b], and traffic [e.g., *Nakata et al.*, 2011], and to non-specific vibrations (so-called *ambient vibration* or *ambient noise*) [e.g., *Sens-Schönfelder and We-*

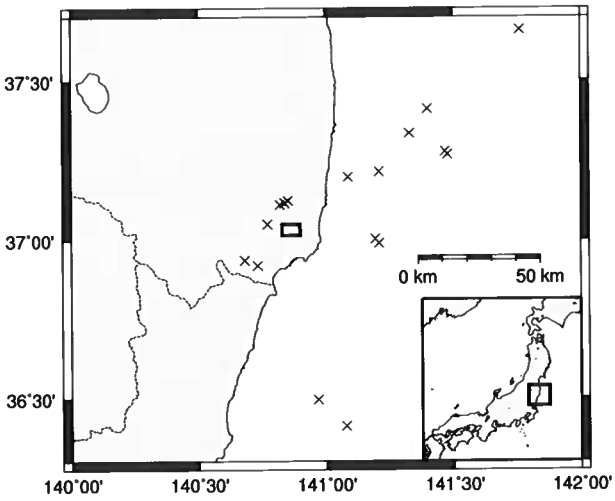

Figure 1. The building (rectangle, not to scale) and epicenters of earthquakes used in Part I (crosses). The lower-right map indicates the location of the magnified area.

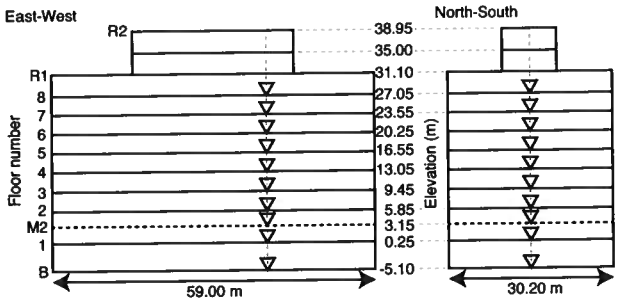

Figure 2. The (left) EW and (right) NS vertical cross sections of the building and the positions of receivers (triangles). Elevations denote the height of each floor from ground level. Receivers are located on stairs 0.19 m below each floor except for the basement (on the floor) and the first floor (0.38 m below). Receiver M2 is located between the first and second floors. Horizontal-receiver components are aligned with the EW and NS directions.

gler, 2006; *Brenguier et al.*, 2008a,b; *Draganov et al.*, 2009; *Minato et al.*, 2012].

In a companion paper (henceforth called Part I: Nakata et al. (2013)), we analyze earthquake data, recorded over the same time period in the same building as in this study, using seismic interferometry. Although several studies apply interferometric approaches to earthquake data recorded in a building [e.g., *Snieder and Şafak*, 2006; *Snieder et al.*, 2006; *Kohler et al.*, 2007; *Todorovska and Trifunac* 2008a,b], few studies apply this technique to ambient vibrations (Prieto et al., 2010). As we explain below, by applying seismic interferometry to ambient vibrations recorded in a building, we not only achieve continuous monitoring in time but also obtain information of the ground coupling and linear response of the building, which we cannot estimate from earthquake data.

We first introduce ambient-vibration data and deconvolved waveforms computed from the observed data. Next, we analytically and qualitatively interpret the deconvolved waveforms using traveling-wave and normal-mode analyses. Then we monitor the building using ambient vibrations based on the interpretation.

2 DECONVOLUTION ANALYSIS USING AMBIENT VIBRATION

We present data acquisition, pre-processing for deconvolution interferometry, and the interferometry using ambient-vibration data in this section. Data are observed in the same building over the same time period as for the earthquake data in Part I (Figure 1). Pre-processing has an important role for obtaining reliable correlograms (Bensen et al., 2007), and here we focus on the pre-processing to exclude large amplitudes caused by earthquakes and human activities.

2.1 Observed records

The building we used is in the Fukushima prefecture, Japan (the rectangle in Figure 1). Continuous ambient seismic vibrations were recorded by Suncoh Consultants Co., Ltd. for two weeks (May 31–June 14, 2011) using 10 MEMS accelerometers developed by Akebono Brake Industry Co., Ltd. The building has eight stories, a basement, and a penthouse (Figure 2). Based on the analysis in Part I, the waves, which propagate vertically inside the building, reflect off the top of the penthouse (R2 in Figure 2). The sampling interval of the accelerometers is 1 ms, and the receivers have vertical, east-west (EW) horizontal, and north-south (NS) horizontal components. In this study we focus on the EW horizontal component to extract horizontal modes.

Figure 3 illustrates the root-mean-square (RMS) amplitude computed over a moving window with a duration of 30 s of unfiltered seismic records observed for the two weeks. The hours of operation of the building are from 8AM to 6PM on weekdays, when the RMS amplitude is elevated. On the weekends we observe lower RMS amplitudes (June 4, 5, 11, and 12 are weekends). The vibrations are probably induced by human activities, elevators, air conditioners, computers, traffic near the building, and other sources. Amplitudes at the upper floors are stronger due to the shape of the fundamental mode of the building (see Figure 4 in Part I for the shape of the fundamental mode). Stronger amplitudes at the first floor compared with nearby floors may be caused by vibrations from traffic outside the building and/or many visitors to that floor. Because the amplitudes at the basement are much smaller than the other

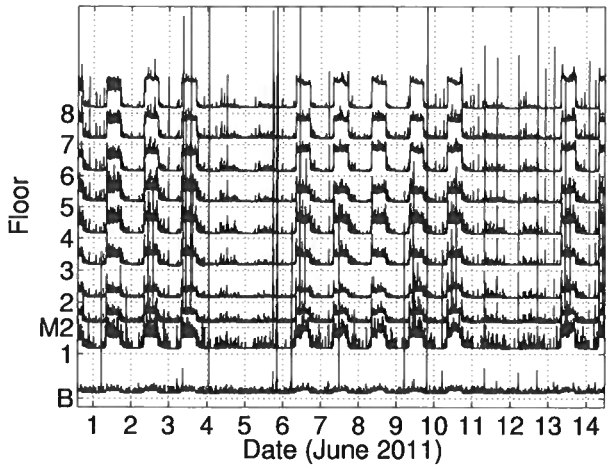

Figure 3. RMS amplitude of the records observed at each floor. The labels of the date are placed at the start of days (midnight). Each trace indicates the RMS amplitude, and the positive axis of amplitude for each trace is upward (dashed horizontal grids describe zero amplitude at each floor).

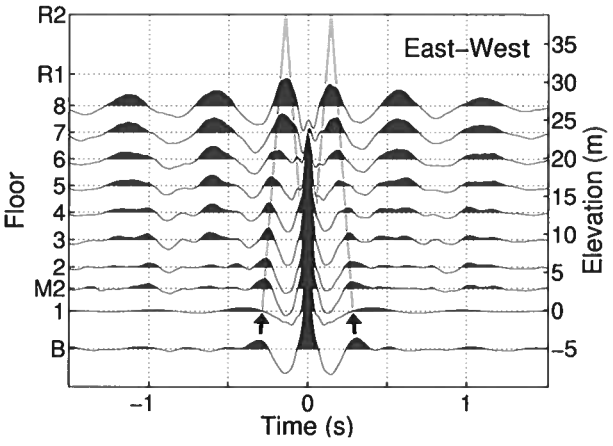

Figure 4. Deconvolved waveforms obtained from ambient vibrations in the EW component (expression 1). Ambient vibrations observed at Floor 1 is used for the denominator in expression 1. The waveforms are averaged over two weeks and applied a bandpass filter 1.3-1.5-15-20 Hz. The shear velocity is estimated from the downgoing waves in the positive time and the upgoing waves in the negative time marked by arrows. Gray lines show the arrival times of the waves propagating with a velocity equal to 270 m/s.

floors, we do not interpret the records at the basement in this study.

2.2 Pre-processing

Before applying deconvolution interferometry, we exclude large-amplitude intervals from the continuous records because we focus on ambient vibrations. Large amplitudes are excited by earthquakes and human interference, such as people touching the accelerometers. Since receivers are often located at places where people can touch them (e.g., on stairs), a technique proposed here to exclude the human interference is useful. To exclude large-amplitude waves, we apply a data-weighting procedure based on the standard deviation of data recorded for one hour in which the data do not include significant earthquakes or human interference (Wegler and Sens-Schönfelder, 2007). When one receiver records a larger amplitude than the threshold, the samples of all receivers at that time are set to zero since we need the waveforms at the same time at all sensors for the deconvolution analysis. After someone touches a receiver, the DC component on the seismograms may change. We subtract the DC component from the data of every 30 s and discard data when the DC component changes during that time interval. Similar to large amplitudes, we exclude time intervals when one receiver indicates a change in the DC component.

2.3 Deconvolution analysis using two-week ambient vibration

We apply deconvolution interferometry to ambient-vibration records observed inside the building. Here, we stack deconvolved waveforms over the two weeks in which data were collected. In the later section *Monitoring the building using ambient vibration*, we stack over four-day intervals for monitoring purposes. We deconvolve each 30-s ambient-vibration record with the first-floor record and then stack the waveforms over the two-week interval:

$$D(z,t) = \sum_{n=1}^{N} \left[\mathcal{F}^{-1} \left\{ \frac{u_n(z,\omega)}{u_n(0,\omega)} \right\} \right] \approx \sum_{n=1}^{N} \left[\mathcal{F}^{-1} \left\{ \frac{u_n(z,\omega) u_n^*(0,\omega)}{|u_n(0,\omega)|^2 + \alpha \langle |u_n(0,\omega)|^2 \rangle} \right\} \right], \quad (1)$$

where N is the number of 30-s intervals (40,080 in this study), $u_n(z,\omega)$ the nth wavefield in the frequency domain recorded at z ($z = 0$ is the first floor), ω the angular frequency, t time, $\mathcal{F}^{-1}$ the inverse Fourier transform, $*$ the complex conjugate, $\langle |u_n|^2 \rangle$ the average power spectrum of u_n, and $\alpha = 0.5\%$ a regularization parameter stabilizing the deconvolution (Clayton and Wiggins, 1976). Our Fourier convention is $f(t) = \int_{-\infty}^{\infty} F(\omega) e^{-i\omega t} d\omega$. We apply a bandpass filter, 1.3-1.5-15-20 Hz, to the deconvolved waveforms (Figure 4).

In Figure 4, we obtain traveling waves and the fun-

3.2 Multiple sources

Using the normal-mode theory (Snieder, 2004b,Ch. 20), we compute the deconvolved waveforms obtained from multiple sources to qualitatively interpret the waveforms in Figure 4. We can express waves using either the summation of traveling waves or normal modes [*Dahlen and Tromp*, 1998, Ch. 4; *Snieder and Şafak*, 2006]. Equations 2–5 are based on traveling waves, and these equations depend on the location of sources. We have to modify all terms in the numerators of equations 2 and 3, and choose equation 2 or 3 depending on the locations of receiver and source. On the other hand, the normal-mode analysis is suitable for multiple sources inside the building because source terms are separated from other terms (see for example equation 20.69 in Snieder (2004b)).

The model for our normal-mode analysis is a one-dimensional string model that includes radiation damping (Snieder, 2004b,Ch. 20.10). This model consists of an open-ended light string with mass density ρ connected to a heavy string with density $\rho_g \gg \rho$ at $z = 0$ (Figure 6). The wave propagation in the light and heavy strings represents the propagation in the building and the subsurface, respectively. Although the string model is primitive, the model qualitatively accounts for the wave propagation in the building because of three reasons; 1) we are only interested in the building, 2) the effect of the ground for the building is limited to the coupling at $z = 0$, and 3) we assume no waves return after the waves propagate to the ground. The ratio of the densities of the light and heavy strings is related to the reflection coefficient at the connection of the strings (at the base of the building) (Coulson and Jeffrey, 1977,Ch. 2):

$$R = \frac{\sqrt{\rho} - \sqrt{\rho_g}}{\sqrt{\rho} + \sqrt{\rho_g}} = \frac{-1 + \epsilon}{1 + \epsilon}, \tag{6}$$

where

$$\epsilon = \sqrt{\rho/\rho_g}. \tag{7}$$

We carry out a perturbation analysis for this small dimensionless parameter.

The eigenfunctions and eigenfrequencies of this string model to first order in ϵ for the mode m ($m = 0, 1, \cdots$) are given by

$$u_m(z) = \sin\left\{\pm\left(m + \frac{1}{2}\right)\frac{\pi z}{H}\right\} - i\epsilon\frac{H - z}{H}\cos\left\{\pm\left(m + \frac{1}{2}\right)\frac{\pi z}{H}\right\}, \tag{8}$$

$$\omega_m^{(r)} = \left\{\pm\left(m + \frac{1}{2}\right)\pi - i\epsilon\right\}\frac{c}{H}, \tag{9}$$

respectively (see Appendix A). Because this string model does not include the intrinsic attenuation of the building, the eigenfrequency in expression 9 does not incorporate the attenuation. The superscript in expression 9 indicates that the complex eigenfrequency accounts only for the radiation loss. Snieder and Şafak (2006) derive the eigenfrequency ($\omega_m^{(a)}$) with the intrinsic attenuation, but without radiation damping:

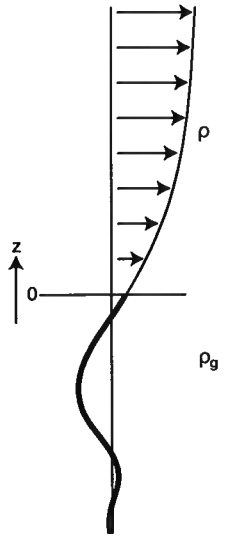

Figure 6. Displacement of radiation damping of the string model. The density of the light string (ρ; $z > 0$; thin line) is much smaller than that of the heavy string (ρ_g; $z < 0$; thick line).

$$\omega_m^{(a)} = \left(m + \frac{1}{2}\right)\frac{\pi c}{H}(\pm 1 - i\gamma). \tag{10}$$

Comparing expressions 9 and 10, we account for the intrinsic attenuation and the radiation damping using the following eigenfrequency:

$$\omega_m^{(ar)} = \left\{\pi\left(m + \frac{1}{2}\right)(\pm 1 - i\gamma) - i\epsilon\right\}\frac{c}{H}, \tag{11}$$

where we assume the intrinsic attenuation to be weak and ignore a cross term between the intrinsic attenuation and radiation damping. In expression 11, the first term ($\pi(m + 1/2)c/H$) is the frequency in case there is no intrinsic attenuation ($\gamma = 0$) and the building has a rigid boundary at the bottom ($R = -1$). The second term ($-i\gamma\pi(m+1/2)c/H$) accounts for the intrinsic attenuation, and the third term ($-i\epsilon c/H$) accounts for the radiation loss at the base of the building. The waveforms in this string model with the intrinsic attenuation are given by the summation of normal modes (Snieder, 2004b):

$$u(z, \omega) = \sum_{m=0}^{\infty} \frac{u_m(z)\int u_m^*(z')F(z')dz'}{(\omega_m^{(ar)})^2 - \omega^2}, \tag{12}$$

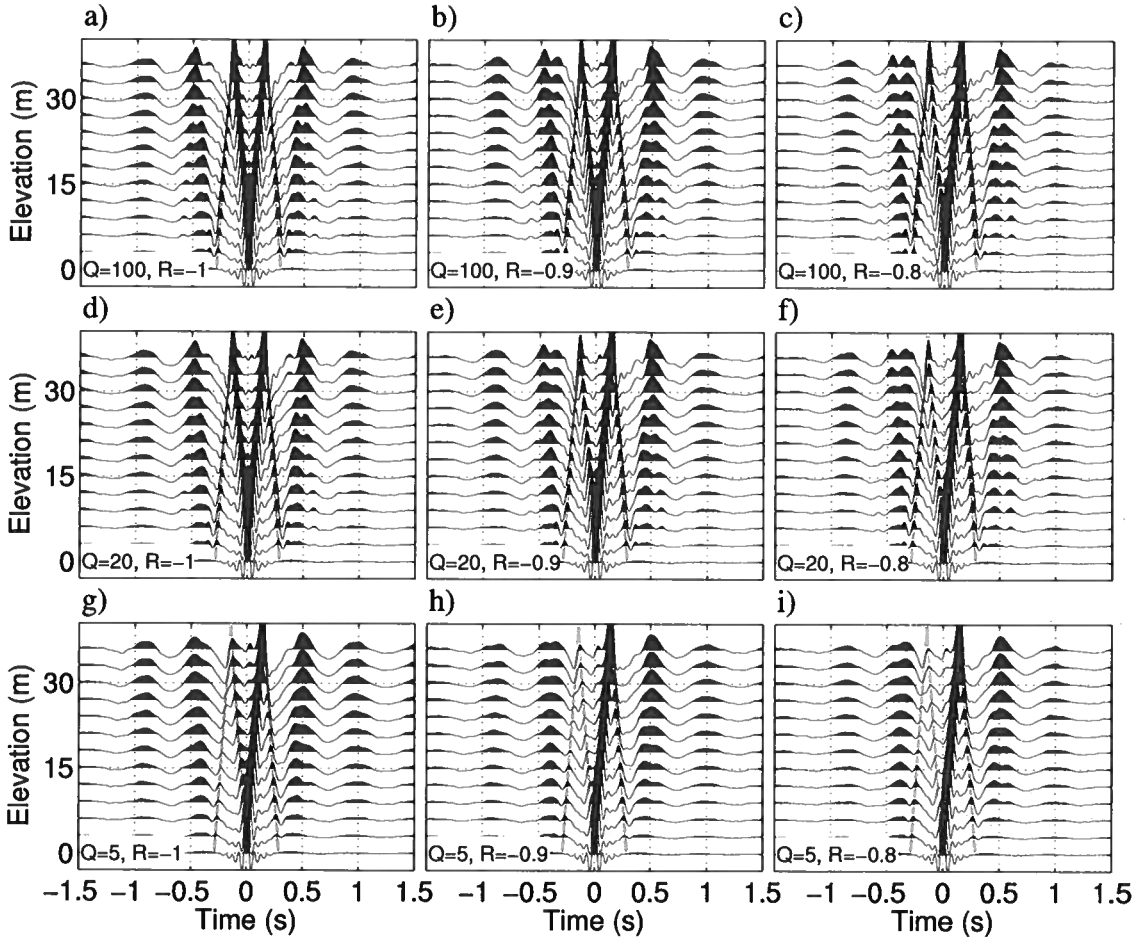

Figure 7. Synthetic deconvolved waveforms using three-hour random vibrations as sources after applying the same bandpass filter as in Figure 4. Panels (a)–(i) are computed by adopting different quality factors Q and reflection coefficients R (see lower-left of each panel). Gray lines indicate the arrival time of the traveling wave with the velocity used for the modeling ($c = 270$ m/s). The scale of the amplitudes at each panel is the same.

where F indicates the forces that excite the vibrations.

We numerically compute the synthetic records using expression 12 for various values of the quality factor Q and the reflection coefficient R with fixed parameters: $H = 39$ m and $c = 270$ m/s. We use random sources (random amplitude, phase, and location) and compute three-hour random-source synthetic observed records. Then we deconvolve the waveforms with the records at the floor at $z = 0$ (Figure 7). All panels in Figure 7 show waves for both positive and negative times, which is consistent with the deconvolved waveforms in Figure 4. Especially for $|t| \gtrsim 1$ s, the waveforms in Figure 7 are similar in character to those in Figure 4. For $|t| \lesssim 0.3$ s, we obtain the traveling waves, propagating with the same velocity as used for the modeling ($c = 270$ m/s; compare the waveforms and the gray lines in Figure 7).

The waveforms are increasingly asymmetric in time as the reflection coefficient differs from $R = -1$, or as the anelastic damping increases (see for example Figures 7def or 7beh). From Figure 7, we learn that the amplitude decay of the waveforms is related to the intrinsic attenuation and the boundary condition. Based on the similarity of the waveforms in Figures 4 and 7, the reflection coefficient and the quality factor of the real building are likely close to those in Figures 7a–7e. Because we can estimate $Q^{(a)}$ independent from the ground coupling using the earthquake data (Part I), the deconvolution using ambient vibrations is potentially useful for estimating R. However, to estimate R, we need a more quantitative analysis, which is a topic of future work. Also, for waveform matching this string model may be too simple. We conclude that the estimated velocity from the waveforms in Figure 4 indicates the true velocity of the traveling wave in the building, and the quality factor estimated from the amplitude decay of the

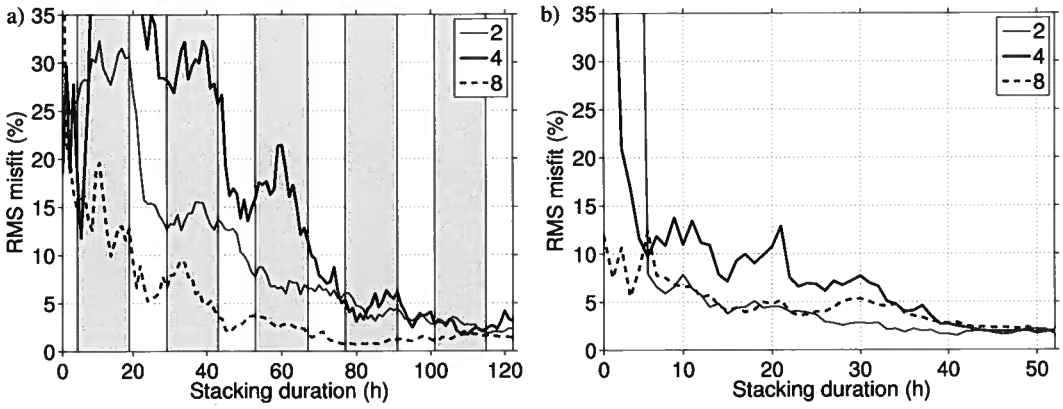

Figure 8. Convergence test of ambient-vibration interferometry based on RMS misfits (equation 13) as a function of the stacking duration. (a) RMS misfits with respect to the stacked waveform over two-week ambient vibrations recorded in both daytime (8AM–6PM) and nighttime (6PM–8AM). The shaded areas correspond to nighttimes. We show the misfits at second, fourth, and eighth floors. (b) RMS misfits with respect to the same waveforms as panel (a) but using only daytime data. We show the RMS misfits for 122 hours (52 hours of daytime and 70 hours of nighttime) in panel (a) and 52 hours in panel (b).

waveforms is $Q^{(ar)}$ not just $Q^{(a)}$. In the next section, we monitor the velocity of the building.

4 MONITORING THE BUILDING USING AMBIENT VIBRATION

For monitoring the velocity of the traveling waves, we need to know the minimum time length to obtain stable waveforms. To determine this time interval, we compute the convergence of the deconvolved waveforms as a function of the stacking duration h using a RMS misfit as used by Prieto et al. (2010):

$$\text{Misfit}(z,h) = \sqrt{\frac{\int_{t_a}^{t_b} \{D_h(z,t) - D_{all}(z,t)\}^2 \, dt}{\int_{t_a}^{t_b} \{D_{all}(z,t)\}^2 \, dt}}, \quad (13)$$

where t_a and t_b define the time interval to compute the misfit (-1.5 s and 1.5 s in this study), h the stacking duration, D_h the deconvolved waves stacked over time period h, and D_{all} the deconvolved waveforms obtained from the entire data set recorded during the two weeks. If the RMS misfit is small, the deconvolved waveform D_h is similar to the deconvolved waveforms obtained from the entire data set.

Figure 8 indicates the convergence of deconvolved waveforms with respect to the stacking duration. In Figure 8a, we use both daytime (8AM–6PM) and nighttime (6PM–8AM) data. Since the RMS misfit is lower than 5% when we use the ambient-vibration data longer than 96 hours, we decide that stacking over 96 hours is sufficient to obtain stable deconvolved waveforms. The RMS misfit in Figure 8a increases during some nighttimes.However, since for example the RMS misfits at $h = 66$ are smaller than the misfits at $h = 52$ at all floors, the vibrations in nighttime also contribute to the convergence. We also compute the waveforms using daytime data only and estimate the RMS misfit (Figure 8b). Interestingly, although Figure 8b shows rapid convergence to 10%, we need about 40 hours (equivalent to four days) to obtain the RMS misfit lower than 5%. In Figure 8, we show the RMS misfits for 122 hours (panel a) and for 52 hours (panel b), which are equivalent because 122 hours include 52 hours of daytime and 70 hours of nighttime.

Figure 9 shows the deconvolved waveforms using the data recorded during both daytime and nighttime (same data as used in Figure 8a), and Figure 10 using the data recoded daytime only (same data as used in Figure 8b). In Figure 9, we stack the data over four-day intervals (96 hours) and overlap these intervals over two days. From the waveforms in Figure 9, we estimate the velocity of the traveling waves using the same method as Figure 4. The estimated velocities are stable during the two weeks, and the uncertainty is about 6 m/s, which is smaller than the uncertainty in the velocity estimated from earthquake data (Figure 12 in Part I). For earthquakes, the estimated velocities vary more than for ambient vibrations, and the acceleration of the observed records also varies (Figure 12b in Part I). These variations indicate that the velocities estimated from earthquakes include nonlinear effects. The velocities estimated from ambient vibrations are not affected by nonlinearity because the acceleration of the observed records is small and does not vary much. Therefore, ambient vibration is appropriate for monitoring the velocity of traveling waves in the linear regime. Deconvolved waveforms in Figure 10 are similar to those in Figure 9, and the difference in estimated velocities are not statistically significant.

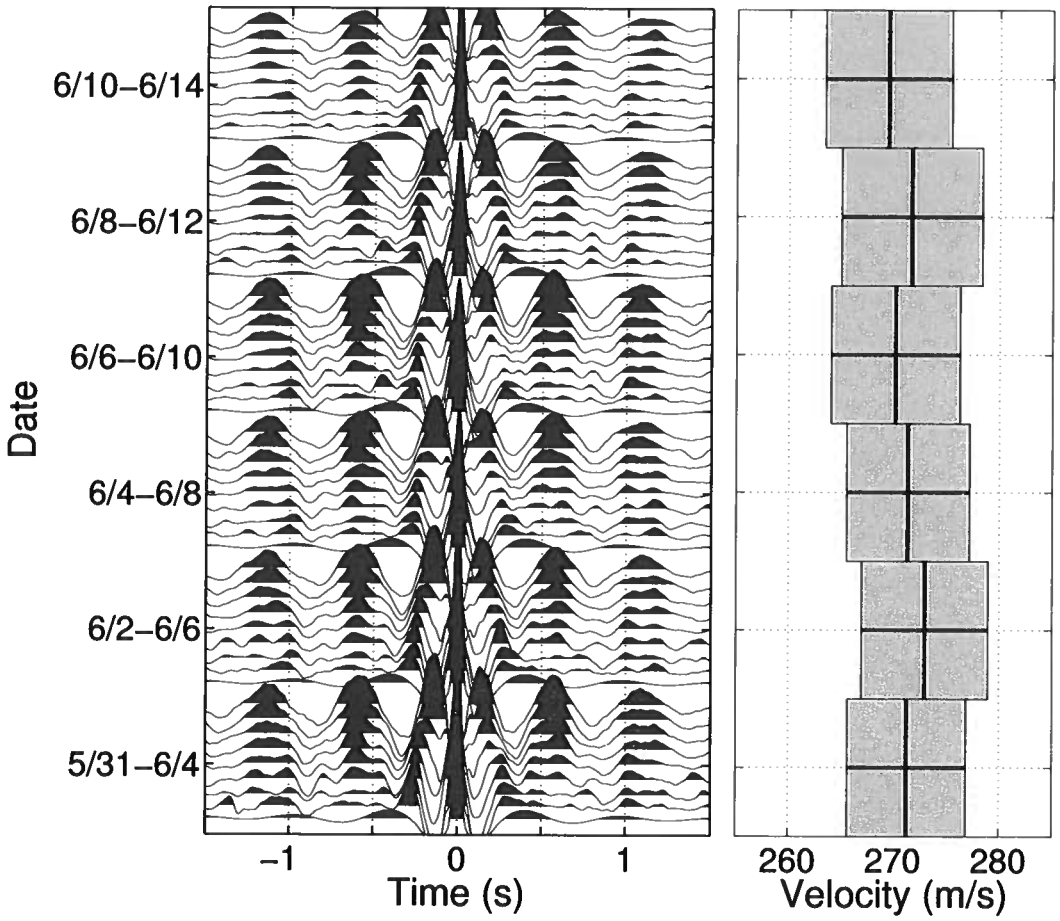

Figure 9. (Left) Time-lapse deconvolved waveforms averaged over 96 hours with a 48-hour overlap using ambient vibrations recorded in both daytime and nighttime. We have applied the same bandpass filter as used in Figure 4. (Right) Shear-wave velocities estimated from the traveling waves in the left panel. The width of each box indicates one standard deviation of estimated velocities at each floor.

5 CONCLUSION

We retrieve traveling waves inside the building by applying seismic interferometry to ambient-vibration data. In contrast to the case when sources are only outside the building, deconvolved waves obtained from ambient vibrations are nonzero for both positive and negative times, which is explained by that multiple sources simultaneously excite inside the building. Based on the normal-mode analysis, we synthetically reconstruct waveforms that are qualitatively similar to the real data using the simple string model. The velocity estimated from the synthetic waveforms with this model is the same as the true velocity although the attenuation estimated from the decay of the amplitude with time is not equal to the intrinsic attenuation of the building. Since the amplitude decay is also influenced by radiation losses at the base of the building, we are, in principle, able to estimate both quality factors and reflection coefficients separately from the amplitude of the waveforms, which requires a more accurate model than the string model used here. For monitoring the building, we find the time interval to obtain stable waveforms using the convergence test, and we need deconvolved ambient vibrations averaged over four days to obtain stable waveforms for this building. The velocity estimated from ambient-vibration data is more stable than that from earthquake data because the ambient vibrations are due to the linear response of the building.

ACKNOWLEDGMENTS

We are grateful to sponsor companies of the Consortium Project on Seismic Inverse Methods for Complex Structures. We want to thank Suncoh Consultant Co.,

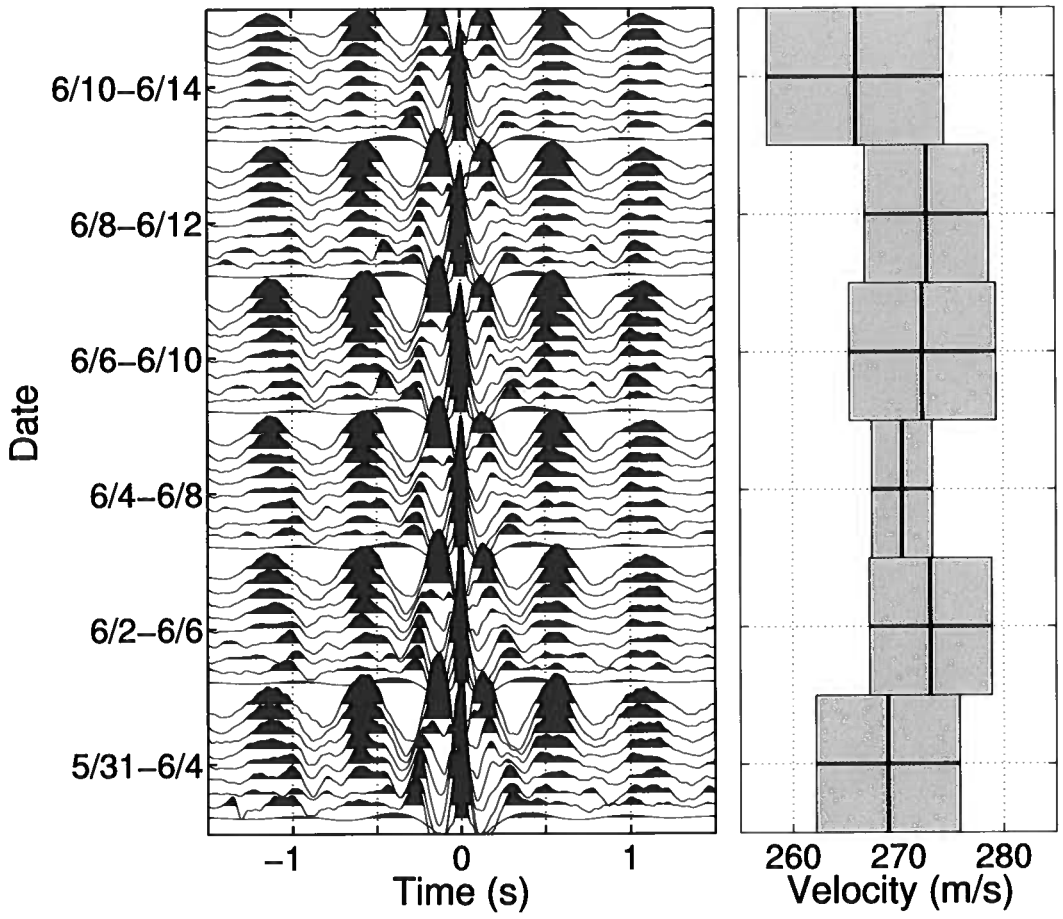

Figure 10. (Left) Time-lapse deconvolved waveforms averaged over 40 hours with a 20-hour overlap using ambient vibration recorded in daytime only. We have applied the same bandpass filter as used in Figure 4. (Right) Shear-wave velocities estimated from the traveling waves in the left panel. The width of each box indicates one standard deviation of estimated velocities at each floor.

Ltd. and Akebono Brake Industry Co., Ltd. for providing the data. We thank Seiichiro Kuroda for his professional comments to improve this work. N.N. thanks the instructor and classmates of the class *Academic Publishing* in Colorado School of Mines for their help in preparing this manuscript.

REFERENCES

Aki, K., 1957, Space and time spectra of stationary stochastic waves, with special reference to microtremors: Bull. Earthq. Res. Inst., **35**, 415–456.

Aki, K., and P. G. Richards, 2002, Quantitative Seismology, 2 ed.: Univ. Science Books.

Bakulin, A., and R. Calvert, 2006, The virtual source method: Theory and case study: Geophysics, **71**, S1139–S1150.

Bensen, G. D., M. H. Ritzwoller, M. P. Barmin, A. L. Levshin, F. Lin, M. P. Moschetti, N. M. Shapiro, and Y. Yang, 2007, Processing seismic ambient noise data to obtain reliable boroad-band surface wave dispersion measurements: Geophys. J. Int., **169**, 1239–1260.

Brenguier, F., M. Campillo, C. Hadziioannou, N. M. Shapiro, R. M. Nadeau, and E. Larose, 2008a, Postseismic relaxation along the San Andreas Fault at Parkfield from continuous seismological observations: Science, **321**, 1478–1481.

Brenguier, F., N. M. Shapiro, M. Campllo, V. Ferrazzini, Z. Duputel, O. Coutant, and A. Nercessian, 2008b, Towards forecasting volcanic eruptions using seimsic noise: Nature Geosci., **1**, 126–130.

Claerbout, J. F., 1968, Synthesis of a layered medium from its acoustic transmission response: Geophysics, **33**, 264–269.

Clayton, R. W., and R. A. Wiggins, 1976, Source shape

estimation and deconvolution of teleseismic body-waves: Geophys. J. R. astr. Soc., **47**, 151–177.

Clinton, J. F., S. C. Bradford, T. H. Heaton, and J. Favela, 2006, The observed wander of the natural frequencies in a structure: Bull. Seismol. Soc. Am., **96**, 237–257.

Coulson, C. A., and A. Jeffrey, 1977, Waves: A mathematical approach to the common types of wave motion, 2 ed.: Longman.

Dahlen, F. A., and J. Tromp, 1998, Theoretical global seismology: Princeton University Press.

Derode, A., E. Larose, M. Tanter, J. de Rosny, A. Tourin, M. Campillo, and M. Fink, 2003, Recovering the Green's function from field-field correlations in an open scattering medium (L): J. Acoust. Soc. Am., **113**, 2973–2976.

Draganov, D., X. Campman, J. Thorbecke, A. Verdel, and K. Wapenaar, 2009, Reflection images from ambient seismic noise: Geophysics, **74**, A63–A67.

Ivanović, S. S., M. D. Trifunac, and M. I. Todorovska, 2000, Ambient vibration tests of structures–a review: ISET J. Earthq. Tech, **37**, 165–197.

Kanai, K., and S. Yoshizawa, 1961, On the period and the damping of vibration in actual buildings: Bull. Earthq. Res. Inst., **39**, 477–489.

Kohler, M. D., T. H. Heaton, and S. C. Bradford, 2007, Propagating waves in the steel, moment-frame Factor building recorded during earthquakes: Bull. Seismol. Soc. Am., **97**, 1334–1345.

Lobkis, O. I., and R. L. Weaver, 2001, On the emergence of the Green's function in the correlations of a diffuse field: J. Acoust. Soc. Am., **110**, 3011–3017.

Mehta, K., J. L. Sheiman, R. Snieder, and R. Calvert, 2008, Strengthening the virtual-source method for time-lapse monitoring: Geophysics, **73**, S73–S80.

Michel, C., P. Guéguen, and P.-Y. Bard, 2008, Dynamic parameters of structures extracted from ambient vibration measurements: An aid for the seismic vulnerability assessment of existing buildings in moderate seismic hazard regions: Soil Dyn. Earthquake Eng., **28**, 593–604.

Minato, S., T. Tsuji, S. Ohmi, and T. Matsuoka, 2012, Monitoring seismic velocity change caused by the 2011 Tohoku-oki earhtquake using ambient noise records: Geophys. Res. Lett., **39**, L09309.

Miyazawa, M., R. Snieder, and A. Venkataraman, 2008, Application of seismic interferometry to exptract P- and S-wave propagation and observation of shear-wave splitting from noise data at Cold Lake, Alberta, Canada: Geophysics, **73**, D35–D40.

Nakata, N., and R. Snieder, 2011, Near-surface weakening in Japan after the 2011 Tohoku-Oki earthquake: Geophys. Res. Lett., **38**, L17302.

———, 2012a, Estimating near-surface shear-wave velocities in Japan by applying seismic interferometry to KiK-net data: J. Geophys. Res., **117**, B01308.

———, 2012b, Time-lapse change in anisotropy in Japan's near surface after the 2011 Tohoku-Oki earthquake: Geophys. Res. Lett., **39**, L11313.

Nakata, N., R. Snieder, S. Kuroda, S. Ito, T. Aizawa, and T. Kunimi, 2013, Monitoring a building using deconvolution interferometry. I: Earthquake-data analysis: Bull. Seismol. Soc. Am. (in press).

Nakata, N., R. Snieder, T. Tsuji, K. Larner, and T. Matsuoka, 2011, Shear-wave imaging from traffic noise using seismic interferometry by cross-coherence: Geophysics, **76**, SA97–SA106.

Prieto, G. A., J. F. Lawrence, A. I. Chung, and M. D. Kohler, 2010, Impulse response of civil structures from ambient noise analysis: Bull. Seismol. Soc. Am., **100**, 2322–2328.

Sawazaki, K., H. Sato, H. Nakahara, and T. Nishimura, 2009, Time-lapse changes of seismic velocity in the shallow ground caused by strong ground motion shock of the 2000 western-Tottori earthquake, Japan, as revealed from coda deconvolution analysis: Bull. Seismol. Soc. Am., **99**, 352–366.

Schuster, G., 2009, Seismic interferometry: Cambridge Univ. Press.

Sens-Schönfelder, C., and U. Wegler, 2006, Passive image interferometry and seasonal variations of seismic velocities at Merapi Volcano, Indonesia: Geophys. Res. Lett., **33**, L21302.

Snieder, R., 2004a, Extracting the Green's function from the correlation of coda waves: A derivation based on stationary phase: Phys. Rev. E, **69**, 046610.

———, 2004b, A Guided Tour of Mathematical Methods for the Physical Sciences: Cambridge Univ. Press.

Snieder, R., and E. Şafak, 2006, Extracting the building response using seismic interferometry: Theory and application to the Millikan Library in Pasadena, California: Bull. Seismol. Soc. Am., **96**, 586–598.

Snieder, R., M. Miyazawa, E. Slob, I. Vasconcelos, and K. Wapenaar, 2009, A comparison of strategies for seismic interferometry: Surveys in Geophysics, **30**, 503–523.

Snieder, R., J. Sheiman, and R. Calvert, 2006, Equivalence of the virtual-source method and wave-field deconvolution in seismic interferometry: Phys. Rev. E, **73**, 066620.

Todorovska, M. I., and M. D. Trifunac, 2008a, Earthquake damage detection in the Imperial Country Services Building III: Analysis of wave travel times via impulse response functions: Soil Dyn. Earthquake Eng., **28**, 387–404.

———, 2008b, Impulse response analysis of the Van Nuys 7-story hotel during 11 earthquakes and earthquake damage detection: Struct. Control Health Monit., **15**, 90–116.

Trifunac, M. D., 1972, Comparisons between ambient and forced vibration experiments: Earthquake Eng. and Structural Dynamics, **1**, 133–150.

Trifunac, M. D., S. S. Ivanović, and M. I. Todorovska, 2001a, Apparent periods of a building. I: Fourier anal-

ysis: J. Struct. Eng., **127**, 517–526.
———, 2001b, Apparent periods of a building. II: Time-frequency analysis: J. Struct. Eng., **127**, 527–537.
Tsai, V. C., 2011, Understanding the amplitudes of noise correlation measurements: J. Geophys. Res., **116**, B09311.
van der Neut, J., J. Thorbecke, K. Mehta, E. Slob, and K. Wapenaar, 2011, Controlled-source interferometric redatuming by crosscorrelation and multidimensional deconvolution in elastic media: Geophysics, **76**, SA63–SA76.
Vasconcelos, I., and R. Snieder, 2008a, Interferometry by deconvolution, Part 1 - Theory for acoustic waves and numerical examples: Geophysics, **73**, S115–S128.
———, 2008b, Interferometry by deconvolution: Part 2 - Theory for elastic waves and application to drill-bit seismic imaging: Geophysics, **73**, S129–S141.
Wapenaar, K., 2004, Retrieving the elastodynamic Green's function of an arbitrary inhomogeneous medium by cross correlation: Phys. Rev. Lett., **93**, 254–301.
Wegler, U., B.-G. Lühr, R. Snieder, and A. Ratdomopurbo, 2006, Increase of shear wave velocity before the 1998 eruption of Merapi volcano (Indonesia): Geophys. Res. Lett., **33**, L09303.
Wegler, U., and C. Sens-Schönfelder, 2007, Fault zone monitoring with passive image interferometry: Geophys. J. Int., **168**, 1029–1033.
Yamada, M., J. Mori, and S. Ohmi, 2010, Temporal changes of subsurface velocities during strong shaking as seen from seismic interferometry: J. Geophys. Res., **115**, B03302.

APPENDIX A: EIGENFUNCTIONS AND EIGENFREQUENCIES OF THE STRING MODEL

In this appendix, we derive the eigenfunctions (expression 8) and eigenfrequencies (expression 9) of the string model (Figure 6) using a perturbation analysis in the small parameter ϵ (expression 7). The normal modes of the unperturbed string ($\epsilon = 0$, $\rho_g = \infty$, and $R = -1$) are given by

$$u(z > 0) = \sin k^{(u)} z, \tag{A1}$$
$$u(z < 0) = 0, \tag{A2}$$

where $k^{(u)}$ is the unperturbed wavenumber. The parameter ϵ accounts for the coupling of the light string to the heavy string (expression 6). For the unperturbed model ($\epsilon = 0$), the string has infinite mass for $z < 0$, and hence it does not move. When $\epsilon \neq 0$, the waveforms, which include perturbed waves, are expressed by

$$u(z > 0) = \sin kz + A \cos kz, \tag{A3}$$
$$u(z < 0) = Be^{-ik_g z}, \tag{A4}$$

respectively. The coefficients A and B depend on ϵ. According to expression A4, waves are radiated downward in the lower (heavy) part of the string (the thick line in Figure 6). The ratio of the wavenumbers in the light and heavy strings (k/k_g) is given by Ch. 2 in Coulson and Jeffrey (1977):

$$k/k_g = \epsilon. \tag{A5}$$

The boundary conditions of the model are $\partial u/\partial z = 0$ at $z = H$, and u and $\partial u/\partial z$ are continuous at $z = 0$. From expressions A3 and A4 and the boundary conditions, we obtain

$$\begin{aligned} &\frac{k}{k_g} \sin kH + i \cos kH \\ =&\frac{\epsilon}{2i}(e^{ikH} - e^{-ikH}) + \frac{i}{2}(e^{ikH} + e^{-ikH}) \\ =&0, \end{aligned} \tag{A6}$$

where we use expression A5 for k/k_g. From expression A6, we obtain

$$e^{2ikH} = -\frac{1-\epsilon}{1+\epsilon}. \tag{A7}$$

Applying a first-order Taylor expansion in ϵ to the wavenumber in expression A7, we obtain the wavenumber for mode m:

$$k_m = \left\{ \pm \left(m + \frac{1}{2} \right) \pi - i\epsilon \right\} \frac{1}{H}, \tag{A8}$$

where the real and imaginary of k_m are the unperturbed and perturbed parts of the wavenumber of mode m, respectively. The perturbation of the wavenumber caused by the radiation damping ($-i\epsilon/H$) is constant for all modes. The eigenfrequency ω_m that corresponds to this wavenumber is given by expression 9.

From expressions A3 and A8, the waveform (eigenfunction) for the mode m within the light string is given by

$$\begin{aligned} u_m(z) &= \sin(k_m z) + A \cos(k_m z) \\ &= \sin(k_m z) + \frac{\cos(k_m H)}{\sin(k_m H)} \cos(k_m z) \\ &= \frac{\cos\{k_m(H - z)\}}{\sin(k_m H)}, \end{aligned} \tag{A9}$$

where we use the boundary condition $\partial u/\partial z = 0$ at $z = H$ at the second equality. Using Taylor expansions to first order in ϵ in the sine and cosine functions, we derive the eigenfunction shown in expression 8.